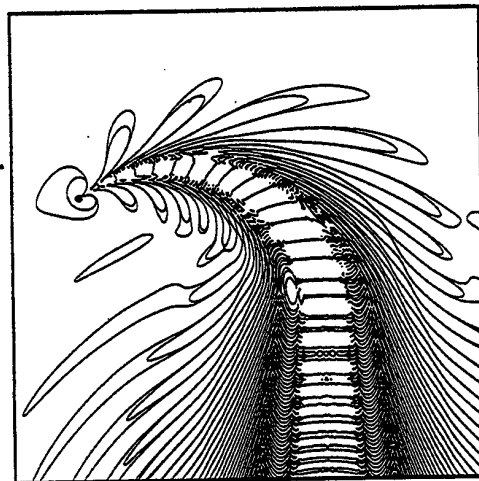


PREPRINTS OF THE PROCEEDINGS OF THE

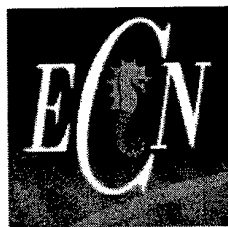
Seventh International Conference on

NUMERICAL SHIP HYDRODYNAMICS



Nantes ~ FRANCE

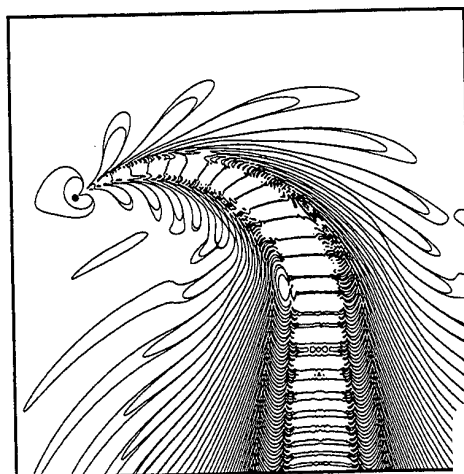
19~22 July 1999



PREPRINTS OF THE PROCEEDINGS OF THE

Seventh International Conference on

NUMERICAL SHIP HYDRODYNAMICS



U.S. Government Rights License

This work relates to Department of the Navy Grant or Contract issued by Office of Naval Research (ONR) International Field Office-Europe. The United States Government has a royalty-free license throughout the world in all copyrightable material contained herein.

Nantes ~ FRANCE

19~22 July 1999

Co-sponsored by : Chantiers de l'Atlantique

Institut de la Recherche en Constructions Navales

David Taylor Model Basin

DSA/DSP Ministère de la Défense

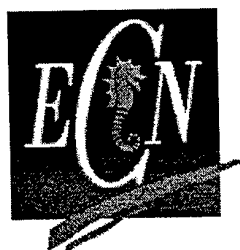
Office of Naval Research

Ministère de l'Education, de la Recherche

et de la Technologie

Ecole Centrale de Nantes

Ville de Nantes



20011130 069

AQ F02-02-0276

REPORT DOCUMENTATION PAGE

Form Approved OMB No. 0704-0188

Public reporting burden for this collection of information is estimated to average 1 hour per response, including the time for reviewing instructions, searching existing data sources, gathering and maintaining the data needed, and completing and reviewing the collection of information. Send comments regarding this burden estimate or any other aspect of this collection of information, including suggestions for reducing this burden to Washington Headquarters Services, Directorate for Information Operations and Reports, 1215 Jefferson Davis Highway, Suite 1204, Arlington, VA 22202-4302, and to the Office of Management and Budget, Paperwork Reduction Project (0704-0188), Washington, DC 20503.

1. AGENCY USE ONLY (Leave blank)		2. REPORT DATE 2001		3. REPORT TYPE AND DATES COVERED 23-26 July 2001 Final Report	
4. TITLE AND SUBTITLE International Conference on Numerical Ship Hydrodynamics (7 th). Held in Nantes, France on 19022 July 1999. Preprints of the Proceedings.				5. FUNDING NUMBERS	
6. AUTHOR(S) J. Piquet, Editor					
7. PERFORMING ORGANIZATION NAME(S) AND ADDRESS(ES)				8. PERFORMING ORGANIZATION REPORT NUMBER	
9. SPONSORING/MONITORING AGENCY NAME(S) AND ADDRESS(ES) Office of Naval Research, European Office PSC 802 Box 39 FPO AE 09499-0039				10. SPONSORING/MONITORING AGENCY REPORT NUMBER	
11. SUPPLEMENTARY NOTES This work relates to Department of the Navy Grant issued by the Office of Naval Research International Field Office. The United States has a royalty free license throughout the world in all copyrightable material contained herein.					
12a. DISTRIBUTION/AVAILABILITY STATEMENT Approved for Public Release; Distribution Unlimited. U.S. Government Rights License. All other rights reserved by the copyright holder.				12b. DISTRIBUTION CODE A	
12. ABSTRACT (Maximum 200 words) This volume gathers preprints of the Seventh International Conference on Numerical Ship Hydrodynamics (NSH&) held in Nantes, France, on 19-22 July 1999. This conference follow the previous one held in Iowa City, IA in 1993. Session topics include: panel methods, free surface viscous flows, lifting surfaces, floating bodies, wave loads & seakeeping, and ship design.					
13. SUBJECT TERMS ONR, Foreign reports, Conference proceedings, Marine engineering, Fluid dynamics				15. NUMBER OF PAGES	
				16. PRICE CODE	
17. SECURITY CLASSIFICATION OF REPORT UNCLASSIFIED	18. SECURITY CLASSIFICATION OF THIS PAGE UNCLASSIFIED	19. SECURITY CLASSIFICATION OF ABSTRACT UNCLASSIFIED	20. LIMITATION OF ABSTRACT UL		

NSN 7540-01-280-5500

Standard Form 298 (Rev. 2-89)
Prescribed by ANSI Std. Z39-18
298-102

SEVENTH INTERNATIONAL CONFERENCE ON

NUMERICAL SHIP HYDRODYNAMICS

SCIENTIFIC COMMITTEE

V. Bertram	Institut für Schiffbau, Germany
L. Doctors	University of South Wales, Australia
R. Eatock-Taylor	University of Oxford, UK
O. Faltinsen	Norw. Inst. Sci. Techn., Norway
H. Haussling	David Taylor Model Basin, USA
B. Molin	ESI Marseille, France
K. Mori	Hiroshima University, Japan
F. Noblesse (cochairman)	David Taylor Model Basin, USA
J. Piquet (chairman)	Ecole Centrale de Nantes, France
H. Raven	MARIN, The Netherlands
P. Slavounos	MIT, USA
F. Stern	IIHR, University of Iowa, USA

LOCAL ORGANIZING COMMITTEE

B. Alessandrini	Division Hydrodynamique Navale
A. Clément	Division Hydrodynamique Navale
G. Delhommeau	Division Hydrodynamique Navale
P. Ferrant	Division Hydrodynamique Navale
J. Piquet (chairman)	Division Modélisation Numérique
M. Visonneau	Division Modélisation Numérique

Proceedings Editor: J. Piquet

Editor's Preface

The present volume gathers preprints of the Seventh International Conference on Numerical Ship Hydrodynamics (NSH7), held in Nantes, France, during 19-22 July 1999. This conference follows the previous one held in Iowa City in 1993. Research in the field of numerical ship hydrodynamics is active worldwide, and altogether 62 abstracts were submitted to the conference. Each of the five-page abstracts was screened by at least three members of the Scientific Committee of NSH7. In the end, 39 preprints have been received prior to the Conference, from all over the world.

Acknowledgements are due to the sponsoring organizations for their generous financial support to the conference and this volume. We are also grateful to the members of the Scientific and Organizing Committee for their various efforts in preparing this Conference.

Nantes
July 1999

J. Piquet

TABLE OF CONTENTS

PANEL METHODS

An introductory treatise on Ship-motion Green functions.

X-B.Chen, Bureau Veritas, France..... 1.1.1-20

Fourier-Kochin extension of fully nonlinear near-field ship waves.

C.Yang¹, **R.Löhner**¹, **F.Noblesse**², **D.Hendrix**².¹ George Mason University, ²David Taylor Model Basin, USA. 1.2.1-14

A mixed source formulation for nonlinear ship motion and wave-load simulations.

W.M.Lin¹, **S.Zhang**¹, **K.Weems**¹, **D.K.P.Yue**².

¹ Science Applications International Corporation, ² Massachusetts Institute of Technology, USA..... 1.3.1-12

Accelerated, nonlinear wave simulations for large structures.

D.Kring, **T.Korsmeyer**, **J.Singer**, **D.Danmeier**, **J.White**. Massachusetts Institute of Technology, USA. 1.4.1-16

FREE-SURFACE VISCOUS FLOWS (1, 2)

Numerical simulation of ship flows in restricted water.

F.Bet, **N.Stuntz**, **D.Hänel**, **S.D.Sharma**. Mercator-Universität Duisburg, Germany. 2.1.1-10

Numerical Simulations of turbulent flows with a free surface.

R.Brogli, **A.Di Mascio**, **R.Muscari**.

Istituto Nazionale per Studi ed Esperienze di Architettura

Navale, Italy..... 2.2.1-7

Free-surface viscous flow around ship models.

A. Cura Hochbaum¹ & **C. Schumann**².

¹ Hamburg Ship Model Basin, ² Flensburger Schiffbau

Gesellschaft, Germany..... 2.3.1-12

Level set methods for predicting viscous free-surface flows.

M.Vogt, **L.Larsson**.

Chalmers University, Sweden..... 2.4.1-19

Computation of the wetted transom stern flow over model 5415.

M.Beddhu, **M-Y.Jiang**, **D.L.Whitfield**, **L.K.Taylor**.

Mississippi State University, USA..... 2.5.1-13

3D RANSE-potential coupling using a Fourier-Kochin approach.

P.E.Guillerm, B.Alessandrini.

Ecole Centrale de Nantes, France.....**2.6.1-11**

Computation of flows around hydrofoils under the free surface.

R.Azcueta¹, S.Muzaferija², M.Peric¹, S.D.Yoo¹.

¹Technical university of Hamburg-Harburg,

²ICCM,Germany.....**2.7.1-10**

PROPULSOR HYDRODYNAMICS

Unsteady RANS simulation of an integrated marine propulsor.

E.G.Patersson, J.Kim, F.Stern.

Iowa Institute of Hydraulic Research, USA**3.1.1-**

Computation of the incompressible viscous flow around a tractor thruster using a sliding mesh technique.

A.Sanchez-Caja¹, P.Rautaheimo², E.Salminen², T.Siikonen².

¹ VTT Manufacturing Technology, ² Helsinki University of Technology, Finland**3.2.1-12**

A numerical lifting surface technique for account of radial velocity component in screw-propeller design problem.

A.S.Achkinadze, V.I.Krasilnikov.

Saint Petersburg State Marine Technical University, Russia.....**3.3.1-14**

VISCOUS FLOWS (1)

Calculation of turbulent flows around VLCC hull forms with stern frameline modification.

W.-J.Kim, D.-H.Kim, S.-H.Van.

Korea Research Institute of Ships & Ocean Engineering, Korea.....**3.4.1-13**

Numerical study of flows around an array of circular cylinders at high Reynolds numbers.

S.Etienne, Y.M.Scolan, B.Molin.

Ecole Supérieure d'Ingénieurs de Marseille, France.....**3.5.1-13**

An example of error quantification of ship-related CFD results.

M.Hoekstra¹, L.Eça².

¹ Maritime Research Institute Netherlands, The Netherlands, ² University of Lisboa, Portugal.**3.6.1-20**

FREE-SURFACE VISCOUS FLOWS (3).

A CFD application to wave-induced floating-body dynamics.

T.Kinoshita, H.Kagemoto, M.Fujino.4.1.1-20
University of Tokyo, Japan.

3D free-surface flow around a ship in forced motion.

L.Gentaz, P.E. Guillerm, B.Alessandrini, G.Delhommeau.
Ecole Centrale de Nantes, France.....4.2.1-12

A finite-element method applied to unsteady viscous-flow around 2D blunt bodies with sharp corners.

R.Tonnesen, O.M.Faltinsen, T.Utno
University of Trondheim, Norway.....4.3.1-20

VISCOUS FLOWS (2) & LIFTING SURFACES (1).

Comparison of explicit algebraic stress models and second-order turbulence closures for steady flows around ships.

G.B. Deng, M.Visonneau.
Ecole Centrale de Nantes, France.....4.4.1-15

Prediction of forces and moments of rudders with flaps and tabs.

C.H.Sung, B.Rhee.
David Taylor Model Basin, USA.4.5.1-10

CFD simulation of three-dimensional motion of a vehicle with movable wings.

N.Takada¹, H.Miyata², T.Sato².
¹ Mitsubishi Heavy Industries, Ltd., ² University of Tokyo, Japan.....4.6.1-15

FLOATING BODIES, WAVE LOADS & SEAKEEPING (1)

A nonlinear 3D approach to simulate green-water dynamics on deck.

Z.Q.Zhou, J.O.DeKat, B.Buchner.
Maritime Research Institute Netherlands, The Netherlands.....5.1.1-15

Linear & non linear flows & responses of ships by a rankine panel method.

Y.W.Kim, S.Kim, D.Renick, P.Sclavounos.
Massachusetts Institute of Technology, USA.5.2.1-16

Seakeeping simulations in nonlinear waves.

P.Ferrant.

Ecole Centrale de Nantes, France.....5.3.1-

Hydroelastic analysis of two-dimensional slamming phenomena.

A.Iafrati, A. Cercaterra, E. Ciappi, E.F. Campana.

Istituto Nazionale per Studi ed Esperienze di Architettura Navale, Italy.....5.4.1-12

LIFTING SURFACES (2).

Numerical investigation on submerged downward lifting body and its optimization with low wave resistance.

S.Nagaya¹, K.H.Mori², Y.Doi².

¹ Ship Res. Institute, ² Hiroshima University, Japan.....5.5.1-10

Numerical analysis of viscous flow past a rounded leading edge of a lifting foil with use of matched asymptotics.

K.V.Rozhdestvenski, Wu-Chun-Kai.

Saint-Petersburg State Marine Technical University, Russia.....5.6.1-16

Combining numerics and asymptotics to account for the influence of the vortex roll-up upon hydrodynamic characteristics of a wing.

K.V.Rozhdestvenski, G.M.Fridman.

Saint-Petersburg State Marine Technical University, Russia.....5.7.1-11

FREE-SURFACE VISCOUS FLOWS (4).

The numerical simulation of the yaw flow of a free-surface ship.

A.Di Mascio, E.F.Campana.

Istituto Nazionale per Studi ed Esperienze di Architettura Navale, Italy.....6.1.1-10

Computation of breaking bow waves for a very full hull ship.

R.Azcueta, S.Muzaferija, M.Peric.

Technical University of Hamburg-Harburg, Germany.....6.2.1-11

Simulation of green water loading using the Navier-Stokes equations.

G.Fekken¹, A.E.P.Veldman¹, B.Buchner².

¹ University of Groningen, ² Maritime Research Institute Netherlands, The Netherlands.....6.3.1-12

FLOATING BODIES, WAVE LOADS & SEAKEEPING (2)

Linear drift-force calculations including all forward speed effects.

T.H.J.Bunnik, A.J.Hermans.

Delft University of Technology, The Netherlands.....**6.4.1-12**

Using differential properties of the Green function in seakeeping computational codes.

A.Clément.

Ecole Centrale de Nantes, France.....**6.5.1-15**

SHIP DESIGN

Shape optimization of practical ship hull forms using Navier-Stokes analysis.

T.Hino.

Ship Research Institute, Japan.....**6.6.1-15**

FRONTIER PROBLEMS IN HYDRODYNAMICS.

Unsteady flow calculations past ventilated hydrofoils.

V.N.Semenenko.

Ukraine National Academy of Science, Ukraine.**7.1.1-11**

Ship wave making over a natural topography.

X-N.Chen.

VBD-EDC for Inland and Coastal Navigation, Germany.....**7.2.1-10**

Periodic wave impact onto an elastic plate.

A.A.Korobkin & T.I.Khabakhpasheva,

Lavrentiev Institute of Hydrodynamics, Russia.....**7.3.1-19**

PANEL METHODS

Chairman : R.Beck

AN INTRODUCTORY TREATISE ON SHIP-MOTION GREEN FUNCTIONS

XIAOBO CHEN

Département Technologie Avancée

BUREAU VERITAS

17bis, Place des Reflet, 92400 Courbevoie, France

Fax: 33-1-4291.3395; E-Mail: xchen@bureauveritas.com

ABSTRACT

This paper gives a survey of newly obtained important results in both analytical and numerical aspects on ship-motion Green functions. First, new formulations of the free-surface component are developed based on the basic decomposition of the double Fourier integral and new expressions of the wavenumber integrals. The resultant wave and local components are both expressed by simple integrals. The asymptotic analysis of the wave component gives analytical expressions of far-field ship waves and reveals their direct relationship with the dispersion relation. The singular and highly-oscillatory properties of potential flows generated by a source located at the free surface are analyzed and expressed in a closed form. The analysis of the line integrals on the free surface shows that they can be evaluated in an analytical way. Finally, efficient numerical developments have been realized to evaluate accurately ship-motion Green functions in all configurations, including the most critical case for which the free-surface effects are most important as both source and field points are located at the free surface.

INTRODUCTION

The potential flow generated by a source pulsating with constant frequency and moving with constant horizontal velocity is fundamental to the analysis of the flow past a moving ship and to the prediction of its motions in waves. The time-harmonic source potentials, called as "ship-motion Green functions" including time-harmonic flows with forward speed and the special cases of Neumann-Kelvin steady flow (zero frequency) and time-harmonic flows without forward speed, play a critical role of theoretical basis due to their intrinsic properties such as proper far-field wavy behavior and radiation condition. Furthermore, the potential-flow analysis of wave diffraction-radiation by a ship or an offshore structure yields calculation methods extremely useful for many practical purposes, notably for design.

Associated with the linearized free-surface boundary condition, the ship-motion Green functions are expressed as the sum of simple (Rankine) singularities satisfying the zero-flow free-surface condition, and the double Fourier integral accounting for the free-surface effects. In the numerical analysis of practical ship-motion problems, the complexity of this double integral and its subse-

quent integration over ship hull-panels and along waterline-segments, as documented in [17], [15], [29], [19], [16], [18], [2] and other similar studies, are the major stumbling block hindering the development of reliable and practical methods.

An alternative approach based on Kochin's formulation is adopted in [23]. Within this approach, the free-surface component of potential flows associated with a distribution of singularities is directly considered as an integration of the double Fourier integral (of ship-motion Green functions associated with a point source), and evaluated by performing the space integration over the hull-panel or the waterline-segment before the Fourier integration. The free-surface potential flow associated with a distribution of singularities is called super Green functions in [7], [8] and [26], as they are given by a similar Fourier integral representation as ship-motion Green functions, which involves a spectrum function defined by the distribution of singularities. The critical advantage of the Fourier-Kochin's approach comes from the fact that the spectrum function associated with a distribution of singularities involving in super Green functions disappears for large wavenumber instead of being constant in ship-motion Green functions. This property of

the spectrum function seems to ensure that super Green functions are not singular so that the complexity of ship-motion Green functions in the limit that the field point approaches to the source point located close to or at the free surface, is avoided. Interesting results recently achieved in [30] to extend nonlinear steady ship flows obtained by using Euler near-field flow solver to the far field, demonstrate the utility of the Fourier-Kochin approach.

However, the other side of the coin is associated with other properties of the spectrum function. The spectrum function depending on the distribution of singularities can be highly oscillatory, and mathematical analyzes on the double integral are more complex. Since the double integral cannot completely be reduced to single integrals, its numerical evaluation is much more time-consuming. Furthermore, the spectrum function associated with smaller hull-panels or shorter waterline-segments decreases more slowly at large wavenumber and super Green functions (and their derivatives) tend to inherit all properties of ship-motion Green functions including their highly-oscillatory and singular behavior.

Fortunately, the recent work on decomposition of free-surface effects given in [25], new results of far-field ship waves obtained in [5], [4] and [9] and new analysis of singular and highly-oscillatory properties of ship-motion Green functions realized in [6] and [13], gives a new lease of life to the Green function approach. Indeed, all this work provides essential elements to construct a sound and solid basis to solve the ship-motion problems. One of objectives of the present paper is to give a summary of the recent work together with some *ad hoc* developments for numerical evaluation of ship-motion Green functions.

The ship-motion Green functions are analyzed in the section after this introduction. Following the analysis performed in [25], the free-surface component expressed by the double Fourier integral is decomposed into a wave component which propagates into the far field, and a local component which is only significant in the near field. This formal decomposition gives a useful expression of the wave component written as a single integral along the dispersion curves, especially in the asymptotic analysis of far-field waves. However, it does not provide suitable formulations for numerical evaluations since the local component remains to be in the form of double integral. Further analysis of the double integral generates new formulations composed by the wave and local components and a complementary term for $\tau > 1/4$. Both wave

and local components are expressed by a single integral along the dispersion curves. The integrand amplitude of wave-component integral is smooth and the integrand of local-component integral is non-oscillatory, so that the single integrals as well as that representing the complementary term are, *a priori*, well suited for numerical evaluation.

Asymptotic analysis of far-field ship waves is presented in the following section. Based on using the stationary-phase analysis of the wave-component line integral, considerable information about far-field features of ship waves is revealed. Especially, the constant-phase curve (e.g. crest-lines) and related wavelength, directions of wave propagation, cusp angles, and phase and group velocities can be determined explicitly from the dispersion function. Indeed, the direct relationship between the dispersion curves in the Fourier plane and the corresponding wave systems on the free surface is established in [4] and [5]. Furthermore, analytical expressions of far-field ship waves are obtained in [9] and summarized in the paper.

An important and complex feature of the ship-motion Green function is its rapid oscillations with singular amplitudes when a field point approaches to the track of the source point at the free surface. This peculiar behavior of the ship-motion Green function is analyzed in [6] by using the wave-component integral along the open dispersion curves. The asymptotic calculation of the integral along the portion of the open dispersion curves at large values of wavenumber yields an analytical expression which captures the behavior of highly oscillations with infinitely increasing amplitude and infinitely decreasing wavelength. The line integrals on the free surface involving the singular and highly-oscillatory terms are further analyzed. It is shown in [13] that the line integral along a contour at infinity, as expected, disappears effectively and the waterline integral can be performed in an analytical way.

In the numerical analysis of ship-motion Green functions, different treatments are needed for the wave component than the local component. The integrand of wave-component integral can be highly oscillatory so that a special algorithm based on analytical integrations after numerical approximations of the amplitude and phase functions of the integrand, is developed. It is shown that the method is effective and accurate to evaluate highly-oscillatory integrals. The integrand of the local component is not oscillatory and the classical Gauss-Legendre quadrature is efficient. However, a logarithmic singularity appears in the integrand

when both the field and source points approach to (or are located at) the free surface. Some technique including integration by part is used to eliminate the difficulty. Finally for illustrations, both wave and local components of the ring waves associated with the closed dispersion curve, and those of the inner-V and outer-V waves associated with the right and left open dispersion curves are presented.

Conclusions are addressed in the end of the paper. Although it remains still some important work in implementing the results of the study to panels codes, we have never been so optimistic to achieve a fully satisfactory solution to ship-motion problems. This paper is then expected to be the beginning of a happy end of this long march.

SHIP-MOTION GREEN FUNCTIONS

The reference system moving with the ship at the mean forward speed U along the positive x -axis, is defined by letting (x, y) plane coincide with the mean free surface and z -axis be positive upward. The velocity potential of the flow generated at a field point $\xi = (\xi, \eta, \zeta)$ by a source of unit strength located at the point $\bar{x}_s = (x_s, y_s, z_s)$ is expressed by

$$G = G^S + G^F$$

Here G^S is the simple singularity component

$$4\pi G^S = -1/r + 1/r'$$

with r and r' the distances between the field point ξ and the source point \bar{x}_s , and between ξ and the mirror image of \bar{x}_s with respect to the mean free surface plane $z = 0$, respectively. The free-surface component G^F is defined by the Fourier superposition of elementary waves, according to [25]

$$4\pi^2 G^F = \lim_{\epsilon \rightarrow 0^+} \int_{-\infty}^{\infty} d\beta \int_{-\infty}^{\infty} d\alpha \frac{e^{kz-i(\alpha x+\beta y)}}{D + i\epsilon \text{sign}(D_f)} \quad (1)$$

where $k = \sqrt{\alpha^2 + \beta^2}$ is the wavenumber and

$$(x, y, z \leq 0) = (\xi - x_s, \eta - y_s, \zeta + z_s)$$

D in (1) is the dispersion function

$$D = (F\alpha - f)^2 - k^2 \quad (2)$$

and $\text{sign}(D_f) = \text{sign}(\partial D / \partial f)$ is given by

$$\text{sign}(D_f) = -\text{sign}(F\alpha - f)$$

The dispersion function (2) is associated with the classical free-surface boundary condition linearized about the uniform stream opposing the forward

speed of the ship. The nondimensional frequency f , the Froude number F , and the Brard number τ are defined as

$$f = \omega \sqrt{L/g} \quad F = U / \sqrt{gL} \quad \tau = Ff = U\omega/g$$

where ω is the encounter frequency of the regular ambient waves exciting the ship motions, L and g are the ship length and the acceleration of gravity.

Decomposition of free-surface component

The free-surface component G^F defined by (1) is now considered. Following the analysis in [25], G^F can be expressed in the basic form

$$G^F = G_1^F + G_2^F \quad (3a)$$

with a single integral

$$4\pi i G_1^F = \sum_{D=0} \int_{D=0} ds \text{sign}(D_f) \frac{e^{kz-i(\alpha x+\beta y)}}{|\nabla D|} \quad (3b)$$

where $\sum_{D=0}$ means summation over all the dispersion curves defined by the dispersion relation $D=0$, and a double integral

$$4\pi^2 G_2^F = \int_{-\infty}^{\infty} d\beta \int_{-\infty}^{\infty} d\alpha \frac{e^{kz-i(\alpha x+\beta y)}}{D} \quad (3c)$$

Furthermore, the double integral G_2^F can be decomposed into two components

$$G_2^F = G_2^W + G^N \quad (4a)$$

with $4\pi i G_2^W =$

$$\sum_{D=0} \int_{D=0} ds \text{sign}(xD_\alpha + yD_\beta) \frac{e^{kz-i(\alpha x+\beta y)}}{|\nabla D|} \quad (4b)$$

and $4\pi^2 G^N =$

$$\lim_{\epsilon \rightarrow 0^+} \int_{-\infty}^{\infty} d\beta \int_{-\infty}^{\infty} d\alpha \frac{e^{kz-i(\alpha x+\beta y)}}{D - i\epsilon \text{sign}(xD_\alpha + yD_\beta)} \quad (4c)$$

In (3b), (4b) and (4c), the notations $|\nabla D|^2 = D_\alpha^2 + D_\beta^2$ with $D_\alpha = \partial D / \partial \alpha$ and $D_\beta = \partial D / \partial \beta$ are used. The two single integrals (3b) and (4b) can be regrouped as $G^W = G_1^F + G_2^W$ then

$$G^F = G^W + G^N$$

where

$$4\pi i G^W = \sum_{D=0} \int_{D=0} ds (\Sigma_1 + \Sigma_2) \frac{e^{kz-i(\alpha x+\beta y)}}{|\nabla D|} \quad (4d)$$

with $\Sigma_1 = \text{sign}(D_f)$ and $\Sigma_2 = (xD_\alpha + yD_\beta)$, is called wave component as it can be shown that $G^F \approx G^W$

in the far field $x^2 + y^2 \rightarrow \infty$ while G^N given by the double integral (4c) is non-oscillatory and only significant in the near field, and then called near-field component or local component.

The single integral (4d) is very useful in the asymptotic analysis of far-field ship waves as presented in [4], [5] and [9]. However, the local component G^N defined by the double integral (4c) remains rudimental and not suited for its numerical evaluation since the integrand is singular across the dispersion curves. A further step realized in [7] and [8], and summarized in [26] gives several decompositions of free-surface effects into wave and local components according to different shapes of dispersion curves. The integrand-amplitude of both components is smooth across the dispersion curves so that the formulations developed in [7] and [8] can be used for numerical calculations. Nevertheless, the local component keeps its form of double integral. The numerical evaluation of oscillatory integrals on the Fourier plane (even with a smooth and decreasing amplitude) is extremely time-consuming from author's experience.

New formulations of ship-motion GF

A new analysis has been performed by starting with (3c) in which we use the remarkable identity derived from (2)

$$D = (F \cos \theta)^2 (k - k^+) (k - k^-) \quad (5a)$$

with $k^\pm(\theta)$ given by

$$k^\pm = (1/2 \pm \sqrt{1/4 + \tau \cos \theta})^2 / (F \cos \theta)^2 \quad (5b)$$

Changing integral variables (α, β) to (k, θ) and using $d\alpha d\beta = k d\theta dk$, (3c) becomes

$$4\pi^2 G_2^F = \int_0^{2\pi} \frac{d\theta}{2\sqrt{1/4 + \tau \cos \theta}} (k^+ \mathcal{K}^+ - k^- \mathcal{K}^-) \quad (6)$$

with the wavenumber integral

$$\mathcal{K}^\pm = \int_0^\infty \frac{e^{k[z - ih \cos(\theta - \gamma)]}}{k - k^\pm} dk \quad (7a)$$

where $h^2 = (x^2 + y^2)$ and $\tan \gamma = y/x$.

For a real $k^\pm > 0$, the integrand of (7a) is singular at $k = k^\pm$ and the wavenumber integral can be written as the sum

$$\mathcal{K}^\pm = \mathcal{W}^\pm + \mathcal{N}^\pm \quad (7b)$$

with the singular term defined by

$$\begin{aligned} \mathcal{W}^\pm &= e^{k^\pm z} \int_{-\infty}^\infty \frac{e^{-(k - k^\pm)^2/4 - ikh \cos(\theta - \gamma)}}{k - k^\pm} dk \\ &= -i\pi \Sigma_2 \operatorname{erf}[k^\pm h] e^{k^\pm(z - ih)} \end{aligned} \quad (7c)$$

with

$$\Sigma_2 = \operatorname{sign}[\cos(\theta - \gamma)] \quad \text{and} \quad h = h \cos(\theta - \gamma) \quad (7d)$$

Furthermore, $\operatorname{erf}(\cdot)$ is the error function defined in [1]. The lower limit of the integral in (7c) is extended to $-\infty$ in order to obtain the analytical expression of \mathcal{W}^\pm . The regular term \mathcal{N}^\pm is defined by the difference between \mathcal{K}^\pm and \mathcal{W}^\pm , given also in a closed form

$$\begin{aligned} \mathcal{N}^\pm &= \mathcal{K}^\pm - \mathcal{W}^\pm = \\ &\operatorname{Cex}[k^\pm(z - ih)] - i\pi \Sigma_2 \operatorname{erfc}[k^\pm h] e^{k^\pm(z - ih)} \end{aligned} \quad (7e)$$

with $\operatorname{erfc}(\cdot)$ the complementary error function and the complex exponential-integral function

$$\operatorname{Cex}(w) = \int_0^\infty \frac{e^{-t}}{t + w} dt = e^w E_1(w) \quad (7f)$$

where $E_1(\cdot)$ is the exponential integral function defined in [1]. It can be shown that \mathcal{N}^\pm is a non-oscillatory function.

Introducing the expression (7b) of \mathcal{K}^\pm into (6), the double integral G_2^F is reduced to the sum of two single integrals and written as $G_2^F = G_2^W + G^N$ with

$$4\pi i G_2^W = \int_0^{2\pi} \frac{k^+ \mathcal{W}^+ - k^- \mathcal{W}^-}{2\sqrt{1/4 + \tau \cos \theta}} d\theta \quad (8a)$$

and

$$4\pi^2 G^N = \int_0^{2\pi} \frac{k^+ \mathcal{N}^+ - k^- \mathcal{N}^-}{2\sqrt{1/4 + \tau \cos \theta}} d\theta \quad (8b)$$

in which the functions \mathcal{W}^\pm and \mathcal{N}^\pm are given in the closed forms (7c) and (7e), respectively.

From the identity (5a), $k = k^\pm$ represents the dispersion curves $D = 0$. In fact, $k = k^+$ describes two open dispersion curves located in the right-half Fourier plane ($-\pi/2 < \theta < \pi/2$) and in the left-half ($\pi/2 < \theta < 3\pi/2$) while $k = k^-$ represents the closed dispersion curve ($0 \leq \theta \leq 2\pi$) around the origin of the Fourier plane, as shown by Fig.1 later on.

The integral (8a) in polar angle can be transformed into a simple integral along the dispersion curve :

$$\begin{aligned} 4\pi i G_2^W &= \\ \sum_{D=0} \int_{D=0} ds \Sigma_2^\pm \operatorname{erf}[\alpha x + \beta y] \frac{e^{kz - i(\alpha x + \beta y)}}{\|\nabla D\|} \end{aligned} \quad (9a)$$

by using the identity

$$\frac{k d\theta}{2\sqrt{1/4 + \tau \cos \theta}} = \frac{k d\theta}{|D_k|} = \frac{ds}{\|\nabla D\|}$$

along the open dispersion curves $k = k^+$ and the closed dispersion curve $k = k^-$. From the expressions (7c) for \mathcal{W}^\pm and (7d) for Σ_2 , the sign function Σ_2^\pm in (9a) is given

$$\Sigma_2^\pm = \pm \text{sign}(\alpha x + \beta y) \quad (9b)$$

along the dispersion curves $k = k^\pm$, respectively.

Regrouping G_1^F given by (3b) and G_2^W by (9a) yields the new formulation for the wave component of ship-motion Green functions

$$4\pi i G^W = \quad (10a)$$

$$\sum_{D=0} \int_{D=0} ds (\Sigma_1 + \Sigma_2^\pm \text{erf}|\alpha x + \beta y|) \frac{e^{kz - i(\alpha x + \beta y)}}{\|\nabla D\|}$$

In the same way, the local component can be expressed by the single integral

$$4\pi^2 G^N = \sum_{D=0} \int_{D=0} ds \frac{\pm \mathcal{N}(kz, \alpha x + \beta y)}{\|\nabla D\|} \quad (10b)$$

involving the non-oscillatory function $\mathcal{N} = \mathcal{N}^\pm$ given by (7e) along the dispersion curves $k = k^\pm$.

The expressions (10a) for the wave component G^W and (10b) for the local component G^N of free-surface ship-motion Green functions are both in a form of single integral. The amplitude of integrand of (10a) is a smooth function and the integrand of (10b) a non-oscillatory function. They are not only adapted to further analysis but also well suited for their numerical evaluations as the special functions including the exponential integral and error functions in (10a) and (10b) can be calculated in an efficient way. Indeed, they are relevant for the further analysis of G^W and G^N and their numerical evaluation as demonstrated in the later part of the paper.

Complementary term for $\tau > 1/4$

The formulations (10a) and (10b) of ship-motion Green functions are valid as far as the values of $k^\pm(\theta)$ are real and positive in a region $\theta_1 \leq \theta \leq \theta_2$. When τ is less than $1/4$, we have $\theta_1 = 0$ and $\theta_2 = 2\pi$ so that $G^F = G^W + G^N$ is complete.

For $\tau > 1/4$, there exists a positive value

$$\theta_c = \arctan \sqrt{16\tau^2 - 1} \quad (11)$$

In the region $\pi - \theta_c < \theta < \pi + \theta_c$, the values of k^\pm are complex and written as $k^\pm = k_R \pm ik_I$ with

$$k_R = (1/2 + \tau \cos \theta) / (F \cos \theta)^2$$

$$k_I = \sqrt{-(1/4 + \tau \cos \theta)} / (F \cos \theta)^2$$

G_2^F given by (6) is then divided into two parts. The part corresponding to the integral in the region of θ from $-\pi + \theta_c$ to $\pi - \theta_c$ can be evaluated in the same way as that expressed by (7a) to (9b) since the values of k^\pm are real and positive. The same expressions as (10a) and (10b) are obtained for the free-surface component.

The complementary term G^C of G_2^F arises from integration in the region of θ from $\pi - \theta_c$ to $\pi + \theta_c$, and is given after some arrangements

$$4\pi^2 G^C = \int_{\pi - \theta_c}^{\pi + \theta_c} \frac{\mathcal{K}_C(\theta)}{(F \cos \theta)^2} d\theta \quad (12a)$$

with the wavenumber integral

$$\mathcal{K}_C = \int_0^\infty \frac{k e^{k[z - ih \cos(\theta - \gamma)]}}{(k - k_R)^2 + k_I^2} dk$$

which can be expressed in a closed form

$$2ik_I \mathcal{K}_C = \text{Cex}(Z^+) - \text{Cex}(Z^-) \quad (12b)$$

$$+ i\pi e^{Z^+} [1 + \text{sign}(\Im_m Z^+)] H(-\Re_e Z^+)$$

$$+ i\pi e^{Z^-} [1 - \text{sign}(\Im_m Z^-)] H(-\Re_e Z^-)$$

where \Re_e and \Im_m mean to take respectively the real part and imaginary part, and the unit step function $H(t)$ is equal to 0 for $t \leq 0$ or equal to 1 for $t > 0$. Furthermore, Z^\pm in (12b) are defined

$$Z^\pm = (k_R \pm ik_I)[z - ih \cos(\theta - \gamma)]$$

Therefore, the ship-motion Green functions can now be expressed by the sum of the wave component G^W , the local component G^N and the complementary term G^C for $\tau > 1/4$

$$G^F = G^W + G^N + H(\tau - 1/4) G^C \quad (13)$$

The wave component G^W and the local component G^N are given respectively by (10a) and (10b) in the form of single integral along the dispersion curves, involving the error function, and the exponential integral function and complementary error function in (7e) to define the non-oscillatory function \mathcal{N} . The complementary term G^C is also given by the single integral (12a) involving the wavenumber integral expressed by a closed form (12b) in which the complex exponential-integral function appears.

FAR-FIELD SHIP WAVES

The far-field ship waves are now considered. The single integral (4d) of the wave component is used without loss of generality as the extension to any

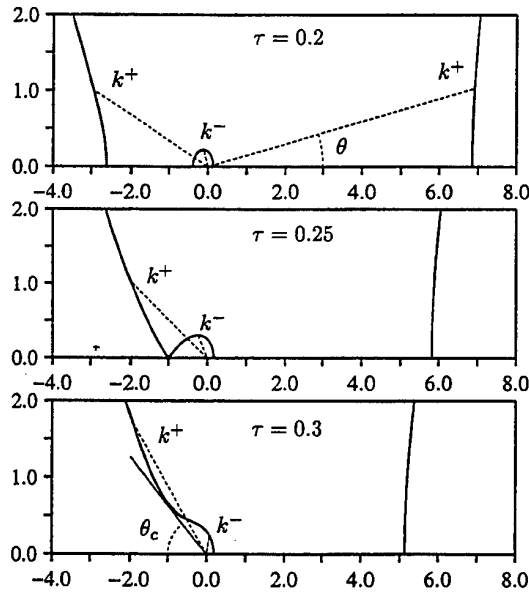
other form like (10a) of simple integral along the dispersion curves is straightforward.

From the expression (2) of the dispersion function, the dispersion relation $D = 0$ defines several dispersion curves which are symmetric with respect to $\beta = 0$ so that only those in the upper half $\beta \geq 0$ of the Fourier plane is now considered. As foregoing analysis, $k = k^\pm$ with $k^\pm(\theta)$ given by (5b) represents two types of dispersion curves : open dispersion curves $k = k^+$ and closed dispersion curve $k = k^-$. In fact, there exist three dispersion curves for $\tau < 1/4$ which intersect the axis $\beta = 0$ at four values of α , which are denoted α_i^\pm and α_o^\pm , and given by

$$\begin{aligned} F^2 \alpha_i^\pm &= \tau \pm (1/2 - \sqrt{1/4 \pm \tau}) \\ F^2 \alpha_o^\pm &= \tau \pm (1/2 + \sqrt{1/4 \pm \tau}) \end{aligned} \quad (14)$$

such that two open dispersion curves are located in the regions $-\infty < \alpha \leq \alpha_o^-$ corresponding to $k = k^+(\theta)$ within $\pi/2 < \theta \leq \pi$ and $\alpha_o^+ \leq \alpha < \infty$ corresponding to $k = k^+(\theta)$ within $0 \leq \theta < \pi/2$, and a closed dispersion curve in the region $\alpha_i^- \leq \alpha \leq \alpha_i^+$ corresponding to $k = k^-(\theta)$ within $0 \leq \theta \leq \pi$.

Fig.1: Dispersion curves in (α, β) or (k, θ) plane



At the special value of $\tau = 1/4$, $\alpha_o^- = \alpha_i^-$ from (14) so that the dispersion curves in the region $-\infty < \alpha \leq \alpha_o^-$ and $\alpha_i^- \leq \alpha \leq \alpha_i^+$ are connected.

For $\tau > 1/4$, we have one open dispersion curve located in the left region $-\infty < \alpha \leq \alpha_i^+$ corresponding to $k = k^+(\theta)$ within $\pi/2 < \theta \leq \pi - \theta_c$ where θ_c is defined by (11), connecting with $k = k^-(\theta)$ within $0 \leq \theta \leq \pi - \theta_c$ at $\theta = \pi - \theta_c$, and another open dispersion curve located in the right region $\alpha_o^+ \leq \alpha < \infty$ corresponding to $k = k^+(\theta)$ within $0 \leq \theta < \pi/2$.

Therefore, four distinct dispersion curves exist : the right open dispersion curve for $F > 0$, the left open dispersion curve for $\tau < 1/4$, the close dispersion curve for $\tau < 1/4$ and the left open dispersion curve for $\tau > 1/4$, associated with which four corresponding wave systems are baptized in [24] as : inner-V waves, outer-V waves, ring waves and ring-fan waves, respectively. The four dispersion curves may be further classified into two types : a closed dispersion curve for $\tau < 1/4$ and two open dispersion curves for $F > 0$. They are depicted for $\tau = 0.2, 0.25$ and 0.3 in Fig.1 where the Fourier plane is scaled with respect to f/F .

Dispersion relation and far-field waves

According to (4d), the wave component associated with one of dispersion curves can be written

$$4\pi i G^W = \int_{D=0} ds (\Sigma_1 + \Sigma_2) A e^{-ih\varphi} \quad (15)$$

with $\Sigma_1 = \text{sign}(D_f)$, $\Sigma_2 = \text{sign}(xD_\alpha + yD_\beta)$ and $h^2 = x^2 + y^2$ as already used, $A = e^{kz}/\|\nabla D\|$ and the phase function $\varphi = \alpha\bar{x} + \beta\bar{y}$ with

$$(\bar{x}, \bar{y}) = (x, y)/h = (\cos \gamma, \sin \gamma)$$

Both (\bar{x}, \bar{y}) and $(\cos \gamma, \sin \gamma)$ are used in the following analysis.

The far-field features of G^W are determined by the stationary points of the phase function φ along the dispersion curves which are defined by $\varphi' = \bar{x}\alpha' + \bar{y}\beta' = 0$ and satisfy

$$\bar{x}D_\beta - \bar{y}D_\alpha = 0 = h\|\nabla D\| \sin(\vartheta - \gamma) \quad (16a)$$

Here ϑ is defined by $(\cos \vartheta, \sin \vartheta) = (D_\alpha, D_\beta)/\|\nabla D\|$ and thus represents the angle between the unit vector normal to a dispersion curve and the α -axis. The wavelength of the waves corresponding to a stationary point (16a) is given by $\lambda = 2\pi/k$ where k is the wavenumber at the stationary point.

Expression (16a) shows that a point of stationary phase on a given dispersion curve is defined by $\vartheta = \gamma$ or $\vartheta = \gamma + \pi$. Thus, a point of a dispersion curve generates waves in the physical space in a direction normal to the dispersion curve. The sign function $\text{sign}(xD_\alpha + yD_\beta)$ in (15) is equal to 1 if $\vartheta = \gamma$ or -1 if $\vartheta = \gamma + \pi$. Expression (4d) therefore indicates that a point of a dispersion curve generates waves in the direction of the normal vector $\|\nabla D\|$ to the dispersion curve if $\text{sign}(D_f) = 1$, or in the opposite direction if $\text{sign}(D_f) = -1$. Furthermore, at the stationary point $\varphi' = 0$, the second derivative of the phase function is expressed as :

$$\varphi'' = c\sqrt{\alpha'^2 + \beta'^2}(\alpha' \cos \gamma - \beta' \sin \gamma)/\sin 2\gamma \quad (16b)$$

where α' and β' are differentiation of α and β with respect to the integral variable along the dispersion curves, and the curvature c is given by :

$$c = (2D_\alpha D_\beta D_{\alpha\beta} - D_\alpha^2 D_{\beta\beta} - D_\beta^2 D_{\alpha\alpha}) / \|\nabla D\|^3$$

As other terms in the expression (16b) cannot be zero, $\varphi'' = 0$ occurs only at the point of inflection where $c = 0$. Using (2) in above expression, the wavenumber at the inflection point is determined by the relation

$$F^4 k_c^2 - (3/2)F^2 k_c + \Sigma_1 4\tau F \sqrt{k_c} - 3\tau^2 = 0 \quad (16c)$$

Two points on both sides of the inflection point may have the same unit normal and then two groups of waves may propagate in the same direction but with different wavenumber. In fact, an inflection point (α_c, β_c) of a dispersion curve, determined by $c = 0$, defines a cusp line along which two distinct wave systems are found with a unique wavelength $\lambda_c = 2\pi/k_c$ and the corresponding angle ϑ_c is defined by

$$\vartheta_c = \arctan(D_\beta/D_\alpha)_c \quad (16d)$$

where the subscript c indicates evaluation at the inflection point (α_c, β_c) .

Tab.1: Cusp angles of wave systems

Wave system	τ	$F^2 k_c$	$\tan \gamma_c$	γ_c
Inner-V waves	0	3/2	$\sqrt{1/8}$	19°28'
	1/4	9/4	$\sqrt{2/25}$	15°48'
Outer-V waves	0	3/2	$\sqrt{1/8}$	19°28'
	1/4	1/4	$\sqrt{2}$	54°44'
Ring-fan waves	1/4	1/4	$-\sqrt{2}$	125°16'
	$\sqrt{2/27}$	1/6	∞	90°00'
	$\sqrt{1/2}$	1/2	$\sqrt{1/2}$	35°26'
	$\sqrt{8/3}$	3/2	$\sqrt{1/8}$	19°28'

The cusp angle defined as the angle between cusp line and the track of the source point is obtained by using (2) and (16c)

$$\gamma_c = \pi - \vartheta_c = \arctan \sqrt{1/(6F^2 k_c - 1)} \quad (17a)$$

for both inner-V and outer-V waves, and for the ring-fan waves at $\tau > \sqrt{2/27}$, and

$$\gamma_c = \pi - \arctan \sqrt{1/(6F^2 k_c - 1)} \quad (17b)$$

for the ring-fan waves in $1/4 < \tau \leq \sqrt{2/27}$. In fact, $\gamma_c = \pi/2$ at $\tau = \sqrt{2/27}$, i.e. strictly no waves

propagate upstream for $\tau \geq \sqrt{2/27}$, an interesting exact result found in [4]. Another interesting value of τ is $\sqrt{8/3}$ at which the unsteady waves (ring-fan waves plus inner-V waves) are contained within the wedges of steady waves. Approximate values of $\tau = \sqrt{2/27} \approx 0.27$ and $\tau = \sqrt{8/3} \approx 1.63$ can also be found in [21]. Other values of cusp angle with respect to τ are given in Tab.1 for inner-V waves, outer-V waves and ring-fan waves.

The curves along which the phase φ is constant, equal to $C_n^\pm = \pm 2\pi - \text{sign}(\varphi'')\pi/4$, are given by

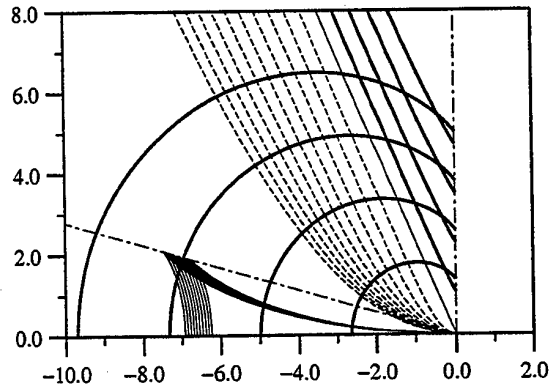
$$(x, y) = C_n^\pm (D_\alpha, D_\beta) / (\alpha D_\alpha + \beta D_\beta) \quad (18a)$$

with a supplementary condition

$$\text{sign}(C_n^\pm) = \Sigma_1 \text{sign}(\alpha D_\alpha + \beta D_\beta) \quad (18b)$$

The formulations (18a) and (18b) are applied to the inner-V waves associated with the right open dispersion curve and the ring-fan waves associated with the left open dispersion curve at the value of $\tau = \sqrt{2/27}$. The constant-phase curves (crest lines) are depicted by Fig.2 hereafter.

Fig.2: Crestlines of wave systems at $\tau = \sqrt{2/27}$



Curves of constant phase corresponding to other values of τ are depicted in detail in [4] and can be found in [7] for typical values of $\tau = 0.24$ and 0.26 .

Following Lighthill's work [21], the wave phase and group velocities are considered now. The phase velocity \vec{v}^f , determined by the stationary-phase relation (16a), is given by

$$\vec{v}^f = -(\alpha, \beta) f / k^2 \quad (19a)$$

which is orthogonal to constant-phase curves (18a) and different, both in magnitude and in direction, from the group velocity \vec{v}^g , at which wave energy is transported, defined by

$$\vec{v}^g = -(\partial f / \partial \alpha, \partial f / \partial \beta) = (D_\alpha, D_\beta) / D_f \quad (19b)$$

Fig.3: Right open dispersion curve and inner-V waves ($F' > 0$)

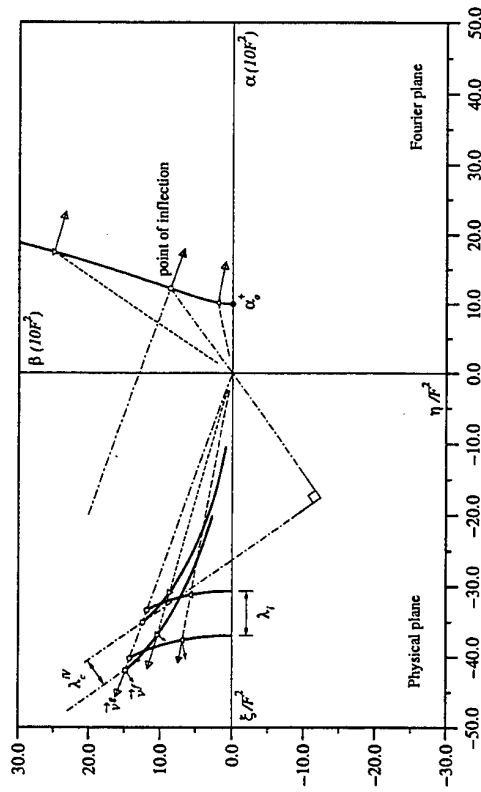


Fig.4: Left open dispersion curve and outer-V waves ($\tau < 1/4$)

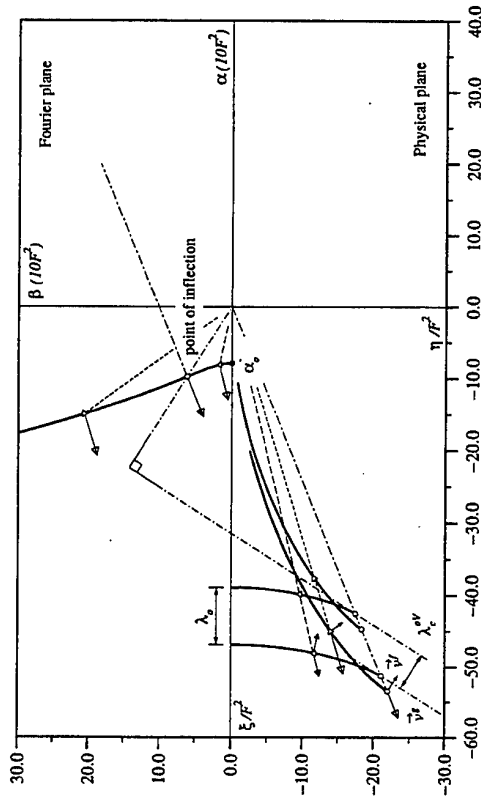


Fig.5: Closed dispersion curve and ring waves ($\tau < 1/4$)

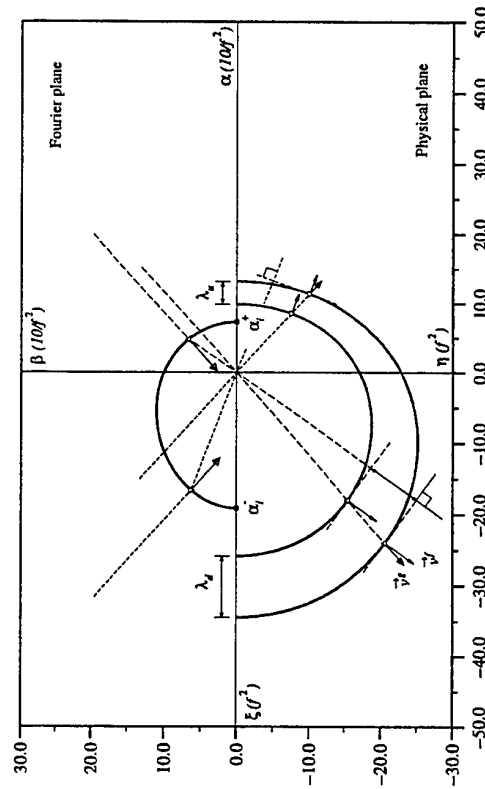
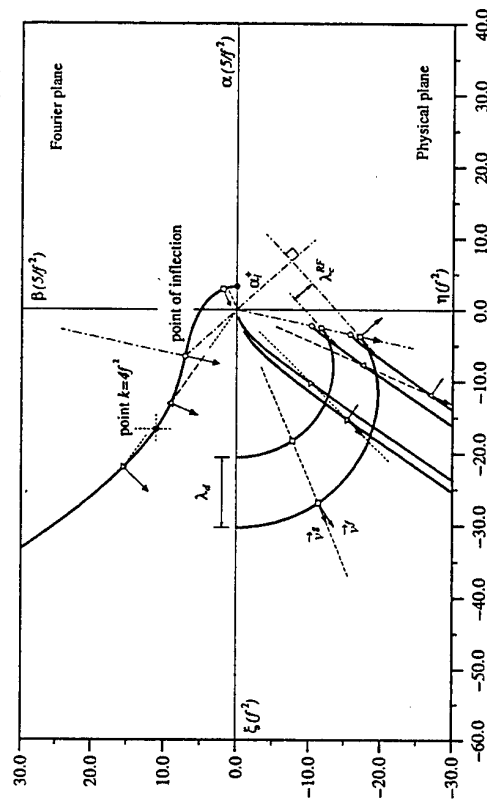


Fig.6: Left open dispersion curve and ring-fan waves ($\tau > 1/4$)



Expressions (19b) and (18a) together with condition (18b) yield $(x, y) \cdot \vec{v}^g > 0$, which shows that wave energy is propagated away from a wave generator in accordance with the radiation condition. Using (2), the group velocity (19b) is written as

$$\vec{v}^g = -[F + \Sigma_1 \alpha / (2k^{3/2}), \Sigma_1 \beta / (2k^{3/2})] \quad (19c)$$

in the system of coordinates moving with the mean forward motion of the ship, and

$$\vec{V}^g = \vec{v}^g + (F, 0) = -\Sigma_1(\alpha, \beta) / (2k^{3/2}) \quad (19d)$$

in the absolute system of coordinates. The absolute velocity \vec{V}^g (19d) is orthogonal to the constant-phase curves, whereas the relative velocity \vec{v}^g (19c) is not.

The foregoing simple analytical relationships between the dispersion curves in the Fourier plane and important features of the corresponding far-field waves in the physical plane are illustrated in Fig.3 for the inner-V waves, Fig.4 for the outer-V waves, Fig.5 for the ring waves and Fig.6 for the ring-fan waves.

Analytical expressions of far-field waves

Analytical expressions of ship wave patterns associated with these two types of distinct dispersion curve are presented in [9] and summarized now.

The ring waves are associated with the closed dispersion curve comprised between α_i^- and α_i^+ for $\tau < 1/4$. The dispersion curve is described by a parametric equation

$$(\alpha, \beta) = k(\cos \theta, \sin \theta)$$

$$\text{with } k = k^- / f^2 = (1/2 + \sqrt{1/4 + \tau \cos \theta})^{-2} \quad (20)$$

in which the variables (α, β, k) are understood to be scaled with respect to f^2 (multiplied by $1/f^2$). The stationary point $(\alpha_r, \beta_r) = k_r(\cos \theta_r, \sin \theta_r)$ satisfying $\varphi' = 0$ is determined by

$$\begin{aligned} \bar{x}\beta_r - \bar{y}(\alpha_r + 2\tau k_r^{3/2}) &= 0 \\ \bar{y}\beta_r + \bar{x}(\alpha_r + 2\tau k_r^{3/2}) &< 0 \end{aligned} \quad (21)$$

At the stationary point $\theta = \theta_r$, we define

$$\begin{aligned} \varphi_0^r &= \alpha_r \cos \gamma + \beta_r \sin \gamma \\ \varphi_2^r &= \varphi_0^r [k_r'' / k_r - 2(k_r' / k_r)^2 - 1] / 2 \\ \varphi_3^r &= \varphi_0^r [(k_r''' - 3k_r' k_r'' / k_r - 2k_r') / (3k_r)] \end{aligned}$$

where $k' = dk/d\theta$, $k'' = d^2k/d\theta^2$ and $k''' = d^3k/d\theta^3$ are used. The analytical expression obtained from asymptotic analysis for the ring waves is written as

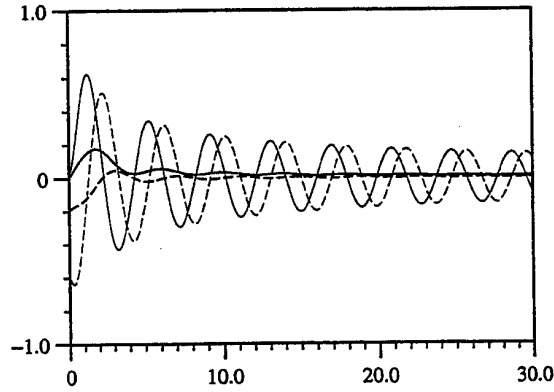
$$G^R = A_0^r \exp(-ih\varphi_0^r) / \sqrt{(\varphi_3^r / \varphi_2^r)^4 + ih\varphi_2^r} \quad (22)$$

$$\text{with } (\sqrt{4\pi}/f^2) A_0^r = ie^{z k_r} k_r^{3/2} / (2 - \sqrt{k_r})$$

which is of order $O(h^{-1/2})$ for $h \rightarrow \infty$ consistent with the classical result. The fact that the analytical expression (22) has finite values at $h \rightarrow 0$ as far as $|\varphi_3^r / \varphi_2^r| \neq 0$, is expected so that it is well suited for numerical evaluations in the near field.

The analytical expression (22) is used to evaluate ring waves for $f = 1$ and $\tau = 0.2$ along a line $\gamma = \pi/4$ (upstream) within $0 \leq hf^2 \leq 30$ on the free surface $z = 0$. The real and imaginary parts of G^R are depicted with thin solid and dashed lines in Fig.7, respectively. The difference between (22) and the line integral (10a) is shown in the figure by the thick solid and dashed lines for the real and imaginary parts.

Fig.7: Approximation of ring waves at $\tau = 0.2$



It can be seen on above figure that the thick lines are close to the zero line rapidly so that (22) is indeed a good approximation of (10a).

Three other wave systems associated with open dispersion curves as defined in [24] are the inner-V waves corresponding to the right one located in $\alpha_o^+ \leq \alpha < \infty$ for $F \geq 0$, the outer-V waves related to left open dispersion curve located in $-\infty < \alpha \leq \alpha_o^-$ for $\tau < 1/4$ and the ring-fan waves associated with left open dispersion curve located in $-\infty < \alpha \leq \alpha_i^+$ for $\tau > 1/4$. All open dispersion curves can be described by a unique parameter equation as

$$\alpha(u) = \tau - \Sigma_1 \sqrt{k}, \quad \beta(u) = \sqrt{k^2 - \alpha^2} \quad (23)$$

with

$$k = k_0(1 + u^2)$$

for $0 \leq u < \infty$, in which the Fourier variables (α, β, k) are understood to be scaled with respect to $1/F^2$ (multiplied by the Froude-scale factor F^2). Furthermore, $\Sigma_1 = -1$ and $k_0 = F^2 \alpha_o^+$ for the

inner-V waves, $\Sigma_1 = 1$ for both outer-V and ring-fan waves while $k_0 = -F^2 \alpha_c^-$ for the outer-V waves and $k_0 = F^2 \alpha_c^+$ for the ring-fan waves.

The open dispersion curve described by (23) has an inflection point at $u = u_c$ (i.e. $k = k_c$) determined by (16c). The cusp angle with respect to the track of the source point is then determined by (17a) and (17b).

Following the analysis given in [5], there exist two points of stationary phase for $\gamma = \arctan \bar{y}/(-\bar{x}) < \gamma_c$ at $u = u_t$ located in $[0, u_c]$ and $u = u_d$ in $[u_c, \infty)$ which are determined by

$$\begin{aligned} \bar{x} \beta_{t,d} - \bar{y}(\alpha_{t,d} + \Sigma_1 2k_{t,d}^{3/2}) &= 0 \\ \text{sign}[\bar{y} \beta_{t,d} + \bar{x}(\alpha_{t,d} + \Sigma_1 2k_{t,d}^{3/2})] &= -\Sigma_1 \end{aligned} \quad (24)$$

with $(\alpha_{t,d}, \beta_{t,d}, k_{t,d}) = [\alpha(u_{t,d}), \beta(u_{t,d}), k(u_{t,d})]$. At the stationary points $u = u_{t,d}$, we define

$$\begin{aligned} \varphi_0^{t,d} &= \alpha_{t,d} \cos \gamma + \beta_{t,d} \sin \gamma \\ \varphi_2^{t,d} &= (\alpha_{t,d}'' \cos \gamma + \beta_{t,d}'' \sin \gamma) / 2 \\ \varphi_3^{t,d} &= (\alpha_{t,d}''' \cos \gamma + \beta_{t,d}''' \sin \gamma) / 3 \end{aligned}$$

where $(\alpha'', \beta'') = (d^2 \alpha / du^2, d^2 \beta / du^2)$ and $(\alpha''', \beta''') = (d^3 \alpha / du^3, d^3 \beta / du^3)$ are used. Corresponding to the stationary points (α_t, β_t, k_t) and (α_d, β_d, k_d) , the transverse waves \mathcal{G}^T and divergent waves \mathcal{G}^D are defined respectively. The analytical expressions for both transverse and divergent waves are written

$$\begin{aligned} \mathcal{G}^T &= A_0^t \exp(-ih\varphi_0^t) (\mathcal{G}_{\frac{1}{2}}^T + \mathcal{G}_{\frac{1}{3}}^T) \\ \mathcal{G}^D &= A_0^d \exp(-ih\varphi_0^d) (\mathcal{G}_{\frac{1}{2}}^D + \mathcal{G}_{\frac{1}{3}}^D) \end{aligned} \quad (25a)$$

where $\mathcal{G}_{\frac{1}{2}}^{T,D}$ and $\mathcal{G}_{\frac{1}{3}}^{T,D}$ are defined

$$\mathcal{G}_{\frac{1}{2}}^{T,D} = \sqrt{\pi / [(\varphi_3^{t,d} / \varphi_2^{t,d})^4 + ih\varphi_2^{t,d}]} \quad (25b)$$

and

$$\mathcal{G}_{\frac{1}{3}}^{T,D} = \frac{2}{3} \frac{|\varphi_2^{t,d} / \varphi_3^{t,d}|}{(\sigma \mp ih\varphi_3^{t,d} / 2)^{\frac{1}{3}}} K_{\frac{1}{3}}(w^{t,d}) \quad (25c)$$

with

$$w^{t,d} = 2(\sigma \mp ih\varphi_3^{t,d} / 2)^{\frac{1}{3}} |\varphi_2^{t,d} / \varphi_3^{t,d}|^3 \quad (25d)$$

where $K_{1/3}(w)$ is the modified Bessel function defined in [1] and σ a positive real constant. Furthermore, the minus/plus signs in the denominator of (25c) and in (25d) are taken for the transverse/divergent waves, respectively.

For $\gamma > \gamma_c$, there is not stationary point any more. To extend continuously ship waves across the cusp line, the values of φ and its derivatives

φ' , φ'' and φ''' at the inflection point $u = u_c$ (i.e. $\varphi_c, \varphi_c', \varphi_c''$ and φ_c'''), are used to define

$$\begin{aligned} \varphi_0^c &= \varphi_c + (1/3)(\varphi_c'')^3 / (\varphi_c''')^2 - \varphi_c' \varphi_c'' / \varphi_c''' \\ \varphi_1^c &= \varphi_c' - (\varphi_c'')^2 / (2\varphi_c'''), \quad \varphi_3^c = \varphi_c''' / 3 \end{aligned}$$

and the transverse and divergent waves by

$$\mathcal{G}^{T,D} = A_0^c \exp(-ih\varphi_0^c) (\mathcal{G}_1^c + \mathcal{G}_{\frac{1}{3}}^c) \quad (26a)$$

with

$$\mathcal{G}_1^c = \frac{e^{-(h\varphi_1^c)^2 (\varphi_1^c / \varphi_3^c)^4}}{2(\varphi_3^c / \varphi_1^c)^2} \quad (26b)$$

and

$$\mathcal{G}_{\frac{1}{3}}^{\pm} = \frac{2}{3} \frac{|\varphi_1^c / \varphi_3^c|}{(\sigma \mp ih\varphi_3^c / 2)^{\frac{1}{3}}} K_{\frac{1}{3}}(w^{\pm}) \quad (26c)$$

with

$$w^{\pm} = 2(\sigma \mp ih\varphi_3^c / 2)^{\frac{1}{3}} |\varphi_1^c / \varphi_3^c|^3 \quad (26d)$$

The amplitude function $A_0^{t,d,c}$ involved in (25a) and (26a) are determined by

$$A_0^{t,d,c} = -\Sigma_1 i e^{z k_{t,d,c}} \frac{\sqrt{k_0 k_{t,d,c} (k_{t,d,c} - k_0)}}{2\pi F^2 \beta_{t,d,c}} \quad (27)$$

The modified Bessel function $K_{1/3}(w)$ involved in (25c) and (26c) can be expressed by using the Airy function $\text{Ai}(\cdot)$ defined in [1]

$$K_{\frac{1}{3}}(w) = \text{Ai}[(3w/2)^{2/3}] \pi \sqrt{3} / (3w/2)^{1/3} \quad (28a)$$

and has the asymptotic expressions

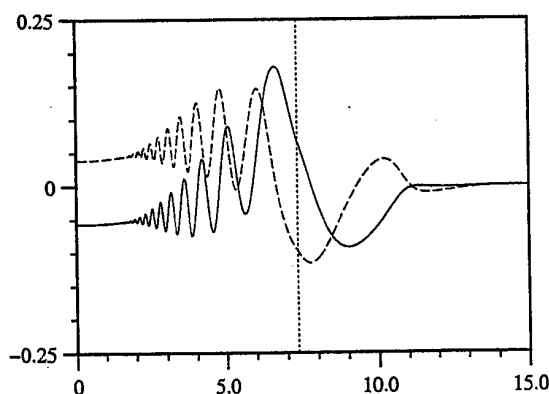
$$K_{\frac{1}{3}}(w) = \begin{cases} e^{-w} \sqrt{\pi / (2w)} & \text{for } |w| \rightarrow \infty \\ \Gamma(1/3) / (4w)^{1/3} & \text{for } |w| \rightarrow 0 \end{cases} \quad (28b)$$

It can be checked by using (28b) that $\mathcal{G}_{1/3}^{T,D}$ given by (25c) involving $K_{1/3}$ decreases exponentially for $h \rightarrow \infty$ as far as $\varphi_2^{t,d} \neq 0$ and that both transverse and divergent waves (25a) decrease then at a rate of order $O(h^{-1/2})$ (leading order of $\mathcal{G}_{1/2}^{T,D}$) within the wedge $\gamma < \gamma_c$.

Along the wedge $\gamma = \gamma_c$, it can be shown that (25a) are of order $O(h^{-1/3})$, the leading order of $\mathcal{G}_{1/3}^{T,D}$ and as $\varphi_c^{t,d} \rightarrow 0$, $\mathcal{G}_{1/2}^{T,D} = 0$, consistent with the classical results. The amplitude of $\mathcal{G}^{T,D}$ represented by (26a) decreases exponentially for $\varphi_1^c \neq 0$, i.e. $\gamma > \gamma_c$, and at a rate of order $O(h^{-1/3})$ when $\varphi_1^c \rightarrow 0$, i.e. $\gamma \rightarrow \gamma_c$, and equal to the results given by (25a).

The four ship-wave systems each of which is associated with a distinct dispersion curve are regrouped here into three classes. The first associated with a closed dispersion curve is called ring waves. The second associated with the portion of open dispersion curves limited between two inflection points located symmetrically in the upper and lower half Fourier plane, is called transverse waves. The third class of unsteady ship waves is associated with the portions of open dispersion curves from the inflection points to infinity, and called divergent waves. The ring waves propagate out in all directions for limited values of the Brard number $\tau < 1/4$ and their amplitude decreases at a rate of order $O(h^{-1/2})$ as $h \rightarrow \infty$. The transverse and divergent waves are limited by a cusp line whose angle defined by (17a) and (17b) is parallel to the direction of the normal vector at the inflection point of corresponding dispersion curve. Within the wedge limited by the cusp line, the amplitude of transverse and divergent waves decreases at the same rate like $O(h^{-1/2})$ while along the wedge the decreasing rate is of $O(h^{-1/3})$. Outside the wedge, the non-oscillatory local component is dominant since the decreasing rate is of order $O(h^{-1})$ while the wave amplitude falls off exponentially. These important features of transverse and divergent waves are well described by (25a) within the wedge and (26a) outside the wedge. Furthermore, the expressions (25a) and (26a) for transverse waves as well as for divergent waves provide the same and correct asymptotic values along the wedge so that they are continuous across the wedge, as shown by Fig.8 which depict $F^2(\mathcal{G}^T + \mathcal{G}^D)$ of the inner-V waves at $\tau = 1/4$ along a transverse line in the downstream $x/F^2 = -26$ within $0 \leq y/F^2 \leq 15$ and close to the free surface $z/F^2 = -0.1$. In the figure, the real and imaginary parts of $\mathcal{G}^T + \mathcal{G}^D$ are presented by the solid and dashed lines, respectively.

Fig.8: $F^2(\mathcal{G}^T + \mathcal{G}^D)$ along $x/F^2 = -26$



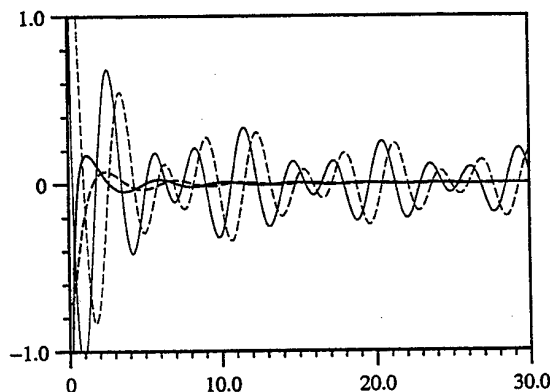
The transverse and divergent waves are shown in Fig.8 to be continuous across the cusp line which is located at $y/F^2 = \sqrt{2/25} x/F^2 \approx 7.35$, according to Tab.1 and marked by the vertical dotted line in the figure.

The classical treatments to the phase function which exhibits two coalescing stationary points were presented in [10] to develop uniform asymptotic expansions of an integral. Very fine results can be obtained as presented in [27] in applying to the Neumann-Kelvin steady waves. However, we prefer here forgoing expressions to describe more complicated *unsteady* ship waves for several reasons.

Firstly, the expressions (25a) for transverse and divergent waves $\mathcal{G}^{T,D}$ are *explicit* in that the wavenumbers $k^{t,d}$, more exactly wavenumber vectors $(\alpha_{t,d}, \beta_{t,d})$, are defined to correspond to the stationary points $k_0 \leq k_t < k_c$ and $k_c < k_d < \infty$ partitioned by k_c given at the inflection point of the corresponding dispersion curve. The decreasing rate is of order $(h^{-1/2})$ since the terms involving $K_{1/3}$ are exponentially small at $h \rightarrow \infty$ for a given $\gamma < \gamma_c$. At the wedge $\gamma = \gamma_c$, we have $k_t = k_c = k_d$ and the terms involving $K_{1/3}$ are reduced to those of order $O(h^{-1/3})$ while the first terms $\mathcal{G}_{1/2}^{T,D}$ in (25a) tend to zero as $\varphi_2^{t,d} \rightarrow 0$.

The transverse waves and the divergent waves $\mathcal{G}^T + \mathcal{G}^D$ involved in the inner-V waves at $\tau = 1/4$, are depicted separately on Fig.9 along $\gamma = \gamma_c/2$ with $0 \leq h/F^2 \leq 30$ close to the free surface with $z/F^2 = -0.01$ with $\tan(\gamma_c) = \sqrt{2/25}$. The real and imaginary parts are represented by solid and dashed lines, respectively. The difference between analytical expressions (25a) and the line integral (10a), represented by the thick solid and dashed lines. It is shown the difference is negligible for $h/F^2 > 10$.

Fig.9: $F^2(\mathcal{G}^T + \mathcal{G}^D)$ along $\gamma = \gamma_c/2$



Concerning divergent waves defined in (25a), as already noted, the decreasing rate is of $O(h^{-\frac{1}{2}})$ in a given direction within the wedge and $O(h^{-\frac{1}{3}})$ along the wedge as well as the transverse waves. However, for a field point in the downstream $x < 0$ with $y \rightarrow 0$, the values of the stationary point (α_d, β_d, k_d) defined by (24) are given approximately

$$\alpha_d \approx \Sigma_1 x / (2y) \quad \text{and} \quad \beta_d \approx x^2 / (4y^2) \approx k_d \quad (29)$$

as the leading term. The amplitude function A_0^d defined by (27) decreases exponentially for a field point approaching to the track of an *immersed* source point ($z < 0$). Furthermore, if $z = 0$ and $y \rightarrow 0$, i.e. a field point approaches to the track of a source located at the free surface, the divergent waves are highly oscillatory with infinitely increasing amplitude and infinitely decreasing wavelength, since $\varphi_2^d \sim k_0 \sin \gamma$ and $\varphi_3^d / \varphi_2^d \sim 0$ involved in (25a). This singular and highly-oscillatory properties of ship waves are analyzed in [6] in great detail.

Secondly, the expressions (22) for ring waves, (25a) and (26a) for transverse and divergent waves are *regular* in the near field, unlike the results from classical asymptotic analysis which are singular for $h \rightarrow 0$. Far-field waves represented by these analytical expressions are then extended to the near field and complementary to the local component. Finally, the last but not the least concerns calculating the line integral (4d) or (10a) in a complete way. Indeed, the asymptotic analysis performed to obtain the analytical expressions, provides formulations well suited for numerical evaluations of the remaining term - another line integral with the integrand of (4d) or (10a) after subtracting the terms related to the analytical expressions.

In summary, we have given the new expressions of unsteady ship wave patterns in an analytical form. These expressions are critically important in calculating the ship-motion Green function in the far field. They may be very useful as well in a number of analyzes such as estimating wave-damping and wave-resistance components.

PECULIARITIES OF SHIP-MOTION GF

Previous studies presented in [27], [14], [28] and [12] on the Neumann-Kelvin steady flow show that the Green function is singular and highly-oscillatory near the singular axis - the track of source point located at the free surface. These studies were mostly based on asymptotic analyzes of the single integral similar to (4d) for steady flows along the complex path of steepest descent. However, it seems more complex to extend this analysis

to general cases such as time-harmonic ship-motion Green functions.

Very recently, an asymptotic analysis based on an asymptotic expansion of open dispersion curves at large wavenumber and properties of the complex error function, has been realized in [6]. The singular and highly-oscillatory properties of ship-motion Green functions are then expressed in an analytical closed form. Further analysis on the line integrals involving the singular and highly-oscillatory term is presented in [13]. A summary of these studies is now given.

Singular and highly-oscillatory terms

According to the analysis in the preceding sections on far-field ship waves, the highly-oscillatory behavior and singular properties of the wave component can only be associated with the open dispersion curves along which wavenumbers tend to infinity. Indeed, the waves in the region near the track of source are associated with stationary points at large wavenumber as given by (29). Asymptotic analysis of the open dispersion curves at large wavenumber is then the starting point.

From (2), the dispersion relation $D = 0$ yields $\beta = \sqrt{(F\alpha - f)^4 - \alpha^2}$ in the Fourier upper-half plane which can be rewritten

$$F^2 \beta = \sqrt{(F^2 \alpha - \tau)^4 - (F^2 \alpha)^2} \quad (30a)$$

which suggests to use the speed-scaled variables and to perform a translation of the Fourier plane such that

$$(a, b) = (F^2 \alpha - \tau, F^2 \beta)$$

and the speed-scaled wavenumber $c = F^2 k$ along the dispersion curves is written simply

$$c = \sqrt{(a + \tau)^2 + b^2} = a^2$$

The equation (30a) defining the dispersion curves can be written now

$$b = \sqrt{a^4 - a^2 - 2\tau a - \tau^2} \quad (30b)$$

The two open dispersion curves defined by (30b) are located in $-\infty < a \leq a^-$ and $a^+ \leq a < \infty$, respectively. It follows from (14) that the values of a^\pm are given by

$$a^- = \begin{cases} -\sqrt{1/4 - \tau} - 1/2 & \text{if } \tau \leq 1/4 \\ -\sqrt{1/4 + \tau} + 1/2 & \text{if } \tau > 1/4 \end{cases}$$

$$a^+ = \sqrt{1/4 + \tau} + 1/2 \quad \text{for } \tau \geq 0$$

and it can be easily verified that $a^- \leq -(\sqrt{2}-1)/2$ and $a^+ \geq 1$. At $\tau = 0$, the open dispersion curves

are symmetrical with respect to $a=0$ and $-a^- = 1=a^+$.

For large values of $|a|$, the expression (30b) can be developed in an asymptotic form

$$b = a^2 - 1/2 + \sum_{n=1}^{\infty} C_n a^{-n} \quad (30c)$$

with first terms

$$C_1 = -\tau, \quad C_2 = -(1+4\tau^2)/8, \quad \dots$$

so that the two open dispersion curves respectively located in $(-\infty, a^-]$ and $[a^+, \infty)$ can be approximated by a unique simple form

$$b + 1/2 = a^2 - \tau/a + O(a^{-2}) \quad \text{as} \quad (30d)$$

for $|a| \rightarrow \infty$, In (30d) the first term is a parabola.

The wave component given by (4d) is now used. In (4d), $\Sigma_1 = \pm 1$ for the left ($a \leq a^-$) and right ($a \geq a^+$) open dispersion curves, respectively. It can also be checked that the values of $\Sigma_2 = \pm 1$ for the left and right dispersion curves, if the field point $x < 0$ in the downstream and $y \rightarrow 0$. Furthermore, the identity $ds/\|\nabla D\| = d\alpha/|D_\beta| = d\alpha(k/\beta) = F^{-2} da(c/b)$ can be used and then the wave components associated with the two open dispersion curves are expressed now

$$2\pi i F^2 \mathcal{G}^W = \left(\int_{-\infty}^{a^-} - \int_{a^+}^{\infty} \right) \frac{c}{b} (\mathcal{E}^+ + \mathcal{E}^-) da \quad (31)$$

in which $b \geq 0$ and the elementary functions \mathcal{E}^\pm are written by

$$\mathcal{E}^\pm = e^{zk - i(x\alpha \pm y\beta)} = e^{zc - ix(a+\tau) - iy^\pm b}$$

with (x, y, z) understood to multiplied by $1/F^2$ and $y^\pm = \pm y$ as $y \geq 0$ is taken here, by the reason of the symmetry of wave patterns. Making use of (30c), it can be shown that

$$\frac{c}{b} (\mathcal{E}^+ + \mathcal{E}^-) = (E^+ + E^-) + \sum_{n=1}^{\infty} (E^+ A_n^+ + E^- A_n^-) a^{-n} \quad (32a)$$

with E^\pm defined by

$$E^\pm = e^{-(z + iy^\pm)a^2 - ixa - i(\tau x - y^\pm/2)} \quad (32b)$$

and

$$A_1^\pm = i\tau y^\pm$$

$$A_2^\pm = (4 + iy^\pm)/8 + \tau^2 iy^\pm (1 + iy^\pm)/2 \quad (32c)$$

...

Introducing (32a) into (31), the wave components can then be expressed by an asymptotic expansion

$$\mathcal{G}^W = \mathcal{G}_0^W + \sum_{n=1}^{\infty} \mathcal{G}_n^W \quad (33)$$

with the first term

$$2\pi i F^2 \mathcal{G}_0^W = \left(\int_{-\infty}^{a^-} - \int_{a^+}^{\infty} \right) (E^+ + E^-) da \quad (34a)$$

in which the integral in $(-\infty, a^-]$ can be converted into one in $[-a^-, \infty)$ by changing integral variable. Furthermore, since the argument of the exponential function E^\pm given (32b) is a parabolic function of the integral variable, the integrals on the right hand side of (34a) can be expressed in a closed form in [6], which involves the complex error function

$$\text{Cef}(w) = we^{w^2} \int_w^\infty e^{-t^2} dt = we^{w^2} \frac{\sqrt{\pi}}{2} \text{erfc}(w) \quad (34b)$$

where $\text{erfc}(\cdot)$ is the usual complementary error function defined in [1]. At large values of $|w|$, the function $\text{Cef}(w)$ has asymptotic expressions

$$\text{Cef}(w) = 1/2 + \sqrt{\pi} we^{w^2} + O(w^{-2}) \quad (34c)$$

for $|\arg(w)| > \pi/2$ otherwise $\text{Cef}(w) = 1/2 + O(w^{-2})$ at $|w| \rightarrow \infty$ if $|\arg(w)| \leq \pi/2$.

Using the asymptotic expression (34c) of $\text{Cef}(w)$, (34a) can be written asymptotically

$$\mathcal{G}_0^W \approx \widetilde{\mathcal{G}}_0^W + O(1)$$

with the singular and highly-oscillatory term $\widetilde{\mathcal{G}}_0^W$ given by

$$\widetilde{\mathcal{G}}_0^W = \frac{e^{zx^2/(4\mathcal{H}^2) - i\tau x}}{F^2 \sqrt{\pi} \mathcal{H}} \sin\left(\frac{\rho - y}{2} - \frac{yx^2}{4\mathcal{H}^2}\right) \quad (34d)$$

where $\mathcal{H} = \sqrt{(-z)^2 + y^2}$ and $\rho = \arctan[y/(-z)]$. The expression (34d) captures the behavior of highly oscillations with infinitely increasing amplitude and infinitely decreasing wavelength of \mathcal{G}^W for $y \rightarrow 0$ at $z=0$, and the finite limit for $\mathcal{H} \rightarrow 0$ at $z < 0$ and a finite value of $x < 0$ as assumed. Thus, the limits are non-uniform depending on $\rho = \pi/2$ ($z=0$) or $\rho < \pi/2$ ($z < 0$).

An interesting feature of the asymptotic expression (34d) is its dependence on the parameter τ as simple as a modification by multiplying $\exp(-i\tau x)$ since other variables involving in (34d) are independent of the frequency $f = \omega \sqrt{L/g}$. This simple result is understood to be associated with the fact

that the parabola $b+1/2=a^2$ is the first leading term of asymptotic expansion for open dispersion curves at all values of τ and $a=F^2\alpha-\tau$ represents a simple translation $(\tau, 0)$ of the Fourier plane $F^2(\alpha, \beta)$, and that a translation of the origin of Fourier plan to (α_0, β_0) yields an oscillatory factor of type $\exp[-i(\alpha_0x + \beta_0y)]$.

In a similar way, the second term in (33)

$$2\pi F^2 \mathcal{G}_1^W = \tau y \left(\int_{-\infty}^{a^-} - \int_{a^+}^{\infty} \right) (E^+ - E^-) / a \, da \quad (35a)$$

can be written as $\mathcal{G}_1^W \approx \widetilde{\mathcal{G}}_1^W + O(1)$ with a highly oscillatory term $\widetilde{\mathcal{G}}_1^W$ written

$$\widetilde{\mathcal{G}}_1^W = \tau \frac{-2ie^{zx^2/(4\mathcal{H}^2)} - i\tau x}{F^2(x/y)\sqrt{\pi/\mathcal{H}}} \cos\left(\frac{\rho+y}{2} + \frac{yx^2}{4\mathcal{H}^2}\right) \quad (35b)$$

and is proportional to τ . The term $\widetilde{\mathcal{G}}_1^W$ is not singular even at $z=0$, since the amplitude of \mathcal{G}_1^W is of order $O(\sqrt{y})$. It is however highly oscillatory due to the trigonometric function of $yx^2/(4\mathcal{H}^2)$ as $\mathcal{H} \rightarrow 0$, same as $\widetilde{\mathcal{G}}_0^W$ represented by (34d).

Although the further components \mathcal{G}_n^W in (33) for $n \geq 2$ can be obtained in the same way, it is enough to take the first two asymptotic terms for \mathcal{G}^W written now $\mathcal{G}^W = \widetilde{\mathcal{G}}^W + O(1)$ with the singular and highly-oscillatory terms (34d) and (35b)

$$\widetilde{\mathcal{G}}^W = \widetilde{\mathcal{G}}_0^W + \widetilde{\mathcal{G}}_1^W = \frac{e^{zx^2/(4\mathcal{H}^2)} - i\tau x}{F^2\sqrt{\pi/\mathcal{H}}} \left[\sin\left(\frac{\rho-y}{2} - \frac{yx^2}{4\mathcal{H}^2}\right) - i2\tau \frac{\mathcal{H}y}{x} \cos\left(\frac{\rho+y}{2} + \frac{yx^2}{4\mathcal{H}^2}\right) \right] \quad (36)$$

for $F > 0$ which means that the above expression of ship-motion Green functions for large values of $x^2/(4\mathcal{H}^2)$ is valid for any values of τ including $\tau=0$ and $\tau=1/4$. Indeed, if we take $\tau=0$, the expression (36) reduces to the simpler form which is in total agreement with previous results given in [27], [28] and [12] for the Neumann-Kelvin steady flow.

Line integrals on the free surface

Within the framework of solving boundary-value problems governed by the Laplace equation, the velocity potential $\phi(\xi, \eta, \zeta)$ can be represented by the integrals over all boundary surfaces including the body boundary, the free surface and a fictitious surface enclosing the body and at infinity. For the ship-motion problem, the free-surface integral is further converted into two line integrals by

using the Stokes' theorem

$$\phi_W + \phi_\infty = \left(\int_W - \int_\infty \right) [(F^2\phi_x + i2\tau\phi)G - F^2\phi G_x] t_y \, dl$$

where $\phi_W = \int_W(\cdot) \, dl$ stands for the waterline integral and $\phi_\infty = -\int_\infty(\cdot) \, dl$ the line integral along a contour at infinity. Furthermore, dl represents the differential element of arc length and t_y the component of the unit vector $\vec{t} = (t_x, t_y, 0)$ tangent to the waterline and the line at infinity, is oriented clockwise.

As already noted, ship-motion Green functions G^F contain the local component and the wave component which is composed of three classes of wave systems. The divergent waves associated with the portion of open dispersion curves at large wavenumber include the singular and highly-oscillatory terms $\widetilde{\mathcal{G}}^W$ represented by (36). It is assumed that the terms other than $\widetilde{\mathcal{G}}^W$ do not induce any difficulty in both mathematical analyzes and numerical evaluations of the line integrals, so that only the first term of \mathcal{G}^W rewritten here for $\zeta+z=0$

$$\widetilde{\mathcal{G}} = \frac{e^{-i\tau X}}{\sqrt{\pi}F^2} Y^{-\frac{1}{2}} \cos\left(\frac{X^2}{4Y} + \frac{Y}{2} + \frac{\pi}{4}\right) \quad (37)$$

where $(X, Y) = (\xi - x, |\eta - y|)/F^2$ and (x, y, z) are the coordinates of source point, is used in the following asymptotic analysis of the line integral at infinity and in the evaluation of influence coefficients corresponding to the waterline integral.

In previous studies, the argument that $\phi \rightarrow 0$ at infinity as required by the radiation condition is usually used to say that the line integral ϕ_∞ vanishes. More elaborately, it is assumed that both ϕ and G decrease at the rate of order $O(h^{-a})$ and the integrals at infinity (surface or line integrals) disappear formally for $a=1$ in the case without free surface effects, and for any values of $a>0$ with free surface effects ($a=1/2$ for ring waves for example) via an analysis using the method of stationary phase. We have, however, a singular and highly-oscillatory term (37) included in G such that the methods used previously are not applicable, and that previous analyzes may not be complete.

To complete the task, we perform an asymptotic analysis of the line integral at infinity by considering a closed curve of rectangular form with length sides located in $-A \leq x \leq A$ at $y = \pm B$ and width sides located in $-B \leq y \leq B$ at $x = \pm A$. The line integrals along the length sides $y = \pm B$ are nil since $t_y = 0$. Furthermore, the values of (ξ, η) are those over ship's hull or a field around the ship,

i.e. $\sqrt{\xi^2 + \eta^2} \ll (A \text{ or } B)$ so that we may take $\xi = 0 = \eta$ without loss of generality. Along the upstream side $x = A$, ϕ decreases at the rate of $O(h^{-1})$ for the local component or $O(h^{-1/2})$ for ring waves at $\tau < 1/4$ while $X = (\xi - x)/F^2 = -A/F^2$ so that \tilde{G} by (37) is applicable. Along the downstream side $x = -A$, the Green function G behaves like $O(h^{-1})$ for its local component or leading terms of ring waves of order $O(h^{-1/2})$ which exist for $\tau < 1/4$, and G doesn't contain the term \tilde{G} since $X = (\xi - x)/F^2 = A/F^2 > 0$. As already noted, we are limited to analyze only line integrals involving the term \tilde{G} so that the line integral at infinity reduced to one

$$\phi_\infty(\xi, \eta) = \int_{-B}^B [(F^2 \phi_x + i2\tau \phi)G - F^2 \phi G_x] dy \quad (38a)$$

along the width sides $x = +A$ at upstream only, which is estimated as

$$|\tilde{\phi}_\infty| < \phi_0 |I_0| + \phi_1 |I_1| \quad (38b)$$

with

$$I_0 = \int_{-B}^B \tilde{G} dy \quad \text{and} \quad I_1 = \int_{-B}^B \tilde{G}_x dy$$

and ϕ_0 and ϕ_1 depending on values of F , τ and distributions of ϕ and ϕ_x along the side $x = A$ are assumed to be of order $O(A^{-1/2})$ since the leading terms in ϕ and ϕ_x are of order $O(h^{-1/2})$ with $h = \sqrt{A^2 + y^2}$ along the upstream side $X = A$ as foregoing analyzed. Now the question is whether I_0 and I_1 are finite. Introducing (37) for \tilde{G} into I_0 and I_1 , we have

$$I_0 = \frac{e^{i\tau A/F^2}}{\sqrt{\pi/2}} \int_0^{B/F^2} \cos \mathcal{Y}(Y) Y^{-\frac{1}{2}} dY$$

$$\text{with} \quad \mathcal{Y}(Y) = \frac{(A/F^2)^2}{4Y} + \frac{Y}{2} + \frac{\pi}{4}$$

and

$$F^2 I_1 = i\tau I_0 + \frac{e^{i\tau A/F^2} A}{\sqrt{\pi} F^2} \int_0^{B/F^2} \sin \mathcal{Y}(Y) Y^{-\frac{3}{2}} dY$$

Using the change of integral variable $Y = \tilde{A}e^u$ with $\tilde{A} = A/(F^2 \sqrt{2})$, both integral $I_0(A)$ and $I_1(A)$ can be evaluated analytically for $B \rightarrow \infty$

$$I_0 = -2\sqrt{\pi} e^{i\tau A/F^2} \sqrt{\tilde{A}} J_{1/2}(\tilde{A})$$

$$F^2 I_1 = i\tau I_0 - \sqrt{2\pi} e^{i\tau A/F^2} \sqrt{\tilde{A}} Y_{1/2}(\tilde{A})$$

where $J_{1/2}$ and $Y_{1/2}$ are the Bessel functions defined in [1]. Therefore, the absolute values of I_0 and I_1 are

$$|I_0| = 2\sqrt{2} \quad \text{and} \quad F^2 |I_1| = 2\sqrt{1 + 2\tau^2} \quad (38c)$$

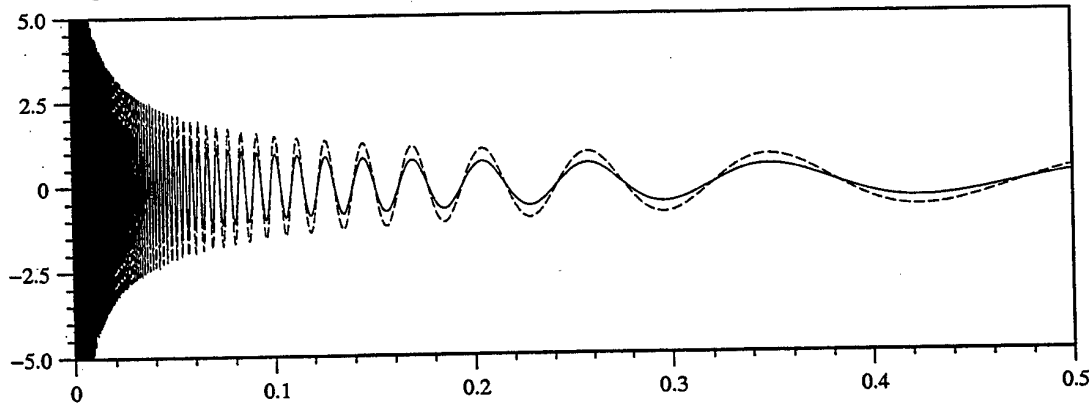
effectively finite for $A \rightarrow \infty$ so that the line integral given in (38b) $|\tilde{\phi}_\infty| = O(A^{-1/2}) \rightarrow 0$ at infinity, since ϕ_0 and ϕ_1 in (38b) are of $O(A^{-1/2})$ as already noted. Another integral on a fictitious surface at infinity can be analyzed in a similar way by using the expression (23a) given in [6] to express the highly-oscillatory term. This surface integral at infinity is expected to disappear as well since the singularity of the integrand is much weaker than the present line integral. This comfortable result is desirable and confirms that the velocity potential is correctly represented by source and dipole distributions on body boundary surface and along the waterline.

To analyze the waterline integral, we denote $\sigma = F^2 \phi_x + i2\tau \phi$ and $\delta = -\phi$ along the waterline and write the waterline integral

$$\phi_W = \int_W \sigma G dy + \int_W \delta F^2 G_x dy \quad (39a)$$

whose numerical evaluations are not a easy task. Indeed, the highly-oscillatory behavior of the integrand in (39a) involving \tilde{G} (37) which is depicted

Fig.10: Singular and highly-oscillatory term $F^2 \tilde{G}(X, Y)$ of ship-motion Green functions



in Fig.10 (real and imaginary parts by solid and dashed lines, respectively) for $\tau = 1/5$ at $X = -5$ and within $Y \leq 0 \leq 0.5$, induces large numerical errors due to dramatic cancelations between very large values with opposite signs in using a quadrature algorithm. The approximation in usual approaches to represent a segment of waterline by its centroids or any other points is simply wrong, according to the analysis in [11].

Fig.11: Real part of $K_\mu(u, v)$

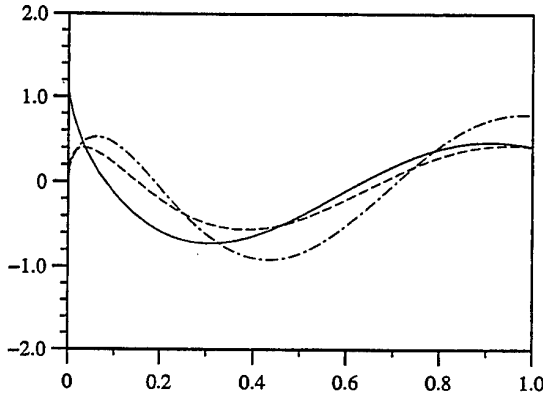
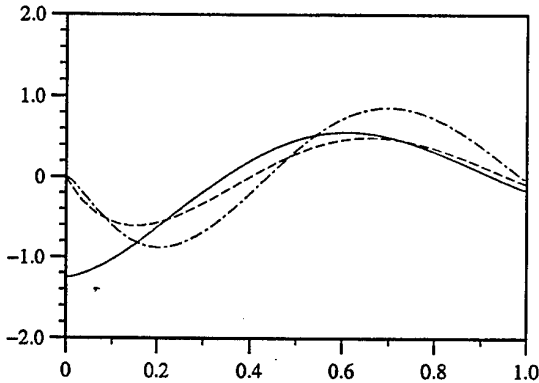


Fig.12: Imaginary part of $K_\mu(u, v)$



A rational and robust way to evaluate (39a) is to perform integrations analytically. In fact, an analytical integration is realized in [13] by assuming a linear distribution of σ and δ and using a special function defined as

$$K_\mu(u, v) = u^{\frac{1}{2}} \int_0^v t^{\mu-1} e^{-iu(t+1/t)} dt \quad (39b)$$

$$= (iu)^\mu u^{\frac{1}{2}} \sum_{n=0}^{\infty} \frac{u^{2n}}{n!} \Gamma(-\mu-n, iu/v)$$

for $\mu = -1/2, 1/2$ and $3/2$. In (39b), $\Gamma(\alpha, w)$ with $\alpha = -(\mu+n)$ and $w = iu/v$ is the complementary incomplete Gamma function defined by (6.5.3) in [1]. The Gamma function $\Gamma(\alpha, w)$ can be evaluated

by using the series developments (6.5.29) in [1] for small to moderate values of $|w|$ and the asymptotic expansions (6.5.32) in [1] for large values of $|w|$.

The integrand of the special function $K_\mu(u, v)$ defined by (39b) is singular and highly-oscillatory while the integration $K_\mu(u, v)$ is regular and depicted in Fig.11 and Fig.12 for the real and imaginary parts, respectively. In both figures, the solid, dashed and dot-dashed lines represent respectively $K_{-1/2}(u, v)$, $5K_{1/2}(u, v)$ and $50K_{3/2}(u, v)$ at $v = 1/5$ for $0 \leq u \leq 1$.

NUMERICAL EVALUATIONS OF GF

The ship-motion Green functions are expressed by the single integrals (10a) and (10b) for the wave and local components. Two single integrals behave in different ways. The integrand-amplitude of wave-component integral is smooth but the integrand may be highly-oscillatory along the portion of dispersion curve at large wavenumber and for large values of h . The integrand of local-component integral is non-oscillatory but has a logarithmic singularity and involves the complex exponential-integral function. Different numerical treatments are then needed for different components. Some numerical aspects are now considered and applications to ring waves, and inner-V and outer-V waves for $\tau = 1/5$ are presented.

Evaluation of highly-oscillatory integrals

The wave-component integral can be written in a generic form

$$I = \int_a^b f(t) e^{-i\varphi(t)} dt \quad (40)$$

in which the functions $f(t)$ and $\varphi(t)$ are called amplitude and phase functions, respectively. Both the amplitude function $f(t)$ and phase function $\varphi(t)$ are assumed to be smooth and nonoscillatory in the interval $[a, b]$. The phase function $\varphi(t)$ is further assumed to be real and may take very large values in $[a, b]$. The integrand of (40) can then be highly oscillatory. Furthermore, the lower and upper bounds a and b may tend to $-\infty$ and ∞ , respectively. Numerical evaluations of (40) by using usual quadrature algorithms, like trapezoidal and Gauss-Legendre rules, is very difficult and not efficient to achieve a good precision, due to dramatic cancelation of oscillatory integrand.

The interval of integration $[a, b]$ of (40) is divided into n subintervals so that the integral (40) is the sum of n integrals in each subinterval. As both the amplitude function $f(t)$ and phase function $\varphi(t)$ are assumed to be smooth and non-oscillatory, a polynomial approximation of $f(u) =$

$a_0 + a_1u + a_2u^2 + a_3u^3$ and $\varphi(u) = p + qu + ru^2$ in the reduced interval $[-1, 1]$, can be obtained (ex. by using a common cubic spline algorithm). The elementary integral over the subinterval

$$I_n = \int_{-1}^1 (a_0 + a_1u + a_2u^2 + a_3u^3) e^{-i(p+qu+ru^2)} du$$

can be evaluated in a closed form :

$$(4r^3 e^{ip}) I_n = iC_3 Q(q, r)/2 + [C_1 r \cos q - i(C_0 + C_2 r^2) \sin q] e^{-ir} \quad (41)$$

with the constants C_0, C_1, C_2 and C_3 defined by

$$\begin{aligned} C_0 &= i4a_1r^2 - i2a_2qr + 4a_3r + ia_3q^2 \\ C_1 &= i4a_2r - i2a_3q \\ C_2 &= i4a_3 \end{aligned}$$

$$C_3 = 8a_0r^3 - 4(a_1q + ia_2)r^2 + 2(a_2q^2 + i3a_3q)r - a_3q^3$$

and the function $Q(q, r)$ written as

$$Q(q, r) = -i \int_{-1}^1 e^{-i(qu+ru^2)} du = \frac{e^{-i(r+q)}}{q/2+r} F\left(\frac{q/2+r}{\sqrt{r}}\right) - \frac{e^{-i(r-q)}}{q/2-r} F\left(\frac{q/2-r}{\sqrt{r}}\right)$$

in which $F(t)$ is connected by $F(t) = \text{Cef}(\sqrt{it})$ with $\text{Cef}(w)$ defined by (34b).

If the constant $r \rightarrow 0$ in the phase function, we have a linear phase function $\varphi(u) = p + qu$. The elementary integral becomes

$$I_n = \int_{-1}^1 (a_0 + a_1u + a_2u^2 + a_3u^3) e^{-i(p+qu)} du$$

The integration by parts yields

$$\frac{q^4 e^{ip}}{2} I_n = (C_1 q + C_3 q^3) \cos q - i(C_0 + C_2 q^2) \sin q \quad (42)$$

$$\begin{aligned} \text{with } C_0 &= ia_0q^3 + a_1q^2 - i2a_2q - 6a_3 \\ C_1 &= ia_1q^2 + 2a_2q - i6a_3 \\ C_2 &= ia_2q + 3a_3 \\ C_3 &= ia_3 \end{aligned}$$

The above defined analytical integrals (41) and (42) respectively corresponding to a quadratic phase function and a linear phase function, are fundamental forms used to evaluate highly oscillatory integrals in a finite interval $[a, b]$.

Extension to an infinite integral with linear phase function can be realized by using the following elementary integral :

$$\begin{aligned} I_n &= \int_{t_0}^{t_1} (a_0 + a_1/t + a_2/t^2 + a_3/t^3) e^{-iht} dt \\ &= I_\infty(t_1) - I_\infty(t_0) \quad (43a) \end{aligned}$$

with $I_\infty(t)$ defined by

$$\begin{aligned} e^{iht} I_\infty(t) &= a_2/t + a_3/(2t^2) - ia_0/h - ia_3h/(2t) \\ &+ (a_1 - a_3h^2/2 - ia_2h) X(ht) \quad (43b) \end{aligned}$$

where the function $X(v)$ is expressed by $X(v) = \text{Cex}(iv)$ with $\text{Cex}(w)$ defined by (7f).

It is useful to divide first the infinite interval $[a, \infty)$ into a finite interval $[a, c]$ and an infinite interval $[c, \infty)$. The integration over $[a, c]$ can be performed by using the algorithm based on the elementary integral (41) et (42). The infinite integral over $[c, \infty)$ can be evaluated by using elementary integral (43a). This way of coupling two algorithms provides a flexibility to choose the point c such that $f(t)$ decreases for $t \geq c$.

Tab.2: Results of an infinity integral

n	$[0, 1/2]$	$[1/2, \infty)$	$[0, \infty)$
3	0.12897568	-0.11825699	0.01071869
5	0.12898053	-0.11839421	0.01058633
7	0.12898099	-0.11839644	0.01058439
10	0.12898113	-0.11839698	0.01058416

This special method based on analytical integrations after numerical approximations of the amplitude and phase functions of the oscillatory integrand, is applied to several examples. One of them concerns an infinity integral in $[0, \infty)$ with $f(t) = (1+t^2)^{-2}$ and $\varphi(t) = 5t$. The interval is divided into a finite part $[0, 1/2]$ and an infinity part $[1/2, \infty)$. Numerical results of the real part of the integral are presented in Tab.2 for several numbers of sampling points in both intervals. It is shown that only 10 points (2×5) are enough to have a precision of 5 figures comparing to $(0.01058394 \dots)$ the exact value.

Evaluation of non-oscillatory integrals

In foregoing developments, there are two special functions - the complex exponential-integral function $\text{Cex}(w)$ defined by (7f) and the complex error function $\text{Cef}(w)$ by (34b) to be evaluated, as other functions like usual error functions are just a special case of (34b). The efficient evaluation of both functions is essential in the numerical evaluation of the wave-component and local-component integrals. The usual way to use the series expansions and continued fractions given in [1] for respectively small to moderate values, and large values of $|w|$

can be used. More efficiently, both special functions can be approximated by Chebychev polynomials following the procedure used in [22] and [3]. Furthermore, for large values of $|w|$, the complex exponential-integral function is approximated by the sum of simple fractions expressed by

$$\mathbf{Cex}(w) = \sum_{n=1}^N \frac{a_n}{w + b_n} + \epsilon \quad (44a)$$

in which the real constants a_n and b_n depending on the number N , and the domain in which $|\epsilon| < 10^{-6}$ are given in Tab.3 hereafter.

Tab.3: Coefficients in (44a) for $\mathbf{Cex}(w)$

N	a_n	b_n	$w = u + iv$
2	0.14644661	3.41421356	$u < -23$ or $u > 18$ or $v > 20$
	0.85355339	0.58578644	
3	0.01038926	6.28994508	$u < -16$ or $u > 8$ or $v > 11$
	0.27851773	2.29428036	
	0.71109301	0.41577456	
5	0.00002337	12.64080084	$u < -15$ or $u > 4$ or $v > 6.8$
	0.00361176	7.08581001	
	0.07594245	3.59642577	
	0.39866681	1.41340306	
	0.52175561	0.26356032	

In the same way, the complex error function is approximated by simple fractions

$$\mathbf{Cef}(w) = \sum_{n=1}^N \frac{c_n}{1 + d_n/w^2} + \epsilon \quad (44b)$$

in which the real constants c_n and d_n depending on the number N , and the domain in which $|\epsilon| < 10^{-6}$ are given in Tab.4 hereafter.

Tab.4: Coefficients in (44b) for $\mathbf{Cef}(w)$

N	c_n	d_n	$w = u + iv$
2	0.04587585	2.72474487	$u > 5$ or $v > 5.5$
	0.45412415	0.27525513	
3	0.00255578	5.52534374	$u > 4$ or $v > 3$
	0.08861575	1.78449275	
	0.40882847	0.19016351	
5	0.00000431	11.80718949	$u > 3.5$ or $v > 2$
	0.00075807	6.41472973	
	0.01911158	3.08593744	
	0.13548370	1.07456201	
	0.34464234	0.11758132	

The integrand of the local-component integral (10b) or (8b) is non-oscillatory but has a logarithmic singularity containing in the complex exponential-integral function $\mathbf{Cex}(w)$ for $|w| \rightarrow 0$. One way to eliminate the logarithmic singularity consists to change the integral (8b) over $[0, 2\pi]$ into

an integral within $[0, \pi/2]$ such that the integrand $F(\theta)$ is singular only at $\theta = 0$. Then integration by part yields

$$\int_0^{\pi/2} F(\theta) d\theta = \frac{\pi}{2} F(\pi/2) - \int_0^{\pi/2} \theta F'(\theta) d\theta \quad (45)$$

where $F'(\theta)$ is the derivative of $F(\theta)$ with respect to θ and assumed to be of order $O(\theta^{-a})$ with $a \leq 1$ as $\theta \rightarrow 0$. The remaining integral on the right hand side of (45) can then be evaluated with ease.

Results for ring waves and V waves

Finally, some results of ring waves, and inner-V and outer-V waves at $\tau = 0.2$ are presented now. The ring waves associated with the closed dispersion curve described by $k = k^-$ with $k^-(\theta)/f^2$ given by (20) are formulated following (10a) for the wave component and (10b) for the local component and using polar angle θ as integral variable. The real and imaginary parts of ring waves for $f = 1$ calculated along $y = 0$ at the free surface ($z = 0$) within $-15 \leq x \leq 5$, are depicted in Fig.13 and Fig.14, respectively. In both figures, the wave and local components are represented respectively by dashed and dot-dashed lines, and their sum by solid lines.

Fig.13: Real part of ring waves along $y = 0$

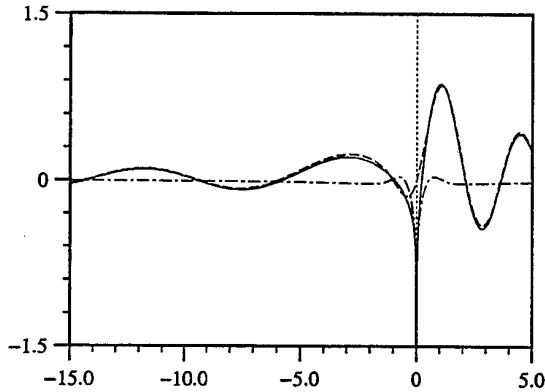


Fig.14: Imaginary part of ring waves along $y = 0$

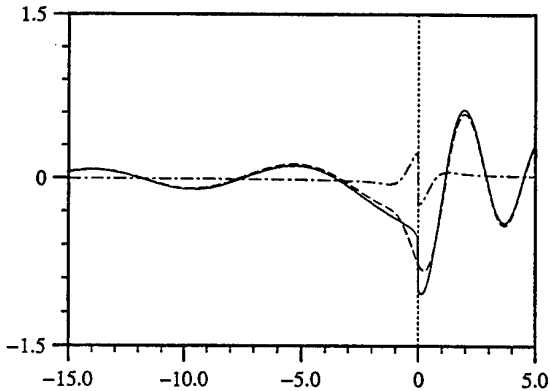


Fig.15: Inner-V waves and outer-V waves

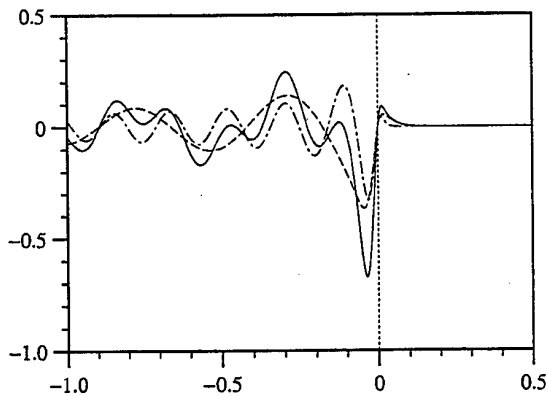


Fig.16: V waves and local component along $y=0$

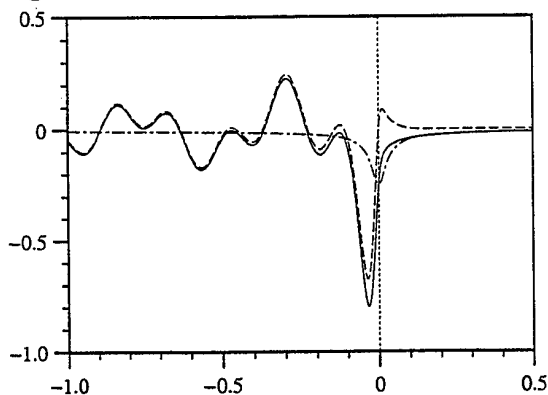
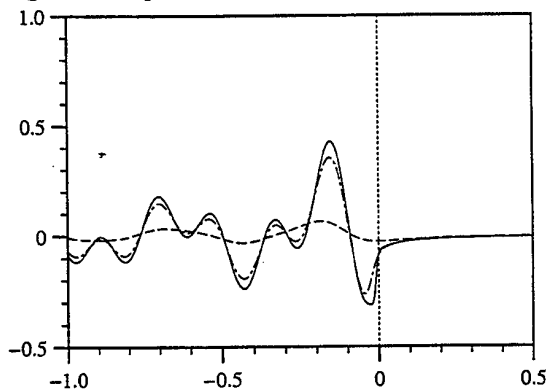


Fig.17: Complete V waves at different values of z



The inner-V waves and outer-V waves are associated with the right open dispersion curve and left open dispersion curve respectively. Both dispersion curves defined by $k = k^+$ are described by the parametric equation (23). The integral expressions for the wave and local components can be derived from (10a) and (10b). The wave component is depicted in Fig.15 for $F=0.2$ at $z=-0.01$ along $y=0$ with $-1 \leq x \leq 0.5$, in which inner-V waves are represented dot-dashed lines, outer-V waves by

dashed lines, and their sum by solid lines and in Fig.16 by dashed lines. The local component is depicted in Fig.16 by dot-dashed lines and the sum of wave and local components by solid lines. It is illustrated that the local component in V waves as well as that in ring waves (Fig.13-14) is only significant in the region close to the singularity.

In both Fig.15 and Fig.16, only the real part is presented. The imaginary part of complete V waves (wave plus local components) is depicted in Fig.17 at different values of z equal to -0.1 , -0.01 and -0.001 represented respectively by dashed, dot-dashed and solid lines. The results confirm foregoing asymptotic analyzes that V waves tend to a finite value in downstream $x < 0$ as $z \rightarrow 0$ but singular at $z=0$ for $y \rightarrow 0$ as shown by Fig.10.

CONCLUSIONS

In this paper, the important results recently achieved on ship-motion Green functions are summarized. New formulations providing different components of the free-surface Green functions are very useful in asymptotic analysis and numerical developments. Indeed, asymptotic analyzes on the wave component reveal the direct and close relationship between far-field ship waves and the dispersion relation, and yield analytical expressions of time-harmonic ship wave patterns. Furthermore, the singular and highly-oscillatory properties of time-harmonic ship-motion Green functions are, for the first time to author's knowledge, analyzed and expressed in a closed form.

All these analyzes not only give deeper understanding on the effect of free-surface in potential flows but also provide the best way to develop efficient methods in numerical analysis of ship-motion Green functions. Indeed, a special algorithm is developed to evaluate highly-oscillatory integrals and approximations by polynomials and simple fractions are used to calculate efficiently the special functions involved in the wave-component and local-component integrals. It is shown that the ship-motion Green functions can now be evaluated with ease in all configurations including the case when both the source and field points are located at the free surface. The results of these studies are being implemented in solvers of boundary-value problems to have a reliable and practical solution to ship-motion problems.

ACKNOWLEDGMENTS

The work is partially supported by a research grant from the DGA, and the European Commission under the BRITE-EURAM Program as part of the research project BE97-4406 entitled "Advanced

Method to Predict Wave Induced Loads for High Speed Ships (WAVELOADS)."

REFERENCES

1. M. Abramowitz & I.A. Stegun (1967) *Handbook of mathematical functions*, Dover Publications
2. M. Ba & M. Guilbaud (1995) *A fast method of evaluation for the translating and pulsating Green's function*, Ship Techn. Res. 42, 68-80
3. X.B. Chen (1993) *Evaluation de la fonction de Green de diffraction-radiation en profondeur d'eau finie - une nouvelle méthode rapide et précise* 4e Journées de l'Hydrodynamique, Nantes, 371-384
4. X.B. Chen (1996) *Évaluation des champs de vagues générés par un navire avançant dans la houle*, BV/DGA Report:95 378
5. X.B. Chen & F. Noblesse (1997) *Dispersion relation and far-field waves*, 12th WWWFB, Carry-le-Rouet, 31-35
6. X.B. Chen (1998) *On singular and highly-oscillatory properties of the ship-motion Green function*, Submitted for publication
7. X.B. Chen & F. Noblesse (1998) *Super Green functions*, 22nd Symp. Naval Hydrodyn., Washington
8. X.B. Chen & F. Noblesse (1998) *Super Green functions for water waves and other dispersive waves*, 3rd Int. Conf. Hydrodyn., Seoul
9. X.B. Chen & L. Diebold (1999) *Analytical expressions of unsteady ship wave patterns*, 14th Int. WWWFB, Michigan
10. C. Chester, B. Friedman & F. Ursell (1956) *An extension of the method of steepest descents*, Proc. Camb. Phil. Soc. 53, 599-611.
11. J.M. Clarisse (1991) *Highly oscillatory behaviors in the Neumann-Kelvin problem*, 6th Int. WWWFB, Woods Hole
12. J.M. Clarisse & J.N. Newman (1994) *Evaluation of the wave-resistance Green function : Part 3 - The single integral near the singular axis*, J. Ship Res. 38, 1, 1-8
13. Y. Doutréleau & X.B. Chen (1999) *Line integrals on the free surface in ship-motion problems*, 14th Int. WWWFB, Michigan
14. D. Euvrard (1983) *Les mille et une facettes de la fonction de Green du problème de la résistance de vagues*, Rapport de recherche, ENSTA, No.144.
15. P. Guével & J. Bougis (1982) *Ship motions with forward speed in infinite depth*, Int. Shipb. Progr. 29, 103-117
16. J.R. Hoff (1990) *Three-dimensional Green function of a vessel with forward speed in waves*, Norwegian Institute of Technology Rep: 1990:71
17. R.B. Inglis & W.G. Price (1982) *A three-dimensional ship motion theory - the hydrodynamic coefficients with forward speed*, Trans. RINA 124, 141-157
18. H. Iwashita & M. Ohkusu (1992) *The Green function method for ship motions at forward speed*, Ship Techn. Res. 39, 3-21
19. J. Jankowski (1990) *Fundamental solution of linear hydrodynamic boundary-value problems*, Polski Rejestr Statkow, Gdansk, Rep:45
20. M.J. Lighthill (1958) *Fourier analysis and generalized functions*, Cambridge Univ. Press, London
21. M.J. Lighthill (1978) *Waves in fluids*, Cambridge Univ. Press, London
22. J.N. Newman (1992) *Approximation of free-surface Green functions*, in Wave Asymptotics ed. by P.A. Martin and G.R. Wickham, Cambridge Univ. Press, 107-135
23. F. Noblesse & C. Yang (1995) *Fourier-Kochin formulation of wave-diffraction-radiation by ships or offshore structures*, Ship Tech. Res. 42, 115-139
24. F. Noblesse, X.B. Chen & C. Yang (1996) *Fourier-Kochin theory of free-surface flows*, 21st Symp. Naval Hydrodyn., Trondheim, 120-135
25. F. Noblesse & X.B. Chen (1995) *Decomposition of free-surface effects into wave and near-field components*, Ship Techn. Res. 42, 167-185
26. F. Noblesse, X.B. Chen & C. Yang (1999) *Generic super Green functions*, Ship Techn. Res. 46, 81-92
27. F. Ursell (1960) *On Kelvin's ship-wave pattern*, J. Fluid Mech. 8, 418-431.
28. F. Ursell (1988) *On the theory of the Kelvin ship-wave source: asymptotic expansion of an integral*, Proc. Royal Society of London A, 418, 81-93
29. G.X. Wu & R. Eatock Taylor (1989) *The numerical solution of the motion of a ship advancing in waves*, 5th Int. Conf. Num. Ship Hydrodyn., Hiroshima, 529-538
30. C. Yang, F. Noblesse & R. Löhner (1999) *Application of the Fourier-Kochin theory to the farfield extension of nonlinear nearfield steady ship waves*, 14th Int. WWWFB, Michigan

FOURIER-KOCHIN EXTENSION OF FULLY-NONLINEAR NEARFIELD SHIP WAVES

C. Yang¹, R. Löhner¹, D. Hendrix², F. Noblesse²

¹Institute for Computational Sciences and Informatics

George Mason University

Fairfax, VA 22030-4444, USA

Fax: 703 993 4064; E-mail: cyang@gmu.edu & lohner@rossini.gmu.edu

²David Taylor Model Basin, NSWC-CD

9500 MacArthur Blvd, West Bethesda, MD 20817-5700, USA

Fax: 301 227 4607; E-mail: hendrix@dt.navy.mil & mathydro@aol.com

ABSTRACT

A practical method — based on an explicit analytical representation of the waves generated by a given nearfield velocity distribution — for extending nearfield steady flows about ships is presented. The farfield analytical representation, based on the Fourier-Kochin theory, is verified by considering the linear free-surface potential flow due to a point source-sink pair. The value of the Fourier-Kochin representation for extending nearfield steady ship waves into the farfield (and more generally for coupling nearfield flow solvers and farfield linear potential flows) is demonstrated by illustrative applications to three hull forms for which the nearfield flow is evaluated using a fully nonlinear calculation method based on the Euler equations.

INTRODUCTION

A number of flow calculation methods — including potential-flow methods based on simple Rankine singularities, and methods that use finite differences or finite elements to solve the Euler or RANS flow equations — can be used to evaluate nearfield steady free-surface flows about ships. A practical method, based on an explicit analytical representation of the waves generated by a given nearfield velocity distribution, for extending nearfield steady flows about ships into the farfield is presented here.

The analytical representation of steady ship waves given in [1] is used. This flow representation is explicit and does not involve the velocity potential. Specifically, the boundary-integral representation given in [1] defines the velocity field $\nabla\phi$ in a potential flow explicitly in terms of the velocity distribution (u, v, w) at a boundary surface Σ . Thus, this flow representation does not involve the potential ϕ at Σ — unlike the usual Green identity which expresses ϕ within a flow domain in terms of boundary values of the potential ϕ and its normal derivative $\partial\phi/\partial n$ — and defines the velocity field $\nabla\phi$ directly, instead of via numerical differentiation of ϕ . The flow representation can therefore be used to extend any given nearfield flow, including flows associated with the Euler or RANS equations for which a velocity potential cannot be defined, into the farfield. Furthermore,

because this flow representation defines the velocity field $\nabla\phi$ explicitly in terms of the boundary velocity distribution (u, v, w) , it is not necessary to solve an integral equation or to evaluate influence coefficients.

The waves generated by distributions of singularities over the matching surface Σ , at which the boundary velocity distribution (u, v, w) is prescribed, are evaluated directly for the entire surface Σ using the mathematical representation of super Green functions given in [2]. This approach makes it possible to evaluate waves accurately and efficiently. Specifically, the Fourier integral defining the wave component in the Fourier-Kochin representation is strongly convergent, and calculation efforts are proportional to the number of panels needed to approximate the matching surface Σ and the number of field points where the flow is evaluated. Thus, calculation times are

$$O(N_{\text{panels}}) + O(N_{\text{points}})$$

instead of

$$O(N_{\text{panels}}) \cdot O(N_{\text{points}})$$

i.e. $O(N)$ rather than $O(N^2)$.

Nearfield waves are evaluated here using the fully nonlinear calculation method presented in [3] and [4]. This calculation method solves the Euler flow equations using unstructured grids. The Euler flow solver, optimized for efficient use of parallel computer hard-

ware, provides predictions of the nearfield wave pattern for typical monohull ships using approximately 1 million tetrahedral elements in a matter of hours on widely available machines.

LINEAR POTENTIAL FLOW DUE TO A VELOCITY DISTRIBUTION

Consider a ship advancing along a straight path, with constant speed U , in calm water of effectively infinite depth and lateral extent. The flow is observed from a Cartesian system of coordinates moving with the ship. The X axis is taken along the path of the ship and points toward the ship bow; thus, the ship advances in the direction of the positive X axis. The Z axis is vertical and points upward, and the mean free surface is chosen as the plane $Z = 0$. The flow appears steady in the translating system of coordinates, and consists of the disturbance flow due to the ship superimposed on a uniform stream opposing the ship's forward speed. The components of the disturbance velocity along the (X, Y, Z) axes are denoted (U, V, W) . Thus, the total velocity is given by $(U - U, V, W)$. Nondimensional coordinates and velocities are defined in terms of a characteristic length L (typically the ship length) and the ship speed U as $(x, y, z) = (X, Y, Z)/L$ and $(u, v, w) = (U, V, W)/U$.

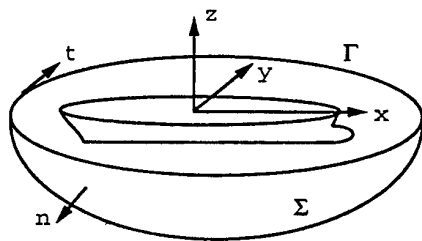


Fig. 1: Definition sketch

A geometrical surface Σ surrounding the ship is considered (Fig. 1). The intersection curve between the surface Σ and the mean free-surface plane $z = 0$ is denoted Γ . The unit vector $\vec{n} = (n^x, n^y, n^z)$ normal to the surface Σ points outside Σ . The unit vector $\vec{t} = (t^x, t^y, 0)$ tangent to the curve Γ is oriented clockwise. The flow in the region outside Σ is assumed to be potential and linear; i.e. the classical Kelvin linear boundary condition $\partial u / \partial \xi + 2\nu w = 0$ is assumed to hold at the mean free-surface plane $z = 0$ outside Γ . Here,

$$\nu = 1/(2F^2) \quad \text{with} \quad F = U/\sqrt{gL}$$

F is the Froude number and g is the acceleration of gravity. The flow in the outer linear potential-flow

region can then be defined using a boundary-integral representation based on the Green function satisfying the Kelvin boundary condition. The boundary-integral representation given in [1] is used here. This boundary-integral representation defines the velocity field $\vec{u}(\vec{\xi})$ — at a field point $\vec{\xi} = (\xi, \eta, \zeta \leq 0)$ of the linear potential-flow region outside a boundary surface Σ — generated by a given velocity distribution $\vec{u}_g(\vec{x})$ at $\Sigma \cup \Gamma$.

The Green function G associated with the Kelvin free-surface boundary condition is given by the sum of a simple-singularity component G^S defined in terms of simple Rankine singularities, and a component G^F that accounts for free-surface effects and is defined by a double Fourier superposition of elementary waves. Thus, the free-surface Green function is expressed in terms of two complementary fundamental solutions of the Laplace equation, the simple Rankine singularity $1/r$ and the elementary wave function $\exp[kz + i(\alpha x + \beta y)]$, which are well suited for representing a local flow disturbance and the system of waves generated by a ship, respectively.

The velocity field \vec{u} can similarly be expressed as the sum of a simple-singularity component \vec{u}^S given by distributions of simple singularities over $\Sigma \cup \Gamma$, and a free-surface component \vec{u}^F given by a double Fourier superposition of elementary waves. The Fourier representation \vec{u}^F of free-surface effects can be further decomposed into a wave component \vec{u}^W and a local component \vec{u}^L , as shown in [2]. Thus, the velocity field \vec{u} can be expressed as

$$\vec{u} = \vec{u}^W + \vec{u}^L + \vec{u}^S \quad (1)$$

This flow decomposition becomes $\vec{u} \approx \vec{u}^W$ at some distance behind the surface Σ , where the local component \vec{u}^L and the simple-singularity component \vec{u}^S are negligible.

Only the wave component \vec{u}^W in the flow decomposition (1) is considered in this study, which mostly considers the *farfield extension* of nonlinear nearfield ship waves. The local component $\vec{u}^L + \vec{u}^S$, required in a *nearfield coupling* of the Fourier-Kochin potential-flow representation with a nearfield flow solver, will be considered elsewhere.

WAVE COMPONENT

The wave component $\vec{u}^W(\vec{\xi})$, at a field point $\vec{\xi} = (\xi, \eta, \zeta \leq 0)$ of a linear potential-flow region outside a boundary surface Σ , due to a given velocity distribution $\vec{u}_g(\vec{x})$ over $\Sigma \cup \Gamma$ is now defined. Both \vec{u} and \vec{u}_g are disturbance velocities. The surface Σ is divided into a set of patches Σ_p associated with reference points $(x_p, y_p, z_p \leq 0)$ located in the vicinity

of Σ_p . The patch reference points $(x_p, y_p, z_p \leq 0)$ attached to the patches Σ_p need not lie on Σ_p .

The wave component $\tilde{u}^W(\xi)$ is given by the single Fourier integral

$$4\pi \begin{Bmatrix} u^W \\ v^W \\ w^W \end{Bmatrix} = \int_{-\infty}^{\infty} \frac{d\beta}{k-\nu} \alpha \Re e \begin{Bmatrix} \alpha \\ \beta \\ i k \end{Bmatrix} \sum_{p=1}^{p=N} [1 + \operatorname{erf}(\frac{x_p - \xi}{\sigma F^2})] S_p e^{\zeta k - i(\xi \alpha + \eta \beta)} \quad (2)$$

The Fourier variable α and the wavenumber $k = \sqrt{\alpha^2 + \beta^2}$ are functions of the Fourier variable β given by

$$k(\beta) = \nu + \sqrt{\nu^2 + \beta^2} \quad \alpha(\beta) = \sqrt{k(\beta)} / F \quad (2)$$

These relations ensure that the dispersion relation $F^2 \alpha^2 = k$ is satisfied.

Summation is performed over all the N patches $\Sigma_p \cup \Gamma_p$ that represent the surface $\Sigma \cup \Gamma$, i.e.

$$\Sigma \cup \Gamma = \sum_{p=1}^{p=N} \Sigma_p \cup \Gamma_p$$

erf is the usual error function (erf varies between -1 and 1), and σ is a positive real constant. The contribution of a patch Σ_p to the wave component \tilde{u}^W is negligible at some distance upstream from the reference point \bar{x}_p attached to Σ_p since

$$1 + \operatorname{erf}[(x_p - \xi)/(\sigma F^2)] \rightarrow 0 \quad \text{as} \quad (x_p - \xi) \rightarrow -\infty$$

Similarly, we have

$$1 + \operatorname{erf}[(x_p - \xi)/(\sigma F^2)] \rightarrow 2 \quad \text{as} \quad (x_p - \xi) \rightarrow \infty$$

The term S_p represents the spectrum function $S_p(\alpha, \beta)$ associated with the patch $\Sigma_p \cup \Gamma_p$, and is defined in terms of distributions of elementary waves $\exp[kz + i(\alpha x + \beta y)]$ over $\Sigma_p \cup \Gamma_p$:

$$S_p(\alpha, \beta) = \int_{\Sigma_p} dA(\bar{x}) e^{kz + i(\alpha x + \beta y)} A^\Sigma(\bar{x}) + F^2 \int_{\Gamma_p} dL(\bar{x}) e^{i(\alpha x + \beta y)} A^\Gamma(\bar{x}) \quad (3a)$$

$dA(\bar{x})$ and $dL(\bar{x})$ are the differential elements of area and arc length of Σ_p and Γ_p at the integration point $\bar{x} = (x, y, z \leq 0)$, and the amplitude functions A^Σ and A^Γ are defined in terms of the given boundary velocity distribution \tilde{u}_g by

$$A^\Sigma = (n^x u_g + n^y v_g + n^z w_g) + i[(n^x w_g - n^z u_g) \alpha / k - (n^z v_g - n^y w_g) \beta / k] \quad (3b)$$

$$A^\Gamma = (t^x t^y + \alpha \beta / k^2) (t^x u_g + t^y v_g) + (t^y)^2 (t^y u_g - t^x v_g) = (t^x u_g + t^y v_g) \alpha \beta / k^2 + t^y u_g \quad (3c)$$

The wave component \tilde{u}^W may be expressed as

$$4\pi \begin{Bmatrix} u^W \\ v^W \\ w^W \end{Bmatrix} \approx \int_0^{\beta_c} \frac{d\beta}{k-\nu} e^{\zeta k - C \beta^4 / \beta_c^4} \sum_{p=1}^{p=N} [1 + \operatorname{erf}(\frac{x_p - \xi}{\sigma F^2})] \begin{Bmatrix} \alpha A_p^\alpha \\ \beta A_p^\beta \\ k A_p^k \end{Bmatrix} \quad (4a)$$

Here, β_c and C are positive real constants satisfying the conditions $\beta_c \gg 1$ and $e^{-C} \ll 1$, and the functions A_p^α , A_p^β , and A_p^k are defined as

$$A_p^\alpha = [(S_r^+ + S_r^-) C_\alpha^\xi + (S_i^+ + S_i^-) S_\alpha^\xi] C_\beta^\eta + [(S_i^+ - S_i^-) C_\alpha^\xi - (S_r^+ - S_r^-) S_\alpha^\xi] S_\beta^\eta \quad (4b)$$

$$A_p^\beta = [(S_i^+ + S_i^-) C_\alpha^\xi - (S_r^+ + S_r^-) S_\alpha^\xi] S_\beta^\eta + [(S_r^+ - S_r^-) C_\alpha^\xi + (S_i^+ - S_i^-) S_\alpha^\xi] C_\beta^\eta \quad (4c)$$

$$A_p^k = [(S_r^+ - S_r^-) C_\alpha^\xi + (S_i^+ - S_i^-) S_\alpha^\xi] S_\beta^\eta - [(S_i^+ + S_i^-) C_\alpha^\xi - (S_r^+ + S_r^-) S_\alpha^\xi] C_\beta^\eta \quad (4d)$$

In these expressions, C_α^ξ , S_α^ξ , C_β^η , and S_β^η are given by

$$\begin{cases} C_\alpha^\xi = \cos(\xi \alpha) \\ S_\alpha^\xi = \sin(\xi \alpha) \end{cases} \quad \begin{cases} C_\beta^\eta = \cos(\eta \beta) \\ S_\beta^\eta = \sin(\eta \beta) \end{cases} \quad (4e)$$

Furthermore, S_r^\pm and S_i^\pm are defined as

$$S_r^\pm = S_p^r(\alpha, \pm \beta) \quad S_i^\pm = S_p^i(\alpha, \pm \beta) \quad (4f)$$

where S_p^r and S_p^i are the real and imaginary parts of the spectrum function S_p associated with the patch $\Sigma_p \cup \Gamma_p$. Thus, the wave component $\tilde{u}^W(\xi)$ is defined in terms of the Fourier representation (4) and the spectrum functions S_p given by (3). The spectrum functions S_p , given by distributions of elementary waves over patches $\Sigma_p \cup \Gamma_p$, are explicitly defined by the velocity distribution \tilde{u}_g over $\Sigma \cup \Gamma$.

For field points $\bar{\xi} = (\xi, \eta, \zeta \leq 0)$ located at a sufficient distance behind the boundary surface Σ , the Fourier-Kochin representation of the wave component $\tilde{u}^W(\bar{\xi})$ given by (4) and (3) takes the simpler form given by (4) and (3) in [5], and there is no need to divide $\Sigma \cup \Gamma$ into a set of patches $\Sigma_p \cup \Gamma_p$. The nearfield representation of the wave component \tilde{u}^W given in this study is verified further on by applying it to the linear free-surface potential flow due to a point

source-sink pair. The simpler *farfield* representation of \bar{u}^W given in [5] is also applied further on in this study to extend the Euler nearfield flows predicted by the calculation method given in [2] and [3] behind three hull forms.

The wave drag $D^W = \rho U^2 L^2 C^W$ can be directly obtained from the spectrum function (3) and the velocity distribution \bar{u}_g over $\Sigma \cup \Gamma$ using the Havelock formula

$$C^W \approx \frac{\nu}{2\pi} \int_{-\beta_c}^{\beta_c} \frac{d\beta}{k-\nu} (S_r^2 + S_i^2) e^{-C\beta^4/\beta_c^4} \quad (5)$$

for the radiated wave energy. Here, S_r and S_i are the real and imaginary parts of the spectrum function $S(\alpha, \beta) = \sum_{p=1}^{p=N} S_p(\alpha, \beta)$ with S_p defined by (3) and k and α given by (2).

VERIFICATION OF FOURIER-KOCHIN FLOW REPRESENTATION

The correctness of the *farfield* Fourier-Kochin representation given by (4) and (3) in [5] is verified in [5] by considering the linear free-surface potential flow due to a submerged point source, i.e. a Green function. The *nearfield* representation (4), (3) of the wave component due to a given velocity distribution over a boundary surface is similarly verified here by considering the linear free-surface potential flow due to a submerged point source and a submerged point sink of same strength, taken equal to 0.002. The source and sink are located at $(0.5, 0, -0.02)$ and at $(-0.5, 0, -0.02)$, respectively.

The disturbance velocity generated by this source-sink pair is evaluated, using integral representations of the gradient of the Green function, at an ellipsoidal boundary surface Σ that encloses the source-sink pair. The ellipsoidal boundary surface Σ is defined by

$$\frac{x^2}{a^2} + \frac{y^2}{b^2} + \frac{z^2}{c^2} = 1 \quad \text{with} \quad \begin{cases} a = 0.55 \\ b = 0.05 \\ c = 0.1 \end{cases}$$

The boundary velocity distributions (u, v, w) generated by the source-sink pair at Σ is depicted in Fig. 2a for $F = 0.316$. This boundary velocity distribution at the matching boundary surface Σ is extended outside Σ using the *nearfield* Fourier-Kochin representation (4), (3), and the outer flow fields (outside Σ) determined directly via integral representations of the gradient of the Green function, and reconstructed via the Fourier-Kochin representation are compared.

The spectrum function S associated with the velocity distribution over the matching boundary surface Σ is considered in Fig. 2b. The left and right columns correspond to the real and imaginary parts S_r and S_i

of S , and the top, center, bottom rows correspond to $F = 0.25, 0.316, 0.408$, respectively. As is indicated in (3a), the spectrum function S associated with a velocity distribution over a matching boundary surface Σ is given by distributions of elementary waves over the surface Σ and the intersection curve Γ of Σ with the plane $z = 0$. Here, Σ is a half ellipsoid and Γ is an ellipse. The contributions of the surface Σ and the curve Γ to the spectrum function S are depicted in Fig. 2b, together with the spectrum function S (given by the sum of the surface and curve components). The real parts (left column) of the surface and curve components entirely cancel out, and the real part of the spectrum function is null. Significant cancellations also occur between the imaginary parts of the surface and curve components (right column).

Fig. 2c depicts the wave patterns generated by the source-sink pair. The top, center, and bottom rows of Fig. 2c correspond to $F = 0.25, 0.316, 0.408$, respectively. The *direct* wave patterns, computed using integral representations of the gradient of the Green function, and the *reconstructed* Fourier-Kochin patterns are identical except near the boundary curve Γ where slight differences can be observed. These nearfield differences stem from the neglect of the local component \bar{u}^L in the flow decomposition (1) in the present implementation of the Fourier-Kochin representation (the simple-singularity component \bar{u}^S yields no contribution to the linear free-surface elevation).

Fig. 2d presents further comparisons of the Green-function (direct) and Fourier-Kochin (reconstructed) wave patterns depicted in Fig. 2c. Specifically, Fig. 2d depicts the free-surface elevations along the 4 wave cuts $y = 0, 0.06, 0.1$, and 0.5 for $F = 0.25$ (top 2 rows), $F = 0.316$ (center 2 rows), and $F = 0.408$ (bottom 2 rows). The Green-function and Fourier-Kochin wave profiles are nearly identical for the cuts $y = 0.1$ and 0.5 (2nd, 4th, and 6th rows). However, nearfield differences can be observed between the Green-function and Fourier-Kochin profiles for the cuts $y = 0$ and 0.06 (1st, 3rd, and 5th rows). These nearfield differences stem from the neglect of the local component \bar{u}^L in (1) as already noted.

EULER NEARFIELD FLOW SOLVER

The incompressible Euler flow equations are solved, using a finite-element method based on unstructured grids, for fully nonlinear boundary conditions at the free surface [3,4]. The Euler solver is optimized for efficient use of parallel computer hardware, and provides steady wave predictions using approximately 1 million tetrahedral elements in a matter of hours on widely available machines, e.g. the SGI Origin 2000.

The numerical procedure is based on a three-dimensional finite-element method for the flow variables (i.e., the velocity u, v, w and the pressure $\psi = p + z/F^2$) coupled to a two-dimensional finite-element method for the free-surface evolution variables (the free-surface elevation e and $\psi = e/F^2$). The computational domain is represented by an unstructured assembly of four-noded tetrahedral elements. The faces on the free surface are extracted from the three-dimensional mesh and renumbered locally to obtain a two-dimensional triangular finite-element mesh.

The discretization of a general three-dimensional computational domain into an unstructured assembly of tetrahedra is accomplished by means of an advancing front grid generation procedure [6]. This procedure requires that the geometry of the computational domain be defined in terms of an assembly of surface patches, and that the spatial variation of element size and shape be prescribed. The first step in the process is the triangulation of the computational boundary surfaces. The assembly of resulting triangles forms the initial front for the three-dimensional grid-generation process. The advancing front method is then used to fill the computational domain with tetrahedra, which are generated so as to meet a user-prescribed distribution of element size and shape.

Both analytical surface patches (planes, Coon's patches, etc.) and discrete surface patches (defined via a surface triangulation) are used to describe the present computational-domain boundaries, which consist of the hull surface, the free surface, and the surface of the computational box. Specifically, the preprocessor FECADE reads in the hull offset data, and a triangulation is generated from the offset data. This triangulation is subsequently used to define the hull surface in a discrete manner. The other boundary surfaces are defined analytically.

The desired element size and shape is prescribed using background grids and sources. The computational domain is covered by a coarse background grid of tetrahedral elements. The desired element size and shape is then specified at the nodes of this background grid. During grid generation, the local element size and shape is obtained using linear interpolation. In addition, both line and surface sources are used on the hull surface and the free surface to further define the element size. The sources on the hull surface ensure the generation of a finer mesh to accurately capture the hull geometry and the complex flow in the bow and stern regions. The sources on the free surface yield a finer mesh in the Kelvin wave pattern region.

The solution domains in the nonlinear nearfield flow calculation method and the Fourier-Kochin flow

representation are respectively bounded by the actual free surface $z = e$, where e stands for the computed free-surface elevation, and the mean free-surface plane $z = 0$. The nearfield flow computed at the Euler matching boundary surface (with $z \leq e$) is therefore mapped onto the Fourier-Kochin boundary surface (with $z \leq 0$) required by the linear potential flow extension. A continuous flow mapping based on linear interpolation is used here.

ILLUSTRATIVE APPLICATIONS

The Fourier-Kochin representation of the wave component generated by a velocity distribution at a boundary surface is now applied to extend nonlinear nearfield flows, determined using the Euler flow solver summarized above, behind the Wigley hull, the Series 60 hull, and Model 5415. These three hull forms are successively considered.

Wigley Hull

The Wigley hull is considered for $F = 0.25, 0.316$ and 0.408 . The waterline profiles predicted by the Euler nearfield flow solver are depicted in Fig. 3a together with experimental measurements obtained at the University of Tokyo. The computational mesh used for the Euler nearfield calculations reported in Fig. 3a consists of 1,003,554 tetrahedra, 184,619 field points and 28,140 boundary points. The free surface contains 28,383 triangular elements and 14,495 points. The Wigley hull is discretized using 18,708 triangular elements and 6,236 points.

The matching boundary surface Σ used for the Fourier-Kochin farfield extension of the Euler nearfield flow is defined by

$$\frac{x^2}{a^2} + \frac{y^2}{b^2} + \frac{z^2}{c^2} = 1 \quad \text{with} \quad \begin{cases} a = 0.6 \\ b = 0.055 \\ c = 0.1 \end{cases}$$

Fig. 3b, which depicts the intersection curves of the Wigley hull and the matching boundary surface Σ with the mean free-surface plane $z = 0$ and the symmetry plane $y = 0$, shows that the matching boundary surface is fairly close to the Wigley hull. The disturbance velocity distribution predicted by the Euler nearfield flow solver, and used in the Fourier-Kochin flow extension, at the matching boundary surface is depicted in Fig. 3c for $F = 0.316$.

The nonlinear Euler nearfield wave patterns and their linear Fourier-Kochin farfield extensions are shown in Fig. 3d for $F = 0.25, 0.316$, and 0.408 . The Fourier-Kochin farfield waves are evaluated at approximately 240,000 points — using approximately 130,000 triangular panels to approximate the

matching boundary surface Σ shown in Fig. 3b — in a few minutes. The nearfield and farfield wave patterns are in fairly good agreement, given the limitations inherent to both the farfield and the nearfield flows. In particular, the local component \bar{u}^L in the flow decomposition (1) is ignored in the present implementation of the Fourier-Kochin flow representation, and the nearfield flow is attenuated away from the Wigley hull due to numerical damping.

The nearfield drag predicted by the Euler nearfield flow solver, via integration of the hull pressure, and the farfield drag obtained in the Fourier-Kochin extension, via the Havelock formula (5) for the wave energy associated with the spectrum function (3), are listed below, together with the corresponding experimental values :

F	Near	Far	Exp
0.408	2.33	2.27	2.31
0.316	1.58	1.55	1.525
0.250	0.97	0.90	0.82

The foregoing theoretical and experimental values of the wave drag coefficient (multiplied by 1000) are in fair agreement. However, the farfield drag obtained via the Fourier-Kochin extension is sensitive to the location of the matching boundary surface Σ .

Series 60 Hull

The Series 60 hull is considered for $F = 0.25$. The waterline profile predicted by the Euler nearfield flow solver is depicted in Fig. 4a together with experimental measurements from the University of Tokyo. The computational mesh used for the Euler calculations reported in Fig. 4a consists of 706,749 tetrahedra, 133,495 field points and 27,314 boundary points. The free surface contains 23,742 triangular elements and 12,199 points. The Series 60 hull is discretized using 15,109 triangular elements and 7,905 points.

The matching boundary surface Σ used for the Fourier-Kochin farfield extension of the Euler nearfield flow is defined by

$$\frac{x^2}{a^2} + \frac{y^2}{b^2} + \frac{z^8}{c^8} = 1 \quad \text{with} \quad \begin{cases} a = 0.58 \\ b = 0.072 \\ c = 0.1 \end{cases}$$

Fig. 4b, which depicts the intersection curves of the Series 60 hull and the related matching boundary surface Σ with the mean free-surface plane $z = 0$ and the symmetry plane $y = 0$, shows that the matching boundary surface is fairly close to the Series 60 hull, as for the Wigley hull. The disturbance velocity distribution predicted by the Euler nearfield flow solver,

and used in the Fourier-Kochin flow extension, at the matching boundary surface is depicted in Fig. 4c.

The nonlinear Euler nearfield wave patterns and their linear Fourier-Kochin farfield extensions are shown in Fig. 4d. As for the Wigley hull, the Fourier-Kochin farfield waves are evaluated at approximately 240,000 points, using approximately 130,000 triangular panels to approximate the matching boundary surface Σ , and the nearfield and farfield wave patterns are in relatively fair agreement.

The nearfield drag predicted by the Euler flow solver, via integration of the hull pressure, and the farfield drag given by the Fourier-Kochin extension and the Havelock formula (5) are listed below, together with the corresponding experimental residuary drag :

F	Near	Far	Exp
0.25	0.63	0.63	0.65

The foregoing theoretical and experimental values of the wave drag coefficient (multiplied by 1000) are in good agreement. However the farfield drag obtained via the Fourier-Kochin extension is sensitive to the location of the matching boundary surface Σ , as for the Wigley hull.

Model 5415

Model 5415 is considered for $F = 0.28$. The waterline profile predicted by the Euler nearfield flow solver is depicted in Fig. 5a together with experimental measurements obtained at the David Taylor Model Basin. The computational mesh used for the Euler nearfield calculations reported in Fig. 5a consists of 2,169,626 tetrahedra, 400,174 field points and 63,702 boundary points. The free surface contains 44,159 triangular elements and 22,560 points. Model 5415 is discretized using 41,693 triangular elements and 21,615 points.

The matching boundary surface Σ used in the Fourier-Kochin farfield extension of the Euler nearfield flow is defined via an outward displacement of the surface of Model 5415 by an approximately uniform distance, equal to 0.0055, as shown in Fig. 5b which depicts the intersection curves of Model 5415 and the related matching boundary surface with the mean free-surface plane $z = 0$ and the symmetry plane $y = 0$. Fig. 5b shows that the matching boundary surface is quite close to the hull. The disturbance velocity distribution predicted by the Euler nearfield flow solver, and used in the Fourier-Kochin flow extension, at the matching boundary surface is depicted in Fig. 5c.

The nonlinear Euler nearfield wave patterns and their linear Fourier-Kochin farfield extensions are

shown in Fig. 5d. As for the Wigley hull and the Series 60 Model, the Fourier-Kochin farfield waves are evaluated at approximately 240,000 points, using approximately 130,000 triangular panels to approximate the matching boundary surface Σ , and the nearfield and farfield wave patterns are in fair agreement.

The nearfield drag predicted by the nonlinear Euler nearfield flow solver, via integration of the hull pressure, and the farfield drag given by the Fourier-Kochin extension and the Havelock formula (5) are listed below, together with the corresponding DTMB experimental residuary drag :

F	Near	Far	Exp
0.28	1.18	1.19	1.51

The foregoing theoretical and experimental values of the wave drag coefficient (multiplied by 1000) are in fair agreement. However, as for the Wigley hull and the Series 60 Model, the farfield drag obtained via the Fourier-Kochin extension is sensitive to the location of the matching boundary surface Σ .

CONCLUSION

The Fourier-Kochin representation of steady and time-harmonic ship waves [1,2] has been applied to the extension of nearfield steady ship waves. The Fourier-Kochin representation defines the farfield steady waves generated by a given velocity distribution \vec{u}_g at a boundary surface $\Sigma \cup \Gamma$ in terms of the single Fourier integral (4) and the spectrum function (3), which is defined explicitly in terms of \vec{u}_g . The wave drag can also be obtained directly from \vec{u}_g and the spectrum function S via the Havelock formula (5).

The Fourier-Kochin representation of the waves generated by a velocity distribution at a boundary surface has been verified by considering the linear free-surface potential flow due to a submerged point source-sink pair. Specifically, the disturbance velocity generated by the source-sink pair has been evaluated at an ellipsoidal boundary surface Σ enclosing the source, and extended outside Σ using the Fourier-Kochin flow representation. The outer flow fields (outside Σ) determined directly, using integral representations of the gradient of the Green function, and reconstructed via the Fourier-Kochin theory are in agreement as expected. This verification study also provides interesting comparisons between the contributions of the surface Σ and of the intersection curve Γ of Σ with the mean free-surface plane $z = 0$ to the spectrum function S .

The potential practical usefulness of the Fourier-Kochin flow representation for extending nearfield steady flows about ships (and more generally for cou-

pling nearfield flow solvers and farfield linear potential flows) is demonstrated by considering illustrative applications to the Wigley hull, the Series 60 hull, and Model 5415. The Fourier-Kochin representation of farfield steady ship waves is coupled here with the nonlinear nearfield calculation method based on the Euler flow equations presented in [3] and [4]. The nonlinear Euler nearfield wave patterns and their linear Fourier-Kochin farfield extensions are in relatively fair agreement, given the limitations inherent to both the farfield and the nearfield flows. In particular, only the wave component \vec{u}^W in the flow decomposition (1) is considered in the present implementation of the Fourier-Kochin flow representation, and the nearfield flow is attenuated away from the ship due to numerical damping.

The wave drags predicted by the Euler nearfield flow solver (via hull-pressure integration) and obtained within the Fourier-Kochin extension (by means of the Havelock formula) are also in fair agreement with one another, and with experiments. However, the farfield drag obtained via the Fourier-Kochin extension is sensitive to the location of the matching boundary surface Σ , which cannot be chosen too close to the ship hull or too far (because free-surface nonlinearities, ignored in the Fourier-Kochin representation, may be important close to the ship, and the quality of the nearfield flow may deteriorate away from the ship, e.g. due to numerical damping).

REFERENCES

1. Noblesse, F., Yang, C. and Chen X.B., "Boundary-Integral Representation of Linear Free-Surface Potential Flows", *Journal of Ship research*, Vol. 41, 1997, pp. 10-16.
2. Noblesse, F., Chen X.B. and Yang, C., "Generic Super Green Functions", *Ship Technology Research*, Vol. 46, 1999, pp. 81-92.
3. Löhner, R., Yang, C., Oñate, E. and Idelsohn, S., "An Unstructured Grid-Based, Parallel Free-Surface Solver", 1997, AIAA-97-1830.
4. Yang, C. and Löhner, R., "Fully Nonlinear Ship Wave Calculation Using Unstructured Grid and Parallel Computing", 3rd Osaka Coll. Advanced CFD Applications to Ship Flow and Hull Form Design, 1998, pp. 125-150.
5. Yang, C., Löhner, R. and Noblesse, F., "Farfield Extension of Nearfield Steady Ship Waves", *Ship Technology Research*, to appear.
6. Löhner, R., "Automatic Unstructured Grid Generators", *Finite Elements in Analysis and Design*, Vol. 25, 1997, pp. 111-134.

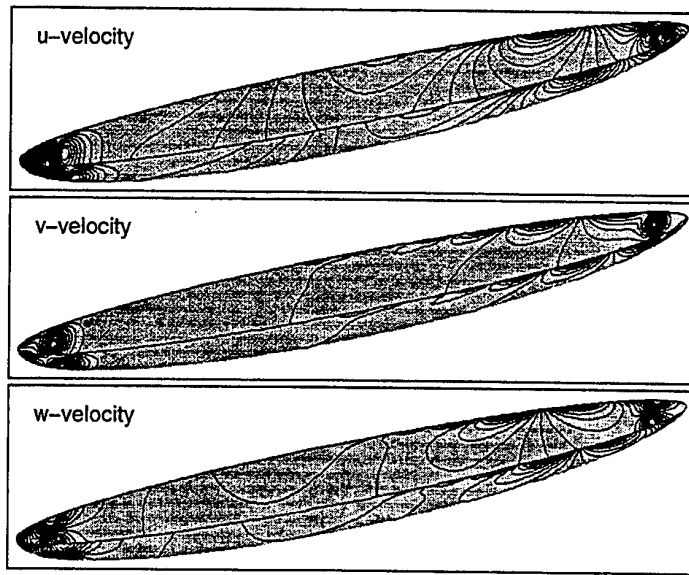


Fig. 2a. Boundary velocity distribution due to a source-sink pair

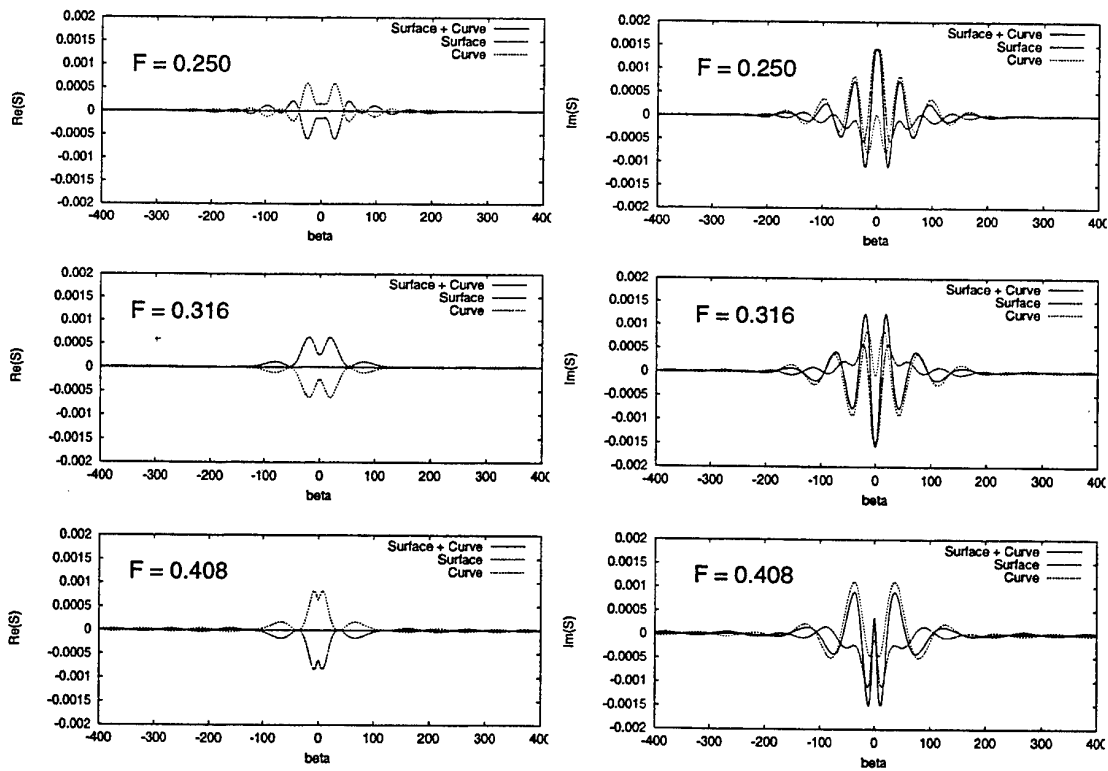


Fig. 2b. Spectrum functions for a source-sink pair

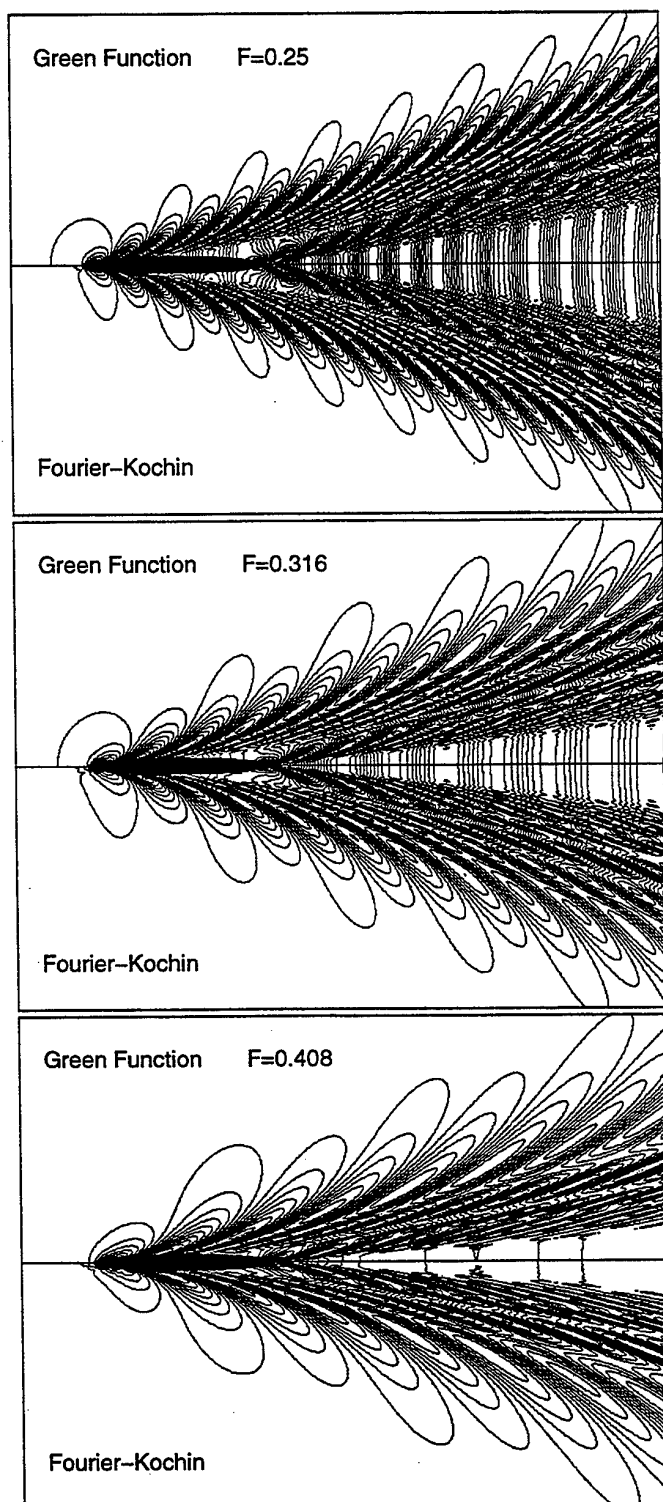


Fig. 2c. Wave patterns generated by a source-sink pair

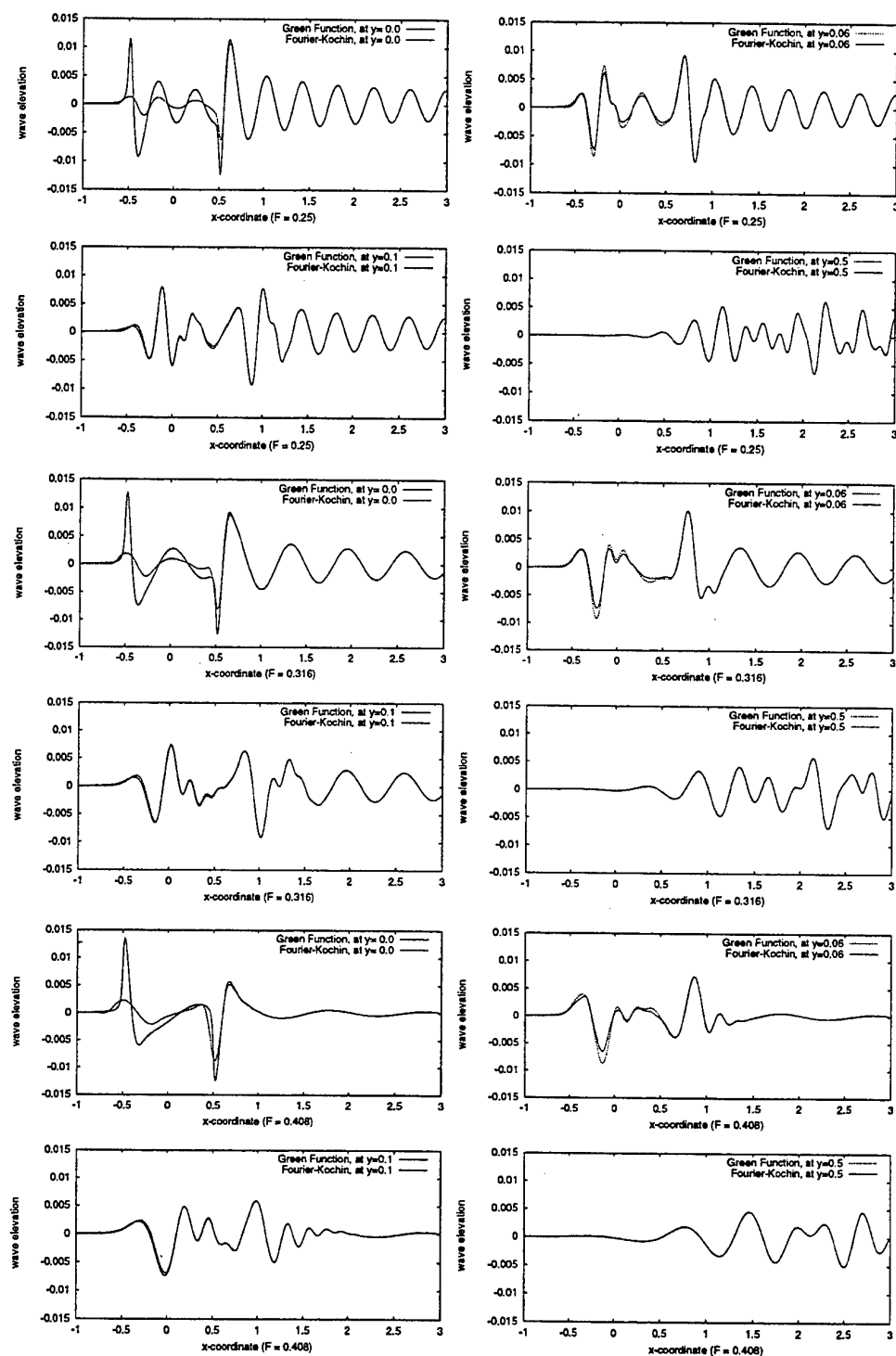


Fig. 2d. Wave profiles along longitudinal cuts for a source-sink pair

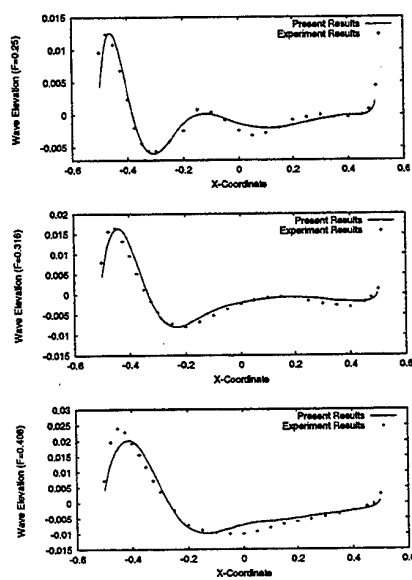


Fig. 3a. Wave profiles for Wigley hull

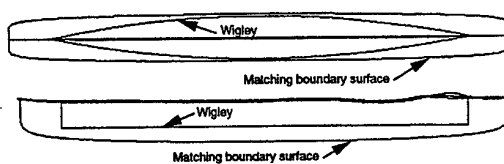


Fig. 3b. Wigley hull and matching boundary surface

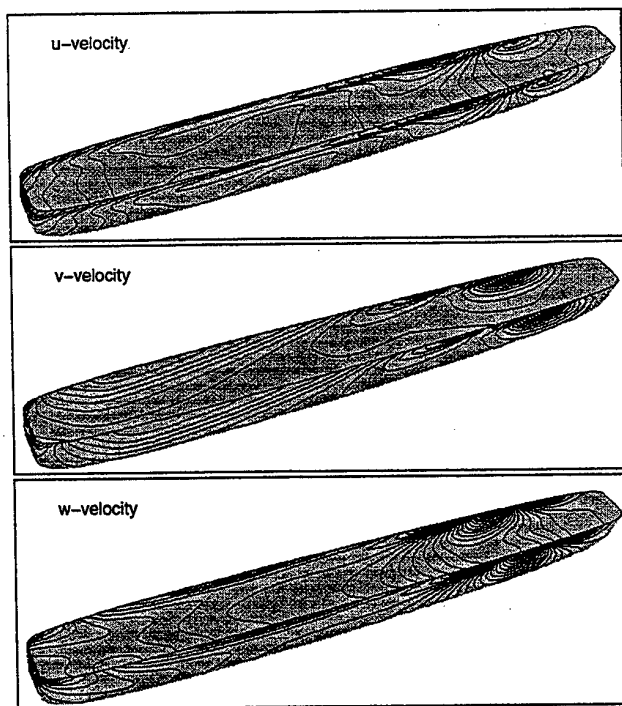


Fig. 3c. Boundary velocity distribution for Wigley hull at $F=0.316$

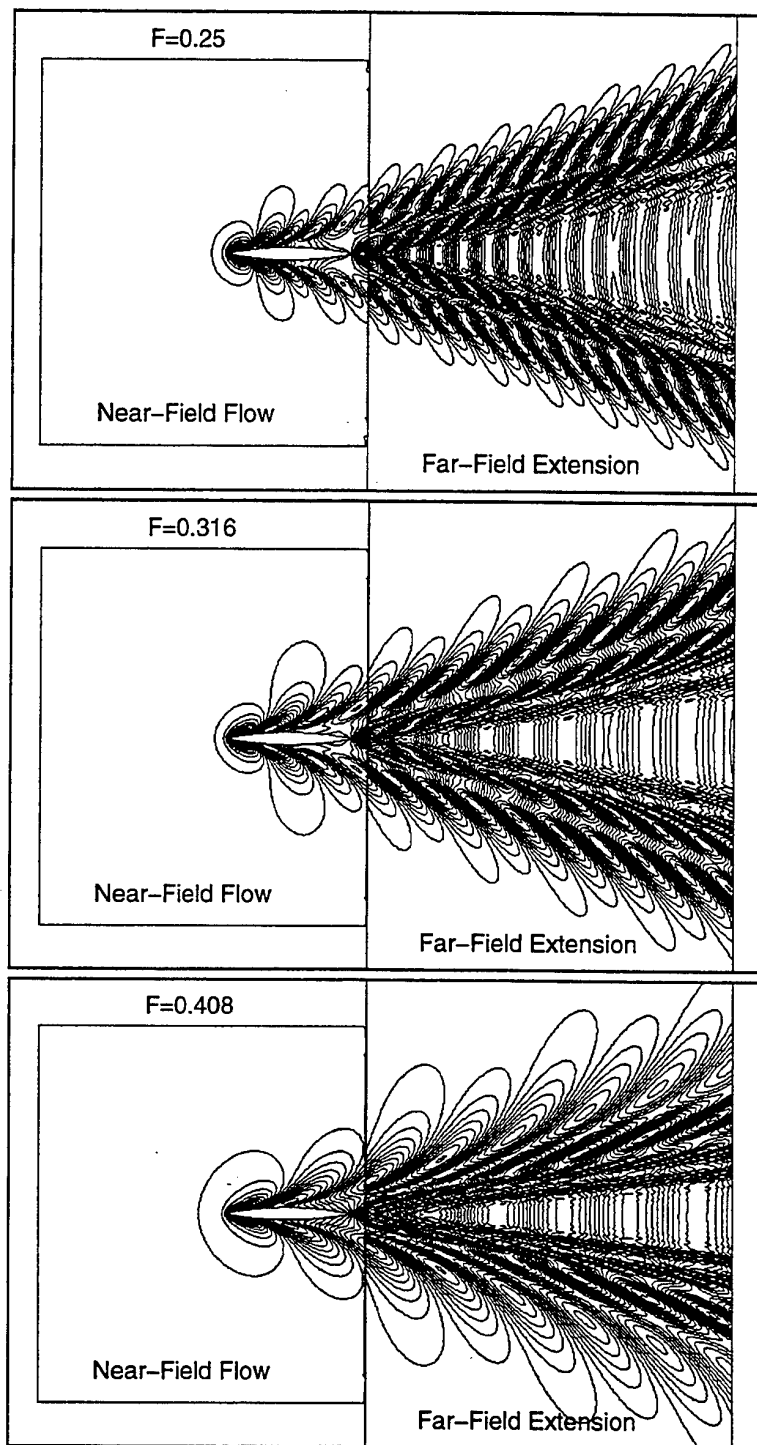


Fig. 3d. Wave patterns for Wigley hull

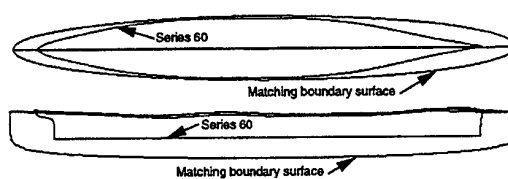
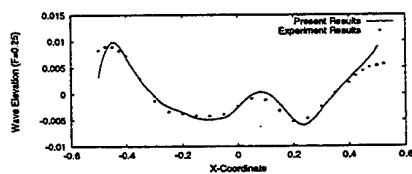


Fig. 4a. Wave profile for Series 60 hull at $F=0.25$ Fig. 4b. Series 60 hull and matching boundary surface

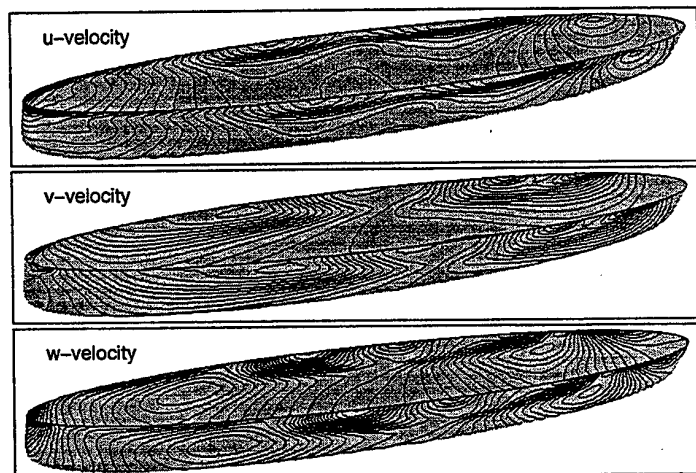


Fig. 4c. Boundary velocity distribution for Series 60 hull at $F=0.25$

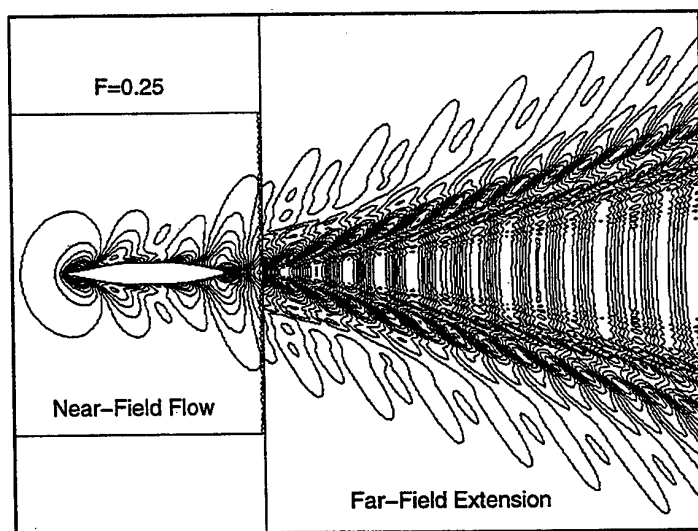


Fig. 4d. Wave pattern for Series 60 hull at $F=0.25$

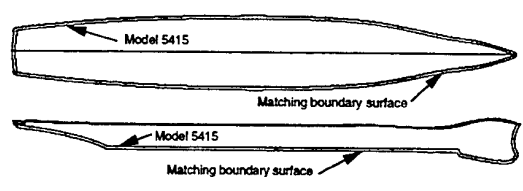
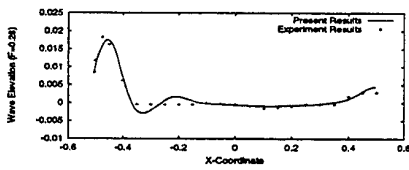


Fig. 5a. Wave profile for Model 5415 at $F=0.28$ Fig. 5b. Model 5415 and matching boundary surface

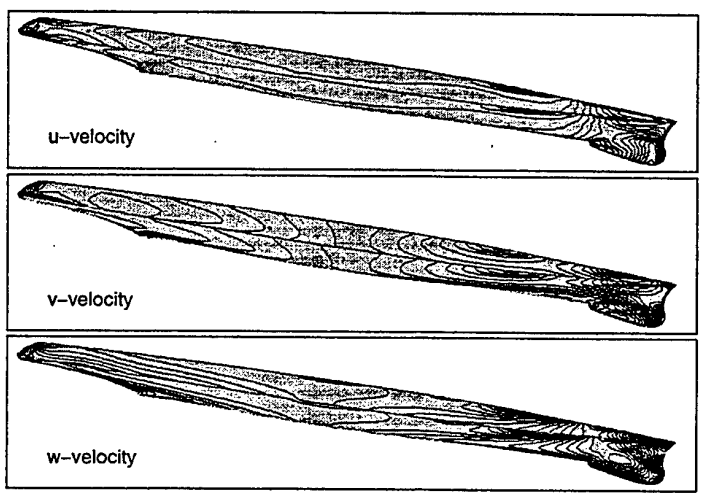


Fig. 5c. Boundary velocity distribution for Model 5415 at $F=0.28$

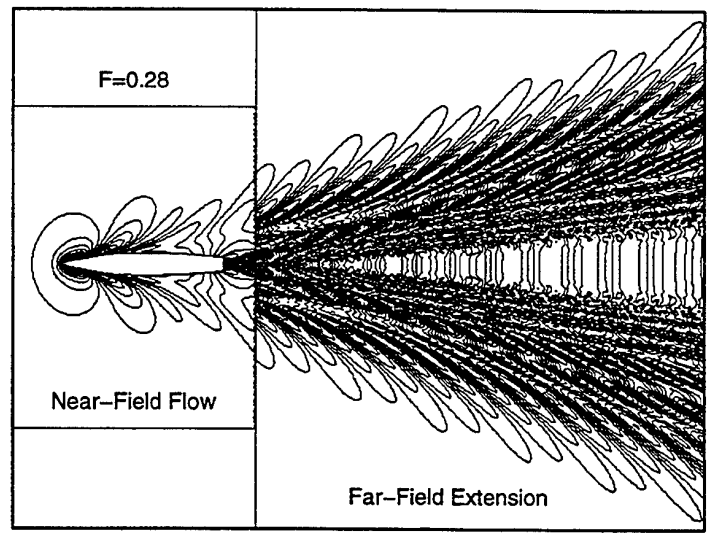


Fig. 5d. Wave pattern for Model 5415 at $F=0.28$

A MIXED SOURCE FORMULATION FOR NONLINEAR SHIP-MOTION AND WAVE-LOAD SIMULATIONS

Woei-Min Lin⁺, Sheguang Zhang⁺, Kenneth Weems⁺, and Dick K.P. Yue⁺⁺

⁺ Science Applications International Corporation, Ship Technology Division,
134 Holiday Court, Suite 318, Annapolis, Maryland 21401 USA.
Fax: 01 410 224 2631 ; E-Mail: lin@ship.saic.com,
szhang@ship.saic.com, ken@ship.saic.com

⁺⁺ Massachusetts Institute of Technology, Department of Ocean Engineering,
77 Massachusetts Avenue, Cambridge, Massachusetts 20139 USA.
Fax: 01 617 258 9389 ; E-Mail: yue@mit.edu

ABSTRACT

This paper presents a three-dimensional time domain boundary-element method using a combination of the transient Green's function and Rankine sources. The focus of the study is to demonstrate the efficiency and robustness of this method in solving free-surface ship hydrodynamics problems involving non-wall-sided ship geometries and large-amplitude ship motions. A computer code based on this approach is developed as part of the LAMP (Large Amplitude Motion program) System for nonlinear ship motion simulations and wave load predictions. To demonstrate the advantages of the new mixed source formulation, numerical examples are presented to show the numerical instability of the original transient Green's function formulation. In addition, radiation, diffraction, and steady forward speed wave patterns are shown for an offshore platform and a naval combatant. Finally, results for ships in storm sea conditions and application of the new method to unconventional hull forms are presented.

INTRODUCTION

As practical applications have increased and computer capabilities have advanced over the past twenty years, there has been a tremendous push in the development of 3-D time-domain methods for solving sea-keeping related problems. In the context of time-domain potential-flow boundary-element methods, the most commonly used approaches fall in two categories: (1) methods that use the transient Green's function and (2) methods that use the Rankine source. For the methods in the first category (e.g. Lin & Yue, 1990, and Lin, *et al.*, 1994), the transient Green's function satisfies the linearized free surface boundary conditions and radiation conditions at the far field, so that the singularities need to be distributed only on the wetted portion of the body surface. For ships with non-wall-sided geometry, numerical difficulties may arise in the area where the intersection angles between the body surface and the free surface become small. This is mainly due to the highly oscillatory nature of the transient Green's function adjacent to the free surface. For the methods in the second category (e.g. Nakos, Kring & Sclavounos,

1993), the Rankine source is used as a kernel in the boundary integral equation. The Rankine source is fairly robust for modeling either wall-sided or non-wall-sided geometry. To satisfy the free surface boundary condition, the Rankine source has to be distributed not only on the body surface but also on the free surface. In order to limit the size of the computation domain, the free surface region is typically truncated at several ship lengths away from the ship and a numerical damping zone is employed to absorb wave energy.

In view of the pros and cons of the two approaches, a natural and optimal choice is to take advantage of the two methods by using both the transient Green's function and the Rankine source in formulating free-surface ship hydrodynamic problems. This so-called mixed source method has recently been developed by the authors for motion and load computations of modern hull forms with highly non-wall-sided geometry. In this method, the fluid domain is divided, through a matching surface, into an inner domain and an outer domain. In the inner domain, the Rankine source is employed. In the outer domain, the transient Green's function is used. The

transient Green's function satisfies both the linearized free surface boundary conditions and radiation condition, implying that the matching surface can be placed fairly close to the body.

The concept of the mixed formulation is not new. Developments based on this type of the method have been made in the past. Dommermuth & Yue (1987) solved a nonlinear axisymmetrical flow with a free surface in the time-domain. Yeung & Cermelli (1993) calculated forced heaving motion of a 2-D submerged body with a free surface. Sierevogel, *et al.* (1996) solved the linear problem of a 3-D floating body with forward speed using a similar approach but a different Green's function in the outer domain. The intent of this paper is to extend the mixed formulation approach to general three-dimensional time-domain non-linear body-wave hydrodynamic problems with or without forward speed. The general formulation and numerical procedure of this approach are described in section 2. As discussed at the beginning of this section, the advantage of the mixed source formulation is that the Rankine source behaves better than the transient Green's function near the body and free surface intersection. As a result, the numerical scheme is much more robust. Numerical examples are presented to show this behavior. The new results are validated against available experimental data.

Another advantage of the mixed formulation is that the local free surface elevation is part of the solution, and no additional evaluation is needed as in the case of using the transient Green's function. To demonstrate this point, numerical results of radiation and diffraction waves of a large offshore platform in waves are presented and compared to results from other computation methods. In addition, the steady state wave pattern of a Navy surface combatant is computed and validated against experimental measurement. Finally, examples are presented to demonstrate the range of application of the current method to non-wall-sided and non-conventional hull forms.

MATHEMATICAL FORMULATION

The new mixed source formulation is developed using an approach similar to the original transient Green's function method. The problem considered is a general three-dimensional body floating on a free surface and undergoing arbitrary six-degree-of-freedom motion in the presence of incident waves. Potential flow theory is used to describe the fluid and the problem is solved in the time domain.

As shown in Figure 1, in the mixed source formulation, the fluid domain is divided into an inner domain (I) and an outer domain (II) by a matching surface S_m . In the inner domain, Rankine sources are distributed on the entire inner domain boundary S_I including the body surface S_b , the local free surface between the body surface and the matching surface S_f , and the matching surface S_m . The outer domain boundary S_{II} consists of the matching surface S_m , the remaining free surface, and an imaginary surface S_∞ at infinity. In the outer domain, the transient Green's function singularities are distributed only on the matching surface S_m because the transient Green's function satisfies both the linearized free-surface boundary conditions and the radiation conditions.

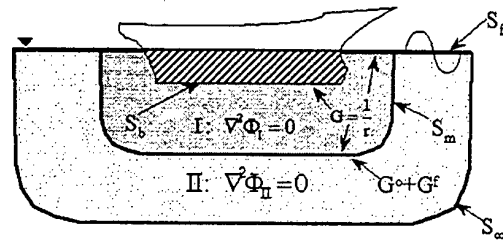


Figure 1: Computation domains in the mixed source formulation

In the inner domain, the total disturbance velocity potential Φ_I satisfies the Laplace's equation. The nonlinear body boundary condition is satisfied on the wetted body surface S_b under the undisturbed incident wave surface (the same as the "body-nonlinear" approach in the original LAMP formulation). The linearized free surface boundary conditions are satisfied on the part of the free surface S_f between the body surface and the matching surface. The boundary integral equation in terms of the Rankine source distribution on S_I can be written as

$$2\pi\Phi_I + \int_{S_I} (\Phi_I G_n - \Phi_n G) dS = 0$$

where $G = 1/|\bar{p} - \bar{q}|$, with \bar{p} and \bar{q} denoting the field point and source point, respectively. The subscript n denotes the directional derivative with

respect to the outward normal \vec{n} on the boundary of the inner domain.

In the outer domain, the total disturbance velocity potential Φ_{II} satisfies the Laplace's equation and the linearized free surface boundary conditions. With transient Green's function distribution on the matching surface, the boundary integral equation can be written as

$$2\pi\Phi_{II} + \int_{S_m} (\Phi_{II} G_n^0 - \Phi_{In} G^0) dS = M(\vec{p}, t)$$

The function $M(\vec{p}, t)$ is defined as

$$M(\vec{p}, t) = \int_0^t d\tau \left\{ \int_{S_m} (\Phi_{II} G_m^f - \Phi_{In} G_\tau^f) dS \right. \\ \left. + \frac{1}{g} \int_{\Gamma_m} (\Phi_{II} G_{\tau\tau}^f - \Phi_{II} G_\tau^f) V_N dL \right\}$$

where Γ_m is the waterline of the matching surface, V_N is the outward normal velocity of Γ_m relative to domain I , \vec{N} is the unit normal to the waterline on the free surface, t is time, and G^0 and G^f are the infinite frequency and memory function part of the transient Green's function (Lin and Yue, 1990).

The matching surface S_m is treated as a control surface. This control surface can be stationary in the case of zero or small horizontal body motions. This control surface can move with the body in the cases where the body has a large horizontal motion. On S_m , the matching conditions are imposed, requiring that the disturbance velocity potentials and their normal derivatives in the inner and outer domains be continuous. These conditions together with the integral equations for Φ_I , Φ_{II} and their normal derivatives form a coupled equation system for the velocity potential Φ_I on S_b , Φ_{In} on S_f , as well as Φ_I and Φ_{In} on S_m .

The solution is obtained at each time step with given Φ_{In} on S_b and Φ_I on S_f . The free surface boundary conditions on S_f are used to update the disturbance velocity potential and the disturbance free surface elevation in time. The time integration is performed using the fourth order Adams-Bashforth-Moulton formula.

As discussed before, one of the advantages of the mixed source formulation is that the Rankine source behaves much better than the transient Green's function near the body and free surface juncture

especially when the intersecting angle of the body geometry and the free surface is large. As a result, the numerical scheme is much more robust. In addition, the local free surface elevation is part of the solution. No additional evaluation is needed as in the case of the original formulation using the transient Green's function distribution on the body surface.

Another important feature of the new mixed source formulation is that the computation is much faster compared to the original formulation for body nonlinear cases. This is mainly due to the number of Green's function evaluation needed. In the original formulation, the memory effects have to be re-evaluated every time step from $t=0$ if the underwater part of the body geometry is changing during time stepping (because of large-amplitude body motions). The re-evaluation of the transient Green's function in the convolution integral is very time consuming. In the mixed source formulation, the transient Green's function singularities are only distributed on the matching surface. As long as the underwater part of the matching surface is the same during time stepping, the transient Green's functions does not have to be re-evaluated even in the case of large-amplitude body motions. In addition, the size and shape of the matching can be selected by the user to render most efficient and robust numerical solution.

DESCRIPTION OF THE LAMP SYSTEM

The new mixed source formulation is completed and has been integrated into the LAMP System as part of the nonlinear motion and load prediction capability. In this section, brief descriptions of the LAMP System and its newly added features are given. Other than the robustness of the method and computation efficiency, the noticeable addition of the updated LAMP System is the availability of the local free surface elevation. As shown in Figure 2, the LAMP System consists of three closely integrated modules. The first module is for the calculation of ship motions and wave-frequency loads. The second module is for the slamming impact computation. The third module is for computing whipping responses using a non-uniform-section dynamic beam method. In addition, the LAMP System includes an interface to provide loading information for finite element analysis. Various post-processing and visualization tools are available as part of the total LAMP System. The principle components of the LAMP System are discussed below.

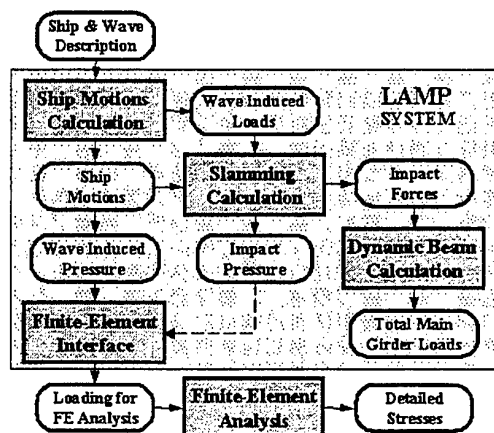


Figure 2: Components of the LAMP System

Linear and Nonlinear Ship Motions and Wave Frequency Loads

As described in the previous section, LAMP solves 3-D time-domain nonlinear motion and load problems using a potential-flow boundary-element method. In LAMP, a so-called "body-nonlinear" approach is used (see Lin and Yue, 1990 and 1993; and Lin, *et al.*, 1994). The body-nonlinear approach satisfies the body boundary condition exactly on the portion of the instantaneous body surface below the incident wave. It is assumed that both the radiation and diffraction waves are small compared to the incident wave so that the free surface boundary conditions can be linearized with respect to the incident wave surface. Note that with this formulation, both the body motions and the incident wave amplitude can be large relative to the draft of the ship. The "body-nonlinear" approach described above is designated as LAMP-4. In addition to 3-D large-amplitude hydrodynamics, LAMP-4 calculates nonlinear hydrostatic restoring and Froude-Krylov wave forces. A weakly nonlinear version of the code is also developed and designated as LAMP-2 that calculates 3-D linear hydrodynamics, but nonlinear hydrostatic restoring and Froude-Krylov wave forces. A complete linear version of the code, LAMP-1, is also available. LAMP-1 solves linear hydrodynamics, linear hydrostatic restoring, and Froude-Krylov wave forces.

In order to calculate the time-domain six-degree-of-freedom coupled motions for any ship heading and

speed, LAMP also includes nonlinear models for non-pressure forces including viscous roll damping, propeller thrust, bilge keels, rudder and anti-rolling fins, etc. For oblique seas cases, a PID (Proportional, Integral, and Derivative) course keeping rudder control algorithm and rudder servo model are implemented.

In addition to motion simulations, LAMP calculates the time-domain wave-induced global loads, including the vertical and lateral bending and torsional moments and shear forces, at any cross-section along the length of the ship. Furthermore, at each time step, LAMP calculates the relative motion of the ship and the wave as well as the hydrodynamic pressure distribution over the instantaneous wetted hull surface below the incident wave surface. The relative motion information is used as input for the impact load calculations. The mapped pressure distribution is used to derive input for finite element structural analysis.

Slamming Calculations for Impact Forces and Pressure

Wave impact loads on the ship can cause high-frequency structural responses. The term "impact" includes keel slam, bow flare impact, and stern overhang impact. As impact occurs, the ship structure responds at its structural natural frequency. The total loads at any section of the ship are the sum of the wave frequency loads and the high-frequency whipping loads. Depending on the severity of the impact, the whipping loads can be of the same order of magnitude as the wave-frequency loads. Therefore, in any extreme wave assessment, the effect of impacts must be included in the hydrodynamic computations.

Most traditional methods for analyzing impact loads rely on semi-empirical force estimates rather than on accurate physics-based prediction of the actual impact pressure distribution. Furthermore, the traditional methods address only head-sea cases with symmetric impact. However, experience indicates that structural failures in oblique seas usually result from asymmetric impact loads. It is important, therefore, that any attempt to resolve the total impact problem include not only the accurate time-domain simulation of the highly nonlinear relative motions in oblique seas, but also the prediction of both the symmetric and asymmetric impact pressures.

In the LAMP System, a post-processor is used for the either symmetrical or non-symmetrical impact

load predictions. It is assumed that the impacts do not affect the global ship motions. The previously computed global ship motions are used to compute relative motion of the ship bow and identify events where impact forces may be significant. The relative ship motion is then used to compute impact loads on 2-D cross sections of the ship for times when impact occurs. The forces from these impact events are then assimilated into an impact force history, which can be used to evaluate whipping loads.

Two levels of impact load computations are currently available. The first one is a simple 2-D empirical model based on momentum theory for global impact forces. The second one is a generalized 2-D Wagner approach based on the fully nonlinear boundary element approach of Zhao and Faltinsen (1993) for calculating impact forces and pressures. More discussion of these approaches and applications can be found in Weems *et al.* (1998).

Dynamic Beam Calculations for Whipping-Associated Loads

Once the sectional impact forces are computed, the main girder responses are computed in LAMP using a non-uniform-section dynamic beam method in order to get high-frequency global loads associated with whipping. The ship is modeled either as a uniform or a variable-mass beam. The total bending moment is obtained by combining the wave-frequency and the high-frequency bending moments with proper phasing.

Interface to Structural Finite-Element Analysis

The LAMP System calculates the pressure distribution over the instantaneous hull surface below the incident wave surface. The hull pressure information, combined with the acceleration data, can be used for finite element structural analysis. A generic interface between the LAMP motion and load calculations and structural finite element codes has been developed. The interface program reads nodal point coordinates and connectivity information (only surface nodes are needed) used in the finite element code and computes the forces acting on the nodal points. At specified time steps, the interface program writes the nodal point forces and ship acceleration information as outputs for the finite element structural analysis program. Other output from the LAMP/FE interface includes nodal pressure

history, sectional main girder loads for FE analysis of partial ship configurations, and external forces (*e.g.* control surfaces) that were modeled in the LAMP simulation but are not included in the pressure distribution. The latter forces must be accounted for so that forces and accelerations are properly balanced in any subsequent structural analysis.

NUMERICAL EXAMPLES

The accuracy and convergence of the mixed formulation were validated for a wide range of geometry including various ship hull forms with or without forward speeds. The results including the impulse response functions, Response Amplitude Operators, local wave elevations, and time history of motions and loads were compared with either existing experimental results or the results obtained by other numerical methods. It was found that the present method performs consistently well.

Selected examples are presented in this paper. These results include a flare body undergoing large-amplitude motions, radiation and diffraction waves of a large offshore platform, steady wave pattern of a naval surface combatant, the U.S. Navy AEGIS cruiser operating in storm sea conditions, and the motion and load predictions for an unconventional "tumblehome" configuration analyzed in a recent design effort.

A Flared Body with Large-Amplitude Motions

To illustrate that the new mixed formulation is suitable (actually better) for non-wall-sided bodies, the calculation of a flared body undergoing forced large-amplitude heaving motion was carried out. This axisymmetric flared body was constructed and tested by Troesch and Wang (1994) in their experimental study for slamming flow and green water on deck. The profile of this body is given in Figure 3 with the mean position of the body located at $Z=0.0$. Numerical results were generated by using the body-nonlinear approach to simulate the large-amplitude body motions. The history of the large-amplitude body motion is illustrated in Figure 4 with the three figures showing the mean, the lowest, and the highest locations of the periodic body motion. The body boundary condition is satisfied on the exact location of the wetted body surface (under the mean surface in this case).

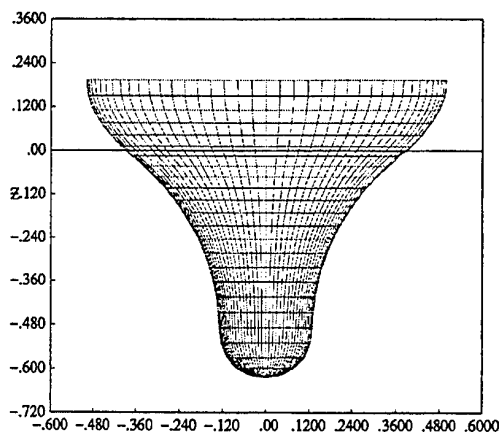


Figure 3: Profile of the flared body

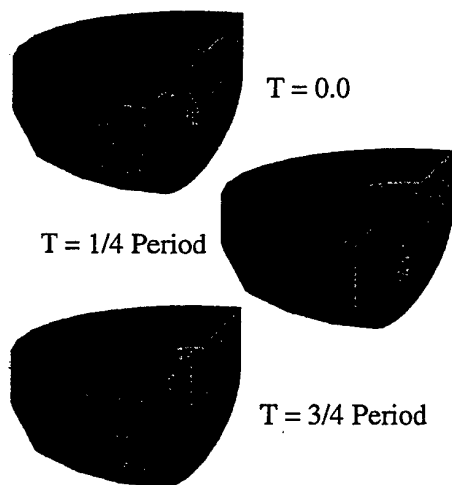


Figure 4: Position of a flared body undergoing large-amplitude motions

Numerical results from the original formulation (with transient Green's function distributed on the body surface) and the new mixed formulation are presented. The calculated hydrodynamic forces from the original formulation are plotted in Figure 5 together with the measured result (Troesch & Wang, 1994) and the results from a fully nonlinear calculation (Yue, 1997). As can be seen in the figure, the results from the original transient Green's function formulation gives non-physical high

frequency oscillations in the hydrodynamic force for this non-wall-sided body. On the other hand, the calculated hydrodynamic force obtained from the mixed formulation as shown in Figure 6 agrees quite well with the experimental result and the fully nonlinear result. This is a significant improvement over the method using the transient Green's function in terms of numerical stability and robustness.

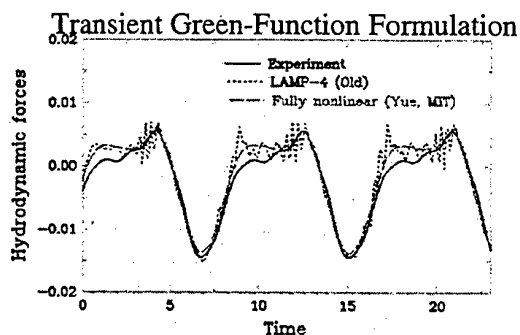


Figure 5: Time-history of the hydrodynamic forces using the original formulation

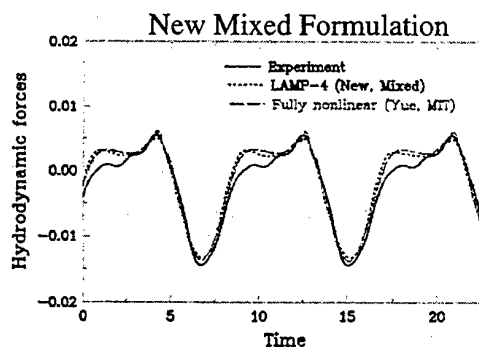


Figure 6: Time-history of the hydrodynamic forces using the new mixed source formulation

Wave Field around A Large Offshore Platform

As discussed previously, one of the advantages of the mixed formulation over the original formulation is that the solution on the local free surface between the body surface and the matching surface is part of the total solution. In other words, the free surface elevation and velocity potential come out directly as part of the solution, and no additional field point memory function evaluations are required. To illustrate this new and important feature of the mixed

formulation, the wave field around a free floating large offshore platform caused by incident waves is presented.

The platform used in this study (as shown in Figure 7) is one module of a conceptual design by the Bechtel National Corp. for the Mobile Offshore Base (MOB) platform (Wung, 1999). MOB is a large offshore platform intended for landing cargo planes in the ocean. The platform can be as long as 2 kilometers and is typically composed of several modules. The platform used in this study is a semi-submersible type platform around 450 meters long.

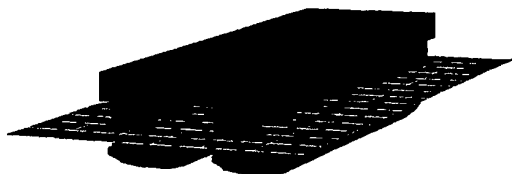


Figure 7: Geometry of one module of the Bechtel MOB design. (Geometry was provided by the Bechtel National Corp.)

One of the important design considerations for a MOB platform is the air gap between the wave surface and the bottom of the upper deck (this is true for offshore platform in general). This is a concern because the wave diffraction and radiation effects could amplify the incident waves under the deck structure. If the clearance between the wave surface and the deck is not large enough, waves may hit the bottom of the deck and cause structural damages.

A sample of the air gap results is given here. A body fitted free-surface grid is utilized for all of the results presented. A systematic study was performed to evaluate several key issues to ensure numerical convergence using the fitted free-surface grid. First the free-surface topology was determined to resolve the multiple waterline intersections with the body. The number of panels necessary to define the MOB geometry proved to be computationally challenging for evaluating the free-surface elevations, so the body and free-surface panel resolution was varied to determine the necessary number of panels to obtain convergence of the free-surface elevation. The effect of the matching surface density, size, and shape were also evaluated to ensure stable and converged calculations.

Numerous LAMP computations using the body fitted free-surface grid were performed to resolve the free-

surface elevations for a free-floating MOB in regular waves. A sample result of maximum free-surface wave amplitude is shown in Figure 8 for the 12-second incident wave coming from the right. The size of the computational domain is 650m. x 160m. The computation was run for 800 time steps (216 seconds) and consisted of 2736 body panels, 11200 free-surface panels, and 800 matching surface panels. As can be seen in the figure, the wave is amplified significantly between the fifth and the sixth set of columns.

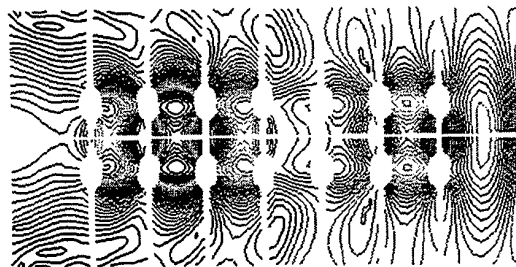


Figure 8: Maximum wave elevation of a MOB platform with a 12-second incident coming from the right - LAMP prediction

The LAMP predictions of the wave elevation at the centerline of the platform in this case are compared with results from WAMIT and MORA in Figure 9. Linear free surface boundary conditions are used in all three computations. LAMP result compares fairly well with results from both WAMIT and MORA. All three results show large wave amplification between column 5 and 6.

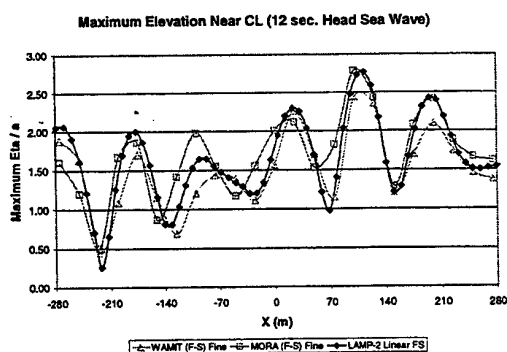


Figure 9: Comparison of free-surface elevation among LAMP, WAMIT, and MORA for 12-second incident wave. (Results from WAMIT and MORA were provided by Bechtel National Inc.).

A similar comparison is given in Figure 10 where the incident wave period is 10 second. As can be seen, LAMP predictions are again compared well with results from both WAMIT and MORA. In this case, the maximum amplification factor is around 1.5. In general, the wave amplification factor can be very different at different incident wave conditions.

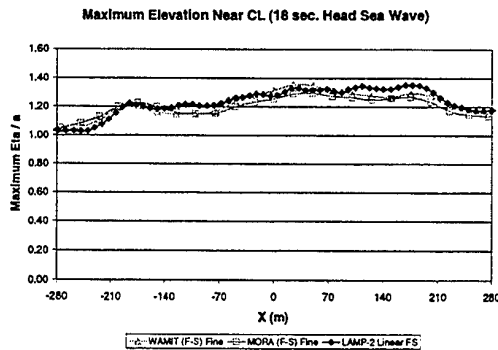


Figure 10: Maximum wave elevation of a MOB platform with 18-second incident wave. (Results from WAMIT and MORA were provided by the Bechtel National Inc.)

Steady Wave Pattern of a Surface Combatant

Calculations were performed to evaluate the ability of the mixed source formulation for predicting the steady wave pattern generated by a ship moving with a constant forward speed. In this section, the steady ship waves for the DTMB Model 5415 surface combatant at Froude numbers 0.2755 is presented and compared with experimental measurement (experiment was performed at NSWCCD Carderock Division). The profile view of the 5415 model geometry is shown in Figure 11. The flow field around this particular model has been systematically studied and compared with results from several Reynolds-Averaged Navier-Stokes and potential flow computation methods (Ratcliffe, 1998).

In the current study, computations were also done by the well-established potential flow code SLAW (Ship Lift and Waves). The SLAW code system is a potential-flow panel-method code for steady ship free-surface flow prediction using a Dawson-type approach. SLAW has been extensively validated and applied to a variety of hull forms, ranging from naval ships to commercial tankers to America's Cup Yachts. The SLAW results were used as a guide in

developing the LAMP free surface model and to evaluate hull and free surface panel models.

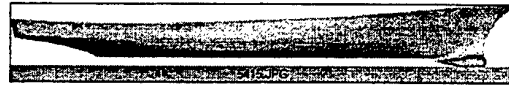


Figure 11: Geometry of Model 5415 (Picture from the web site: <http://www50.dt.navy.mil/5415>)

The LAMP computations of the steady wave pattern for the DTMB Model 5415 surface combatant used 896 hull body panels, 800 outer boundary panels, and 5300 free surface panels in an O-grid topology. The O-grid was used in this case to better resolve the region near the transom stern.

In Figure 12, the wave elevations at the waterline are shown for both the experimental data and the LAMP calculation. As can be seen in the figure, the LAMP calculation significantly under-predicts the waterline elevation in the bow region. It can be observed in the experiment in this case that the bow wave is very steep and near breaking. It is believed that nonlinear free surface boundary conditions are required for more accurate prediction. To confirm this behavior, the wave elevation prediction was done by SLAW. It was found that the SLAW, with linearized free surface boundary conditions, gives a similar prediction as that predicted by LAMP in the bow region. The remainder of the LAMP-calculated waterline seems to reasonably follow the elevation trend, especially in the stern region. It may be noted that LAMP captures the trend of the experimental data well, although the trough and peak just after the bow are under-predicted. More details of wave pattern prediction for this hull form can be found in Ratcliffe (1998).

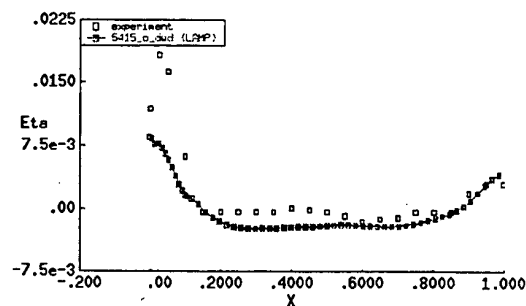


Figure 11: Wave profile comparison along the waterline for DTMB Model 5415.

In Figure 13 and 14, the free surface elevation contours from the experimental data and the LAMP calculation for the DTMB Model 5415 are shown. As can be seen in the Figure, the general feature of the wave pattern predicted by LAMP compares reasonably well with experimental measurement indicating the linear free surface boundary conditions are adequate for most of the flow region.

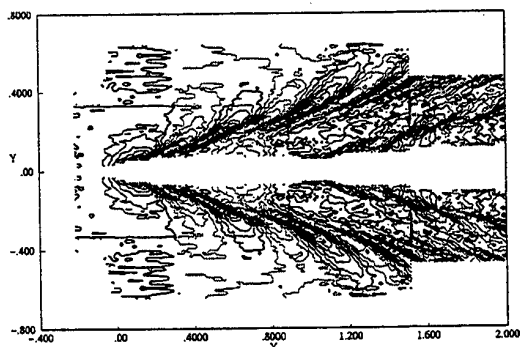


Figure 13: Wave contours for the DTMB Model 5415 at constant forward speed - experiment

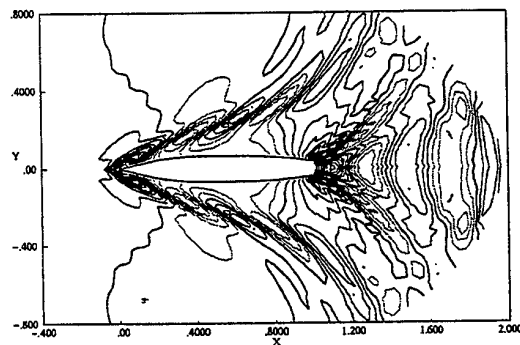


Figure 14: Wave contours for the DTMB Model 5415 at constant forward speed - LAMP

Naval Cruiser in Storm Waves

Further validation of the method is performed of a modern Navy ship (CG47) traveling in storm sea conditions. This case was studied before using the original transient Green's function formulation (Engle, *et al.* 1997; and Weems, *et al.* 1998). It is now tested again using the new mixed formulation to study the robustness of the code for body with large-amplitude motions.

The U.S. Navy's AEGIS cruiser (CG-47) is a typical modern combatant hull form for which a large amount of model and full-scale motion and load data is available (Hay, *et al.*, 1994). A view of the CG-47 cruiser, with its fine U-shaped bow, sonar dome, and large bow flare, is shown in Figure 15. The penalization of this hull form for the mixed formulation is show in Figure 16.

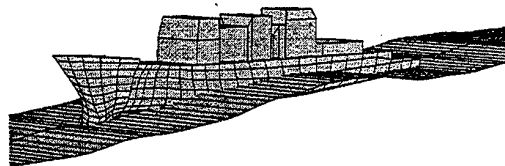


Figure 15: CG-47 AEGIS Cruiser in Waves

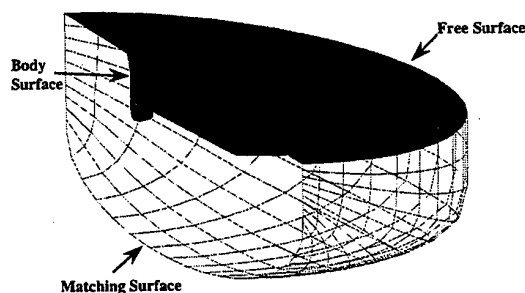


Figure 16: Numerical grid for the CG-47 hull

Figure 17 shows a comparison of LAMP-1 results and experimental measurements for a two-minute real time record of this ship moving at 10 knots in storm sea conditions. In the top plot, which shows the incident wave elevation at the ship's center of gravity, it can be seen that the maximum wave height in this record reaches about 55 ft (16.8m). The remaining three plots show heave and pitch motions and the vertical bending moment at Frame 174 of the model, which is located just forward of the deckhouse. Except for an initial transient period in the calculation, the motion comparisons are excellent. However, comparison for the sectional vertical bending moment is not as good. These typical results show how linear hydrodynamics are adequate for predicting head seas motion but underpredict peak wave loads, especially near maximum sagging situations.

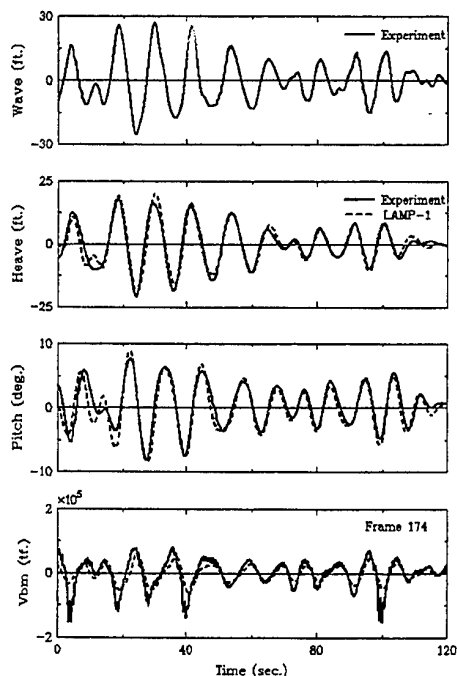


Figure 17: Computation vs. Experiment for CG-47 AEGIS Cruiser in Head Storm Seas

Again, to illustrate the importance of nonlinear geometry and hydrodynamics, LAMP-2 results are shown in Figure 18 for the sagging peak at $T=100$ seconds. These results include the bending moment components at both the wave frequency and high frequency whipping responses due to impact. Near the peak of the sagging moment, not only the magnitude of the moment is comparable, but the frequency and amplitude of the calculated whipping response agree well with the experimental results. The whipping responses are mainly caused by impact on the bow flare. The whipping responses significantly increase the total bending moment during the sagging cycle. Similar results can be obtained using a LAMP-4 computation, indicating that hydrostatic and incident wave effects dominate these vertical loads.

It is worthwhile to note that in the computation is about 40 times faster using the mixed formulation compared than using the original transient Green's function approach. This is due to the fact that the matching surface is remained the same in the mixed formulation while the body is performing large-amplitude motions. Therefore, the memory functions in the convolution integral do not have to be re-evaluated from at beginning at every time step.

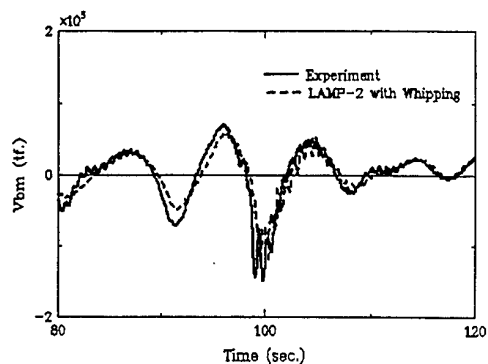


Figure 18: Time History of Vertical Bending Moment Comparison of CG-47 at Frame 174

Wave Piercer Hull Form Design

The LAMP System was employed recently for a "wave piercer" high-speed hull form concept under development at Bath Iron Works (General Dynamics/Marine). Because of the unconventional "tumblehome" hull configuration, there was considerable concern about operability and loads in extreme seas. We are also interested in the ability of current computation techniques to evaluate the ship's seakeeping performance. A view of the hull is shown in Figure 19. In addition to the tumblehome bow shape, this ship has very long overhanging stern.

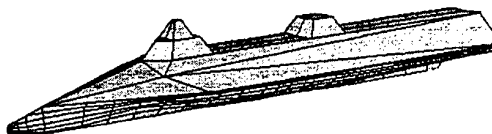


Figure 19: Conceptual "Wave Piercer" Geometry

To address these concerns, a seakeeping study was performed, including both model tests at the U.S. CD-NSWC and computational analysis with the LAMP System. Computations using the original transient Green's function approach were done with special treatment of the panels on the long overhanging stern. In this region, the intersection angle of the hull geometry and the free surface is small. Transient Green's function distribution on panels in this area exhibits highly oscillatory behavior. Contributions from some of the panels have to be removed to avoid unrealistic solution.

The new mixed formulation was used to re-examine the computation of this ship. It was found that the numerical scheme was very robust and results were very stable. The results of the original computation can be found in Weems (1998). The computation results using the new method are not reproduced in this paper.

CONCLUSION

A new mixed source formulation is presented here for solving 3-D free-surface ship and platform hydrodynamic problems in the time domain. In addition to computing linear and nonlinear ship motions and wave loads, the new method can also be used to calculate the local free surface elevation. Examples presented in the paper demonstrate the robustness and effectiveness of the new method especially for non-wall-sided geometry. Further validation of the new method is currently ongoing. The mixed formulation is developed in the framework of the LAMP System to provide a systematic and integrated solution for practical application to ship and platform design, evaluation, and assessment.

ACKNOWLEDGEMENTS

The development of the mixed source formulation has been supported by the Naval Sea System Command (NAVSEA) and the Office of Naval Research (ONR) under the Dynamic Assessment of Surface Ship (DASS) project. The development of the LAMP System has been supported by DARPA, the U.S. Coast Guard, NAVSEA, ONR, American Bureau of Shipping (ABS), and SAIC. The authors would like to thank Mr. Allen Engle and Dr. Edwin Rood for their encouragement and support. The authors are also grateful to Mike Meinhold, Thomas Treacle, and Marian Weems for their assistance in the LAMP System development.

REFERENCES

- Hay, W., J. Bourne, A. Engle, & R. Rubel, "Characteristics of Hydrodynamics Loads Data for a Naval Combatant," Hydroelasticity in Marine Technology, Rotterdam, the Netherlands, 1994.
- Dommermuth, D.G. & Yue, D.K.P., "Numerical Simulations of Nonlinear Axisymmetric Flows with a Free Surface," Journal of Fluid Mechanics, 1987, Vol. 178, pp. 195-219
- Engle, A., Lin, W., Salvesen, N., & Shin, Y., "Application of 3-D Nonlinear Wave-Load and Structural Response Simulations in Naval Ship Design," Naval Engineering Journal, 1997, Vol. 109, No. 3.
- Nakos, D.E., D. Kring, & P.D. Sclavounos, "Rankine Panel Methods for Transient Free-Surface Flows," Proceedings of the Sixth International Conference on Numerical Ship Hydrodynamics, Iowa, U.S.A. 1993.
- Lin, W.M., & Yue, D.K.P., "Numerical Solutions for Large-Amplitude Ship Motions in the Time-Domain," Proceedings of the Eighteenth Symposium of Naval Hydrodynamics, The University of Michigan, U.S.A., 1990.
- Lin, W.M., & Yue, D.K.P., "Time-Domain Analysis for Floating Bodies in Mild-Slope Waves of Large Amplitude," Proceedings of the Eighth International Workshop on Water Waves and Floating Bodies, Newfoundland, Canada, 1993.
- Lin, W.M., Meinhold, M.J., Salvesen, N., & Yue, D.K.P., "Large-Amplitude Ship Motions and Wave Loads for Ship Design," Proceedings of the Twentieth Symposium of Naval Hydrodynamics, The University of California, U.S.A., 1994.
- Ratcliffe, T., "Validation of Free Surface Reynold's Averaged Navier Stokes and Potential Flow Codes," Proceedings of the Twenty-Second Symposium on Naval Hydrodynamics, Washington, D.C. U.S.A., 1998.
- Sierevogel, L., Hermans, A. & Huijsmans, R., "Time-Domain Calculations of First- and Second-Order Forces on a Vessel Sailing in Waves", Proceedings of the Twenty-First Symposium of Naval Hydrodynamics, Trondheim, Norway, 1996
- Troesch, A.W. & Wang, M., "An Experimental Study for Slamming Flow and Green Water on Deck", Technical Report No. 327, Department of Naval Architecture and Marine Engineering, University of Michigan, 1994.
- Yeung, R. & Cermelli, C.A., "The Shell Functions: A Global Method for Computing Free-Surface Time-Dependent Flows", Proceedings of the 8th International Workshop Water Waves & Floating Bodies, St. John's, Newfoundland, 1993.
- Yue, D.K.P., "Fully Nonlinear Computation for A Flared Body with Large-Amplitude Motions," Private Communication, 1997.
- Weems, K., Zhang, S., Lin, W., Shin, Y., & Bennett, J., "Structural Dynamic Loadings Due to Impact and Whipping," Proceedings of the Seventh International Symposium on Practical Design of Ship and Mobile Units, The Hague, The

Netherlands, 1998.

Wung, C., "Design Tools Benchmark Study,"
The Fourth Mobile Offshore Base Technology
Exchange Conference, Rosslyn, VA, 1999

Zhao, R., & O. Faltinsen, "Water Entry of Two-
Dimensional Bodies," Journal of Fluid Mechanics,
1993, vol. 246, pp. 593-612.

ACCELERATED, NONLINEAR WAVE SIMULATIONS FOR LARGE STRUCTURES

D. Kring, T. Korsmeyer, J. Singer, D. Danmeier, J. White
Research Laboratory of Electronics
Massachusetts Institute of Technology
Cambridge, MA, USA 02139-4307
E-Mail: kring@rle-vlsi.mit.edu

ABSTRACT

A method is presented for the solution of nonlinear wave-body interactions. The exact free-surface boundary conditions are solved in a Zakharov framework with surface piercing bodies and forward speed effects. This potential flow problem is solved by a high-order, geometry-independent, BEM in a Rankine, time-domain approach. Low and high-order acceleration schemes reduce computational CPU time and memory costs, which allows the method to be used for large, complicated structures.

INTRODUCTION

Ocean structures and ships, subject to extreme wave events, often possess complicated geometry and dynamics. While linear wave theory is sufficient in many cases, a solution of the exact free-surface and body boundary conditions is necessary for some problems. However, most current implementations of fully nonlinear theory have been restricted to simple bodies. Engineering applications that require local accuracy over large, complicated geometries motivates a search for a stable, efficient simulation of nonlinear seakeeping.

A high-order, geometry-independent, boundary element method (BEM) combined with order- N acceleration offers a numerical solution with the necessary efficiency and accuracy. Using this high-order discretization, a stable method results for a Zakharov formulation of the exact free-surface conditions. Acceleration algorithms make this method suitable for complicated free-surface problems.

This fully nonlinear formulation uses the linear Rankine theory introduced in [1] and [2]. Its numerical solution adapts the high-order BEM of [3] to the Rankine approach. Elements are placed on the elevated free surface and the wetted body surface to discretize the boundary-integral form of the Laplace equation.

This nonlinear Zakharov formulation differs from previous work that used a spectral representation of the free surface and considered only submerged bodies [4]. Spectral methods are difficult to extend to sur-

face piercing bodies, but the method presented here allows surface piercing bodies, forward speed, and varying degrees of nonlinearity in the boundary conditions. This last feature provides a convenient framework for gauging the significance of different nonlinearities.

Using a conventional iterative procedure for solving the boundary-integral equation, this method is only practical for simple problems. The large and complex problems contemplated here require so-called "fast" algorithms such as fast-multipole or pre-corrected Fast Fourier Transform (pFFT) to make the potential solution tractable. Based on the fast summation techniques used in many-particle problems, these algorithms were first combined with BEM for electrostatic analysis [5] [6]. Applied to BEM, these fast or "acceleration" algorithms effectively render the dense linear systems sparse. An unaccelerated or dense solution technique requires order- N^2 cost to set up and iteratively solve the linear system, where N is the number of unknowns. Fast algorithms avoid all but an order- N subset of the system setup and pFFT, for instance, only requires order- $N \log(N)$ effort for the solve. Since the solution of the boundary-integral equation is the dominant computational cost in these free-surface problems, acceleration allows for complicated problems to be solved in a reasonable time.

An example of a large structure that requires an accelerated solution is seen in the Mobile Offshore Base (MOB) project. At over a mile in length, the base must operate and survive in the most extreme environments in any ocean. One concept for this float-

ing air and sea port consists of five connected semi-submersibles. This large, complicated geometry includes a total of fifty vertical columns and ten horizontal pontoons. Even a linearized analysis of such a structure is computationally challenging by classical BEM. However, this structure has been analyzed by a pFFT accelerated, linear, frequency domain method using almost 100,000 boundary elements on an engineering workstation [7].

This paper first presents the Zakharov nonlinear formulation and discusses the implementation of the high-order, geometry-independent BEM. Stability and convergence of the method are demonstrated for a simple body in heave and surge using the dense solution. The paper then describes solution acceleration algorithms for a low and high-order BEM. A unit of the MOB is simulated in heave in order to demonstrate the computation advantage of acceleration. Forward speed capabilities are also demonstrated.

The intent of the present study is to demonstrate a method that is stable, convergent, and applicable to complicated problems.

NONLINEAR, TIME-DOMAIN SIMULATION

The following nonlinear, time-domain method considers three-dimensional potential flow with the exact free-surface and body boundary conditions. Surface tension and viscous effects are not included and the wave elevation is assumed to be single valued. Therefore, wave breaking and spray are not considered.

This section presents the Zakharov nonlinear formulation of the problem and its numerical implementation using the high-order boundary elements of [8] and [3]. The Rankine approach for discretizing the boundary value problem in the time-domain follows the linear theory introduced by [1].

Formulation

The Laplace equation governs the velocity potential, $\phi(x, y, z, t)$,

$$\nabla^2 \phi = 0 \quad \text{in } \mathcal{V}, \quad (1)$$

in the fluid volume, \mathcal{V} , bounded by the elevated free surface, $S_F(t)$, and wetted body surfaces, $S_B(t)$.

The exact free-surface conditions, with the wave elevation, $\zeta(x, y, t)$, assumed to be single valued, are posed in the inertial frame. Here z represents the vertical direction and a gravitational constant, g , is assumed. A kinematic condition defines the motion of the material free surface,

$$\left(\frac{\partial}{\partial t} + \nabla \phi \cdot \nabla \right) [z - \zeta(x, y, t)] = 0, \quad \text{on } z = \zeta, \quad (2)$$

and a dynamic condition poses a constant pressure at the air-water interface,

$$\frac{\partial \phi}{\partial t} = -g\zeta - \frac{1}{2} \nabla \phi \cdot \nabla \phi, \quad \text{on } z = \zeta. \quad (3)$$

In existing methods, this is sometimes linearized through a perturbation expansion for small wave slope about the mean free surface, $z = 0$, with a basis flow such as free stream or double-body. In the present method the exact free-surface conditions are imposed on the instantaneous free surface at $z = \zeta$.

The exact "no-flux" body-boundary condition states that the normal derivative of the velocity potential must be equal to the normal component of the body velocity, \vec{V} , over its entire, instantaneous wetted surface,

$$\nabla \phi \cdot \hat{n} = \vec{V} \cdot \hat{n}. \quad (4)$$

This boundary condition can be linearized by a Taylor expansion about the mean body surface below $z = 0$. A variant called the body-nonlinear formulation uses a linearized free surface condition but retains the exact body-boundary condition below $z = 0$. In the present fully-nonlinear formulation the exact body boundary conditions are imposed up to the waterline at $z = \zeta$ defined by the exact free surface.

The body velocity is specified for radiation or diffraction problems, or it can be determined by solving the equations of motion for the body according to [9], [10], or [11].

A radiation condition closes the problem. Radiated and scattered waves are absorbed by a numerical beach [1] [12].

Zakharov nonlinear free-surface conditions

The exact free surface conditions (2) and (3) are applied in a Zakharov framework that tracks the potential at a point that follows the free surface. This differs from the Eulerian frame, fixed at a point in the volume, and the Lagrangian frame, that tracks moving fluid particles. The frame of reference defines the partial time derivative which has important numerical implications.

An Eulerian point does not follow the moving free surface. At one moment a Eulerian point may be above the free surface and at the next moment it may be below. The numerical extrapolation needed to evaluate the time derivative from one Eulerian point to another can lead to non-convergence in the temporal integration.

The Lagrangian point that follows a physical fluid particle has a numerically consistent expression for the time derivative, but creates other difficulties since particles may gather at stagnation points or violate

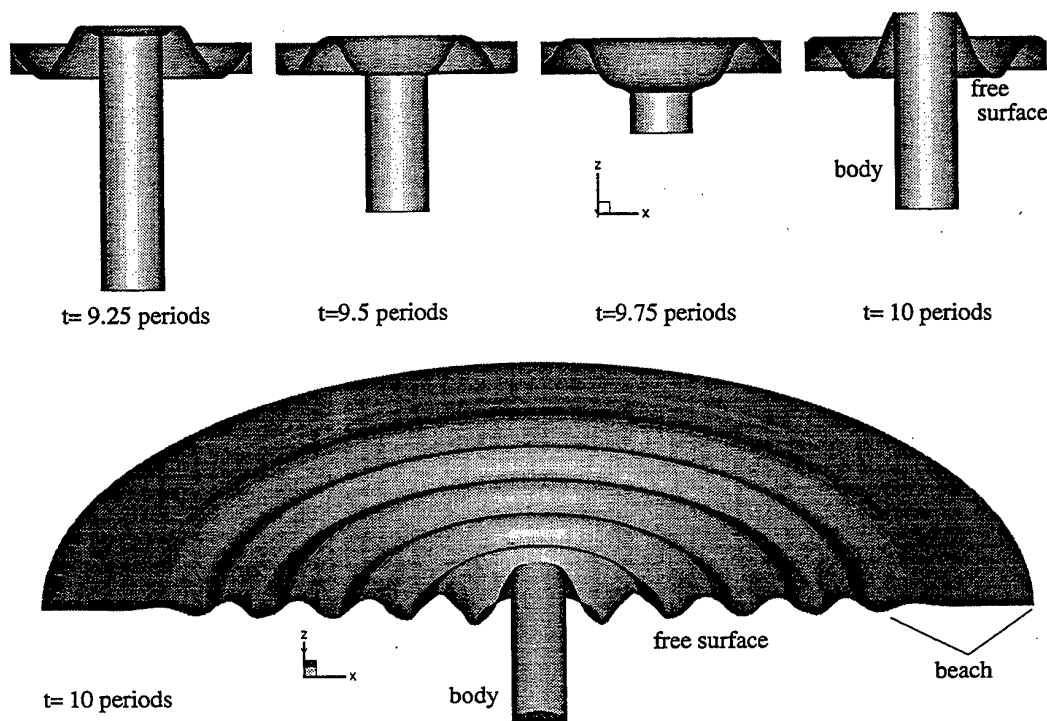


Figure 1: Snapshots of free surface and wetted body geometry for a heaving cylinder through one period. The cylinder has a radius, a , and depth, $0.5a$. The heave period is $T\sqrt{g/a} = 4$. Vertical scale $\times 10$.

material boundaries. Regridding to compensate for these problems leads to numerical error. This was one reason that the Zakharov formulation was chosen over the Mixed Eulerian-Lagrangian approach of [13]. Other reasons for this choice include the numerical stability properties of MEL schemes and a desire to avoid wave breaking in the simulation.

The Zakharov formulation allows a consistent treatment of the time-derivative in the free-surface conditions without violating boundary conditions since mathematical points can be constrained. This method, using a parametric representation of the flow and geometry, can track points that lie on a moving waterline, for instance.

The Zakharov formulation has been implemented previously in a spectral method study of nonlinear wave interactions for periodic free-surface domains [4]. This method was extended in [14] to include a submerged sphere. A mixed spectral/BEM for general submerged bodies was presented in [15]. These methods all posed a series of integral equations about the mean free surface through a Taylor expansion

of the vertical flux, ϕ_z .

The re-formulation of the exact free-surface conditions (2) (3) begins by defining a surface potential, φ , on the moving free surface,

$$\varphi(x, y, t) \equiv \phi(x, y, \zeta(x, y, t), t). \quad (5)$$

This surface potential is equivalent to the volume potential, ϕ , at the instantaneous position of the free surface. Its purpose is to provide a mathematical marker on which to apply the boundary conditions. By applying the chain rule, the Eulerian time-derivative of the volume potential can be consistently modified for the partial time-derivative that tracks the moving free surface. This is a Galilean transform of the free-surface conditions moving along a vertical column:

$$\frac{\partial}{\partial t} \phi = \frac{\partial}{\partial t} \varphi - \phi_z \frac{\partial}{\partial t} \zeta. \quad (6)$$

Since the surface potential contains no information about the vertical velocity of the fluid, ϕ_z must be retained in the conditions. Through another application of the chain rule, this leads to a type of stretching

for the horizontal gradient of the surface potential that depends on the local wave slope:

$$\nabla\phi - \phi_z = \nabla\varphi - \phi_z \nabla\zeta. \quad (7)$$

Here, the gradient for the surface potential is understood to mean only the horizontal components.

At this point, a modification to the Zakharov formulation is offered in order to allow for surface piercing bodies. Except for heaving wall-sided bodies, a vertical column cannot be defined. Looking down on the free surface, the waterline defines a "footprint" that changes shape as a function of body and wave motion. To account for this, a horizontal Gallilean transformation is applied.

A parametric space (u, v) , which is fixed for all time, is defined for the body and free-surface geometry. The physical motion of any geometric point in parametric space is defined through a three-dimensional mapping that is a function of time. The waterline intersection of the body and free surface are always fixed in parametric space even though the physical waterline and its footprint may vary. Parametric space provides the frame of reference in which to pose the free-surface conditions. The Zakharov surface potential tracks the vertical motion and the Gallilean transform tracks the horizontal motion at parametric points,

$$\begin{aligned} \frac{\partial}{\partial t} \varphi(\vec{x}(u, v, t)) &= \frac{\partial}{\partial t} \varphi(u, v, t) \\ &\quad - \frac{\partial \vec{x}(u, v, t)}{\partial t} \cdot \nabla \varphi(u, v, t) \end{aligned} \quad (8)$$

A similar horizontal Gallilean transformation is applied for the wave elevation, ζ . On the body, where only the volume potential is defined, the three-dimensional transform is used for the temporal derivative.

Forward speed for the entire domain can also be included, so that the total motion for the frame of reference at any point, (u, v) , is now $(\vec{W} + \frac{\partial \vec{x}}{\partial t})$. This forward speed, \vec{W} , is imposed uniformly at all points. If there are multiple bodies moving in different directions, an inertial frame of reference must be used and all forward speed effects will be in the time-dependent part of the transform.

An important implication of this horizontal motion is that both the body boundary and free-surface conditions are imposed consistently the waterline. This consistency means that three sources of numerical error are avoided. First, there is no accumulation of error in the time derivative that can occur with an Eulerian scheme, where errors at each time-step of order ΔT summated over $n = 1/(\Delta T)$ time-steps lead

to global errors of order 1. Second, there is no numerical regridding. This can occur when Lagrangian points are interpolated or extrapolated to new positions to compensate for particles that collect in areas of high spatial gradients or artificially pierce the body. Third, the free surface and body boundary conditions are both satisfied at the waterline. The importance of numerically imposing both these conditions is discussed in [16].

Another consideration that must be addressed is the presence of a waterline singularity in the potential flow formulation for impulsive body motion perpendicular to the free surface [17]. This issue will be discussed with the numerical results for a surging body since it depends on a combination of theoretical, numerical, and practical considerations.

The final form with surface-piercing bodies and forward speed follows for the kinematic free-surface condition:

$$\begin{aligned} \left[\frac{\partial}{\partial t} - (\vec{W} + \frac{\partial \vec{x}}{\partial t}) \cdot \nabla \right] \zeta &= (1 + \nabla \zeta \cdot \nabla \zeta) \phi_z \\ &\quad - \nabla \varphi \cdot \nabla \zeta, \quad \text{on } z = \zeta, \end{aligned} \quad (9)$$

and for the dynamic free-surface condition:

$$\begin{aligned} \left[\frac{\partial}{\partial t} - (\vec{W} + \frac{\partial \vec{x}}{\partial t}) \cdot \nabla \right] \varphi &= -g\zeta - \frac{1}{2} \nabla \varphi \cdot \nabla \varphi \\ &\quad + \frac{1}{2} (1 + \nabla \zeta \cdot \nabla \zeta) \phi_z^2, \quad \text{on } z = \zeta. \end{aligned} \quad (10)$$

Boundary-integral equation

The boundary value problem for the velocity potential, ϕ , is recast as a boundary-integral equation through Green's second identity,

$$\begin{aligned} 2\pi\phi(\vec{x}) - \iint_{S_F \cup S_B} \frac{\partial \phi(\vec{x}')}{\partial n} G(\vec{x}'; \vec{x}) dx' \\ + \iint_{S_F \cup S_B} \phi(\vec{x}') \frac{\partial G(\vec{x}'; \vec{x})}{\partial n} dx' = 0 \end{aligned} \quad (11)$$

where $G(\vec{x}'; \vec{x})$ is the Rankine source potential,

$$G(\vec{x}'; \vec{x}) = \frac{1}{|\vec{x} - \vec{x}'|}. \quad (12)$$

This Green function is the fundamental solution of the governing equation and also satisfies a vanishing potential condition in the fluid domain far from any bodies. In this time-domain formulation, (11) is solved as a mixed first- and second-kind Fredholm equation. On the body boundary the Neumann condition is specified by (4). On the free surface the Dirichlet condition is specified by the wave potential from the temporal integration of the free-surface conditions (9) and (10).

Numerical Implementation

At each time instant after the startup, two computational procedures are undertaken. First, the free-surface conditions are numerically integrated in time and then the boundary-integral equation for the potential is satisfied.

Before startup, initial conditions are specified for the wave elevation and potential. Typically, these are assumed to be trivial. The startup, at $t = 0^+$, is impulsive and the boundary integral equation is satisfied to obtain the vertical flux, ϕ_z , that forces the evolution of the free-surface waves.

Temporal integration

The numerical integration of the Zakharov free-surface conditions uses the same mixed explicit-implicit Euler scheme used for the linear problem [1]. In this scheme the kinematic free-surface condition is integrated with an explicit Euler integration and the dynamic free-surface condition is integrated with an partially-implicit Euler integration. A higher-order variant, a mixed Trapezoidal-Leapfrog scheme, could also be used. These schemes, designed through an error analysis for the propagation of waves over a discrete free surface, result in a neutrally stable free surface evolution that has no numerical dissipation.

The linear terms in the dynamic condition are considered implicitly, which is necessary for numerical stability. The nonlinear terms are treated explicitly in both the kinematic and dynamic condition. The weak nonlinear terms do not seem to affect numerical stability. This combination of implicit linear terms and explicit nonlinear terms is referred to as "partially-implicit".

The temporal integration scheme for the Zakharov formulation is,

$$\zeta^{n+1} = \zeta^n + \Delta t \left[\left(\vec{W} + \frac{\partial \vec{x}^n}{\partial t} \right) \cdot \nabla \zeta^n + (1 + \nabla \zeta^n \cdot \nabla \zeta^n) \phi_z^n - \nabla \varphi^n \cdot \nabla \zeta^n \right], \quad (13)$$

and

$$\begin{aligned} \varphi^{n+1} - \Delta t \left[\left(\vec{W} + \frac{\partial \vec{x}^n}{\partial t} \right) \cdot \nabla \varphi^{n+1} \right] = \\ \varphi^n + \Delta t \left[-g \zeta^{n+1} - \frac{1}{2} \nabla \varphi^n \cdot \nabla \varphi^n + \frac{1}{2} (1 + \nabla \zeta^{n+1} \cdot \nabla \zeta^{n+1}) (\phi_z^n)^2 \right], \quad (14) \end{aligned}$$

The spatial discretization of the unknowns, ζ , φ , and ϕ_z , are expressed by arbitrary-order B-splines consistent with the basis functions used to solve the governing boundary-integral equation.

High-order, geometry-independent BEM

With the wave potential obtained from the evolution of the free-surface conditions and the normal flux obtained from the body boundary conditions, satisfying the governing boundary-integral equation closes the problem for the present time-step.

This mixed Neumann-Dirichlet, boundary-integral equation is solved using a high-order, geometry-independent BEM. The main feature of this spatial discretization is the independent treatment of the fluid flow and body geometry by parametric mappings. This allows for a consistent formulation at the moving waterline.

The method is geometry-independent. Unlike a traditional panel method there is no fixed relation between the discretization of the fluid flow and the body geometry. The velocity potential on the body is expressed as a collection of arbitrary-order B-splines in parametric space,

$$\phi(u, v) = \sum_{m=1}^{M+k-1} \sum_{n=1}^{N+k-1} \hat{\phi}_{mn} B_m(u) B_n(v), \quad (15)$$

where, M, N are the number of high-order elements in either direction, k is the order of the B-spline, $\hat{\phi}_{mn}$ are the spline coefficients, and B are the basis functions of order k . Clamped splines are used to improve numerical conditioning. On the free surface, the wave elevation, ζ , and normal flux, ϕ_z , are treated as separate unknowns using this B-spline form.

There are no restrictions on the representation of body geometries. The method only requires a mapping from the parametric to the physical space from which the physical coordinates, normal vector, and Jacobian can be obtained. The body geometry can be expressed analytically or numerically, through a library of shapes, a CAD package, or by a set of NURBS, for example. One advantage of this approach is that accuracy now depends upon the discretization of the flow alone which facilitates automatic convergence and error control. The mapping automatically defines the wetted body surface at each time step through an intermediate Gordon-Coon's mapping [18] that trims the complete structure. This geometry-independent approach is not used on the free surface since the B-spline for the wave elevation, ζ , defines the wave geometry.

The boundary-integral equation is solved with a Galerkin procedure. While the Galerkin method has the same asymptotic convergence rate as collocation, it is usually more accurate, for both local and global error metrics, for a given discretization. In coupling this hydrodynamic simulation to structural analysis programs, for instance, the ability of the BEM to

have good local accuracy on geometries that match the structure is very important. For the Rankine approach, high-order discretization of the flow is important for numerical stability.

At forward speed, a low-pass spatial filter (as developed for the linear formulation) is applied to eliminate spurious grid-scale waves that have the wrong group velocity. These short waves are not unstable in the sense of the sawtooth waves of MEL schemes and only need to be spatially filtered once every 50 to 100 time steps. At zero speed, filters are never used.

Truncated, vertical cylinder

The high-order BEM has been implemented with the unaccelerated (dense) solution of the boundary integral equation. Both the linear and fully nonlinear free-surface conditions are applied for a truncated, vertical cylinder forced to heave. The results are non-dimensionalized for a cylinder of radius, a , and draft, $d/a = 0.5$. For this simulation, a period of $T\sqrt{g/a} = 4$ and heave amplitude of $A/a = 0.25$ was chosen. The heave amplitude is the maximum that keeps at least part of the cylinder wet at all times. The method was tested to insure that the nonlinear results approach the linear results in the limit of small wave steepness.

The simulation of heave, illustrated by the wave pattern snapshots shown in Figure 1, was run for ten periods, at which point the wave pattern reached the beach. A large domain of radius, $18a$, was chosen for this simulation to illustrate the wave pattern in the far field. Sensitivity studies showed that a much smaller domain could be used if the solution were required only on the body.

The spatial convergence of the heave force for the fully nonlinear radiation problem of Figure 1 is demonstrated by the left plot in Figure 2. Three discretizations are shown, using 20×4 , 30×6 , and 40×8 , quadratic B-spline elements on the free surface. The total number of elements on the body and free surface are 112, 252, and 448, for the three discretizations. The time-step for each of these runs, $\Delta t \sqrt{g/a} = 0.1$, was chosen through a temporal convergence study.

The right plot in Figure 2 compares the fully nonlinear results with the linear results (linearized free-surface and body boundary conditions). The negative shift in the force is due to the introduction of the quadratic velocity component in the nonlinear pressure. This will occur with any surface piercing body, but for submerged bodies, the difference in quadratic pressure between top and bottom surfaces creates a positive suction towards the free surface.

Local quantities often converge more slowly than integrated, global quantities. While the heave force

is graphically converged for the coarsest mesh, the wave elevation requires a finer discretization. Figure 3 demonstrates the convergence of the wave elevation along a cut on the positive x -axis. In this figure the cylinder waterline is at $x/a = 1$ with three discretizations for the nonlinear free surface. Only the converged result is shown for the linear free surface. On the left, a snapshot of the wave profile was taken after two periods. This illustrates the sensitivity of the local solution to discretization and nonlinearity. The nonlinear heave force differs from the linear by about 10% while the nonlinear wave elevation at the waterline differs from the linear by almost 100%. The plot on the right shows that some difference persists between the linear and nonlinear results away from the body.

Surge motion must be considered carefully since it can generate a singularity in the potential flow solution at the waterline. The cylinder was started impulsively at $t = 0$ into a surge oscillation of period, $T\sqrt{g/a} = 4$. Figure 5 shows the vertical flux along the x -axis just after the impulsive startup at $t = 0^+$. Before the startup this flux was zero everywhere. Figure 4 examines the surge nonlinear wave run-up near the cylinder after steady-state has been achieved. A domain of radius, $9a$, was used.

The surging cylinder is an impulsive response, similar to the moving two-dimensional wall problem [17] which has a log-type singularity. This singularity may not be as severe in for the three-dimensional cylinder, but this is open to question. The numerical solution converges at some distance away from the cylinder wall, but, at the wall at $t = 0^+$, there appears to be a singularity. As the solution progresses and the startup transients decay, the wave elevation run-up becomes well behaved. This failure of convergence at the startup at the waterline does not cause the method to break down.

Energy at length scales that are too small for the discretized free surface to resolve are aliased into larger waves. In this particular case, the energy in the singularity is not significant for the global solution since the method is convergent after the transients decay or at locations away from the waterline. For the local problem, experimental validation for cases such as this would be useful. The evidence may indicate that waterline models for viscosity or surface tension, for instance, are necessary for an accurate analysis of wave runup for impulsive problems.

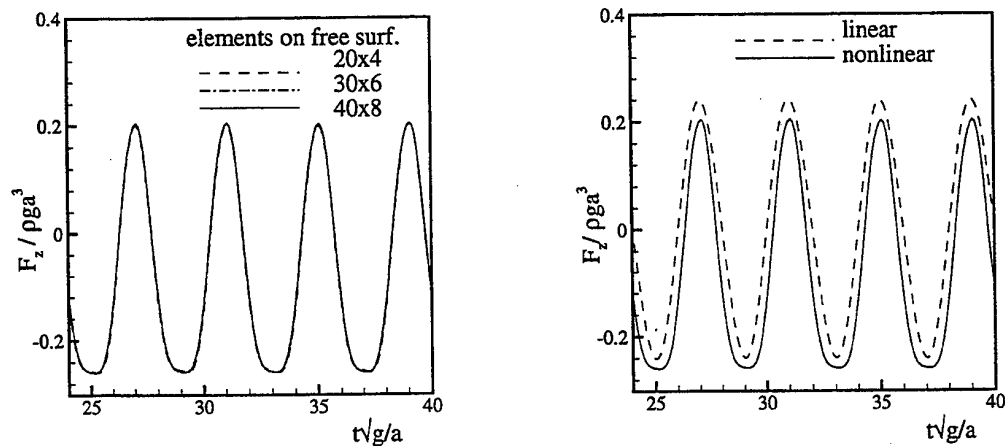


Figure 2: Heave force for a cylinder heaving at period, $T\sqrt{g/a} = 4$. Spatial convergence of the nonlinear simulation and the converged linear result.

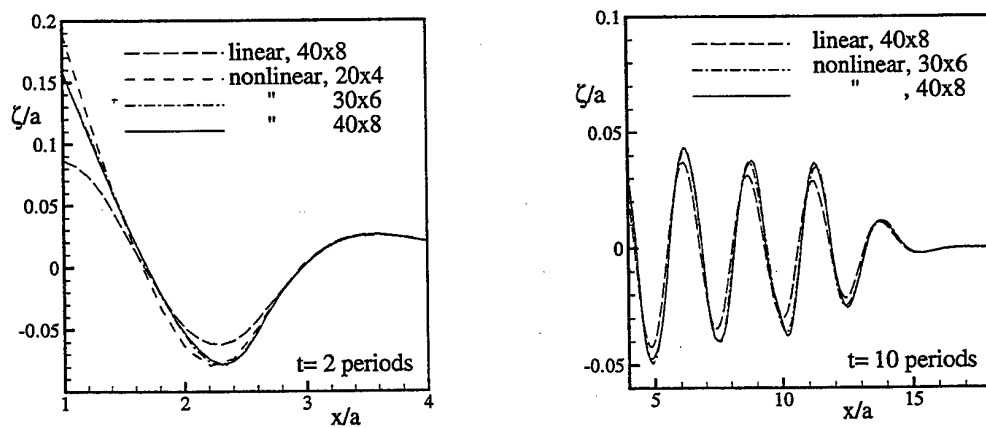


Figure 3: Wave elevation along a radial cut; $x/a = 1$ is the cylinder wall. Spatial convergence of the nonlinear simulation and the converged linear result.

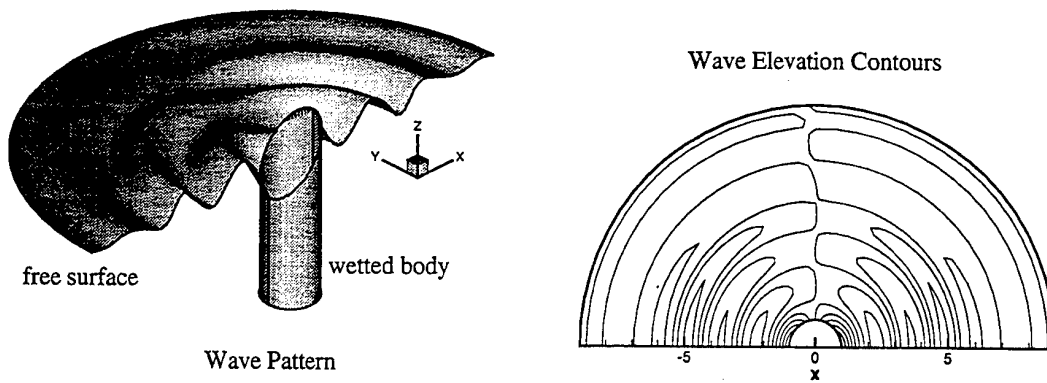


Figure 4: Nonlinear wave pattern, vertical scale $\times 10$, and elevation contours for a cylinder surging with period $T\sqrt{g/a} = 4$. The wetted body is shown with half the free surface cut away.

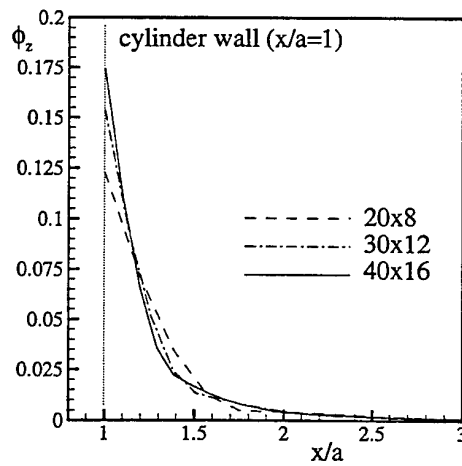


Figure 5: Vertical flux on the free surface at $t = 0^+$ along a radial cut for the surging cylinder.

SOLUTION ACCELERATION

The Rankine formulation of the (possibly nonlinear) free-surface problem may be considered as an interior problem regardless of whether it is closed by material surfaces as in a wave-tank simulation or by beaches and a bottom or decay condition. Therefore either surface or volume methods are appropriate avenues for solution. Volume methods such as FEM or FD may be preferred over classical BEM as their discretizations lead to sparse linear systems of equations. Consider that n elements are needed for each spatial direction to resolve the geometry and wavelengths in the problem. Then the computational cost of solving a volume formulation may be as low as n^3 , while that of solving a classical BEM formulation will be order n^6 as the resulting linear system is dense. However BEM acceleration algorithms effectively sparsify the dense linear systems of equations usually associated with these methods. For instance, the fast-multipole algorithms have order- N cost, where N is the total number of unknowns. This means that in the context of the above example their cost is order n^2 ; that is, lower than a volume method.

The pFFT method is a newer sparsification algorithm that is particularly attractive for hydrodynamic applications as it retains its low asymptotic cost even for wavy Green functions, which is not true of fast-multipole methods. For the acceleration of problems using the Rankine kernel as addressed here, either method is suitable. The pFFT method may be preferred even though its asymptotic cost is order $N \log N$ for cpu time expended (it is order N for memory allocated) as the constant factors are lower than for fast-multipole. For the size of problem considered here, pFFT is probably more efficient.

The pFFT algorithm has been implemented to accelerate both low- and high-order BEM formulations. Experiments were conducted accelerating the high-order element discrete form directly and time-integrating the high-order element form, while solving the Laplace problem at each time step with a derivative low-order element form. The explanation of the pFFT algorithm is most comprehensible in the low-order element context so that approach is covered in detail. Then a discussion is provided on how the algorithm must be modified to handle high-order elements and results from the two approaches are contrasted.

Low-Order Element Algorithm

Consider the common and straightforward method for solving (11) on general three-dimensional structures by discretizing the surface $S_B \cup S_F$ with N pla-

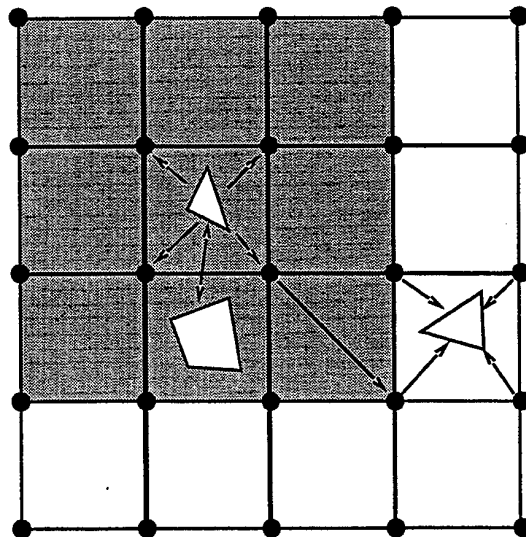


Figure 6: 2-D representation of the steps of the precorrected-FFT algorithm. For the triangular element at the upper left, its influence on nearby elements (any in the grey area) is computed directly and precorrected, its influence on distant elements is computed via the FFT on the uniform grid.

nar elements upon which the potential and its normal derivative are taken to be constant and enforcing the discrete equation at N collocation points, usually taken to be the element centroids. Proceeding in this manner, there will be a linear equation system to solve

$$Dq = p, \quad (16)$$

in which q is a column vector with elements ϕ and ϕ_n , depending on which surface the element is on and D is a matrix of influence coefficients that appear as source or dipole distributions over the elements. The vector Dq , then, may be viewed as a potential.

If equation (16) is sufficiently well conditioned, it may be solved by an iterative method, such as GMRES [19], with order- N^2 cost. The order- N^2 cost arises from the dense-matrix fill of D and the application of D to q^k (k denoting the k -th iterate) to arrive at a solution.

The acceleration of the solution of (16) is accomplished by filling only an order- N subset of D and computing the application of D to q^k in two parts, that is:

$$p^k = D_{sparse}q^k + p_{far}^k \quad (17)$$

and with D_{sparse} an order- N subset of D and p_{far}^k computed by an approximate technique. This technique relies on the fact that in the computation of any

$p_i^k = p^k(\vec{x}_i)$ the singularity distributions on any elements sufficiently far from x_i can be accurately represented by a small set of point singularities and that this accuracy may be increased by simply increasing the number of point singularities associated with any given element. The details of the algorithm are available in [6], but an overview is presented in Figure 6, a schematic of the steps in the algorithm to compute p^k . Instead of computing all interactions directly, there is a series of steps as follows:

Grid set-up: Overlay the problem geometry with a uniform right-parallelepiped grid and sort the low-order elements into the cells formed by the grid. The nearby elements of a given element are those elements in the 27 cells that share a vertex with the given element's cell. Set point singularities on the grid at at least the cell vertices (grid-order = 2), or at half the spacing of the vertices (grid-order = 3), etc, as desired for accuracy.

Projection operators: Numerically evaluate the operators (one for each cell that contains elements) that can replace the set of element singularity distributions in the cell with an equivalent set of point singularities on the grid. These are matrices deduced from a collocation problem for each cell that matches, at a set of test points, the potential due to the singularities at the points on the grid with the potential due to the singularity distributions on the elements.

Interpolation operators: Numerically evaluate the interpolation operators. These are essentially the transpose of the projection operators, although not precisely, because the interpolation is done to collocation points, not element distributions.

Direct interaction and precorrection: Directly compute the small number of nearby influences for each element using the same algorithms that would be used in a conventional approach. Use the projection operators, the Green function, and the interpolation operators to precompute and subtract from these nearby influences the grid-based influences for these same nearby elements that will be included inaccurately when the far influences are added from the potential interpolated off the grid.

Projection: Project the element singularity distributions to point singularities on the uniform grid by applying the projection operators to the element singularity distributions.

Convolution: Compute the potentials at the grid points due to the singularities at the grid points

according to the Green function (12) by FFT-accelerated convolution [20].

Interpolation: Interpolate the grid point potentials onto the elements by applying the interpolation operators to the grid potentials and add these to the precorrected direct influences.

High-Order Element Algorithm

In the high-order element method B-spline basis functions represent the solution and the boundary conditions and the problem is to determine the unknown coefficients. The support of the basis functions overlaps the element boundaries and this lack of a one-to-one correspondance between unknowns and elements makes the determination of the division between the near and far influence for any evaluation point more complex and more costly.

The high-order acceleration algorithm follows the same principal steps for grid calculations as the low-order method with some qualifications and extensions. All quadrature rules on the elements in the far field must be independent of the distance to the evaluation point. Hence, the domain of the direct calculation has to include all sufficiently close elements to properly characterize the singular nature of the kernel. Unlike the low-order element algorithm the determination of the close elements is not based on neighbor cells as this would impose undue constraints on the pFFT grid size, rather it is based on a grid-independent radius centered at each high-order element. In the far-field, function values at quadrature points, instead of element density values, are projected to and interpolated from the FFT grid. It should be noted that the order of the interpolation and projection methods must be consistent with the degree of the basis functions to retain the high-order convergence rate.

The Galerkin procedure and the high-order elements themselves result in a higher cost for the computation of D_{sparse} . For this case, the sparse matrix associated with the direct calculations tends to be less sparse than for low order because the support of a basis function extends over several elements. Moreover, locating the entries in this sparse matrix is more expensive than in the low-order case due to the lack of a one-to-one correspondance of entries to elements. Consequently, compared to low order, the construction of the sparse matrix for the direct part of the computation is more expensive at high order.

A benefit of near and far sorting of any sparsification algorithm is that an effective preconditioning strategy for BEM is natural. The overlapping block preconditioner of [21] is implemented in the high-

order acceleration method and has proved to be effective, although like the direct computations it is expensive to compute.

Since high-order methods are more efficient than low order to begin with, the efficiency gains from accelerating them are less dramatic than for low order, at least for the size of problem shown here.

Low vs. High-Order Acceleration

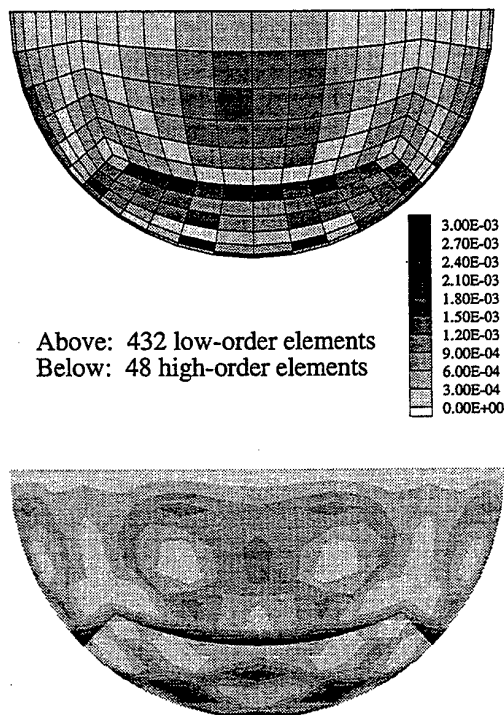


Figure 7: Comparison of absolute error for low- and high- order acceleration schemes for a floating sphere in heave at $t = 0^+$.

There are three issues to weigh in the choice of low versus high-order BEM schemes. First, there is a balance in the local accuracy of the problem at any instance in time. Second, there is the global accuracy of the problem as it progresses in time. Global accuracy is a question about numerical stability when the BEM is used in the evolution of the discrete free surface. These first two issues are the same when considering the unaccelerated solution. The third issue is computational efficiency, which depends upon the implementation of the low and high-order acceleration schemes.

The high-order method has a faster convergence rate and better local accuracy for a given number of elements, but this is offset by a need for more computations per element. Numerical experiments have found that nine low-order elements produced a comparable accuracy to one quadratic spline element for a typical free-surface problem. This is illustrated in Figure 7, which compares the accelerated solutions to the analytic solution for a floating sphere that moves impulsively in heave at $t = 0$. The maximum local error is comparable in these two results.

Global accuracy is considered through numerical stability. Linear analysis holds that a low-order (constant) discretization of the free surface cannot produce a neutrally stable integration in time. Only a high-order discretization can produce a stable scheme. However, for the present study a hybrid method was developed to test the efficiency of the low-order acceleration scheme. In the scheme, the free-surface conditions are discretized with a high-order B-spline while the boundary-integral equation is solved by low-order acceleration. A Galerkin interpolation is used to pass the solution between the high- and low-order discretizations.

This hybrid method is stable for the linear free surface, but is only stable for the nonlinear free surface with submerged bodies. The high-order accelerated method is expected to be stable for surface piercing bodies but it has only been fully implemented for the linear, frequency-domain problem and for the impulsive startup which can be solved with Neumann conditions. It has not been extended to the mixed Neumann-Dirichlet conditions needed for the nonlinear, time-domain problem yet.

In this study, a body-nonlinear problem for a MOB semi-submersible and a fully-nonlinear problem of a sub moving with forward speed are solved using the hybrid scheme to demonstrate the advantages of acceleration.

	CPU (sec)	Memory (MB)
Low dense	11000	3800
Low accel.	400	600
High dense	3800	200
High accel.	200	30

Table 1: Computational time and memory costs for one time-step with 5,000 high-order (quadratic) elements or 50,000 low-order (constant) elements on a 433Mhz Alpha workstation.

As an example of the capabilities of acceleration, a generic BEM example can be considered. For the

high-order scheme, estimates of computational time and memory requirements are interpolated from the linear, frequency-domain problem. The costs for the dense, low-order solution are projections. Table 1 compares 5,000 high-order elements to 50,000 low-order elements which can be considered to give comparable accuracy. This is the number of elements that would produce good local accuracy for a typical ship or offshore platform problem and represents the time needed for each time-step in a simulation. Typical simulations range from 100 to 1000 time-steps depending upon the application.

Low-order elements tend to benefit more from acceleration than high-order elements since the gains over dense methods scale as order N and N is larger using low-order elements. Also, the high-order acceleration scheme has a higher constant factor from its implementation. Even so, the high-order scheme has some advantages, especially in memory usage. Computational efficiency and the need for numerical stability dictate that the high-order scheme is preferred.

Semi-Submersible

A 260m long semi-submersible, one part of a five unit MOB concept, is simulated in heave using the body-nonlinear simulation. The hybrid high-order free surface, low-order acceleration scheme was applied. The linear free-surface condition was used with the body-nonlinear condition since the hybrid method became unstable using the fully nonlinear free surface. The body-nonlinear simulation requires the same number of boundary-integral evaluations as the fully nonlinear simulation so it gives an indication of the computational efficiency to be gained from acceleration.

The steady-state wave pattern is illustrated in Figure 8. The body consists of sixteen separate B-spline patches and the free surface has twenty-three. Even though no continuity is specified between free-surface patches, the boundary-integral formulation provides a smooth transition across their boundaries. This 260m semi-sub is heaving at a period of 6 seconds. A snapshot of the wave pattern was taken 30 seconds after an impulsive startup.

Three discretizations were run for this structure using roughly 17000, 36000, and 63000 low-order elements. This corresponds to 1900, 4000, and 7000 quadratic elements respectively. No planes of symmetry were used since these would not be available in the nonlinear diffraction or free motion simulations. The wave elevation contours converge to about 1%. Figure 9 shows the convergence of the heave force for this problem. Convergence is better for this global integrated quantity than for the wave elevation.

The fully nonlinear, dense solution was run for the

coarsest discretization for less than one period and did not exhibit signs of instability. It was not run longer or run with a finer discretization because the computational cost was prohibitive. For the finest mesh with a 30 second simulation time (300 time-steps), the total computational time for the accelerated solution was 40 hours, and required 800 megabytes of memory on a 433Mhz Alpha workstation. For this case, the direction solution with low-order elements would require 1800 hours (2.5 months) and 7.5 gigabytes of memory; the high-order dense solution would require 600 hours and 400 megabytes of memory. The high-order acceleration scheme, when implemented, is expected to reduce the memory and time requirements even farther than the low-order scheme and allow for fully nonlinear free-surface computations. For the fine mesh, it would require only 20 hours of computation time and less than 50 megabytes of memory.

Submarine With Forward Speed

For fully submerged bodies, the hybrid method proved to be stable at forward speed with the spatial filtering adapted from linear theory.

Figure 10 shows a steady-state wave pattern from the nonlinear simulation for a sub travelling at a Froude number of $U/\sqrt{gL} = 0.3$, where U is the forward speed and L is the length overall. The vertical scale has been magnified by a factor of ten to highlight the wave elevation, but the scale of the sub has been not been magnified. Its depicted depth of submergence is also not to scale. Its centerline is 1.6 hull radii below the mean free surface.

Figure 11 shows the wave elevation at a cut along the axis of travel centered on the sub. There is relatively little difference between the linear and nonlinear wave elevations. For surface piercing ships, the difference is expected to be larger. However, the differences in the linear and nonlinear resistance is quite significant. The linearized calculation used the Kelvin, free stream, basis flow. A linearization that uses the double-body flow may have a much better agreement with the nonlinear results. The Kelvin model contains no component of the quadratic pressure, which is known to be important in wave resistance studies.

The point of this nonlinear study is not to demonstrate nonlinear effects, but to prove that the numerical solution is convergent and can be obtained at a reasonable computational cost.

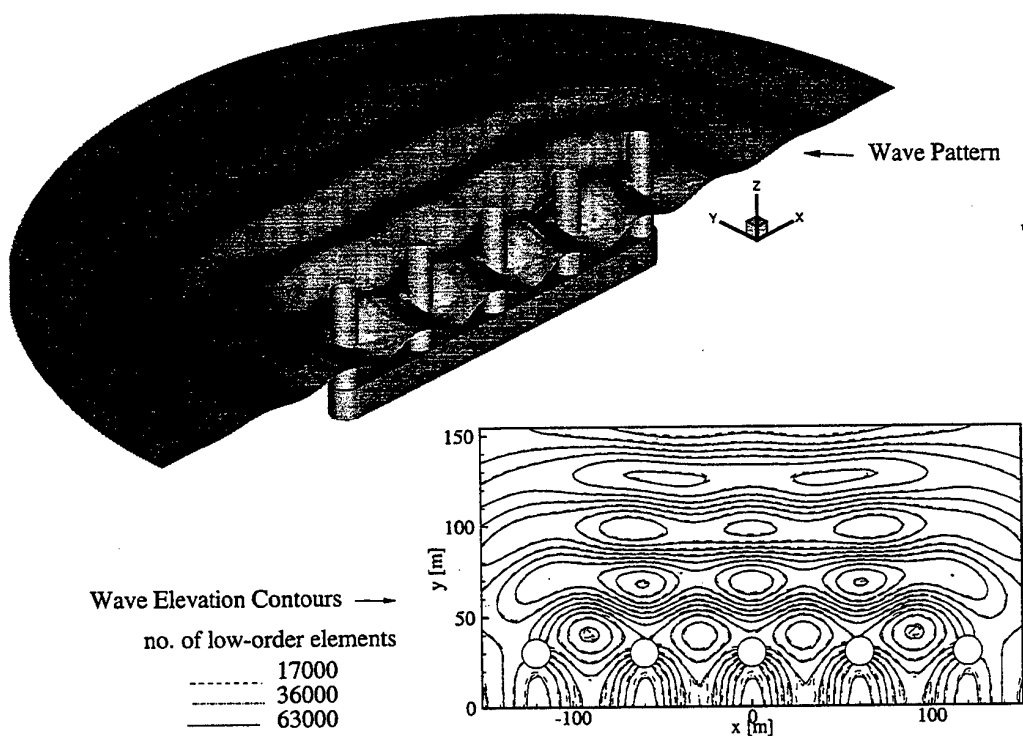


Figure 8: Body-nonlinear wave pattern and wave elevation contours for a MOB semi-sub heaving at period, $T = 6$ sec. Vertical scale x2.

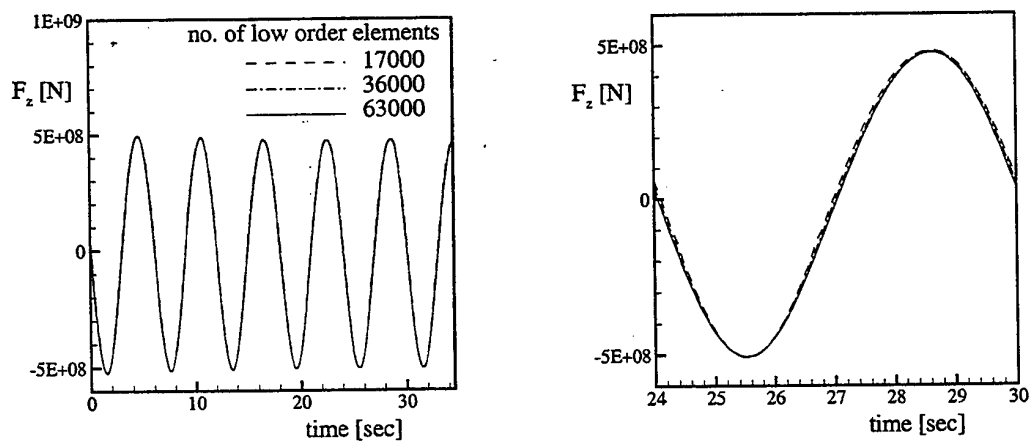


Figure 9: Convergence of heave force for a MOB semi-sub in heave motion.

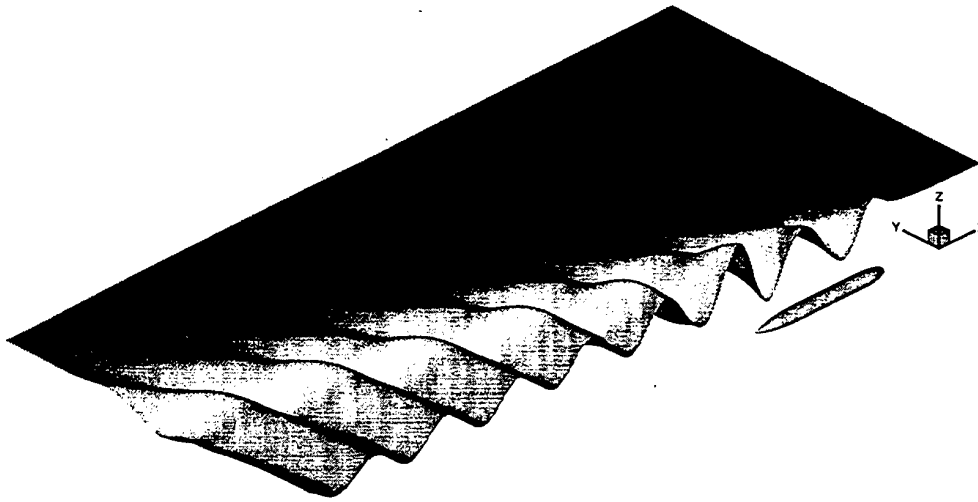


Figure 10: Nonlinear steady wave pattern for a submarine travelling at Froude number $U/\sqrt{gL} = 0.3$. Vertical scale $\times 10$.

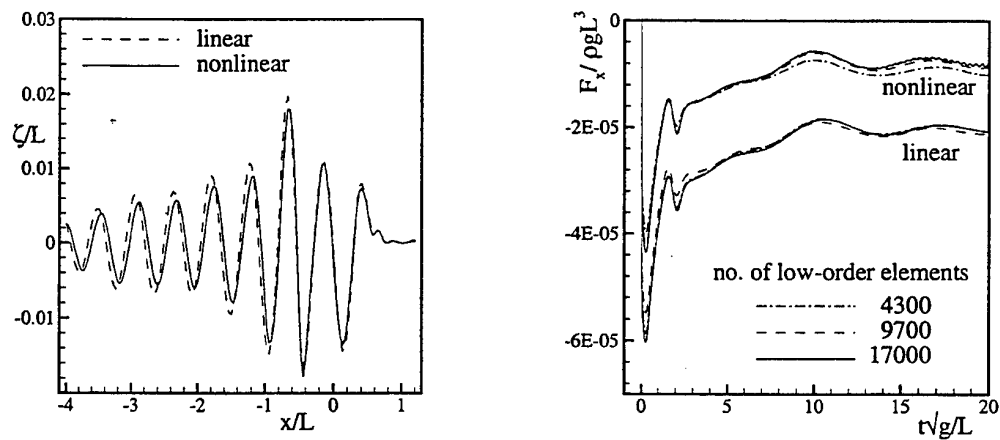


Figure 11: Linear and nonlinear Wave Elevation cut along axis of motion centered above sub (left plot), and convergence of Wave Resistance after impulsive startup for Froude number, 0.3 (right plot). The sub spans (bow to stern), $x/L = 0.5$ to $x/L = -0.5$

CONCLUSION

A nonlinear, time-domain, free-surface BEM has been developed using a dense solution of the boundary-integral formulation that is numerically stable. A semi-Lagrangian Zakharov formulation avoids some of the reported difficulties of the Mixed Eulerian-Lagrangian schemes and considers both surface piercing bodies and forward speed effects. The high-order, geometry-independent implementation is accurate and well-suited for use with structural analysis or other physical models. However, the dense solution can only be applied to simple bodies such as a floating cylinder for a reasonable computational cost.

Acceleration was added to the BEM to make it practical for large, complicated geometries such as ships and offshore structures. An existing low-order acceleration scheme has been added to the high-order free-surface discretization in a hybrid scheme and work has begun on implementing an existing high-order acceleration procedure.

For these realistic problems, acceleration can offer decreases of up to two orders in magnitude in CPU time and memory requirements. More importantly, larger problems can be solved, up to 150,000 high-order elements with one gigabyte of memory.

This initial work has proven that the presented BEM is convergent and efficient for nonlinear radiation, but it requires further validation. By identifying some strongly nonlinear effects, appropriate experimental validation studies can be chosen. After this validation and the implementation of the high-order acceleration scheme, the BEM will be a good candidate for nonlinear seakeeping studies. To address seakeeping, the nonlinear diffraction and free motion problems must be solved for open ocean conditions. The nonlinear incident waves and computational domain of [11] or the wave-generating singularities of [22] offer some direction towards this goal.

Some possible applications for a nonlinear seakeeping method include the analysis of structural loads, wave run-up, wave and added resistance, slamming, and transom stern and lifting effects. This method may also be suitable for coupling to near-body viscous solvers.

ACKNOWLEDGEMENTS

This work is supported by ONR Grant N00014-97-1-0827, under the direction of NFESC; and by the industry consortium: Numerical Analysis of Wave Loads on Offshore Structures, with participants: Chevron, DNV-Software, Exxon, Mobil, Norsk-Hydro, NSWC-CD, OTRC, Petrobras, Saga, Shell, and Statoil.

REFERENCES

1. Nakos, D. E., Kring, D. E. and Sclavounos, P. D. "Rankine panel methods for time-domain free surface flows," 6th Int. Conf. on Numerical Ship Hydrodynamics, Iowa City, 1993.
2. Sclavounos, P. D., Kring, D. C., Huang, Y., Mantzaris, D. A., Kim, S. and Kim, Y., "A ship flow computational method as an advanced cfd tool of design," SNAME Transactions, 1997.
3. Danmeier, D. G., A higher-order panel method for large-amplitude simulations of bodies in waves. PhD thesis, Massachusetts Institute of Technology, Cambridge, 1994.
4. Dommermuth, D. G. and Yue, D. K. P., "A high-order spectral method for nonlinear gravity waves," J. Fluid Mechanics, Vol. 184, 1987, pp. 267-288.
5. Nabors, K., Korsmeyer, F. T., Leighton, F. T. and White, J., "Preconditioned, adaptive, multipole-accelerated iterative methods for three-dimensional first-kind integral equations of potential theory," SIAM J. Sci. Comp., Vol. 15, No. 3, 1994, pp. 713-735.
6. Phillips, J. R. and White, J. K., "A precorrected-FFT method for electrostatic analysis of complicated 3-d structures," IEEE Trans. on Computer-Aided Design, Vol. 16, No. 10, 1997, pp. 1059-1072.
7. Korsmeyer, T., Klemas, T., Phillips, J. and White, J. "Fast hydrodynamic analysis of large offshore structures," ISOPE'99, Brest, 1999.
8. Maniar, Hiren Dayalal, A three dimensional higher order panel method based on b-splines. PhD thesis, Massachusetts Institute of Technology, Cambridge, MA, 1995.
9. Kring, D. C. and Sclavounos, P. D., "Numerical stability analysis for time-domain ship motion simulations," J. Ship Research, Vol. 39, No. 4, 1995, pp. 313-320.
10. Beck, R. F., Cao, Y. and Lee, T.-H. "Fully nonlinear water wave computations using the desingularized method," 6th Int. Conf. on Numerical Ship Hydrodynamics, Iowa City, 1993.
11. Ferrant, Pierre "Simulation of strongly nonlinear wave generation and wave-body interactions using a 3D MEL model," Proceedings of the 21st Symposium on Naval Hydrodynamics, Trondheim, Norway, Jun 1996, pp. 226-241.
12. Cointe, R., "Nonlinear simulations of transient free surface flows," 5th Intl. Conf. on Numerical Ship Hydrodynamics, 1989.
13. Longuet-Higgins, M. S. and Cokelet, E. D.,

"The deformation of steep surface waves on water," Proc. Roy. Soc., Vol. Series A, 350, 1976, pp. 1-26.

14. Liu, Y., Dommermuth, D. G. and Yue, D. K. P., "A high-order spectral method for nonlinear wave-body interactions," J. Fluid Mechanics, Vol. 245, 1992, pp. 115-136.

15. Thomas, Gregory Robert, A combined high-order spectral and boundary integral equation method for modeling wave interactions with submerged bodies. PhD thesis, Massachusetts Institute of Technology, Cambridge, MA, 1996.

16. Raven, H. C., "Nonlinear ship wave calculations using the RAPID method," 6th Intl. Conf. on Numerical Ship Hydrodynamics, 1993.

17. Roberts, A. J., "Transient free surface flows generated by a moving vertical plate," J. Mech. Appl. Math., Vol. 40, 1986, pp. 129-158.

18. Gordon, W. J., "Blending function methods of bivariate and multivariate interpolation and approximation," Siam J. Num. Anal., August 1971.

19. Saad, Y. and Schultz, M. H., "GMRES: A generalized minimal residual algorithm for solving nonsymmetric linear systems," SIAM J. Sci. Stat. Comp., Vol. 7, No. 3, July 1986, pp. 856-869.

20. Van Loan, C., Computational Frameworks for the Fast Fourier Transform, SIAM, Philadelphia, 1992.

21. Vavasis, S. A., "Preconditioning for boundary integral equations," SIAM Journal of Matrix Analysis and Applications, Vol. 13, No. 3, July 1992, pp. 905-925.

22. Clement, A. "The spinning diopole: an efficient unsymmetrical numerical wavemaker," 14th Intl. Workshop on Water Waves and Floating Bodies, Port Huron, Michigan, 1999.

FREE SURFACE VISCOUS FLOWS

Chairmen : T.Hino, F.Noblesse.

NUMERICAL SIMULATION OF SHIP FLOW IN RESTRICTED WATER

F. Bet¹, N. Stuntz², D. Hänel¹, S.D. Sharma²

¹Institute of Combustion and Gasdynamics; ²Institute of Ship Technology
Gerhard-Mercator-University Duisburg, D-47048 Duisburg, Germany

ABSTRACT

The paper presents a numerical solution method for the three-dimensional Euler and Navier-Stokes equations for the prediction of ship flow in unbounded and restricted water. A Finite Volume discretisation is applied to body conform, structured grids with a level-set method for tracking the free surface.

The algorithm is based on the concept of artificial compressibility which enables the application of efficient algorithms originally developed for compressible flows. The integration in time is accomplished by an explicit Runge-Kutta multi-stage time stepping scheme.

INTRODUCTION

A task of major concern in the field of ship hydrodynamics is the accurate calculation of the drag forces of a ship and its characteristic features of propulsion, to make obligatory predictions of these characteristics in the state of project. Due to the high complexity of the real flow around a ship's body and due to the interaction of the ship and the moving water surface one still depends on small-scale experiments in water channels. Maintaining the Froude-similarity in experimental setups leads generally to a violation of the Reynolds-similarity. Thus the experimental results are generally not similar. The traditional decomposition of the total drag into two independent parts due to waves and friction is physically inadequate due to the correlations between waves and the viscous flow around the ship. In addition, the empirical correction of friction in shallow water commonly used is too inaccurate to transfer solution from the model to the real-scale prototype.

The present work intends to overcome the weaknesses of small-scale experiments (high costs, time consuming, influence of scale) by the determination of a most possible commonly valid theoretical solution using means of modern computational fluid dynamics (CFD).

Our interest is directed to the development of efficient and accurate algorithms for the incompressible Navier-Stokes equations with applications to flow around ships in restricted water. The algorithmic de-

velopment is based on previous experiences with the artificial compressibility concept [1] and on multi-grid acceleration [2]. The numerical formulation of free surfaces influences remarkably the accuracy and efficiency of the computation. Several attempts exist; a review about them is given by e.g. *Mijata* [3]. In the following the solution method and some computational results will be presented.

METHOD OF SOLUTION

The governing equations are the Navier-Stokes equations for an incompressible fluid influenced by gravity. Normalised by the length of the body L , the undisturbed flow velocity U , the fluid density ρ , and viscosity ν , the equations can be written as follows:

$$\frac{\partial u}{\partial x} + \frac{\partial v}{\partial y} + \frac{\partial w}{\partial z} = 0 \quad (1)$$

$$\frac{\partial u}{\partial t} + \frac{\partial uu}{\partial x} + \frac{\partial vu}{\partial y} + \frac{\partial wu}{\partial z} + \frac{\partial \tilde{p}}{\partial x} = \frac{1}{Re} \Theta_x \quad (2)$$

$$\frac{\partial v}{\partial t} + \frac{\partial uv}{\partial x} + \frac{\partial vv}{\partial y} + \frac{\partial wv}{\partial z} + \frac{\partial \tilde{p}}{\partial y} = \frac{1}{Re} \Theta_y \quad (3)$$

$$\frac{\partial w}{\partial t} + \frac{\partial uw}{\partial x} + \frac{\partial vw}{\partial y} + \frac{\partial ww}{\partial z} + \frac{\partial \tilde{p}}{\partial z} = \frac{1}{Re} \Theta_z \quad (4)$$

with \tilde{p} denoting the total pressure, which consists of a static part (p_s) and a geodetic part, both normalised with $\rho \cdot U^2$

$$\tilde{p} = p_s + \frac{y}{Fn^2} \quad (5)$$

where y is the coordinate in direction of gravity. The Froude number based on the reference value is defined as $Fn = U/\sqrt{gL}$, and the corresponding Reynolds number is $Re = UL/\nu$ where ν represents the kinematic viscosity of water.

The viscous terms σ are defined as follows:

$$\Theta_x = \frac{\partial}{\partial x}\sigma_{xx} + \frac{\partial}{\partial y}\sigma_{xy} + \frac{\partial}{\partial z}\sigma_{xz}$$

$$\Theta_y = \frac{\partial}{\partial x}\sigma_{xy} + \frac{\partial}{\partial y}\sigma_{yy} + \frac{\partial}{\partial z}\sigma_{yz}$$

$$\Theta_z = \frac{\partial}{\partial x}\sigma_{xz} + \frac{\partial}{\partial y}\sigma_{yz} + \frac{\partial}{\partial z}\sigma_{zz}$$

with:

$$\begin{aligned} \sigma_{xx} &= 2\nu \frac{\partial u}{\partial x} & \sigma_{xy} &= \nu \left(\frac{\partial u}{\partial y} + \frac{\partial v}{\partial x} \right) \\ \sigma_{yy} &= 2\nu \frac{\partial v}{\partial y} & \sigma_{yz} &= \nu \left(\frac{\partial v}{\partial z} + \frac{\partial w}{\partial y} \right) \\ \sigma_{zz} &= 2\nu \frac{\partial w}{\partial z} & \sigma_{zx} &= \nu \left(\frac{\partial u}{\partial z} + \frac{\partial w}{\partial x} \right) \end{aligned}$$

The equations are transformed to general coordinates as sketched in figure 1:

$$\tau = t, \quad \xi(x, y, z), \quad \eta(x, y, z), \quad \zeta(x, y, z)$$

and are discretized by a finite-volume method in a node-centred arrangement on block-structured curvilinear grids.

The transformed equations can be written as:

$$\frac{\partial Q}{\partial t} + \frac{\partial \tilde{E}}{\partial \xi} + \frac{\partial \tilde{F}}{\partial \eta} + \frac{\partial \tilde{G}}{\partial \zeta} = \frac{\nu}{Re} \left(\frac{\partial \tilde{R}}{\partial \xi} + \frac{\partial \tilde{S}}{\partial \eta} + \frac{\partial \tilde{T}}{\partial \zeta} \right) \quad (6)$$

where:

$$Q = J^{-1} \begin{bmatrix} 0 \\ u \\ v \\ w \end{bmatrix}, \quad \tilde{E} = J^{-1} \begin{bmatrix} \hat{U} \\ \hat{U}u + \tilde{p}\xi_x \\ \hat{U}v + \tilde{p}\xi_y \\ \hat{U}w + \tilde{p}\xi_z \end{bmatrix}$$

$$\tilde{F} = J^{-1} \begin{bmatrix} \hat{V} \\ \hat{V}u + \tilde{p}\eta_x \\ \hat{V}v + \tilde{p}\eta_y \\ \hat{V}w + \tilde{p}\eta_z \end{bmatrix}, \quad \tilde{G} = J^{-1} \begin{bmatrix} \hat{W} \\ \hat{W}u + \tilde{p}\zeta_x \\ \hat{W}v + \tilde{p}\zeta_y \\ \hat{W}w + \tilde{p}\zeta_z \end{bmatrix}$$

$$\tilde{R} = J^{-1} \begin{bmatrix} 0 \\ \sigma_{xx}\xi_x + \sigma_{xy}\xi_y + \sigma_{xz}\xi_z \\ \sigma_{xy}\xi_x + \sigma_{yy}\xi_y + \sigma_{yz}\xi_z \\ \sigma_{xz}\xi_x + \sigma_{yz}\xi_y + \sigma_{zz}\xi_z \end{bmatrix}$$

$$\tilde{S} = J^{-1} \begin{bmatrix} 0 \\ \sigma_{xx}\eta_x + \sigma_{xy}\eta_y + \sigma_{xz}\eta_z \\ \sigma_{xy}\eta_x + \sigma_{yy}\eta_y + \sigma_{yz}\eta_z \\ \sigma_{xz}\eta_x + \sigma_{yz}\eta_y + \sigma_{zz}\eta_z \end{bmatrix}$$

$$\tilde{T} = J^{-1} \begin{bmatrix} 0 \\ \sigma_{xx}\zeta_x + \sigma_{xy}\zeta_y + \sigma_{xz}\zeta_z \\ \sigma_{xy}\zeta_x + \sigma_{yy}\zeta_y + \sigma_{yz}\zeta_z \\ \sigma_{xz}\zeta_x + \sigma_{yz}\zeta_y + \sigma_{zz}\zeta_z \end{bmatrix}$$

with

$$\begin{aligned} \hat{U} &= u\xi_x + v\xi_y + w\xi_z \\ \hat{V} &= u\eta_x + v\eta_y + w\eta_z \\ \hat{W} &= u\zeta_x + v\zeta_y + w\zeta_z \end{aligned}$$

The metric factors are defined as:

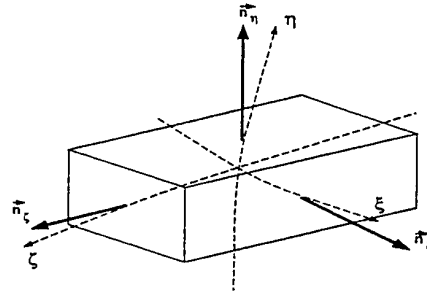


Figure 1: Discrete Control Volume and Coordinate System

$$\begin{aligned} \xi_x &= J(y_\eta z_\zeta - y_\zeta z_\eta) & \eta_x &= J(z_\xi y_\zeta - z_\zeta y_\xi) \\ \xi_y &= J(z_\eta x_\zeta - z_\zeta x_\eta) & \eta_y &= J(x_\xi z_\zeta - x_\zeta z_\xi) \\ \xi_z &= J(x_\eta y_\zeta - x_\zeta y_\eta) & \eta_z &= J(y_\xi x_\zeta - y_\zeta x_\xi) \end{aligned}$$

$$\begin{aligned} \zeta_x &= J(y_\xi z_\eta - z_\xi y_\eta) \\ \zeta_y &= J(z_\xi x_\eta - x_\xi z_\eta) \\ \zeta_z &= J(x_\xi y_\eta - y_\xi x_\eta) \end{aligned}$$

and with the Jacobian determinante:

$$J^{-1} = x_\xi(y_\eta z_\zeta - y_\zeta z_\eta) + x_\eta(z_\xi y_\zeta - z_\zeta y_\xi) + x_\zeta(y_\xi z_\eta - z_\xi y_\eta)$$

Concept of Artificial Compressibility

The pressure in a rigorous incompressible flow acts like a relaxation parameter to satisfy the continuity equation $\nabla \cdot \vec{v} = 0$.

A possible way to determine the pressure field is the coupling of mass and momentum equations by the concept of artificial compressibility in analogy of the compressible flow [4]. This is applied here based on previous computations in [5] for steady and unsteady

incompressible flows.

The original continuity equation (1) is modified by adding an artificial time derivative of pressure representing the artificial compressibility:

$$\frac{\partial \tilde{p}}{\partial t} + \beta^2 \left(\frac{\partial u}{\partial x} + \frac{\partial v}{\partial y} + \frac{\partial w}{\partial z} \right) = 0 \quad (7)$$

where β acts as a compressibility parameter.

Equation (7) can be deduced from the continuity equation for compressible fluids, by using the equation of state:

$$\tilde{p} = \beta^2 \rho \quad (8)$$

The modified inviscid system of partial differential equations reads now:

$$\frac{\partial Q}{\partial t} + \frac{\partial \tilde{E}}{\partial \xi} + \frac{\partial \tilde{F}}{\partial \eta} + \frac{\partial \tilde{G}}{\partial \zeta} = 0 \quad (9)$$

with:

$$Q = J^{-1} \begin{bmatrix} \tilde{p} \\ u \\ v \\ w \end{bmatrix}, \tilde{E} = J^{-1} \begin{bmatrix} \beta^2 \hat{U} \\ \hat{U}u + \tilde{p}\xi_x \\ \hat{U}v + \tilde{p}\xi_y \\ \hat{U}w + \tilde{p}\xi_z \end{bmatrix}$$

$$\tilde{F} = J^{-1} \begin{bmatrix} \beta^2 \hat{V} \\ \hat{V}u + \tilde{p}\eta_x \\ \hat{V}v + \tilde{p}\eta_y \\ \hat{V}w + \tilde{p}\eta_z \end{bmatrix}, \tilde{G} = J^{-1} \begin{bmatrix} \beta^2 \hat{W} \\ \hat{W}u + \tilde{p}\zeta_x \\ \hat{W}v + \tilde{p}\zeta_y \\ \hat{W}w + \tilde{p}\zeta_z \end{bmatrix}$$

The system is of hyperbolic type, in analogy to the compressible case. Its eigenvalues in the $\xi - t$ plane are e.g.:

$$\lambda_1 = \hat{U} \quad \lambda_2 = \hat{U} \quad \lambda_3 = \hat{U} + c \quad \lambda_4 = \hat{U} - c \quad (10)$$

The value of c is given by:

$$c = \sqrt{\hat{U}^2 + \beta^2 (\xi_x^2 + \xi_y^2 + \xi_z^2)} \quad (11)$$

A comparison with the eigenvalue of the Euler equations for a compressible fluid shows that c corresponds to an artificial speed of sound.

In analogy to the compressible case, an artificial Mach-number can be defined by the relation of the flow velocity to the artificial speed of sound:

$$Ma_k = \frac{\hat{U}}{c} = \frac{\hat{U}}{\sqrt{\hat{U}^2 + \beta^2 (\xi_x^2 + \xi_y^2 + \xi_z^2)}} < 1 \quad (12)$$

$(\beta > 0)$

Small disturbances in pressure propagate in an incompressible fluid with infinite velocity. The artificial compressibility limits the propagation speed and

in contrast to an incompressible fluid, the effects of disturbances will be delayed. The degree of delay depends on the value of β . For $\beta > 0$ the pseudo-compressible flow is comparable to subsonic flows.

The solution of the system with modified continuity equation is unphysical for transient flows but however, at steady-state the time-derivative $\frac{\partial \tilde{p}}{\partial t}$ vanishes and the original continuity equation for incompressible fluids will be remained.

The propagation speed of a pressure wave in a pseudo-compressible flow is influenced considerably by the selection of the parameter β . An increase of the parameter β results in a disturbance spreading faster into the zone of flow, and the solution will approach more closely to the solution of a completely incompressible flow.

Thus the selection of a suitable value for β is subject to certain restrictions. An upper boundary can be calculated from the relation K between the maximum and the minimum eigenvalue of the differential equation system:

$$K = \frac{|\lambda_{max}|}{|\lambda_{min}|} = \frac{|u + \sqrt{u^2 + \beta^2}|}{|u - \sqrt{u^2 + \beta^2}|} \quad (13)$$

In the literature different models exist, where the value of β is assumed to be proportionally to the local flow velocity [6], [7]:

$$\beta^2 = \gamma \cdot \max[(u^2 + v^2 + w^2), \beta_{min}^2] \quad (14)$$

where the parameter γ is a factor of the order of magnitude 1.

The value for β received from equation (14) is a local variable. This can lead to difficulties in convergence since the flow rate can become locally very large and thus the parameter β also increases.

A reasonable lower boundary for β can be estimated from the condition that artificial pressure waves propagate faster than the viscous effects.

Suitable values for β lay between 0.4 and 2.0 depending on the flow problem examined in the context of this word. Figure 2 shows the convergence behaviour of a two dimensional laminar boundary layer flow at different values of the parameter β .

Numerical Flux Discretisation

The similarity of the modified system equations (9) to a system for subsonic flow enables the construction of numerical fluxes corresponding to well proved shock-capturing schemes developed for compressible flow. Therefore several upwind formulations of the artificial compressibility concept were derived and

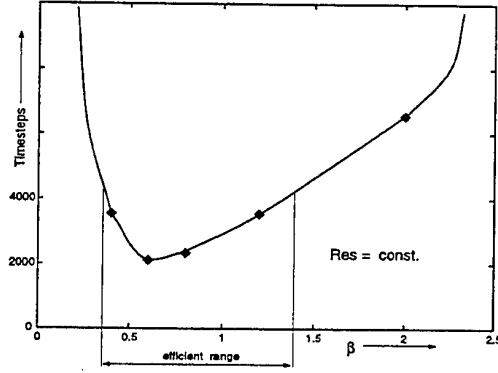


Figure 2: Comparison of the convergence behaviour of the solution procedure at differently values of the parameter β

tested in previous studies, like AUSM splitting, flux-vector splitting or Roe splitting. Among them, Roe's flux-difference-splitting has found to be well suited to achieve a close coupling between the continuity and momentum equations. The flux splitting is derived from a diagonal transformation of the flux Jacobian matrices (for example in the ξ direction)

$$A = \frac{\partial \tilde{E}}{\partial Q} = R \cdot \Lambda \cdot R^{-1}$$

and by splitting of the eigenvalue matrix

$$\Lambda = \text{diag.} (\hat{U}, \hat{U}, \hat{U} + c, \hat{U} - c)$$

in

$$\Lambda = \Lambda^+ + \Lambda^-$$

An efficient variant of the Roe splitting at a cell interface $i + \frac{1}{2}$ is used in the form

$$\tilde{E}_{i+1/2} = \tilde{E}_{i+1/2}^+ + A^-(\tilde{Q}_{i+1/2}) (Q_{i+1/2}^- - Q_{i+1/2}^+) \quad \text{if } \hat{U} > 0$$

$$\tilde{E}_{i+1/2} = \tilde{E}_{i+1/2}^- - A^+(\tilde{Q}_{i+1/2}) (Q_{i+1/2}^- - Q_{i+1/2}^+) \quad \text{if } \hat{U} < 0$$

where $A^\pm(\tilde{Q}) = R \cdot \Lambda^\pm \cdot R^{-1}$ is the Jacobian matrix build with its positive and negative eigenvalues, respectively which are formed with the averaged quantities $\tilde{Q} = (Q^+ + Q^-)_{i+1/2}$. A MUSCL extrapolation is used for the left and right extrapolated values Q^\pm to achieve second order accuracy.

Treatment of Free Surface

The free surface corresponds to the phase boundary between water and air which is moving according to the flow velocity \vec{v} .

The free surface can be defined by isolines of a function $\psi(x, y, z, t) = \psi_0 = 0$. The total differential of this function yields to the transport equation of the position of the surface which satisfies the kinematic condition at the surface:

$$\frac{\partial \psi}{\partial t} + u \frac{\partial \psi}{\partial x} + v \frac{\partial \psi}{\partial y} + w \frac{\partial \psi}{\partial z} = 0 \quad (15)$$

The dynamic condition describes the continuity of stress across the phase boundary. Neglecting the viscous terms at the surface and the surface tension the dynamic condition reduces to the condition of constant pressure normal to the interphase

$$p(\psi_0(x, y, z, t)) = p_a$$

where p_a is the atmospheric pressure. The boundary condition of the total pressure reads now:

$$\tilde{p} = p_a + \frac{h}{Fn^2} \quad (16)$$

The combination of equation (15) with the system (6) leads to the following system of equations:

$$Q = \begin{bmatrix} \vdots \\ \psi \end{bmatrix}, \tilde{E} = \begin{bmatrix} \vdots \\ \hat{U}\psi \end{bmatrix}$$

$$\tilde{F} = \begin{bmatrix} \vdots \\ \hat{V}\psi \end{bmatrix}, \tilde{G} = \begin{bmatrix} \vdots \\ \hat{W}\psi \end{bmatrix}$$

The additional equation for ψ has no influence on the eigenvalues $\lambda_{1...4}$ (10) of the system. Just a further eigenvalue $\lambda_5 = \hat{U}$ was introduced.

The function $\psi(x, y, z)$ divides the integrational domain into three sections as shown in Figure 3.

$$\begin{aligned} \psi &> 0 \rightarrow \text{Air} \\ \psi &= 0 \rightarrow \text{Surface} \\ \psi &< 0 \rightarrow \text{Water} \end{aligned}$$

The initial condition for ψ is chosen as:

$$\psi_{i,j,k} = y_{i,j,k} - h_0$$

with $y_{i,j,k}$ and h_0 being the distance of each point to the undisturbed free surface and its height respectively.

The new position of the free surface is calculated by linear interpolation of $\psi_{i,j,k}$ after every integration

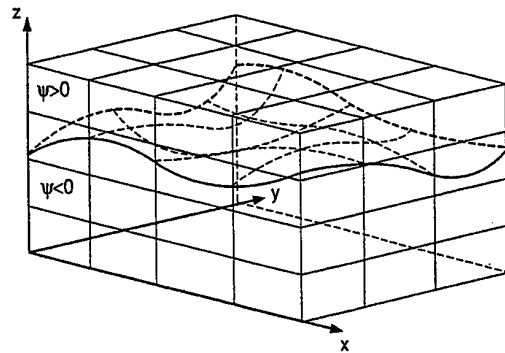


Figure 3: Position of the Free Surface into the Computational Grid

time step.

As far as the air phase is of no interest, the corresponding grid points can be used as dummy points to set the dynamic boundary condition given by Eq. (16) at the free surface which is satisfied at $\psi_o = 0$ by an extrapolation of \tilde{p} sketched in Figure 4. This con-

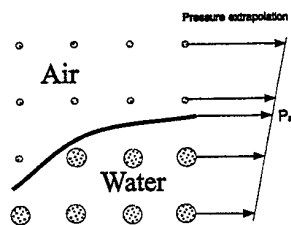


Figure 4: Interpolation Law to Calculate the New Location of the Free Surface

cept is similar to the level-set approach in [8]. with its main advantages:

- The level set ψ is differentiable over the surface.
- There is no interruption of the calculations over the surface.
- Arbitrary surface-inclination up to braking may be possible.
- Immiscible fluid-fluid interaction can be calculated. (e.g. oil-water).

Turbulence Model

For turbulent boundary layer computations the laminar viscosity ν is replaced by

$$\nu_{eff} = \nu + \nu_t \quad (17)$$

where the turbulent viscosity ν_t is computed by using a standard $k - \omega$ model [9]. Using the summation convention the two equations for the determination of k and ω have the following form:

$$\frac{\partial k}{\partial t} + v_k \frac{\partial k}{\partial x_k} = P - c_\mu k \omega + \frac{\partial}{\partial x_k} \left[\left(\nu + \frac{\nu_t}{\sigma_k} \right) \frac{\partial k}{\partial x_k} \right] \quad (18)$$

$$\frac{\partial \omega}{\partial t} + v_k \frac{\partial \omega}{\partial x_k} = c_1 P \omega - c_2 \omega^2 + \frac{\partial}{\partial x_k} \left[\left(\nu + \frac{\nu_t}{\sigma_\omega} \right) \frac{\partial \omega}{\partial x_k} \right] \quad (19)$$

The production term P read as follows:

$$P = \nu_t \left(\frac{\partial v_j}{\partial x_k} + \frac{\partial v_k}{\partial x_j} \right) \frac{\partial v_j}{\partial x_k} \quad (20)$$

The turbulent viscosity is given by:

$$\nu_t = \frac{k}{\omega} \quad (21)$$

and the constant coefficients are:

c_1	c_2	c_μ	σ_k	σ_ω
0.55	0.075	0.09	0.5	0.5

The turbulent transport equations (18) and (19) contain time scales much smaller than the characteristic scales of the flow. So the explicit solution of the System would proceed with significant smaller time steps, prescribed by the numerical stability. To avoid this, an operator splitting is employed to the turbulent equations:

$$\frac{\tilde{Q}_t^{(1)} - \tilde{Q}_t^{(n)}}{\Delta t} + L_1 \left(\tilde{Q}_t^{(n)} \right) = 0 \quad (22)$$

$$\frac{\tilde{Q}_t^{(n+1)} - \tilde{Q}_t^{(1)}}{\Delta t} + L_2 \left(\tilde{Q}_t^{(n+1)} \right) = 0 \quad (23)$$

with the vector of the turbulent transport properties

$$\tilde{Q}_t = \begin{pmatrix} k \\ \varepsilon \end{pmatrix},$$

the convective-diffusive part

$$L_1 \left(\tilde{Q}_t^{(n)} \right) = \vec{v} \nabla \tilde{Q}_t - \nabla \left[\left(\frac{\nu_t}{\sigma_Q} + \nu_l \right) \nabla \tilde{Q}_t \right], \quad (24)$$

and the dissipative part:

$$L_2 \left(\tilde{Q}_t^{(n+1)} \right) = \begin{pmatrix} -P + c_\mu k \omega \\ -c_1 P \omega + c_2 \omega^2 \end{pmatrix}. \quad (25)$$

Equation (22) now is an equation of transport only and can be solved by a standard upwind method while equation (23) contains all source terms which are solved implicitly in order to obtain a more stable behaviour of the solution.

Boundary Conditions

Figure 5 shows the principle arrangement for ship flow calculations and the position of the coordinate system. The x-coordinate coincides with the ship's length direction from bow to stern, the y-coordinate is positive upwards and the z-coordinate defines the transverse direction.

The ship hull is fixed during the calculation i.e. so far sinkage and trim are not taken into account. The

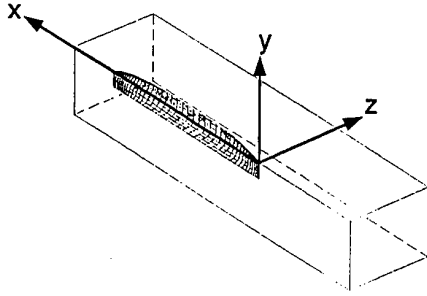


Figure 5: Reference Frame and Ship Location

integrational domain is bounded by different types of boundaries as they are free surfaces, walls, inflow/outflow boundaries and a symmetry plane.

The boundary conditions at the free surface are set according to the description above.

Walls are defined by a zero velocity in normal direction:

$$\vec{v}_n = 0$$

In viscous flow all velocity components are set to zero according to Stokes no-slip condition.

$$u_r = 0, \quad v_r = 0, \quad w_r = 0$$

Values of pressure at a wall have to be deducted from compatibility conditions. For walls with high Reynolds numbers Re the pressure gradient can be neglected because of the boundary layer character of the flow near to the wall, so that on the boundary the pressure can be extrapolated from the flow field with:

$$\frac{\partial p}{\partial n} = 0$$

At inviscid flows over curved walls e.g. in [10] and [11], the pressure gradient at the wall is not zero. In this case the wall pressure is updated by extrapolation from the interior.

At inflow and outflow boundaries the effect of friction is neglected. Then boundary conditions can be derived from the characteristic solution \vec{W} of the corresponding Euler equations, with:

$$\vec{W}(x_n, t) = \vec{W}(x_n - \lambda t)$$

where x_n is the coordinate normal to the boundary and λ is the eigenvalue in that direction.

The boundary conditions at the inflow edge (index r) are determined by the formulation of the variables \vec{W} with the inflow conditions (index ∞) and by compatibility conditions (index e), which are determined by extrapolation from the field.

For the inflow boundary follows

$$u_r = \frac{p_\infty - p_e + (u_\infty + u_e) \sqrt{u_e^2 + \beta^2}}{2(u_e - u_\infty) \sqrt{u_e^2 + \beta^2}}$$

$$p_r = p_\infty - (u_r - u_\infty) \left(u_r + \sqrt{u_e^2 + \beta^2} \right)$$

$$v_r = 0$$

$$w_r = 0$$

At the outflow boundaries a non-reflecting condition for the pressure is used permitting disturbance waves to pass the boundary without reflecting [12]:

$$\frac{\partial}{\partial t} \left(p - \vec{v}_n \sqrt{\vec{v}_n^2 + \beta^2} \right) + \alpha (p - p_\infty) = 0 \quad (26)$$

where \vec{v}_n is the velocity component normal to the boundary. The square root term $\sqrt{\dots}$ represents the artificial speed of sound at the boundary and α is an iteration parameter with the value $0.1 \div 0.2$. All other variables at the outflow are extrapolated.

At the symmetry plane the gradients normal to the symmetry plane have to be zero and further the normal velocity components vanish completely ($\vec{v}_n = 0$).

Integration in Time

Equation (6) is integrated in time by an explicit Runge-Kutta multi-stage scheme. Equation (9) can be written in a semi-discrete form:

$$\frac{dQ}{dt} + Res(Q) = 0 \quad (27)$$

where $Res(Q)$ is the discrete space approach of equation (9). The multi-stage time stepping scheme is formulated as:

$$\vec{Q}^0 = \vec{Q}^\nu$$

$$\vec{Q}^1 = \vec{Q}^0 - \alpha_1 [\delta_1] \Delta t Res(\vec{Q}^0)$$

$$\vec{Q}^2 = \vec{Q}^0 - \alpha_2 [\delta_2] \Delta t Res(\vec{Q}^1)$$

...

$$\vec{Q}^m = \vec{Q}^0 - \alpha_m [\delta_m] \Delta t Res(\vec{Q}^{m-1})$$

$$\vec{Q}^{\nu+1} = \vec{Q}^m$$

The coefficients (α_n) are chosen to maximise the stability of the system and the optional coefficients (δ_n) are employed in the equation for ψ to allow an individual optimisation towards best stability.

A five stage-scheme with three evaluations of the level-set equation has been found to be particularly effective. Its coefficients are:

$$\begin{array}{ll} \alpha_1 = 1/4 & \delta_1 = 0 \\ \alpha_2 = 1/6 & \delta_2 = 0 \\ \alpha_3 = 3/8 & \delta_3 = 1 \\ \alpha_4 = 1/2 & \delta_4 = 1 \\ \alpha_5 = 1 & \delta_5 = 1 \end{array}$$

COMPUTATIONAL RESULTS

A number of calculations of viscous and inviscid flow, mainly in 2-D, were performed to validate the present solution concept and the treatment of free surfaces [10].

In the following, two classical 3-D examples are presented which enable the comparison with other results, in particular for the wave pattern. To enable direct comparisons with inviscid computations in [6] and to eliminate effects of insufficient turbulence modelling, the following calculations are performed likewise for inviscid flow.

The flow past the wigley hull and the serie-60 ship are presented here as computational examples, since for both configurations many numerical and experimental results are available [6] [13].

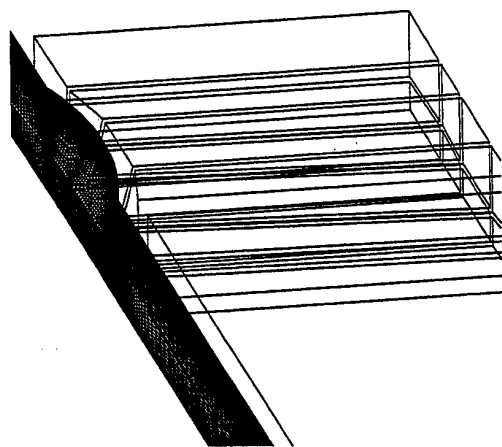


Figure 6: Blocksplitting for the Shallow Water Channel Geometrie, Wigley-Hull

For the simulation of ship flow in restricted water the geometry of the Duisburg towing tank was modeled. In this case the meshing procedure becomes more

difficult so the grids are generated with the commercial ICFM CFD/CAE Hexa code which provides different meshing topologies. Figure 6 shows the principle block splitting of the flow domain for the wigley hull shallow water channel. The block faces are projected onto the geometry surfaces and after a preliminary grid generation, the grid was improved by smoothing operations.

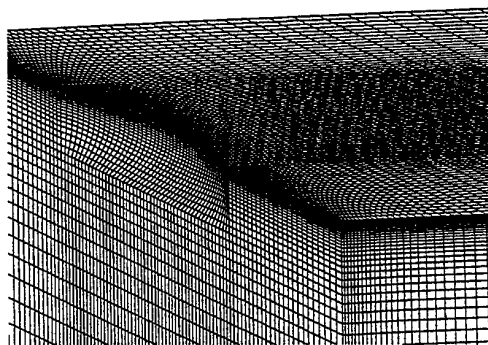


Figure 7: Calculations Grid for Wigley-Hull Computation in Deep Water

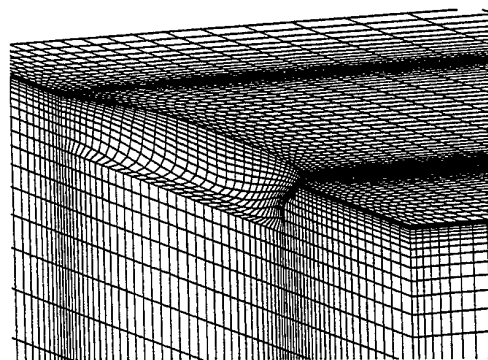


Figure 8: Calculations Grid for Serie-60 Model Computation in Deep Water

The Figures 7 and 8 show portions of the generated grids. The grid points are clustered near the bow and stern in the x -direction, near the free surface in the y -direction and near the ship hull in the z -direction. The grid extends a half ship length upstream from the bow, $1\frac{1}{2}$ ship lengths downstream from the stern, $1\frac{1}{2}$ ship lengths in the transverse direction and 1 ship length down below the undisturbed free surface for the deep water case and $\frac{1}{16}$ ship length for the shallow water case respectively.

Figure 9 shows the calculated wave patterns of the serie-60 model at a Froude number $Fn = 0.316$, the wigley-hull at a Froude number $Fn = 0.250$ and Figure 10 shows the wave patterns for the wigley-hull in the shallow water channel at a Froude number $Fn = 0.250$ with a depth to draft ratio of $h/T = 2.0$.



Figure 9: Wave Patterns for the Serie-60 Model at $Fn = 0.316$ (Top) and for the Wigley-Hull at $Fn = 0.250$ (Bottom) (Wave Heights are 3 times magnified)

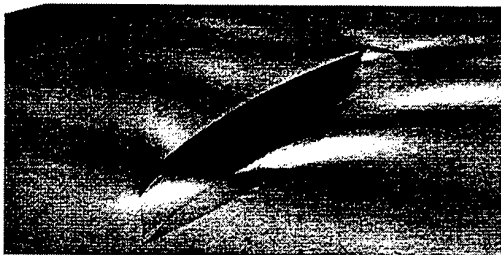


Figure 10: Wave Patterns for the Wigley-Hull in the Shallow Water Channel at $Fn = 0.250$, $h/T = 2.0$ (Wave Heights are 3 times magnified)

The surface elevations along the ship hulls compared with experimental results [14] are shown in Figure 11 and 12. For the shallow water case the wave elevation is plotted against the deep water calculation.

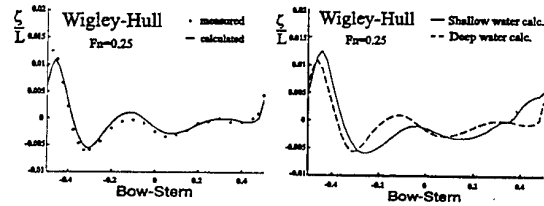


Figure 11: Computed Surface Elevation, Wigley-Hull, Deep and Shallow Water

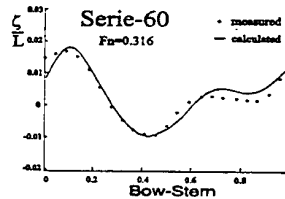


Figure 12: Computed Surface Elevation Serie60 Model, Deep Water

Figure 14 and Figure 13 show the comparison of the computed and measured wave resistance with $C_{w(exp)} = 0.821 \cdot 10^{-3}$ for the wigley hull in deep and shallow water and $C_{w(exp)} = 2.6 \cdot 10^{-3}$ for the serie-60 model in deep water. The overhead wave profiles, computed for both ship configurations, are presented in Figure 15. Further shallow water calculations for will be presented on the conference.

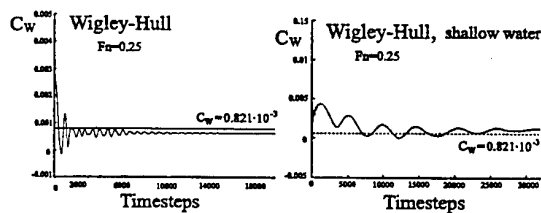


Figure 13: Computed vs. Experimental Wave Resistance, Wigley-Hull, Deep and Shallow Water

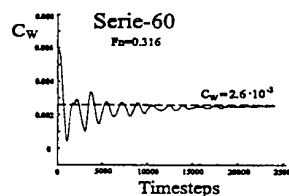


Figure 14: Computed vs. Experimental Wave Resistance, Serie-60 Model, Deep Water

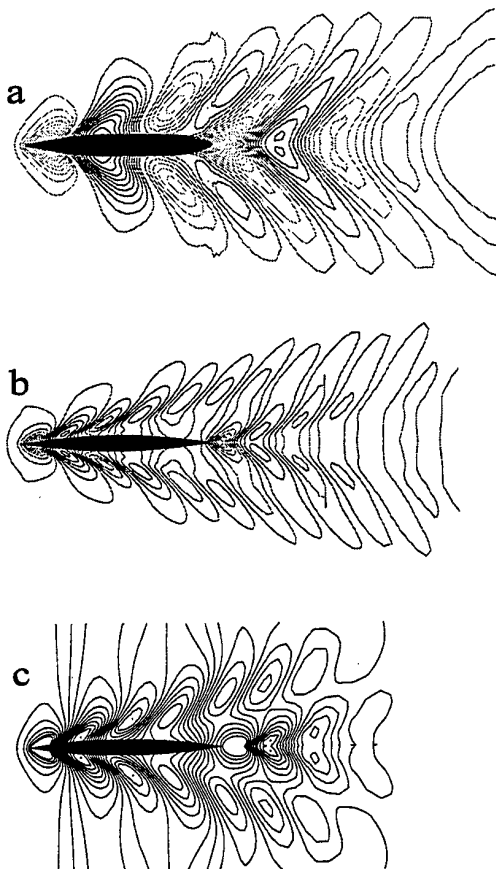


Figure 15: Computed Overhead Wave Profiles, Serie-60 Model, $Fn = 0.319$ (a), Deep Water, Wigley-Hull, $Fn = 0.250$, Deep Water (b), Wigley-Hull, $Fn = 0.250$, Shallow Water $h/T = 2.0$ (c)

The simulation of viscous flow with free surface is of particular interest. In order to validate the model calculations with and without free surface have been performed.

An example of a viscous flow with free surface is represented in figure 16. The deformation of the free water surface, which is due to the formation of the boundary layer in the flow at a flat partly immersed plate, is shown. The friction coefficient c_f is given at different water levels in figure 17. The difference relative to the theoretical (Blasius) value is very small at large distance from the free water surface, only near to the free surface the values differ considerably. This difference is a consequence of the interaction of the free surface with the boundary layer.

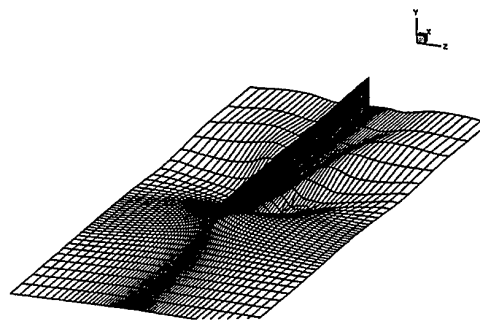


Figure 16: Boundary layer and wave Patterns for a flat plate at $Re = 1000$. (Wave Heights are 3 times magnified)

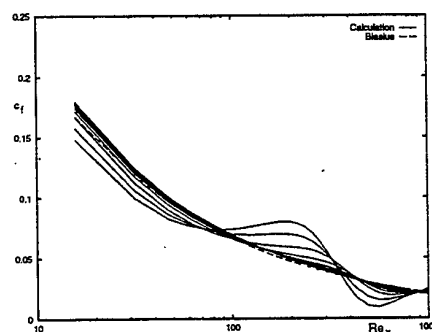


Figure 17: c_f vs. Re_x comparison between calculation and theory (Blasius)

REFERENCES

1. Hänel, D., Breuer, M., Klöcker, J. and Meinke, M., "Computation of unsteady vortical flows," *Computer & Fluids*, Vol. 22, 1993, pp. 229-237.
2. Hänel, D., Meinke, M. and Schröder, W., "Multigrid solutions for the navier-stokes equations," *Finite Approximations in Fluid Mechanics II. Notes on Num. Fluid Mechanics*, Hirschel, E.H., ed., Vol. 25, , Vieweg Verlag Braunschweig, 1989.
3. Miyata, H., "Free-surface flow simulations by finite difference techniques," *Computational Fluid Dynamics 94*, 1994.
4. Chorin, A. J., "A numerical method for solving incompressible viscous flow problems," *Journal of Computational Physics*, Vol. 2, 1967, pp. 12-26.
5. Breuer, M., *Numerische Lösung der Navier-Stokes-Gleichungen für dreidimensionale inkompressible instationäre Strömungen zur Simulation des Wirbelaufplatzens*. PhD thesis, RWTH Aachen, 1991.
6. Farmer, J., Martinelli, L. and Jameson, A. "A fast multigrid method for solving the nonlinear ship wave problem with a free surface," *6th International*

Conference on Numerical Ship Hydrodynamics, Iowa City, Iowa, 2-5 August 1993.

7. Hino, T., Martinelli, L. and Jameson, A., "A finite-volume method with unstructured grid for free surface flow simulations." Sixth International Conference on Numerical Ship Hydrodynamics, 1993.

8. Sussman, M., Smereka, P. and Osher, S., "A level set approach for computing solutions to incompressible two-phase flow," Journal of Computational Physics, Vol. 114, 1994, pp. 146-159.

9. Wilcox, D. C., Turbulence Modeling for CFD, DCW Industries, Inc., La Cañada, California, 1993.

10. Bet, F., Hänel, D. and Sharma, S. D. "Simulation of hydrodynamical free-surface flow," Proc. of Eccomas96, INRIA, Paris, John Wiley & Sons, Ltd., 1996.

11. Bet, F., Hänel, D. and Sharma, S. D. "Simulation of ship flow," Proc. of Numerical Methods in Laminar and Turbulent Flow, 10th International Conference, Swansea 1997, Pineridge Press Limited, 1997.

12. Jameson, A., Schmidt, W. and Turkel, E. "Numerical solutions of the euler equations by finite volume methods using runge-kutta time-stepping schemes," Proc. of AIAA 14th Fluid and Plasma Dynamics Conference, AIAA, Palo Alto, California, 1981.

13. Miyata, H., Zhu, M. and Watanabe, O., "Numerical study on a viscous flow with free-surface waves about a ship in steady straight course by a finite volume method," Journal of Ship Research, Vol. 36, 1992, pp. 332-345.

14. Toda, Y., Stern, F. and Longo, J., "Mean flow measurements in the boundary layer and wake and wave field of a serie 60 cb = 0.6 ship model for froude numbers .16 and .316," Tech. Rep. 352, 1991, Iowa Institute of Hydraulic Research, The University of Iowa.

15. Meinke, M. and Hänel, D. "Time accurate multigrid solutions of the navier-stokes equation," Proc. of Third European Conference on Multigrid Methods, Oct 1990.

NUMERICAL SIMULATIONS OF TURBULENT FLOWS WITH A FREE-SURFACE

R. Broglia¹, A. Di Mascio¹ and R. Muscari¹

¹I.N.S.E.A.N., Istituto Nazionale per Studi ed Esperienze di Architettura Navale

Via di Vallerano 139, 00128-Roma, Italia

Fax: +39-06-5070619; E-Mail: r.brogli@insean.it

ABSTRACT

Large Eddy Simulations of turbulent channel flow with and without free surface are performed. Unsteady Navier Stokes equations are numerically resolved by a spatial second order difference scheme on non-staggered grid; time integration is obtained by a second order two steps semi-implicit Runge-Kutta scheme. Both iterative Successive Over Relaxed Gauss-Seidel scheme and FACR technique are employed to resolve the Poisson equation for the pressure, which resolution is required only at the final sub-step of the integration algorithm. Smagorinsky eddy viscosity approach is adopted to model subgrid-scale stress tensor. Calculations are performed at Reynolds number equal to 180 (based on wall shear velocity, channel half height and kinematic viscosity). Agreement with DNS data for channel flow and free surface effects on turbulent structures are emphasised.

NOMENCLATURE

		τ_{ij}	Subgrid-Scale Stress Tensor
		$\overline{S_{ij}}$	Large-Scale Strain Tensor
$x_i \quad i = 1, 2, 3$	Cartesian Coordinate	u_τ	Friction Velocity
x, y, z	Cartesian Coordinate	$(\cdot)^+$	Wall Unit Non-Dimensionalized Quantities
t	Time	Δ	Filter Width
$u_i \quad i = 1, 2, 3$	Velocity Components	$f(z^+)$	Wall Dumping Function
u, v, w	Velocity Components	C_s	Smagorinsky Constant
p	Pressure	A	Model Constant
$N(u_i)$	Convective Terms		
$L(u_i)$	Diffusive Terms		
$\frac{\partial}{\partial x_i}$	Discrete Difference Operator		
Re	Reynolds Number		
Δt	Time Stepping		
ν_t	Eddy Viscosity		
$\overline{(\cdot)}$	Large Eddy Quantities		
$(\cdot)'$	Subgrid Quantities		
$(\cdot)_{rms}$	Root-Mean-Square Value		

INTRODUCTION

Interaction of turbulent structures with a free-surface is one of the major problems in the field of the numerical simulations of naval flows. Most CFD codes exploit turbulence models developed, calibrated and tested for aeronautical applications; these models do not take into account the effects of the moving boundary, which strongly influences the coherent structures of turbulence [1, 2]. In this paper we begin to analyse this interactions by a numerical studies of a fully developed channel flow with a free surface; our attention is essentially pointed to verify global behaviour of turbulence fluctuations near a free surface, which

are already noted by [1, 2] in the case of juncture flows. Unsteady Navier–Stokes equations are solved by a second order centred scheme. Particular attention is pointed to develop a scheme with low memory storage and computational cost; these intentions have been reached by the use of a second order semi implicit time integration scheme of Runge–Kutta genre, with the Poisson equation solved only at the final sub-step. The method is explained in the first section. Validation and capabilities of the scheme are tested considering the case of turbulent channel flow where DNS results are available. Finally the test case of turbulent channel flow bounded at the top by a rigid lid is analysed.

MATHEMATICAL AND NUMERICAL MODEL

The flow of an incompressible fluid is mathematically modelled by the Navier–Stokes and the continuity equations, that can be written as:

$$\frac{\partial u_i}{\partial t} + \frac{\partial u_i u_j}{\partial x_j} = -\frac{\partial p}{\partial x_i} + \frac{1}{Re} \frac{\partial u_i^2}{\partial x_j \partial x_j} \quad (1)$$

$$\frac{\partial u_j}{\partial x_j} = 0 \quad (2)$$

which have been non-dimensionalized by a characteristic length and velocity (channel half height and friction velocity, are used).

Numerical Model

Time integration of (1) is achieved by means of a two step Runge–Kutta semi-implicit scheme; present method, originally developed by Chorin [3], is a modification of that presented in [4]. Actual scheme is composed by a first fully explicit step:

$$u_i^{(1)} = u_i^n + \Delta t \left[N(u_i^n) + L(u_i^n) - \frac{\delta p^n}{\delta x_i} \right] \quad (3)$$

and a second semi-implicit one:

$$u_i^{n+1} = \frac{u_i^{(1)} + u_i^n}{2} + \frac{\Delta t}{2} \left[N(u_i^{(1)}) + L(u_i^{n+1}) - \frac{\delta p^{n+1}}{\delta x_i} \right] \quad (4)$$

In the previous equations the non-linear (convective) and linear (diffusive) operators have been indicated with N and L :

$$N(u_i) = -\frac{\delta u_i u_j}{\delta x_j} \quad (5)$$

$$L(u_i) = \frac{1}{Re} \frac{\delta u_i^2}{\delta x_j \delta x_j}$$

and the finite difference operator with $\delta/\delta x_i$. Second order centred discretization on non-staggered grid is used for both convective and diffusive terms. Implicit treatment of diffusive terms provides a higher time step, which is limited by the explicit treatment of the advective terms; the stability limit, $CFL = \Delta t \max(u/\Delta x + v/\Delta y + w/\Delta z)$, is 1. Overall accuracy is second order in time and space. As can be noted, explicit calculations of the pressure is needed only at the final step. Fractional step technique is employed for the final step; first a non solenoidal velocity field is evaluated eliminating the pressure term in (4):

$$u_i^{(2)} = \frac{u_i^{(1)} + u_i^n}{2} + \frac{\Delta t}{2} \left[N(u_i^{(1)}) + L(u_i^{(2)}) \right] \quad (6)$$

The divergence free velocity field is then calculated by projecting the non solenoidal field by means of a scalar function ϕ :

$$u_i^{n+1} = u_i^{(2)} - \frac{\Delta t}{2} \frac{\delta \phi}{\delta x_i} \quad (7)$$

Equation (6) is solved by a implicit factorization written in delta form:

$$\delta u_i + L(\delta u_i) \simeq \prod_{j=1,3} \left(1 - \frac{\Delta t}{2Re} \frac{\partial^2}{\partial x_j^2} \right) \delta u_i \simeq \frac{u_i^n - u_i^{(1)}}{2} + \frac{\Delta t}{2} \left[N(u_i^{(1)}) + L(u_i^{(1)}) \right] \quad (8)$$

and then:

$$u_i^{(2)} = u_i^{(1)} + \delta u_i \quad (9)$$

Taking the divergence of the equation (7), and enforcing (2), i.e. the solenoidal condition for the velocity at $n+1$ time level, a Poisson equation for the scalar function ϕ is obtained:

$$\frac{\delta \phi^2}{\delta x_j \delta x_j} = \frac{\Delta t}{2} \frac{\delta u_j^{(2)}}{\delta x_j} \quad (10)$$

This scalar function is related to the pressure field by the following relation:

$$p^{n+1} = \phi - \frac{\Delta t}{2} L(\phi) \quad (11)$$

Poisson Solvers

Solution of the Poisson equation (10) has been obtained by means of either a successive over relaxed method of the Gauss–Seidel type (in conjunction with a multigrid acceleration technique) or a FACR (Fourier Analysis and Cyclic Reduction) method (see [5] and [6] for more details).

Turbulence Model

Large Eddy Simulation idea is to decompose the flow field into a large scale part, which is resolved and a small scale part, the subgrid scale, which is modelled. This decomposition is obtained applying a filter operation in the domain; in a finite difference framework the filter function is simply a top-hat filter, with length corresponding to the grid size itself:

$$\bar{f}(x_i) = \frac{1}{\Delta x_1 \Delta x_2 \Delta x_3} \int_{\mathcal{D}} G(x_i - x'_i) d^3 x'_i \quad (12)$$

where f is the variable to be filtered, with \bar{f} its filtered part and f' its subgrid part; \mathcal{D} is the control volume, that is the finite difference cell.

Applying the filter operation to the incompressible equations (1) and (2), the equations for the resolved field are obtained:

$$\frac{\partial \bar{u}_i}{\partial t} + \frac{\partial \bar{u}_i \bar{u}_j}{\partial x_j} = -\frac{\partial \bar{p}}{\partial x_i} + \frac{1}{Re} \frac{\partial \bar{u}_i^2}{\partial x_j \partial x_j} - \frac{\partial \tau_{ij}}{\partial x_j} \quad (13)$$

$$\frac{\partial \bar{u}_j}{\partial x_j} = 0 \quad (14)$$

The subgrid-scale stress tensor:

$$\tau_{ij} = \bar{u}_i \bar{u}_j - \bar{u}_i \bar{u}_j \quad (15)$$

represents the effect of the small scale (that are filtered out) upon the filtered quantities; it involves quantities that are unknown, and therefore has to be modelled in order to close the system. In the present work the simply Smagorinsky eddy viscosity model [7] has been used; the subgrid-scale stress tensor is modelled as:

$$\tau_{ij} - \frac{\delta_{ij}}{3} \tau_{kk} = -2\nu_t \bar{S}_{ij} \quad (16)$$

The trace of the subgrid-scale stress tensor is incorporated in the pressure term. In the previous \bar{S}_{ij} is the resolved scale strain rate tensor:

$$\bar{S}_{ij} = \frac{1}{2} \left(\frac{\partial \bar{u}_i}{\partial x_j} + \frac{\partial \bar{u}_j}{\partial x_i} \right) \quad (17)$$

where ν_t is the Smagorinsky eddy viscosity:

$$\nu_t = (C_s \Delta)^2 |\bar{S}| f(z^+) \quad (18)$$

and where $|\bar{S}| = \sqrt{2\bar{S}_{ij}\bar{S}_{ij}}$ is the magnitude of the large-scale strain rate tensor, C_s is the Smagorinsky constant ($C_s = 0.1$ has been adopted), and Δ is the filter width, that, for finite difference discretization, is:

$$\Delta = (\Delta x \Delta y \Delta z)^{\frac{1}{3}} \quad (19)$$

In the equation (18) has been considered a wall dumping function for the eddy viscosity:

$$f(z^+) = \left(1 - e^{-Az^+}\right)^2 \quad (20)$$

where $A = 0.04$ and z^+ is the distance from the wall, non-dimensionalized by viscosity and friction velocity. In what follows bar over filtered variables will be omitted, explicit notations will be used where doubts can occur.

RESULTS

In this section some results about fully developed turbulent channel flow and free surface flow are presented. Focused case is characterised by a physical domain with extensions of $(5/2)\pi\delta$, $(1/2)\pi\delta$ and 2δ (for channel flow, δ for free surface flow) along streamwise (x), spanwise (y) and normal to wall (z) direction respectively. The flow is periodic along stream and spanwise direction; in the normal direction, no-slip wall is present at the bottom for both test cases, whereas at the top, either a no-slip wall (channel flow) or a rigid lid (free surface flow) is present. The rigid-lid boundary conditions is often used as a representation of a free surface boundary with negligible waves. Mass flow is maintained by a constant forcing term on x -component of momentum equation. Reynolds number based on wall shear velocity u_τ , half channel height δ and kinematic viscosity ν is 180, which correspond to a Reynolds number of about 3300 based on mean centerline velocity U_c , half channel height and kinematic viscosity. Physical domain is uniformly discretized along x - and y -directions, whereas non-uniform mesh is used in the z -direction; hyperbolic tangent function is used to cluster points near the wall. In the case of free surface flow, a power law is also adopted in order to cluster points also on the top rigid lid. The initial condition used in the present work for the velocity field is the theoretic logarithmic turbulent profile with random fluctuations superimposed. The intensities of the fluctuations are modulated by the value of the mean velocity. The numerical simulations are carried until a statistically steady condition is reached, which is identified by a linear profile of the total shear stress; time average statistics are then computed over ten non-dimensional unit of time. Mean profile are obtained averaging in time and along the homogeneous directions. In order to reduce the computational cost, the extension of the physical domain is less than the similar test case considered by J. Kim et al. [8]; as a consequence the turbulent fluctuations are not completely uncorrelated at a distance of one half period in the streamwise and spanwise homogeneous directions (see figures (1) and (2)). How-

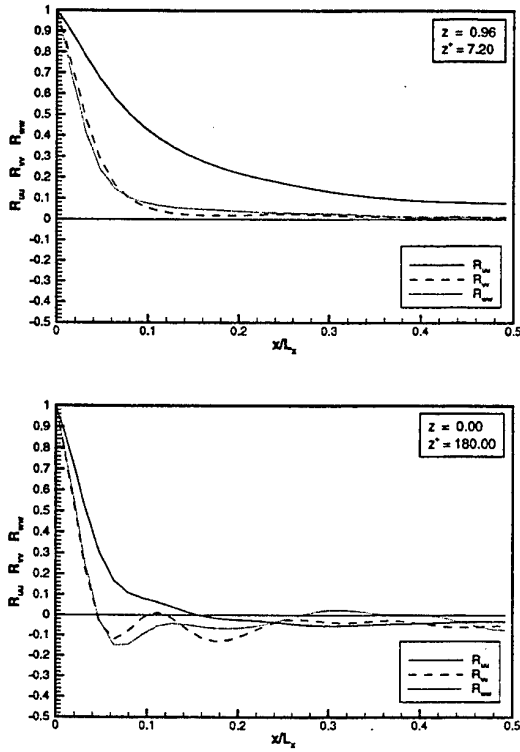


Figure 1: Two-points streamwise correlations. Upper: close to the wall; down: close to the centerline.

ever, as demonstrate by J. Jiménez et al. [9], physical domain is wider enough to provide good agreement in the statistical quantities.

Channel Flow

In this section some results about fully developed turbulent channel flow are presented in order to both show the capabilities of the scheme and setting model constant C_s . Finest grid is composed by $66 \times 66 \times 65$ points; the distance from the wall of the first point is 0.1 wall unit; about 20 points are within 30 wall unit from the solid boundary. Streamwise and spanwise discretization steps are about $\Delta x^+ \simeq 22$ and $\Delta y^+ \simeq 4.4$ wall unit respectively. In order to set the Smagorinsky constant, some simulations were performed for different values of C_s ; in figure (3) logarithmic profile for these simulations are presented. As it can be noted, good agreement with the theoretic lin-log law is obtained for $C_s = 0.10$, which is the value used for all the following simulations, if not otherwise specified. Comparing the logarithmic profile obtained with $C_s = 0.10$ and without small-grid scale model, it can also be noted that the grid con-

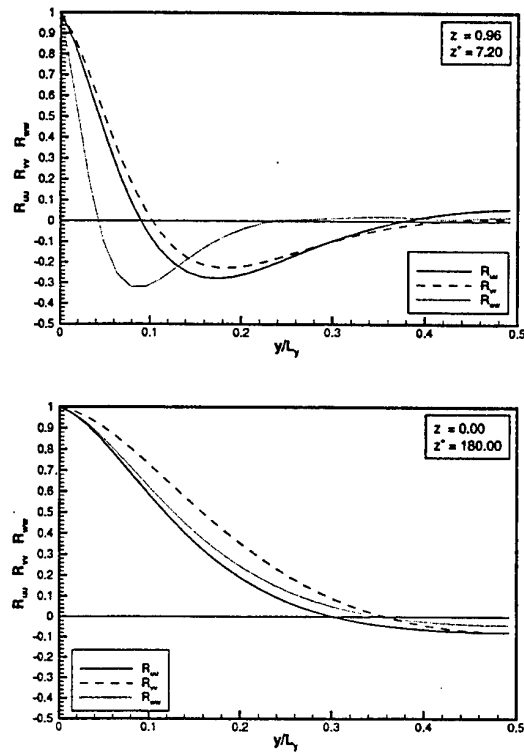


Figure 2: Two-points spanwise correlations. Upper: close to the wall; down: close to the centerline.

sidered in this work is not enough refined in order to perform direct numerical simulations. However comparison with a coarser grid (figure (4)) shows that the grid employed is refined enough for large eddy simulations. Capabilities of the presented scheme and of the sub-grid scale model adopted are tested by comparisons with DNS data of [8]. Logarithmic profile obtained with the finest grid, is in very good agreement with DNS data (not reported here) and with theoretic law (see figure (4)); moreover good agreement can be observed for root-mean-square velocity fluctuations and Reynolds shear stresses, reported in figure (5) and (6). Poorer agreement can be observed for the x component of velocity root-mean-square fluctuations, particularly in the peak value: this can be due to the subgrid-scale model.

Free Surface Flow

In this section results obtained considering the presence of a free surface at the centerline of the channel are presented. A rigid lid is used as model for the free surface, thus null gradient of tangential velocity and pressure, and zero normal velocity are enforced on

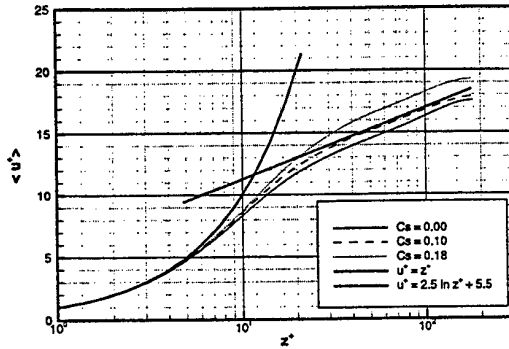


Figure 3: Logarithmic profiles for different values of C_s ; grid $66 \times 66 \times 65$.

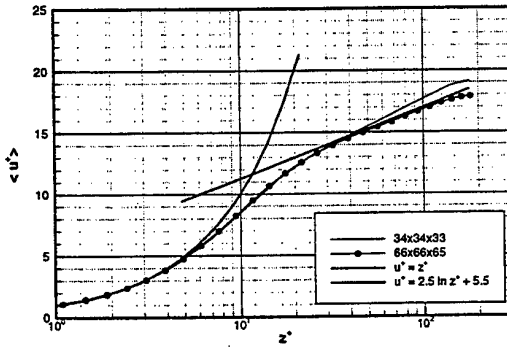


Figure 4: Logarithmic profiles for different grid; $C_s = 0.10$.

the upper boundary. Numerical simulations were carried out on a $66 \times 66 \times 65$ grid, uniformly distributed along homogeneous directions; in the transversal direction the points are clustered in the solid wall region and in the rigid lid boundary by means of hyperbolic tangent function and power law. The distance of the first point from the rigid wall is $\Delta z^+ = 0.1$ wall unit and more than 25 points are within 30 wall unit from the solid boundary. Instead from the rigid lid, the first point is located at a distance of about $\Delta z^+ \simeq 1.0$ wall unit. Streamwise and spanwise discretization steps are about $\Delta x^+ \simeq 22$ and $\Delta y^+ \simeq 4.4$ wall unit respectively. Attention is pointed on the difference between the results on the two test case, such to evidence the interaction between turbulent structures with a free surface. Such presence is already evident on the mean and the logarithmic profiles (figures (7) and (8)), where the presence of a free surface seems to have a dissipative behaviour on mean quantities.

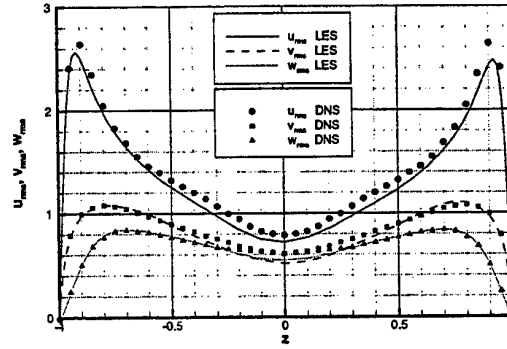


Figure 5: Comparison with DNS data: root-mean-square velocity fluctuations.

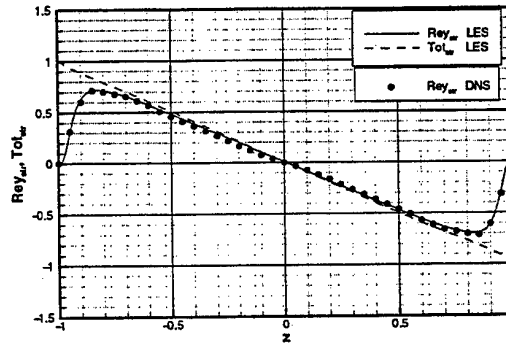


Figure 6: Comparison with DNS data: total shear $(-u'w' + \frac{1}{Re} \frac{\partial u}{\partial y})$ and Reynolds $(-u'w')$ stresses.

Similar behaviour can be noted on the fluctuations in the near wall region; in fact (see figure (9)) the peak value of root-mean-fluctuations is reduced. In the same figure can be also observed, near the free surface, an intensification of the fluctuations of the tangential component velocities and a great dissipation of the normal component, leading to a bidimensionalization of the turbulence structures. The net behaviour is pointed out in figure (10) where the turbulent kinetic energy profile is presented; while a dissipation is present near the wall, a production of turbulent fluctuations are evident near the free surface. These effects are in agreement with what has been observed numerically by Sreedhar et al. [2] and experimentally by Longo et al. [10] in the case of solid/rigid-lid junction.

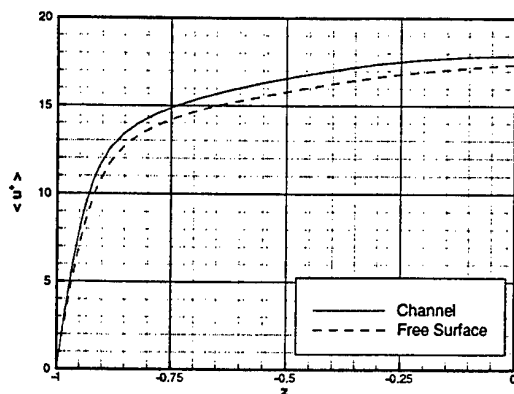


Figure 7: Streamwise mean velocity profiles: comparison between channel and free surface flow.

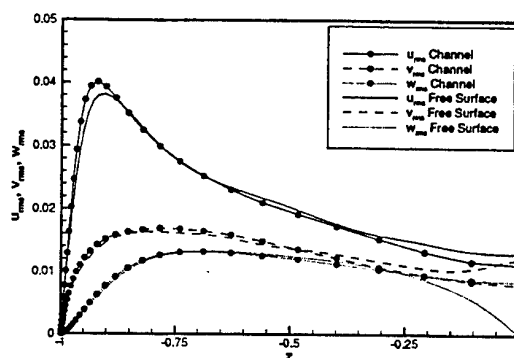


Figure 9: Root-mean-square profiles: comparison between channel and free surface flow.

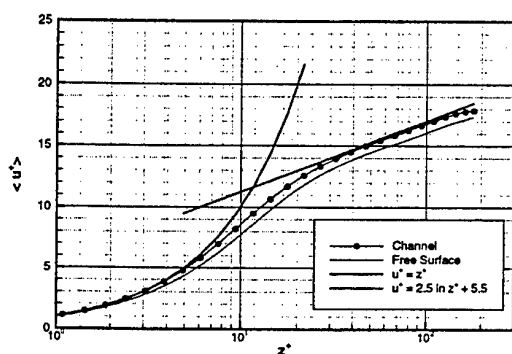


Figure 8: Logarithmic profiles: comparison between channel and free surface flow.

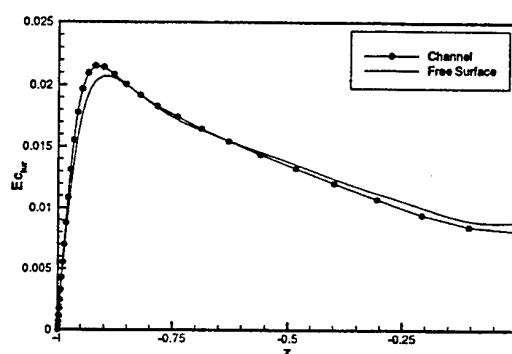


Figure 10: Turbulent kinetic energy: comparison between channel and free surface flow.

CONCLUSIONS

Large eddy simulations of fully developed channel turbulent flow with and without free surface has been performed. Numerical capabilities of the scheme and subgrid scale-model has been validated by comparisons with DNS data; good agreement has been shown. Numerical results about free surface flow have been shown qualitative agreement with both available numerical and experimental observations. Further development and analysis are required in order to better understand interactions between free surface and turbulent structures.

ACKNOWLEDGEMENTS

This work was supported by the Italian Ministry of Transportation in the frame of INSEAN research plan 1997-99.

REFERENCES

1. Choi, J.E. and Stern, F. "Solid-fluid juncture boundary layer and wake with waves," VI Int. Conf. on Num. Ship Hydrod., Iowa City, Iowa, USA, Vol. 1, 1993, pp. 215-238.
2. Sreedhar, M. and Stern, F., "Large eddy simulation of temporally developing juncture flows," Int. J. for Num. Methods, Vol. 28, 1998, pp. 47-72.
3. Chorin, A.J., "On the convergence of discrete approximations to the navier-stokes equations," Math. Comput., No. 23, 1969, pp. 341-353.
4. Le, H. and Moin, P., "An improvement of fractional step methods for the incompressible navier-stokes equations," J. Comp. Phys., No. 92, 1991, pp. 369-379.
5. Hirsh, C., "Iterative methods for the resolution of algebraic systems," Numerical Computation for Internal and External Flows, 1st ed., Vol. 1, Jhon Wiley and Sons, New-York, 1988, pp. 469-473.
6. Press, W.H., Flannery, B.P., Teukolsky, S.A. and Vetterling, W.T., "Partial differential equations," Numerical Recipes, 1st ed., Cambridge Univerity Press, Cambridge, 1987, pp. 646-652.
7. Smagorinsky, J., "General circulation experiments with the primitive equations. i. the basic experiment," Mon. Weather Rev., No. 91, 1963, pp. 99-164.
8. Kim, J., Moin, P. and Moser, R., "Turbulence statistics in fully developed channel flow at low reynolds number," J. Fluid Mech., Vol. 177, 1987, pp. 133-166.
9. Jiménez, J. and Moin, P., "The minimal flow unit in near-wall turbulence," J. Fluid Mech., Vol. 225, 1991, pp. 213-240.
10. Lqngo, J., Huang, H.P. and Stern, F., "Solid/free-surface juncture boundary layer and wake, piercing flat plate," Exp. Fluids, in press.

FREE SURFACE VISCOUS FLOW AROUND SHIP MODELS

A. Cura Hochbaum¹, C. Schumann²

¹Hamburg Ship Model Basin, Bramfelder Strasse 164, D-22305 Hamburg, Germany,
FAX: +40 69203 345, E-Mail: cura@hsva.de;

²Flensburger Schiffbau Gesellschaft, Batteriestrasse 52, D-24939 Flensburg, Germany,
FAX: +461 4940 514, E-Mail: cschuman@fsg-ship.de

ABSTRACT

The free surface viscous flow around a ship model moving steadily straight ahead is computed by solving the Reynolds-averaged Navier-Stokes equations (RANSE) with a finite-volume method. Reynolds-stresses are modelled with the $k - \omega$ turbulence model, and the free surface is captured with a Level Set technique considering a two-phase flow. The dynamic sinkage and trim are not yet taken into account. After describing the mathematical model and its numerical implementation, results for the Series 60 ship $C_B = 0.6$ at $R_n = 5.27 \cdot 10^6$, $F_n = 0.316$ are presented and compared with available experimental data.

INTRODUCTION

One of the major interests in numerical ship hydrodynamics is the computation of the viscous free surface flow around a ship aiming to avoid model tests, which suffer from empirical corrections and scaling problems. Computations at model scale neglecting the free surface (double-body flow) are state of the art. The accuracy achieved is sufficient for ship hull improvement. In comparison, methods which take into account the free surface are still in development. Methods for determining the free surface can be classified in two groups: i) Methods in which one boundary of the computational domain coincides with the free surface and the grid is moved, stretched and compressed during the iteration process and ii) Methods in which the numerical grid is fixed and the free surface is defined by some kind of scalar function. This function divides the domain into grid zones, which are either filled with water or not. We chose a method of the second type, because of its potential to handle complicated ship forms (e.g. protruding bulbous bows, barge sterns) and flow phenomena such as breaking waves or spray. Among the existing algorithms of this type we chose a two-phase flow formulation and the Level Set technique to 'capture' the free surface as the interface between water and air.

We will describe the Level Set method and its numerical implementation. The results obtained for the flow around the Series 60 model will be presented and discussed, and goals and limits of the method indicated.

MATHEMATICAL MODEL

Mass and Momentum Conservation

We consider the free surface flow around a ship as the flow of one fluid with two immiscible phases (water and air). The interface between both phases represents the free surface. Because each phase is incompressible, the global flow can as such be handled as incompressible. The governing equations are the Reynolds-averaged Navier-Stokes equations, in which the eddy viscosity approach is used for approximating the Reynolds-tensor, and the continuity equation:

$$\frac{\partial v_i}{\partial t} + \frac{\partial(v_i v_j)}{\partial x^j} = \frac{\cos \alpha_i}{F_n^2} - \frac{1}{r_1} \frac{\partial(p + 2/3 r_1 k)}{\partial x^i} + \frac{\partial}{\partial x^j} \left[\left(\frac{r_2}{R_n} + \nu_t \right) \left(\frac{\partial v_i}{\partial x^j} + \frac{\partial v_j}{\partial x^i} \right) \right] \quad (1)$$

$$\frac{\partial v_j}{\partial x^j} = 0 \quad (2)$$

All variables have been nondimensionalised by the ship speed U_0 , the ship length L and the water den-

sity ρ_w . The surface tension has not been taken into account in equation (1).

v_i is the mean velocity component in the cartesian direction i and x^i the corresponding cartesian coordinate. The directional cosine of the gravity force referred to the cartesian direction i is denoted by $\cos \alpha_i$, p is the mean pressure, k the turbulent kinetic energy and t the time. The eddy viscosity ν_t is determined by using the $k - \omega$ turbulence model from Wilcox [17]. $r_1 = \rho/\rho_w$ and $r_2 = \nu/\nu_w$ are the ratios between the local density and kinematic viscosity and the corresponding values for water. These ratios have constant values ρ_l/ρ_w and ν_l/ν_w in air, ρ_l and ν_l being the density and viscosity of air, and both equal one in water. $F_n = U_0/\sqrt{gL}$ is the Froude number, g denoting the acceleration due to gravity, and $R_n = U_0 L/\nu_w$ is the Reynolds number.

Instead of solving the two corresponding conservation equations for the density and viscosity, which would cause numerical difficulties, ρ and ν are determined by the Level Set technique (see below).

In reality, the transition from water to air occurs suddenly, at the interface between the fluids. Nevertheless, it is advantageous from a numerical point of view, to smooth this transition to some extent. For this reason, a thin region in the neighbourhood of the interface is considered, in which the density and the viscosity, i.e. r_1 and r_2 , are interpolated between the values for water and air. An important feature of the Level Set method used in this work is that the thickness of this region can be prescribed, making it possible to choose it just large enough for stability.

When deriving equation (1) from the usual equation for one phase, the variability of the density was not taken into account in the diffusion term. Although this and other simplifications made in the transition region do not seem to deteriorate the results, their consequences have yet not been analysed in detail.

The conservation equations (1) and (2) are solved throughout the computational domain. No special treatment is necessary for the different phases. The continuity of the velocity and pressure fields enforced in this way at the slightly smeared interface substitutes the usual boundary conditions when considering only one phase. This continuity also avoids numerical problems when solving the equations of the turbulence model used (see below), for which the smoothness of the numerical grid and the discrete approximation of the solution is very important.

Turbulence Model

The eddy viscosity is determined with the $k - \omega$ turbulence model from Wilcox [17]. In this model ν_t is defined as the quotient of the turbulent kinetic energy

k and its specific dissipation rate ω , for which two additional conservation equations have to be solved:

$$\frac{\partial k}{\partial t} + \frac{\partial(v_i k)}{\partial x^i} = \frac{\partial}{\partial x^i} \left[\left(\frac{r_2}{R_n} + \sigma^* \nu_t \right) \frac{\partial k}{\partial x^i} \right] \quad (3)$$

$$+ \nu_t \left(\frac{\partial v_i}{\partial x^j} + \frac{\partial v_j}{\partial x^i} \right) \frac{\partial v_i}{\partial x^j} - \beta^* \omega k$$

$$\frac{\partial \omega}{\partial t} + \frac{\partial(v_i \omega)}{\partial x^i} = \frac{\partial}{\partial x^i} \left[\left(\frac{r_2}{R_n} + \sigma \nu_t \right) \frac{\partial \omega}{\partial x^i} \right] \quad (4)$$

$$+ \gamma \left(\frac{\partial v_i}{\partial x^j} + \frac{\partial v_j}{\partial x^i} \right) \frac{\partial v_i}{\partial x^j} - \beta \omega^2$$

All variables are nondimensionalised in the same manner as in the momentum equations. The model constants are:

$$\sigma^* = \sigma = 0.5, \quad \beta^* = 0.09, \quad \beta = 0.075, \quad \gamma = 0.555$$

The usual equations for one phase have been slightly modified here by introducing the ratio r_2 in the diffusion terms to account for the two phases. The variability of the density in these terms was again neglected. Despite the non-physical modifications affecting the (rather thin) transition region between water and air, the turbulence model behaves as expected in this region and yields good results overall (see explanation of figure 4, TESTCASE).

To make things easier, we decided to use wall functions in our first applications of the method to calculate free surface ship flows, making it possible to choose a much coarser grid resolution at the ship wall. It should be noted that no changes are necessary in the equations of the turbulence parameters (3) and (4) when using wall functions.

The law of the wall, written in nondimensional form and our two-phase flow notation, is used to determine the magnitude τ_w of the wall shear stress assuming a known velocity field:

$$\tau_w = \frac{U^2 r_1}{\left[\frac{1}{0.41} \ln \left(\sqrt{\frac{\tau_w}{r_1} \frac{n}{r_2} R_n} \right) + 5 \right]^2} \quad (5)$$

U is the component of the velocity parallel to the wall and n the distance to the wall from the first cell center next to the wall. In every new iteration step, the argument of the logarithmic function is evaluated using the previous value of τ_w . Once τ_w has been calculated, the values of the turbulence parameters in the

first cell center and the wall shear stress field (for output purposes) are determined with the following formulae, instead of solving (3) and (4):

$$k = 3.333 \frac{\tau_w}{r_1} \quad (6)$$

$$\omega = \frac{1}{0.123 \pi} \sqrt{\frac{\tau_w}{r_1}} \quad (7)$$

$$\tau_i = \tau_w \frac{v_i}{v_j v_j} \quad (8)$$

Level Set Technique

The Level Set Method from *Osher & Sethian* [6] is used to capture the interface between water and air. This technique was further developed and applied for the computation of (2D) free surface flows by *Sussman et al.* [12, 13]. *Vogt* [16] applied the method to calculate the flow around submerged profiles, getting better results than with a moving grid technique.

At each point of time, the interface can be expressed in an implicit way as $\Phi(x^i, t) = 0$. This is also true if the interface has a complicated shape, e.g. in the case of breaking waves. Therefore, the material derivative of Φ is zero on all points of the interface. In the Level Set technique, a scalar field Φ having a zero level set (isosurface $\Phi = 0$) coinciding with the interface is defined throughout the computational domain. Extending the condition $\frac{D\Phi}{Dt} = 0$ to all points of the domain leads to the transport equation for the level set function:

$$\frac{\partial \Phi}{\partial t} + \frac{\partial(v_i \Phi)}{\partial x^i} = 0 \quad (9)$$

Due to the continuity of the Level Set Function Φ at the interface, no numerical difficulties arise when solving this equation with usual convection schemes. In every point (cell center) of the computational domain, the initial value of Φ is chosen to be the distance (with sign) to the initial position of the interface. According to equation (9), Φ is exclusively transported by convection and always remains positive in one phase and negative in the other.

The density would be $\rho = \rho_w$ (water) for $\Phi > 0$ and $\rho = \rho_l$ (air) for $\Phi < 0$. In the same way, the molecular viscosity of the fluid would suddenly change its value when Φ changes its sign, both affecting the stability and the convergence of the numerical method. In order to smooth these discontinuities, density and viscosity are determined with the following formulae:

$$r_1 = \frac{\rho}{\rho_w} = (1 - c) \frac{\rho_l}{\rho_w} + c$$

$$r_2 = \frac{\nu}{\nu_w} = (1 - c) \frac{\nu_l}{\nu_w} + c \quad (10)$$

$$c = 1 \quad \Phi > \alpha \text{ (water)}$$

$$c = 0 \quad \Phi < -\alpha \text{ (air)}$$

$$c = \frac{1}{2} \left[1 + \sin \left(\frac{\pi \Phi}{2\alpha} \right) \right] \quad -\alpha \leq \Phi \leq \alpha$$

The parameter α allows for prescribing the thickness of the transition region. As long as Φ is the nondimensionalised distance from the considered point to the interface, this thickness is 2α , as can be seen in (10). We choose α so it roughly equals the vertical grid spacing near the waterline of the ship at rest.

During the time marching process (see NUMERICAL METHOD), the velocity equations (momentum conservation), the pressure-correction equation (derived from mass conservation) and the equations of the turbulence parameters are solved first, assuming a known Φ distribution. After that, a new approximation of Φ is calculated with equation (9). This equation moves the interface correctly but Φ does not remain a distance function. Keeping Φ as a distance is crucial for keeping the thickness of the interface constant, which is important for stability and for limiting mass losses. Thus, it is recommendable to 'reinitialize' Φ before starting a new time step.

Reinitialization

The reinitialization is simply the replacement of the Φ distribution resulting from (9) by another distribution $\hat{\Phi}$, which in each point again represents the distance to the interface and behaves better than Φ . Because in all points on the interface the distance is zero, the interface remains unchanged while doing so, i.e. the isosurfaces $\hat{\Phi} = 0$ and $\Phi = 0$ coincide.

Theoretically, the reinitialization could be done in a geometric way. This would demand an enormous CPU time and would in addition be unfavourable from a numerical point of view, due to the resulting non-smooth distribution. An elegant alternative to perform the reinitialization consists in determining $\hat{\Phi}$ as the steady state solution of the following equation, with the initial condition $\hat{\Phi}(x^i, 0) = \Phi(x^i, t)$:

$$\frac{\partial \hat{\Phi}}{\partial \tau} + S(\Phi) \left(\sqrt{\frac{\partial \hat{\Phi}}{\partial x^i} \frac{\partial \hat{\Phi}}{\partial x^i}} - 1 \right) = 0 \quad (11)$$

$S(\Phi) = \Phi / \sqrt{\Phi^2 + \epsilon^2}$ is a smoothed sign function. Following *Sussman et al.* [13] we choose ϵ to be roughly as large as α . When the steady state is achieved, the first term in (11) vanishes. Thus, it must

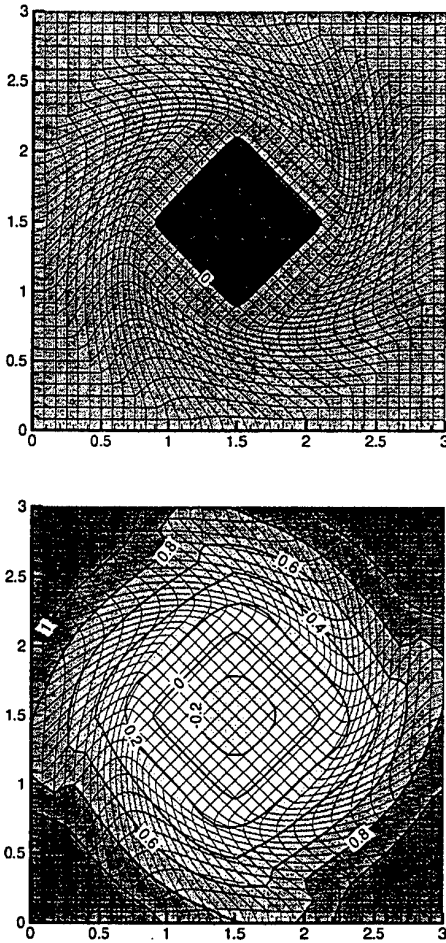


Figure 1: 2D test for reinitialization algorithm. Initial distribution (top) and achieved distance distribution (bottom).

be $|\nabla \hat{\Phi}| = 1$. This is exactly the constraint which must be fulfilled by $\hat{\Phi}$ to be a distance function. Strictly speaking, the reinitialization has nothing to do with the flow. Therefore, usual convection schemes are not suitable for the discretisation of equation (11). The 1st order ENO scheme described in [12, 13] was extended here for 3D curvilinear grids, and the explicit Euler method is used for integrating (11) in time.

Figure 1 shows the result of a 2D test of the implemented reinitialization technique. The initial values of $\hat{\Phi}$ (upper picture) were chosen to be $\hat{\Phi} = -1$ inside the square, $\hat{\Phi} = 1$ outside of it, and $\hat{\Phi} = 0$ on the square contour, which plays the role of the interface. The lower picture shows isolines of $\hat{\Phi}$ after achieving the steady state solution of equation (11) after some hundreds steps. Despite grid and boundary effects, the solution represents satisfactorily the

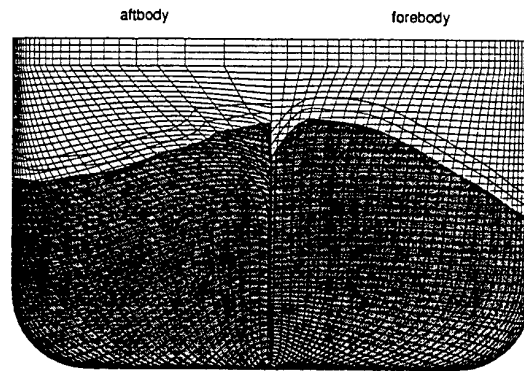


Figure 2: Wetted area and transition zone on the hull of the Series 60 ship at $F_n = 0.316$.

distance to the square contour.

It is not necessary in practice to solve (11) exactly. Moreover, a few steps are usually sufficient, because $\hat{\Phi}$ must be reinitialized in the neighbourhood of the interface only and, when solving (11), the solution is first achieved at the interface and then at more and more distant points [7]. Additionally, the initial values of $\hat{\Phi}$ are much better in practice than in this test. Thus, only three steps were sufficient in our computations to keep the chosen thickness of the interface constant, as can be seen from the 'wetted' area on the hull of the Series 60 ship shown in figure 2. The white band represents the transition region between water and air, i.e. the region in which $-\alpha < \Phi < \alpha$. When integrating equation (11), the nondimensionalised time step was chosen to be $\alpha/10$. The reinitialization hardly increased the CPU time. The most probable explanation is that the behavior of the Level Set function improves with reinitialization, leading to less iterations needed for solving equation (9).

Despite the implemented reinitialization, global mass conservation cannot be guaranteed. Nevertheless, mass losses were not relevant in all computed steady flow cases. The difference between the mass fluxes at inlet and outlet of the computational domain is typically less than 10^{-4} , the mass flux at the inlet being of order one.

NUMERICAL METHOD

The conservation equations are discretised on a non-orthogonal body fitted grid by using a finite volume method. All unknowns (pressure, velocities, turbulent parameters and Level Set function) are defined at the cell centers. The Diffusion terms are approximated with the Central Differencing Scheme (CDS) and the convected velocities in the momentum fluxes, with the

Linear Upwind Differencing Scheme (LUDS). The mass fluxes are calculated by the technique of *Rhie & Chow* [8]. The SIMPLE algorithm is used to solve the resulting non-linear equations set. This method is similar to the method described in [1]. Except for the implementation of the Level Set technique in the Navier-Stokes solver NEPTUN, only minor changes were necessary to extend the method for two-phase flows.

The boundary conditions on the boundaries of the computational domain have remained almost unchanged compared to the double-body flow computed in the past. The no-slip condition on the hull is enforced indirectly, through the wall functions. The centerplane represents a plane of symmetry. Therefore, the free-slip condition is set there and both the convection and diffusion fluxes are set to zero in the turbulence equations. At the inlet, undisturbed flow is assumed. Thus, velocities and turbulence parameters are prescribed there. At the outlet, zero gradient conditions are used for all these variables, while the pressure is assumed to be undisturbed. Because the gravity is taken into account in the momentum equations, the undisturbed pressure corresponds to a hydrostatic distribution referred to the waterline of the ship at rest. At the outer lateral boundary, a free-slip condition is set. The boundary conditions on the upper boundary of the computational domain are not important now, because the grid is extended as much towards the main deck as necessary to prevent the water from reaching this boundary. Moreover, the clearance between the interface and the upper boundary should be large enough to avoid wall effects and convergence problems. Boundary conditions are not necessary on every boundary for the Level Set function, because the transport equation (9) is a hyperbolic rather than an elliptic equation. The values of Φ are prescribed at the inlet, but are extrapolated on to all other boundaries.

Due to the changes made in the momentum equations to account for the two phases, slight modifications had to be made in the *Rhie & Chow* term of the mass fluxes, as well as in the coefficients of the pressure-correction equation and in the formulae for the correction of velocities and mass fluxes. These changes simply involve adding the density ratio r_1 to the denominators of the corresponding terms.

As opposed to double-body flow computations, which are performed by using a steady iteration process, free surface flow computations are performed with a (pseudo) time marching process. Integration in time is achieved with the backward Euler scheme for all time derivatives.

Because the time integration simply represents an

aid to achieve the steady state solution, the governing equations are solved approximately in every time step. The momentum and mass conservation equations (1) and (2), the latter one via the pressure-correction equation, are solved first. Then, the equations (3) and (4) for k and ω are solved, completing a SIMPLE loop. After that, the transport equation (9) for the Level Set function is solved and the reinitialization (11) completes the time step. For stability reasons, more than one SIMPLE loop are sometimes necessary during certain periods of the time marching procedure. Additionally, very small time steps are necessary to avoid divergence, both making the solution procedure much less effective than the usual procedure for double-body flows (see TESTCASE).

To avoid the generation of waves due to a violation of mass and momentum conservation by the initial values, computations usually start from rest. The Level Set function is initialized with the distance to the water surface. The ship is then accelerated until it reaches the desired speed. The velocity at the inlet plane is currently updated and an inertial force acts during the acceleration period, which typically takes a third of the total number of time steps.

Several types of non-reflecting boundary conditions to prevent wave reflections (especially at the inlet and outlet planes) have been tested, but none of them were really satisfactory yet. For the time being, a numerical beach, consisting in damping waves in the far field by a fictive vertical force implemented in the momentum equation in vertical direction, is used. Although this does not completely avoid reflections, it has proved to be helpful in reducing them.

For the accuracy of the computed forces on the hull, it is important that the gravitational forces balance the pressure forces in the momentum equations. In the case of an undisturbed flow with hydrostatic pressure distribution, e.g., these forces should cancel. The usual interpolation technique does not guarantee this balance on curvilinear grids. Therefore a secondary flow will arise affecting the prediction of forces on the hull clearly. A special treatment of the gravity force terms reduces this problem.

TESTCASE

One testcase is presented and compared with the detailed flow measurements of [14], [15] and [11]. It is the flow around a Series 60 ship model with length 3.048m (scale 1 : 40), block coefficient 0.6 and a Froude number of 0.316 which results in a Reynolds number of $5.27 \cdot 10^6$. Trim and sinkage were fixed. First attempts to calculate the free surface flow on a block-structured grid with non-matching interfaces led to steps in the wave elevation near to those inter-

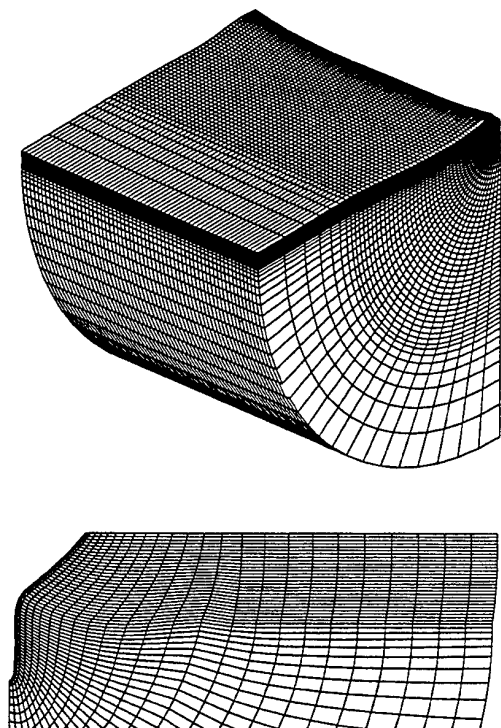


Figure 3: Views of the numerical grid with proper resolution for the computation of free surface flow. Perspective view along the hull (above), partial view in a cross section (below).

faces. To avoid such problems we decided to discretise the numerical domain with a single block structured grid with a length of approx. $3L$, depth L and width L , see figure 3. The grid has an O-topology on transverse grid surfaces and H-topology on longitudinal radial grid surfaces. Due to the symmetry of the flow only the port side of the hull is meshed. The computational domain is shaped like a quarter of a cylinder. In addition to the usual high spatial resolution at the hull to resolve the boundary layer, a fine and regular grid resolution beside and behind the hull as well as in the neighbourhood of the expected free surface is required to capture the waves well. These requirements yield a grid of $121 \cdot 60 \cdot 55 = 399300$ cells in longitudinal, radial and lateral direction respectively. At the hull, the thickness of the cells results in a nondimensional wall distance $y^+ \approx 200$. The grid used allows for resolving one wave length with about 45 cells and the wave height with 20 cells. Former calculations with wider domains showed that no channel effect is expected in this domain.

Through testing we found the thickness of the transition zone $2\alpha \approx 3\Delta z$ to be sufficient for numerical

stability, Δz being the vertical grid spacing.

The ratios of densities and viscosities were chosen to $\rho_l/\rho_w = 0.0012$ and $\nu_l/\nu_w = 15$, which correspond to usual conditions. Additional computations were carried out on a coarse grid with half the resolution in space and also on the fine grid neglecting the viscosity.

Calculations on the fine grid were carried out over 5000 time steps, starting with the ship at rest. The ship speed was then accelerated until time step 1500. The time step was $\delta t = 0.003$ and could not be chosen much larger because of stability. For the same reason we needed two SIMPLE loops in every time step and this yielded a total CPU time of about 150h on a medium HP workstation. Viscous and inviscid flow computations demanded roughly the same CPU time. On the coarse grid a time step of $\delta t = 0.005$ was sufficient, and 3000 time steps were used. In both cases the number and magnitude of time steps yielded the same covered distance of $15L$ for the ship at design speed.

Some general features of the technique used to determine the interface are shown in figures 2, 4, and 5. In these figures the small transition zone around the free surface is plotted showing the isolines $\Phi = -\alpha, 0, \alpha$. The wall shear stress practically vanishes in air because of its very low density and varies smoothly, but rapidly in the transition zone as expected, figure 4. In a steady flow, the velocity vector field (as well as the wall shear stress field) is tangential to the interface, which can be seen in figure 4 and in a cut near the bow, figure 5. The thickness of the transition zone is kept constant throughout the domain. This is important to attain convergence and to avoid too strong smearing of the interface. Figure 2 shows the bandwidth of the interface along the hull. Somewhat unexpected, the overall features of the Level Set method and of the two-phase flow model seem to be satisfactory from a physical and numerical point of view.

Figure 6 shows the resulting frictional, pressure and total resistance coefficients C_F , C_P and C_T , on the coarse and on the fine grid. All coefficients are built with the wetted area of the hull at rest, the water density and the design speed of the ship (model). The pressure resistance includes the viscous pressure and wave resistance and is determined by integration of the pressure on the hull. The frictional resistance is obtained by integration of the wall shear stresses. The integration was performed over the 'wetted' part of the hull ($\Phi \geq 0$). It was found that the resistance is less sensitive to the size of the integration domain. Extending the integration to the whole hull yields practically the same results, because of the very low density of air. Even if the integration is carried

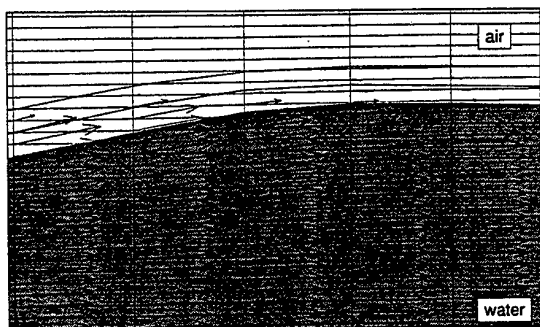


Figure 4: Partial view of the wall shear stress field on the bow in the neighbourhood of the interface. The white band represents the transition region.

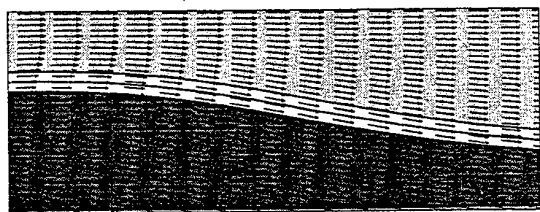


Figure 5: Velocity vectors near the free surface. Iso-lines represent $\Phi = -\alpha, 0, \alpha$.

out only up to the lower bound of the transition zone ($\Phi = \alpha$), the total resistance on the fine grid is predicted just 3% smaller.

We can see as a general characteristic an oscillation of the pressure resistance, figure 6, which is caused by long waves of very small amplitudes, which are trapped inside the computational domain. They are reflected at the inlet and outlet boundaries and vanish very slowly in time. These waves are damped by the numerical beach near the boundaries. Nevertheless, we did not achieve a fully steady solution after 5000 time steps, respectively 3000 steps. Accelerating the ship speed at the beginning of the computation was found to be helpful to reduce the amplitude of the trapped waves: The slower the acceleration, the smaller the wave height. The oscillations are more severe on the fine grid than on the coarse grid, because waves are damped numerically stronger on the coarse grid anyway.

Determining the mean resistance values at the end of the computation, we recognize that the coarse grid solution underestimates the frictional resistance and overestimates the pressure resistance. This explains the relatively small difference in total resistance when comparing the solutions on the coarse and fine grid.

The results on the fine grid are still far from a grid independent solution. The pressure resistance computed on the fine grid $C_P = 2.05 \cdot 10^{-3}$ includes an error caused by numerical diffusion of about $0.35 \cdot 10^{-3}$ which was estimated by an inviscid computation neglecting the free surface. Theoretically no resistance is expected for this case (D'Alembert's paradox). The predicted frictional resistance coefficient on the fine grid $C_F = 3.25 \cdot 10^{-3}$ is close to the empirical value $C_F = 3.36 \cdot 10^{-3}$ yielded by the ITTC57 formula. A further grid refinement would lead to a clear decrease of the pressure resistance and a slight increase of the frictional resistance.

The total resistance of $C_T = 5.95 \cdot 10^{-3}$ reported in [15] seems not to be very reliable considering other experimental data. Several measurements reported in [4] give a range of the total resistance coefficient varying from $C_T = 5.15$ to $5.80 \cdot 10^{-3}$, with emphasis on the smaller values, for models which were free to trim and sink. Results for the total resistance with a fixed model (as in our calculation) would be even smaller because of the neglected sinkage. Having all this in mind the result of the computation of about $C_T = 5.30 \cdot 10^{-3}$ is reasonable, but not accurate enough for practical use. The fine grid used is still too coarse, although the geometry of the slender Series 60 hull is simple. For an estimation of the numerical error, a computation on a much finer grid with e.g. 3 200 000 cells would be necessary.

Figures 7 and 8 compare the wave pattern of an inviscid and viscous flow computation on the fine grid (at time step 5000) with the measurements of [15]. Temporary changes in wave pattern are very small at the end of the computation, and only indirectly visible in the resistance curves, so the depicted wave pattern should be considered as stationary. The numerical prediction is accurate from the ship stem to $2/3 L$ behind it for both viscous and inviscid flow computations. In this area viscous effects are negligible. The results of the inviscid flow computation tend to overpredict slightly the first wave trough. From $2/3 L$ on the agreement between measurement and computations becomes poorer, due to numerical diffusion which damps the waves. The stern wave is computed more accurately by the viscous flow, because the more realistic (smaller) pressure recovery at the stern reduces the stern wave distinctly.

Figure 9 compares the wave profile on the hull and centerplane, and the two wave cuts at $y/B = 1.057$ and $y/B = 2.039$ with the experimental data. The agreement of the wave profile on the hull is quite good, but the results deteriorate with increasing distance to the hull. Outer cuts tend to underpredict wave elevations and suffer from a larger phase lag. Both ef-

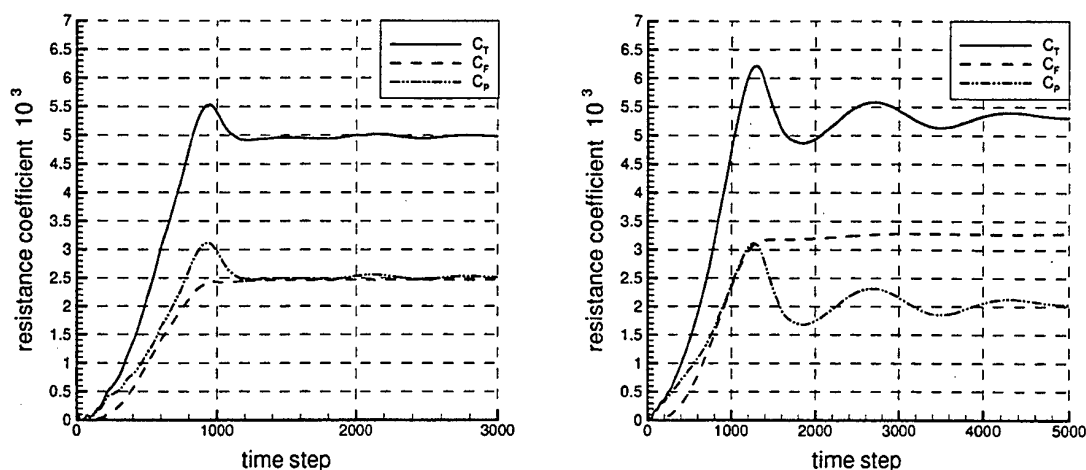


Figure 6: Resistance coefficients for the Series 60 ship computed on the coarse (left) and on the fine (right) grid, $R_n = 5.27 \cdot 10^6$, $F_n = 0.316$.

fects are typically caused by numerical diffusion on a coarse grid.

The comparison with another method developed at the HSVA is very interesting. It is a Volume of Fluid (VOF) method for a single phase fluid, [9] and [10]. In this method the numerical treatment of the free surface is much more complicated than here. A strict subdivision in filled, partially filled and empty cells which are treated in different ways is necessary. Both the VOF method and the current method practically coincide in the liquid phase. At the beginning of the development we thought that the mixture of water and air in the transition zone and the application of the Level Set method would cause a strong damping of waves. This assumption proved to be true on coarse grids, but not on finer grids (like the one used here)! We assume that with increasing resolution the weak part of the algorithm for resolving the waves is no longer the treatment of the free surface/interface itself, but the discretisation of the convective terms in the momentum equations. These terms are discretised in the same way in both methods. While the VOF method still shows some advantages concerning stability and CPU time, the Level Set method offers advantages concerning the turbulence modelling.

Figure 10 shows the nondimensional pressure distribution $C_p = (p - \rho g z) / (\frac{1}{2} \rho_w U_0^2)$ on the hull, and the predicted free surface depicted as a black line. The results are comparable to the measurements of [11] with a Froude number of 0.3, which show similar contours of isobars at the bow and amidship.

Figures 11 and 12 compare the computed velocity fields in the two cross sections at $0.9 L$ and $1.0 L$ from

the forward perpendicular with the measurements of [15]. The agreement is quite good at $0.9 L$. Despite the wall functions used, the $k - \omega$ model works well for this slender ship. Nevertheless, the agreement becomes less accurate in the wake, as can be seen at $1.0 L$. This is probably due to the rather coarse grid resolution in this region and the omission of the propeller bossing in the numerical description of the hull.

CONCLUDING REMARKS

A Navier-Stokes solver has been further developed for the computation of free surface viscous ship flows. The method described yielded in most aspects accurate results for the Series 60 model at $F_n = 0.316$. In particular the quality of predicted waves is comparable to moving grid methods, but the Level Set method has several advantages for handling more complicated geometries. The grids used, containing roughly 400000 cells are still too coarse for quantitative accurate resistance predictions. Computational time and stability are not currently acceptable for practical use, and these items will be the subject of future research.

We have some additional computational experience with other hull forms, e.g. full tankers, which often lead to breaking bow waves. Wave breaking did not affect the stability of the method. These tests showed that for the typical small Froude numbers of such ships, the spatial resolution presently used is too coarse in relation to the wave length. Thus, waves are not resolved sufficiently. We hope to improve these results and present them in the near future.

ACKNOWLEDGEMENT

This work was supported by the German Ministry of Education and Research.

REFERENCES

1. Cura Hochbaum A., *A Finite-Volume Method for Turbulent Ship Flows*, Ship Technology Research 41/3 1994
2. Cura Hochbaum A., *Computation of the Turbulent Flow Around a Ship Model in Steady Turn and in Steady Oblique Motion*, 22nd ONR Symp. on Naval Hydrodyn., August 1998 Washington D.C.
3. Cura Hochbaum A., *Computation of the total resistance of a ship*, HSVA Report 1632, March 1999 (in German)
4. Kajitani H., *A Wandering in some Ship Resistance Components and Flow*, Ship Technology Research 34, 1987
5. Longo J., Stern F., Toda Y., *Mean-Flow Measurements in the Boundary Layer and Wake and Wave Field of a Series 60 $CB=0.6$ Ship Model - Part 2 : Scale Effects on Near-Field Wave Patterns and Comparisons with Inviscid Theory*, Journal of Ship Research Vol.37 No.1, March 1993
6. Osher S., Sethian J.A., *Fronts Propagating with Curvature-Dependent Speed: Algorithms Based on Hamilton-Jacobi Formulations*, Journal of Computational Physics 79, 1988
7. Peng D., Merriman B., Osher S., Zhao H., Kang M., *A PDE Based Fast Local Level Set Method*, UCLA CAM Report 98-25, 1998
8. Rhie C.M., Chow W.L., *Numerical Study of the Turbulent Flow Past an Airfoil with Trailing Edge Separation*, AIAA Journal Vol.21 No.11, November 1983
9. Schumann C., *Computation of the inviscid ship flow using a volume of fluid method to determine the free surface*, Report of Technical University of Hamburg Harburg, 1999, to appear (in German)
10. Schumann C., *Computing Free Surface Ship Flows with a Volume of Fluid Method*, PRADS 1998, The Hague
11. Stern F., Longo J., Zhang Z.J., Subramani A.K., *Detailed Bow-Flow Data and CFD for a Series 60 $CB=0.6$ Ship Model for Froude Number 0.316*, Journal of Ship Research Vol.40 No.3, 1996
12. Sussman M., Smereka P., Osher S., *A Level Set Approach for Computing Solutions to Incompressible Two-Phase Flow*, Journal of Computational Physics 114, 1994
13. Sussman M., Fatemi E., Smereka P., Osher S., *An Improved Level Set Method for Incompressible Two-Phase Flows*, UCLA CAM Report 95-27, 1995
14. Toda Y., Stern F., Longo J., *Mean-flow Measurements in the Boundary Layer and Wake and Wave Field of a Series 60 $CB=0.6$ Ship Model - Part 1 : Froude Numbers 0.16 & 0.316*, Journal of Ship Research Vol.36 No.4, 1992
15. Toda Y., Stern F., Longo J., *Mean-flow Measurement in the Boundary Layer and Wake and Wave Field of a Series 60 $CB=0.6$ Ship Model for Froude Numbers .16 and .316*, Iowa Institute of Hydraulic Research Report No. 352 August 1991
16. Vogt M., *A Numerical Investigation of the Level Set Method for Computing Free Surface Waves*, Diploma Thesis of the Chalmers University of Technology, Gothenburg, 1998
17. Wilcox D.C., *Turbulence Modeling for CFD*, DCW Industries, La Cañada, California, 1993

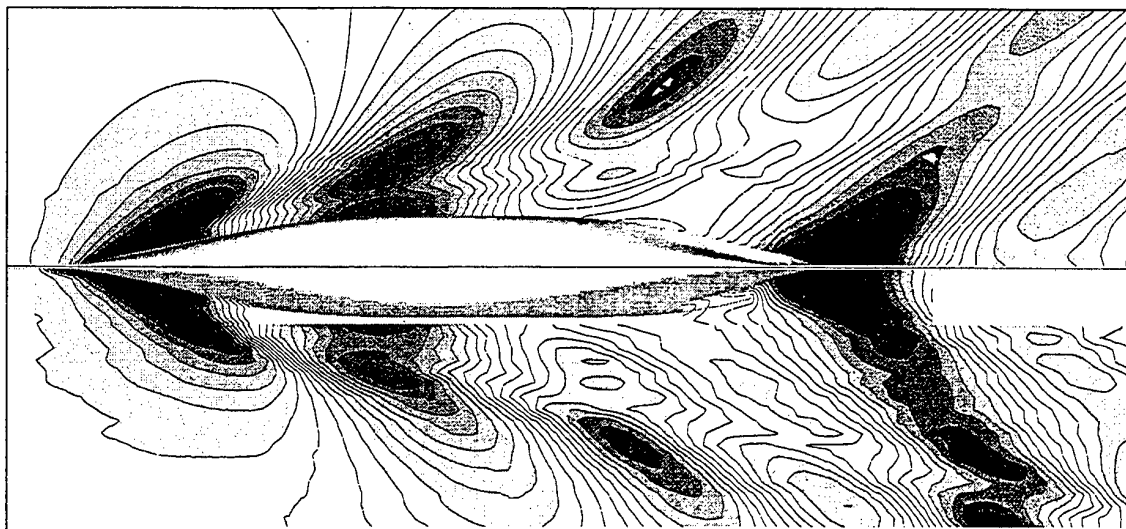


Figure 7: Computed (top) and measured (bottom) wave pattern. Contour interval 0.00115. Series 60, inviscid flow, $F_n = 0.316$.

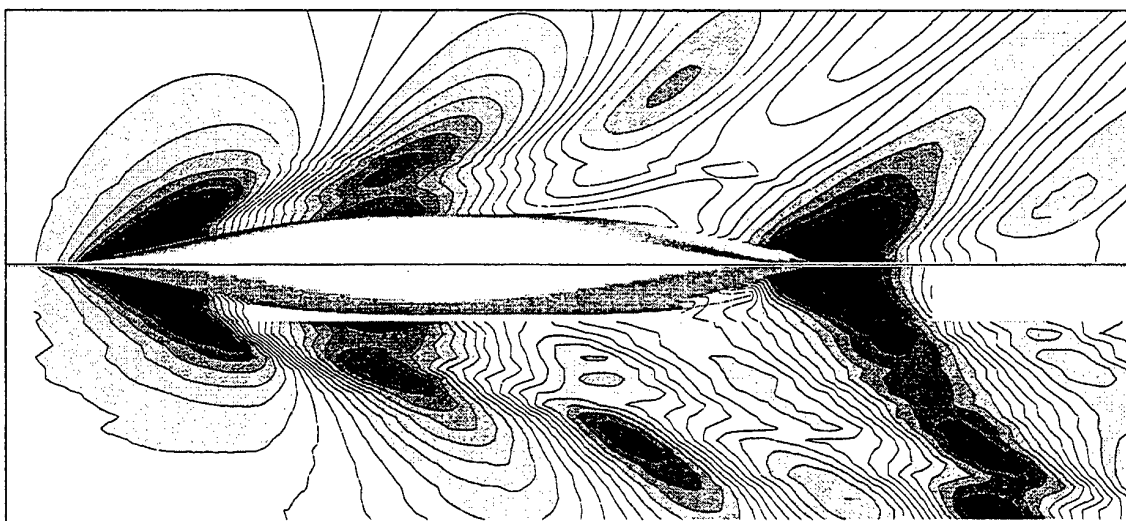


Figure 8: Computed (top) and measured (bottom) wave pattern. Contour interval 0.00115. Series 60, viscous flow, $R_n = 5.27 \cdot 10^6$, $F_n = 0.316$.

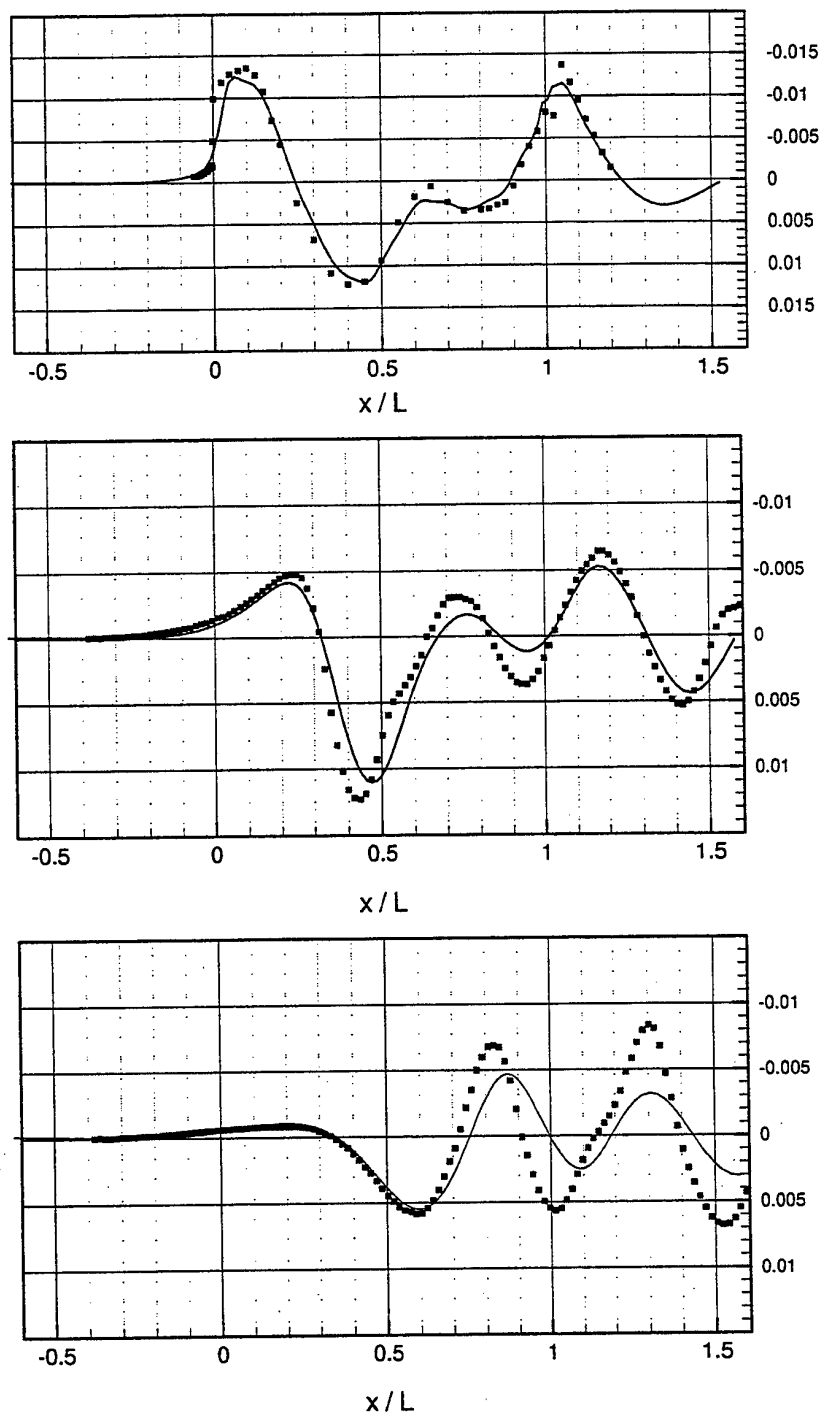


Figure 9: Wave elevation on the hull, at $y/B = 1.057$ and $y/B = 2.039$ (from top to bottom). Symbols represent measurements, lines represent viscous flow computation. Forward and aft perpendiculars at $x=0$ and $x=1$, respectively. z -axis shows downward.

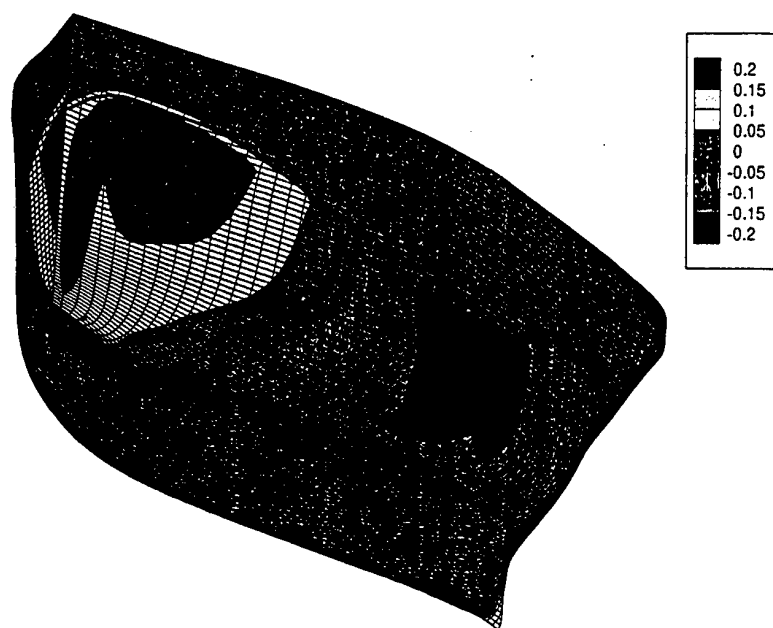


Figure 10: Computed pressure distribution on the hull. Series 60, $R_n = 5.27 \cdot 10^6$, $F_n = 0.316$.

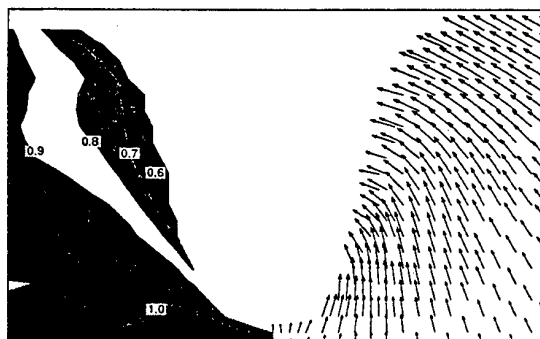
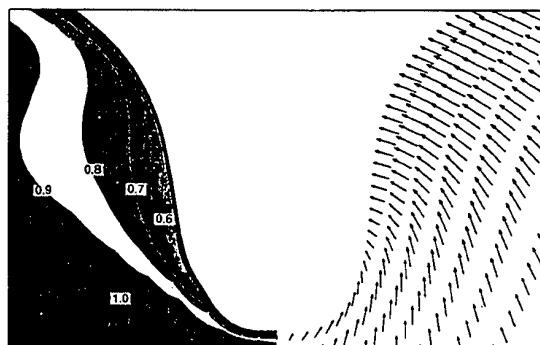


Figure 11: Computed (top) and measured (bottom) velocity field in a cross section at $0.9L$ from F.P. Series 60, $R_n = 5.27 \cdot 10^6$, $F_n = 0.316$.

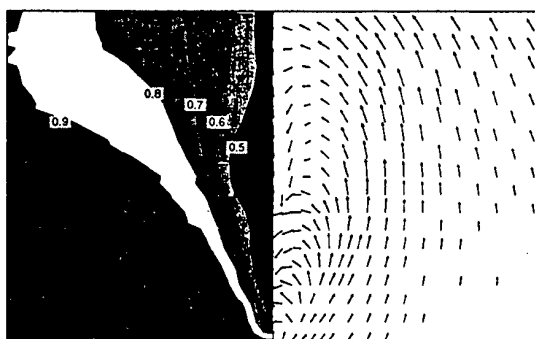
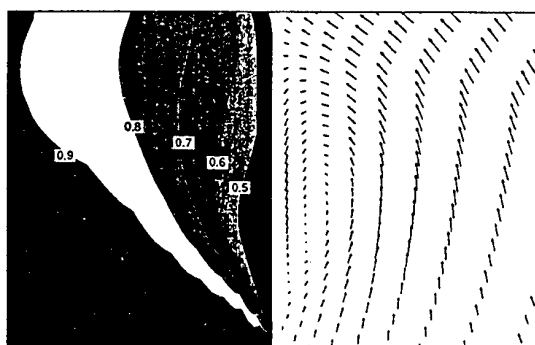


Figure 12: Computed (top) and measured (bottom) velocity field in the propeller plane. Series 60, $R_n = 5.27 \cdot 10^6$, $F_n = 0.316$.

LEVEL SET METHODS FOR PREDICTING VISCOUS FREE SURFACE FLOWS

M. Vogt (*)¹, L. Larsson (*)

(*) Dept. of Naval Architecture and Ocean Engineering,
Chalmers University of Technology, S-412 96 Göteborg, Sweden
Fax: +46 31-772 36 99 ; E-Mail: larsl@na.chalmers.se

(*) Flowtech International AB
Box 24001, S-400 22 Göteborg, Sweden

ABSTRACT

A two-phase level set formulation and a one-phase level set formulation are used to compute two-dimensional free surface flows around a submerged wing section by solving the incompressible Reynolds averaged Navier-Stokes equations. The interface between the water and the air i.e. the free surface is identified as the zero level set of a smooth function. In the two-phase method the computational domain includes both water and air regions while in the one-phase method only the water flow is simulated. In the latter method dynamic boundary conditions are applied at the free surface. Spatial discretization is based on a finite volume method and velocity and pressure are coupled in a fractional step manner. Reynolds stresses are modelled with the $k-\epsilon$ model with wall functions. Results from inviscid and viscous calculations of the wave profile as well as predictions of the onset of breaking for various Froude numbers with both methods are compared to experiments.

NOMENCLATURE

Roman symbols

b_i^j	Jacobian matrix of the coordinate transformation
c	Chord length of the foil
d	Normal distance to the free surface
e_{ij}	Rate of strain tensor
Fn	Froude number
g	Gravitational acceleration
g^{ij}	Contravariant metric tensor
H	Heaviside's unit function
J	Jacobian of the coordinate transformation
k	Turbulent kinetic energy
L	Characteristic length
n_i	Unit normal vector
p	Total pressure
q	von Karman constant
Re	Reynolds number
s	Submergence of the foil
t	Time
t_a	Time of acceleration
U_i	Contravariant velocity components
U_o	Free stream velocity
u_i	Cartesian velocity components

u_p	Velocity parallel to the wall
u_τ	Friction velocity
u^+	Non-dimensional velocity
\vec{u}	Velocity vector
We	Weber number
x_i	Cartesian coordinates
\vec{x}	Cartesian coordinate vector
y_n	Distance to the wall
y^+	Non-dimensional wall distance

Greek symbols

α	Half the prescribed width of the band where the physical properties change
β	Sign function smoothing parameter
γ	Damping function
δ	Dirac delta function
δ_{ij}	Kronecker delta
ϵ	Dissipation rate of k
η	Wave elevation
κ	Curvature of the free surface
λ	Relation between the properties in air and water
μ	Dynamic viscosity
ν	Kinematic viscosity
ξ_j	Curvilinear coordinates
ρ	Density
σ	Surface tension coefficient
τ	Pseudo time
τ_{ij}	Stress tensor

¹ Presently at Hamburg ship model basin
Bramfelder Str. 164, D-222 305 Hamburg, Germany
Fax: + 49 40-69 203 345; E-Mail: vogt@hsva.de

τ_w	Shear stress at the wall
ϕ	Level set function
ψ	Pressure excluding hydrostatic pressure
ω	Filter smoothing parameter

INTRODUCTION

It is well known that the wave resistance cannot be correctly predicted without a method that can accurately compute the wavy surface and that the total resistance is not predictable if the viscosity is not taken into account. Concerning the wave resistance, panel methods including non-linear free surface techniques for steady state flow in calm water are sufficiently accurate for qualitative judgements of hull shape changes for many hull forms. However, the calculated magnitude of the wave resistance cannot be relied upon due to viscous effects mainly near the stern and even negative values of the wave resistance are possible numerical solutions [1].

There are many methods developed for viscous flows with moving boundaries and for those intended for free surfaces the following problems have to be considered:

The component of ship resistance associated with a breaking wave at the bow can be substantial [2] and the wave system behind a multihull tends to break at certain speed ranges. So, it is of interest to be able to capture the major features of the breaking phenomenon within a numerical method.

Further, since the density and the viscosity change sharply at the free surface, the two-phase schemes in which the momentum equations are solved both in the water and in the air will either incur excessive numerical diffusion when solving the convection equations for the density and the viscosity or give the surface a finite thickness with a mixture of air and water, which is an unphysical approximation too.

Also, for CFD to be a useful tool in practical ship hydrodynamics a converged solution must be reached in the order of hours. In recent years the rate of increase of processor speed has decreased but parallel computing has become a common way to increase the overall performance of numerical calculations. Hence, it is an advantage if the free surface formulation is suitable for implementation on a parallel computer.

Lastly, the no-slip condition that is imposed on a surface piercing body may conflict with the kinematic condition on the free surface and inhibit the rise of the free surface along the side of the hull. This problem is out of the scope of this investigation.

One of the earliest numerical algorithms for viscous flow to treat free surfaces is the marker-and-cell (MAC) method which was introduced by Harlow and Welch [3]. Massless marker particles are distributed to define the liquid region and the interface. These markers are then used in a Lagrangian sense,

to trace the motion of fluid particles at the free surface and within the fluid.

In the volume-of-fluid (VOF) [4] method a step function advected by the flow in the Eulerian grid is used instead of marker particles. The step function is unity everywhere in one fluid and zero in the other. The average value of the step function in each cell then represents the fraction of each cell containing the first fluid. At any time, the interface can be reconstructed from these volume fractions.

Advantages of these methods include the ability to treat complex interfacial shapes of the surface, fixed grid formulations and, so, easier implementation of adaptive mesh refinement. However, they define the different regions of fluids instead of the exact interface and the determination of intrinsic geometric properties such as normal vectors and curvature requires a large computing effort.

Today the moving grid method [5] is commonly used for viscous hydrodynamics calculations. The grid is fitted to the boundaries and moves with the free surface. This facilitates the implementation of boundary conditions there and the interface stays sharp. The system of equations are solved in either the physical domain or they are transformed into a uniform rectangular computational domain. For the latter, the singular transformation that occurs, i.e. for breaking waves and merging, needs special treatment and regridding around practical hull forms are computationally expensive.

A modern Eulerian approach based on a fixed grid is the level set technique [6]. The method has had a large number of applications but has only recently been applied to free surface waves [7,8]. In this method the subset with a value of zero of a level set function that moves with the fluid defines the free surface. Even though this interface may change topology, break and merge, the level set function itself always remains a function. So, geometric properties of the free surface are easily determined from this function. Since the level set technique is derived to follow the motion of an $N-1$ dimensional surface in N -dimensional space there are no significant difference between two and three dimensions. However, for water wave problems the free surface has to be given a finite thickness.

This leads to objective of this study. A level set formulation in which the two fluids are treated simultaneously is compared to a formulation in which the momentum equations are solved in the water region only. In the latter the level set function is still used to capture the free surface at which, however, boundary conditions are applied.

In the next two Sections, the mathematical models for the two- and one-phase methods respectively are formulated. Then the numerical method and the solution procedure are described. After that, discussions of numerical results for flows around a submerged

wing are presented and finally, concluding remarks are provided.

TWO-PHASE FORMULATION

In this section the mathematical model of a two-phase formulation of the level set technique is described, including governing equations, reinitialization procedure, turbulence model and boundary conditions.

Governing Equations

A level set function, $\phi(\bar{x}, t)$, where $\bar{x} = (x_1, x_2)$ is a Cartesian coordinate vector, is a smooth scalar function defined in the whole domain including both fluids. At any time t , the free surface Γ coincides with the subset with a value of zero of this function i.e.

$$\Gamma(t) = \{\bar{x} : \phi(\bar{x}, t) = 0\}. \quad (1)$$

Initially, ϕ is set equal to the distance with sign from the interface such that ϕ is positive in the water region and negative in the air region,

$$\phi(\bar{x}, 0) = \begin{cases} d, & \bar{x} \in \Omega^w \\ 0, & \bar{x} \in \Gamma \\ -d, & \bar{x} \in \Omega^a \end{cases} \quad (2)$$

where d is the distance from the free surface and Ω^w and Ω^a denote the water and air regions respectively. Then the level set function moves with the fluid as an extra quantity and the free surface may always be found from the location of the zero level set, even under topological changes. Depending on the sign of the level set function the density and the viscosity are given appropriate values.

μ_w and μ_a denote the dynamic viscosity of water and air respectively and ρ_w and ρ_a are the corresponding properties of the density. For viscous incompressible immiscible fluids the equations of motion are the Reynolds Averaged Navier-Stokes equations and the conservation of mass is enforced by the continuity equation. Non-dimensionalized by the reference length L , the free stream velocity U_o and the density and viscosity of water, the system of equations to be solved are written in Cartesian tensor notation form as

$$\frac{\partial u_i}{\partial t} + \frac{\partial}{\partial x_j} (u_i u_j) = -\frac{1}{Fn^2} \frac{\partial x_2}{\partial x_i} - \frac{1}{\rho(\phi)} \frac{\partial p}{\partial x_i} + \quad (3)$$

$$\frac{\partial}{\partial x_j} \left(\left(\frac{v(\phi)}{Re} + v_t \right) \frac{\partial u_i}{\partial x_j} \right) + \frac{1}{\rho(\phi)} \frac{1}{We} \kappa(\phi) \delta(\phi) \frac{\partial \phi}{\partial x_i}$$

$$\frac{\partial u_i}{\partial x_i} = 0 \quad (4)$$

$$\frac{\partial \phi}{\partial t} + u_i \frac{\partial \phi}{\partial x_i} = 0 \quad (5)$$

where u_i is the velocity, p is the pressure and x_i is the Cartesian coordinate system where the horizontal x_1 -axis is pointing to the right and the vertical x_2 -axis is positive upwards. $Re = U_o L \rho_w / \mu_w$ is the Reynolds number, $Fn = U_o / \sqrt{gL}$ the Froude number and $We = \rho_w L U_o^2 / \sigma$ is the Weber number. g is the gravitational acceleration, σ is the surface tension coefficient, κ is the curvature of the free surface and δ is the Dirac delta function. $v(\phi) = \mu(\phi) / \rho(\phi)$ is the kinematic viscosity and Reynolds stresses are related to the mean rate of strain through an isotropic kinematic eddy viscosity v_t , here determined with a k - ϵ turbulence model.

The variable non-dimensional viscosity and density fields $\mu(\phi)$ and $\rho(\phi)$ respectively are determined from:

$$\begin{aligned} \mu(\phi) &= \lambda_\mu + (1 - \lambda_\mu) H(\phi) \\ \rho(\phi) &= \lambda_\rho + (1 - \lambda_\rho) H(\phi) \end{aligned} \quad (6)$$

where $\lambda_\mu = \mu_a / \mu_w$ and $\lambda_\rho = \rho_a / \rho_w$ are the ratios between air and water properties for the viscosity and density respectively and $H(\phi)$ is Heaviside's unit function.

The density changes sharply at the free surface, λ_ρ is very small and the Dirac delta function in the surface tension force term in equation (3) is difficult to handle numerically. Therefore, the free surface is given a finite thickness, 2α . Now, physical properties that are smoothed across the free surface can be introduced. This is done by using the following Heaviside function

$$H(\phi) = \begin{cases} 0 & \phi < -\alpha \\ \frac{1}{2} \left(1 + \frac{\phi}{\alpha} + \frac{1}{\pi} \sin\left(\frac{\pi\phi}{\alpha}\right) \right) & |\phi| \leq \alpha \\ 1 & \phi > \alpha \end{cases} \quad (7)$$

The smooth Dirac delta function follows from the definition $\delta(\phi) = dH(\phi)/d\phi$ which yields

$$\delta(\phi) = \begin{cases} \frac{1}{2\alpha}(1 + \cos(\frac{\pi\phi}{\alpha})) & |\phi| < \alpha \\ 0 & \text{otherwise} \end{cases} \quad (8)$$

The curvature is obtained from the divergence of the unit normal vector to the free surface

$$\kappa(\phi) = \frac{\partial n_j}{\partial x_j} \quad (9)$$

where

$$n_j = (\partial\phi/\partial x_j) / |\partial\phi/\partial x_k|. \quad (10)$$

Or, if the normal vectors are not computed and stored, equation (9) can in non-conservative form in two dimensions be rewritten as

$$\kappa(\phi) = \frac{\phi_{xx}\phi_y^2 - 2\phi_{xy}\phi_x\phi_y + \phi_{yy}\phi_x^2}{(\phi_x^2 + \phi_y^2)^{3/2}}, \quad (11)$$

here the subscript x and y denotes derivatives in the x_j - and x_2 -directions respectively. It follows from the definition of ϕ that the normal vector is pointing into the water region.

The equations are partially transformed from the physical domain in Cartesian coordinates x_i into the computational domain in body fitted non-orthogonal curvilinear coordinates ξ_j . ξ_1 is taken in the longitudinal direction from the leading edge to the trailing edge of the wing section and ξ_2 in the normal direction from the body surface or from the centre line in front of the leading edge and behind the trailing edge to the bottom and top boundaries. Velocity components are retained in Cartesian coordinates and only the independent variables are transformed [9]. The momentum (3) and continuity (4) equations and the convection equation for the level set function (5) are now written as

$$\begin{aligned} J \frac{\partial u_i}{\partial t} + \frac{\partial}{\partial \xi_j} (J u_i U_j) &= -\frac{1}{Fn^2} \frac{\partial}{\partial \xi_j} \left(J b_i^j \frac{\partial x_2}{\partial \xi_j} \right) + \\ \frac{1}{\rho(\phi)} \frac{\partial}{\partial \xi_j} (J p b_i^j) + \frac{\partial}{\partial \xi_j} \left(\left(\frac{v(\phi)}{Re} + v_t \right) J g^{jk} \frac{\partial u_i}{\partial \xi_j} \right) &+ \\ + \frac{1}{\rho(\phi)} \frac{1}{We} b_k^j \frac{\partial n_k}{\partial \xi_j} \delta(\phi) b_r^s \frac{\partial \phi}{\partial \xi_s} & \quad (12) \end{aligned}$$

$$\frac{1}{J} \frac{\partial}{\partial \xi_j} (J U_j) = 0 \quad (13)$$

$$\frac{\partial \phi}{\partial t} + U_j \frac{\partial \phi}{\partial \xi_j} = 0 \quad (14)$$

where $b_i^j = \partial \xi_j / \partial x_i$ is the matrix of the coordinate transformation, $J = \det(b_i^j)^{-1}$ is the Jacobian of

the coordinate transformation, $g^{ij} = \frac{\partial \xi_i \partial \xi_j}{\partial x_k \partial x_k}$ are

contravariant components of the metric tensor, $U_i = u_k b_k^i$ are contravariant components of veloc-

ity and $n_k = b_k^l \frac{\partial \phi}{\partial \xi_l} / \left| b_m^n \frac{\partial \phi}{\partial \xi_n} \right|$.

Reinitialization

It is seen in equations (6)-(10) that the density and viscosity, which are smoothed around the free surface in a band that has a uniform thickness as well as the normal vector and the curvature are dependent upon the level set function being a distance function. If a steep gradient arises in the level set function i.e. $|\partial\phi/\partial x_j|$ is much larger than one, a steep gradient will be introduced in the density and the viscosity, opposite to the intention with the smoothed physical properties and with numerical difficulties as a result. Equation (5) moves the zero level set $\phi = 0$ according to the velocity field but the level set function ϕ will no longer be a distance function. Therefore, the level set function is reinitialized i.e. ϕ is given new values everywhere but on the free surface as follows. Define a function $d(x_i, \tau)$ and solve the equation

$$\frac{\partial d}{\partial \tau} = S(d_o) \left(1 - \left| \frac{\partial d}{\partial x_k} \right| \right) \quad (15)$$

with the initial conditions $d(x_i, 0) = \phi(x_i, t)$ where S is a smooth sign function

$$S(d_o) = \frac{d_o}{\sqrt{d_o^2 + \beta^2}} \quad (16)$$

and $d_o(x_i) = d(x_i, 0)$ to steady state [10]. Now, $d(x_i, \tau)$ is a distance function. Its gradient is equal to one and it has the same zero level set as $\phi(x_i, t)$. Then, let ϕ take the values of d i.e. set $\phi(x_i, t) = d(x_i, \tau)$ and the level set function is reinitialized. Note that the time τ is an artificial pseudo

time different from the global time t in the momentum equations. Figure 1 shows contours of the level set function for free surface waves generated by a submerged wing section. First waves are generated with reinitialization. Then the computation is restarted with and without reinitialization for another $0.3T$ where T is time units. The dashed lines in figure 1 indicate the bandwidth with the free surface in the middle.

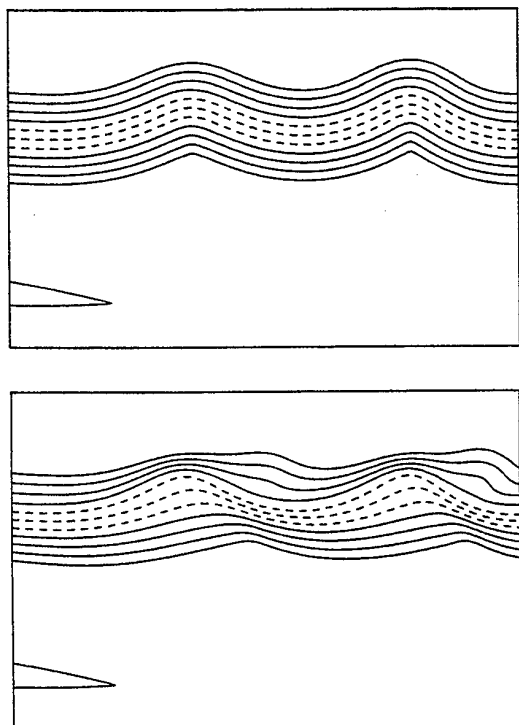


Figure 1. Waves generated by a submerged hydrofoil, the last $0.3T$ still with reinitialization (top) and without reinitialization (bottom).

Without reinitialization the level set function does not remain a distance function, especially not in the air region. The bandwidth will not be constant neither in space nor in time and the free surface will be distorted. In figure 2 the free surface heights from figure 1 are compared. The dashed line shows the waves with reinitialization and the solid line the waves when reinitialization is taken away. It is seen that already after $0.3T$ the wave profile has changed.

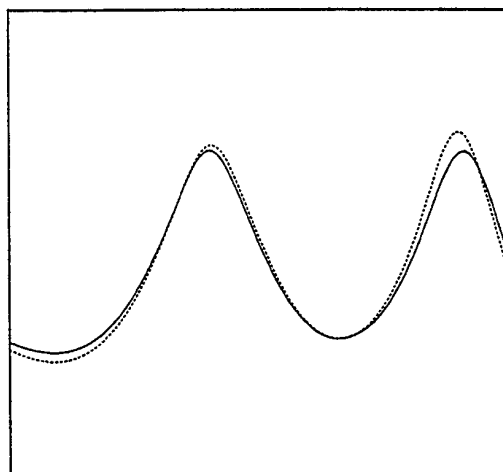


Figure 2. Comparison of wave heights of the waves shown in figure 1. '—' without reinitialization and '---' with reinitialization the last $0.3T$.

Turbulence Model

So far, no turbulence model exists that can be successfully applied to turbulent flows in general, so the model has to be selected from case to case. It has been shown that the Baldwin-Lomax model is unstable combined with free surface boundary conditions [11]. These are not needed in the two-phase level set formulation but will be partly applied in the one-phase formulation. Even though the standard $k-\epsilon$ model is not the best two-equation model for predictions of the turbulence in flows with pressure gradients e.g. flows over curved surfaces, it is widely used and reasonably stable, at least with wall functions. The better stability properties due to wall functions mainly follow from the fact that the aspect ratio of cells close to a wall gets smaller when wall functions are used. Further, it is not obvious how to determine the value of ϵ at the a wall, so difficulties arise when the ϵ -equation is integrated up to the wall boundary and also since the details of the boundary layer are of less interest in this investigation a $k-\epsilon$ -model with wall functions [12] is implemented.

$k-\epsilon$ model

In the $k-\epsilon$ model the eddy viscosity is

$$\nu_t = C_\mu \frac{k^2}{\epsilon} \quad (17)$$

and the equations for the kinetic energy k and its dissipation rate ϵ are

$$\frac{\partial k}{\partial t} + u_i \frac{\partial k}{\partial x_i} =$$

$$\frac{\partial}{\partial x_i} \left(\left(\frac{v(\phi)}{Re} + \frac{v_i}{\sigma_k} \right) \frac{\partial k}{\partial x_i} \right) + P_k - \epsilon \quad (18)$$

$$\frac{\partial \epsilon}{\partial t} + u_i \frac{\partial \epsilon}{\partial x_i} =$$

$$\frac{\partial}{\partial x_i} \left(\left(\frac{v(\phi)}{Re} + \frac{v_i}{\sigma_\epsilon} \right) \frac{\partial \epsilon}{\partial x_i} \right) + \frac{\epsilon}{k} C_{\epsilon 1} P_k - C_{\epsilon 2} \frac{\epsilon^2}{k} \quad (19)$$

where

$$P_k = v_i \left(\frac{\partial u_i}{\partial x_j} + \frac{\partial u_j}{\partial x_i} \right) \frac{\partial u_i}{\partial x_j} \quad (20)$$

and the constants to close the problem are $C_\mu=0.09$, $C_{\epsilon 1}=1.44$, $C_{\epsilon 2}=1.92$, $\sigma_k=1.0$ and $\sigma_\epsilon=1.3$.

Wall functions

In the viscous sublayer where $y^+ < 11.63$, the friction velocity, u_τ , is given by the near wall linear law

$$\frac{u_p}{u_\tau} = y^+ \quad (21)$$

and for $y^+ \geq 11.63$, u_τ is given by the log law

$$\frac{u_p}{u_\tau} = \frac{\ln[Ey^+]}{q} \quad (22)$$

where $y^+ = u_\tau y_n \rho_w / \mu_w$, y_n is the normal distance to the solid boundary, u_p the velocity component parallel to the wall, $E = 9$ and $q = 0.41$, the von Karman constant.

Under the assumption that, in the near wall region, the production of kinetic energy equals its dissipation rate, the turbulent quantities are related to the friction velocity at the first node adjacent to the wall as

$$k = \frac{u_\tau^2}{\sqrt{C_\mu}}, \quad \epsilon = \frac{u_\tau^3}{q y_n}, \quad v_i = \frac{u_\tau y_n q}{\ln[Ey^+]} \quad (23)$$

Very close to the wall there is no balance between production and dissipation and the first grid point adjacent to the wall must not be closer than approximately $y^+ \approx 40$.

Boundary Conditions

Inlet Boundary

A uniform flow $u_1 = 1$ and $u_2 = 0$, $\partial p / \partial n = 0$ where $\partial / \partial n$ is the normal derivative and extrapolation of ϕ from inside the computational domain are imposed. k and ϵ are set to a small value different from zero.

Outlet Boundary

To avoid reflections from the outlet boundary the computational domain is extended with a dissipation zone [13,14]. Here, fictitious damping forces are added to the level set function and the grid is made coarser towards the outlet. The level set function is damped with an artificial wave damping function, γ , as follows

$$\frac{\partial \phi}{\partial t} = -u_i \frac{\partial \phi}{\partial x_i} - \gamma(x_1) \eta \quad (24)$$

where

$$\gamma(x_1) = \begin{cases} A \left(\frac{x - x_d}{x_o - x_d} \right)^2 & \text{if } x_d \leq x_1 \leq x_o \\ 0 & \text{otherwise} \end{cases} \quad (25)$$

η is the wave elevation, A is a constant, x_o is the x_1 -coordinate at the outflow boundary and x_d is defined as $x_d = x_o - 2\pi F n^2$. With no waves at the outlet it is appropriate to use Neumann condition for the velocity field $\partial u_i / \partial n = 0$ and for the pressure $\partial p / \partial n = 0$ and ϕ , k and ϵ are extrapolated.

Bottom Boundary

At the bottom $u_2 = 0$, $\partial u_1 / \partial n = 0$, the pressure is extrapolated, $\partial k / \partial n = 0$ and $\partial \epsilon / \partial n = 0$.

Top Boundary (air region)

$\partial u_i / \partial n = 0$, the pressure is extrapolated,

$\partial k / \partial n = 0$ and $\partial \epsilon / \partial n = 0$.

Body Boundary (viscous)

$u_i = 0$ and according to the boundary layer theory the pressure gradient near the body surface is zero, $\partial p / \partial n = 0$. Wall functions are used for k and ϵ .

Body Boundary (inviscid)

Neglecting curvature effects the normal component of the velocity must vanish $u_i \cdot n_i = 0$. For inviscid flows the pressure gradient is not zero close a curved wall, so the pressure is extrapolated.

The level set function is introduced and used to capture the free surface and to smooth the density and viscosity around the free surface. Nowhere else in space must the level set function be known. Therefore, ϕ is updated and reinitialized only in a region around the free surface. This means that boundary conditions for ϕ are just needed at the in- and outlet.

ONE-PHASE FORMULATION

Since ship flow calculations mostly concern the water flow only, and due to the fact that the introduction of a band in which the physical properties change is an unphysical approximation, it is favourable to keep the air domain and the band width to a minimum. It is shown in [7] that for stationary non-breaking waves at least three cells are required in the band in the normal direction to the free surface. The air domain only needs to be about 10 cells from the free surface and thus does not affect the computational cost significantly if the wave height is approximately known apriori. The band in which the physical properties change has little influence on the wave profile when the thickness relative the curvature is small. However, for breaking waves the thickness relative to the curvature will usually no longer be small. Level set contours of the free surface and the band borders of an overturning wave are shown in figure 3. The water volume of the fluid - the volume inside the inner contour - in the tongue must not be much smaller than the volume inside the free surface (middle) contour to be a representative of a water tongue.

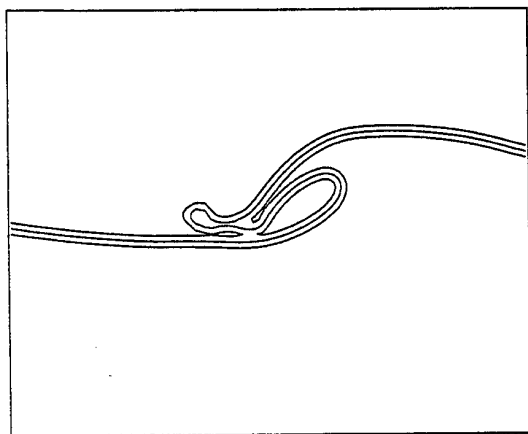


Figure 3. Bandwidth around a breaking wave.

Even though a turbulence model is included in the level set formulation the stresses close to the free surface might not be correct since the density and the viscosity are artificial near it. To get forces on a surface vessel the pressure is integrated over the wetted surface. However, the hydrostatic pressure does not vary linearly from the free surface and through the band. These disadvantages of the level set method presented in the last section can be related to one problem - the smooth density and viscosity distribution through the free surface. For this reason a level set method with a sharp free surface is presented in this and partially the next sections.

Governing Equations

Let the computational domain be a fixed grid covering both water and air regions as before. The idea is to solve the equations of motion in the water domain only and still capture the free surface with the zero level set of a level set function. The coupling between the level set function and the equations of motion is not accomplished by a level set formulation of the equations of motion but instead through boundary conditions at the free surface.

Now, the bulk flow is governed by

$$\frac{\partial u_i}{\partial t} + \frac{\partial}{\partial x_j}(u_i u_j) = -\frac{\partial \psi}{\partial x_i} + \frac{\partial}{\partial x_j} \left(\left(\frac{1}{Re} + v_t \right) \frac{\partial u_i}{\partial x_j} \right) \quad (26)$$

$$\frac{\partial u_i}{\partial x_i} = 0$$

$$\frac{\partial \phi}{\partial t} + u_i \frac{\partial \phi}{\partial x_i} = 0$$

where $\psi = p + x_2/Fn^2$ is the pressure with the hydrostatic pressure excluded and v_t is the kinematic ($\nu = \mu/\rho$) eddy viscosity. In the two-phase formulation the pressure, ψ , cannot be used because of the different hydrostatic pressure in air and water.

Reinitialization

Since the equations of motion are solved only in the water domain, boundary conditions are needed at the free surface. It is convenient to use the level set function to get the distance to the free surface when these conditions are implemented and when to decide whether a node is inside, here in the water, or outside the free surface. The level set function is then reinitialized to keep it a distance function to facilitate implementation of boundary conditions and not to smooth the density and the viscosity. The reinitialization procedure is the same as described in the two-phase formulation.

Turbulence Model

The k - ϵ turbulence model often referred to as the standard k - ϵ turbulence model with wall functions is used here.

The kinematic eddy viscosity is

$$\nu_t = C_\mu \frac{k^2}{\epsilon} \quad (27)$$

The transport equations for k and ϵ are

$$\frac{\partial k}{\partial t} + u_i \frac{\partial k}{\partial x_i} = \frac{\partial}{\partial x_i} \left(\left(\frac{1}{Re} + \frac{\nu_t}{\sigma_k} \right) \frac{\partial k}{\partial x_i} \right) + P_k - \epsilon \quad (28)$$

$$\frac{\partial \epsilon}{\partial t} + u_i \frac{\partial \epsilon}{\partial x_i} =$$

$$\frac{\partial}{\partial x_i} \left(\left(\frac{1}{Re} + \frac{\nu_t}{\sigma_k} \right) \frac{\partial \epsilon}{\partial x_i} \right) + \frac{\epsilon}{k} (C_{\epsilon 1} P_k - C_{\epsilon 2} \epsilon) \quad (29)$$

where the production P_k and the constants are the same as in the two-phase formulation

$$P_k = \nu_t \left(\frac{\partial u_i}{\partial x_j} + \frac{\partial u_j}{\partial x_i} \right) \frac{\partial u_i}{\partial x_j}$$

and $C_\mu=0.09$, $C_{\epsilon 1}=1.44$, $C_{\epsilon 2}=1.92$, $\sigma_k=1.0$ and $\sigma_\epsilon=1.3$.

For a description of the wall functions, see the two-phase formulation.

Boundary Conditions

Below, only the boundary conditions different from those given above are presented.

Top Boundary

No boundary conditions are needed at the top boundary.

Free Surface Boundary Condition

At the free surface the difference between normal stresses across the interface are proportional to the surface tension and tangential stresses and tangential velocity components are continuous across the interface [15]. In the absence of surfactants this yields a boundary condition at the interface between the two fluids

$$\tau_{ij} n_j = \tau_{ij}^* n_j + \frac{\kappa}{We} n_i \quad (30)$$

where the stress tensors τ_{ij} and τ_{ij}^* are

$$\tau_{ij} = -p \delta_{ij} + \frac{1}{Re} e_{ij} \text{ and } \tau_{ij}^* = -p^* \delta_{ij} + \frac{1}{Re^*} e_{ij}^*$$

for water and air respectively. $e_{ij} = \frac{\partial u_i}{\partial x_j} + \frac{\partial u_j}{\partial x_i}$ is the rate of strain tensor and δ_{ij} is the Kronecker delta. Neglecting viscous stresses in the air, equation (30) written in normal and tangential components give the two dynamic conditions

$$\tau_{ij} n_i n_j = -p^* + \frac{\kappa}{We} \text{ and } \tau_{ij} n_i t_j = 0. \quad (31)$$

Inviscid boundary conditions are obtained under the additional assumption that viscous stresses in the water are negligible whereupon equations (31) reduce to

$$p = p^* - \frac{\kappa}{We}.$$

This is not a very crude assumption since the stresses are proportional to $1/Re$. With the atmospheric pressure p^* set to zero, the dynamic boundary condition for ψ at the free surface is

$$\psi = \frac{\eta}{Fn^2} - \frac{\kappa}{We}.$$

$$\partial u_i / \partial n = 0, \partial k / \partial n = 0 \text{ and } \partial \epsilon / \partial n = 0.$$

NUMERICAL METHOD

Momentum Equations

The continuity and momentum equations are solved with a fractional step method using a finite-volume formulation. Time integration is carried out with Euler forward differencing, convective terms are approximated by a third order upwind scheme while other spatial derivatives are discretized by second order central differences.

The momentum equations are written with discrete operators in explicit form for the velocity vector u^n and implicit form for the pressure as

$$\frac{u^{n+1} - u^n}{\Delta t} = F(u^n) - \nabla p^{n+1} \quad (32)$$

where p is ψ or p in the one- or two-phase formulations respectively, $F(u^n)$ is the combined convective and diffusive operator in the one-phase formulation, the combined convective and diffusive operator

including surface tension and gravitational forces in the two-phase formulation and n is the number of the timestep. Define the intermediate velocity $\tilde{u} = u^n + \Delta t F(u^n)$ and rewrite equation (32)

$$u^{n+1} = \tilde{u} - \Delta t \nabla p^{n+1}. \quad (33)$$

The corrector equation is

$$u^* = \tilde{u} - \Delta t \nabla p^n. \quad (34)$$

Taking the difference of the last two equations, defining the pressure difference

$$dp = p^{n+1} - p^n \quad (35)$$

and using $\nabla \cdot u^{n+1} = 0$ will provide the Poisson equation for the pressure difference

$$\nabla^2(dp) = \frac{1}{\Delta t} (\nabla \cdot u^*) \quad (36)$$

p^{n+1} is given by equation (35) and u^{n+1} by equation (33).

Acceleration

To decrease start-up transients the following smooth acceleration of the flow field is used:

$$u_1^n = u_1^{n-1} + u_a^n \quad (37)$$

$$u_a^n = \begin{cases} \sin^2\left(\frac{r^n \pi}{t_a}\right) - \sin^2\left(\frac{r^{n-1} \pi}{t_a}\right) & 0 < r^n \leq t_a \\ 0 & r^n > t_a \end{cases} \quad (38)$$

$r^0 = 0$, t_a is the time of acceleration - typically one time unit, and r^n is the time at time level n . The gravitational force in the two-phase formulation is accelerated likewise since it appears explicitly in the equations.

Level Set Function

The level set function, equation (5), is solved with a finite-difference scheme. Convection terms are approximated by a third order upwind scheme. Central differences are used at boundaries to avoid dummy nodes. As for the momentum equations Euler forward is used for discretization in time.

Reinitialization

Equation (15) may be written in the form

$$\frac{\partial d}{\partial \tau} + w_i \cdot \frac{\partial d}{\partial x_i} = S(d_o) \quad (39)$$

where

$$w_i = S(d_o) \left(\frac{\partial d}{\partial x_i} / \left| \frac{\partial d}{\partial x_k} \right| \right). \quad (40)$$

Equation (39) is a nonlinear hyperbolic equation. To reduce both dissipation and dispersion errors even in the presence of large gradients, a second order upwind ENO scheme [16] is used for the spatial derivatives. Equation (15) is solved by iterating

$$d^{m+1} = d^m - \Delta \tau S(d_o) G(d^m) \quad (41)$$

to steady state. $G(d^m)$ is the discrete ENO operator applied to $|\partial d / \partial x_k| - 1$

$$G(d^m) = \begin{cases} D^+ & S(d_o) > 0 \\ D^- & S(d_o) < 0 \\ 0 & S(d_o) = 0 \end{cases} \quad (42)$$

where

$$\begin{aligned} D^+ &= \left[\max((A_1^1 + |A_1^1|)^2, (A_1^2 - |A_1^2|)^2) \frac{1}{4} + \right. \\ &\quad \left. \max((A_2^3 + |A_2^3|)^2, (A_2^4 - |A_2^4|)^2) \frac{1}{4} \right]^{1/2} - 1 \\ D^- &= \left[\max((A_1^1 - |A_1^1|)^2, (A_1^2 + |A_1^2|)^2) \frac{1}{4} + \right. \\ &\quad \left. \max((A_2^3 - |A_2^3|)^2, (A_2^4 + |A_2^4|)^2) \frac{1}{4} \right]^{1/2} - 1 \end{aligned} \quad (43)$$

and

$$A_i^r = b_i^r \frac{\partial d^k}{\partial \xi_j} + \frac{1}{2} Q \left(b_i^r \frac{\partial d^{kk}}{\partial \xi_j}, b_i^r \frac{\partial d^c}{\partial \xi_j} \right) \quad (44)$$

where

$$Q(x, y) = \begin{cases} x & \text{if } |x| \leq |y| \\ y & \text{if } |x| > |y| \\ 0 & \text{if } xy < 0 \end{cases} \quad (45)$$

is the switch function that turns higher order differencing off when a chock is detected and the superscript k and c denotes the order and kind of differencing. c means second order central differencing. One k means first order while two k (kk) means second order differencing and b is backward and f is forward differencing as

$$k = \begin{cases} b \begin{cases} b_i^j > 0, & r = 1, 3 \\ b_i^j < 0, & r = 2, 4 \end{cases} \\ f \begin{cases} b_i^j < 0, & r = 1, 3 \\ b_i^j > 0, & r = 2, 4 \end{cases} \end{cases} \quad (46)$$

This means that the direction of the upwinding is influenced by the sign of the coefficient of the Jacobian matrix of the coordinate transformation b_i^j .

Figure 4 demonstrates the effectiveness of the reinitialization procedure. Initially, the value of the level set function ϕ is one in the space between the wing boundary and the zero level set, the ellipse, and minus one outside the ellipse. Figure 5 shows the contours of ϕ after a few iterations. It is seen that ϕ first becomes a distance function close to the zero level set. Thus, since the density and the viscosity are smoothed around the free surface and nowhere else, ϕ does not have to be defined in the whole domain or if ϕ is defined in the whole domain it is not necessary to reach a steady state solution. The unevenness at the two fronts just indicates that steady state has not been reached. After another few iterations steady state is reached, figure 6. Initially ϕ was not at all a distance function. In a real flow simulation ϕ is reinitialized every, or say every tenth, iteration and the function to be reinitialized is close to a distance function. So, typically only one to three iterations are needed to reach steady state. The zero level set plotted as a dotted line in figures 5-6 coincide totally with the reinitialized ϕ and is therefore not visible in the figures.

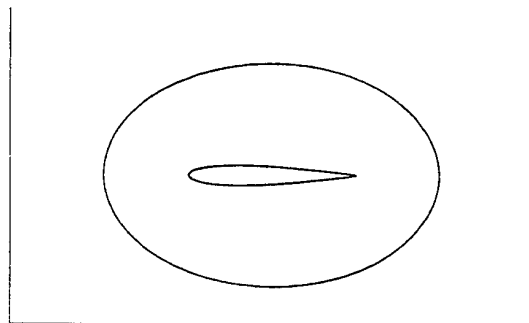


Figure 4. The zero level set around a wing section.

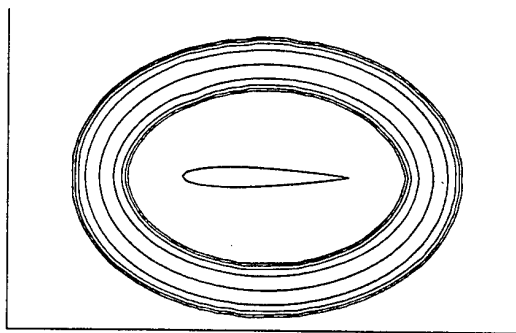


Figure 5. After a few steps of reinitialization of the level set function in figure 4.

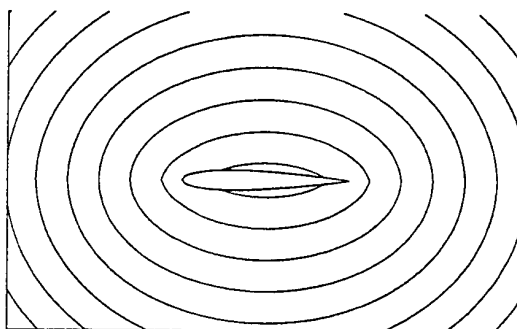


Figure 6. The level set function in figure 4 and 5 reinitialized.

Free Surface Boundary Conditions

In the one-phase formulation boundary conditions are to be applied at the free surface. However, since a fixed grid is used the free surface usually does not coincide with neither the positions of the variables in question nor a gridline, so boundary conditions at the free surface have to be implemented with care.

Pressure Condition

The pressure is defined in the cell centre and the pressure free surface boundary condition is to be applied e.g. at point k in figure 7.

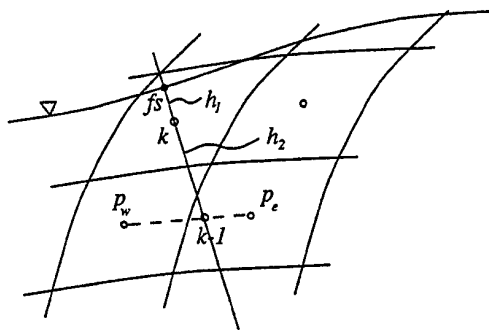


Figure 7. Definitions for pressure free surface boundary condition implementation.

Taylor expand ψ around k in the normal direction to the free surface

$$\psi_{fs} = \psi_k + \frac{\partial \psi_k}{\partial n} h_1 + \frac{1}{2} \frac{\partial^2 \psi_k}{\partial n^2} h_1^2 + O(h^3). \quad (47)$$

The value of the pressure at the free surface is known. Neglecting curvature effects it is $\psi_{fs} = \eta / Fn^2$, $\eta = x_{2,k} - n_2 h_1$, $h_1 = \phi|_k$. And the pressure at $k-1$ is interpolated from ψ_w and ψ_e in figure 7. With central differences for both first and second derivatives and non-equidistant grid spacing equation (47) is

$$\psi_{fs} = \psi_k + \frac{h_1}{h_1 + h_2} (\psi_{fs} - \psi_k) +$$

$$\frac{h_1^2}{2(h_1^2 + h_2^2)} \left(\frac{2h_2}{h_1 + h_2} \psi_{fs} - 2\psi_k + \frac{2h_1}{h_1 + h_2} \psi_{k-1} \right) \quad (48)$$

which yields an equation for ψ_k . But h_2 and the position $k-1$ has to be found. Find the intersection points between the line normal to the free surface l_1 and the two dashed lines l_2 and l_3 , shown in figure 8, take $k-1$ to the intersection point nearest k and set $h_2 = \overline{kk-1}$. It is not known beforehand between which two pressure points $k-1$ lies. So, if l_1 is the dotted line in figure 8, i.e. the free surface has a steeper slope, the pressure points to interpolate from will be k_w and k_n .

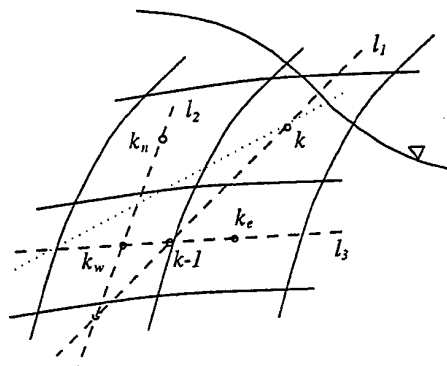


Figure 8. Definitions for pressure free surface boundary condition implementation.

l_1 which is parallel to n_i and shall go through point k is expressed as

$$x_i = x_i^k + rn_i \quad (49)$$

and l_2 as

$$x_i = a_2^i + sx_i^{k_w} \quad (50)$$

where $-\infty < r, s < \infty$ and $a_j^i = \partial x_i / \partial \xi_j$. r and s are given from $x_i^k + rn_i = a_2^i + sx_i^{k_w}$. For example

$$s = \frac{n_1(a_2^2 - x_2^k) + n_2(x_1^k - a_2^1)}{n_2x_1^{k_w} - n_1x_2^{k_w}}. \text{ Applying } s \text{ to}$$

equation (50) yields the intersection point between l_1 and l_2 . Then the intersection point between l_1 and l_3 is found in the same way and all is set for calculating the pressure boundary condition at point k .

Normal derivatives

Normal derivatives at the free surface are approximated by weighting the contravariant components of the normal vector to the free surface and the distance to three neighbour points, figures 9 and 10.

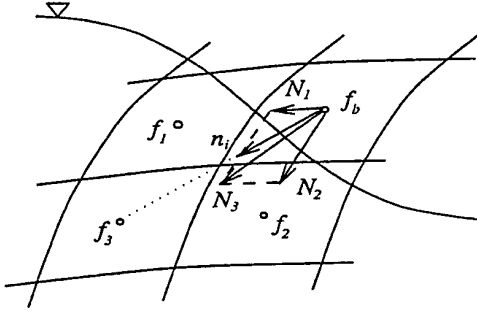


Figure 9. Definitions for implementation of normal derivatives at the free surface.

For any scalar f defined e.g. in the cell centre

$$f_b = \frac{\sum f_k |N_k| / L_k}{\sum |N_k| / L_k} \quad (51)$$

where

$$N_k = b_i^k n_i$$

is the contravariant normal vector and

$$L_1 = \frac{\sqrt{g^{22}}}{J}, \quad L_2 = \frac{\sqrt{g^{11}}}{J}$$

and

$$L_3 = \frac{1}{J} (g^{11} + g^{22} - 2g^{12})^{1/2}.$$

N_3 can lie in the plane between N_1 and n_i or between N_2 and n_i , compare figure 9 and 10. Therefore, N_3 is calculated from

$$\frac{|N_3|}{L_3} = \begin{cases} \frac{|N_1|}{L_1} & \text{if } \frac{\hat{N}_1}{\hat{L}_1} \leq \frac{\hat{N}_2}{\hat{L}_2} \\ \frac{|N_2|}{L_2} & \text{otherwise} \end{cases}$$

where $\hat{\cdot}$ denotes normalized components.

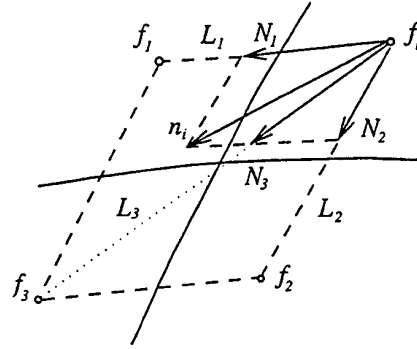


Figure 10. Definitions for implementation of normal derivatives at the free surface.

Extrapolation

In the one-phase formulation the system of equations is solved in the water region only and the level set function is used to capture the free surface that is now a sharp interface. However, to get the zero level set, velocities on both sides of the zero level set i.e. water and air velocities are needed. The values in the air are extrapolated in the normal direction to the free surface in a similar manner as the normal derivatives are calculated. The level set function in the air is updated by the reinitialization.

Free Surface Outlet Condition

In the wave damping term in equation (24) η is the wave elevation. The level set function is a distance function so, $\phi|_{\text{ifss}}$ is the normal distance with sign from the free surface to the initial flat free surface ifss and the wave elevation $\eta = n_2 \phi|_{\text{ifss}}$. In this way the level set function does not have to be found explicitly to apply the damping function at the outlet. Since ifss does not necessarily coincide with a node, $\phi|_{\text{ifss}}$ is calculated by linear interpolation. The damping function $\gamma(x_1)$ is calculated once and stored.

Filtering

It is obvious that the normal vector plays an important role in computing boundary conditions at the free surface in the one-phase formulation. Therefore, a smooth distribution of the normal vector is required for the methods of applying boundary conditions at the free surface as described in the last section to be accurate. The normal vector is expressed in terms of the level set function, equation (10), which is a smooth function. However, in numerical computations this may not always be true. For example at large curvature in relation to the resolution i.e.

cell sizes. If the level set function then includes high frequency dispersion errors not really visible when judging the shape of the level sets the normal vector will be influenced by these. Usually, the small fluctuations in the normal vector field will be damped by numerical diffusion but in the worst case they will not and the oscillations will increase and the computation will crash. To avoid this the level set function can be filtered. Here the following equation is solved

$$\tilde{\phi} + \omega \nabla^2 \tilde{\phi} = \phi. \quad (52)$$

where $\tilde{\phi}$ is the filtered level set function, ∇^2 is the discrete laplacian operator and ω is a smoothing parameter, typically the size of the cell. The filtered level set function is a new quantity and does not replace the original level set function. It is used only to compute the normal vector and curvature and for nothing else. So, the introduction of a filtered level set function will not affect the capturing of the free surface i.e. this will not be smoothed.

RESULTS

Profiles of the waves generated by a submerged NACA0012 hydrofoil have been extensively measured by Duncan [17]. The case is two-dimensional and in the present work a submerged NACA0012 wing section with an angle of attack of 5 degrees is simulated. For $Fn=0.567$, $Re=1.62 \cdot 10^5$ and the non-dimensional depth of submergence $s/c=1.034$ some prior checking of the code has been carried out and the free surface height for stationary waves computed. The onset of breaking was predicted for three speeds, $Fn=0.425$, $Fn=0.567$ and $Fn=0.709$. Viscous flows were computed with both methods and inviscid flows with the two-phase method. The computational domain extended five chord lengths in front of the foil and between seven and twelve chord lengths, including damping zone, behind the foil depending on the speed. Note the position and scaling of the foil in the figures below.

Prior checking

The residual, R , is here defined as a weighted L_2 -norm of the acceleration

$$R = \sqrt{\frac{1}{N} \sum_{i=1}^N \sum_{k=1}^2 (F(u) - \nabla p)_i^2} \quad (53)$$

where N is the number of grid nodes. The residual is shown in figure 11. There are no fundamental differences in the solution algorithm between the two methods and the residuals of the two methods behaves in a similar manner.

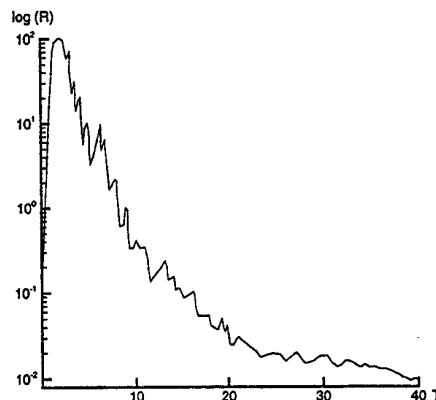


Figure 11. The residual of the acceleration.

To get an estimation of the order of the scheme computations on three different grids successively refined a factor two finer in all directions can be compared. A weighted L_2 -norm of a vector valued function $\vec{u} = (u_1, u_2)$ is defined as

$$\|\vec{u}\|_2 = \sqrt{\frac{1}{N} \sum_{k=1}^N ((u_1^k)^2 + (u_2^k)^2)} \quad (54)$$

and of a scalar θ as

$$\|\theta\|_2 = \sqrt{\frac{1}{N} \sum_{k=1}^N \theta_k^2} \quad (55)$$

Denote the fields $\vec{u}^{4h_k}, \theta^{4h_k}, \vec{u}^{2h_k}, \theta^{2h_k}$ and $\vec{u}^{h_k}, \theta^{h_k}$ superindexed by the spatial resolution and the time steps used are $4\Delta t, 2\Delta t$ and Δt respectively. Let the difference in L_2 -norm be

$$* = \begin{cases} \|\vec{u}^{4h_k} - \vec{u}^{2h_k}\|_2 & \text{or} \quad \|\theta^{4h_k} - \theta^{2h_k}\|_2 \end{cases} \quad (56)$$

and

$$** = \begin{cases} \|\vec{u}^{2h_k} - \vec{u}^{h_k}\|_2 & \text{or} \quad \|\theta^{2h_k} - \theta^{h_k}\|_2 \end{cases} \quad (57)$$

In table 1 and table 2 these differences and the convergence obtained are given for the velocity, the pressure and the level set function for the two- and

one-phase methods respectively. In the two-phase formulation only the water region is considered.

Variable	*	**	order
u	$8.53 \cdot 10^{-2}$	$3.16 \cdot 10^{-2}$	1.43
p	$6.43 \cdot 10^{-2}$	$2.76 \cdot 10^{-2}$	1.22
ϕ	$5.69 \cdot 10^{-2}$	$1.84 \cdot 10^{-2}$	1.63

Table 1. Order of convergence for the velocity, the pressure and the level set function for the two-phase formulation.

Variable	*	**	order
u	$8.69 \cdot 10^{-2}$	$3.37 \cdot 10^{-2}$	1.41
p	$6.64 \cdot 10^{-2}$	$2.97 \cdot 10^{-2}$	1.16
ϕ	$5.90 \cdot 10^{-2}$	$2.00 \cdot 10^{-2}$	1.53

Table 2. Order of convergence for the velocity, the pressure and the level set function for the one-phase formulation.

The convergence rates for the velocity field and the level set function is close to 1.5 and for the pressure a little bit better than 1. The values are slightly lower with the one-phase formulation than with the two-phase formulation. Even though essentially all parts contributing to the spatial convergence are at least second order accurate the total order of convergence is far from that. Skewed cells, cells with high aspect ratio and influences from boundary conditions are examples of effects that yield a lower order convergence.

Pressure and velocity contours beneath the free surface and the velocity field around the foil computed with the one-phase method and turbulence model are shown in figures 12-14.

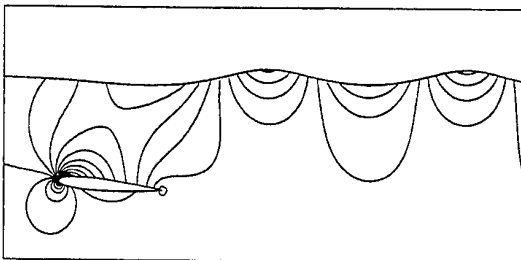


Figure 12. Pressure contours.

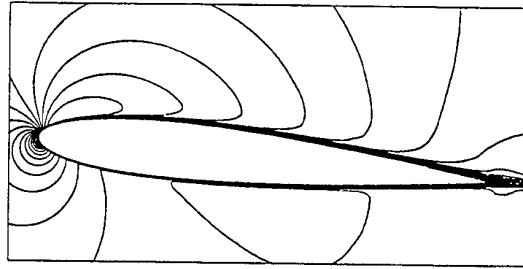


Figure 13. Velocity contours.

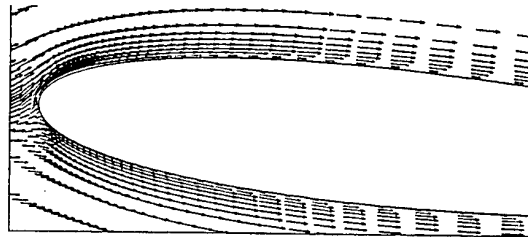


Figure 14. Velocity vectors.

Stationary waves

Stationary waves have been investigated for $Fn=0.567$ and depth of submergence $s/c=1.034$. It is seen in figures 15 and 16 that results from the two methods are almost on top of each other even though the one-phase formulation under predicts the wave heights a little more than the two-phase formulation for both inviscid and viscous solutions. Figure 17 shows inviscid and viscous one-phase formulation results. The RANSE wave amplitude is noticeably lower than the Euler wave amplitude which was also observed by other investigators [18]. It should be pointed out that the pretty pictures shown in this subsection are snapshots of the profile of waves that has not mathematically speaking reached steady state but a rather periodic state. Start up transients and reflections from mainly the outlet and inlet boundaries are bouncing back and forth between the boundaries which are not completely non-reflecting. Two wave profiles at time t and $t+dt$ could not be separated by inspection of the wave amplitude covering the whole screen. Also, two wave profiles at time t and $t+ndt$ where n is of the order of hundred (explicit scheme) and n happens to be the periodicity would coincide. Avoiding the periodic n the difference might be visible see figure 18. However, all comparisons are at least made at the same time t .

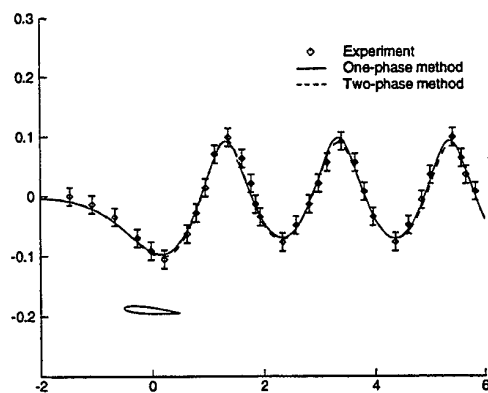


Figure 15. Comparison between inviscid one- and two-phase methods.

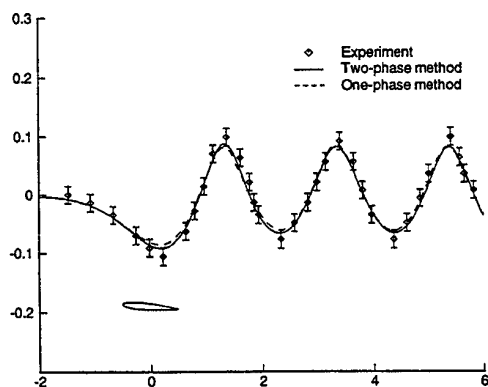


Figure 16. Comparison between viscous one- and two-phase methods.

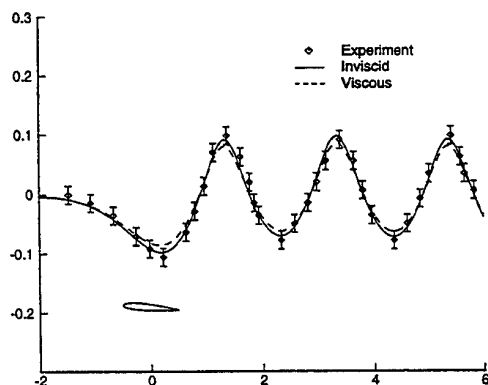


Figure 17. Comparison between inviscid and viscous results with the one-phase method.

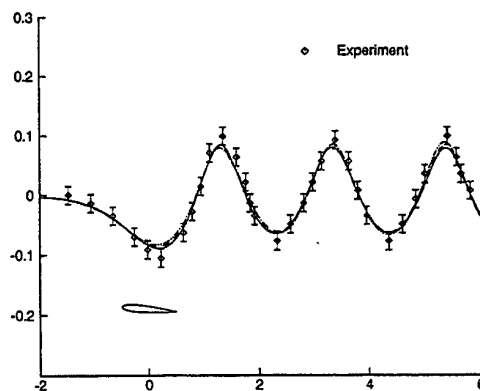


Figure 18. Oscillating wave amplitude.

Figure 19 shows a close up of Euler and RANSE velocity vectors around the free surface computed with the two-phase method. The largest gradients appear in the air at the interface between the band and the air due to the relatively largest changes in the density there. For the viscous calculation these gradients are a little less pronounced.

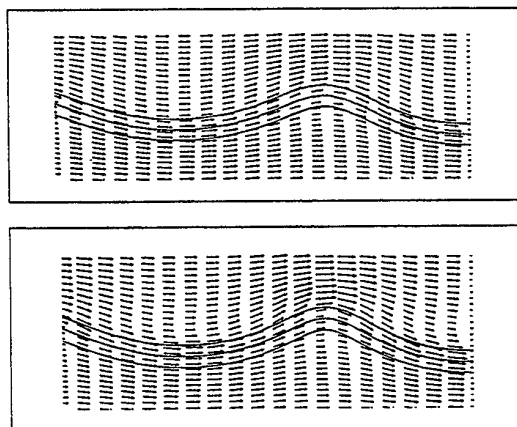


Figure 19. Velocity vectors around the free surface, viscous top and inviscid bottom.

Onset of breaking

The onset of breaking has been numerically investigated for three different Froude numbers, $Fn=0.425$, $Fn=0.567$ and $Fn=0.709$ solving the Euler and RANS equations with the two-phase formulation and the Euler equations with the one-phase formulation. Computations were carried out for different depths of submergence s/c of the foil in whole steps in the second decimal of s/c . At the lowest Froude number $Fn=0.425$ the onset of breaking is generally well predicted. The inviscid two-phase method over predicts

the depth of submergence of the foil for the two higher speeds i.e. waves are breaking for deeper depths than measured, figure 20.

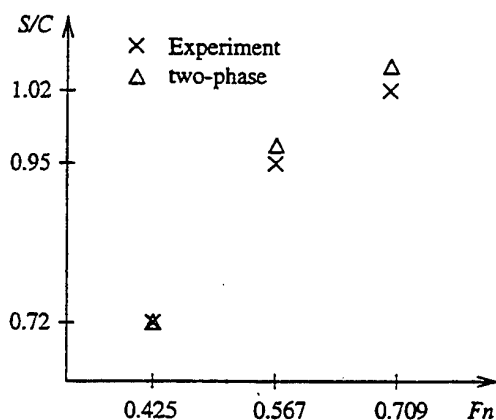


Figure 20. Wave breaking predictions as a function of foil submergence and speed with inviscid two-phase method.

For viscous calculations both methods under predict the depth of submergence and the discrepancies are getting larger with higher Froude number, figure 21.

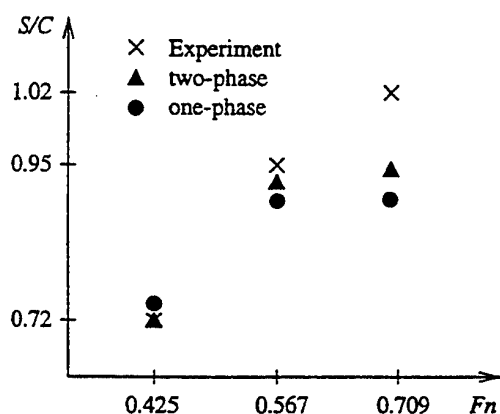


Figure 21. Wave breaking predictions as a function of foil submergence and speed with viscous one- and two-phase methods.

Figure 22 shows the difference between viscous and inviscid computations with the two-phase method. The viscous results are under predicted and the inviscid results are slightly over predicted. The trend that viscous results are under predicted follows the one observed for stationary waves, compare figure 17.

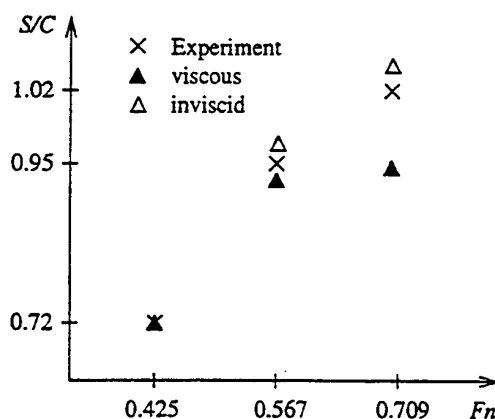


Figure 22. Wave breaking predictions as a function of foil submergence and speed for inviscid and viscous two-phase method.

Duncan found that for $Fn=0.567$ steady state was obtained for $s/c=0.950$. For $s/c=0.951$ no breaking occurred if no disturbances were added but with disturbances (a cloth was used in front of the foil at the free surface) the waves broke. With such large differences in depths between various runs as used in the present work there were three kinds of wave profiles observed. Plunging breaking, a sort of cyclic slightly overturning breaking and no breaking. A typical plunging breaking with a break-off of a 'water drop' is shown in figure 23 for $Fn=0.425$ and $s/c=0.50$ computed with the two-phase method.

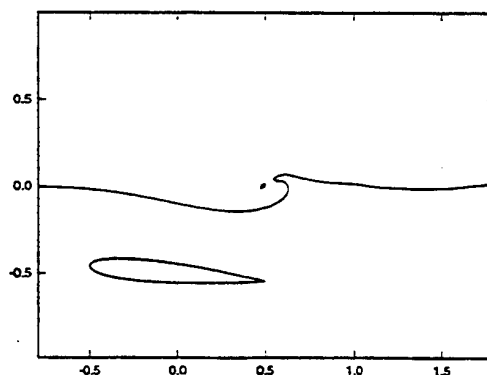


Figure 23. Overturning wave and the break-off of a 'water drop', $Fn=0.425$ and $s/c=0.5$.

The resolution in figure 23 is far from satisfactory and this wave profile has probably little to do with real wave shapes for this case. Later, the overturning wave merges. Figure 24 shows a merged overturning wave computed with the one-phase method at $Fn=0.567$ and $s/c=0.88$. Values at dummy nodes

were not implemented in a general way so, merging will not be correctly treated even though it is possible to compute. However, the divergence is large, many more than three iterations were needed to reinitialize the level set function and filtering was required.

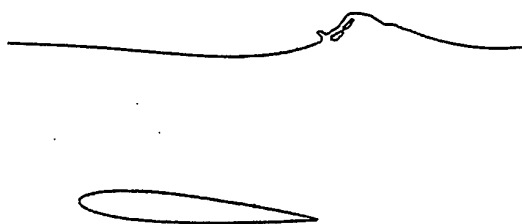


Figure 24. Merging overturning wave, $Fn=0.567$ and $s/c=0.88$.

In figure 25 one cycle (in order: solid, dashed dot, dashed, dashed dot dot, dotted and long dashed) of the slightly overturning breaking wave with the two-phase method at $Fn=0.567$ and $s/c=0.93$ is shown. Two kinds of breaking, shown in figures 23 and 25 were observed. It was such, obvious whether breaking occurred or not.

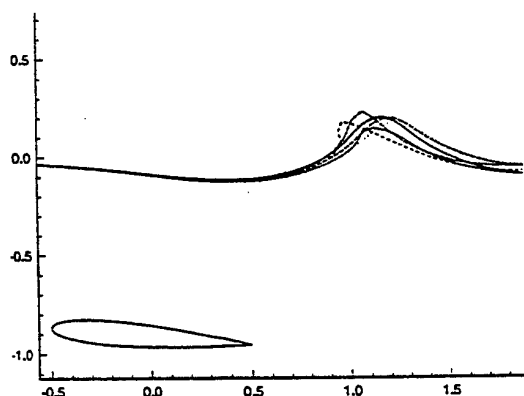


Figure 25. Slightly overturning breaking wave, $Fn=0.567$ and $s/c=0.93$.

CONCLUSIONS

Two variations of a finite volume method solving the Reynolds averaged Navier-Stokes equations for two-dimensional free surface flows on fixed grids are presented here. The level set technique is used to

capture the free surface in both a two-phase formulation and in a one-phase formulation. In the latter, dynamic boundary conditions are applied at the free surface. Also the $k-\epsilon$ turbulence model is formulated in the level set formulation.

In the two-phase method, the possibility for the free surface to change topology is embedded in the formulation. This is achieved at the expense of an interface with a finite thickness, in terms of number of cells around the free surface. To avoid this disadvantage a sharp free surface level set method has been developed. However, in this method the flexibility is so far restricted and it is more complicated to implement which applies particularly to the extension to three dimensions.

The computed wave profiles of steady waves generated by a submerged wing section with the two methods are close to each other for both inviscid and viscous flows and the inviscid results are in better agreement with experiments than viscous results are.

Regarding predictions of the onset of breaking the depths at which breaking waves were predicted were compared to experiments for three different Froude numbers. For viscous flows, predictions with both methods agree well with experiments for the lowest Froude number $Fn=0.425$ and are more and more underpredicted with higher speeds. Euler computations were carried out with the two-phase formulation and compared to RANSE solutions. The Euler solutions are in better agreement with experiments but over predicts the depth of submergence for the higher Froude numbers $Fn=0.567$ and $Fn=0.709$.

The two variations show similar results for the cases computed. So, the benefit with the sharp free surface method can be argued. In case the effects of the free surface boundary layer are important, on one hand, a sharp interface should represent the free surface better than one including a mixing of water and air. On the other hand, boundary conditions are implemented at an interface not coinciding with a gridline and the method is slightly less accurate, see table 1 and 2, than the two-phase method.

ACKNOWLEDGEMENTS

This work was funded by the Swedish National Research Program for Naval Architecture. Thanks are due to Hamburg Ship Model Basin where this report was partially written.

REFERENCES

1. Raven H. C. "Nonlinear ship wave calculations using RAPID method," Sixth international conference on numerical ship hydrodynamics, Iowa City, Iowa, USA, Aug. 1993, Naval Studies Board of the U.S. National Research Council, IIHR, DTRC and ONR, Aug. 1993, pp.95-113.
2. Baba E., "A new component of viscous resistance of ships," Journal of the society of naval

architects of Japan, 1969, Vol.125, pp.23-34.

3. Harlow F. H. and Welch J. P., "Numerical calculation of time-dependent viscous flow of fluid with free surface," Physics of Fluids, Vol.8, 1965, pp.2182-2189.

4. Hirt C. W. and Nichols B. D., "Volume of fluid (VOF) method for the dynamics of free boundaries," Journal of computational physics, Vol.39, 1981, pp.201-225.

5. Mori K. and Hinatsu M., Proceedings of CFD workshop Tokyo 1994, an international workshop for improvement of hull form designs, Tokyo, Japan, Vol.1, mar.1994

6. Osher S. and Sethian J. A., "Fronts propagating with curvature-dependent speed: algorithms based on Hamilton-Jacobi formulations," Journal of computational physics, Vol.79, No.1, 1988, pp.12-49.

7. Vogt M., "A numerical investigation of the level set method for computing free surface waves," 1998, Department of Naval Architecture and Ocean Engineering, Chalmers University of Technology, report CHA/NAV/R-98/0054

8. Dommermuth D., Innis G., Luth T., Novikov E., Schlageter E. and Talcott J., "Numerical simulation of bow waves," Twenty-second symposium on naval hydrodynamics, Washington, D.C., Vol.2, aug.1998, pp.159-172.

9. Thompson J. F., Thames F. C. and Mastin C. W., "Automatic numerical generation of body-fitted curvilinear coordinate system on fields containing any number of arbitrary two-dimensional bodies," Journal of computational physics, Vol.15, 1974, pp.299-.

10. Sussman M., Smareka P. and Osher S., "A level set approach for computing incompressible two-phase flows," Journal of computational physics, Vol.114, 1994, pp.146-159.

11. Alessandrini B. and Delhommeau G., "Numerical calculation of three-dimensional viscous free surface flow around a serie 60 $C_b=0.6$ ship model," Proceedings of CFD workshop Tokyo 1994, an international workshop for improvement of hull form designs, Tokyo, Japan, Vol.1, mar.1994, pp.95-104.

12. Launder B. E. and Spalding D. B., "The numerical computation of turbulent flows," Computer methods in applied mechanics and engineering, Vol.3, 1974, pp.269-289.

13. Hino T., Martinelli L. and Jameson A., "A finite-volume method with unstructured grid for free surface flow simulations," Sixth international conference on numerical ship hydrodynamics, Iowa City, Iowa, USA, Aug. 1993, Naval Studies Board of the U.S. National Research Council, IIHR, DTRC and ONR, Aug.1993, pp.173-193.

14. Lungu A. and Mori K., "A study on numerical schemes for more accurate and efficient computations of free surface flows by finite difference method," Journal of the society of naval architects of Japan, Vol.173, 1993, pp.9-17.

15. Wehausen J. V. and Laitone E. V., "Surface waves," Handbuch der Physik, Vol.9, Springer, Berlin, 1960.

16. Shu C. W. and Osher S., "Efficient implementation of essentially non-oscillatory shock capturing schemes, II," Journal of computational physics, Vol.83, 1989, pp.32-78.

17. Duncan J. H., "The breaking and non-breaking wave resistance of a two-dimensional hydrofoil," Journal of Fluid Mechanics, Vol. 126, 1983, pp.507-520.

18. Hino T., "An unstructured grid method for compressible viscous flows with a free surface," AIAA, 1997.

APPENDIX

Volume computation

To take the difference between the mass flow at the in- and outlet is one way to check the global conservation of an incompressible stationary solution. This should be appropriate if the boundary conditions are correctly implemented. But if a free surface is present, first, the mass in- and outflow through the surface may not always be numerically zero, so even if the difference between the mass flow at the in- and outlet is zero this does not necessarily imply global conservation. Second, as the solution proceeds in time the net mass flow might be negligible. However, if the number of time steps needed to reach a stationary solution is large and the sign of the difference between the mass flow at the in- and outlet does not oscillate i.e. the differences are not cancelling each other the total or in time integrated mass difference might be substantial. This means leakage or filling of mass into the domain before a stationary solution is reached which could be the correct solution, but if not, only checking the difference of mass between the in- and outlet could be misleading. Another way to check global conservation is to compute the volume of the fluid domain. With a free surface cutting cells in a fixed grid there are three kinds, in 2D, of partially filled cells at the surface. a) one node in the water region and three nodes in the air region, b) two nodes in both the water and air regions and c) three nodes in the water region and one node in the air region. The volume fraction of water v_{fw} is here for the three cases:

$$a) v_{fw} = \frac{J - |A|}{J}$$

$$b) v_{fw} = \frac{|A|}{J}$$

$$c) v_{fw} = \frac{J}{J}$$

where

$$A = \frac{1}{2} \begin{vmatrix} x_1^1 & x_2^1 & 1 \\ x_1^2 & x_2^2 & 1 \\ x_1^3 & x_2^3 & 1 \end{vmatrix} \text{ see figure A1 and}$$

$J = \det(a_j^i)|_c$ where a_j^i at point c is interpolated from the values in the points 1, 2, 3 and 4 in figure A2. These are computed with different grid spacing.

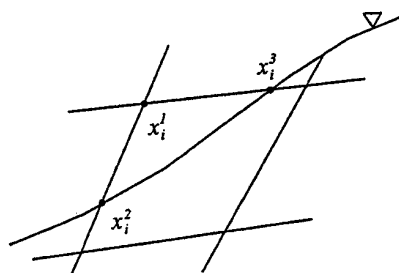


Figure A1. Definitions for volume calculation of free surface cells.

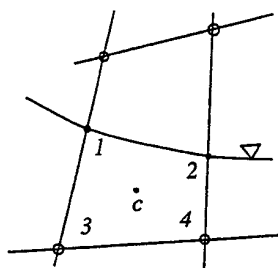


Figure A2. Definitions for volume calculation of free surface cells.

The coordinates of the points where the free surface cuts the cell faces are interpolated from the level set function. Since the level set function is a distance function this yields exactly the position of the free surface at the cell faces.

Computation of the Wetted Transom Stern Flow over Model 5415

Murali Beddhu, Min-Yee Jiang, David L. Whitfield and
Lafayette K. Taylor

CFD Laboratory, NSF Engineering Research Center, Mississippi State University

POB Box 9627 Mississippi State MS 39762 USA

Fax: 601-325-7692 ; E-mail: murali@erc.msstate.edu

ABSTRACT

The importance of model 5415 stems from the facts that it represents an important class of existing ships and detailed experimental data are available for validating Computational Fluid Dynamics (CFD) codes. The code UNCLE incorporates an algorithm for tracking unsteady free surface flows in a time accurate manner. In this algorithm, to facilitate the tracking of the free surface, a background grid is employed. Using the background grid the free surface grid points are forced to move along predetermined paths in order to simplify the grid regeneration process at the new time level. Newton's method is used to find the intersection of the background grid lines with the free surface. This allows the preservation of the shape of the free surface during various grid operations at a given time level. The governing equations of the flow field are cast with respect to an unsteady Eulerian coordinate system and solved using the modified artificial compressibility method. The kinematic condition has been formulated from first principles such that it is valid for breaking waves up to the point of reentry. The resulting numerical algorithm is implicit and time accurate and is formulated based on a finite volume approach. Roe's formulation is used for obtaining the first order inviscid numerical fluxes and van Leer's MUSCL approach is used for obtaining higher order (third) corrections. Central differencing is used for the viscous terms and a two point backward Euler formula is used for the time derivative. The same algorithm is also used for implicitly solving the free surface kinematic condition which is cast with respect to surface curvilinear coordinates. The numerical results are compared with the experimental results. The flow conditions are $Fr = 0.2756$ and $Re = 12,020,000$. This set of parameters correspond to the so called wetted transom case which is difficult to compute. The results are quite encouraging.

1. INTRODUCTION

Fluid flow over a full scale ship involves very high Reynolds number and may involve physical phenomena such as wave breaking. So far, the approach adopted for designing a ship to operate under such conditions is mainly based on experimental data and experience. Experiments are usually conducted at a scaled down Reynolds number. On the other hand, the computational tools currently being employed in ship design use approximations that simplify the equations that represent the physical model. These techniques are robust and fast but may not be reliable. CFD techniques usually involve solving the Reynolds averaged Navier-Stokes equation which can provide more accurate and reliable solution. As a step towards using such codes in ship

design, one needs to validate them against known experimental results. Since much work needs to be done in understanding the physics of unsteady flows at very high Reynolds number and, since one may want to use the codes for conditions for which one may not be able to conduct experiments, the validation of codes against known experimental results is crucial in their acceptance as a design tool.

Numerical approaches for solving the free surface flows can be divided into two categories based upon the frame in which the governing equations are solved. Methods, such as the Marker and Cell approach (Harlow and Welch [1]) as well as the volume of fluid approach (Hirt and Nichols [2]) cast the governing equations in an inertial frame. The recently developed level set approach (Osher and Sethian [3]) also casts the governing equations in an inertial frame. Thus in all these approaches a grid that is fixed in time

$$\bar{\sigma} = \mu (\nabla \underline{u} + \nabla^T \underline{u}) \quad (2.3)$$

where, $\mu = \mu^*/\mu_0$, is the non-dimensional coefficient of viscosity. The superscript 'T' in Eq. (2.3) denotes the transpose operation.

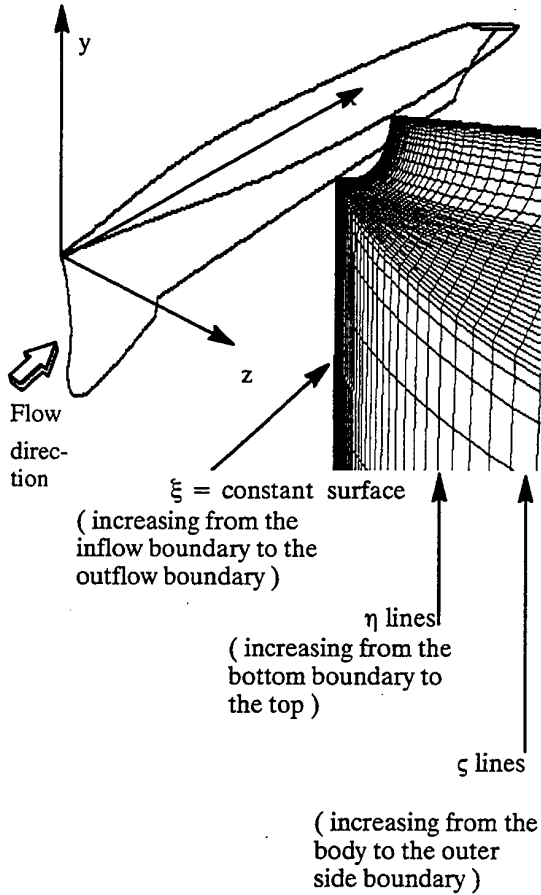


Fig. 1. Schematic illustrating the Cartesian and curvilinear coordinates chosen.

Casting the governing equations (2.1) and (2.2) with respect to a curvilinear coordinate system (ξ, η, ζ, τ) and using the so-called partial transformation in which the vectors and tensors that appear within the divergence operator are expressed with respect to the underlying Cartesian coordinates whereas the divergence operator itself is expressed in terms of the curvilinear coordinates, one can obtain the so-called numerical vector form which is as follows:

$$\frac{\partial Q}{\partial \tau} + \frac{\partial F}{\partial \xi} + \frac{\partial G}{\partial \eta} + \frac{\partial H}{\partial \zeta} + \frac{\partial F^v}{\partial \xi} + \frac{\partial G^v}{\partial \eta} + \frac{\partial H^v}{\partial \zeta} = 0 \quad (2.4)$$

where,

$$Q = \sqrt{g} \begin{bmatrix} p' \\ u \\ v \\ w \end{bmatrix} \quad F = \sqrt{g} \begin{bmatrix} \beta u^1 \\ u(u^1 + \xi_t) + p' \xi_x \\ v(u^1 + \xi_t) + p' \xi_y \\ w(u^1 + \xi_t) + p' \xi_z \end{bmatrix}$$

$$F^v = \sqrt{g} \begin{bmatrix} 0 \\ \sigma_{xx} \xi_x + \sigma_{xy} \xi_y + \sigma_{xz} \xi_z \\ \sigma_{xy} \xi_x + \sigma_{yy} \xi_y + \sigma_{yz} \xi_z \\ \sigma_{xz} \xi_x + \sigma_{yz} \xi_y + \sigma_{zz} \xi_z \end{bmatrix}$$

$$u^1 = u \xi_x + v \xi_y + w \xi_z$$

u, v , and w , are the components of the absolute velocity vector with respect to a Cartesian coordinate system, σ_{xx} , etc., are the Cartesian components of the Stokes tensor, ξ_x, ξ_y and ξ_z , are the Cartesian components of the contravariant base vector $\text{grad } \xi$. Expressions for G and H are similar to F and can be obtained from F by replacing ξ by η and ζ respectively. Similarly G^v and H^v can be obtained from F^v . Figure 1 indicates the coordinate systems chosen.

Equation (2.4) is the system of non-linear equations to be solved numerically, using a set of physical and numerical boundary conditions. The physical boundary conditions include the noslip condition ($\underline{v} = 0 \Rightarrow \underline{u} = -\underline{w}$) on the body and the kinematic and dynamic free surface boundary conditions.

The kinematic condition used in this work can be derived as follows. Assume that the free surface is represented by the function $\phi = 0$. Then the kinematic condition implies [12]

$$\frac{\partial \phi}{\partial t} + \underline{u} \cdot \nabla \phi = 0 \quad (2.5)$$

In terms of a set of *inertial* curvilinear coordinates ($\phi = \phi(\xi, \eta, \zeta, t)$), Eq. (2.5) can be written as

$$\frac{\partial \phi}{\partial t} + u^1 \frac{\partial \phi}{\partial \xi} + u^2 \frac{\partial \phi}{\partial \eta} + u^3 \frac{\partial \phi}{\partial \zeta} = 0 \quad (2.6)$$

where the contravariant velocity component u^1 is defined below Eq. (2.4) and u^2 and u^3 can be similarly defined. On the other hand, in terms of a set of *non-inertial* curvilinear

is used and the free surface is allowed to move between grid points. Thus, locating the free surface, maintaining it as a sharp discontinuity as well as imposing the boundary conditions on it, are not trivial in these approaches. On the other hand, the second approach which has been variously called moving grid approach, alternate Lagrangian-Eulerian formulation and unsteady Eulerian coordinates, uses a non-inertial frame and the free surface coincides with a grid surface exactly at all times. Thus, application of the boundary conditions on the free surface as well as tracking the free surface in time is straight forward. However, this approach involves grid regeneration at every time step which may not be feasible for all cases.

Some of the precursory works in free surface flow computations about surface ships were performed by Miyata and Nishimura [4], Kodama [5], Hino [6] and Farmer et al [7]. Recent works are that of Tahara and Stern [8] and Beddhu et al [9], [10], [11]. Tahara and Stern use a Poisson equation for pressure and use the pressure-implicit split-operator (PISO) algorithm to solve the mean flow equations and the Beam and Warming approach with artificial dissipation for solving the free surface equation. They use the so-called finite analytic method to discretize the governing equations. In addition, they use separate grids for solving the mean flow and the free surface and use interpolation for transferring data between the grids. Beddhu et al [10] use the modified artificial compressibility approach, introduced earlier in Beddhu et al [9], for the mean flow equations and use an explicit method for calculating the free surface motion. They use a finite volume, implicit scheme patterning their numerical scheme after compressible flow solvers. Thus, Roe scheme is used for obtaining first order numerical fluxes and van Leer's MUSCL approach is used to obtain third order corrections. The viscous terms are approximated using second order central differences and the time derivative is approximated using either first order or second order backward differences.

In [11], Beddhu et al use an implicit method for calculating the free surface. The method was chosen to be the same as the one used for the mean flow. In addition, a novel way of tracking the free surface in time was introduced which preserves the shape of the free surface at each time step during various grid operations. Since the geometries of actual ships are very complex such an approach is necessary for advancing the free surface along curvilinear coordinates. In essence, a background grid was used which is fixed in time. Grid points on the free surface are allowed to move along a particular family of coordinate lines, chosen a priori, of the background grid. The portion of the coordinate lines below the free surface is then used to rebuild the actual grid

at the next time level using the arclength distribution of the actual grid line at the current time level.

In the present paper a consistent formulation of the free surface kinematic boundary condition using surface curvilinear coordinates applicable to breaking waves up to the point of reentry is given from first principles. The formulation differs from other published formulations in that the curvilinear coordinates are introduced on a curved surface as opposed to a flat surface. The results presented herein supplement and complement those presented in [11].

The rest of the paper is organized as follows: In Section 2, the governing equations and boundary conditions are presented. In Section 3, numerical methods for solving the mean flow equations and the free surface kinematic condition are presented. In Section 4, the method of updating the free surface and the interior grid is presented. In Section 5, results are presented and in Section 6, conclusions are drawn.

2: GOVERNING EQUATIONS

The governing equations in this work are cast with respect to a non-inertial frame. In tensor invariant form the continuity equation in the modified artificial compressibility method (Beddhu et al [9], [10]) is given by

$$\frac{\partial p'}{\partial \tau} + \beta \operatorname{div} \underline{u} = 0 \quad (2.1)$$

where β is the artificial compressibility parameter. The momentum equation for viscous, incompressible flows in a non-inertial frame of reference, in a gravitational field, in non-dimensional, vector invariant form is given by (Beddhu et al [9], [10])

$$\frac{1}{\sqrt{g}} \frac{\partial(\sqrt{g} \underline{u})}{\partial \tau} + \nabla \cdot [\underline{v} \underline{u} + p' \underline{\tilde{I}} - \frac{1}{Re_0} \underline{\tilde{\sigma}}] = 0 \quad (2.2)$$

In Eqs. (2.1) and (2.2), $\underline{u} = \underline{u}^*/U_0$, is the non-dimensional absolute velocity vector, $\underline{v} = \underline{u} + \underline{w}$ is the non-dimensional relative velocity vector, \underline{w} is the non-dimensional grid velocity vector, $\tau = tU_0/L$, is the non-dimensional time, $\underline{\tilde{\sigma}}$, is the Stokes tensor and $p' = p + \chi/Fr^2$ where $p = (p^* - p_0)/\rho_0 U_0^2$ is the non-dimensional pressure and χ is the body force potential due to gravity. Re_0 is the Reynolds number, $Re_0 = \rho_0 U_0 L / \mu_0$, where, ρ_0 is a reference density, U_0 is a reference velocity, L is a reference length, and, μ_0 is a reference coefficient of viscosity. Fr is the Froude number given by $Fr = U_0 / \sqrt{aL}$, where, a is the acceleration due to gravity. Note that when the positive y -direction is aligned in the direction opposite to the gravity vector, one obtains $\chi = y$. A tilde over a quantity denotes that it is a tensor and an underscore denotes that it is a vector. The Stokes tensor is given by

coordinates $(\phi = \phi(\xi(t), \eta(t), \zeta(t), \tau); (\tau = t))$, Eq. (2.5) can be written as

$$\frac{\partial \phi}{\partial \tau} + (u^1 + w^1) \frac{\partial \phi}{\partial \xi} + (u^2 + w^2) \frac{\partial \phi}{\partial \eta} + (u^3 + w^3) \frac{\partial \phi}{\partial \zeta} = 0 \quad (2.7)$$

where w^1, w^2 and w^3 are the contravariant components of the grid velocity vector. Choosing $\eta = y$, Eq. (2.7) becomes

$$\frac{\partial \phi}{\partial \tau} + (u^1 + w^1) \frac{\partial \phi}{\partial \xi} + v \frac{\partial \phi}{\partial y} + (u^3 + w^3) \frac{\partial \phi}{\partial \zeta} = 0 \quad (2.8)$$

Up to this point the notion of surface curvilinear coordinates is not needed. Note that there is no restriction placed on the coordinates ξ and ζ . In general, $\xi = \xi(x, y, z, t)$ and $\zeta = \zeta(x, y, z, t)$. Now, let the surface $\phi = 0$ be represented by

$$\phi(\xi, y, \zeta, t) = y - Y(\xi, \zeta, t) = 0 \quad (2.9)$$

Substituting, Eq. (2.9) in Eq. (2.8), one obtains

$$\frac{\partial Y}{\partial \tau} + (u^1 + w^1) \frac{\partial Y}{\partial \xi} + (u^3 + w^3) \frac{\partial Y}{\partial \zeta} - v = 0 \quad (2.10)$$

In Eqs. (2.9) and (2.10) the curvilinear coordinates ξ and ζ need to be interpreted as surface curvilinear coordinates. However, ξ and ζ are still of the form $\xi = \xi(x, y, z, t)$ and $\zeta = \zeta(x, y, z, t)$. The velocity components u^1 and u^3 , and the grid velocity components w^1 and w^3 are now surface contravariant components.

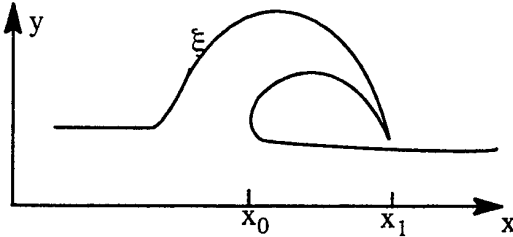


Fig. 2. Breaking wave representation.

$Y(x)$ is multi-valued for $x_0 \leq x \leq x_1$.

$Y(\xi)$ is however single-valued until reentry.

Note that Eq. (2.10) is identical in form to the one obtained by Farmer et al [7]. However, they have explicitly assumed that $\xi = \xi(x, z)$ and $\zeta = \zeta(x, z)$. The formulation introduced here is completely general and is valid as long as Y remains a single valued function of ξ and ζ . Thus, the formulation introduced here is valid for tracking breaking waves up to the point of reentry (see Fig. 2). The conceptual difference between the present formulation and that of Ref.

[7] is that Farmer et al [7] introduce the curvilinear coordinates on a flat surface (i.e. xz -plane) whereas the present formulation introduces them on the actual free surface.

Any book on differential geometry, Warsi [13] for example, can be consulted for obtaining the metrics of the surface curvilinear coordinates using which the surface contravariant velocity components used in Eq. (2.10) can be obtained. Briefly, at any point on the free surface, one can obtain the covariant base vectors

$$\underline{a}_1 = \frac{\partial \underline{r}}{\partial \xi}; \underline{a}_3 = \frac{\partial \underline{r}}{\partial \zeta} \quad (2.11)$$

where \underline{r} is the position vector. From \underline{a}_1 and \underline{a}_3 one obtains the surface contravariant base vectors \underline{a}^1 and \underline{a}^3 using standard tensor operations [13].

The surface contravariant components of the flow velocity and the grid velocity can now be obtained as follows:

$$u^1 = \underline{u} \cdot \underline{a}^1; u^3 = \underline{u} \cdot \underline{a}^3 \quad (2.12)$$

$$w^1 = -\frac{\partial \underline{r}}{\partial \tau} \cdot \underline{a}^1; w^3 = -\frac{\partial \underline{r}}{\partial \tau} \cdot \underline{a}^3 \quad (2.13)$$

Since, Eq. (2.10) is cast in terms of curvilinear coordinates, the numerical scheme for solving it can be patterned after that of Eq. (2.4).

In the absence of surface tension, continuity of the stress vector across the interface is the exact dynamic free surface boundary condition that one needs to impose. This condition was originally obtained by Hirt and Shannon [14]. An efficient way of implementing these exact conditions is outlined in Beddhu et al [15]. However, in the present study exact dynamic boundary conditions are not used. Since the external tangential stresses are neglected and only the atmospheric pressure is considered in the normal stress component and also since the grid near the free surface is not fine enough to resolve the weak surface layer, the dynamic boundary condition has been approximately implemented by many authors for computing ship related flows. For example, commonly used approximate conditions are

$$\frac{\partial u}{\partial z} = 0; \quad \frac{\partial v}{\partial z} = 0; \quad \frac{\partial w}{\partial z} = 0$$

where, z is the direction opposite to the direction of the gravity vector. In the present work, a characteristic variable based approach is used which can be outlined as follows. First, every term in Eq. (2.4) is neglected except the unsteady term and the inviscid term in the η -direction. The resultant equation is linearized and cast in a diagonal form as outlined in Taylor [16]. Thus, one obtains

$$\frac{\partial W}{\partial \tau} + \bar{\Lambda} \frac{\partial W}{\partial \eta} = 0 \quad (2.14)$$

where, $W = T_0^{-1}Q$ is the characteristic variable vector, T_0^{-1} is the left eigenvector of the flux Jacobian $\partial G/\partial Q$ and $\bar{\Lambda}$ is the diagonal matrix containing the eigenvalues of the flux Jacobian $\partial G/\partial Q$. The subscript '0' in T_0^{-1} denotes that it is treated as a constant matrix. The eigenvalues are given by

$$\left. \begin{aligned} \lambda_{1,2} &= \eta_t + u\eta_x + v\eta_y + w\eta_z \\ \lambda_3 &= u\eta_x + v\eta_y + w\eta_z + k_t/2 + c \\ \lambda_4 &= u\eta_x + v\eta_y + w\eta_z - k_t/2 - c \end{aligned} \right\} \quad (2.15)$$

where,

$$c = \sqrt{(u\eta_x + v\eta_y + w\eta_z + \eta_t/2)^2 + \beta(\eta_x^2 + \eta_y^2 + \eta_z^2)}$$

On a $\eta = \eta_{\max}$ boundary which is typically chosen as the free surface, λ_1 and λ_2 are zero, λ_3 is positive and λ_4 is negative. Thus the characteristic variable W_4 needs to be prescribed and W_3 needs to be extrapolated from within the computational domain. However, since λ_1 and λ_2 are zero one can either extrapolate or specify W_1 and W_2 . In this work, W_2 and W_3 are extrapolated from within the computational domain, and instead of prescribing W_1 and W_4 one uses the conditions $\eta_t + u\eta_x + v\eta_y + w\eta_z = 0$ and $p' = y/Fr^2$. A 3x3 matrix is solved for the velocity components at each grid point using W_2 , W_3 and the kinematic condition. Even though, this is an inviscid approximation to the exact viscous dynamic boundary condition, it works quite well for the cases considered and very good agreement has been obtained with measured wave profiles.

The numerical boundary conditions are imposed on artificial (outer) boundaries which are introduced to truncate the computational domain to a finite size so that the resulting problem can be solved using a computer. The assumption is that the artificial boundaries are far removed from the physical body that they won't affect the accuracy of the solution in the vicinity of the body. In this work the fluid flow is assumed to be along the positive x direction with the body fixed at the origin. Thus, far upstream of the body one uses a characteristic variable based inflow boundary condition and a characteristic variable based outflow boundary condition far downstream of the body. The upstream and downstream boundaries are located at least at 5 body lengths each from the origin. At the far away side boundary and the bottom boundary either characteristic variable based inflow or outflow boundary condition is used depending upon the local velocity vector. The side boundary and the bottom boundaries are located at 5 body lengths from the origin. At the $z = 0$ boundary, flow symmetry is imposed. In addition, the computational domain is subdivided into arbitrary sub-domains and at the boundaries of these domains a two point symmetry condition is used.

The following procedure is used to advance the solution from time step n to time step n+1 :

- 1) Solve for the interior of the flow field using the Discretized Newton Relaxation method.
- 2) Update the boundary conditions on the flow variables on all surfaces.
- 3) Use the kinematic condition to find the new position of the free surface.
- 4) Find the intersection of the background η lines with the updated free surface.
- 5) Recreate the volume grid from the free surface obtained in step 4.
- 6) Obtain the new metric coefficients and grid speeds.
- 7) Update the free surface dynamic boundary condition once again. This is done since the shape of the free surface has changed (in step 2 the free surface at the previous time level n was used) and is found to enhance the stability of the scheme.
- 8) go to step 1.

An integral quantity of immense practical interest is the total resistance of a ship. The total resistance is calculated using the following expression:

$$F_x = \int - \left(p' - \frac{y}{Fr^2} \right) n_x \sqrt{g} |\nabla \zeta| d\xi d\eta + \int (T_{xx}n_x + T_{xy}n_y + T_{xz}n_z) \sqrt{g} |\nabla \zeta| d\xi d\eta$$

where

$$T_{xx} = \frac{2\mu_t}{Re} u_x ; \quad T_{xy} = \frac{\mu_t}{Re} (u_y + v_x) ;$$

$$T_{xz} = \frac{\mu_t}{Re} (u_z + w_x)$$

In the actual computation, the integral is replaced by summation over all the surface grid cells. n_x is the component of the unit normal in the x direction at any point on the body. The quantity $|\nabla \zeta| d\xi d\eta$ is the surface elemental area where $|\nabla \zeta| = \sqrt{\zeta_x^2 + \zeta_y^2 + \zeta_z^2}$. Note that the body is represented by a $\zeta = \text{constant}$ surface everywhere except the transom surface which is a $\xi = \text{constant}$ surface. This fact is properly accounted for in the result presented in Fig. 16.

3: NUMERICAL PROCEDURE

The numerical scheme used in this study is similar to that proposed by Pan and Chakravarthy [17] and is discussed in detail by Taylor [16], and, Whitfield and Taylor [18]. An extensive discussion of the methodology has been

presented by Whitfield and Taylor [19] applicable to two dimensional flows. The approach taken in this work is to solve Eq (2.4) implicitly using the Discretized Newton-Relaxation (DNR) scheme of Whitfield and Taylor [18], where the fluxes at the cell faces are obtained using the Roe scheme [20] with higher order accuracy achieved using the MUSCL approach (van Leer [21]; Whitfield and Taylor [19]). Writing Eq. (2.4) in discrete form,

$$\begin{aligned} & \frac{Q^{n+1} - Q^n}{\Delta\tau} + \\ & F_{i+\frac{1}{2}}^{n+1} - F_{i-\frac{1}{2}}^{n+1} + G_{j+\frac{1}{2}}^{n+1} - G_{j-\frac{1}{2}}^{n+1} + H_{k+\frac{1}{2}}^{n+1} - H_{k-\frac{1}{2}}^{n+1} + \\ & F_{i+\frac{1}{2}}^{vn+1} - F_{i-\frac{1}{2}}^{vn+1} + G_{j+\frac{1}{2}}^{vn+1} - G_{j-\frac{1}{2}}^{vn+1} + H_{k+\frac{1}{2}}^{vn+1} - H_{k-\frac{1}{2}}^{vn+1} = 0 \end{aligned} \quad (3.1)$$

where $F_{i+\frac{1}{2}}^{n+1} = F(Q_{i-1}^{n+1}, Q_i^{n+1}, Q_{i+1}^{n+1}, Q_{i+2}^{n+1})$ and so on. Note that for a higher order flux representation $F_{i+\frac{1}{2}}^{n+1}$ depends on Q_{i-1}^{n+1} and Q_{i+2}^{n+1} as well. If Eq. (3.1) is expanded for each grid cell, a system of algebraic equations are obtained in terms of q^{n+1} at each grid cell where $q^{n+1} = Q^{n+1}/\sqrt{g^{n+1}}$. Strictly speaking F^{n+1} is a function of both q^{n+1} and the metrics at $n+1$. Since the metrics at $n+1$ are known, no linearization needs to be done with respect to the metrics. Hence Eq. (3.1) is regarded as a function of q^{n+1} alone. In functional form, Eq. (3.1) can be represented as

$$X(q^{n+1}) = 0 \quad (3.2)$$

Solving Eq. (3.2) involves finding the roots of a system of non-linear algebraic equations. Using Newton's method, the solutions of Eq. (3.2) are obtained from the following linear equations:

$$\left(\frac{\partial X}{\partial q} \right)^{n+1,m} (q^{n+1,m+1} - q^{n+1,m}) = -X(q^{n+1,m}) \quad (3.3)$$

In order to limit the band width of the matrix, the operator $(\partial X/\partial q)$ is obtained using higher order fluxes in a special manner and is rearranged along the lines of Whitfield and Taylor [19], into a strong diagonal form. The viscous flux Jacobians are obtained using the thin layer approximation whereas the residue $X(q^{n+1,m})$ contains all the viscous terms. Within each Newton iteration symmetric Gauss-Seidel passes are used. The resulting algorithm is termed the Discretized Newton-Relaxation (DNR) procedure. When the iteration in m converges, q^{n+1} is obtained

and the calculation procedure is extended to the next time level. As the iteration in m converges, the LHS of Eq (3.3) goes to zero. Hence time accuracy is introduced into the scheme by multiplying the local time derivative term in $X(q^{n+1,m})$ by a conditioning matrix I_a where $I_a = \text{diag}(0, 1, 1, 1)$. The inviscid fluxes on the RHS of Eq (3.3) are obtained using a third order MUSCL-type flux and the viscous fluxes using a second order central differencing.

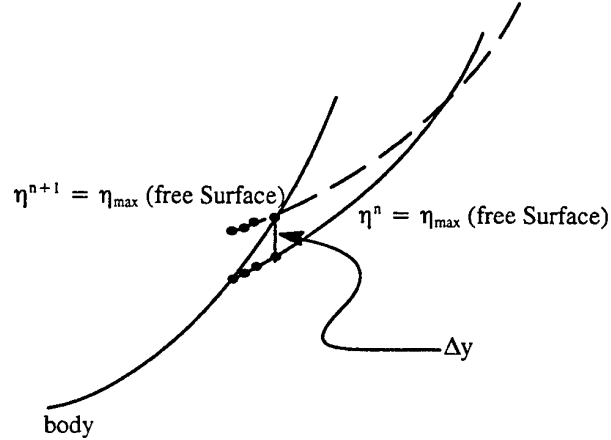


Fig. 3. Schematic illustrating the need for the intersection approach near the body

4. FREE SURFACE UPDATE AND GRID REGENERATION

The present approach utilizes an initial grid that has a flat free surface. It has been sub-divided into several sub-domains or blocks. Blocks that have the free surface as a boundary are called free surface blocks and the rest are bottom blocks. By extending the free surface blocks well above the flat free surface (or the $y = 0$ plane) the so-called background grid is constructed. Thus part of the background grid is below the free surface and part of it is above the free surface. The only purpose of the background grid is to help in the grid regeneration process once the free surface is allowed to evolve.

At each time step the free surface kinematic condition is solved to find the incremental ΔY that needs to be applied at each point on the free surface and then the free surface is updated as mentioned in the previous section. A smoothing technique as mentioned in Beddhu et al [10] is used to smooth the newly updated free surface. This method is originally due to Miyata et al [22]. In general, grid points on the new free surface will not lie on the η lines of the back-

ground grid. This is because the η lines of the background grid need not be aligned along the y -direction. Since, the grid regeneration process expects the free surface points to be on the background η lines one needs to find the intersection of the background η lines with the current free surface. Another motivation for using the intersection approach comes from the following observation. In Fig. 3, assume that the free surface at two consecutive time steps are as shown. Also, assume that the shape of the body is as shown. Since, the free surface points are moved by applying the corresponding ΔY , the point at the intersection of the free surface and the body has moved inside the body after an increment in time. Thus, in order to find the correct point of intersection of the free surface with the body at the new time level one has to resort to techniques that are similar to the one described below.

A grid point on the free surface has two curvilinear coordinate values i and k corresponding to ξ and ζ respectively. Initially, the background η line through that point has the same i and k values. After an increment in time the Y value of the grid point changes and it may no longer lie on the background η line through (i, k) . In order to find the intersection of the background η line through (i, k) with the free surface, a search algorithm is used such that one finds the line segment between consecutive points (i, j_c, k) and $(i, j_c + 1, k)$ on the background η line that intersects the new free surface at the quadrilateral (i_s, j_0, k_s) , $(i_s + 1, j_0, k_s)$, $(i_s + 1, j_0, k_s + 1)$ and $(i_s, j_0, k_s + 1)$ where j_0 is the η value of the free surface. The position vector \underline{r}^c of an intermediate point on the line segment is given by

$$\underline{r}^c(t_2) = \underline{r}_c + t_2 (\underline{r}_{c+1} - \underline{r}_c) \quad (4.1)$$

where \underline{r}_c is the position vector of the point (i, j_c, k) , \underline{r}_{c+1} is the position vector of the point $(i, j_c + 1, k)$ and t_2 is a parameter $(0 \leq t_2 \leq 1)$. Using bilinear interpolation or the so-called tensor product form (Thompson et al [23]), the position vector \underline{r}^s of an interior point within the above quadrilateral is given by

$$\begin{aligned} \underline{r}^s(t_1, t_3) = & (1 - t_1)(1 - t_3) \underline{r}(i_s, j_0, k_s) \\ & + t_1(1 - t_3) \underline{r}(i_s + 1, j_0, k_s) \end{aligned}$$

$$\begin{aligned} & + (1 - t_1) t_3 \underline{r}(i_s + 1, j_0, k_s + 1) \\ & + t_1 t_3 \underline{r}(i_s, j_0, k_s + 1) \end{aligned} \quad (4.2)$$

where t_1 and t_3 are two parameters such that $(0 \leq t_1, t_3 \leq 1)$. At the point of intersection, one has,

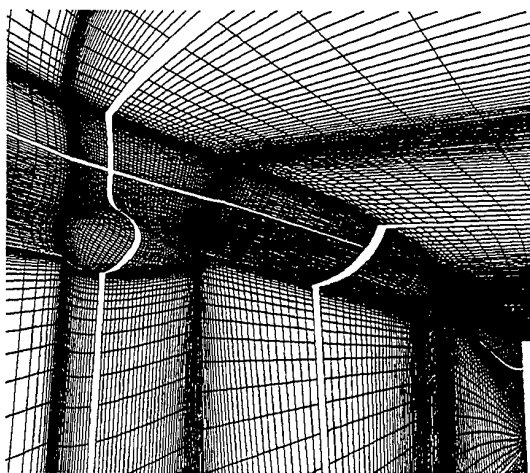
$$N(\underline{t}) \equiv \underline{r}^s(t_1, t_3) - \underline{r}^c(t_2) = 0 \quad (4.3)$$

where $\underline{t} = (t_1, t_2, t_3)$. Equation (4.3) is solved using Newton's method as described in the previous section. Suppose, the value of one or more parameters exceeds the upper or lower limits then the Newton's algorithm is continued in an adjacent quadrilateral or line segment indicated by that parameter until the convergence criterion is met. Thus, if t_3 exceeds 1 then k_s is incremented by one and Newton's iteration is continued in that quadrilateral.

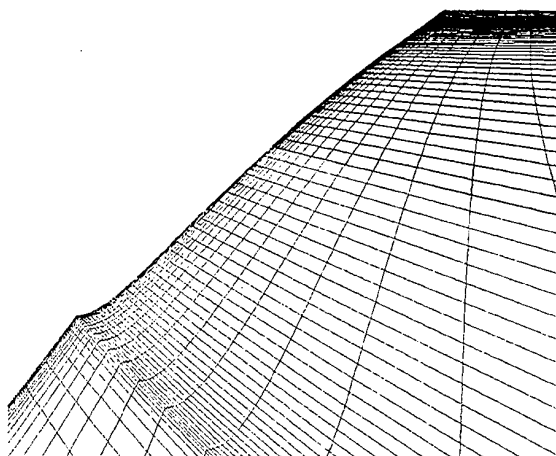
The purpose of the search algorithm is to provide a good initial guess for the Newton's algorithm. This is especially true for points near the body and in particular in the vicinity of the bow. This is because the bow wave has a large gradient and rises sharply. Thus, the angle between the quadrilaterals on the free surface and the η lines of the background grid can become very small. In such regions, if a good initial guess is not provided then the Newton's algorithm may not converge.

Since the time step $\Delta\tau$ is small, the increment ΔY would also be small and hence the new Y value of the point (i, k) would be in the neighborhood of the old value. Hence the search is limited on the free surface to a patch of ± 5 points on either side of (i, k) . However, the entire background η line is included in the search. Through consecutive points on the η line, straight lines are constructed. This means that in Eq. (4.1) the parameter t_2 is allowed to take all possible values. On the free surface, on every quadrilateral the point $(i_s + 1, j_0, k_s + 1)$ is ignored and through the remaining three points a plane is constructed. The point of intersection of a straight line with a plane is straight forward to obtain. Then, it is checked to find whether the x and z values of each of the intersection points lie within the rectangle constructed by using the minimum and maximum x and z values of the vertices of the corresponding quadrilateral. By the way the background grid is constructed such a point always exists. Once that point is found, its normalized projections on the line segments $\underline{r}(i_s, j_0, k_s) \underline{r}(i_s + 1, j_0, k_s)$,

and $\bar{\Gamma}(i_s, j_0, k_s) \bar{\Gamma}(i_s, j_0, k_s + 1)$ are used as the initial values for t_1 and t_3 .



Bow region



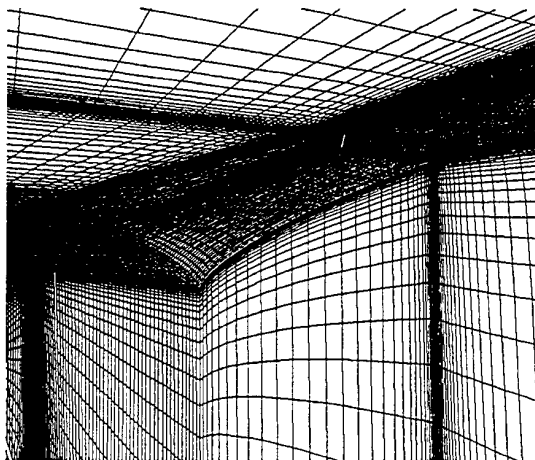
Bow region – Free surface

Fig 4. DTMB 5415 – Bow Region

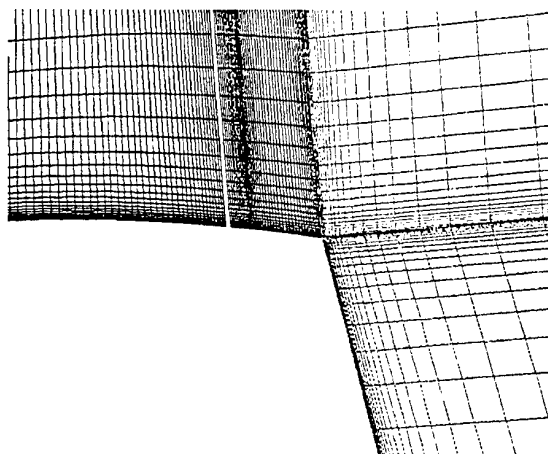
In the vicinity of the bow wave and in the blocks behind the transom the following procedure is found to be more stable. Instead of finding the intersection of the background η line with the free surface, one can alternately find the intersection of the ξ lines on the free surface with the $\xi = \text{constant}$ surfaces of the background grid. Thus, one obtains a curve that lies on the $\xi = \text{constant}$ surface. Then, in order to distribute points on this curve in the ζ direction one computes the intersection of the η lines on the $\xi = \text{constant}$ surface with it.

Once the points of intersection are found for all the i and k values, then the process of grid regeneration is quite simple. One uses a simple arclength redistribution method that preserves the normalized arclength of the original rigid lid grid.

5. RESULTS



Stern region



Stern region – Free surface

Fig 5. DTMB 5415 – Stern Region

The code UNCLE incorporates the method presented in Sections 3 and 4 and has been used to compute the flow field over a variety of geometries. Results for Wigley hull can be found in [10] and for Series 60 $C_B = 0.6$ hull can be found in [24]. In the present paper it is used to compute the flow field around DTMB Model 5415 which has a sonar dome and a transom stern. Two sets of experiments corresponding to Froude numbers of 0.2756 and 0.4136 respec-

tively were conducted for this model in a towing basin at DTMB (David Taylor Model Basin at Carderock, MD). The experimental Reynolds number based on model length is 12.02 million for the $Fr = 0.2756$ case. The case corresponding to $Fr = 0.2756$ is supposed to be computationally more challenging since it involves a wetted transom as opposed to the $Fr = 0.4143$ case which has a dry transom. The geometry file for the model was provided by DTMB.

The grid consists of twenty-six blocks with ten free surface blocks. Two of the free surface blocks are behind the transom. The spacing off the wall for this grid was chosen to be $1. \times 10^{-5}$. This spacing yields a minimum y^+ value of 0.3 off the solid surface. The upstream boundary was placed at $x=-5.0$ and the downstream boundary was placed at $x=6.0$. The lateral and bottom boundaries were placed at locations corresponding to the model basin dimensions. Thus the bottom boundary was placed at $y=-1.2$ and the side boundary is placed at $z=1.36$. The grid structure is shown in Figs. 4 and 5.

Figure 6 shows a comparison of the computed

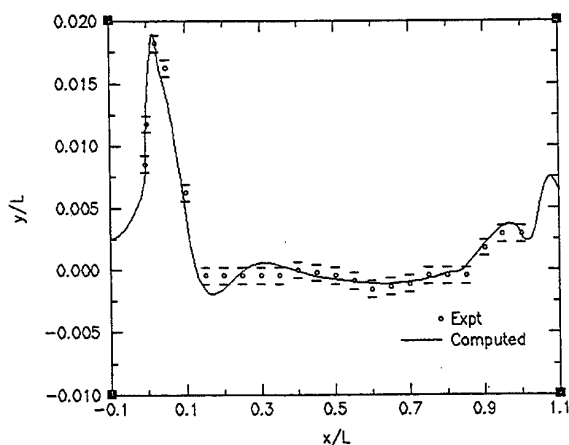


Fig. 6. Comparison of experimental and computed hull profiles (first grid)

wave profile along the hull with the experimental wave profile. An error bar of ± 0.1 inches was added to the experimental profile by DTMB. It can be seen that the computed profile mostly falls within the error bars. An important flow feature of free surface flows is the Kelvin wave like structure. A comparison between the experimental and computed wave structures is shown in Fig. 7 for the first grid. Again the agreement seems to be reasonable.

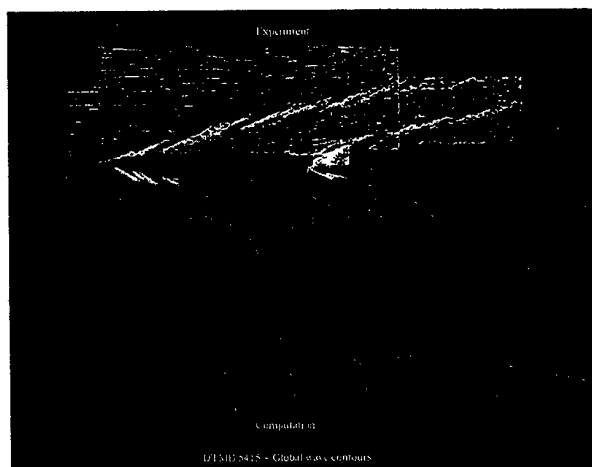


Fig. 7. Comparison of experimental and computed wave contours

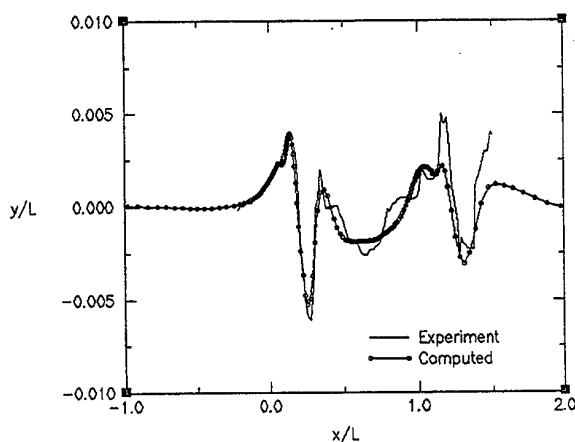


Fig. 8. Comparison of experimental and computed longitudinal wavecuts at $z = 0.108$

A comparison of this longitudinal wavecut with the computed wavecut is presented in Fig. 8 which shows reasonable agreement with the experimental results.

In Fig. 9, comparisons of experimental and computed wavecuts in the transverse direction at various x locations in the bow region are presented. In each row of these figures the scale for the vertical axis is the same as the left-most figure. From these transverse wavecuts, it can be seen that the agreement between experiment and computation is quite good.

In the next set of figures, detailed comparisons are shown in the stern region which is shown in Fig. 10. First is a comparison of the wave contours shown in Fig. 11. Next is a set of detailed comparisons at various transverse locations

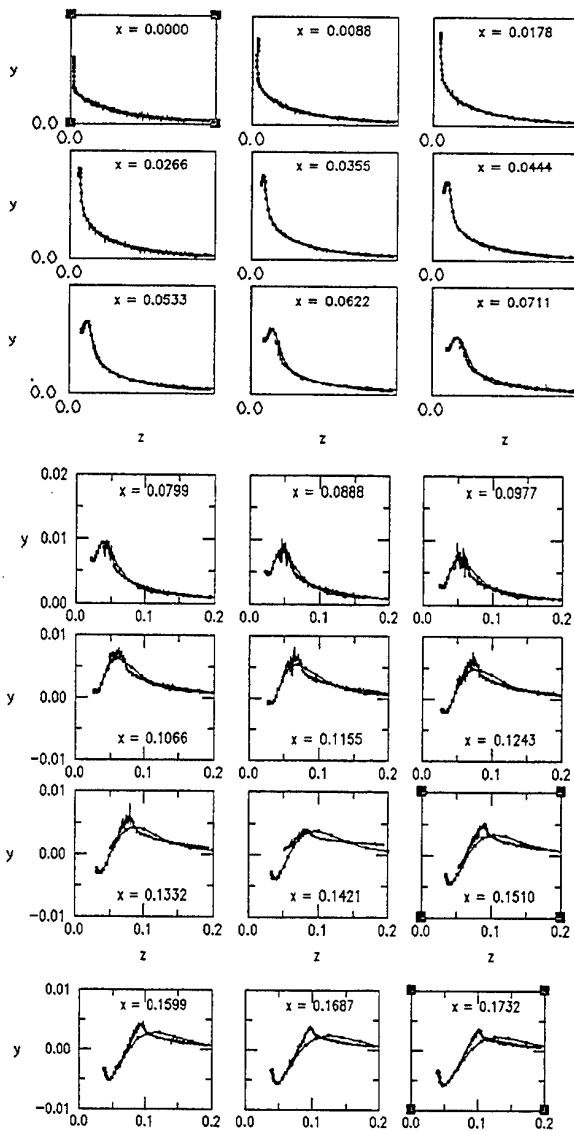


Fig. 9. Comparison of experimental and computed transverse wavecuts near the bow

from $x = 1.025$ to $x = 1.22$ shown in Fig. 12. Dimensional values are used in this figure. It can be seen from these figures that the comparison is quite reasonable given the difficulties associated with tracking the free surface and generating a volume grid in the stern region.

So far, detailed comparisons of the free surface computations with the experimental data have been shown. In the next set of figures computed velocity field is compared with the measured velocity field. In the experiments, the velocity field was measured at the propeller plane which is of immense interest. The propeller itself was not included in

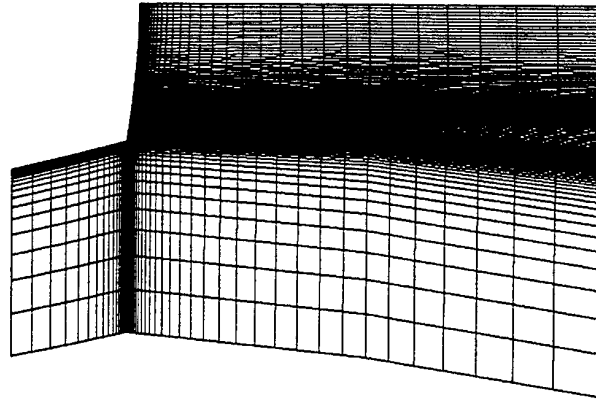


Fig. 10. DTMB Model 5415 - Initial Free Surface Grid (Transom Region)
 $0.95 \leq x \leq 1.2$; $0.0 \leq y \leq 0.1$

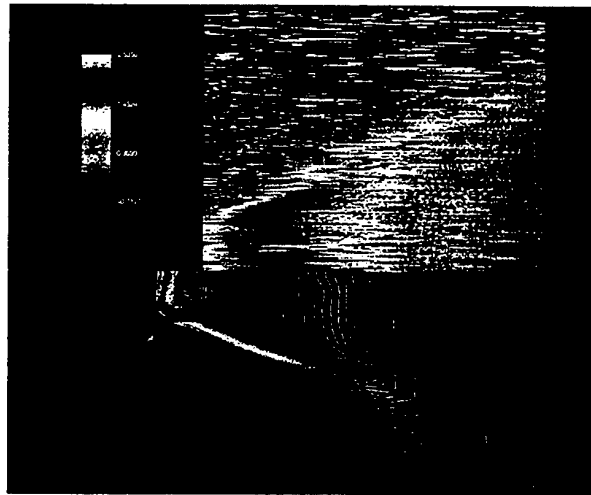


Fig. 11. Comparison of experimental and computed stern wave contours

these measurements. A comparison of the contours of the u component of velocity is shown in Figs. 13. Comparison of the contours of cross plane velocity magnitude is shown in Fig. 14 and that of cross plane velocity vectors is shown in Fig. 15. These comparisons show that the flow field has been computed quite reasonably and that the two equation turbulence model chosen does a reasonably good job in predicting the mean flow.

Finally, in Fig 16 the comparison of experimental and computed total resistance is shown. The comparison is quite good.

CONCLUSION

As mentioned in the introduction, a necessary condition for an unRANS code to be considered for design ap-

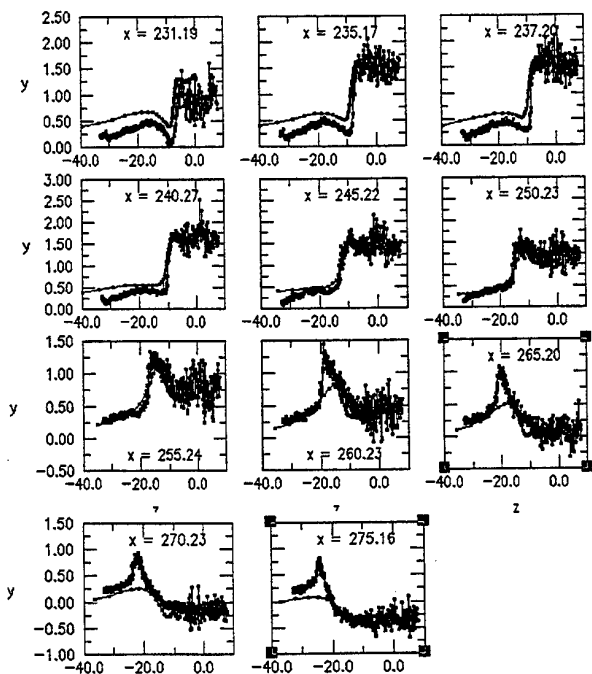


Fig. 12. Comparison of experimental and computed transverse stern wave contours

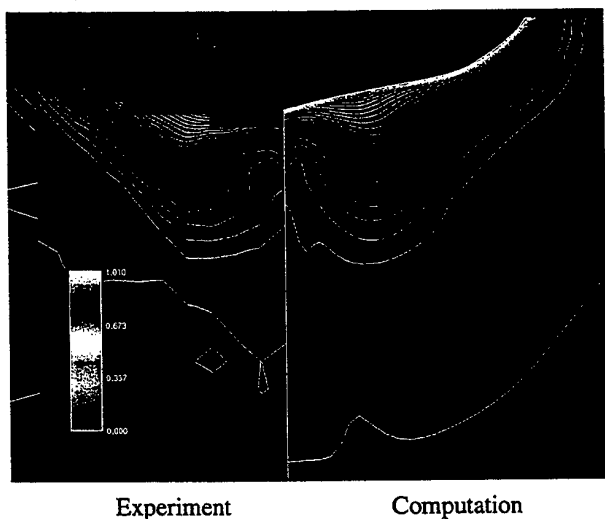


Fig. 13. Comparison of experimental and computed u component of velocity on the $x = 0.935$ plane.

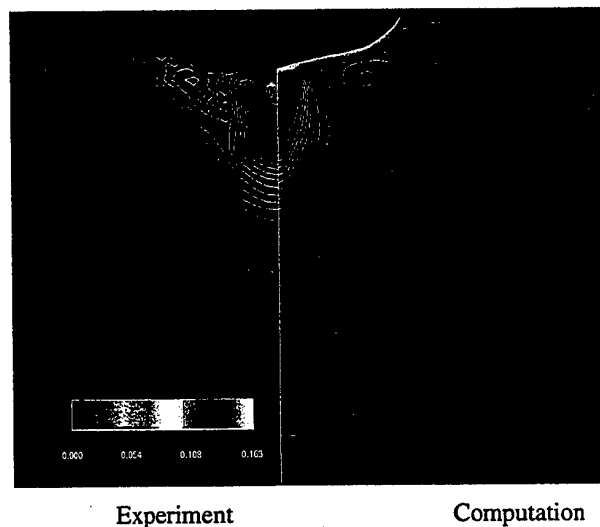


Fig. 14. Comparison of experimental and computed cross plane velocity magnitude contours on the $x = 0.935$ plane.

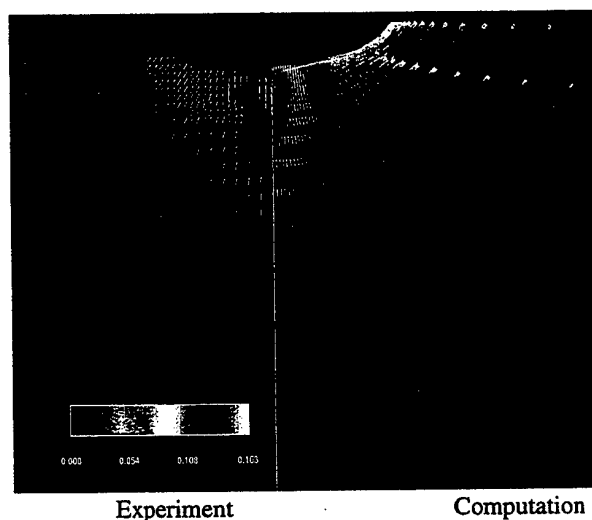


Fig. 15. Comparison of experimental and computed cross plane velocity vectors on the $x = 0.935$ plane.

plications is that it reproduce known experimental results with reasonable accuracy. Series 60 $C_B = 0.6$ and Model 5415 are two important geometries which have been studied extensively using experiments. In [24] the UNCLE solver has been shown to reproduce the flow field around Series 60 $C_B = 0.6$ at the Froude number of 0.316 fairly accurately when compared against the experimental results obtained at

University of Iowa. In the current work, the UNCLE solver is shown to reproduce the experimental results of Model 5415 fairly accurately for the wetted transom case. Currently, efforts are underway to validate the UNCLE solver against other available experimental results. Efforts are also underway to make the free surface algorithm more robust and to parallelize the solver. These will be reported in the future.

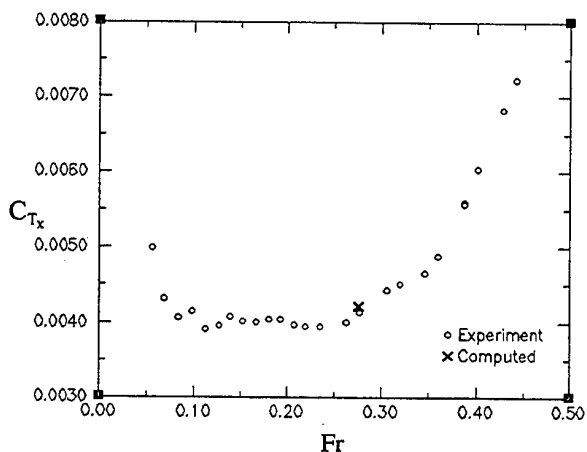


Fig. 16. Experimental and Computed Total Resistance vs Froude Number

ACKNOWLEDGEMENTS

This work was supported by grant N00014-97-1-0959 from the Office of Naval Research. The grant monitor is Dr. Edwin Rood. This support is greatly appreciated.

REFERENCES

1. Harlow, F. H. and Welch, J. E. "Numerical Calculation of Time-Dependent Viscous Incompressible Flow of Fluid with Free Surface," *Physics of Fluids*, Vol. 8, 1965, pp. 2182-2189.
2. Hirt, C. W. and Nichols, B. D., "Volume of Fluid (VOF) Method for the Dynamics of Free Boundaries," *Journal of Computational Physics*, Vol. 39, 1981, pp. 201-225.
3. Osher, S. and Sethian, J. A., "Front Propagation with Curvature-Dependent Speed: Algorithms Based on Hamilton-Jacobi Formulations," *Journal of Computational Physics*, Vol. 79, 1988, pp. 12-49.
4. Miyata, H. and Nishimura, S., "Finite Difference Simulation of Nonlinear Ship Waves," *Journal of Fluid Mechanics*, Vol. 157, 1985, pp. 327-357.
5. Kodama, Y., "Grid Generation and Flow Computation for Practical Ship Hull forms and Propellers Using the Geometrical Method and the IAF Scheme," *Proceedings, Fifth International Conference on Numerical Ship Hydrodynamics*, 1989, pp. 71-85.
6. Hino, T., "Computation of Free Surface Flow Around an Advancing Ship by the Navier-Stokes Equations," In *Proceedings, Fifth International Conference on Numerical Ship Hydrodynamics*, 1989, pp. 103-117.
7. Farmer, J., Martinelli L., and Jameson A., "A Fast Multi-grid Method for Solving Incompressible Hydrodynamic Problems With Free Surfaces," *AIAA Journal*, Vol. 32, No. 6, 1993, pp. 1175-1182.
8. Tahara, Y., and Stern, F. "A Large-Domain Approach for Calculating Ship Boundary Layers and Wakes and Wave Fields for Nonzero Froude Number," *Journal of Computational Physics*, Vol. 127, 1996, pp. 398-411.
9. Beddhu, M., Taylor, L. K. and Whitfield, D. L., "A Time Accurate Calculation Procedure for Flows with a Free Surface Using a Modified Artificial Compressibility Formulation," *Applied Mathematics and Computation*, Vol. 65, 1994, pp. 33-48.
10. Beddhu, M., Jiang, M. Y., Taylor, L. K. and Whitfield, D. L., "Computation of Steady and Unsteady Flows with a Free Surface Around the Wigley Hull," *Applied Mathematics and Computation*, Vol. 89, 1998, pp. 67-84.
11. Beddhu, M., Jiang, M. Y., Whitfield, D. L. Taylor, L. K. and Arabshahi, A., "CFD Validation of the Free Surface Flow Around DTMB Model 5415 Using Reynolds Averaged Navier-Stokes Equations," *Proceedings, Third Osaka Colloquium on Advanced CFD applications to Ship Flow and Hull Form Design*, Osaka, Japan, May 25-27, 1998.
12. Warsi, Z. U. A., "Fluid Dynamics: Theoretical and Computational Approaches," 1st. ed., CRC Press, Boca Raton, 1993, p.10
13. Warsi, Z. U. A., "Ruminations on Applied Tensor Analysis," MSSU-EIRS-ASE-98-1, Oct. 1998, Mississippi State, MS 39762, p.78.
14. Hirt, C. W. and Shannon, J. P., "Free-Surface Stress Conditions for Incompressible-Flow Calculations," *Journal of Computational Physics*, Vol. 2, 1968, pp. 403-411.
15. Beddhu, M., Jiang, M. Y., Whitfield, D. L, Taylor, L. K., and Arabshahi, A. "Computational Physical Oceanography - A Comprehensive Approach based on Generalized CFD/Grid Techniques for Planetary Scale Simulations of Oceanic Flows," MSSU-EIRS-ERC-97-5, Mississippi State, MS 39762, Feb., 1997.
16. Taylor, L. K. "Unsteady Three - Dimensional Incompressible Algorithm Based on Artificial Compressibility," Ph. D. Dissertation, Department of Aerospace Engineering, Mississippi State University, Mississippi State, May 1991.

17. Pan, D. and Chakravarthy, S., "Unified Formulation for Incompressible Flows," AIAA-89-0122, Jan., 1989.
18. Whitfield, D. L. and Taylor, L. K., "Discretized Newton-Relaxation Solution of High Resolution Flux-Difference Split Schemes," AIAA-91-1539, June 1991.
19. Whitfield, D. L. and Taylor, L. K., "Numerical Solution of the Two-Dimensional Time-Dependent Incompressible Euler Equations," MSSU-EIRS-ERC-93-14, Mississippi State University, Mississippi MS 39762 April, 1994.
20. Roe, P. L., "Approximate Riemann Solvers, Parameter Vectors, and Difference Schemes," Journal of Computational Physics, Vol. 43, 1981, pp. 357-372.
21. van Leer, B., "Towards the Ultimate Conservation Difference Scheme V, A Second Order Sequel to Guderlin's Method," Journal of Computational Physics, Vol. 32, 1979, pp. 101-136.
22. Miyata, H., Sato, T., and Baba, T., "Difference Solution of a Viscous Flow with Free-Surface Wave about an Advancing Ship," Journal of Computational Physics, Vol. 72, 1987, pp. 393-421.
23. Thompson, J. F., Warsi, Z. U. A., and Mastin, C. W., "Numerical Grid Generation - Foundation and Applications", North Holland, New York 1986.
24. M. Beddhu, S. Nichols, M. Y. Jiang, C. Sheng, D. L. Whitfield and L. K. Taylor, "Comparison of EFD and CFD Results of the Free Surface Flow Field about the Series 60 $C_B = 0.6$ Ship," Proceedings of the Twenty-Fifth American Towing Tank Conference, Iowa City, IA, September 24-25, 1998.

3D RANSE-POTENTIAL COUPLING USING A FOURIER-KOTCHIN APPROACH

Pierre-Emmanuel GUILLERM and Bertrand ALESSANDRINI
Division Hydrodynamique Navale, Laboratoire de Mécanique des Fluides,
Ecole Centrale de Nantes, 1 rue de la Noë, 44321 Nantes Cedex 03, France

ABSTRACT

This paper presents a coupling method for the numerical simulation of steady free-surface flow past ship hull. The fluid domain in the neighbourhood of the hull is divided in two overlapping zones. Reynolds Averaged Navier-Stokes Equations (RANSE) are solved near the ship hull with a fully coupled method for the velocities, pressure and free surface elevations discrete unknowns [1]. In the external domain potential flow theory with linearized free-surface conditions is used to provide boundary condition for the RANSE solver and to calculate free-surface wave pattern. The Fourier-Kotchin method [2][3] (based on the Fourier-Kotchin formulation), which defines the velocity field in a potential flow region in terms of the velocity distribution at a boundary surface is used for that purpose. Numerical simulations are presented on serie 60 CB=0.6 hull, for two different Froude numbers and mesh refinements.

INTRODUCTION

The main features of the flow around ship hull are the existence of a three dimensional turbulent boundary layer, the presence of a free-surface wave pattern and its interaction with the boundary layer and the wake. The viscous and wave effects can be calculated using Reynolds averaged Navier-Stokes equations (RANSE) with appropriate free-surface boundary conditions. However this computation requires a large number of grid nodes and amount of CPU time to achieve resolution of the entire flow field. Moreover the solution is perturbed by the decreasing concentration of nodes away from the hull. Since viscous effects are confined to a small region surrounding the hull and the wake, a zonal approach which combines viscous flow near the hull and inviscid theories away from the ship can therefore be an effective method to solve ship free-surface problems.

This solution was already used by Tahara and Stern for a Wigley hull [4]. The RANSE method was coupled with a source doublet Dawson method. A displacement-body concept was used to account for viscous effects in the potential calculation, but this method can not be used in the presence of flow separation. Campana et al. [5] discretized the RANSE by a finite volume method in the neighbourhood of the hull and used the linearized model of Dawson in the inviscid domain.

The external flow is splitting in a double model flow and a perturbation term. So they first compute an iterative RANSE/potential double-body solution, then the free-surface flow is computed. This solution is consistent with the potential formulation, but requires iterating RANSE and potential calculations twice; first the double-body calculation and then with the free-surface effects accounted for. Moreover only the normal component of the velocity on the matching surface is computed from the viscous flow solution, then used as Neumann condition for the potential flow problem. Chen et al. [6] use the same solution, but they iterate with the complete (with free surface) RANSE and potential solutions from the beginning, using the complete RANSE velocity on the matching surface as boundary condition for the double-body and free surface potential calculations. This procedure requires only one iterating calculation, but velocities used as boundary condition for the double-body calculation are no longer "double-body" velocities.

In the present paper steady free-surface flow past ship hull are studied. RANSE are solved by a fully coupled velocity, pressure and free-surface elevation method in the internal domain. In the external domain the Fourier-Kotchin method [2][3] (based on the Fourier-Kotchin formulation), which defines the velocity field in a potential flows region in terms of the velocity distribution at a boundary surface, is used.

The great advantage of this method is that the three components of the velocity on the boundary surface are used to provide the fluid characteristics in the potential domain. So this method seems to be well suited to make the coupling successful. The fluid domain is divided in two overlapping zones. In the inner domain, RANSE and continuity equation are written through partial transformation from cartesian space (x^i) to curvilinear space (ξ^i) fitted to the hull and the free-surface at each time. General discretization method is based on second order (in space and time) implicit finite differences. The fully coupled system is solved by iterative algorithm using matrix preconditionning. The fluid domain is then re-gridded using the new free-surface wave pattern. In the potential flow domain, the Fourier-Kotchin formulation of Green function satisfying this linearized free-surface condition is used to provide boundary condition for the RANSE calculation. The velocity components on S^i are computed from the viscous flow solution (figure 1), and used as velocity distribution at the boundary surface of the inviscid domain. Potential calculation provide wave field pattern in the outer region and velocities and pressure on the viscous boundary surface S^o .

In the following sections, the viscous and inviscid solver are described and some numerical examples are discussed and compared with experimental data and with fully viscous calculations.

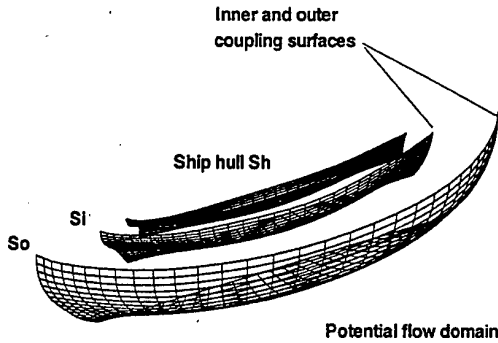


Figure 1: sketch of the coupling surfaces

RANSE SOLVER

Governing equations

The convective form of Reynolds Averaged Navier-Stokes Equations are written through partial transformation from cartesian space (x^1, x^2, x^3) to curvilinear

space (ξ^1, ξ^2, ξ^3) fitted to the hull and the free surface at each iteration. Free surface elevation, the three cartesian velocity components (u^i), pressure (p) including gravitational effects ($\rho g x^3$) and turbulent kinetic energy ($2/3 \rho k$) are the dependant unknowns.

Mean momentum transport equations are written in a moving referential attached to the hull :

$$u_{,t}^\alpha + \left(a_i^j (u^i - u_g^i) - \nu_{eff} f^j - a_k^i \nu_{t,i} a_k^j \right) u_{,j}^\alpha + \frac{1}{\rho} a_\alpha^k p_{,k} - \nu_{eff} g^{ij} u_{,ij}^\alpha - a_k^i \nu_{t,i} a_j^\alpha u_{,j}^k + q_i = 0 \quad (1)$$

Where (a^i) is the contravariant basis, (g^{ij}) the contravariant metric tensor, (f^i) the control grid functions and (u_g^i) the grid velocity which traduces the displacement of the mesh. Inertia forces due to non galilean referential (rotating motion, accelerated translation) are taking into account in the (q_i) terms. In translation case (with or without drift angle) inertia forces are expressed as follows where U_a is the hull velocity :

$$\begin{cases} q^1 = q_d^1 = U_{a,t} \cos(\theta) \\ q^2 = q_d^2 = U_{a,t} \sin(\theta) \\ q^3 = q_d^3 = 0 \end{cases} \quad (2)$$

Mass conservation is expressed as the classical continuity equation :

$$a_i^j u_{,j}^i = 0 \quad (3)$$

To close the equation set we use a classical $k - \omega$ model proposed by Wilcox [7][8][9], introducing a specific dissipation rate ω without low Reynolds formulation requirement. Transport equation of turbulent kinetic energy and dissipation rate are written as follows :

$$\left(a_i^j (u^i - u_g^i) - (\nu + \sigma^* \nu_t) f^j - a_k^i \sigma^* \nu_{t,i} a_k^j \right) k_{,j} - (\nu + \sigma^* \nu_t) g^{ij} k_{,ij} - Pr + \beta^* \omega k + k_{,t} = 0 \quad (4)$$

$$\left(a_i^j (u^i - u_g^i) - (\nu + \sigma \nu_t) f^j - a_k^i \sigma \nu_{t,i} a_k^j \right) \omega_{,j} - (\nu + \sigma \nu_t) g^{ij} \omega_{,ij} - \gamma \omega Pr/k + \beta \omega^2 + \omega_{,t} = 0 \quad (5)$$

with :

$$\nu_t = \gamma^* \frac{k}{\omega} \quad (6)$$

and :

$$\begin{cases} \beta = 3/40; \sigma = 0.5; \gamma = 5/9 \\ \beta^* = 0.09; \sigma^* = 0.5; \gamma^* = 1 \end{cases} \quad (7)$$

Free surface conditions

Free surface boundary conditions are one kinematic condition, two tangential dynamic conditions and one normal dynamic condition. The kinematic condition, coming from the continuity hypothesis, expresses that the fluid particles of the free surface stay on it :

$$h_{,t} + \left(b_i^j (u^i - u_g^i) h_{,j} \right)_{(i,j) \in \{1,2\}} - u^3 = 0 \quad (8)$$

where b^i are the bi-dimensional contravariant basis.

Dynamic conditions are given by the continuity of strains at the free surface. If the pressure is assumed to be constant above free surface, normal dynamic condition is :

$$p - \rho gh - 2 \frac{\rho \nu_{eff}}{|a^3|^2} a_i^3 a_j^3 a_j^k u_{,k} - \frac{\gamma}{r} = 0 \quad (9)$$

where γ is the superficial tension coefficient (that is a physical way to smooth free surface near the hull) and r the free surface medium curvature radius. Tangential dynamic conditions are simply given by a linear combination of first order velocities derivatives :

$$a_{\alpha i} g^{j3} u_{,i}^j = 0 \quad (10)$$

Discretization

General discretization is based on second order (in space and time) implicit finite differences. Discrete unknowns are distributed on a structured curvilinear grid fitted to the hull and the free surface. Velocity cartesian components, kinetic turbulent energy, and specific dissipation rate are located on the grid nodes. Pressure is located on the center of each elementary volume and free surface elevation is located on the center of free surface interfaces.

Convection terms are computed using an upwind second order scheme that needs a 13 nodes cell. Diffusion terms need 7 nodes for second order derivatives and 12 nodes to express cross second order derivatives (equation 1) while pressure gradient requires 8 nodes for each component [1][10].

Concerning free surface calculation, it has been shown that classical way using normal dynamic condition as Dirichlet condition on the pressure and uncoupled kinematic equation as transport equation to compute free surface elevation induces some problems connected to difficulties to exactly solve mass conservation under free surface [1]. Efficient solution consists in using fully coupled algorithm [1] that requires at each iteration the linear solution of mean

momentum equations, continuity equation and whole boundary conditions including free surface condition.

$$\begin{pmatrix} M_{11} & M_{12} & M_{13} & M_{14} \\ M_{21} & M_{22} & 0 & 0 \\ 0 & M_{32} & M_{33} & 0 \\ 0 & 0 & M_{43} & M_{44} \end{pmatrix} \begin{pmatrix} U \\ \tilde{U} \\ P \\ H \end{pmatrix} = \begin{pmatrix} fu \\ f\tilde{u} \\ fp \\ fh \end{pmatrix} \quad (11)$$

Unfortunately the most efficient iterative algorithms (CGSTAB+ILU, Multigrid) are unable to invert this system because of the very bad matrix conditioning of pressure block M_{33} . The solution consists in modifying the system using free-surface boundary conditions to express the flux through free surface. In this case, conditioning number decreases and fully coupled system becomes invertible by iterative algorithms. Resulting linear system for velocity (U) and pseudo velocity (\tilde{U}) components, pressure (P) and free surface elevation (H) is written as follows :

$$\begin{pmatrix} M_{11} & M_{12} & M_{13} & 0 \\ M_{21} & M_{22} & 0 & 0 \\ 0 & M_{32} & M_{33} & 0 \\ 0 & 0 & M_{43} & M_{44} \end{pmatrix} \begin{pmatrix} U \\ \tilde{U} \\ P \\ H \end{pmatrix} = \begin{pmatrix} fu \\ f\tilde{u} \\ fp \\ fh \end{pmatrix} \quad (12)$$

POTENTIAL SOLVER

General formulation

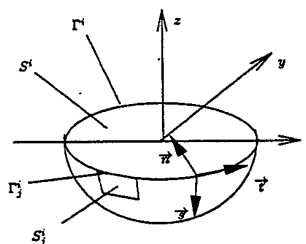


Figure 2: sketch of the potential region

We consider a ship advancing at constant speed along a straight path in water of effectively infinite depth and lateral extent. Steady waves are analysed within the classical linear potential-flow theory, based on a free-surface boundary condition linearized about

the uniform stream opposing the forward speed of the ship. Moreover the free-surface Green function satisfying this linearized free-surface condition is used. Non dimensional coordinates $\vec{x} = (x, y, z)$, time t , velocity potential ϕ and related flow variables are defined with respect to the ship length L , the acceleration of gravity g , and the density of water ρ as basic reference units. The flow is observed from a moving system of coordinates (x, y, z) in steady translation with the mean forward speed U of the ship. The Froude number is defined as $F = U/\sqrt{gL}$. The x axis is along the path of the ship and points toward the bow. The z axis is vertical and points upward, and the undisturbed free surface is taken as the plane $z = 0$.

The velocity potential satisfies the linear free-surface boundary condition

$$[F^2 \partial_x^2 + \partial_z] \phi = 0 \quad (13)$$

The Green function G , associated with the boundary condition (13), is expressed as the sum of a Rankine term and a free-surface component:

$$G = G^S + G^F \quad (14)$$

G^S is defined as:

$$4\pi G^S = -\frac{1}{R} + \frac{1}{R'} \quad (15)$$

with:

$$\begin{cases} R = \sqrt{(x-\xi)^2 + (y-\eta)^2 + (z-\zeta)^2} \\ R' = \sqrt{(x-\xi)^2 + (y-\eta)^2 + (z+\zeta)^2} \end{cases}$$

G^F is given by the Fourier superposition of elementary waves:

$$4\pi^2 G^F = \lim_{\epsilon \rightarrow 0^+} \int_{-\infty}^{+\infty} \int_{-\infty}^{+\infty} \frac{e^{Z.k - i.(X.\alpha + Y.\beta)} . d\alpha . d\beta}{F^2 . \alpha^2 - k - i.\epsilon . \text{sign}(\alpha)} \quad (16)$$

with:

$$k = \sqrt{\alpha^2 + \beta^2}$$

$$(X, Y, Z \leq 0) = (\xi - x, \eta - y, \zeta + z)$$

$(x, y, z \leq 0)$ and $(\xi, \eta, \zeta \leq 0)$ respectively stand for the singularity and flow-observation point.

Furthermore, D is the dispersion function

$$D = (F.\alpha)^2 - k \quad (17)$$

Fourier-Kotchin formulation

Practical calculations involve distributions of singularities of the form:

$$\rho = \int_{P_0} \left\{ \frac{G.\sigma}{\nabla G.\vec{\delta}} \right\} \quad (18)$$

where P_0 stands for a hull panel or a waterline segment near a point $\vec{x}_0 = (x_0, y_0, z_0)$ (in presents calculations \vec{x}_0 stands for the middle of the hull panel) and σ and $\vec{\delta} = (\delta_x, \delta_y, \delta_z)$ are source and dipole densities, respectively. In usual approach G and ∇G are evaluated using (16) and integrated over a panel or a segment as in (18). However the space integration (with respect to the point \vec{x}) can be performed first and the Fourier integration (with respect to the Fourier variables α and β) last. Thus the Green function is not evaluated directly in this approach, which is based on a Fourier representation of the free surface component of the velocity potential. This approach corresponds to the classical method used by Kotchin [11][12] for the problems of steady flow about a ship. Thus the free-surface component ρ_F is given by the double Fourier integral

$$4\pi^2 \rho_F = \lim_{\epsilon \rightarrow 0^+} \int_{-\infty}^{+\infty} \int_{-\infty}^{+\infty} \frac{S . e^{Z.k - i.(X.\alpha + Y.\beta)} . d\alpha . d\beta}{F^2 . \alpha^2 - k - i.\epsilon . \text{sign}(\alpha)} \quad (19)$$

where $(X, Y, Z \leq 0) = (\xi - x_0, \eta - y_0, \zeta + z_0)$ and S is the spectrum function defined as

$$S = \int_{P_0} \epsilon \left\{ i.\alpha.\delta_x + i.\beta.\delta_y + k.\delta_z \right\} \quad (20)$$

with $\epsilon = e^{k(z-z_0) + i[\alpha(x-x_0) + \beta(y-y_0)]}$

For coupling problems, sources and dipoles densities are evaluated on the boundary surface S^i and on its intersection curve Γ^i with the mean free-surface plane $z = 0$, using the Green identity. Moreover these densities can be expressed as functions of the velocity components on S^i and Γ^i (figure 2). Specifically, the function $S(\alpha, \beta)$ is given by

$$S(\alpha, \beta) = \int_{S^i} A^{S^i} . e^{k(z-z_0) + i.(\alpha(x-x_0) + \beta(y-y_0))} dA - F^2 \int_{\Gamma^i} A^{\Gamma^i} . e^{-k.z_0 + i.(\alpha(x-x_0) + \beta(y-y_0))} dL \quad (21)$$

where dA and dL stand for the differential elements of area and arc length of the surface S^i and the curve Γ^i . Functions A^{S^i} and A^{Γ^i} are defined as:

$$A^{S^i} = \vec{u} . \vec{n} + i . \left(\frac{\beta}{k} . t_x - \frac{\alpha}{k} . t_y \right) \vec{u} . \vec{s} - i . \left(\frac{\beta}{k} . s_x - \frac{\alpha}{k} . s_y \right) \vec{u} . \vec{t} \quad (22)$$

$$A^{\Gamma^i} = t_y^2 \vec{u} \cdot \vec{\nabla} + \left(t_x t_y + \frac{\alpha\beta}{k^2} \right) \vec{u} \cdot \vec{t} \quad (23)$$

Near-field and far-field components

It is shown in [2], [13] and [14] that the double Fourier integral (19) can be expressed as the sum of a wave component φ^W , which is dominant in the far field, and a local component φ^N , negligible in the far field but significant in the near field.

$$\varphi^F = \varphi^W + \varphi^N \quad (24)$$

For steady free-surface flows, the dispersion function D defines two dispersion curves, which are symmetric with respect to both $\alpha = 0$ and $\beta = 0$. The dispersion curves $D = 0$ are given by $\alpha = \pm \alpha_d(\beta)$ where the function $\alpha_d(\beta)$ is defined by $F^2 \alpha_d = \sqrt{F^2 k_d}$ with $F^2 k_d = K$,

$$K = 1/2 + \sqrt{1/4 + b^2} \quad (25)$$

and $-\infty < b = F^2 \beta < +\infty$. The wave component φ^W and the local component φ^N (24) of the free-surface potential (19) can be represented in terms of the speed-scale coordinates $(X^u, Y^u, Z^u) = (X, Y, Z)/F^2$.

The wave component is given by :

$$\varphi^W = \frac{[erf(X^u) - 1]}{4\pi F^2} \int_{-\infty}^{+\infty} db \frac{\sqrt{K} e^{K Z^u}}{\sqrt{0.25 + b^2}} \cdot \Im \left\{ S \left(\frac{\sqrt{K}}{F^2}, \frac{b}{F^2} \right) \cdot e^{-i(X^u \sqrt{K} + Y^u b)} \right\} \quad (26)$$

The local component φ^N can be expressed as :

$$2\pi^2 F^2 \varphi^N = I^N + \frac{\pi S_0}{\sqrt{(X^u)^2 + (Y^u)^2 + (\nu - Z^u)^2}} \quad (27)$$

where $S_0 = S(0, 0)$ is the value of the spectrum function S at the origin of the Fourier plane, ν is a real positive number, and I^N is given by the double Fourier integral :

$$I^N = \Re \int_{-\infty}^{+\infty} db e^{-i Y^u b} \int_0^\infty da e^{-i X^u a} \Lambda \quad (28)$$

with Λ defined as

$$\Lambda = \frac{S e^{c Z^u}}{a^2 - c} - \frac{S_0 e^{-c(\nu - Z^u)}}{c} - \frac{\sqrt{K} e^{K Z^u}}{\sqrt{1 + 4b^2}} \left(\frac{E^- S^+}{a - \sqrt{K}} - \frac{E^+ S^-}{a + \sqrt{K}} \right) \quad (29)$$

Here $(a, b, c) = F^2(\alpha, \beta, k)$, K is the function (25), E^\pm are localizing functions defined as

$$E^\pm = e^{-(a \pm \sqrt{K})^2 / 4} \quad (30)$$

S, S_0 and S^\pm stand for :

$$S = S(a/F^2, b/F^2)$$

$$S_0 = S(0, 0)$$

$$S^\pm = S(\pm \sqrt{K}/F^2, b/F^2)$$

MATCHING CONDITIONS

The boat starts from rest and accelerates until its final velocity. The coupling procedure uses the Green function for steady flow, so the first coupling is computed when the hull has reached his final velocity. During the first part of the computation, the RANSE solver is used with a very large grid. After the first coupling the surface S^o is the outer boundary, and the condition is given by the potential flow calculation; The velocity components on S^i , given by RANSE method, are used to calculate the viscous flow (velocity and pressure) in internal domain on S^o and the wave field in the outer region. Once this calculation is made, a new time step of the RANSE calculation is performed with the updated boundary condition on S^o .

In practical computation surface S^i and its intersection curve Γ^i with the mean free surface are divided in panels and segments (figure 2). The velocity is assumed constant on each panels and segments, then the spectrum function can be expressed as a sum on panels and segments .

$$S(\alpha, \beta) = \sum_{j=1}^{np} \int_{S_j^i} A^{S_j^i} \cdot e^{k(z - z_{oj}) + \omega_j} dA^j - F^2 \sum_{j=1}^{ns} \int_{\gamma_j^i} A^{\gamma_j^i} \cdot e^{-k \cdot z_{oj} + \omega_j} dL^j \quad (31)$$

with :

$$\omega_j = i \cdot (\alpha(x - x_{oj}) + \beta(y - y_{oj}))$$

np and ns represents respectively number of panels on S^i and number of segment on Γ^i .

Moreover functions $A^{S_j^i}$ and $A^{\gamma_j^i}$ are written as functions of velocity components on each panels and segments :

$$A^{S_j^i} = \vec{u}_j^i \cdot \vec{n}_j^i + i \frac{\alpha}{k} (\vec{u}_j^i \cdot \vec{t}_j^i \cdot s_{yj} - \vec{u}_j^i \cdot \vec{s}_j^i \cdot t_{yj}) + i \frac{\beta}{k} (\vec{u}_j^i \cdot \vec{s}_j^i \cdot t_{xj} - \vec{u}_j^i \cdot \vec{t}_j^i \cdot s_{xj}) \vec{u}_j^i \cdot \vec{t}_j^i \quad (32)$$

$$A_{ij}^{\Gamma^i} = (t_{yj}^2 \vec{u}_j \cdot \vec{n}_j + t_{xj} t_{yj} \vec{u}_j \cdot \vec{t}_j) + \frac{\alpha \beta}{k^2} \vec{u}_j \cdot \vec{t}_j \quad (33)$$

By inverting sums on np and ns (31) with integrals in a and b (26)(28), the far-field and near-field components can be expressed as the sum of functions of the velocity on surface S^i and on waterline Γ^i , multiplying influence coefficients. These influence coefficients only depend on panels geometry and on flow-observation points. Thus they are evaluated at the beginning of the computation. When the outer boundary condition on S^o is updated, only functions of the velocity are re-evaluated. Calculations of the free-surface elevations in the potential flow domain present in the next section, are not necessary for the RANSE computation, but they allow us to observe connexions between the two computations.

RESULTS

In order to valid the method, a self-consistency calculation is first performed. Then a serie 60 CB=0.6 merchant ship is used for all the calculations. Only symetric cases are studied, hence one half of the fluid domain around the ship is discretized. For the calculations two O-O grids were used (fig 3). The coarse grid has 33 nodes in streamwise direction, 33 nodes in normal direction and 17 nodes in girthwise direction. The fine grid has 89 nodes in streamwise direction, 65 nodes in normal direction and 33 nodes in girthwise direction. Calculations were made on the coarse grid with a Froude number of 0.316 and on the fine grid with Froude number of 0.316 and 0.2. Moreover with this last Froude number the coupling was made with two differents coupling surfaces. Nondimensional values are defined with respect to the ship length L , the acceleration of gravity g , the density of water ρ and the hull velocity U_a .

Self-consistency test

In a first step the problem of steady flow past a source is solved with the Fourier-Kotchin formulation of the Green function. Green function and velocity are computed on the free surface and on a surface surrounding the source. In a second step, velocity components on the surface surrounding the source are used to distribute sources and dipoles panels over this surface. Both far-field and near-field flow are then computed using the Fourier-Kotchin coupling method explained in section 2. This second step is then similar to a coupling. The computed free-surface elevations behind the source panels for the two steps are then compared. The figure 4 and 5 show far-field and near-field components of the Green function on the free surface due

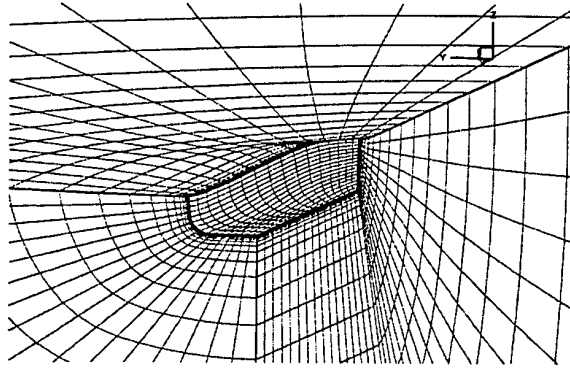


Figure 3: Partial view of the coarse grid around serie 60

to a source advancing at constant speed. On figures 4, 5, 6 results of the self-consistency test are presented for differents numbers of panels. This figures show the Green function in the wake of the source ($y=0$) on the free surface ($z=0$) at several location in the x direction. The source is located at $x=0$ and the vertical line show the position of the coupling surface in the $y=0$ plane. The coupling calculation is valid only in the outer domain behind the source ($x < -0.4$).

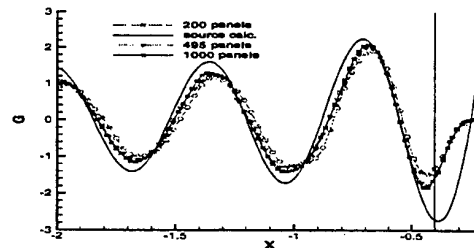


Figure 4: self-consistency test on far-field component

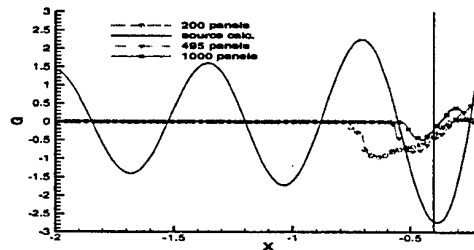


Figure 5: self-consistency test on near-field component

The self-consistency test show a good agreement

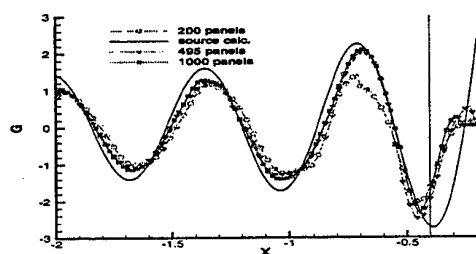


Figure 6: self-consistency test on total free-surface component

between the two calculations, the wave crests and holes are at the same location in the x direction for the two calculations (fig 4 and 6). We notice small differences on the waves magnitudes between the two calculations. Nevertheless the self-consistency calculations confirming the validity of the Fourier-Kochin method for the flow computation in the inviscid domain and on the outer coupling surface.

We notice that the near-field component is only significant in a small domain near the coupling surface (fig 5). Moreover the far-field component converges faster than the near-field component; The far-field component converges for 495 panels, while we notice differences between near-field calculations with 495 and 1000 panels. For these reasons, the near-field component will not be used in coupling computations.

Coupling on coarse grid $Fn = 0.316$

In this section, numerical results of the coupling procedure are compared with RANSE calculations and with experiments. The calculations are performed on a serie 60 CB=0.6 hull, for a Froude number $Fn = Ua/\sqrt{gL} = 0.316$, a Reynolds number $Rn = Ua.L/\nu = 2.5.10^6$ and a non dimensional time step $\sqrt{\frac{g}{L}}.\Delta t = 0.078$. The ship reaches its final velocity after 75 time steps, and the first coupling is performed after 180 time steps and then every five. The inner and outer coupling surfaces are the fifteenth and nineteenth surfaces in the normal direction, and the inner coupling surface is discretized in 300 panels.

On figure 17 pressure on the free-surface is represented for the RANSE calculation on the top side and for RANSE calculation with coupling on the bottom side. The two black curves represent sights of inner and outer coupling surfaces on the free surface. On this figure we can see the good connexion between the viscous and potential calculations on the outer coupling surface and the numerical damping away from the hull with RANSE calculation.

On figure 7 free-surface elevation on the hull with

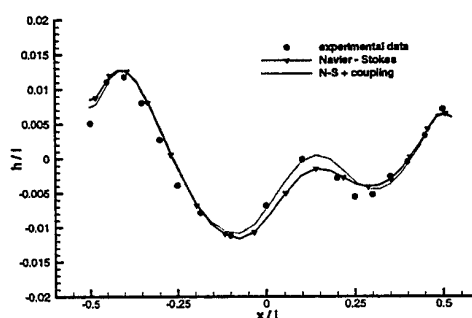


Figure 7: Free-surface elevation on the hull (coarse grid, $Fn = 0.316$)

the coupling approach is compared with results of RANSE calculation and with experimental data [15]. The crest and hole are better estimated with the coupling method than with the RANSE method. For this calculation we use a very coarse grid, numerical damping is then important, the coupling method provides boundary conditions without damping in the inner region, which leads to more accurate results on the waterline.

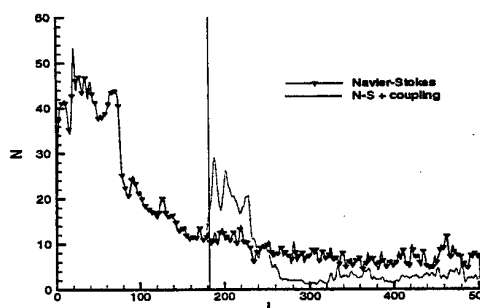


Figure 8: Number of solver iteration versus time iteration (coarse grid, $Fn = 0.316$)

Figures 8 and 9 represent numbers of iterations of the solver at each time step and CPU time per time step versus the number of iteration in time, respectively. These figures show that number of solver iterations and CPU time decrease when the coupling procedure is used. After the first coupling the RANSE domain is smaller, the fully coupled system to solve is then smaller.

Coupling on fine grid $Fn = 0.316$

As in the previous section, numerical results of the coupling procedure are compared with RANSE cal-

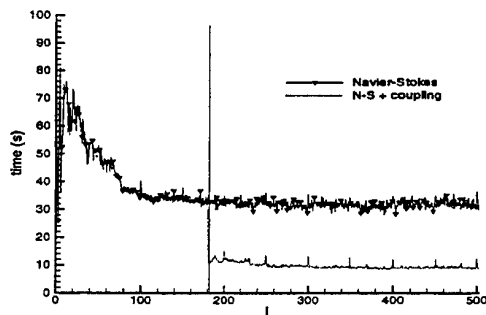


Figure 9: CPU time in second versus time iteration (coarse grid, $Fn = 0.316$)

culations and with experiments. The calculations are performed with the same Froude and Reynolds numbers and non dimensional time step. The ship reaches its final velocity after 75 time steps, and the first coupling is performed after 150 time steps and then every five. The inner and outer coupling surfaces are the thirty-fifth and forty-fifth surfaces in the normal direction, and the inner coupling surface is discretized with 300 panels.

On figure 18 we notice a good connexion between the potential and viscous calculations on the outer coupling surface. Figure 10 shows free-surface elevation on the hull. RANSE calculation and RANSE with coupling calculation are very closed. The RANSE with coupling free-surface elevation is close to the previous calculation with a coarse grid (fig 7), while the fully RANSE calculation curve gets closer to the RANSE with coupling curve. Pressure and

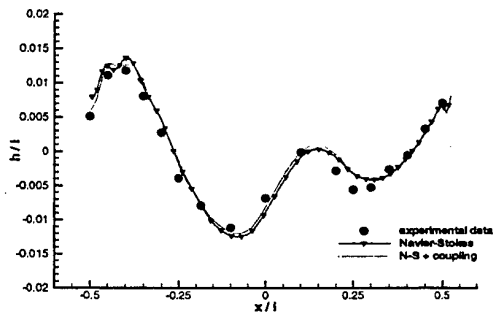


Figure 10: Free-surface elevation on the hull (fine grid, $Fn = 0.316$)

streamlines on the hull are represented on figure 19. Results of the two calculations are very close, and show that the coupling procedure does not perturb the

RANSE solution on the hull when the mesh is sufficiently refined. Figures 11 and 12 represent numbers of iterations of the solver at each time step and CPU time per time step versus the number of iteration in time, respectively. Moreover figure 12 shows that number of solver iterations and CPU time decrease of a factor two when the coupling procedure is used.

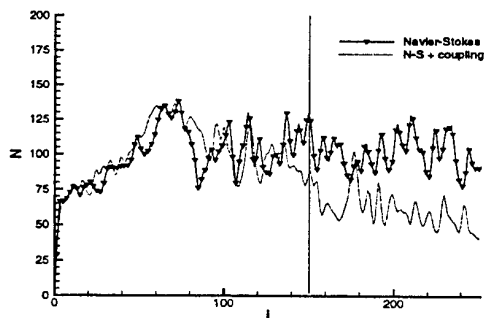


Figure 11: Number of solver iterations versus time iteration (fine grid, $Fn = 0.316$)

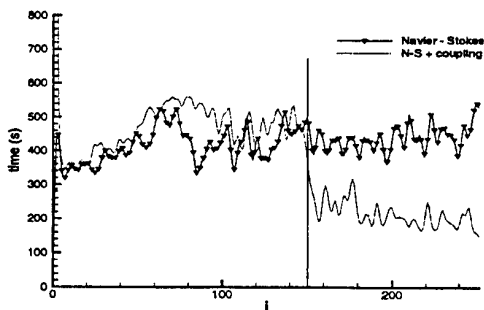


Figure 12: CPU time in second versus time iteration (fine grid, $Fn = 0.316$)

Coupling on fine grid $Fn = 0.2$

In this section, we compare numerical results of the coupling procedure for two couples of inner and outer coupling surfaces. In the first calculation the inner and outer coupling surfaces are respectively thirty fifth and forty fifth surfaces in the normal direction, while the thirtieth and thirty fifth surfaces are used in the second computation. The calculations are performed for a Froude number $Fn = Ua/\sqrt{gL} = 0.2$, a Reynolds number $Rn = Ua.L/\nu = 2.5.10^6$ and a non dimensional time step $\sqrt{\frac{L}{g}}.\Delta t = 0.078$. The ship reaches its final velocity after 75 time steps, and

the first coupling is performed after 180 time steps and then every five. The inner coupling surface is discretized in 300 panels.

Figures 20 and 21 show pressure levels on the free-surface. Potential solver has a great influence in the second computation. In the first computation the inner coupling surface seems to be too far of the hull. Velocity components used for the potential calculations are then softened. Waves elevations are smaller in the outer region (fig 20 and 21) and outer computation has no influence on the inner domain (fig 13). In the second computation the inner coupling surface and the hull are closer, RANSE calculations are then modified by potential solution (fig 14 and 22). Fig-

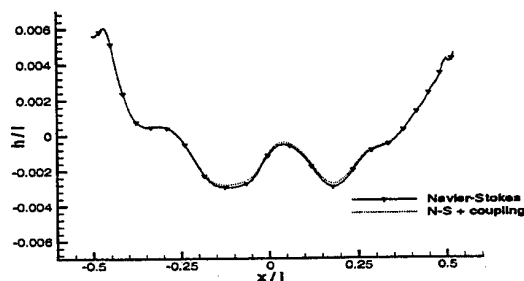


Figure 13: Free-surface elevation on the hull (fine grid, $Fn = 0.2$, coupling surfaces (35; 45))

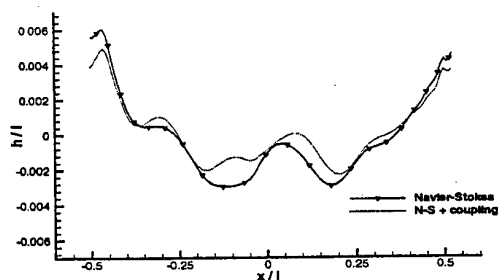


Figure 14: Free-surface elevation on the hull (fine grid, $Fn = 0.2$, coupling surfaces (30; 35))

ures 15 and 16 show that the coupling calculation decrease CPU time of a factor two, while the number of solver iterations remains roughly constant.

CONCLUSION

An iterative numerical method which combines the Reynolds Averaged Navier-Stokes equations

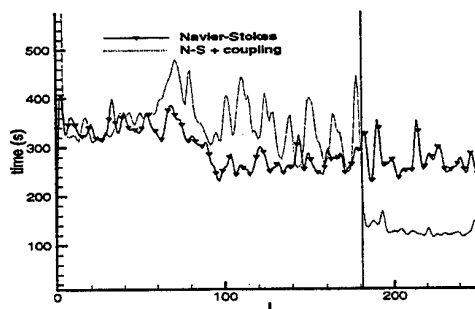


Figure 15: CPU time in second versus time iteration (fine grid, $Fn = 0.2$, coupling surfaces (35; 45))

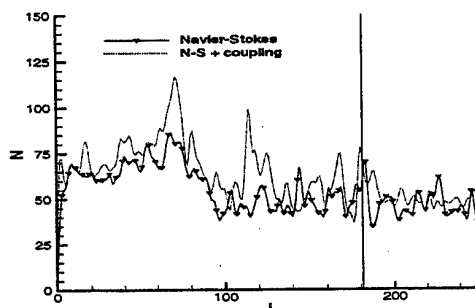


Figure 16: Number of solver iterations versus time iteration (fine grid, $Fn = 0.2$, coupling surfaces (35; 45))

(RANSE) and a free-surface potential flow calculation is presented here. RANSE are solved by a fully coupled velocity, pressure and free-surface elevation method, while Fourier-Kotchin formulation of Green function is used in the potential domain.

On coarse grid, the coupling approach decrease numerical damping, which leads to more accurate results in the RANSE domain. On fine grid the coupling approach decrease of a factor two CPU time for each time step, but modify wave elevation and pressure on the hull for $Fn = 0.2$. Further numerical experiments are needed to study the behaviour of the algorithm with this Froude number. Nevertheless calculations performed on a serie 60 hull form for two Froude numbers and mesh refinements show the ability of the method. Moreover the coupling approach can be generalized for the study of diffraction and radiation flow around structures, and for ship motion in waves, which is the main aim of this method.



Figure 17: Pressure levels on free-surface. RANSE calculation (top half) and RANSE calculation with coupling (bottom half) for the coarse grid $Fn = 0.316$.

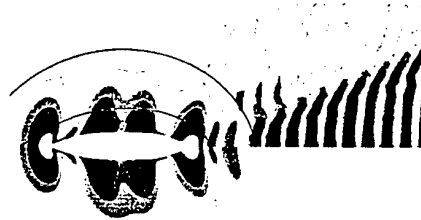


Figure 20: Pressure levels on free-surface for the fine grid $Fn = 0.2$ and coupling surfaces (35;45). RANSE calculation (bottom half) and RANSE calculation with coupling (top half).



Figure 18: Pressure levels on free-surface for the fine grid $Fn = 0.316$. RANSE calculation (top half) and RANSE calculation with coupling (bottom half).



Figure 21: Pressure levels on free-surface for the fine grid $Fn = 0.2$ and coupling surfaces (30;35). RANSE calculation (bottom half) and RANSE calculation with coupling (top half).

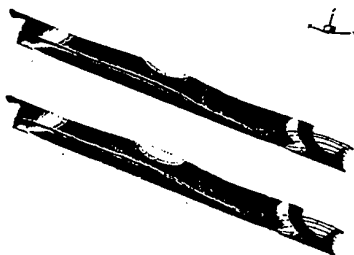


Figure 19: Pressure levels and streamtraces on the hull (fine grid, $Fn = 0.316$). RANSE calculation (top half) and RANSE with coupling calculation (bottom half)

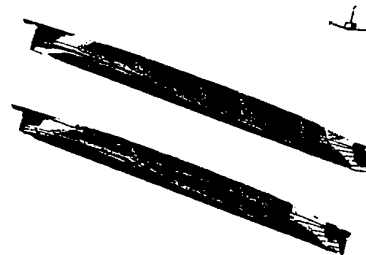


Figure 22: Pressure levels and streamtraces on the hull (fine grid, $Fn = 0.2$, coupling surfaces (30;35)). RANSE calculation (top half) and RANSE with coupling calculation (bottom half)

REFERENCES

1. Alessandrini, B. and Delhommeau, G. "A multigrid velocity-pressure-free surface elevation fully coupled solver for calculation of turbulent incompressible flow around a hull," Proceedings of the 21st ONR Symposium on Naval Hydrodynamics, Trondheim, 1996.
2. Chen, X.-B. and Noblesse, F. "Green functions and super green functions in free-surface hydrodynamics," EUROMECH, Poitiers, 1998.
3. Noblesse, F. and Yang, C., "Fourier-kochin formulation of wave diffraction-radiation by ships or offshore structures," Ship technology research, Vol. 42, 1995.
4. Tahara, Y. and Stern, F., "Validation of an iterative approach for calculating ship boundary layers and wakes for nonzero froude number," Computers fluids, Vol. 23, 1994.
5. E. Campana, A. Di Mascio, P.G. Esposito and Lalli, F., "Viscous-inviscid coupling in free surface ship flows," International journal for numerical methods in fluids, Vol. 21, No. 10, 1995.
6. H.-C. Chen, W.-M. Lin and Weems, K.M., "Interactive zonal approach for ship flows including viscous and nonlinear wave effects," Computers fluids, Vol. 23, 1994.
7. Menter, F. R. "Zonal two equation $k - \omega$ turbulence models for aerodynamics flows," Fluid Dynamics Conference, Orlando, Vol. 1, 1993.
8. Wilcox, D. C., "Reassessment of the scale determining equation for advanced turbulence models," AIAA Journal, Vol. 26, 1988, pp. 1299-1310.
9. Wilcox, D. C., "Multiscale model for turbulent flows," AIAA Journal, Vol. 26, 1988, pp. 1311-1320.
10. Alessandrini, B. and Delhommeau, G. "A multigrid velocity-pressure-free surface elevation fully coupled solver for turbulent incompressible flow around calculation," Proceedings of 9th International Conference on Numerical Methods in Laminar and Turbulent flow, Atlanta, Vol. 1, 1995.
11. Kotchin, N. E., "On the wavemaking resistance and lift of bodies submerged in water," tech. rep., 1937, translated in SNAME Tech. and Res. Bull. 1-8 (1951).
12. Kotchin, N. E., "The theory of waves generated by oscillations of a body under the free surface of a heavy incompressible fluid," tech. rep., 1940, translated in SNAME Tech. and Res. Bull. 1-10 (1952).
13. Chen, X. B. and Noblesse, F. "Super green functions," Proceedings of 22nd Symposium on Naval Hydrodynamics, Washington, USA, Vol. 1, 1998.
14. Noblesse, F. and Chen, X. B., "Decomposition of free-surface effects into wave and near-field components," Ship Technology Research, Vol. 42, 1995, pp. 167-185.
15. Y. Toda, F. Stern and Longo, J., "Ihr report 352," tech. rep., 1991, Iowa Institute of Hydraulic Research, The University of Iowa, USA.

COMPUTATION OF FLOWS AROUND HYDROFOILS UNDER THE FREE SURFACE

R. AZCUETA¹, S. MUZAFERIJA², M. PERIĆ¹, S.-D. YOO¹

¹Fluid Dynamics and Ship Theory Section, Technical University of Hamburg-Harburg
Lämmersieth 90, D-22 305 Hamburg, Germany
Fax: +49 40 42832 3331; E-Mail: peric@schiffbau.uni-hamburg.de

²ICCM Institute of Computational Continuum Mechanics GmbH,
Bramfelder Str. 164, D-22 305 Hamburg, Germany

ABSTRACT

Results of numerical simulations of flows above a submerged hydrofoil are presented. The computations were performed using a finite volume method with block-structured or unstructured meshes and either an interface-tracking or an interface-capturing scheme to determine the shape of the free surface. In the case of small submergence depths and high Froude numbers, wave breaking occurred above the hydrofoil. The effects of hydrofoil velocity on the breaking pattern for a given submergence were investigated. Comparisons were also made with the flow around hydrofoil in deep water.

INTRODUCTION

Hydrofoils are often used to generate lift for marine vessels. When a hydrofoil is close enough to the free surface and when its velocity exceeds a certain level, waves are generated at the free surface above it; they can be smooth or they may undergo breaking. The smooth waves are usually steady (when the hydrofoil moves at a constant speed), while breaking waves can be both quasi-steady and fully unsteady.

The wave breaking causes fluctuations of both drag and lift; this can lead to vibrations on board of the vessel and may also cause structural damage. It is therefore of great practical importance to be able to predict the flow around submerged hydrofoils.

The lift created by submerged hydrofoils in the presence of smooth, non-breaking waves can be predicted – often with an accuracy sufficiently high for practical purposes – using potential flow methods. However, breaking waves require the use of methods based on the Navier-Stokes equations.

The computation of flow around a hydrofoil close to a free surface requires also that the shape and position of the free surface be computed. There are basically two classes of methods that can be used for this purpose: *interface-tracking* and *interface-capturing methods*.

Interface-tracking methods compute the flow of water only, treating thereby the free surface as the (unknown) boundary of the solution domain. The nu-

merical grid is fitted to the free surface and moves with it as it changes its position and shape. The location of the free surface is usually found by using the kinematic boundary condition, which requires that no flow occurs through the free surface. This approach is usually used only when the free surface does not deform beyond certain limits so that the initial grid topology can be used throughout the simulation; otherwise, complicated re-gridding operations are necessary. Examples of such methods are described in [1–4].

Interface-capturing methods compute usually the flow of both air and water on a grid which is only adapted to the shape and position of solid boundaries but which does not deform or move as a result of free-surface movement. There are many variants of this class of methods; the most widely used are the MAC-method [5], the VOF-method [6] and the schemes that treat both air and water as a single fluid with variable properties [7–11]. These methods can handle both breaking waves and isolated air bubbles in water or water drops in air.

We present here computations of flows around submerged hydrofoils for two configurations: one that was studied experimentally by Duncan [12] with non-breaking waves, to which both kinds of solution methods could be applied, and one with breaking waves, for which no experimental data is available and where only the interface-capturing approach can be employed. The two solution methods are first

briefly described, before the results of computations are presented and discussed.

NUMERICAL SOLUTION METHOD

Both solution methods employed in this study are based on the same discretization procedure, which will be described first before the features specific to each method are described. More details about these two methods can be found in [4] and [11].

The Basic Method

The starting point are the mass and momentum conservation equations, which read in integral form:

$$\frac{d}{dt} \int_V \rho dV + \int_S \rho(\mathbf{v} - \mathbf{v}_b) \cdot \mathbf{n} dS = 0, \quad (1)$$

$$\begin{aligned} \frac{d}{dt} \int_V \rho u_i dV + \int_S \rho u_i \mathbf{v} \cdot \mathbf{n} dS = \\ \int_S (\tau_{ij} \mathbf{i}_j - p \mathbf{i}_i) \cdot \mathbf{n} dS + \int_V \rho b_i dV, \end{aligned} \quad (2)$$

where V is the CV-volume bounded by a closed surface S with a unit normal vector \mathbf{n} directed outwards, \mathbf{v} is the fluid velocity vector, ρ is fluid density, p is the pressure, b_i are the body forces per unit mass (here the gravity), and τ_{ij} are the effective stresses (the sum of viscous and Reynolds-stresses, the latter being modeled using the standard k - ϵ model based on the eddy-viscosity approach; only incompressible flows are considered):

$$\tau_{ij} = \mu_{\text{eff}} \left(\frac{\partial u_i}{\partial x_j} + \frac{\partial u_j}{\partial x_i} \right), \quad (3)$$

with $\mu_{\text{eff}} = \mu + \mu_t$ being the effective dynamic viscosity of the fluid.

When the grid is moving (either due to the movement of the solid walls or due to its adaptation to the free surface), the so called *space conservation law* must also be considered:

$$\frac{d}{dt} \int_V dV - \int_S \rho \mathbf{v}_b \cdot \mathbf{n} dS = 0. \quad (4)$$

In the case of turbulent flows, additional transport equations for the turbulent kinetic energy and its dissipation rate (which will not be given here) are solved; their form is similar to that of the momentum equations and they can be discretized and solved using the same principles.

The solution domain is first subdivided into a finite number of non-overlapping control volumes (CVs), which in principle can be of any shape; for accuracy

reasons, hexahedral CVs are used whenever possible. The CVs can be locally refined by subdividing an existing CV into several smaller ones; in this case the non-refined neighbor CVs – although geometrically still of hexahedral shape – have to be treated as polyhedra, since some of their faces are then replaced by several smaller faces common to the non-refined CV and the newly created smaller CVs. Also, grid blocks of different fineness and topology can be “glued” together, and the grids do not have to match at the interface, cf. Fig. 1. The numerical grid is therefore unstructured; the number of neighbors can vary from CV to CV and has no upper limit.

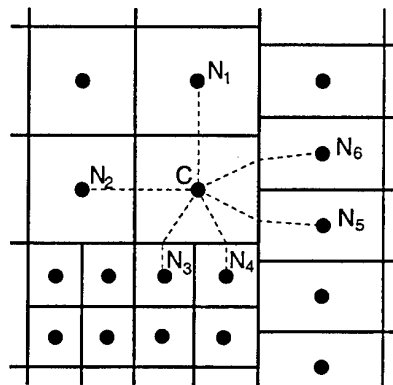


Fig. 1: An example of a two-dimensional grid with local refinement and a non-matching block interface, showing one quadrilateral CV centered around node C, which is treated as a hexagon since it has six neighbors, N_1 to N_6 .

The conservation equations are applied to each CV, with the aim to derive one algebraic equation per CV and variable, linking the unknown at the CV center C with those at k immediate neighbor CVs, N_1 to N_k . To this end, three levels of approximation are employed:

- Surface, volume, and time integrals are approximated using midpoint rule, i.e. replacing the integral with a product of the integrand evaluated at the center of the integration domain (cell-face center k , cell center C, or time instant t_n) and the integration domain (surface, volume, or time over which the integration takes place).
- Since all quantities are either prescribed (like fluid properties) or computed at the CV center C only, they need to be interpolated to other locations at which they are needed, e.g. cell-face centers. Here, linear interpolation in space and linear or quadratic interpolation in time are used.
- The derivatives of variables are computed using

approximations which are equivalent to central differences of second order.

More details on these and other possible approximations are given in [13]. Deferred-correction approach is used to reduce the implicit part of the discretized equations to the nearest neighbors only; the difference between the simplified and full approximations is included at the right-hand side of the algebraic equations. This makes the matrix of the algebraic equation system smaller and allows the use of simpler iterative solvers [11,13].

When the grid is moving, the volume swept by a cell face over one time step is used to represent the velocity of the CV surface; see [13,14] for more details on the conservative treatment of moving grids.

Since the equations are both non-linear and coupled, an iterative solution method is necessary. Here, the widely used SIMPLE-type approach [15] is used to solve the linearized momentum equations sequentially and then correct the velocities and pressure by applying a pressure correction derived from an equation obtained by combining the discretized mass and momentum equations. This sequence is called an *outer iteration*; it is repeated within each time step until the residual norms of mass and momentum are reduced below prescribed level (typically three to four orders of magnitude compared to the initial level). Linear equation systems are solved using ICCG (for symmetric matrices) or BI-CGSTAB [16] (for non-symmetric matrices) solvers from the conjugate gradient family (*inner iterations*). Here, it is sufficient to reduce the residual levels by one order of magnitude.

Interface-Tracking Method

In the interface-tracking version of the method, the initial interface location is prescribed and the dynamic boundary condition is used to prescribe the pressure at the current free-surface location (the effects of surface tension and shear are neglected here):

$$p_l - 2\mu \left(\frac{\partial v_n}{\partial n} \right)_l = p_g, \quad (5)$$

$$\left(\frac{\partial v_t}{\partial n} \right)_l = 0, \quad (6)$$

where n describes the local coordinate normal to the free surface, v_n and v_t are the velocity components in the direction normal and tangential to the free surface, respectively, and the subscripts "l" and "g" denote liquid and gas. Often the normal viscous stresses can also be neglected, meaning that the pressure on the liquid side of the free surface is equal to the atmospheric pressure. Velocities are extrapolated to the

free surface when they are needed there, while the pressure is treated as known.

The prescribed pressure is used in the momentum equations and provides a Dirichlet boundary condition for the pressure-correction equation. However, since the pressure at CV centers is corrected, there result corrections of the velocity components at the free surface so that the kinematic condition is not necessarily satisfied upon solving the momentum and pressure-correction equations:

$$\int_{S_{fs}} \rho(\mathbf{v} - \mathbf{v}_b) \cdot \mathbf{n} dS = \dot{m}_{fs} \neq 0. \quad (7)$$

In order to enforce the kinematic condition at the free surface, it is moved so that the displacement volume compensates the previously computed volume flux, \dot{m}_{fs}/ρ . This means that the free-surface velocity is corrected. More details on this technique can be found in [4].

Interface-Capturing Method

In the interface-capturing method, the solution domain covers both water and air regions. Both fluids are considered as an effective fluid with variable properties, which are at any spatial location determined according to the volume fraction of one constituent fluid (e.g. water). The volume fraction c is obtained by solving the corresponding conservation equation, which reads:

$$\frac{d}{dt} \int_V c dV + \int_S c \mathbf{v} \cdot \mathbf{n} dS = 0. \quad (8)$$

The discretization of this equation requires special attention. The usual higher-order schemes violate the boundedness requirement, which demands that $0 \leq c \leq 1$; on the other hand, numerical diffusion of low-order schemes must be avoided in order to retain a sharp interface between the two fluids. Here, the high-resolution interface-capturing scheme (HRIC) is used, which computes the cell-face value of c as a blend of the upwind, downwind, and centered interpolation; see [11] for a detailed description. The choice of the blending factor depends on the local value of the Courant number,

$$Co = \frac{\mathbf{v} \cdot \mathbf{n} S_k \Delta t}{V_C}, \quad (9)$$

where S_k is the area of the CV-face k , V_C is the volume of the cell centered around node C, and Δt is the time step. The Courant number indicates how much of one fluid is available in the donor cell and the scheme is tuned not to allow to drain more fluid out of one CV within one time step than was available in

it. Another important factor is the orientation of the interface relative to the CV-face. The normal to the interface – which is assumed to lie where the volume fraction has the value $c = 0.5$ – is obtained by computing the gradient of c ; it is equal to zero everywhere except in the interface region.

Finally, the cell-face value of c is computed as:

$$c_k = \gamma c_C + (1 - \gamma) c_{N_k}, \quad (10)$$

where γ is a non-linear function of the profile of c , Courant number, and the orientation of the interface, and C and N_k denote the nodes on either side of the CV-face k . For more details, see [11].

With this approach, the interface is usually smeared across two or three cells. The fluid properties are computed as:

$$\rho = \rho_1 c + \rho_2 (1 - c), \quad \mu = \mu_1 c + \mu_2 (1 - c), \quad (11)$$

where subscripts 1 and 2 denote the two fluids (e.g. liquid and gas). If one CV is partially filled with one and partially with the other fluid (i.e. $0 \leq c \leq 1$), it is assumed that both fluids have the same velocity and pressure.

The free surface does not represent a boundary and no boundary conditions need to be prescribed at it. If surface tension is significant at the free surface, this can also be taken into account by transforming the resulting surface-tension force into a body force [8,9].

RESULTS OF COMPUTATIONS

The computations were performed for two configurations with a NACA0012 hydrofoil under the free surface: one with non-breaking and one with breaking waves. They are described in the following two sections.

Non-Breaking Waves

The flows around a submerged hydrofoil that were studied experimentally by Duncan [12] are often used as test cases for methods designed to compute free-surface flows. The hydrofoil with a NACA0012 profile had the chord length of $l_c = 203$ mm; the maximum thickness of 25.4 mm was located 61 mm behind the nose. The hydrofoil was towed at an angle of attack of 5° at several submergence depths. The towing velocity was 0.8 m/s. We present here results of computations for the submergence depth of 210 mm, in which case the waves did not break so that both interface-tracking and interface-capturing methods could be applied. The Froude number based on foil speed and chord length was $Fr = 0.567$.

In both cases the computations start with a flat free surface and proceed to the steady-state solution by time marching. Both inviscid (Euler equations) and viscous (turbulent) flows were computed; the differences in wave profiles were of the order of few per cent, with wave amplitudes being lower in the viscous case. The grid used in the interface-tracking method is shown in its final shape in Fig. 2.

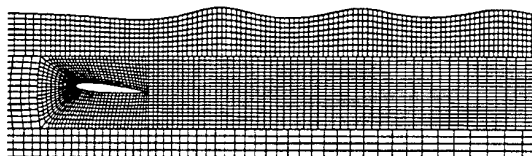


Fig. 2: Numerical grid used to compute the flow around a submerged NACA0012 hydrofoil by the interface-tracking method at the final, steady state.

The computations were performed using four systematically refined grids with 1004, 4016, 16064, and 64256 CVs, respectively, in order to assess the discretization errors. Figure 3 shows the wave profiles computed on the four grids using the interface-tracking method, compared with experimental data of Duncan [12]. The difference between solutions on subsequent grids is reducing with grid refinement, indicating convergence towards a grid-independent solution. The comparison with experimental data shows that the grid-independent numerical solution will still appreciably differ from experimental observation. While the maximum elevation appears to be almost the same in the experiment and in the simulation, the trough depths and the wavelength are smaller in the simulation than in the experiment. This observation was also made by other authors who computed these flows [1]; an explanation might lie in slight differences between boundary conditions in the simulation and in the experiment.

The comparison of solutions obtained using the two methods on the same grid (whereas for the interface-capturing method an additional grid block is added for the air region above the free surface) shows only minor differences, cf. Figs. 3 and 4. This was found also in other applications, see [11].

When the wave breaking takes place, the interface-tracking method can not be used. However, the interface-capturing method can be applied even for extreme situations, as will be shown below.

Breaking Waves

A series of computations was conducted using the NACA0012 hydrofoil with chord length of 1000 mm, submergence depth of 140 mm (measured from the

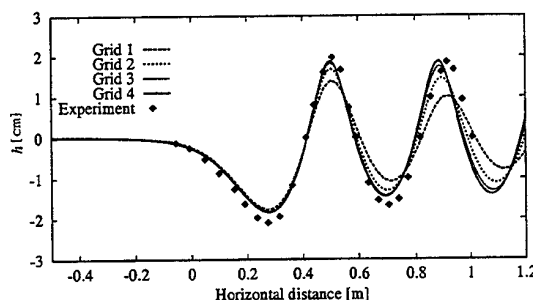


Fig. 3: The free-surface profile in the flow around a submerged NACA0012 hydrofoil computed by the interface-tracking method on four systematically refined grids, compared to experimental data of Duncan [12].

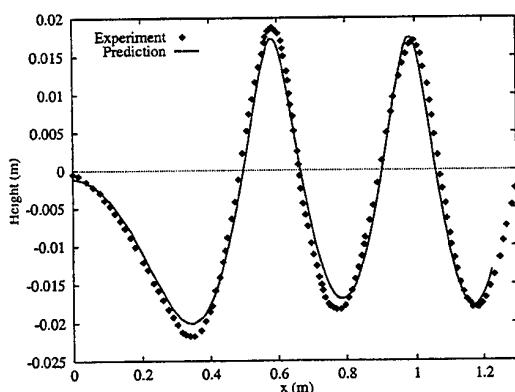


Fig. 4: The free-surface profile in the flow around a submerged NACA0012 hydrofoil computed by the interface-capturing method on the third grid from Fig. 3 (16 064 CV plus an additional 2 000 CVs in the air region above free surface), compared to experimental data of Duncan [12].

mid-point on the profile nose), and various speeds. The grid extends five chord lengths ahead and seven chord lengths behind the foil; three chord lengths were covered above and below the foil. Figure 5 shows the grid around the foil; it was locally refined in regions of large velocity changes and expected breaking waves, and was kept coarse far from the hydrofoil. The grid consists of 21 503 CVs.

For the foil speed of 0.2 m/s, no appreciable waves appeared in the simulation.

For the speed of 0.5 m/s, an unsteady breaking wave occurred. The water accelerates over the suction side of the foil and the Froude number, based on the water velocity and free-surface distance from the wall, becomes greater than unity. The flow becomes supercritical and continues to accelerate; the water depth over hydrofoil reduces and the Froude number

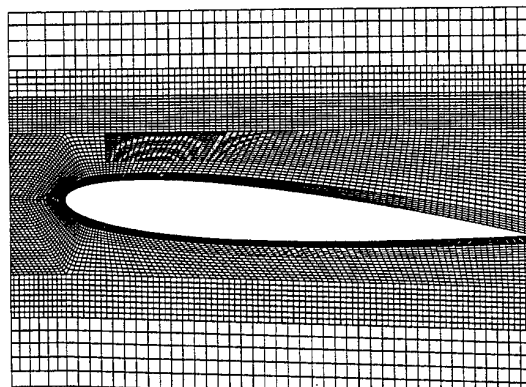


Fig. 5: Locally refined numerical grid around the hydrofoil that was used to compute flows with breaking waves.

reaches nearly the value of 1.3. However, since the foil tail is submerged 227 mm below the still water level, the acceleration can not continue all the way along the suction side – the downstream conditions require a change in the flow regime. Therefore, a hydraulic jump takes place, with a violent wave breaking, at about mid-chord distance from the nose. Figure 6 shows velocity vectors and free-surface shapes at two time instants 0.4 seconds apart. Due to the sudden slowing down of water flow behind the breaking wave, a vortex is generated on the suction side of the foil near trailing edge, which interacts with the breaking wave and results in vortex shedding and build-up.

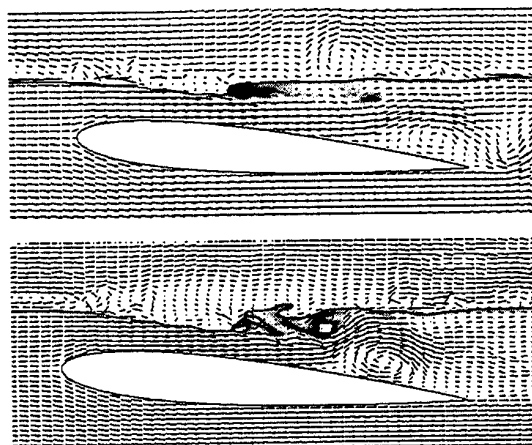


Fig. 6: Computed velocity vectors (in a coordinate frame attached to the foil) and free-surface shapes at two time instants for the foil speed of 0.5 m/s.

When the speed of hydrofoil is further increased, the wave-breaking region moves towards the trail-

ing edge. Figure 7 shows velocity vectors and free-surface shapes at four time instants from the simulation for the foil speed of 1 m/s. The hydrofoil starts suddenly moving at full speed; this leads to a build-up of a very steep, but smooth wave just above the trailing edge. This wave then overturns, as indicated in the top figure of Fig. 7. After that, the breaking region moves slightly forward and remains in the range between 0.8 and 0.9 chord lengths from the nose. In the initial stage of simulation, some vortex shedding at the trailing edge is observed; later, the flow becomes smooth all around the hydrofoil. Note that the velocity scale is not the same in all figures, and that in the breaking region the velocities are very low.

The dark-colored region represents volume fractions around 0.5; where the interface is sharp, this region is narrow. Large spreading of this region in the wave-breaking area indicates (although this is not accurately modelled) intensive mixing of water and air.

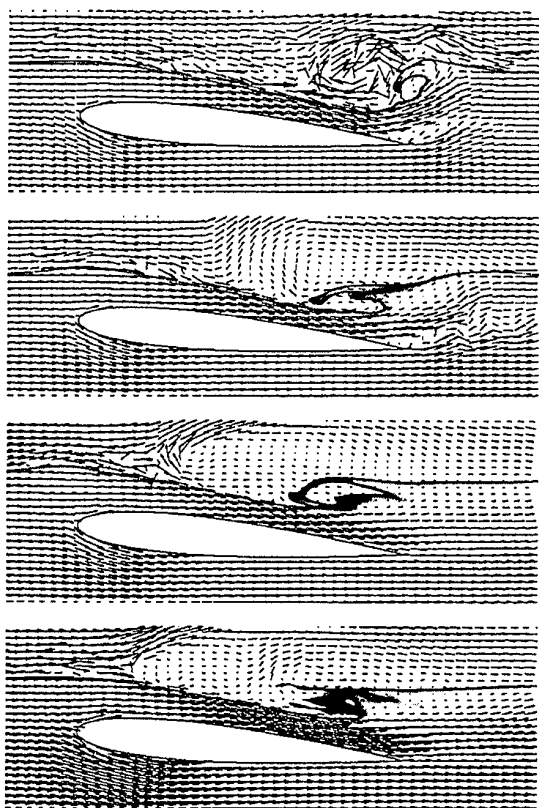


Fig. 7: Computed velocity vectors (in a coordinate frame attached to the foil) and free-surface shapes at four time instants about one second apart, for the foil speed of 1.0 m/s.

Finally, the hydrofoil speed was increased to 1.5

m/s. Figure 8 shows free-surface shapes and velocity vectors at six time instants during the simulation. Again, one steep wave builds up first and overturns (top figure). The splash caused by the overturning wave hitting the free surface is seen in the second figure of the sequence shown in Fig. 8. At later times, violent wave breaking with air entrainment takes place in a region extending from the trailing edge to about half chord length behind the foil. Also, the crest of the wave that forms above the leading edge starts breaking at the later stage of the simulation.

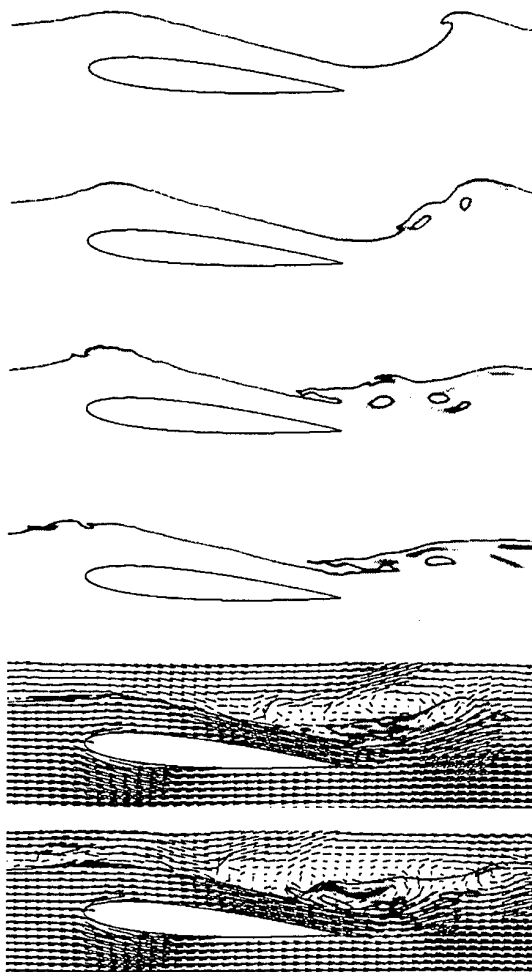


Fig. 8: Computed velocity vectors (in a coordinate frame attached to the foil) and free-surface shapes at six time instants about one second apart, for the foil speed of 1.5 m/s.

The analysis of velocity distribution and distance to free surface above the hydrofoil reveals that the critical Froude number is reached at about 15% of chord length; before the breaking starts, the Froude number

of about 2.0 is reached.

The predicted turbulent kinetic energy is very low in water, except in the wave-breaking region; the turbulence appears to be high only in the air above wave-breaking regions, cf. Fig. 9. However, while this appears plausible, there is no guarantee that the turbulence quantities from this simulation are quantitatively correct.

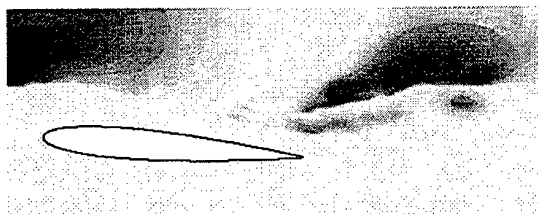


Fig. 9: Predicted distribution of the turbulent kinetic energy at one time instant for the hydrofoil under the free surface at the speed of 1.5 m/s.

The flow around hydrofoil close to the free surface is substantially different from the flow around hydrofoil with large submergence. Computations were also performed at hydrofoil speed of 1.5 m/s in deep water; in this case, a steady solution was obtained. The difference in flow patterns for the two different submergences are best illustrated by looking at the profiles of the streamwise and vertical velocity component along the lines at $y = 45$ mm (above hydrofoil) and at $y = -101$ mm (below hydrofoil), from one chord length ahead to one chord length behind the foil (the coordinate origin is at the midpoint of the foil nose).

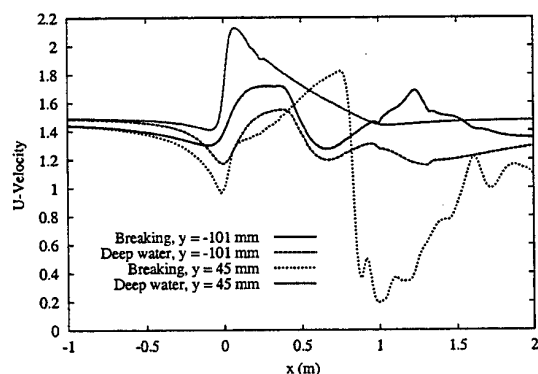


Fig. 10: Comparison of predicted profiles of the streamwise velocity component along the line at $y = 45$ mm and $y = -101$ mm for the hydrofoil in deep water and under the free surface at the speed of 1.5 m/s.

In the case of deep water, the streamwise velocity

at $y = 45$ mm drops from 1.5 m/s to about 1.46 m/s above the stagnation point and rises then sharply to a maximum of about 2.15 m/s at 5% of chord length. Thereafter, the velocity reduces steadily over the suction side until it reaches about 1.45 m/s at the trailing edge. Further downstream the velocity rises again until it reaches the foil velocity of 1.5 m/s.

Along the line $y = -101$ mm, the streamwise velocity drops to about 1.2 m/s below the stagnation point and then rises to a maximum of about 1.6 m/s at about 40% of chord length. It drops then again to a second minimum at about 70% of chord length, increases again towards trailing edge, reduces again slightly and thereafter increases steadily until the foil speed is reached further downstream.

When the hydrofoil is close to the free surface, the water level rises ahead of it and the velocity reduces; as Fig. 10 shows, the streamwise velocity at $y = 45$ mm drops substantially in front of the hydrofoil and is only 1 m/s above the stagnation point. At this location, the water level has risen to about 191 mm (from 140 mm in the undisturbed state). The velocity rises then sharply, but much less than in the case of deep water; after reaching about 1.3 m/s over a short distance, the velocity continues rising at a slower pace along the whole suction side. The line $y = 45$ mm crosses the free surface at about $x = 760$ mm, which can be recognized in Fig. 10 by a sudden drop in velocity from about 1.83 m/s (at the free surface) to about 0.4 m/s (in air). There follows the breaking wave region with very low velocities; further downstream the velocity rises again.

Along the line $y = -101$ mm, the situation in front of the hydrofoil is just opposite to the deep-water case: now, the streamwise velocity drops only slightly to about 1.3 m/s. From here on the profile has a very similar shape to that in the deep-water case, only at a higher level. In particular, a higher velocity is reached at the trailing edge, and it continues to rise for a short distance behind it, while in the deep-water case the velocity was reducing after the trailing edge. The line $y = -101$ mm passes just 14 mm below the trailing edge. In the deep-water case, the streamwise velocity on the suction side is at the trailing edge much lower than on the pressure side, so a mixing layer is created; it leads to a reduction of velocity below and increase above the trailing-edge level further downstream. When the foil is close to the free-surface, the velocity on the suction side is larger than on the pressure side and the mixing layer behind the trailing edge has now the opposite profile: the upper layer is decelerated and the lower layer is accelerated.

Figure 11 shows profiles of the vertical velocity along the same lines as in Fig. 10 for the two sub-

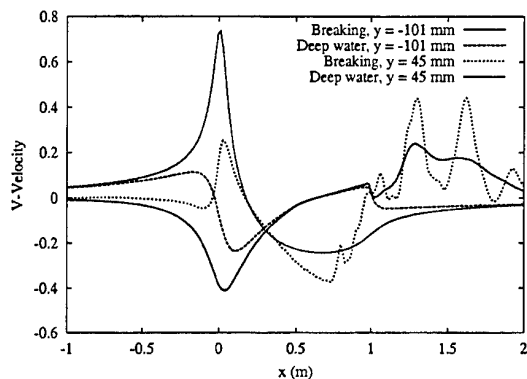


Fig. 11: Comparison of predicted profiles of the vertical velocity component along the lines at $y = 45$ mm and $y = -101$ mm for the hydrofoil in deep water and under the free surface at the speed of 1.5 m/s.

mergences. The profiles have a similar shape in both cases, but the quantitative differences are large. In particular, the peak at $y = 45$ mm just after the leading edge is much more pronounced in the deep-water case, where the vertical velocity component reaches about 50% of the foil speed, while in the free-surface case, the peak is much lower. Also, in the free-surface case, the vertical velocity components reduces first approaching the leading edge along both lines, while it is increasing in the deep-water case. The minimum shortly after trailing edge on the line $y = -101$ mm is lower in the free-surface case, while at the trailing edge, almost the same velocity prevails in both cases. In the free-surface case, the velocity oscillates in the breaking-wave region.

Figures 10 and 11 show instantaneous velocity profiles in the case of free-surface flow; since this flow is unsteady, the velocities vary in time, but the profiles shown indicate the typical features and highlight the differences compared to the deep-water case. Another appreciation of the different flow patterns for the two submergences is provided in Fig. 12, which shows the velocity vectors around the nose section of the hydrofoil. In the case of deep-water flow, the stagnation point is located on the lower foil surface and the flow approaches it at an angle of about 20° , measured from the direction of undisturbed flow. In the case of low submergence, the stagnation point moves to the upper foil surface and the flow direction changes to about -6° .

The changes in velocity distribution around the foil are reflected in different pressure and shear stress distributions, thus leading to different drag and lift forces. Figures 13 and 14 show the drag and lift coefficient for the free-surface and deep-water case

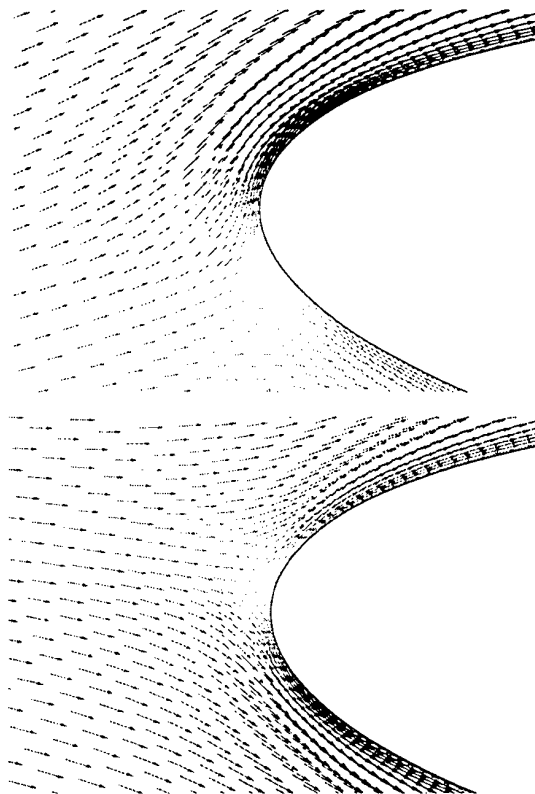


Fig. 12: Computed velocity field around the hydrofoil nose in deep water (above) and under the free surface (below) at the speed of 1.5 m/s.

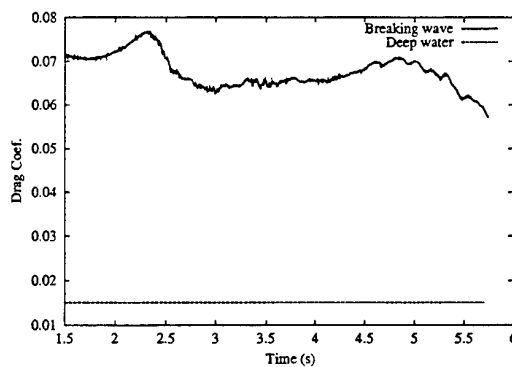


Fig. 13: Comparison of predicted drag coefficient as a function of time for the hydrofoil in deep water and under the free surface at the speed of 1.5 m/s.

as a function of time. The deep-water case has a steady solution, so these coefficients are constant; the free-surface case is unsteady and both coefficients vary with time, especially the lift coefficient. However, while the drag coefficient is almost five times large

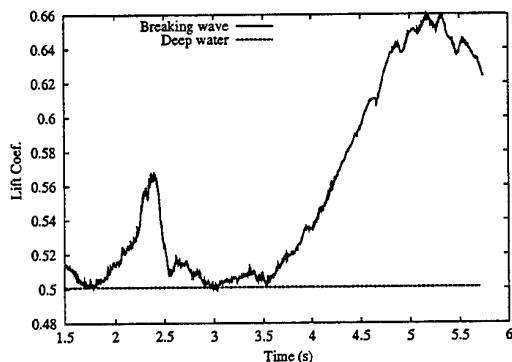


Fig. 14: Comparison of predicted lift coefficient as a function of time for the hydrofoil in deep water and under the free surface at the speed of 1.5 m/s.

in the free-surface case due to the wave generation, the lift coefficient varies between the value obtained in the deep-water case and a 30% higher value. The simulated period is not long enough to evaluate the mean frequency of the drag oscillation; the high-frequency oscillations may also be due to numerical effects and their analysis is not so meaningful, unless a real three-dimensional direct or large-eddy simulation of the turbulent flow is conducted.

DISCUSSION

The results of computations presented in preceding sections demonstrate the capabilities of the interface-capturing method to compute flows around submerged hydrofoils under severe wave-breaking conditions. Although:

- no experimental data is available for the wave-breaking cases studied here to validate the simulations,
- no grid- and time-step-dependence tests have been performed so far to estimate the discretization errors,
- the two-equation (high-Re $k-\epsilon$) turbulence model used here most probably does not account accurately for the turbulence effects, neither at the hydrofoil wall nor at the free surface,
- the two-dimensional simulation of wave breaking may also not fully correspond to the averaged truly three-dimensional process expected in the nature,

it is believed that the main features of the free-surface flows as a function of hydrofoil speed are qualitatively correctly predicted. In particular, the fact that

the wave-breaking region moves towards the trailing edge and beyond as the speed is increased and that the hydraulic-jump conditions are obtained above the hydrofoil appear plausible. The comparisons of numerical solutions obtained using both interface-tracking and interface-capturing method with experimental data for the non-breaking conditions – in spite of the non-perfect agreement – suggest that the simulation results are at least qualitatively correct. In the water-entry simulations performed earlier, where the wave breaking also occurs, relatively good agreement with experimental data was achieved, which also supports the above conclusions [17].

The use of Reynolds-averaged Navier-Stokes equations (RANSE) and two-equation turbulence models in unsteady simulations of wave breaking is another issue that needs further analysis. Normally, unsteady RANSE are appropriate if there is a gap between the turbulence scale and flow unsteadiness; this is usually the case in vortex-shedding flows behind bluff bodies, but whether the wave breaking fulfils these conditions and under which circumstances is not quite obvious.

Computations on a substantially finer grid are in progress and in the future also the experiments will be conducted to enable quantitative verification of the simulation results. Especially the increase in drag due to wave breaking requires further analysis.

REFERENCES

1. Farmer, J., Martinelli, L. & Jameson, A., Fast multigrid method for solving incompressible hydrodynamic problems with free surfaces, *AIAA J.*, Vol. 32, pp. 1175–1182, 1994.
2. Raithby, G.D., Xu, W.-X. & Stubley, G.D., Prediction of incompressible free surface flows with an element-based finite volume method, *Comput. Fluid Dynamics J.*, Vol. 4, pp. 353–371, 1995.
3. Hinatsu, M., Numerical simulation of unsteady viscous nonlinear waves using moving grid system fitted on a free surface, *J. Kansai Soc. Naval Arch.*, Vol. 173, pp. 45–50, 1993.
4. Muzaferija, S. & Perić, M., Computation of free-surface flows using finite volume method and moving grids, *Numer. Heat Transfer, Part B*, Vol. 32, pp. 369–384, 1997.
5. Harlow, F.H. & Welsh, J.E., Numerical calculation of time dependent viscous incompressible flow with free surface, *Phys. Fluids*, Vol. 8, pp. 2182–2189, 1965.

6. Hirt, C.W. & Nicholls, B.D., Volume of fluid, (VOF) method for dynamics of free boundaries, *J. Comput. Phys.*, Vol. 39, pp. 201–221, 1981.
7. Kawamura, T. & Miyata, H., Simulation of non-linear ship flows by density-function method, *J. Soc. Naval Architects Japan*, Vol. 176, pp. 1–10, 1994.
8. Lafaurie, B., Nardone, C., Scardovelli, R., Zaleski, S. & Zanetti, G., Modelling merging and fragmentation in multiphase flows with SURFER, *J. Comput. Phys.*, Vol. 113, pp. 134–147, 1994.
9. Ubbink, O., Numerical prediction of two fluid systems with sharp interfaces, *PhD thesis*, University of London, 1997.
10. Zaleski, S., Li, J. & Succi, S., Two-dimensional Navier-Stokes simulation of deformation and breakup of liquid patches, *Phys. Rev. Lett.*, Vol. 75, pp. 244–277, 1995.
11. Muzaferija, S., Perić, M., Computation of free surface flows using interface-tracking and interface-capturing methods, chap. 2 in O. Mahrenholtz and M. Markiewicz (eds.), *Nonlinear Water Wave Interaction*, pp. 59–100, WIT Press, Southampton, 1999.
12. Duncan, J.H., The breaking and non-breaking wave resistance of a two-dimensional hydrofoil, *J. Fluid Mech.*, Vol. 126, pp. 507–520, 1983.
13. Ferziger, J.H., Perić, M., *Computational Methods for Fluid Dynamics*, Springer, Berlin, 1996.
14. Demirdžić, I., Perić, M., Finite volume method for prediction of fluid flow in arbitrarily shaped domains with moving boundaries, *Int. J. Num. Methods in Fluids*, Vol. 10, pp. 771–790, 1990.
15. Patankar, S.V., Spalding, D.B., A calculation procedure for heat, mass and momentum transfer in three-dimensional parabolic flows, *Int. J. Heat Mass Transfer*, Vol. 15, pp. 1787–1806, 1972.
16. Van den Vorst, H.A., BI-CGSTAB: a fast and smoothly converging variant of BI-CG for the solution of non-symmetric linear systems, *SIAM J. Sci. Stat. Comput.*, Vol. 13, pp. 631–644, 1992.
17. Muzaferija, S., Perić, M., Sames, P.C., Shellin, T., A two-fluid Navier-Stokes solver to simulate water entry, *Proc. 22nd Symposium on Naval Hydrodynamics*, pp. 277–289, August 09–14, 1998, Washington, D.C.

PROPULSOR HYDRODYNAMICS

Chairman: J.Piquet

RANS Simulation of Integrated Marine Propulsors

Eric G. Paterson, Jin Kim, and Fred Stern

Iowa Institute of Hydraulic Research

The University of Iowa

Iowa City, Iowa 52242-1585 U.S.A.

ABSTRACT

Integrated marine propulsors are more frequently being considered as design options for future Naval ships and submarines. This is due to their potential in reducing signature-producing phenomenon such as cavitation and unsteady-flow-induced vibrations and acoustics. This paper reports work which focuses upon development of unsteady Reynolds-averaged Navier-Stokes tools which can provide the basis for future modeling efforts. Although lacking validation data, the MIT Sirenian Propulsor is used as a verification/demonstration geometry. Steady flow solutions are presented for the machine without and with the rotor, the latter of which is obtained using a circumferentially-averaged information transfer to and from the overset rotor grid blocks. The integrated nominal wake provides the speed of advance and sets the rpm of the rotor. Details of the flow are discussed and directions for future time-accurate unsteady simulations are outlined.

INTRODUCTION

Integrated marine propulsors offer many advantages over their open-water counterparts. Duct and stator design can increase static pressure at the rotor (for the case of a decelerating nozzle) and can control both preswirl and inflow circumferential-harmonic content. Together these provide options for the naval architect to try to reduce cavitation and unsteady-flow-induced vibrations and acoustics.

The flows associated with such machinery are inherently unsteady and are dominated by viscous flow phenomenon such as propulsor-hull and rotor-stator interactions, and unsteady boundary layer, wake, and tip and leakage vortices. Current state-of-the-art design tools are based upon coupled viscous/potential-flow methods (e.g., Kerwin et al., 1994). While these methods are valuable for initial design studies, they are incapable of resolving the physics required for modeling real flows and addressing signature issues.

Future simulation-based design tools will be based upon unsteady Reynolds-averaged Navier-Stokes (RANS), and possibly large-eddy simulation (LES), methods. These methods provide a physics-based approach which are theoretically capable of resolving, although at different scales, the critical unsteady, viscous hydrodynamics found in modern propulsors. In addition, they are amenable to inclusion of phenomenological models and optimal design algorithms.

Current status of RANS is that over the past 10 years, steady-flow application to propulsors has become commonplace and has demonstrated capability to predict detailed blade flows. Examples include study of design- and off-design conditions for open-water propellers (Stern et al., 1994), an ONR program focusing on validation of tip-vortex simulations and prediction of trends for tip-geometry variants (Chesnaka and Jessup, 1998; Hsiao and Pauley 1998) and prediction of 4-quadrant performance (Chen and Stern, 1998). For multiple-blade-row machines, much work has focused upon steady-flow approximations (e.g., average-passage equations [Dreyer and Zierke, 1994], and circumferentially-averaged mixing plane approach [Lee et al., 1994; Hall, 1997]) and resolution of rotor tip-gap flows (e.g., Lee et al., 1996),

Use of unsteady RANS is not yet as common. This is due to the fact that unsteady simulations for practical geometries are massive computations, which require the largest available supercomputers and a high-level of grid generation expertise. However, there are a number of notable examples already in the propulsor hydrodynamics literature. They include simulation of an open-water propeller with an idealized screen-wake inflow (Chen et al., 1994), of the Series 60 $C_b=0.6$ with rotating propeller (Abdel-Maksoud et al., 1998), and of a maneuvering submarine with appendages and rotating propeller (Taylor et al., 1998). Similar development, but for compressible flows, has also taken place in the aerospace and gas-turbine communities as evidenced by the large number of papers at specialty conferences (e.g., ASME Gas

Turbine & Aeroengine Congress). Although the machines, in comparison to marine propulsors, tend to have significantly different design and flow physics (and therefore different modeling requirements), the numerical issues and CFD status are very similar.

The work reported herein is part of a program of research that is focused upon development of future simulation-based design tools capable of resolving unsteady propulsor flows at a level of fidelity which can support development of models for multi-phase flow and cavitation. Herein, the CFD code CFDSHIP-IOWA is described and a building-block study and demonstration of capability is provided using the MIT Sirenian Propulsor. Steady-flow solutions are presented for the machine without and with the rotor, the latter of which is accomplished using a circumferentially-averaged information transfer. Details of the flow are discussed along with plans for verification and future time-accurate unsteady simulations.

CFDSHIP-IOWA

CFDSHIP-IOWA is a general purpose CFD code developed at IIHR specifically for naval hydrodynamics. It has been verified and validated for a number of surface-ship and propulsor flow problems. The most recent development (version 3.0) has focused upon accuracy, distributed parallel computing, generality, modularity, and efficiency, and is described by Paterson and Sinkovits (1999) and Wilson et al. (1998). These references and other online information can be found at <http://www.iihr.uiowa.edu/~cfdschip/>.

Governing equations

The code solves the three-dimensional unsteady incompressible Reynolds-averaged Navier-Stokes and continuity equations in either Cartesian, inertial cylindrical-polar, or non-inertial cylindrical-polar base-coordinate systems. The effects of rotating machinery are included through boundary conditions and the addition of either grid-velocity or non-inertial terms for inertial or non-inertial formulations, respectively.

Reynolds-stress closure is accomplished using a standard linear stress-strain relationship. Eddy-viscosity is calculated using either the Baldwin-Lomax model, a blended $k-\omega/k-\epsilon$ model (Menter, 1994), or the near-wall $k-\epsilon$ model of Chen and Patel (1985).

Numerics

The solution scheme is based upon the PISO algorithm and is fully implicit. The governing equations are reduced to algebraic form using finite-difference operators. The convective terms are discretized with a general 5-point stencil which permits user-specified accuracy ranging from 1st-order upwind to 4th-order central. The viscous terms are discretized with a 2nd-order central finite-difference. Temporal terms are discretized with either a first- or second-order backward finite-differences for steady or unsteady flow, respectively. The pressure equation is derived by taking the divergence of the momentum equations and by projecting the velocity into a divergence-free field at time level (n). Since a collocated grid approach is used, fourth-order dissipation is added to prevent oscillations by taking a linear combination of full- and half-cell operators. Algebraic equations are solved using line-ADI and a penta-diagonal algorithm. Wilson et al. (1998) provides further description of the core algorithm.

Boundary conditions

Twenty-three boundary conditions are available in CFDSHIP-IOWA. They can be grouped as physical, computational, and multi-block types. The physical conditions include no-slip and free-surface boundaries. Computational conditions include inlet, exit, far-field, impermeable slip, zero-gradient, periodic, branch-cut, pole singularity, cylindrical zero gradient, cylindrical periodic, and symmetry-plane boundaries. Block-to-block communication can take the form of either patched or overset (a.k.a., Chimera) conditions. For overset boundaries, parametrically-mapped tri-linear interpolation is used. For unsteady moving-grid problems, donor cells are found for each unique grid position (i.e., for the first period) using a stencil-jumping search algorithm.

Boundary conditions are specified as index ranges in an external input file. Each face of a computational domain can be sub-divided into arbitrary number of boundary-condition types. Gradient conditions are evaluated using either first- or second-order (as specified by user) one-sided finite differences.

High-performance computing

The code and data structures were designed for scalable, parallel-multi-block implementation and ease of 2nd-party model subroutine development. The

approach is based upon message-passing interface (MPI) and the single-program multiple data (SPMD) paradigm. As such, each processor executes its own copy of the executable and only has its own block of data in memory. As such, load balancing is achieved statically via domain decomposition. Except for the input and output routines, communication between processors occurs only at the boundary condition subroutines and, as already mentioned, can take the form of either patched- or overset-grid multi-block interfaces.

Portability is achieved through the use of MPI, the C preprocessor CPP, and the UNIX make utility. CPP is used to build either the parallel or serial versions from a single source code where MPI- and serial-specific code is isolated through the use of CPP directives. The makefile builds platform specific versions by invoking the correct compiler options and the CPP directives. The code has been run on the SGI Origin 2000, Cray T3E, Cray T90, DEC Alpha, HP and SGI workstations, and Intel Pentium-based PC.

GEOMETRY, CONDITIONS, AND GRIDS

The MIT Sirenian Propulsor is a notional design developed for use by the University code-development community. The geometry consists of an axisymmetric hull, modified NACA 65A duct, 11 stator blades, and 6 rotor blades. There is no rotor tip-gap.

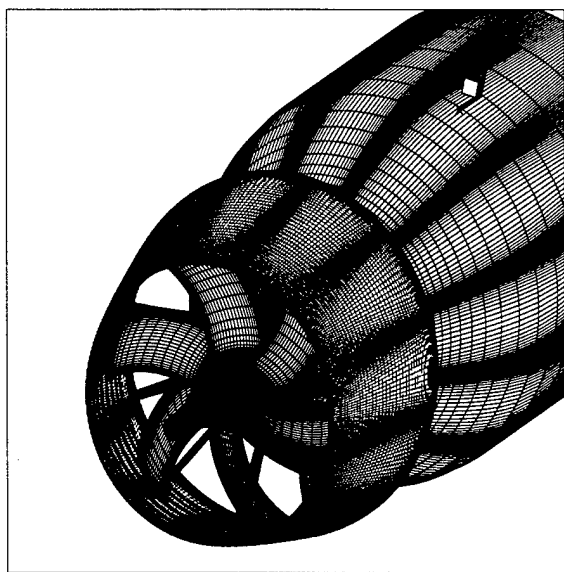


Figure 1. Overall view of geometry and surface grid.

For the simulations shown here, the geometry has been modified by adding one stator

blade (i.e., 12:6 ratio). This permits spatially-periodic simulation of a domain consisting of 2-stator passages and 1 rotor passage. Figures 1 and 2 show the geometry.

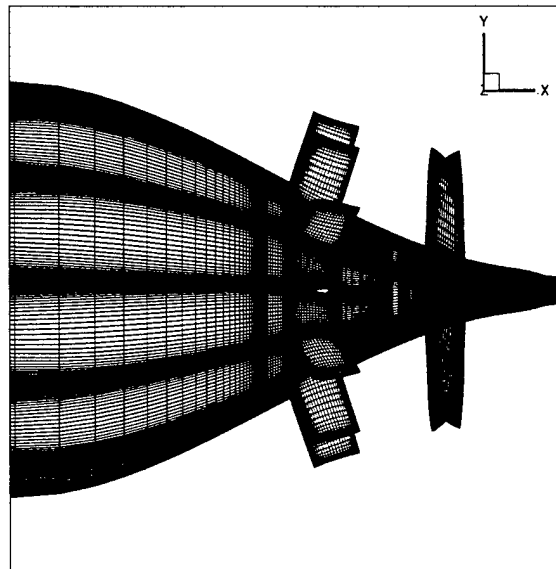


Figure 2. Stern view of geometry and surface grid, duct removed.

The design condition corresponds to an advance coefficient $J = V_A/nD_r = 1.52$ and Reynolds number based upon hull length $Re_L = UL/\nu = 3.2 \times 10^6$, where V_A is the speed of advance, D_r is the rotor diameter, U and L are ship speed and length, respectively, n is rpm, and ν is kinematic viscosity. The non-dimensional circumferential angular velocity is $\omega = 2\pi V_A/D_r J$ and the period of one complete revolution is $T = 2\pi/\omega$. The computational time step is related to T , the number of stator wakes $N_s = 12$, and the number of time steps per period N_p , i.e., $\Delta t = 2\pi/\omega N_s N_p$. An important parameter governing the unsteady response of a lifting surface, is the frequency parameter ξ . It is defined as $\xi = \omega_r C_r / (V_A + \omega_r r)$ and, for the Sirenian, is approximately 13, where $C_r = 0.027L$ is the rotor chord length and $\omega_r = \omega N_s$ is the frequency of encounter seen by the rotor.

Computational conditions are as follows. The code is run in inertial cylindrical coordinates using the blended $k-\omega/k-\epsilon$ model. Accuracy of the convective terms is set to 2nd-order upwind. Reynolds number is set to the design value $Re = 3.2 \times 10^6$. The number of time steps per period N_p is set to 60 which when coupled with $N_s = 12$, corresponds to 720 time steps per revolution or 0.5° per time step. Time step and ω is set using the CFD-determined speed-of-

advance, i.e., integration of the nominal wake from the unpropelled simulation.

To reduce the size of the domain, inlet boundary conditions are interpolated from a bare-hull simulation at $x/L=0.6$. As already mentioned, spatially-periodic boundary conditions are used upstream and downstream of the stator and rotor blade surfaces. Both patched and overset multi-block boundaries are used. For steady-flow simulation of the machine without the rotor, a uniform-flow initial condition is used. All other solutions then build upon this solution to provide initial conditions.

Grid generation is accomplished using GRIDGEN from Pointwise, Inc. H-type topologies were used around all foil sections and a sting was added to eliminate the pole singularity in the wake, the latter of which improves convergence. The domain inlet is at $x/L=0.6$, the exit is at $x/L=2.0$, and the far-field is at a radius of $1.0L$. The grid was generated with near-wall spacings set to $\Delta y=1.0 \times 10^{-5}$, which corresponds to $y^+ \approx 1.5$. Five blocks were initially generated in Cartesian coordinates and then decomposed into a 54-block system in cylindrical coordinates. The largest block is 27,500 points and the total grid system is approximately 1.1 million points.

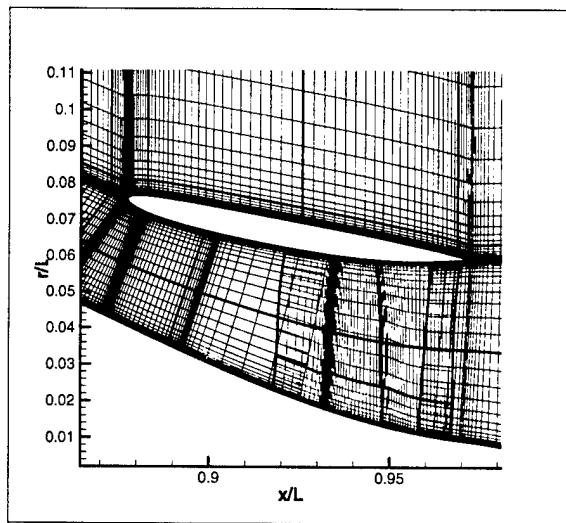


Figure 3. Grid system. k-constant plane (x-r) showing overset grids, blanked region, and block boundaries.

The grid system is shown in Figs. 3 and 4. Domain decomposition boundaries, which are located at arbitrary locations determined by load balancing requirements, are shown. The rotor blocks move with a grid speed of ωr and are coupled to the rest of the domain using an overset mesh as shown in the

figures. There is a corresponding region that is blanked out downstream of the stators.

The extent of this region is selected to maintain a minimum two grid-cell overlap. This approach, as opposed to an abutted "clicking" plane, is advantageous since the grid size and time step can be adjusted independently. For unsteady simulations, the coefficients are calculated "on-the-fly" for each time-step of the first period and saved to temporary files. Subsequent periods read the coefficients from these files. This greatly reduces computational effort since the search and calculation costs more than the CFD solution for a given time step.

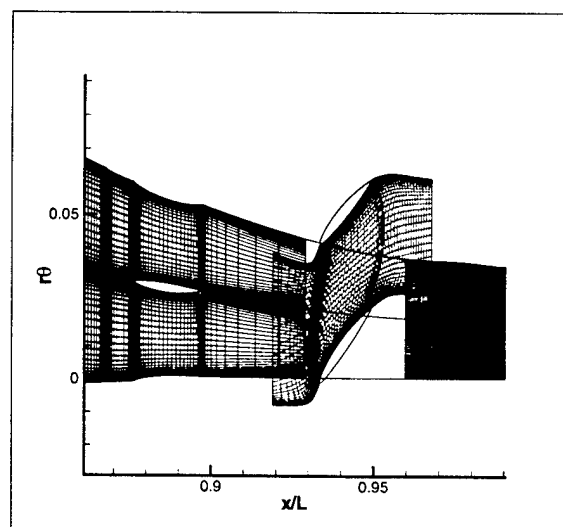


Figure 4. Grid system. j-constant plane (x-rθ) showing overset grids, blanked region, and block boundaries.

DISCUSSION

The integrated nature of this type of propulsor required the solution to be built-up in a progression of steps. First, steady-flow solution of the flow without the rotor was obtained. Then, the rotor was added but using circumferentially-averaged inflow. Finally, the unsteady simulation was turned on using the previous solution as the initial condition. In the following, each step of the process is discussed.

For steady flow without the rotor (i.e., body-duct-stator only), one stator passage is simulated. Figure 5 shows the velocity, pressure, and eddy-viscosity contours at mid passage. The duct is shown to be embedded in the thick stern boundary layer and the pressure side of the duct is on the inside of the machine. There is a small amount of separation on the body. It is not yet known if this is due to grid

resolution, turbulence model, or lack of rotor suction. Further study and verification is required. The eddy viscosity shows resolution of body, duct, and stator boundary layers and wakes and good continuity between blocks. It should be pointed out that the complex geometry and domain decomposition precludes use of the Baldwin-Lomax model. This type of application takes full advantage of the blended $k-\omega/k-\epsilon$ model wherein wall-proximity variables (e.g., normal distance) are not required.

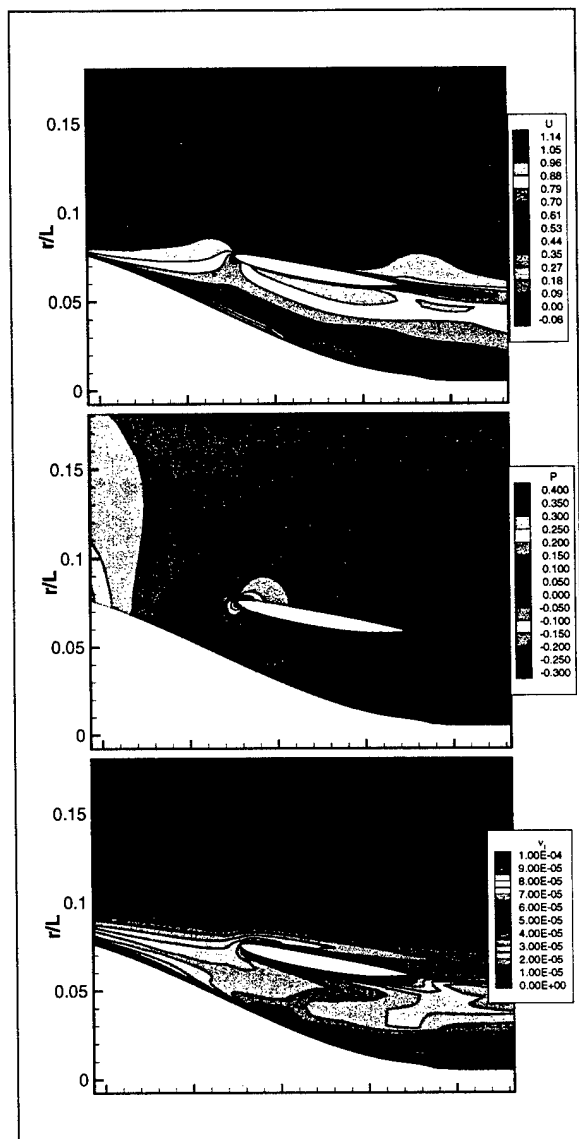


Figure 5. Body-duct-stator solution. (a) axial-velocity contours, (b) pressure contours, (c) eddy-viscosity contours.

Figure 6 shows the axial velocity at the location of the rotor-block inlet, i.e., $x/L=0.92$. Part (a) shows the spatial variation on the grids that pass through the stator passage, whereas part (b) shows

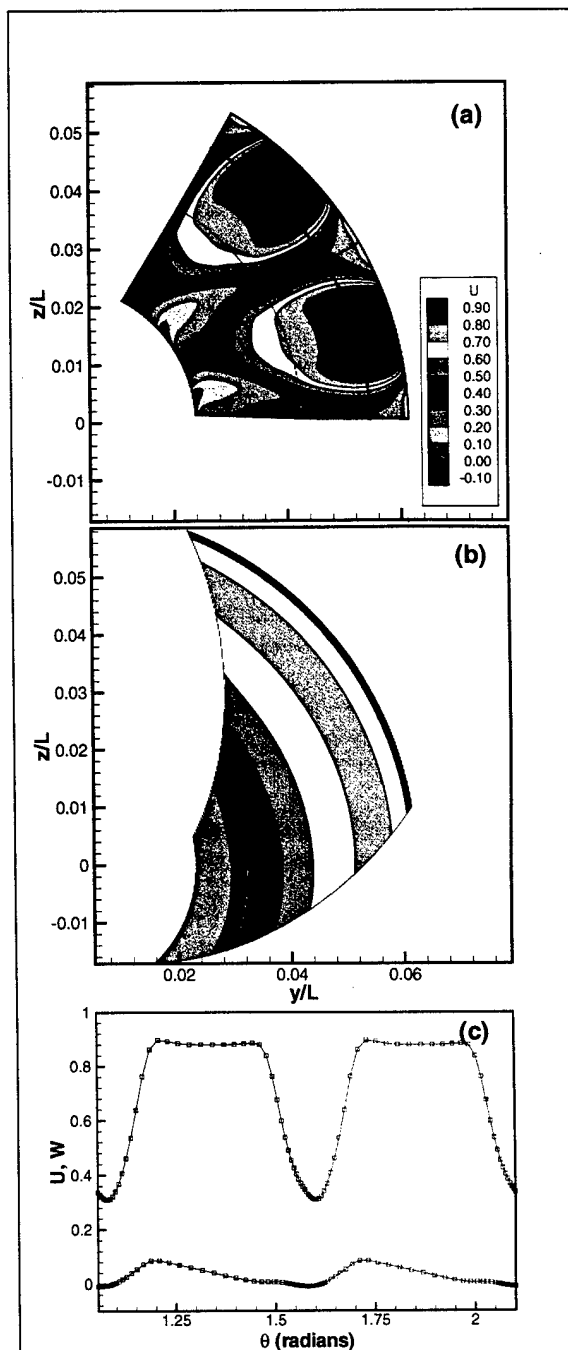


Figure 6. Body-duct-stator solution at inlet to rotor blocks. (a) axial-velocity, stator wakes, (b) axial-velocity, circumferential average, (c) circumferential variation of U- and W-components at $r/D_r=0.375$.

the circumferential average interpolated onto the inlet of the rotor blocks. A plot of the circumferential variation of U, W at $r/D_r \approx 0.375$ is shown in 6(c). The wake deficit is shown to be $U=0.5$ and the maximum pre-swirl is 0.125. The wakes appear to be fairly broad, however, the lack of verification prevents conclusions concerning performance of the

turbulence model. It should be noted that the stator Re is about 50,000.

If the velocity is integrated further downstream at the rotor plane, i.e., $x/L=0.94$, the average velocity is found to be 0.7. This is assumed to be the speed of advance V_A and is used for both setting ω and Δt and for putting the forces into the form of the traditional thrust and torque coefficients.

Flow unsteadiness and rotor-stator interaction is due to the rotor operating in the stator wakes. The predicted rotor inflow presents a high-frequency, large-amplitude unsteadiness ($\xi \approx 13$, $\Delta U = 0.5$). Implications for real machines are unknown, however, as shown by Paterson and Stern (1999), this would represent an extreme condition for a 2D gust-flow model, such as the MIT Flapping-Foil Experiment, which itself was a high-frequency experiment, wherein $\xi = 7.2$ and $\Delta U = 0.044$.

Steady-flow solutions are obtained with the rotor by using circumferentially-averaged information transfer between blocks. At upstream faces, all quantities are interpolated from the donor block and then averaged in the circumferential direction. Downstream faces use extrapolation of the velocity field and interpolation of the averaged pressure field. Using $J=1.52$ and $V_A=0.7$ as determined from the previous solution, the angular velocity is set to $\omega = -23.93$.

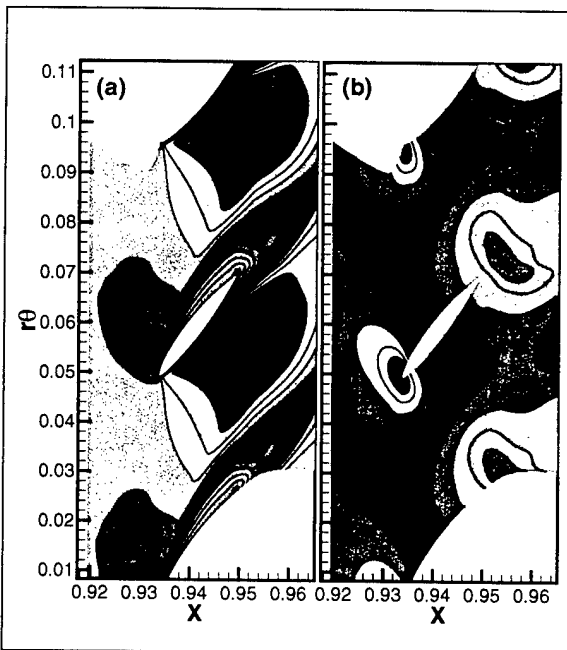


Figure 7. Steady-flow solution, contours in rotor passage, $r/D_p=0.375$. (a) axial-velocity, (b) pressure.

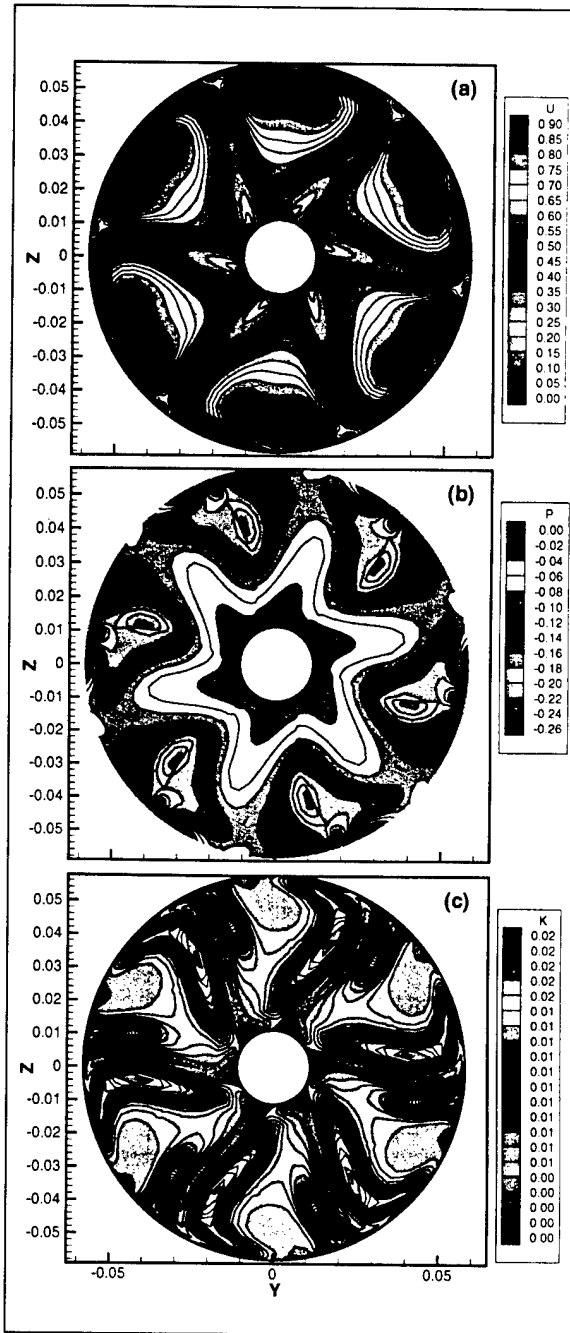


Figure 8. Steady-flow solution, rotor wake contours at $x/L=0.96$. (a) axial-velocity, (b) pressure, (c) turbulent kinetic energy.

Figure 7 shows flow contours in the rotor passage at $r/D_p=0.375$. Flow acceleration through the passage is clearly displayed, however, the rotor displays a thick boundary layer on the suction side of the lifting surface. This suggests that ω (i.e., rpm) needs to be adjusted to produce the correct angle-of-attack and loading. Several other J were investigated (1.82, 1.65, 1.45, 1.06), however each of these speeds resulted in large separation on the rotor. Further

study is required wherein J is adjusted by matching the design K_T and K_Q values. For reference, it is noted that potential-flow simulations using MIT PBD14 predict performance values of $K_T=0.215$, $K_Q=0.044$ (Kerwin, 1998).

Figure 8 shows contours of the rotor wake at $x/L=0.96$ (i.e., approx. $0.75C_T$ downstream of the rotor trailing edge). Part (a) shows axial-velocity contours. Rotor wakes and mid-passage flow acceleration are clearly shown. Even though a tip gap is not modeled, a tip juncture vortex is shown in both the velocity and pressure contours. Part (c) shows the turbulent kinetic energy. It is worth noting that the wake of both boundary layers is shown in the contours and that, in general, the blended $k-\omega/k-\epsilon$ model performs very well and is quite robust.

CONCLUDING REMARKS

Code development work for unsteady Reynolds-averaged Navier-Stokes simulation of integrated marine propulsors was presented. The goal of this work is to develop a physics-based simulation tool capable of predicting unsteady pressure fields at a level of fidelity sufficient for supporting model development. The MIT Sirenian Propulsor was used as verification/demonstration geometry. Steady flow solutions were presented for the machine without and with the rotor, the latter of which was obtained using a circumferentially-averaged information transfer to and from the overset rotor grid blocks. The integrated nominal wake provided the speed of advance and set the rpm of the rotor. Details of the flow were discussed.

Clearly, there is much work remaining. Foremost, verification and validation are required to provide a foundation for future modeling efforts. Following Stern et al. (1999), estimation of grid and temporal errors/uncertainty require solutions on 3 grids and 3 time steps. Steady flow verification will be performed for the geometry and conditions used herein to evaluate grid and model performance. Also, steady rotor simulation will be conducted by adjusting J so that K_T and K_Q match the loading predicted by potential flow codes.

Time-accurate simulations are currently underway. Preliminary work indicates that to prevent the stator wakes from dissipating when entering the rotor block, a good match in the circumferential distribution between blocks is required. This will be critical in accurate prediction of rotor-stator interaction and unsteady response of the rotor viscous flow.

With respect to physics and modeling, the capability for non-integer ratio of stator-to-rotor blades must be developed. There are two approaches to this problem, either complete 360° resolution (i.e., approx. 6M points at current gridding density) or development of periodic-phase-shift boundary conditions. Clearly, the latter is preferred from the perspective of computer resources. Also, a rotor-tip gap must be modeled and gridded so that the unsteady tip- and leakage-vortex system is resolved. The possible unsteady interactions of this system with the stator wakes are potentially important from the perspective of cavitation inception. Finally, while turbulence modeling is important, improvements require validation data.

With respect to code development, CFDShip-IOWA has achieved a fairly high level of sophistication. However, the solver and high-performance computing algorithms can be improved to speed convergence and reduce user workload in preparing large multi-block grid systems. This includes evaluation of Krylov vs. multigrid solvers for the pressure equation and implementation of a multi-level parallelism based upon both MPI and OpenMP.

ACKNOWLEDGEMENTS

This work was sponsored by Office of Naval Research grant N00014-97-1-0151 under the administration of Dr. Edwin Rood. All simulations were conducted using Department of Defense High-Performance Computing Modernization Program resources at the Naval Oceanographic Office (Bay St. Louis, MS) Major Shared Resource Center.

REFERENCES

1. Abdel-Maksoud, M., Menter, F.R., and Wuttke, H., "Numerical Computation of the Viscous Flow Around the Series 60 $C_b=0.6$ Ship with Rotating Propeller," Proceedings of the 3rd Osaka Colloquium on Advanced CFD Applications to Ship Flow and Hull Form Design, May 25-27, 1998, Osaka, Japan.
2. Chen, B., Stern, F., and Kim, W., "Computation of Unsteady Viscous Marine Propulsor Blade and Wake Flow," Proceedings of the 21st ONR Symposium on Naval Hydrodynamics, Santa Barbara, CA, 1994.
3. Chen, B. and Stern, F., "Computational Fluid Dynamics of Four-Quadrant Marine-Propulsor Flow," ASME Symposium on Advances in

- Numerical Modeling of Aerodynamics and Hydrodynamics in Turbomachinery," Washington D.C., 21-25 June 1998.
4. Chen, H.C., and Patel, V.C., "Near-Wall Turbulence Models for Complex Flows Including Separation," AIAA J., Vol. 26, No. 6, pp. 641-648, 1988.
 5. Chesnakas, C.J., and Jessup, S.D., "Propeller Tip-Vortex Measurements Using 3-Component LDV," Proceedings of the 22nd ONR Symposium on Naval Hydrodynamics, Washington D.C., 1998.
 6. Dreyer, J.J., and Zierke, W.C., "Solution of the Average-Passage Equations for the Incompressible Flow Through Multiple-Blade-Row Turbomachinery," Penn State Applied Research Laboratory, Technical Report No. TR 94-05, 1994.
 7. Hall, E.J., "Aerodynamic Modeling of Multistage Compressor Flowfields - Part 1: Analysis of Rotor/Stator/Rotor Aerodynamic Interaction," Proceedings of the 1997 International Gas Turbine & Aeroengine Congress & Exposition, Orlando, FL, June 1997.
 8. Hsiao, C.T., and Pauley, L.L., "Numerical Computation of Tip Vortex Flow Generated by Marine Propeller," ASME FED Summer Meeting, Washington D.C., 1998.
 9. Kerwin, J., Keenan, D., Black, S., and Diggs, J., "A Coupled Viscous/Potential Flow Design Method for Wake-Adapted, Multi-Stage, Ducted Propulsors Using Generalized Geometry," SNAME Transactions, Vol. 102, 1994, pp. 23-56.
 10. Kerwin, J., ONR Propulsor Hydrodynamics Workshop, Washington D.C., September, 1998.
 11. Lee, Y.T., Hah, C., Loellbach, J., "Three-Dimensional Navier-Stokes Solutions for a One-Stage Axial-Flow Pump," Proceedings of the 21st ONR Symposium on Naval Hydrodynamics, Santa Barbara, CA, 1994.
 12. Lee, Y.T., Feng, J., Merkle, C., and Tse, M., "Effects of Tip-Clearance Flows," Proceedings of the 22nd ONR Symposium on Naval Hydrodynamics, Trondheim, Norway, 1996.
 13. Menter, F.R., "Zonal Two Equation $k-\omega$ Turbulence Model for Aerodynamic Flows," AIAA Paper 93-2906, 1993.
 14. Paterson, E.G., and Sinkovits, R.S., "Performance, Scalability, and Portability of a MPI-based version of CFDSHIP-IOWA: Results of a NAVO PET Tiger-Team Collaboration," Proceedings of the 9th Department of Defense High-Performance Computing Modernization Program Users Group Meeting, Monterey, CA, July 1999.
 15. Paterson E.G., and Stern, F., "Computation of Unsteady Viscous Marine-Propulsor Blade Flows-Part 2: Parametric Study," ASME Journal of Fluids Engineering, Vol. 121, March 1999.
 16. Stern, F., Zhang, D., Chen, B., Kim, H., Jessup, S., "Computation of Viscous Marine Propulsor Blade and Wake Flow," Proceedings of the 21st ONR Symposium on Naval Hydrodynamics, Santa Barbara, CA, 1994.
 17. Stern, F., Paterson, E.G., and Tahara, Y., "CFDSHIP-IOWA: Computational Fluid Dynamics Method for Surface-Ship Boundary Layers, Wakes, and Wave Fields," IIHR Report #381, September 1996.
 18. Stern, F., Wilson, R.V., Coleman, H., and Paterson, E.G., "Verification and Validation of CFD Simulations," to appear in Proceedings 3rd ASME/JSME Joint Fluids Engineering Conference, San Francisco, July 1999.
 19. Taylor, L.K., Pankajakshan, R., Jiang, M., Sheng, C., Briley, W.R., Whitfield, D.L., Davoudzadeh, F., Boger, D.A., Gibeling, H.J., Gorski, J., Haussling, H., Coleman, R., and Buley, G., "Large-Scale Simulations for Maneuvering Submarines and Propulsors," AIAA Paper No. 98-2930, 29th AIAA Plasmadynamics and Lasers Conference, Albuquerque, NM, June 1998.
 20. Wilson, R., Paterson, E., and Stern, F., "Unsteady RANS Simulation of Model 5415 in Waves," Proceedings of the 22nd Symposium on Naval Hydrodynamics, Washington D.C., August 1998.

COMPUTATION OF THE INCOMPRESSIBLE VISCOUS FLOW AROUND A TRACTOR THRUSTER USING A SLIDING-MESH TECHNIQUE

Antonio Sánchez-Caja¹, Patrik Rautaheimo², Esa Salminen² and Timo Siikonen²

¹VTT Manufacturing Technology, Maritime and Mechanical Engineering
P.O.Box 1705, FIN-02044 VTT, Finland

Fax: 358-9-456 0619; E-Mail: Antonio.Sanchez@vtt.fi

² Helsinki University of Technology, Laboratory of Applied Thermodynamics
P.O.Box 4400, FIN-02015 HUT, Finland

Fax: 358-9-451 3418; E-Mail: Patrik.Rautaheimo@hut.fi,
Esa.Salminen@hut.fi, Timo.Siikonen@hut.fi

ABSTRACT

The unsteady flow around a tractor thruster is simulated by solving the RANS equations with a sliding mesh technique. A multiblock Navier–Stokes solver (FINFLO) developed at Helsinki University of Technology is used in the calculations. In this paper a computational method with special emphasis on the sliding mesh technique is described. The flow over a BB series propeller is analysed and a comparison with experimental data is made. This calculation is made with a fine grid and used as a reference for the rest of the computations, where the flow around the tractor thruster is simulated. The thruster consists of the BB-series propeller, a pod and a strut. The sliding surface is located between the propeller and strut. The calculations are performed in two different ways. In the first case the flow quantities are circumferentially averaged on the sliding surface in order to reduce computing time. The second calculation is time-accurate.

INTRODUCTION

Azimuthing propulsor systems have long been confined to low propulsive power levels. The reason is the limitation of torsional moments that can be transmitted by Z-drive units. Podded propulsors have removed such a limitation. An electric motor coupled directly to the propeller is housed inside a pod and located as a separated unit outside the ship hull. Podded propulsors have many advantages over conventional ones, e.g. improved wake to the propeller, and, consequently, reduction of vibrations and noise, better manoeuvrability, simpler engine control and more flexibility for the selection of ship forms in the hydrodynamic design of the stern. This also allows space savings as well as higher propulsion efficiency. Over the last decade Kvaerner Masa-Yards and ABB have pioneered the use of this innovative Diesel-electric propulsion system for high propulsive power levels. They have named it Azipod (azimuthing podded drive).

In recent years Reynolds Average Navier–Stokes (RANS) solvers have been increasingly applied at several research institutions around the world for the prediction of the flow around marine propeller blades. At the Technical Research Centre of Finland (VTT) the application of RANS solvers to marine propeller analysis started in 1995 with encouragingly good res-

ults [1]. Since then the application of RANS solvers have been extended to more complex propeller configurations, e.g. to podded propulsors. In such complicated geometries the flow is basically unsteady, which should be taken into account in the computational model.

There are different approaches to solving the Navier–Stokes equations in the case of rotating machinery. The most accurate and straightforward one is to divide the computational mesh into stationary blocks fixed to the non-rotating part of the machinery and into rotating blocks. They are connected to each other through a sliding surface. The problem with this approach is that the flow is modelled as being time dependent, which requires a great deal of computing time. Another and cheaper method is to find a steady-state solution in a rotating coordinate system. Then the velocities are expressed in the rotating frame and extra Coriolis and centrifugal forces are introduced into the Navier–Stokes equations. A disadvantage of this approach is that there might be numerical problems far away from the rotating axis, and also for turbulence modelling one must keep in mind what velocities should be used to define the strain and vorticity rates. An alternative approach is to use the absolute Cartesian velocities in the rotating frame. This method is accurate only with axisymmetric flows, but is applied in the present study for the

unsteady flow around the Azipod, and compared to the time-accurate calculation with the sliding mesh.

The multiblock Navier-Stokes solver (FINFLO) used in this study has been developed at Helsinki University of Technology [2]. The original code has been extended for incompressible flows using a pseudo-compressibility method [3]. In the following, the physical modelling and the solution methods used are described. Next, the steady-state analysis of a BB series propeller is provided, and the results are compared with experimental data. This calculation is made with a very fine grid to serve as a reference for the rest of the computations. A quasi-steady analysis is then performed for the tractor thruster using circumferentially averaged conditions on the sliding surface. The thruster consists of the above mentioned BB-series propeller, a pod and a strut. The final calculation for the thruster is time-accurate and the sliding-mesh technique is applied. Comparison between the calculated and the mean experimental thrust and torque forces is provided, and some details of the flow are illustrated. The validation presented in this paper has been possible thanks to the release of some experimental data from some of the first preliminary versions of the Azipod system.

SOLUTION METHODS

Governing Equations

The flow simulation is based on the solution of the Reynolds averaged Navier-Stokes equations in a coordinate system which rotates around the x -axis with an angular velocity Ω . Turbulence is modelled using the $k-\epsilon$ -model. The rotational speed of the domain is $\vec{\Omega} \times \vec{r} = [0, -\Omega z, \Omega y]^T$. The equations can be written in a conservative form without the energy equation as

$$\frac{\partial U}{\partial t} + \frac{\partial(F-F_v)}{\partial x} + \frac{\partial(G-G_v)}{\partial y} + \frac{\partial(H-H_v)}{\partial z} = Q \quad (1)$$

where U is a vector of conservative variables $U = [\rho, \rho u, \rho v, \rho w, \rho k, \rho \epsilon]^T$, ρ is the density, u, v and w are the absolute velocity components in a Cartesian coordinate system, and Q is a source term. In the steady-state solution the time-derivative term is meaningless and is only utilized in the numerical solution. Instead, a source term is introduced in the momentum equation [4]. Altogether with the turbulence equations, the source term becomes $Q = [0, 0, \rho \Omega w, -\rho \Omega v, Q_k, Q_\epsilon]^T$. Thus in the quasi-steady simulation the source term Q has non-zero components for the equations for y - and z -momentum and turbulence. In the time-accurate integration the source terms for the turbulence equations are retained,

but there are no source terms in the momentum equation and the time-derivative must be discretized accurately. However, the differences in these two simulation approaches are small.

The inviscid fluxes are

$$F = \begin{pmatrix} \rho \hat{u} \\ \rho u \hat{u} + p + \frac{2}{3} \rho k \\ \rho v \hat{u} \\ \rho w \hat{u} \\ \rho \hat{u} k \\ \rho \hat{u} \epsilon \end{pmatrix} \quad G = \begin{pmatrix} \rho \hat{v} \\ \rho v \hat{v} + p + \frac{2}{3} \rho k \\ \rho w \hat{v} \\ \rho \hat{v} k \\ \rho \hat{v} \epsilon \end{pmatrix} \quad H = \begin{pmatrix} \rho \hat{w} \\ \rho u \hat{w} \\ \rho v \hat{w} \\ \rho w \hat{w} + p + \frac{2}{3} \rho k \\ \rho \hat{w} k \\ \rho \hat{w} \epsilon \end{pmatrix} \quad (2)$$

where p is the pressure. The kinetic energy of turbulence $2/3 \rho k$ is connected with the pressure and appears here in the convective, i.e. inviscid fluxes. Above the convective, i.e. the relative speeds are

$$\hat{u}_i = u_i - (\vec{\Omega} \times \vec{r})_i \quad (3)$$

In this case the individual components are

$$\begin{aligned} \hat{u} &= u \\ \hat{v} &= v + \Omega z \\ \hat{w} &= w - \Omega y \end{aligned} \quad (4)$$

The viscous fluxes are

$$F_v = \begin{pmatrix} 0 \\ \tau_{xx} + \frac{2}{3} \rho k \\ \tau_{xy} \\ \tau_{xz} \\ \mu_k (\partial k / \partial x) \\ \mu_\epsilon (\partial \epsilon / \partial x) \end{pmatrix} \quad G_v = \begin{pmatrix} 0 \\ \tau_{xy} \\ \tau_{yy} + \frac{2}{3} \rho k \\ \tau_{yz} \\ \mu_k (\partial k / \partial y) \\ \mu_\epsilon (\partial \epsilon / \partial y) \end{pmatrix} \quad H_v = \begin{pmatrix} 0 \\ \tau_{xz} \\ \tau_{yz} \\ \tau_{zz} + \frac{2}{3} \rho k \\ \mu_k (\partial k / \partial z) \\ \mu_\epsilon (\partial \epsilon / \partial z) \end{pmatrix} \quad (5)$$

where the viscous stress tensor is

$$\tau_{ij} = \mu \left[\frac{\partial u_j}{\partial x_i} + \frac{\partial u_i}{\partial x_j} \right] - \overline{\rho u_i'' u_j''} \quad (6)$$

The anisotropic and the shear stress parts of the Reynolds stresses $\rho u_i'' u_j'' - \frac{2}{3} \rho k \delta_{ij}$ are included in the viscous fluxes. The stress tensor (6) contains a laminar and a turbulent part. For the Reynolds stresses the Boussinesq approximation is used

$$-\rho u_i'' u_j'' = \mu_T \left[\frac{\partial u_j}{\partial x_i} + \frac{\partial u_i}{\partial x_j} \right] - \frac{2}{3} \rho k \delta_{ij} \quad (7)$$

where μ_T is a turbulent viscosity. The diffusion coefficients of the turbulence quantities are written as

$$\mu_k = \mu + \frac{\mu_T}{\sigma_k} \quad \mu_\epsilon = \mu + \frac{\mu_T}{\sigma_\epsilon} \quad (8)$$

where σ_k and σ_ϵ are the appropriate Schmidt's numbers.

Turbulence Modeling

In the low-Reynolds number $k-\epsilon$ model, the solution is extended to the wall instead of using a wall-function approach [5]. The source term for Chien's model is given as

$$Q = \begin{pmatrix} P - \rho \bar{\epsilon} - 2\mu \frac{k}{y_n^2} \\ c_1 \frac{\bar{\epsilon}}{k} P - c_2 \frac{\rho \bar{\epsilon}^2}{k} - 2\mu \frac{\bar{\epsilon}}{y_n^2} e^{-y^+/2} \end{pmatrix} \quad (9)$$

where y_n is the normal distance from the wall, and y^+ is defined by

$$y^+ = y_n \frac{\rho u_\tau}{\mu_w} = y_n \frac{\sqrt{\rho \tau_w}}{\mu_w} \approx y_n \left[\frac{\rho |\nabla \times \vec{V}|}{\mu} \right]_w^{1/2} \quad (10)$$

In Chien's model $\bar{\epsilon}$ is solved instead of ϵ . The variable $\bar{\epsilon}$ is defined so that it obtains a zero value at the wall and the true dissipation can be expressed as $\epsilon = \bar{\epsilon} + \frac{2\mu}{\rho} \frac{k}{y_n^2}$. The production of turbulent kinetic energy is modelled using Eq. (7)

$$\begin{aligned} P &= -\rho u_i'' u_j'' \frac{\partial u_i}{\partial x_j} \\ &= \left[\mu_T \left(\frac{\partial u_j}{\partial x_i} + \frac{\partial u_i}{\partial x_j} \right) - \frac{2}{3} \delta_{ij} \rho k \right] \frac{\partial u_i}{\partial x_j} \\ &= \left[\mu_T \left(\frac{\partial u_j}{\partial x_i} + \frac{\partial u_i}{\partial x_j} \right) \right] \frac{\partial u_i}{\partial x_j} \end{aligned} \quad (11)$$

In the $k-\epsilon$ model the turbulent viscosity is calculated from

$$\mu_T = c_\mu \frac{\rho k^2}{\bar{\epsilon}} \quad (12)$$

In order to avoid unphysical growth of the turbulent viscosity μ_T , e.g., near the stagnation point, the production of turbulent kinetic energy P is limited as

suggested by Menter [6]

$$P = \min(P, 20 \rho \bar{\epsilon}) \quad (13)$$

According to the conducted tests [6], the maximum of the ratio $P/\rho \bar{\epsilon}$ inside shear layers is about two and, therefore, this limit should not affect the well-behaving regions of the flow field. Only the problems encountered near the stagnation point will disappear.

The equations for k and ϵ contain empirical coefficients. In this study the following coefficients are applied

$$\begin{aligned} c_1 &= 1.44 & \sigma_k &= 1.0 \\ c_2 &= 1.92(1 - 0.22e^{-Re_T^2/36}) & \sigma_\epsilon &= 1.3 \\ c_\mu &= 0.09(1 - e^{-0.0115y^+}) \end{aligned} \quad (14)$$

where the turbulence Reynold's number is defined as

$$Re_T = \frac{\rho k^2}{\mu \bar{\epsilon}} \quad (15)$$

Numerical Methods

Basic Features

Since the flow is incompressible, the time derivative of density in Eq. (1) disappears. In a pseudocompressibility approach [3] this is replaced by an artificial time derivative of pressure, and the continuity equation $\nabla \cdot \vec{V} = 0$ is replaced by

$$\frac{1}{\beta^2} \frac{\partial P}{\partial \tau} + \nabla \cdot \vec{V} = 0 \quad (16)$$

where $P = p/\rho$. In the present approach the original conservative fluxes are retained, but utilizing the chain rule we obtain

$$\frac{\partial \rho}{\partial \tau} \approx \frac{\partial \rho}{\partial p} \frac{\partial p}{\partial \tau} = \frac{1}{\beta^2} \frac{\partial p}{\partial \tau} \quad (17)$$

i.e. the derivative $\partial \rho / \partial p$ is replaced by an artificial pseudocompressibility factor $1/\beta^2$ [7]. The following continuity equation is obtained

$$\frac{1}{\beta^2} \frac{\partial p}{\partial \tau} + \nabla \cdot \rho \vec{V} = 0 \quad (18)$$

The flow equations are solved using Roe's method [8], which was originally designed for compressible flow, but can be applied with the artificial compressibility concept. In the derivation of the Jacobian matrix of the flux-vector, the pseudolinearization $\partial \rho / \partial p = 1/\beta^2$ is applied for each density-derivative term. In the original method (16) a pressure-derivative term is added only into the continuity equation. In the present

way the characteristic speeds reduce to simple expressions of $\lambda_{1,2} = u \pm \beta$. With a compressible flow the corresponding speeds are $\lambda_{1,2} = u \pm c$, where c is the speed of sound. This makes the flux calculation straightforward and similar to the compressible formulae. The flux is calculated as

$$\hat{F} = T^{-1}F(TU) \quad (19)$$

where T is a rotation operator that transforms the dependent variables to a local coordinate system normal to the cell surface. In this way, only the Cartesian form F of the flux is needed. This is calculated from

$$\begin{aligned} F(U^l, U^r) &= \frac{1}{2} [F(U^l) + F(U^r)] \\ &- \frac{1}{2} \sum_{k=1}^K r^{(k)} |\lambda^{(k)}| \alpha^{(k)} \end{aligned} \quad (20)$$

where U^l and U^r are the solution vectors evaluated on the left and right sides of the cell surface, $r^{(k)}$ is the right eigenvector of the Jacobian matrix $A = \partial F / \partial U = R \Lambda R^{-1}$, the corresponding eigenvalue is $\lambda^{(k)}$, and $\alpha^{(k)}$ is the corresponding characteristic variable obtained from $R^{-1} \delta U$, where $\delta U = U^r - U^l$. A MUSCL-type approach has been adopted for the evaluation of U^l and U^r . In the evaluation of U^l and U^r , primary flow variables (p, u, v, w), and conservative turbulent variables ($\rho k, \rho \epsilon$) are utilized. For the turbulence quantities, flux calculation utilizes second-order upwinding with a limiter of van Albada [9].

It should be noted that the flux calculation based on Eq. (20) can be interpreted as a central difference + a damping term. With an incompressible flow this damping term is based on β and is non-physical, but works properly. Since the damping term is not physically accurate, as is the case with the compressible flow assumption, it has been simplified and only significant terms are maintained.

Discretization

The quasi-steady approach and the time-accurate solution utilize the same basic steady-state algorithm. Since the differences between the two approaches are small, in the following the main features of the steady-state solution are firstly described. In the present solution, a finite-volume technique with a structured grid is applied. The flow equations have a discrete form

$$V_i \frac{dU_i}{d\tau} = \sum_{\text{faces}} -S(\hat{F} - \hat{F}_v) + V_i Q_i = R_i \quad (21)$$

where the sum is taken over the faces of the computational cell. The inviscid part of the flux is

$$\hat{F} = \begin{pmatrix} \rho \hat{U} \\ \rho u \hat{U} + n_x p \\ \rho v \hat{U} + n_y p \\ \rho w \hat{U} + n_z p \\ e \hat{U} + p \end{pmatrix} \quad (22)$$

Here $n_x \vec{i} + n_y \vec{j} + n_z \vec{k}$ is the unit normal vector of the cell face, $\hat{U} = n_x u + n_y v + n_z w$ is the velocity component normal to a stationary cell surface, and \hat{U} is the convective velocity relative to the moving cell surface. The same flux formula is applied in the case of the time-accurate solution. In both cases the viscous fluxes are evaluated using a thin-layer approximation. The thin-layer model is activated in all coordinate directions.

Eq. (21) is integrated in time implicitly by applying the DDADI-factorization [10]. This is based on the approximate factorization and on the splitting of the Jacobians of the flux terms. The resulting implicit stage consists of a backward and forward sweep in every coordinate direction. The boundary conditions are treated explicitly, and a spatially varying time step is utilized. Hence, the integration is not accurate in time, but provides an iterative way to approach the steady-state. In order to further accelerate the convergence, multigrid cycling is used. The method of Jameson [11] with a simple V-cycle has been adopted. When the multigrid is activated, turbulence is not evaluated on the coarse levels. Instead, the turbulent viscosities are transformed onto the coarse grid levels, as are the other flow variables. This treatment is essential when the $k - \epsilon$ -model is used, and it may also improve the stability with the algebraic model. More details of the solution algorithm are given in [4] and [12].

The time-accurate integration shares the same basic features described above, but now the pseudo time-integration is performed inside a physical time step and a true time derivative is added on the right-hand side of Eq. (21). A three-level fully implicit scheme is applied for the time-integration [13]. Then the residual R_i defined by the right-hand side of Eq. (21) is discretized in time as

$$\begin{aligned} R_i = & - V_i \frac{3U^{n+1} - 4U^n + U^{n-1}}{2\Delta t} \\ & - \sum_{\text{faces}} S(\hat{F}^{n+1} - \hat{F}_v^{n+1}) + V_i Q_i^{n+1} \end{aligned} \quad (23)$$

Here n indicates the time level and Δt is a physical time step. From Eq. (23) it is seen that the time-derivative term is treated as a source term. It should

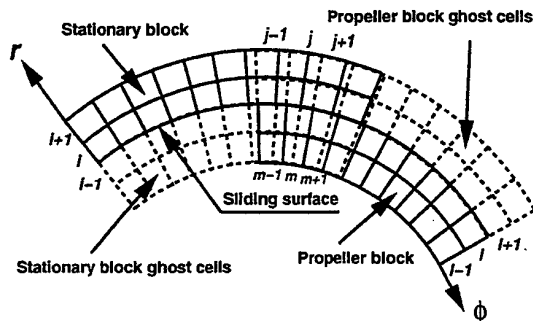


Figure 1: Interface between a moving block and a stationary block.

be noted that the time-derivative term replaces the additional source terms caused by the rotation and here Q only stands for the sources in the turbulence equations (9).

In the time-accurate case a kind of steady-state integration inside the true time step is performed using the solution methods described above. The left-hand side of Eq. (21) is utilized in the iteration exactly in the same way as in the steady-state calculation. The iteration converges as the residual of Eq. (23) approaches zero. During the solution the grid block describing the impeller rotates and a new position as well as the geometrical properties including the new rotational speeds are calculated as the calculation proceeds to the next time level. The impeller is connected to the rest of the domain using a sliding mesh technique. As a result the grid lines between the impeller blocks and the stator are discontinuous. A mass conserving interpolation is made between the connecting blocks at every time step [14]. This is discussed in the next section.

The flow solver utilizes a multiblock grid. The boundary conditions between the blocks are treated explicitly and only on the highest grid level. In order to decrease computational times the code is parallelized. The parallelization is done over the blocks. The details concerning the parallelization can be found from Ref. [15].

Sliding Mesh Model

The sliding mesh technique is ideally suited for problems involving rotor/stator interactions, e.g. propeller/ship hull geometry. In the sliding mesh technique two grids are employed: one for the stationary components and another for the propeller. The propeller grid moves with respect to the stationary grid along a sliding surface. Fig. 1 illustrates the interface between a propeller block and a stationary block.

Since the grid lines across the sliding surface are

not continuous, the information transfer across the surface has to be done using interpolation. A conservative interpolation can be evaluated discretely as follows: Let C_j be the discrete flux in the propeller block to be interpolated at a particular ϕ position from the discrete flux in the stationary block. A piecewise constant projection of C from one grid on to the other is [14]

$$C_j = \sum_m C_m N_j^m$$

where

$$N_j^m = \begin{cases} 0, & \text{if } \phi_{m+1/2} < \phi_{j-1/2} \\ 0, & \text{if } \phi_{m-1/2} > \phi_{j+1/2} \\ \frac{1}{\Delta\phi_j} \int_{\max(\phi_{m-1/2}, \phi_{j-1/2})}^{\min(\phi_{m+1/2}, \phi_{j+1/2})} d\phi, & \text{otherwise} \end{cases}$$

The N_j^m represent the relative area (angle) of overlap of cell m onto the cell j , ($0 \leq N_j^m \leq 1$). The discrete flux balance is maintained as

$$\sum_j C_j \Delta\phi_j = \sum_m C_m \Delta\phi_m$$

since $\sum_j N_j^m \Delta\phi_j = \Delta\phi_m = \phi_{m+1/2} - \phi_{m-1/2}$.

In the flow solver used in this study, it is required that at one time step (e.g. $t = 0$) the surface grids on the opposite sides of the sliding surface match each other. This means that the grid point clustering in the circumferential direction must be the same on both grids. The information transfer across the sliding surface is handled in two phases. In the first phase, the values in the ghost cells are updated by assuming a zero rotation angle. The values in the ghost cells of the moving block are copied from the corresponding stationary block cells, and the values in the stationary block ghost cells are copied from the appropriate moving grid cells. In the second phase, the ghost cell values are rotated according to the rotation angle. In this phase the interpolation weights N_j^m are utilized.

Assuming N computational cells in the circumferential direction, we get $(N+2) \times (N+2)$ interpolation weight matrix. The "+2"s represent the first ghost cells at the ends of the circular arc. These ghost cells are not shown in Fig. 1. The weight matrix is valid for all the circumferential cell rows, so it needs to be computed only once for each sliding patch.

PROPELLER IN A UNIFORM FLOW

Geometry and Meshing

The propeller selected for the RANS calculations is a 0.219 m diameter, four-bladed propeller of the BB-series. Measurements from open water tests performed at MARIN for the BB-series are found in [16].

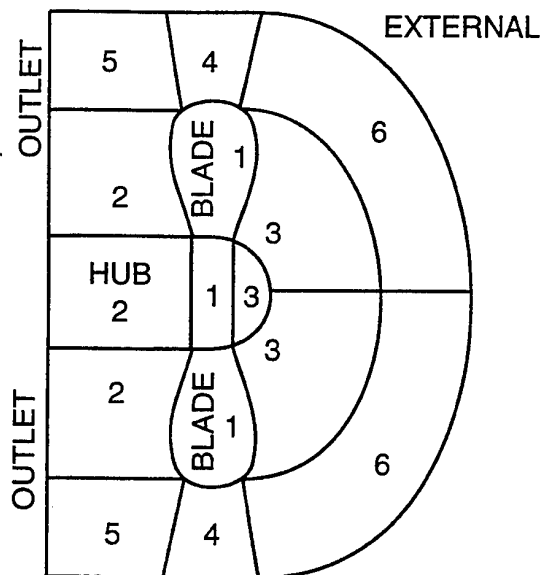


Figure 2: Position of the grid blocks and boundary conditions for the propeller.

Model tests have also been conducted at VTT. The Troost BB propeller in the VTT open water tests had a modified hub, i.e. the hub diameter ratio (about 0.23) was larger than that of the standard BB propeller and the coning angle was different. The same hub was also used in the Azipod tests made at VTT. The calculations presented in this paper correspond to the VTT geometry with an advance ratio $J = 0.8$, and Reynolds number $Re = 4 \times 10^5$.

For the RANS calculation only the space between two contiguous propeller blades was modelled to take full advantage of the periodicity of the flow and geometry. The grid consists of six blocks, and the topology is schematically shown in Fig. 2. The grid has the inlet boundary modelled by a spherical sector located at three diameters from the propeller centre. The outlet boundary is a plane located at $x/D = -3.0$, i.e. three diameters downstream of the propeller plane. Both boundaries are connected to each other by an external boundary consisting in a cylindrical surface placed at $r/D = 3.0$, i.e. at three diameters from the propeller axis. The total number of cells is about 1,300,000. Fig. 3 shows the surface grid of the whole propeller. Fine grid spacings are used in the vicinity of the leading and trailing edges of the propeller blades in the chordwise direction, and near the blade tip and hub in the radial direction. The minimum grid spacing in the circumferential direction for the resolution of the boundary layer is 0.3×10^{-5} m. After computations the parameter y^+ was found to be lower than 0.6 along most of the blade. Only at the tip the

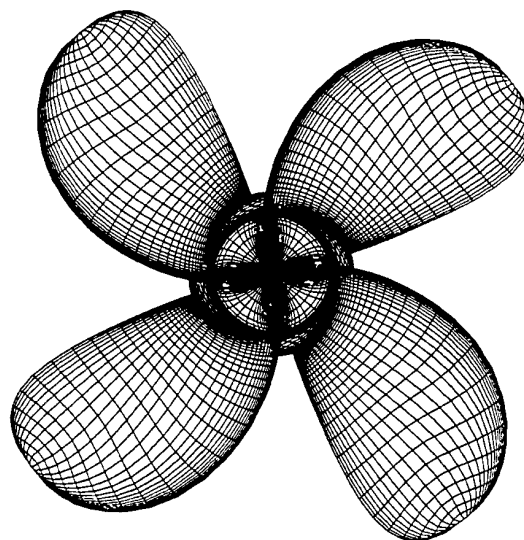


Figure 3: Surface grid of the propeller. Every other grid line is drawn.

mean value of y^+ is a little higher than one.

The hub and blade surfaces of the propeller are rotating solid walls. The lateral surfaces adjacent to the propeller blades have a cyclic boundary condition. Block boundaries, where two adjacent block surfaces are coincident, are defined as connectivities. Uniform and inviscid flow conditions are applied to the inlet and external boundary surfaces, and the streamwise gradients of the flow variables are set to zero at the outlet.

Results

The computations were performed on a SGI Origin 2000 machine. Three processors were used. The computation time was 45 seconds per iteration cycle. For the second and third grid levels the CPU times are 1/8 and 1/64 times those of the first grid level, respectively. A satisfactory convergence was obtained with a Courant number of 0.5 and two multigrid levels. The convergence histories of the overall lift and drag coefficients are presented in Figs. 4 and 5.

Differences less than 1.5 % in the calculated thrust and torque coefficients and about 1.5 % in efficiency are found relative to measurements from MARIN, where, in fact, the Reynolds number was five times higher than that in the simulation. If experimental values obtained at VTT are chosen as the reference, calculations over-predict the thrust and torque coefficients by 5 %. However, the error in efficiency is only about 0.3 %. The discrepancies in the experimental measurements can be attributed to the differences in

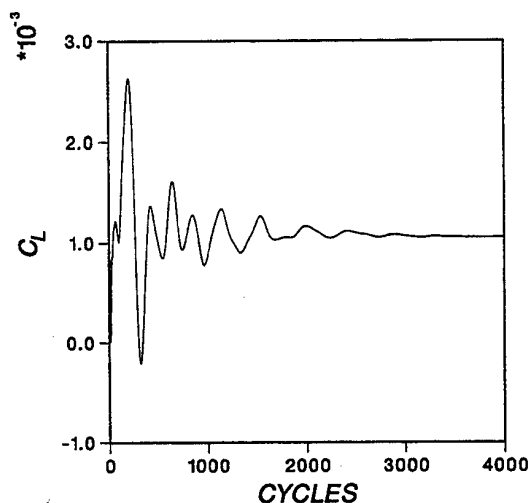


Figure 4: Convergence history of the lift coefficient for the propeller.

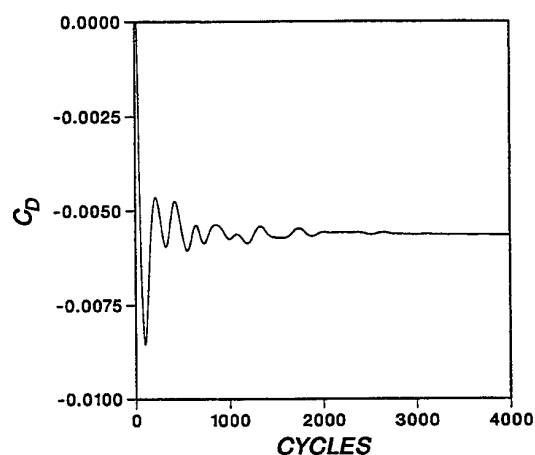


Figure 5: Convergence history of the drag coefficient for the propeller.

both the Reynolds number used in the tests and the shape of the hub in the experimental models. In fact, the Reynolds number for which VTT tests were performed for this tentative Azipod version was close to 4×10^5 , which is small compared to 2×10^6 used in MARIN data. The experimental apparatus may also be responsible for part of the discrepancies, as it has been recognised in comparative tests performed at various towing tanks with identical propeller models.

When passing from the second grid level (coarse grid) to the first grid level (finest grid) the improvement of the efficiency prediction is about 4 % and that

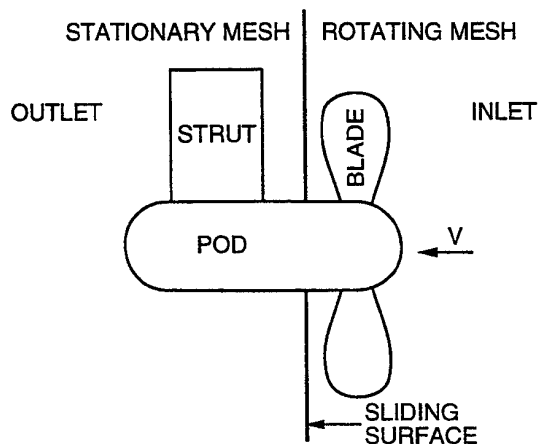


Figure 6: Geometry and boundary conditions for the tractor thruster.

of the thrust prediction about 2 %. This data will be useful when interpreting the correlation with experiments for the Azipod calculation.

THE TRACTOR THRUSTER

Geometry and Mesh

The thruster consists of the BB-series propeller mentioned in the preceeding section, a pod and a strut. A sketch of the geometry is shown in Fig. 6. The flow around the tractor thruster is no longer cyclic, as was for the case of the propeller alone. The strut breaks the symmetry. Consequently, periodic or cyclic boundary conditions cannot be applied anymore to reduce the computational domain, and the entire flow region must be meshed.

The grid consists of 17 blocks divided into two groups representing the space near and far away from the pod. The space near the pod extends from the pod to a distance of about one propeller radius. The space far away from the pod extends from the propeller radius to the outermost external boundary. The grid has a C-O topology in the axial-circumferential direction for the group of blocks far away from the pod, and a O-O topology for the blocks contiguous to the pod. The sliding surface is located between the propeller and the strut. The total number of cells is 814,080. The grid on the thruster surfaces is shown in Fig. 7.

The minimum grid spacing in the circumferential direction for the resolution of the boundary layer is about twice that of the grid of the computation for the propeller alone. This is enough to have the mean value of y^+ close to 1 at the 0.7 nondimensional radius of the propeller.

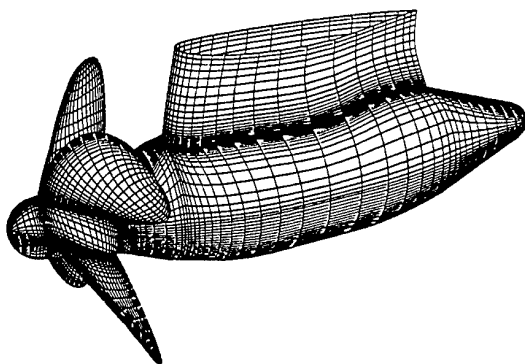


Figure 7: Grid on the thruster surface.

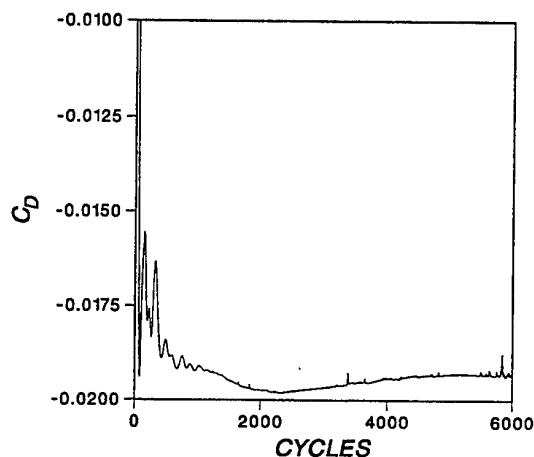


Figure 8: Convergence history of the drag coefficient for the tractor thruster. Quasi-steady simulation.

Convergence

Quasi-Steady Calculation

In these calculations the Courant number was 0.5, and the number of multigrid levels was two. The convergence history of the overall drag coefficient is presented in Fig. 8. The computation time with four processors was 19.8 seconds per iteration cycle.

Time-Accurate Calculation

The computation was started by taking as an initial guess the results obtained from the quasi-steady calculation. For the first grid level the Courant number was 5, the number of internal iterations per time step 50, and the time increment Δt corresponds to an angular step of 0.625° . It should be noted that the Cour-

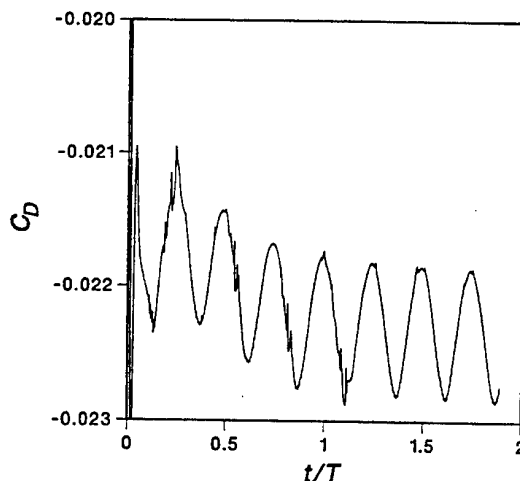


Figure 9: Convergence history of the drag coefficient for the tractor thruster. Time-accurate simulation.

ant number corresponds to the step-size of $\Delta \tau$ utilized inside the true time-step. In the time-accurate case $\Delta \tau$ can be larger than in the quasi-steady calculation. Slightly more than one thousand time steps were taken until a sufficiently stable periodic solution was established. The total computation time was almost 300 hours with four processors. The total CPU time required to obtain converged results for the forces and the moments is about 9 times that of the quasi-steady calculation.

The convergence history of the overall drag coefficient residuals for the first grid level is presented in Fig. 9. The corresponding history of the L_2 -norm of the x -momentum residuals within five physical time steps is shown in Fig. 10.

In order to verify the precision of the time-accurate method, the simulation was performed on the second grid level using time-step sizes that correspond to angular steps of 0.625° and 1.25° . This coarser grid has a number of cells equal to $1/8$ of the first grid level (half of the cells in each one of the three block directions). The differences in the thrust and the torque coefficients between the calculations with different time steps are only about 1 %, which shows that the time-step size is adequate.

Analysis of Results

Quasi-Steady Calculation

After 3,000 iterations most of the forces, especially those on the propeller surfaces, have converged to one percent accuracy. Differences from experimental values in thrust of 8.5 % and in efficiency of about 6.5 % appear. They can be attributed to several reasons:

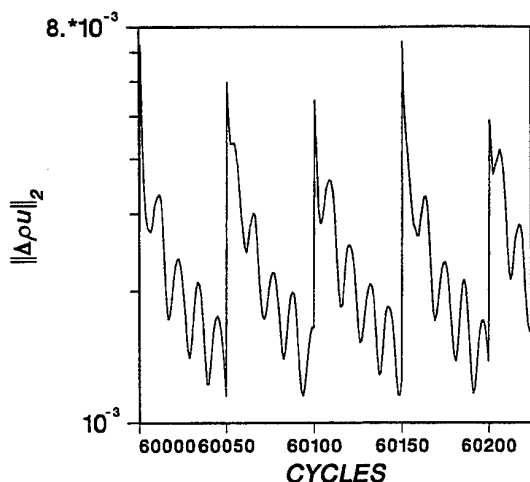


Figure 10: Convergence history of the L_2 -norm of x -momentum residuals within five time steps.

1. The grid used for the Azipod calculations in the first level represents the propeller geometry with a little less precision than the second grid level of the propeller-alone grid. This means that the error could have been reduced by about 4-5 % in efficiency and 2-2.5 % in thrust, if a denser grid had been used. This error is estimated from the improvement of efficiency when passing from the second grid level to the first one in the propeller-alone calculations.
2. The unsteadiness of the flow, not modelled in the quasi-steady calculation, reduces the mean thrust and torque coefficients due to the generation of the so-called shed vortices in the wake in addition to the free vortices always present in the steady-state results. The error can be estimated by comparing the quasi-steady results to the time-accurate results presented in the next section. It was found to be 0.9 % in the efficiency and 0.8 % in the thrust.
3. The tests were conducted with a plate located on the upper part of the Azipod. The calculations have been done without the plate. The strut has been progressively reduced in breadth at the plate location.
4. For the propeller-alone calculations the experimental thrust and torque coefficients from MARIN were about 5 % larger than those found at VTT. As mentioned before, the differences in the hub shape are not solely responsible for the large difference. Reynolds number effects and

the experimental set up may well have some influence on it.

If a provision were made for the sources of the errors, the prediction of efficiency could be improved by about 4.9-5.9 % with a finer grid and a full unsteady calculation, and the remaining error of 0.6-1.6 % would be attributed to the deficiencies in the computational approach, e.g. limitations of the turbulence modelling, etc. As far as the thrust coefficient is concerned, the improvement would be 2.8-3.3 % relative to the VTT measurements. If the trend observed in the propeller-alone calculation for MARIN data is extrapolated to the Azipod calculation, the error when MARIN is chosen as a reference for the magnitude of the thrust could be further reduced by no more than 5%. This does not concern the efficiency, which would be more or less the same.

The calculated pressure distribution on the thruster surface is given in Figs. 11 and 12. The minimum pressures are located both on the leading edge of the propeller blades, close to the tip, and on the suction side of the strut. Tractor thrusters have the pod and strut located in the high-velocity region of the propeller wake. This means that higher viscous forces are expected on the pod and the strut surfaces than is the case with pushing thrusters. Non-symmetric struts and fins could be designed to alleviate to some extent this problem providing additional thrust, and they can also be shaped to reduce low pressure peaks.

Time-Accurate Calculation

After a rotation of 180° the propeller forces have converged to one percent accuracy. However, the forces on the strut require about two revolutions to converge. The strut forces converge before the pod ones, the latter being smaller. The mean propeller thrust and torque are reduced from the quasi-steady calculations by 0.8 and 1.7 %, respectively. The normalized fluctuations in time of propeller thrust, torque and efficiency are illustrated in Fig.13. The fluctuations in thrust (3.2%) are higher than those of torque (2.8%). This means that at the maxima of the thrust the instantaneous efficiency grows, and vice versa. The fluctuations of the efficiency are not as high as those of the thrust and the torque. A small shift between the thrust and the torque fluctuations is observed.

The forces on the strut exhibit less fluctuation amplitude than those on the propeller. Only the portion of the strut within the slipstream is affected by unsteady forces. This means that in the case of designing non-symmetric struts the lack of symmetry in the strut geometry should be confined to the part washed by the propeller slipstream. The fluctuations on the

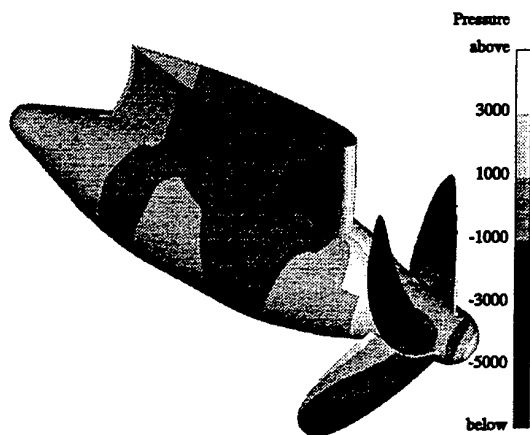


Figure 11: Distribution of pressure difference on the starboard side of the thruster surface. Quasi-steady simulation.

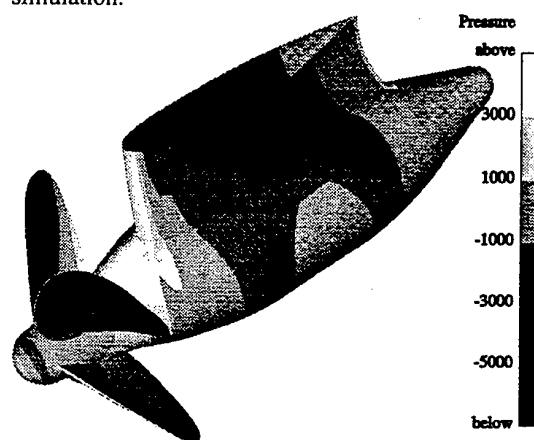


Figure 12: Distribution of pressure difference on the port side of the thruster surface. Quasi-steady simulation.

hub are very small.

The calculated pressure distribution on the thruster surface is given in Figs. 14-16 for different angular positions of the propeller (30° of angular increment) and in Fig. 17 for the propeller blades.

The minimum pressures are located both on the leading edge of the propeller blades, close to the tip, and on the suction side of the strut as it was in the case of the quasi-steady computation. However, the low pressure region on the suction side of the strut is not as extensive as before. This is probably a consequence of the higher loads present in the quasi-steady case due to the lack of the so-called shed vorticity found in unsteady potential-based methods. Fig. 17 reveals a non-uniform distribution of pressure near the leading

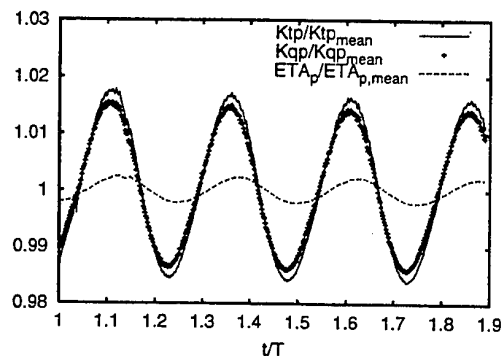


Figure 13: Fluctuations in time of propeller thrust, torque and efficiency.

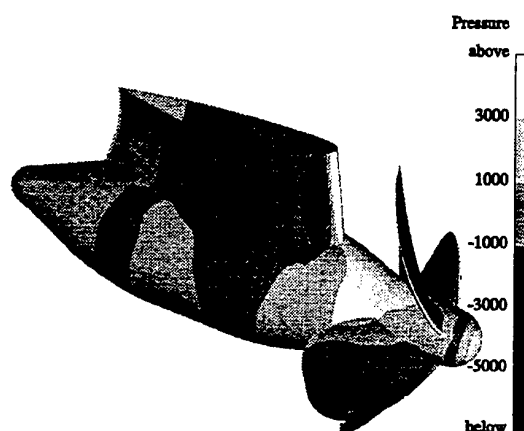


Figure 14: Distribution of pressure difference on the thruster for a reference angular position of the propeller. Time-accurate simulation.

edges of the blades, accompanied with low pressure peaks at the leading edges. Blade sections of NACA mean line $a = 0.8$ or modern blade sections, such as those designed with the Eppler method to delay cavitation inception, would display distinctly different pressure patterns in this area. It can be observed that the region of lowest pressure is larger for the blade located in front of the strut, as would be expected due to the higher wake at the propeller plane.

CONCLUSIONS

In this paper the unsteady flow around a tractor thruster (pulling type) has been analysed by solving the RANS equations in combination with the sliding mesh technique.

First, the flow around a BB series propeller in steady flow has been computed using the $k - \epsilon$ tur-

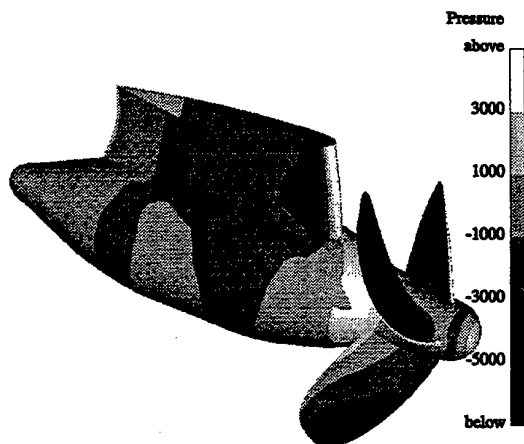


Figure 15: Distribution of pressure difference on the thruster for 30° deviation from the reference angular position of the propeller. Time-accurate simulation.

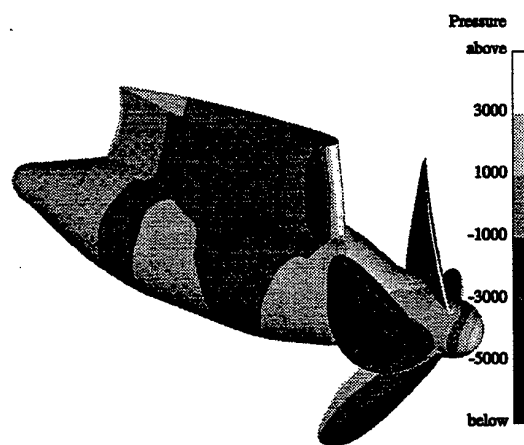


Figure 16: Distribution of pressure difference on the thruster for 60° deviation from the reference angular position of the propeller. Time-accurate simulation.

bulence model. The open water tests performed at MARIN and VTT have been used as validation data. Differences less than 1.5 % in the calculated thrust coefficient and about 1.5 % in the efficiency are found relative to measurements from MARIN. If experimental values obtained at VTT are chosen as a reference, calculations over-predict the thrust coefficient by 5 %. However, the error in efficiency is about 0.3 %. The discrepancies in the experimental measurements can be attributed to differences in both the Reynolds number used in the tests and the shape of the hub in the experimental models. The experimental apparatus may also be responsible for part of the discrepancies, as it has been recognised in comparative

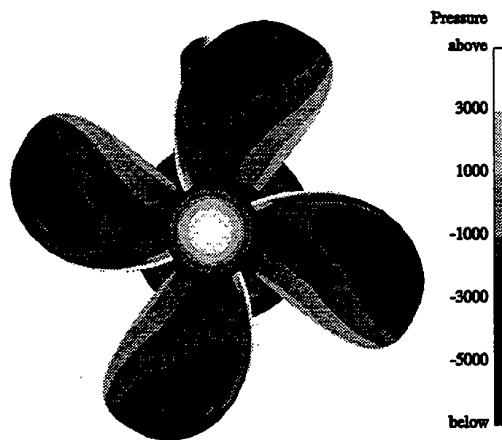


Figure 17: Distribution of pressure difference on the surface of the blades. Time-accurate simulation.

tests performed at various towing tanks with identical propeller models.

Secondly, simulations have been performed for the flow around the tractor thruster using the sliding-mesh technique. The computations have been performed in two different ways. For computations with circumferentially averaged flow through the sliding surface, larger differences from the experimental results appear in the computed thrust, torque and efficiency. This can mainly be attributed to several reasons: the mesh used for Azipod calculations is not as dense as that used in the propeller-alone computations; the unsteadiness of the flow tends to reduce the mean values of thrust and torque; uncertainty in the measurements at VTT and MARIN; and deficiencies of turbulence modelling.

Finally, a time-accurate computation has been conducted for the tractor thruster. Improvements in the prediction of the thrust and the torque coefficients by 0.8 and 1.7 % respectively, and of efficiency close to 1 % were achieved as compared to the quasi-steady calculation. Since the same relative coarse grid as in the quasi-steady case was utilized, the difference from the experimental data remains high. This is mainly due to the relatively coarse mesh used in the calculations. It should be noted that by utilizing parallelization more efficiently, the time-accurate computation could have been made in a dense grid with about 300 CPU hours.

Considering the two simulation approaches, the quasi-steady calculation allows the computer time to be reduced to about 1/10 compared to the latter. Its main merit consists of reducing the CPU time maintaining a full representation of the propeller geometry, i.e. without introducing simplified models for simulating the propeller action, such as actuator disk mod-

els or body force models like that presented in [17].

Tractor thrusters have the pod and strut located in the high-velocity region of the propeller wake. This means that higher viscous forces are expected on the pod and strut surfaces than is the case with pushing thrusters. Non-symmetric struts and fins could be designed to alleviate to some extent this problem providing additional thrust, and they can also be shaped to reduce the observed low pressure peak.

ACKNOWLEDGEMENTS

This research has been supported by the Technology Development Centre (TEKES) under the Computational Fluid Dynamics Technology Programme. The Centre for Scientific Computing of Finland has provided its computing facilities. The validation presented in this paper has been possible thanks to the release of some experimental data by ABB-Azipod Ltd.

REFERENCES

1. Sanchez-Caja, A. "DTRC propeller 4119 calculations at VTT," 22nd ITTC Propulsion Committee Propeller RANS/Panel Method Workshop, ITTC, April 1998.
2. Siikonen, T., Hoffren, J. and Laine, S. "A multigrid LU factorization scheme for the thin-layer Navier-Stokes equations," Proceedings of the 17th ICAS Congress, Stockholm, Sept. 1990, pp. 2023-2034. ICAS Paper 90-6.10.3.
3. Chorin, A.J., "A numerical method for solving incompressible viscous flow problems," Journal of Computational Physics, Vol. 2, 1967, pp. 12-26.
4. Siikonen, T. and Pan, H. "Application of Roe's method for the simulation of viscous flow in turbomachinery," Proceedings of the First European Computational Fluid Dynamics Conference, Brussels, Elsevier Science Publishers B.V., Sept. 1992, pp. 635-641.
5. Chien, K.-Y., "Predictions of channel and boundary-layer flows with a low-Reynolds-number turbulence model," AIAA Journal, Vol. 20, No. 1, Jan 1982, pp. 33-38.
6. Menter, Florian R. "Zonal two equation $k - \omega$ turbulence models for aerodynamic flows," 24th AIAA Fluid Dynamics Conference, Orlando, Florida, Jul 1993. AIAA Paper 93-2906-CP.
7. Rahman, M.M., Rautahaimo, P. and Siikonen, T. "Numerical study of turbulent heat transfer from a confined impinging jet using a pseudo-compressibility method," Proceedings of the 2nd International Symposium on Turbulence, Heat and Mass Transfer, Delft, June 1997, pp. 511-520.
8. Roe, P.L., "Approximate Riemann solvers, parameter vectors, and difference schemes," Journal of Computational Physics, Vol. 43, 1981, pp. 357-372.
9. Van Albada, G.D., Van Leer, B. and Roberts, W.W., "A comparative study of computational methods in cosmic gas dynamics," Astronom. and Astrophys., Vol. 108, No. 76, 1982.
10. Lombard, C.K., Bardina, J., Venkatapathy, E. and Olinger, J. "Multi-dimensional formulation of CSCM — an upwind flux difference eigenvector split method for the compressible Navier-Stokes equations," 6th AIAA Computational Fluid Dynamics Conference, Danvers, Massachusetts, Jul 1983, pp. 649-664. AIAA Paper 83-1895-CP.
11. Jameson, A. and Yoon, S., "Multigrid solution of the Euler equations using implicit schemes," AIAA Journal, Vol. 24, No. 11, 1986.
12. Siikonen, T., "An application of Roe's flux-difference splitting for the $k - \epsilon$ turbulence model," International Journal for Numerical Methods in Fluids, Vol. 21, 1995, pp. 1017-1039.
13. Hoffren, J., Siikonen, T. and Laine, S., "Conservative multiblock Navier-Stokes solver for arbitrarily deforming geometries," Journal of Aircraft, Vol. 32, No. 6, 1995, pp. 1342-1350.
14. Rai, M.M., "A relaxation approach to patched-grid calculations with the euler equations," Journal of Computational Physics, No. 66, Dec 1986, pp. 99-131.
15. Rautahaimo, P., Salminen, E. and Siikonen, T. "Parallelization of a multi-block Navier-Stokes solver," Proceedings of the Third ECCOMAS Congress, Paris, John Wiley & Sons, Ltd., Sept. 1996.
16. Kuiper, G., "The wageningen propeller series," MARIN Publication, No. 92-001, May 1992.
17. Kerwin, J.E., Keenan, D.P., Black, S.D. and Diggs, J.G., "A coupled viscous/potential flow design method for wake-adapted, multi-stage, ducted propulsors using generalized geometry," SNAME Transactions, Vol. 102, 1994, pp. 23-56.

A NUMERICAL LIFTING SURFACE TECHNIQUE FOR ACCOUNT OF RADIAL VELOCITY COMPONENT IN SCREW PROPELLER DESIGN PROBLEM.

Alexander S. Achkinadze, Vladimir I. Krasilnikov

Theory of Ship Department, State Marine Technical University,
3 Lotsmanskaya Street, 190008 St.Petersburg, Russia.

E-mail: achkin@mail.ru.

ABSTRACT

An account of radial velocity component (as propeller self-induced as inflow) doesn't make difficulties in screw propeller analysis with the help of panel methods when blades' geometry is fixed. It isn't like this in propeller design where blades' shape isn't known beforehand and is to be derived from the problem solution. In the present paper a quite reliable and effective iterative algorithm taking into account radial velocities is constructed for design problem. For this case a kinematic boundary condition is applied to the mean blade surface without any simplifications. Some important elaboration in the calculation of forces on the blades is provided by the present method.

NOMENCLATURE

b - blade section chord length;
 D - propeller diameter;
 e_0 - maximum thickness of blade section;
 f_0 - maximum camber of blade section;
 J - advance ratio;
 K_T - propeller thrust coefficient;
 K_Q - propeller torque coefficient;
 \vec{n} - unit normal vector to blade chord surface;
 \vec{n}_C - unit normal vector to blade mean surface;
 P - blade section pitch;
 q - strength of the source/sink layer;
 r - radial coordinate;
 V - ship speed;
 V_E - transversal velocity;
 V_R - total relative velocity of fluid;
 V_∞ - inflow velocity;
 \vec{W} - propeller induced velocity;
 x - axial coordinate in propeller fixed coordinate system;
 x_R - blade section displacement along the propeller axis;
 x_S - blade section rake: x -coordinate of the midchord point;

Z - number of propeller blades;

β_{FVS} - pitch angle of free vortex surface in GLM;
 β_{PFV} - pitch angle of pseudofree vortex threads inside the blade contour;
 β_{WTV} - pitch angle of trailing vortex threads in the wake behind the blades;
 Γ - circulation around the blade section;
 γ - strength of the vortex layer;
 η_0 - open-water propeller efficiency;
 η'_C - ordinate of the blade section mean line;
 θ - angular coordinate in propeller fixed coordinate system;
 θ_S - blade section skew angle;
 φ - blade section pitch angle;

$F'(\xi', \eta')$ - orthogonal coordinate system fixed on blade section: ξ' - helical coordinate directed along the chord, η' - perpendicular to ξ' in the plane of cylindrical blade section;
 $M(x^0, y^0, z^0)$ - local coordinate system fixed on given point at the section chord: x^0 - coordinate tangential to ξ' , y^0 - coordinate directed radially outward; z^0 - coordinate perpendicular to ξ' .

INTRODUCTION

A well-known paper by Beek & Vorst (1994) gives an example of screw propeller design with use of unsteady propeller analysis based on non-linear lifting surface theory [1]. Jessup & Wang (1997) solve the analogous problem by means of unsteady panel method [2]. As a matter of fact this approach is the method of trials and errors. In authors' opinion although such method takes into account the unsteady effects it can not allow to look over all possible variants of problem solution and, consequently, it can not guarantee the acceptable precision in differential blade geometry characteristics. In one word a propeller analysis of itself can not substitute for propeller design because only the last one gives a possibility to determine the radial distributions of the pitch, camber, chord length, thickness, skew and rake which meet the definite requirements. An example of such requirements is the specified thrust (or torque) value under certain supplementary conditions connected with blade strength, cavitation performances, propeller-induced pressure pulses level on the hull, airborne noise etc.

At the present paper the authors describe the development of steady non-linear lifting surface theory as applied to propeller design in non-uniform velocity field. The main case of such design procedure consists in determination of the radial distributions of the pitch and camber, which correspond to given thrust (or torque) and prescribed normalized circulation distributions along the chord and radius (though radial circulation can be optimized for maximum propulsion efficiency also). A special attention is paid to account of the radial component of the total velocity field in which propeller operate.

Apparently the paper by Kerwin (1973) was one of the first publications devoted to this problem [3]. An account of the radial velocity component induced by vortex and source systems had been carried out for satisfaction of the kinematic boundary condition on the blade mean surface and for blade section geometry calculation on its base. The radial velocity component of external inflow wasn't taken into consideration. Meanwhile the necessity of the account for this component has been demonstrated by Brockett (1983) [4].

In 1982 the famous and widely cited paper by Greeley & Kerwin [5] was published. The original propeller design algorithm and code (PBD-10) based on non-linear lifting surface theory used such hydrodynamic singularities as discrete vortex threads and discrete sources that replace the blade mean surface by the lattice of concentrated straight-

line elements. The elements were of constant strength and the endpoints of each element were located on the blade mean surface. A special semi-empiric 6-parametric vortex model was used for simulation of the trailing vortex wake behind the blades. The geometry of the mean surface was derived from special iterative procedure. The propeller forces' values were obtained in the frameworks of lifting surface theory through the application of the Kutta-Jowkowski's law with subtracting the thickness-induced velocity from the total velocity before performing the calculation. According to the authors' opinion there are the following drawbacks in the PDB-10 algorithm: 1). discrete (non-continuous) manner for representation of the blade singularities; 2). quite complex (especially for design) semi-empiric model for trailing vortex wake; 3). slow convergence of the iterative procedure for blade geometry computation; 4). non-evident accounting for radial velocity component in forces computation; 5). lack of the adequate comprehension of the thickness effects. The last drawback may be overcome by means of thickness/loading coupling method submitted by Kinnas [6] for propeller analysis. Kinnas has shown that accuracy of his technique for analysis calculations proves to be close to one reached with the help of panel methods.

In Russia the investigations connected with non-linear lifting surface theory application to propeller design were being conducted by Zavadovsky [7], [8]. However it didn't result in complete and debugged computer code.

The facts rehearsed above say about the topicality of the further study in considered field.

A new propeller design algorithm and code FRSPD-98 elaborated by authors are outlined in the present paper. Authors' method has a number of essential advantages in comparison with method by Greeley & Kerwin [5]. First, the continuous distribution of the hydrodynamic singularities on the blade is adopted instead of discrete one. Second, the authors use the simple and effective Generalized Linear Model (GLM) for trailing vortex wake has been put forward earlier by Achkinadze (1989) [9]. Third, cumbersome iterative procedure employed in PBD-10 code is replaced by rather fast converged and logical iterative process which demands about 3-5 steps only for real blade configurations in place of 10 as it is pointed out in [5]. Lastly, the authors have realized the direct accounting of forces appear on the blade pseudofree (directed along the chord) vortices due to its interaction with radial component of relative velocity.

KINEMATIC BOUNDARY CONDITION ON THE BLADE MEAN SURFACE

The discussed design calculation has to result in definition of the blade mean surface ordinates $\bar{\eta}'(\bar{r}, \bar{\xi}')$ and blade sections' pitch angles $\varphi(\bar{r})$. For this case it is necessary to integrate the chordwise derivative $\partial \bar{\eta}' / \partial \bar{\xi}'$ along the chord. Below we shall obtain the equation for this derivative including all the velocity components (and radial one among others).

Let us consider three-dimensional blade mean surface that is represented by means of function $\bar{\eta}'(\bar{\xi}')$ at each of the cylindrical blade sections $\bar{r} = \text{const}$. Here $\bar{\xi}'$ is the helical coordinate directed along the section chord from trailing edge to leading edge in the standard coordinate system $F'(\bar{r}, \bar{\xi}', \bar{\eta}')$ fixed on propeller blade section. The $\bar{\eta}'$ coordinate is perpendicular to $\bar{\xi}'$ in given cylindrical blade section plane and it is directed from pressure side to suction side (see Fig.1).

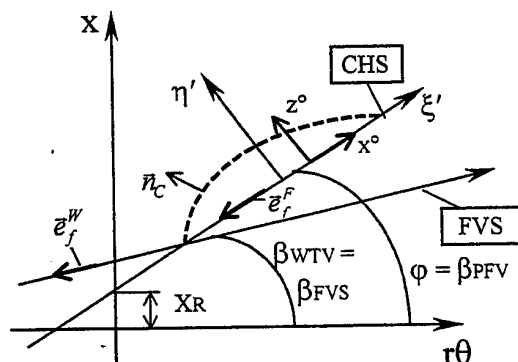


Fig.1 Coordinate systems and location of the vortex singularities.

Further all the non-dimensional geometry quantities marked with the dash above the item are the rate of propeller radius R and all the non-dimensional kinematic quantities are the rate of ship speed V .

Let us put into consideration an auxiliary coordinate system $M(\bar{x}^0, \bar{y}^0, \bar{z}^0)$ fixed on given point at the section chord. The axes x^0 and z^0 are situated in the plane tangential to the cylinder of radius r , moreover x^0 is tangential to $\bar{\xi}'$ and z^0 is normal to $\bar{\xi}'$. Finally, axis y^0 completes the right-hand system and is directed radially outward.

One can describe the blade mean surface in the local coordinate system M by the function

$$z^0 = z_C^0(\bar{x}^0, \bar{y}^0). \quad (1)$$

In general steady problem kinematic boundary condition on the blade mean surface is formulated in vector form as follows

$$\vec{V}_R \cdot \vec{n}_C = 0, \quad (2)$$

where total (including external inflow) relative velocity is

$$\vec{V}_R = \vec{W} + \vec{V}_\psi - \vec{V}_E, \quad (3)$$

and transversal velocity is

$$\vec{V}_E = V \cdot \vec{i} + \Omega r \cdot \vec{i}_\theta. \quad (4)$$

The external inflow velocity vector contains each of the three components in arbitrary case (for instance, axial, tangential and radial ones prescribed in the cylindrical coordinate system):

$$\vec{V}_\psi = V_{\psi\alpha} \vec{i} + V_{\psi\theta} \vec{i}_\theta + V_{\psi r} \vec{i}_r. \quad (5)$$

It has to be noted that external inflow velocity field can prove to be non-potential. The authors assume this fact in spite of using the hypothesis upon flow potentiality. Such an approach is valid if the external inflow is considered as pre-set and invariable during the design procedure. On principle the described method allows more accurate definition of the external inflow working out step by step the elaboration of \vec{V}_ψ at every iteration as it has been done in [12] for wake adapted propeller behind the hull.

As one can see the normal vector \vec{n}_C in equation (2) has no to be unit vector without fail. The arbitrary constant non-zero multiplier can not change the validation of the identity (2) for scalar vector product. It is known [11] that vector proportional to unit normal to the mean surface coincides with the following gradient

$$\vec{n}_C = \text{grad} F = \frac{\partial F}{\partial \bar{x}^0} \vec{i}^0 + \frac{\partial F}{\partial \bar{y}^0} \vec{j}^0 + \frac{\partial F}{\partial \bar{z}^0} \vec{k}^0, \quad (6)$$

where $F(\bar{x}^0, \bar{y}^0, \bar{z}^0) = 0$ is the equation for blade mean surface in local coordinate system M . By virtue of the equation (1) for the same mean surface one can obtain

$$F(\bar{x}^0, \bar{y}^0, \bar{z}^0) = \bar{z}^0 - z_C^0(\bar{x}^0, \bar{y}^0) = 0, \quad (7)$$

and then

$$\vec{n}_C = -\frac{\partial z_C^0}{\partial \bar{x}^0} \vec{i}^0 + \frac{\partial z_C^0}{\partial \bar{y}^0} \vec{j}^0 + \vec{k}^0. \quad (8)$$

Taking into account formula (8) the kinematic boundary condition (2) can be transformed as follows

$$-\vec{V}_{R\alpha^0} \frac{\partial z_C^0}{\partial \bar{x}^0} - \vec{V}_{R\beta^0} \frac{\partial z_C^0}{\partial \bar{y}^0} + \vec{V}_{R\gamma^0} = 0, \quad (9)$$

where \bar{V}_{Rz^0} , \bar{V}_{Ry^0} , \bar{V}_{Rx^0} are the non-dimensional (related to V) components of total relative velocity in local coordinate system M . This formulation of the kinematic boundary condition has been obtained without any simplifications and, consequently, it can be examined as the basis design equation we have to solve for definition of the blade mean surface shape.

In the strict sense we have to solve this equation concerning partial derivative $\partial \bar{z}_C^0 / \partial \bar{x}^0$, integrate this derivative along the chord and obtain final geometry of the searching surface in every section. Further numerical solution of the design equation (9) is based on the iterative method demands some transformations of (9), namely

$$\frac{\partial \bar{z}_C^0}{\partial \bar{x}^0} = \frac{1}{\bar{V}_{Rz^0}} \left(\bar{V}_{Rz^0} - \bar{V}_{Ry^0} \frac{\partial \bar{z}_C^0}{\partial \bar{y}^0} \right). \quad (10)$$

Using standard symbols of coordinate system F' we rewrite (10) as follows

$$\frac{\partial \bar{\eta}'}{\partial \bar{\xi}'} = \frac{1}{\bar{V}_{R\xi'}} \left(\bar{V}_{R\eta'} - \bar{V}_{Rr} \frac{\partial \bar{z}_C^0}{\partial \bar{y}^0} \right). \quad (11)$$

It is important that radial component of the total fluid relative velocity \bar{V}_{Rr} get in above-treated design equation side by side with other components that locate in the plane of cylindrical blade section (tangential to chord $\bar{V}_{R\xi'}$ and normal to chord $\bar{V}_{R\eta'}$).

The obtained form of the design equation is useful to direct estimation of the radial velocity effect on the design outputs. It is not possible to take into account such effect within the frameworks of conventional linear approach. But we need in linear theory as departure in our design procedure. The first linear iteration follows just from (11) after the rejection of the quantity $\bar{V}_{Rr} \left(\partial \bar{z}_C^0 / \partial \bar{y}^0 \right)$.

BLADE SINGULARITIES DISTRIBUTION AND COMPUTATION OF THE PROPELLER BLADE FORCES

Characteristic feature of propeller design problem connects with the fact that blade mean surface ordinates are not known beforehand. As it was pointed out above to define these ordinates we employ the iterative procedure. The first step of this algorithm use the regular helicoid with constant pitch corresponding to Generalized Linear Model (GLM) as the surface hydrodynamic singularities (vortices and sources) are lying on [9], [13]. The pitch angle β_{FVS} of this so-called free vortex surface (see FVS on Fig.1) was already found to this step according to special algorithm at the lifting line design stage [9], [13]. Instead of full form of the

design equation (11) we use its linearized variant at the initial iteration. The linearization means the withdrawal of the radial velocity component, i.e. $\bar{V}_{Rr} = 0$ in identity (11). Thus, the initial iteration of the advanced algorithm utterly correspond to generalized linear lifting surface technique SPD-96 elaborated by the authors earlier and described in detail in [14], [15]. The calculated values of the pitch angle $\varphi_{(1)}$ and mean surface ordinates $\bar{\eta}'_{C(1)}$ fix blade mean surface of first (linear) iteration and yield blade geometry for the next step of the alignment procedure. At the new step the hydrodynamic singularities is situated on the blade chord surface (CHS on Fig.1) of pitch angle $\beta_{PFV} = \varphi_{(1)}$ within the blade contour. Then iteration process gives the possibility to refine the shape of the mean surface and chord surface at each of the following steps (i.e. to find $\varphi_{(2)}$, $\bar{\eta}'_{C(2)}$; $\varphi_{(3)}$, $\bar{\eta}'_{C(3)}$, ... , etc.) using full form of the equation (11) without any simplifications. As the comparative calculations have shown such a feature that singularities are lying not on the mean surface but on the chord surface does not bring down the calculation precision when blade section camber is small. The latter is typical for conventional propellers.

According to correct problem formulation within the frameworks of steady non-linear lifting surface theory (without additional assumptions) we have to dispose the hydrodynamic singularities of two kinds on the above-mentioned blade chord surface. These singularities are the continuous vortex layer characterized with vector strength $\vec{\gamma}$ and the continuous source/sink layer with scalar strength \bar{q} . Besides that the elementary trailing vortex filaments coincided with flow streamlines and stretched to the infinity must be situated in the wake behind each of the blades. The strength of the enumerated singularities can be defined by the following identities

$$\vec{\gamma} = (\text{grad} \Gamma) \times \vec{n}, \quad (12)$$

$$q = \bar{e}_0 \frac{dF_T}{d\xi'} \frac{\bar{V}_{R1} \cos(\varphi - \beta_1)}{\Lambda_n}. \quad (13)$$

In the identity (12) Γ is velocity circulation along the arbitrary reserved contour which pass throw given vortex surface once at given point (actually Γ depends on radial and chordwise coordinate of the given point only), while \vec{n} is unit normal vector to vortex surface at given point (see Fig.2). In the identity (13) \bar{e}_0 is prescribed maximum blade section thickness; F_T is normalized chordwise thickness distribution function; \bar{V}_{R1} is relative

velocity calculated on lifting line design stage; Λ_n is factor for accounting of the difference between the direction of normal vector \vec{n} and the direction of η' axis lying on the plane tangential to cylindrical section of radius \bar{r} (see Fig.1); multiplier $\cos(\varphi - \beta_i)$ accomplish the correction needed because the sources are located along the helix with pitch angle φ just as the direction of \vec{V}_{Ri} velocity is characterized by hydrodynamic pitch angle β_i . The test calculations have shown the small effect due to the last correction.

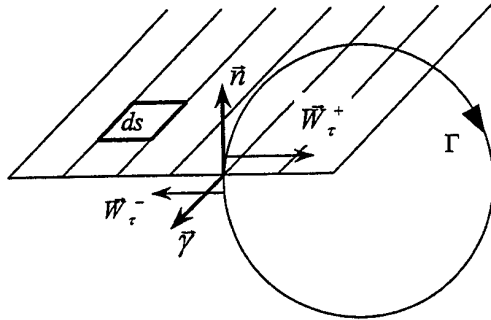


Fig.2 Definition of the strength of the vortex layer.

It has to be noted that the authors do not distinguish bound and free vortices within the blade contour unlike conventional linear theory. Such an approach requires the account of forces appear on all vortex singularities inside the blade contour without exception.

In the wake behind the blade the trailing vortex threads are formed. To define its' real location it is enough to employ the equation (12), continuity condition in the trailing edge neighbourhood and condition of coincidence of this threads with flow streamlines. However in the present paper similar problem is not examined in view of its quite cumbersome algorithm. Instead of this full formulation the authors use some more one assumption and consider the elementary free vortex threads beginning at the trailing edge as helices of constant pitch equal to pitch of the free vortex surface (FVS) at the initial (linear) iteration, i.e. adopt $\beta_{WTV} = \beta_{FVS}$. It would be more correct to call these vortices as "pseudofree". At the second and following iterations free (rather pseudofree) vortex surface is already not a regular helicoid. In general case the cylindrical sections of this surface have the rake depend on rake, skew and pitch of the blade chord surface. The axial displacement of the FVS

sections at non-linear steps can be defined by the formula given below

$$\bar{x}_{R_{FVS}} = \bar{x}_R + r \theta_{TE} (tg \varphi - tg \beta_{FVS}), \quad (14)$$

where \bar{x}_R is the analogous characteristic of the chord surface and θ_{TE} is the angular coordinate of the trailing edge in cylindrical coordinate system fixed on propeller.

The forces on the pseudofree vortices outside the blade contour are not taken into account. Certainly the described scheme does not claim upon the detail representation of the real vortex wake geometry but offers its mite to guarantee the adequate definition of the induced velocities due to the trailing vortex wake under design conditions. As it is shown in the present paper the latter case is obtained successfully. For instance, one can see it from Fig.4 where the comparison in terms of induced velocity components between present algorithm and data by Greeley & Kerwin [5] is demonstrated. Examining this comparison it is to bear in mind that calculations in [5] have been worked out with use of far more complex non-linear trailing vortex wake model claims upon the similitude with real flow in the vortex wake for the case of isolated propeller.

Within the bounds of the blade contour we can find the vorticity vector $\vec{\gamma}$ for each of the points on the blade chord surface from the identity (12). In the considering problem a scalar quantity Γ characterizes the flow potential jump (or jump in tangential induced velocity as it is shown on Fig.2) on the lifting surface is actually prescribed since the chordwise loading distribution is specified for each cylindrical blade section. In the present paper the authors adopt the standard *NACA*, $a = 0.8$ loading type for all calculations as the most widespread in marine propellers design practice.

To make the accepted model more suitable for practical computations the total vorticity vector $\vec{\gamma}$ lying in the plane tangential to the vortex surface is decomposed on two perpendicular components: one direct along the blade section chord and other is normal to it. We shall call the chordwise projection of $\vec{\gamma}$ as elementary pseudofree vortex thread (by analogy with linear theory) while another one will be elementary bound vortex thread. The unit vectors define the directions of both vorticity components in cartesian coordinates are represented by the following identities:

for pseudofree vortices

$$\vec{e}_f^F = -\sin \varphi \cdot \vec{i} + \cos \varphi \sin \theta \cdot \vec{j} - \cos \varphi \cos \theta \cdot \vec{k}, \quad (15)$$

and for bound vortices

$$\vec{e}_b = \vec{e}_f^F \times \vec{n}, \quad (16)$$

where \vec{n} is unit normal to the blade chord surface.

Generally, as it has been noted above the authors refuse from rigorous agreement in location of the free vortices and flow streamlines assuming the non-real (along the chord) direction of the former. Taking such an approach we haven't to lose sight of forces appear on the pseudofree vortices within the blade contour. It is interesting to note that mentioned forces contribute to the total thrust and torque values due to the interaction of the pseudofree vortices with radial relative velocity component only. Thus, the present technique allows calculating the part of the force (thrust or torque) which is conditioned by radial velocity separately and evaluating its quantum in total force magnitude. For computation of the forces we use the generalized differential form of Jowkowski's theorem [16]:

$$dF = \rho V_R \times \vec{\gamma} ds, \quad (17)$$

where ds is vortex surface element (see Fig.2). This formulation of the Jowkowski's theorem is different from conventional because it takes into account the relative velocity component normal to vortex surface. Emphasized fact is quite important for numerical algorithm described here because the kinematic boundary condition on the blade mean surface is satisfied approximately at the intermediate steps of the iterative alignment process. Obviously the practical realization of the forces calculation on the base of (17) requires to construct the another once more iterative process (besides the general iterative alignment procedure necessary for solution of the design equation (11)) for refinement of the agreement between the actual propeller force and its prescribed magnitude. This "external" iterative process in terms of forces is necessary because at the beginning we define the singularities' strength by the lifting line theory identities. And, consequently, the calculated thrust and torque values will correspond to the prescribed ones if and only if we define its in the frameworks of the lifting line theory. At the second step of the forces' refinement iterative process the prescribed force value, for example K_T^* (or K_Q^*) is to be corrected on the magnitude equal to difference between this value and the value obtained after lifting surface calculation with use of generalized Jowkowski's theorem K_T^{LS} (17). Thereby the required thrust coefficient on which the design is renewed at j -iteration as to forces can be evaluated by formula

$$K_T^{(j)} = K_T^{(j-1)} - (K_T^{LS(j-1)} - K_T^*). \quad (18)$$

The difference between the lifting surface calculated force value and its departure prescribed magnitude is taken as the convergence criterion in forces' elaboration process. The programming realization of

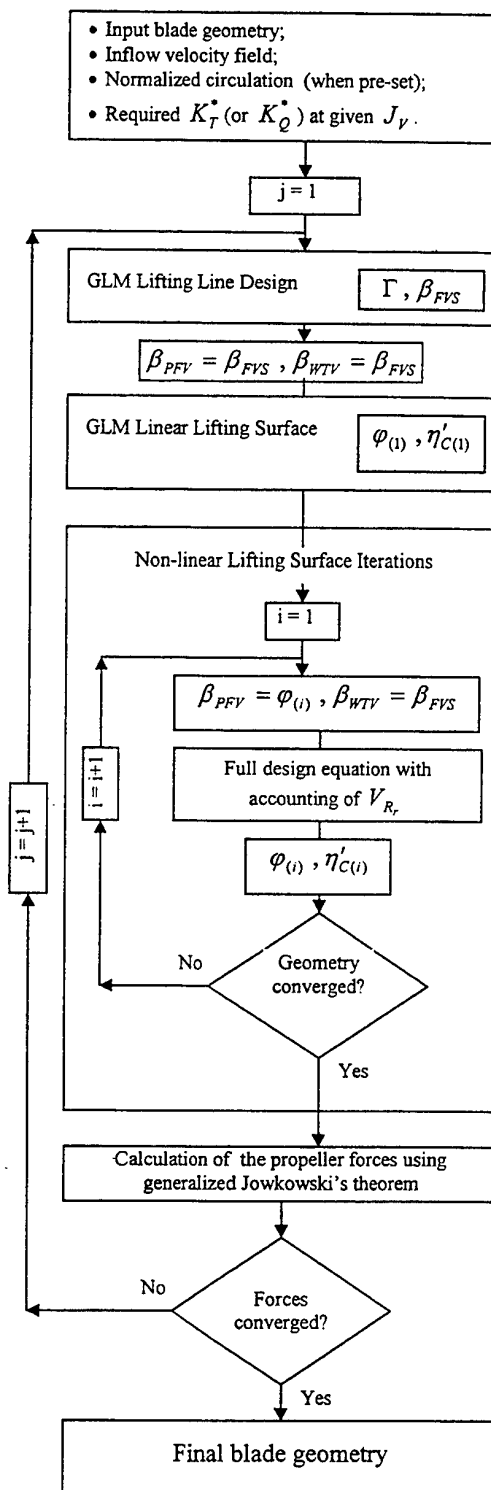


Fig.3 Principal flowchart for FRSPD-98 design technique.

this double-loop algorithm (with external cycle as to propeller forces refinement and embedded cycle as to blade geometry alignment) has resulted in creation of the design code named as FRSPD-98. The principal flowchart of these algorithm and code is shown on Fig.3.

The blade thickness is represented by continuous source/sink distribution on the blade chord surface with strength defined according to formula (13). In the present procedure of the forces calculation the authors employ the following approach. The thickness-induced velocities enter into kinematic boundary condition (i.e. into design equation (11)) but are not taken into account during the forces calculation. Greeley & Kerwin have used the analogous ruse in [5]. To explain the reason of such approach we have to consider the proof of the differential Jowkowski's theorem. This proof can be performed through the application of the impulse theorem to differential element like thin parallelepiped constructed around the given point on the lifting surface. If we work with the thin lifting surface we can consider the points belonged to the opposite sides of the parallelepiped as the points are lying on the same streamline. When crossing the lifting surface a jump of Bernulli constant does not occur along this streamline although a jump of tangential velocity takes place. In presence of the source/sink layer on the lifting surface this statement and, consequently, formula (17) are wrong. The using of (17) in this case can result in so-called "thickness paradox". An account of the Lagally forces does not change this situation. The examples of the calculations as to propeller forces based on generalized Jowkowski's theorem are given in the next item.

MAIN PARTICULARITIES OF THE NUMERICAL ITERATION PROCESS AND RESULTS OF THE COMPARATIVE CALCULATIONS

The calculation of the induced velocities is worked out with use of Biot-Savard relation for vortex surface and its counterpart for source/sink layer. To compute the surface singular integrals the authors employ the same special "symmetrical double compound Gaussian rule" that in their code-predecessor SPD-96 [14],[15]. The employment of the Biot-Savard relation involves the inevitable assumption about the potential character of the induced velocity field.

By definition of the induction due to trailing vortex wake at the first (linear) iteration we have a right to use a well-known Pien's approach because the free vortex surface is the regular helicoid. At the

following steps when free vortex surface is characterized by the rake presence such method is inadmissible. That is why the explicit integration along the semi-infinite wake is the only method in this case. This integration can be performed by means of both continuous singularities' distribution method and discrete vortex method similarly. According to the author's opinion the first method has some advantages. First, it allows to escape of the possible waste in precision when compute the induced velocities at the control points which are near from the trailing edge. The integration rule used in this case is similar to one used by the integration on the blade and it is based on symmetrization of the integration domain concerning the control point. This symmetrization is implemented by analogy with "symmetrical double compound Gaussian rule" but only from above and from below the radius control point is situated. Besides that the right choice of the integration quadratures makes it feasible the accounting of the singularities in behaviour of $d\Gamma/dr$ function at the "hub" and "tip" bounds of the wake. Although the discrete method is more preferable in the standpoint of reduction of the computation time. The account of the $d\Gamma/dr$ singularities at the integration domain's bounds is attained by the corresponding disposition of the discrete vortices. As the test calculations have shown the axial extension of the integration domain in the vortex wake must be equal to 10 propeller diameters at least to one can guarantee the sufficient accuracy of the induced velocity computation.

The crucial stage in the elaboration of the new design code is its debugging and practical verification. In view of tight possibilities for direct experimental tests the comparison with other programs that have gained a foothold is the matter of great concern. The well-known DTMB series propellers used time and again by many authors in their calculations assure the good reliable base for this comparison.

Allow to begin with highly skewed (72°) warped propeller DTMB4498 design [5], [17]. Firstly let us consider the different methods of determination of the propeller blade forces. In the Table 1 the comparative estimation of the thrust, torque and efficiency values for propeller DTMB4498 obtained using different methods is demonstrated. All the input data correspond to the Table 4. Since the authors set their mind on doing the comparison between the calculation methods the iterations as to forces values have not been worked out, i.e. the results of the first step of iteration process in terms of forces refinement have been used.

An account of the viscous effects in forces calculations has been reduced to using of the corrections factors by Mishkevich [14], [15]. On the basis of fulfilled comparison one can infer that accounting for radial velocity component (by the third method) is necessary in design of the propeller with such complex geometry like DTMB4498. The forces values obtained by the third method are in the good agreement with analogous results by Greeley & Kerwin had been given in [5]. It is illustrated in Table 2.

The results of the calculation without accounting for radial velocity component (the second method) stay close to the lifting line theory data. The said fact is not unexpected because in the case of symmetrical blade without rake the both methods in question must yield nearly the same results when chordwise loading distribution close to equable.

In passing it can be noted that for the case pointed out above (symmetrical blade contour without rake) the third method predicts the thrust and torque values which are approximately on (1-2)% greater than the lifting line prognosis. The difference between lifting line and non-linear lifting surface evaluations of the propeller forces has a tendency to increase with increase of skew and for warped blade configuration. The propeller efficiency stays practically invariable in these cases (the variance in its value predicted by both methods does not exceed the 1%). The data summarized in the Table 3 confirm the inferences have been done. The additional makeweight due to the thickness-induced (sources-induced) velocities as with Lagally forces as without its leads to the improbable results that conform with above-mentioned features of the generalized Jowkowski's theorem application.

Hereby, the authors can recommend the third method for elaboration of integral propeller performances and just this method has been adopted for iterative forces' refinement procedure in the final version of the FRSPD-98 design code.

Let us consider now the definition of the blade geometry immediately that is the main task of the design calculation. First of all it is important to evaluate the practical convergence of the iterative alignment process in terms of blade geometry used when numerical solution of the design equation (11) is executed. The camber and pitch values from linear and first five non-linear iterations are shown in the Tables 5 (a) and (b) at the several radial blade sections.

One can see that accuracy attained already after three iterations is quite enough for practical calculations. Thus the presented technique has demonstrated a very good convergence even in the case of such complex blade configuration. The data

Table 1. Comparison of the different methods of blade forces determination in the design example for DTMB4498 propeller.

	Integral performances	K_T	K_Q	η_0
	Absolute value according to lifting line theory	0.213	0.0438	0.6872
I	Lifting line	100%	100%	100%
II	Linear lifting surface (SPD-96)	99.28%	99.38%	99.90%
III	Non-linear lifting surface with accounting for radial velocity due to loading only (FRSPD-98)	105.3%	104.2%	101.0%
IV	The same but with accounting for induced velocities due to thickness also	110.4%	112.2%	98.37%
V	The same but with accounting as for thickness-induced velocities as for Lagally forces	114.4%	110.3%	94.65%

Table 2. Comparison of the integral performances predicted by authors' method with PBD-10 code results for DTMB4498 propeller design example (at design $J = 0.889$).

Integral performances	FRSPD-98 III method	PBD-10 8×8 grid	PBD-10 16×34 grid
K_T	0.224	0.224	0.224
K_Q	0.0456	0.0458	0.0461
η_0	0.694	0.693	0.689

Table 3. Evaluation of the integral performances for DTMB series propellers with different blade configuration by non-linear lifting surface theory with accounting of the radial velocity (III method).

4381: skew 0° ; 4382: skew 36° ;

4383: skew 72° ; 4497: skew 36° Warp.

Lifting line prognosis: $K_T = 0.213$; $K_Q = 0.438$;

$$\eta_0 = 0.6872.$$

Integral performances	4381	4382	4383	4497
K_T	101.54%	102.81%	104.15%	103.31%
K_Q	101.63%	103.19%	104.49%	102.40%
η_0	99.91%	99.64%	99.68%	100.89%

on Fig.5 and in Table 6 illustrate the comparison between authors' method and PBD-10 design code [5] as to calculated induced velocities and final design blade geometry. The plots of chordwise distributions of the induced velocity components $\bar{W}_x, \bar{W}_\theta, \bar{W}_r$ at the $\bar{r} = 0.7$ radius are presented on Fig.5 together with the product of the radial component and the derivative is included in the design equation $\bar{W}_m = \bar{W}_r (\partial z_c^0 / \partial y^0)$.

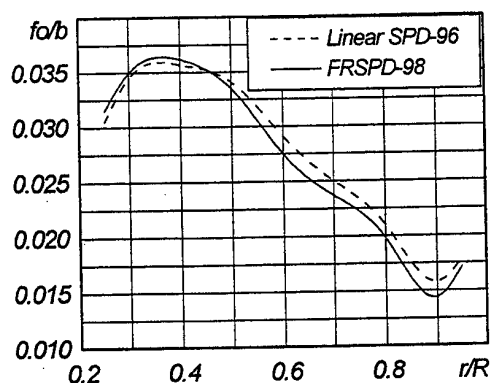


Fig.4(a) Comparison of the radial camber distributions obtained with use of linear (SPD-96) and non-linear (FRSPD-98) authors' lifting surface techniques for DTMB4498 propeller.

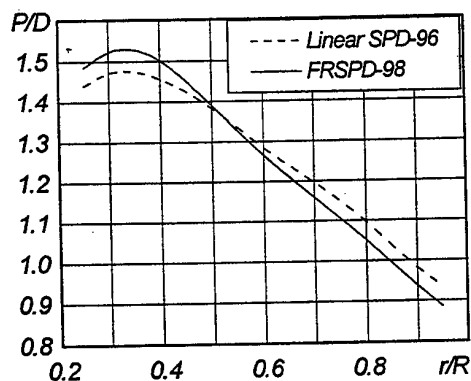


Fig.4(b) Comparison of the radial pitch distributions obtained with use of linear (SPD-96) and non-linear (FRSPD-98) authors' lifting surface techniques for DTMB4498 propeller.

Table 4. Input information for design of the DTMB4489 propeller.

Skew 72° Warp.
Diameter $D = 0.2$ m;
Rotational speed $n = 30.0$ rps;
Hub radius $r_H / R = 0.2$;
Number of blades $Z = 5$;
Expanded area ratio $A_E / A_O = 0.725$;
Design $K_T = 0.213$;
Advance coefficient $J = 0.889$;
Chordwise loading distribution: NACA-a=0.8;
Chordwise thickness distribution: NACA-66 mod.

r/R	b/D	e_0/D	$\theta_s, ^\circ$	x_s/D	$\Gamma/\Gamma_{0.5}$
0.20	0.174	0.0434	0.0	0.0	0.0
0.25	0.202	0.0396	-4.647	0.0	0.240
0.30	0.229	0.0358	-9.293	0.0	0.445
0.40	0.275	0.0294	-18.816	0.0	0.810
0.50	0.312	0.0240	-27.991	0.0	0.987
0.60	0.337	0.0191	-36.770	0.0	1.0
0.70	0.347	0.0146	-45.453	0.0	0.953
0.80	0.334	0.0105	-54.245	0.0	0.760
0.90	0.280	0.0067	-63.102	0.0	0.525
0.95	0.210	0.0048	-67.531	0.0	0.355
1.00	0.000	0.0029	-72.000	0.0	0.0

Table 5. Convergence of the iterative alignment process as to design blade geometry.

(a). Camber f_0/b

r/R	L	NL(1)	NL(2)	NL(3)	NL(4)	NL(5)
0.4	0.0357	0.0352	0.0367	0.0361	0.0362	0.0362
0.5	0.0341	0.0337	0.0335	0.0335	0.0335	0.0335
0.6	0.0291	0.0280	0.0276	0.0275	0.0275	0.0275
0.7	0.0250	0.0239	0.0237	0.0237	0.0237	0.0237
0.8	0.0210	0.0199	0.0198	0.0198	0.0198	0.0198
0.9	0.0158	0.0144	0.0144	0.0144	0.0144	0.0144
0.95	0.0179	0.0168	0.0171	0.0172	0.0172	0.0172

(b). Pitch P/D

r/R	L	NL(1)	NL(2)	NL(3)	NL(4)	NL(5)
0.4	1.4564	1.5060	1.5081	1.5012	1.5020	1.5020
0.5	1.3831	1.3924	1.3909	1.3896	1.3897	1.3897
0.6	1.2839	1.2667	1.2677	1.2662	1.2662	1.2662
0.7	1.1966	1.1586	1.1604	1.1591	1.1591	1.1591
0.8	1.0970	1.0508	1.0527	1.0518	1.0518	1.0518
0.9	0.9812	0.9363	0.9379	0.9372	0.9372	0.9372
0.95	0.9342	0.8855	0.8864	0.8859	0.8859	0.8859

Table 6. Comparison of the pitch and camber distributions for propeller DTMB 4498 obtained by the authors (FRSPD-98 code) with PBD-10 design code outputs.

(a). Camber f_0/b

r/R	PBD-10	FRSPD-98 (F-1)	FRSPD-98 (F-3)
0.4	0.0378	0.0362	0.0337
0.5	0.0336	0.0335	0.0315
0.6	0.0282	0.0275	0.0261
0.7	0.0227	0.0237	0.0225
0.8	0.0181	0.0198	0.0188
0.9	0.0151	0.0144	0.0137
0.95	0.0175	0.0172	0.0165

(b). Pitch P/D

r/R	PBD-10	FRSPD-98 (F-1)	FRSPD-98 (F-3)
0.4	1.460	1.5020	1.4735
0.5	1.375	1.3897	1.3698
0.6	1.273	1.2662	1.2520
0.7	1.160	1.1591	1.1495
0.8	1.044	1.0518	1.0464
0.9	0.937	0.9372	0.9364
0.95	0.884	0.8859	0.8850

(c). Convergence of the forces refinement procedure.
Design $K_T = 0.213$.

Iteration number	(F-1)	(F-2)	(F-3)
K_T	0.22410	0.21185	0.21384

This magnitude (and its symbol W_m) corresponds to the projection of the total induced velocity on the outward axis in local coordinate system fixed on blade mean surface used in [5] from where all the data for comparison were borrowed. The agreement of the velocity components' values has appeared quite satisfactory. The greatest difference was registered for radial velocity when relative variance in the middle point on the chord of considered section amounted 20% approximately. Withal it is interesting to note that magnitude W_m has proved very close to PBD-10 results. The some disagreement was in W_θ and W_r velocity components didn't lead to the significant difference in the final pitch and camber distributions predicted by both programs (see Tables 6(a) and (b)). All the above-discussed results correspond to the FRSPD-98 code outputs after the first step of the

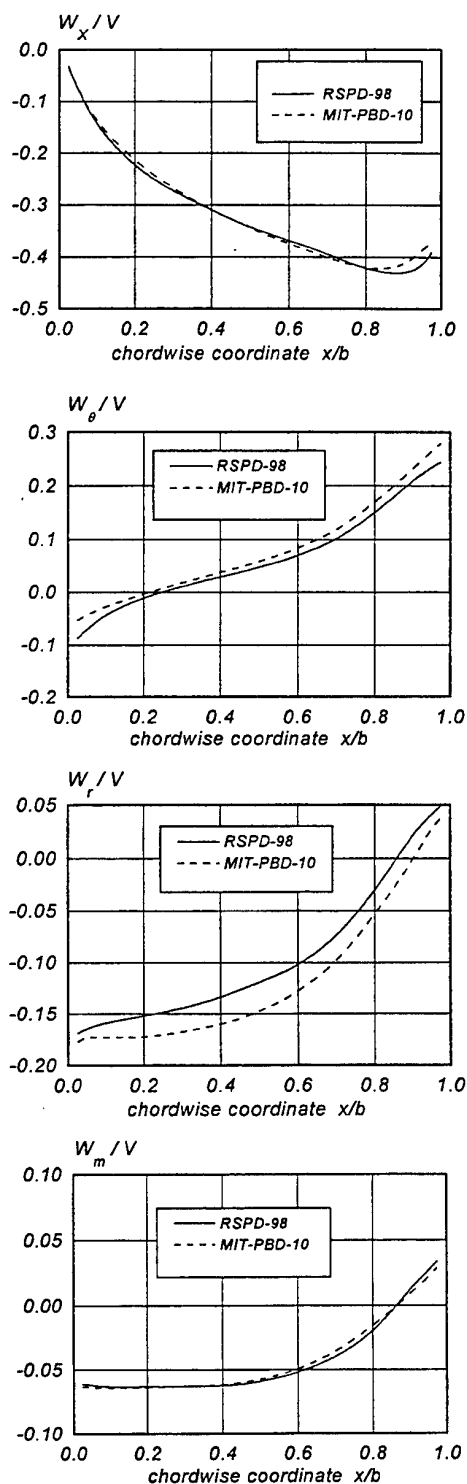


Fig.5 Computation data on induced velocity components at $r = 0.7$ radius for DTMB4498 propeller design example.

external cycle in terms of propeller forces refinement. To have a complete information about the presented design procedure the results of geometry definition after the elaboration of the integral propeller performances with use of generalized Jowkowski's theorem are given in the same Tables 6(a) and 6(b). The convergence of the refinement process as to forces has been attained in three iterations that one can see from the Table 6(c).

SOME RESULTS ON RADIAL VELOCITY EFFECT ON THE DESIGN BLADE GEOMETRY

From the above-considered design example of DTMB4498 propeller one can conclude that accounting for radial velocity component is absolutely necessary in the definition of the blade geometry elements of the propeller with such complex blade configuration characterized by the high skew and warp. The radial pitch distributions presented on Fig.4(b) clearly demonstrate the difference between usual linear theory and non-linear lifting-surface method takes place in this case. It is obvious from the design equation (11) that said difference determines by the accounting of the radial velocity component above all.

Meanwhile as the authors have shown [14], [15] the linear lifting surface theory allows the quite accurate prediction of the camber and pitch in the case of purely skewed propellers without rake's warp. Moreover the diapason of the skew investigated in these references was rather wide. To elaborate the boundaries of this diapason and to compare directly the linear and nonlinear design methods concerning to effect of the radial velocity on the skewed propellers' blade geometry the authors have worked out the special calculations. Some results of these calculations are presented below.

The DTMB series skewed propellers already used by the forces estimation were the objects of this study. All these propellers have the same main input elements as given in the Table 4 and differ only due to maximum skew angle which vary as follows: propeller 4381 ($\theta_s^* = 0^\circ$, symmetrical contour), propeller 4382 ($\theta_s^* = 36^\circ$), propeller 4383 ($\theta_s^* = 72^\circ$). The considered propellers have not rake's warp and are designed on equal operation conditions ($K_T = 0.213$; $J = 0.889$). Besides that we dispose of the information about the model geometry characteristics and experimental performances for these propellers designed and tested in DTMB [5], [17], [18]. These data are presented in the Table 7 together with computation distributions of the camber and pitch predicted by

both linear and non-linear lifting surface algorithms. The authors' computation data correspond to the first step of the external forces' refinement procedure, i.e. it were obtained without elaboration of the propeller forces by the lifting surface calculation. The fulfilled comparison allows to judge about the concordance of the calculated geometry elements to model ones and, consequently, to experimental propeller performances.

In particular as one can see from the Tables 7(a) and (b) the both algorithms yield quite close results in the case of symmetrical blade contour (propeller 4381) and in the case of skewed blade with total skew angle $\theta_s^* = 36^\circ$ (propeller 4382). These results appear in good agreement with DTMB model geometry. Taking into account the fact that two said models have shown the required thrust coefficient in the experiment with tolerance $\pm 2\%$ we can infer that both linear and final FRSPD-98 projects will ensure the prescribed integral performance.

The difference between linear and non-linear techniques rises with increase of skew. As it is sprung out from the analysis of 4383 propeller data the disagreement between the calculation and model geometry increase also especially at the exterior radii ($\bar{r} \geq 0.8$). However, it has to be noted that in the test DTMB4383 model has revealed the thrust coefficient approximately on 7% greater than required while authors' non-linear design procedure has reduced the pitch in comparison with model one (on 1.6% at $\bar{r} = 0.8$ and on 2% at $\bar{r} = 0.9 - 0.95$). In view of this fact it is logical to assume that FRSPD-98 design will approve better with regards to required thrust coefficient particularly after the corrective of the forces' values (compare the variance in thrust coefficient registered in the Tables 3 and 7(c)).

The distinction of the FRSPD-98 design from linear version design and DTMB project worked out also with use of linear lifting surface program [18] is referred by the accounting of the radial velocity effect. The magnitude of the makeweight due to radial velocity increases with upsurge of skew that in particular is illustrated by the data presented in the Table 8. In this table the magnitude $\bar{W}_m = \bar{W}_r (\partial z_c^\circ / \partial y^0)$ represented the contribution of the radial component in the kinematic boundary condition is compared with normal induced velocity component \bar{W}_n lying in the plane of cylindrical blade section, i.e. component which de facto is taken into account in the frameworks of linear theory.

All the design examples studied heretofore answer the case of isolated propeller in zero uniform velocity field, i.e. the open-water conditions.

Table 7. Calculated camber and pitch of the skewed series propellers defined with use of both linear and non-linear lifting surface techniques in comparison with DTMB tested model geometry.

Design conditions: $K_T = 0.213$; $J = 0.889$.

K_T^{test} is taken from DTMB open-water curves for model propellers [5].

(a). Propeller 4381 (skew 0°)

$$\Delta K_T = (K_T^{test} - K_T) / K_T^{test} = -1.43\%$$

r/R	camber f_0/b			pitch P/D		
	SPD-96	FRSPD-98	DTMB model	SPD-96	FRSPD-98	DTMB model
0.40	0.0323	0.0351	0.0348	1.3261	1.3139	1.3580
0.50	0.0304	0.0313	0.0307	1.3169	1.3140	1.3361
0.60	0.0250	0.0246	0.0245	1.2605	1.2623	1.2797
0.70	0.0207	0.0199	0.0191	1.2078	1.2099	1.2099
0.80	0.0168	0.0157	0.0148	1.1442	1.1464	1.1366
0.90	0.0125	0.0114	0.0123	1.0638	1.0673	1.0660
0.95	0.0154	0.0139	0.0128	1.0427	1.0443	1.0310

(b). Propeller 4382 (skew 36°)

$$\Delta K_T = (K_T^{test} - K_T) / K_T^{test} = +2.29\%$$

r/R	camber f_0/b			pitch P/D		
	SPD-96	FRSPD-98	DTMB model	SPD-96	FRSPD-98	DTMB model
0.40	0.0318	0.0335	0.0344	1.3936	1.3975	1.4117
0.50	0.0303	0.0302	0.0305	1.3520	1.3603	1.3613
0.60	0.0254	0.0244	0.0247	1.2723	1.2806	1.2854
0.70	0.0214	0.0201	0.0199	1.2008	1.2047	1.1999
0.80	0.0178	0.0161	0.0161	1.1179	1.1136	1.1117
0.90	0.0133	0.0127	0.0134	1.0186	1.0150	1.0270
0.95	0.0161	0.0151	0.0140	0.9844	0.9857	0.9850

(c). Propeller 4383 (skew 72°)

$$\Delta K_T = (K_T^{test} - K_T) / K_T^{test} = +6.99\%$$

r/R	camber f_0/b			pitch P/D		
	SPD-96	FRSPD-98	DTMB model	SPD-96	FRSPD-98	DTMB model
0.40	0.0357	0.0368	0.0385	1.4564	1.4826	1.4588
0.50	0.0341	0.0337	0.0342	1.3831	1.4034	1.3860
0.60	0.0291	0.0279	0.0281	1.2839	1.2979	1.2958
0.70	0.0250	0.0231	0.0230	1.1966	1.1982	1.1976
0.80	0.0209	0.0190	0.0189	1.0970	1.0783	1.0959
0.90	0.0158	0.0155	0.0158	0.9812	0.9639	0.9955
0.95	0.0179	0.0172	0.0168	0.9342	0.9266	0.9450

Table 8. The allotment due to induced radial velocity related to normal induced velocity component lying in the plane of cylindrical blade section.

$r/R = 0.3$

x/b	$ W_m/W_\eta $				
	4381	4382	4383	4497	4498
0.100	0.00068	0.00957	0.01662	0.02666	0.07232
0.300	0.00079	0.00298	0.00091	0.03017	0.05582
0.500	0.00000	0.00209	0.00864	0.03138	0.04900
0.700	0.00107	0.00597	0.01506	0.03012	0.04295
0.900	0.00121	0.00253	0.00443	0.01850	0.02993

$r/R = 0.6$

x/b	$ W_m/W_\eta $				
	4381	4382	4383	4497	4498
0.100	0.00280	0.00180	0.01730	0.10579	0.27437
0.300	0.00135	0.00332	0.01975	0.07846	0.15943
0.500	0.00000	0.00698	0.02224	0.06636	0.11619
0.700	0.00120	0.00920	0.02199	0.05255	0.07410
0.900	0.00209	0.00683	0.00969	0.02011	0.02459

$r/R = 0.9$

x/b	$ W_m/W_\eta $				
	4381	4382	4383	4497	4498
0.100	0.00170	0.18489	0.51134	0.25557	0.88470
0.300	0.00042	0.04250	0.25082	0.10761	0.46592
0.500	0.00000	0.03379	0.13183	0.10094	0.22948
0.700	0.00026	0.02751	0.06702	0.06236	0.10124
0.900	0.00046	0.01987	0.00557	0.02740	0.03525

At once the authors' design method and corresponded design code FRSPD-98 allow to realize the direct accounting for inflow velocity field in which propeller operate. In the general case inflow velocity vector can embrace all three components: axial, tangential and radial if we use the cylindrical coordinate system. An accounting for radial inflow velocity component deserves special attention. It can be hugely important as in the case of single propeller design adapted to the hull wake as when the marine integrated propulsors (counter-rotated and tandem propellers, AZIPOD system, stator-rotor combination) are studied.

There are not many references in which the effect of radial velocity on the propeller design geometry is examined separately. The paper by Brockett [13] gives an example of such exclusive investigations. In mentioned paper the design of DTMB4498 propeller has been carried out in the velocity field

characterized by radial component $\bar{V}_{\psi r} = -0.05$ constant along the radius.

Using the FRSPD-98 design code the authors have conducted the systematic design calculations for propellers operating in the wakes embrace the radial velocity. Some results of these calculations are discussed below.

First of all it has to be noted that qualitative conclusions about the importance of the accounting for induced radial velocity effects made above are all-out valid in relation to inflow radial velocity. Scilicet such an account is more indispensable in the cases of highly skewed and warped blades because for symmetrical or small skewed blades the radial velocity effect is noticeably reduced due to small (close to zero) values of the $\partial \bar{z}_c^0 / \partial \bar{y}_0$ derivative (see design equation (11)) even if the radial velocity itself is not small.

In the Table 9 and on the Fig.6(a) and (b) the results of two propeller designs in the wakes with radial velocity component are summarized. These examples correspond to the warped propellers DTMB 4497 (skew 36°) and DTMB4498 (skew 72°) at the same design conditions as given in the Table 4 barring spanwise circulation distribution (it was determined as optimal). In pursuance of Brockett's wake sample the authors adopt the constant inflow radial velocity $\bar{V}_{\psi r} = \pm 0.05$ along the radius. Hereby two cases are examined for each of propellers: the first case when radial velocity direct outward to the blade tip (positive $\bar{V}_{\psi r}$) and the second when it direct to the hub (negative $\bar{V}_{\psi r}$).

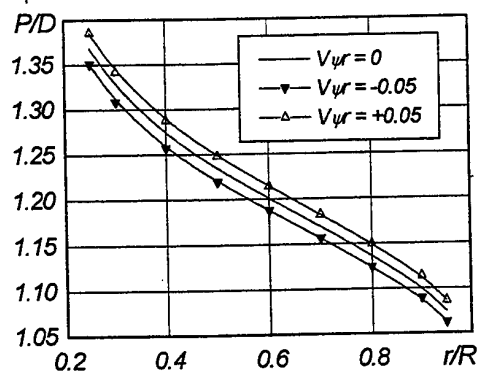


Fig.6(a) The effect of radial inflow velocity component on the design spanwise pitch distribution for propeller DTMB4497.

Table 9. The effect of radial inflow velocity component on the design spanwise camber f_0/b distribution.

(a). Propeller 4497 (skew 36° Warp.)

r/R	$\bar{V}_{\psi r} = 0$	$\bar{V}_{\psi r} = -0.05$	$\bar{V}_{\psi r} = +0.05$
0.25	0.0236	0.0232	0.0239
0.40	0.0227	0.0224	0.0230
0.60	0.0189	0.0187	0.0191
0.80	0.0185	0.0183	0.0187
0.95	0.0240	0.0238	0.0242

(b). Propeller 4498 (skew 72° Warp.)

r/R	$\bar{V}_{\psi r} = 0$	$\bar{V}_{\psi r} = -0.05$	$\bar{V}_{\psi r} = +0.05$
0.25	0.0179	0.0173	0.0185
0.40	0.0205	0.0200	0.0210
0.60	0.0201	0.0199	0.0204
0.80	0.0212	0.0210	0.0215
0.95	0.0251	0.0248	0.0254

Table 10. The relative alterations of the design camber and pitch due to radial inflow velocity effect for DTMB 4498 propeller.

r/R	camber $\Delta(f_0/b)$		pitch $\Delta(P/D)$	
	FRSPD-98	Brockett	FRSPD-98	Brockett
0.40	-2.5 %	+0.3 %	-2.4 %	-2.5 %
0.60	-1.3 %	-1.0 %	-2.2 %	-2.4 %
0.80	-1.0 %	-1.6 %	-2.3 %	-2.3 %

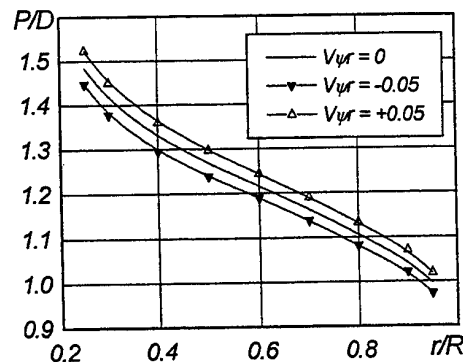


Fig.6(b) The effect of radial inflow velocity component on the design spanwise pitch distribution for propeller DTMB4498.

The calculated results as to camber are presented in the Tables 9(a) and (b). The analogous estimations for pitch are shown on the Fig.6(a) and (b).

The main inferences one can make on the base of these results are following. The radial inflow velocity practically has no influence on the blade sections' camber. The effect of this velocity leads to the increase of the pitch values when \bar{V}_{vr} directs outward and to the decrease when \bar{V}_{vr} directs to the hub. The alterations in the pitch amounted respectively +1.3% and -1.3% for 4497 propeller (lesser skew) whereas +2.3% and -2.3% for propeller 4498 (higher skew). As to the latter design (propeller 4498) the obtained results are in the good agreement with the data by Brockett [13] as it is reflected in the Table 10.

CONCLUSIONS

A new lifting surface technique has been presented for account of the real blade configuration and radial velocity component in propeller blade design problem. In spite of obvious necessity of the further direct experimental testing of the developed algorithm the results presented in this paper confirm quite high quality and precision of the design procedure under consideration.

The special calculations worked out by the authors have demonstrated the importance of the accounting for induced radial velocity component in the case of the high blade skew and complex rake distribution.

An essential advantage of the presented algorithm consists in the direct accounting for radial inflow velocity effects on the design blade geometry. The latter feature of the described technique is rather important in the refinement of the blades geometry for propeller operating as the element of AZIPOD system when inflow radial velocities can measure up formidable magnitudes due to non-cylindrical pod and hub configurations.

In terms of practical calculations the presented method guarantees the more fast convergence than well-known PBD-10 algorithm by Kerwin et. al. described in [5].

REFERENCES

1. Beek, T., Vorst, H., "On the Validation of an Unsteady Lifting Surface Method for Propeller Design Analysis," Proceedings of the Propellers / Shafting'94 Symposium, SNAME, 1994, pp.11/1-24.
2. Jessup, S.D., Wang, H.-C., "Propeller Design and Evaluation for a High Speed Patrol Boat Incorporating Iterative Analysis with Panel Methods," Proceedings of the Propellers/Shafting'97 Symposium, SNAME, 1997, pp.11/1-20.
3. Kerwin, J.E., "Computer Techniques for Propeller Blade Section Design," Transactions of the Second Lips Propeller Symposium, Drunen, Holland, 1973, pp.7-34.
4. Brockett, T.E., "Effect of Freestream Radial Velocity Component on Hydrodynamic Analysis of Propellers," Journal of Ship Research, Vol.27, No.2, 1983.
5. Greeley, D.S., Kerwin, J.E., "Numerical Methods for Propeller Design and Analysis in Steady Flow," Transactions of SNAME, Vol.90, 1982, pp.415-453.
6. Kinnas, S.A., "A General Theory for the Coupling Between Thickness and Loading for Wings and Propellers," Revised version for JSR, Oct.1990, pp.1-29. (published in Journal of Ship Research, No.36, 1992).
7. Zavadovski, N.Y., "Theoretical Foundations of the Hydrodynamic Calculations for Propellers with Complex Blade Geometry," The Problems of the Shipbuilding, series: Ship Designing, 1984, Vol.39, pp.39-54. (in Russian).
8. Zavadovski, N.Y., "On the Identity between the Free and Bound Vortices Strength in Unsteady Lifting Surface Theory," Transactions of Leningrad State University, 1985, No.15, pp. 40-45. (in Russian).
9. Achkinadze, A.S., "Design of Optimal Screw Propellers, Turbines and Freely Rotating Turbopropellers Adapted for Radial Non-uniform Swirled Flow," Proc. of the 4th PRADS Symp., 1989, Varna, Bulgaria, Vol.3, pp. 124/1-13.
10. Bavin, V.F., Zavadovski, N.Y., Levkovski, Y.L. and Mishkevich, V.G., "Marine Propellers: Modern Calculation Methods," Sudostroenie, Leningrad, 1983, 296 p. (in Russian).
11. Kochin, N.E., Vector Analysis and the Foundations of Tensor Analysis, ONTI, GTTI, Leningrad, 1934, 456 p. (in Russian).
12. Kerwin, J.E., Keenan, D.P., Black, S.D. and Diggs, J.G., "A Coupled Viscous/Potential Flow Design Method for Wake-adapted, Multi-stage, Ducted Propulsors Using Generalized Geometry," Transactions of SNAME, Vol. 102, 1994, pp.23-56.
13. Achkinadze, A.S., "Design of Optimal Wake Adapted Screw Propeller Using Vortex Theory," Textbook, St.Petersburg State Marine Technical University, 1996, 86 p. (in Russian).
14. Achkinadze, A.S., Krasilnikov, V.I., "A Generalized Optimum Condition for Wake Adapted Screw Propeller," Proceedings of

Propellers/Shafting'97 Symposium, SNAME, 1997, pp. 22/1-28.

15. Krasilnikov, V.I., "Hydrodynamic Design for Non-cavitating Screw Propeller Using Generalized Linear Model of the Vortex Wake," PhD thesis, Theory of Ship Department, St.Petersburg State Marine Technical University, 1997, 188 p. (in Russian).

16. Artyushkov, L.S., Achkinadze, A.S., and Rousetski, A.A., "Marine Propulsors," Sudostroenie, Leningrad, 1988, 296 p. (in Russian).

17. Kerwin, J.E., Lee, C.S., "Prediction of Steady and Unsteady Marine Propeller Performance by Numerical Lifting Surface Theory," Transaction of SNAME, Vol.86, 1978.

18. Cumming, R.A., Morgan, Wm.B., and Boswell, R.J., "Highly Skewed Propellers," Transactions of SNAME, Vol.80, 1972, pp.98-135.

APPENDIX

Expression for partial derivative $\partial z_c^0 / \partial y_0$ in design equation

It is important for practical employment of the design equation (11) in numerical procedure to deduce the convenient identity for partial derivative $\partial z_c^0 / \partial y_0$. Let us write the equations of the blade mean surface in parametric form using local coordinate system $M(x^0, y^0, z^0)$:

$$\left. \begin{aligned} x_c^0 &= x_c^0(\bar{r}, \xi') \\ y_c^0 &= y_c^0(\bar{r}, \xi') \\ z_c^0 &= z_c^0(\bar{r}, \xi') \end{aligned} \right\} \quad (19)$$

The differentials of local coordinates dx_c^0, dy_c^0, dz_c^0 are represented via the differentials of parameters \bar{r} and ξ' by following identities:

$$\left. \begin{aligned} dx_c^0 &= \frac{\partial x_c^0}{\partial \bar{r}} d\bar{r} + \frac{\partial x_c^0}{\partial \xi'} d\xi' \\ dy_c^0 &= \frac{\partial y_c^0}{\partial \bar{r}} d\bar{r} + \frac{\partial y_c^0}{\partial \xi'} d\xi' \\ dz_c^0 &= \frac{\partial z_c^0}{\partial \bar{r}} d\bar{r} + \frac{\partial z_c^0}{\partial \xi'} d\xi' \end{aligned} \right\} \quad (20)$$

To get the searching derivative we have to write the relation dz_c^0 / dy_0 at $dx_c^0 = 0$ condition that just corresponds to treatment of the partial derivative

$\partial z_c^0 / \partial y_0$. Using first equation from (20) and $dx_c^0 = 0$ condition one can obtain

$$\frac{d\xi'}{d\bar{r}} = - \frac{\partial x_c^0}{\partial \bar{r}} / \frac{\partial x_c^0}{\partial \xi'} \quad (21)$$

The latter formula characterizes the local direction of $x_c^0 = \text{const}$ line. Like that by means of second and third equations from (20) and taking into account (21) we find the derivative of interest:

$$\frac{\partial z_c^0}{\partial y_0} = \frac{\frac{\partial z_c^0}{\partial \bar{r}} + \frac{\partial z_c^0}{\partial \xi'} \frac{d\xi'}{d\bar{r}}}{\frac{\partial y_c^0}{\partial \bar{r}} + \frac{\partial y_c^0}{\partial \xi'} \frac{d\xi'}{d\bar{r}}} \quad (22)$$

After the substitution of (21) in (22) we obtain final expression available for proximate calculations:

$$\frac{\partial z_c^0}{\partial y_0} = \frac{\frac{\partial z_c^0}{\partial \bar{r}} \frac{\partial x_c^0}{\partial \xi'} - \frac{\partial z_c^0}{\partial \xi'} \frac{\partial x_c^0}{\partial \bar{r}}}{\frac{\partial y_c^0}{\partial \bar{r}} \frac{\partial x_c^0}{\partial \xi'} - \frac{\partial y_c^0}{\partial \xi'} \frac{\partial x_c^0}{\partial \bar{r}}} \quad (23)$$

It does not make difficulties to compute the partial derivatives in numerator and denominator of (23) when relations between local and global cartesian propeller fixed coordinates $(\bar{x}, \bar{y}, \bar{z})$ are determined:

$$\left. \begin{aligned} x^0 &= \bar{x} \cos(\bar{x}^0, \bar{x}) + \bar{y} \cos(\bar{x}^0, \bar{y}) + \bar{z} \cos(\bar{x}^0, \bar{z}) - \bar{x}_A \\ y^0 &= \bar{x} \cos(\bar{y}^0, \bar{x}) + \bar{y} \cos(\bar{y}^0, \bar{y}) + \bar{z} \cos(\bar{y}^0, \bar{z}) - \bar{y}_A \\ z^0 &= \bar{x} \cos(\bar{z}^0, \bar{x}) + \bar{y} \cos(\bar{z}^0, \bar{y}) + \bar{z} \cos(\bar{z}^0, \bar{z}) - \bar{z}_A \end{aligned} \right\} \quad (24)$$

where directive cosines for local coordinate system M are following

$$\left. \begin{aligned} \cos(x^0, x) &= \sin \varphi_A \\ \cos(x^0, y) &= -\cos \varphi_A \sin \theta_A \\ \cos(x^0, z) &= \cos \varphi_A \cos \theta_A \\ \cos(y^0, x) &= 0 \\ \cos(y^0, y) &= \cos \theta_A \\ \cos(y^0, z) &= \sin \theta_A \\ \cos(z^0, x) &= \cos \varphi_A \\ \cos(z^0, y) &= \sin \varphi_A \sin \theta_A \\ \cos(z^0, z) &= -\sin \varphi_A \cos \theta_A \end{aligned} \right\} \quad (25)$$

and $(\bar{x}_A, \bar{y}_A, \bar{z}_A)$ are coordinates of point local coordinate system M fixed on.

VISCOUS FLOWS

Chairman : M.Visonneau

CALCULATION OF TURBULENT FLOWS AROUND VLCC HULL FORMS WITH STERN FRAMELINE MODIFICATION

Wu-Joan Kim, Do-Hyun Kim, Suak-Ho Van

Marine Transportation Systems Research Center
Korea Research Institute of Ships & Ocean Engineering
Jang-dong 171, Yusung-gu, Taejon 305-343, KOREA
(Fax) +82 42 868 7274 (e-mail) wjkim@mailgw.kimm.re.kr

ABSTRACT

For the designers in ship yards to use CFD tools in judging their hull forms, it is a prerequisite to prove that the computational modeling is affordable and sufficient to provide right information within short period of time. In order to ascertain the above request, turbulent flow calculations are performed for the two modern practical VLCCs with the same forebody and the slightly different afterbody, i.e., KRISO 300K VLCC F1+A1(KVLCC) and F1+A2(KVLCC2). The Reynolds-averaged Navier-Stokes equations for turbulent flows around model ships are solved using the cell-centered finite-volume scheme. Several variations of two-equation turbulence models, such as the standard $k-\epsilon$ model(SKE), the RNG-based $k-\epsilon$ model(RNG), and the realizable $k-\epsilon$ model(RKE), are tested to identify the differences caused by the turbulence models. The calculated results around the two VLCC hull forms using O-O grid topology and profile-fitted surface meshes are compared to the measured data from towing tank experiment. It is observed that the realizable $k-\epsilon$ model provided realistic wake distribution with hook-like shape, while other two models failed. It is very encouraging to see that the CFD with relatively simple turbulence closure can tell the difference quantitatively as well as qualitatively for the two hull forms with stern frameline modification.

INTRODUCTION

In the initial stage of hull form design, it is customary to develop a new hull form based on a parent ship. Thus, it is essential for a designer to get enough information on changes of the flow characteristics due to the hull form variation. Traditionally towing tank tests have been carried out for the performance prediction of commercial ships such as tanker, bulk carrier, and container ship. However, it usually takes several months and costs lots of money. Recently some shipyards are trying to utilize Computational Fluid Dynamics(CFD) for the performance prediction during the initial hull form design. It is very probable that the application of CFD as a colander, can reduce the number of model tests required for the hull form optimization. However, before declaring that CFD is a useful tool, it should be confirmed that it can tell the difference of flow characteristics due to the amount of hull form change as much as typically made in the shipyards. Another important issue to point out is that the users in ship yards are not familiar

with the details of computational methods, stating that the numerical methods should be robust. Furthermore, CFD tools should provide the results within short period of time, since ship yards usually allow to get the results overnight.

There have been several workshops on viscous flow around a ship (e.g., 1990 SSPA-CTH-IIHR Workshop[1], 1994 Tokyo Workshop[2], and 1998 Osaka Colloquium[3], etc.). For the workshops, relatively simple hull forms without any bulbs such as HSVA/Dyne tanker and Series 60 models were used for the validation of the numerical methods and turbulence models. However, the hull forms used in those experiments are quite different from the modern hull forms of actual ships today. For better understanding of the flow around a modern ship, it is necessary to validate the computational modeling against the reliable experimental data of practical commercial hull forms.

In the present study turbulent flow calculations are performed for the two modern practical VLCCs with the same forebody and the slightly different

afterbody(i. e., KRISO 300K VLCC F1+A1, F1+A2). The Reynolds-averaged Navier-Stokes equations for turbulent flows around model ships are solved using the cell-centered finite-volume schemes with several variation of the $k-\epsilon$ turbulence model. Two-equation model like $k-\epsilon$ model is still cost-effective to be used for design purpose. Furthermore, the so-called Launder and Spalding's wall function is utilized to bridge the fully turbulent region and the wall to save computational efforts. Kim et al.[4] tested various turbulence models with wall function, showing the possibility of application to ship flow calculation. For the calculation, hull surface is depicted as a spline net, where bow and stern profiles are considered as grid lines with the same indices. Field grid system with O-O topology is generated using the solution of three-dimensional Poisson equation and trans-finite interpolation. The calculated results around the two VLCC hull forms are compared to the measured data from towing tank experiment.

In the followings the details of computational modeling and calculated results are described. It is interesting to see that the CFD with relatively simple turbulence closure can tell the difference quantitatively as well as qualitatively for the two hull forms with stern frame modification.

HULL FORM AND EXPERIMENT

To confirm the capability of CFD as a design tool, two VLCC hull forms are chosen with the same forebody and slightly different afterbody. At first, a 300K VLCC hull form(F1+A1, namely, KVLCC) was designed and experiments were performed. Later, another 300K VLCC hull form(F1+A2, namely, KVLCC2) with the same forebody and different afterbody was tested. The second one(KVLCC2) has more U-shaped stern frame lines, as shown in Fig. 1. The principal particulars of the test ships are given in Table 1. Two model ships of KRISO VLCCs with the scale ratio of 1/58, are made of wood. Turbulence stimulators are studded at 19 station and at the middle of bow bulb with 10 mm interval, so as to make sure that the flow becomes fully turbulent afterwards. The details of measurement device, techniques and the uncertainty analysis results are already reported in other papers(e.g., Van et al.[5]). Thus, in the present paper, only the brief descriptions are given.

The experiments were carried out in the towing tank of Korea Research Institute of Ships and Ocean Engineering(KRISO). The model ship is fixed at the towing carriage by using two clamping devices for local mean velocity measurements, in order to prevent the difficulties in positioning the probes in the

experiments and in computing the flow for validation. However, the resistance tests were performed in the free condition, since towing force measurement is not very accurate in the fixed condition. It is believed that the difference of resistance performance between the fixed and free condition is very small for the present VLCC hull forms. For the local measurement of three-dimensional velocity field around the stern region, a 5-hole Pitot tube rake was utilized. However, local flow angles sometimes were out of calibration range of $\pm 40^\circ$ of pitch and yaw angles, especially just behind a stern cap or transom. In case that the local flow angle is out of calibration range, the measured data was discarded and velocity components could not be determined.

For both ships, the stern cap of semi-sphere was attached to prevent the abrupt change at the end of stern bossing. Thus, the propeller plane(St. 0.35) is located just behind the stern cap. The propeller diameter is 9.8 m. The shaft center line of the VLCC is located at 5.8 m above the base line(i. e., $Z/L_{pp} = -0.04688$ from calm free surface). The measured mean velocity components at the propeller plane of the 300K VLCC models are compared in Fig. 2. The shape of wake contours are not much different since the hull form variation is not so great. However, it is observed that wake contours are more of circular shape and have stronger hook for KVLCC2. For details of wake distribution will be discussed later along with calculated results.

GOVERNING EQUATIONS

The governing equations for turbulent flow in the present study are Reynolds-averaged Navier-Stokes equations for momentum transport and the continuity equation for mass conservation. The Cartesian coordinates are used, where (x, y, z) denotes downstream, starboard, and upward direction, respectively. The origin of the coordinates is located at the midship and calm free surface. All the quantities are non-dimensionalized by ship speed (V), length (L_{pp}), and fluid density(ρ).

Continuity equation

$$\frac{\partial u_k}{\partial x_k} = 0 \quad (1)$$

Momentum transport equation

$$\frac{\partial u_i}{\partial t} + \frac{\partial(u_i u_j)}{\partial x_j} = -\frac{\partial p}{\partial x_i} + \frac{\partial \tau_{ij}}{\partial x_j} \quad (2)$$

, where $u_i = (u, v, w)$ are velocity components in $x_i = (x, y, z)$ directions, while p is static pressure. Stress tensor τ_{ij} can be written using Boussinesq's isotropic eddy viscosity hypothesis as follows.

$$\tau_{ij} = \nu_e \left(\frac{\partial u_i}{\partial x_j} + \frac{\partial u_j}{\partial x_i} \right) - \frac{2}{3} \delta_{ij} k \quad (3)$$

Here, k is turbulent kinetic energy and ν_e is effective viscosity, i.e., the sum of turbulent eddy viscosity (ν_t) and molecular kinematic viscosity (ν).

$$\nu_e = \nu_t + \frac{1}{Re} \quad (4)$$

and Re is Reynolds number ($VL\rho\rho/\nu$).

For turbulence closure, three $k-\varepsilon$ models are utilized. Those are the standard $k-\varepsilon$ model (hereafter SKE)[6], the RNG-based $k-\varepsilon$ model (RNG)[7], and the realizable $k-\varepsilon$ model (RKE)[8]. With the $k-\varepsilon$ two-equation turbulence model, the eddy viscosity ν_t can be written as

$$\nu_t = C_\mu \frac{k^2}{\varepsilon} \quad (5)$$

In the standard $k-\varepsilon$ model (SKE) $C_\mu=0.09$, while in the RNG-based model (RNG) $C_\mu=0.085$. For the Realizable $k-\varepsilon$ model (RKE) C_μ has rather complicated form given in the followings.

$$C_\mu = \frac{1}{A_o + A_s \frac{U^* k}{\varepsilon}}$$

, where the terms are defined as

$$U^* = \sqrt{S_{ij}S_{ij} + \Omega_{ij}\Omega_{ij}},$$

$$S_{ij} = \frac{1}{2} \left(\frac{\partial u_i}{\partial x_j} + \frac{\partial u_j}{\partial x_i} \right),$$

$$\Omega_{ij} = \frac{1}{2} \left(\frac{\partial u_i}{\partial x_j} - \frac{\partial u_j}{\partial x_i} \right),$$

$$A_o = 4.0, \quad A_s = \sqrt{6} \cos \phi,$$

$$\phi = \frac{1}{3} \arccos(\sqrt{6} W),$$

$$W = \frac{S_{ij}S_{jk}S_{ki}}{\widetilde{S}^3}, \quad \widetilde{S} = \sqrt{S_{ij}S_{ij}}$$

Turbulent kinetic energy k can be obtained by the solution of the following transport equation. For

all three $k-\varepsilon$ models, equation for k has the same form as given by

Turbulent kinetic energy transport equation

$$\frac{\partial k}{\partial t} + \frac{\partial(u_j k)}{\partial x_j} = \frac{\partial}{\partial x_j} \left(\left(\nu + \frac{\nu_t}{\sigma_k} \right) \frac{\partial k}{\partial x_j} \right) + G - \varepsilon \quad (6)$$

, where ε represents the dissipation rate of turbulent kinetic energy and G is production term as given below.

$$G = \nu_t \left(\frac{\partial u_i}{\partial x_j} + \frac{\partial u_j}{\partial x_i} \right) \frac{\partial u_i}{\partial x_j} \quad (7)$$

In the standard $k-\varepsilon$ model (SKE) and the Realizable $k-\varepsilon$ model (RKE), $\sigma_k=1.0$, while in the RNG-based model (RNG) $\sigma_k=0.719$.

Transport equation for dissipation rate ε is written by

Dissipation rate of turbulent kinetic energy equation

$$\frac{\partial \varepsilon}{\partial t} + \frac{\partial(u_j \varepsilon)}{\partial x_j} = \frac{\partial}{\partial x_j} \left(\left(\nu + \frac{\nu_t}{\sigma_\varepsilon} \right) \frac{\partial \varepsilon}{\partial x_j} \right) + S_\varepsilon \quad (8)$$

In SKE and RNG,

$$S_\varepsilon = C_{\varepsilon 1} \frac{\varepsilon}{k} G - C_{\varepsilon 2} \frac{\varepsilon^2}{k}$$

where for SKE, $\sigma_\varepsilon=1.3$, $C_{\varepsilon 1}=1.44$, and $C_{\varepsilon 2}=1.92$, while for RNG, $\sigma_\varepsilon=0.719$, $C_{\varepsilon 1}=1.42$, and $C_{\varepsilon 2}$ is given by

$$C_{\varepsilon 2} = 1.68 + \frac{C_\mu \eta^3 (1 - \eta/4.38)}{1 + 0.012 \eta^3}$$

$$\text{where } \eta = S \frac{k}{\varepsilon}, \quad S = \sqrt{2 S_{ij} S_{ij}}.$$

In RKE,

$$S_\varepsilon = C_{\varepsilon 1} S_\varepsilon - C_{\varepsilon 2} \frac{\varepsilon^2}{k + \sqrt{\nu \varepsilon}}$$

where $\sigma_\varepsilon=1.2$, $C_{\varepsilon 2}=1.9$, and

$$C_{\varepsilon 1} = \max \left[0.43, \frac{\eta}{\eta + 5} \right].$$

It is advisory to use a near-wall turbulence model to resolve boundary layer up to the wall, however, it will require usually twice of grids. For the present study the so-called Launder and Spalding's wall function[5] is utilized to bridge the fully turbulent

region and the wall. The first grid point in the wall function approach is approximately 100 times off the wall compared to that in the near wall turbulence model. It provides the economy and robustness for CFD tools. Since the flows around a ship of the present interest, the so-called singular separation with back flow is not expected, although the formation of longitudinal vortices is often observed. The wall function is known to give good results for such a mild flow. The wall function adopted in the present calculation is given by

Launder and Spalding's wall function

$$\frac{U_P C_\mu^{1/4} k_P^{1/2}}{\tau_w} = \frac{1}{\chi} \ln(E n_P^*) \quad (9)$$

$$\chi = 0.41, \quad E = 8.342$$

where τ_w is wall shear stress, U_P and k_P are the magnitude of velocity and turbulent kinetic energy at the center of the first cell off the wall. The non-dimensionalized normal distance from the wall n_P^* is given by

$$n_P^* = \frac{C_\mu^{1/4} k_P^{1/2} n_P}{\nu}$$

Generation of turbulent kinetic energy at the first cell off the wall is given as follows.

$$\overline{G_P} = \tau_w \left(\frac{\partial U}{\partial n} \right)_P = \frac{\tau_w^2}{\chi C_\mu^{1/4} k_P^{1/2} n_P}$$

, while dissipation at that cell is written by

$$\overline{\varepsilon_P} = \frac{C_\mu^{3/4} k_P^{3/2}}{\chi n_P}$$

GRID GENERATION

To make it easier to apply the CFD to calculating turbulent flow around a practical hull form such as the present VLCC hull form, an efficient pre-processor is developed for surface and field grid generation[8].

A hull surface mesh generating program based on given station offsets along with stern and bow profiles has been developed. This new method employs non-uniform parametric splines with predetermined waterline end-shapes of natural spline, normal spline, ellipse, parabola, hyperbola, and their combinations. It takes less than ten minutes in PC to obtain hull surface meshes, starting from a given

offset table. Mesh topology chosen in the present study, to present hull surface with bulbous bow and stern end bulb, can be transformed into a rectangle. It implies that flow solvers are able to accommodate the mesh easily and their own accuracy does not deteriorate especially when turbulent quantities are determined by the so-called wall coordinate. The generated hull surface meshes can be used immediately as boundary surface grids for field grid generation

Utilizing the generated surface meshes, Poisson equation is solved to constitute the field grid system of O-O topology. In the present study outer boundary surface resembles a bullet, where appropriate boundary conditions are easily identified. Sorenson's method[9] is extended into three-dimensional one to specify grid-control functions. Weighted trans-finite interpolation is also utilized to specify the better initial guess and to make smooth transition of 3D grids into 2D boundary grids[10]. Fig. 3 shows obtained grid system for turbulent flow calculation around a VLCC hull form. Surface meshes near bow and stern are well fitted with profiles of the ship. Since the present calculation employs the so-called wall function approaches, the distance of the first grid point off the wall is around 0.5×10^{-3} . For the present calculation, three grid systems of 81X29X25, 97X33X33, and 113X37X41 grids are generated to investigate grid dependence of the solution. The calculated radial distribution of circumferentially averaged axial velocity components at propeller plane, which is the most important information for propeller design, is compared when the realizable $k-\varepsilon$ model is utilized. From Fig. 4, it is clear that 97X33X33 grids are sufficient for the practical applications. From now on, all calculated results shown in the paper are obtained with 97X33X33 grids.

NUMERICAL METHODS

The cell-centered finite-volume method is utilized to discretized governing equations, as discussed in Ferziger and Peric[11]. Governing equations are integrated over a grid cell Ω with boundary surface S , resulting in the following equations.

$$\begin{aligned} \int_S \vec{v} \cdot \vec{n} dS &= 0 \\ \frac{\partial}{\partial t} \int_\Omega u_i d\Omega + \int_S u_i \vec{v} \cdot \vec{n} dS \\ &= \int_S \tau_{ij} \vec{i}_j \cdot \vec{n} dS - \int_S p \vec{i}_i \cdot \vec{n} dS \end{aligned}$$

where \vec{i}_j is unit vector in x_j direction.

The first term of momentum transport equation, temporal derivative is ignored by putting very big time step, since only the steady solution is of the present interest. Convection terms are discretized using QUICK scheme of the third order. But the QUICK scheme requires 13 point stencil, resulting in complicated algebraic equations. Thus, the so-called deferred correction approach is adopted, which a simple upwind scheme is used with lagged higher order terms. The deferred correction makes 7 point stencil with simple linear equations.

Rewriting the third term of stress tensor,

$$\begin{aligned} \int_S \tau_{ij} \vec{i}_j \cdot \vec{n} dS &= \int_S \nu_t \left(\frac{\partial u_i}{\partial x_j} + \frac{\partial u_j}{\partial x_i} \right) \vec{i}_j \cdot \vec{n} dS \\ &= \int_S \nu_t \left(\text{grad}(u_i) \cdot \vec{n} + \frac{\partial u_j}{\partial x_i} \vec{i}_j \cdot \vec{n} \right) dS \end{aligned}$$

where the term with turbulent kinetic energy is included in pressure gradient. Central difference scheme is utilized for diffusion terms, while the terms coming from grid non-orthogonality is deferred. Linear equations obtained from 7 point stencil are solved using strongly implicit procedure[12].

If the pressure field is known a prior, momentum equations will give correct velocity field. However, those velocity components will not satisfy the continuity equation. To ensure divergence-free velocity field, the SIMPLEC method[13] is employed. Since the collocated grid arrangement is chosen, the artificial dissipation term in pressure correction equation is added, as discussed in Rhie and Chow[14]. As mentioned in the above momentum equation, pressure correction equation also have the terms related to grid skewness. In the present study, as recommended in Ferziger and Peric[11], the second correction is added to compensate for deferred correction terms in pressure correction equation. Again, the resulting linear equations are solved using strongly implicit procedure until the equation residual drops by an order of magnitude each iteration.

To complete the solution procedures, at first, hull surface meshes are generated as mentioned earlier. Taking the generated surface as a boundary surface, three-dimensional field grids are obtained. With the generated grid system, flow calculation is initiated, starting from uniform stream (i.e., abrupt start). With the grids and initial guess for flow field ready, iteration begins for coupled partial differential equations. After three momentum transport equations are solved sequentially to obtain preliminary velocity components, pressure correction equations is solved to get pressure field. Then, velocity components are corrected using new pressure field. In the next turbulence equations are solved and eddy viscosity

is updated. Iteration continues until total residuals of each momentum equation are less than 10^{-5} , which is about five order less than the initial residuals.

RESULTS AND DISCUSSIONS

In the followings the calculated results are compared with experiments. At first, for KVLCC, the results with three different turbulence models are discussed to investigate the effect of turbulence model on flow prediction. In the next, propeller plane wakes are investigated carefully for two hull forms with stern frameline modification to see that the present computational modelling can identify the difference of stern hull form quantitatively as well as qualitatively. It should be noted that the measurements were carried out in towing tank, thus, flow field was certainly affected by wave generation on the free surface. However, the present calculation ignores the effect of waves, since wave generation of the VLCC is not significant because of low Froude number. Instead, Neumann condition is applied on the calm free surface.

In Figs. 5 ~ 7, calculated velocity fields with SKE, RNG, and RKE are compared to experiments at station 2 and 0.35. The calculated results with SKE shows thicker boundary layer at station 2, while little bilge vortices are found at the propeller plane. For RNG, boundary layer thickness are predicted better, however, the RNG-based $k-\epsilon$ model still failed to predict distortion of axial velocity contours at the propeller plane. On the other hand, the realizable $k-\epsilon$ model(RKE) provides correct boundary layer thickness with hook-like distortion of axial velocity contours. It is rather surprising, since the wall function is utilized to skip the details of near wall turbulence phenomena. In Fig. 8 propeller plane wakes are compared. As expected from Fig. 5 and 6, SKE and RNG failed to predict the hook in U-contours, while RKE succeeded. The sharp turning of wake contours around lower part of 0.4R is observed, which is believed to come from the numerical method or grid topography.

Calculated turbulent kinetic energy and eddy viscosity are shown in Fig. 9 and 10. RNG provided lower level of turbulence than the others. Eddy viscosity contours of SKE and RNG show similar shapes, as expected from the axial velocity contours. RKE has lower eddy viscosity values than SKE and RNG except at the location above hub and near vortex core, where high eddy viscosity is concentrated. These figures might give some clues on that RKE gives nice hook-like shape as in Fig. 8. It is noteworthy

that coefficient C_μ in (5) of RKE is not a constant but a function of mean strain rate and vorticity, and the contours of C_μ in RKE resembles those of eddy viscosity. It would be premature to tell which turbulence model is superior in predicting wake distribution, but RKE seems to have an edge.

In practical application of viscous flow calculation to design of commercial ships, the most common usage will be to provide nominal wake distribution for propeller design in advance. Fig. 11 shows radial distribution of circumferentially averaged axial velocity components at propeller plane of KVLCC and KVLCC2. As already shown in Fig. 8, SKE shows poor results for both ship. The RNG-based $k-\epsilon$ model(RNG) gives a little better results, but still far from the experiment. However, the realizable $k-\epsilon$ model(RKE) yields to fairly good agreement with experiments for both ships. The discrepancy near hub (0.3~0.4R) might be coming from the simple extrapolation of velocity fields of the experiment, since the measured local flow angles are out of calibration range beneath the hub, thus, discarded in the experiment. If the velocity distribution outside of 0.5R is considered, RKE gives directly applicable results, which is very encouraging. The answer for question that the present computational modeling can tell the difference of stern frameline modification will be addressed later.

Calculated surface pressure distribution and surface friction lines are demonstrated in Fig. 12 and 13 for KVLCC with RKE model. The calculated pressure around the bow bulb of KVLCC migrate smoothly into low pressure region around a bow shoulder. Pressure gradient in diagonal direction is seen which is also the direction of limiting streamlines. Since the bulb of the VLCC is relatively small, pressure change across the bulb is not so radical as ships with long bulb, e.g., container ships. Low pressure region near the bottom bilge is also observed. The pressure variations near the stern of both hull forms are much milder than near the bow region, since thick boundary layer near the stern prohibits the rapid change of pressure field. The flow patterns from bow bulb to midship can be considered mainly as a potential flow with thin boundary layer. However, as focus moves downstream towards stern, thick boundary layer and wake flows developed along the streamlines will clearly demonstrate the effect of turbulence in viscous flow. The formation of stern bilge vortices are clearly seen in Fig. 13. Surface friction lines are converged near the stern bilge, which is shown as a thick line.

In the next, measured and calculated wake

distribution for KVLCC and KVLCC2 will be discussed. As mentioned earlier KVLCC2 has been modified to fortify bilge vortices, which is clearly seen in Fig. 14-(a). KVLCC2 has stronger hook-like U-contours. All three turbulence models make some difference in wakes, although those of SKE and RNG are quite different from the experiment. RKE provides very reasonable difference between KVLCC and KVLCC2. To see the difference between KVLCC and KVLCC2, circumferentially averaged axial velocity distributions are shown in Fig. 15. Surprisingly all three models give almost the same amount of difference between the two ships, except near hub. This observation probably makes CFD applicants of ship yards happy. If the viscous calculation was used only for the qualitative purpose, SKE with wall function should have given the right answer, although the values are not in agreement with the experiment. The other point from the present calculation is that calculated wake distribution with the realizable $k-\epsilon$ model(RKE) gives fairly good agreement with the experiment. One of the conclusion drawn from the present computation is that it is possible to predict nominal wake distribution in pretty good accuracy with RKE and wall function.

Surface pressure and friction lines on KVLCC and KVLCC2 with RKE is shown in Fig.16. There is little difference in pressure, however, this difference will make some difference in viscous pressure drag, since normal vectors near the stern region will affect the pressure drag. Limiting streamlines of KVLCC2 near the stern region shows a little stronger convergence into open separation line than in KVLCC, but difference is not very notable. However, it should be mentioned here that this amount of change is usually applied in ship yards for hull form improvement.

Finally integrated parameters are compared in Table 2. Surface friction coefficients of KVLCC and KVLCC2 with the same turbulence model are very similar, while a little of difference is found between the turbulence models. However, there are bigger difference in viscous pressure drag coefficients and nominal wake. SKE again failed to predict the pressure drag. RKE are the closest, since the wave making resistance coefficient of the present VLCCs at the Froude number of 0.142 is about 0.15×10^{-3} . In nominal wake prediction, as noted earlier, RKE gives pretty close values to the experiment. With 97X33X33 grids, the computing time was around 1.5 hours in SGI Onyx 2 (344 MFLOPS). It is believed that hull form designers can get the viscous flow solution in engineering workstations within working hours, starting from the station offset table.

CONCLUDING REMARKS

In order to confirm that the viscous flow calculation with affordable difficulties can predict nominal wake distribution correctly, flow calculations are performed for the two modern practical VLCCs with the same forebody and the slightly different afterbody, i.e., KVLCC and KVLCC2. The focus is laid upon the application of relatively simple computational modeling to provide the enough information to hull form designers, when they really modify hull forms in ship yards. The Reynolds-averaged Navier-Stokes equations for turbulent flows around model ships are solved using the cell-centered finite-volume schemes. Several variations of two-equation turbulence models, such as the standard $k-\epsilon$ model(SKE), the RNG-based $k-\epsilon$ model(RNG), and the realizable $k-\epsilon$ model(RKE), with Launder and Spalding's wall function are tested to identify the differences caused by the turbulence models. The calculated results around the two VLCC hull forms using O-O grid topology and profile-fitted surface meshes are compared to the measured data from towing tank experiment.

It is observed that the realizable $k-\epsilon$ model(RKE) provided realistic wake distribution with hook-like shape, while other two models failed. Furthermore, it is found that simple turbulence modeling is still effective to use for hull form evaluation purpose, since the predicted values in resistance coefficients and nominal wake fractions are in good agreement to the experiment if the proper turbulence model is chosen. It is very encouraging to see that the CFD with relatively simple turbulence closure can tell the difference quantitatively as well as qualitatively for the two hull forms with stern frameline modification.

ACKNOWLEDGEMENT

The present work is based on the projects of "Improvement of Resistance Performance of Ships," supported by Ministry of Industry and Resources, and "Development of Hydrodynamic Performance Analysis System," supported by Ministry of Science and Technology. Turbulent flow calculations are performed in SGI Onyx 2 (R10000 CPU, 195 MHz).

REFERENCES

[1] Larsson, L., Patel, V. C., and Dyne, G.(editors), "Ship Viscous Flow," Proceedings of 1990 SSPA-CTH-IIHR WORKSHOP. Gothenburg, Sweden, 1991.

[2] Proc. of CFD Workshop Tokyo- an

international workshop for improvement of hull form designs, Tokyo, Japan, 1994.

[3] Himeno, Y. et al., Proc. of Osaka Colloquium on advanced application of CFD on hull form design, Osaka, Japan, 1998.

[4] Kim, S.E, et al., "A Reynolds-averaged Navier-Stokes solver using unstructured mesh-based finite-volume scheme," AIAA 98-0231, 1998.

[5] Van, S.H. et al., "Experimental study on the flow characteristics around VLCC with different stern shapes," Proc. of the Third International Conference on Hydrodynamics(ICHHD), Seoul, Korea, 1998.

[6] Launder, B.E., and Spalding, D.B., "The Numerical Computation of Turbulent Flows," Comp. Meth. Appl. Mech. Eng., Vol. 3, pp. 269-289, 1974.

[7] Yakhot, V., Orszag, S.A., Thangam, S., gatski, T.B., Speziale, C.G., "Development of turbulence models for shear flows by a double expansion technique," Physics of Fluids A, Vol. 4, No. 7, pp. 1510-1520, 1992.

[8] Shih, T.-H., Liou, W.W., Shabir, A., and Zhu, J., "A New $k-\epsilon$ Eddy Viscosity Model for High Reynolds Number Turbulent Flows - Model Development and Validation," Computers and Fluids, Vol. 24, No. 3, pp. 227-238, 1995.

[9] Sorenson, R.L., "A computer program to generate two-dimensional grids about airfoils and other shapes by the use of Poisson equation," NASA TM 81198, 1980.

[10] Kim, W.J. et al., "Computational study on turbulent flow around practical hull forms with efficient grid generator," Proc. of Osaka Colloquium on advanced application of CFD on hull form design, Osaka, Japan, 1998.

[11] Ferziger, J.H., and Peric, M., *Computational Methods for Fluid Dynamics*, Springer-Verlag, 1996.

[12] Stone, H.L., "Iterative Solution of Implicit Approximations of Multi-directional Partial Differential Equations," SIAM J. Numer. Anal., Vol. 5, pp. 530-558, 1968.

[13] Van Doormal, J.P., and Raithby, G.D., "Enhancements of the SIMPLE method for Predicting Incompressible Fluid Flows," Numerical Heat Transfer, Vol. 7, pp. 147-163, 1984.

[14] Rhie C.M., and Chow, W.L., "A Numerical Study of Turbulent Flow Past an Isolated Airfoil with Trailing Edge Separation," AIAA Journal, Vol. 21, pp. 307-357, 1983.

Table 1 Principal particulars of test ships (KRISO 300K VLCC)

Ship Name		F1+A1 (KVLCC)		F1+A2 (KVLCC2)	
Designation		Ship	Model	Ship	Model
Scale ratio (λ)		58.0			
Design speed (kts, m/sec)		15.5 knots	1.047 m/sec	15.5 knots	1.047 m/sec
Length B.P.	L_{PP} (m)	320.0	5.5172	320.0	5.5172
Breadth	B (m)	58.0	1.0000	58.0	1.0000
Depth	D (m)	30.0	0.5172	30.0	0.5172
Draft	T_F (m)	20.8	0.3586	20.8	0.3586
	T_A (m)	20.8	0.3586	20.8	0.3586
Length of waterline	L_{WL} (m)	325.5	5.6121	325.5	5.6121
Wetted surface area	S (m^2)	27320.0	8.1213	27194.0	8.0838
Rudder area	S_r (m^2)	273.3	0.0812	273.3	0.0812
Displacement volume	∇ (m^3)	312737.5	1.6029	312621.7	1.6023
Block coefficient	C_B	0.8101		0.8098	
Load waterline coeff	C_W	0.9077		0.9016	
Midship section coeff	C_M	0.9980		0.9980	
LCB(fwd.+)	%	3.4800		3.5000	

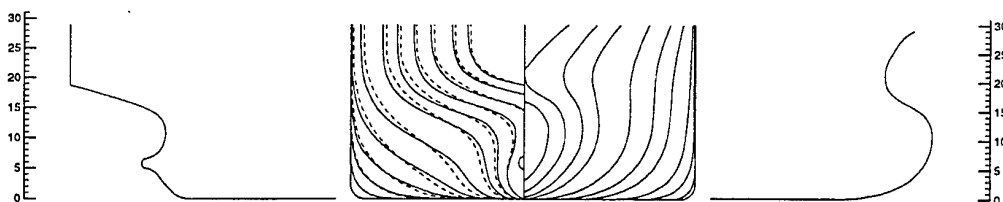


Fig. 1 Body plans & side profiles of 300K VLCC(solid: A1, dashed: A2)

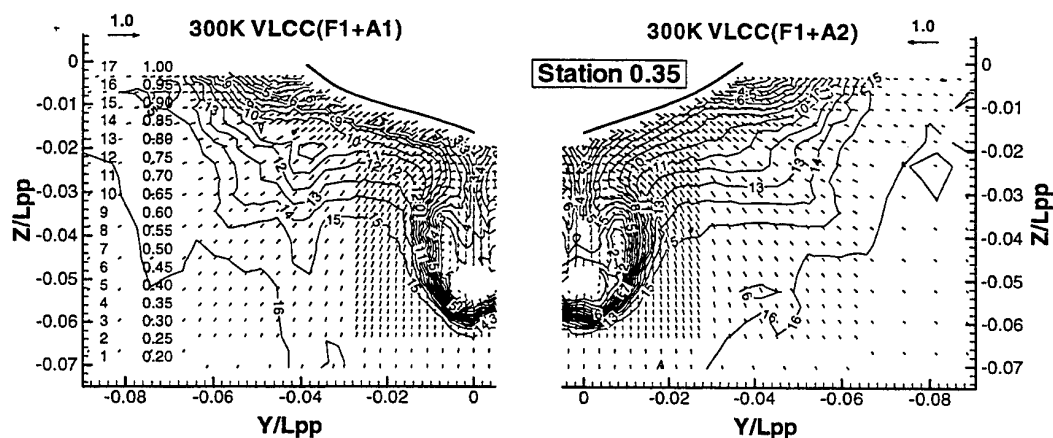


Fig. 2 Measured velocity fields of KVLCC and KVLCC2 at St. 0.35

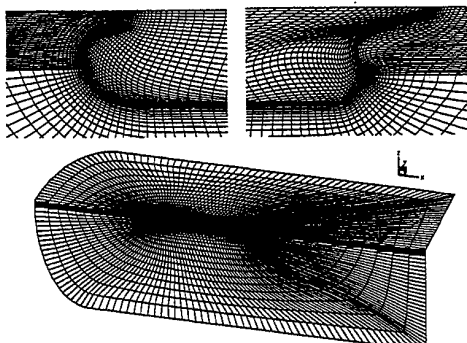


Fig. 3 Generated grid system of O-O topology

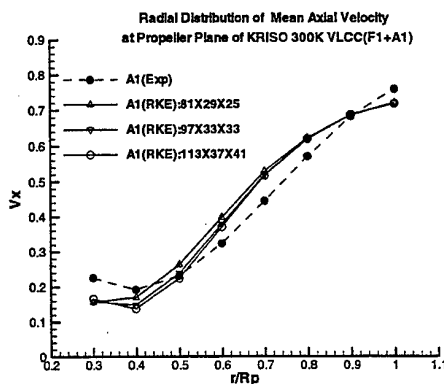


Fig. 4 Wake distribution with 3 grid levels

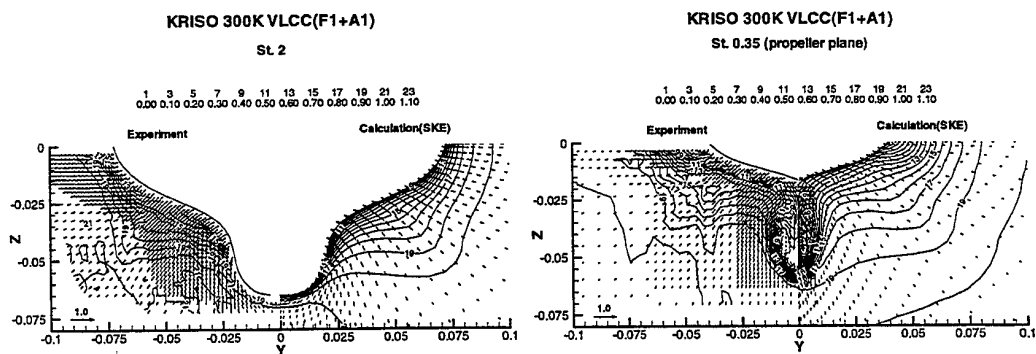


Fig. 5 Comparison of velocity fields(KVLCC) with the standard $k-\epsilon$ model(SKE)

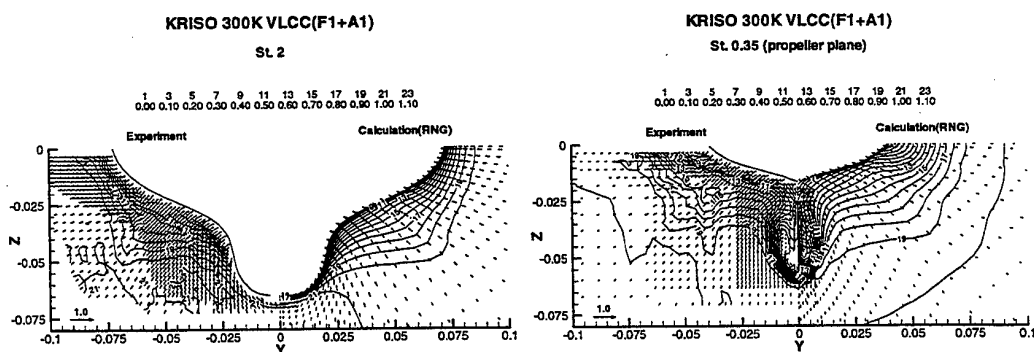


Fig. 6 Comparison of velocity fields(KVLCC) with the RNG-based $k-\epsilon$ model(RNG)

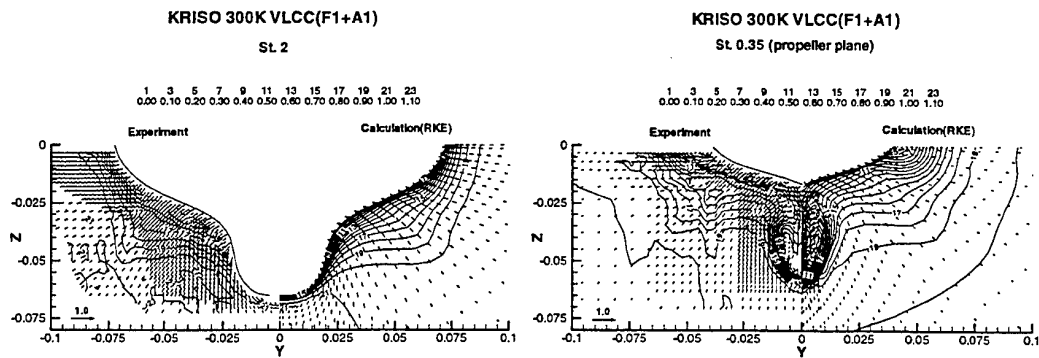


Fig. 7 Comparison of velocity fields(KVLCC) with the realizable $k-\varepsilon$ model(RKE)

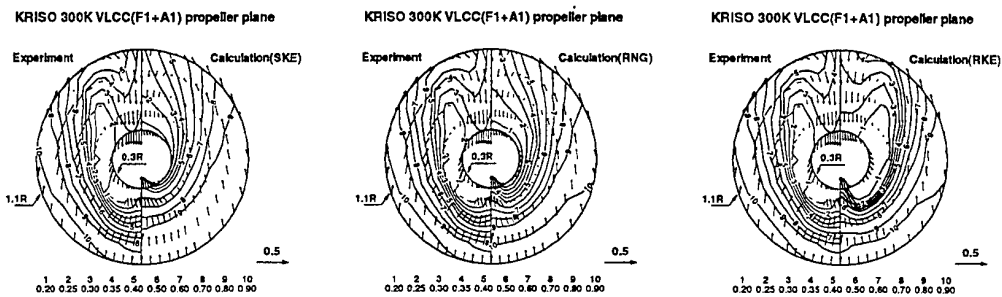


Fig. 8 Extracted velocity fields(KVLCC) at the propeller plane

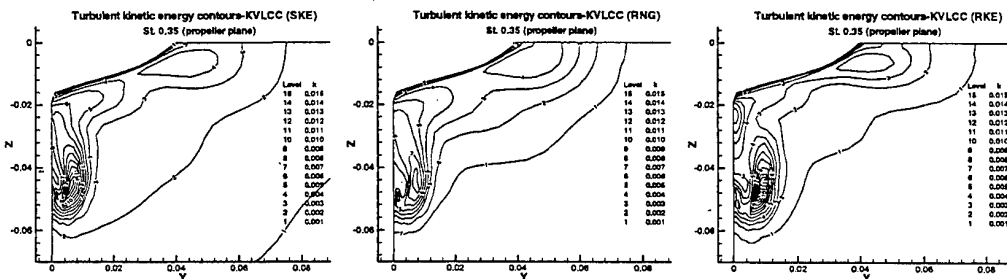


Fig. 9 Calculated turbulent kinetic energy contours at the propeller plane

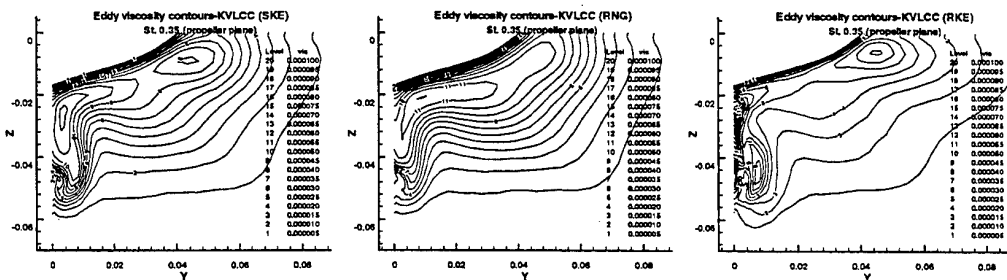


Fig. 10 Calculated eddy viscosity contours at the propeller plane

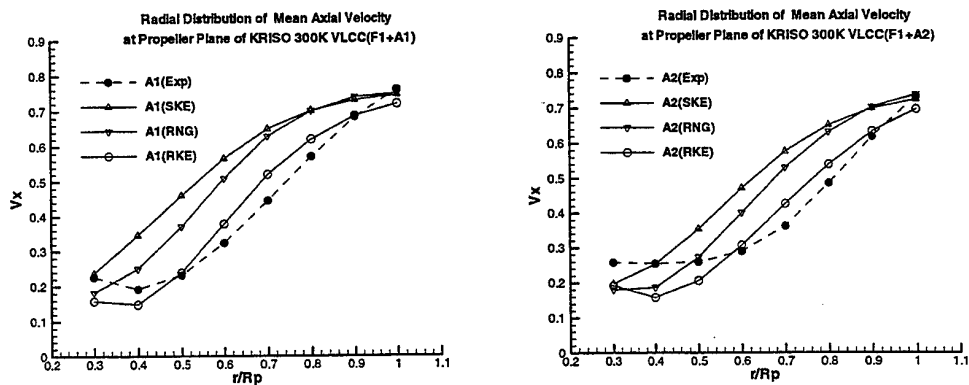


Fig. 11 Radial distribution of circumferentially averaged axial velocity components at the propeller plane of KVLCC and KVLCC2

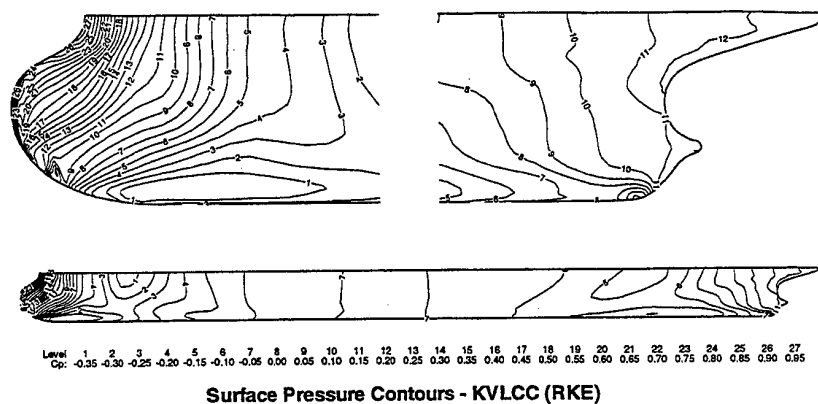


Fig. 12 Calculated surface pressure distribution of KVLCC with the realizable $k-\epsilon$ models

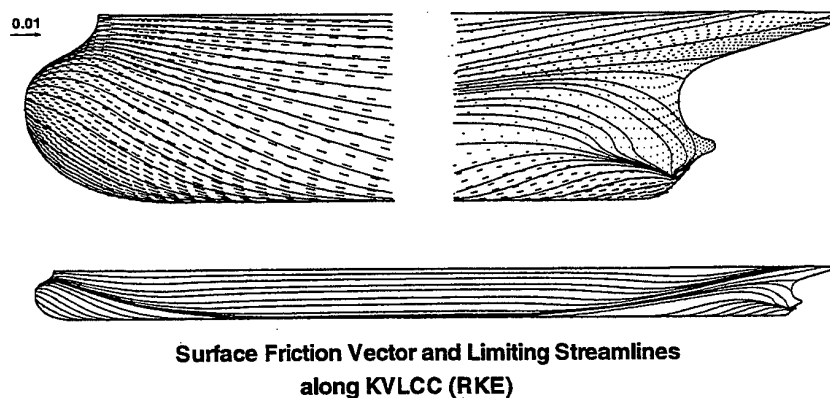


Fig. 13 Calculated friction vectors and limiting streamlines on KVLCC with the realizable $k-\epsilon$ models

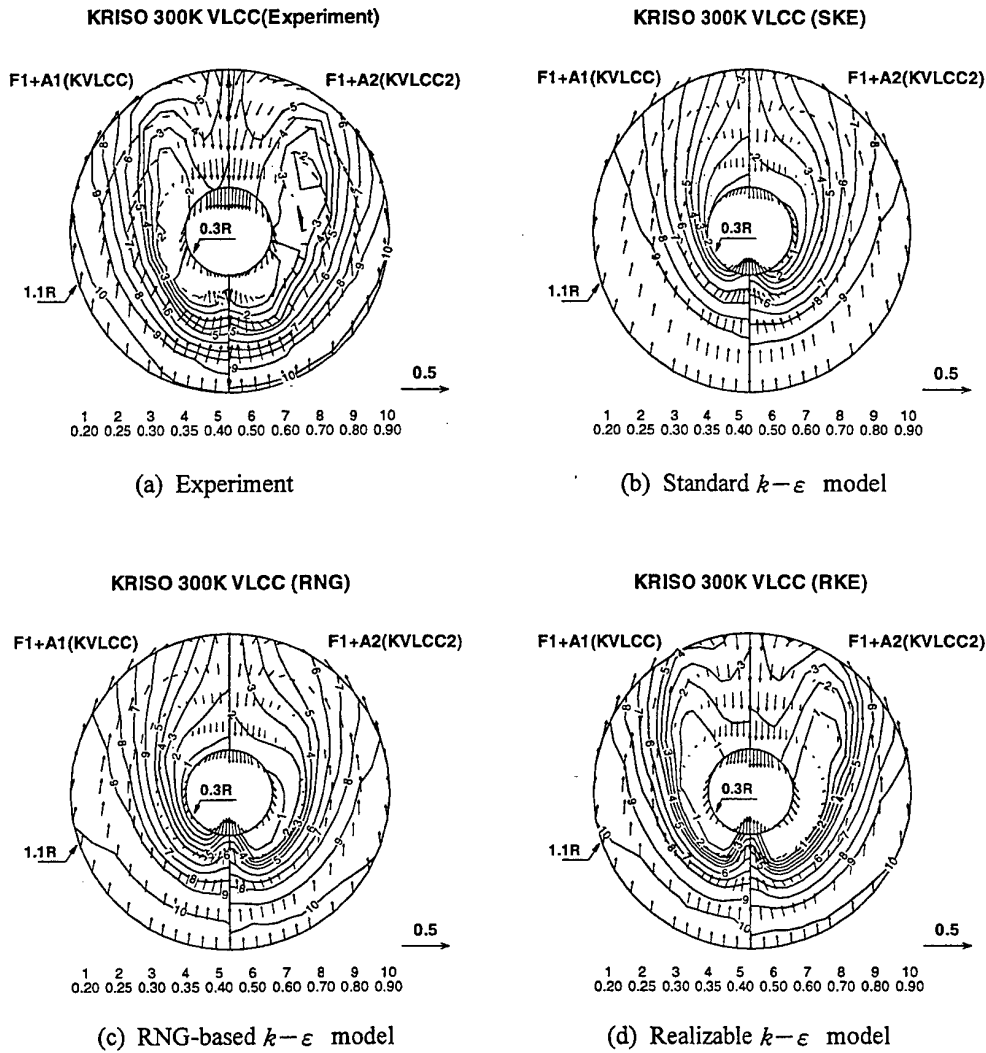


Fig. 14 Comparison of wake distribution of KVLCC and KVLCC2 at the propeller plane

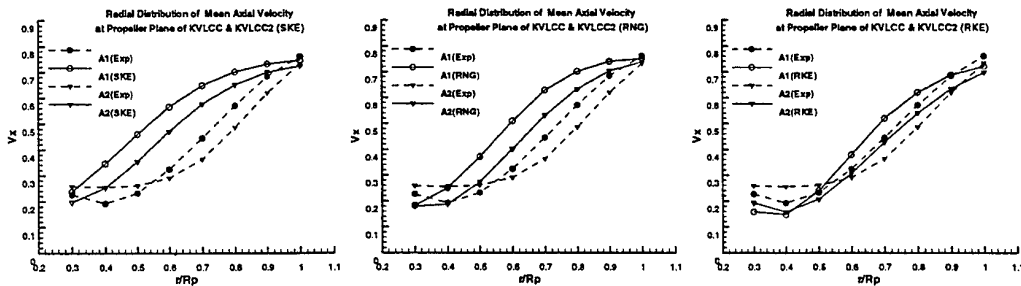


Fig. 15 Comparison of circumferentially averaged axial velocity distribution of KVLCC and KVLCC2 at the propeller plane with three $k-\epsilon$ models

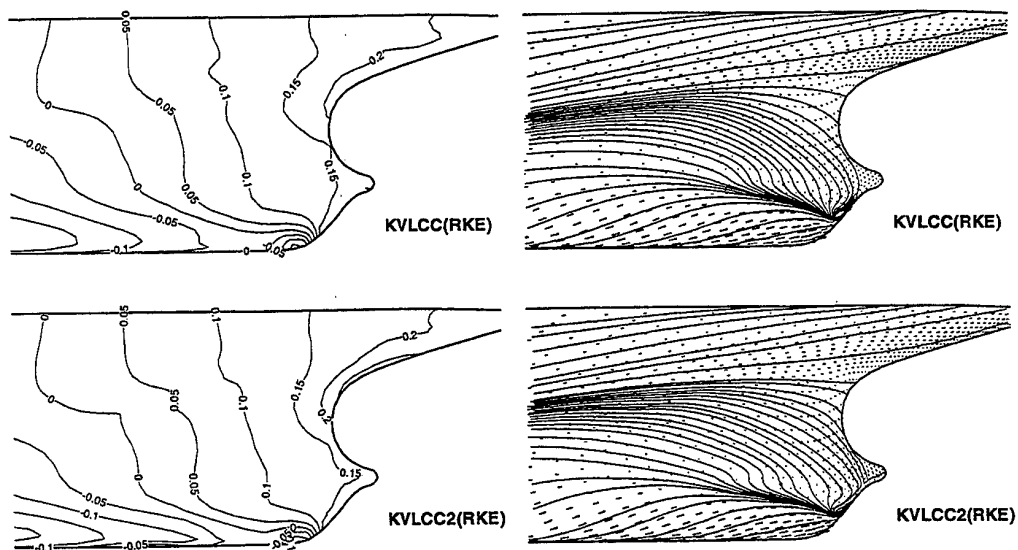


Fig. 16 Calculated surface pressure and friction lines on KVLCC and KVLCC2 with the realizable $k-\epsilon$ model(RKE)

Table 2 Resistance coefficients and nominal wakes

	KRISO 300K VLCC F1+A1 (KVLCC)				KRISO 300K VLCC F1+A2 (KVLCC2)			
	Exp	SKE	RNG	RKE	Exp	SKE	RNG	RKE
Reynolds Number	4.6×10^6				4.6×10^6			
$C_F \times 1000$	3.450*	3.694	3.431	3.346	3.450*	3.697	3.433	3.351
$C_{VP} \times 1000$	0.638*	0.908	0.312	0.481	0.660*	0.944	0.347	0.524
Norm.wake	0.523	0.387	0.417	0.503	0.561	0.450	0.484	0.556

* C_F and C_R based on 1957 ITTC formula (experiments were performed with rudder in free condition)

NUMERICAL STUDY OF FLOWS AROUND AN ARRAY OF CIRCULAR CYLINDERS AT HIGH REYNOLDS NUMBERS

S. Etienne^{1,2}, Y.M. Scolan¹, B. Molin¹

¹Ecole Supérieure d'Ingénieurs de Marseille, 13451 Marseille cedex 20, France.

²Institut Français du Pétrole, 1 et 4 Avenue de Bois Préau, 92852 Rueil-Malmaison Cedex, France.
e-mail: etienne@gesim.imt-mrs.fr

Abstract

A domain decomposition method is developed in order to investigate the flow around multiple circular cylinders. In the inner domains, which surround each cylinder, the Reynolds Averaged Navier-Stokes (RANS) equations are solved in vorticity-stream function formulation with $k - \omega$ turbulence models by Wilcox (1985) and Menter (1992). In the outer domain, a Lagrangian method is used where particles are convected with a Fast Vortex Method. Lagrangian turbulence modeling is also implemented. We present comparisons with experimental results in the case of one circular cylinder at $Re = 140000$ and multiple circular cylinder arranged in line at $Re = 22000$. The aim is to study the interactions between relative motions of the cylinders in the ambient flow, in order to model Vortex Induced Vibrations. We also present results for a single moving cylinder at $Re < 150$, $Re = 1000$ and $Re = 140000$.

INTRODUCTION

The development of offshore oil production in very deep water requires more knowledge about the dynamic behavior of long flexible pipes (risers) joining the sea level to the sea bed. This problem has to be properly solved in order to prevent Vortex Induced Vibrations (VIV) and/or strong interactions between the long cylinders that are often assembled in arrays. This is not a purely academic configuration hence the choice of a formulation (geometry and variables) must be judicious.

First of all, simplifications are imposed concerning the geometry. Here the equations are established for two-dimensional configurations. This is justified due to the significant correlation in the direction of the body slenderness. Then the velocity/pressure conservation equations need not be necessarily solved. The vorticity/stream-function equations are preferred for reasons of CPU-time and computer resources savings.

Other aspects of the physical problem are the strong flow unsteadiness combined to the dynamics of moving bodies. The resulting flow is clearly turbulent and large excursions of bodies are expected. The formulation is hence chosen to be as grid-free as possible and a lagrangian approach fits particularly well. However in the immediate vicinity of solid boundaries, this approach does not work correctly; a purely eulerian formulation is preferable in closed domains

near each bodies where the boundary layers develop.

These considerations lead to the context in which a domain decomposition is developed in order to investigate the flows around multiple circular cylinders. The inner domains consist of annular surfaces which surround each cylinder. There the Reynolds Averaged Navier-Stokes (RANS) equations are solved in vorticity-stream function eulerian formulation. The turbulent effects are modeled with the $k - \omega$ equations. In the outer domain, the properties are transported in a lagrangian way. Two sets of particles carry the vorticity on one hand, the turbulent kinetic energy and rate of dissipation on the other hand. Overlapping between the two formulations enables a good mutual transfer of information. This lagrangian approach is justified for several reasons: 1) the convection is better handled since the discretization of the nonlinear quadratic term is avoided, 2) the transport of properties creates less numerical diffusion and 3) the incoming information (wake of one cylinder impacting another cylinder) is better transmitted between each inner domains.

After the presentation of the numerical method, we will discuss the results obtained for the case of one cylinder, first fixed then on elastic support. The Reynolds number studied are $Re = UD/\nu < 150$, $Re = 1000$ and $Re = 140000$ with U the uniform free stream velocity, D the cylinder diameter and ν

the kinematic viscosity. Finally, we present and discuss results around 2 and 3 circular cylinders arranged in tandem.

NUMERICAL METHOD

In the following developments each formulation is described. First the equations are given. Then the numerical methods are outlined according to the type of formulation.

Basic equations and turbulence modeling

The equations are formulated in terms of vorticity ζ and stream-function ψ :

$$\begin{aligned}\zeta_t + \text{rot}(\psi \mathbf{k}) \cdot \text{grad} \zeta &= \nu \Delta \zeta \\ \Delta \psi &= -\zeta \\ \mathbf{U} &= \text{rot}(\psi \mathbf{k})\end{aligned}\quad (1)$$

where \mathbf{U} , ν , \mathbf{k} denote the velocity, the kinematic viscosity and the normal vector to the plane of the flow respectively.

The equations for the averaged quantities ζ and \mathbf{U} reduce to:

$$\zeta_t = -U_j \zeta_{,j} + (\nu_e \zeta)_{,jj} + S_\zeta \quad (2)$$

where ν_e is the total viscosity: kinematic ν and turbulent ν_t . In the right hand side, S_ζ is a source term; it is negligible for the studied flows. Numerically its influence on the mean flow is much weaker than that of the turbulent diffusion (Sugavanam & Wu (1980)). The turbulent viscosity ν_t is derived from the Boussinesq hypothesis. The turbulence model is chosen in order to provide a good agreement with available experimental data. Different two-equations models are tested:

- a standard $k - \omega$ model as described pp 84–87 in Wilcox (1995); it is better suited to mild adverse pressure gradients than the $k - \epsilon$ model but it might be sensitive to the arbitrary far field condition for ω ,
- a first alternative, proposed by Menter (1992), allows a progressive change from $k - \omega$ on the body to standard $k - \epsilon$ as described pp 87–89 in Wilcox (1995); it is called the Baseline or BSL model,
- another alternative, proposed by Menter (1992), is to integrate the Bradshaw assumption into the BSL method; that constitutes the Shear Stress Transport (SST) model.

As the constant coefficients of the models originate from three-dimensional experiments, they are supposed to partly take into account three-dimensional effects of turbulence, even though the flow is restricted to a plane. The use of models has another interest, against Direct Numerical Simulation for example, since one can identify the different effects of convection, diffusion, dissipation and production. This is useful for lagrangian transport of particles through an Operator Splitting Technique (OST).

The standard $k - \omega$ model, BSL and SST models are used. The associated equations are:

$$\begin{aligned}k_{,t} + U_j k_{,j} &= \tau_{ij} U_{i,j} - \beta^* \omega k + [(\nu + \sigma_k \nu_t) k_{,j}]_{,j} \\ \omega_{,t} + U_j \omega_{,j} &= \frac{\gamma}{\nu_t} \tau_{ij} U_{i,j} - \beta \omega^2 \\ &\quad + [(\nu + \sigma_\omega \nu_t) \omega_{,j}]_{,j}\end{aligned}\quad (3)$$

The turbulent viscosity and the constant coefficients are:

$$\nu_t = \gamma^* \frac{k}{\omega} \quad \left\{ \begin{array}{lll} \beta^* = 0.09 & \sigma_k = 0.5 & \gamma = \frac{5}{9} \\ \gamma^* = 1.0 & \sigma_\omega = 0.5 & \beta = \frac{3}{40} \end{array} \right. \quad (4)$$

The usual boundary conditions are:

$$\begin{aligned}\text{on the walls} &\quad \left\{ \begin{array}{l} k = 0 \\ \omega \xrightarrow{y \rightarrow 0} \frac{6\nu}{\beta y^2} \end{array} \right. \\ \text{far in the free stream} &\quad \left\{ \begin{array}{l} k_\infty = \nu_{t_\infty} \omega_\infty \\ \omega_\infty = (1 \rightarrow 10) \frac{U_\infty}{L} \\ \nu_{t_\infty} = 10^{-3} \nu \end{array} \right.\end{aligned}\quad (5)$$

where L is a length scale for example the cylinder diameter and y denotes the normal distance from the wall.

The BSL model is described as :

$$\begin{aligned}k_{,t} + U_j k_{,j} &= \tau_{ij} U_{i,j} - \beta^* \omega k + [(\nu + \sigma_k \nu_t) k_{,j}]_{,j} \\ \omega_{,t} + U_j \omega_{,j} &= \frac{\gamma}{\nu_t} \tau_{ij} U_{i,j} - \beta \omega^2 + [(\nu + \sigma_\omega \nu_t) \omega_{,j}]_{,j} \\ &\quad + 2(1 - F_1) \sigma_{\omega 2} \frac{1}{\omega} k_{,j} \omega_{,j}\end{aligned}\quad (6)$$

The following constants change from $k - \omega$ Wilcox to $k - \epsilon$ Jones-Lauder ones, as ϕ does :

$$\phi = F_1 \phi_1 + (1 - F_1) \phi_2 \quad (7)$$

and:

$$\begin{aligned}\bullet \phi_1 (k - \omega \text{ Wilcox}): \\ \sigma_{k1} = 0.5 \quad \sigma_{\omega 1} = 0.5 \quad \beta_1 = 0.075 \\ \gamma_1 = \frac{\beta_1}{\beta^*} - \sigma_{\omega 1} \frac{\kappa^2}{\sqrt{\beta^*}}\end{aligned}$$

$$\bullet \phi_2(k - \epsilon)$$

$$\sigma_{k2} = 1.0 \quad \sigma_{\omega 2} = 0.856 \quad \beta_2 = 0.0828$$

$$\gamma_2 = \frac{\beta_2}{\beta^*} - \sigma_{\omega 2} \frac{\kappa^2}{\sqrt{\beta^*}}$$

$\kappa = 0.41$ is the Karman constant. Finally we have :

$$F_1 = \tanh(\zeta_1^4) \quad (8)$$

with,

$$\zeta_1 = \min \left[\max \left(\frac{\sqrt{k}}{0.09\omega y}, \frac{500\nu}{y^2\omega} \right), \frac{4\sigma_{\omega 2}k}{CD_{k\omega}y^2} \right] \quad (9)$$

and,

$$CD_{k\omega} = \max \left(2\sigma_{\omega 2} \frac{1}{\omega} k_{j,j}, 10^{-20} \right) \quad (10)$$

As the $k-\omega$ model behaves better than the $k-\epsilon$ model in the logarithmic zone, transition from $k-\omega$ to $k-\epsilon$ can take place in the outer zone and ζ_1 is rewritten as:

$$\zeta_1 = \min \left(\frac{500\nu}{y^2\omega}, \frac{4\sigma_{\omega 2}k}{CD_{k\omega}y^2} \right) \quad (11)$$

Boundary conditions are identical to Wilcox's ones

The SST model is alike the BSL model except for some constants and the turbulent viscosity which are rewritten as :

$$\sigma_{k1} = 0.85 \quad \sigma_{\omega 1} = 0.65 \quad \beta_1 = 0.075$$

$$\gamma_1 = \frac{\beta_1}{\beta^*} - \sigma_{\omega 1} \frac{\kappa^2}{\sqrt{\beta^*}} = 0.44$$

and,

$$\nu_t = \frac{a_1 k}{\max(a_1\omega; \Omega F_2)} \quad (12)$$

with $a_1 = 0.3$, Ω the absolute value of vorticity and F_2 :

$$F_2 = \tanh(\arg_2^2) \quad (13)$$

with,

$$\arg_2 = \max \left(2 \frac{\sqrt{k}}{0.09\omega y}, \frac{400\nu}{y^2\omega} \right) \quad (14)$$

Eulerian inner problem in the annuli

Figure 1 shows the decomposition of the flow domain into annuli (Ω_i), associated with each circular section, and the complementary domain (Ω_0). Since only simple circular sections are studied, the method of resolution is well suited to a polar mesh.

The main two equations are solved in an uncoupled way. The Poisson equation is discretized by means of a Finite Difference Method and FFT in the radial and azimuthal directions respectively. The precision is of fourth order for ψ and the velocity and velocity derivatives are directly obtained by the hermitian formulas.

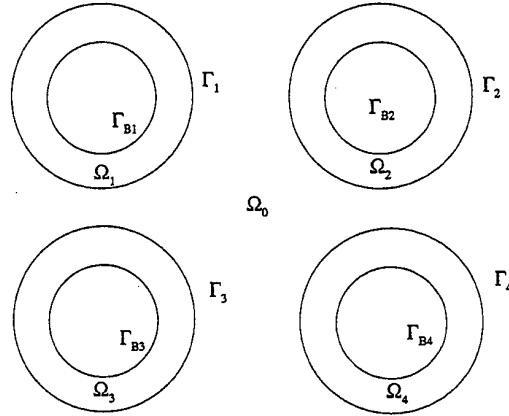


Figure 1: $N_c = 4$ cylinders configuration; Ω_0 is the outer domain, Ω_i , Γ_i , Γ_{B_i} ; $i \in [1, 4]$ are respectively inner domains, external boundaries and walls

The transport equations are solved by a Finite Volume Method (FVM) in space and an Alternate Directions Implicit (ADI) technique to forward in time. The convective flux are discretized with either a second order QUICK scheme or different second or third order Total Variation Diminishing (TVD) schemes which reduce unphysical oscillations in spite of accuracy loss near the vorticity extrema. Both give identical results at low Reynolds number but the latter improves substantially the stability of the turbulent quantities transport.

The mesh of the inner domain is regular in the azimuthal direction because of the FFT. An exponentially decreasing mesh size in the radial direction is controlled with the following law:

$$x + i.y = (e^{\xi - \xi_0} - a)e^{i\theta} \quad (15)$$

where ξ and θ are the new polar exponential variables, ξ_0 and a are adjusted so that the first point lies approximately $0.1/\sqrt{Re}$ far from the wall.

The boundary conditions for the stream function must be defined on all the solid walls $(\Gamma_{B_i})_{i \in [1, N_c]}$:

$$\begin{cases} \psi_{\Gamma_{B_i}} = C_i & \text{fixed body} \\ \psi_{\Gamma_{B_i}} = \Im(\alpha_i Z) + C_i & \text{moving body} \end{cases} \quad (16)$$

where \Im denotes imaginary part, C_i is a constant for each body which ensures pressure continuity along B_i . The complex number Z is the position of a point on Γ_{B_i} . The characteristics of the body motion appear in α_i which corresponds to the conjugate

of $V_{Bx} + iV_{By}$. On the control surface $(\Gamma_i)_{i \in [1, N_c]}$ the two components of the velocity are matched from both sides:

$$\text{rot}(\psi_{\Gamma_i}, \mathbf{k}) = \mathbf{V}_{\Gamma_i}, i \in [1, N_c] \quad (17)$$

There exists no natural boundary condition for the vorticity. Woods' second order condition can be applied. Alternatively numerical tests show that the following condition is more stable:

$$\begin{aligned} \zeta_{\Gamma_B} = & e^{2\xi_0} \frac{16\psi_{\Gamma_B}/5 - \psi_2 - \psi_3}{5\Delta\xi^2} \\ & + \frac{-\psi_4 - \psi_5 + 4\psi_6/5 + 6\psi_{\Gamma_B, \xi}}{5\Delta\xi^2} \quad (18) \\ & - a\psi_{\Gamma_B, \xi} \end{aligned}$$

where $\psi_{\Gamma_B}, \psi_2, \psi_3, \dots$ are ψ values on the body and at the two nearest points in the radial direction into the fluid. Other conditions like Mukhopadhyay's (1993) is very stable as well but it does not respect the Poisson equation at the adjacent points on the body. On the control surfaces $(\Gamma_i)_{i \in [1, N_c]}$, the vorticity is explicitly calculated from the outer solution in an overlapping area where eulerian and mixed formulations coexist.

Lagrangian solution in the outer domain

Only two sets of particles are required to transport the three properties of the flow: one for the vorticity ζ and the other set transports both the energy k and the rate of dissipation ω . The reason for that follows from the Operator Splitting Technique (OST): it is clear from equation (3), that convection and diffusive terms (where space derivatives appear) are similar whatever the turbulent quantities considering only the standard Wilcox model.

Convection transport

The convective step requires the calculation of the velocity since the corresponding equation reduces to Euler's. Let one note Q a vector whose components are (ζ, k, ω) , one should solve:

$$Q_{,t} = -\vec{U} \cdot \vec{\nabla} Q \quad (19)$$

A lagrangian particle located at $X(t)$ is followed through the equation:

$$\frac{d\vec{X}}{dt} = \vec{U}(\vec{X}, t) \quad (20)$$

where $\vec{U}(\vec{X}, t)$ is the local velocity at instant t .

This equation is solved with a second order scheme of Runge-Kutta type:

$$\begin{aligned} \mathbf{X}^{n+1/2} &= \mathbf{X}^n + \frac{\Delta t}{2} \mathbf{U}^n(\mathbf{X}^n) \\ \mathbf{X}^{n+1} &= \mathbf{X}^n + \Delta t \mathbf{U}^{n+1/2}(\mathbf{X}^{n+1/2}) \quad (21) \end{aligned}$$

where Δt is the time step and n its number.

The velocity is calculated with the Fast Vortex Method (FVM) developed by Greengard & Rokhlin (1987). The principle is as follows:

- building a fictitious grid which covers the only part of the flow where particles exist,
- treatment of "far" cells where the velocity, induced by the vorticity, is represented by series of multipoles; in the frame of Complex Variable Theory these series can be afterwards transported wherever in the flow plane; in particular the Circle Theorem is used in order to take into account the presence of the solid boundaries,
- treatment of the other cells, *i.e.* the nearest adjacent cells where the Biot-Savart law provides the velocity.

Numerical experiments show that, for a fixed truncature of the multipoles series, there exists a minimum CPU-time defined by a combination of grid size and number of particles (see Etienne *et al.*, 1998).

As the Poisson equation is linear, one can distinguish three main contributions to the total stream-function:

$$\psi = \psi_{PF} + \psi_{\zeta} + \psi_B \quad (22)$$

where each term corresponds respectively to:

- the undisturbed flow which is well known since it follows from Potential Flow theory (under the perfect fluid hypothesis). Its expression for an unsteady flow of intensity $|C(t)|$ and direction $-\arg[C(t)]$, is:

$$\psi_{PF}(Z) = \Im(C(t)Z) \quad (23)$$

- the stream-function induced by the whole vorticity all over the fluid domain. Either the FVM method or the Vortex-In-Cell (VIC) method is used,
- the stream-function which takes into account the presence of the bodies *i.e.* it follows from an impermeability condition on all solid surfaces. It can be expressed as:

$$\psi_B(Z) = \Im \left(\sum_{j=1}^{N_c} \sum_{n=1}^{\infty} a_{jn} \left[\frac{R_j}{Z_j} \right]^n \right) \quad (24)$$

where Z_j corresponds to Z in the coordinate system attached to the j^{th} body and R_j is its radius. The coefficients a_{jn} are new unknowns. For that ψ_{PF} and ψ_ζ are first expressed in term of multipole series then a_{jn} are calculated by prescribing the following boundary conditions on the bodies:

$$\psi_{PF}(Z) + \psi_\zeta(Z) + \psi_B(Z) = f_i(Z) \quad (25)$$

where

$$\begin{cases} f_i(Z) = C_i & \text{fixed cylinder} \\ f_i(Z) = \alpha_i Z + C_i & \text{moving cylinder} \\ \forall Z \in \Gamma_{B_i}, & \forall i \in [1, N_c] \end{cases} \quad (26)$$

where constants are as described by equation (16).

Diffusion of the properties

For the vector Q defined above, the diffusion reduces to the heat equation:

$$Q_{,t} = \begin{pmatrix} \Delta \nu_e \zeta \\ (\nu + \sigma_k \nu_t) \Delta k \\ (\nu + \sigma_\omega \nu_t) \Delta \omega \end{pmatrix} \quad (27)$$

Here again a fictitious grid is built and renewed at each time step. This grid follows from a remeshing of the patterns as described later in the text. Its nodes are the supports of the variables. Each isolated particle distributes its own transported property onto the neighbouring particles according to the Particle Strength Exchange (PSE) method. This is a serious improvement compared to the Random Walk (RW) method. First, as for convergence criteria, those are discussed in Degond and Mas-Gallic (1989) for the PSE method and in Beale and Majda (1981) or Roberts (1985) for the RW method. Secondly the PSE method is deterministic contrarily to the RW method and hence the stochastic component, which pollutes the time variations of all the variables, is completely removed.

The PSE method consists in solving the following differential equation. One uses a simple first order explicit Euler scheme. The particle $N^o i$ located in X_i , transports the property $\nu_i f_i$ and receives a contribution from the neighbouring particles whose numbers are in ensemble J :

$$\frac{df_i}{dt} = \epsilon^4 \sum_{j \in J} x_g (\nu_j f_j - \nu_i f_i) \sigma_4 \left(\frac{X_j - X_i}{\epsilon} \right), \forall i \in J \quad (28)$$

The surface of local cell is x_g ; it also measures the averaged vacuum surface around the j^{th} particle. The diffusion kernel is σ_4 and ϵ denotes its size (see Ould

Salihi, 1998):

$$\sigma_4(r) = 6 \frac{3 - r^2}{(1 + r^2)^4} \quad (29)$$

where r is a radial coordinate centered at the particle location. This kernel vanishes rapidly and consequently the corresponding CPU-time is proportional to the total number of particles in the flow.

Equation (28) works for ζ , but for k and ω , the viscosity must be extracted from the summation since it does not appear in the Laplacian operator.

Correction of convection for k and ω

For the turbulent properties k and ω , an additive convection transport is calculated. The corresponding velocity is proportional to $\vec{\nabla} \nu_t$:

$$\begin{pmatrix} k \\ \omega \end{pmatrix}_{,t} = \begin{pmatrix} \sigma_k(\nu_{t,j}) \cdot (k_{,j}) \\ \sigma_\omega(\nu_{t,j}) \cdot (\omega_{,j}) \end{pmatrix} \quad (30)$$

Effects of the Production/Dissipation

According to the Operator Splitting technique, there remains a system of time differential equations to solve for k and ω :

$$k_{,t} = \tau_{ij} U_{i,j} - \beta^* \omega k \quad \text{et} \quad \omega_{,t} = \frac{\gamma}{\nu_t} \tau_{ij} U_{i,j} - \beta \omega^2 \quad (31)$$

The order of the integration scheme is strictly larger than 1 since the velocity gradients follows from the intermediate step of the convection step.

Their calculation derives from the multipole series expansion represented with the complex potential of the flow $F(Z)$ whose imaginary part is ψ given in equation (22). As a matter of fact one can show that:

$$S^2 = \frac{1}{2} (U_{i,j} + U_{j,i})^2 = 4 \left| \frac{d^2 F}{dZ^2} \right|^2 \quad (32)$$

where $Z = x + iy$ is a current point of the flow plane.

Remeshing of the variables

In order to properly simulate the diffusion and the overlapping, an intermittent remeshing is achieved for each variable. This defines the fictitious grid used for the diffusion step. After positioning an isolated particle in a cell, its property is distributed onto its 16 neighbouring particles according to a biquadratic law (see Ould Salihi, 1998):

$$M'_4(x) = \begin{cases} \frac{3x^3 - 5x^2 + 2}{2} & \text{if } 0 < x < 1 \\ \frac{-x^3 + 5x^2 - 8x + 4}{2} & \text{if } 1 < x < 2 \\ 0 & \text{if } x > 2 \end{cases} \quad (33)$$

where x is the distance between the particle and the grid nodes. This technique allows the conservation of the first three moments: total circulation (Kelvin Theorem), linear impulse and angular impulse. Another interest of the technique is to smooth possible irregularities.

Control of the solution in the overlapping domain

The overlapping domain is useful to provide the external boundary conditions for inner domains and the boundary conditions for the outer domain for transported flow quantities, here ζ , k and ω .

We take advantage of the remeshing technique to perform assignation from one domain to the boundary of the other domain. This procedure requires that at least two cells of the assigned domain are recovered by the assignating one. This explains why the overlapping area must be at least 4 cells large. We generally take wider distances since it permits to verify that the solution obtained in one domain is exactly the same in the other.

RESULTS

Validation tests for the laminar code have been done and compiled in Etienne *et al.* (1998). Here we will show results for the multidomain method in the case of single body and multiple bodies configuration.

Turbulent flows around single body

Fixed body

The uniform flow around a circular cylinder at Reynolds number 140000 has been studied experimentally by Cantwell & Coles (1980). This flow is a challenging one for conventional modelisation. Indeed, the flow is laminar until a transition takes place after the first separation.

We chose to compare the mean radial velocity profile at the rear of the cylinder. First, we use the pure eulerian method to evaluate how turbulent models behave in such conditions. The grids used are 200×256 in radial and angular directions.

Figure 2 shows the mean radial velocity profile along the centerline from experiments and other numerical results compiled by Kassera & Stromheier (1997). The Wilcox $k - \omega$ and SST models give reasonable results regarding to other models and comparing with the experimental profile. The BSL model which corresponds to the $k - \epsilon$ model doesn't permit to reproduce this profile. The results are different from those obtained by Franke *et al.* (see Kassera, 1997) using the standard $k - \epsilon$ model. Nevertheless, the trend is similar in the sense that velocity is largely

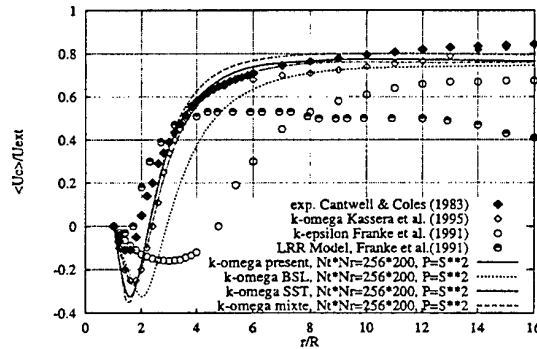


Figure 2: Mean streamwise velocity component on the centerline at the rear of the cylinder. $Re = 140000$

underestimated up to $r/R = 8$. Such results can be explained by the fact that the $k - \epsilon$ model generates more turbulent viscosity than the $k - \omega$ model. An improvement could be obtained using the SST model. The Bradshaw's assumption limits explicitly the turbulent viscosity in the boundary layer. This counterbalances the overproduction induced by the standard $k - \epsilon$ model. From $r/R = 2.5$ to 10, the SST model induces results very close to experiments. This is not the case for lower radii. For $r/R < 2.5$, results obtained by Kassera show that this underestimation of the velocity is induced by the Wilcox $k - \omega$ model.

Figure 3 shows the force coefficients as a function of nondimensional time $t^* = Ut/D$ where U denotes the uniform velocity at infinity. The mean value of the drag coefficient is equal to 1.05 when using the $k - \omega$ model, it is equal to 0.65 when using the BSL model and 0.9 when using the SST model. The experimental value of the drag coefficient is 1.1. The best result is obtained with the standard $k - \omega$ model. This Reynolds number value is subcritical and low values obtained with the BSL and SST models may be due to an overproduction of turbulent viscosity generated by the equivalent $k - \epsilon$ model in the wake at $Re = 140000$. Indeed, these values correspond to higher Reynolds number flows. Experimentally the drag crisis begins at $Re = 250000$.

To validate the multidomain method we have chosen to compare, at $t^* = 4$, the different properties of the flow. Comparisons couldn't be done at later times since dissipation in the eulerian solution due to important cells far from the body induces a different solution in the wake. The turbulence model chosen is the standard $k - \omega$ model since it is easier to implement with this method than others.

Figures 4 and 5 show the distribution of nodes for the annular domain and the lagrangian domain re-

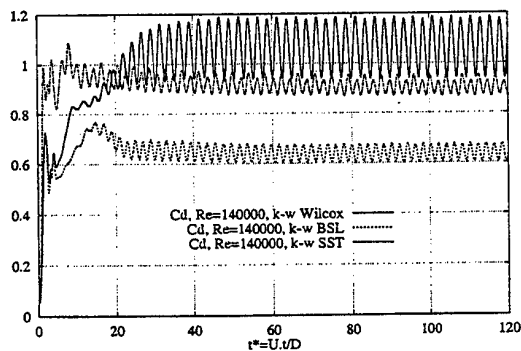


Figure 3: Drag coefficient as a function of non-dimensional time at $Re = 140000$

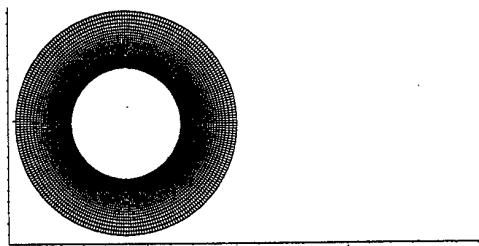


Figure 4: Annular grid around the body

spectively. The annular mesh satisfies the condition $y^+ = y_w \sqrt{\zeta_B Re} < 1$ where y_w denotes the non-dimensional distance to the wall and ζ_B the non-dimensional vorticity at wall. Figures 6 through 13 show comparisons between the pure eulerian properties fields and the mixed Euler-Lagrange properties fields. We can appreciate that properties are correctly transferred from one domain to the other.

Moving body

We have simulated the Vortex Induced Vibrations of a single cylinder for $Re < 150$, $Re = 1000$, $Re =$

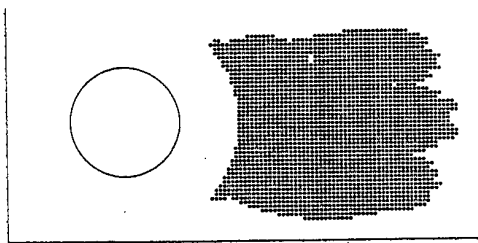


Figure 5: Eulerian position of particles

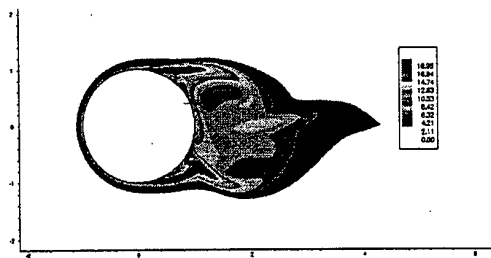


Figure 6: Uniform flow: ω field at $t^* = 4$; eulerian.

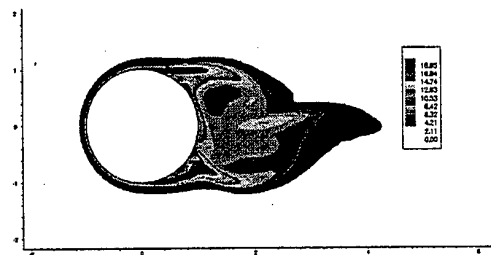


Figure 7: Uniform flow: ω field at $t^* = 4$; Euler/Lagrange.

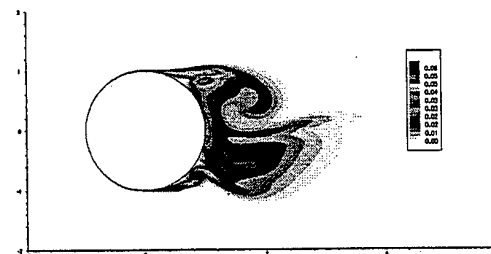


Figure 8: Uniform flow: k field at $t^* = 4$; eulerian.

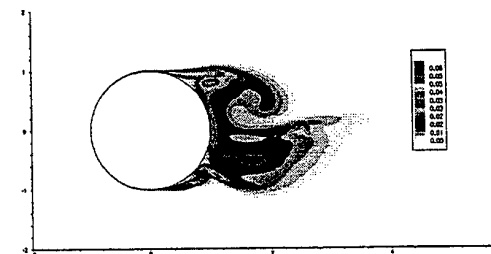


Figure 9: Uniform flow: k field at $t^* = 4$; Euler/Lagrange.

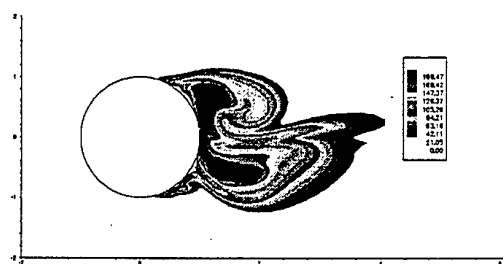


Figure 10: Uniform flow: ν_t field at $t^* = 4$; eulerian.

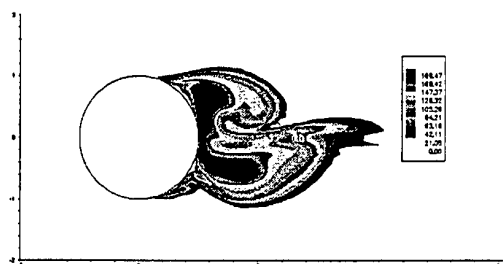


Figure 11: Uniform flow: ν_t field at $t^* = 4$; Euler/Lagrange.

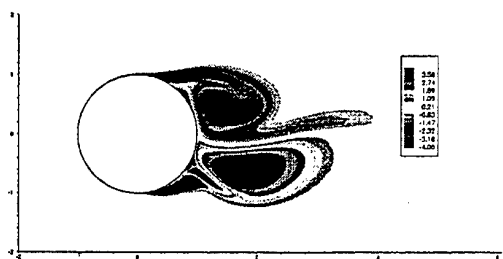


Figure 12: Uniform flow: ζ field at $t^* = 4$; eulerian.

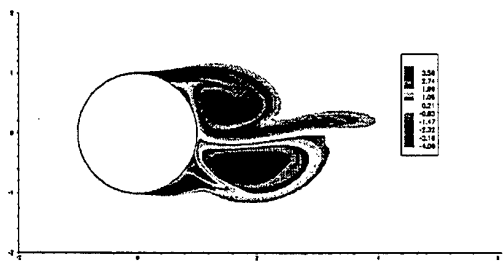


Figure 13: Uniform flow: ζ field at $t^* = 4$; Euler/Lagrange.

140000. The two latter Reynolds numbers are sub-critical but nevertheless sufficiently high from an engineering point of view. Results are obtained using the Wilcox $k - \omega$ model only.

The nondimensionalised transverse motion equation of the body (see equation 34) is solved by a 4th order Runge-Kutta procedure.

$$\ddot{y} + \frac{4\pi\zeta}{U_r}\dot{y} + \frac{4\pi^2}{U_r^2}y = \frac{F_H(t)}{\mu} \quad (34)$$

with y the transverse displacement nondimensionalised by the cylinder diameter, superscripts the time derivatives, ζ the percentage of structural critical damping, $U_r = U/(fD)$ the reduced velocity with U the uniform velocity at infinity, f the natural frequency in air of the cylinder, $\mu = m/(\rho D^2)^1$ the reduced mass and F_H the nondimensional transverse hydrodynamic load.

Figure 14 shows the amplitudes of oscillations as a function of R_e . Comparisons are done with the experimental results of Anagnostopoulos & Bearman (1992) and other numerical results. For this case, the reduced mass in water μ is equal to 148, the percentage of structural critical damping is equal to 0.0012, and, when R_e varies from 80 to 150, U_r varies from 4.5 to 8.3. The time step is equal to 0.02 and there are 128×100 nodes in angular and radial directions. The present results underestimate the experimental results of Anagnostopoulos by nearly 10 to 20 per cent. This is the case for all numerical methods except the results of Graziani (1998) which overestimate results by at least 50 per cent. For those Reynolds number values, it is difficult to have a representative phenomenon of Vortex Induced Vibrations (VIV). Indeed, the Strouhal number grows from 0.1 to 0.2 between $R_e = 100$ and $R_e = 200$. So we performed calculations for $R_e = 1000$ since, around this value, the Strouhal number is constant and equal to 0.21.

Figure 15 shows the amplitude of oscillations as a function of reduced velocity U_r for $R_e = 1000$. At this Reynolds number, even though the wake is turbulent, the flow is essentially laminar. The mass ratio is equal to 10. The structural damping is chosen also negligible as 1 per cent of the critical damping. The time step is equal to 0.01 and there are 128×100 nodes in angular and radial directions. The amplitude of oscillation reaches a maximum value of 1.05 diameters. Reduced velocities that generate lock-on range from 4 to 7. Those results are quite in accordance with experimental ones which for that mass ratio predict amplitudes of the order of 1.1 diameters.

¹ m is the mass of the cylinder per unit length and ρ is the density of the fluid

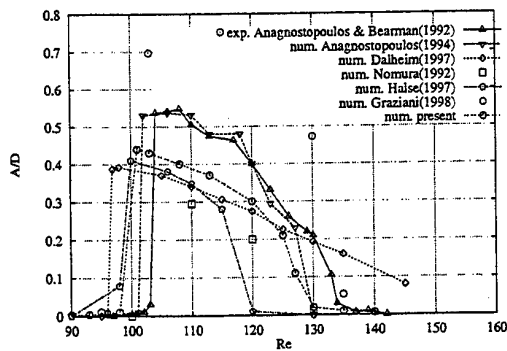


Figure 14: Cylinder oscillation amplitude as a function of Re

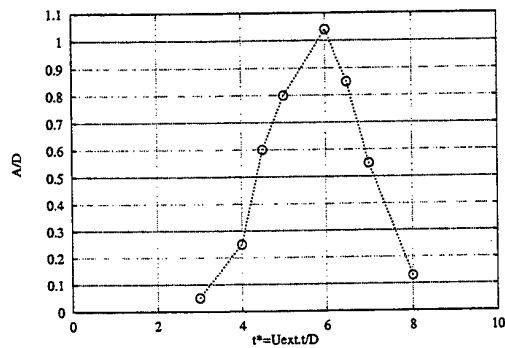


Figure 15: Cylinder oscillation amplitude as a function of U_r . $Re = 1000$

To illustrate those results, figures 16 and 17 show respectively the amplitude of oscillation as a function of t^* and the corresponding drag coefficient for $U_r = 5$. The corresponding drag coefficient more than doubles compared with the non-oscillating case.

Figure 18 shows the amplitude of oscillations as a function of reduced velocity U_r at $Re = 140000$. The structural characteristics are the same as for $Re = 1000$. The time step is equal to 0.005 and there are 256×150 nodes in angular and radial directions. At this Reynolds number, the flow is turbulent just after the separation point. This Reynolds has been chosen since comparisons have been performed with experiments in the uniform flow case (see above paragraph).

Figures 19 and 20 show respectively the amplitude of oscillation as a function of t^* and the corresponding drag coefficient for $U_r = 5$. Compared with figures 16 and 17, the amplitude of oscillation has slightly grown up and the mean drag coefficient has decreased. Nevertheless, the differences between

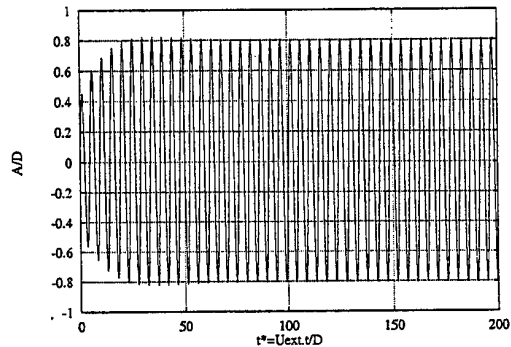


Figure 16: Cylinder oscillation amplitude as a function of nondimensional time. $Re = 1000$, $U_r = 5$

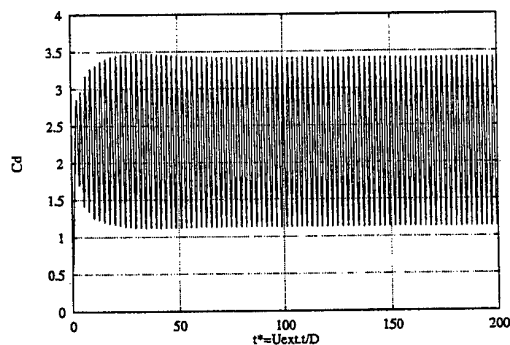


Figure 17: Drag coefficient as a function of nondimensional time. $Re = 1000$, $U_r = 5$

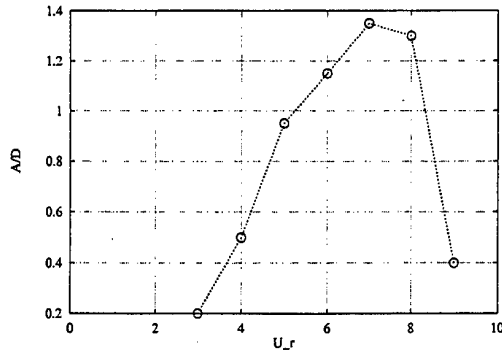


Figure 18: Cylinder oscillation amplitude as a function of U_r . $Re = 140000$

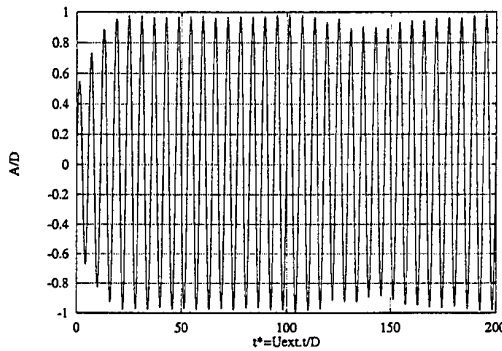


Figure 19: Cylinder oscillation amplitude as a function of nondimensional time. $Re = 140000$, $U_r = 5$

maximum and minimum values of the drag coefficient follow the same trend as the amplitude.

Laminar and turbulent flows around multiple bodies

For multiple circular cylinder configurations, validations have been done and are presented in Etienne *et al.* (1998). Here we chose to validate the calculation of force coefficients. We chose the case of two cylinders in tandem arrangement. The nondimensional distance center-to-center T/D is equal to 2. Figures 21 and 22 show the instantaneous vorticity field and streamlines at $t^* = 25$ for a subcritical Reynolds number equal to 200. That shows that the lagrangian method doesn't diffuse the wake and that continuity is ensured between each domain for transported quantities and for the velocity field.

Figure 23 shows the drag coefficient for each cylinder as a function of t^* . These results are in agreement with experiments reported by Zdravkovich (1977)

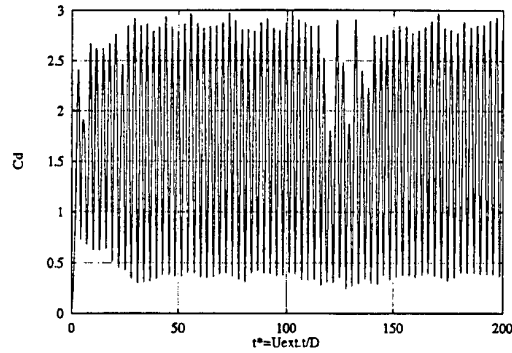


Figure 20: Drag coefficient as a function of nondimensional time. $Re = 140000$, $U_r = 5$

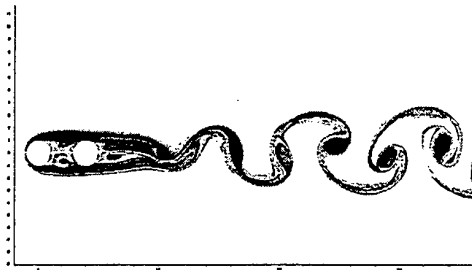


Figure 21: Instantaneous vorticity field for two cylinders in tandem arrangement at $t^* = 25$. $Re = 200$, $T/D = 2$

which show that for $T/D = 2$, the first cylinder experiences a drag coefficient C_d around 1. (for a single circular cylinder $C_d=1.35$) and the second cylinder experiences a drag coefficient around -0.2. There is nevertheless a discrepancy concerning the Strouhal number which is overestimated at 0.19 when, from experiments, it is equal to 0.16. To make sure, longer simulations should be performed.

For the turbulent case, few experiments exist. The comparison will be done with the experiments performed by Igarashi (1984) around three circular cylinders in tandem arrangement at Reynolds number 22000. Igarashi gives the drag coefficients for the three cylinders for several center-to-center distances in the range $[1, 4]$. We choose a center-to-center distance of 2.5 diameters.

Figures 24 to 27 show the instantaneous vorticity ζ , turbulent kinetic energy k , characteristic frequency ω and turbulent viscosity ν_t fields respectively at $t^* = 20$. maximum values of the turbulent viscosity reach 10 times the kinematic one. Maximum values

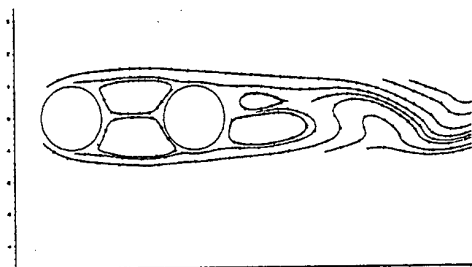


Figure 22: Instantaneous streamlines for two cylinders in tandem arrangement at $t^* = 25$. $Re = 200$, $T/D = 2$

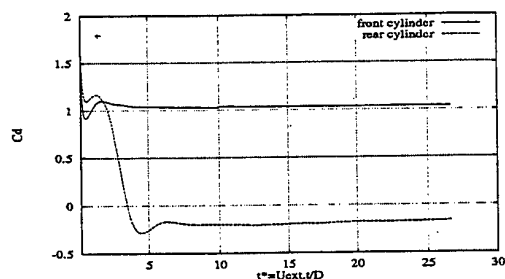


Figure 23: Drag coefficients for the two cylinders in tandem arrangement. $Re = 200$, $T/D = 2$

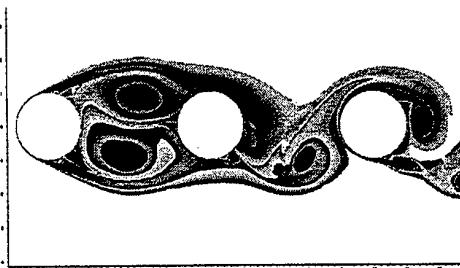


Figure 24: Instantaneous vorticity field for three cylinders in tandem arrangement at $t^* = 20$. $Re = 22000$, $T/D = 2.5$.

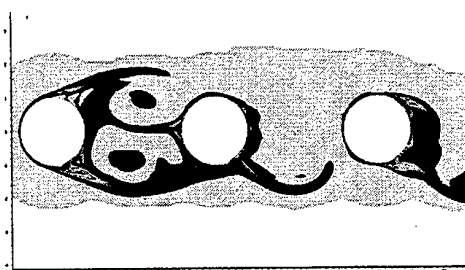


Figure 25: Instantaneous field of k for three cylinders in tandem arrangement at $t^* = 20$. $Re = 22000$, $T/D = 2.5$.

are localised at the rear of separation points. Maximum values of k are of 7%.

The two large circulation areas at the rear of the first cylinder generate a negative drag on the second cylinder. This in return doesn't produce vorticity which could attract the third cylinder. This explains that, in mean, the second cylinder experiences a negative drag and the third cylinder a positive one. Igarashi's experiments demonstrate the same trends. Figure 28 shows the drag coefficient for each cylinder. For $L/D = 2.5$, Igarashi measured a drag coefficient of 1. for the first cylinder, -0.3 for the second cylinder and 0.6 for the third cylinder. Nevertheless, the simulation is too short to yield stable mean values for the different drag coefficients.

CONCLUSION

The present method clearly shows that the mixed Euler/Lagrange method enables an accurate solution for the studied configuration in laminar but also turbulent flows. This is due to a good transfer of turbulent properties between each sub-domain covering the

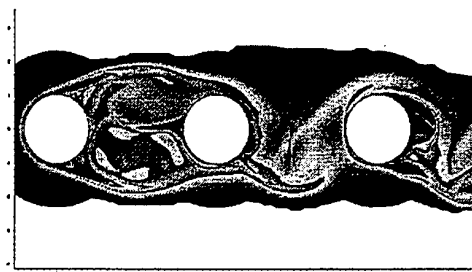


Figure 26: Instantaneous field of ω for three cylinders in tandem arrangement at $t^* = 20$. $Re = 22000$, $T/D = 2.5$.

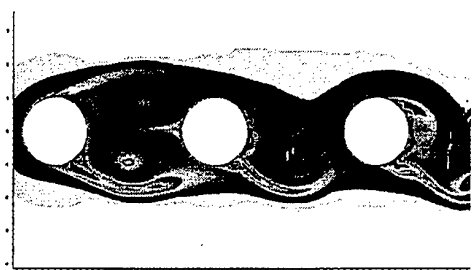


Figure 27: Instantaneous field of ν_t for three cylinders in tandem arrangement at $t^* = 20$. $Re = 22000$, $T/D = 2.5$.

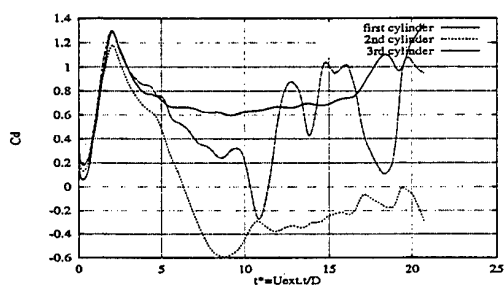


Figure 28: Drag coefficients for three cylinders in tandem arrangement. $Re = 22000$, $T/D = 2.5$.

flow plane. Computational efforts are concentrated in the region of interest thanks to the lagrangian formulation and the growth of the boundary layer is properly handled in an eulerian framework.

Concerning the phenomenon of Vortex Induced Vibrations for one cylinder, using the pure eulerian method, it is well recovered in laminar but also turbulent flow configurations. Amplitudes of oscillations for the case $Re = 140000$ show that for subcritical values of the Reynolds number, amplitudes of oscillations are of the order of one diameter. Calculations should be done at higher Reynolds numbers to quantify the impact of drag crisis on the VIV phenomenon.

Acknowledgement This work is part of a thesis project financed by Institut Français du Pétrole.

REFERENCES

- Anagnostopoulos, P. & Bearman, P.W., 1992,
"Response characteristics of a vortex excited
cylinder at low reynolds numbers ", *Journal of
fluids and structures*, Vol. 6, pp. 39-50.
- Cantwell, B. & Coles, D., 1983,
"An experimental study of entrainment and
transport in the turbulent near wake of a circular
cylinder", *J. Fluid Mech.*, Vol. 136, pp. 321-
374.
- Etienne, S., Sclan Y.M. & Molin B., 1998,
"Numerical study of complex flow around an ar-
ray of circular cylinders", *Proc. 2nd Hydroe-
lasticity in Marine Technology Conference*, pp.
145-153.
- Greengard, L. & Rokhlin, V., 1987,
"A fast algorithm for Particle Simulations", *J.
Comp. Phys.*, Vol. 73, pp. 325-348.
- Igarashi, T. & Suzuki, K., 1984,
"Characteristics of the flow around three circular
cylinders arranged in line", *Bulletin of the JSM*,
Vol. 27
- Kassera, V. & Stromheier, K., 1997,
"Simulation of tube bundles vibrations induced
by cross-flow", *J. Fluid & Struct.*, Vol. 11, pp.
909-928.
- Menter, F.R., 1992,
"Improved Two-Equation $k-\omega$ Turbulence mod-
els for aerodynamic flows", *NASA Technical
Memorandum 103975*
- Ould Salihi, M.L., 1998,
"Couplage de méthodes numériques en simu-
lation directe d'écoulements incompressibles",
*Thèse de doctorat de l'université Joseph
Fourier-Grenoble, Science et Géographie.*
- Wilcox, D.C., 1995,
"turbulence modeling for CFD", *DCW Indus-
tries, Inc. La cañada, California.*
- Sugavanam A., Wu J.C., 1980,
"Numerical Study of Separated Turbulent Flow
over Airfoils", *AIAA Journal*, Vol. 20, N4, pp.
464-470
- Zdravkovich M., 1977,
"Review of flow interference between two circu-
lar cylinders in various arrangements", *ASME*

AN EXAMPLE OF ERROR QUANTIFICATION OF SHIP-RELATED CFD RESULTS

M. Hoekstra¹ and L. Eça²

¹Maritime Research Institute Netherlands

P.O. Box 28, 6700 AA Wageningen, The Netherlands

Fax: +31 317 493245; E-Mail: M.Hoekstra@marin.nl

²Department of Mechanical Engineering, Instituto Superior Técnico

Avenida Rovisco Pais, 1096 Lisboa Codex, Portugal

Fax: +351 1 841 7398; E-Mail: eca@marine.ist.utl.pt

abstract

Grid convergence studies are reported for our RANS code PARNASSOS, applied to various flow cases. First, the laminar boundary layer and wake of a flow-aligned flat plate is dealt with, followed by the axisymmetric turbulent flow at the tail of a modified 6:1 prolate spheroid. Subsequently, two 3D flow fields are considered, viz. the flow at the stern of the Wigley hull and of the Mystery tanker. The most elaborate study is carried out for the latter case by comparing solutions on 24 grids of different density. The tentative recommendations of the ITTC on error analysis are followed and their adequacy is considered.

INTRODUCTION

Numerical analysis of the viscous flow around a ship, based on the solution of the Reynolds-averaged Navier-Stokes (RANS) equations, is being pursued for some 20 years now. The goal is to establish tools which can be used as an alternative or a complement to model testing in towing tanks or water/wind tunnels for analysis of ship designs. The technology has not matured in the sense that it can be generally applied without supporting experiments, but the increasing number of applications to real-world problems indicates that useful design information can often be extracted, or a better understanding and interpretation of model test results can be achieved.

With the increased frequency of applications in the design environment, however, the question about the credibility of the CFD-results is more often posed (where of course the required level of credibility may depend on the purpose of the application). Following the developments in aeronautics [1], the Resistance and Flow Committee of the ITTC has made a strong effort to emphasize the importance of error quantification of numerical simulation as well as of experimental work. It is expected that tentative guidelines for ITTC-members, i.e. the ship-hydrodynamics community at large, will be issued in the forthcoming ITTC proceedings. A preliminary version of these recommendations can be found in [2]. We endorse this approach and this paper is meant as a contribution to the

exploration of the field of error/uncertainty analysis of CFD results in ship-hydrodynamic applications.

In error quantification a distinction must be made between numerical or discretisation errors (related to discretisation method, grid resolution and lay-out, insufficient convergence, influence of round-off error, etc.) and modelling errors (shortcomings of the mathematical model, notably the turbulence modelling, as a representation of the physics). In this paper we attempt to get an impression of these errors – with the emphasis on the discretisation errors – by application of our RANS code PARNASSOS to a variety of flow fields. A brief description of the code is given in Section 2. Subsequently, we present and discuss results of grid-refinement studies applied to four cases. Beginning with the laminar flow at the trailing edge of a flow-aligned flat plate, we proceed with an axisymmetric turbulent flow and an analysis of the stern-flow field of the Wigley hull, to end with an elaborate study for the Dyne (Mystery) tanker.

DESCRIPTION OF FLOW CODE

All computational results presented in this paper have been obtained by application of our RANS code for ship stern flows, called PARNASSOS. It assumes free surface disturbances to be negligible. The solution algorithm is based on a coupled solution of the continuity and momentum equations in a space-marching iteration process. Each global iteration consists of a downstream predictor sweep, followed by an

algebraic update of the pressure field in an upstream corrector sweep. The procedure avoids reference to a Poisson equation for the pressure or introduction of artificial compressibility, which has several advantages for robustness and efficiency. As far as the turbulence models used are based on transport equations, these equations are solved segregated from the continuity and momentum equations. Two versions of the code are used, viz. the finite-difference (FD) version, recently described in [3], solving the RANS equations in weak-conservation form, and the finite-volume (FV) version, details of which are given in [4], solving the same equations in conservation form. In both cases the flow field is computed down to the wall without reliance on wall functions. Discretisation is of second or higher order, so that both methods are considered theoretically second-order accurate.

ESTIMATION OF ORDER OF ACCURACY

The estimation of the order of accuracy, n , for a given variable, ϕ , requires the solution of the flow field on at least three geometrically similar grids of different density, [5]. The estimation of this order of accuracy is based on the principle that the error of each of the three numerical solutions can be expressed as

$$e_{\phi_a} = \phi_a - \phi_{exact} = \alpha h_a^n, \quad (1)$$

where h_a stands for the (representative) grid cell size of the grid on which the solution ϕ_a has been obtained. This presupposes that the solutions are in the asymptotic range, i.e. additional terms of higher order on the right-hand side of (1) are negligible with respect to the leading order term. If three solutions ϕ_1, ϕ_2, ϕ_3 of any local or integral scalar quantity ϕ on three grids with $h_1 < h_2 < h_3$ are available, it is possible to derive from eq. (1) for any of the three grid pairs:

$$\frac{e_{\phi_b}}{e_{\phi_a}} = \left(\frac{h_b}{h_a}\right)^n, \quad (2)$$

or

$$e_{\phi_b} - e_{\phi_a} = \phi_b - \phi_a = e_{\phi_a} \left(\left(\frac{h_b}{h_a}\right)^n - 1 \right). \quad (3)$$

From eq. (3) two alternatives for the estimation of order of accuracy n can be derived:

$$\frac{(\phi_3 - \phi_1)}{(\phi_2 - \phi_1)} = \frac{\left(\left(\frac{h_3}{h_1}\right)^n - 1 \right)}{\left(\left(\frac{h_2}{h_1}\right)^n - 1 \right)}, \quad (4)$$

or, using (2):

$$\left(\frac{h_2}{h_1}\right)^n = \frac{(\phi_3 - \phi_2)}{(\phi_2 - \phi_1)} \frac{\left(\left(\frac{h_2}{h_1}\right)^n - 1 \right)}{\left(\left(\frac{h_3}{h_2}\right)^n - 1 \right)}. \quad (5)$$

It is easy to see that equations (4) and (5) are perfectly equivalent. If the ratios h_2/h_1 and h_3/h_2 are equal, n follows directly; else n must be determined iteratively. Grid convergence is achieved if $n > 0$.

CASE 1: LAMINAR WAKE OF A FLAT PLATE

The laminar flow past a flow-aligned flat plate of finite length is a suitable first case for numerical verification. The geometry is simple and allows the use of rectangular Cartesian grids; boundary layer and triple-deck theories provide a good framework for comparison; and possibly disturbing influences of turbulence modelling are avoided. At the same time it represents the most fundamental form of trailing edge flows.

For the numerical tests we have chosen a Reynolds number based on the length of the plate of $Re = 10^5$. A rectangular coordinate system x, y was adopted with the origin at the leading edge of the plate and the x -axis along the plate. The computation domain extended in lengthwise direction from $x/L = 0.5$ to $x/L = 1.5$, while the domain width was $y_{max} = 0.125L$, which is approximately 8 times the boundary-layer thickness at the trailing edge. The boundary conditions $u = u_\infty$ and $p = 0$ were applied on the external boundary $y = y_{max}$, while on the inlet boundary a close approximation of the Blasius solution [6] was imposed.

Five rectangular grids were generated with the grid points uniformly distributed in x -direction, but stretched towards the plate and the wake centreline in the normal direction. The grids had respectively 33×33 , 45×45 , 65×65 , 89×89 and 129×129 nodes. If the typical grid size of the finest grid is h , the covered sequence of grid sizes is: $h, 1.45h, 2h, 2.91h, 4h$.

The convergence histories of the solutions on the various grids, obtained with the FV version of PAR-NASSOS, are compared in Fig. 1, where the maximum change of C_p between successive global iterations (i.e. the L_∞ norm of ΔC_p) has been chosen as the measure of convergence. The convergence is seen to be uniform and fast, but the rate of convergence decreases somewhat with the increase of the grid density.

In Fig. 1 the change in the pressure variable is employed to measure the convergence. This is not unreasonable, since the residual of the momentum equation is dominated by the pressure change as a result

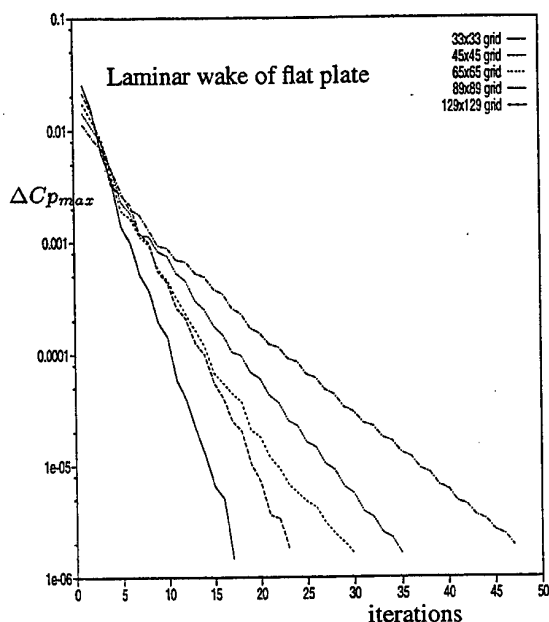


Figure 1: Convergence behaviour on five grids

of the chosen iterative solution strategy. But convergence is properly obtained if it can be shown that besides variable changes between successive iterations, also the residuals of the equations being solved tend to zero. Therefore, as an example, the convergence of the global iteration process on the 65×65 grid is alternatively presented in Fig. 2, showing the maximum residuals of the three equations per iteration.

The oscillatory behaviour in the y -momentum residual is due to invoking an approximate multigrid cycle in every second global iteration. The residual of the continuity equation does not appear because it is in this case at machine accuracy level (10^{-17}) from the beginning, and thus outside the range of the figure. By the construction of our iteration scheme, this residual is only affected by the convergence tolerance of the local or inner iteration process. In the global iteration process it is therefore orders of magnitude smaller than the residual of the momentum equation. This is a characteristic feature of PARNASSOS. While the velocity and pressure fields gradually adjust to satisfy the momentum equation, all intermediate velocity fields satisfy the continuity equation. This is a major distinction from the Marker-and-Cell or the Artificial Compressibility method.

From the (sufficiently converged) solutions on a set of three similar grids, varying in density, the apparent order of accuracy of a numerical method for a particular test case can be established as described above

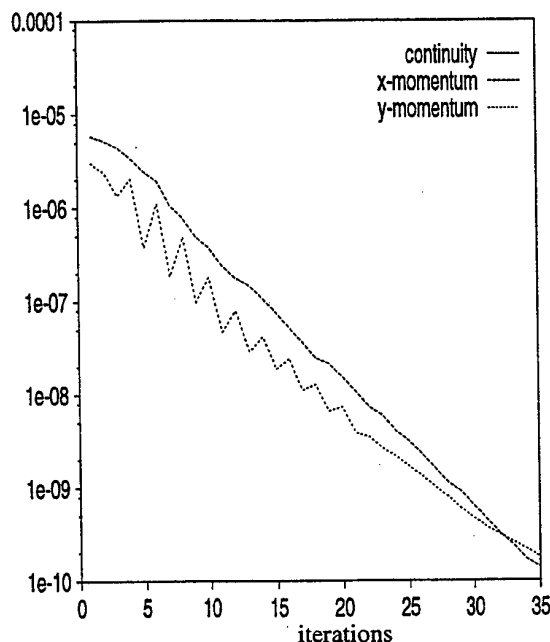


Figure 2: Convergence history on the 65×65 grid - maximum residuals

from eq. (4) or (5). For ϕ , any local or integral quantity can be chosen. We have selected four quantities, viz. C_D , the total drag of the plate, determined from

$$C_D = \frac{2}{u_\infty^2 L} \int_0^{y_{max}} (p + u(u_\infty - u))_{outlet} dy,$$

C_{fx} , the drag of the aft half of the plate (obtained by skin friction integration), C_{pte} , the pressure at the trailing edge and u_{cl} , the centreline velocity at the outlet plane for the order verification of our method. The computed values of these quantities are listed in Table 1, while the order of accuracy derived from various grid triplets is presented in Table 2.

The results are rather diverse. For the total drag C_D the order seems to be better than 2, but for the frictional drag of the aft half of the plate it falls in the mean below 2. The conjecture that the latter result might be due to using simple mid-point integration in the evaluation of C_{fx} did not come true; with Simpson integration, essentially the same figures for the order of convergence were obtained. Turning to the local quantities C_{pte} and u_{cl} , we see that the result is uniformly 1.1 for the pressure at the trailing edge, but approximately 2 for the centreline velocity at the outlet, provided the results involving the coarsest grid (case 5) are left out. The low convergence order for the pressure at the trailing edge is not unusual, considering the fact that this quantity is evaluated at the location where

#	grid	C_D $\times 10^3$	C_{fx} $\times 10^4$	C_{pte} $\times 10^2$	u_{cl} $\times 10$
1	129 × 129	4.3147	6.4203	-1.2675	5.4184
2	89 × 89	4.3139	6.4178	-1.2483	5.4195
3	65 × 65	4.3121	6.4141	-1.2250	5.4212
4	45 × 45	4.3062	6.4076	-1.1845	5.4259
5	33 × 33	4.2972	6.3942	-1.1344	5.4305

Table 1: Key quantities for order derivation

cases	$n(C_D)$	$n(C_{fx})$	$n(C_{pte})$	$n(u_{cl})$
1+3+5	2.52	1.68	1.09	1.75
1+2+3	2.84	1.61	1.04	1.65
2+3+4	2.92	1.15	1.12	2.48
3+4+5	1.70	2.59	1.09	0.46
1+2+4	2.88	1.43	1.07	2.00
2+3+5	2.46	1.70	1.11	1.78
1+3+4	2.90	1.29	1.10	2.26
2+4+5	1.97	2.23	1.10	0.96

Table 2: Apparent order of grid convergence

it reveals a sharp peak. We verified that with a first-order two-point discretisation of the mainstream pressure gradient the order drops to even lower values (approximately 0.65).

The drag converges to $C_D = 0.0043153$ for $h \rightarrow 0$ which is in good agreement with triple deck theory that gives (see [7])

$$\begin{aligned}
 C_D &= \frac{D}{\frac{1}{2}\rho u_\infty^2 L} \\
 &= 1.32824Re^{-1/2} + 2.651Re^{-7/8} + O(Re^{-1}) \\
 &= 0.004312 + O(10^{-5}).
 \end{aligned}$$

Taking $C_{D,h \rightarrow 0}$ as a reference, the relative error in the drag obtained on the five grids is 0.014, 0.032, 0.074, 0.211 and 0.419 per cent, respectively.

CASE 2: FLOW AT THE TAIL OF A MODIFIED SPHEROID

For a further verification of our numerical method we move on to the turbulent flow around the aft end of an axisymmetric body. As the body we have chosen a 6:1 prolate spheroid, modified at the tail to avoid flow separation. The modification consists of replacing the blunt aft end by a pointed tail, thus making the body about 3.57 per cent longer.

More precisely, the body geometry is given by:

$$\begin{cases} y = \frac{1}{6}\sqrt{x(0.9655L - x)} & 0 \leq x \leq 0.9333L \\ y = 0.4333(L - x) & 0.9333L \leq x \leq L \end{cases}$$

The flow around this body at a Reynolds number of $Re = 1.264 \times 10^6$ was simulated in a domain extending in lengthwise direction from $x/L = 0.4828$ (the location of maximum thickness of the body) to $x/L = 1.4483$. The external boundary was put at $y_{max} = 0.1448L$. The boundary conditions imposed there were derived from a potential flow solution; on the inlet boundary suitable velocity profiles were prescribed.

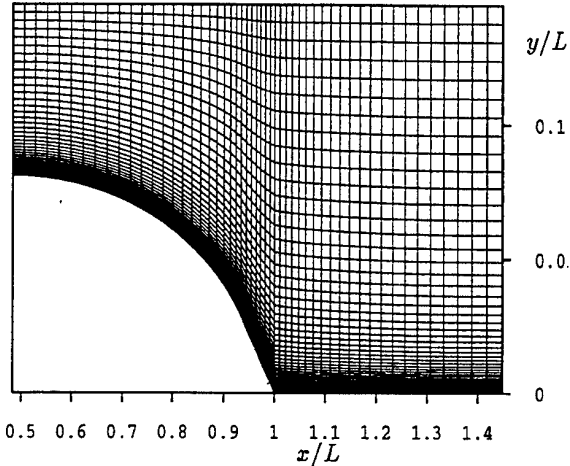


Figure 3: Coarsest grid (49 × 65) for modified 6:1 spheroid

In the chosen domain five grids were generated: 49 × 65, 61 × 81, 73 × 97, 85 × 113 and 97 × 129. The coarsest grid is shown in Fig. 3 (notice that the horizontal and vertical axes are scaled differently); the other grids were similar, but with greater density. Except for the number of grid nodes, the parameters for grid generation were kept the same, so that for instance the amount of stretching to the body surface and the wake centreline is the same for all grids, implying that the thickness of the cells adjacent to the surface decrease with an increase of the grid density.

Again the FV-version of the program was applied, employing an algebraic turbulence model.

The apparent order of accuracy was determined for the frictional and the pressure drag of the aft part of the body (*i.e.* the part inside the computation domain). Results were obtained with third order (QUICK) discretisation of the streamwise pressure gradient, but also with a first-order two-point downstream discretisation. The results are summarized in Table 3, while the derived order for several grid combinations is presented in Table 4. We like to point out that the five digits given for C_{fx} and C_{px} are free of iterative convergence errors.

With the standard method (with QUICK discretisation for the mainstream pressure gradient) the order of

#	grid	Quick $\partial p/\partial \xi$		2-pnts $\partial p/\partial \xi$	
		$C_{fx} \times 10^4$	$C_{px} \times 10^4$	$C_{fx} \times 10^4$	$C_{px} \times 10^4$
1	97×129	3.3536	1.1755	3.3501	1.2748
2	85×113	3.3527	1.1756	3.3486	1.2893
3	73×97	3.3514	1.1759	3.3465	1.3082
4	61×81	3.3489	1.1768	3.3429	1.3354
5	49×65	3.3443	1.1796	3.3372	1.3773

Table 3: Modified spheroid - Key quantities for order derivation

cases	Quick $\partial p/\partial \xi$		2-pnts $\partial p/\partial \xi$	
	$n(C_{fx})$	$n(C_{px})$	$n(C_{fx})$	$n(C_{px})$
1+2+3	1.55	6.57	1.34	0.84
2+3+4	2.87	5.46	2.19	1.16
3+4+5	2.00	4.53	1.27	1.13
1+3+5	2.34	5.18	1.72	1.10

Table 4: Modified spheroid - Apparent order of grid convergence

accuracy of C_{fx} is about 2, of C_{px} about as much as 5. A lower-order discretisation for the pressure gradient results evidently in a lower order of accuracy. But the solutions for both discretisations plausibly converge to the same result for $h \rightarrow 0$, as illustrated in Fig. 4. This figure shows C_{fx} and C_{px} plotted on a basis of the characteristic cell size h , taking $h = 1$ for the finest grid; moreover, for each data set a close fit is given by a simple power law formula, which reflects the mean of the accuracy orders of Table 4. The same figure also might give a clue to why the order of accuracy of C_{px} is unexpectedly high: the pressure drag value happens to be almost independent of the grid resolution. The evaluation of the order of accuracy becomes very sensitive to minor deviations in the data; at the same time, its significance for the uncertainty in the result becomes small.

Taking the extrapolated values for C_{fx} and C_{px} as a reference, the numerical errors of the various solutions can be directly inferred from Fig. 4.

CASE 3: STERN FLOW OF THE WIGLEY HULL

For numerical verification in 3D applications, we begin with analysing the flow at the stern of the Wigley hull, a ship-like form defined by the simple offset function:

$$y = \frac{B}{2} \left[\frac{4x}{L} \left(1 - \frac{x}{L} \right) \right] \left[1 - \left(\frac{z}{H} \right)^2 \right],$$

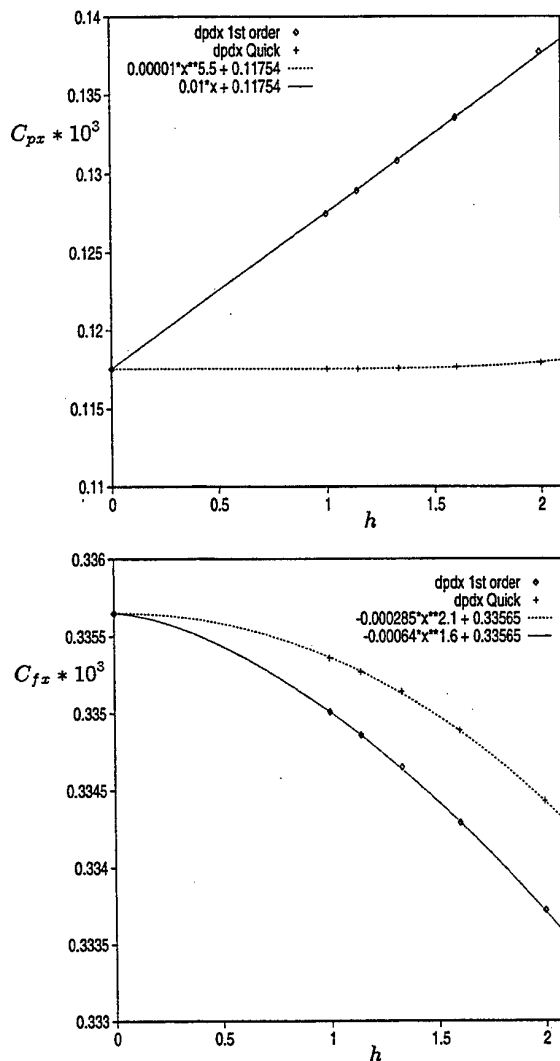


Figure 4: C_{fx} and C_{px} for various grid densities

with x and z in the range

$$0 \leq x \leq L \quad -H \leq z \leq 0,$$

while

$$B = 0.1L \quad H = 0.0625L.$$

The flow around this slender and sharp-keeled body was simulated at a Reynolds number of $Re = 7.4 \times 10^6$. The computation domain, extending in lengthwise direction from $x/L = 0.52$ to $x/L = 1.48$, was bounded externally by the relevant part of the elliptic cylinder

$$(y/0.07)^2 + (z/0.09)^2 = L^2; \quad x \text{ arbitrary.}$$

The FV version of PARNASSOS was applied. The boundary conditions imposed on the external bound-

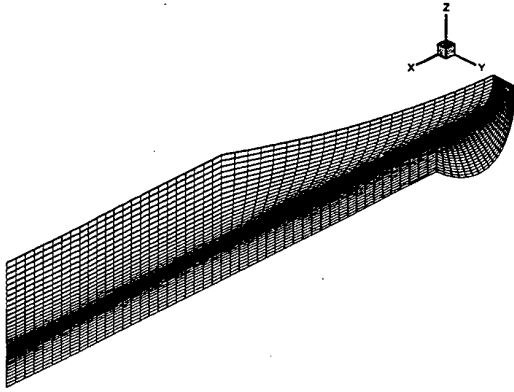


Figure 5: Grid planes $i=1, j=1, k=1$ for Wigley hull

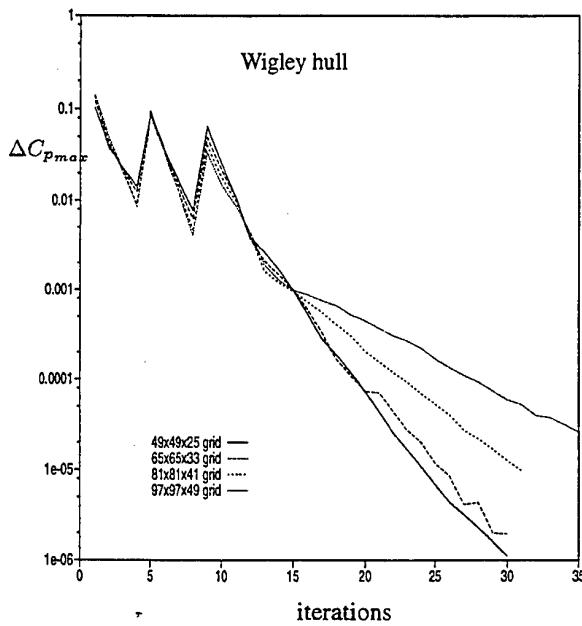


Figure 6: Convergence behaviour on various grids

ary were derived from a potential flow solution, while on the inlet boundary suitable velocity profiles were prescribed.

Computations were made on four H-O type grids, generated by stacking 2D grids obtained with the Schwarz-Christoffel technique described in [8], with $49 \times 49 \times 25$, $65 \times 65 \times 33$, $81 \times 81 \times 41$, $97 \times 97 \times 49$ nodes, respectively. The grid distribution on the domain boundaries is displayed for the coarsest of these grids in Fig. 5. The other grids are geometrically similar. The grid line along the keel and extending straight into the wake is a singular line; \sqrt{g} , the Jacobian of the transformation, vanishes there.

It may be worthwhile to mention that the grids were somewhat coarse near the body surface. The maxi-

mum y^+ value associated with the thickness of the grid cells adjacent to the body was about 3 for the finest grid, so about 6 for the coarsest grid.

#	grid	size	Algeb.	Menter	Spalart
1	$97 \times 97 \times 49$	1.0	9.633	9.334	9.492
2	$81 \times 81 \times 41$	1.2	9.622	9.268	9.511
3	$65 \times 65 \times 33$	1.5	9.607	9.142	9.542
4	$49 \times 49 \times 25$	2.0	9.590	8.882	9.643

Table 5: Wigley hull - $C_{fx} \times 10^5$ data for three turbulence models with FV version

#	grid	size	Algeb.	Menter	Spalart
1	$97 \times 97 \times 49$	1.0	2.850	2.573	2.578
2	$81 \times 81 \times 41$	1.2	2.890	2.610	2.616
3	$65 \times 65 \times 33$	1.5	2.960	2.672	2.679
4	$49 \times 49 \times 25$	2.0	3.092	2.792	2.799

Table 6: Wigley hull - $C_{px} \times 10^5$ data for three turbulence models with FV version

cases	Algebraic		Menter		Spalart	
	C_{fx}	C_{px}	C_{fx}	C_{px}	C_{fx}	C_{px}
1+2+3	0.53	1.75	2.17	1.54	1.41	1.49
1+2+4	0.11	1.63	2.01	1.56	2.46	1.50
1+3+4	-0.23	1.54	1.90	1.57	3.11	1.51
2+3+4	-0.50	1.48	1.83	1.58	3.57	1.52

Table 7: Wigley hull - Apparent order of grid convergence

The convergence history, measured again by the L_∞ norm of the pressure change between successive iterations, is shown in Fig. 6. Obviously, the L_∞ norm is more demanding than the often used L_2 norm, which would be a lot smaller. As revealed by the two jumps in the convergence curves in the figure, we have applied grid sequencing (step size halving in main-stream direction) in three stages.

#	size	Algeb.-2		Menter	
		$C_{fx} \times 10^5$	$C_{px} \times 10^5$	$C_{fx} \times 10^5$	$C_{px} \times 10^5$
1	1.0	9.161	2.443	9.843	2.443
2	1.2	9.255	2.451	9.763	2.452
3	1.5	9.362	2.467	9.567	2.469
4	2.0	9.515	2.502	9.243	2.507

Table 8: Wigley hull - Results of FD-version

The apparent order of accuracy was determined for the frictional and the pressure drag of the aft part of the body (*i.e.* the part inside the computation domain). Results are presented for a Cebeci/Smith-type algebraic turbulence model and for two one-equation turbulence models, *viz.* those proposed by Spalart-Allmaras [9] and by Menter [10] in Tables 5 and 6. The derived orders for several grid combinations are presented in Table 7. Although the results for all models are monotonous, the convergence order is quite different for the frictional resistance. We suspected that the low order found for the algebraic model might be due to the conditional statements used in the determination of the outer length scale, but the maximum eddy viscosity appeared to differ for the various grids only near the stern and in the near wake, where the differences were systematic. More likely, therefore, the cause is to be found in the rather high value of $(y_2^+)_{max}$ in these calculations.

All results above were computed with the FV version. On the same four grids, we repeated the calculations with the FD-version. Ideally, this would give us an impression of the influence of different discretisation techniques (which should vanish for grid cell sizes tending to zero), but unfortunately there are several implementation differences between the FV and FD version. For example, the FD version does not use the flux limiters included in the FV version, while also the turbulence models are not in all details the same. Nevertheless the results are given in Table 8. Taking all results of FV and FD version together, we see a variation in the total drag of the aftbody ($C_{fx} + C_{px}$) with a bandwidth of about ± 2.5 per cent on the finest grid. This is greater than the numerical errors derived per data set with eq. (3).

CASE 4: DYNE (MYSTERY) TANKER

An elaborate study has been carried out for the Dyne or Mystery tanker, a variant of the HSVA tanker with U-shaped afterbody sections. The hull has been a test case in both the Gothenburg [11] and the Tokyo [12] workshop. Solutions of the flow field at $Re = 5 \times 10^6$ were obtained with the FD version of our code, using the algebraic, Cebeci/Smith-type turbulence model, on no less than 24 grids, the number of grid nodes varying from about 7×10^3 to 2.15×10^6 . The computation domain covered only the flow field near the stern, the inlet station being located at $x/L = 0.5$ and the outlet at $x/L = 1.25$ ($x = 0$ at the forward perpendicular). The remaining boundaries of the computational domain are the ship surface, the external boundary, the ship symmetry plane and the free surface (which is treated as a symmetry plane). The ship surface was represented by a 2-D cubic spline and

the external boundary was an elliptic cylinder, given by:

$$\left(\frac{y}{0.149}\right)^2 + \left(\frac{z - 0.056L}{0.140}\right)^2 = L^2,$$

where $y = 0$ in the vertical symmetry plane and $z = 0$ on the keel plane. Fig. 7 shows the general lay-out of the grid.

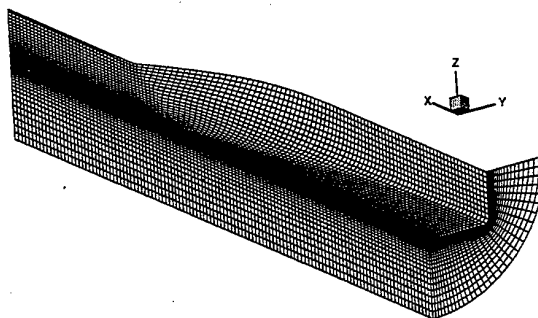


Figure 7: Impression of grid lay-out for Mystery tanker

The volume grids were created with a proprietary elliptic PDE grid generator, based on the GRAPE approach [13]. The plane and surface grids on the boundaries of the computational domain were generated with elliptic PDE orthogonal grid generators or the 2D version of the GRAPE method. The grid node distribution is uniform on only one of the eight edges of the computational domain, *viz.* the keel line. At the waterline and at the lengthwise edges of the external boundary, the grid node distribution is obtained from the boundary condition of the 2-D and surface grid generators to ensure grid orthogonality at the boundaries. Along the four edges in the direction normal to the ship surface, one-dimensional stretching functions were applied to adjust the maximum value of y^+ for the layer of grid cells adjacent to the hull, $(y_2^+)_{max}$.

It is important to note that the strategy for generating the grids of this study was slightly different from the foregoing applications. First, 8 grids were generated with the procedure described above. In this set of grids, the parameter that governs the stretching towards the hull surface increases with the coarsening of the grid. In fact the parameter for the finest grid was multiplied with $r_i = h_i/h_{fine}$, where h_i is the representative grid cell size of the coarser grids. Next grid doubling was applied twice to each of these 8 grids. Thus we have three grid groups; each member of a group has a geometrically similar counterpart in the other two groups, but within a group the grids are not exactly similar. This procedure causes

that Richardson extrapolation may formally be applicable only across groups. All grids were made to have $(y_2^+)_\text{max}$ less than 1; the actual values are given in Table 9.

All solutions were converged until changes in C_p and in the velocity were less than 2×10^{-6} ; iterative convergence errors are therefore negligible with respect to the grid convergence errors.

Selected results are presented in Table 9. They comprise two global quantities, viz. the frictional and the pressure drag of the afterbody, as well as extrema of the main variables. Some data are also displayed graphically in Figs. 8, 9 and 10. A reasonable quadratic data-fit has been added, so that an impression is obtained how well the theoretical second order grid-convergence is realised in practice.

In Table 10 we present, for a limited set of three-grid combinations, the order of grid convergence for seven quantities.

We make the following observations:

- Immediately apparent in Figs. 8, 9 and 10 is an appreciable scatter in the data, which causes that orders derived from various grid combinations are scattered as well. In 3D turbulent flows there are of course several factors that may obscure or violate the convergence behaviour expected on theoretical grounds (see also [5]). A conditional statement, as used in turbulence models or in flux limiter implementations, is one such factor. Also, grid resolution may still be insufficient to reach the asymptotic range. An aspect undoubtedly relevant for the results of the Mystery tanker presented here is that the grid does not nicely conform to the stern contour, which is a knuckle line in the domain boundary surface. For the grids of all previous cases up to and including the Wigley hull, we were careful to let all grids have a node at the tail of the body or a grid-line along the stern contour. For the single-block H-O grid of the Mystery tanker this is not feasible. It is likely that the scatter with respect to quadratic convergence, observed in Fig. 8 for both C_{px} and C_{pmax} , is at least partly caused by this anomaly. Clearly the minimum value of the pressure, C_{pmin} , occurring in the bilge region, thus in a smoother part of the grid, is less affected. This quantity might be said to exhibit quadratic convergence – even over the whole range of h_i/h_1 – but still with considerable scatter. For C_{px} the bandwidth of the scatter narrows with h_i/h_1 approaching 1. For all grids with $h_i/h_1 \leq 3.2$, except grid 10, we find $0.533 < C_{px} \times 10^4 < 0.552$.

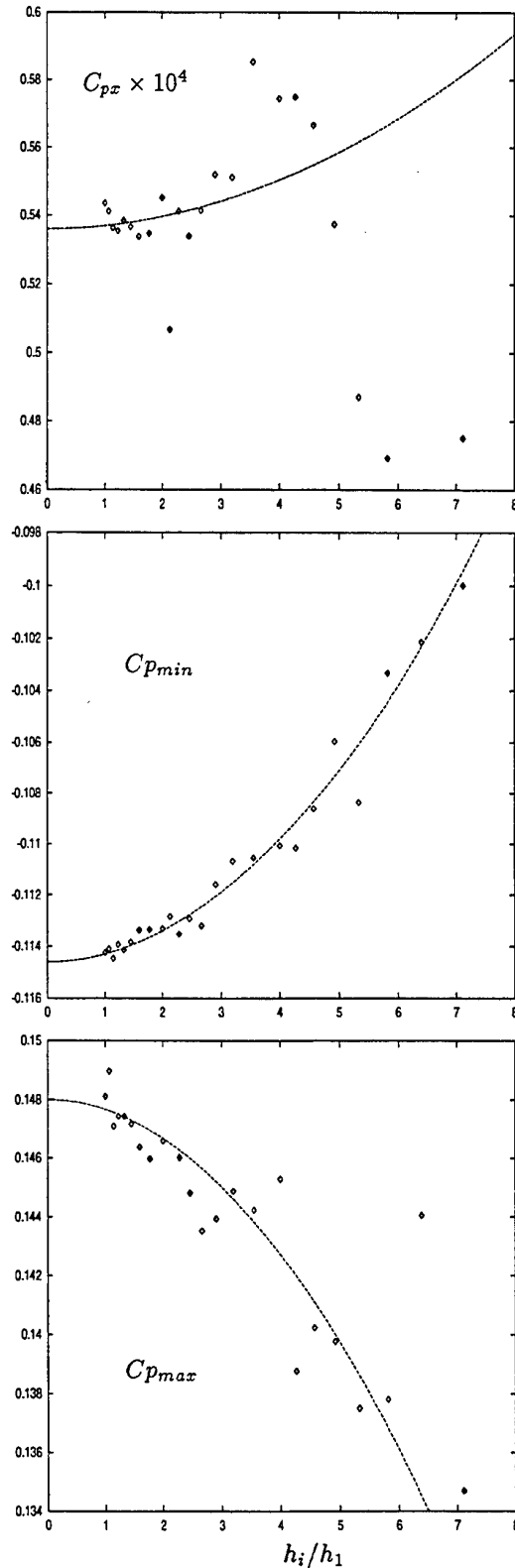


Figure 8: Results for Mystery tanker

#	grid	cell size	$(y_2^+)_\text{max}$	$C_{fx} \times 10^4$	$C_{px} \times 10^5$	$u_\text{min} \times 10^2$	vw_max	$C_{p\text{min}}$	$(\nu_t)_\text{max} \times 10^4$
1	257×129×65	h	0.191	1.48986	5.43524	-4.7509	0.29078	-0.11424	2.9299
2	241×121×61	1.0667h	0.184	1.48952	5.41176	-4.6984	0.29086	-0.11410	2.9166
3	225×113×57	1.1429h	0.159	1.48864	5.36324	-4.3891	0.29065	-0.11446	2.9095
4	209×105×53	1.2308h	0.148	1.48803	5.35423	-4.3388	0.28968	-0.11393	2.8840
5	193×97×49	1.3333h	0.138	1.48722	5.38449	-4.5550	0.29005	-0.11414	2.8575
6	177×89×45	1.4545h	0.127	1.48621	5.36630	-3.7880	0.28942	-0.11384	2.8480
7	161×81×41	1.6000h	0.114	1.48467	5.33770	-3.3333	0.28910	-0.11338	2.8505
8	145×73×37	1.7778h	0.102	1.48309	5.34693	-3.2637	0.28762	-0.11335	2.7815
-									
9	129×65×33	2h	0.344	1.48630	5.45183	-3.1181	0.28811	-0.11332	2.7996
10	121×61×31	2.1333h	0.311	1.48487	5.06692	-2.5469	0.28602	-0.11285	2.8099
11	113×57×29	2.2857h	0.315	1.48419	5.41143	-2.6245	0.28641	-0.11354	2.7351
12	105×53×27	2.4615h	0.283	1.48261	5.33877	-2.0603	0.28563	-0.11294	2.6861
13	97×49×25	2.6667h	0.267	1.48141	5.41408	-1.3547	0.28229	-0.11321	2.5929
14	89×45×23	2.9091h	0.232	1.48053	5.51944	-0.7377	0.28271	-0.11160	2.5715
15	81×41×21	3.2000h	0.217	1.47767	5.51145	-0.5905	0.27926	-0.11068	2.4768
16	73×37×19	3.5555h	0.209	1.47601	5.85325	-0.5163	0.27844	-0.11054	2.4947
-									
17	65×33×17	4h	0.683	1.48073	5.74357	-0.6250	0.27321	-0.11006	2.5117
18	61×31×16	4.2667h	0.727	1.47842	5.74851	-0.4443	0.27103	-0.11016	2.5869
19	57×29×15	4.5714h	0.626	1.47377	5.66504	-0.5606	0.27192	-0.10862	2.5502
20	53×27×14	4.9231h	0.549	1.47329	5.37421	-0.0128	0.27224	-0.10596	2.6144
21	49×25×13	5.3333h	0.480	1.46932	4.87081	-0.0897	0.27082	-0.10836	2.5934
22	45×23×12	5.8182h	0.491	1.46178	4.69209	0	0.26823	-0.10332	2.6716
23	41×21×11	6.4000h	0.367	1.46331	3.13399	0	0.26054	-0.10213	2.7199
24	37×19×10	7.1111h	0.422	1.46052	4.75042	0	0.25605	-0.09999	2.6444

Table 9: Mystery tanker - results on various grids for Cebeci-Smith model

grids	h_2/h_1	h_3/h_2	order						
			C_{fx}	C_{px}	u_min	vw_max	$C_{p\text{min}}$	$C_{p\text{max}}$	$(\nu_t)_\text{max}$
1+9+17	2.000	2.000	0.65	4.13	0.61	2.48	1.82	-0.23	1.14
2+10+18	2.000	2.000	0.47	-	-0.03	1.63	1.11	-	1.06
3+11+19	2.000	2.000	1.23	2.39	0.23	1.77	2.41	2.44	0.09
4+12+20	2.000	2.000	0.78	-	-0.15	1.66	2.81	0.95	-1.46
1+5+8	1.333	1.333	1.55	-1.05	6.55	4.16	7.18	2.65	0.17
1+6+11	1.455	1.571	-1.91	-	0.00	1.44	-1.15	0.03	0.32
1+6+12	1.455	1.692	-0.79	-2.89	0.54	1.48	1.02	1.25	0.75
1+7+13	1.600	1.667	-1.12	-	0.51	2.66	-3.56	0.84	2.21
1+9+14	2.000	1.455	2.17	4.21	1.96	2.65	2.49	2.32	2.34
3+6+8	1.273	1.222	1.99	-	0.21	2.55	-0.26	-	1.19
3+7+13	1.400	1.667	-1.48	-	0.49	2.44	-5.83	2.22	2.41

Table 10: Mystery tanker - grid convergence order (Cebeci-Smith model)

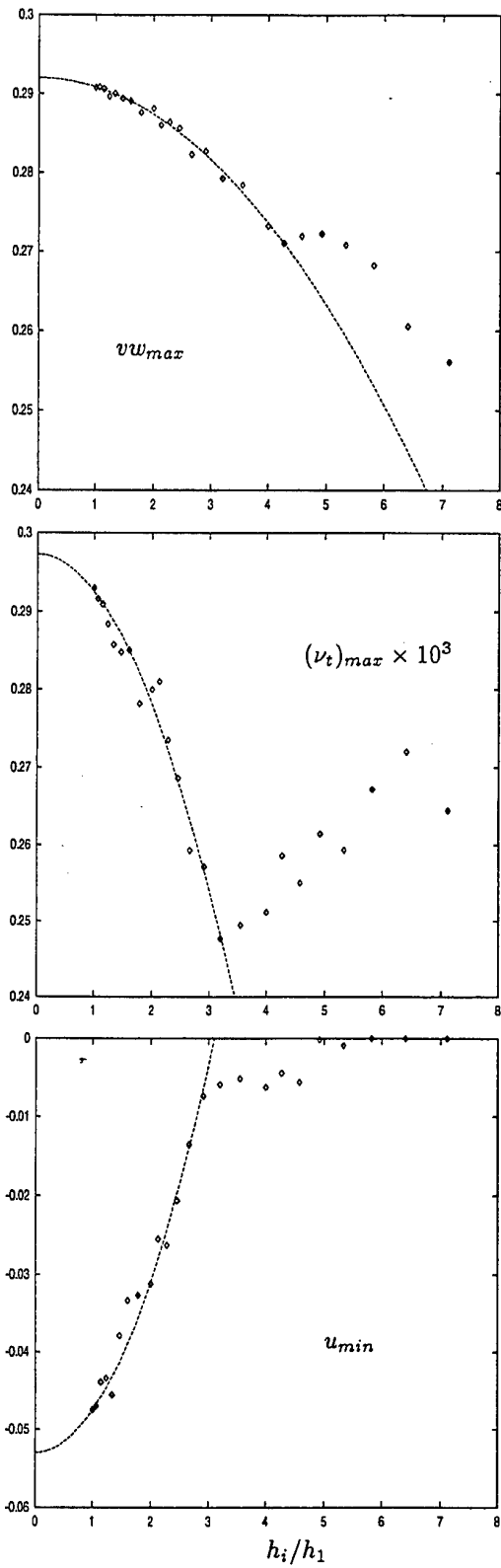


Figure 9: Results for Mystery tanker

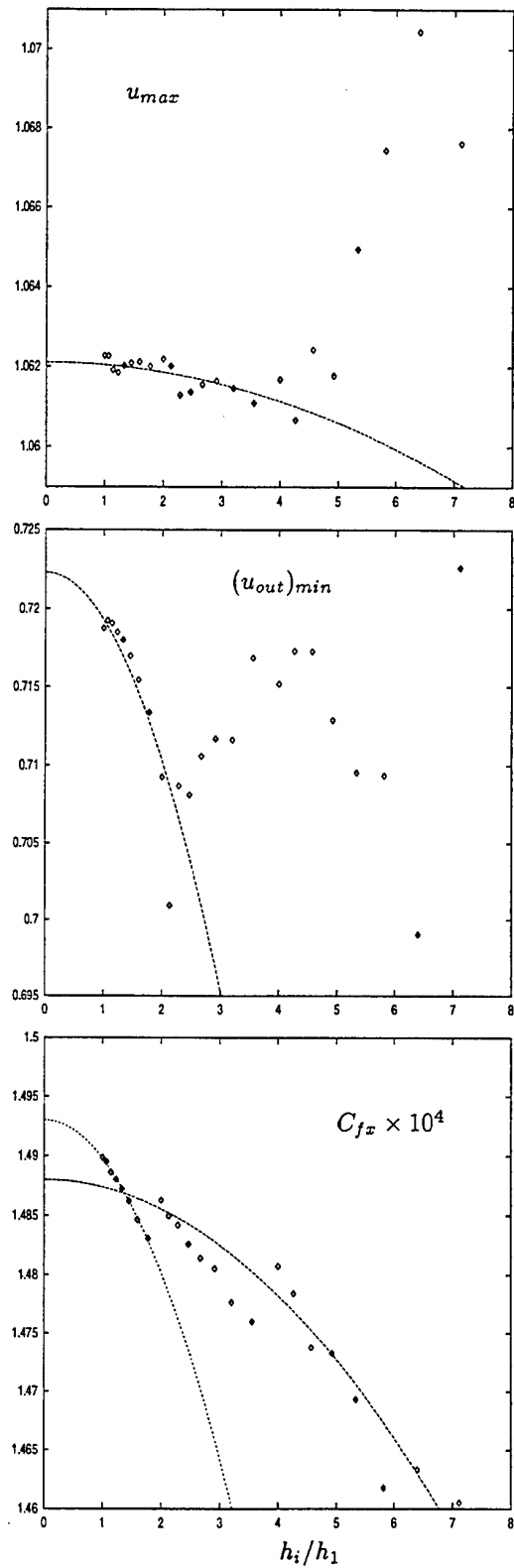


Figure 10: Results for Mystery tanker

- The results for the maximum transverse velocity vw_{max} show the trend that one would like to see: marginal scatter with respect to quadratic convergence behaviour for $h_i/h_1 \leq 4$. This is reflected in Table 10, which shows the least variation in the order derived from various grid combinations for vw_{max} .
- The minimum axial velocity u_{min} , indicative of the velocity in the reversed-flow zone, is a grid-sensitive quantity. On the coarse grids, reversed flow does not occur. With grid refinement the minimum velocity decreases and the results seem to indicate that for $h \rightarrow 0$ a further reduction is to be expected.
- The maximum axial velocity u_{max} is almost grid-independent up to $h_i/h_1 = 4$. Even on the coarsest grids the deviation from the finest grid solution is within 1 per cent.
- The maximum eddy viscosity $(\nu_t)_{max}$ seems to reach the asymptotic range only for $h_i/h_1 < 3$. But since the maximum eddy viscosity is likely to occur at or near the separation region a direct bearing on the results for u_{min} is plausible.
- The results for the frictional drag C_{fx} fall clearly apart into three groups. This is of course due to our choice to generate all grids with good resolution near the hull surface (see the column for $(y_2^+)_{max}$ in Table 9). There are two trends: an increase of C_{fx} with grid refinement, a decrease of C_{fx} with reduction of $(y_2^+)_{max}$. At the beginning of this section we suspected that Richardson extrapolation might not be applicable within each of the three grid groups. For C_{fx} this is clearly true. Encouraging is that the friction drag on the coarsest and the finest grid differ by only 2 per cent.
- The variation of the minimum velocity at the outlet plane, $(u_{out})_{min}$ is quite irregular and it is hard to say what the result for $h \rightarrow 0$ would be. Even so, the range of the data as a fraction of the reference speed is less than for vw_{max} .

As has been observed by several others (e.g. in [14]), order derivation from local quantities usually gives highly scattered results, even for 2D flows. Therefore we have chosen to compare mean values of several quantities along some of the edges of the computation domain (e.g. keel and waterline) and along straight lines in the interior of the domain. Along the chosen line, 10, 50 or 100 equally-spaced nodes were determined where the variable values were derived

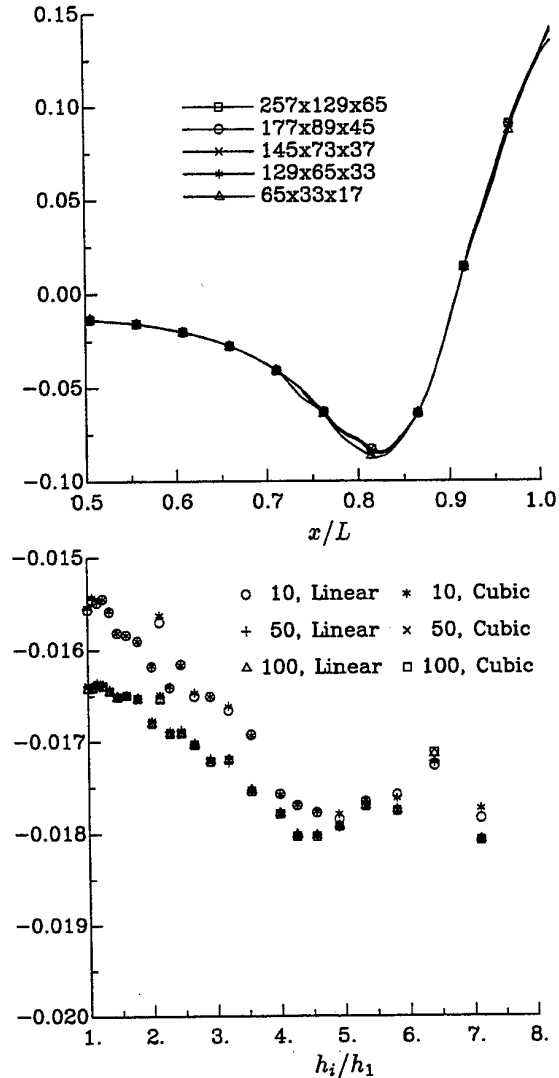


Figure 11: Mystery tanker - Pressure along the waterline (top) and its average value as a function of grid cell size (bottom)

by interpolation along grid lines, using two different techniques:

a) Linear interpolation. For $\xi_i < \xi_0 \leq \xi_{i+1}$

$$\phi_0 = \phi_i + \frac{\xi_0 - \xi_i}{\xi_{i+1} - \xi_i} (\phi_{i+1} - \phi_i) \quad (6)$$

b) Cubic interpolation. For $\xi_{i-1} \leq \xi_0 < \xi_i$

$$\phi_0 = \psi_1 \phi_{i-2} + \psi_2 \phi_{i-1} + \psi_3 \phi_i + \psi_4 \phi_{i+1} \quad (7)$$

$$\lambda = (\xi_0 - \xi_{i-1}) / (\xi_i - \xi_{i-1})$$

$$\psi_1(\lambda) = \frac{1}{6}(\lambda - 1)(2 - \lambda)\lambda$$

$$\begin{aligned}\psi_2(\lambda) &= \frac{1}{2}(1 - \lambda^2)(2 - \lambda) \\ \psi_3(\lambda) &= \frac{1}{2}(\lambda + 1)(2 - \lambda)\lambda \\ \psi_4(\lambda) &= \frac{1}{6}(\lambda^2 - 1)\lambda\end{aligned}$$

Subsequently, the line-mean variable value has been determined according to

$$\overline{\phi}_k = \frac{\int_{\xi_{begin}}^{\xi_{end}} \phi_k dx}{\xi_{end} - \xi_{begin}},$$

where the index k is the grid identification number. The integral is evaluated with the trapezoidal rule.

We have evaluated a lot of these line averages, but the limits on the length of this paper do not allow us to present them all. As an example, we show the pressure along the waterline for five grids and the line-average for all grids in Fig. 11. We have chosen this example in particular to show that one might – by visual inspection of a plot, displaying the spatial variation of a variable – easily conclude the solutions to be grid independent. The pressure distributions along the waterline are very little affected by the grid resolution; even the coarse $65 \times 33 \times 17$ grid gives an acceptable result. However, the plot of the line-average values indicates that there are small but systematic differences.

In general, these line-averages reveal a similar behaviour as found for minimum and maximum values of variables: systematic trends, but with scatter so that the evaluation of the order of grid-convergence based on one grid triplet gives strongly varying results, depending on the particular grid triplet that is chosen.

Having established the grid-convergence behaviour of our RANS code with the algebraic turbulence model, an intriguing question is how the results would be affected by a change of turbulence model. Moreover, considering the effect of different grid stretching towards the hull surface on C_{fx} (Fig. 10), one wonders what the influence would be of a better geometric similarity of the grids. Therefore, we decided to extend the study in two directions. First, we repeated the calculations on the grids as used for the algebraic turbulence model with Menter's one-equation model [10]. Secondly, we generated a new set of 24 grids, now with equal stretching parameters; this new grid set will be indicated as grid set B, while we refer to the original grid set as set A.

Results are summarized in Tables 11 and 13. The latter table shows that $(y_2^+)_{max}$ is now increasing from fine to coarse grids. All three data sets are compared graphically in Figs. 12, 13 and 14.

The differences between the results for the Menter model on the two grid sets A and B are very modest;

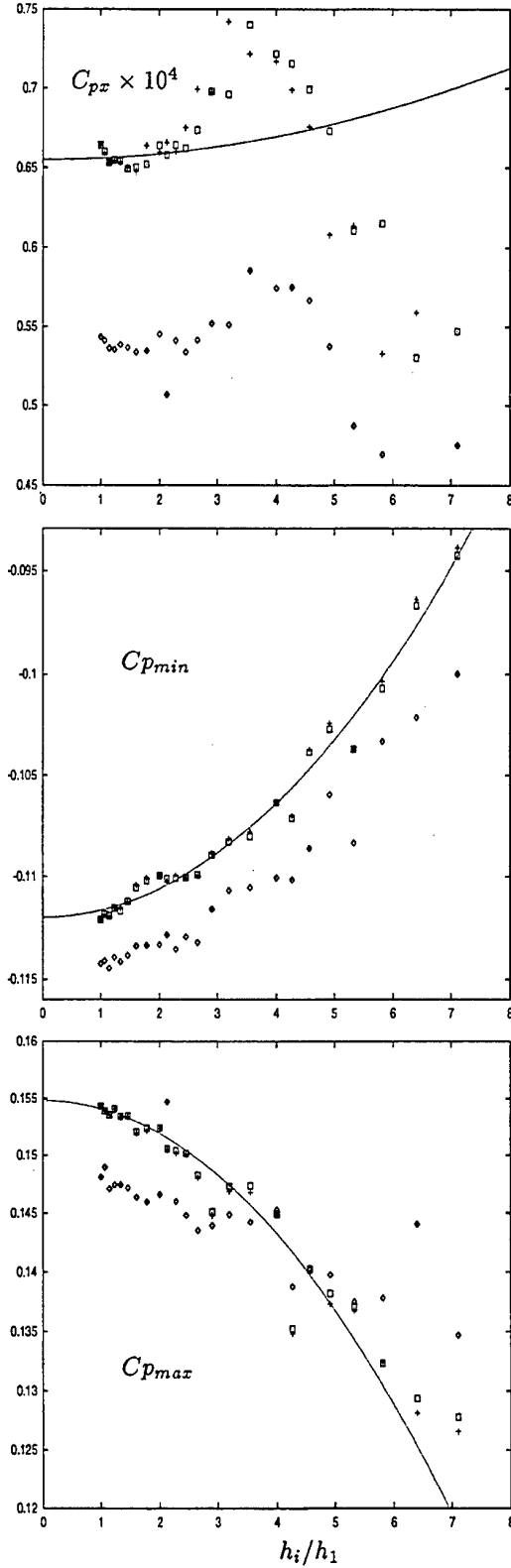


Figure 12: Results for Mystery tanker. \square : Menter, set A; $+$: Menter, set B; \diamond : Algebraic, set A

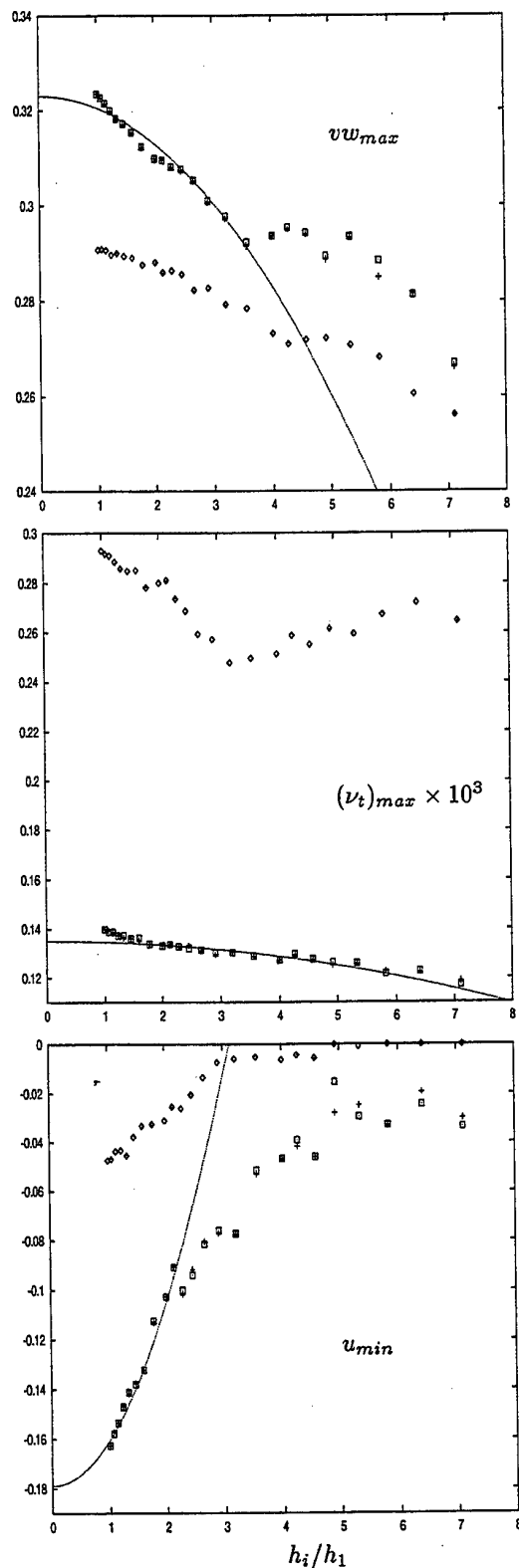


Figure 13: Results for Mystery tanker. \square : Menter, set A; $+$: Menter, set B; \diamond : Algebraic, set A

they are found for the fine grids ($h_i/h_1 < 4$) primarily in C_{fx} , C_{px} and u_{max} .

The differences between the results of the one-equation and the algebraic model (related to modelling errors) are greater than a reasonable estimate of the numerical error for each model. Notice that the maximum eddy viscosity for the algebraic model is roughly twice the value for the one-equation model.

With the Menter model the pressure drag of the afterbody is higher than with the algebraic model. But in both cases the data are found around an S-shaped line with a peak near $h_i/h_1 \approx 3.5$. This S-shape is apparently a grid-related feature.

Also C_{pmin} and C_{pmax} tend to a different level for $h \rightarrow 0$ for the two turbulence models.

From the results for the minimum longitudinal velocity u_{min} it can be concluded that the flow separation is more pronounced with the Menter model. The parabolic fit to the Menter model data is a poor one; a linear fit might be more appropriate. This would imply that u_{min} could reach a value of about -0.22 for $h \rightarrow 0$. This may be an indication of high sensitivity of the turbulence model, but we might also be reaching here the limits of the applicability of our code, that assumes in the discretisation of reversed flow that the separation zone is of modest extent. This is to be investigated further.

Also from the results for the Menter one-equation turbulence model we have determined line averages. As an illustration we shall give results for a straight line in the interior of the calculation domain, viz. the horizontal line defined by $x = 0.989L$, $z = 0.016L$ and $0 < y < 0.03L$. This is the line crossing the core of the bilge vortex, as follows from Figs. 15 and 16, which show plots of the relevant variables in the plane $x = 0.989L$ obtained on the finest grid. Fig. 17 shows the variation of the three Cartesian velocity components along the line, while Fig. 19 gives similar results for the pressure and the eddy viscosity. Figs. 18 and 20 show the corresponding line-averages on the basis of h_i/h_1 . The interpolations according to eqns. (6) and (7), required to derive the line averages, were carried out so as to get first data for $x = 0.989L$, then $z = 0.016L$ and finally $y = const..$

DISCUSSION

The 21st and 22nd ITTC Resistance Committee's have been working on the establishment of a recommended practice for error and uncertainty analysis. As the outcome on the forthcoming Conference may be expected to have a strong bearing on what is proposed in [2], we can now consider the suitability and adequateness of the suggestions and recommendations

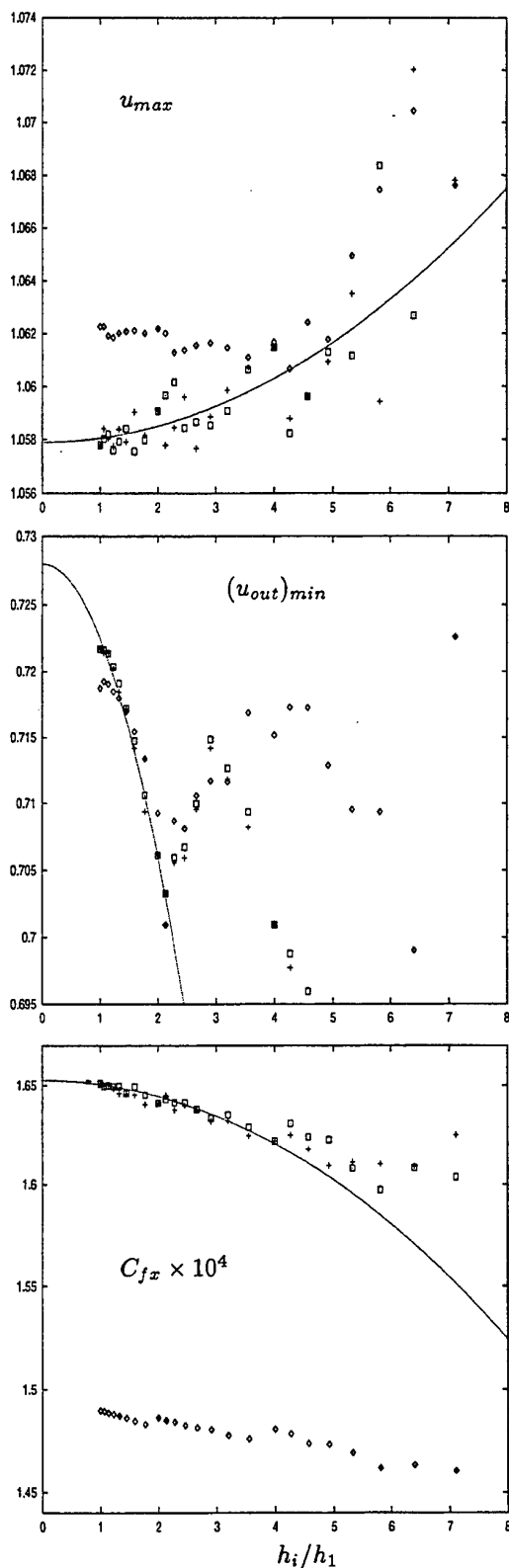


Figure 14: Results for Mystery tanker. \square : Menter, set A; $+$: Menter, set B; \diamond : Algebraic, set A

made therein.

The basic assumption of the proposed procedure is that reasonable quantitative estimates of error and uncertainty can be obtained with the data obtained on three geometrically similar grids. The results in the present paper suggest that there are many obstacles for these estimates to be conclusive and reliable. In the very simple case of a 2D laminar flow, computations on three or four grids may suffice for a good estimate. But for a 3D turbulent flow as at the stern of a ship there are apparently so many disturbing factors that solutions on more than three grids are required to give some confidence in the observed order of accuracy and to make a reliable error estimate. This is disappointing, because it means that error quantification becomes a heavy task.

We cannot exclude that particularities of our code PARNASSOS are responsible for (some of) the scatter, but unless others can show a markedly better behaviour with another code, we tend to consider our results as representative.

In [2] it is assumed that solutions are obtained on three grids with representative grid cell size ratio's $h_3/h_2 = h_2/h_1 = \sqrt{2}$. The grid convergence criterion can then be formulated as

$$R = \frac{\phi_2 - \phi_1}{\phi_3 - \phi_2} < 1.$$

As a guideline for the *approximate* magnitude of the grid refinement ratio, the value of $\sqrt{2}$ is an acceptable minimum. But the strict value $\sqrt{2}$ is practically inconvenient because the refinement ratio is hard to keep equal for all three coordinate directions. Indeed, in the example given in section 4 of [2], the refinement ratio's vary between 1.36 and 1.43 in different directions and thus the grids cannot be called geometrically similar, which is an unnecessary source of uncertainty in using Richardson extrapolation. We think that in future recommendations of the ITTC, formulas for convergence criteria and order estimates are to be generalised, as in [5].

Also the results presented here suggest that a step size ratio of at least 2 between the finest and the coarsest of a grid triplet is needed to establish the convergence trend with some confidence. But the danger of using too coarse grids in the determination of the order of accuracy is also evident. For the Mystery tanker, the solutions on the grids beyond $h_i/h_1 = 4$ seem to be outside of the asymptotic range. However, how would one know to be outside that range in a simple three-grid study?

With lots of mystifications, a correction factor C_k for error estimation is introduced in section 3.2.3 of [2]. What this factor actually implies is that errors are

#	grid	cell size	$(y_2^+)_\text{max}$	$C_{fx} \times 10^4$	$C_{px} \times 10^5$	$u_\text{min} \times 10$	vw_max	C_{pmin}	$(v_t)_\text{max} \times 10^4$
1	257×129×65	h	0.319	1.65093	6.64235	-1.6277	0.32340	-0.11211	1.3980
2	241×121×61	1.0667h	0.299	1.65010	6.59048	-1.5730	0.32249	-0.11187	1.3939
3	225×113×57	1.1429h	0.271	1.65025	6.53528	-1.5348	0.32135	-0.11194	1.3845
4	209×105×53	1.2308h	0.254	1.64838	6.54357	-1.4687	0.31974	-0.11153	1.3726
5	193×97×49	1.3333h	0.233	1.64605	6.53328	-1.4179	0.31821	-0.11154	1.3635
6	177×89×45	1.4545h	0.215	1.64590	6.50084	-1.3756	0.31704	-0.11124	1.3610
7	161×81×41	1.6000h	0.188	1.64527	6.47399	-1.3219	0.31524	-0.11042	1.3540
8	145×73×37	1.7778h	0.167	1.64042	6.53147	-1.1299	0.31220	-0.11008	1.3371
-									
9	129×65×33	2h	0.565	1.64110	6.63858	-1.0280	0.30985	-0.10995	1.3306
10	121×61×31	2.1333h	0.535	1.64493	6.59702	-0.9068	0.30955	-0.11021	1.3356
11	113×57×29	2.2857h	0.515	1.63767	6.65625	-1.0185	0.30805	-0.10993	1.3262
12	105×53×27	2.4615h	0.444	1.64008	6.60148	-0.9185	0.30730	-0.11007	1.3302
13	97×49×25	2.6667h	0.421	1.63740	6.75154	-0.8052	0.30511	-0.10993	1.3095
14	89×45×23	2.9091h	0.373	1.63187	6.99319	-0.7719	0.30072	-0.10885	1.2939
15	81×41×21	3.2000h	0.320	1.63208	6.97544	-0.7754	0.29729	-0.10817	1.3044
16	73×37×19	3.5555h	0.321	1.62451	7.42103	-0.5311	0.29145	-0.10781	1.2861
-									
17	65×33×17	4h	0.963	1.62186	7.21563	-0.4688	0.29366	-0.10635	1.2714
18	61×31×16	4.2667h	0.996	1.62480	7.16799	-0.4189	0.29509	-0.10702	1.2912
19	57×29×15	4.5714h	0.626	1.61772	6.98834	-0.4616	0.29402	-0.10373	1.2730
20	53×27×14	4.9231h	0.803	1.60947	6.75576	-0.2798	0.28865	-0.10242	1.2501
21	49×25×13	5.3333h	0.708	1.61123	6.08043	-0.2492	0.29321	-0.10370	1.2562
22	45×23×12	5.8182h	0.636	1.61029	6.13445	-0.3308	0.28497	-0.10035	1.2257
23	41×21×11	6.4000h	0.517	1.60917	5.32874	-0.1950	0.28155	-0.09637	1.2226
24	37×19×10	7.1111h	0.513	1.62496	5.58916	-0.3014	0.26606	-0.09392	1.1864

Table 11: Mystery tanker - results on various grids for Menter model

grids	h_2/h_1	h_3/h_2	order						
			C_{fx}	C_{px}	u_min	vw_max	C_{pmin}	C_{pmax}	$(v_t)_\text{max}$
1+9+17	2.000	2.000	0.97	-	-0.10	0.26	0.73	1.95	-0.19
2+10+18	2.000	2.000	1.96	6.45	-0.45	0.16	0.95	2.19	-0.39
3+11+19	2.000	2.000	0.67	1.46	0.11	0.08	1.63	1.61	-0.13
4+12+20	2.000	2.000	1.88	1.41	0.22	0.59	2.39	1.69	0.92
1+5+8	1.333	1.333	0.51	-14.25	1.10	0.52	3.26	0.69	-0.93
1+6+11	1.455	1.571	0.74	-	0.39	0.38	0.54	2.57	0.60
1+6+12	1.455	1.692	-0.43	-	0.56	0.19	-0.10	2.01	-1.17
1+7+13	1.600	1.667	0.50	-	0.90	0.27	-2.72	0.81	-0.15
1+9+14	2.000	1.455	1.07	-	-0.43	0.42	-0.12	4.12	0.01
3+6+8	1.273	1.222	1.89	-	2.82	1.35	3.18	10.85	0.92
3+7+13	1.400	1.667	0.09	-	1.09	0.21	-3.87	1.03	-0.10

Table 12: Mystery tanker - grid convergence order (Menter model)

#	grid	cell size	$(y_2^+)_{max}$	C_{fx} $\times 10^4$	C_{px} $\times 10^5$	u_{min} $\times 10$	vw_{max}	C_{pmin}	$(\nu_t)_{max}$ $\times 10^4$
1	257×129×65	h	0.319	1.65093	6.64235	-1.6277	0.32340	-0.11211	1.3980
2	241×121×61	1.0667h	0.339	1.64962	6.59980	-1.5793	0.32256	-0.11183	1.3872
3	225×113×57	1.1429h	0.351	1.64994	6.53259	-1.5365	0.32141	-0.11192	1.3872
4	209×105×53	1.2308h	0.380	1.64937	6.54782	-1.4712	0.31989	-0.11154	1.3717
5	193×97×49	1.3333h	0.406	1.64957	6.54068	-1.4127	0.31824	-0.11168	1.3734
6	177×89×45	1.4545h	0.442	1.64608	6.49322	-1.3811	0.31720	-0.11121	1.3597
7	161×81×41	1.6000h	0.465	1.64936	6.50268	-1.3221	0.31539	-0.11054	1.3621
8	145×73×37	1.7778h	0.492	1.64519	6.52071	-1.1253	0.31236	-0.11019	1.3378
-									
9	129×65×33	2h	0.565	1.64110	6.63858	-1.0280	0.30985	-0.10995	1.3306
10	121×61×31	2.1333h	0.605	1.64297	6.57862	-0.9095	0.30947	-0.11010	1.3358
11	113×57×29	2.2857h	0.663	1.64139	6.64248	-1.0012	0.30811	-0.11008	1.3276
12	105×53×27	2.4615h	0.660	1.64133	6.62235	-0.9399	0.30764	-0.11005	1.3198
13	97×49×25	2.6667h	0.729	1.63793	6.73599	-0.8154	0.30533	-0.10991	1.3124
14	89×45×23	2.9091h	0.761	1.63349	6.97854	-0.7602	0.30101	-0.10894	1.3010
15	81×41×21	3.2000h	0.785	1.63510	6.95987	-0.7737	0.29778	-0.10829	1.3031
16	73×37×19	3.5555h	0.931	1.62894	7.40082	-0.5150	0.29233	-0.10804	1.2883
-									
17	65×33×17	4h	0.963	1.62186	7.21563	-0.4688	0.29366	-0.10635	1.2714
18	61×31×16	4.2667h	1.125	1.63075	7.15384	-0.3920	0.29543	-0.10713	1.2964
19	57×29×15	4.5714h	1.164	1.62389	6.99096	-0.4609	0.29434	-0.10384	1.2757
20	53×27×14	4.9231h	1.186	1.62245	6.73095	-0.1540	0.28946	-0.10270	1.2628
21	49×25×13	5.3333h	1.203	1.60827	6.10401	-0.2961	0.29350	-0.10370	1.2586
22	45×23×12	5.8182h	1.274	1.59725	6.15033	-0.3290	0.28848	-0.10070	1.2165
23	41×21×11	6.4000h	1.240	1.60839	5.30364	-0.2454	0.28133	-0.09666	1.2271
24	37×19×10	7.1111h	1.444	1.60374	5.47222	-0.3364	0.26693	-0.09427	1.1710

Table 13: Mystery tanker - results on various grids, Menter model, grid set B

grids	h_2/h_1	h_3/h_2	order						
			C_{fx}	C_{px}	u_{min}	vw_{max}	C_{pmin}	C_{pmax}	$(\nu_t)_{max}$
1+9+17	2.000	2.000	0.97	-	-0.10	0.26	0.73	1.95	-0.19
2+10+18	2.000	2.000	0.88	-	-0.37	0.10	0.78	2.20	-0.38
3+11+19	2.000	2.000	1.03	1.67	0.01	0.05	1.76	1.69	-0.20
4+12+20	2.000	2.000	1.23	0.54	0.57	0.57	2.30	1.61	0.14
1+5+8	1.333	1.333	4.06	-5.66	1.01	0.46	4.28	0.57	1.28
1+6+11	1.455	1.571	-0.53	-	0.59	0.47	0.09	2.59	-0.88
1+6+12	1.455	1.692	-0.80	-	0.53	0.21	-0.20	2.18	-0.66
1+7+13	1.600	1.667	3.83	-	0.86	0.29	-2.06	0.91	0.49
1+9+14	2.000	1.455	0.69	-	-0.35	0.36	-0.27	4.03	-0.38
3+6+8	1.273	1.222	-5.70	-	3.11	1.46	2.50	12.61	-0.17
3+7+13	1.400	1.667	5.64	-	1.03	0.22	-2.96	1.23	0.63

Table 14: Mystery tanker - grid convergence order, Menter model, grid set B

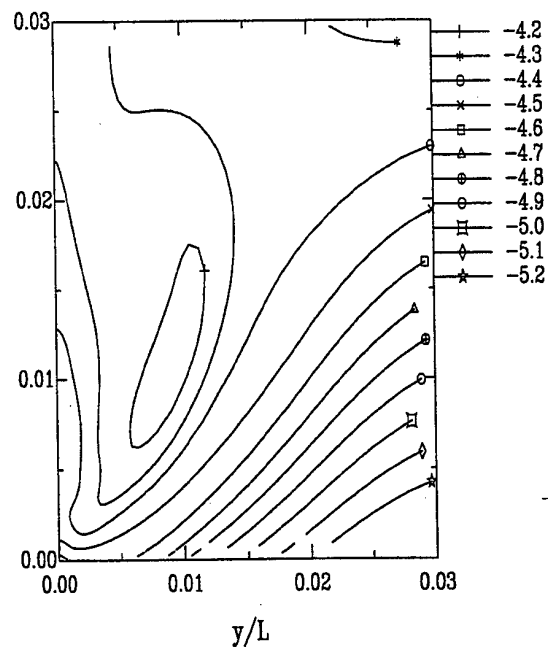
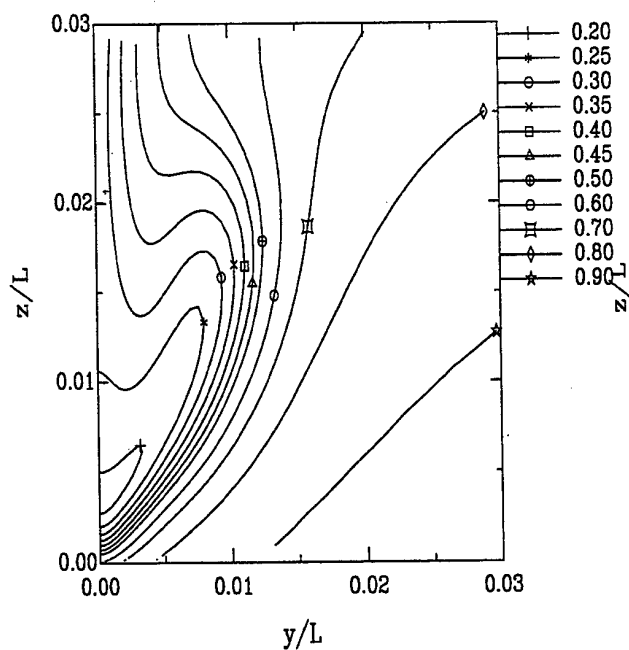
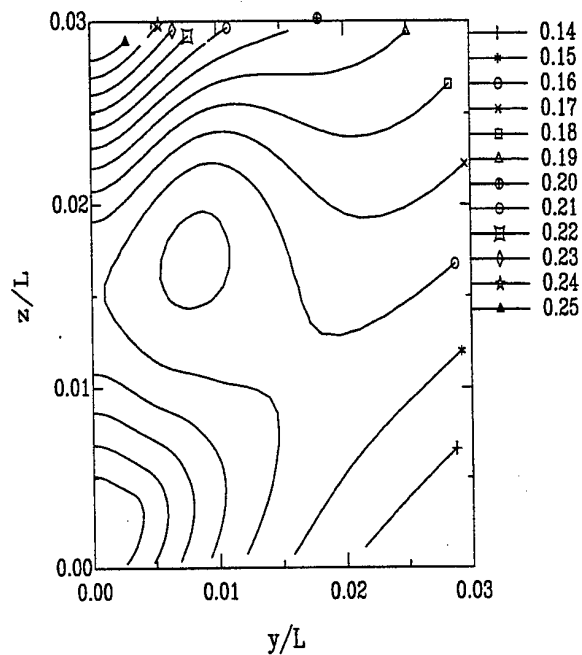
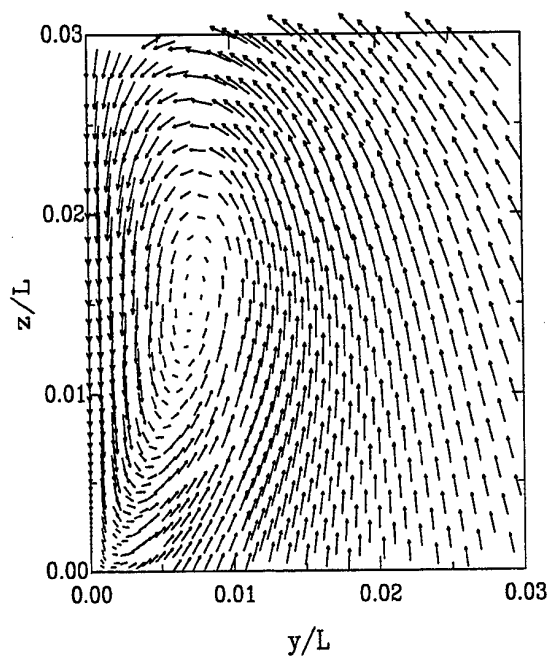


Figure 15: Mystery tanker - results at $x=0.989L$. Top: transverse velocities; Bottom: axial velocity

Figure 16: Mystery tanker - results at $x=0.989L$. Top: pressure; Bottom: eddy viscosity ($10 \log \nu_t$)

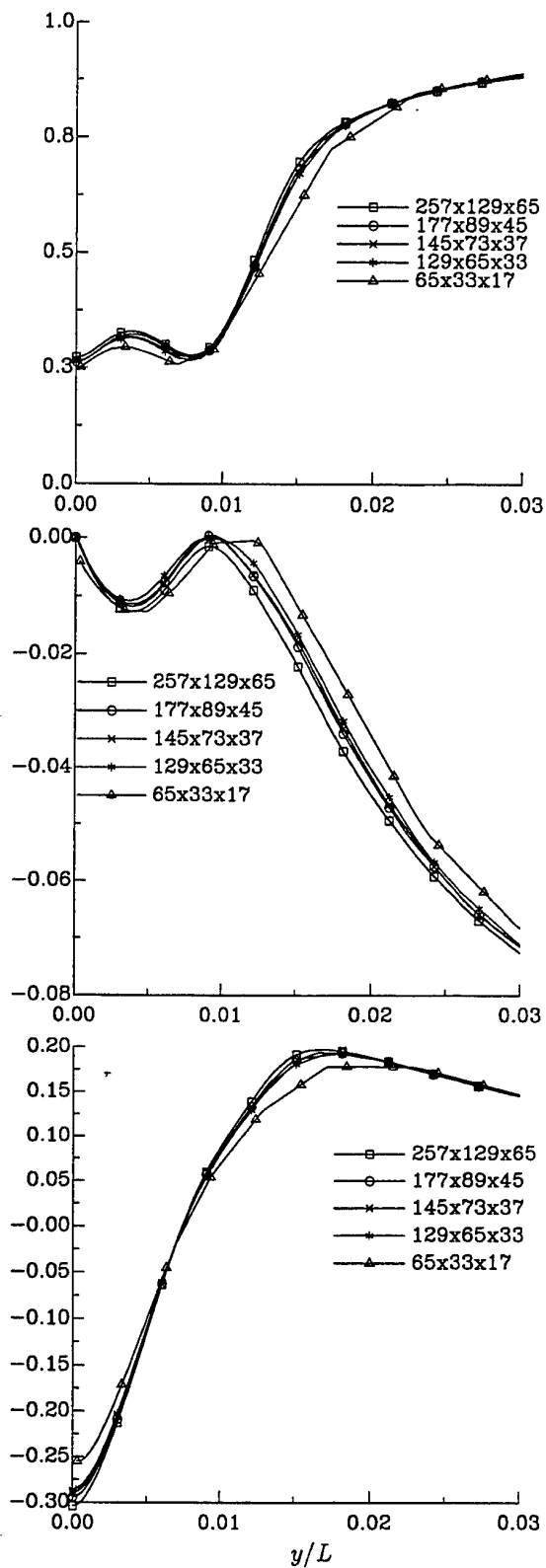


Figure 17: Mystery tanker - u/U_∞ (top), v/U_∞ (middle) and w/U_∞ (bottom) along $x = 0.989L$; $z = 0.016L$.

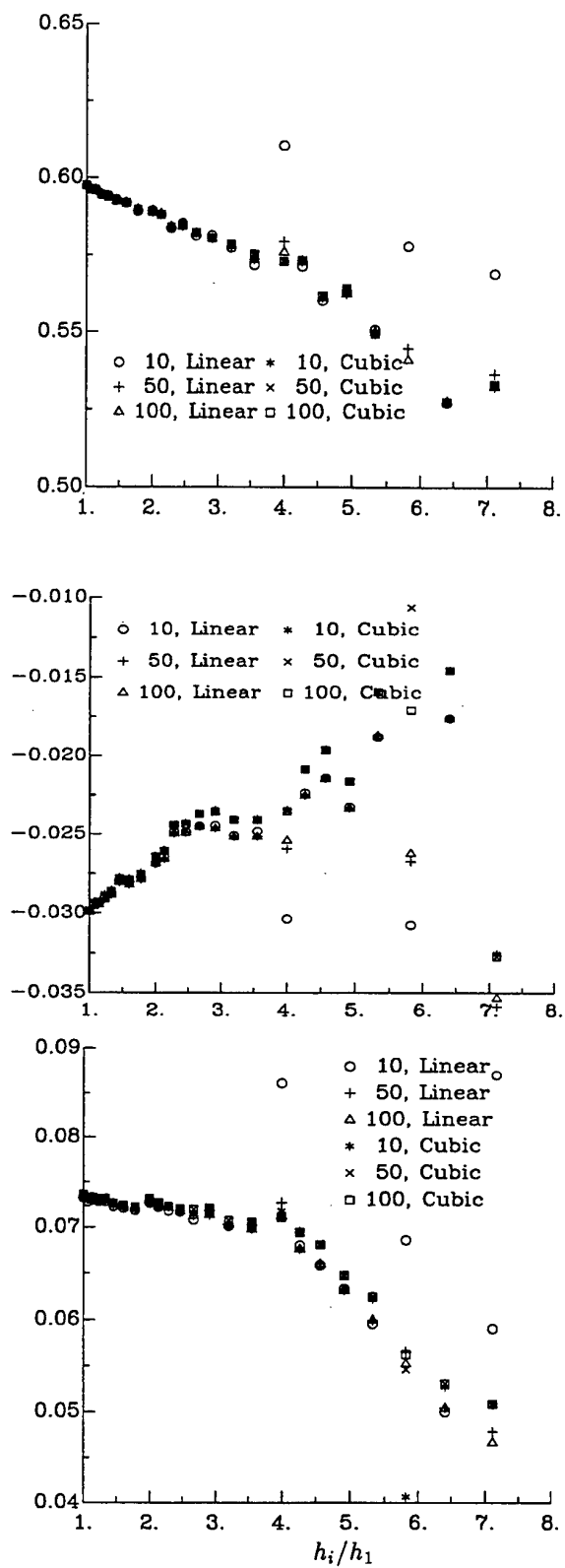


Figure 18: Mystery tanker - Line averages for u/U_∞ (top), v/U_∞ (middle) and w/U_∞ (bottom) along $x = 0.989L$; $z = 0.016L$.

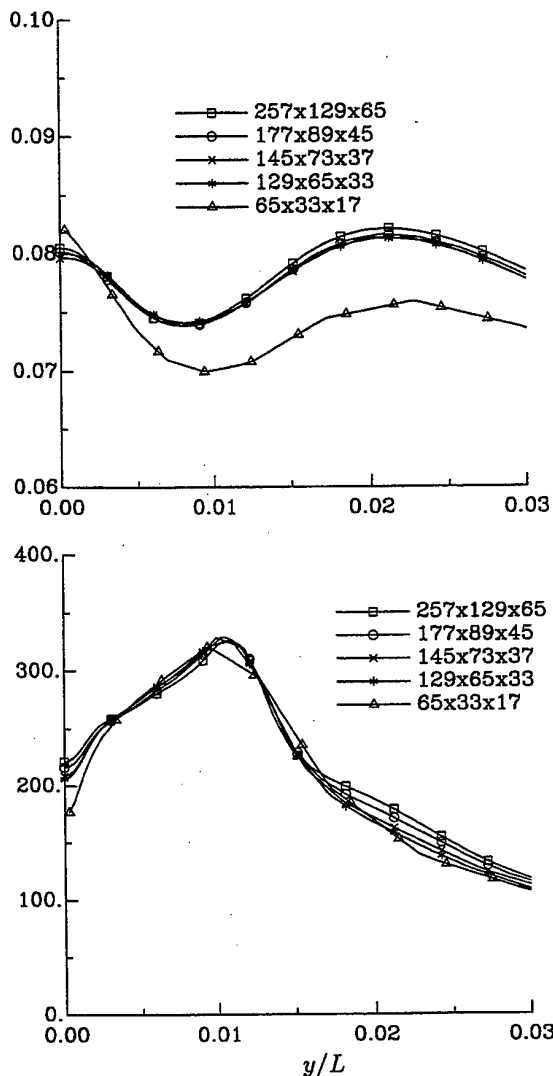


Figure 19: Mystery tanker - Variation of C_p (top) and v_t/v (bottom) along $x = 0.989L$; $z = 0.016L$.

estimated with Richardson extrapolation based on the theoretical (formal) order rather than the apparent order of accuracy. This is the way to go if solutions on only two grids are available (so that the apparent order cannot be established), but there seems to be no reasonable argument in favour of using C_k if solutions on three grids are at hand. Clearly C_k has nothing to do with the safety factor proposed in [5]. This safety factor is meant to make the error estimate deliberately conservative. The results in the present paper confirm that for some grid combinations a straightforward error estimate would be too optimistic and that Roache's factor is quite appropriate; but there are also cases for which the safety margin would yield an unduly pessimistic estimate. The use of more than three grids

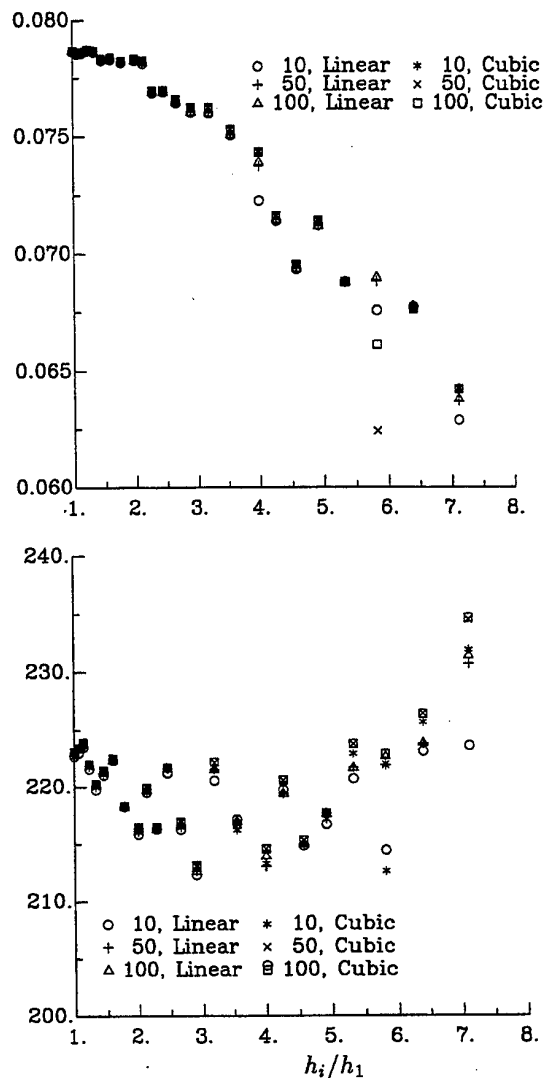


Figure 20: Mystery tanker - Line averages of C_p (top) and v_t/v (bottom) along $x = 0.989L$; $z = 0.016L$.

seems therefore unavoidable.

To verify and validate wave profile data, Stern *et al.* in [2] suggest to use the L_2 -norm of solution changes. Although this L_2 -norm is a valid measure to quantify the difference between two solutions, it is of course wrong to derive an order of accuracy from two such norms, because the norm is not a property of the solution on a single grid. The right procedure is to calculate the L_2 (or any other suitable) norm of the wave height (instead of a wave height difference) obtained on each of three grids, and then derive the convergence order from (5).

CONCLUSIONS

Supporting the idea that more attention should be given to the evaluation of the uncertainty or error bandwidth of CFD results, we have done grid convergence studies for various flows with two versions of our RANS code PARNASSOS. We summarize the conclusions of these studies as follows:

- Even in rather simple flows the grid-convergence order, derived from solutions on three grids, may not be very reliable. It can vary a lot for a single variable, or can be widely different for different variables, dependent on the particular grid triplet chosen.
- Convergence studies applied to the 3D turbulent flow around a ship seem to require more than three grids for a proper error or uncertainty estimate.
- As far as differences between solutions based on distinct turbulence models are representative for modelling errors, the latter tend to be greater than discretisation errors on grids with a density that would typically be used nowadays in the analysis of a ship design.
- The recommendations for verification and validation of CFD simulations given in [2] are useful, but with the elaborate data of this paper available, some of them appear to be immature or misleading. Further work is needed to scrutinize the suitability of current recommendations.
- In any error analysis of CFD results for ships special attention must be given to the geometrical similarity of the grids.

References

- [1] Various authors (1998) *AIAA Journal*, Vol. 36, No. 5.
- [2] Stern, F., Coleman, H.W., Wilson, R.V. & Paterson, E.G. (1999) "Verification and validation of CFD simulations". Proceedings of the 3rd ASME/JSME joint Fluids Engineering Conference, San Francisco, California.
- [3] Hoekstra, M. & Eça, L. (1998) "PARNASSOS: An efficient method for ship stern flow calculation". In proceedings of *Third Osaka Colloquium*, Osaka, Japan, pp.331-357.
- [4] Hoekstra, M. (1999) "Numerical simulation of ship stern flows with a space-marching Navier-Stokes method". *PhD thesis*, Delft University of Technology (to appear).
- [5] Roache, P.J. (1997) "Quantification of uncertainty in computational fluid dynamics". *Annual Review of Fluid Mechanics*, Vol. 29, pp. 123-160.
- [6] Schlichting, H. (1968) *Boundary Layer Theory*, 6th edition, McGraw-Hill, New York.
- [7] Veldman, A.E.P. (1976) "Boundary layer flow past a finite flat plate". *PhD thesis*, University of Groningen.
- [8] Hoekstra, M. (1986) "Coordinate generation in symmetrical interior, exterior or annular 2-D domains, using a generalised Schwarz-Christoffel transformation". In *Numerical Grid Generation in Computational Fluid Dynamics*, eds. J. Häuser and C. Taylor, Pineridge Press Ltd., Swansea, U.K., pp. 59-70.
- [9] Spalart, P.R. & Allmaras, S.R. (1994) "A one-equation turbulence model for aerodynamic flows". *Recherche Aéronautique*, Vol. 1, pp. 5-21.
- [10] Menter, F.R. (1997) "Eddy viscosity transport equations and their relation to the $k-\epsilon$ model". *J. of Fluids Eng.*, Vol. 119, pp.876-884.
- [11] Larsson, L., Patel, V.C. & Dyne, G. (editors) (1991) *Ship Viscous Flow*, Proceedings of the 1990 SSPA-CTH-IIHR Workshop, Flowtech Report No. 2, Gothenburg.
- [12] Kodama, Y. (editor) (1994) Proceedings of the CFD Workshop, Ship Research Institute, Tokyo, Japan.
- [13] Sorenson, R.L. (1986) Three-dimensional elliptic grid generation about fighter aircraft for zonal finite-difference computations. *AIAA-86-0429*, AIAA 24th Aerospace Sciences Conference, Reno, NV.
- [14] Celik, I. & Karatekin, O. (1997) "Numerical experiments on application of Richardson extrapolation with nonuniform grids", *Transactions of the ASME*, Vol. 119, pp. 584-590.

FREE-SURFACE VISCOUS FLOWS

Chairman : P.Sclavounos.

A CFD application to wave-induced floating-body dynamics

T.Kinoshita, H.Kagemoto and M.Fujino

Department of Environmental Studies

Graduate School of Frontier Sciences, The University of Tokyo

7-3-1 Hongo, Bunkyo-ku, Tokyo 113-0033, JAPAN.

Fax:81-3-3815-8360;E-Mail:kagemoto@k.u-tokyo.ac.jp

ABSTRACT

The techniques of computational fluid dynamics(CFD) are applied to the computations of wave-induced motions of floating bodies. It is demonstrated that a wide variety of problems associated with floating-body dynamics in waves can be dealt with in almost the same manner by a single computer code. Practically important problems such as the motions resonant to waves in a viscous fluid or the motions of a ship advancing in large waves are calculated.

1.INTRODUCTION

Although ship motions and associated loads on a ship hull can now be predicted fairly accurately when the waves are relatively small, a strong need has recently been emerging for numerical tools that can predict the motions and the loads in large waves. Shipyard companies exposed to keen international competition need such tools so that they can design their ships based on rational predictions of long-term extreme hull loads(e.g.[1]). Many of the current research works on the development of such numerical tools are based on a boundary-integral-equation method(BIEM) using velocity potentials and few works can be found that solve Navier-Stokes equations directly. In the present study, the techniques of computational fluid dynamics(CFD) are applied to the computation of wave-induced motions of a floating body. CFD, which solves Navier-Stokes equations(or Euler equations) directly by making use of a powerful computer machine, has been applied in many engineering fields and has succeeded in showing us the detailed insight into the various physical phenomena, which could not be known even in a well-devised experiment. In the field of ship hydrodynamics, CFD has mainly been applied to the computation of forces on a ship advancing with constant speed in a calm water. Although applications to unsteady ship hydrodynamics are appearing recently, most of them are limited to

slow motions such as manoeuvring motions in a calm water[2] and few attempts have been made in applying CFD to the computation of wave-induced, relatively high-frequency motions. The reason for this may be attributed to the fact that wave-induced floating-body dynamics are dominated mainly by inertial forces, which can be accounted for fairly well by the inviscid potential theory, whereas slow(or zero-frequency) motions of a ship are dominated mainly by viscous forces, which require the analysis of Navier-Stokes equations.

Despite of these facts, we attempt in this paper to apply CFD to wave-induced floating-body dynamics for the reasons that:

(1)Although motions in waves are usually dominated by inertial forces, there still exist quite a few practically important phenomena in which viscous forces play a dominant role. They include resonant motions in waves, slow-drift oscillations of a moored body, etc.

(2)Even in an inviscid fluid, direct numerical computations of Euler equations(inviscid version of Navier-Stokes equations) together with the equations of motion of a floating body may sometimes be easier than conventional numerical methods based on a BIEM. This is particularly true when strong nonlinear phenomena such as the motions in large waves, capsizing or slamming are involved, because large deformations of a free surface and/or large displacement of a body can be

dealt with fairly easily by CFD. Besides, a single CFD code may be able to deal with a wide variety of physical problems while a potential-theory-based computation has to contrive certain techniques in order to cope with coherent natures of each problem.

The validity of the present method and the advantages of the present method over the conventional methods described above will be demonstrated through comparisons to analytical solutions, other validated numerical results as well as experimental data.

2. FORMULATION

2.1 Governing equations of fluid motion

Two coordinate systems shown in Fig.2.1 are used in the present formulation. One is a space-fixed coordinate system (x, y, z) and the other one is a body-fixed coordinate system (X, Y, Z) . The x, y axes lay on the undisturbed free-surface and the z axis stretches vertically upward. The origin of the body-fixed coordinate system (X, Y, Z) coincide with the center of gravity(G) of the body. The X, Y axes are parallel to the undisturbed free-surface while Z axis points vertically upward when the body is at rest. The governing equations of

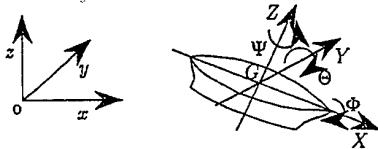


Fig.2.1: Coordinate systems

fluid motions, that is, the continuity equation and the equations of motion (Navier-Stokes equations) of fluid particles, are described in terms of the space-fixed coordinate system as follows.

The continuity equation

$$\frac{\partial u}{\partial x} + \frac{\partial v}{\partial y} + \frac{\partial w}{\partial z} = 0 \quad (1)$$

Navier-Stokes equations

$$\begin{aligned} \frac{\partial u}{\partial t} + u \frac{\partial u}{\partial x} + v \frac{\partial u}{\partial y} + w \frac{\partial u}{\partial z} \\ = -\frac{1}{\rho} \frac{\partial p}{\partial x} + \nu \left(\frac{\partial^2 u}{\partial x^2} + \frac{\partial^2 u}{\partial y^2} + \frac{\partial^2 u}{\partial z^2} \right) \end{aligned} \quad (2)$$

$$\begin{aligned} \frac{\partial v}{\partial t} + u \frac{\partial v}{\partial x} + v \frac{\partial v}{\partial y} + w \frac{\partial v}{\partial z} \\ = -\frac{1}{\rho} \frac{\partial p}{\partial y} + \nu \left(\frac{\partial^2 v}{\partial x^2} + \frac{\partial^2 v}{\partial y^2} + \frac{\partial^2 v}{\partial z^2} \right) \end{aligned} \quad (3)$$

$$\begin{aligned} \frac{\partial w}{\partial t} + u \frac{\partial w}{\partial x} + v \frac{\partial w}{\partial y} + w \frac{\partial w}{\partial z} \\ = -g - \frac{1}{\rho} \frac{\partial p}{\partial z} + \nu \left(\frac{\partial^2 w}{\partial x^2} + \frac{\partial^2 w}{\partial y^2} + \frac{\partial^2 w}{\partial z^2} \right) \end{aligned} \quad (4)$$

where u, v, w represent the x, y, z components of the fluid velocity and p, g, ν represent the fluid pressure, the gravitational acceleration and the kinematic viscosity of the fluid respectively. The dynamic boundary condition, or the equilibrium of forces, on the free-surface is written as follows.

$$p = p_0 \quad (5)$$

where p_0 denotes the air pressure, which is assumed to be of constant value. The tangential stress on the free-surface that may be caused by such things as wind is not accounted for and the surface tension is also not taken into account, because they are irrelevant to the subject of the present study. The kinematic boundary condition on the free-surface that is used in the present study is written as follows.

$$\frac{\partial \zeta}{\partial t} = w - u \frac{\partial \zeta}{\partial x} - v \frac{\partial \zeta}{\partial y} \quad (6)$$

Here ζ represents the vertical displacement of the free-surface. As for the boundary condition on a body-surface, the fluid velocity relative to the body in the direction normal to the surface should be zero because no water can penetrate the body surface, whereas, in tangential direction, the no-slip condition is imposed when viscous effects are taken into account and the free-slip condition is imposed when viscous effects are neglected. The free-surface conditions as well as the body boundary condition are imposed on the instantaneous position of the corresponding surface. The dynamic condition on the body surface is given by the equations of motion of the body that will be described below.

2.2 Governing equations of body motion

For the description of body motions, the body-fixed coordinate system (X, Y, Z) is more convenient. The equations of motion of a floating body in terms of the body-fixed coordinate system are given as follows.

$$m (\dot{U}_G + QW_G - RV_G) = \iint_S (-pn_X + \tau_X) dS \quad (7)$$

$$m (\dot{V}_G + RU_G - PW_G) = \iint_S (-pn_Y + \tau_Y) dS \quad (8)$$

$$m (\dot{W}_G + PV_G - QU_G) = \iint_S (-pn_Z + \tau_Z) dS \quad (9)$$

$$\begin{aligned}
& I_{XX}\dot{P} - I_{XY}\dot{Q} - I_{XZ}\dot{R} + (I_{ZZ} - I_{YY})QR \\
& - I_{XZ}PQ + I_{YX}RP - I_{YZ}Q^2 + I_{YZ}R^2 \\
& = \iint_S \{p(-r_Z n_Y + r_Y n_Z) + r_Z \tau_Y - r_Y \tau_Z\} dS
\end{aligned} \quad (10)$$

$$\begin{aligned}
& - I_{YX}\dot{P} + I_{YY}\dot{Q} - I_{YZ}\dot{R} + (I_{XX} - I_{ZZ})RP \\
& + I_{YZ}PQ - I_{XY}QR + I_{ZX}P^2 - I_{XZ}R^2 \\
& = \iint_S \{p(-r_X n_Z + r_Z n_X) + r_X \tau_Z - r_Z \tau_X\} dS
\end{aligned} \quad (11)$$

$$\begin{aligned}
& - I_{ZX}\dot{P} - I_{ZY}\dot{Q} + I_{ZZ}\dot{R} + (I_{YY} - I_{XX})PQ \\
& + I_{XZ}QR - I_{YZ}RP - I_{YX}P^2 + I_{XY}Q^2 \\
& = \iint_S \{p(-r_Y n_X + r_X n_Y) + r_Y \tau_X - r_X \tau_Y\} dS
\end{aligned} \quad (12)$$

In the above equations, the 'dot' indicates differentiation with respect to time. m represents the mass of the body and $I_{XX}, I_{YY}, I_{ZZ}, I_{XY}, I_{YZ}, I_{ZX}$ denote the mass moment of inertia of the body about the axes indicated by the subscripts. U_G, V_G, W_G represent the X, Y, Z components of the velocity of G , the center of gravity. P, Q, R represent the angular velocities around the X, Y, Z axes while Φ, Θ, Ψ represent the angular displacements around the X, Y, Z axes. τ_X, τ_Y, τ_Z represent the X, Y, Z components of the tangential stress along the body surface. n_X, n_Y, n_Z are the X, Y, Z components of a unit normal vector on the corresponding body surface and r_X, r_Y, r_Z represent the X, Y, Z components of the vector from G to the corresponding point on the body surface (see Fig.2.2).

If we denote the (x, y, z) coordinates of G as

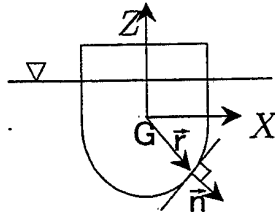


Fig.2.2: Definitions

(x_g, y_g, z_g) , then the time derivatives of the coordinates x_g, y_g, z_g are written as follows.

$$\begin{aligned}
\frac{dx_g}{dt} &= U_G \cos \theta \cos \psi \\
&+ V_G (\sin \phi \sin \theta \cos \psi - \cos \theta \sin \psi) \\
&+ W_G (\cos \phi \sin \theta \cos \psi + \sin \phi \sin \psi)
\end{aligned} \quad (13)$$

$$\frac{dy_g}{dt} = U_G \cos \theta \sin \psi$$

$$\begin{aligned}
& + V_G (\sin \phi \sin \theta \sin \psi - \cos \theta \cos \psi) \\
& + W_G (\cos \phi \sin \theta \sin \psi + \sin \phi \cos \psi)
\end{aligned} \quad (14)$$

$$\begin{aligned}
\frac{dz_g}{dt} &= -U_G \sin \theta \\
&+ V_G \sin \phi \cos \theta + W_G \cos \phi \cos \theta
\end{aligned} \quad (15)$$

where ϕ, ψ, θ are the Eulerian angles that identify the attitudes of the body with respect to the space-fixed coordinate system as shown in Fig.2.3. The

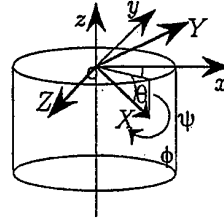


Fig.2.3: The definition of Eulerian angles

time derivatives of those angles are expressed as follows.

$$\frac{d\phi}{dt} = P + Q \sin \phi \tan \theta + R \cos \phi \tan \theta \quad (16)$$

$$\frac{d\theta}{dt} = Q \cos \phi - R \sin \phi \quad (17)$$

$$\frac{d\psi}{dt} = Q \sin \phi / \cos \theta + R \cos \phi / \cos \theta \quad (18)$$

By integrating the equations (13)~(18), the locations and the attitudes of the body with respect to the space-fixed coordinate system can be updated at each time step.

3. GRID SYSTEM

Since the present method solves Navier-Stokes equations (or Euler equations) directly, the fluid volume should be discretized into grids. In the present calculations, a hybrid hexahedral grid system is used in which a body-fixed boundary-fitted grid system is used in the neighborhood of the body whereas a space-fixed grid system is used away from the body as shown in Fig.3.1. The two grid systems are overlapped partially at the

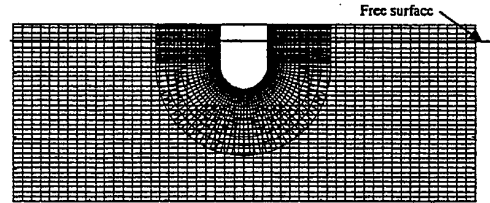


Fig.3.1: The hybrid grid system

perimeter of each grid system as shown in Fig.3.1. Although the body-fixed grids are fitted to the body surface, they are not fitted to the free-surface, because it is quite time-consuming if they are adjusted at each time to the deformation of the free-surface. Instead, the volume area above the free-surface is also discretized into grids as schematically shown in Fig.3.1 and the free-surface is displaced such that the mass continuity is satisfied in the grids located along the free-surface. If the whole computational area is discretized into a body-fixed grid system, the grids located away from the body may be forced to move excessively even by a tiny rotational motion of the body. On the other hand, if the whole region is discretized into a space-fixed grid system, which was actually adapted at the beginning of our study, the computations are sometimes destabilized probably because the body surface crosses the neighboring grids back and forth with relatively high frequencies as the body moves in waves. For these reasons, the hybrid grid system used in the present study seems to be an adequate strategy for the computations of wave-induced motions.

4.COMPUTATION PROCEDURE

4.1 Numerical tank

Our numerical tank consists of a fluid domain bounded by a free-surface, a bottom surface and four vertical boundaries installed at the four sides of the fluid domain as shown in Fig.4.1. The ver-

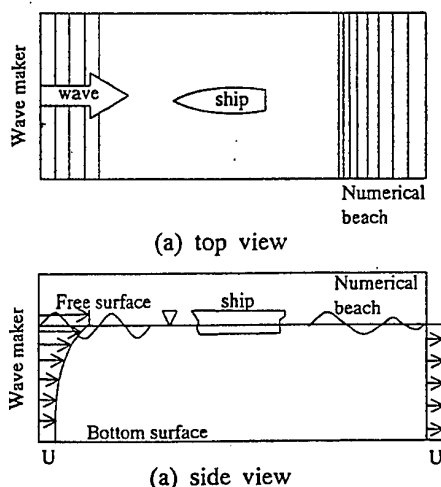


Fig.4.1: Schematic view of the numerical tank

tical boundaries can be physical ones if the fluid is really bounded but otherwise they are imaginary ones that are introduced in order to reduce the computational domain. At one(if head/following

waves are to be generated) or two(if oblique waves are to be generated) boundaries of the four vertical boundaries, certain normal velocities are imposed for the wave generation as will be elaborated later. Numerical beaches are incorporated near the other imaginary boundaries so that no waves are reflected at the corresponding boundaries. Waves propagating toward the wave-making boundaries are also dissipated in order to keep them from reflecting at the wave-making boundaries.

4.2 Wave generation

Waves are generated by imposing the following boundary condition over one or two sides of the numerical tank.

$$v_{wn}(x, y, t) = v_{bn}(x, y, t) \quad (19)$$

where v_{wn} represents the water velocity normal to the corresponding boundary and v_{bn} is a certain given velocity. For the generation of regular waves of period $2\pi/\omega$, amplitude ζ_a , for example, the following distribution of normal velocities are imposed over the corresponding boundary.

$$v_{bn} = \zeta_a \omega \frac{\cosh kz}{\sinh kh} \sin \omega t \quad (z \leq 0)$$

$$v_{bn} = \zeta_a \omega \frac{1}{\sinh kh} \sin \omega t \quad (z > 0) \quad (20)$$

The upper one of eqn.(20) corresponds to the velocity distribution given by the linear water-wave theory based on an assumption of infinitesimal amplitude ζ_a . As will be shown later, this practice really reproduces waves of specified amplitude ζ_a when ζ_a is small. However, as ζ_a in eqn.(20) becomes large, the real amplitude of the waves produced due to the velocity distribution of eqn.(20) deviates from ζ_a because of the nonlinear effects involved in the free-surface condition. For nonlinear waves, even the definition of 'amplitude' is ambiguous because the wave profile is not pure sinusoidal anymore. Therefore, for the generation of nonlinear large waves, the wave generation may be repeated while varying ζ_a of eqn.(20) systematically until waves of specified crest-trough height are reproduced. For the two-side generation of oblique waves, the following velocity distributions are given over the respective side of the numerical tank.

At side-1($x=\text{constant}$)

$$v_{bn1} = \zeta_a \omega \cos \chi \frac{\cosh kz}{\sinh kh} \sin(\omega t - ky \sin \chi) \quad (z \leq 0)$$

$$v_{bn1} = \zeta_a \omega \cos \chi \frac{1}{\sinh kh} \sin(\omega t - ky \sin \chi) \quad (z > 0) \quad (21)$$

At side-2($y=\text{constant}$)

$$v_{bn2} = \zeta_a \omega \sin \chi \frac{\cosh kz}{\sinh kh} \sin(\omega t - kx \cos \chi) \quad (z \leq 0)$$

$$v_{bn2} = \zeta_a \omega \sin \chi \frac{1}{\sinh kh} \sin(\omega t - kx \cos \chi) \quad (z > 0) \quad (22)$$

where χ represents the wave direction defined counter-clockwise from the x axis.

The generation of irregular waves is also possible if the velocity distribution over the wave-maker(s) is specified. It is, however, difficult at present to reproduce waves of specified time history.

4.3 Wave absorption

If the vertical boundaries are not physical ones but imaginary ones, waves should not be reflected there. Although there exist numerous techniques that prevent waves from reflecting at such boundaries (e.g. [3][4][5]), they may be categorized into two. One is a so-called no-reflection boundary on which a certain no-reflection boundary condition is imposed so that waves go through the boundary without feeling any resistance. The other one is a numerical beach where the energy of outgoing waves is dissipated numerically. Among these two methods, the latter one may be preferable for the present purpose, because it is quite difficult to achieve complete no-reflection with the no-reflection boundaries and therefore a tiny residual reflection may eventually force the computation break down as the reflected waves are accumulated. Supposing that we use a numerical beach, two kinds of waves exist that should be dissipated. One is the waves propagating toward the wave-maker boundary and the other one is the waves propagating toward the other boundaries. For the absorption of the latter waves, the grid size is enlarged gradually toward the corresponding boundary and an upwind finite-difference scheme is used for the evaluation of the convection terms of Navier-Stokes equations (or Euler equations). Since an upwind finite-difference scheme entails numerical viscosity, which is amplified in proportion to the corresponding grid size, waves are damped gradually on the numerical beach as they propagate toward the corresponding boundary. As for the absorption of waves propagating toward the wave-maker boundary, since there co-exist waves propagating from the wave-maker, a special treatment is needed so that only the waves propagating toward the wave-maker are dissipated. For that purpose, the following velocity is used at the damping zone in the vicinity of the wave-

maker (see Fig.4.2).

$$u = u^* - \frac{1}{i}(u^* - u') \quad (23)$$

where u^* represents the velocity that is obtained when no dissipation mechanism is introduced for the waves propagating toward the wave-maker, whereas u' represents the velocity that is obtained when no floating bodies exist and thus no waves propagating toward the wave-maker exist. With the use of eqn.(23), the velocity u is equal to u^* away from a wave-maker whereas it reaches u' at the place of the wave-maker.

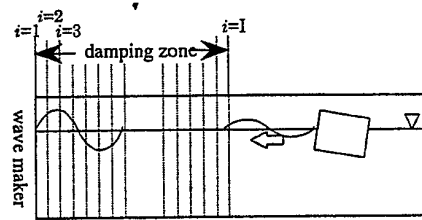


Fig.4.2: Dissipation of waves propagating toward a wave-maker

4.4 Treatment of an advancing body

For the computation of a ship advancing in waves with velocity U , the most naive way may be to let the ship advance with the velocity U in the corresponding numerical tank. This requires, however, a large computational domain because the domain should be large enough to let the ship advance at least until the initial disturbance is subdued. An alternative way may be to let the whole computational domain advance with the velocity U . If the velocity U is of a constant value, there is no need to modify the governing equations. On the other hand, if the velocity is time dependent, additional terms should be added to the equations of flow motion (Navier-Stokes equations) in order to account for the acceleration. For example, when a ship is advancing in x direction with velocity $U(t)$, a body force proportional to the acceleration $\dot{U}(t)$ should be added to the righthand-side of the equation as follows.

$$\frac{\partial u}{\partial t} + u \frac{\partial u}{\partial x} + v \frac{\partial u}{\partial y} + w \frac{\partial u}{\partial z} = -\frac{1}{\rho} \frac{\partial p}{\partial x} + \nu \left(\frac{\partial^2 u}{\partial x^2} + \frac{\partial^2 u}{\partial y^2} + \frac{\partial^2 u}{\partial z^2} \right) + \dot{U} \quad (24)$$

Even in the computation of a ship advancing with constant velocity U , it is efficient to let the entire

flow field be accelerated from zero to U gradually, because if a finite velocity U is imposed impulsively at $t = 0$, free-surface oscillations, the wavelength of which is equal to two times the tank length, are induced by the initial disturbance, which last quite a long duration until finally they disappear.

4.5 The calculation flow

After discretizing the fluid domain into grids as described in Section 3, velocity components u, v, w and a pressure p are defined in each grid. In each grid, the pressure is evaluated at the volume center of the grid while velocities are evaluated at the midpoint of each of the six sides of the grid. The derivatives in the governing equations of the flow motions are evaluated by a finite-difference scheme. The time derivatives are evaluated by the first-order Eulerian scheme. As for the spatial derivatives, the upwind-difference scheme is used for the convection terms while the second-order central-difference scheme is used for the other terms. It is a common practice to use the upwind-difference scheme for the convection terms for the sake of the stability of numerical calculations. In the present computations, third-order upwind-difference scheme is used except in the computations of a 3-D ship advancing in wave, in which the first-order upwind-difference scheme is used in order to enhance the stability of the computation because the third-order scheme did not work in that particular case. The location and the attitude of the body are increased by an amount of the finite difference from the previous time step. The calculation flow is tabulated in Table 4.1. Since a pressure p is obtained after determining velocities u, v, w in the present method, the following equation (Euler equation) is imposed as the body-boundary condition for p .

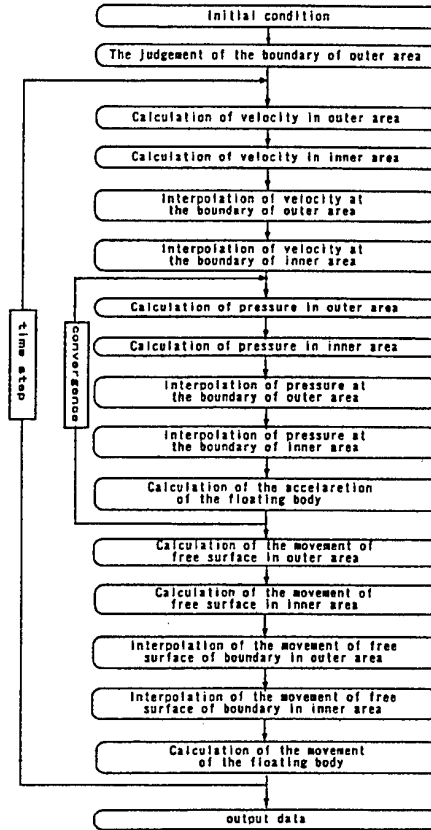
$$\frac{Dv_n}{Dt} = -\frac{1}{\rho} \frac{\partial p}{\partial n} \quad (25)$$

where v_n represents the normal velocity of the fluid on the body-surface.

5. RESULTS AND DISCUSSION

In this section, results obtained by the method described so far will be shown and its validity is discussed. After confirming the validity, it will be applied to the computations of some nonlinear problems of practical importance. Most of the computations that will be shown hereafter are based on an Euler-equation-based CFD and thus viscous forces are neglected unless otherwise specified. A Navier-Stokes-equation-based CFD

Table 4.1: The calculation flow



is performed for a calculation of wave-induced motions of a 2-D body.

5.1 Some basic computations

Some basic computations such as wave generation, wave absorption, etc. are carried out in order to examine the basic performances of the present numerical tank.

5.1.1 Wave generation

Regular waves were produced without the existence of a floating body.

(a) Waves of small amplitude

Regular waves of radian frequency ω and of very small amplitude ζ_a were generated and the results were compared to those given by the linear water-wave theory. As already described in 4.2, the following normal velocities were imposed over the wave-maker boundary.

$$v_{bn} = \zeta_a \omega \frac{\cosh kz}{\sinh kh} \sin \omega t \quad (z \leq 0)$$

$$v_{bn} = \zeta_a \omega \frac{1}{\sinh kh} \sin \omega t \quad (z > 0) \quad (26)$$

This distribution corresponds to the liner water

wave of amplitude ζ_a and wave-number k . The specific values of ζ_a, ω used in the computation were $\zeta_a = 1.00$ mm, $\omega = 6.28$ sec⁻¹. Since, with these values, the wave slope $k\zeta_a$ is as small as 0.0040, the linear water wave of amplitude ζ_a may be considered as a right answer which the present calculation should coincide with. Fig.5.1(a),(b) compare the vertical distribution of the horizontal velocity amplitude and that of the vertical velocity amplitude at about 6m away from the wave-maker obtained by the present calculation with the corresponding values given by the linear water-wave theory. The agreements are almost complete. The instantaneous displacement of the free surface obtained 10 seconds after the wave generation was commenced is shown in Fig.5.2. The amplitude and the wave-length identified from the figure are 1.00mm, 1.57m respectively, which coincide with the corresponding values of the linear water-wave theory.

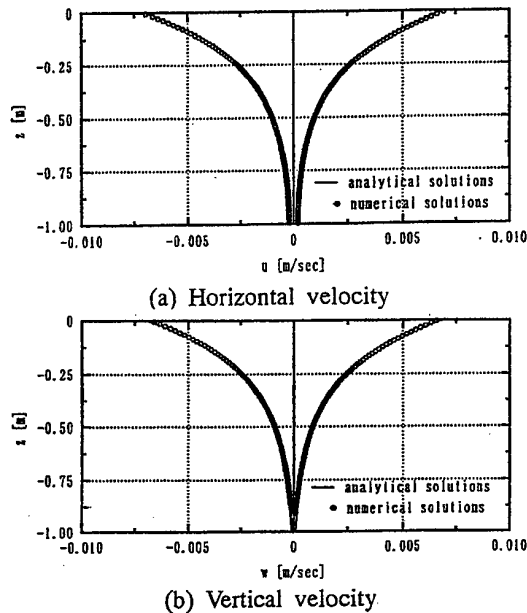


Fig.5.1: The vertical distributions of the velocity components

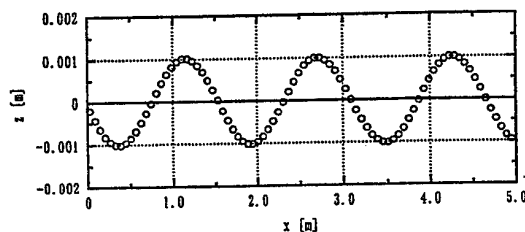


Fig.5.2: The instantaneous displacement of the free surface

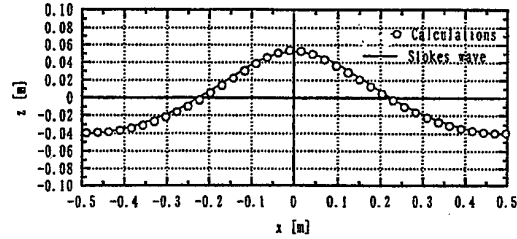


Fig.5.3: The comparison of the wave profile generated in the numerical tank with the 3rd-order Stokes waves

(b) Waves of large amplitude

Fig.5.3 shows an example wave profile of large amplitude generated in the present numerical tank while substituting a certain large value in ζ_a of eqn.(26). As can be observed, the wave profile is unsymmetric about $z = 0$, its crest is larger by quite an amount than its trough, which is a typical feature of large nonlinear waves. For comparison, the nonlinear 3rd-order Stokes wave given by the following equation is shown in the same figure.

$$\eta = \zeta \cos(\omega t - kx) + \frac{\zeta^2 k}{2} \frac{\cosh kd}{2 \sinh^3 kd} (2 + \cosh 2kd) \cos \{2(\omega t - kx)\} + \frac{\zeta^3 k^2}{4} \frac{3}{16} \frac{8 \cosh^6 2kd + 1}{\sinh^6 kd} \cos \{3(\omega t - kx)\} \quad (27)$$

As for k in eqn.(27), the corresponding value of the linear water waves was used and the value of ζ were determined so that the crest and the trough are well fitted to the present calculation.

(c) Oblique waves

As described, if oblique waves are needed to be generated in the entire free-surface in the numerical tank, two sides of the tank must be used as wave-makers. The main concern about the generation of oblique waves is that if the crest-lines of the waves generated by each of the two wave-makers are continually connected with each other. The iso-height contours of example oblique waves generated in our tank are shown in Fig.5.4, in which little distortion is observed in their crest-lines.

5.1.2 Wave absorption

In order to examine if the wave absorption scheme employed in the present numerical tank works as anticipated, two example calculations were conducted. In the first example, waves were generated in the numerical tank shown in Fig.5.5. The

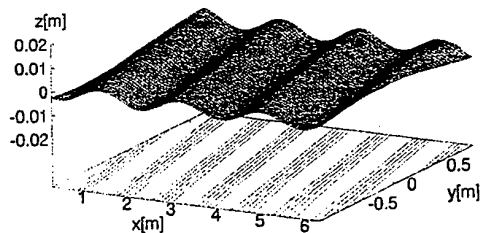


Fig.5.4: The generated oblique waves in the numerical tank

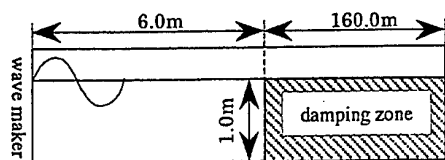


Fig.5.5: A numerical tank with a numerical beach at the opposite side from a wave-maker

waves are regular ones and their period was fixed to be 1.00 second. Fig.5.6 shows the instantaneous wave profile obtained 200 seconds after the wave generation was initiated at $t=0$. The horizontal axis indicates the distance from the wave-maker. A wave train of at least graphically identical amplitude is generated and no distortions are observed in the waves, which suggests that no reflection is occurring at the opposite side of the numerical tank from the wave-maker. In fact, the amplitude of the free-surface displacement 4.00m away from the wave-maker at $t=200\text{sec}$. differed only by as small as less than 1% from the corresponding value obtained at $t=20\text{sec}$. In the second example, waves were generated in the numerical tank shown in Fig.5.7, in which a numerical beach is incorporated in the vicinity of the wave-maker so that the waves propagating toward the wave-maker are

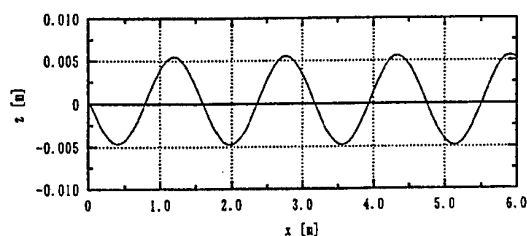


Fig.5.6: The instantaneous free surface displacement at $t=200\text{sec}$

damped, whereas the other side of the tank, where no numerical beaches exist, is assumed to be a rigid wall of complete reflection. If no numerical beaches existed in the entire numerical tank, standing waves of ever increasing amplitude should be induced as the wave generation is continued, because the wave energy is trapped in the numerical tank without any dissipation. Fig.5.8 compares

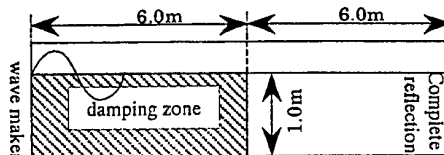


Fig.5.7: A numerical tank with a numerical beach in the vicinity of a wave-maker

the time history of the free-surface displacement in the vicinity of the wave-maker (0.09m from the wave-maker) obtained in the duration between $t=90\text{sec}$ and $t=100\text{sec}$ with the wave train produced in another numerical tank which is long enough so that no reflected waves come back to the corresponding point at the time between $t=90\text{sec}$ and $t=100\text{sec}$. The amplitude remains of almost the

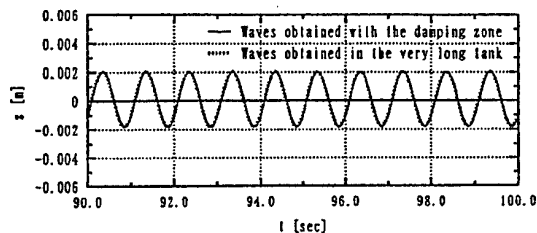


Fig.5.8: The time history of the free surface displacement near the wave-maker

same value during that time period and it differs only by less than 1% from the amplitude of the wave train produced in the very long tank. These results indicate that the numerical beaches used in the present numerical tank work as well as expected.

5.1.3 Continuity of various physical quantities between the two grid systems

Since two grid systems are used and they are partially overlapped with each other, where such physical quantities as the velocity or the pressure are evaluated separately in the two grid systems, care must be taken so that such physical quantities are continuous over the two grid systems. Fig.5.9

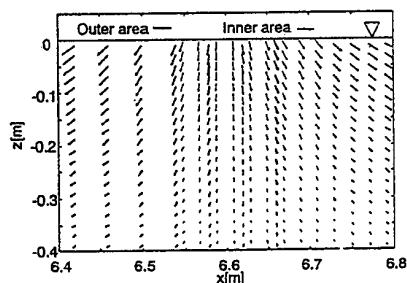


Fig.5.9: The continuity of the velocity vectors between the two grid systems (without a body)

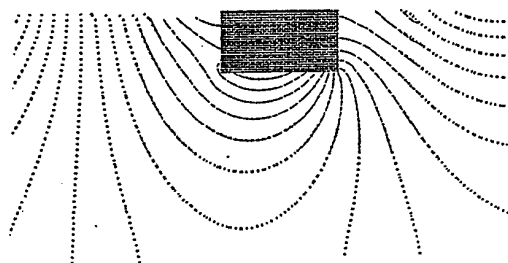


Fig.5.10: The continuity of the pressure contours between the two grid systems

shows the velocity vectors in waves without a body. It is observed that the velocity vectors evaluated separately in the two grid systems at the overlapped region are smoothly connected between the two grid systems. Fig.5.10 shows the pressure iso-contours around a 2-D box-shaped barge at a certain instant. Again no discontinuity is observed between the two grid systems and therefore it can be concluded that the two-grid system is working well.

5.1.4 Computation of the acceleration of body motions

Although the acceleration of a floating body may be obtained by a backward finite difference from the body velocity obtained at the previous time step, it is desirable from the viewpoints of numerical accuracy and numerical stability that the acceleration itself is calculated at each time step as already indicated in many places (e.g. [6]). In order to examine this fact, an example calculation was carried out in which a 2-D body shown in

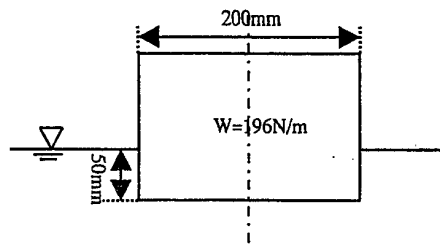


Fig.5.11: A 2-D body used for the free-oscillation calculation

Fig.5.11 was displaced vertically upward from its equilibrium position by a small amount and released at $t = 0$ with zero velocity. Two kinds of computations are compared in this example. In one computation, the acceleration of the body was calculated by a backward finite difference of the body velocities. In the other one, the acceleration itself was calculated at each time step together with the velocities and the pressures. Fig.5.12(a),(b),(c) compare the time histories of the displacement, the velocity and the acceleration of the body obtained by the two methods. It is quite characteristic that the displacement and the velocity are almost identical in the two methods, whereas unrealistic oscillations of high frequency are observed in the acceleration at the initial stage of the calculation when the backward difference scheme is used. Although at $t = 0$, when the body is released with zero velocity, the body should have a certain acceleration, if backward difference scheme is used, since the velocity is zero at $t = 0$ and no previous time step exists, the evaluation of the acceleration by a backward finite-difference scheme can not be carried out accurately. This may be the main cause of the unrealistic oscillations observed in the acceleration.

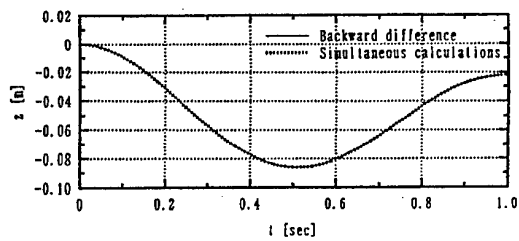
5.2 Comparisons with other results

Since it has been confirmed that the basic performances of the present numerical tank are good enough for practical computations associated with wave-induced motions, computations were conducted for several problems for which reliable results that can be compared with the present calculations exist.

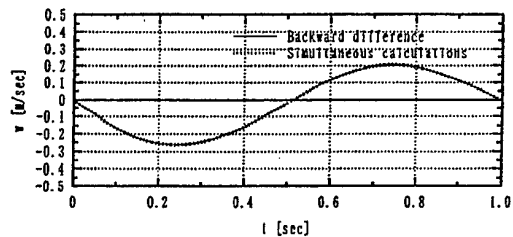
5.2.1 2-D problems

(1) Motions in regular waves of small amplitude

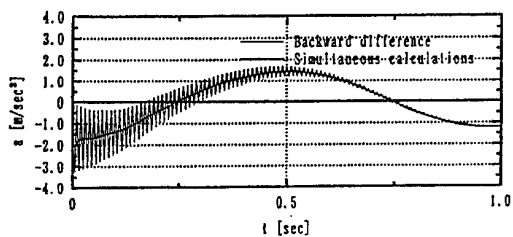
When the amplitude of incident waves is small compared to their wavelength, the solutions given by the linear potential theory may be considered as the right answers which the present calculation



(a) displacement



(b) velocity



(c) acceleration

Fig.5.12: The comparisons of the two schemes for the calculation of the body displacement, velocity and acceleration

should coincide with. Therefore, motions of a 2-D body in regular waves of small amplitude were chosen as the first example and the results were compared with the ones obtained by a singularity distribution method which is based on the linear potential theory. Experiments were also carried out for the comparison. The set-up of the experiments is shown in Fig.5.13. Two bodies of different geometries were used for both the experiments and the calculations. One has a semi-circular cross section and the other one has a triangular cross section as shown in Fig.5.14(a),(b). Fig.5.15(a),(b),(c) and Fig.5.16(a),(b),(c) show the RAOs(response amplitude operators) of the semi-circular body and those of the triangular body respectively. In the present calculations, the obtained time history was decomposed into Fourier components and the component which has the same frequency as that of the incident waves was chosen for the comparison. Since the present calculations were conducted using Euler equations as the governing equations of water-particle motions and thus the viscous ef-

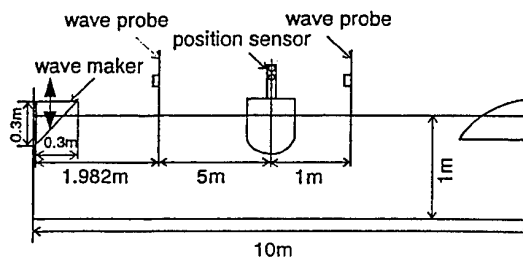
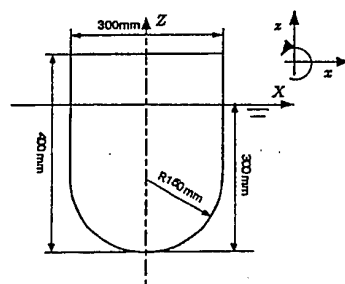
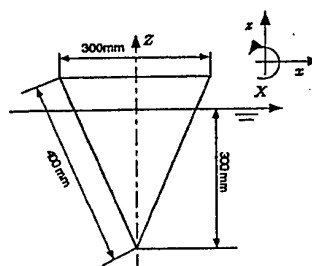


Fig.5.13: The set-up of the experiment



(a) semi-circular body



(b) triangular body

Fig.5.14: The bodies used for both the experiments and the calculations

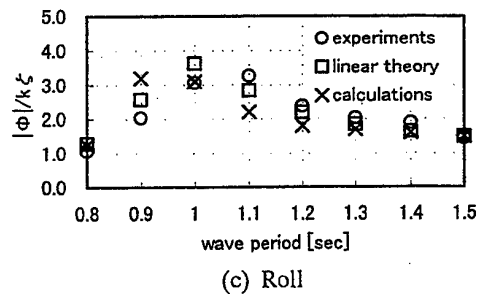
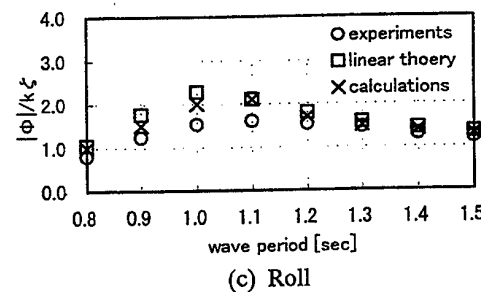
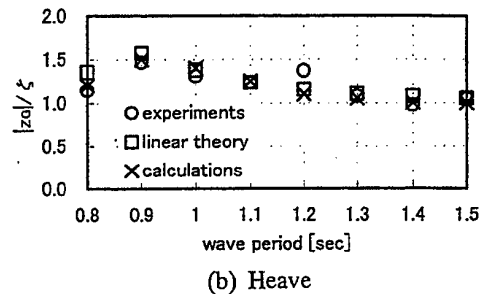
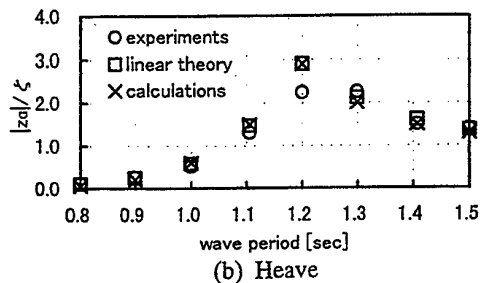
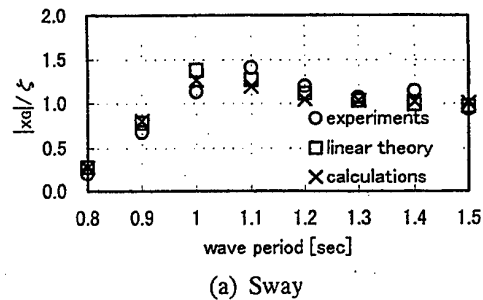
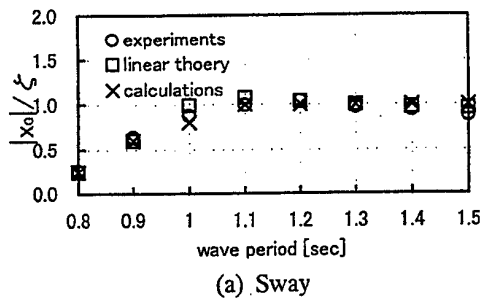


Fig.5.15: The RAOs of the semi-circular body

Fig.5.16: The RAOs of the triangular body

fects are not accounted for, it is reasonable if they coincide with the results obtained by the linear potential theory. They, in fact, agree quite well with the linear theory except in the rotational motion of the triangular body(Fig.5.16(c)). The slight difference that is also observed in the rotational motion of the semi-circular body may be attributed to the numerical damping that is inevitable in the calculations based on a finite-difference scheme. As for the comparison with the experimental results, both the linear theory and the present calculations agree fairly well with the experiments except at around the natural periods of the motions. This is probably because damping forces caused by viscous effects, which are known to play a dominant role in motions resonant to external excitations, are not accounted for in the calculations. In order to confirm the effect of viscosity, computations based on Navier-Stokes equations were

also performed for the semi-circular body. Since grids should be fine enough to reproduce characteristic features of viscous flows such as boundary layers, much finer grids were used, especially near the body surface as shown in Fig.5.17, although a turbulence model was used as will be described below. The Reynolds number of this computation is estimated to be $10^3 \sim 10^4$ and thus the flow is estimated to be turbulent. Since computations carried out by the authors using a two-parameter turbulence model broke down probably due to the complexity of the necessary computation scheme near the body surface, a simple mixing-length theory was used as the turbulence model. Fig.5.18 shows the instantaneous velocity vectors near the body surface obtained in the calculation. Fig.5.19 compares the RAOs of the motions obtained by 1)Euler-equation-based CFD(already shown in Fig.5.15) 2)Navier-Stokes-equation-based

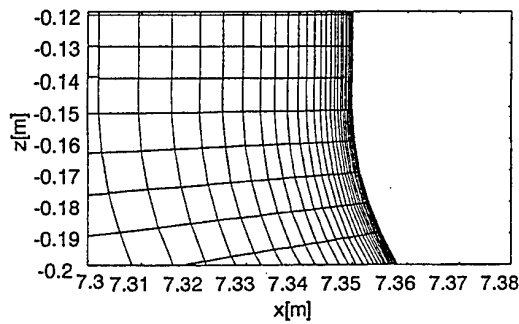


Fig.5.17: The grid near the body surface for the Navier-Stokes calculation

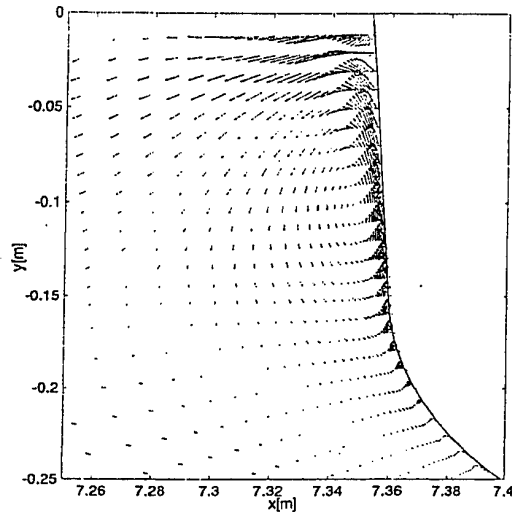
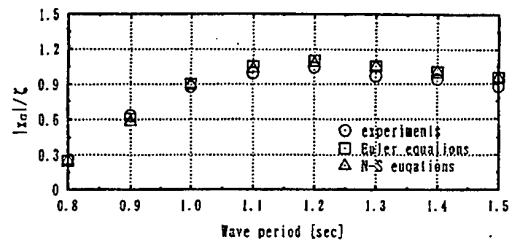


Fig.5.18: The instantaneous velocity vectors near the body surface

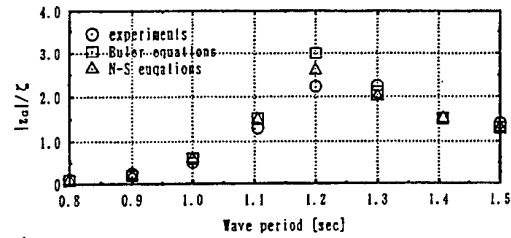
CFD and 3) Experimental data. The effect of the additional damping on the motions induced by the viscous forces is manifested around the resonant period in the results obtained by the Navier-Stokes-equation-based CFD although a slight difference from the experimental data still exists. The computation based on Euler equations and that based on Navier-Stokes equations can be carried out with the same computer code by simply eliminating or adding viscous forces in the equations, which is one of the significant feature of the present method.

(2) Nonlinear motions in large transient waves

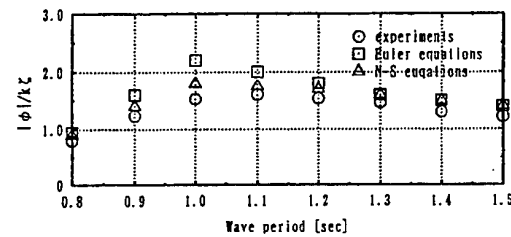
After confirming that the Euler-equation-based CFD can predict motions in small waves with the same degree of accuracy as that of the linear potential theory, the present method was applied to the computation of nonlinear motions in large waves. Viscous effects were not taken into account and thus Euler equations were used in the calculation. Since the linear potential theory can



(a) Sway



(b) Heave



(c) Roll

Fig.5.19: The comparison of the RAOs of the semi-circular body with/without viscous effects

no longer be used as a benchmark because of the nonlinearity of the phenomena, experiments were carried out to obtain the data that can be compared to the present calculations. The semi-circular model already shown in Fig.5.14(a) was used in the experiment and the experimental set-up is the same as that already shown in Fig.5.13. Prior to the computation, large waves were generated without placing the body in the tank. Fig.5.20 compares the time history of the free-surface displacement measured in the real water tank with the corresponding time history reproduced in the present numerical tank. As can be observed, the waves were generated in such a way that they concentrate at the place where the body was supposed to be located. In the present calculation, the same time history of the wave-maker velocity as that given in the experiment were imposed at the wave-maker boundary. It is observed that almost the same time history is reproduced in the present numerical tank although there exists a little discrepancy at a little time after the waves

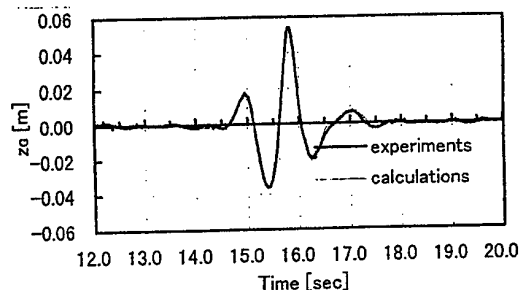


Fig.5.20: The comparison of the large transient waves produced in the experiment and those generated in the numerical tank

concentrated. Fig.5.21 compares the time histories of the motions of the semi-circular body placed in the waves. The motion in x direction coincides with the measured one almost completely. Even the horizontal excursion after the body encountered the wave packet is perfectly predicted. The motions in z direction and the rotational motions about y axis are also reproduced quite well including the free oscillations after the encounter to the concentrated wave.

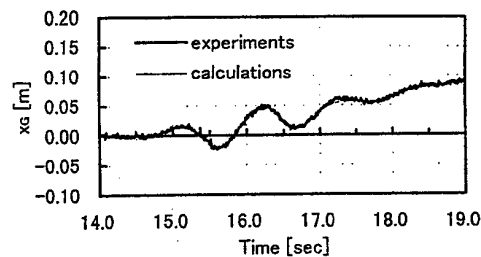
(3) Steady drift force on a submerged horizontal circular cylinder

As an example for which an analytical solution exists[7], the steady drift force on a submerged horizontal circular cylinder was chosen (see Fig.5.22). Since the analytical solution of the horizontal steady drift force on a submerged horizontal circular cylinder is zero, the vertical steady drift force was compared with the present computation. In the present calculation, an averaged value of the calculated vertical force over one wave period was taken as the steady drift force that is to be compared. The comparison is shown in Fig.5.23. Despite the fact that a steady drift force is a second-order small quantity, the agreement is quite good for all the wavelength and for all the submerged depth shown in the figure.

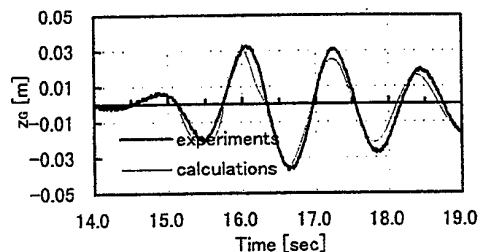
5.2.2 3-D problems

(1) Motions in regular waves of small amplitude with zero forward speed

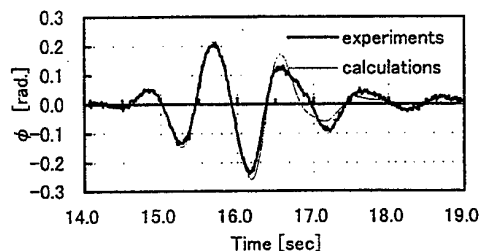
The first example of 3-D problems is the motions of a simple box-shaped floating barge in regular waves of small amplitude. As in 2-D problems, this example was chosen because solutions obtained by the linear potential theory may be considered as benchmark results. The main particulars of the barge are indicated in Fig.5.24. The incident angle of the waves was assumed to be 20 deg. as shown in the figure. Results ob-



(a) motion in x direction



(b) motion in z direction



(c) rotational motion about y axis

Fig.5.21: The time histories of the motions of a semi-circular body in large waves

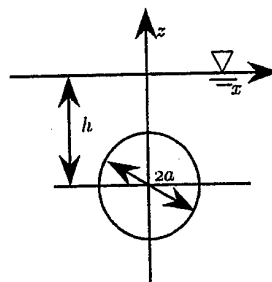


Fig.5.22: The submerged horizontal cylinder used for the calculation of steady drift force in waves

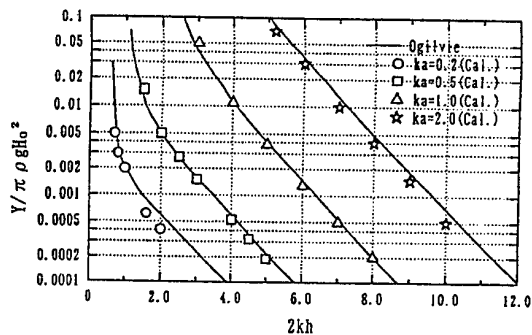


Fig.5.23: The steady vertical drift force on the submerged circular cylinder

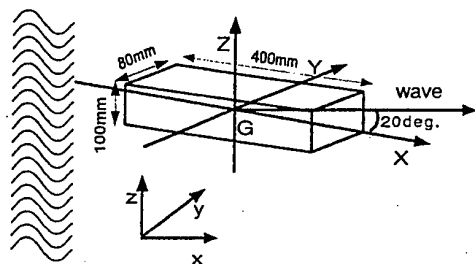
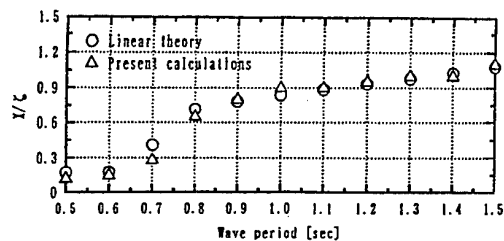


Fig.5.24: A 3-D floating barge in oblique waves

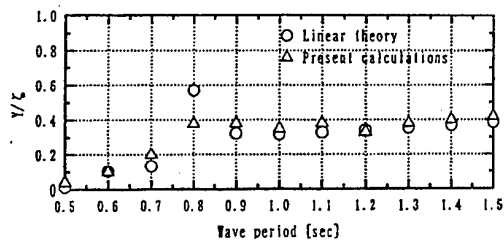
tained by a singularity distribution method based on the linear potential theory were used for the comparison. The present calculation is based on Euler equations and thus the viscous forces are not taken into account. Fig.5.25 and Fig.5.26 show the RAOs of the motions. It is observed that the present calculations give almost identical results with those obtained by the linear potential theory except at the vicinity of the resonant periods of the roll and the pitch motions, where the present results are noticeably smaller than the linear theory. These discrepancies may be attributed to the numerical damping which entails in finite-difference calculations. This numerical damping is amplified in the vicinity of the corner points because the velocities become very large. (The discrepancy that is also observed at around 0.8 sec. in the sway motion is considered to be caused through the coupling with the roll motion.)

(2) Motions of a Series-60 ship advancing in head waves

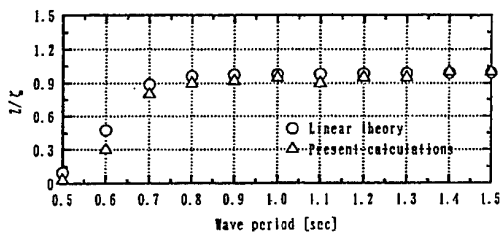
Next, as a practical example, a Series-60 ship ($C_b=0.7$) advancing in regular head waves with $F_n=0.2$ was selected for the computation. The reason for choosing this particular example is that experimental results conducted by Gerritsma et al.[8] exist. The body-fixed grid system used in the computation is a H-H type one, which is shown



(a) Surge



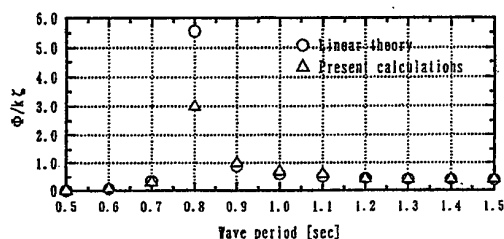
(b) Sway



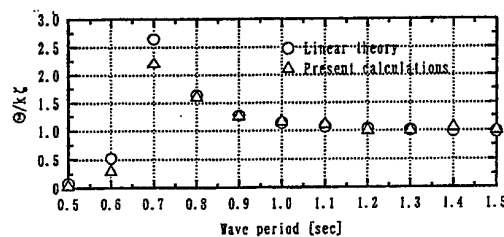
(c) Heave

Fig.5.25: The RAOs of the barge in oblique waves

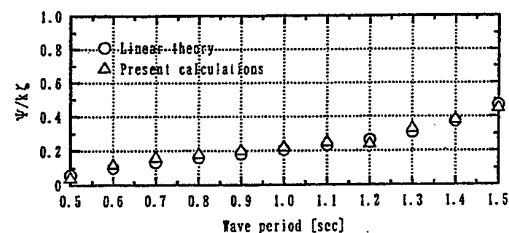
in Fig.5.27. Fig.5.28(a),(b) compare the RAOs of the heave and the pitch motions computed by the present method with the experiments. The agreement with the experimental data is satisfactory, which is quite encouraging, because, despite the fact that the predictions of wave loads and associated motions of a ship advancing in waves are vital for the design of the ship, the conventional methods such as a Green-function method or a Rankine source method still have certain difficulties in actual computations even within the linear potential theory. The present method can be applied in practically identical manner to the computation of wave loads and associated motions of a ship regardless of the existence of a forward speed. This feature is quite significant if compared to the conventional methods, in which the calculation becomes quite complicated once a



(d) Roll



(e) Pitch



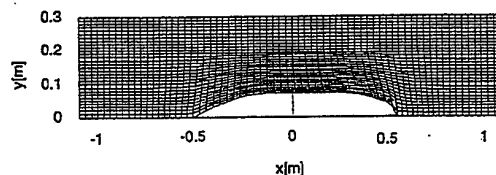
(f) Yaw

Fig.5.26: The RAOs of the barge in oblique waves (continued from Fig.25)

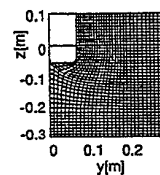
forward speed is involved.

5.3 An application to a ship advancing in large waves

As an example application of the present method to practically important nonlinear problems, wave loads and motions of a ship advancing in large waves were calculated. As described in *INTRODUCTION*, predictions of wave loads and motions of a practical ship advancing in large waves are now in great demand because a rational design of a cost effective ship is necessary to compete in the keen international market. For this reason, significant efforts are now being devoted around the world by many researchers to the development of reliable numerical tools that enable such predictions. Although most of the current

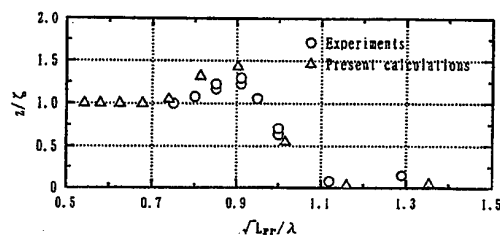


(a) Water-line

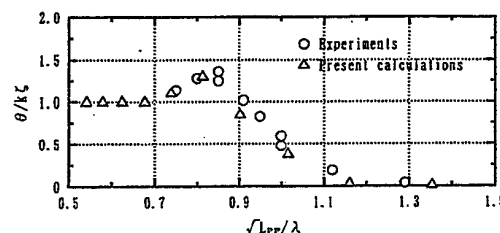


(b) Midship

Fig.5.27: The grid used for the calculation of a Series-60 ship



(a) Heave



(b) Pitch

Fig.5.28: The RAOs of the Series-60 ship running in heave waves with $F_n=0.2$.

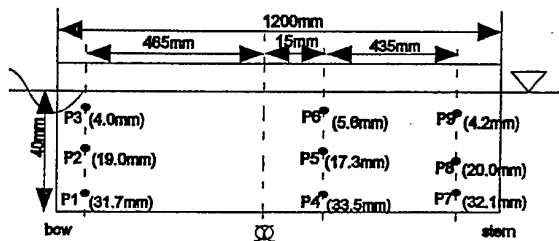
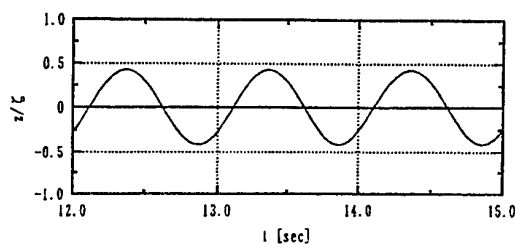
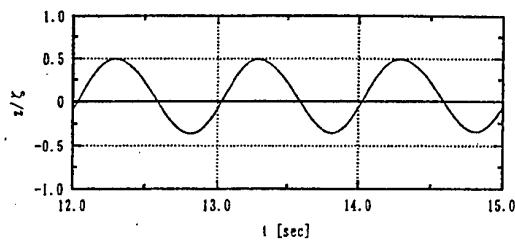


Fig.5.29: The calculated points of the pressures on a Wigley hull

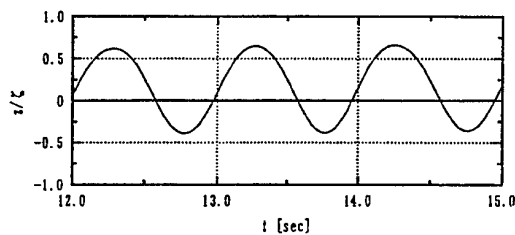
efforts are based on a boundary-integral-equation method(BIEM), the present method, which discretizes the fluid volume into grids, may be advantageous over the BIEM, because the nonlinear boundary conditions at the free-surface as well as at the body surface can be dealt with sometimes much easier than a BIEM. To demonstrate this efficaciousness of the present method, wave loads, pressures and motions of a Wigley hull advancing in large regular head waves were calculated. The places where the pressures were calculated are shown in Fig.5.29. The computations were conducted for three different wave-height, $\zeta_a/d = 0.25, 0.5, 1.0$, where ζ_a, d represent the wave amplitude and the draft of the ship respectively. The wavelength(λ) was kept to be $\lambda/L=1.3$ and the ship speed was $F_n=0.1$. Although motions in large waves are affected significantly by the hull geometry above the still-water level, a so-called double model, in which the geometry of the ship hull above the still-water level is a mirror image of the hull geometry below the still-water surface, was used in the present calculation for the sake of the simplicity of grid generation. Fig.5.30(a)(b)(c), Fig.5.31(a)(b)(c) show the time histories of the heave and the pitch motions respectively in the three different wave-height. Fig.5.32(a)(b)(c), Fig.5.33(a)(b)(c) show the time histories of the heave force and the pitch moment(about the midship section) in the three different wave-height. It is quite characteristic that little distortions are observed in the time histories of the motions even in quite large waves, whereas the time histories of the heave force and the pitch moment are deviated significantly from sinusoidal curves. These results are at least qualitatively consistent with the known fact that nonlinearities are manifested in wave loads while motions remain sinusoidal up to fairly large wave-height. Fig.5.34, Fig.5.35, Fig.5.36 show the time histories of the pressures in the three different wave-height. In some of the time histories, the pressures level



(a) $\zeta_a/d = 0.25$



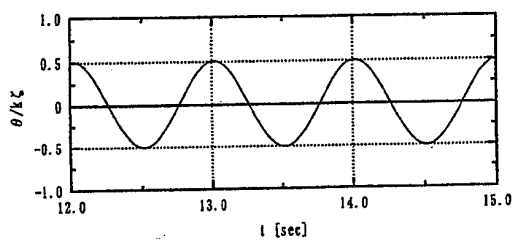
(b) $\zeta_a/d = 0.5$



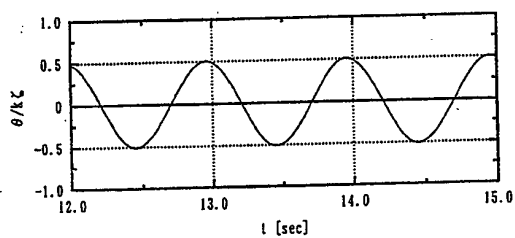
(c) $\zeta_a/d = 1.0$

Fig.5.30: The time histories of the heave motion in three different wave-height

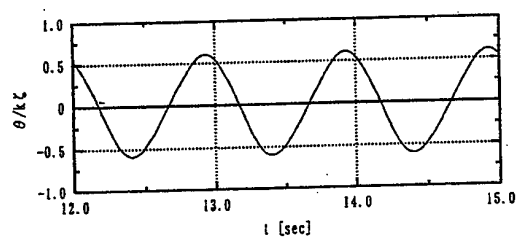
off once they reach $p = 0$ (air pressure). This happens as the corresponding place is exposed to the air due to large motions. In relatively small wave-height, $\zeta_a/d = 0.25$, such phenomenon is only observed in P3, which is located close to the still-water surface, whereas as the wave-height increases, the pressure at P9 also levels off together with that at P3 in $\zeta_a/d=0.5$. Even the pressure at such a place as P1, which is located well below the still-water surface, level off in the largest waves ($\zeta_a/d=1.0$). Since no experimental data nor other calculation results corresponding to the present ones are available at present, the validation of the presented results is one of the urgent future tasks. It is also necessary from the practical point of view to deal with a ship which has a realistic hull geometry above the still-water level.



(a) $\zeta_a/d = 0.25$

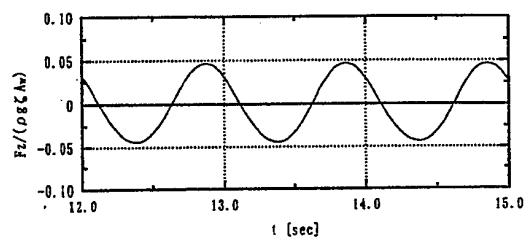


(b) $\zeta_a/d = 0.5$

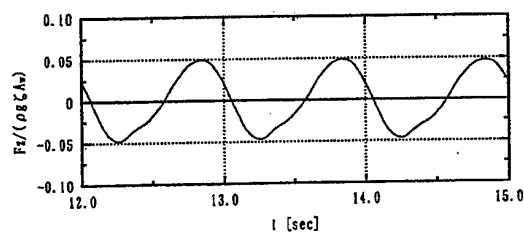


(c) $\zeta_a/d = 1.0$

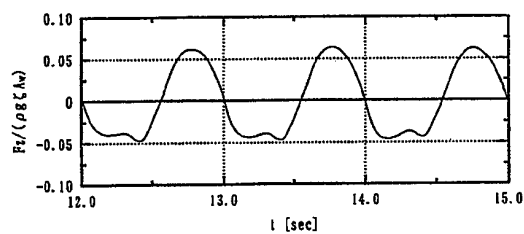
Fig.5.31: The time histories of the pitch motion in three different wave-height



(a) $\zeta_a/d = 0.25$

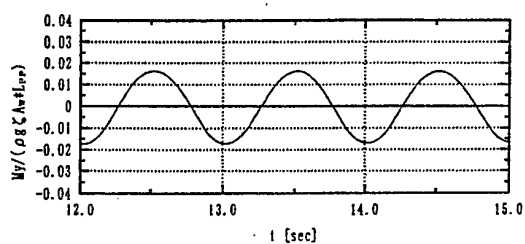


(b) $\zeta_a/d = 0.5$

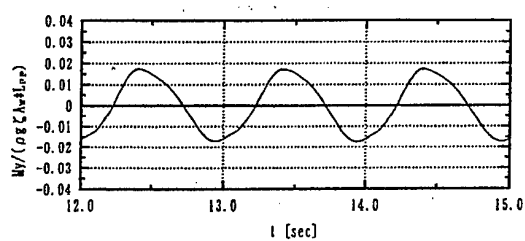


(c) $\zeta_a/d = 1.0$

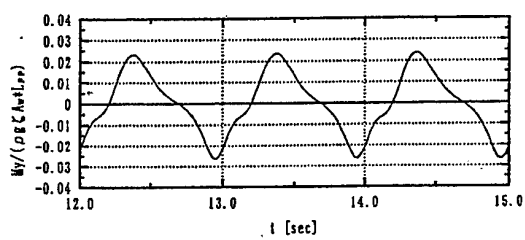
Fig.5.32: The time histories of the heave force in three different wave-height



(a) $\zeta_a/d = 0.25$

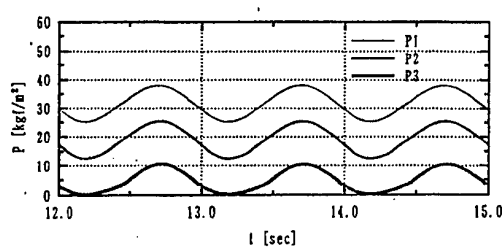


(b) $\zeta_a/d = 0.5$

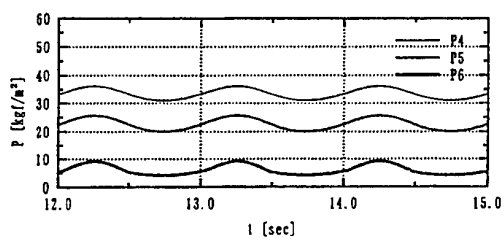


(c) $\zeta_a/d = 1.0$

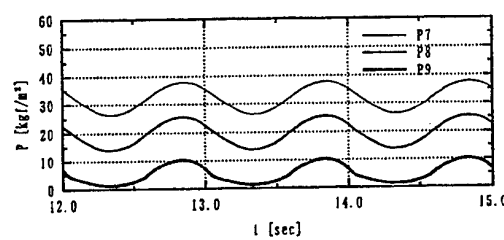
Fig.5.33: The time histories of the pitch moment in three different wave-height



(a) Bow

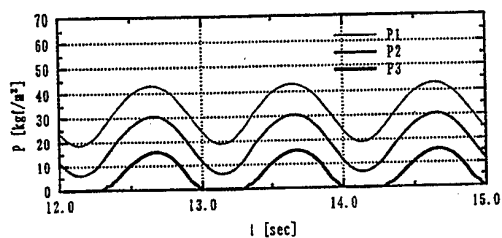


(b) Center

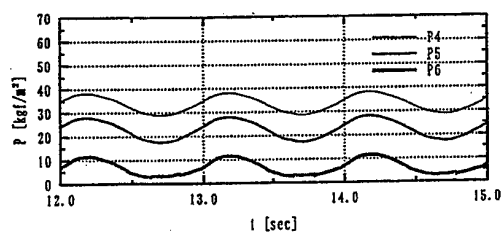


(c) Stern

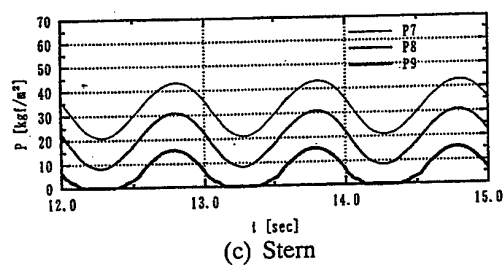
Fig.5.34: The time histories of the pressure in waves($\zeta_a/d = 0.25$).



(a) Bow

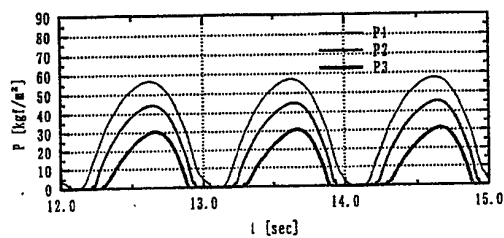


(b) Center

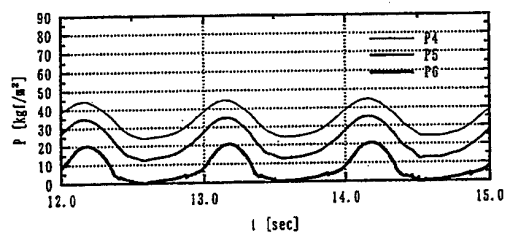


(c) Stern

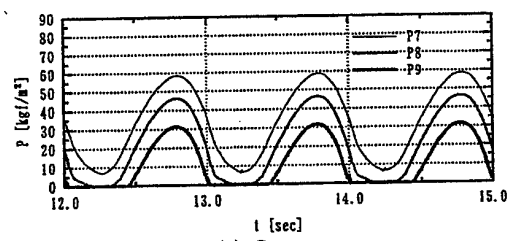
Fig. 5.35: The time histories of the pressure in waves ($\zeta_a/d = 0.5$)



(a) Bow



(b) Center



(c) Stern

Fig. 5.36: The time histories of the pressure in waves ($\zeta_a/d = 1.0$).

6.CONCLUSIONS

With an Euler-equation-based CFD, it has been shown that wave-induced motions of a floating body in small regular waves can be calculated with the same degree of accuracy as that attained by the conventional linear potential theory. By adding the viscous-force terms to Euler equations, it was demonstrated that a Navier-Stokes-equation-based CFD can be actually carried out with essentially the same computer code and the results were obtained that account for the additional damping effect on the motions resonant to waves. It has also been shown that the present method can be used for the calculations of wave loads and associated motions of a ship advancing in waves in practically the same manner as the computation of a ship with no forward speed. Considering that the conventional methods such as a Green-function method or a Rankine source method require significant numerical efforts once a forward speed is involved even in the linear theory, the above mentioned feature of the present method is a significant advantage over the conventional methods. With the present method, even the calculation of wave loads and the resultant motions of a ship advancing in large waves can be carried out without any major difficulty. Overall it has been demonstrated that the CFD computations of wave-induced motions of a floating body can be done with reasonable accuracy in a wide variety of practically important problems by essentially a single computer code. Although the right direction of the future strategy for the development of reliable numerical tools that can predict the wave loads and resultant motions of a ship advancing in large waves may yet be determined, the present strategy could be one of the promising candidates for that purpose.

REFERENCE

1. R.Torhaug, S.R.Winterstein and A.Braathen, "Nonlinear ship loads: Stochastic models for extreme response", Journal of Ship Research, Vol.42, No.1, March 1998, pp.46-55.
2. T.Ohmori, "Finite-volume simulation of flows about a ship in maneuvering motions", Journal of Marine Science and Technology, Vol.3, No.2, 1998, pp.82-93.
3. I. Orlanski, "A simple boundary condition for unbounded hyperbolic flows", Journal of Computational Physics, Vol.21, 1976, pp.251-269.
4. R.Cointe, P.Geyer, B.King, B.Molin and M.Tramoni, "Nonlinear and linear motions of a rectangular barge in a perfect fluid", Proc.18th

Symp. on Naval Hydrodynamics, Ann Arbor, Michigan, 1991, pp.85-99.

5. J.E.Romate, "Absorbing boundary conditions for free surface waves", Journal of Computational Physics, Vol.99, 1992, pp.135-145.

6. K.Tanizawa, "A nonlinear simulation method of 3D body motions in waves: formulation with the acceleration potential", Abstract submitted to 10th Intl. Workshop on Water Waves and Floating Bodies, Oxford, 1995.

7. T.F.Ogilvie, "First- and second-order forces on a cylinder submerged under a free surface", Journal of Fluid Mechanics, Vol.16, 1963, pp.451-472.

8. J.Gerritsma, W.Beukelman and C.Glansdrop, "The effects of beam on the hydrodynamic characteristics of ship hulls", Proc.10th Symp. on Naval Hydrodynamics, Cambridge, Massachusetts, 1974, pp.3-43.

THREE-DIMENSIONAL FREE SURFACE VISCOUS FLOW AROUND A SHIP IN FORCED MOTION

L. Gentaz, P.E. Guillerm, B. Alessandrini, G. Delhommeau

Division Hydrodynamique Navale, Laboratoire de Mécanique des Fluides, Ecole Centrale de Nantes
1, rue de la Noë 44072 Nantes Cedex 03, France

ABSTRACT

This article deals with numerical simulation of wave radiation by the force heave or pitch motion of a ship at forward speed. A viscous, turbulent and unsteady flow is considered. The motions of the hull are written in a cartesian frame moving at the mean hull velocity. The hydrodynamic loads acting on the hull are calculated at each time step during the unsteady simulation and the hydrodynamic coefficients are then obtained through Fourier analysis.

The Navier-Stokes equations with nonlinear free surface boundary conditions are solved by a fully-coupled method for velocity, pressure and free surface elevation unknowns [1]. The discretisation of the governing equations by finite difference schemes provides a linear system which is solved by an iterative algorithm based on conjugate gradient or multigrid methods. A $k-\omega$ model based on the solution of two transport equations is used to evaluate turbulent viscosity.

The hydrodynamic loads computed with this method are compared with perfect fluid flow calculations and experiments for a free surface piercing hemisphere and a merchant ship Series 60, CB=0.60.

INTRODUCTION

The numerical method to solve the Reynolds-Averaged Navier-Stokes (RANS) equations with nonlinear free surface boundary conditions presented in the following has been already used to simulate cases of ships in rectilinear motion in an initially calm water [1]. This method has been modified here in order to take supplementary forced motions into account. The final purpose of this study is to devise a coupling method between the present RANS equations approach and a potential flow method [7]. Indeed the main interest of computations around ships in viscous flow is the capability to compute boundary layer, effects of turbulence or vorticity which occur in the vicinity of the hull. On the other hand it is difficult to compute free surface field far from the hull in long term simulations. Moreover influence of turbulence, viscosity or vorticity is weak far from the hull. So it can be very interesting to use a method based on potential flow theory (with linear approximation or not) to compute this far field. So a coupling between a method solving RANS equations and another one solving

potential flow equations is an original way to use advantages of each one : flow in the vicinity of the hull is solved by computing Navier-Stokes-Reynolds equations with nonlinear free surface boundary conditions and flow far from the hull by Laplace equation $\Delta\phi = 0$ and free surface boundary conditions. The potential flow solution is used to provide boundary conditions on the external boundary for the problem in viscous fluid.

For the present problem of hydrodynamic loads on a body in forced oscillating motions, many references can be found in literature. Solutions in perfect fluid flow based on perturbation methods have been first developed. First analytical solutions have been obtained by Havelock [11] and three-dimensional problem for a floating body has been formulated by John [12]. In 1960 Wehausen and Laitone [23] proposed formulations of the Green function for the three-dimensional problem. The first approach of the 3D problem has been done by Korvin-Kroukowsky [13] with a method based on the strip theory. Other authors like Faltinsen [6] and Telste [21] have solved the fully nonlinear 2D problem by developing some BEM methods. Three dimensional

seakeeping problem with forward speed has been undertaken too since the middle of the 80's. First studies treated the linear and steady problem in the frequency domain (Sclavounos and Nakos [20] or Ohkusu and Iwashita [17] among many others contributors). More recently time-domain solution has been developed and the nonlinear problem is still in progress [14]. In 1998 no fully nonlinear code was available in the industry.

Concerning viscous approach of this problem Nichols and Hirt [16] for bodies in heave motion or Yeung and Ananthakrishnan [26] and other authors have developed numerical algorithms based on 2D Navier-Stokes equations. Today solvers based on RANS equations can treat problem of ship with forward speed in initially calm water (with calculation of wave and viscous resistances). So such solvers should from now on treat the 3D seakeeping problem (without incoming waves).

In present article RANS equations with fully nonlinear free surface boundary conditions are solved by an original fully-coupled method for velocity, pressure and free surface elevation unknowns. Governing equations are written in a set of curvilinear coordinates fitted to the body and free surface. A linear system for all discrete unknowns (velocity, pressure and free surface elevations) is solved at each iteration by a CGSTAB algorithm and mesh of the fluid domain is regrided according to the new shape of the free surface (moving grid technique). A $k - \omega$ model is used to compute the turbulent effects but the kinetic energy k and the turbulent dissipation rate ω are not included in the fully coupled linear system.

The hydrodynamic loads (pressure effects and viscous effects) are computed on the hull at each time step, allowing for the influence of viscosity on added masses or damping coefficients to be studied.

DEFINITION OF COORDINATE SYSTEMS

The motion of the ship is assumed to be the sum of a rectilinear motion with the average speed (U_a) plus a sinusoidal motion. The equations are written in a cartesian system $(R_0) = (O; \vec{x}; \vec{y}; \vec{z})$ which is moving with the constant forward speed (U_a). The x axis of this coordinate system is parallel to the average speed of the ship but oriented in the opposite direction. The y axis is on the free surface at rest and the y axis is vertically upward oriented.

The ship can have movements of translation along the three axis of the system (R_0) or move-

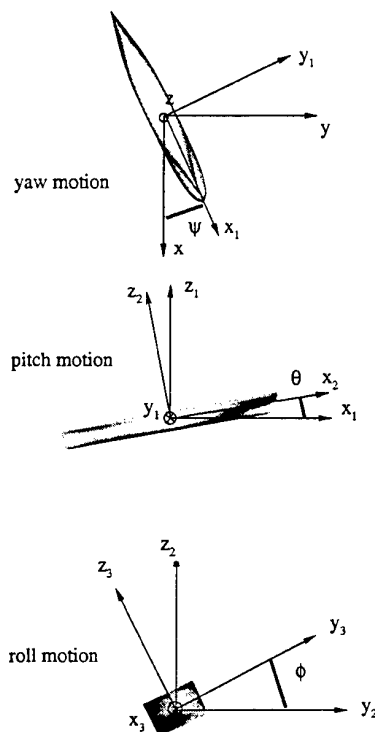


Figure 1: Used frames

ments of rotation. These rotations are defined as following (see figure 1) :

the yaw movement is a rotation around $(O; \vec{z})$ axis and (R_0) becomes $(R_1) = (O; \vec{x}_1; \vec{y}_1; \vec{z})$.
the pitch movement is a rotation around $(O; \vec{y}_1)$ axis and (R_1) becomes $(R_2) = (O; \vec{x}_2; \vec{y}_1; \vec{z}_2)$.
the roll movement is a rotation around $(O; \vec{x}_2)$ axis and (R_2) becomes $(R_3) = (O; \vec{x}_2; \vec{y}_3; \vec{z}_3)$ where (R_3) is a coordinate system connected to the hull.

GOVERNING EQUATIONS

Transport equations and turbulence transport equations

RANS equations are written under a convective form for a three-dimensional turbulent flow of a Newtonian and incompressible fluid. The three components of velocity (u^i), pressure (p) including gravitational effects ($\rho g x^3$) and turbulent kinetic energy ($2/3 \rho k$) are the dependent unknowns of the problem. The independent unknowns are

the three coordinates of the cartesian basis and the time (t). A curvilinear system (ξ^1, ξ^2, ξ^3) fitted to the physical fluid domain is defined in order to simplify the implementation of the boundary conditions on the hull and on the free surface. So $\xi^2 = 0$ and $\xi^3 = 0$ are the equations of the wetted part of the hull and the free surface respectively. At each time step a partial transformation is defined between the moving cartesian coordinate system and the fixed curvilinear system : in the sequel, the independent unknowns will be the curvilinear components (ξ^1, ξ^2, ξ^3) and time (t). The metric of this transformation uses covariant basis (a_i), contravariant basis (a^i), contravariant metric tensor (g^{ij}), control grid functions (f^i) and grid velocities. These geometric elements are computed at each time step at each node of the mesh.

The transport equations in the non Galilean frame (R_0) are written :

$$u_{,t}^\alpha + \left(a_i^j (u^i - u_g^i) - \nu_{eff} f^j - a_k^i \nu_{t,i} a_k^j \right) u_{,j}^\alpha + \frac{1}{\rho} a_{\alpha,p,k}^k p_{,k} - \nu_{eff} g^{ij} u_{,ij}^\alpha - a_k^i \nu_{t,i} a_j^\alpha u_{,j}^k + \delta_{1\alpha} U a_{,t} = 0 \quad (1)$$

and the mass conservation implies :

$$a_i^j u_{,j}^i = 0 \quad (2)$$

A two transport equations turbulence model $k - \omega$ [15] [24] [25] is used to close the set of equations. ω denotes a specific dissipation rate defined by

$$\omega = \frac{\varepsilon}{k \beta^*} \quad (3)$$

By using the above partial transformation, the transport equations for k and ω become :

$$k_{,t} + \left(a_i^j (u^i - u_g^i) - (\nu + \sigma^* \nu_t) f^j - a_k^i \sigma^* \nu_{t,i} a_k^j \right) k_{,j} - (\nu + \sigma^* \nu_t) g^{ij} k_{,ij} - P_\tau + \beta^* \omega k = 0 \quad (4)$$

$$\omega_{,t} + \left(a_i^j (u^i - u_g^i) - (\nu + \sigma \nu_t) f^j - a_k^i \sigma \nu_{t,i} a_k^j \right) \omega_{,j} - (\nu + \sigma \nu_t) g^{ij} \omega_{,ij} - \frac{\gamma \omega}{k} P_\tau + \beta \omega^2 = 0 \quad (5)$$

with

$$\begin{cases} \beta^* = 0.09; \sigma = 0.5; \gamma = \frac{5}{9} \\ \gamma^* = 1; \sigma^* = 0.5; \beta = \frac{3}{40} \end{cases} \quad (6)$$

P_τ and ν_t are the production term and the turbulent viscosity respectively.

Standard boundary conditions

This formulation needs boundary conditions for velocity, turbulent kinetic energy k and dissipation rate ω . No other pressure boundary condition is necessary at the boundary. Let us denote by Γ_c the boundary defined by the hull, Γ_e the external boundary, Γ_a the symmetry vertical plane and Γ_s the free surface. x^1, x^2, x^3 are the cartesian coordinates in the frame (R_0) corresponding to the directions $\vec{x}, \vec{y}, \vec{z}$ respectively.

For closure of the turbulence equations, we use the following boundary conditions for k and ω

$$\begin{aligned} \text{on } \Gamma_s : k &= k_{min}; \omega = \omega_{max} \\ \text{on } \Gamma_e : k &= k_{min}; \omega = \frac{U_a}{\beta d} \\ \text{on } \Gamma_c : k &= k_{min}; \omega \sim \frac{\delta \nu}{\beta d^2} \\ \text{on } \Gamma_a : \frac{\partial k}{\partial x^2} &= \frac{\partial \omega}{\partial x^2} = 0 \end{aligned} \quad (7)$$

where l and d are the ship length and the distance to the hull respectively.

The boundary conditions for the velocity field all other boundaries, except the free surface Γ_s , are given by no-slip or symmetry conditions :

$$\begin{aligned} \text{on } \Gamma_e : u^1 &= U_a; u^2 = u^3 = 0 \\ \text{on } \Gamma_c : u^1 &= u^2 = u^3 = 0 \\ \text{on } \Gamma_a : u^2 &= 0; \frac{\partial u^1}{\partial x^2} = \frac{\partial u^3}{\partial x^2} = 0 \end{aligned} \quad (8)$$

Free surface boundary conditions

On the free surface, the available boundary conditions on (Γ_s) are : one kinematic condition, two tangential dynamic conditions and one normal dynamic condition.

The kinematic condition expresses that the fluid particles of the free surface remain on it :

$$h_{,t} + \left(b_i^j (u^i - u_g^i) h_{,j} \right)_{(i,j) \in \{1,2\}} - u^3 = 0 \quad (9)$$

In this equation (b^i) is a the bidimensional contravariant basis computed on the free surface.

The dynamic conditions arise from the continuity of stresses at the free surface. When the pressure above the free surface is supposed to be constant, the normal dynamic condition is given by :

$$p - \rho g h - 2 \frac{\rho \nu_{eff}}{|\alpha^3|^2} a_i^3 a_j^3 a_k^k u_{,k}^i - \frac{\gamma}{r} = 0 \quad (10)$$

where γ is the superficial tension coefficient and r is an averaged free surface curvature radius. At last the tangential dynamic conditions are a linear combination of the first derivatives of the cartesian velocity components.

$$a_{\alpha i} g^{j3} u_{,j}^i = 0 \quad \alpha \in \{1, 2\} \quad (11)$$

Body motions

The present numerical method has been first implemented to compute viscous free surface flows around a hull in rectilinear motion. In this case the hull was fixed in the frame (R_0). In order to study seakeeping with forward speed, the motions of the calculation frame have to be taken into account. At each time step (n), the location of the hull is defined in the frame (R_0) (the supplementary sinusoidal motion of the hull being an explicit time function); the fluid domain around the hull is then regridded by considering the new hull and free surface positions computed in the previous time step ($n - 1$).

When the hull is forced to oscillate in translation or rotation, the no-slip condition implies that the fluid velocity on the hull and the velocity of the hull itself must be identical. If we consider a point of the hull P merged into a node of the grid at a time (t), the velocity of (P) is equal to zero in the frame (R_3). The velocity of this point (P) in the frame (R_0) is then

$$\left. \frac{d\vec{OP}}{dt} \right|_{R_0} = \left. \frac{d\vec{OP}}{dt} \right|_{R_3} + \vec{\Omega}_{03} \wedge \vec{OP} = \vec{\Omega}_{03} \wedge \vec{OP} \quad (12)$$

where $\vec{\Omega}_{03}$ is the rotation velocity of frame (R_3) with respect to (R_0).

DISCRETISATION OF THE SET OF EQUATIONS BY THE FULLY-COUPLED METHOD

Today most of numerical methods solving RANS equations including free surface effects are weakly-coupled methods. In these approaches discrete transport equations and continuity equation at time step (n) are solved by some iterative algorithms like SIMPLER [18] which provide approximate solutions for velocity and pressure fields. The free surface elevation is then updated separately from them by using the normal dynamic condition or by integrating the kinematic condition.

Unfortunately these algorithms lead to a weak coupling between velocity and pressure fields. Complete free surface boundary conditions cannot be taken into account. Integration of the kinematic condition requires non physical boundary conditions; Moreover using of the normal dynamic condition under Dirichlet form inhibits the mass conservation under the free surface. An original method has been developed to improve

the theoretical and numerical resolution of these problems [1]. In this method three dimensional RANS equations with the Newtonian closure are written under convective form in a curvilinear computational space fitted at each time step to the hull and to the moving free surface. The $k - \omega$ turbulence model gives two linear systems solved at each time step (n) with velocity field computed at previous step ($n - 1$). The transport equations are discretised at the nodes of the grid. The Rhie & Chow interpolation [19] with extra pseudo-velocity unknowns is used to set up the pressure equation discretised at the center of each elementary volume. The two tangential dynamic conditions and the kinematic condition give a set of three velocity boundary conditions on the free surface. The normal dynamic condition is used to provide an implicit relation between pressure and free surface elevation.

The original aspect of the present "fully-coupled" method is that a single linear system for velocity components, pseudo-velocity components, pressure and free surface elevation is built and solved at each iteration using a CGSTAB algorithm [22]. This method leads to a strong velocity-pressure coupling which is essential for good convergence on non-linearities. Moreover, the complete nonlinear free surface boundary conditions (with viscous and surface tension terms) are properly taken into account.

In the following, the discrete components of velocity (U_i^α), pseudo-velocity ($U_i^{*\alpha}$), kinetic energy (K_i), turbulent dissipation rate (W_i) are located along the curvilinear coordinates lines of the volumic grid (Ω), which allows to write easily boundary conditions on ($\partial\Omega$). The pressure unknowns (P_k) are located at the centre of elementary volumes (Ω_v) to ensure mass conservation without special treatment at boundaries. The free surface elevation unknowns (H_k) are located at the centre of free surface interfaces ($\partial\Omega_{si}$) in order to avoid singularity of the kinematic free surface condition. ($\partial\Omega_s$) are the nodes of the grid (Ω) belonging to free surface only; ($\partial\Omega_b$) represent the nodes of the grid belonging to the boundaries except the free surface (we have $\partial\Omega = \partial\Omega_s \cup \partial\Omega_b$).

All equations are discretised by second-order finite differences schemes (in space or time).

Discretisation of the transport equations

The transport equations are first linearised : that means that the convection terms and a part of the turbulence terms and the diffusion terms (cross second derivative terms) are computed at the

previous time step. Then they are discretised at nodes of the grid : the convection terms are computed under implicit form with an upward second-order scheme and need a 13 points stencil and the non crossed diffusion terms need a 7 points stencil. The pressure gradient is discretised on the nodes too with a 8 points stencil. Finally we obtain for the transport equations at node i for the three cartesian components ($\alpha \in \{1, 2, 3\}$) :

$$U_i^\alpha + (\chi u)_{ij} U_{j \neq i}^\alpha + (\chi p)_{ik} P_k = f u_i^\alpha \text{ on } \Omega \setminus \partial\Omega \quad (13)$$

Discretisation of the transport equations for the turbulence model

The transport equations for k and ω are first linearised under following form :

$$\begin{cases} (\nu + \sigma^* \nu_t) g^{jj} k_{,jj} + A_k^j k_{,j} - k_{,t} = S_k \\ (\nu + \sigma \nu_t) g^{jj} \omega_{,jj} + A_\omega^j \omega_{,j} - \omega_{,t} = S_\omega \end{cases} \quad (14)$$

with :

$$\begin{cases} A_k^j = -a_i^j (u^i - u_g^i) + (\nu + \sigma^* \nu_t) f^j + a_k^i \sigma^* \nu_{t,i} a_k^j \\ A_\omega^j = -a_i^j (u^i - u_g^i) + (\nu + \sigma \nu_t) f^j + a_\omega^i \sigma \nu_{t,i} a_\omega^j \end{cases} \quad (15)$$

and :

$$\begin{cases} S_k = -(\nu + \sigma^* \nu_t) (g^{ij} k_{,ij})_{i \neq j} - P_r + \beta^* \omega k \\ S_\omega = -(\nu + \sigma \nu_t) (g^{ij} \omega_{,ij})_{i \neq j} - P_r \frac{\gamma_\omega}{k} + \beta \omega^2 \end{cases} \quad (16)$$

In the equations (14), $(\nu + \sigma^* \nu_t) g^{jj}$, $(\nu + \sigma \nu_t) g^{jj}$, A_k^j , A_ω^j , S_k and S_ω are computed at previous time step. Other terms of the equations (14) (unsteady term, first derivatives and non crossed second derivatives in space) are discretised under implicit form with schemes similar to those used for the convection-diffusion equations (1).

After discretisation the equations (14) can be written under following form :

$$\begin{cases} (\chi k)_{ij} K_j + \gamma_i W_i = f k_i \text{ on } \Omega \setminus \partial\Omega \\ (\chi \omega)_{ij} W_j = f \omega_i \text{ on } \Omega \setminus \partial\Omega \end{cases} \quad (17)$$

At each time step (n) new values of the kinetic energy field (K_i) and the turbulent dissipation rate field (W_i) are solved by using velocity field computed at previous time step ($n-1$). These fields allow the calculation of ν_t and other turbulent terms in the transport equations (13) or in the free surface boundary condition (10).

Discretisation of free surface boundary conditions

The kinematic condition (9) is linearised as an implicit relation between the three velocity cartesian components and the free surface elevation :

$$h_{,t} + A^1 u^1 + A^2 u^2 - u^3 = A^1 u_g^1 + A^2 u_g^2 \quad (18)$$

This equation is then discretised on the nodes ($\partial\Omega_s$) of the free surface. The spatial derivatives of free surface elevation in the terms A^1 and A^2 are expressed with second-order centred schemes on a 4 points stencil. The unsteady term is implicitly written by a 3 points non-centred scheme. H is the discrete free surface elevation defined at the center of free surface cells and \hat{H} its interpolation at the nodes of the grid. Finally we have for the discrete kinematic condition :

$$\lambda_i^{1,1} U_i^1 + \lambda_i^{1,2} U_i^2 + \lambda_i^{1,3} U_i^3 + \eta_i^{1,4} \hat{H}_i = f c c_i \text{ on } \partial\Omega_s \quad (19)$$

The discretisation of the two tangential dynamic conditions (11) on a 6 points stencil can be written under following form :

$$\begin{cases} \lambda_i^{2,1} U_i^1 + \lambda_i^{2,2} U_i^2 + \lambda_i^{2,3} U_i^3 + \\ \left(\eta_{ij}^{2,1} U_j^1 + \eta_{ij}^{2,2} U_j^2 + \eta_{ij}^{2,3} U_j^3 \right)_{j \neq i} = 0 \\ \lambda_i^{3,1} U_i^1 + \lambda_i^{3,2} U_i^2 + \lambda_i^{3,3} U_i^3 + \\ \left(\eta_{ij}^{3,1} U_j^1 + \eta_{ij}^{3,2} U_j^2 + \eta_{ij}^{3,3} U_j^3 \right)_{j \neq i} = 0 \end{cases} \text{ on } \partial\Omega_s \quad (20)$$

The three equations (19) and (20) are the boundary conditions for the velocity field on the free surface. In order to obtain a fully-coupled linear system with better conditioning the linear system of these equations is analytically solved for the unknowns U_i^α ($\alpha \in \{1, 2, 3\}$) on each node i . The boundary conditions for velocity on free surface become :

$$U_i^\alpha + (\chi s u)_{ij}^\alpha U_{j \neq i}^\alpha + (\chi s h)_i^\alpha \hat{H}_i = f s_i^\alpha \text{ on } \partial\Omega_s \quad (21)$$

For the discretisation of the normal dynamic condition (10) the viscous terms are computed under explicit form. The pressure unknowns are located at the centre of elementary volumes. Thus the pressure on the free surface is linearly extrapolated with the two pressure unknowns located just under free surface. Finally the discretised normal dynamic condition is written :

$$H_k + (\chi s p)_{kj} P_j = f h_k \text{ on } \partial\Omega_{si} \quad (22)$$

Discretisation of pressure equation and use of generalised Rhie & Chow interpolation

The Rhie & Chow method is commonly used to obtain a pressure equation from continuity equation. The fully-coupled linear system with the transport equations, the pressure equation and all boundary conditions is of course invertible but it is not true for the single pressure block that leads to a bad conditioning. To avoid this problem the Rhie & Chow procedure is modified for elementary volumes in contact with free surface. In such cases free surface boundary conditions are introduced for calculation of the divergence.

In the equations hereafter \hat{X} and \bar{X} mean interpolation of the discrete variable X on the nodes of the grid and at the centre of free surface interfaces respectively.

Free surface elevation is eliminated of equation (21) by using the normal dynamic condition (22) :

$$U_i^\alpha + (\chi su)_{ij}^\alpha U_{j \neq i}^\alpha - (\chi sh)_i^\alpha (\widehat{\chi sp})_{il} \hat{P}_l = f s_i^\alpha - (\chi sh)_i^\alpha \widehat{f h}_i \quad \text{on } \partial \Omega_s \quad (23)$$

By introducing the pseudo-velocity unknowns ($U_i^{*\alpha}$), the transport equations (13) and three free surface boundary conditions (23) can be expressed at the centre of each interface (Ω_i) :

$$\overline{U_n^\alpha} - \overline{U_n^{*\alpha}} + \sigma_\nu (\overline{\chi p})_{nk}^\alpha P_k - \sigma_s (\overline{\chi sh})_n^\alpha (\chi sp)_{nj} P_j = 0 \quad \text{on } \Omega_i \quad (24)$$

with :

$$\left\{ \begin{array}{l} U_i^{*\alpha} + \sigma_\nu \left((\chi u)_{ij} U_{j \neq i}^\alpha - f u_i^\alpha \right) + \\ \sigma_s \left((\chi su)_{ij} U_{j \neq i}^\alpha - f s_i^\alpha + (\chi sh)_i^\alpha \widehat{f h}_i \right) = 0 \quad \text{on } \Omega \\ \sigma_\nu = 1 \quad \text{on } (\Omega \cup \Omega_i) \setminus (\partial \Omega \cup \partial \Omega_i) \\ \sigma_\nu = 0 \quad \text{on } \partial \Omega \cup \partial \Omega_i \\ \sigma_s = 1 \quad \text{on } (\Omega \cup \Omega_i) \setminus (\partial \Omega_s \cup \partial \Omega_{si}) \\ \sigma_s = 0 \quad \text{on } \partial \Omega_s \cup \partial \Omega_{si} \end{array} \right. \quad (25)$$

To summarize, the pseudo-velocity ($U_i^{*\alpha}$) regroups the convection terms and the right hand second members for the transport equations and the free surface boundary conditions, except the normal dynamic condition (25).

The pressure equation is obtained by cancellation of the divergence on each elementary volume.

The case $\sigma_s = 0$ is the classical Rhie and Chow method. With $\sigma_s = 1$ the free surface boundary conditions are put in the calculation of the divergence under free surface that gives a fully coupled linear system easy to solve. Finally the pressure equation is written :

$$(\chi mp)_{kl} P_l + (\chi d)_{ki}^\alpha U_i^{*\alpha} = 0 \quad \text{on } \Omega_v \quad (26)$$

THE FULLY-COUPLED SOLUTION

The linear system (17) allowing to obtain the kinetic energy and the turbulent dissipation rate is solved separately as explained before. The equations used for the fully-coupled linear system in velocity, pseudo-velocity, pressure and free surface elevation are the following : the transport equations (13) on $\Omega \setminus \partial \Omega$, the relation between velocities and pseudo-velocities (25) on $\Omega \setminus \partial \Omega$, the free surface boundary conditions for velocities (21) on $\partial \Omega_s$, the implicit relation between velocities and pseudo-velocities (25) on $\partial \Omega_s$ (with corresponding values of σ_ν and σ_s), the boundary conditions for velocities on $\partial \Omega_b$ (practically, no-slip or symmetry conditions; see (8)), the implicit relation between velocities and pseudo-velocities (25) on $\partial \Omega$, the pressure equation (26) on Ω_v and the normal dynamic condition on $\partial \Omega_{si}$ (22).

The resulting coupled linear system is solved at each iteration by the CGSTAB algorithm [22] with an incomplete LU preconditioning of the pressure block χmp only.

$$Ax = b$$

with :

$$A = \begin{bmatrix} Id & & -Id & & \chi p \\ & Id & & -Id & \chi shp \\ \chi cl & \chi cl & \chi cl & & \\ \chi u & \chi u & \chi u & Id & \\ \chi su & \chi su & \chi su & Id & \\ & & -Id & & \\ & & & \chi d & \chi d & \chi d & \chi mp \\ & & & & & \chi sp & Id \end{bmatrix}$$

$$x = \begin{bmatrix} U(\Omega \setminus \partial \Omega) \\ U(\partial \Omega_s) \\ U(\partial \Omega_b) \\ U^*(\Omega \setminus \partial \Omega) \\ U^*(\partial \Omega_s) \\ U^*(\partial \Omega_b) \\ P(\Omega_v) \\ H(\partial \Omega_{si}) \end{bmatrix}; \quad b = \begin{bmatrix} fcl \\ fu \\ fssh \\ fh \end{bmatrix} \quad (27)$$

RESULTS

Hydrodynamic loads

Forces $Rp_i(t)$ and $Rf_i(t)$ due to the pressure and the friction respectively are acting on the hull and are computed at each time step on the exact wetted part of this one. In order to compute the hydrodynamic coefficients we have to taken hydrodynamic restoring forces $Rh_{di}(t)$ into account. In formula (28), n_i represents the i^{th} component of unit normal vector pointing outside and P the total pressure :

$$\begin{aligned} Rp_i(t) + Rf_i(t) + Rh_{di}(t) = \\ - \int_{body} P n_i dS + \int_{body} \rho \cdot \nu \cdot \left(\frac{\partial u^i}{\partial x^j} + \frac{\partial u^j}{\partial x^i} \right) \cdot n_j \cdot dS \\ - \int_0^h \int_{\Gamma_0} \rho g (h - x^3) n_i dS \end{aligned} \quad (28)$$

Hydrodynamic coefficients

The prescribed forced motion in heave and pitch are given under nondimensionalised form :

$$\tilde{\eta} = \tilde{A} * \sin(\tilde{\omega} \tilde{t} + \varphi) \quad (29)$$

$$\theta = \Theta * \sin(\tilde{\omega} \tilde{t} + \varphi) \quad (30)$$

All variables are undimensionalised with the hull length L , the average forward speed U_a and the water density ρ . This leads to the following relations for : amplitude \tilde{A} , frequency $\tilde{\omega}$, motion $\tilde{\eta}$, time \tilde{t} , force \tilde{F} and torque \tilde{M} .

$$\begin{cases} \tilde{A} = \frac{A}{L}; \tilde{\omega} = 2\pi \cdot \tilde{f}; \tilde{f} = f \cdot \sqrt{\frac{L}{g}}; \tilde{\eta} = \frac{\eta}{L}; \\ \tilde{t} = t \cdot \sqrt{\frac{g}{L}}; \tilde{F} = \frac{F}{\rho \cdot g \cdot L^3}; \tilde{M} = \frac{M}{\rho \cdot g \cdot L^4} \end{cases} \quad (31)$$

The hydrodynamic loads are then expressed as a Fourier analysis :

$$\tilde{F}_\eta(\tilde{t}) = \tilde{F}_0 + \tilde{F}_1 \cos(\tilde{\omega} \tilde{t} + \varphi) + \tilde{F}_2 \sin(\tilde{\omega} \tilde{t} + \varphi) + \dots \quad (32)$$

$$\tilde{M}_\theta(\tilde{t}) = \tilde{M}_0 + \tilde{M}_1 \cos(\tilde{\omega} \tilde{t} + \varphi) + \tilde{M}_2 \sin(\tilde{\omega} \tilde{t} + \varphi) + \dots \quad (33)$$

and :

$$\tilde{F}_\eta(\tilde{t}) = \tilde{F}_0 + \tilde{C}_{a33} \frac{\partial \tilde{\eta}}{\partial \tilde{t}} + \tilde{M}_{a33} \frac{\partial^2 \tilde{\eta}}{\partial \tilde{t}^2} \quad (34)$$

$$\tilde{M}_\theta(\tilde{t}) = \tilde{M}_0 + \tilde{C}_{a55} \frac{\partial \theta}{\partial \tilde{t}} + \tilde{M}_{a55} \frac{\partial^2 \theta}{\partial \tilde{t}^2} \quad (35)$$

Finally non-dimensionalised added mass coefficients \tilde{M}_a and damping coefficients \tilde{C}_a for heave and pitch motion are obtained :

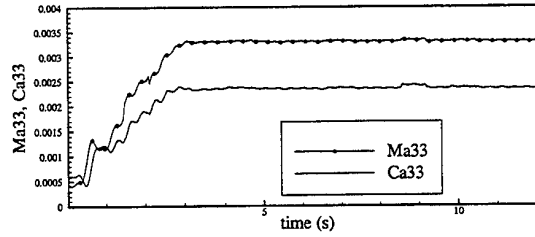


Figure 2: Hydrodynamic coefficients \tilde{M}_{a33} and \tilde{C}_{a33} versus time

for heave motion

$$\tilde{M}_{a33} = -\frac{\tilde{F}_2}{\tilde{A} \tilde{\omega}^2}; \tilde{C}_{a33} = \frac{\tilde{F}_1}{\tilde{A} \tilde{\omega}} \quad (36)$$

for pitch motion

$$\tilde{M}_{a55} = -\frac{\tilde{M}_2}{\Theta \tilde{\omega}^2}; \tilde{C}_{a55} = \frac{\tilde{M}_1}{\Theta \tilde{\omega}} \quad (37)$$

The Fourier analysis is performed in a moving window of one period long. This method allows to determine transient or stationary part of the signal versus time with accuracy. On figure 2, the hydrodynamic coefficients \tilde{M}_{a33} and \tilde{C}_{a33} are shown in function of time : transient part of the signal can be observed.

Results for a hemisphere

In order to validate the implementation of supplementary sinusoidal motions in the present RANSE solver [1] computations have first been performed for heaving hemisphere without forward speed. In such a case theoretical results [10] and experiments [4] can be found in literature. So excitation forces, hydrodynamic coefficients and pressure on hemisphere are reachable. The theoretical results have been obtained under assumption of potential flow and linearised free surface boundary conditions.

The radius of the hemisphere R is equal to 0.152 m and the entire body used in calculations or experiments is formed by a hemisphere topped by a vertical circular cylinder. The heave amplitude is $amp=0.0127$ m, leading to a nondimensionalised amplitude ratio $\frac{amp}{R}$ of 0.08. An O-O topology grid with 92169 cells (57 along the hemisphere, 49 in the radial direction and 33 in the third direction) was used in RANSE computations. The first point in the boundary layer is located at $\frac{e}{R} = 0.001$ from the hull and the numerical value of the time step is chosen in order

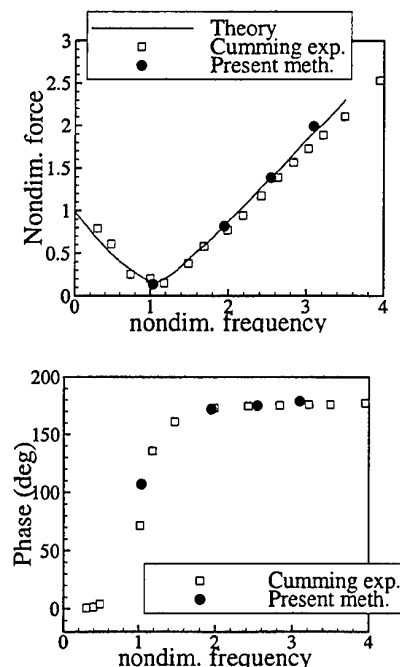


Figure 3: Non dimensional forces on semi-sphere in forced heave motion

to have 40 iterations during one period of oscillating. During the first five periods, the amplitude is gradually increased from 0 to its final value in order to manage a smooth transition. The calculations were performed at various frequencies and are shown in figures 3 to 6.

The numerical results in viscous fluid simulation are in good agreement with theoretical results but little discrepancies can be observed between present numerical results and experimental data from R. A. Cumming [4]. No computation has been undertaken for nondimensional frequency lower than 1. Under this value, experimental results are not reliable because of reflections on the walls of the wave tank walls.

The point located just under the hemisphere is defined by angle $\theta = 0$ degree and the points of the semi-sphere located on the free surface at rest are defined by the angle $\theta = 90$ degrees. For the points located at angles between 0 and twenty degrees (the top pictures of the figure 5), pressures given by computation in viscous fluid are very close from theoretical results and experimental data for low frequencies. In the high frequencies range, present results and perfect fluid flow calculations are out of phase with experiments.

For $\theta = 40$ degrees there is a good agreement between experiments, results in perfect fluid flow

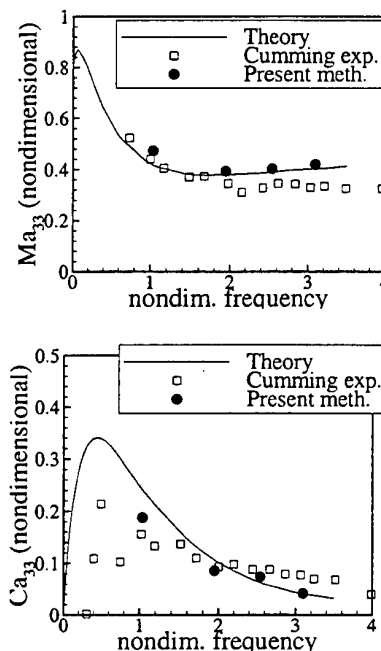


Figure 4: Added mass coefficient \widetilde{Ma}_{33} and damping coefficient \widetilde{Ca}_{33} for the semi-sphere in forced heave motion

theory and present results for all frequencies (figure 5, bottom left).

For $\theta = 80$ degrees, our results are in good agreement with theoretical results but discrepancy with experiments is noticeable (figure 5, bottom right).

Series 60 CB=0.6 in forced heave motion

Another case is the merchant ship Series 60, CB=0.6 in forced heave motion and a constant forward speed. For this case, experimental data [8] [9] and numerical results based on approximation of encounter frequency [5] in linear perfect fluid flow theory are available.

The parameters of computation are the same as those used during experiments. The Froude number is 0.2 and Reynolds number is $8.3 \cdot 10^5$. In all computations the nondimensional amplitude of forced heave motion is $\frac{am^2}{L} \simeq 0.01$. Computations have been performed on a coarse grid - 33 cells along the hull, 33 cells in the direction perpendicular to hull and 17 in the third direction - and on a finer grid - 57 cells along the hull, 49 cells in the direction perpendicular to hull and 33 in the third direction. For the coarse grid, the first node in the boundary layer is located at

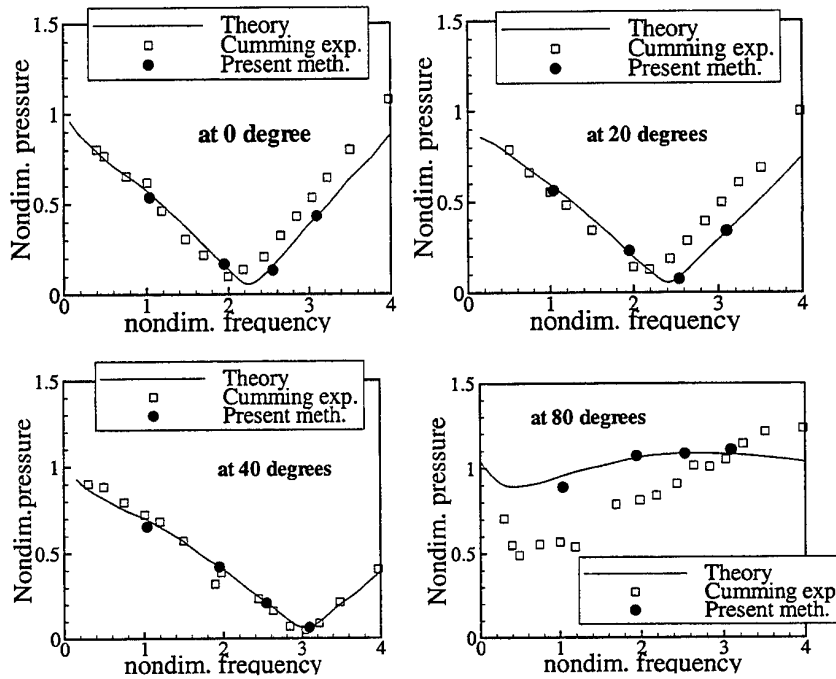


Figure 5: Nondimensional pressures on the semi-sphere

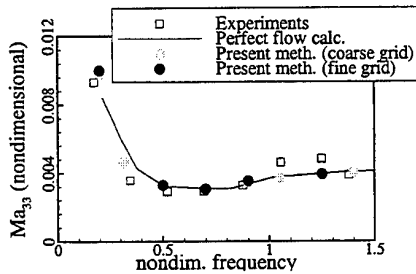


Figure 6: Added mass coefficient \widetilde{Ma}_{33} for the Series 60 in forced heave motion

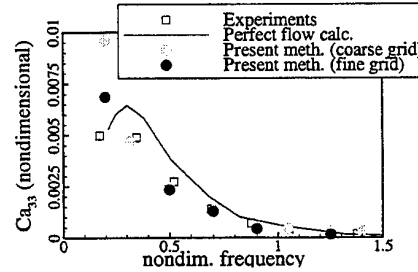


Figure 7: Damping coefficient \widetilde{Ca}_{33} for the Series 60 in forced heave motion

$\frac{\varepsilon}{L} = 1.1 \cdot 10^{-4}$ and at $\frac{\varepsilon}{L} = 8 \cdot 10^{-5}$ for the finer grid. As before we use 40 time steps per period of forced motion.

On figure 6 results given by the present method are in good agreement with experiments and perfect fluid flow calculations for the added mass \widetilde{Ma}_{33} . For the damping coefficient \widetilde{Ca}_{33} (see figure 7) the present method leads to results close to experimental data. For low frequencies, RANSE computations give results closer to experiments than perfect fluid flow theory. This highlights influence of viscosity. Computations with finer grid do not improve results except for the \widetilde{Ca}_{33} coefficient at lower frequencies (figure 7). So we can

consider that the grid convergence is almost verified for the coarser grid.

On figure 10 the turbulent viscosity is shown in several sections around the hull Series 60. One can notice an increase of turbulent viscosity near the hull and the formation of two vortices located near the stern of the hull.

Finally the wave pattern around the hull is represented on figure 11. The numerical wave damping becomes noticeable far from the hull due to the gradual increase of the cells size. A coupling between the present method and a perfect fluid flow theory seems necessary in order to increase the accuracy of the far field simulation [7].

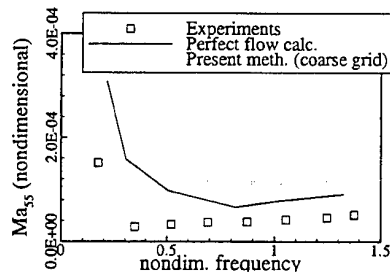


Figure 8: Added mass coefficient \widetilde{Ma}_{55} for Series 60 in forced pitch motion

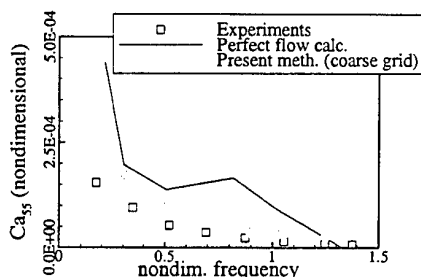


Figure 9: Damping coefficient \widetilde{Ca}_{55} for Series 60 in forced pitch motion

Series 60 CB=0.6 in forced pitch motion

Experimental results [8] [9] and numerical results [2] [3] in perfect fluid flow theory are available for Series 60 CB=0.6 in forced pitch motion with forward speed.

Computations with the previous coarse grid (33*33*17) have been performed for this case. The pitch amplitude is 1.5 degrees; that leads to a nondimensional amplitude $\frac{amp}{L} \simeq 0.013$ at the bow and at the stern of the hull.

Results for added mass and damping coefficient are shown on figures 8 and 9 respectively.

For variation of added mass coefficients versus frequency (see figure 8), present computations give overestimated results. For damping coefficients (figure 9) our results are in quite good agreement with experiments for high frequencies but experimental values for low frequencies are overestimated. Computations with finer grid should probably improve results for both added mass and damping coefficients.

CONCLUSION

Computation of three-dimensional turbulent and viscous flow with fully nonlinear free surface effects by an original fully coupled solver for velocity, pressure and free surface elevation unknowns

has been already validated for hull in rectilinear motion [1]. In the present paper this solver has extended to seakeeping with or without forward speed. For the hemisphere in forced heave motion it gives results in good agreement with theoretical results and experiments. For the hull Series 60 CB=0.6 in forced heave motion and forward speed our results are in good agreement with experiments for damping coefficient; that shows interest to take viscosity into account. For the Series 60 in forced pitch motion and forward speed, the agreement between experiments and present results is not good for added mass but it remains quite good for damping coefficient.

The results seem to show that our RANSE solver is able to simulate correctly wave radiation seakeeping problem with forward speed. A coupling method combining such RANSE solver with potential flow far field simulation is an very interesting development. Such developments have already been undertaken and are still in progress [7].

REFERENCES

1. Alessandrini A., Delhommeau G. (1995), A multigrid velocity-pressure-free surface elevation fully coupled solver for calculation of turbulent incompressible flow around a hull. 9th International Conference on Methods in Laminar and Turbulent Flows, Atlanta, 1995.
2. Brument A. (1998), Evaluation numérique de la fonction de Green de la tenue à la mer avec vitesse d'avance", Thèse de doctorat, université de Nantes.
3. Brument A., Delhommeau G., Maury C., Gaillard L., Guilbaud M. (1998), Comparison between numerical computations and experiments for seakeeping on ship's models with forward speed. Euromech, Poitiers.
4. Cumming R.A. (1963), The experimental determination of forces and pressures acting on a hemisphere oscillating on a free surface. report NA-63-1 Inst. Eng. Res. Univ. Berkeley.
5. Delhommeau G. (1987), Les problèmes de diffraction-radiation et de résistance de vagues : étude théorique et résolution numérique par la méthode des singularités. Thèse de doctorat ès Sciences, Laboratoire d'Hydrodynamique Navale, Ecole Centrale de Nantes.
6. Faltinsen O.M. (1977), Numerical solutions of transient nonlinear free-surface motion outside or inside moving bodies. Proc. 2nd Int. Conf.

on Num. Ship Hydrodyn. Univ. of California, Berkeley, 347-357.

7. Guillermin P.E. et Alessandrini A. (1999), 3D RANSE-Potential coupling using a Fourier-Kotchin approach. Seventh Numerical Ship Hydrodynamics, Nantes.

8. Guyot F. (1995), Etude expérimentale de la résistance ajoutée d'une maquette de navire soumise à des oscillations forcées harmoniques. Etude du champ de vagues instationnaires associé. Thèse de doctorat, Université de Poitiers.

9. Guyot F. et Guilbaud M. (1995), Force and free surface elevation measurements on a serie 60 CB=0.6 ship model in forced oscillations. Proc. 5th ISOPE conference, La Haye.

10. Havelock T.H. (1955), Waves due to a floating sphere making periodic heaving oscillations. Proc. Royal Soc. serie A vol. 231 pp.1-7.

11. Havelock T.H., The pressure of water waves on a fixed obstacle. Proc. Roy. Soc. vol A 175 London pp. 409-421.

12. John F., On the motion of floating bodies (1 and 2). Communication on pure and applied mathematics Vol. 2 and 3 New York.

13. Korvin-Kroukowski B.V. (1961), Theory of Seakeeping. S.N.A.M.E. New York.

14. Kring D., Huang Y.-F., Sclavounos P. (1996), Nonlinear Ship Motions and Wave-Induced Loads by a Rankine Method. 23th Symposium on Naval Hydrodynamics, Trondheim, Norway.

15. Menter F.R. (1993), Zonal two equation $k - \omega$ turbulence models for aerodynamics flows. AIAA Paper, 93-2906, Fluid Dynamics Conference, Orlando.

16. Nichols B.D., Hirts C.W. (1977), Non linear Hydrodynamic forces on floating bodies. Proc. 2nd Int. Conf. on Num. Ship Hydrodyn. Univ. of California, Berkeley, 382-394.

17. Ohkusu M., Iwashita H. (1991), Evaluation of the Green Function for Ship Motions at Forward Speed and Application to Radiation and Diffraction Problems. 4th International Workshop on Water Waves and Floating Bodies, Norway.

18. Patankar S.V. (1980), Numerical Heat Transfert and Fluid Flow. Series in Computational Methods in Mechanics and Thermal Sciences, Mac Graw Hill Book Compagny.

19. Rhie C.M., Chow W.L. (1983), A Numerical Study of the Turbulent Flow Past an

Isolated Airfoil with Trailing Edge Separation. AIAA Journal.

20. Sclavounos P.D., Nakos D.E. (1988), Stability Analysis of Panel Methods for Free Surface Flows with Forward Speed. 17th Symposium on Naval Hydrodynamics, The Hague, The Netherlands.

21. Telste J.G. (1985), Calculation of fluid motion resulting from large amplitude forced heave motion of two dimensionnal cylinder in a free surface. Proc. fourth Int. Conf. on Numerical Ship Hydrodynamics, Washington D. C.

22. Van der Vorst H.A. (1992), BiCGSTAB : a fast and smoothly converging variant of Bi-CG for the solution of non-symmetric systems. J. Sci. Stat. Comp. vol 13.

23. Wehausen J.V., Laitone E. (1960), Surface waves. Handbuch der physik vol. 9 Springer Verlag.

24. Wilcox D.C. (1988), Multiscale model for turbulent flows. AIAA journal, vol. 26, pp. 1211-1320.

25. Wilcox D.C. (1988), Reassessment of the scale determining equation for advanced turbulence models. AIAA journal, vol. 26, pp. 1299-1310.

26. Yeung R.W., Ananthakrishnan P. (1992), Oscillation of a floating body in a viscous fluid. Journal of Engineering Mathematics 26, 211-230, 1992.

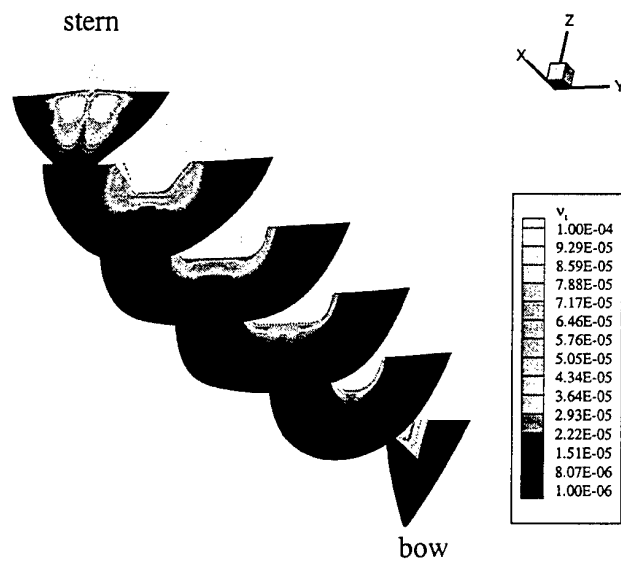


Figure 10: Turbulent viscosity for forced heave motion with forward speed

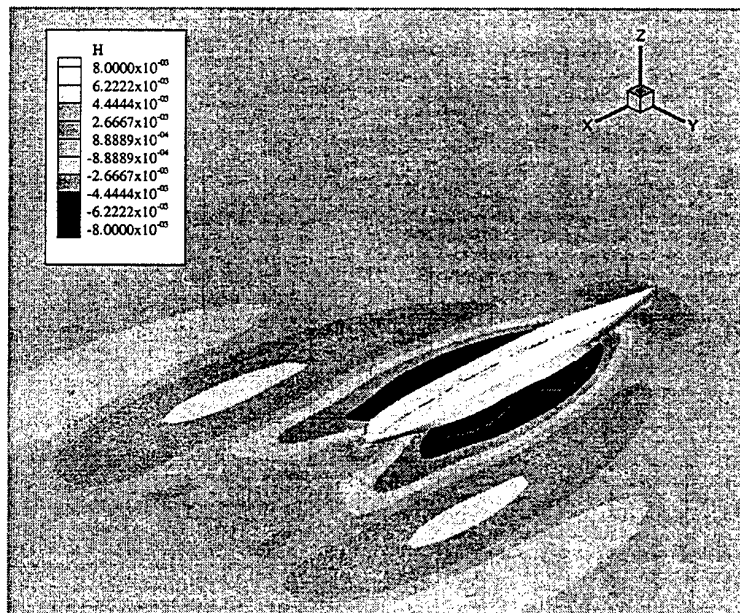


Figure 11: Free surface field around hull for forced heave motion with forward speed

A FINITE ELEMENT METHOD APPLIED TO UNSTEADY VISCOUS FLOW AROUND 2D BLUNT BODIES WITH SHARP CORNERS

Rune Tønnessen¹, Odd M. Faltinsen¹ and Torbjørn Utnes²

¹Faculty for Marine Technology, Norwegian University of
Science and Technology (NTNU), N-7491 Trondheim, Norway

²SINTEF Applied Mathematics, N-7491 Trondheim, Norway

ABSTRACT

A computer code based on the Finite Element Method has been developed for the incompressible 2D Navier-Stokes equations. The momentum equations are projected onto a divergence free velocity field by the semi-implicit Fractional-Step formulation. For oscillating flow a second order time integration scheme is applied whereas a first order scheme is used for steady ambient flow. The emphasis has been on flow around sharp corners. Weaknesses with linear triangular elements and with lumped mass matrix approximation were discovered and corrected for. A problem of numerical instability at the outflow boundary was solved by introducing a turbulent wake. Detailed studies of ambient steady and oscillating crossflow past a flat plate were carried out. Mesh refinement towards the tip was important, but only during the period of the formation of the vortex street. Mesh refinement was shown to be less important for low- and moderate KC-number oscillating flow. Conservation of mass and momentum was shown. Results for oscillating ambient flow compare well with experimental results.

INTRODUCTION

The need for a consistent method to calculate the eddy making damping of ships with bilge keels has been the main motivation for this work. Since the main contribution to the viscous damping comes from the bilge keels, the method will have to accurately calculate the vortex shedding from a flat plate in ambient flow normal to the plate. Other methods, such as vortex sheet methods, e.g. [1, Braathen & Faltinsen] have shown good results in this respect but have proven to be less robust. Another possibility is to use the vortex-in-cell method in combination with the Operator Splitting Technique. This has for instance been used by Scolan & Faltinsen [2]. Good results were demonstrated. We have decided in this paper to use the Finite Element Method to solve the Navier-Stokes equations. The current method represents a further development of the method by Herfjord [4]. Further studies should include the combined effect of free surface waves and forward speed (Faltinsen [3]).

A semi-implicit projection method frequently denoted the Fractional-Step method [6] has been applied in combination with the Finite Element method, ref. [7] and [8]. First an ambient steady flow past a diamond square was studied. Using linear triangular elements in combination with a lumped mass

matrix resulted in an unphysical asymmetric flow. It was shown that higher order element interpolation in combination with a consistent mass matrix solved this problem. A traction free condition was applied on the outflow boundary. This is a frequently used condition that has proven to work for boundaries far downstream of the body. The implementation of a consistent mass matrix then introduced a problem of instability at this boundary. A numerical beach, obtained by adding eddy viscosity consistent with the turbulent wake theory [9] resolved this problem, leaving no upstream effect. The steady ambient flow normal to a flat plate was also studied. Steady state drag forces are greatly overpredicted compared to experimental results, but are in good agreement with other numerical results. It was found that the mesh refinement towards the tip of the plate was important, but only during vortex street formation. Finally, the ambient oscillating cross flow past a flat plate was studied. To achieve proper conservation of momentum, a scheme correct to second order was required. It was found little mesh dependency for this case, and the results showed good agreement with experimental results for the considered KC number range. It was shown that the flow might change its main characteristics during a time series, especially for KC numbers around 7. This implies that the estimated drag and mass coef-

ficients will be strongly influenced by the time window used for the analysis. The study also revealed the importance of plate thickness and edge sharpness, which is considerable even for oscillating flow at low KC-numbers.

THE FINITE ELEMENT FORMULATION

Two dimensional laminar flow of an incompressible fluid around a fixed bluff body in infinite fluid is considered. Gravity is neglected. The governing equations are the Navier-Stokes equations and the continuity equation, i.e.

$$\frac{\partial \mathbf{u}}{\partial t} + (\mathbf{u} \cdot \nabla) \mathbf{u} = -\frac{1}{\rho} \nabla p + \nu \nabla^2 \mathbf{u}, \quad (1)$$

$$\nabla \cdot \mathbf{u} = 0. \quad (2)$$

$\mathbf{u} = (u, v)^T$ is the velocity vector in the 2D plane, p is the pressure, ρ is the mass density and ν is the kinematic viscosity coefficient. t means the time variable.

The Reynolds number is defined as $Re = \frac{U D}{\nu}$ for steady ambient flow, and as $Re = \frac{U_A D}{\nu}$ for unsteady ambient flow. Here U is the steady ambient flow velocity, U_A the velocity amplitude of the oscillating ambient flow and D a characteristic cross-sectional dimension. The equations are non-dimensionalized in the numerical solution procedure.

The equations have been solved by the Fractional-Step formulation [6]. The method projects the Navier-Stokes equations onto a divergence free velocity field and enables an explicit solution procedure including an implicit pressure term. Let superscript n denote the time step number so that $t^{n+1} = t^n + \Delta t$. The time-discretized non-dimensionalized Navier-Stokes equations may be written

$$\mathbf{u}^{n+1} = \mathbf{u}^n - \Delta t (\theta \nabla p^n + (1 - \theta) \nabla p^{n+1}) - \int_{t^n}^{t^{n+1}} ((\mathbf{u}^n \cdot \nabla) \mathbf{u}^n - \frac{1}{Re} \nabla^2 \mathbf{u}^n) dt. \quad (3)$$

This is a semi-implicit equation in p if $0 \leq \theta < 1$ and fully explicit if $\theta = 1$. The Fractional-Step formulation consists of three steps. A fully explicit time integration of the velocity terms is performed in Step-1. Normally pressure terms are excluded from this scheme, but the present method may also include a pressure term from the previous time step n . If $\theta = 0.5$, the scheme will be correct to second order in pressure as well as in velocity. Several explicit time integration methods may be used for the advection-diffusion parts. We have chosen a version of the Taylor-Galerkin method [10] but adding the pressure terms. Step-1 is then

$$(a) \quad \tilde{\mathbf{u}}^{n+\frac{1}{2}} = \mathbf{u}^n - \frac{\Delta t}{2} (\mathbf{u}^n \cdot \nabla) \mathbf{u}^n$$

$$- \frac{\Delta t}{2} \theta \nabla p^n \quad (4)$$

$$(b) \quad \hat{\mathbf{u}}^{n+1} = \mathbf{u}^n - \Delta t (\tilde{\mathbf{u}}^{n+\frac{1}{2}} \cdot \nabla) \tilde{\mathbf{u}}^{n+\frac{1}{2}} - \Delta t \theta \nabla p^n \quad (5)$$

$$(c) \quad \tilde{\mathbf{u}}^{n+1} = \hat{\mathbf{u}}^{n+1} + \Delta t \frac{1}{Re} \nabla^2 \hat{\mathbf{u}}^{n+1} \quad (6)$$

Here $\tilde{\mathbf{u}}$ is an intermediate variable so that

$$\mathbf{u}^{n+1} = \tilde{\mathbf{u}}^{n+1} - \Delta t (1 - \theta) \nabla p^{n+1} \quad (\text{Step-3}) \quad (7)$$

according to eq. (3). Since \mathbf{u}^{n+1} is a divergence free velocity field while $\tilde{\mathbf{u}}$ is not, the divergence of (7) gives the following Pressure Poisson Equation (PPE)

$$\nabla^2 p^{n+1} = \frac{1}{\Delta t (1 - \theta)} \nabla \cdot \tilde{\mathbf{u}}^{n+1}. \quad (\text{Step-2}) \quad (8)$$

This is valid for $\theta < 1$.

The Fractional-Step formulation is combined with the Galerkin Finite Element formulation. Both triangular and quadrilateral elements are used to discretize the computational domain (Ω). According to the Finite Element approximation

$$u(\mathbf{x}, t) \approx \sum_{i=1}^{nel} N_i^e(\mathbf{x}) u_i^e = \mathbf{N}^e T \mathbf{u}^e, \quad (9)$$

$$v(\mathbf{x}, t) \approx \sum_{i=1}^{nel} N_i^e(\mathbf{x}) v_i^e = \mathbf{N}^e T \mathbf{v}^e, \quad (10)$$

$$p(\mathbf{x}, t) \approx \sum_{i=1}^{nel} N_i^e(\mathbf{x}) p_i^e = \mathbf{N}^e T \mathbf{p}^e, \quad (11)$$

where \mathbf{x} is a spatial vector pointing into element e . $\mathbf{N}^e T = [N_1^e N_2^e \dots N_{nel}^e]$ are interpolation functions over the element e , and nel is the number of nodes for the element, being 3 for triangular elements and 4 for quadrilateral elements. $\mathbf{u}^e = [u_1^e u_2^e \dots u_{nel}^e]$, $\mathbf{v}^e = [v_1^e v_2^e \dots v_{nel}^e]$ and $\mathbf{p}^e = [p_1^e p_2^e \dots p_{nel}^e]$ as the vectors of the primary variables defined at the nodes of the element, and $\mathbf{u}, \mathbf{v}, \mathbf{p}$ are the vectors containing the nodal values of the primary variables of the whole mesh. This means that \mathbf{u} used in combination with the Finite Element Method is different from \mathbf{u} defined in combination with eqs. (1)-(8).

The second order derivatives are reduced to first order by the *weak formulation*. We may therefore use linear interpolation functions N_i^e , $i = 1, \dots, nel$. N_1^e to N_{nel}^e are also used as weighting functions (Galerkin method). The choice of equal order interpolation functions can create spurious pressure modes (Babuska-Brezzi condition [7]) but the Fractional-Step method circumvents this problem. However the pressure term in Step-1 is likely to create such modes.

Guermond and Quartapelle [11] circumvent this by a mixed interpolation procedure.

The Fractional-Step procedure may now be written in matrix form as:

Step-1:

x-direction:

$$(a) \quad M \tilde{u}^{n+1/2} = M u^n - \frac{\Delta t}{2} A^n u^n + \frac{\Delta t}{2} \theta (D_x^T p^n - D_{Sx}(p^n)) \quad (12)$$

$$(b) \quad M \hat{u}^{n+1} = M u^n - \Delta t A^{n+1/2} \tilde{u}^{n+1/2} + \Delta t \theta (D_x^T p^n - D_{Sx}(p^n)) \quad (13)$$

$$(c) \quad M \tilde{u}^{n+1} = M \hat{u}^{n+1} + \frac{\Delta t}{Re} L \hat{u}^{n+1} \quad (14)$$

Similar we get in the y-direction by replacing u by v , \tilde{u} by \tilde{v} , \hat{u} by \hat{v} , D_x^T by D_y^T and D_{Sx} by D_{Sy} .

Step-2:

$$L p^{n+1} = -\frac{1}{\Delta t(1-\theta)} (D_x \tilde{u}^{n+1} + D_y \tilde{v}^{n+1}) + N_S(p^{n+1}) \quad (15)$$

Step-3 on standard form (used when $\theta = 0$):

$$M u^{n+1} = M \tilde{u}^{n+1} - \Delta t D_x p^{n+1} \quad (16)$$

$$M v^{n+1} = M \tilde{v}^{n+1} - \Delta t D_y p^{n+1} \quad (17)$$

Step-3 on weak form in p -terms (used when $\theta > 0$):

$$M u^{n+1} = M \tilde{u}^{n+1} + \Delta t (1-\theta) D_x^T p^{n+1} - \Delta t (1-\theta) D_{Sx}(p^{n+1}) \quad (18)$$

$$M v^{n+1} = M \tilde{v}^{n+1} + \Delta t (1-\theta) D_y^T p^{n+1} - \Delta t (1-\theta) D_{Sy}(p^{n+1}) \quad (19)$$

The equation system is reduced to the weak form by integrating the diffusion terms by parts leaving a line integral as well as the weak diffusion term. In eq. (14) and the corresponding expression in the y-direction the line integrals at the outer boundaries are zero by using the Traction free condition. This has relevance for steady ambient flow. The velocity Dirichlet conditions on the body result in no contribution from the line integrals along the body surface.

The pressure parts in eqs. (12), (13), (18) and (19) have been written on a weak form. The resulting line integrals include Dirichlet values of the pressure. In oscillatory ambient flow, the pressure is known at the outer boundaries and implemented in the line integrals.

In the present studies $\theta = 0$ for steady ambient flow and $\theta = 0.5$ for oscillating ambient flow, when a higher order time discretization in the pressure is required.

The matrices are defined as

$$M = \int_{\Omega} N^T N d\Omega \quad (20)$$

$$D_x = \int_{\Omega} N_{,x}^T N d\Omega, \text{ where } N_{,x} = \frac{\partial N}{\partial x} \quad (21)$$

$$D_y = \int_{\Omega} N_{,y}^T N d\Omega \quad (22)$$

$$L = \int_{\Omega} N_{,x}^T N_{,x} d\Omega + \int_{\Omega} N_{,y}^T N_{,y} d\Omega \quad (23)$$

$$A^n = \sum_{Nel} (\bar{u}^n D_x^e + \bar{v}^n D_y^e) \quad (24)$$

$$D_{Sx} = \int_{S_D} N n_x dS \quad (25)$$

$$D_{Sy} = \int_{S_D} N n_y dS \quad (26)$$

$$N_S = \int_{S_N} N_{,n} dS, \text{ where } N_{,n} = \frac{\partial N}{\partial n} \quad (27)$$

where M is the mass matrix, $D = (D_x, D_y)$ is the divergence matrix (D_x^e and D_y^e being element divergence matrixes) and L is the Laplacian matrix. S_D is the part of the boundary where a Dirichlet condition for the pressure is enforced and S_N is the part of the boundary where a pressure Neumann condition is enforced. The advection matrix A^n is simplified by the *centroid advection* method (Gresho et al. [12]). This saves considerable computational time without loosing accuracy. \bar{u}^n and \bar{v}^n are the averaged nodal values of the velocity at time step n and Nel is the total number of elements in the mesh.

The diagonal dominance of the mass matrix makes the equation systems in Step-1 and Step-3 easy to solve. An approximate solution can be found by lumping the mass matrix. This means projecting all non-diagonal matrix elements onto the diagonal. This gives an uncoupled equation system. However lumping will induce dispersion in advection dominated flows, and as we will see later, may lead to non-physical asymmetric flow around a symmetric body. We will demonstrate the benefit of using a Jacobi-iteration procedure to obtain a solution consistent with the non-lumped mass matrix.

Step-2 solves the Poisson equation. This leads to a linear equation system $Ax = b$. The A matrix is not diagonal dominant and have to be solved by an inverting process. We use Gaussian elimination process. The upper triangle of A is compactly stored in so-called Skyline matrix, [13]. Since the mesh is

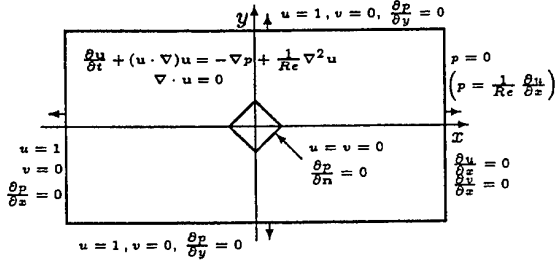


Figure 1: The boundary value problem (BVP) for steady ambient flow past a blunt body

fixed throughout the simulation, the time consuming triangularization process is only carried out once.

Our governing equations are general in the sense that they may solve problems that are both elliptic, hyperbolic and parabolic in nature. The flows currently studied will be a mixture of all. This generality must be reflected in the complete boundary value problem (BVP). Since the Pressure Poisson Equation (PPE) is elliptic, a closed boundary value problem is required in order to have a well posed equation system. Fig. 1 shows the BVP for a steady ambient flow around a diamond square. The unit normal vector on the body is pointing into the body.

We distinguish between essential boundary conditions and natural boundary conditions. The essential boundary conditions are most often of Dirichlet type and are implemented by enforcing the desired Dirichlet value onto the selected boundary nodes. The natural boundary conditions consist of line integrals occurring as a consequence of the weak formulation. The integrand consists of a weighted normal derivative (Neumann type). Neglecting the integral will weakly enforce (in an integrated manner) a zero normal derivative on this boundary. When the ambient flow is oscillatory, inviscid flow is assumed outside the computational domain. (This is difficult to satisfy for very high Keulegan-Carpenter numbers and if vortex pairing occurs. Vorticity may as a consequence be convected far away). The inviscid solution can then be used to express the boundary condition for u^{n+1} at the outer boundary. If the ambient oscillatory flow is planar with velocity $u_0 = U_A \sin \omega t$ and $v_0 = 0$, it follows that eq. (7) can be rewritten as

$$\bar{u}^{n+1} = U_A \sin \omega t^{n+1} - \Delta t (1 - \theta) U_A \omega \cos \omega t^{n+1} \quad (28)$$

and $\bar{v}^{n+1} = 0$.

On the body boundary we use ∇p^n instead of ∇p^{n+1} since ∇p^{n+1} is not known a priori. We also neglect the normal derivative of the pressure since the variation of pressure normal to the boundary layer is

of higher order [9][Ch. VII]. However, this may be questionable around a separation point. The boundary condition can be written

$$\bar{u}^{n+1} = \Delta t (1 - \theta) \tau_x \frac{\partial p^n}{\partial \tau} \quad (29)$$

$$\bar{v}^{n+1} = \Delta t (1 - \theta) \tau_y \frac{\partial p^n}{\partial \tau} \quad (30)$$

by using eqs. (16) and (17), and that $u^{n+1} = 0$ and $v^{n+1} = 0$ on the body. $\tau = (\tau_x, \tau_y)$ is the unit vector tangential to the body. For simplicity this body boundary condition (b.b.c.) is also used for the other intermediate velocities used in the Taylor-Galerkin scheme.

The same type of body boundary conditions are used by e.g. [14] who used the Finite Difference method. Chorin [6], did also use a special boundary condition for \bar{u}^{n+1} . Since then, most authors applying the Fractional-Step formulation simply use the same condition for \bar{u}^{n+1} as for u^{n+1} . This may be acceptable as long as the variation of pressure tangential to the body is small. But, the flow around the tip of a flat plate accelerates strongly when approaching the tip. Hence $\frac{\partial p^n}{\partial \tau}$ may have a significant value in this area. This is why the boundary conditions (29) and (30) should be applied in flows around sharp edged bodies.

Let us assume that correct body boundary conditions were applied throughout Step-1 in the Fractional-Step method. Then, after the pressure correction in Step-3 (eq.7), u^{n+1} would end up with the value assumed for the velocity Dirichlet condition on the boundary, revealing a no-slip condition. In any case, the correct boundary condition for u^{n+1} will be enforced after the operations in Step-3 is completed. This will locally result in a flow field that does not satisfy the continuity equation. We will now illustrate how much u^{n+1} deviate from the correct b.b.c before u^{n+1} is set equal to zero. Impulsively started cross flow at constant speed past a flat plate is investigated. Fig. 2 shows the average value of u^{n+1} (left) and v^{n+1} (right) over the plate before the b.b.c. is enforced in Step-3. Since the correct velocity on the body is zero, this gives a measure on the error in velocity accumulated on this body during one time step. We note that the v -velocity (almost parallel to the plate) is very well predicted with the introduction of the more consistent b.b.c for \bar{u}^{n+1} (eqs. (29) and (30)). The velocity normal to the plate (left) is not so much influenced by this b.b.c. An error source in the formulation is that $\frac{\partial p}{\partial n}$ is neglected on the body.

Let us now consider the outflow boundary condition and analyze a fixed body in steady ambient flow. After some time vorticity will cross the downstream

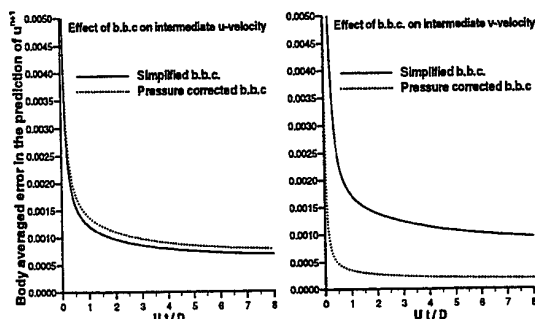


Figure 2: Impulsively started flow normal to a flat plate. The error in predicted velocity u^{n+1} (left) and v^{n+1} (right) averaged over the body, as a function of non-dimensionalized time.

boundary. A physically correct boundary condition is difficult to formulate at the outer boundary. The traction free condition ([15] and [16]) is most frequently used. It states the following Dirichlet condition for the pressure

$$p = \mu \frac{\partial u}{\partial x} \quad (31)$$

and

$$\frac{\partial v}{\partial x} = 0 \quad (32)$$

equivalent to the natural boundary condition $\frac{\partial v}{\partial x} = 0$. The pressure condition is most often simplified to a $p = 0$ Dirichlet condition without any impact on the result. $\frac{\partial p}{\partial x} = 0$ is another outflow condition that might be applied. This condition is consistent with the mean wake flow solution far downstream from the body [9]. But it does not account for unsteady flow due to vortex shedding. Neither of the above mentioned conditions represent the actual physics at the outflow boundary. However, a pressure condition is required in order to close the Boundary Value Problem. We used a $p = 0$ condition, but experienced serious instability problems at the outflow boundary for denser meshes. These instability problems occurred also when using eq. (31) and were not due to stability constraints reflected by the cell Courant number. If this had been the case, the instability should have occurred close to the body and especially close to the corners of the body where the elements are small and the velocity high.

The numerical instability problem at the outer downstream boundary has been cured by introducing a numerical beach far downstream. This numerical beach has a physical explanation. The present formulation assumes laminar flow. In reality this is valid for quite high Reynolds numbers close to the body. But the wake becomes turbulent at relatively

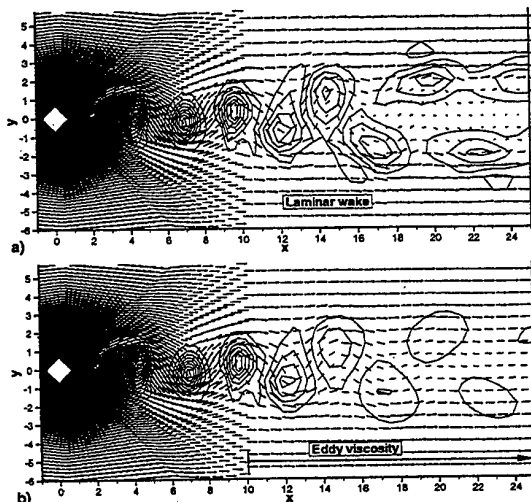


Figure 3: The effect of eddy viscosity added in the wake (b) relative to a laminar wake (a). Eddy viscosity is added in (b) from $x=10$, increasing smoothly to $x=15$, and being at its maximum thereafter. Both velocity vectors and vorticity contours are plotted. The contour lines in (a) and (b) represent equivalent vorticity levels.

low Reynolds numbers. We therefore decided to use a turbulent formulation in the wake behind a body in steady ambient flow. The eddy viscosity formulation by Schlichting [9] was used. In the wake, ν was replaced smoothly by the eddy viscosity coefficient

$$\nu_e = 0.0222 U \overline{Cf_x} D. \quad (33)$$

$\overline{Cf_x}$ is the mean value of the drag coefficient (Cf_x) taken over one vortex shedding period and is continuously calculated during the simulation. The effect of introducing eddy viscosity is illustrated in fig. 3.

As part of the verification process we check the conservation of mass and momentum. To obtain a measure on how well the mass is conserved, we integrate the left hand side of eq. (2) over the domain (Ω), and call this $\frac{dV}{dt}$, i.e.

$$\frac{dV}{dt} = \int_{\Omega} \nabla \cdot \mathbf{u} d\Omega = \int_S (n_x u + n_y v) dS. \quad (34)$$

We can interpret $\rho dV/dt$ as the time rate of change of computational fluid mass. $\frac{dV}{dt}$ should of course be zero. This is what we have to check by calculating the right hand side of eq. (34). We relate the degree of mass conservation achieved to the non-dimensionalizing emptying time

$$T_e[-] = \frac{A_{\Omega}}{\frac{dV}{dt}}. \quad (35)$$

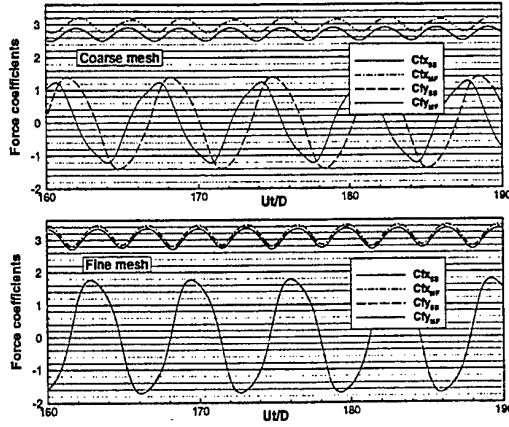


Figure 4: Steady ambient cross-flow past a diamond square. Conservation of momentum is shown by calculating the force coefficients based on integrating the stress over the body (SB) and by using conservation of fluid momentum (MF) respectively. Convergence with respect to mesh fineness is shown.

Since the equations have been non-dimensionalized by U (or U_A) and D , it means that T_e is emptying time times U (or U_A) divided by D .

The momentum in the x - and y - directions within the fluid domain Ω are defined by

$$\mathbf{M} = (M_x, M_y)^T = \rho \int_{\Omega} \mathbf{u} d\Omega. \quad (36)$$

Applying the transport theorem and using the Navier-Stokes equations (1) give

$$\begin{aligned} \frac{d\mathbf{M}}{dt} = & -\rho \int_{S_O} \mathbf{n} \cdot (\mathbf{u} \mathbf{u}) dS - \int_{S_B + S_O} \mathbf{n} p dS \\ & + \rho \int_{S_B + S_O} \nu_e \mathbf{n} \cdot \nabla \mathbf{u} dS - \rho \int_{\Omega} \frac{\partial \nu_e}{\partial x} \frac{\partial \mathbf{u}}{\partial x} d\Omega \end{aligned} \quad (37)$$

The force on the body is calculated using the x - and y -component of eq. (37). The integrals over the body (S_B) are the force obtained by direct integration of stresses over the body (SB). The remaining part of the equation gives us the force based on conservation of fluid momentum (MF). Comparison of SB and MF is a good measure of the quality of the numerical procedure and the chosen mesh. If SB and MF deviate significantly like in fig. 4, we know that the mesh has to be refined. If SB and MF are very close, it does not necessarily mean that the mesh with the closest value of SB and MF is the most converged result.

The forces are non-dimensionalized as

$$Cfx = \frac{Fx}{\frac{1}{2} \rho U^2 D}, \quad (38)$$

$$Cfy = \frac{Fy}{\frac{1}{2} \rho U^2 D}. \quad (39)$$

Cfx and Cfy are the in-line and transverse force coefficients, or drag- and lift coefficients. D used for the diamond square is the length of one of the sides. When not otherwise stated, D for the flat plate is the width of the plate.

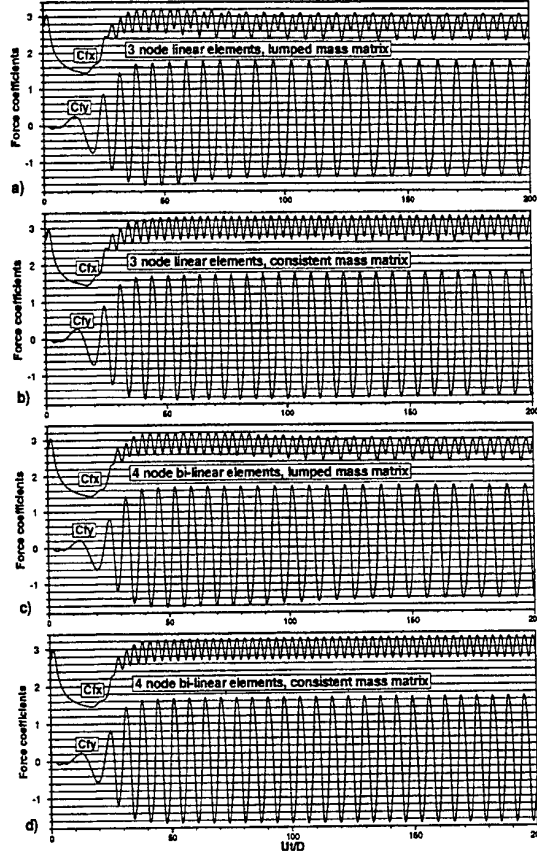


Figure 5: Lift (Cfy) and drag (Cfx) coefficients for a diamond square in steady ambient flow. $Re=200$. The effect of consistent relative to lumped mass matrix is shown and the effect of linear triangular elements relative to bi-linear quadrilateral elements is shown. It is shown that a mesh with elements of higher order than the linear triangular element, and a consistent mass matrix is needed in order to obtain symmetric vortex shedding.

During the present study the code went through a number of serious changes, some of them due to instability problems, but others due to problems now to be discussed.

The original code used linear triangular elements, lumped mass matrix and a Forward Euler time integration scheme for the advection diffusion part, with Balancing Tensor Viscosity (BTV) added to compensate for the under-diffusivity of the Euler scheme. This is similar to [4]. However this code showed a weakness when applied to a diamond square in steady ambient flow. For this case $\theta = 0$ is applied. Fig. 5 (a) shows that the force coefficient in the transverse direction (C_{fy}), or lift coefficient, has a non-zero mean. This is believed to be non-physical. The in-line force coefficient (C_{fx}) has also an unexpected behavior indicating that the vortices shed from the upper and lower corners of the diamond square are not of opposite strength. It was found that both a consistent mass representation, in contrast to a lumped mass matrix, as well as an element representation with higher degree of accuracy than the linear triangular elements were necessary to obtain a symmetric lift force. Fig. 5 (b) demonstrates that a consistent mass representation helps but is not sufficient to keep the mean flow symmetric. Fig. 5 (c) shows that increasing the accuracy of the element representation is still not sufficient by itself.

The behavior of the force curves in figs. 5 (a)-(c) implies periodic asymmetry of the flow. This asymmetry is visualized in figs. 6 (a) and (b). Figs. 6 (c) and (d) representing the zero mean lift case in fig. 5 (d) show vortical regions that looks mirrored as expected. The two plots represent the vortical scenario when the lift force is at its minimum and maximum respectively. Even small details in (c) are represented mirrored in (d). This is absolutely not the case in fig 6 (a) and (b) representing the flow calculated by using linear triangular elements in combination with a lumped mass matrix. The vortices shed from the upper and lower corners are looking quite different. We will elaborate more on the use of a consistent mass matrix and why we should avoid linear triangular elements.

Eqs.(12) to (14) and eqs. (16) to (19) can be written as

$$\mathbf{M} \mathbf{u} = \mathbf{f}. \quad (40)$$

Similarly can be done for the \mathbf{v} -velocity. \mathbf{M} is the mass matrix and \mathbf{f} the vector containing everything on the right hand side, and (\mathbf{u}, \mathbf{v}) is the velocity at any stage in the Fractional-Step formulation. Now, our initial solution \mathbf{u}_k and \mathbf{v}_k when $k = 1$, is obtained using the lumped mass matrix \mathbf{M}_L . Correcting this solution according to the consistent mass, the follow-

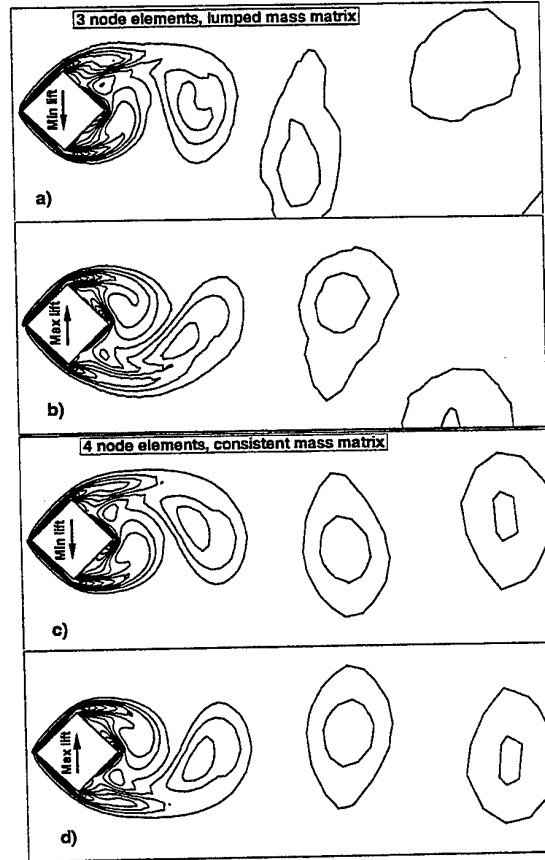


Figure 6: Vorticity contours are plotted at times representing maximum and minimum lift force. The effect of linear triangular elements in combination with a lumped mass matrix is shown in (a,b) (equivalent to fig. 5 (a)) The effect of quadrilateral elements in combination with consistent mass matrix is shown in (c,d) (equivalent to fig. 5 (d))

ing Jacobi-iteration scheme may be used

$$\mathbf{u}_{k+1} = \mathbf{u}_k + \mathbf{M}_L^{-1}(\mathbf{f} - \mathbf{M} \mathbf{u}_k) \quad (41)$$

Alternatively, and much more computationally efficient, is to rewrite the equations in the form

$$\mathbf{M} \Delta \mathbf{u} = \hat{\mathbf{f}}, \quad (42)$$

where $\Delta \mathbf{u}$ may be either $\hat{\mathbf{u}}^{n+\frac{1}{2}} - \mathbf{u}^n$ according to eq. (12), $\hat{\mathbf{u}}^{n+1} - \mathbf{u}^n$ or $\hat{\mathbf{u}}^{n+1} - \hat{\mathbf{u}}^{n+1}$ according to eqs. (13) and (14), or $\mathbf{u}^{n+1} - \hat{\mathbf{u}}^{n+1}$ according to eqs. (16) and (18).

The Jacobi-iteration scheme now takes the form

$$\Delta \mathbf{u}_{k+1} = \Delta \mathbf{u}_k + \mathbf{M}_L^{-1}(\hat{\mathbf{f}} - \mathbf{M} \Delta \mathbf{u}_k). \quad (43)$$

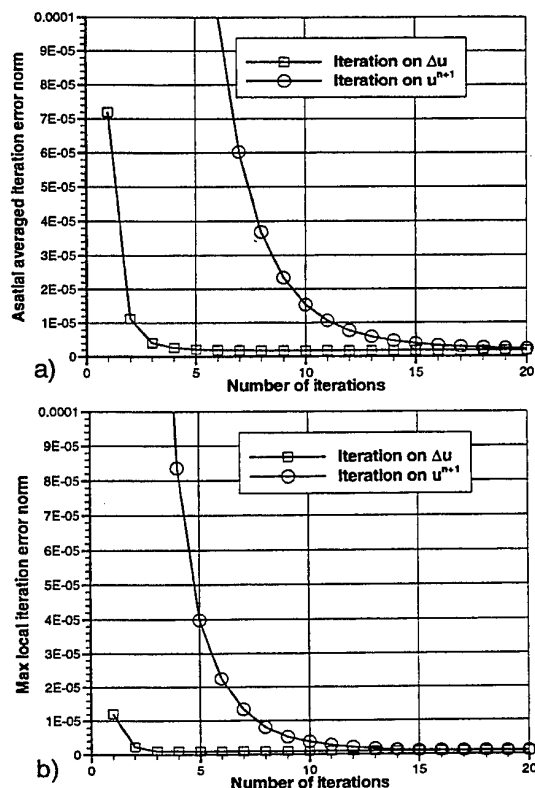


Figure 7: Convergence of Jacobi-iteration schemes (43) (iteration on Δu) and (41) (iteration on u). (a) shows the field averaged iteration error norm. (b) shows the maximum local iteration error norm. The local iteration error norm is defined as $\sqrt{(u_{k+1} - u_k)^2 + (v_{k+1} - v_k)^2}$.

The latter scheme is according to [7] while the first is used by e.g. [18]. Scheme (41) results in more operations per iteration loop than scheme (43), and converges considerably slower. This is shown in fig. 7 (a) where the field averaged iteration error norm for each scheme is plotted. In fig. 7 (b) the maximum iteration error norm within the field is plotted. The spatial iteration error norm is defined as $\sqrt{(u_{k+1} - u_k)^2 + (v_{k+1} - v_k)^2}$. Both figures show that scheme (41) needs only 3 to 5 iterations to converge while scheme (43) requires about 15 iterations. If scheme (43) is used without reaching proper convergence, the field will be over-diffusive. Using only 1 iteration with this scheme, resulted in no vortex shedding even for a sharp edged body.

Now, why should linear triangular elements not be used in this kind of problem? The reason is that the element Laplacian matrix for elements with a right angle does not include any coupling terms between

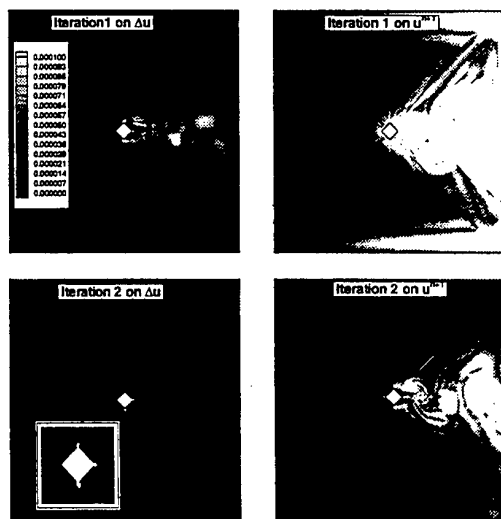


Figure 8: Spatial ratio of convergence for the Jacobi iteration schemes (43) (left) and (41) (right). The spatial iteration error norm ($\sqrt{(u_{k+1} - u_k)^2 + (v_{k+1} - v_k)^2}$) is plotted. Black areas are considered converged.

the nodes on the element diagonal. This contradicts with what is expected from the elliptic Poisson equation. In order to investigate this we created a unit square (fig. 9) and established the Laplacian matrix using both a formulation with one bi-linear quadrilateral element (L_6^4) and by using two linear triangular elements ($L_6^{2 \times 3}$). (44) shows the Laplacian matrix for the unit square modeled by two triangular elements and (45) shows the Laplacian matrix using one bi-linear quadrilateral element. There are no coupling terms along the diagonal of the square ($L_{13}^{2 \times 3}, L_{31}^{2 \times 3}, L_{24}^{2 \times 3}$ and $L_{42}^{2 \times 3}$ are all zero) when triangular elements are used. All matrix elements are non-zero for the quadrilateral element. Refining the square into more triangular elements does not help. Similar phenomena are experienced within the field of structural mechanics. The text book [19] refers to a convergence study on the deflection of a beam subjected to an external load. It was found that the CST elements (linear triangular elements) converged very poorly both with respect to the deflection and the stress level relative to using elements of higher order. Even bi-linear elements converged considerably better.

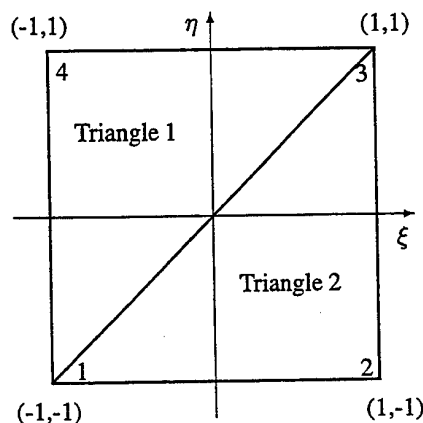


Figure 9: A unit element. It may be modeled by one bi-linear element or two linear triangular elements.

$$\mathbf{L}_{square}^{2 \times 3} = \begin{bmatrix} 1.0 & -0.5 & 0.0 & -0.5 \\ -0.5 & 1.0 & -0.5 & 0.0 \\ 0.0 & -0.5 & 1.0 & -0.5 \\ -0.5 & 0.0 & -0.5 & 1.0 \end{bmatrix} \quad (44)$$

$$\mathbf{L}_{square}^4 = \begin{bmatrix} 0.67 & -0.17 & -0.33 & -0.17 \\ -0.17 & 0.67 & -0.17 & -0.33 \\ -0.33 & -0.17 & 0.67 & -0.17 \\ -0.17 & -0.33 & -0.17 & 0.67 \end{bmatrix} \quad (45)$$

The bad representation of the Laplacian matrix is probably also the reason why the pressure field looks very scattered when using linear triangular elements. Fig. 10 shows that there are large node to node variations in the pressure for the upper mesh with triangular elements relative to a smooth pressure field for the mesh with bi-linear quadrilateral elements. Large discrepancies are also seen for the mass conservation. Fig. 11 shows that a mesh with linear triangular elements conserves mass poorly during simulation relative to a mesh with bi-linear elements.

STEADY AMBIENT CROSS FLOW PAST A FLAT PLATE

Plates used in numerical and experimental studies differ in geometry. The basic plate that we have used is shown in fig. 12 (left). The plate used by Bearman et al. [20] is seen in fig. 12 (middle). It has a 60 degree chamfer angle and a thickness to width ratio of approximately 0.215. The plate used by Fage & Johansen [21] is a three edge plate with a flat front face and a thickness to width ratio of 0.03. The plate used by Chua et al. [22] in their experiments looks like the right half of the plate in figure 12 (middle) with a flat

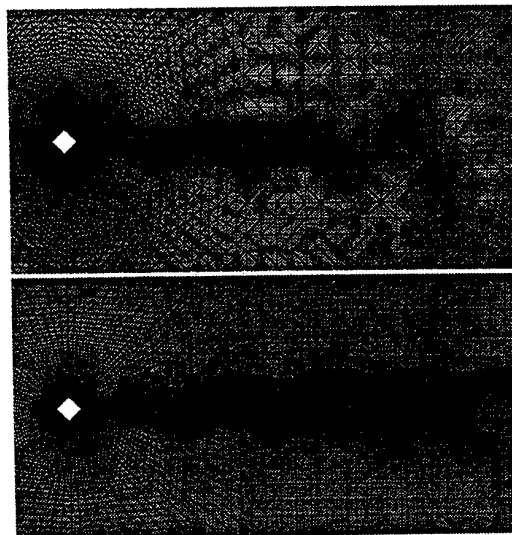


Figure 10: Pressure field around a diamond square in steady ambient flow. Mesh with linear triangular elements (upper) and with bi-linear quadrilateral elements (lower).

front face to the left, chamfered to 30 degree chamfer angle and having a thickness to width ratio of 0.2. The plates used by the vortex methods have either zero or close to zero thickness.

Four meshes were generated for the flattest plate. The coarsest one (p1) have 13139 elements and the finest one (p2) has 25564 elements. Mesh p3 and p4 have 19452 and 24123 elements respectively. Mesh p1 is the basic mesh. Mesh p2 is refined relative to p1 by dividing the elements closest to the body into five in the direction normal to the body leaving the same element dimension tangential to the body. Meshes p3 and p4 are refined towards the tip. The elements closest to the plate are refined by dividing the elements from the p1-mesh into three and six respectively, but only refining in the direction tangential to the body leaving the same element thickness normal to the plate. (See fig. 13). Only one mesh density is used for the middle and right plates in fig. 12. This density is similar as p1. The meshes are named pc60 and pc30, respectively. All meshes consist of 4 noded quadrilateral elements. The computational domain extends 15D along the positive x-direction (downstream) and 10D along the negative x-direction. The mesh extension in the y-direction is $\pm 10D$. Meshes used for oscillating ambient flow are equal to the those mentioned above only extending the domain in the negative x-direction so that the domain becomes symmetric about $y=0$.

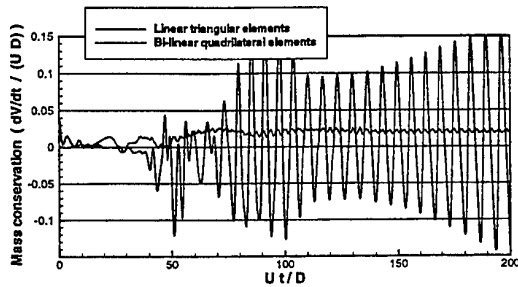


Figure 11: The rate of change of mass in the computational domain as a function of non-dimensionalizing time.

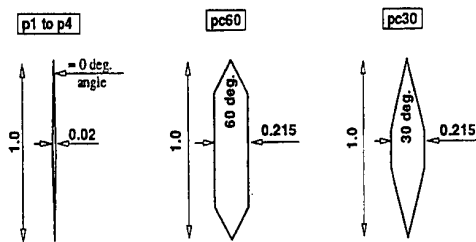


Figure 12: Geometries of the plates used in the numerical studies.

The present method has been compared to other numerical methods based on vortex sheet methods [23, 24, 25, 27]. The start-up problem of crossflow past a flat plate is analyzed. The similarity solution by Wedemeyer [23] assumes a semi-infinite plate. Pullin [24] and Faltinsen & Pettersen [25] use a Rott vortex [26] as an initial solution. The vortex sheet then rolls up around this discrete vortex. One major difference between the method by Faltinsen and Pullin, is that Pullin considers a semi-infinite plate even after the startup (similarity solution), while Faltinsen & Pettersen consider a finite plate width. Fink & Soh [27] start the computation by shedding one vortex sheet segment, which they represent by one equivalent vortex. Their solution seems to converge towards the other methods by decreasing the segment size ΔS_n , where n denotes the final segment shed (see fig. 15).

The start-up flow is interesting also from the perspective of ambient oscillatory flow. When the ambient flow turns, the oscillatory flow problem has similarities to the start-up problem.

A major difference between the present method and the vortex sheet methods, is the way diffusion is handled. A vortex sheet method assumes that all the vor-

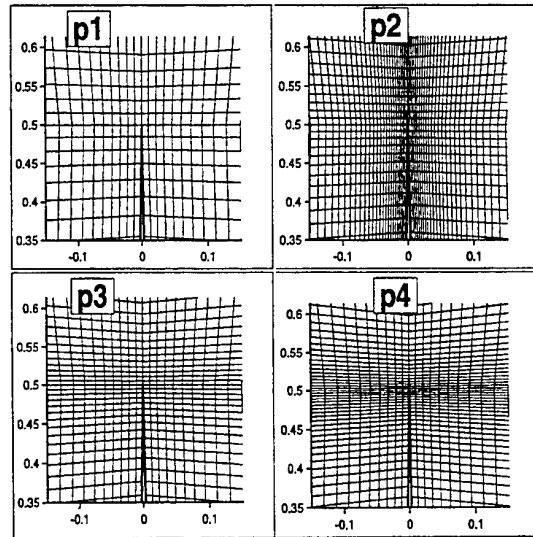


Figure 13: Detailed view of the upper tip of the plate for mesh p1 to p4.

ticity is contained within zero thickness boundary layers and free shear layers. In other words, the vortex sheet methods do not solve for the flow in the boundary layer nor for the flow inside the free shear layers. Therefore, for comparison reasons, a slip condition has been enforced on the body when using the present method. Due to the near vertical edges of the plate, the node of the plates have been given a $u=0$ Dirichlet condition for the velocity in the x -direction (normal to the plate) and no Dirichlet condition for the velocity in the y -direction (tangential to the plate). In this case the weak Neumann condition $\int_{S_B} w \partial v / \partial n ds = 0$, as is the leftover line integral due to the weak FEM-formulation, is valid (w being the weighting function).

For the present case only upper half of the plate and the domain is meshed. The new dimensioning length is $H=0.5$ which is now the height of the plate. The meshes are renamed p1-h, p2-h, p3-h and p4-h respectively.

The vorticity shed into the fluid is calculated and compared to the other methods. This is for the vortex sheet methods equivalent to the time dependent circulation around the rolled up vortex shed at the tip of the plate. Since a slip condition on the body is used, the total circulation calculated by the present method should be comparable to the predicted values by the vortex sheet methods. Fig. 14 (a) shows a small mesh-dependency. Meshes p3-h and p4-h are closest to Wedemeyer's solution. Fig. 14 (b) shows that the vortex sheet methods start up in very similar manner.

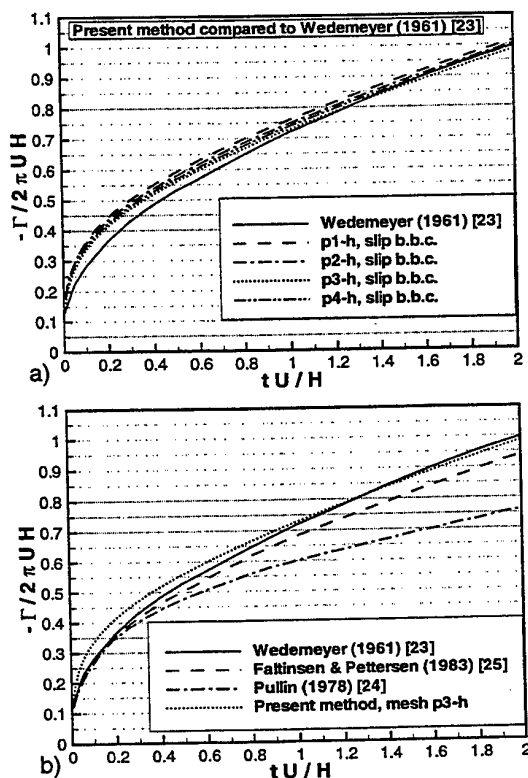


Figure 14: An impulsively started flow normal to a flat plate. The vorticity ($\Gamma = \int_{\Omega} (\frac{\partial u}{\partial y} - \frac{\partial v}{\partial x}) d\Omega$) shed into the fluid as a function of non-dimensionalized time. H is the height of the half plate. $Re=200$ is used for present method.

When time goes on, the similarity solution by Pullin deviates from the other vortex sheet methods. The current method shows some initial difference with the other methods, but keep up nicely with the method by Wedemeyer [23] and Faltinsen & Pettersen [25] as time goes on. The reason to the initial difference may be that no similarity solution was assumed at the start up. A similarity solution implies that for any small time there is present shed vorticity. This was found impractical with the way we start up the solution.

The normal force on the plate is also investigated and compared with results by the vortex sheet methods. The forces from the present method are calculated by directly integrating stresses over the body (SB). The effect of a slip and a no-slip condition on the plate is investigated. Fig. 15 (a) shows that the body boundary condition (b.b.c.) have in particular an influence initially. We note the small mesh dependency on the force. Fig. 15 (b) shows good agreement

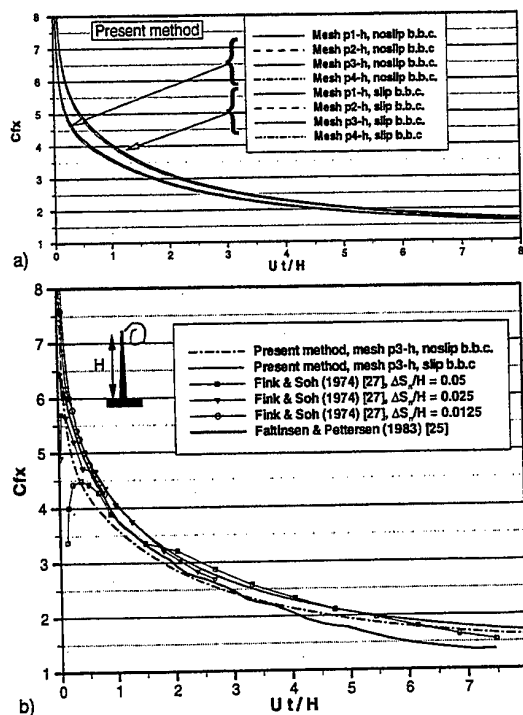


Figure 15: An impulsively started flow normal to a flat plate. Drag coefficient as a function of non-dimensionalized time. $Re=200$ is used for the present method.

with the vortex sheet methods when a slip condition is applied. After some time the present method seems to overestimate the force relative to the method by Faltinsen & Pettersen [25], but not so much relative to the method by Fink & Soh [27]. Scolan & Faltinsen [2] showed good agreement between the vortex-in-cell method and the vortex sheet method by Faltinsen & Pettersen [25].

We have continued the simulations with meshes p1-p4 until a steady state vortex shedding is reached. Asymmetry of the flow was triggered by a small vertical velocity orthogonal to the ambient velocity. This was done similarly for all meshes. Limited studies showed that the results were not sensitive to this perturbation. The first order (in pressure) version of the Fractional-Step procedure is used, i.e. $\theta = 0$. The results presented in table 1 are based on analyzing the time window: $(80 \leq Ut/D \leq 110)$. Table 1 shows mean values (\overline{Cfx}) of the drag coefficient. Momentum is conserved relatively good since there is small difference between calculating the force by directly integrating stresses over the body (SB) and by using conservation of momentum (MF). Fig. 16 shows that

Table 1: Convergence study of steady ambient cross-flow past a flat plate. Mean drag (\overline{Cfx}) is calculated by both integrating the stresses over the body (SB) and by using conservation of momentum (MF). The Strouhal number is estimated from half the oscillation frequency of Cfx based on (SB). Satisfaction of conservation of mass is expressed by the non-dimensionalized emptying time $T_e[-]$ (eq. 35).

Mod.	\overline{Cfx}		Strouhal number		$T_e[-]$
	SB	MF	SB	MF	
p1	3.310	3.387	0.1648	0.1645	1.8E5
p2	3.162	3.278	0.1600	0.1600	5.5E5
p3	2.937	3.038	0.1442	0.1440	1.9E5
p4	2.962	3.066	0.1432	0.1436	3.8E5
pc60	2.755	2.854	0.1870	0.1870	4.4E5
pc30	2.712	2.825	0.1568	0.1565	3.1E6

the drag force oscillating with twice the vortex shedding frequency has an envelope variation over four to five oscillation periods. But this time variation has a small influence on the estimated mean drag. Table 1 shows that refinement towards the tip of the plate is far more important than refinements normal to the plate. The refinements of the mesh causes a reduction in \overline{Cfx} until convergence is reached (p4 relative to p3). We also notice by comparing results from p1, pc30 and pc60 that the sharpness of the plate influences the drag coefficient. A sharper plate gives higher drag coefficient.

Table 1 shows two regimes of Strouhal numbers. Meshes p1 and p2 have higher Strouhal numbers than meshes p3 and p4. Considerable difference in Strouhal number usually means that the flow pattern is different. This is the case here. Fig. 17 shows that mesh p1 (fig. a) produces a different flow pattern than mesh p3 (fig. b). Flow pattern (b) looks more like a regular vortex street normally seen in laminar wakes while it seems like the vortices shed in (a) are getting paired after some time, again influencing on the shedding frequency. Similar differences were observed between the denser meshes p2 and p4.

Fig. 16 shows the time series of the drag coefficient from start-up and until some time after steady state is reached. Only results from meshes p1 and p3 are shown, but simulations based on the other meshes show a similar behavior until the drag stabilizes in either of the two levels. A detailed view of the start-up shows similar behavior for all meshes. This is consistent with the results presented in fig. 15. An exper-

iment was carried out to investigate the effect of the mesh in more details. The velocity and pressure field from the simulation with mesh p1 were mapped onto the p3 mesh, and the simulation was continued from there. The same was done by mapping from the p3 mesh onto the p1 mesh. It was found that the drag coefficient keeps its level after having been mapped over to the coarser mesh even after 30 shedding cycles. The same happens when mapping the field the other way around. It was also found that the different flow patterns survive the mapping. Mesh refinements for such fine mesh considered is mainly of importance in the transient phase when the vortex street is being formed. But the transient phase is shown to be of considerable importance for the steady state vortex shedding.

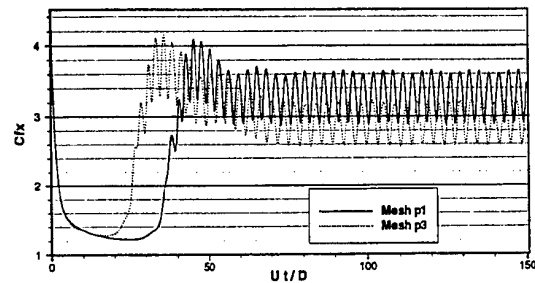


Figure 16: Flat plate in steady ambient crossflow. $Re=200$. Drag coefficient is shown for two meshes. Mesh p1 is the reference mesh while the mesh p3 is refined towards the tip of the plate (tangential to the body). (See fig. 13.)

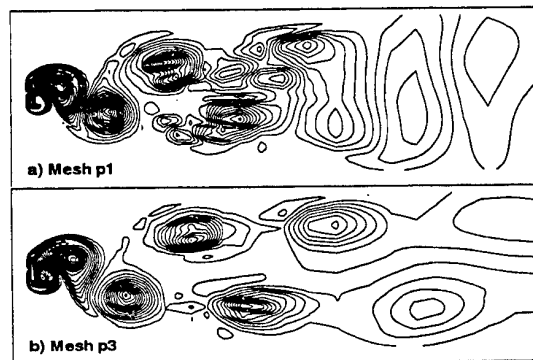


Figure 17: Flat plate in steady ambient crossflow. $Re=200$. Vorticity contours shown. Mesh p1 (a) is the reference mesh whereas mesh p3 (b) is refined towards the tip of the plate (tangential to the body). (See fig. 13.)

Chua et al. [22] collected different numerical and experimental results. We have retabulated these in table 2 and added the results from the present method and from Bearman et al. [20]. The values by [20] are obtained by extrapolating their high KC-number experimental results by relation (7.32) in Faltinsen [5].

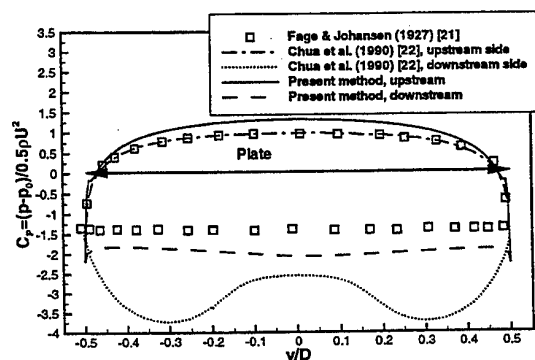


Figure 18: Time averaged pressure coefficient on a flat plate in steady ambient crossflow. Comparisons between the present Navier-Stokes solver ($Re=200$), a vortex blob method by Chua et al. (1990) ($Re=10^4$) and wind tunnel experiments by Fage & Johansen (1927) ($Re=1.5 \cdot 10^5$).

The large scatter in the Strouhal numbers tabulated in table 2 indicates that various methods, either numerical or experimental, reach different steady state situations, not only for the value of the drag but also for the behavior of the flow pattern.

Table 2 shows that the numerically predicted values, which are all based on 2D methods, in general greatly overpredicts the drag compared to experimental values. The present method overestimates the drag with 38% compared to the experimental results by Fage & Johansen [21]. However, somewhat comforting is the good agreement for the predicted Strouhal number.

Possible causes to the difference between our predicted drag and the experimental results will be discussed.

The time rate of shed vorticity into the fluid ($d\Gamma/dt$) is of importance to the drag. The degree of sharpness of the shedding edge has a strong effect on $d\Gamma/dt$. This is reflected in table 2. The plate with the sharpest edge has higher drag coefficient than the chamfered plates.

Large differences between the computed and experimental values for drag force are often explained by three-dimensional effects in the experiments. Two 3D effects are considered important. One is due to end effects of finite span bodies. Another effect is the

Table 2: Comparison of drag coefficients ($\overline{Cf_x}$) and Strouhal numbers (St) between different numerical methods and experiments. The table is taken from Chua et al. [22] adding the results from the present method and extrapolated experimental results by Bearman et al. [20]. ⁽¹⁾ Empirical circulation decay models are used to reduce $\overline{Cf_x}$ from higher values.

Method	Ref.	$\overline{Cf_x}$	St	Re
NS	Pres.	2.9-	0.144	200
sim.	met.	3.0		
—	[29]	2.8	0.15	200
Vortex	[22]	3.5	0.11	10^4
met.		± 0.1		
—	[30]	3.4	—	—
—	[31] ⁽¹⁾	2.4-	0.14-	—
—		2.8	0.16	—
—	[32] ⁽¹⁾	2.8	0.14	—
—	[33]	3.0-	—	—
—		4.0	—	—
Wind	[21]	2.13	0.146	$1.5 \cdot 10^5$
tunnel				
—	[34]	2.0	—	$10^3 - 10^5$
—	[35]	1.74	0.135	$10^3 - 10^4$
Towing	[22]	2.05	0.133	$5 \cdot 10^3$
tank		± 0.05		
High KC	[20]	2.10	—	—
exp.			—	—

spanwise lack of correlation of vortex shedding due to 3D instabilities of the shed vortices. This effect is Reynolds number dependent. It does generally not occur for $Re < 180$ where one may achieve 2D flow even in experiments if care is taken to control end effects. The effect of the spanwise correlation was briefly investigated by Chua et al. [22]. They did numerical simulations in 2D as well as experiments (3D) on an oscillating plate in steady ambient crossflow. The oscillation direction was orthogonal to the steady ambient flow. They obtained perfect spanwise correlation and the agreement between the 2D numerical results and 3D experiments increased considerably.

Chua et al. [22] have compared the time averaged pressure coefficient over a flat plate with measured values by [21]. Fig. 18 shows a comparison with our

2D numerical results. The results by Chua et al. [22] show a very large base suction with a concentration of the suction towards the tips of the plate. Fage & Johansen [21] obtained experimentally a nearly spatially constant suction pressure. Our numerical results show also small spatial variations of the suction pressure. Chua et al. [22] have more confidence into the shape of the pressure distribution obtained by their numerical method than what Fage & Johansen measured. This is also discussed by Roshko [28]. He suggests that the nearly spatially uniform base pressure is due to loss of spanwise phase coherence, i.e. 3D effects. Since the present method is 2D and showing similar constant base pressure as Fage & Johansen, one cannot relate this to 3D effects only. Instead we suggests another explanation for the varying base suction: Chua et al. [22] reports that the roll-up vortices from their numerical calculations form closer to the body than what is observed from experiments. The location of the roll-up vortex relative to the body is believed to be important for the base pressure, and hence the drag.

OSCILLATING AMBIENT FLOW NORMAL TO A FLAT PLATE

When analyzing ambient oscillating flow, the Keulegan-Carpenter (KC) number is important. This is defined as

$$KC = \frac{U_A T}{D}, \quad (46)$$

where T is the oscillation period of the ambient flow.

We will analyze our results by fitting them to Morison's equation

$$F_m = \frac{1}{2} \rho D C_d |U| U + \frac{\pi D^2}{4} \rho C_m \frac{dU}{dt}, \quad (47)$$

where F_m is the total force per unit length in direction of the ambient flow velocity. C_d and C_m are the drag- and mass- coefficients.

We express the free stream velocity as

$$U = U_A \sin \frac{2\pi t}{T} = U_A \sin \omega t. \quad (48)$$

There is no y-component of the ambient velocity.

C_d and C_m are found by the "method of Fourier Averaging" [36], i.e.

$$C_d = \frac{3}{8} \frac{1}{\rho U_A^2 D} \int_0^{2\pi} F \sin \omega t d(\omega t) \quad (49)$$

$$C_m = \frac{4}{\rho D^2 U_A \pi \omega} \int_0^{2\pi} F \cos \omega t d(\omega t) \quad (50)$$

where F is the computed force.

The physics that the boundary conditions at the outer boundaries represent are somewhat simpler in the oscillatory problem. We simply say that we have undisturbed free stream at the outer boundaries. This free stream may be introduced by giving Dirichlet-conditions for u as $u = U_A \sin \omega t$ on the outer boundaries. This is what Herfjord [4] does in his thesis. Since we should avoid having both pressure Dirichlet and velocity Dirichlet conditions on the same boundary, such a method will leave no boundaries where to impose pressure Dirichlet condition. If no pressure Dirichlet condition is given, the total pressure will be wrong. The error is space independent, but varies with time. However the pressure gradient, which is actually what we solve for, and what is needed to correctly calculate the integrated pressure force over the body, will in principle be correct. This is only in principle since the space independent error will affect the numerical accuracy as time goes on. Because this constant error is so large, it uses so many significant digits that only a few is left to the physical pressure. If no pressure is given, then the weak Neumann condition $\int_{\Gamma} w \frac{\partial p}{\partial n} d\Gamma = 0$ (n being the unit normal vector out of the domain) will be satisfied because in general the line integral is simply neglected. Since $\frac{\partial p}{\partial z} = -\rho \frac{\partial U}{\partial t}$ at the outer boundary for the oscillatory flow problem, the line integral should be implemented in the method.

Many combinations of Dirichlet conditions for the velocity and the pressure have been tested. It was found that implementing pressure Dirichlet conditions on the inflow and outflow boundaries, thus letting the Froude-Kriloff (ambient) flow be driven by the pressure gradient, was more robust and gave better conservation of momentum than implementing Dirichlet conditions for the u velocity at these boundaries. It was also shown that better momentum conservation was achieved by disregarding the Dirichlet conditions for u at the upper and lower boundaries, leaving the weak Neumann condition there. The applied boundary conditions are shown in fig. 19.

Vortex pairing may occur for KC numbers as low as 1. The vortex pairs may travel at any angle between 0 and 45 degrees from the x-axis and at quite high speed due to their mutual influence. They may therefore hit the outer boundaries and thereby contradict the assumption of planar inviscid flow outside the domain. Also when the KC-number is high, vorticity may cross the outer boundaries. This may eventually lead to numerical instability of the kind that was discussed earlier for steady ambient flow. The resulting numerical instabilities were cured by adding eddy viscosity on both sides of the plate in a similar manner as we discussed for the steady ambient flow. The

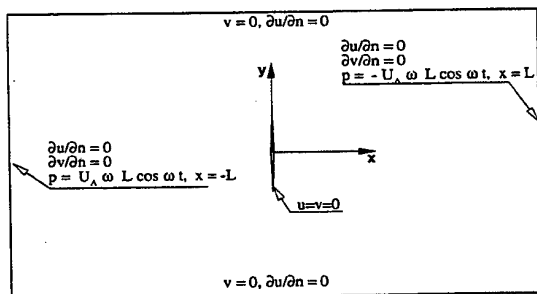


Figure 19: Boundary conditions for planar oscillating ambient flow normal to a flat plate.

eddy viscosity can only be related to the C_d in a quasi-steady manner for high KC -numbers.

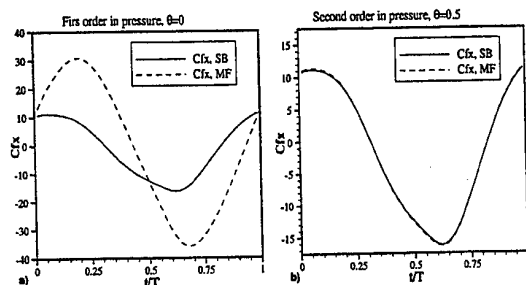


Figure 20: Oscillating ambient flow normal to a flat plate. One oscillation period is simulated with $KC = 1$. Force coefficients in x -direction based on stress integration over the body (SB) and by conservation of momentum (MF) are compared. (a) shows conservation of momentum with pressure accurate to $O(\Delta t)$ and (b) shows conservation of momentum with pressure accurate to $O(\Delta t^2)$.

In problems with ambient steady flow past blunt bodies we normally say that we have a convection dominated flow, which is not always true because diffusion is important in the inner part of the boundary layer. However, in such problems when trying to improve the accuracy of the time integration one normally concentrate on the advection terms leaving the pressure term to first order in time. This is the case with the Taylor-Galerkin time integration scheme with $\theta = 0$. Fig. 20 (a) shows clearly that a first order scheme for the pressure does not conserve momentum in the computational domain. Other studies not reported here with a body oscillating in calm fluid give conservation of momentum even with a first order scheme. The only difference between these two cases is the presence of a Froude-Kriloff (ambient) pressure in fig. 20 (a) which is the driving force in

the problem, and is dominating. The morale is then that we do not need higher order schemes on all the terms in Navier-Stokes equations. Their importance in the problem studied should be investigated before proceeding to a higher order scheme. But obviously the pressure driven ambient flow requires a higher order time integration scheme. Therefore, the results shown for oscillating flow in the rest of paper are calculated by the second order scheme, i.e. $\theta = 0.5$.

Results

Oscillatory crossflow past a flat plate has not been as extensively reported as oscillatory flow past a circular cylinder. Experiments have been carried out by Keulegan & Carpenter [36] mounting the plate beneath a standing wave, and by Singh et al. [39] using a U-tube. Shih & Buchanan [40] did experiments with plates oscillating in fluid at low Reynolds numbers. Graham [41] did numerical simulations at low KC numbers using a discrete vortex method around an isolated edge. Faltinsen & Pettersen [42] and Lian [43] used a vortex sheet method. Scolan & Faltinsen [2] used the vortex-in-cell method.

When proceeding to the oscillatory problem from the steady ambient flow problem, a legitimate question is whether a converged mesh in the steady ambient flow problem should be considered converged for the oscillatory flow problem. Mesh p3 was considered converged for steady ambient flow while mesh p1 was not. The influence of the mesh on the force occurred after the von-Karman vortex street was established. No significant differences were seen during the start up phase. Since the oscillatory problem for low KC is similar to the start-up problem, mesh p1 may be appropriate for the oscillatory problem even if it was not for steady ambient flow. This is confirmed in table 3 for $KC=1$. Since the denser mesh p3 requires considerably more cpu-time per step and shorter time steps, mesh p1 is used in the comparative studies with other numerical methods and experimental results.

Table 3 shows the effect of Reynolds number (Re). Re is varied between 94 and 940. C_d increases with about 15% in this Reynolds number range. Most of the increase occurs between $Re=94$ and $Re=188$. The effect of Re on C_m is minor. Since the effect of Re for values above 200 is small, the following calculations are done with $Re=200$.

Our numerical results have been compared with experiments and with Graham's isolated edge theory, presented in Bearman et al. [44] and Graham [41]. This theory is a non-viscous ($Re \rightarrow \infty$) low KC number theory. The experiments originate from Singh [39]. Another set of experimental results were taken from [36]. They do not describe the detailed

Table 3: Influence of Reynolds number, mesh and time step (Δt) for oscillating crossflow past a flat plate at $KC=1$. σ is the respective standard deviation defined as $\sigma = \frac{1}{n-1} \sum_{j=1}^n (C_{dj} - \bar{C}_{dj})$, C_{dj} being the C_d calculated from cycle j where j goes from 1 to n . \bar{C}_{dj} is the value averaged over n cycles. Similarly for C_m . W_m and W_c are the work carried out on the body by the flow using the Morison force F_m in eq. (47) or the force F in eqs. (49)-(50) respectively. 50 oscillations are considered except for the the two last rows where 25 and 35 oscillations are considered.

Mesh	Re	$U_A \Delta t / D$	C_d , σ	C_m , σ	W_m/W_c
p1	94	0.001	9.96 0.01	1.26 0.00	1.03
p3	94	0.0005	10.05, 0.01	1.26, 0.00	1.03
p1	188	0.001	11.24, 1.01	1.27, 0.02	1.02
p3	188	0.0005	11.52, 0.98	1.29, 0.02	1.02
p1	376	0.001	11.38, 1.32	1.25, 0.08	1.05
p1	564	0.001	11.59, 1.15	1.28, 0.06	1.04
p1	940	0.001	11.20, 1.64	1.25, 0.08	1.06
p1	940	0.0005	11.50, 1.46	1.26, 0.12	1.05

shape of the plates they use. The Reynolds number range is between 4500 and 11400. The results from [36] are plotted in figs. 21 and 22. We have also compared with the results from Lian [43] and Scolan & Faltinsen [2].

Shih & Buchanan [40] compared their experimental results with Keulegan & Carpenter's experiments [36], and found good agreement. Their results are therefore not presented here. However, they constructed a formula that describes C_d as a function of KC and Re , when KC is between 1.57 and 4.71 and Re is between 1.01 and 1057. The formula is

$$C_d = 15 KC^{-\frac{1}{2}} \exp\left(\frac{1.88}{Re^{-0.547}}\right). \quad (51)$$

This is plotted in fig. 21. Other similar formulas are

$$C_d = 8 KC^{-\frac{1}{2}} \quad (\text{Graham}), \quad (52)$$

$$C_d = 9.555 KC^{-\frac{1}{2}} \quad (\text{Himeno}). \quad (53)$$

Graham uses a factor 8 based on experimental results instead of 11.8 which he numerically calculated by his

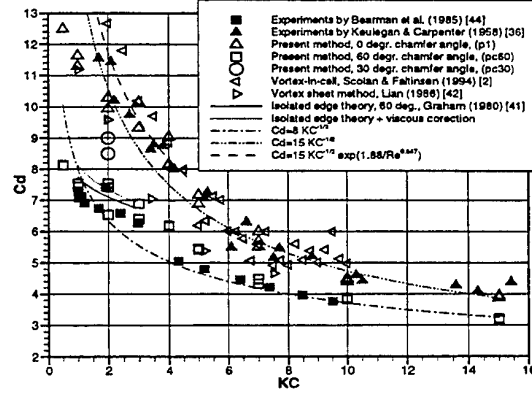


Figure 21: Drag coefficients for oscillating crossflow past a flat plate.

isolated edge theory, ref. [41]. The exponent $-1/3$ follows from Graham's low KC -number theory. Himeno's formulae is found in [45]. The formula

$$C_d = 15 KC^{-\frac{1}{2}} \quad (54)$$

was found to fit our calculated values for a plate of zero thickness in a KC range between 2 and 15.

Numerical simulations with the present method are carried out on plate meshes p1, pc60 and pc30. The first two meshes were used for KC between 0.5 and 15. The last model was used only for $KC=2$. Results in terms of drag- and mass-coefficients for plate mesh p1 is tabulated in table 4. At least two time windows are analyzed for each KC number. Values from all time windows are plotted in figs. 21 and 22. The scatter in the results for some KC numbers are relatively large.

Figs. 21 and 22 have to be analyzed together with table 4. For instance, fig. 22 shows large scatter for C_m at $KC = 7$. Some values deviate significantly from experimental results. However, table 4 shows that C_m estimated from the last time window, when the flow pattern is supposed to have stabilized, is in fact not so far from the experimental values. The standard deviation σ presented in table 4 measures the spread of C_d or C_m . This is due to the changing flow characteristics within the time window.

Fig. 21 shows that the scatter in C_d is small at high KC and larger for smaller KC , and especially for KC between 2 and 7. Since the contribution from the drag force to the total force is small for small KC -numbers, the extraction of C_d from the computed force can be sensitive. This is true for a circular cylinder. But, the C_d -values are higher for flat plates than for circular cylinders. The scatter in estimated C_d for $KC < 2$ is

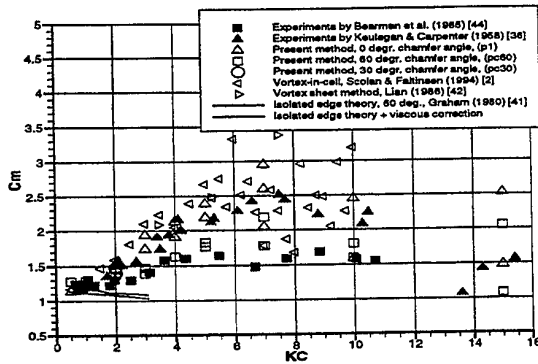


Figure 22: Mass coefficients for oscillating crossflow past a flat plate.

low. We note that the scatter is more pronounced for the plate (p1) with zero degree internal angle, relative to the Bearman type plate (pc60) with 60 degree internal angle. A similar effect is seen in fig. 22 where C_m is plotted. The spread in C_m is large for higher KC, especially for the flattest plate. However, going back to table 4, and choosing C_m from the last time window for $KC=10$ and $KC=15$, we see a good fit with the experimental results in spite that this is a KC range considerably influenced by the drag. The flow in the KC range between approximately 4 and 8 is unstable and the relative importance between the mass and drag terms changes as the flow develops. The results for different time windows for $KC=7$ in table 4 indicate this. It means that a very long simulation time (or experimental time) is needed for these KC-numbers. Another thing about the intermediate KC numbers is the relatively bad estimation of the estimated work done per cycle of the Morison force relative to real work done based on the computed force. Deviations of up to 13% is seen, and again, being more pronounced at intermediate KC numbers indicating errors in estimated drag- and mass- coefficients. It indicates also that Morison's equation is not an accurate representation of the force. Tønnessen [46] uses also a least square fit to extract the drag- and mass coefficients from the computed force. However, the Morison force calculated with these coefficients seem to overpredict the work done even more. Overpredictions of up to 22% were shown.

Table 4: C_d and C_m for a flat plate in oscillating crossflow. Mesh p1 is used. $Re=200$ and $U_A \Delta t/D=0.001$ for all cases. σ is the respective standard deviation. The W_m/W_c -factor indicates how well the Morison force predicts the work done over one period (1=perfect). N.O. is the number of oscillations in the time window considered.

KC	Time window	N.O.	C_d , σ	C_m , σ	W_m/W_c
0.5	2.5-27.5	50	12.50, 0.01	1.14, 0.00	1.02
	15-27.5	25	12.50, 0.03	1.14, 0.00	1.02
1.0	5-55	50	11.30, 1.14	1.28, 0.02	1.02
	30-55	25	11.64, 1.28	1.28, 0.01	1.02
2.0	10-110	50	9.95, 1.11	1.51, 0.09	1.04
	60-110	25	10.29, 1.03	1.53, 0.07	1.04
3.0	15-165	50	10.15, 1.84	1.94, 0.29	1.08
	102-165	21	9.33, 1.46	1.74, 0.18	1.08
4.0	20-220	50	9.04, 1.69	2.13, 0.56	1.09
	80-220	35	8.16, 1.18	1.91, 0.45	1.08
5.0	25-250	45	7.17, 1.04	2.39, 0.52	1.11
	80-250	34	6.89, 0.89	2.19, 0.32	1.11
7.0	35-210	25	5.52, 0.50	2.95, 0.67	1.13
	105-210	15	5.70, 0.49	2.60, 0.65	1.13
	154-210	8	6.01, 0.44	2.05, 0.23	1.13
10.0	50-300	25	4.41, 0.50	2.42, 1.40	1.13
	130-300	17	4.50, 0.59	1.59, 0.63	1.09
15.0	75-450	25	3.88, 0.60	2.52, 1.44	1.03
	240-450	14	3.95, 0.59	1.48, 0.54	0.98

The sharpness of the plate influences the results. This was also documented for steady ambient cross-flow. The effect on C_d is clearly visible in fig. 21. Fig. 22 demonstrates also an effect on C_m for $KC = 10$. The details of the body, i.e. the sharpness of the edges are more important for the lower KC numbers. C_d at $KC = 2$ for plate pc30 is between the results for the flattest plate (p1) and Bearman's plate (pc60). Since it has a sharpness between p1 and pc60, this looks reasonable. The scatter due to the chosen time window is generally larger for the flattest plate, however not in the vicinity of $KC=2$ and 3 where also the plate pc60, and as a matter of fact also Bearman's experimental results show scatter.

We find surprisingly good agreement by comparing our numerical results, based on plate pc60, with the experimental results from Berman et al. [44] plotted in figs. 21 and 22. The same can be said about the numerical results based on model p1 (0 degree internal angle) compared with the results from Keulegan & Carpenter [36] plotted in the same figures. One might have expected an overestimation of C_d for high KC numbers due to the absence of 3D effects, but no such effects are seen. Thus, for KC about 4 to 5 we can see that C_d is slightly overestimated for the plate (pc60). The same can be said about C_m shown in fig. 22 but in the range of KC from 5 to 7. At the same time it was found that $W_m/W_c = 1.1$ for this KC range, meaning that the Morison's equation overestimates the work done during a cycle with about 10% compared to the work done by the numerically calculated force. Eq. (54) fits very well the experimental results by Keulegan & Carpenter for $KC > 2$. But the scatter in the experimental results at $KC = 2$ is large. Comparing the mass coefficient we see similar good agreement and similar large scatter for high KC numbers. We also note the relatively large discrepancy between results based on the chamfered plate and the flattest plate.

The results by Scolan & Faltinsen [2] using a vortex-in-cell method, and Lian [43] using a vortex sheet method are also plotted in figs. 21 and 22. Both use a plate with close to zero thickness. While the present method tends to underestimate C_d for low KC numbers, the vortex-in-cell method tends to overestimate, but the agreement is in general very good compared to experiments. The vortex-in-cell method shows also large scatter in C_d for KC numbers around 7. The vortex sheet method seems to underestimate C_d for all KC numbers. A large scatter is shown in C_m for the vortex-in-cell method especially for KC numbers greater than 5 and the values are in general overestimated. Also the vortex-sheet method seems to overestimate C_m for KC numbers greater than 5.

CONCLUSIONS

Steady ambient flow

- Both a consistent mass matrix, in contrast to a lumped mass matrix, and higher order accuracy of the element formulation (at least bi-linear quadrilateral elements) are recommended.
- The introduction of consistent mass matrix introduced instabilities at the outflow boundary for some denser meshes and some time steps. Use of well recognized outflow boundary conditions do not help. Adding eddy viscosity based on turbulent wake theory cured the instability problem.
- Crossflow past a flat plate in steady ambient flow normal to the plate is studied. The refinement of the mesh towards the tip of the plate is important while refinement normal to the plate is relatively unimportant. The refinement is only important in the transient phase after the start up of the flow and before steady state is reached. The relatively small differences in meshes used in the study may result in quite different flow patterns in the wake.
- The start-up of impulsively started crossflow past a flat plate agrees well with other methods.
- The drag on a flat plate in crossflow is overpredicted by 38% relative to experimental results with a similar plate. Compared to other numerical methods, the present method seems to show drag closer to experimental results, than most other numerical methods (without any artificial simulation of 3D effects). Prediction of Strouhal number is satisfactory.
- It is shown numerically that the drag on a flat plate with zero thickness in cross flow is higher than the drag on plates with relatively larger thickness and hence larger internal angles at the tips (chamfer angle). This is confirmed by available experimental results.

Oscillating flow

- The chamfer angle, or thickness to width ratio, of the plate has a large influence on C_d and C_m .
- The present numerical method predicts very well the forces on flat plates, no matter whether the plate has a nonzero chamfer angle or close to zero thickness.
- Empirical formulas for C_d must include the effect of sharpness of the plate. It is also important

to state what KC number range one is considering. $C_d = 15 KC^{-0.5}$ gives a good representation of C_d for KC between 2 and 16 for a plate with close to zero thickness.

- The choice of time window influences estimated C_d and C_m . The flow may change its characteristics even after a long time of simulation. This is especially true for KC in the range from 3 to 7.
- Fourier averaging has been used to estimate C_d and C_m . The force based on the extracted values of C_d and C_m do generally overpredict the work done during a cycle. For the intermediate KC numbers, the overprediction may be up to 13%. Using a least square fit method to extract C_d and C_m gives even worse result.

ACKNOWLEDGMENTS

This work has received support from The Research Council of Norway, both directly and by providing CPU-time on the Cray T3E through the Programme for Supercomputing. The first author have also received support from the Faculty of Marine Technology at NTNU as well as from the Educational Fund by Det Norske Veritas (DNV).

This work is part of the PhD thesis by the first author [46].

REFERENCES

1. Braathen, A. and Faltinsen, O. M., "Application of a vortex tracking method to roll damping," Int. Conference on Technology Common to Aero and Marine Engineering, London, 1988
2. Scolan, Y.-M. and Faltinsen, O. M., "Numerical studies of separated flow from bodies with sharp corners by the Vortex In Cell method," Journal of Fluids and Structures, Vol. 8, 1994, pp. 201-230.
3. Faltinsen, O. M., "On Seakeeping of Conventional and High-Speed Vessels," Journal of Ship Research, Vol. 37, 1993, pp. 87-101.
4. Herfjord, K., A study of two-dimensional separated flow by a combination of the Finite Element Method and Navier-Stokes Equations, PhD thesis No. 1996:2, The Norwegian Institute of Technology (NTH), Trondheim, Norway, 1996.
5. Faltinsen, O. M., Sea loads on ships and offshore structures, Cambridge University Press, 1990.
6. Chorin, A. J., "Numerical Solution of the Navier-Stokes Equations," Mathematics of Computation, Vol. 22, 1968, pp. 742-762.
7. Zienkiewicz, O. C. and Taylor, R. L., The Finite Element Method, 4 ed., Vol. 2, McGraw-Hill Book Company, 1991.
8. Gresho, P. M., Sani, R. L., Incompressible Flow and the Finite Element Method, John Wiley & Sons Ltd., 1990.
9. Schlichting, H., Boundary-layer theory, 7 ed., McGraw-Hill Book Company, 1979.
10. Lewis, R. W., Ravindran, K. and Usmani, A. S., "Finite element solution of incompressible flows using an explicit segregated approach," Archives of Computational Methods in Engineering, Vol. 2, 1995, pp. 69-93.
11. Guermond, J.-L. and Quartapelle, L., "On stability and convergence of projection methods based on pressure Poisson equation," International Journal for Numerical methods in Fluids, Vol. 26, 1998, pp. 1039-1053.
12. Gresho, P. M., Chan, S. T., Lee, R. L., Upson, C. D., "A modified finite element method for solving the time-dependent, incompressible Navier-Stokes equations. Part2: Applications," International Journal for Numerical Methods in Fluids, Vol. 4, 1984, pp. 619-640.
13. Dhatt, G. and Touzot, G., The Finite Element Method Displayed, John Wiley & Sons, 1984.
14. Yeung, R. W. and Ananthakrishnan, P., "Oscillation of a floating body in viscous fluid," Journal of Engineering Mathematics, Vol. 26, 1992, pp. 211-230.
15. Gartling, D. G., "A test problem for outflow boundary conditions-flow over a backward facing step," International Journal for Numerical Methods in Fluids, Vol. 11, 1990, pp. 953-967.
16. Engelman, M. S. and Jamnia, M.-A., "Transient flow past a circular cylinder: A benchmark solution," International Journal for Numerical Methods in Fluids, Vol. 11, 1990, pp. 985-1000.
17. Newman, J.N., Marine Hydrodynamics, MIT Press., 1977.
18. Dalheim, J. M., Numerical prediction of ivortex-nduced vibration by the Finite Element Method, PhD thesis No. 1997:63, The Norwegian Institute of Technology (NTH), Trondheim, Norway, 1997.
19. Fiskvatn, A., Elementmetoden, TAPIR, 1984.
20. Bearman, P. W., Graham, J. M. R. and Singh, S., "Forces on Cylinders in Harmonically Oscillating Flow," Proceedings in Mechanics of Wave-Induced Forces on Cylinders, Shaw, T.L., ed., London: Pitman, 1979, pp. 437-449.
21. Fage, A. and Johansen, F. C., "On the Flow

of Air behind an Inclined Flat Plate of Infinite Span," Proc. Roy. Soc., Vol. 116, 1927, pp. 170-197.

22. Chua, K., Lisoski, D., Leonard, A. and Roshko, A., "A numerical and experimental investigation of separated flow past an oscillating flat plate," International Symposium on Nonsteady Fluid Dynamics, Miller and Telionos, ed., Vol. 92, USA, 1990, pp. 455-464.

23. Wedemeyer, E., "Ausbildung eines Wirbel-paares an den kanten einer Platte," Ingenieur-Archiv, Vol. 30, 1961, pp. 187-200.

24. Pullin, D. I., "The large-scale structure of unsteady self-similar rolled-up vortex sheets," Journal of Fluid Mechanics, Vol. 88, 1978, pp. 401-430.

25. Faltinsen, O. M. and Pettersen, B., "Vortex Shedding Around Two-Dimensional Bodies at High Reynolds Numbers," Fourteenth Symposium on Naval Hydrodynamics, Michigan, USA, 1983, pp. 1171-1213.

26. Rott, N., "Diffraction of weak shock with vortex generation," Journal of Fluid Mechanics, Vol. 1, 1956, pp. 111-128.

27. Fink, P. T. and Soh, W. K., "Calculation of Vortex Sheets in Unsteady Flow and Applications in Ship Hydrodynamics," Tenth Symposium in Naval Hydrodynamics, Cambridge, Mass., 1974, pp. 463-491.

28. Roshko, A., "Perspectives on bluff body aerodynamics," Journal of Wind Engineering and Industrial Aerodynamics, Vol. 49, 1993, pp. 79-100.

29. Raghavan, V., McCroskey, W. J., Van Dalsem, W. R. and Baeder, J. D., "Calculations of the Flow Past Bluff Bodies, Including Tilt-rotor Wing Sections at $\alpha = -90^\circ$," Tech. Rep. AIAA-90-0032, 1990.

30. Dutta, P. K., Discrete Vortex Method For Separated AND Free Shear Flows, PhD thesis, Indian Institute of Science, Banglora, 1988.

31. Kiya, M., Arie, M., "Discrete-vortex Simulation of Unsteady Separated Flow Behind a Nearly Normal Plate," Bull. JSME, Vol. 23, 1980

32. Chein, R. and Chuang, J. N., "Discrete Vortex Simulation Of Flow Over Inclined And Normal Plates," Comp. and Fluids, Vol. 16, 1988, pp. 405-427.

33. Kuwahara, K., "Numerical Study Of Flow Past An Inclined Flat Plate By An Inviscid Model," J. Phys. Soc. Japan, Vol. 35, 1973, pp. 1545-1551.

34. Flachsbart, O., "Messungen an Ebenen und Gewölbten Platten," Ergben. Aerodyn. Versuchsanstalt Göttingen, Vol. 4, 1932

35. Roshko, A., "On The Drag And Shedding Frequency Of Two-dimensional Bluff Bodies," tech. rep. NACA-TN-3169, 1954

36. Keulegan, G. H. and Carpenter, L. H., "Forces on Cylinders and Plates in an Oscillating Fluid," Journal of Research of the National Bureau of Standards, Vol. 60, May, 1958, pp. 423-440.

37. Sarpkaya, T. and Isaacson, M., Mechanics of Wave Forces on Offshore-Structures, Van Nostrand Reinhold Company, 1981.

38. Maull, D. J. and Milliner, M. G., "Sinusoidal flow past a circular cylinder," Coastal Engineering, 1978.

39. Singh, S., Forces on bodies in oscillatory flow, PhD thesis, Imperial College, London, UK, 1978.

40. Shih, C. S., Buchanan, H. J., "The drag on oscillating flat plates in liquids at low Reynolds numbers," Journal of Fluid Mechanics, Vol. 48, 1971, pp. 229-239.

41. Graham, J. M. R., "The forces on sharp-edged cylinders in oscillatory flow at low Keulegan-Carpenter numbers," Journal of Fluid Mechanics, Vol. 97, 1980, pp. 331-346.

42. Faltinsen, O. M. and Pettersen, B., "Application of a vortex tracking method to separated flow around marine structures," J. Fluids Struct., Vol. 1, 1987, pp. 217-237.

43. Lian, W., A numerical study of two-dimensional separated flow past bluff bodies at moderate KC-numbers, PhD thesis, The Norwegian Institute of Technology (NTH), Trondheim, Norway, 1986.

44. Bearman, P. W., Downie, M. J., Graham, J. M. R. and Obasaju, E. D., "Forces on cylinders in viscous oscillatory flow at low Keulegan-Carpenter numbers," Journal of Fluid Mechanics, Vol. 154, 1985, pp. 337-356.

45. Ikeda, Y. and Tanaka, N., "On viscous drag of oscillating bluff bodies," 12th Scientific and Methodological Seminar of Ship Hydrodynamics (SMSSH'83), Varna, Bulgaria, 1983

46. Tønnessen, R., A Finite Element Method applied to unsteady viscous flow around 2D blunt bodies with sharp corners, PhD thesis, The Norwegian University for Science and Technology (NTNU), Trondheim, Norway, To be defended in 1999.

VISCOUS FLOWS & LIFTING SURFACES.

Chairman : K.H.Mori

COMPARISON OF EXPLICIT ALGEBRAIC STRESS MODELS AND SECOND-ORDER TURBULENCE CLOSURES FOR STEADY FLOWS AROUND SHIPS

G.B. Deng & M. Visonneau

Laboratoire de Mécanique des Fluides, Ecole Centrale de Nantes

1 Rue de la Noë, B.P. 92101, 44321 Nantes Cedex 3, France

Fax: (33) 2 40 37 25 23;

E-Mail: Ganbo.Deng@ec-nantes.fr, Michel.Visonneau@ec-nantes.fr

ABSTRACT

The flow around the HSVA tanker is computed with an explicit algebraic stress model (EASM) and a Reynolds stress model. Near-wall models based on a transport equation for the turbulent frequency are proposed for both closures such that the same pressure-strain model can be employed. The EASM model improves the prediction in all aspects compared with simple linear eddy-viscosity model. Further improvements on the prediction of the longitudinal vortex are obtained with the Reynolds stress model. The analysis of the computational results reveals the limitation of the linear eddy-viscosity model as well as the existence of flow regions where the local equilibrium assumption, on which the algebraic stress model is based, is no longer valid.

INTRODUCTION

This paper is devoted to the assessment of the most recent turbulence models for steady flows around ships. The so-called HSVA Tanker, intensively studied experimentally by Dr. J. Kux at the Institute of Shipbuilding in Hamburg, is chosen as test case because it is one of the best experimental ship flow databases (Wieghardt and Kux, 1980) [1]. The flow is characterized by a strong thickening of the boundary layer, the generation of an intense longitudinal vortex motion creating complex "hook-shaped" velocity contours in the central part of the wake near the location of propeller and many other characteristics which are not recalled here for the sake of brevity (see Figs. 1 and 2).

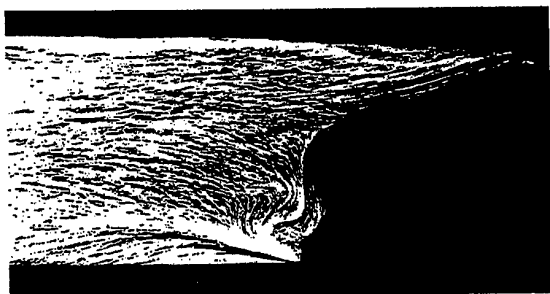


Figure 1: HSVA Tanker – $Re = 5.0 \cdot 10^6$ Experimentally observed wall flow.

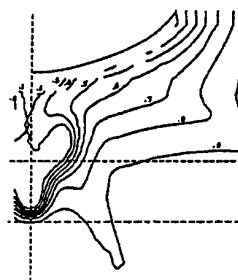


Figure 2: HSVA Tanker – $Re = 5.0 \cdot 10^6$ Experimental isowake contours at $x/L=0.978$

Even though classical $k-\epsilon$ models with near-wall low-Reynolds-number modifications are able to predict the gross features of the flow and the wall flow, the characteristic hook shape present in the measured velocity contours is not captured by the computations.

A detailed analysis conducted by Deng, Queutey & Visonneau (1993) [2] and confirmed by Sotiropoulos & Patel (1994) [3], have established that the $k-\epsilon$ turbulence models used at that time were responsible for these inaccuracies because of too high a level of turbulent viscosity generated in the core of the longitudinal vortex. This analysis was confirmed during the 1994 Tokyo Workshop for Improvement of Hull Form Design (Tokyo Workshop, 1994, [4]).

Although the $k-\omega$ model developed by Wilcox (1993) [5] and its variants due to Menter (1993) [6]

bring noteworthy improvements in the simulation of the near-wake flow, as indicated by Deng & Visonneau (1996) [7] and confirmed recently by [8], they cannot be considered as a fully satisfactory answer. A recent computation of a wing-body junction flow performed by the authors shows that both $k - \epsilon$ and $k - \omega$ models are not able to predict accurately the intensity of the horse-shoe vortex [9]. In addition to the inability to simulate turbulence anisotropy, the limitations of eddy-viscosity models for modeling complex flows are related to models' inability to account for the selective amplification or attenuation of Reynolds stresses by curvature-related strain components, which explains their bad performances on flows characterized by intense longitudinal vortices.

Whereas second-order closures (RST models) are based on the solution of a modeled form of the full Reynolds stress transport (RST) equations, the explicit algebraic stress models (EASM) are derived from equilibrium hypotheses imposed on the convective and diffusive terms in the RST equations. Both models are able to provide an anisotropic description of the turbulence but the RST closures include additional physical terms such as the convection and the turbulent diffusion of the Reynolds stresses which makes possible a more accurate description of turbulent complex flows. However, the current generation of RST closures does not perform outstandingly well on flows far from equilibrium. This observation suggests that EASM could be a good compromise for some three-dimensional flows.

Therefore, the main goal of this paper will be to evaluate the relative importance of transport and diffusion mechanisms of the Reynolds stresses for the steady flows around ships. The EASM model proposed by Gatski & Speziale [10] will be used in conjunction with a turbulent frequency ω equation proposed by the authors which allows direct integration of the EASM model up to the wall. In order to facilitate the evaluation of the role played by these additional physical terms, the same models for the pressure-strain and turbulent dissipation term will be implemented in both EASM and RST closures.

Sotiropoulos & Patel (1994) [3] have shown a successful prediction of ship flow with the low Reynolds number Reynolds stress model proposed by Shima. However, our personal experience with the Shima model was not so positive since our implementation of this closure was systematically unable to give a satisfactory prediction because of stability problems (Deng & Visonneau (1996) [7]). Attempts were made to stabilize the Shima model by replacing the ϵ equation with an ω equation (Deng & Visonneau (1996) [11]). Unfortunately, the proposed model was also unable

to give a stable prediction for the ship flow. This is the reason why a completely new near wall model is proposed in the present study. Without modifying the numerical method, a stable solution is obtained with the new near wall model. Although it is calibrated only on a simple boundary layer flow, a good agreement between the computations and the experiments is observed for the flow around the HSV A tanker.

NUMERICAL METHOD

The simulation has been performed with the HORUS code developed in our CFD group. The solution of the Reynolds Averaged Navier-Stokes Equations is obtained by using finite difference method with a body-fitted structured grid. A cell-centered layout is employed in which the pressure, turbulence and velocity unknowns share the same location. The momentum and continuity equations are coupled through the PISO procedure and several implicit first and second order accurate schemes are implemented for the space and time discretizations. In the present computation, convection terms written in convective form are discretized with a third order upwind-biased scheme which is similar to the well known Quick scheme for the conservative formulation. Finally, preconditioned conjugate gradient solvers (CGS, CGSTAB) are used to solve the linear systems.

Implementation of Reynolds stress transport model in a non-staggered layout is not straightforward. Due to the absence of numerically stabilizing eddy viscosity and the predominant influence in the momentum transport equations of the equilibrium between several strong and opposite source terms, namely the pressure and Reynolds stress gradients, a special numerical stabilizing technique has to be implemented. The main characteristics are listed below:

- To build the mass flux at the interface such that the equilibrium between the pressure and the Reynolds stress gradients is preserved.
- To keep the relaxation of the pressure field consistent with that of Reynolds stress so that the balance between them is maintained.
- To design an appropriate procedure to solve the coupling between the velocity, the pressure and the Reynolds stresses.

Details of the implementation have been given in Deng & Visonneau (1996) [7]. Such numerical treatments are also applied in the implementation of explicit algebraic stress model. In addition to the above mentioned technique, a defect correction approach is used to take into account the contribution of the Reynolds

stress in the momentum transport equation, which makes the computation with the new near wall Reynolds stress model as stable as a simulation using a two-equation model. The defect correction approach will be described later in the paper.

TURBULENCE MODEL

Reynolds Stress Model

The Reynolds stress transport equations can be written as:

$$\frac{D\overline{u_i u_j}}{Dt} = P_{ij} + \phi_{ij} - \varepsilon_{ij} - \frac{\partial}{\partial x_k} \left(C_{ijk} - \nu \frac{\partial}{\partial x_k} \overline{u_i u_j} \right)$$

The production terms are given by:

$$P_{ij} = - \left(\overline{u_j u_k} \frac{\partial U_i}{\partial x_k} + \overline{u_i u_k} \frac{\partial U_j}{\partial x_k} \right)$$

An isotropic model for the dissipation rate is used:

$$\varepsilon_{ij} = \frac{2}{3} \delta_{ij} \varepsilon$$

A linear model with wall reflection terms is retained in the present study for the pressure-strain terms:

$$\phi_{ij} = \phi_{(1)ij} + \phi_{(2)ij} + \phi_{(w)ij}$$

where

$$\phi_{(1)ij} = -C_1 \varepsilon b_{ij}$$

$$\begin{aligned} \phi_{(2)ij} = & C_2 k S_{ij} \\ & + C_3 k \left(b_{ik} S_{jk} + b_{jk} S_{ik} - \frac{2}{3} b_{mn} S_{mn} \delta_{ij} \right) \\ & + C_4 k (b_{ik} W_{jk} + b_{jk} W_{ik}) \end{aligned}$$

and the wall reflection terms proposed by Gibson & Launder (1978) [12] are given by:

$$\begin{aligned} \phi_{(w)ij} = & C_{w1} \frac{\varepsilon}{k} \left(\overline{u_k u_m} n_k n_m \delta_{ij} - \frac{3}{2} \overline{u_i u_k} n_k n_j \right. \\ & \left. - \frac{3}{2} \overline{u_k u_j} n_k n_i \right) \frac{k^{3/2}}{C_l \varepsilon y_w} \\ & + C_{w2} \left(\phi_{(2)km} n_k n_m \delta_{ij} - \frac{3}{2} \phi_{(2)ki} n_k n_j \right. \\ & \left. - \frac{3}{2} \phi_{(2)kj} n_k n_i \right) \frac{k^{3/2}}{C_l \varepsilon y_w} \end{aligned}$$

In the above formula, S_{ij} and W_{ij} are the strain rate and the rotation rate tensors respectively:

$$S_{ij} = \frac{1}{2} \left(\frac{\partial u_i}{\partial x_j} + \frac{\partial u_j}{\partial x_i} \right)$$

Model	C_1	C_2	C_3	C_4
LRR	3.0	0.8	1.75	1.31
IP	3.6	0.8	1.2	1.2
SSG	6.8	0.36	1.25	0.4

Table 1: Pressure-strain model constants

$$W_{ij} = \frac{1}{2} \left(\frac{\partial u_i}{\partial x_j} - \frac{\partial u_j}{\partial x_i} \right)$$

b_{ij} is the Reynolds stress anisotropy tensor defined as

$$b_{ij} = \frac{\overline{u_i u_j}}{2k} - \frac{1}{3} \delta_{ij}$$

n_i is the wall normal vector, and y_w is the wall normal distance. The Daly & Harlow model is used for the diffusion correlation terms:

$$C_{ijk} = -C_s \frac{k}{\varepsilon} \overline{u_k u_l} \frac{\partial \overline{u_i u_j}}{\partial x_l}$$

A variety of linear pressure-strain correlation models have been proposed. The most popular models are the Launder, Reece and Rodi (1975) [13] LRR model, the isotropization-of-production (IP) model, and more recently, the Speziale, Sarkar and Gatski (1991) [14] (SSG) model. For high-Reynolds-number flows, the model constants are given in the following table.

In the original version, the SSG model contains a quadratic term

$$C'_1 \varepsilon \left(b_{ik} b_{kj} - \frac{1}{3} b_{mn} b_{mn} \delta_{ij} \right) \text{ with } C'_1 = 4.2$$

which is neglected in the present study, since it prevents the solution of the algebraic stress model to be obtained explicitly. Originally, the C_1 and C_2 coefficients take the form

$$C_1 = 3.4 + 1.8 \frac{P}{\varepsilon}, C_2 = 0.8 - 1.3 \sqrt{b_{mn} b_{mn}}$$

The coefficients in table 1. are taken from Gatski and Speziale (1993) [10] for equilibrium flows. It may be noticed that, when using the IP model, the $\phi_{(2)ij}$ can be simplified as:

$$\phi_{(2)ij} = -\frac{1}{2} C_3 \left(P_{ij} - \frac{2}{3} \delta_{ij} P \right)$$

The above model is only valid for high Reynolds number flows. A near wall modification needs to be included in order to be able to apply the model in the wall region. When calibrating a near wall model, the most important requirements that should be taken into account are the following:

- To satisfy the numerical constraints so that all equations can be integrated to the wall.
- To predict a correct behavior of the law of wall and a good estimation of the wall friction velocity for simple wall flow. This requirement is guaranteed by the good prediction of the shear stress.
- To predict correctly the normal stress anisotropy.
- To predict a correct wall limiting behavior of the Reynolds stresses.

The complexity and the numerical stiffness of the model increase with the constraint imposed on the model. In the present study, we try to construct a near wall model which is as simple as possible. Consequently, only the first two requirements are taken into account.

The numerical requirement concerns only the C_1 coefficient. Near the wall, the turbulent dissipation is in balance with the viscous diffusion of the turbulent kinetic energy:

$$\nu \frac{\partial^2 k}{\partial x_k^2} - \varepsilon = 0$$

At the same time, the balance of each Reynolds stress component is governed by:

$$\nu \frac{\partial^2 \overline{u_i u_j}}{\partial x_k^2} - C_1 \varepsilon b_{ij} - \frac{2}{3} \delta_{ij} \varepsilon = 0$$

It can be easily shown that the above system of equations admits a solution when and only when $C_1 \rightarrow 2$ when $y \rightarrow 0$. This solution does not satisfy the correct wall limiting behavior for the Reynolds stresses, since all Reynolds stresses are of the same order when $y \rightarrow 0$. We believe that the correct wall limiting behavior of Reynolds stresses is not mandatory to obtain a good prediction of the mean flow. It is more important to use a model which does not increase significantly the numerical stiffness. As a consequence, we prefer to retain the isotropic dissipation model even if it is responsible for the drawback just mentioned. In the present near wall model, the C_1 coefficient is just replaced by :

$$C_1 \Rightarrow 2 + (C_1 - 2) \tanh \left(\frac{0.0018 k^2}{\nu \varepsilon} \right)$$

The remaining coefficients are given below:

$$\begin{aligned} C_{w1} &= 0.4 \\ C_{w2} &= \min(0.3, A) \\ C_l &= 2.5 \end{aligned}$$

$$\begin{aligned} C_s &= 0.22 \\ A &= 1 - \frac{9}{8} A_2 + \frac{9}{8} A_3 \\ A_2 &= a_{ij} a_{ji} \\ A_3 &= a_{ij} a_{jk} a_{ki} \end{aligned}$$

The C_{w2} formula proposed by Hanjalic & Jakirlic (1998) [15] is used here since it is found useful to avoid any unphysical separation. The same near wall treatment is adopted for the LRR model, the IP model, and the SSG model. Calibration for different models are done only in the turbulent frequency equation presented below.

The Reynolds stresses determined from transport equations are not directly used in the momentum transport equations. Actually, the effective Reynolds stresses in the momentum equations are computed as :

$$\begin{aligned} \tau_{ij} &= -2\nu_t S_{ij}^n + \frac{2}{3} \delta_{ij} k \\ &+ f_c \left(2\nu_t S_{ij}^{n-1} + \overline{u_i u_j} - \frac{2}{3} \delta_{ij} k \right) \end{aligned}$$

where

$$\begin{aligned} \nu_t &= 0.09 f_\mu \frac{k^2}{\varepsilon} \\ f_\mu &= 1 - e^{-\frac{R_y}{30}} \\ R_y &= \max \left(\frac{y_w \sqrt{k}}{\nu}, 0.006 \frac{y_w |u|}{\nu} \right) \end{aligned}$$

where the function f_c remains to be defined.

The first two terms representing a linear eddy viscosity model are treated implicitly, while the last term is treated explicitly. The f_μ function is calibrated such that the implicit term gives a good approximation of the shear stress for simple wall boundary layer flow. The choice of the correction function f_c is flexible. With $f_c = 0$, the present model is reduced to an eddy-viscosity model even Reynolds stress transport equations are solved to determine k and ε . Although this choice is not interesting for turbulence modelization, a first run with $f_c = 0$ can give a good initialization of the Reynolds stress. With $f_c = 1$, the above implementation can be considered as a defect correction approach. However, even with this choice, the implicit term does not cancel the corresponding explicit term. In one-dimension for example, the implicit discretization of the implicit term involves grid points $(i-1, i, i+1)$, while the explicit discretization of the source term involves grid points $(i-2, i, i+2)$. The difference between the implicit and the explicit discretization provides a numerical dissipation which is beneficial for the numerical stabilization.

For the computation of complex flows such as the flow around the HSVA tanker, it is found that the computation with $f_c = 1$ fails to converge. For such a complex flow, the validation of the wall reflection model calibrated from simple wall boundary layer flow becomes questionable. However, this term has no direct contribution to the prediction of the turbulent kinetic energy. Therefore, we may expect that reasonable prediction of the kinetic energy can still be obtained when solving the Reynolds stress transport equation. Consequently, an eddyviscosity model based on the predicted kinetic energy can provide a reasonable approximation. To obtain a stable solution, we have chosen the correction f_c as

$$f_c = 1 - e^{-\frac{R_y}{15}}$$

In this case, the present model is reduced to eddyviscosity model in the near wall region.

Turbulent Frequency Equation for the Reynolds Stress Model

The turbulent dissipation ε is determined from a turbulent frequency ω equation rather than from a turbulent dissipation equation. When $y \rightarrow 0$, the ω equation is decoupled from any other equations. Consequently, it is less stiff compared with the ε equation. In addition, a near wall model for ω is easier to implement than for ε . The transport equation for ω used in the present study is given below.

$$\begin{aligned} \frac{D\omega}{Dt} &= \alpha \frac{\omega}{k} P_k - \beta \omega^2 \\ &+ \frac{\partial}{\partial x_k} \left(C_\omega \frac{k}{\varepsilon} \overline{u_k u_l} \frac{\partial \omega}{\partial x_l} + \nu \frac{\partial \omega}{\partial x_k} \right) \\ &+ f_\omega^2 \frac{2}{k} \left(\nu \delta_{kl} + C_\omega \frac{k}{\varepsilon} \overline{u_k u_l} \right) \frac{\partial \omega}{\partial x_k} \frac{\partial k}{\partial x_l} \end{aligned}$$

Where

$$\begin{aligned} \alpha &= (C_{\varepsilon 1} - 1) f_\omega + C_{\alpha\omega} (1 - f_\omega) \\ \beta &= C_\mu (C_{\varepsilon 2} - 1) \\ C_\omega &= 0.18 \\ f_\omega &= \tanh \left[\left(\frac{0.002 \sqrt{k} y_w}{\nu} \right)^2 \right] \\ \varepsilon &= C_\mu k \omega \\ C_\mu &= 0.09 \end{aligned}$$

The coefficients $C_{\varepsilon 1}$, $C_{\varepsilon 2}$ and $C_{\alpha\omega}$ given in the following table are calibrated for different pressure-strain model by using the experimental data for a boundary layer under zero pressure gradient.

Model	$C_{\varepsilon 1}$	$C_{\varepsilon 2}$	$C_{\alpha\omega}$
LRR	1.55	1.90	0.63
IP	1.53	1.92	0.60
SSG	1.53	1.92	0.60

Table 2: Model coefficients for the ω transport equation

Away from the wall, the ω equation returns to the classical ε equation with the constants $C_{\varepsilon 1}$ and $C_{\varepsilon 2}$ given in table 2. Unlike in a near wall model for ε where a damping function is often used to change the order of the dissipation term, the damping function f_ω in the above model is used to change the value of the α coefficient as well as to cancel the cross diffusion term in the near wall region. Therefore, such a model is more universal.

Explicit Algebraic Stress Model

By using a local equilibrium assumption, Rodi [16] has deduced an algebraic stress model (ASM) from the Reynolds stress transport model. The ASM model can be explicitly solved. Such an explicit algebraic stress model (EASM) has been first proposed by Pope [17] for two-dimensional flows. EASM models for 3D flow have been developed by Gatski & Speziale [10] and widely used. In this study, we use the EASM model proposed by Gatski & Speziale [10] based on a three-term basis which is the exact solution of the ASM model only for 2D flow. For 3D flow, it can be only considered as an approximation. However, it is expected that it can improve the prediction compared with linear eddy-viscosity model.

With the EASM model, the Reynolds stresses are given by

$$\begin{aligned} \overline{u_i u_j} &= \frac{2}{3} k \delta_{ij} - 2\nu_t S_{ij} \\ &- 2\nu_t^* \frac{k^*}{\varepsilon} \alpha_2 (S_{ik} W_{kj} + S_{jk} W_{ki}) \\ &+ 4\nu_t^* \frac{K^*}{\varepsilon} \alpha_3 \left(S_{ik} S_{kj} - \frac{1}{3} S_{kl} S_{kl} \delta_{ij} \right) \end{aligned}$$

where

$$\begin{aligned} \nu_t &= C_\mu \frac{k^{*2}}{\varepsilon}, \quad \nu_t^* = C_\mu^* \frac{k^{*2}}{\varepsilon} \\ C_\mu &= \frac{3(1 + \eta^2) + 0.2(\eta^6 + \zeta^6)}{3 + \eta^2 + 6\eta^2 \zeta^2 + 6\zeta^2 + \eta^6 + \zeta^6} \alpha_1 \\ C_\mu^* &= \frac{3(1 + \eta^2)}{3 + \eta^2 + 6\eta^2 \zeta^2 + 6\zeta^2 + \eta^6 + \zeta^6} \alpha_1 \\ \eta &= \frac{\alpha_3 k^*}{\varepsilon} \sqrt{S_{ij} S_{ij}}, \quad \zeta = \frac{\alpha_2 k^*}{\varepsilon} \sqrt{W_{ij} W_{ij}} \end{aligned}$$

Model	SSG	LRR	IP
$C_{\alpha w}$	0.61	0.63	0.61

Table 3: Values of $C_{\alpha w}$

$$\alpha_1 = \left(\frac{4}{3} - C_2\right) \frac{g}{2}, \quad \alpha_2 = (2 - C_4) \frac{g}{2},$$

$$\alpha_3 = (2 - C_3) \frac{g}{2}, \quad g = \frac{1}{C_1/2 + C_5 - 1}$$

C_1, C_2, C_3 and C_4 are the coefficients of the linear pressure-strain model given previously. The value of C_5 is 2.09 for the LRR and the IP model, and 1.89 for the SSG model. We use the formula proposed by Gatski [10] for the coefficients C_μ and C_μ^* .

To take into account the wall effect, k^* is employed instead of k . Its definition is given by:

$$k^* = k(1 - e^{-R_t/65}), \quad R_t = k^2/(\nu\varepsilon)$$

To determine k and ε , we solve a two-equation $k - \omega$ model which reads as follow:

$$\frac{Dk}{Dt} = P_k - \varepsilon + \frac{\partial}{\partial x_k} \left[\left(\nu + \frac{\nu_t}{C_k} \right) \frac{\partial k}{\partial x_k} \right]$$

$$\frac{D\omega}{Dt} = \alpha \frac{\omega}{k} P_k - \beta \omega^2 + \frac{\partial}{\partial x_k} \left[\left(\nu + \frac{\nu_t}{C_\omega} \right) \frac{\partial \omega}{\partial x_k} \right]$$

$$+ f_\omega^2 \frac{2}{k} \left(\nu + \frac{\nu_t}{C_\omega} \right) \frac{\partial \omega}{\partial x_j} \frac{\partial k}{\partial x_j}$$

with

$$\alpha = (C_{\varepsilon 1} - 1)f_\omega + C_{\alpha w}(1 - f_\omega)$$

$$\beta = C_\mu(1 - C_{\varepsilon 2})$$

$$C_k = 1.0$$

$$C_\omega = 1.3$$

$$f_\omega = \tanh \left(\frac{0.03k}{\nu\omega} \right)$$

$$\varepsilon = C_\mu k\omega$$

$$C_\mu = 0.09$$

$$C_{\varepsilon 1} = 1.45$$

$$C_{\varepsilon 2} = 1.92$$

The coefficient $C_{\alpha w}$ depends on the pressure strain model. The following table summarizes the values for each model:

At high Reynolds numbers where $f_\omega = 1$, the ω equation is equivalent to the ε equation with the $C_{\varepsilon 1}$ and $C_{\varepsilon 2}$ coefficients given above. The reason for retaining the ε equation for High Reynolds Number flows is that the ε equation is well established with

well calibrated coefficients. Besides, it is well known that the solution of the ω equation may be sensitive to the free stream value of ω . By retaining the cross diffusion term, this problem can be avoided.

NUMERICAL RESULTS

Computations have been performed on a domain covering the whole ship with $120 \times 81 \times 34$ nodes in the streamwise, radial and girthwise directions respectively. A third order upwind-biased scheme is used to discretize the convection term. The convergence is ensured by checking the evolution of the wall friction velocity. Several thousand iterations are necessary to achieve convergence. Computational time with the Reynolds stress model is about twice more important than with the EASM or two-equation models.

The influence of the different linear pressure-strain models presented previously will be studied only with the EASM model. Computations show that the LRR model gives results which are similar to those obtained with the IP model. Consequently, only the results obtained with the IP and SSG models will be presented. With the Reynolds stress model, computation has only been done with the IP model for the pressure-strain term at the present time. For comparison, results obtained with a linear eddy-viscosity model are also given. The linear eddy-viscosity model selected is the SST model proposed by Menter [6].

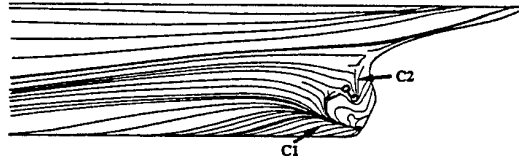


Figure 3: Wall limiting streamlines predicted with the Menter's SST model

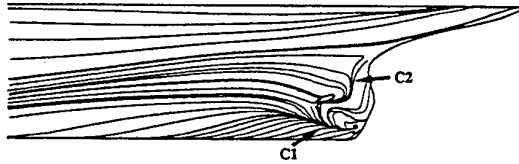


Figure 4: Wall limiting streamlines predicted with the EASM model using the IP pressure-strain model

The wall limiting streamlines are found to be very sensitive to turbulence model. The limiting streamlines predicted with the SST model, the EASM-IP model (explicit algebraic stress model with isotropi-

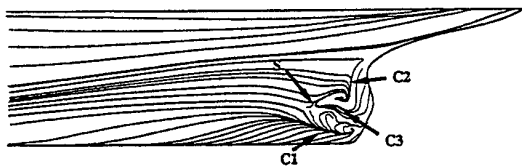


Figure 5: Wall limiting streamlines predicted with the EASM model using the SSG pressure-strain model

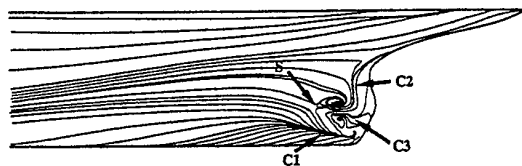


Figure 6: Wall limiting streamlines predicted with the Reynolds stress model.

zation-of-production pressure-strain model), the EASM SSG model, and the Reynolds stress model are shown in figures 3 to 6 respectively. All turbulence models predict the main features of the wall limiting streamlines observed in the experiments: an horizontal line of convergence C1, a vertical line of convergence C2, and a reversed flow region. Among the computational results, two different patterns can be distinguished. With the EASM-SST model and the Reynolds stress model, a line of convergence C3 can be observed in the reverse flow region. Above this line, a spiraling flow can also be identified. A saddle point S associated with the line of convergence C3 can be also identified in front of the reversed flow region. Although experimentally visualized limiting streamlines seem to be in better agreement with the computed limiting streamlines obtained with the EASM-IP model and the SST model for which the above mentioned features are not observed, flows with the former limiting streamlines pattern give better agreements concerning prediction of the mean velocity field. The existence of the spiraling flow above the C3 line is associated with a strong longitudinal vortex. Although the EASM-IP model and the Reynolds stress model are based on the same pressure-strain model, the predicted limiting streamlines are quite different. However, with the SSG pressure-strain model, the EASM model predicts similar results (figure 5) as the Reynolds stress model (figure 6).

The distributions of the pressure coefficient along the keel and the waterline predicted with different turbulent models are compared with the measurements in figure 7. The similar predictions provided by differ-

ent turbulent models suggest that the pressure field is mainly determined by the shape of the ship. Discrepancies between the prediction and the measurements are likely due to a blockage effect.

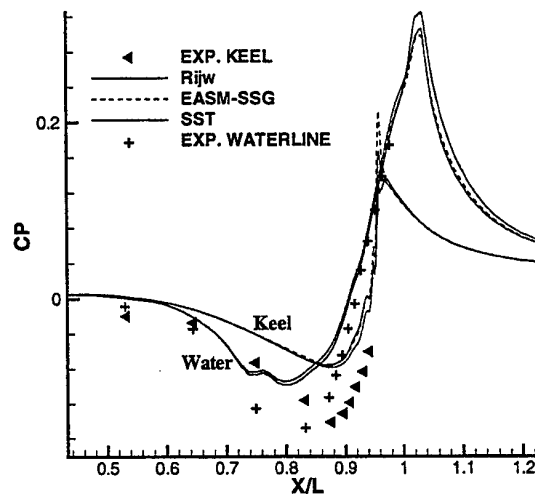


Figure 7: Pressure coefficient distribution

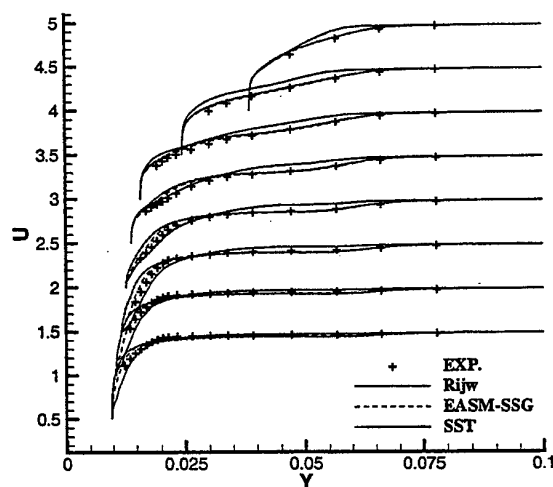


Figure 8: Streamwise velocity profiles at $x/L=0.941$ as function of y for several depths

The predicted mean streamwise and vertical velocity components will be compared with the experimental data at several horizontal sections. Since the

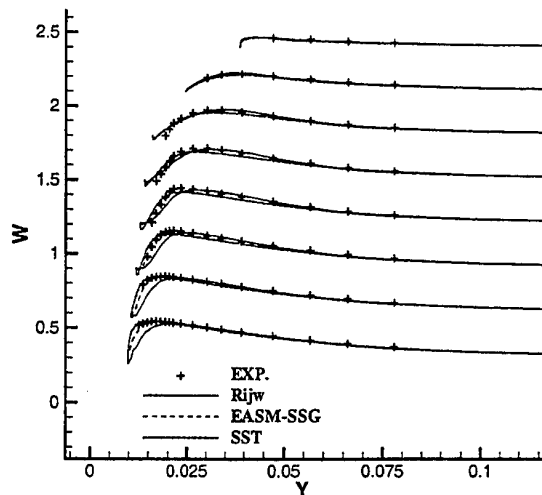


Figure 9: Vertical velocity profiles at $x/L=0.941$ as function of y for several depths

EASM-IP model gives similar result as the EASM-SSG model, we will mainly compare the SST model, the Reynolds stress model, and the EASM-SSG model. At section $x/L=0.941$, the Reynolds stress model gives a better prediction of the streamwise velocity component near the keel where the curvature (profiles in the lower part of the figure 8). Improvement is also observed in the region with the EASM-SSG model compared with the SST model. Near the water surface however, the Reynolds stress model fails to capture correctly the growth of the turbulent boundary layer, while both the EASM model and the SST model provide a good prediction. The imperfections of the Reynolds stress model are also observed in the free stream region where a low momentum domain exists because of the convection of lower momentum from the upwind station. Comparison of the vertical velocity component (figure 9) also indicates that the most satisfactory result is obtained with the EASM-SSG model, while the Reynolds stress model underestimates the vertical velocity component near the wall.

The EASM model is deduced from the Reynolds stress model under a local equilibrium assumption. Thus, the domain of validation of the Reynolds stress model is expected to be larger than that of the EASM model. However, the opposite conclusion must be drawn in the present computation. Since the same pressure-strain model is used in both models, the only differences between the Reynolds stress model and the EASM model concern the local equilibrium as-

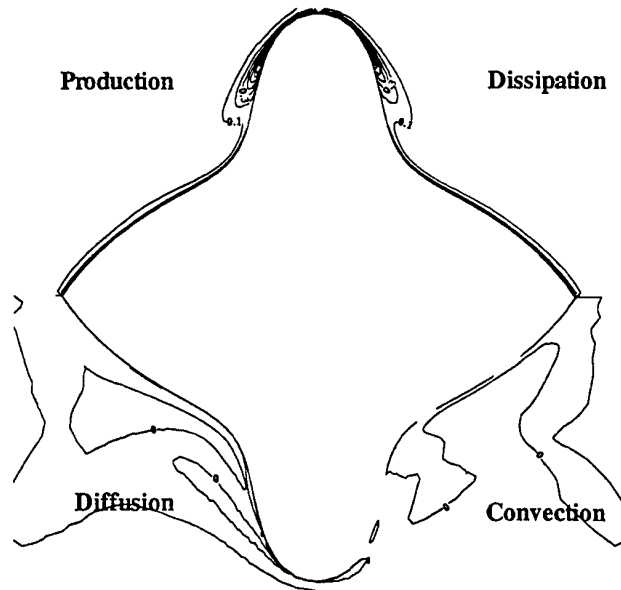


Figure 10: Budget of the kinetic energy equation predicted by the SST model at the section $x/L=0.941$

sumption, the approximations employed to obtain the explicit solution of the algebraic stress model, and the wall reflection terms used only in the Reynolds stress model. The local equilibrium assumption can be easily checked with the budget of the kinetic energy transport equation. From the budget predicted with the SST model shown in figure 10, it can be observed that, at this station, both convection and turbulent diffusion terms are small, compared with the production and turbulent dissipation terms. Therefore, the flow can be considered in local equilibrium. It is unlikely that the approximations employed to obtain the explicit solution of the algebraic Reynolds stress model significantly improve the deficiencies presented in the original model. This is the reason why we believe that the deficiencies of the Reynolds stress model at this station is mainly due to the modelization of the wall reflection term.

At a station further downstream $x/L=0.962$, the convection and the turbulent diffusion become more important. At the center of the longitudinal vortex, the sum of these two terms represents about 40% of the production (figure 11). However, the prediction obtained with the EASM-SSG model remains globally the best for the streamwise and vertical velocity components compared with the SST model and the Reynolds stress model (figures 12 and 13). By using different initializations and doing more iterations, it has been checked that the unsatisfactory solution provided by the Reynolds stress model was not due to

possible numerical problems. It is neither due to the correction function f_c used in the numerical implementation. Figures 14 and 15 present the results obtained with different correction functions. With $f_c = 0$, the linear eddy-viscosity model is recovered and the solution of the Reynolds stress transport equation is only used to determine the turbulent velocity scale. With this choice, a very good prediction of the velocity field is obtained at this station. However, it exhibits similar drawbacks as other linear eddy-viscosity model at downstream stations, and should not be considered as an acceptable model. Similar results are obtained when two different correction functions $f_c = 1 - e^{-\frac{R_y}{50}}$ and $f_c = 1 - e^{-\frac{R_y}{500}}$ are used (figures 14 and 15).

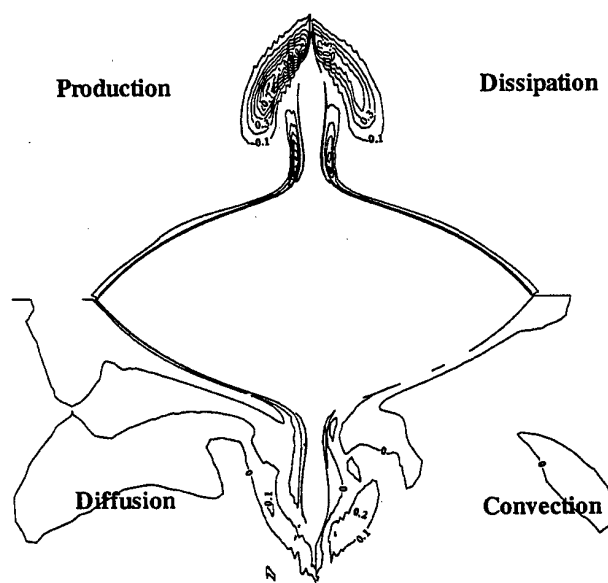


Figure 11: Budget of the kinetic energy equation predicted by the SST model at the section $x/L=0.962$

$X/L=0.978$ is the station where the propeller should be present. The successful prediction of the hook-shaped mean streamwise velocity contours observed in the measurements has always been considered as a key criterion for assessing the performance of a turbulence model designed for ship flows. In the center of the longitudinal vortex, the streamwise velocity profiles are correctly predicted, while the SST model and the EASM-SSG model predict a lower value (figure 16). The width of the longitudinal vortex is however better captured with the EASM-SSG model. Compared with the previous stations, the prediction of the vertical velocity with the Reynolds stress model is dramatically improved. This results provides further justification that the poor prediction of the vertical ve-

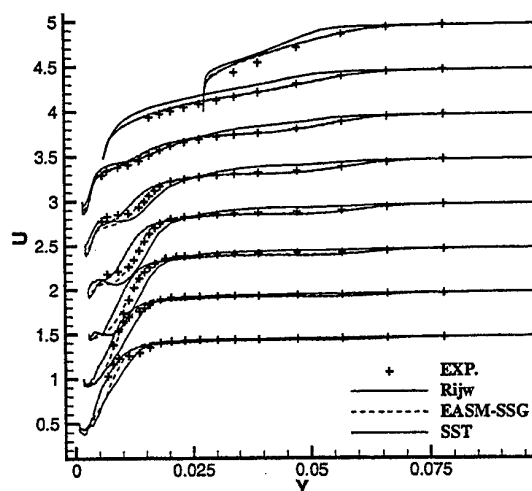


Figure 12: Streamwise velocity profiles at $x/L=0.962$ as function of y for several depths

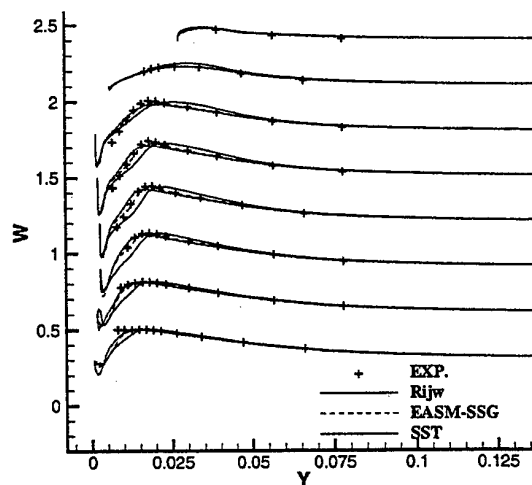


Figure 13: Vertical velocity profiles at $x/L=0.962$ as function of y for several depths

locity component with the Reynolds stress model is due to the wall reflection term.

By comparing the predicted mean streamwise velocity contours with the experimental measurements at this station (figures 18 to 21), it can be observed that the hook-shaped velocity contours are remarkably well captured with this new Reynolds stress model

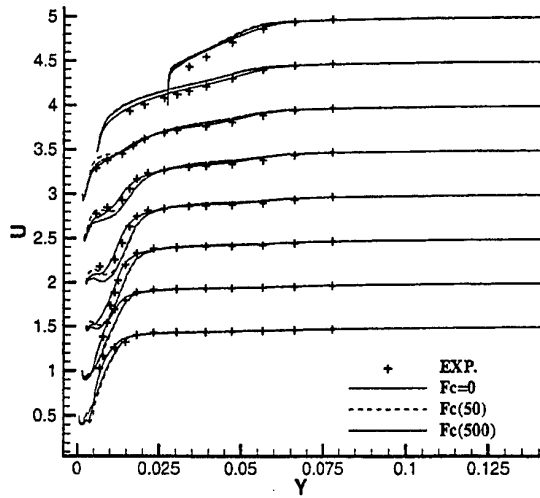


Figure 14: Prediction of the streamwise velocity profiles at $x/L=0.962$ by the Reynolds stress model with different correction functions

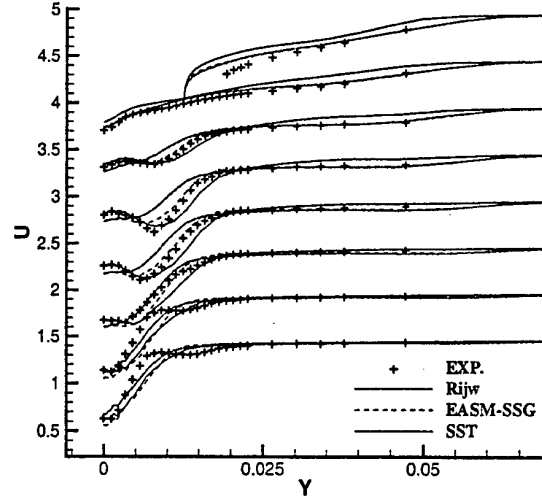


Figure 16: Streamwise velocity profiles at $x/L=0.978$ as function of y for several depths

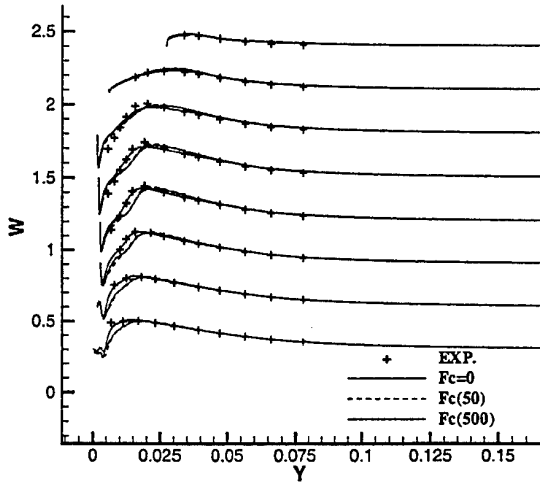


Figure 15: Prediction of the vertical velocity profiles at $x/L=0.962$ by the Reynolds stress model with different correction functions

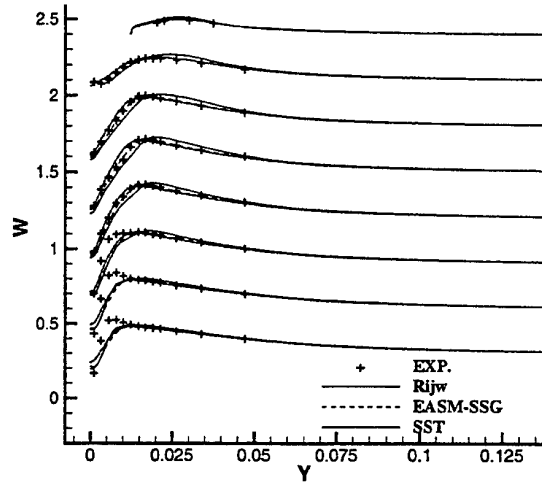


Figure 17: Vertical velocity profiles at $x/L=0.978$ as function of y for several depths

(figure 21). With the EASM model and the SST model, the streamwise velocity at the center of the longitudinal vortex is under-predicted. Compared with the IP model (figure 19), the SSG model provides a simulated flow in better agreement with the experiments (figure 20). The improved performance of the EASM

and Reynolds stress models reveals the limitation of linear eddy-viscosity model for the prediction of complex three-dimensional turbulent flows.

In a previous study using an algebraic model [2], the authors have found that the prediction of turbulent velocity and length scales was a key issue. Figures 22 and 23 show the predicted turbulent kinetic

energy and turbulent length scales obtained with different models. The good agreement between all tested turbulent models suggests that the performance of a turbulence model does not depend only on its ability to provide a good estimation of the turbulent velocity and length scales. The turbulent kinetic energy budget at the station $x/L=0.978$ shown in figure 24 reveals that the sum of the convection and the turbulent diffusion terms is almost as important as the turbulent dissipation term. Consequently, the convection and the turbulent diffusion terms, intrinsically present in the Reynolds stress transport equations, can not be neglected. In the algebraic stress model, the convection and the diffusion effects are taken into account by employing a local equilibrium assumption. For example, the convection term is approximated by

$$\frac{D\tau_{ij}}{Dt} = \frac{\tau_{ij}}{K} \frac{DK}{Dt}$$

To check the validity of this assumption, the correlation maps between $k \frac{D\tau_{ij}}{Dt}$ and $\tau_{ij} \frac{DK}{Dt}$ are plotted for the normal and shear stresses, respectively, for the station $x/L=0.978$ by using the solution of the Reynolds stress model. If the local equilibrium assumption can be accepted for the normal stress as illustrated by figures 25, the figure 26 indicates that the same assumption is not valid for the shear stress. Since the convection of the Reynolds stresses is not negligible, it is not possible to obtain the details of the velocity distribution at this station with the EASM model or the exact solution of algebraic stress model. A full Reynolds stress transport model is the only alternative.

The turbulence relaxation in the wake is unfortunately not very well captured with the Reynolds stress model. This is illustrated by the prediction of the velocity profiles shown in figures 27 and 28. The budget of the kinetic energy transport equation shown in figure 29 indicates that, while the production, dissipation and the convection term decrease compared with the situation at upstream stations, the turbulent diffusion term is increased and becomes important at this station. Since the EASM model provides a reasonable prediction for the vertical velocity component, the modelization of the turbulent diffusion term with the Daly & Harlow model is likely responsible for the inadequacy of the Reynolds stress in the wake.

CONCLUDING REMARKS

The flow around the HSVA tanker has been calculated by using different turbulent models ranging from linear eddy-viscosity model, the explicit algebraic stress model, to full Reynolds stress transport model. A stable solution of the Reynolds stress transport equations has been obtained by implementing a new near-

wall model and a defect correction approach. On one hand, non-linear models obtained from an approximate explicit solution of the algebraic stress models improve the prediction in all aspects compared with simple linear eddy-viscosity models. On the other hand, the solution of the Reynolds stress transport equations shows that the local equilibrium assumption on which the algebraic stress model is based is not valid in the region where the longitudinal vortex is intense. Physically accurate computations of this flow can only be obtained by solving the Reynolds stress transport equations. However, although an improved prediction has been obtained in the region where the convection of the Reynolds stress is important, the present Reynolds stress model provides a relatively less satisfactory prediction elsewhere compared with less sophisticated turbulence models. The weaknesses of the proposed Reynolds stress model are likely due to the modelization of the wall reflection and the turbulent diffusion terms. Finally, the computational results suggest that the exact representation of the convection and production terms is mandatory but not sufficient to improve the prediction in the whole fluid domain. It is necessary to improve simultaneously the modelization of the pressure-strain, turbulent diffusion and turbulent dissipation terms, otherwise the solution may be globally less accurate than the one provided by cruder turbulence closures.

ACKNOWLEDGMENTS

Thanks are due to the Scientific Committee of IDRIS and the DS/SPI for attributions of CPU on the Cray C98, the Cray T3E and the VPP machines.

REFERENCES

1. Wiegardt, K. and Kux, J., "Nomineller nachstrom auf grund von windkanal versuchen," Jahrb. der Schiffbau Technischen Gesellschaft (STG), 1980.
2. Deng, G.B., Queutey, P. and Visonneau, M. "Navier-stokes computations of ship stern flows: A detailed comparative study of turbulence models and discretisation schemes," Proc. 6th Int. Conf. on Numerical Ship Hydrodynamics, Patel, V.C. and Stern, F., eds., National Academy Press, 1993, pp. 367-386.
3. Sotiropoulos, F. and Patel, V.C., "Application of Reynolds-stress transport models to stern and wake flows," Journal of Ship Research, Vol. 39-4, 1995, pp. 263-283.
4. Institute, Ship Research, ed., Proc. CFD Workshop for Improvement of Hull Form Designs - Tokyo, 1994.

5. Wilcox, D.C., "Reassessment of the scale-determining equation for advanced turbulence models," *AIAA Journal*, Vol. 26, 1988, pp. 1299-1310.

6. Menter, F.R. "Zonal two-equations $k - \omega$ turbulence models for aerodynamic flows," *AIAA 24th Fluid Dynamics Conf.*, AIAA Paper 93-2906, 1993.

7. Deng, G.B. and Visonneau, M. "Evaluation of eddy-viscosity and second-moment turbulence closures for steady flows around ships," *21st Symposium on Naval Hydrodynamics*, 1996.

8. Kawamura, T., "Numerical simulation of 3d turbulent free-surface flows," Tech. Rep. (Thesis), 1998, ICCH.

9. Deng, G.B. and Visonneau, M. "Computation of a wing-body junction flow with a new Reynolds-stress turbulence model," *22nd Symposium on Naval Hydrodynamics*, 1998.

10. Gatski, T.B. and Speziale, C.G., "On explicit algebraic stress models for complex turbulent flow," *J. Fluid Mech.*, Vol. 254, 1993, pp. 59-78.

11. Deng, G.B. and Visonneau, M. "Near-wall modelization for dissipation in second-moment closures," *Proc. 11th Turbulent Shear Flows*, 1997.

12. Gibson, M.M. and Launder, B.E., "Ground effects on pressure fluctuations in the atmospheric boundary layer," *J. Fluid Mech.*, Vol. 86, 1978, pp. 491-511.

13. Launder, B.E., Reece, G.J. and Rodi, W., "Progress in the development of a Reynolds stress turbulent closure," *Journal of Fluid Mechanics*, Vol. 183, 1975, pp. 63-63.

14. Speziale, C.G., Sarkar, S. and Gatski, T.B., "Modeling the pressure-strain correlation of turbulence: An invariant dynamical systems approach," *Journal of Fluid Mechanics*, Vol. 227, 1991, pp. 245-272.

15. Hanjalić, K. and Jakirlić, S., "Contribution Towards the Second-Moment Closure Modelling of Separating Turbulent Flows," *Computers & Fluids*, Vol. 27, 1998, pp. 137-156.

16. Rodi, W., "A new algebraic relation for calculating the Reynolds stresses," *ZAMM*, Vol. 56, 1976, pp. 219-221.

17. Pope, S.B., "A more general effective viscosity hypothesis," *J. Fluid Mech.*, Vol. 72, 1975, pp. 331-340.

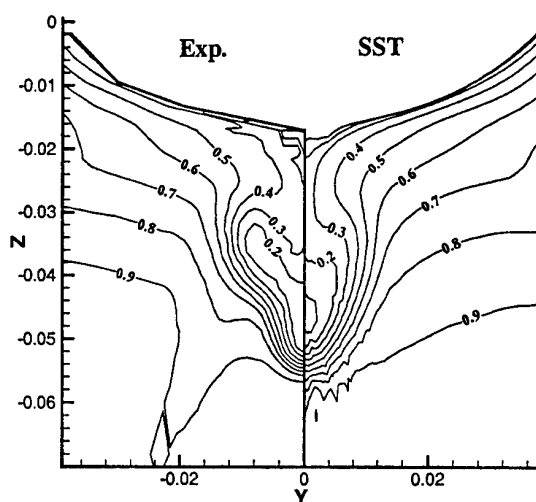


Figure 18: SST model - Comparison between experimental and computed isowakes at $x/L=0.978$

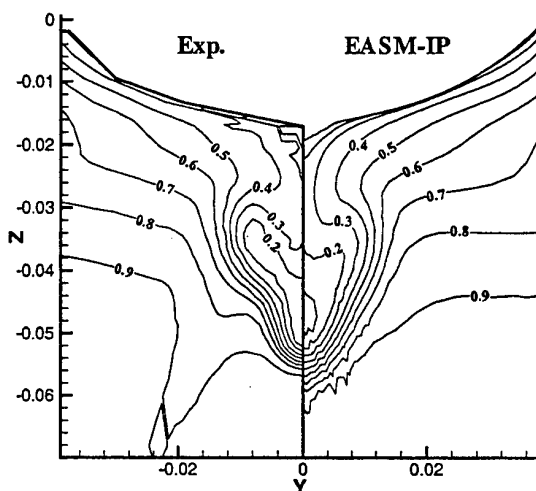


Figure 19: EASM-IP model - Comparison between experimental and computed isowakes at $x/L=0.978$

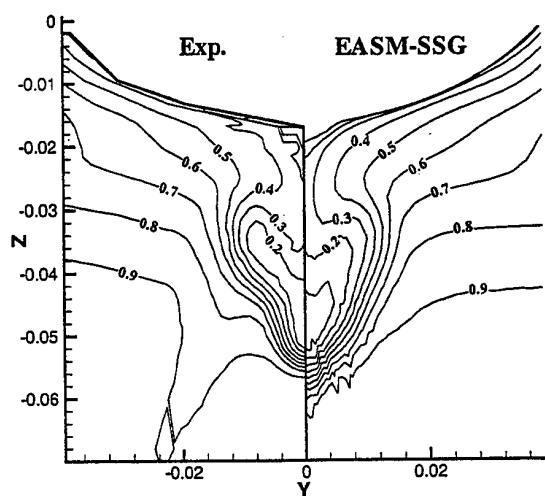


Figure 20: EASM-SSG model - Comparison between experimental and computed isowakes at $x/L=0.978$

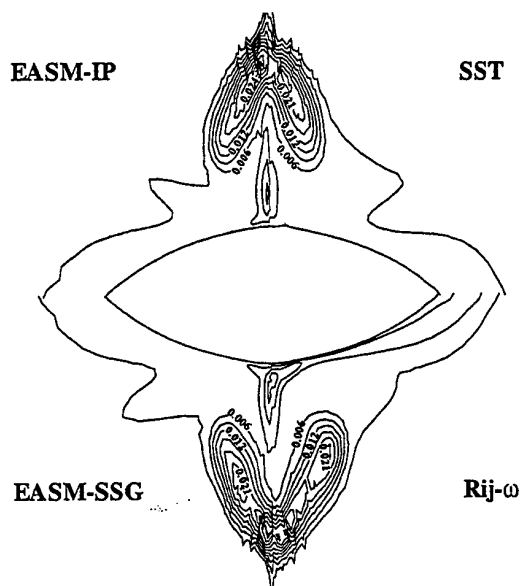


Figure 22: Comparison of predicted turbulent kinetic energy at station $x/L=0.978$

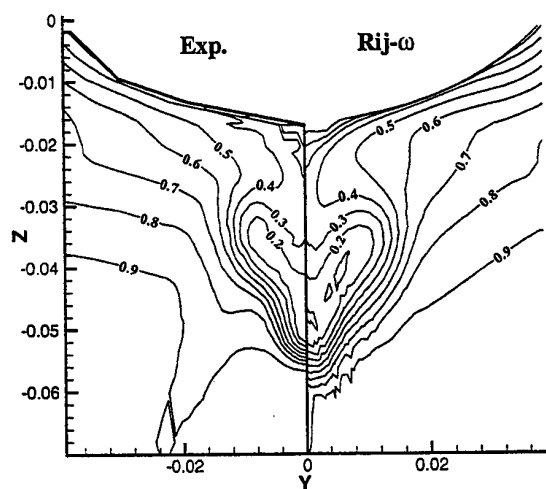


Figure 21: Reynolds stress model - Comparison between experimental and computed isowakes at $x/L=0.978$

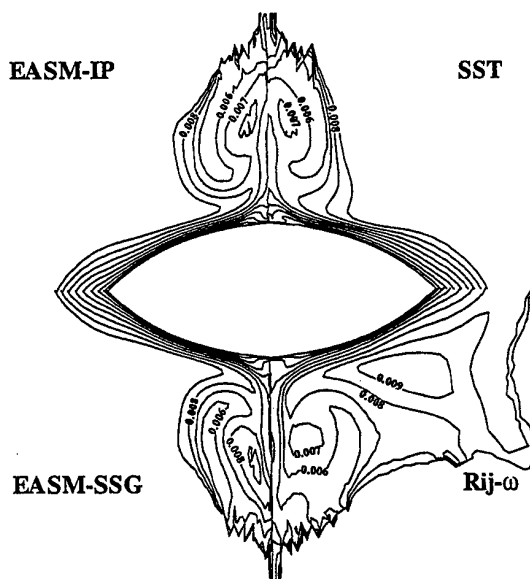


Figure 23: Comparison of predicted turbulence length scale \sqrt{k}/ϵ at station $x/L=0.978$

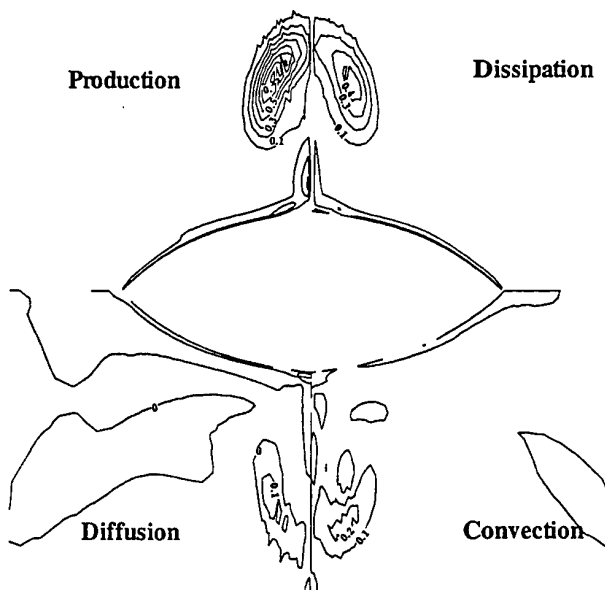


Figure 24: Budget of the kinetic energy equation predicted by the SST model at the station $x/L=0.978$

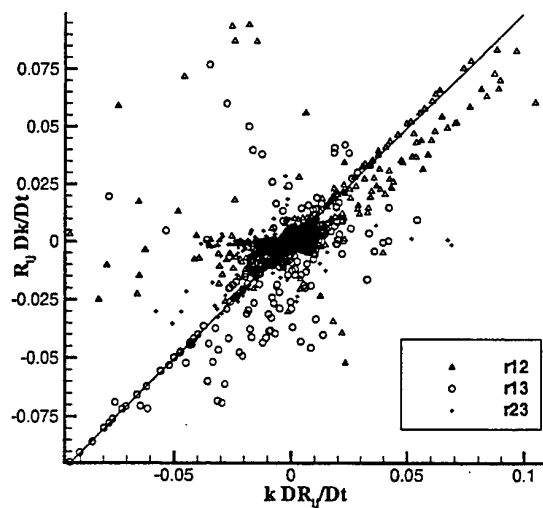


Figure 26: Correlation map for the shear stress at the station $x/L=0.978$

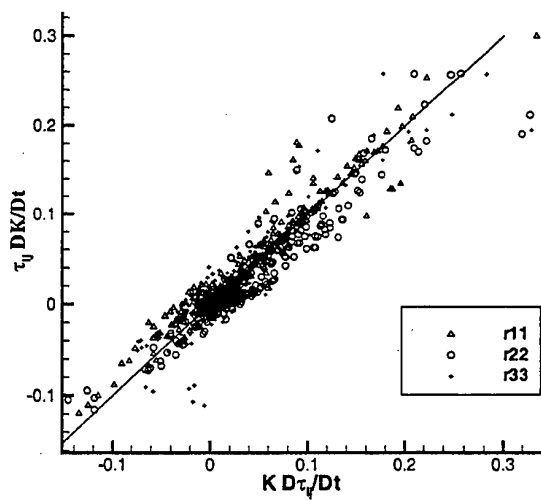


Figure 25: Correlation map for the normal stress at the station $x/L=0.978$

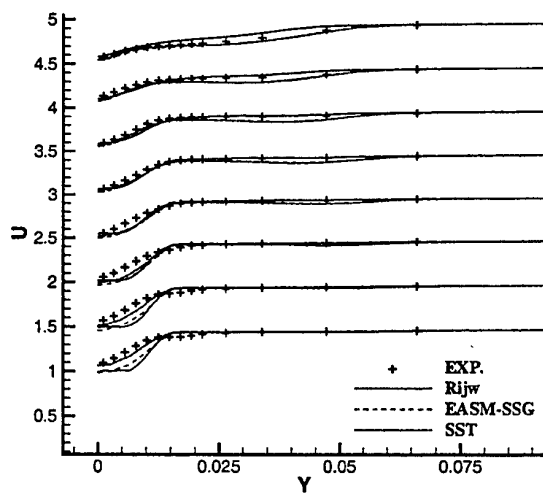


Figure 27: Streamwise velocity profiles at $x/L=1.045$ as function of y for several depths

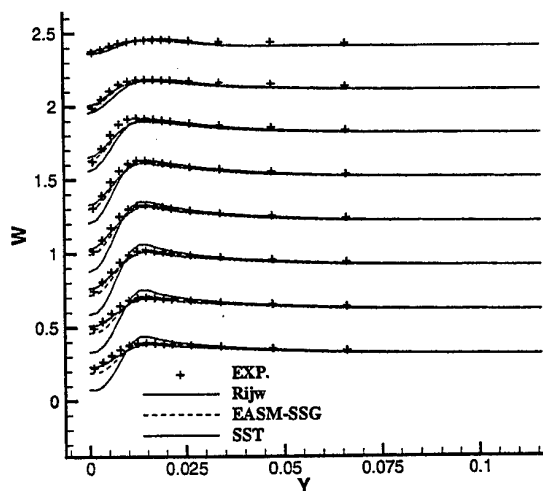


Figure 28: Vertical velocity profiles at $x/L=1.045$ as function of y for several depths

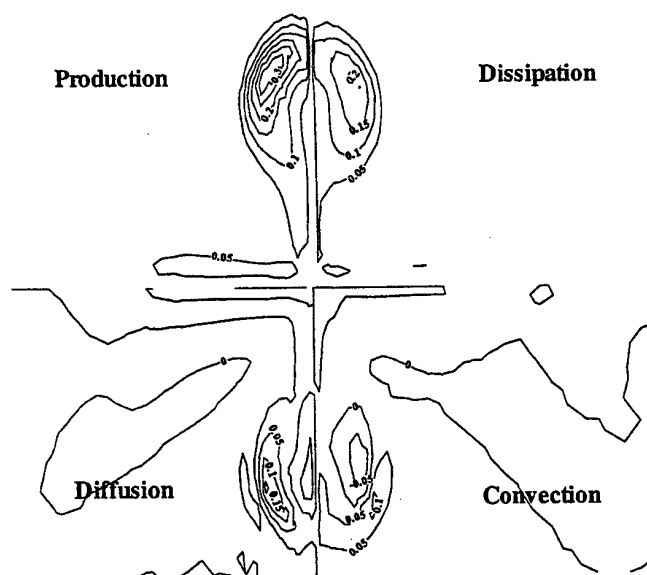


Figure 29: Budget of the kinetic energy equation predicted by the SST model at the station $x/L=1.045$

Paper Submitted to the
Seventh International Conference on Numerical Ship Hydrodynamics
July 19-22, 1999, Nantes, France

**Prediction of Forces and Moments of Rudders with Flap and Tab
Part I. 2D Airfoil with Flap and Tab**

Chao-Ho Sung and Bong Rhee
David Taylor Model Basin, CDNSWC, MD 20817-5700, U.S.A.

ABSTRACT

A numerical procedure for the prediction of the forces and moments of a 2D airfoil with a flap and a tab has been developed. The procedure is based on solving the incompressible Reynolds-averaged Navier-Stokes equations coupled with a κ - ω turbulence model. Some features of the numerical method use have been highlighted. In particular, the preconditioning method, multigrid method, nonreflecting far field boundary condition, wall boundary condition for the specific dissipation rate and the approach to obtain good convergence in solving the κ - ω equations have been discussed. Computed results of the airfoil section lift coefficients, airfoil section pitching moment coefficients, flap hinge moment coefficients and tab hinge moment coefficients have been compared with the measured data. The trend of the variation of forces and moments has been accurately captured. The airfoil section lift coefficients have been predicted within 5 percent discrepancy from the data even at high angles of attack and high flap deflections. The discrepancy of the airfoil section pitching moment coefficients is slightly higher at about 15 percent. Higher discrepancy occurs when values of the moments are small. The flap hinge moment coefficients are in general overpredicted. The prediction of the tab hinge moment coefficients can only capture the trend properly with uneven discrepancy. In general, the predictive procedure is believed to be useful for design applications.

INTRODUCTION

A control surface here will be defined as consisting of a main control surface, a flap and a tab. The main control surface may be fixed or movable but the flap and tab are always movable. Control surfaces have at least three major functions applicable to both aircraft and marine vehicles. (1) The main control surface, flap and tab can be aligned to form a high cambered control surface to increase the lift significantly. In aerospace industry, this is the so called high-lift multi-element airfoil (or wing). (2) Control surfaces are normally designed for low speed operation, because undesirable excessive control may occur at high speed. A smoother control at high speed may be achieved by keeping the main control surface fixed and using the flap and/or tab for control. (3) At high speed, an excessively large hinge moment can arise in the main control surface. This large moment can be reduced by deflecting the flap and/or tab in the direction opposite to the direction of the angle of attack of the incoming flow. The purpose of this paper is to report the progress made in the development of a predictive capability of the forces and moments of control surfaces. The design of efficient control surfaces using the predictive capability will be left for future work.

This paper will also be confined to 2D configurations. A 2D study in the development stage of a predictive capability has a great advantage over a 3D study. Because of a much smaller grid size requirement, it is much easier to do grid refinement study to determine a good grid distribution and size required to achieve grid-independent solution. This information is invaluable to 3D studies. Progress in the 3D study will be reported in the future.

There is an extensive literature on both experiments and computations on the high-lift multi-element airfoil (wing). Many references can be found in [1]. For marine applications, work on control surfaces (rudders) is mostly experimental and very little computational work has appeared in the literature. Forces and moments on control surfaces (no flap nor tab) has been measured by Whicker et al.[2] and those on a flapped control surface (no tab) has been measured by Bowers[3]. Water tunnel experiments on a series of 12 rudders with systematic variations of flap area and flap balance have been performed by Kerwin et al.[4]. Three variations of skeg-rudders (i.e., fixed main control surfaces with movable flaps) have been investigated in the wind tunnel in[5]. The effect of gaps between the rudder and the skeg has also been investigated. It has been observed that the effect from

gap is insignificant. Unlike aerospace industry, there are not too many computational works on control surfaces. Recently, Soding [6] discussed the application of potential theory in Rudder flow predictions. The effects of flaps and tabs were not discussed. Computations for rudders (no flap nor tab) based on solving the Reynolds-averaged Navier-Stokes (RANS) equations with a $k-\epsilon$ turbulence model have been reported by Chau [7]. The 2D computations to be reported in this paper will be compared with the data of a NACA-0015 airfoil with flap and tab measured by Sears et al. [8]. The 3D computations to be reported later will be compared with the data to be reported in [9]. All the investigations discussed so far assumed that the control surface was operating in a uniform flow without the influence of the hull boundary layer, horse-shoe vortex shed by appendages and finally propeller.

In the next section, the governing equations of the incompressible Reynolds-averaged Navier-Stokes equations and the two equations of a $k-\omega$ turbulence model will be described. The numerical method used will be discussed next. Only some special features of the numerical schemes will be highlighted omitting most of the details. The experiment performed on the airfoil with flap and tab will be described and the comparisons between computations and measurements will then be discussed. Finally some conclusions are mentioned.

GOVERNING EQUATIONS

The incompressible Reynolds-averaged Navier-Stokes (RANS) equations and a nonlinear $k-\omega$ turbulence model are to be solved. The nonlinear $k-\omega$ model used here is a standard $k-\omega$ turbulence model developed by Wilcox [10] coupled with a nonlinear Reynolds stress model.

$$\frac{\partial u_i}{\partial x_i} = 0 \quad (1)$$

$$\frac{\partial u_i}{\partial t} + \frac{\partial u_i u_j}{\partial x_j} = -\frac{\partial p^*}{\partial x_i} + \frac{\partial}{\partial x_j} (\nu \frac{\partial u_i}{\partial x_j} - \tau_{ij}) \quad (2)$$

$$\begin{aligned} \frac{\partial k}{\partial t} + \frac{\partial}{\partial x_j} (u_j k) - \frac{\partial}{\partial x_j} [(\nu + \sigma_k \nu_t) \frac{\partial k}{\partial x_j}] = \\ -\tau_{ij} \frac{\partial u_i}{\partial x_j} - \beta^* \omega k \end{aligned} \quad (3)$$

$$\begin{aligned} \frac{\partial \omega}{\partial t} + \frac{\partial}{\partial x_j} (u_j \omega) - \frac{\partial}{\partial x_j} [(\nu + \sigma_\omega \nu_t) \frac{\partial \omega}{\partial x_j}] = \\ -\alpha \frac{\omega}{k} \tau_{ij} \frac{\partial u_i}{\partial x_j} - \beta \omega^2 \end{aligned} \quad (4)$$

where u_i is the Cartesian velocity component, p^* is the pressure p divided by a constant density ρ , κ is the turbulent kinetic energy, ω is the specific dissipation rate, ν is the kinematic viscosity, ν_t is the eddy viscosity given as κ/ω and τ_{ij} is the Reynolds stress tensor. A quadratic Reynolds stress model developed by Speziale [11] will be used here and an explicit expression can be found there. Standard modeling coefficients are used: $\beta^* = 0.09$, $\beta = 3/40$, $\alpha = 5/9$ and $\sigma_k = \sigma_\omega = 1/2$.

NUMERICAL METHOD

The incompressible RANS equations are solved by the artificial compressibility approach first proposed by Chorin [12] and subsequently generalized and improved by Turkel [13]. A finite volume method is used. The mean flow (i.e., Eqns (1) and (2)) is discretized by a second-order accurate central difference method with fourth-order dissipation terms. The turbulent flow (i.e., Eqns (3) and (4)) is discretized by one of the several upwind schemes suggested by Yee [14]. The reason for using an upwind scheme to solve the turbulent flow is that the matrix is already diagonal; therefore there is no additional cost in doing characteristic formulation. The time step is based on an explicit one-step multi-stage Runge-Kutta method to reach a steady-state solution. This approach can also be extended in a very simple manner to solve the time dependent problems as discussed by Jameson [15] and Liu [16]. Several convergence acceleration techniques including multigrid, local time step, implicit residual smoothing, preconditioning and bulk viscosity damping have been implemented. To handle complex geometry, the multi-block grid structure is adopted.

These numerical techniques have been implemented in a code named IFLOW, synonymous with Incompressible FLOW. IFLOW is intended to be a production code for solving 2D, 3D, steady and unsteady problems. The code is highly modular in structure so different turbulence models and higher order schemes can be easily implemented. Some special features of the numerical schemes used will be highlighted. Detailed derivations will be mostly omitted.

Preconditioned Method

The preconditioned method is developed based on a system of hyperbolic equations, but the idea goes back to the effort to reduce the condition number of a matrix in linear algebra. For hyperbolic equations, the objective is to make the various speeds of different

wave modes more or less the same so that convergence can be significantly accelerated. This is particularly important if the artificial compressibility approach is adopted to solve incompressible flows. The reason is that the sound speed, which is one of the wave modes in the incompressible flow, propagates much faster than the fluid speed. The result is a very slow convergence as often encountered in the attempts to compute low Mach number flows using a compressible flow code.

The preconditioned mean flow (i.e., Eqns (1) and (2)) can be written in the conservative form as

$$P_o^{-1} q_t + F_x + G_y + H_z = 0 \quad (5)$$

where the preconditioned matrix P_o and the three components of fluxes F , G , and H are defined as

$$P_o^{-1} = \begin{bmatrix} (1+\gamma)\beta^{-2} & \gamma\beta^{-2}u & \gamma\beta^{-2}v & \gamma\beta^{-2}w \\ (1+\alpha+\gamma)\beta^{-2}u & 1+\gamma\beta^{-2}u^2 & \gamma\beta^{-2}uv & \gamma\beta^{-2}uw \\ (1+\alpha+\gamma)\beta^{-2}v & \gamma\beta^{-2}vu & 1+\gamma\beta^{-2}v^2 & \gamma\beta^{-2}vw \\ (1+\alpha+\gamma)\beta^{-2}w & \gamma\beta^{-2}wu & \gamma\beta^{-2}wv & 1+\gamma\beta^{-2}w^2 \end{bmatrix}$$

$$q = \begin{bmatrix} p^* \\ u \\ v \\ w \end{bmatrix}, \quad F = \begin{bmatrix} u \\ u^2 + p^* - \tau_{xx} \\ uv - \tau_{xy} \\ uw - \tau_{xz} \end{bmatrix}, \quad G = \begin{bmatrix} v \\ uv - \tau_{yx} \\ v^2 + p^* - \tau_{yy} \\ vw - \tau_{yz} \end{bmatrix},$$

$$H = \begin{bmatrix} w \\ uw - \tau_{wx} \\ vw - \tau_{wy} \\ w^2 + p^* - \tau_{zz} \end{bmatrix} \quad (7)$$

where α , β^{-2} and γ are preconditioning parameters, τ_{ij} , $i, j = x, y, z$, are Reynolds stresses. For mathematical analysis, it is easier to write Eqn (5) in a non-conservative form. Neglecting the viscous terms, it can be derived as:

$$P^{-1} q_t + A q_x + B q_y + C q_z = 0 \quad (8)$$

The explicit forms of matrices A , B , and C are omitted here. The preconditioning matrix P^{-1} is different from the previous one P_o^{-1} and is given by

$$P^{-1} = \begin{bmatrix} (1+\gamma)\beta^{-2} & \gamma\beta^{-2}u & \gamma\beta^{-2}v & \gamma\beta^{-2}w \\ \alpha\beta^{-2}u & 1 & 0 & 0 \\ \alpha\beta^{-2}v & 0 & 1 & 0 \\ \alpha\beta^{-2}w & 0 & 0 & 1 \end{bmatrix} \quad (9)$$

The condition $\alpha = \gamma$ ensures the system of partial differential equations is well-posed. However, the implication of well-posedness to numerical solution is not clear. In this paper, it is equal to $\alpha = \gamma = 0$ and β^{-2} is given as

$$\beta^{-2} = \max(|u|^2, \epsilon), \quad \epsilon = 0.7 \quad (10)$$

Through rather tedious algebraic manipulations, the eigenvalues and left and right eigenfunctions can be found. The maximum of eigenvalues is used to define a local time step. The eigenfunctions are of no use to central difference schemes except for establishing a nonreflecting boundary condition at far field. The final system of equations to be solved in the conservative form is

$$P_o^{-1} q_t + F_x + G_y + H_z = (P_o^{-1} | PA | q_{xxx})_x + (P_o^{-1} | PB | q_{yyy})_y + (P_o^{-1} | PC | q_{zzz})_z \quad (11)$$

Since the formulation is based on hyperbolic equation only, viscous terms should be added to the fluxes F , G and H as shown in Eqn (7). The right-hand side of Eqn (11) is the fourth-order matrix dissipation terms. The matrix dissipation gives the most accurate solution but is less stable because a smaller amount of dissipation is added. As a compromise between accuracy and robustness, vector dissipation is adopted in this paper. For vector dissipation, matrices PA , PB and PC are replaced by their corresponding radius spectra. In the curvilinear coordinates, ξ^I , $I=1,2,3$, the maximum eigenvalue in the i -direction is given by

$$\lambda_{\max}^i = \frac{1}{2} \left(|U^i| + \sqrt{U^i{}^2 + 4\beta^2 |a^i|^2} \right);$$

$$U^i = u \cdot a^i, \quad a^i = \nabla \xi^i \quad (12)$$

Multigrid Method

Multigrid is one of the most effective methods to accelerate the rate of convergence and should be used routinely in every production code. The approach in IFLOW follows mostly the ideas of Brandt [17] and Jameson [18]. Several variations including V-, W- and F-cycles have been implemented. In general, W- and F-cycles are more efficient but not significantly so. More levels of multigrid cost a little more but are more efficient. For simplicity, most computations performed with IFLOW use three levels of multigrid in V-cycle. The multigrid method is used routinely in IFLOW. For large scale computations on complex geometries, the starting of computation is often jumpy.

To obtain a smoother start, a multigrid starting procedure is used. Consider a 3-level multigrid computation: A 2-level multigrid consisting of the medium and coarse grids is run for about 50 cycles. The solution is then extrapolated to the fine grid to start the 3-level multigrid computation. In general, a solution adequate for engineering applications can be achieved in 100-500 multigrid cycles. This efficiency is at least as good as the best Computational Fluid Dynamics (CFD) codes available but is far from the Textbook Multigrid Efficiency (TME, less than 10 cycles) advocated by Achie Brandt [19]. Achieving TME is a noble endeavor and will have a significant impact on engineering applications of CFD.

Boundary Conditions

Only the solid wall and the farfield boundary conditions need to be discussed. At the wall, the three components of velocity and the turbulent kinetic energy κ are set equal to zero, the pressure p is derived from the zero normal pressure gradient at the wall. Finally, the wall boundary condition of specific dissipation rate ω originally given by Wilcox (p. 148 in [10]) is modified as

$$\omega_w = \frac{a_o}{\beta} \Omega_w, \beta = \frac{3}{40} \quad (13)$$

where Ω_w is the vorticity at the wall and a_o is a constant varying from a value of 6 given by Wilcox to 20. The choice of a_o may vary the convergence rate slightly but once the convergence is achieved the solution is about the same. The motivation in deriving the modified wall boundary condition (13) is to get rid of the requirement that the first grid normal distance must be given. The non-dimensional normal distance y^+ requirement creates difficulty for coarser grids because the first grid normal distances tend to be too large in the coarse grids. With Eqn (13), the normal distance does not appear and the y^+ of the first grid normal distance of the finest mesh should be in the order of 1 or 2.

At the far field, the gradients of the three components of velocity and the gradients of the two turbulence quantities κ and ω are set to zero. The pressure is obtained by a non-reflecting condition discussed by Hedstrom [20], Rudy and Strikverda [21] and Sung [22]. This is one of the most important boundary conditions for external flows and will be outlined. The idea is based on the characteristic formulation of hyperbolic equations, such that the outgoing solution modes will not be reflected back into the

computational domain to corrupt the solution. To do this, the time derivatives of the characteristic variables ϕ_i corresponding to the positive eigenvalue λ_+ at the left boundary $\xi = 0$ and the negative eigenvalue λ_- at the right boundary $\xi = 1$ are set equal to zero, i.e.,

$$\text{for } \lambda_+ > 0 \text{ at } \xi^i = 0$$

$$\phi_{1,i} = t_{11}p_i^* + t_{12}u_i + t_{13}v_i + t_{14}w_i = 0$$

$$\text{for } \lambda_- < 0 \text{ at } \xi^i = 1$$

$$\phi_{2,i} = t_{21}p_i^* + t_{22}u_i + t_{23}v_i + t_{24}w_i = 0 \quad (14)$$

$$\text{where } \phi = R^{-1}q, R^{-1} = \{t_{ij}\} \quad (15)$$

q is the vector defined in Eqn (7) and R^{-1} is the matrix of the left eigenvectors. The matrix R^{-1} is quite complex for general preconditioning. For the simpler case of non-symmetric preconditioning, Eqn (14) is quite simple and is given as

$$\text{for } \xi^i = 0$$

$$P_i^* + \left(\frac{U - \lambda_-}{|a|^2 - \alpha\beta^{-2}U\lambda_-} \right) (a_x u_i + a_y v_i + a_z w_i) = 0$$

$$\text{for } \xi^i = 1$$

$$P_i^* + \left(\frac{U - \lambda_+}{|a|^2 - \alpha\beta^{-2}U\lambda_+} \right) (a_x u_i + a_y v_i + a_z w_i) = 0 \quad (16)$$

$$\text{where } U = u \bullet a, \quad a = \nabla \xi,$$

$$\lambda_{\pm} = \frac{(1-\alpha)U}{2} \pm \sqrt{(1-\alpha)^2 U^2 + 4\beta^2 |a|^2} \quad (17)$$

Eqn (17) is used as the outflow far field boundary condition of P^* after the three components of velocity are specified.

Two-Equation Turbulence Models

It is well known that the convergence of the two-equation turbulence models is rather temperamental. Two techniques have been used in IFLOW and as a result the same convergence rate as using the Baldwin-Lomax turbulence model has been achieved. One of the techniques is the point-implicit method for source terms. Here, the positive part of the source term is treated explicitly, the negative part implicitly. This technique is in fact quite widely used. The other technique is to establish a lower bound for the specific dissipation rate ω by Schwartz inequality. To illustrate the method, it is sufficient to consider a linear Reynolds stress model

$$\tau_{ij} = \overline{u_i u_j} = \frac{2}{3} \kappa \delta_{ij} - c_\mu f_\mu \frac{K}{\beta^* \omega} (2S_{ij}) \quad (18)$$

$$\text{where } S_{ij} = \frac{1}{2} \left(\frac{\partial u_i}{\partial x_j} + \frac{\partial u_j}{\partial x_i} \right)$$

By Schwartz inequality, it can be shown that

$$\overline{u_i u_j}^2 \leq 4\kappa^2 \quad (19)$$

Taking square of the both sides of Eqn (18) gives

$$\tau_{ij}^2 = \frac{4}{3} \kappa^2 + 2(c_\mu f_\mu \frac{K}{\beta^* \omega})^2 P_o, \quad P_o \equiv 2S_{ij}S_{ij} \quad (20)$$

A lower bound for ω is then obtained by combining Eqns (19) and (20) as

$$\omega \geq \frac{c_\mu f_\mu}{\beta^*} \sqrt{\frac{3}{4} P_o} \quad (21)$$

The proportionality factor in Eqn (21) can be taken as a value in the neighborhood of 2. Different values for this factor can affect the convergence rate. But once the convergence is achieved, they all give about the same answer. The value used in this paper is 2.1.

DESCRIPTION OF EXPERIMENT

An experiment was performed in the NACA 4- by 6-foot vertical tunnel of an NACA-0015 airfoil equipped with a plain flap and a plain tab. The effective Reynolds number was approximately 2.76×10^6 based on the chord length ($c = 24$ inches) of the entire airfoil. The aerodynamic center was at $0.23c$. The hinge axes of flap and tab were located at $0.7c$ and $0.94c$, respectively. Thus the flap chord length was defined as $c_f = 0.3c$ and the tab chord length was $c_t = 0.06c$. The noses of the flap and tab were semicircles with the centers at the corresponding hinge axes. The flap gap was $0.005c$ and the tab gap was $0.001c$. The cases with both sealed and unsealed gaps were considered.

Airfoil section lift coefficient C_l , airfoil section pitch-moment coefficient C_m , flap section hinge-moment coefficient C_{hf} and tab section hinge-moment coefficient C_{ht} were measured under variations of angles of attack and deflections of flap and tab. The angle of attack varied from $+16$ to -18 degrees and flap deflection varied from 0 to 30 degrees. With the flap at 0 degree, tab deflection varied from 0 to 25 degrees; with the flap deflected at 5 degrees, tab deflection varied from 15 to -20 degrees; with the flap deflected at 15 and 25 degrees, tab deflection varied from 0 to 20

degrees. Airfoil section lift coefficient C_l was defined as (l/qc) , where l is the lift, c is the airfoil chord length, and q is the dynamic pressure defined by $1/2 \rho u_\infty^2$. Airfoil section pitch-moment coefficient C_m was defined by (m/qc^2) , where m is the airfoil section moment. Flap section hinge-moment coefficient C_{hf} was defined by (h_f/qc_f^2) and tab section hinge-moment coefficient C_{ht} was defined by (h_t/qc_t^2) , where h_f was the flap hinge moment and h_t was the tab hinge moment. The accuracy of data was claimed to be ± 0.2 degrees.

DISCUSSION OF RESULTS

Convergence and Grid-Independent Solution

As CFD plays an increasingly important role in practical engineering applications, it is important to have some idea about how accurate and reliable the computed solutions are. It is possible to perform meaningful error analysis on a simple problem in a Cartesian computational domain with a uniform grid for inviscid or laminar flows. However, it is not possible to analyze the order of accuracy of a spatial discretization scheme in a highly stretched computational domain in a curvilinear coordinate system. The situation becomes much worse with the additional complication from turbulence models. Efforts to quantify the errors in RANS computations for practical problems are dubious. From our experience and that of other researchers as in e.g., [23], it appears that a careful check of convergence history and mesh refinement to obtain grid-independent solution remains the most effective approach to establish confidence on solution.

The size of the computational domain and how the grid cells are distributed significantly affect the convergence rate and the quality of the solution. Originally, a smaller computational domain was used. The inflow was set at $3c$ ahead of the airfoil and the outflow was set at about $5c$ after the airfoil tail. The convergence was bumpy and hung after about 3 orders of magnitude drop in residue. A larger computational domain was later used. Now the inflow was at $5c$ and the outflow at $12c$ and the grid lines immediately after the tail were also forced to align with the streamlines as shown in Figure 1. Convergence rate is significantly improved. Figure 1 shows a typical grid with 3 blocks. Block 1 covers the entire airfoil, block 2 and 3 are for the flap gap and the tab gap, respectively. Since the effect of gaps is not significant, all the computed results shown are based on sealed gaps. Nevertheless, the grid distributions of block 1 used for computations of the sealed case are the same as if there were gaps. This is to demonstrate that good

solutions can be obtained even with rather awkward-looking grids. Several grid sizes have been investigated for mesh refinement. To investigate the effect of the changes in the grid size in the transverse direction (j-direction) with the grid size in the longitudinal (i-direction) fixed, three grids 184x48, 184x64 and 184x96 were used for computations. Then another three grids 184x64, 256x64 and 368x64 were used to investigate the effect of the changes in the grid size in the i-direction with the grid size in the j-direction fixed.

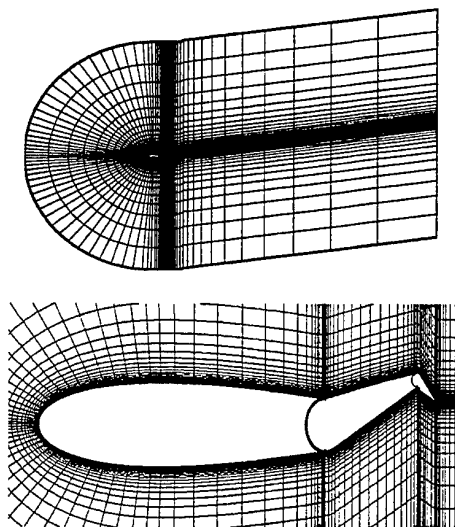


Fig 1. Grid used in the computation of flow over an NACA 0015 airfoil with flap and tab

Figure 2 shows that the forces and moments C_l , C_m , and C_{hf} all become steady after about 100 multigrid cycles for all five grids. The deviations from the experimentally measured forces and moments are less than 7 percent. The reductions of the root-mean-square residues of the pressure of the five grids mentioned above are shown in Figure 3. It is noted that all 5 convergence curves are decreasing at about the same rate after 500 multigrid cycles. It should also be noted that the residual reduction due to the multigrid starting procedure has not been included in Figure 3. This explains why $\log(\text{residue})$ starts at -1 or -2 instead of 0. It is concluded from Figures 2 and 3 that the solutions are converged and grid-independent solutions have been achieved. The above results justify the use of the grid 184x64 for the comparison of computed and measured forces and moments to be discussed.

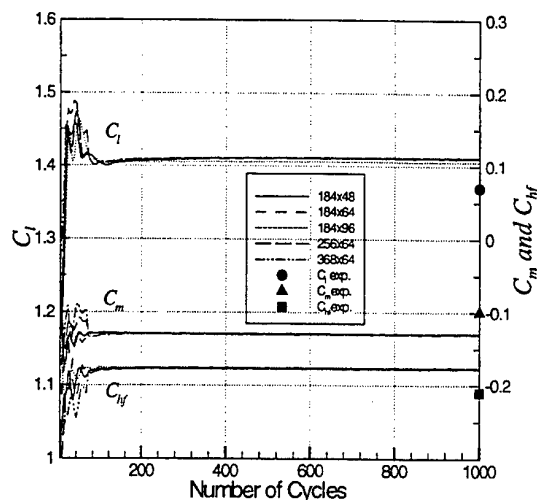


Fig 2. Convergence of C_l , C_m , and C_{hf} vs. multigrid cycles

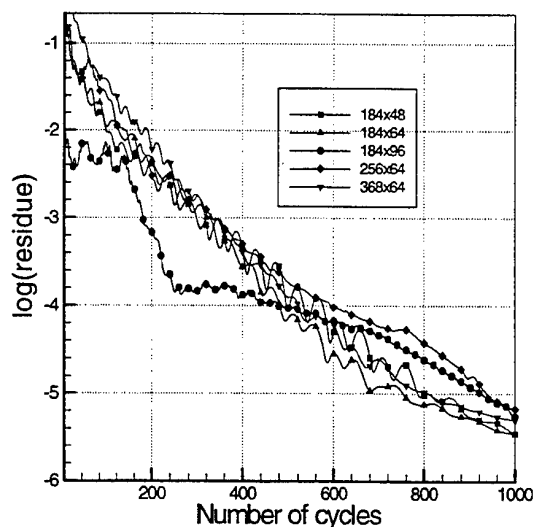


Fig 3. Root-mean square residue of pressure vs. multigrid cycles

Forces and Moments

In the following discussion, the grid used is 184x64 and the Reynolds number based on the airfoil chord length is 2.7×10^6 . As mentioned earlier the effects of flap and tab gaps are not particularly significant. Therefore, only the results with the sealed case will be presented despite of the fact that computations have been done for both the sealed and the unsealed cases. It should also be noted that the uncertainty bounds of

the measured data have not been defined. Thus when a discrepancy of a certain percent is mentioned in the following discussion, it will mean the discrepancy between computation and experiment without taking into account the experimental uncertainty. Obviously, the discrepancy to be mentioned represents the upper bound of the actual discrepancy. Figure 4 shows the comparison of computed and measured airfoil section lift coefficient C_l as the angle of attack α_o varies from -12 to +12 degrees and the flap deflections varies from 0 to 30 degrees.

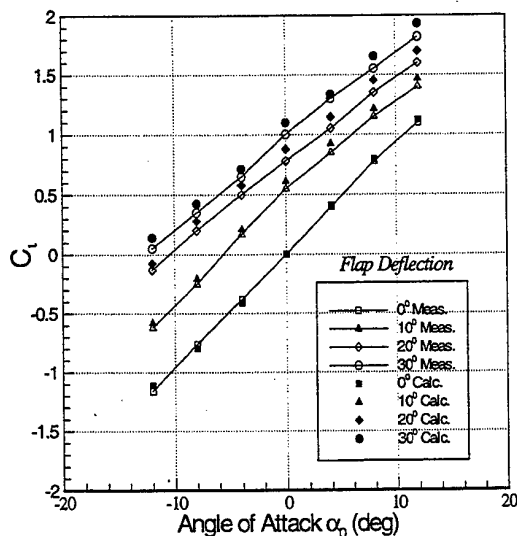


Fig 4. Comparison of calculated and measured airfoil section lift coefficients (sealed gap), 184x64 grid, $Re = 2.7 \times 10^6$

The agreement is very good. The deviation is larger at higher angles of attack. But even at an angle of attack of 12 degrees and a flap deflection of 30 degrees, the discrepancy between computation and measurement is no more than 5 percent. Figure 5 shows the comparison of computed and measured airfoil pitching moment coefficient C_m with the same variations in angles of attack and flap deflections as Figure 4. The agreement between computation and measurement are still quite good although the discrepancies are larger than the case with C_l . The largest discrepancies occur at an angle of attack of 12 degrees. The discrepancy is about 50 percent at a flap deflection of 10 degrees, about 15 percent at a flap deflection of 20 degrees and about 8 percent at a flap deflection of 30 degrees. The large percentage in discrepancy at a flap deflection of 10 degrees is not particularly alarming because the moments are rather small. Figure 6 shows the comparison of computed and measured flap hinge

moment coefficient C_{hf} with again the same variations in angles of attack and flap deflections as Figure 4. The agreement between computation and measurement are still quite good. The trend is completely captured. The computations tend to overpredict consistently. At present, the reason can not be explained.

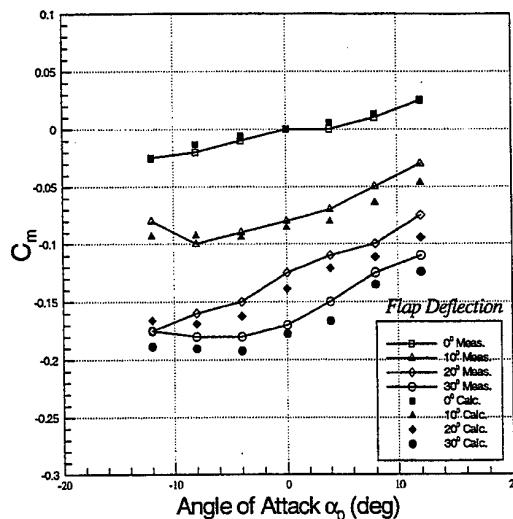


Fig 5. Comparison of calculated and measured airfoil pitching moment coefficients (sealed gap), 184x64 grid, $Re = 2.7 \times 10^6$

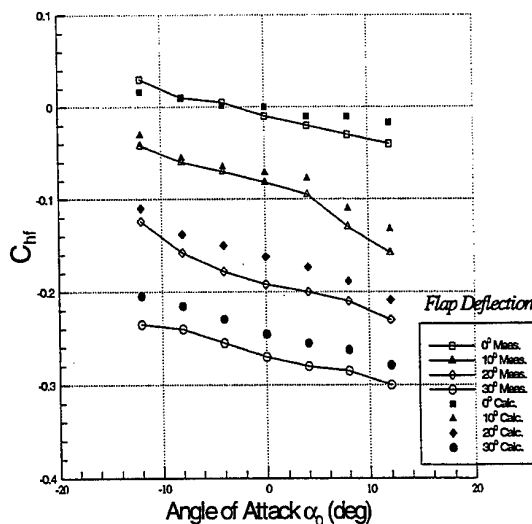


Fig 6. Comparison of calculated and measured flap hinge moment coefficients (sealed gap), 184x64 grid, $Re = 2.7 \times 10^6$

Tab Deflection

The increments of airfoil section lift coefficient ΔC_l , flap section hinge-moment coefficient ΔC_{hf} and tab section hinge-moment coefficient C_{ht} are compared with the measured values at a flap deflection of 5 degrees, angles of attack from -8 to $+8$ degrees and tab deflections from -15 to $+15$ degrees as shown in Figs 7-9. The increment of airfoil section lift coefficient ΔC_l is obtained by deducting the coefficient with tab neutral from that with the tab deflected, with all other factors constant. ΔC_{hf} and C_{ht} are defined similarly. It can be seen from Figs 7-9 that the slopes of the curves have been captured quite well. In general, the discrepancies are within 10 percent with occasional discrepancies in the order of 20 percent.

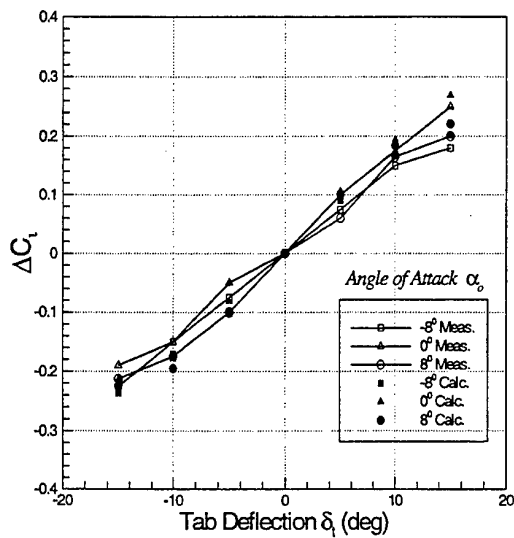


Fig 7. Comparison of calculated and measured increment of airfoil lift coefficients with flap

CONCLUSIONS

A numerical procedure for the prediction of the forces and moments of a 2D airfoil with a flap and a tab has been developed. The procedure is based on solving the incompressible Reynolds-averaged Navier-Stokes equations coupled with a κ - ω turbulence model. Computed results of the airfoil section lift coefficients, airfoil section pitching moment coefficients, flap hinge moment coefficients and tab hinge moment coefficients have been compared with the measured data. The trend of the variation of forces and moments has been accurately captured. The airfoil section lift coefficients have been predicted within 5 percent

discrepancy from the data even at high angles of attack and high flap deflections. The discrepancy of the airfoil section pitching moment coefficients is slightly higher at about 15 percent. Higher discrepancy occurs when values of the moments are small. The flap hinge moment coefficients are in general overpredicted. The prediction of the tab hinge moment coefficients can only capture the trend properly with uneven discrepancy. In general, the predictive procedure is

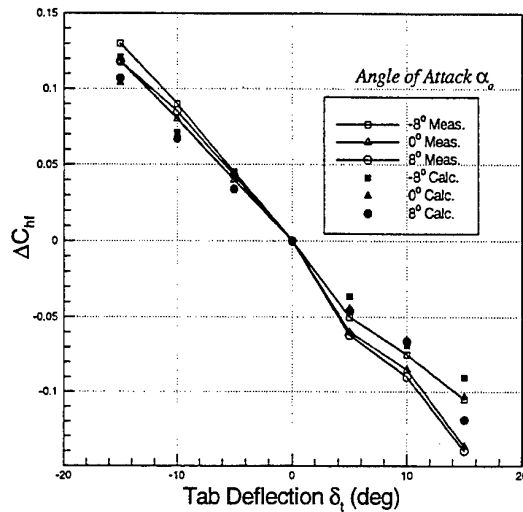


Fig 8. Comparison of calculated and measured increment of flap hinge moment coefficients with flap deflection 5° (sealed gap), 184×64 grid, $Re = 2.7 \times 10^6$

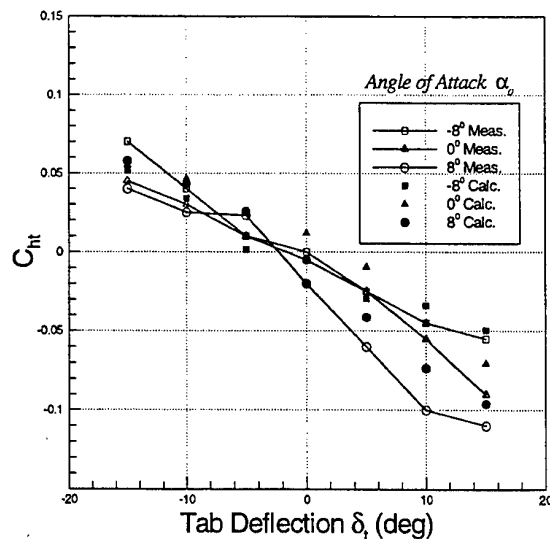


Fig 9. Comparison of calculated and measured tab hinge moment coefficients with flap deflection 5° (sealed gap), 184×64 grid, $Re = 2.7 \times 10^6$

believed to be useful for design applications.

ACKNOWLEDGMENT

This work was funded by the Office of Naval Research, Code 333, under the Mechanics and Energy Conversion Science and Technology Division (PE0602121). Dr. Patrick Purtell is the technical monitor of this program. Dr. Nguyen Thang is the monitor at David Taylor Model Basin. The Department of Defense High Performance Computing Modernization Office (DOD-HPCMC) provided the Cray C90 computer resources for this work.

REFERENCES

1. AGARD Conference Proceedings 515 on "High-Lift System Aerodynamics", September, 1993.
2. Whicker, L. Folger and Leo F. Fehlner, "Free-Stream Characteristics of a Family of Low-Aspect Ratio, All-Movable Control Surfaces For Application to Ship Design", David Taylor Model Basin Report 933, December 1958.
3. Bowers, Allen, "Wind Tunnel Investigation of the Characteristics of a Flapped Control Surface Mounted on a Simulated Submarine Hull", University of Maryland Wind Tunnel Report No. 259, June, 1959.
4. Kerwin, Justine E., Philip Mandel and S. Dean Lewis, "An Experimental Study of a Series of Flapped Rudders", Journal of Ship Research, December, 1972.
5. Goodrich, G. J. and A. F. Molland, "Wind Tunnel Investigation of Semi-Balanced Ship Skeg-Rudders", The Royal Institute of Naval Architects, pp. 285-307, 1979.
6. Soding, H., "Limits of Potential Theory in Rudder Flow Predictions", Twenty-Second Symposium on Naval Hydrodynamics, Washington, D.C., pp. 264-276, August 9-14, 1998.
7. Chau, Shiu-Wu, "Computation of Rudder Force and Moments in Uniform Flow", Ship Technology Research Vol. 45, pp. 3-13, 1998.
8. Richard I. Sears and Robert B. Liddell, "Wind-Tunnel investigation of Control-Surface Characteristics, VI - A 3 Percent-Chord Plain Flap On the NACA 0015 Airfoil". NACA Wartime Report-454, June 1942.
9. Gowing, Scott, Thang Nguyen and David Bochinski, "T.A.C. Test Static Results in the 24" Water Tunnel", not yet published, 1999.
10. Wilcox, D. C., Turbulence Modeling for CFD, DCW Industries, Inc. CA, 1993.
11. Speziale, Charles G., "Comparison of Explicit and Traditional Algebraic Stress Models of Turbulence", AIAA Journal vol. 35, No. 9, September 1997.
12. Chorin, A. J., "A Numerical Method for Solving Incompressible Viscous Flow Problem", Journal of Computational Physics, vol. 2, 275, 1967.
13. Turkel, E., "Preconditioned Methods for Solving the Incompressible and Low Speed Compressible Equations", Journal of Computational Physics, vol. 72, 277, 1987.
14. Yee, H. C., "A Class of High-Resolution Explicit and Implicit Shock-Capturing Methods", NASA Technical Memorandum 101088, February, 1989.
15. Jameson, A., "Time Dependent Calculations Using Multigrid with Applications to Unsteady Flows Past Airfoils and Wings", AIAA 91-1596, June 1991.
16. Liu, C., X. Zheng and C. H. Sung, "Preconditioned Multigrid Methods for Unsteady Incompressible Flows", Journal of Computational Physics, vol. 139, 35-57, 1998.
17. Brandt, A., "Multigrid Techniques: 1984 Guide, with Applications to Fluid Dynamics", 1984, 191 pages, ISBN-3-88457-081-1; GMD-Studien Nr 85; Available from GMD-AIW, Postfach 1316, D-53731, St. Augustin 1, Germany, 1984.
18. Jameson, A., "Multigrid Algorithms for Compressible Flow Calculations", Lecture Notes in Mathematics, No. 1228, Proceedings of the Second European Conference on Multigrid Methods, Cologne, pp. 166-201, October 1-4, 1985.
19. Brandt, A., "Barriers to Achieving Textbook Multigrid Efficiency (TME) in CFD", NASA/CR-1998-207647, ICASE Interim Report No. 32, April 1998.
20. Hedstrom, G. W., "Nonreflecting Boundary Conditions for Nonlinear Hyperbolic System", Journal of Computational Physics, vol. 30, pp. 222-237, 1979.
21. Rudy, D. H., and J. C. Strikwerda, "Boundary Conditions for Subsonic Compressible Navier-Stokes

Equations", Computers and Fluids, vol. 9, pp. 327-338, 1981.

22. Sung, C. H., "An Explicit Runge-Kutta Method for 3D Incompressible Turbulent Flows", DTNSRDC/SH - 1244-01, July 1987.

23. Jameson, A. and L. Martinelli, "Mesh Refinement and Modeling Errors in Fluid Simulation", AIAA Journal vol. 36, No. 5, May 1998.

CFD simulation of 3-dimensional motion of a vehicle with movable wings

Takada N. (+) , Miyata H. (++) , Sato T. (++)

(+) R+D Center Nagasaki, Mitsubishi Heavy Industries, Ltd.,

3-48 Bunkyo-Machi, Nagasaki, Japan

Fax: +81-95-845-7701 ; E-mail: takada@ngsrdc.mhi.co.jp

(++) Dept.of Environmental and Ocean Engineering, School of Engineering,

The university of Tokyo, Hongo 7-3-1, Bunkyo-ku, Tokyo, Japan

Fax: +81-3-5802-3374 ; E-mail: miyata@triton.naoe.t.u-tokyo.ac.jp ,

sato@triton.naoe.t.u-tokyo.ac.jp

ABSTRACT

A CFD simulation method has been developed for simulating unsteady motions of a vehicle with movable lifting surfaces. The coordinate system used in this simulation method is fixed to the moving body and inertia forces such as Coriolis's force and the centrifugal force are treated as body forces in the incompressible Navier-Stokes equation. A multi-block grid scheme is introduced for the body having a number of lifting surfaces and the control of movable lifting surfaces is treated in a moving grid scheme. *Motion Simulation System* (MSS) can be constructed by coupling these CFD techniques and the equations of motion of a vehicle. The concept of MSS and the method of the simulation are explained and some results of the simulation by using MSS applied to the keel of a racing yacht and under water vehicle are presented.

INTRODUCTION

The evolution of hardware computational resources has lead Computational Fluid Dynamics (CFD) to undergo thorough development in the last years. CFD is used for configuration design, performance improvement, environmental assessment, etc., for a lot of aircraft, machines, structures, etc. In the field of ship and ocean engineering, CFD is used for the design of a hull form as a powerful tool. There are many CFD codes, which can simulate the flow field around a vehicle in steady straight, oblique, and circling motion, and their outputs are useful for the development and design of hull forms. However, in these simulations running attitude of a vehicle is assumed and they are useful to evaluate only a part of hydrodynamic performances. For high-speed ships and underwater vehicles, not only resistance but also running attitude, maneuverability and interaction with appendages generating lifting forces must be

carefully considered. Therefore, the design of hull forms mostly relies upon experts who can consider various complex conditions. It would be very convenient for a designer if we could construct a system, which can simulate six-degree of freedom motion and evaluate all hydrodynamic performances of a running vehicle. When this system is wholly completed, most part of the design of mobile vehicles is done by design-by-simulation procedure.

The coupling of the equations of motion of vehicles and the flow equations can be an answer to this assignment. Kaiden et al.[1] have applied the such a method to the simulation of SRB (Solid Rocket Booster) separation on the H-II rocket. Their numerical method for the flow simulation was based on the Chimera technique. The motion of the SRB after the separation from the H-II core was calculated by solving the equations of motion. Arnaud et al.[2][3] have simulated the launching of a torpedo from a moving submarine. Their numerical model is based on an original coupling between unsteady NS

equations in a moving grid attached to the torpedo and an intersection model based on a VOS method (volume of solid) to represent the independent motion of the submarine. Akimoto et al.[4] have applied the above numerical method to the simulation of a maneuvering motion in 1996. They have introduced a technique that solves the flow around the hull of a racing yacht in unsteady motion with moving grid scheme and simulated the maneuvering motion. However, there was a difficulty that the fair grid following the movement of the hull was generated in a large amplitude motion. Therefore, Sato et al.[5] have introduced a method that solves NS equations in the coordinate system fixed to a ship making the planar motion and simulated the maneuvering motion of tankers in the horizontal plane. In these simulations, however, the hydrodynamic or aerodynamic forces and moments acting on appendages such as a rudder and a propeller were estimated from mathematical models on the basis of experimental databases. Davoudzadeh et al.[6][7] have introduced a rotating propeller in the flow simulation about a fully-appended SUBOFF by using the technique of a rotating dynamic grid scheme. However, their maneuvering control is not made by pure CFD, but either by fixed appendages with pre-determined angles or directly-given external yawing moment.

The present study introduces a technique that solves the flow around a vehicle in steady or unsteady motion with the movement of lifting surfaces as motion control system. And we construct motion simulation system, so that it can simulate overall hydrodynamic performances of a vehicle advancing in fluid.

MOTION SIMULATION SYSTEM

Motion Simulation System (MSS) is a system, which is coupled a NS-solver with equations of six-degree of freedom and a prediction system of hydrodynamic performances of vehicles advancing in fluid as shown in Fig.1. MSS consists of four modules that are the flow simulator, i.e. NS-solver, the grid generator, equations of six-degree of freedom motion and the control system of lifting

surfaces. First of all, when movable lifting surfaces of a vehicle are moved, the computational grid fitted it is generated. Next, NS-solver solves the flow about it and consequent hydrodynamic forces and moments acting on the vehicle are calculated in this grid. When the equations of six-degree of freedom motion are solved by using this hydrodynamic forces and moments, translational and angular velocities and accelerations of the vehicle are obtained. They are fed back to the NS-solver and the control of the movable lifting surfaces. The trajectory of the vehicle can be obtained by iterating this procedure. There are three of this simulation method ways of application. One is the simulation of forced motion that solves the flow around and the hydrodynamic forces and moments acting on the vehicle in the compulsorily given steady or unsteady motion. The second one is the simulation of free-motion that obtains the trajectory of the vehicle with given control of movable lifting surfaces by solving the equations of motion coupled with NS-solver. The last one is the control simulation with the addition of the control system of movable lifting surfaces so that the vehicle can move autonomously. Using this system, not only hydrodynamic performances in steady state but also overall maneuverability can be predicted. For such a purpose, NS-solver should provide with the following conditions. That is, the flow about a vehicle in the unsteady motion of large amplitude with controllable lifting surfaces can be solved at each time step time-evolutionarily.

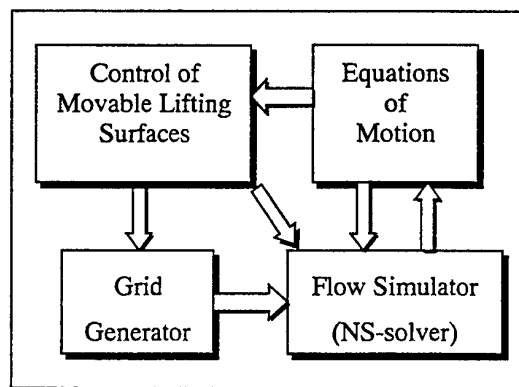


Fig.1 Flow chart of Motion Simulation System

In the following sections, description is made of the equations of six-degree of freedom motion and the NS-solver by which such a simulation can be enabled. And, some results of simulations of forced motions and a free-motion for the keel of a racing yacht and under water vehicle, respectively are presented.

NUMERICAL METHOD

Equations of six-degree of freedom motion

The equations of six-degree of freedom motion are expressed in the coordinate system fixed to a vehicle shown in Fig.2. The origin of this coordinate system is on the center of gravity (C.G.) of the vehicle. The x-axis lies along the centerline of the vehicle and is oriented backward. The y-axis is oriented in the starboard direction and the z-axis is oriented upward.

When (F_x, F_y, F_z) and (M_x, M_y, M_z) are the total forces acting on the vehicle and the total moments working at the C.G. of the vehicle, respectively, the equations of six-degree of freedom motion are

$$m(\dot{U} + QW - RV) = F_x \quad (1)$$

$$m(\dot{V} + RU - PW) = F_y \quad (2)$$

$$m(\dot{W} + PV - QU) = F_z \quad (3)$$

$$I_{xx}\dot{P} - I_{xz}\dot{R} + (I_{zz} - I_{yy})QR - I_{xz}PQ = M_x \quad (4)$$

$$I_{yy}\dot{Q} + (I_{xx} - I_{zz})RP + I_{xz}(P^2 - R^2) = M_y \quad (5)$$

$$-I_{xz}\dot{P} + I_{zz}\dot{R} + (I_{yy} - I_{xx})PQ - I_{xz}QR = M_z \quad (6)$$

where m is the mass and I_{xx} , I_{yy} , I_{zz} , and I_{xz} are the moments of inertia of the vehicle. Since the geometry of the vehicle is generally symmetry about the x-z plane, I_{xy} and I_{yz} are zero. The change of moments of inertia caused by moving the lifting surfaces is ignored in this study. (U, V, W) and (P, Q, R) are the translational and the angular velocities. By solving these equations, the trajectory of the vehicle are obtained. The attitude of the

vehicle is defined as Euler's angles (roll angle ϕ , pitch angle θ , and yaw angle ψ).

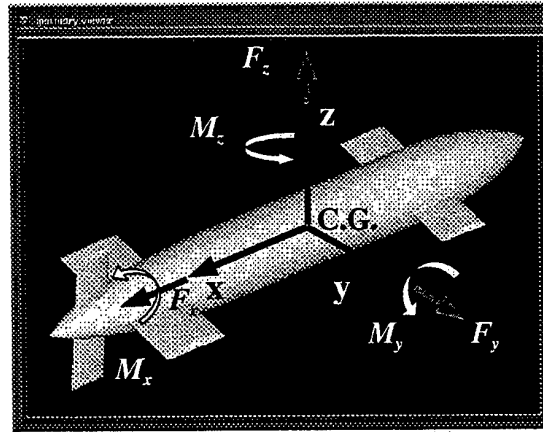


Fig.2 Definition of a body-fixed coordinate system

NS-solver

The present NS-solver is developed on the basis of WISDAM-V[8][9][10][11], which has been successfully used for the flow simulation about ships dealing with wave-making, viscous boundary layer, turbulence, etc. The method adopts staggered allocation of pressure and velocity components in the Cartesian coordinates with the MAC-type algorithm for incompressibility, finite-volume formulation in a curvilinear body-fitted grid system. The convection and the diffusion terms are discretized in the third-order upwind differencing scheme constructed within flux-difference splitting framework and the second-order central differencing scheme, respectively. The Poisson equation for pressure is discretized in the second-order central differencing scheme and is solved iteratively by the Successive Over Relaxation (SOR) procedure. See the references on each computational procedure for more details. In this study, we have provided the WISDAM-V code with some modifications for motion simulations, which are described in the following sections.

Fluid flow equations for motion simulations

The Navier-Stokes equations in the conservative form for an incompressible fluid in a coordinate system fixed to the moving body are formulated as follows:

Continuity equation:

$$\nabla \cdot \hat{u} = 0 \quad (7)$$

Momentum equation:

$$\frac{\partial \hat{u}}{\partial t} + \nabla \cdot [\hat{u} \cdot (\hat{u} - \hat{v}) + pI - \tau] - \hat{f} = 0 \quad (8)$$

where \hat{u} is the absolute velocity and \hat{v} the velocity of the grid points. \hat{v} is needed since the movement of movable lifting surfaces is treated in a moving grid scheme. p is the pressure and τ the viscous stress tensor. \hat{f} is the inertia force caused by the transformation of coordinate and is given by

$$\hat{f} = -2\hat{\omega} \times \hat{u} - \hat{\omega} \times (\hat{\omega} \times \hat{r}) - \dot{\hat{\omega}} \times \hat{r} - (\dot{\hat{V}} + \omega \times \hat{V}) \quad (9)$$

where $\hat{\omega}$ is the angular velocity vector (P, Q, R) and \hat{r} the position vector (x, y, z) of the point defining the fluid velocity and \hat{V} the translational velocity vector (U, V, W). Four terms in the RHS of Equation (9) indicate the Coriolis force, the centrifugal force and the unsteady forces due to angular and translational accelerations, respectively.

Time integration scheme

The original WISDAM-V adopted explicit time integration scheme with MAC-type algorithm and the time increment has to be so small as to be sufficient for the expression of the motion. Therefore, a semi-implicit time integration scheme, which is explained as follows, is introduced in order to increase the time increment and shorten the calculation period.

In this scheme, the Equation (8) is time-discretized as follows:

$$\begin{aligned} (I - \Delta t(C_i^{\text{impl}} + D_i^{\text{impl}}))u_i^* &= u_i^n \\ &+ \Delta t(C_i^{\text{expl}} + C_i^{\text{expl}} + f_i^n) \end{aligned} \quad (10)$$

and

$$u_i^{n+1} = u_i^* - \nabla p^n \quad (11)$$

In the first equation, u^* and Δt are the "intermediate" velocity and the time increment, respectively, and the superscript n denotes the time level. C_i^{impl} and D_i^{impl} are implicit convection and diffusion operators, and C_i^{expl} and D_i^{expl} are explicit parts of the convection term and diffusion term, respectively. The convection term is split into implicit and explicit parts as follows:

$$C_i^{\text{impl}} = \sum_j U^{jn} A^j(u_i^*) \quad (12)$$

$$C_i^{\text{expl}} = \sum_j U^{jn} (Q^j(u_i^n) - A^j(u_i^n)) \quad (13)$$

where U^j is the volume flux at the cell face. $A^j()$ and $Q^j()$ are the first-order and the third-order upwind interpolations, respectively. And the diffusion term is split into implicit and explicit parts as follows:

$$D_i^{\text{impl}} = \frac{1}{2} \frac{\partial}{\partial x_f} \left(v_e \frac{\partial u_i^*}{\partial x_f} \right) \quad (14)$$

$$D_i^{\text{expl}} = \frac{1}{2} \frac{\partial}{\partial x_f} \left(v_e \frac{\partial u_i^n}{\partial x_f} \right) + \frac{\partial}{\partial x_f} \left(v_e \frac{\partial u_f^n}{\partial x_i} \right) \quad (15)$$

where v_e is the effective viscosity defined from the eddy-viscosity type turbulence model used in this study. The linear equation system Equation (10) is solved iteratively by the SOR procedure and intermediate velocity u^* is obtained. Then, substituting Equation (11) into Continuity equation (7), we obtained the Poisson equation as follows:

$$\nabla^2 p^n = \nabla \cdot \hat{u}^* \quad (16)$$

This equation is also solved iteratively by SOR procedure and the pressure field is obtained. Finally the velocity field is incremented by Equation (11). In this scheme, the time increment can be 10 times as large as that in the original explicit scheme and the computational time is shortened by about 60 %.

Computational grid

Multi-block grid scheme

In this study, a multi-block grid scheme is employed for a body having a number of lifting surfaces. For example, the grid of the keel with

wings of a racing yacht made up of 3 blocks is shown in Fig.3. Each block is a rectangular parallelepiped in computational coordinate. On the interface of the blocks, discontinuity of grid points is not allowed. Therefore, sweeps for the solution procedure for pressure throughout the whole computational domain are capable and the efficiency of the calculation can be kept to the level of the case of a single grid. The body boundary conditions are easily controlled since surfaces of the body are defined on boundary surfaces of the grid.

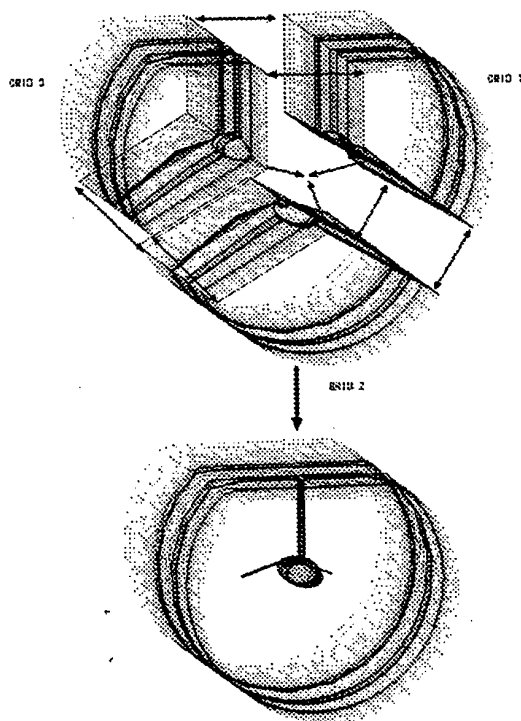


Fig.3 Multi-block grid system for a keel with wings

Moving grid system

The movement of movable lifting surfaces is treated by a moving grid scheme. In the present scheme, when lifting surfaces is moved, the grid fitted is accordingly regenerated at each time step. Since the magnitude of movement of lifting surfaces is equivalent to the angle on the coordinate system

fixed to an arbitrary moving vehicle, it is not very difficult that the fairness of the grid fitted to surfaces of the vehicle is retained. For example, the grid in the vicinity of the rudder of an underwater vehicle is shown in Fig.4 (a) and (b). (a) is the case of rudder angle 0 degrees and (b) is the case of rudder angle 10 degrees. The algebraic interpolation method is adopted to generate a grid in order to save computational time.

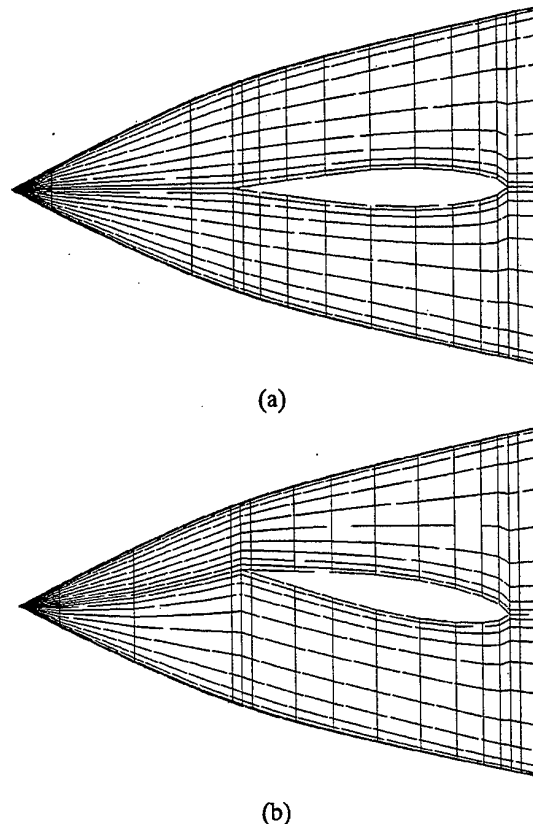


Fig.4 Grid for the rudders of an underwater vehicle
rudder angle is 0 degrees (a) and 10 degrees
(b)

Boundary condition

The boundary conditions for the NS-solver are time-dependent, since the computational region is fixed to an arbitrary moving vehicle. At the inflow boundary, the velocity is given as

$$\hat{u}(\hat{r}_0) = -\hat{V} - \hat{\omega} \times \hat{r}_0 \quad (16)$$

where \hat{r}_0 is the position vector on the boundary. On the body boundary, no-slip condition is given, i.e. the velocity on the body surface \hat{u}_{srf} is given as

$$\hat{u}_{srf} = \hat{v}_w \quad (17)$$

where \hat{v}_w is the velocity on moving lifting surfaces and set at zero on the other body surfaces. The outflow boundary condition is zero-normal-gradient Neumann condition.

The Neumann-type pressure condition on the body boundary has to be

$$\nabla p = -\frac{\partial \hat{v}_w}{\partial t} + \hat{f} \quad (18)$$

A Dirichlet condition ($p=0$) is imposed at the inflow boundary and a zero-normal-gradient condition at the outflow boundary.

On the interface of the blocks, boundary information is given on each boundary surface of a block.

Turbulence model

There are two kinds of eddy-viscosity type turbulence model used in this study. One is a combination of a Smagorinsky-type subgrid scale and a Baldwin-Lomax turbulence models (Hybrid model). Another is a Dynamic SGS model (DSM), which is proposed by Germano et al[12].

SIMULATION OF RACING YACHT KEEL IN FORCED MOTION

Firstly, we apply MSS to three simulations of forced motions for the keel of a racing yacht. The keel of a racing yacht shown in Fig.5 consists of a bulb, a strut, and wings, and is attached to the bottom of the hull at the top of the strut. The length of the bulb is 4.6 m and the depth from the top of the strut to the bottom of the bulb is 3.1 m. A part of the trailing edge of the strut consists of the trim-tab such as a flap.

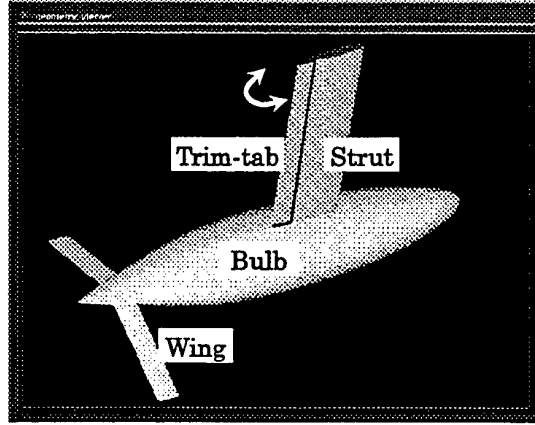


Fig.5 Geometry of the keel with wings of a racing yacht

The racing yacht, which we focus on, is generally required to sail in two conditions, i.e. downwind sailing and upwind sailing (close-hauled condition). In the former condition, the keel of a yacht works only for stability. On the other hand, the keel works not only for stability but also for generating lifting forces preventing the drift of the boat in the close-hauled condition. Therefore, the hydrodynamic performance of the keel in this condition is very important for the design of a high performance racing yacht. In this condition, the racing yacht sails with an angle between the windward direction and the advancing direction of the boat. The angle, which depends on the wind velocity however, is generally 40 degrees. Fig.6 shows the state of the balance of forces acting on the racing yacht at this point. The keel has to generate a side force opposing the side force generated by the sails to prevent the drift of the boat.

Oblique tow motion

Before the simulation of the flow about the keel in an upwind sailing condition, computation is made for the flow about the keel without wings in an oblique tow condition in order to validate the NS-solver. The hydrodynamic drag and side force and the flow field of the simulation with the Hybrid model and the DSM are compared with those of experiments, which are measured with 1/5 scale

model of the keel without wings in the circulating water channel of Kobe University of Mercantile Marine. The leeway (drift) angle and the trim-tab angle are set at -2 degrees and 6 degrees, respectively. The Reynolds number of the simulation is 1.0×10^6 , which is almost consistent with that of the experiment (9.2×10^5). The grid of the keel without wings is made up of a single block and the number of grid points are 103,402 ($97 \times 26 \times 41$ in the longitudinal, radial, and circumferential directions, respectively).

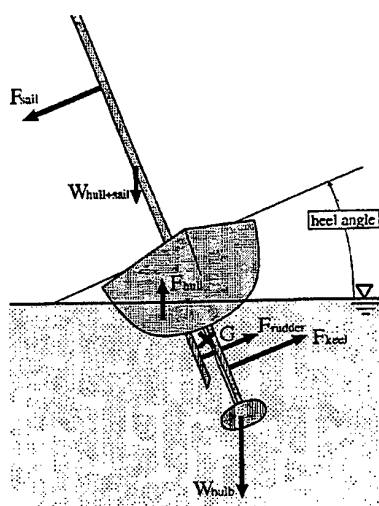


Fig.6 Balance of force and moment on the vertical plane normal to the axis of advancement

The comparison of the drag and side force non-dimensionalized by $\rho V_0^2 L^2$ between the simulations and the experiment is shown in Fig.7. ρ is the density of water, V_0 the velocity of uniform flow (the boat speed) and L the length of the bulb. Henceforth, hydrodynamic forces are non-dimensionalized in the same manner. And the drag and the side force directs backward along the axis of advancement and the starboard side normal to it, respectively. The calculated drag by the Hybrid model and the DSM are smaller than the measured value by 17.7% and 13.3%, respectively. The calculated side forces are 10.5% and 24.5% smaller than the side force measured, respectively. The

comparison of the ratio of the side force to the drag is shown in Fig.8. For the ratio of the side force to the drag, the agreement of the simulation by the Hybrid model with the experiment is superior to the simulation by the DSM.

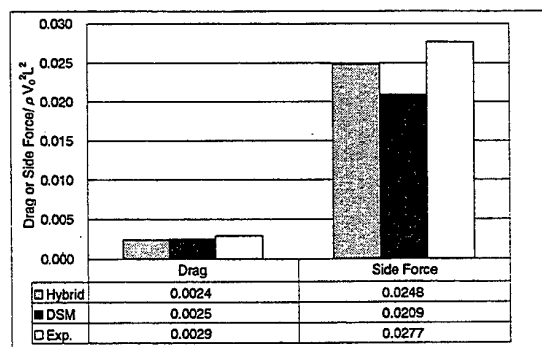


Fig.7 Comparison of drag and side force

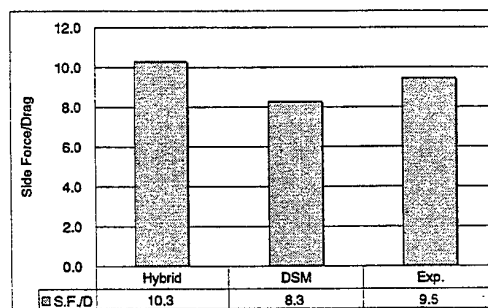


Fig.8 Comparison of the ratio of side force to drag

The comparison of the velocity vector of the fluid in the transverse plane at the aft end of the bulb between computation by the Hybrid model and measurement is shown in Fig.9. The rotational flow is generated about the bulb in the clockwise direction, which is caused by the circulation of the strut. This rotational flow is realized in the computation, and it qualitatively accords with the experimental results. In the following simulations about the keel, the Hybrid model is used as a turbulence model, since the calculated side force accords with the measured better.

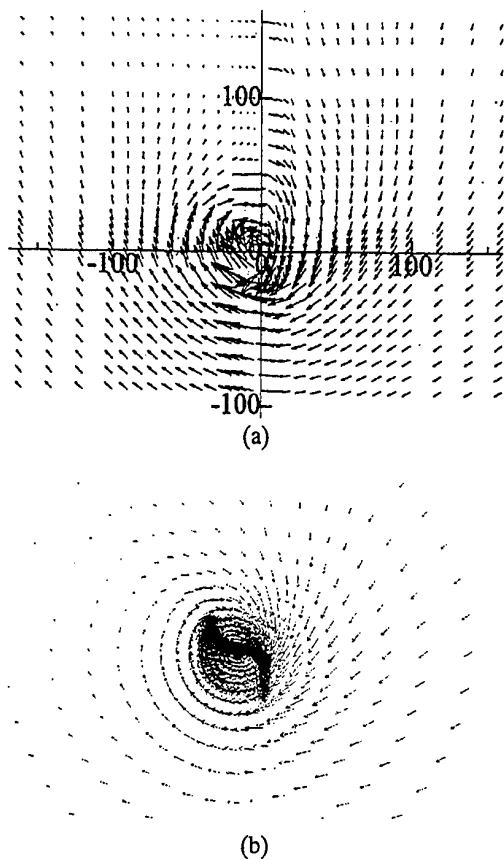


Fig.9 Comparison between measured (a) and computed (b) velocity vector field on the transverse plane at the aft end of bulb

Steady upwind sailing

The keel is required to generate large side force accompanied with low drag and is equipped with wings as devices to improve efficiency. However, the scale of wings and the location must be carefully optimized. Therefore, simulation is performed for the flow around the keel with wings in steady upwind sailing in order to obtain hydrodynamic forces acting on wings and the structure of the flow field.

Conditions of Simulation

The keels without wings and with wings are taken as objects of the simulation. The leeway angle,

the heel (roll) angle, and the trim-tab angle, are set to -2 degrees, -25 degrees, and 6 degrees, respectively. The geometry of the wings is rectangle, the chord is 0.25m and span is 1.1m . The wings are assumed to be installed at the position 4m from the fore end of the bulb in the longitudinal direction.

As shown in Fig.3 above, the computational region of the keel with wings is made up of 3 blocks. The number of grid points are $128,622$ ($97 \times 26 \times 17 \times 3$ in the longitudinal, radial, circumferential directions, and the number of blocks, respectively). The grid of the keel without wings is same with that of simulation of the previous section.

Results of Simulation

Fig.10 shows the ratio of the hydrodynamic forces acting on the starboard and port side wings relative to the forces acting on the keel without wings. The drag of the wing on the windward (port) side is larger than that on the leeward (starboard) side and the drag increase of the keel when the wings are equipped becomes 12.4% . The rate that both wings contribute to the increase of the side force of the keel does not come up to as much as 1% . Therefore, the ratio of the side force to the drag of the keel with wings decreases by 11% compared with the keel without wings as shown in Fig.11.

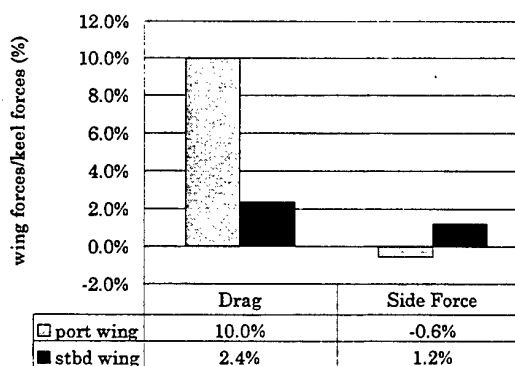


Fig.10 Comparison of the ratio of wing forces to keel forces

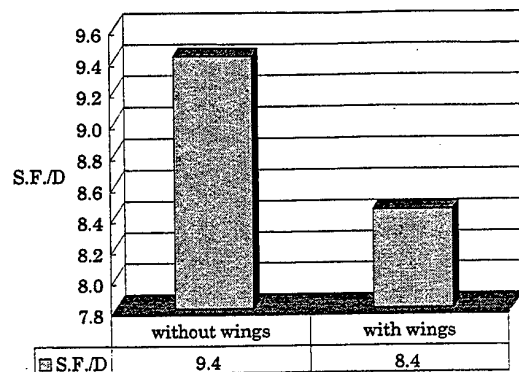


Fig.11 Comparison of the ratio of side force to drag

Fig.12 (a) and (b) indicate the velocity vector of the fluid in the transverse plane at the aft end of the bulb. The clockwise rotational flow can be observed in each figure, although the intensity of the rotational flow of the keel with wings is smaller than that of the keel without wings.

The contour map of the pressure on the surface of wings is shown in Fig.13. The pressure is non-dimensionalized by ρV_0^2 where V_0 is the boat speed. Solid and dashed lines indicate the positive and negative pressure, respectively.

It is shown that the simulation using multi block scheme is effective to the analysis of the flow around a body having a complicated configuration like the keel with wings. It seems that this simulation method can be applied to the design of the keel.

Tacking motion

Tacking of a racing yacht is a maneuvering motion accompanied by large rolling (heel) angle changes in a short period. In general, the maximum rolling angle changes from positive 20 degrees to the opposite value, as the heading angle of the boat varies 90 degrees within 15 seconds. The hydrodynamic forces acting on the keel of a racing yacht in this kind of large amplitude motion are not exactly clarified. The trim-tab of the keel is moved during the tacking and it isn't well clarified how the trim-tab is moved for an effective tacking. Therefore, the flow is solved for the keel without wings in a tacking motion in order to know hydrodynamic

forces and find out effective steering methods for the trim-tab.

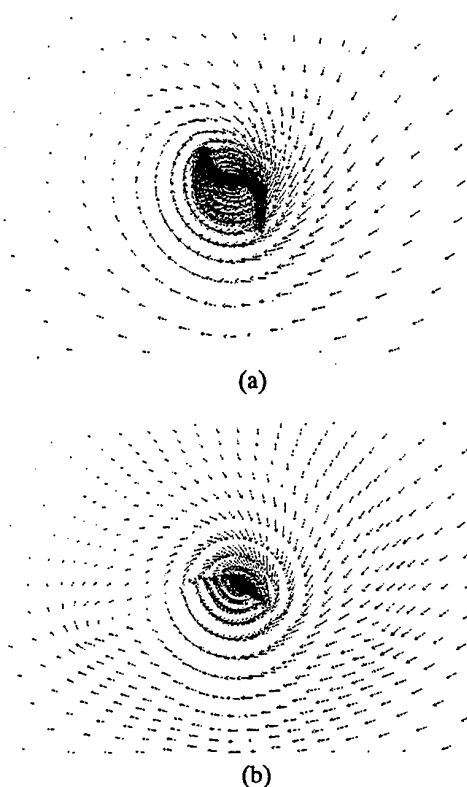


Fig.12 Computed velocity vector field on the transverse plane at the aft end of bulb (a) without wings, (b) with wings

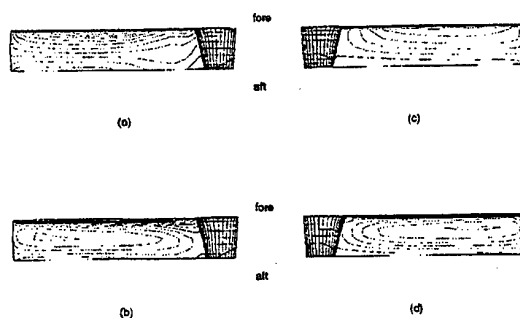


Fig.13 Contours of computed pressure on the surface of wings, (a) port upper surface, (b) port lower surface, (c) stbd upper surface, (d) stbd lower surface

Conditions of Simulation

Tacking motion is assumed as follows:

$$\alpha(t) = \alpha_0 \left(\frac{1}{\pi} \sin \frac{2\pi t}{T^*} \right) - \frac{2t}{T^*} + 1 \quad (19)$$

where $\alpha(t)$ are roll angle ϕ , pitch angle θ , heading angle ψ defined as Euler's angles and leeway (drift) angle β . α_0 is initial angle before tacking motion. t is non-dimensional time and T^* is time during tacking motion. $\alpha(t)$ change smoothly from α_0 to $-\alpha_0$ in T^* . Initial β , ϕ and ψ are -2 degrees, -25 degrees and -40 degrees, respectively. Pitch angle does not change and is set at 0 degrees. T^* is 15 seconds ($t=3 \sim 18$) and 1 second is 1 as non-dimensional time. The velocity of the racing yacht is assumed constant. Fig.14 shows the path of C.G. and attitude of the keel. X_g -axis lies along wind direction in the still horizontal plane.

The trim-tab angle changes from 6 degrees to -6 degrees in 5 seconds. There are 3 simulation cases with differences in the start time of steering trim-tab. The start time of Case 1, 2, and 3 are 3 , 8 , and 13 , respectively. The time histories of the trim-tab angle and leeway angle are shown in Fig.15.

Results of Simulation

The time histories of the hydrodynamic forces are shown in Fig.16. (a) is the drag and (b) is the side force acting on the keel. They indicate the differences of the hydrodynamic forces in each of cases caused by the difference of the trim-tab movement. Drags in all cases reduce in tacking motion and the result of Case 1 shows the longest time during drag reduction. The drag reduces rapidly from $t=3.5$ to $t=6.5$ and at $t=6.5$ the drag is 60% of the drag before tacking. Side forces in all cases vary along with the variation of trim-tab angle and leeway angle. Negative values of the side force mean that the side force directs the port side.

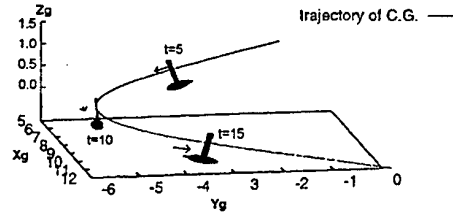


Fig.14 Trajectory of the keel (3D-View)

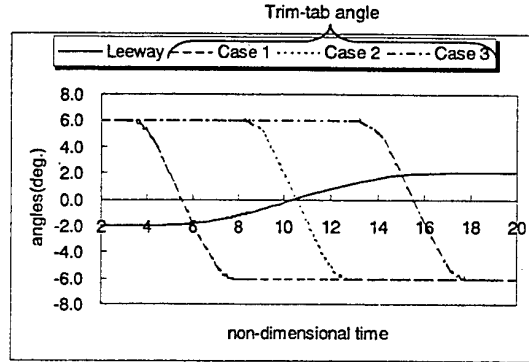
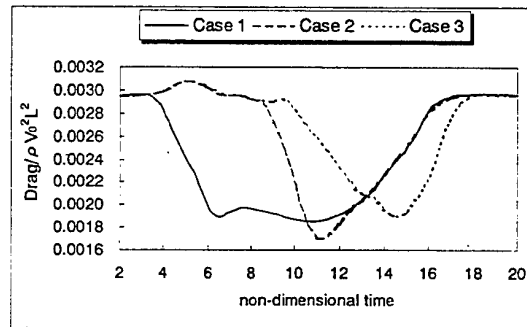
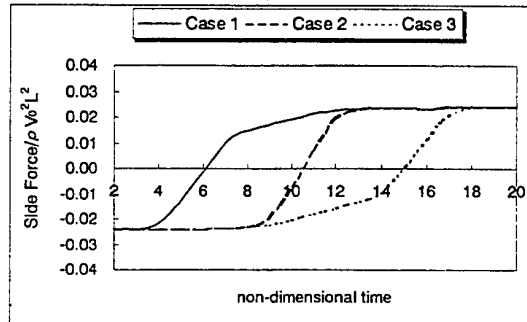


Fig.15 Time history of the tab angle and the leeway angle



(a)



(b)

Fig.16 Time history of drag coefficient (a) and side force coefficient (b) of the keel

The developed NS-solver can simulate the flow around the keel in the large amplitude motion such as tacking and with movement of the trim-tab. This simulation clarified that the hydrodynamic forces acting on the keel in the tacking motion depend on the difference of the start time of steering trim-tab. Therefore, it can be said that the steerage of the trim-tab is important for the effective tacking.

SIMULATION OF UNDERWATER VEHICLE WITH CONTROLLABLE SURFACES

Secondly, we apply MSS coupled NS-solver with equations of motion to the simulation of a free-motion (maneuvering). We focus on underwater vehicle, the geometry of which is shown in Fig.17. The underwater vehicle consists of the fuselage of body of revolution, the length of which is 3.7m, with fore and aft horizontal wings and upper and lower vertical tails. The fore horizontal wings equipped with elevators and the vertical tails namely rudders are wholly movable. The mass of the vehicle is 243.3kgf and the inertia moments I_{xx} , I_{yy} , I_{zz} , and I_{xz} are 4.7, 32.8, 34.4, and 0kgf · m · s², respectively. The location of the center of gravity is consistent with the location of center of buoyancy. The initial velocity of the vehicle is 2.0m/s.

The grid system consists of 4 blocks and 110,292 grid points as shown in Fig.18 and the dynamic SGS model is used as the turbulence model. Hydrodynamic forces and moments needed in this maneuvering simulation are obtained from the NS-solver except thrust. Thrust is assumed point-wise load given at the aft end of the vehicle, of which value is assumed same with the simulated negative resistance to the vehicle in straight course and is also regarded as constant during the vehicle motion.

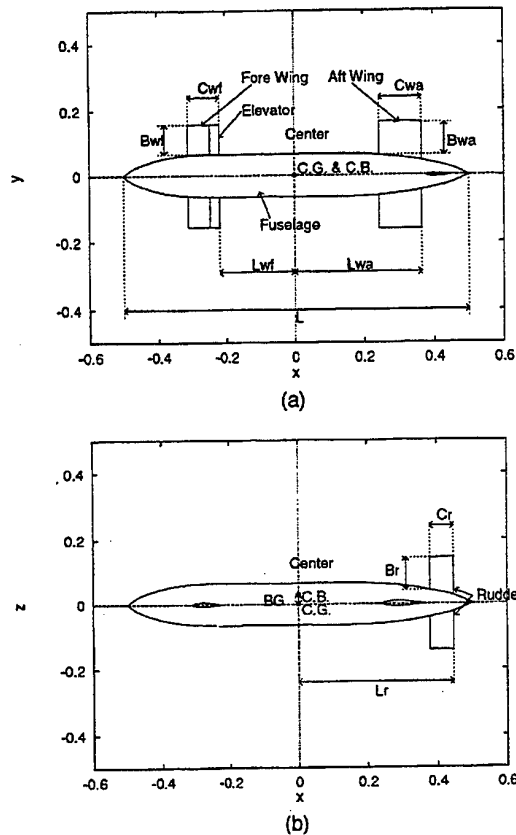


Fig.17 Notation, plan view (a), profile (b)

First of all, the steady-state flow in straight course is simulated until $t=3$. Then, the maneuvering simulation is started and elevators and rudders are moved as shown in Fig.19. The port and starboard side elevators start moving upward and downward, respectively until their angles become 5 degrees, from $t=3$ to $t=3.25$. And the rudders also start rotating clockwise at the top view until their angles become 10 degrees in the same time interval. After that angles of elevators and rudders are fixed constant until $t=20$.

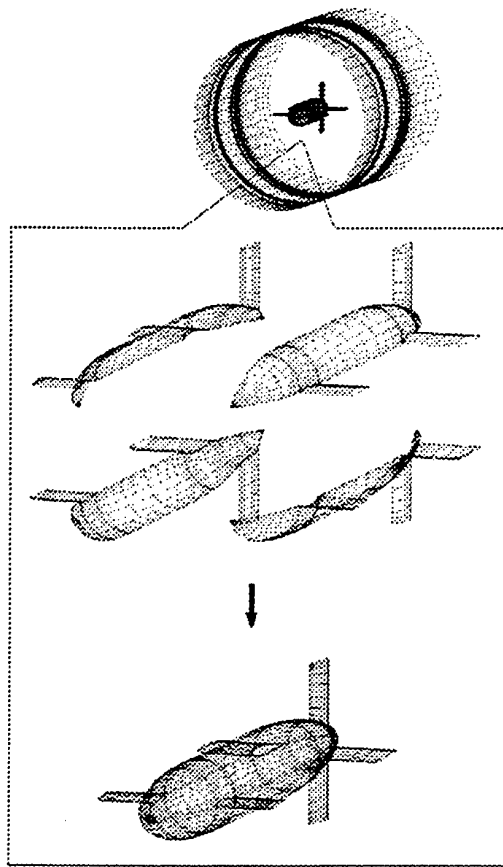


Fig.18 Grid system for underwater vehicle

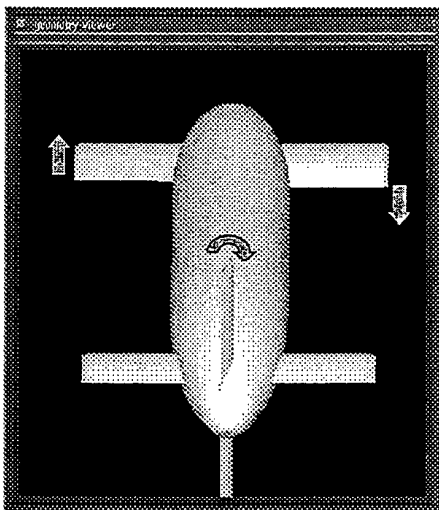


Fig.19 Control of elevators and rudders

Fig.20 (a), (b), and (c) show the path of the vehicle and the attitude of the vehicle at $t=3, 5, 10, 15$, and 20 in the horizontal, transverse, and vertical plane, respectively and at 3-dimensional view is shown in Fig.21. From $t=3$ to $t=5$, the vehicle gradually turns left with rolling to the inside of turn and then starts to nose down as the roll angle increases. From $t=10$ to $t=15$, the vehicle nose-dives in the vertical state and start to nose up from $t=15$. At the end of simulation ($t=20$), the vehicle resumes horizontal state and the attitude almost becomes consistent with that at the start time of the motion ($t=3$). The attitude of the vehicle at $t=3, 5, 7, 9, 11, 13, 15, 17$, and 19 is shown in Fig.22. The view-direction of these figures is fixed to the centerline of the vehicle at $t=3$ and the viewpoint moves with the C.G. of the vehicle. Pressure distribution on the surface of the vehicle is shown in color.

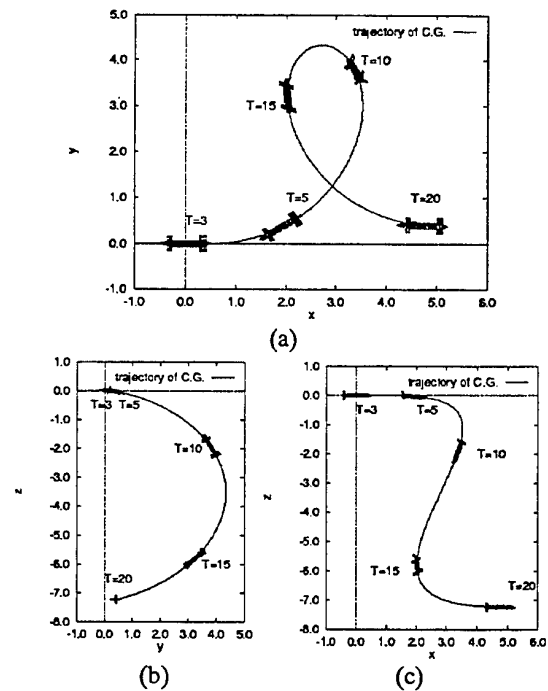


Fig.20 Trajectory of the underwater vehicle, horizontal (a), transverse (b) and vertical (c) plane

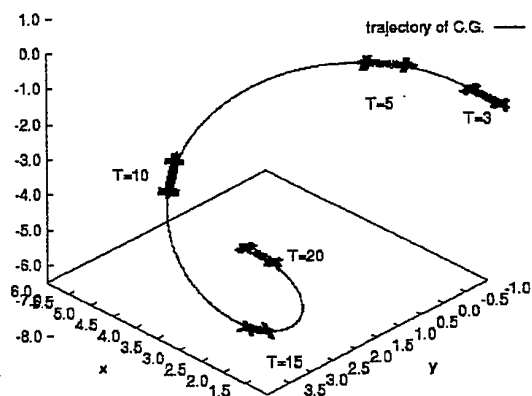


Fig.21 Trajectory of the underwater vehicle (3D-view)

CONCLUSIONS

Motion Simulation System has been constructed for predicting the hydrodynamic performances of a body having a number of lifting surfaces. The numerical simulation method has been developed for solving maneuvering motion of a vehicle by coupling the equations of motion and the flow equations. Since these equations are solved in a coordinate system fixed to the arbitrarily moving vehicle, inertia forces are incorporated into the flow equations. The multi-block grid scheme is introduced into our NS-solver for the body having a number of lifting surfaces and the control of movable lifting surfaces is treated in the moving grid scheme.

We applied MSS to the simulation of forced motion about the keel of a racing yacht at the first stage. It was confirmed that our NS-solver could simulate flow around the body having a number of lifting surfaces in the steady and unsteady motion with control of the movable lifting surfaces. We obtained the properties of hydrodynamic forces acting on the keel in steady or unsteady motion. At the second stage, we applied MSS to the simulation of free-motion about an underwater vehicle. The hydrodynamic forces and moments acting on the vehicle including controlling forces of the movable lifting surfaces are obtained by the NS-solver. It was shown that the present numerical simulation method could simulate the maneuvering arbitrary motion of the underwater vehicle.

Though the validation of the accuracy of the computed motion is left for the future study, it is shown that MSS is useful for evaluating the hydrodynamic performances of arbitrarily moving vehicles. Moreover, this system has a wide-ranging available possibility, and be able to applied to general ships and underwater vehicles.

ACKNOWLEDGEMENT

The authors would like to express to Dr. Toda at Kobe University of Mercantile Marine special gratitude for providing the authors the experimental results of the keel.

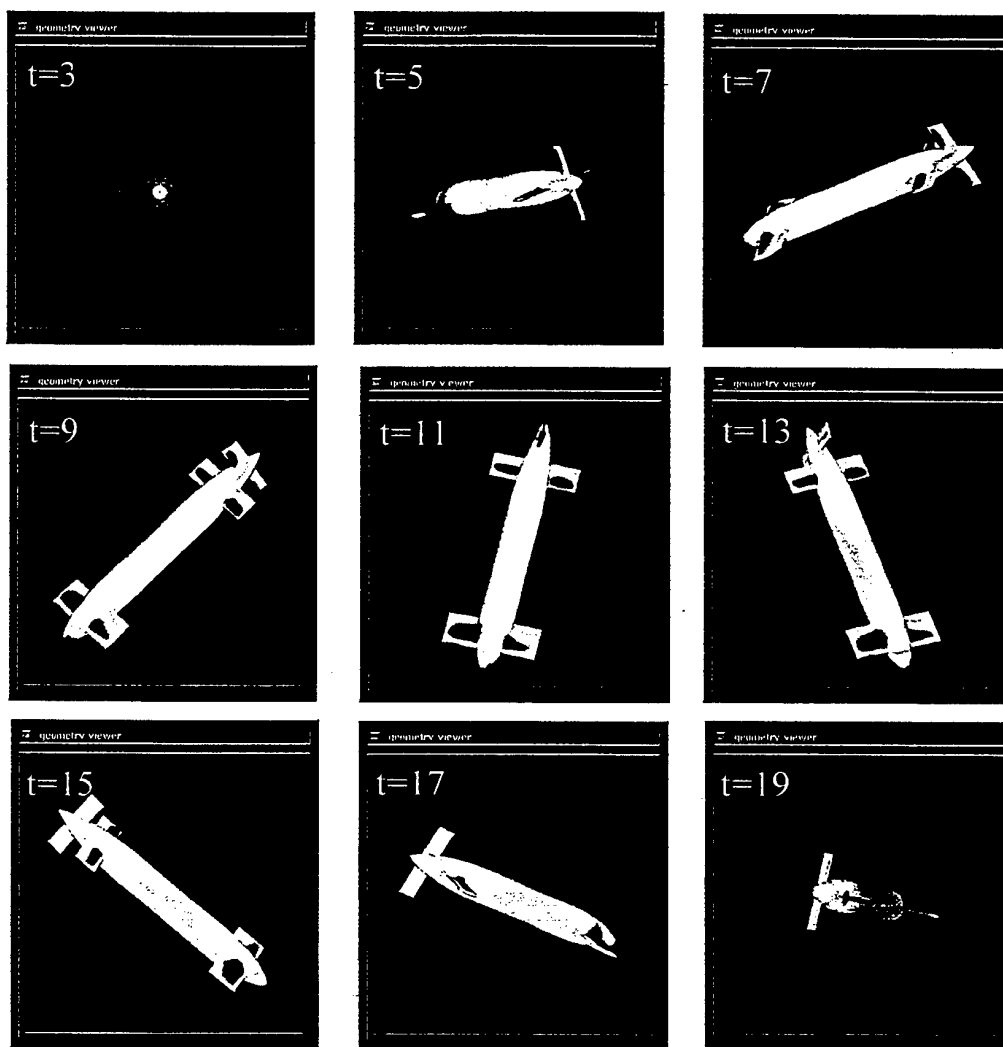


Fig.22 Time series of computed pressure distribution on the surface of the vehicle in the spiral motion. Red, yellow, green, and blue in sequence mean from positive to negative pressure.

REFERENCES

1. Kaiden, T., and Tamura, Y., "Time-Accurate Numerical Simulation of Separation between H-II and SRB", 5th ISCFD-Sendai, Sep. 1993
2. Arnaud, M., Legouez, J.M., and Rouault, M.C., "Simulation 3D of the launching of a Torpedo from a moving submarine", UDT 97, Hambourg, 1997.
3. Arnaud, M., Boheas, M.A., and Rouault, M.C., "The launching of an undersea mobile", UDT 98, London, 1998.
4. Akimoto, H., Hiroshima, F. and Miyata, H., "Hydrodynamic Design of a Sailing Boat by CAD/CFD system with Moving Coordinates", Proc. 3rd Korea-Japan Joint Workshop on Ship & Marine Hydrodynamics, 1996
5. Sato, T., Izumi, H. and Miyata, H., "Numerical Simulation of Maneuvering Motion", 22nd Symposium on Naval Hydrodynamics, Preprints, Thursday/Friday Session, 1998, pp.16-26.
6. Davoudzadeh, F., Taylor, L. K., Zlerke, W. C., Dreyer, J. J., McDonald, H. and Whitfield, D. L., "Coupled Navier-Stokes and Equations of Motion

- Simulation of Submarine Maneuvers Including Crashback", Proceedings of Fluids Engineering Division Summer Meeting, ASME, 1997, FEDSM 97-3129, pp.1-8.
7. Dreyer, J. J., Taylor, L. K., Zlerke, W. C. and Davoudzadeh, F., "A First-Principal Approach to the Numerical Prediction of the Maneuvering Characteristics of Submerged Bodies", Proceedings of Fluids Engineering Division Summer Meeting, ASME, 1997, FEDSM97-3130, pp. 1-8.
 8. Miyata, H., Zhu, M. and Watanabe, O., "Numerical Study on a Viscous Flow with Free-Surface Waves about a Ship in Steady Straight Course by a Finite-Volume Method", Journal of Ship Research, Vol.36, No. 4, 1992, pp. 332-345.
 9. Kanai, A. and Miyata, H., "Numerical Analysis of Structure of Free-Surface Shock Wave About a Wedge Model", Journal of Ship Research, Vol. 40, No. 4, 1996, pp.278-287.
 10. Kawamura, T., Mashimo, K., Masuda, S., Kimura, K., Mitsutake, H. and Ando, J., "Finite-Volume Simulation of self-propelled Tanker Models", Proceedings of the 3rd Korea-Japan Joint Workshop on Ship and Marine Hydrodynamics, Society of Naval Architects of Korea and Society of Naval Architects of Japan, 1996, pp. 105-114.
 11. Ohmori, T., Fujino, M. and Miyata, H., "A Study on Flow Field around Full Ship Forms in Maneuvering Motion", Journal of Marine Science and Technology, to appear.
 12. Germano, M. et al., "A dynamic subgrid-scale eddy viscosity model", Phys. Fluids, Vol.3, No.7, 1991, pp.1760-1765.

FLOATING BODIES, WAVE LOADS & SEAKEEPING.

Chairman : R.Eatock-Taylor.

A NONLINEAR 3-D APPROACH TO SIMULATE GREEN WATER DYNAMICS ON DECK

Z.Q. Zhou¹, J.O. De Kat and B. Buchner
Maritime Research Institute Netherlands (MARIN)
P.O. Box 28, 6700 AA Wageningen, The Netherlands

ABSTRACT

This paper presents a numerical method to predict the 3-D flow of water on deck and resulting loads using the shallow water equations. The numerical simulation of water flow on deck has been coupled to the prediction of large amplitude ship motions in waves.

The large amplitude relative motions at bow in head seas are obtained by using a nonlinear ship motion program. An empirical formula based on an experimental database estimates the water height at the deck boundary. Glimm's method has been used to simulate the three-dimensional shallow water flow over deck. An algorithm of flow flux deals with the water interaction along the deck boundary.

Extensive comparison studies have been carried out to validate the method. Numerical results have been compared with the following: 1) theoretical results of dam-breaking theory; 2) model test measurements of a reservoir-breaking impact on a structure; 3) experimental data of green water impact tests with moored tankers having different bow flare configurations in regular waves.

INTRODUCTION

Green water impact loads have an important influence on the design of turret moored Floating Production Storage and Offloading (FPSO) structures. Due to the weathervaning properties of turret moored system, the bow of the vessel is always exposed to waves in harsh environments. The impact of green water can cause serious damage to critical equipment at the bow. Green water is also a factor that limits the sustained sea speed for seagoing ships.

In recent years, efforts have been made towards understanding the physics of green water and the flow properties. The influence of the impact of green water on FPSO design was investigated by Buchner [1,2,3] experimentally. The water height on the deck of a container ship model was measured, and the shipping of water was investigated numerically with the method of characteristics by Mizoguchi [4].

In his work, the ship model was held captive, the initial conditions along the deck boundary were given by the measured results, and the simulation terminated when a bore formed. Buchner and Cozijn [5] simulated the water onto deck in a 2-D simplified configuration by a fully nonlinear boundary integral method. Dillingham [6] studied the motions of sway and roll of a vessel with shallow water on a two dimensional deck by using Glimm's method. Dillingham and Falzarano [7], and Pantazopoulos [8], extended and applied the shallow water equations approach to the 3-D case. Huang and Gu [9] considered the influence of water on deck on rolling prediction. Huang and Hsiung [10] introduced a flux-difference splitting method to predict shallow water flow on deck.

This paper presents a numerical method to predict the 3-D flow of green water on deck and resulting impact loads with shipping water on and off the deck boundary in head sea. It includes a de-

¹ Address at present: School of Naval Architecture and Marine Engineering, University of New Orleans, New Orleans, LA 70148-2225

scription of the theory, numerical procedures and validation against experimental data.

The objective of the numerical model in this paper is to simulate the following sequential phases of water on deck dynamics:

- 1) the large amplitude relative motion around the bow;
- 2) the green water flow onto the deck boundary;
- 3) the green water flow across the deck;
- 4) the impact of green water on a deck structure.

To account for these distinct aspects, the approach consists of the combination of nonlinear theory and experimentally derived formulations:

- The large amplitude relative motions at the bow are obtained in the time domain using a nonlinear, large amplitude ship motion program.
- An empirical formula based on model test data estimates the water height at the deck boundary as a function of relative motion, flare angle and location along the deck edge.
- Glimm's method is used to simulate the 3-D nonlinear, shallow water flow across the deck, while applying time-dependent boundary conditions and local deck motions obtained from the large amplitude ship motion program.
- A hydraulic model simulates water flow through scuppers and over the bulwarks.

To validate the water on deck simulation model, numerical results for water height on deck and pressure have been compared with the following:

- theoretical results of dam-breaking theory.
- model test measurements of a reservoir-breaking impact on a structure.
- experimental data of green water loading tests with moored tankers having different bow flare configurations in regular waves.

The paper discusses the influence of different formulations for impact pressure, the influence of computational grid selection, the numerical stability, and methods for dealing with the numerical simulation.

LARGE AMPLITUDE RELATIVE MOTION

Experimental investigation has shown that although the wave-induced motion of a ship is determined quite accurately by linear theory, the relative motion can exhibit strong nonlinearity especially in the bow region, mainly due to the flare of the bow and due to deformation of the wave surface.

The correct prediction of the ship's absolute motion and relative wave motion is an important step in the simulation of water flow on deck. The relative wave motion has a direct relation with water height at the deck boundary. Since deck motion is a

result of absolute ship motions at every time instant, the ship absolute motion has an influence on the phase of water flow. Without correct prediction of ship motion, the water flow on deck will be out of phase with experimental measurements.

In present analysis, the ship motion and relative wave motion prediction in head sea have been performed with a large amplitude ship motion program, which is based on a nonlinear time-domain strip method by Zhou et al. [11]. In this method, nonlinearities flare and large amplitude motion are modelled due to the integration of the wave pressure over the instantaneous wetted surface of a ship hull in waves. The sectional hydrodynamic forces are estimated according to the time-varying submerged portion at each time step based on 2-D solutions, then integration along the longitudinal direction of ship hull is carried out to obtain the total hydrodynamic forces and moments acting on the ship.

The equations of motion in head seas for heave and pitch are as follows in the model by Zhou et al. [11]:

$$[M_0 + a_{zz}(t)]\ddot{z}_g + a_{z\psi}(t)\ddot{\psi} = F_{sw}(t) + \text{Re}[F_{dz}(t)e^{i\omega_0 t}] - M_0 g + b_{zz}(t)\dot{z}_g + b_{z\psi}(t)\dot{\psi} \quad (1)$$

$$a_{\psi z}(t)\ddot{z}_g + [I_{\psi\psi} + a_{\psi\psi}(t)]\ddot{\psi} = M_{sw}(t) + \text{Re}[M_{d\psi}(t)e^{i\omega_0 t}] + b_{\psi z}(t)\dot{z}_g + b_{\psi\psi}(t)\dot{\psi} \quad (2)$$

The relative motions are calculated with respect to the disturbed wave surface. The relative motion components resulting from the diffracted and radiated waves are obtained by following equation:

$$S(x, y, t) = \zeta_w(x, t) + \zeta_r(x, t) + \zeta_d(x, t) - z_p(x, y, t) \quad (3)$$

where:

$S(x, y, t)$: the relative motion;

$\zeta_w(x, t)$: the incident wave elevation;

$\zeta_r(x, t)$: the radiation wave elevation;

$\zeta_d(x, t)$: the diffraction wave elevation;

$z_p(x, y, t)$: the vertical displacement of ship.

WATER ONTO DECK BOUNDARY

How to deal with water flow onto the deck boundary is a key question in green water simulation. It is very difficult to predict water onto deck boundary by an exact nonlinear method [5].

In typical methods for the prediction of deck wetness or green water, it is assumed that:

1. Every freeboard exceedance results in deck wetness;
2. Water height on deck boundary is equal to the exceedance of freeboard by the relative wave motion beside the bow.

However, experimental investigations on water onto deck [1,12] suggest the following:

1. The water height at deck boundary is different from freeboard exceedance at the corresponding position;
2. In regular wave case, the relation between the water height on deck boundary and the freeboard exceedance is almost independent of the wave length.

Lloyd [13,14] observed that in head sea the relative motion at the stem determines the probability of deck wetness. Experimental investigation [1,12] supported this conclusion. During the test, a large number of freeboard exceedances occurred at the side of the bow, without resulting in green water on deck, or with only very little green water from the sides. Only at the most forward point of the bow, the stem, every freeboard exceedance resulted in green water on deck.

Green water onto bow deck is a complex phenomenon affected by many strong nonlinear factors. It is influenced by: a) Ship motion; b) Geometric hull form, especially the bow flare effect of bow flare is not only pushing the water around bow swell-up, but also push the water away from the bow; c) Sea waves: including the wave height, period and progressing direction as well as the effect of wave deformations; d) Ship forward speed.

If we predict the relative motion based on a ship motion theory, we may consider that all the influence on green water onto deck, have been taken into account by the relative wave motion and freeboard exceedance calculation, except for the influence of above water bow flare.

This influence of bow flare on green water onto deck is difficult to predict by a theoretical method. In Fig. 1 an example is given of the relation between the water depth on deck compared to the freeboard exceedance for different regular wave tests. From this type of figure empirical relations between freeboard exceedance and water depth on deck can be determined [12]. By using such relations, the time history of water height at the deck edge can be generated, which will be the outer region condition for deck flow simulation (see Fig. 21).

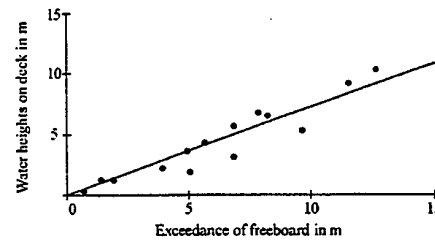


Fig. 1 Relation of water height on deck boundary and freeboard exceedance

WATER FLOW ON DECK

The problem of water flow on deck is, in fact, a dynamic coupling problem. Since the flow of deck water depends on the vessel motion, which in turn may be influenced by the forces exerted on the vessel by the deck water. The first part of this coupling problem is to describe the vessel motions given the forces acting on it, which has been performed in this paper by using a large amplitude ship motion program. The second part of the problem is to determine the water flow on deck and the forces exerted on the vessel by the water given the motion of the ship, which will be described in detail in following sections. It is assumed that the ship motion is not affected by the water on deck.

Coordinate Systems

Four coordinate systems are employed to describe the shallow water flow on a three-dimensional deck and a six-degree-of-freedom ship motion, as shown in Fig. 2.

Earth-Fixed Coordinate System

A right-handed coordinate system $O_0 - x_0 y_0 z_0$ is fixed in space. The (x_0, y_0) plane lies on the still water surface, x_0 is directed as the wave propagation direction and z_0 is directed upwards.

Ship-Fixed Reference Coordinate System

Let $\tilde{O} - \tilde{x}\tilde{y}\tilde{z}$ define a right-handed coordinate system with the origin located at the mean position of center of gravity, which translates forward with a constant ship speed U without rotation. The (\tilde{x}, \tilde{y}) plane parallel to (x_0, y_0) plane, and $\tilde{O} - \tilde{z}$ axis is positive upwards. Let η_1, η_2, η_3 be the translation displacements of the vessel in the $\tilde{x}, \tilde{y}, \tilde{z}$

directions respectively, and η_4, η_5, η_6 be the rotational displacements about the $\tilde{x}, \tilde{y}, \tilde{z}$ axes.

Moving Coordinate System

Let $G-xyz$ define a coordinate system attached to the ship with G at the ship's gravity center. The directions of the axes are: x in the longitudinal forward direction, y in the lateral port side direction and z upwards. The (x, y) plane is parallel to the still water surface when the ship is at its static equilibrium position. This coordinate system moves with the vessel.

Deck Coordinate System

Let Z_d-xyz define a deck-flow coordinate system attached to the ship, Z_d-xy plane coincides with the deck bottom plane well. The origin locates above G with distance Z_d , and the z axis is directed vertically upward. In Z_d-xyz coordinate system, the water depth is h and the free surface elevation is $\eta(x, y, t)$, measured from $z = h$. Fluid particle velocities u, v, w are expressed in this system.

It is convenient to describe the water flow on deck in Z_d-xyz system and the oscillating ship motion in $\tilde{O}-\tilde{x}\tilde{y}\tilde{z}$ system.

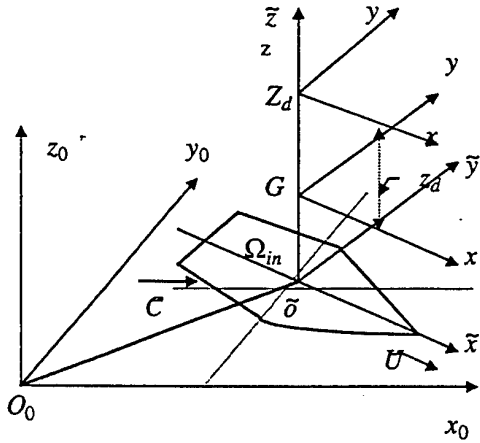


Fig. 2 Coordinate systems

Governing Equations

The problem of the flow on deck may be formulated as a nonlinear hyperbolic system of equations using the shallow water wave theory.

Assuming the water on deck is shallow comparing with the radius of curvature of the water surface. The ship undergoes arbitrary motions in waves in a six degree of freedom. By satisfying the conditions of conservation of mass and momentum, and the kinematics condition on the free surface and the bottom, the dynamic condition on the free surface, the nonlinear shallow water wave equations are obtained [8]:

$$\frac{\partial u}{\partial t} + u \frac{\partial u}{\partial x} + v \frac{\partial u}{\partial y} = -g \frac{\partial \eta}{\partial x} \quad (4)$$

$$\frac{\partial v}{\partial t} + u \frac{\partial v}{\partial x} + v \frac{\partial v}{\partial y} = -g \frac{\partial \eta}{\partial y} \quad (5)$$

$$\frac{\partial [u(\eta+h)]}{\partial x} + \frac{\partial [v(\eta+h)]}{\partial y} = -\frac{\partial \eta}{\partial t} \quad (6)$$

These equations represent the movement of water in a stationary and level reference frame. To couple the vessel motion with the water flow on deck, these equations must be transformed into the coordinate system Z_d-xyz attached to the moving vessel.

Thus, in a moving vessel, the equations of motion of water are written as [8]:

$$\frac{\partial u}{\partial t} + u \frac{\partial u}{\partial x} + v \frac{\partial u}{\partial y} = -a_{(z)} \frac{\partial \lambda}{\partial x} + f_1(x) \quad (7)$$

$$\frac{\partial v}{\partial t} + u \frac{\partial v}{\partial x} + v \frac{\partial v}{\partial y} = -a_{(z)} \frac{\partial \lambda}{\partial y} + f_2(y) \quad (8)$$

$$\frac{\partial \lambda}{\partial t} + u \frac{\partial \lambda}{\partial x} + v \frac{\partial \lambda}{\partial y} + \lambda \frac{\partial u}{\partial x} + \lambda \frac{\partial v}{\partial y} = 0 \quad (9)$$

where $\lambda = \eta + h$ and $t_0 < t < t_0 + Dt$, Dt is the time interval of ship motion.

Initial conditions and boundary conditions are (see Fig. 4):

$$\lambda = \lambda_0(x, y), u = u_0(x, y), v = v_0(x, y) \\ t \leq t_0, (x, y, z) \text{ on } \Omega_{in}$$

$$\lambda = \lambda(x, y, t_0), u = u(x, y, t_0), v = v(x, y, t_0) \\ t = t_0, \quad (x, y, z) \text{ on deck boundary}$$

where $f_1(x)$ and $f_2(y)$ represent the various body force contributions acting on the fluid in local x and y direction in the ship fixed coordinate system (for detailed expressions see e.g. Pantazopoulos [8]). a_z represents the total acceleration acting on the fluid in vertical direction in the moving coordinate system $Z_d - xyz$.

With a proper initial condition and boundary condition at every time step, these equations represent the three-dimensional shallow water flow on deck in the moving coordinate system $Z_d - xyz$.

Method Of Solution

The main difficulty of finding the solution for Eq. (7) ~ Eq. (9) is the handling of the hydraulic jumps which almost inevitably appear. Dillingham [6] initiated the shallow water flow computation in 2-D deck by applying Glimm's method.

Glimm's method is used in this paper to simulate a three-dimensional water flow on deck. This method consists of two steps. First the analytical solutions of a local Riemann problem (the dam-breaking problem) in each time interval are obtained by solving the initial value problem using the solution of the previous time step. Then the solution in the whole spatial domain is constructed as piecewise constant solutions, by using a random sampling procedure to sample a series of the obtained explicit solutions of the local Riemann problems.

By using Glimm's method, the solution of water elevation and the velocities u and v with respect to the x and y -direction at each grid point are obtained at each time step. The resulting estimates of elevation and velocity, which are random over short time spans, converge to the exact solution of Eq. (7) ~ Eq. (9), as the number of time steps becomes large.

Glimm's method is in particular attractive because it handles relatively complex flows with multiple hydraulic jumps without any special treatment of the discontinuities, as well as the case where the deck becomes partially dry. Glimm's method is unconditionally stable and numerical errors can be reduced to a relatively small size by satisfying the Courant-Friedrichs-Levy (CFL) condition.

In this paper, at every time step Δt of ship motion, the calculation of shallow water flow on deck consists of first a calculation in x -direction followed by a calculation in y -direction as has been applied by Dillingham and Falzarano [7].

During the x -direction calculation, Eq. (7) ~ Eq. (9) are reduced by retaining derivatives in the x -direction only, and the following equations are solved:

$$\frac{\partial u}{\partial t} + u \frac{\partial u}{\partial x} = -a_{(z)} \frac{\partial \lambda}{\partial x} + f_1(x) \quad (10)$$

$$\frac{\partial \lambda}{\partial t} + u \frac{\partial \lambda}{\partial x} + \lambda \frac{\partial u}{\partial x} = 0 \quad (11)$$

$$\frac{\partial v}{\partial t} + u \frac{\partial v}{\partial x} = 0 \quad (12)$$

During the y -direction calculation, using as initial conditions the solutions found in the x -sweep, after dropping the derivatives in x -direction, Eq. (7) ~ Eq. (9) become:

$$\frac{\partial v}{\partial t} + v \frac{\partial v}{\partial y} = -a_{(z)} \frac{\partial \lambda}{\partial y} + f_2(y) \quad (13)$$

$$\frac{\partial \lambda}{\partial t} + v \frac{\partial \lambda}{\partial y} + \lambda \frac{\partial v}{\partial y} = 0 \quad (14)$$

$$\frac{\partial u}{\partial t} + v \frac{\partial u}{\partial y} = 0 \quad (15)$$

Glimm's Method

To illustrate the algorithm of Glimm's method in some detail, we introduce the x -direction solution of Eq. (10) ~ Eq. (12) as an example. More details of the method can be found in [6].

The first step is to apply the technique of operator splitting to remove the inhomogeneous term $f_1(x)$ from the right side of Eq. (10). At each time step, we obtain an approximate solution to the following equations by Glimm's method:

$$\frac{\partial u}{\partial \tau} + u \frac{\partial u}{\partial x} + a_{(z)} \frac{\partial \lambda}{\partial x} = 0 \quad (16)$$

$$\frac{\partial \lambda}{\partial \tau} + u \frac{\partial \lambda}{\partial x} + \lambda \frac{\partial u}{\partial x} = 0 \quad (17)$$

and then solve the following equation by a simple Runge-Kutta integration:

$$\frac{\partial u}{\partial \tau} = f_1(x) \quad (18)$$

We divide the deck length into intervals of length Δx and approximate the water elevation λ

and velocity u by piecewise constant functions of position x and the time interval $\Delta\tau$.

The procedure for finding the solution for Eq. (16) and Eq. (17) consists of two steps.

Step 1

Let $U_n(x, \tau)$ be the exact solution to the following initial value problem for $n\Delta\tau < \tau \leq (n+1)\Delta\tau$, $n=0,1,2,\dots,M-1$.

$$U_i^n = \begin{cases} \lambda_i & (i-\frac{1}{2})\Delta x < x < (i+\frac{1}{2})\Delta x, \tau = n\Delta\tau \\ u_i & (i-\frac{1}{2})\Delta x < x < (i+\frac{1}{2})\Delta x, \tau = n\Delta\tau \end{cases} \quad i = 1, 2, \dots, N_x \quad (19)$$

The initial data consist of intervals where the solution is constant, separated by jump discontinuities (Fig. 3a):

$$\begin{aligned} U(x, n\Delta\tau) &= U_{i+1}^n & x > (i+1/2)\Delta x \\ U(x, n\Delta\tau) &= U_i^n & x < (i+1/2)\Delta x \end{aligned} \quad (20)$$

Eq. (16), (17) and Eq. (20) represent a Riemann problem. The initial conditions at two sides of an imaginary dam are known at time $n\Delta\tau$. The new solution at time $\tau + \Delta\tau$ is sought, after breaking of the imaginary dam. The method for solving the Riemann problem can be found in [6].

If the Courant-Friedrichs-Lewy (CFL) condition

$$\frac{\Delta x}{2\Delta\tau} > (|u| + C) \quad (21)$$

is satisfied, where C is the local celerity, the waves generated by Riemann problem at every grid point cannot propagate more than one-half the length of a cell (Fig. 3c). Consequently, the local solutions of Riemann problem at each grid point can be obtained analytically [6]. A random choice method is used to obtain a solution for the whole space domain.

Let $f_u[x, (n+\frac{1}{2})\Delta\tau]$, $f_\lambda[x, (n+\frac{1}{2})\Delta\tau]$ ($i\Delta x < x < (i+1)\Delta x$) be the exact local solution to Riemann problems at time $(n+1/2)\Delta\tau$. Let r_n be a random number from a uniform distribution in the interval $[-1/2, 1/2]$.

Defining at every $i + \frac{1}{2}$ position:

$$\begin{aligned} (u)_{i+\frac{1}{2}}^{n+\frac{1}{2}} &= f_u[(i+\frac{1}{2}+r_n)\Delta x, (n+\frac{1}{2})\Delta\tau] \\ (\lambda)_{i+\frac{1}{2}}^{n+\frac{1}{2}} &= f_\lambda[(i+\frac{1}{2}+r_n)\Delta x, (n+\frac{1}{2})\Delta\tau] \\ i &= 0, \pm 1, \pm 2, \dots \end{aligned} \quad (22)$$

then the piecewise constant solution is constructed as (Fig. 3b):

$$\begin{aligned} u[x, (n+\frac{1}{2})\Delta\tau] &= (u)_{i+\frac{1}{2}}^{n+\frac{1}{2}} \\ \lambda[x, (n+\frac{1}{2})\Delta\tau] &= (\lambda)_{i+\frac{1}{2}}^{n+\frac{1}{2}} \end{aligned} \quad (23)$$

where $i\Delta x \leq x < (i+1)\Delta x$.

In this way the solution advances half a time step from time $\tau = n \cdot \Delta\tau$ to time $(n+\frac{1}{2})\Delta\tau$.

Step 2

To advance the solution an additional half time step we repeat the above procedure, but with a different choice of random number. The second step is finding the solution of Eq. (16) and Eq. (17) in time $\tau = (n+1) \cdot \Delta\tau$, taking Eq. (38) as the initial condition.

The same procedure as before, let $f_u[x, (n+1)\Delta\tau]$, $f_\lambda[x, (n+1)\Delta\tau]$ ($(i+\frac{1}{2})\Delta x < x < (i+\frac{3}{2})\Delta x$) be a sequence of the exact local solutions to Riemann problems. Then we construct the piecewise constant solution in time $\tau = (n+1) \cdot \Delta\tau$ by using random number $r_n < 0$ (Fig. 3c).

Defining at every $i+1$ position:

$$\begin{aligned} (u)_{i+1}^{n+1} &= f_u[(i+1+r_n)\Delta x, (n+1)\Delta\tau] \\ (\lambda)_{i+1}^{n+1} &= f_\lambda[(i+1+r_n)\Delta x, (n+1)\Delta\tau] \\ i &= 0, \pm 1, \pm 2, \dots \end{aligned} \quad (24)$$

The piecewise constant solution is given by

$$u[x, (n+1)\Delta\tau] = (u)_i^{n+1} \quad (25)$$

$$\lambda[x, (n+1)\Delta\tau] = (\lambda)_i^{n+1}$$

where $(i + \frac{1}{2})\Delta x \leq x < (i + \frac{3}{2})\Delta x$.

At this stage, we have found the solution of equations of (16) and (17) at time $(n+1)\Delta\tau$, given the initial condition at time $n\Delta\tau$.

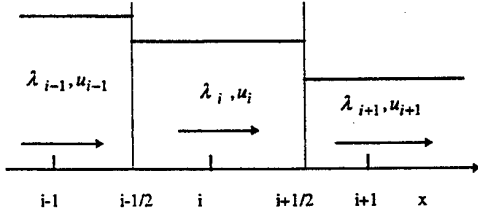


Fig. 3a

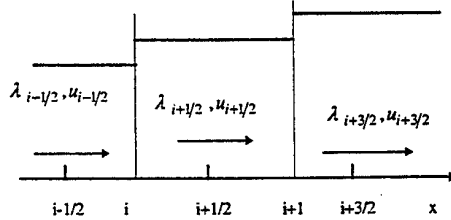


Fig. 3b

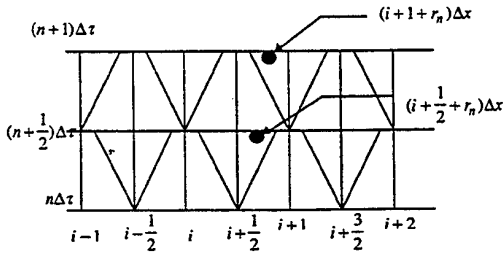


Fig. 3c

Green Water Loads

Pressure

The forces and moments exerted on deck and deck structures are mainly caused by the hydraulic jump and the impinging water jet. The pressure exerted on deck is estimated as follows:

$$p(x, y, z, t)|_{z=0} = \rho a_z(x, y, z_d, t) \lambda(x, y) \quad (26)$$

The pressure exerted on a structure on the deck is given by:

$$p(x, y, z, t) = \rho a_z(x, y, z_d, t) (\lambda(x, y) - z) \quad (27)$$

where (x, y, z) in deck-flow coordinate system $Z_d - xyz$.

Forces on Structures

The forces exerted on deck structures (as well as bulwarks) are given by:

$$\bar{F}(x, y, z, t) = \iint_S p(x, y, z, t) \bar{n} ds \quad (28)$$

and the moment about an origin is:

$$\bar{M}(x, y, z, t) = \iint_S p(x, y, z, t) \bar{r} \times \bar{n} ds \quad (29)$$

where \bar{n} is unit exterior normal to the wall.

Forces on Deck

The green water force exerted on deck is:

$$F_z(t) = \iint_S p(x, y, z, t) n_3 ds = - \sum_i \sum_j \rho a_z(x, y, z_d, t) \lambda(x_i, y_j, t) \Delta x_i \Delta y_j \quad (30)$$

The roll moment exerted on deck about the x-axis is:

$$M_x(t) = \iint_S p(x, y, z, t) n_4 ds = - \sum_i \sum_j \rho a_z(x, y, z_d, t) \lambda(x_i, y_j, t) y_j \Delta x_i \Delta y_j \quad (31)$$

The pitch moment exerted on deck about the y-axis is:

$$M_y(t) = \iint_S p(x, y, z, t) n_5 ds = \sum_i \sum_j \rho a_z(x, y, z_d, t) \lambda(x_i, y_j, t) x_i \Delta x_i \Delta y_j \quad (32)$$

WATER INTERACTION AT DECK BOUNDARY

The solution of shallow water flow found by Glimm's method is based typically on the assumption that the bulwark height is infinitely high, so that no water interaction takes place at the boundary. In fact, water flow across the deck boundary depends upon the deck motion and the water flow on deck. A flow flux method has been adopted to deal with flow interaction at the boundary.

Deck Geometry Boundary

The deck profile defined in the simulation model can be either the bow deck, or the complete ship deck, even a part of deck. The computational area consists of $N_x \times N_y$ rectangular cells. The deck profile then automatically is distributed on the computational grids. The computation starts at the deck boundary grid. The computational domain consists of two areas: Ω_{in} and Ω_{out} (Fig. 4). Ω_{out} is an imaginary area outside the deck boundary.

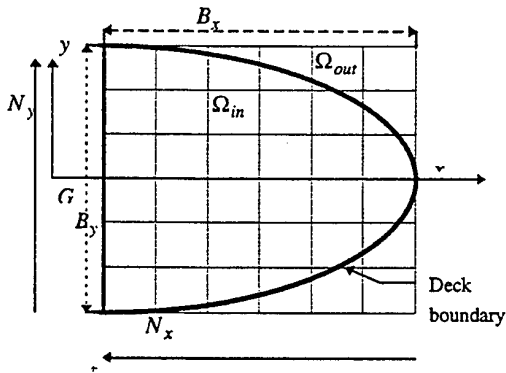


Fig. 4 Computational domain

Hydraulic flow model

Usually a vessel has bulwarks around the bow and some openings along the deck. The flow through freeing ports depends upon the pressure difference along the boundary between the outer region Ω_{out} and inner region Ω_{in} .

In a practical way, we may assume that the flow can be treated as steady flow over a weir. The water elevation along the deck boundary in the outer region is estimated at each time step by using the empirical correction procedure described in Fig. 1. Total water elevation at the deck boundary may be corrected at each time instant by adding or subtract-

ing water amount based on the water elevation difference at two sides of the deck boundary.

The interaction of deck water with water in the outer region is illustrated for the following two cases.

Case 1: $h_b > 0, h_a < 0$

In Fig. 5, ζ is the reference coordinate, h_a, h_b are the water depths at two sides of a bulwark relative to the top of bulwarks. The ideal flow velocity at depth ζ may be easily computed by converting the static head ζ into a velocity head according to Bernoulli's equation $v = \sqrt{2g\zeta}$.

Integrating over the depth we obtain the flow rate over the bulwark:

$$Q^+ = \int_0^{h_b} v d\zeta = \int_0^{h_b} \sqrt{2g\zeta} d\zeta = \frac{2}{3} h_b \sqrt{2gh_b} \quad (33)$$

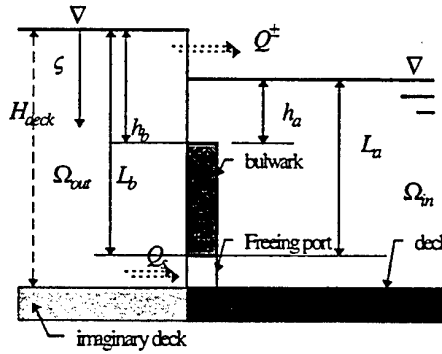


Fig. 5 Flow through scuppers and over bulwarks

Case 2: $h_a > h_b > 0$

In this case, the flow rate will be:

$$Q^- = -\frac{1}{3} (2h_a + h_b) \sqrt{2g(h_a - h_b)} \quad (34)$$

Water elevation on Deck Boundary Grid in Inner Domain

Assuming water flow rate Q to be constant in the ship motion interval Dt , the water amount in or off the deck boundary will be:

$$V_w = A_{x,y} \times Q \times Dt \quad (35)$$

where $A_{x,y}$ is the area coefficient, equal to $\Delta y \times 1.0$ in the x-direction and $\Delta x \times 1.0$ in y-direction.

Assuming this part of water amount V_w only distributed over the boundary cell at initial time t_0 , thus the water depth translated onto the boundary cell will be.

$$h_{out}(x, y, t) = \frac{V_w}{\Delta x \times \Delta y} \quad (36)$$

The total water height on boundary cell at initial time t_0 will be the combined results of the new coming water with water in last time step.

$$h(x_0, y_0, t_0) = h(x_0, y_0, t_0 - Dt) + h_{out}(x_0, y_0, t_0) \quad (37)$$

This water depth is added to the two grid points of first cell. The similar procedure is applied to the boundary in y-direction.

According to experimental observations for a moored vessel, the piled up water around the bow like a vertical wall in the outer region translates onto deck boundary, its horizontal velocity being almost zero [12]. Thus the horizontal velocity of the water column at the grid points along deck boundary at initial time is assumed to be zero.

RESULTS

Based on the method described above, a prediction tool of green water dynamics has been designed. To validate the method of the time domain simulation module, extensive comparative studies have been carried out.

Dam-Breaking Problem: Comparison with Theory

Using Glimm's method the dam-breaking problem [15] can be solved numerically. Values of water depth and velocity are computed at grid points. In initial state, the water depth is taken to be 10.m on right side of the dam, the left side without water. Fig. 6 and Fig. 7 show the values of water height and velocity obtained analytically [15] and numerically at the instant of $t = 1.0$ s.

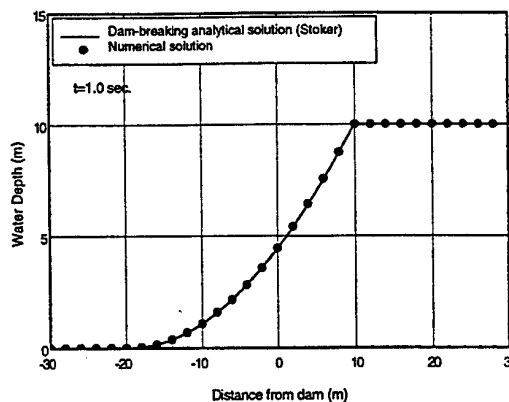


Fig. 6 Comparison of water depth of dam-breaking problem

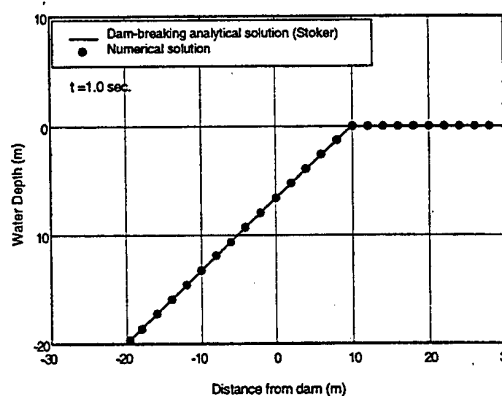


Fig. 7 Comparison of velocity of dam-breaking problem

Dam-Breaking Impact Model Test

Model tests of a reservoir-breaking impact on a structure were performed at MARIN to investigate green water impact. A set up overview of the test is given in Fig. 8.

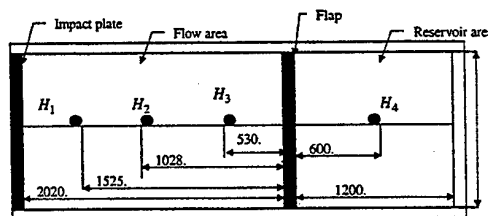


Fig. 8a The locations of water depth probes (in mm)

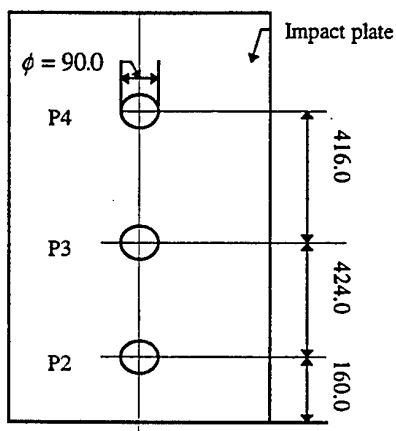


Fig. 8b The location of pressure transducers (in mm)

At the beginning of the test, water was located in the reservoir area on the right hand side of the flap with a depth of 0.60 m. At the moment the flap was lifted, the vertical wall of water in the reservoir area crashed into the flow area, resulting in a high speed jet impact on the impact plate at the left side of the flow area.

The comparisons of simulation results with experimental measurements are presented in Fig. 9 to Fig.11. The total simulation time length $T_N = 6.0\text{ s}$, the corresponding ship motion time interval $Dt = 0.1\text{ s}$. The grid space length $\Delta x = 0.01\text{ m}$ and the time step of flow simulation $\Delta\tau = Dt/n_t$, n_t is determined according to CFL condition at every ship motion time interval Dt . The pressure formula used in this simulation is simplified to the normal hydrostatic pressure $p = \rho g(\lambda - z)$.

The figures, suggest that the water flow progression and the water jet impact are simulated quite well. The vertical motion of flap is assumed to have an infinite vertical velocity at the beginning instant. Test records showed that even for a repeat test, the test results are not exactly same. The high frequency fluctuation of pressure records in Fig. 11 may result from the dynamic response of the transducer attached to the impact plate. Experiments and simulations carried out by Stansby et al. [16] also suggest that dam-break flow is modelled correctly by means of shallow water theory.

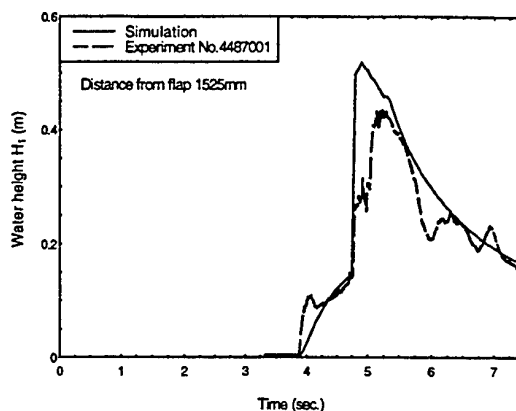


Fig. 9 Water depth at H_1

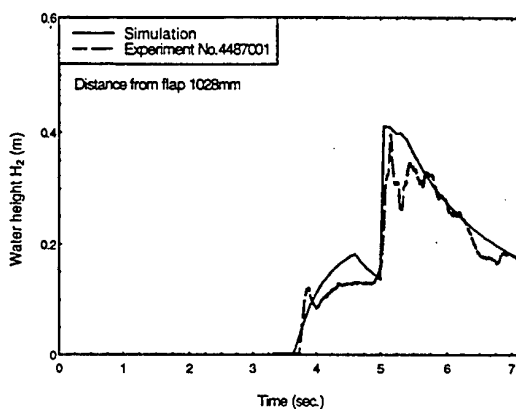


Fig. 10 Water height at H_2

Green Water Impact Model Test On A Typical Tanker With A Large Flare Bow

A comparative study has been carried out with green water impact model test of a typical 160,000 tDWT tanker moored in regular head waves.

The model tests have been reported by Buchner [1]. To investigate the effect of flare on the relative motion and green water, a significant flare above the waterline was made shown in Fig. 12 with the dash lines. A drawing of the instrumented fore-deck of the ship is shown in Fig. 13. No bulwark was placed around the bow. To simulate a turret protection house or superstructure, an instrumented vertical wall was used in this test (see Fig. 14). The main particulars are given in Table 1.

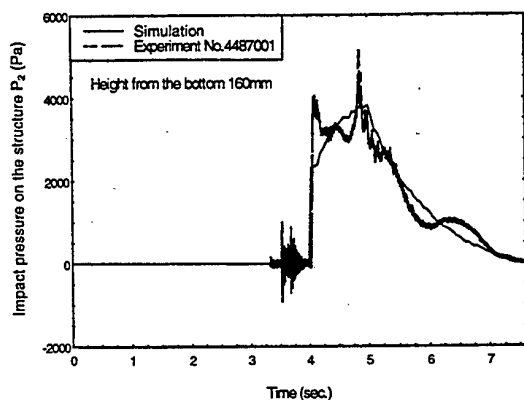


Fig. 11 Impact pressure on vertical plate at P_2

Table 1
Main particulars and stability data of a tanker

Denomination	Dimension
Length (between perpendiculars)	260.34 m
Breadth	47.10 m
Draft (even keel)	17.52 m
Freeboard	8.88 m
Depth	26.40 m
Displacement weight	183053. t
COG above base	14.22 m
COG forward of midship	+6.72 m
Longitudinal radius of gyration	65.10 m
Pitch period	11.0 s
Heave Period	11.3 s

The dimension of the bow deck in the simulation is as following: $B_x = 34.6875$ m, $B_y = 47.50$ m. The grid number used is $N_x \times N_y = 21 \times 25$. The flare angle at station 19.5 is 27 deg.

Fig. 15 to Fig. 17 are the water depths on deck. The hydraulic jumps have been well simulated. Especially the very steep water front has been captured with accurate phase. The phenomena of double peak due to water interfere has been well described in Fig. 17 and Fig. 16. The water height of bores at forward part of deck is almost constant during flowing and be reduced in height due to the interfere of transverse water fronts. In Fig. 17, in front of the structure, due to the piled up of water jet, the hydraulic jump reaches two times as high as in location H_4 in Fig. 16. Fig. 20 is the impact pressure on deck; Fig. 21 is the impact pressure on the structure (see Fig. 14). In Fig. 18 and Fig. 19, the maximum peak pressure has been correctly predicted.

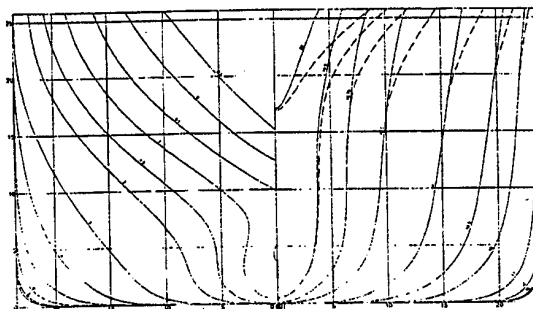
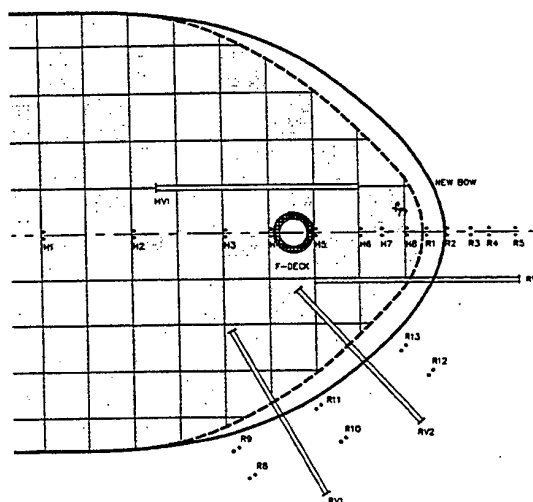


Fig. 12 Body plan of a 160,000 t DWT tanker



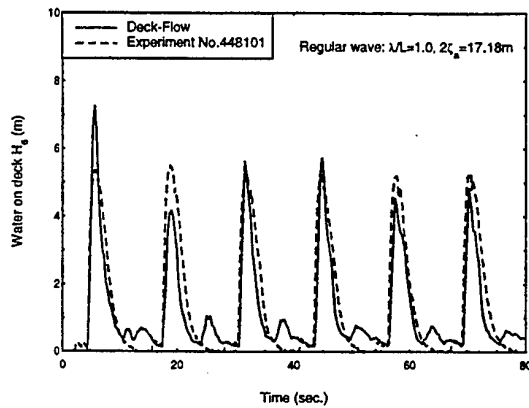


Fig. 15 Water depth on deck at location H_6 (0.69 m from the bow stem)

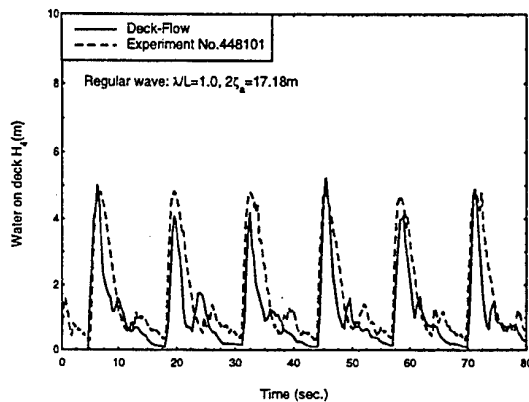


Fig. 16 Water depth on deck at location H_4 (19.69 m from stem)

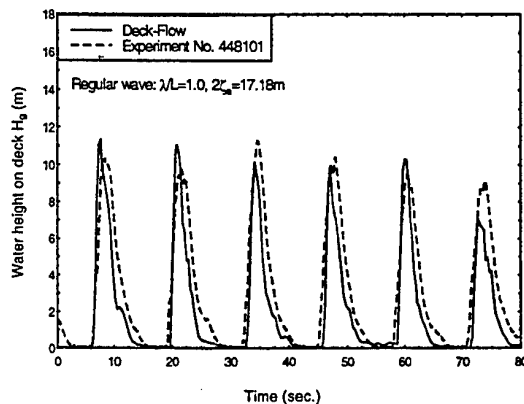


Fig. 17 Water height on deck at location H_9 , in front of impact plate (33.84 m from the stem)

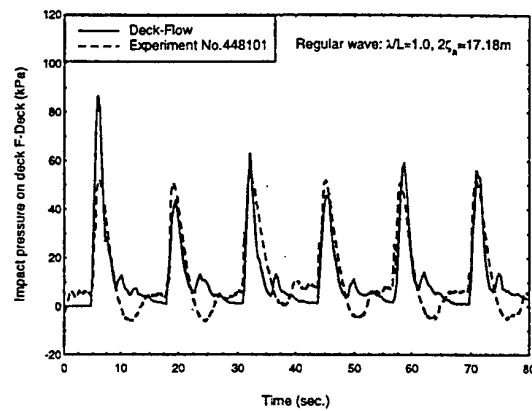


Fig. 18 Pressure on deck (17.19 m from the stem)

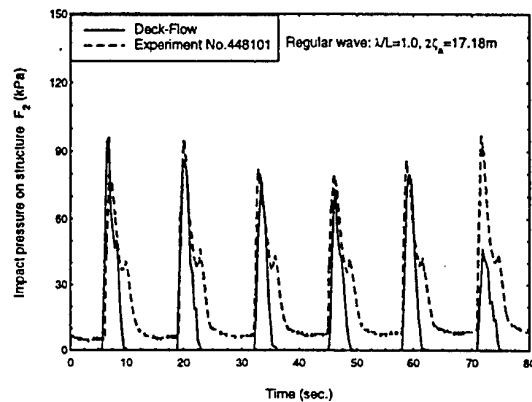


Fig. 19 Impact pressure on transducer F_2 (34.69 m bulkhead from stem)

Additional comparisons between simulations and model tests have been made for a tanker with a different bow shape. A few relevant results are shown below. A bulwark with a height of 1.4 m was placed around the ship bow. Flare angle of ship hull is 30 deg. The computational grid is $N_x \times N_y = 41 \times 21$, the time interval of ship motion simulation is about 0.36 s.

Fig. 20 shows a comparison of the relative motion at F.P., which is an example of ship motion results obtained by using the large amplitude ship motion code referred to in [11]. Fig. 21 shows the time series of water height on outer deck boundary. The prediction of relative motions at bow and absolute motions of the ship ensure the correct amplitude and phase of the deck motion.

The height and phase of the hydraulic jumps show similar agreement as in the previous case. Fig. 22 shows the green water pressure on deck. Fig. 23 and Fig. 24 shows the total water impact moment exerted on the vertical bulkhead.

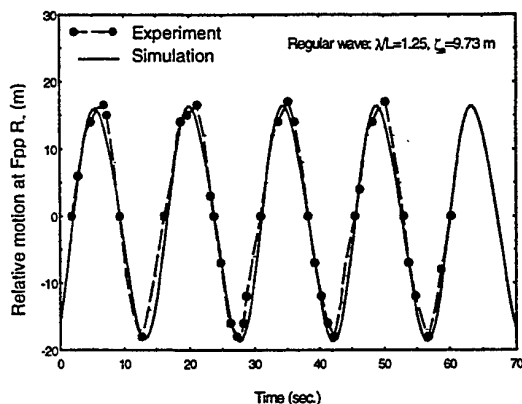


Fig. 20 Relative motion at F.P. in severe head waves (amplitude: 9.73 m)

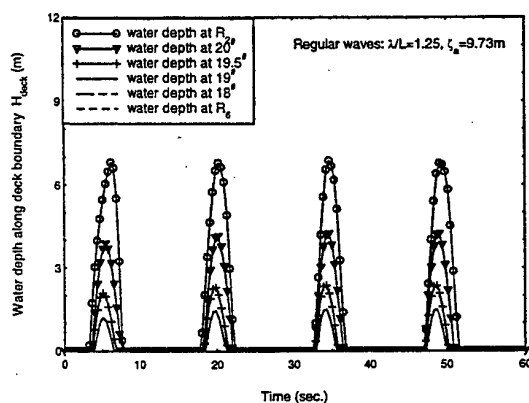


Fig. 21 Measured time series of water height along deck boundary in bow region.

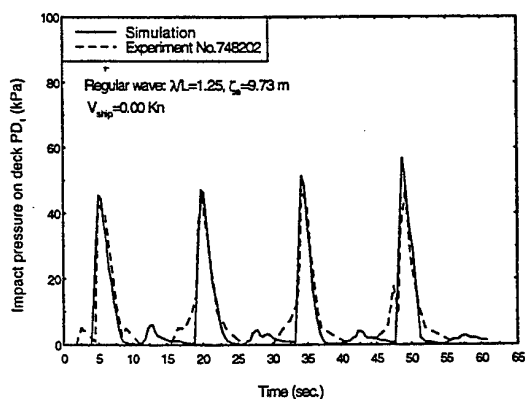


Fig. 22 Pressure on deck (13.26 m from the bow stem)

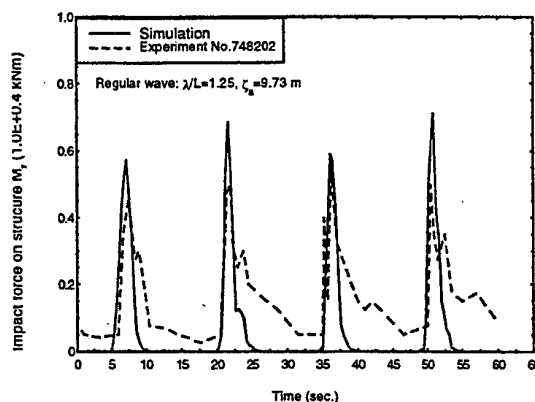


Fig. 23 Impact moment exerted on vertical bulkhead aft of F.P.

DISCUSSION

Influence of Green Water on Ship Motions

The influence of deck water on the ship motions and on the bending moment lies outside the scope of this paper. However, it should be pointed out that, the pitch motion and phase in short waves can be influenced by water flow on deck, whereas the influence in the longer waves small [2]. The computation examples presented in this paper apply to long waves. In this case, the predicted relative motion of the ship is quite accurate without the influence of the deck water effect.

Influence of Grid Size

Grid size may influence simulation results. The first factor of influence is the application of Glimm's method in which different cell numbers or the space step size $\Delta x, \Delta y$ were adopted. If the CFL condition is satisfied, the influence of grid size on simulation results can be limited to a known acceptable level. The second factor is induced by imposing the deck boundary condition on the boundary grid. Since a fluid flux method was adopted to deal with the water interaction at boundary, see Eq. (38), the water height on the boundary grid varies according to the size of grid, which will influence the computations. However, according to dam-breaking theory, the possible maximum difference will be less than $\frac{4}{9} \Delta h$ at the boundary grid.

Fig. 24 is an example of the influence of the grid number on water height. The figure shows

that the influence of grid size in the method presented in this paper is fairly limited.

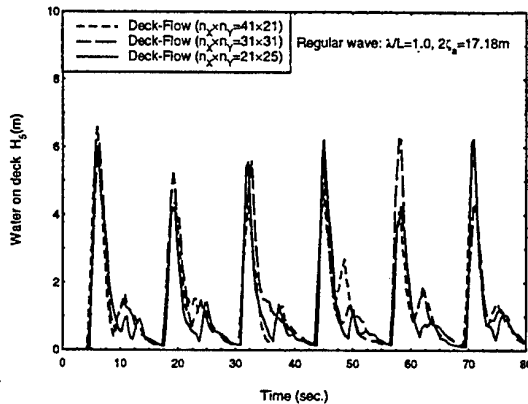


Fig. 24 Influence of grid size on water height simulation

Numerical Stability

Since Glimm's method is unconditionally stable, the method presented in this paper to simulate the 3-D green water dynamics does not suffer from any numerical stability problems.

Fig. 25 is an example of the water height on deck comparison for duration simulation. The simulation is stable, which suggests that the treatment of the boundary conditions is successful without disturbing the inner domain computation.

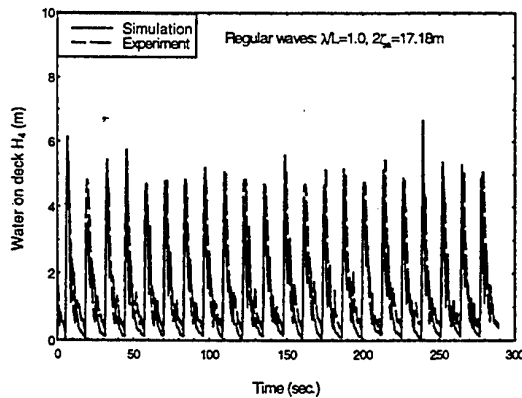


Fig. 25 Long duration simulation of water height on deck (tanker in head waves).

Pressure Formulation

In the present method the pressure exerted by water on deck is based on a hydrostatic concept with the absolute vertical (ship-fixed) deck acceleration, see eq. (26) and (27). Fig. 26 shows for one case a comparison between this pressure formulation and a similar formulation where the vertical acceleration $a_z(t)$ is replaced with the gravitational acceleration. In this case, the static pressure component is still a predominant part. However, the correct prediction of hydraulic jump height is very important in the pressure computation.

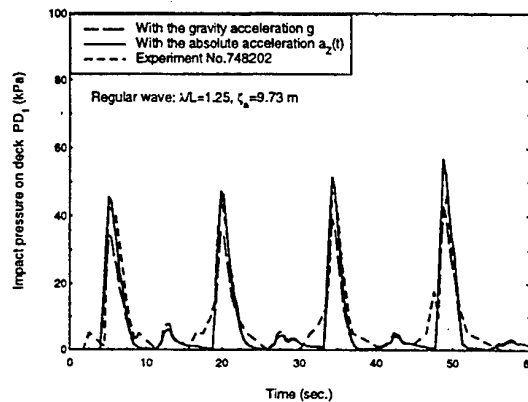


Fig. 26 Comparison between different pressure formulations

CONCLUSIONS

The three-dimensional nonlinear green water has been studied systematically. A time domain simulation approach has been developed. Extensive comparisons have been carried out to validate the accuracy of the method. The following conclusions apply:

1. Coupling the 3-D shallow water equations to a large amplitude ship motion model is a reliable approach for predicting water on deck dynamics in terms of height and pressures.
2. The water height at the deck edge is not the same as the relative motion exceedance at the location. Therefore, the methodology does require some empirically based input: model tests provide quantitative information on water height at the deck edge as a function of relative motion.

3. Maximum deck pressures are predicted well using a quasi-hydrostatic formulation based on the instantaneous hydraulic jump height and absolute vertical (ship-fixed) acceleration at a point on the deck.

REFERENCES

1. Buchner, B., "The impact of Green Water on FPSO Design", OTC 1995, No. OTC 7698, Houston, May 1995.
2. Buchner, B., "On the Impact of Green Water Loading on Ship and Offshore Unit Design", PRADS'95, Seoul, Korea, 1995.
3. Buchner, B., "The Influence of the Bow Shape of FPSOs on Drift Forces and Green Water", OTC 1996, No. OTC 8073, Houston, 1996.
4. Mizoguchi, S., "Analysis of Shipping Water with the Experiments and the Numerical Calculations", J.S.N.A., Japan, Vol. 163, June 1988.
5. Buchner, B. and Cozijn, J.L., "An Investigation into the Numerical Simulation of Green Water", Boss'97, Delft, July 1997.
6. Dillingham, J., "Motion Studies of a Vessel with Water on Deck", Marine Technology, Vol. 18, No. 1, Jan. 1981, pp. 38-50.
7. Dillingham, J. and Falzarano, J., "Three Dimensional Numerical Simulation of Green Water on Deck", STAB'86, Sep. 1986, pp. 57-64.
8. Pantazopoulos, M.S., "Three-Dimensional Sloshing of Water on Decks", Marine Technology, Vol. 25, No. 4, Oct. 1988, pp. 253-261.
9. Huang, X. and Gu, X., "Time Simulation of Ship Rolling with Shipping Water", Shipbuilding of China, No. 3, 1993.
10. Huang, Z. and Hsiung, C.-C., "Nonlinear Shallow-Water Flow on Deck", Journal of Ship Research, Vol. 40, No. 4, Dec. 1996, pp. 303-315.
11. Zhou, Z.Q., He, W.Z. and Cheng, J., "A Practical Algorithm of Predicting Ship Motions and Wave Loads in Large Amplitude Waves of Head Sea", Technology Report, No. 96337, Aug. 1996, China Ship Scientific Research Center.
12. Buchner, B. and Ballegoyen, G. van, "F(P)SO Green Water Loading, Vol. A1: Discussion Report", MARIN Report, No. 1.13644, Dec. 1997, Maritime Research Institute Netherlands.
13. Lloyd, A.J.R.M., Salsich, J.O. and Zselezky, J.J., "The Effect of Bow Shape on Deck Wetness in Head Seas", RINA, 1985.
14. Lloyd, A.J.R.M., Seakeeping, Ship Behavior in Rough Weather, Ellis Horwood Limited, Chichester, 1989.
15. Stoker, J.J., Water Waves, In Pure and Applied Mathematics, Vol. 9, The Mathematical Theory with Applications, R. Courant, L. Bers, and J.J. Stoker, Eds., Interscience, New York, 1957.
16. Stansby, P.K., Chegini, A., and Barnes, T., "The Initial Stages of Dam-Break Flow", J. Fluid Mech., Vol. 374, 1998, pp. 407-427.

Linear and Nonlinear Flows and Responses of Ships by a Rankine Panel Method

Yonghwan Kim¹, Sungeun Kim², Dirk Renick³ and Paul D. Sclavounos³

¹ American Bureau of Shipping, Two World Trade Center 106th Fl., New York, NY 10048, U.S.A.

² Boston Marine Consulting Inc., 25 Mt. Auburn St., Suite 306, Cambridge MA 02138, U.S.A.

³ Massachusetts Institute of Technology, 77 Massachusetts Ave. Cambridge, MA 02139, U.S.A

ABSTRACT

The paper presents progress with the development of the time-domain Rankine Panel Method SWAN for the simulation of steady and unsteady free surface flows, forces and responses of realistic ships in calm water and in waves. The relevant free surface boundary value problems are reviewed, the fundamental stability analysis underlying the spatial and temporal discretization of the governing equations is presented and applications of the method are discussed. They include the prediction of the resistance of a sailing yacht, a high-speed transom stern semi-displacement ship, the wave pattern and motions of multi-hull vessels, the second-order maneuvering forces of a ship in waves and the nonlinear seakeeping of a containership in steep oblique waves.

1. INTRODUCTION

Computation is gaining ground as a versatile, reliable and inexpensive tool in ship design. The last two decades have witnessed the development of a broad spectrum of computational methods for the simulation of ideal and viscous flows past realistic ship forms, which are finding their way to the desk of ship designers and naval architects. A survey of such developments is presented by Beck, Reed and Rood (1996), Larson (1996) and Sclavounos (1996). Recent progress has been reported in the proceedings of the Naval Hydrodynamics Symposia and the Numerical Ship Hydrodynamics Conferences.

An important class of Computational Fluid Dynamic (CFD) methods has been developed for the solution of the potential flow past ships in calm water and in waves. Ideal fluid effects are known to be important for the prediction of the ship wave pattern, flow properties along the ship hull, the wave resistance, a portion of the induced resistance of ships and the ship seakeeping

properties. The flow within the ship boundary layer, its wake and into the flow regime where propulsors are located as well as into a significant portion of the ship wake requires the solution of the free surface Navier Stokes equations, a task currently undertaken by several studies.

A variety of free surface conditions have been considered for the solution of potential flows past ships, ranging from the classical linear Neumann-Kelvin condition to the fully nonlinear forward speed free surface condition. All have their merits and limitations. The pioneering work of Dawson (1977) demonstrated that such ship flows may be treated numerically by the distribution of Rankine sources and dipoles over the ship hull and the free surface and the majority of solution methods today fall into that category. The use of methods based on free-surface Rankine singularity distributions however revealed that a careful study of their numerical stability properties was necessary for the solution to be robust, accurate and capable to resolve the broad range of length scales which are present in steady and unsteady

ship wave patterns. This task was undertaken in a sequence of rational stability studies by Sclavounos and Nakos (1988), Nakos and Sclavounos (1990), Vada and Nakos (1993), and Kring (1995).

Early versions of the method solved the linearized steady-state and time-harmonic linear free surface flows past ships [cf. Nakos and Sclavounos (1990, 1993)], hence treating analytically time derivatives in the free surface condition and ship motion equations. This approach enjoys unique advantages when it comes to the simulation of details of wave patterns generated by ships advancing in calm water and in regular waves. It is however limited when it comes to the simulation of second-order and nonlinear effects which can be treated more naturally in the time domain. Such an extension of the method was therefore developed. The linear time domain ship seakeeping problem was treated by Kring, Nakos and Sclavounos (1993), the second-order problem with forward speed by S. Kim and Sclavounos and Nielsen (1997) and S. Kim (1998), the nonlinear ship seakeeping problem by Huang and Sclavounos (1996) and the second-order zero-speed problem around floating structures by Y. Kim, Kring and Sclavounos (1996). The application of SWAN to a broad range of ship and offshore structure problems has been reviewed by Sclavounos et. al. (1996) and its use as a CFD ship design method was recently addressed by Sclavounos and S. Kim (1999).

This article reports on recent developments of SWAN for the treatment of linear and nonlinear ship flows. Section 2 formulates the free-surface boundary value problems for the linear, second-order and nonlinear forward-speed flows and responses of ships. More details may be found in the above references and in several doctoral dissertations completed at MIT over the past 10 years which detail the various stages in the development of the method. Sections 3 and 4 summarize the Rankine panel method and the stability properties of the discretization algorithms underlying the solution of the zero- and forward-speed time-domain flows past ships.

Section 5 describes the performance of the linear version of SWAN in predicting the wave resistance and seakeeping of realistic hull forms, including an America's Cup yacht, a high-speed semi-displacement mono-hull and a tri-maran hull form. Section 6 addresses the solution of the second-order forward-speed problem around ships with finite steady-state or slowly-varying velocities in surge-sway-yaw. Second-order effects are important in a variety of contexts in ship hydrodynamics. They include the evaluation of the slowly-varying wave forces acting on vessels undergoing a maneuver in waves. Such wave effects are time-dependent, quadratic in the wave amplitude and important in the evaluation of the course keeping in waves. A second problem of critical interest to the offshore industry is the position keeping of FPSO's, ship-like vessels moored offshore for the exploration and extraction of hydrocarbons from deep-water reservoirs.

Section 7 describes recent extensions of SWAN to the nonlinear seakeeping problem of ships in steep oblique waves. The weak scatterer method which has been demonstrated in earlier SWAN studies to be very accurate in steep head waves has been extended to oblique waves. Computations of the motions of a containership advancing with forward velocity in oblique waves are presented and shown to be in very good agreement with experiments, presenting a significant improvement over the linear version of the method. Section 8 presents a summary.

2. FREE-SURFACE BOUNDARY VALUE PROBLEMS

Consider a ship in the presence of incoming waves. A body-fixed Cartesian coordinate system, $\bar{x} = (x, y, z)$, is defined in Fig.1 with the positive z -axis pointing upwards and the positive x -axis pointing upstream. The ship is assumed to translate with velocity \bar{U} .

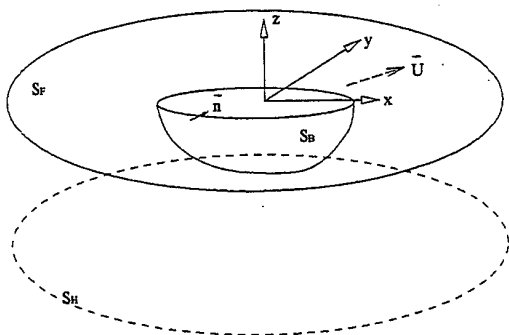


Fig.1 Coordinate system

Assume that the fluid is ideal and the flow irrotational. A total flow velocity potential $\Psi(\vec{x}, t)$ may thus be defined, governed by the Laplace equation in the fluid domain. In this study, three distinct formulations are considered for the linear, second-order and nonlinear forward-speed problems, respectively.

2.1 Linear and Second-Order Forward-Speed Problems

Perturbation series expansions for the velocity potential $\Psi(\vec{x}, t)$ and wave elevation $\eta(\vec{x}, t)$ are assumed, leading to the definition of linear, second- and higher-order quantities,

$$\Psi(\vec{x}, t) = \Phi(\vec{x}, t) + \varphi_1(\vec{x}, t) + \varphi_2(\vec{x}, t) + \dots \quad (1)$$

$$\eta(\vec{x}, t) = \zeta_1(\vec{x}, t) + \zeta_2(\vec{x}, t) + \dots \quad (2)$$

Here, Φ is the basis flow potential, and φ_1 and φ_2 are the linear and second-order wave potentials, respectively. Up to second-order, the free-surface boundary conditions take the form:

Linear

$$\left[\frac{\partial}{\partial t} - (\vec{U} - \nabla\Phi) \cdot \nabla \right] \varphi_1 + g\zeta_1 = \vec{U} \cdot \nabla\Phi - \frac{1}{2} \nabla\Phi \cdot \nabla\Phi \quad (3)$$

$$\left[\frac{\partial}{\partial t} - (\vec{U} - \nabla\Phi) \cdot \nabla \right] \zeta_1 - \frac{\partial \varphi_1}{\partial z} = \zeta_1 \frac{\partial^2 \Phi}{\partial z^2} \quad (4)$$

Second-Order

$$\left[\frac{\partial}{\partial t} - (\vec{U} - \nabla\Phi) \cdot \nabla \right] \varphi_2 + g\zeta_2 = -\zeta_1 \left[\frac{\partial}{\partial t} - (\vec{U} - \nabla\Phi) \cdot \nabla \right] \frac{\partial \varphi_1}{\partial z} - \frac{1}{2} \nabla \varphi_1 \cdot \nabla \varphi_1 \quad (5)$$

$$\left[\frac{\partial}{\partial t} - (\vec{U} - \nabla\Phi) \cdot \nabla \right] \zeta_2 - \frac{\partial \varphi_2}{\partial z} = -\nabla \varphi_1 \cdot \nabla \zeta_1 + \zeta_1 \frac{\partial^2 \varphi_1}{\partial z^2} + \zeta_2 \frac{\partial^2 \Phi}{\partial z^2} \quad (6)$$

The velocity potential is decomposed into the incident-wave and perturbation potentials. The linear and second-order incident wave potentials can be expressed as follows:

$$\varphi_{1,0} = \text{Re} \left\{ \sum_j \varphi_{1,j}(x, y, z) e^{i\omega_j t} \right\} \quad (7)$$

$$\varphi_{2,0} = \text{Re} \left\{ \sum_l \sum_m [\varphi_{2,l}^+(x, y, z) e^{i(\omega_l + \omega_m)t} + \varphi_{2,l}^-(x, y, z) e^{i(\omega_l - \omega_m)t}] \right\} \quad (8)$$

where ω_j is the frequency of the j -th wave component. The second-order wave consists of two distinct components arising from the sum- and difference-frequency contributions.

The linear and second-order hydrodynamic forces can be obtained by integrating the pressure of the respective order,

$$\vec{F}_1 = -\rho \iint_{S_B} \frac{\partial \varphi_1}{\partial t} \vec{n} \, ds \quad (9)$$

$$\vec{F}_2 = -\rho \iint_{S_B} \left(\frac{\partial \varphi_2}{\partial t} + \frac{1}{2} \nabla \varphi_1 \cdot \nabla \varphi_1 \right) \vec{n} \, ds + \frac{1}{2} \rho g \oint_{wl} \zeta_1^2 \vec{n} \, dl$$

where ρ, \vec{n} are the water density and the unit vector normal to the ship hull and pointing out of the fluid domain. The line integral in the definition of the second-order force is defined over the static water line, and involves the square of the wave elevation.

2.2 Nonlinear Forward-Speed Problem

When the ship advances with a constant forward speed \bar{U} in steep waves, the seakeeping problem is treated by the weak-scatterer approximation. In this formulation, the total velocity potential is decomposed as follows:

$$\Psi(\bar{x}, t) = \Phi(\bar{x}, t) + \phi(\bar{x}, t) + \varphi_0(\bar{x}, t) + \varphi(\bar{x}, t). \quad (10)$$

Here, Φ and ϕ are the basis and impulsive flow potentials, while φ_0 and φ are the prescribed incident wave and the memory potentials, respectively. In particular, the basis flow is the solution of a boundary value problem, which assumes a no-flux condition on all solid boundaries and the free surface defined by the known incident wave elevation. Similarly, the total wave elevation $\eta(x, y, t)$ is decomposed into two components,

$$\eta(x, y, t) = \zeta_0(x, y, t) + \zeta(x, y, t) \quad (11)$$

where ζ_0, ζ denote the incident and disturbance wave elevations, respectively.

Assuming that the basis flow, Φ , the impulsive flow, ϕ , and the incident wave flow, φ_0 provide the dominant contributions to the total wave flow, the free surface conditions with respect to φ and ζ may be linearized about $z = \zeta_0(x, y, t)$, as follows:

$$\begin{aligned} \left[\frac{\partial}{\partial t} - (\bar{U} - \nabla\Phi - \nabla\phi - \nabla\varphi_0) \cdot \nabla \right] \zeta = & \\ - \left[\frac{\partial}{\partial t} - (\bar{U} - \nabla\Phi - \nabla\phi - \nabla\varphi_0) \cdot \nabla \right] \zeta_0 & \quad (12) \\ + \frac{\partial}{\partial z} (\Phi + \phi + \varphi + \varphi_0) - \nabla\varphi \cdot \nabla\zeta_0 + & \\ \left[\frac{\partial^2\Phi}{\partial z^2} + \frac{\partial^2\varphi_0}{\partial z^2} - \nabla \left(\frac{\partial\Phi}{\partial z} + \frac{\partial\varphi_0}{\partial z} \right) \cdot \nabla\zeta_0 \right] \zeta & \end{aligned}$$

$$\begin{aligned} \left[\frac{\partial}{\partial t} - (\bar{U} - \nabla\Phi - \nabla\phi - \nabla\varphi_0) \cdot \nabla \right] \zeta = & \frac{1}{2} \nabla\varphi_0 \cdot \nabla\varphi_0 \\ - \left[\frac{\partial}{\partial t} - (\bar{U} - \nabla\Phi - \nabla\phi - \nabla\varphi_0) \cdot \nabla \right] \varphi_0 - & \\ \left[\frac{\partial}{\partial t} - (\bar{U} - \nabla\Phi) \cdot \nabla \right] \Phi + \frac{1}{2} \nabla\Phi \cdot \nabla\Phi - & \quad (13) \\ \left[\frac{\partial}{\partial t} - (\bar{U} - \nabla\Phi - \nabla\phi) \cdot \nabla \right] \phi + \frac{1}{2} \nabla\phi \cdot \nabla\phi - & \\ g(\zeta + \zeta_0) - \left[\frac{\partial}{\partial t} - (\bar{U} - \nabla\Phi - \nabla\phi - \nabla\varphi_0) \cdot \nabla \right] \times & \\ \zeta \frac{\partial}{\partial z} (\Phi + \phi + \varphi_0) & \end{aligned}$$

The ship motion equations take the form,

$$(\mathbf{M} + a_0)\ddot{\xi} + b_0\dot{\xi} + (C + c_0)\xi = F_m(\ddot{\xi}, \dot{\xi}, \xi, t) \quad (14)$$

where the matrix coefficients a_0, b_0, c_0 represent the impulsive flow forces proportional to the ship acceleration $\ddot{\xi}$, the velocity $\dot{\xi}$ and the displacement ξ , respectively. \mathbf{M} and \mathbf{C} are the mass and restoring coefficient tensors. In addition, F_m is the integrated memory force arising from surface wave effects, obtained from the solution of the surface wave flow around the ship in waves.

3. RANKINE PANEL METHOD

The solution algorithm is based on a three-dimensional Rankine panel method derived from the studies of Sclavounos & Nakos (1988) for the steady wave flow problem and Nakos and Sclavounos (1990) for the time harmonic problems. Recently, extensions of this method were introduced by Y. Kim, Kring and Sclavounos (1997), S. Kim, Sclavounos and Nielsen (1997) and Huang and Sclavounos (1998).

The boundary of the fluid domain is discretized into quadrilateral panels, and the physical variables are represented with a higher-order B-spline basis function. The velocity potential adopts the representation,

$$\phi(\bar{x}_i, t) \approx \sum_j \phi_j(t) B_j(\bar{x}_i) = \sum_j \phi_j(t) b^{(p)}(\xi_1; \bar{x}_i) b^{(q)}(\xi_2, \bar{x}_i) \quad (15)$$

where $B_j(\bar{x}_i)$ is the B-spline basis function of order (p, q) , defined relative to the local panel coordinates (ξ_1, ξ_2) . The same approximation is applied to the wave elevation and normal velocity over the fluid boundaries.

According to Green's theorem, the velocity potential and normal velocity over the fluid boundaries are related by the integral relation

$$(\phi_k)_j^{n+1} B_{ij} + (\phi_k)_j^{n+1} \iint_S B_{ij}(\bar{\xi}) \frac{\partial}{\partial n} G(\bar{x}; \bar{\xi}) d\bar{\xi} - \left(\frac{\partial \phi_k}{\partial n} \right)_j^{n+1} \iint_S B_{ij}(\bar{\xi}) G(\bar{x}; \bar{\xi}) d\bar{\xi} = 0 \quad (16)$$

where the superscript denotes the time step, and the Green function is the Rankine source. Here, ϕ_k symbolizes all velocity potentials involved.

The free surface conditions are integrated using a modified Euler scheme. In this scheme, the free surface elevation is obtained from the kinematic free surface condition,

$$\frac{(\zeta_k)_j^{n+1} - (\zeta_k)_j^n}{\Delta t} = P(\phi_k^n, \zeta_k^n, \dots), \quad (17)$$

and the velocity potential from the dynamic condition,

$$\frac{(\phi_k)_j^{n+1} - (\phi_k)_j^n}{\Delta t} = Q(\phi_k^n, \zeta_k^{n+1}, \dots). \quad (18)$$

P and Q are the forcing terms, which are defined in equations (3), (4) or (12), (13). It should be noted that the wave elevation obtained from equation (17) is used as input in equation (18). Combining equations (17) and (18) with the boundary integral equation (16), allows the values of the velocity potentials on the submerged body surface and the normal velocities on the free surface to be updated.

The nonlinear equation of motion, (14), is numerically integrated using a fourth-order Adam-Bashford-Moulton predictor-corrector scheme. The first four time steps were integrated by a fourth-order Runge-Kutta scheme. Kring and Slavounos (1995) showed that this method is stable as long as a set of conditions governing temporal and spatial discretization are met. Note that, in the weak-scatter formulation, the nonlinear restoring force has been included in C , while only the linear inertia has been considered in M .

The enforcement of the radiation condition is also necessary over the truncated region of the free surface computational domain. In the present computation, a numerical dissipative beach is employed. Over this artificial beach, the method introduces a Newtonian-type cooling term, $\mu_1 \zeta_k$, into the kinematic free surface condition together with an extra term, $\mu_2 \phi_k$, added to ensure no change of the linear dispersion relation when $\mu_2 = -\mu_1^2 / 4g$. Details are presented in Nakos(1993).

4. STABILITY ANALYSIS

The stability analysis for the current Rankine panel method using B-spline basis functions can be found in the studies of Slavounos & Nakos (1988) for the steady state and Nakos and Slavounos (1990) for the time-harmonic problems, respectively. Nakos (1993) extended the method to the unsteady time-domain problem.

The stability analysis considers the propagation of surface waves over a discrete domain, hence only the free surface is considered. Furthermore, it is assumed that the panel dimensions in the x- and y-directions are constant, $\Delta x, \Delta y$. The spatial-temporal discrete Fourier transform and its inverse are introduced in the form:

$$\tilde{f}(u, v, \omega) = \Delta x \Delta y \Delta t \times \sum_l \sum_m \sum_n f_{l,m}^{(n)} e^{i(u l \Delta x + v m \Delta y - \omega n \Delta t)} \quad (19)$$

$$f_{l,m}^{(n)} = \frac{1}{(2\pi)^3} \int_{-\pi/\Delta x}^{\pi/\Delta x} \int_{-\pi/\Delta y}^{\pi/\Delta y} \int_{-\pi/\Delta t}^{\pi/\Delta t} \tilde{f}(u, v, \omega) \times e^{-i(u\Delta x + v\Delta y - \omega\Delta t)} du dv d\omega \quad (20)$$

Their use plays a central role in the Neumann stability analysis discussed next.

4.1 Zero-Speed Problem

When the discrete Fourier transform is applied to Green's theorem, (16), and free surface conditions, (17) and (18) with zero speed, the velocity potential takes the form:

$$\varphi_{l,m}^{(n)} = \frac{1}{(2\pi)^3} \iiint \frac{\tilde{R}}{\tilde{W}} e^{-i(u\Delta x + v\Delta y - \omega\Delta t)} du dv d\omega \quad (21)$$

where the denominator, \tilde{W} , contains all information about the dispersion relation governing the propagation of surface waves over the discrete free surface. It takes the form:

$$\tilde{W} = \beta^2 Z^2 - (2\beta^2 - S)Z + \beta^2 \quad (22)$$

where $Z = e^{i\omega\Delta t}$, $\beta = \sqrt{\Delta x / g\Delta t^2}$, and $S = \Delta x \tilde{B} / \tilde{S}_0$. Here, \tilde{B} and \tilde{S}_0 are the Fourier transforms of the basis function and its integral with the Rankine source potential,

$$\begin{aligned} \tilde{B} &= \Delta x \Delta y \times \sum_{m=-\infty}^{\infty} \sum_{n=-\infty}^{\infty} \frac{\sin^{p+1}(\hat{u}\pi + m\pi) \sin^{q+1}(\hat{v}\pi + n\pi)}{(\hat{u}\pi + m\pi)^{p+1} (\hat{v}\pi + n\pi)^{q+1}} \\ \tilde{S}_0 &= \frac{\Delta x^2 \Delta y}{2\pi} \times \sum_{m=-\infty}^{\infty} \sum_{n=-\infty}^{\infty} \frac{\sin^{p+1}(\hat{u}\pi + m\pi) \sin^{q+1}(\hat{v}\pi + n\pi)}{(\hat{u}\pi + m\pi)^{p+1} (\hat{v}\pi + n\pi)^{q+1} \sqrt{(\hat{u} + m)^2 + (\hat{v} + n)^2}} \end{aligned} \quad (23)$$

where $\hat{u} = u\Delta x / \pi$, $\hat{v} = v\Delta y / \pi$. The discrete dispersion relation, (22), must reduce to the continuous dispersion relation when $\Delta x, \Delta y, \Delta t$ tend to zero. When $O(\Delta x, \Delta y) = O(\Delta t)$ and $\Delta t \rightarrow 0$, the series expansion of $\Delta x / S$ becomes

$$\begin{aligned} \Delta x / S &= \frac{1}{\sqrt{u^2 + v^2}} + \frac{(-1)^{p+1} \Delta t (v\Delta t)^{q+1}}{(v\Delta t + 2\pi)^{q+1} \sqrt{(u\Delta t)^2 + (v\Delta t + 2\pi)^2}} + \\ &\quad \frac{(-1)^{q+1} \Delta t (u\Delta t)^{p+1}}{(u\Delta t + 2\pi)^{p+1} \sqrt{(u\Delta t + 2\pi)^2 + (v\Delta t)^2}} + \\ &\quad \frac{(-1)^{p+q+2} \Delta t (u\Delta t)^{p+1} (v\Delta t)^{q+1}}{(u\Delta t + 2\pi)^{p+1} (v\Delta t + 2\pi)^{q+1} \sqrt{(u\Delta t + 2\pi)^2 + (v\Delta t + 2\pi)^2}} \\ &\quad + O(\Delta t^{p+q+3}) \end{aligned} \quad (25)$$

Therefore, as $\Delta t \rightarrow 0$, it is easy to prove that the discrete dispersion relation becomes

$$\tilde{W} = \omega^2 - g\sqrt{u^2 + v^2} + O(\Delta t^{p+3}, \Delta t) = 0 \quad (26)$$

when $p = q$. This result proves consistency, namely that the discrete problem reduces to the continuous one in the limit as the panel size and time step tend to zero.

A separate issue is temporal stability, which can be studied using the above results. For temporal stability, the roots Z of equation (22) must reside inside of unit circle in the complex frequency plane. Especially, when Z is on a unit circle, the scheme becomes neutrally stable. In the present scheme, the condition for neutral stability becomes

$$\beta \geq \frac{\sqrt{S}}{2} \quad (27)$$

Fig.2 shows the continuous and discrete dispersion relations when $\alpha = 1.0$ and $\beta = 1.0$. As shown above, when $\Delta x, \Delta t \rightarrow 0$, the two solutions approach the same limit. This figure supports the fact that the primary source of discretization error is not the spatial but the time discretization. Therefore, increasing the order of the basis function does not improve the solution accuracy. Moreover, the group velocity becomes zero when $u\Delta x / 2\pi = 0.5$, leading to the generation of the familiar saw-tooth waves, present in many free surface Rankine panel methods.

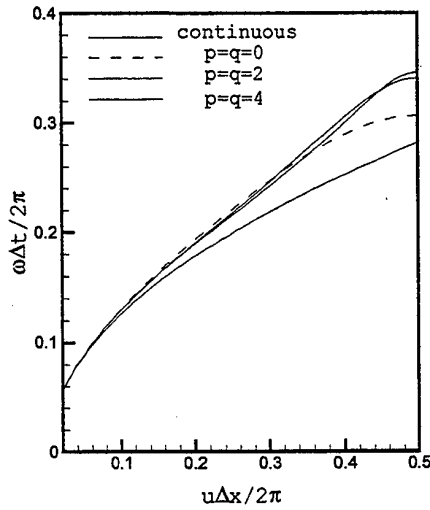


Fig.2 Continuous and discrete dispersion relation;
 $\alpha = 1, \beta = 1, v = 0, U = 0$

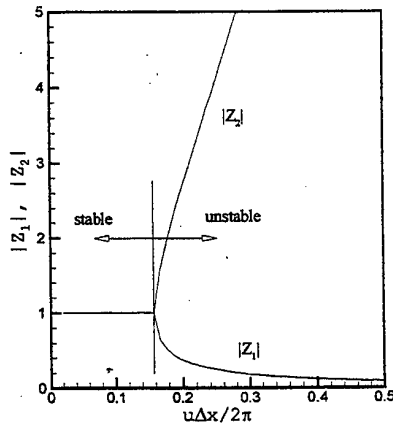


Fig.3 Magnitude of two solutions of equation (22);
 $\alpha = 1.0, \beta = 0.5, U = 0, p = q = 2$

Fig.3 shows the magnitude of the two solutions of equation (22) when $\alpha = 1.0$ and $\beta = 0.5$. In this case, a bi-quadratic basis function was applied. The magnitude of Z_2 becomes larger than 1 from a certain value of $u \Delta x / 2\pi$, and the computation will be unstable at this condition. Fig.4 is a contour plot of $S/4\beta^2$ when $\alpha = 1.0$. Therefore, stable computation is expected when $S/4\beta^2 \leq 1.0$.

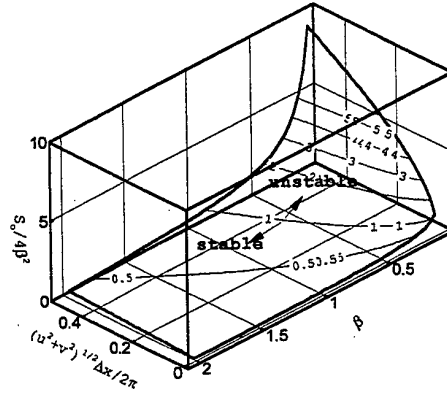


Fig.4 Contour plots of $S/4\beta^2$ and stability zone;
 $\alpha = 1.0, U = 0, p = q = 2$

4.2 Forward-Speed Problem

The stability analysis for the weak-scatterer formulation is too complex to undertake over the surface of the ambient wave. However, when the incident wave steepness is small, the classical linear problem is recovered and its stability properties often persist in the nonlinear problem. For the linear free surface conditions,

$$\frac{\partial \phi}{\partial t} + U \frac{\partial \phi}{\partial x} = -g\zeta \quad (28)$$

$$\frac{\partial \zeta}{\partial t} + U \frac{\partial \zeta}{\partial x} = \frac{\partial \phi}{\partial z}, \quad (29)$$

the discrete dispersion relation takes the form:

$$\tilde{W} = (\beta^2 - i\beta F_h D)Z^2 - (2\beta^2 - S + F_h^2 D^2)Z + \beta^2 + i\beta F_h D \quad (30)$$

where $F_h = U/\sqrt{g\Delta x}$ and $D = \tilde{D}_1/\tilde{B}$. Moreover, \tilde{D}_1 is the Fourier transform of the first derivatives of the basis function with respect to x . D takes the form,

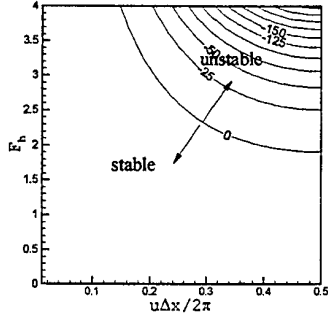
$$\tilde{D}_1 = \sum_{m=-\infty}^{\infty} \frac{\sin^p(\hat{u}\pi + m\pi)}{(\hat{u}\pi + m\pi)^p} \quad (31)$$

$$\sum_{m=-\infty}^{\infty} \frac{\sin^{p+1}(\hat{u}\pi + m\pi)}{(\hat{u}\pi + m\pi)^{p+1}}$$

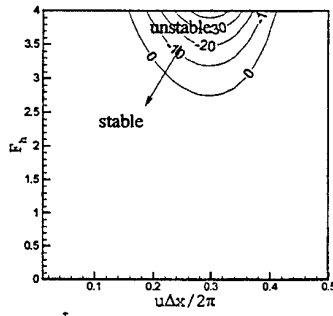
Here, \tilde{B} is defined in equation (23). We can easily determine that D is a function of \tilde{u} only and it is written as

$$D = u\Delta x + O(\Delta x^{p+1}) \quad (32)$$

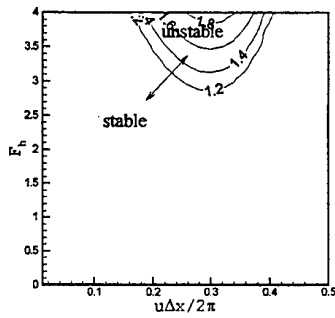
Equations (31), (32) and in the zero-speed case, equations (23)-(26), are the general forms of Nakos's result, which is valid for a basis function of arbitrary order.



(a) H contour, $p=q=0$



(b) H contour, $p=q=2$



(c) $|Z_1|$ contour, $p=q=2$

Fig.5 Contour plots of H and $|Z_1|$ and the stability zone; $\alpha = 1.0, \beta = 3.0, \tilde{v} = 0.5$

From equations (25) and (32), the limit case of equation (30) becomes

$$\tilde{W} = (\omega - Uu)^2 - g\sqrt{u^2 + v^2} + O(\Delta x^{p+1}, \Delta t) = 0, \quad (33)$$

recovering the continuous dispersion relation. As in the zero-speed problem, a condition for temporal neutral stability may be derived from equation (30) in the form

$$H = \beta^2 - \frac{(F_h^2 D^2 - S)^2}{4S} \geq 0 \quad (34)$$

Nakos (1993) suggested a similar condition, but equation (34) is a preferable form, which takes into account the negative values of S and $F_h^2 D^2 - S$.

Fig.5 (a) and (b) show the contour plots of H for the piece-wise constant and bi-quadratic basis functions. When the piece-wise constant basis function is applied, this result corresponds to the two-point central difference method. It is obvious that the bi-quadratic basis function offers a wider stability zone. Figure (c) shows the contour of $|Z_1|$ in the same condition as figure (a) and (b). The computation will be unstable if $|Z_1|$ is greater than 1.0, and this contour plot is consistent with figure (b), proving that equation (34) is correct.

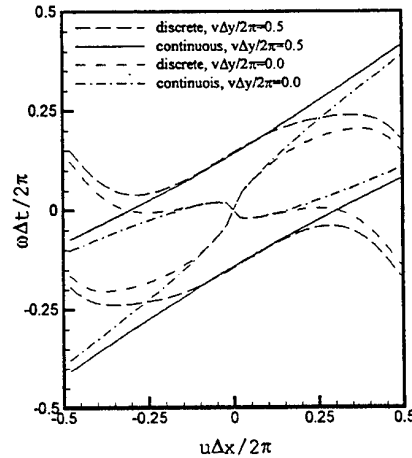


Fig.6 Continuous and discrete dispersion relations; $\alpha = 1.0, \beta = 2.0, F_h = 1.0$

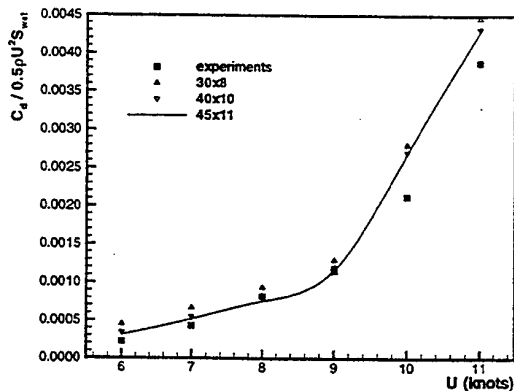


Fig.7 Residuary resistance of an America's Cup yacht.

Fig.6 shows the continuous and discrete dispersion relations for different wave numbers, ν . As shown in equation (33), the two solutions are very close near $(u\Delta x, \omega\Delta t)/2\pi = (0,0)$. However, in shorter waves, a larger discrepancy is found. Moreover, there exist frequencies where the group velocity vanishes. These pose a significant threat to the overall performance of the computation, it is therefore very important to keep a fine spatial resolution.

5 Linear Forward-Speed Problem

The prediction of the ship wave pattern and resistance is important in ship design. This section presents comparisons between measurements and computations of the wave resistance and seakeeping of three realistic hull forms, using the linear version of SWAN.

Fig.7 compares the residuary resistance of an America's Cup yacht cruising upright at a Froude number of 0.3. At each speed the yacht is allowed to sink and trim. Moreover, the apparent lengthening of the wetted length of the yacht due to the overhangs near the bow and stern has also been taken into account.

Fig.8 and Fig.9 illustrate the steady wave pattern and the residuary power of the FastShipTM, a 770ft 40knot containership being considered for service across the Atlantic with a wide and shallow transom stern.

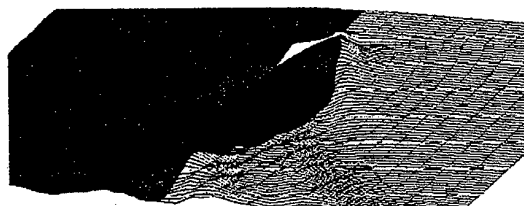


Fig.8 Steady wave pattern of FastShipTM

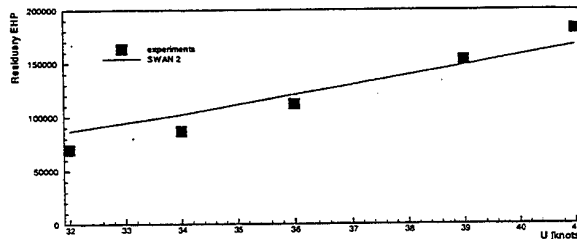


Fig.9 Residuary power of FastShipTM

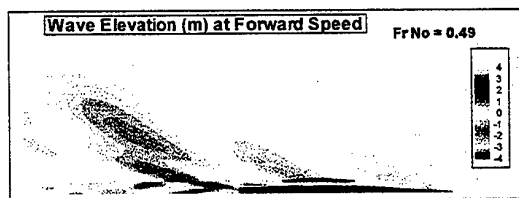


Fig.10 Kelvin wave pattern of a trimaran vessel advancing at Froude numbers 0.42 and 0.49

In Fig.9, the residuary resistance of the FastShipTM predicted by SWAN is compared with the measured values. The residuary resistance was evaluated as the sum of the wave resistance computed by SWAN and an induced resistance component that depends on the geometry of the transom stern. The induced resistance of the FastShipTM is found to be significant and relatively constant across the speed range shown in Fig.9.

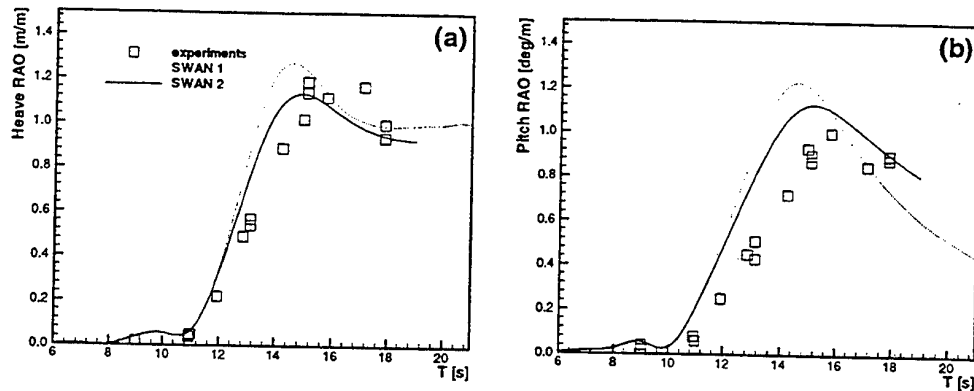


Fig.11 Heave and pitch RAO's of the FastShip™

Fig.10 presents the Kelvin wave pattern of a trimaran vessel advancing at Froude numbers 0.42 and 0.49. In recent years such hull forms have emerged as attractive alternative to monohulls or catamarans, both from the point of view of their calm and rough water performance.

Fig.11 illustrates the SWAN computations of the heave and pitch RAO's of the FastShip™ hull and their correlation with experiments in waves of moderate steepness.

6. Second-Order Forward-Speed Problem

SWAN has been extended to the solution of the second-order forward-speed problem around ships in the time domain. The free surface boundary conditions are defined in equation (3) and (4), where the body velocity vector \vec{U} can be a constant or a slowly-varying velocity in the surge-sway-yaw modes. Second-order wave effects acting on the ship undergoing a maneuver in waves with a time-dependent velocity \vec{U} can be very important in the evaluation of the vessel course- or station-keeping properties.

Unlike conventional ships which cruise with forward-speed, moored floating structures are designed to operate at a stationary position in an environment which includes waves, wind and current. Due to their compliant mooring systems, the floating structures often undergo large

excursions about their mean positions, called the 'slow-drift' motions. The yaw slow-drift motion is of practical importance for the design of FPSO vessels subject to the 'weathervaning' motions when positioned by Turret mooring systems. The wave-current-body interaction may thus cause an instability in the yaw slow-drift motion of FPSO's or ship-like vessels.

The yaw drift moment and wave-drift damping of a mathematical hull has been studied by Grue and Palm (1996) in the frequency domain. The geometry of a mathematical hull they considered is defined as follows

$$r(x) = 0.5B \left[1 - \left(\frac{2x}{L} \right)^4 \right],$$

where L is the ship length, B is the ship beam and $L/B=5.6$. In the present study, the hull surface is discretized with 40 stations, 1428 panels and the entire free surface is discretized with 4268 panels.

Time domain simulations for the yaw drift moment on the mathematical hull were carried out, considering the diffraction problem only. The time history of the force acting on the hull is converted to the frequency domain using Fourier analysis in order to compare with the results of Grue and Palm.

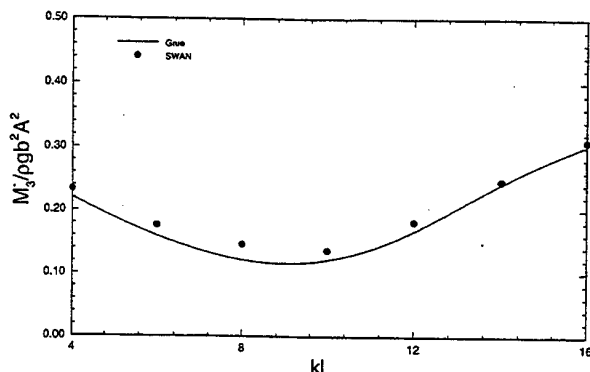


Fig.12 Yaw drift moment of a mathematical hull in waves of heading $\beta=135^\circ$

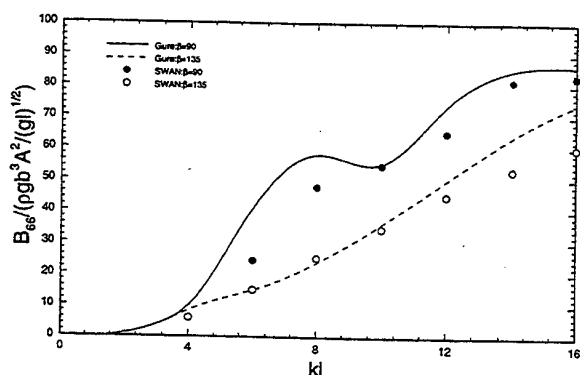


Fig.13 Yaw drift damping of a mathematical hull in waves of heading $\beta=90^\circ$ and 135°

Fig.12 shows the yaw drift moment acting on the hull in waves of heading $\beta=135^\circ$. The yaw drift damping coefficient is defined as follows:

$$B_{66} = - \left. \frac{\partial M_3}{\partial \Omega_3} \right|_{\Omega_3=0},$$

where ∂M_3 is a variation of the yaw drift moment and $\partial \Omega_3$ is a variation of the yaw velocity about $\Omega_3 = 0$. Fig.13 shows the yaw wave-drift damping B_{66} of the hull in beam waves, $\beta=90^\circ$, and in oblique waves, $\beta=135^\circ$.

7. Nonlinear Forward-Speed Problem

In the present paper, the oblique wave seakeeping problem is considered. The head wave problem, using the weak-scatterer formulation, was solved by Huang and Slavounos (1998). The present study extends their work.

In oblique seas, a ship undergoes motions in 6-D.O.F., experiencing lateral and torsional loads as well as vertical loads. From the computational viewpoint, a new set of problems must be addressed. Firstly, proper numerical modeling is needed for the sway, yaw and surge motions. Since these motions are subject to no restoring forces, the body may undergo a drifting motion in these modes. This results in a numerical instability and/or poor accuracy. Adopting an auto-pilot or soft-spring concept are candidates to address this problem, but a thorough related study has not been reported. Furthermore, in oblique sea computations, the symmetry of the hull geometry with respect to the x-z plane is absent, therefore the solution grids must be distributed over the entire computational domain. As a result, the CPU time and memory size are larger than those in head waves.

In the present study, two wave headings, 120° and 150° , are considered for the S175 containership. The hull surface was extended smoothly up to 8m above the mean water level, and 600 panels were distributed on the wetted surface at every time step. On free surface, an annular O-type body-fitted grid system with about 2000 panels was applied. In this computation, the surge, sway and yaw motions are not allowed, and the computations concentrated on heave and pitch. Since the heave and pitch motions are generally weakly coupled with other motions, restraining the surge, sway and yaw motions provides almost no effect on heave and pitch. Furthermore, the frequency range considered in the present study is far from the roll resonance frequency, so the roll amplitude is not large.

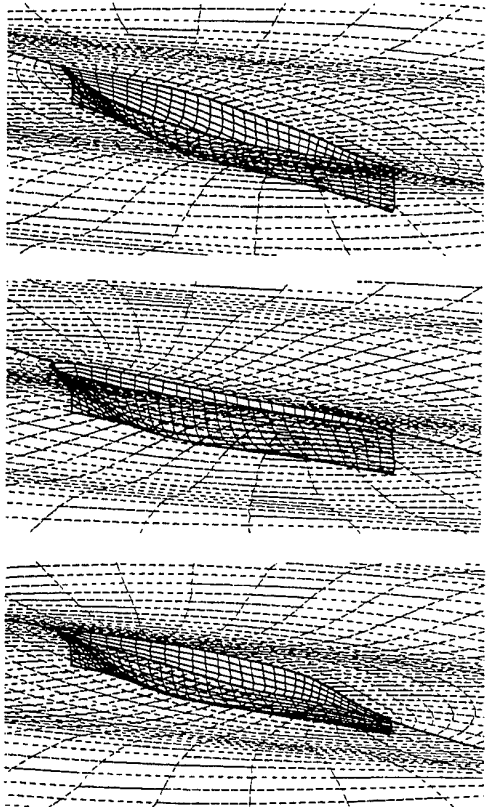


Fig.14 Solution grids on the ship hull and free surface at different time steps

Fig.14 shows the solution grids on ship hull and free surface at three time steps. In the weak-scatterer formulation, the solution grid is redistributed at every time step since the free surface conditions are imposed on the exact position of the incident wave profile and the exact nonlinear body boundary condition is enforced.

Fig.15 shows the instantaneous hydrodynamic pressure distribution over the hull wetted surface for two cases. Both correspond to the same

incident wave frequency, but the encounter frequencies are different. The Froude number in this case is 0.275. A large pressure variation is shown in the bow and stern regions, and sometimes around the bottom.

Fig.16 shows snapshots of the surface wave elevation contours, and the evolution of the surface wave disturbance may also be observed in these figures. In particular, strong reflection waves may be observed on the weather side of ship, which are then carried downstream.

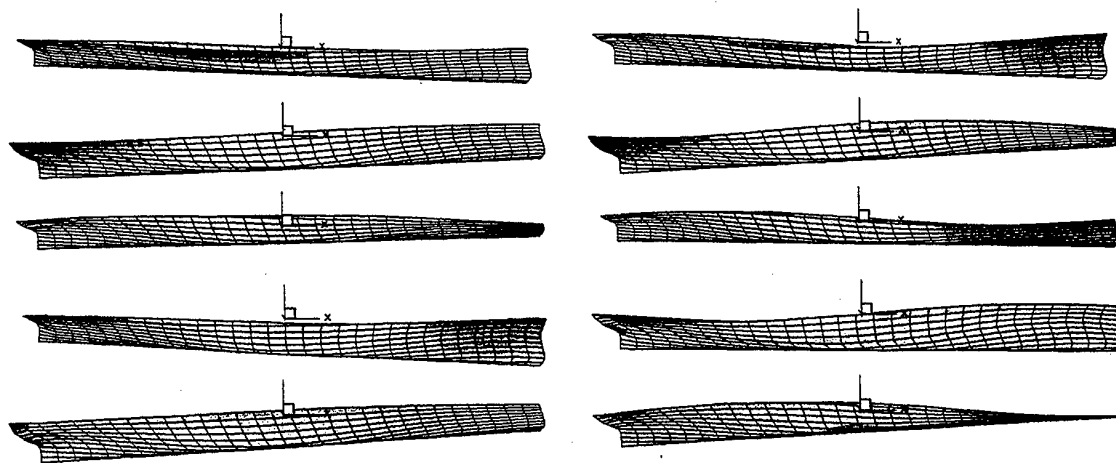
Fig.17 illustrates the heave and pitch motion RAOs. In head seas, Huang and Sclavounos (1998) reported that the weak-scatterer formulation provides much better agreement to experiments than linear theory. As expected, the same accuracy is found in the oblique sea problem. The experimental data in this figure correspond to an incident wave amplitude to ship length ratio of 1/50, and the same steepness was used in the computation. Generally strip theory is known to predict a highly tuned resonance. The weak-scatterer computation leads to less pronounced peaks, particularly when the incident wave amplitude is large, a trend also confirmed by the experimental measurements.

8. SUMMARY

The treatment of linear, second-order and nonlinear potential flows past realistic ships advancing with forward speed in waves of moderate or large steepness was presented using the time-domain Rankine panel method SWAN. The versatility of the solution method allows the enforcement of a progression of free surface conditions appropriate for the problem under study. This approach is demonstrated to lead to robust, accurate and efficient simulation of a variety of flows past ships.

ACKNOWLEDGMENTS

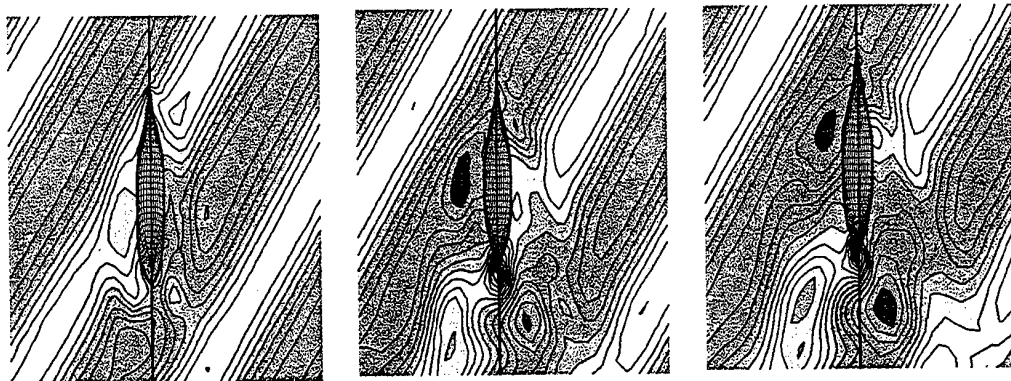
Financial support for this study has been provided by the Office of Naval Research and it is greatly



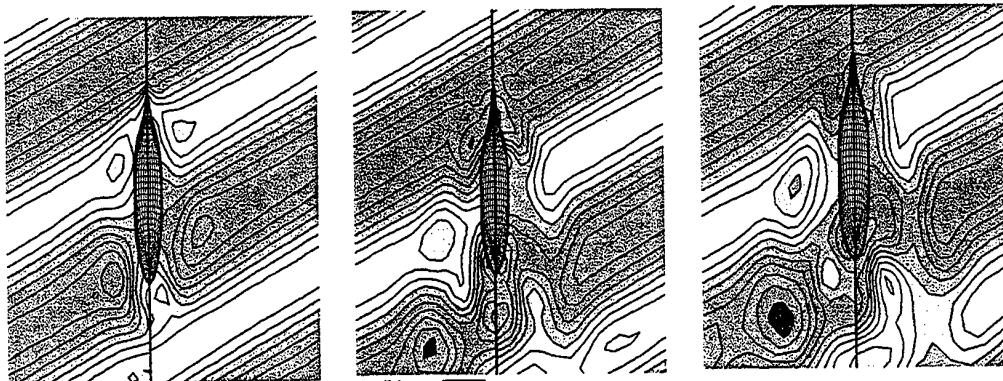
(a) $\omega\sqrt{L/g} = 2.5, \beta = 120^\circ$

(b) $\omega\sqrt{L/g} = 2.5, \beta = 150^\circ$

Fig. 15 Instantaneous hydrodynamic pressure on the wetted-hull surface, Froude No.=0.275



(a) $\omega\sqrt{L/g} = 2.75, \beta = 120^\circ$



(b) $\omega\sqrt{L/g} = 2.5, \beta = 150^\circ$

Fig. 16 Snapshots of instantaneous wave elevation contour around the body, Froude No.=0.275

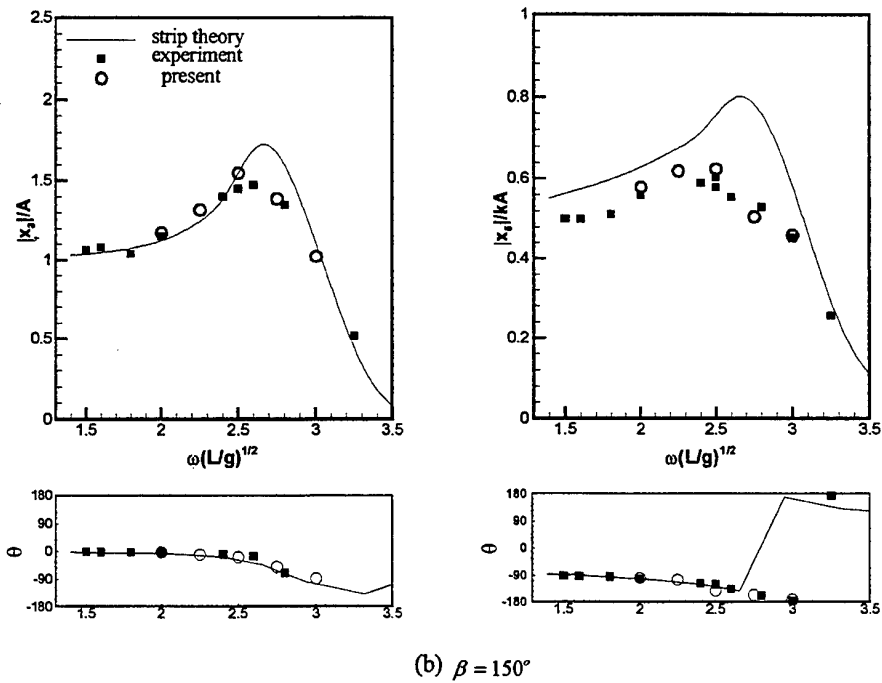
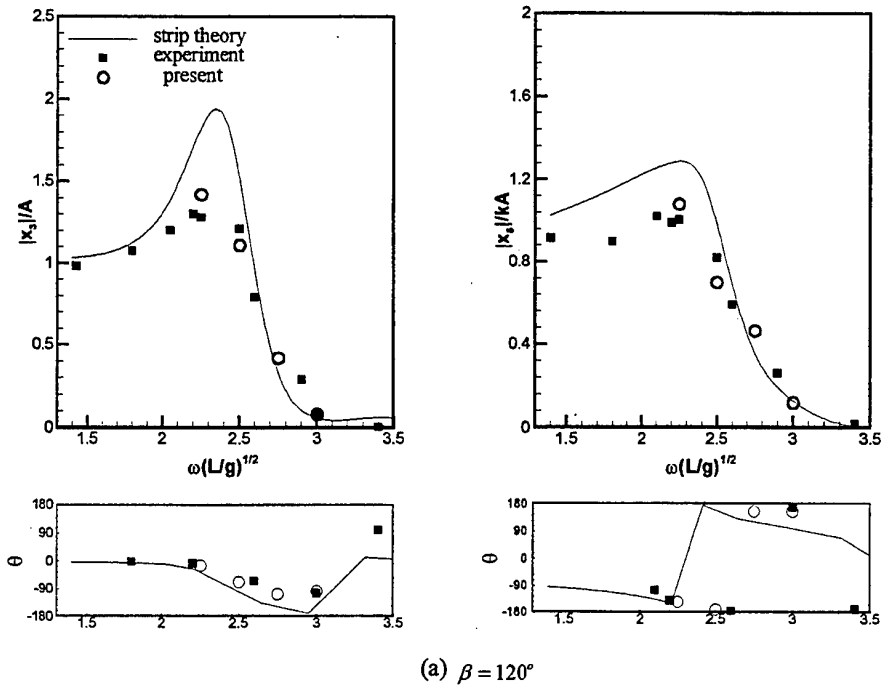


Fig.17 Heave and pitch motion RAOs of S175 container ship at oblique sea, Froude No.=0.275

appreciated. Several results presented in the article have been obtained from design studies conducted at Boston Marine Consulting Inc. for the marine industry.

REFERENCES

1. Baker, G.H., Meiron, D.I., and Orszag, S.A., "Application of a generalized vortex method to free surface flows," Proc. of the 3rd International Conference on Numerical Ship Hydrodynamics, Paris, 1981.
2. Dalzell, J.F., Thomas III, W.L. and Lee, W.T., "Correlations of model data with analytical load predictions for three high speed ships," Department Report, Ship Hydrodynamics Department, Naval Surface Warfare Center, 1986.
3. Dawson, C.W., "A practical computer method for solving ship-wave problems," Proc. of the 2nd International Conference on Numerical Ship Hydrodynamics, Berkeley, CA, 1977.
4. Emmerhoff, O.J., & Sclavounos, P.D., "The slow-drift motion of arrays of vertical cylinders," Journal of Fluid Mechanics, Vol.242, 1992.
5. Israeli, M., and Orszag, S.A., "Approximation of radiation boundary conditions," Journal of Computational Physics, Vol.41, 1981.
6. Kim, M.H., "The complete second-order diffraction solution for an axisymmetric body : Part 1. Monochromatic incident waves," Journal of Fluid Mechanics, Vol.200, 1989.
7. Kim, S., Sclavounos, P.D., and Nielsen, F.G., "Slow-drift response of moored platforms," Proc. of BOSS conference, Hague, The Netherlands, 1997.
8. Kim, S., "Nonlinear Interaction of Water Waves with Three-Dimensional Floating Bodies in a Current," Doctoral Dissertation, MIT, 1998.
9. Kim, S., Sclavounos, P.D., "Tank Testing vs Computational Fluid Dynamics(CFD) in Ship Design," ICCAS'99, MIT, 1999.
10. Kim, Y., Kring, D.C., Sclavounos, P.D., "Linear and nonlinear interactions of surface waves with bodies by a three-dimensional Rankine panel method," Applied Ocean Research, Vol.19, 1997.
11. Kim, Y., "Computation of higher-order hydrodynamic forces on ships and offshore structures in waves," Doctoral Dissertation, MIT, 1998.
12. Kim, Y., and Sclavounos, P.D., "Numerical Simulation of the Linear and Second-Order Surface Flows around Circular Cylinders in Random Waves", Proc. of the 8th International Workshop on Water Waves and Floating Bodies, Port Huron, MI, 1999.
13. Korsmeyer, F.T., Lee, C.H., Newman, J.N., and Sclavounos, P.D., "The analysis of wave interactions with tension leg platforms", Proc. of OMAE conference, 1988.
14. King, B.W., Beck, R.F., and Magee, A.R., "Seakeeping calculations with forward speed using time domain analysis," Proc. of the 17th Symposium on Naval Hydrodynamics, Hague, Netherlands, 1988.
15. Kring, D.C., and Sclavounos, P.D., "Numerical stability analysis for time-domain ship motion simulations", Journal of Ship Research, Vol.39, No.4, 1995.
16. Kring, D.C., Huang, Y.F., Sclavounos, P.D., Vada, T. and Braathen, A., "Nonlinear ship motions and wave induced loads by a Rankine panel method," Proc. of the 21st Symposium on Naval Hydrodynamics, Troheim, Norway, 1996.

17. Lin, W.M. and Yue, D.K.P., "Numerical solutions for large-amplitude ship motions in time domain," Proc. of the 18th Symposium on Naval Hydrodynamics, Ann Arbor, MI, 1990.
18. Longuet-Higgins, M.S. and Cokelet, E.D., "The deformation of steep surface waves on water (I) --- A numerical method of computation", Proc. of the Royal Society of London, Vol. 350, 1976.
19. Nakos, D.E., Kring, D.C. and Sclavounos, P.D., "Rankine panel methods for transient free surface flows," Proc. of the 6th International Conference on Numerical Ship Hydrodynamics, Iowa City, IA. 1993.
20. Nakos, D.E., "Stability of transient gravity waves on a discrete free surface," MIT Report, 1993.
21. Pawlowski, J., "A nonlinear theory of ship motions in waves", Proc. of the 19th Symposium on Naval Hydrodynamics, Seoul, Korea, 1992.
22. Sclavounos, P.D., and Nakos, D.E., "Stability analysis of panel methods for free-surface flows with forward speed," Proc. of the 17th Symposium on Naval Hydrodynamics, Hague, The Netherlands, 1988.
23. Sclavounos, P.D., "On the quadratic effect of random gravity waves on a vertical boundary," Journal of Fluid Mechanics, Vol.242, 1992.
24. Sclavounos, P.D., "Computation of Wave Ship Interactions," Advances in Marine Hydrodynamics, Computational Mechanics Publications, Southampton, 1996.
25. Sclavounos, P.D., Kring, D.C., Huang, Y.F., Mantzaris, A.D., Kim, S. and Kim, Y., "A ship flow computational method as an advanced CFD tool of design," Trans. of SNAME, 1997
26. Vada, T., and Nakos, D.E., "Time marching schemes for ship motion simulations," Proc. of the 8th International Workshop on Water Waves and Floating Bodies, St. John's, Newfoundland, Canada, 1993
27. Huang Y. and Sclavounos, P.D., "Nonlinear ship motions," Journal of Ship Research, Vol.42, No.2, 1998.

SEAKEEPING SIMULATIONS IN NON LINEAR WAVES*

Pierre FERRANT

Division Hydrodynamique Navale/LMF, Ecole Centrale de Nantes, B.P.92101, 44321 Nantes Cedex 3

ABSTRACT

This paper is dedicated to the study of non-linear wave forces and free surface motions in the vicinity of three dimensional surface-piercing structures. This topic, which is of the utmost interest in many aspects of marine engineering, is addressed using a time domain simulation method for non-linear potential flows with a free surface. The model is based on a formulation of the fully non-linear diffraction problem in which the incident wave is given explicitly, with sensible advantages in terms of efficiency and accuracy over more conventional formulations.

Original results using this model have already been published, with emphasis on higher order forces in long waves ([11], [12]), or non-linear wave-current-body interactions ([1][10]). In these calculations, the incident wave was given by the stream function model of Rienecker & Fenton [23], and waves were diffracted by a vertical circular cylinder. This latter restriction allowed an easy implementation of bi-cubic splines interpolations, for accurate estimations of slopes and fluid velocity at free surface markers.

In this paper, we present the extension of this fully nonlinear diffraction model to arbitrary 3D geometries. This extension is essentially based on the implementation of more flexible schemes for the computation of slopes and fluid velocities around free surface piercing structures of complex shape. After a review of validation results obtained in the simplified case of a vertical surface-piercing cylinder, the new capabilities of the model are illustrated by the simulation of the diffraction of non linear waves by a four-column structure.

INTRODUCTION

The accurate calculation of forces and free surface motions in the vicinity of sea going structures is a topic of permanent interest both for offshore engineers and naval architects. In the domain of offshore structure design, free-surface motions, including wave runup on cylindrical columns, as well as resonant interaction effects between columns have a direct incidence on the airgap (or deck clearance). The airgap estimation is a major design parameter, with considerable consequences on the building and operational costs of structures.

Beyond linear diffraction theory, the usual practice for estimating loads and free surface motions is to rely on frequency domain second order theory. This theoretical basis is now well established, and a number of numerical implementations for general geometries have been published, see e.g. [4], [19], [6]. Meanwhile, semi analytic solutions for simplified geometries appeared [15], and proved to be particularly useful for the validation of the above mentioned fully numerical schemes. However, for realistic offshore structures, the computation of the full quadratic transfer function (QTF) matrix remains a difficult task, relying on the computation of slowly convergent integrals on the free surface.

An interesting alternative is to solve the second order diffraction problem in the time domain. This solution presents a number of advantageous features. First, the truncation of the free surface, and the associated radiation condition may be easily handled by including an absorbing zone on the outer part of the free surface mesh. Secondly, we have the possibility of directly simulating the interaction of a complex wave system with a body, once a second order representation of the incoming wave field has been derived. On the condition that computer time requirements reduce to a sufficiently low level, this approach will ultimately allow the direct estimation of design parameters such as significant or extreme loads and runup, by applying usual statistical analysis to second order simulated signals, just as what can be achieved by exploiting experimental time series. Time domain solutions to second order

*Paper presented at the 7th International Conference on Numerical Ship Hydrodynamics, Nantes, July 1999

diffraction problems in three dimensions include the early work of Isaacson & Cheung [14], based on a low order panel method, and more recently Skourup et al [26], and Kim et al [16]. These applications, however, mostly concern simple geometries such as vertical cylinders. The extension to more complex geometries is limited not only by the larger computer resources necessary, but also by the more essential difficulty of accurately evaluating derivatives of the first order solution on a general free surface mesh.

Furthermore, in a number of situations, important non linear phenomena are induced by higher than second order effects. This includes the so-called ringing phenomenon, causing high frequency loads on offshore structures in steep waves. Ringing has been proved to be related to third or higher order diffraction phenomena, and the best solution here is to abandon perturbation theory and to build a fully non linear diffraction model. Such a model has been applied to a submerged geometry by Ferrant[7]. The scheme has then been improved and applied to surface-piercing cylinders (see e.g.[9]). Extensive validation, both with refined experiments or third order perturbation theory may be found in Ferrant [11], or Ferrant *et al* [12]. Meanwhile, a non linear diffraction scheme has been proposed by Di Mascio *et al* [5], in which the incident field is modeled by a fifth order Stokes wave, while in the present scheme the incident wave is a fully non linear stream function wave[23]. The use of an explicit incident wave results in considerable advantages in terms of accuracy and computational efficiency. Other fully non linear wave-body interaction results in three dimensions have been obtained using numerical wave tank models, in which the full process of incident wave generation and propagation towards the model has to be simulated [2]. The resulting computing demand is very high, and up to now, fully validated results using this latter approach have not been reported.

In the present paper, we wish to present the extension of our fully nonlinear diffraction model ([9], [11], [12]) to the case of arbitrary three dimensional structures. This extension has required a substantial modification of the free surface geometry and fluid velocity calculation procedure, in order to be able to cope with general mesh arrangements. The issues associated with these new developments of the model, as well as results of the fully non linear diffraction of a regular wave on a four-legged structure are presented and discussed.

MATHEMATICAL FORMULATION

Semi-Lagrangian approach

We consider a three-dimensional fluid domain (D), bounded by a free surface F and a set of N solid boundaries S_i . These boundaries include the surface of a marine structure, as well as the sea floor at finite distance. The domain is of infinite extent in the horizontal directions. The fluid flow problem is formulated in the frame of potential flow theory. The fluid velocity thus derives from a scalar potential satisfying Laplace's equation at any point of the fluid domain:

$$\vec{\nabla} \cdot (\vec{M}, t) = \vec{\nabla} \Phi(M, t) ; \text{ for } M \in (D) \quad (1)$$

$$\Delta \Phi(M, t) = 0 ; \text{ for } M \in (D) \quad (2)$$

On the free surface, both kinematic and dynamic conditions must be satisfied. The kinematic condition states that the mass flux through the free surface is zero, and writes, in Lagrangian form:

$$\frac{D\vec{M}}{Dt} = \vec{\nabla}[\Phi(M)] ; \text{ for } M \in F \quad (3)$$

If surface tension is ignored, the dynamic condition expresses the continuity of the pressure across the free surface, and derives from Bernoulli's equation:

$$\frac{D\Phi(M, t)}{Dt} - z + \frac{1}{2}|\vec{\nabla}\Phi|^2 ; \text{ for } M \in F \quad (4)$$

where D/Dt stands for the material derivative. Equations (3) and (4) suppose a fully Lagrangian description of the free surface, with markers identified as material points. In the present paper, the formulation will be modified by inhibiting the horizontal motions of free surface markers, leading to a semi-Lagrangian description. In such a formulation, the free surface vertical co-ordinate becomes implicitly single-valued, and may be expressed as:

$$z = \eta(x, y, t) ; \text{ for } M(x, y, z, t) \in F \quad (5)$$

Plugging this notation into (3) and (4), and after some manipulations, we obtain new forms of the non-linear kinematic and dynamic boundary conditions, in which a fixed projection of free surface markers in the x-y plane is implied:

$$\frac{d\eta}{dt} = \frac{\partial \Phi}{\partial z} - \frac{\partial \Phi}{\partial x} \frac{\partial \eta}{\partial x} - \frac{\partial \Phi}{\partial y} \frac{\partial \eta}{\partial y}; \text{ for } z = \eta(x, y, t) \quad (6)$$

$$\frac{d\Phi}{dt} = -\eta + \frac{1}{2} |\vec{\nabla} \Phi|^2 + \frac{\partial \eta}{\partial t} \frac{\partial \Phi}{\partial z}; \text{ for } z = \eta(x, y, t) \quad (7)$$

where η is the free surface elevation, z is positive upwards with its origin on the mean position of the free surface. Non dimensional quantities are assumed, based on a reference length L and with the acceleration of gravity g as the acceleration of reference. In the present paper, L is the water depth h .

On fixed material boundaries, no-flux Neumann conditions are applied:

$$\frac{\partial \Phi}{\partial n} = 0; \text{ for } M \in S_i, i = 1, N \quad (8)$$

Separation of an explicit part of the solution

In some situations, it is practical to re-formulate the general problem described in the preceding section, by subtracting from the total flow a contribution which may be explicitly described. The aim of such a procedure is to be left with a modified problem for the remaining part of the flow which will be easier to solve. This is what is usually achieved in linearized radiation-diffraction theory when prescribing the incident wave potential and solving the problem for the diffracted flow alone. Here the situation is sensibly more complicated, since the boundary-value problem is non linear. However, the field equation itself, namely Laplace's equation, remains linear so that we may write:

$$\Phi = \Phi_e + \Phi_d; \text{ for } M \in (D) \quad (9)$$

where Φ_e is a scalar potential satisfying Laplace's equation in the whole fluid domain. In the same manner, in a single-valued description of the free surface, we may write:

$$\eta(x, y, t) = \eta_e(x, y, t) + \eta_d(x, y, t) \quad (10)$$

where η_e is some explicit time dependent function of the horizontal co-ordinates. Plugging (9) and (10) into (6) and (7), we are left with free surface conditions for Φ_d and η_d , in which terms depending on Φ_e and η_e are supposed to be evaluated explicitly.

$$\frac{d\eta_d}{dt} = \quad (11)$$

$$\frac{\partial \Phi}{\partial z} - \frac{\partial \Phi}{\partial x} \frac{\partial \eta}{\partial x} - \frac{\partial \Phi}{\partial y} \frac{\partial \eta}{\partial y} - \frac{\partial \eta_e}{\partial t}; \text{ for } z = \eta(x, y, t)$$

$$\frac{d\Phi_d}{dt} = \quad (12)$$

$$-\eta + \frac{1}{2} |\vec{\nabla} \Phi|^2 + \frac{\partial \eta}{\partial t} \frac{\partial \Phi_d}{\partial z} - \frac{\partial \Phi_e}{\partial t}; \text{ for } z = \eta(x, y, t)$$

Note that at this point, Φ_e and η_e are totally independent of each other, the only constraint is on Φ_e which have to satisfy Laplace's equation throughout the fluid domain. Up to this point (9) and (10) simply represent changes of variables for Φ and η . The usefulness of this operation appears when Φ_e and η_e are identified to the incoming flow components.

Specification of the incoming flow

In the present study, the incoming flow is composed of non linear regular waves, modeled by a stream function model [23]. In this model, which is valid for both deep and shallow water, the velocity potential and elevation of a periodic wave traveling over a horizontal bottom are expressed as Fourier series. Nonlinear free surface conditions are satisfied exactly at some equidistant points distributed over one wave length, so that the error in the solution is driven by the truncation of the Fourier series only. The incident wave elevation is given by:

$$\eta_i(x, y, t) = \frac{a_0}{2} + \sum_{j=1}^{N_w} a_j \cos[jk(x - x_0 - ct)] \quad (13)$$

and the potential

$$\Phi_i(x, y, z, t) = \quad (14)$$

$$\sum_{j=1}^{N_w} B_j \frac{\cosh[jk(z + h)]}{\cosh(jkh)} \sin[jk(x - x_0 - ct)]$$

where c is the wave celerity, k the wave number and N_w the order of truncation of the Fourier series.

Coefficients of the series (13) and (14) are obtained through an optimization procedure leading to the minimization of an objective function based on the error on the kinematic and dynamic free surface

conditions evaluated at the control points. In current applications, i.e. for amplitudes sensibly lower than the limiting amplitude leading to a sharp crest, we use about 50 points distributed on half a wavelength ($N_w = 50$), and coefficients converge to machine accuracy within less than 10 iterations. The resulting truncated series expressions for η and Φ may thus be considered as exact analytical representations of the incident non linear wave. Note that (14) is continuous in the whole fluid domain. This property is essential to the success of the formulation derived in the following section.

The incoming flow being specified, conditions at infinity simply write:

$$\Phi(M, t) \rightarrow \Phi_i(M, t) ; \text{ for } M \rightarrow \infty \quad (15)$$

Formulation for the perturbation flow

The most evident choice for Φ_e is of course Φ_i . With this choice, a major contribution to the total flow will be represented analytically, with advantages in terms of global accuracy. Furthermore, conditions at infinity reduce to $\Phi_d(M, t) \rightarrow 0 ; \text{ for } M \rightarrow \infty$. For identical reasons, we shall also adopt $\eta_e = \eta_i$. The resulting boundary value problem to be solved for (Φ_d, η_d) is thus:

Laplace equation in the fluid domain

$$\Delta \Phi_d(M, t) = 0 ; \text{ for } M \in (D) \quad (16)$$

Non linear kinematic and dynamic free surface conditions applied for ($z = \eta(x, y, t)$)

$$\frac{d\eta_d}{dt} = \frac{\partial \Phi_d}{\partial z} - \vec{\nabla}^T(\Phi_i + \Phi_d) \cdot \vec{\nabla}^T(\eta_i + \eta_d) \quad (17)$$

$$-\frac{\partial \eta_i}{\partial t} + \frac{\partial \Phi_i}{\partial z} - \nu(R)\eta_d$$

$$\frac{d\Phi_d}{dt} = -(\eta_i + \eta_d) + \frac{1}{2}|\vec{\nabla} \Phi_i + \vec{\nabla} \Phi_d|^2 \quad (18)$$

$$+ \frac{\partial(\eta_i + \eta_d)}{\partial t} \cdot \frac{\partial \Phi_d}{\partial z} - \frac{\partial \Phi_i}{\partial t} - \nu(R)\Phi_d$$

In these equations, $\vec{\nabla}^T$ stands for $\vec{i} \partial/\partial x + \vec{j} \partial/\partial y$, and terms involving Φ_i and η_i will be evaluated exactly from the stream function model. Damping terms involving functions $\nu(R)$ have also

been included. The role of these terms is to absorb the diffracted waves on the outer part of the free surface mesh. More details on the implementation of this absorbing zone technique are given in a following section.

Initial conditions (undisturbed incident wave)

$$\Phi_d(M, t = 0) = 0 ; \text{ for } M \in (D) \quad (19)$$

Body boundary condition

$$\frac{\partial \Phi_d}{\partial n} = -\alpha(t) \frac{\partial \Phi_i}{\partial n} ; \text{ for } M \in S_1 \quad (20)$$

where $\alpha(t)$ is a smooth ramp function varying from 0 to 1 during the beginning of the simulation (typically 1 to 2 wave periods). This gradual imposition of the body boundary condition for the diffracted potential avoids a shock at the beginning of the simulation, which would result in the generation of spurious short wave components.

Conditions at infinity

$$\Phi_d(M, t) \rightarrow 0 ; \text{ for } M \rightarrow \infty \quad (21)$$

The quasi-analytical representation of incident waves, combined with the formulation of the problem in terms of the non linear perturbation potential (radiation and/or diffraction) thus results in a simple and clean account of conditions at infinity, even in the case of steep non linear incident waves.

It must be emphasized that the boundary-value problem being non-linear, equations (17) and (18) are satisfied on the instantaneous free surface position, so that the incident potential Φ_i may possibly be evaluated above the undisturbed incident wave $z = \eta_i(x, y, t)$. This is possible here because the stream function potential has a continuous prolongation above the incident wave. One of the advantages of this formulation is that the non linear incident wave is handled analytically, so that it is not altered during its propagation from the outer surface of the computational domain to the body. In addition, perturbations represented by (Φ_d, η_d) are essentially composed of waves propagating in radial directions, allowing relatively coarse meshes to be adopted far from the body, in the absorbing zone. This results in considerable savings in computer resources, without loss of accuracy. On the other hand, this formulation is not universal and relies on the availability of an explicit model for the incident wave, with appropriate continuity properties across the incident wave profile.

Boundary integral equation method:

The initial boundary problem being properly posed, a solution procedure based on a boundary integral equation method is set-up. Applying Green's identity to the velocity potential and to the free space Green function (Rankine source) $G(M, M') = -1/4\pi MM'$, we obtain an integral representation of the velocity potential Φ_d :

$$\frac{\Omega(M)}{4\pi} \Phi_d(M, t) = \quad (22)$$

$$\int_{\Sigma} \left[\Phi_d(M', t) \frac{\partial G}{\partial n'} - G \frac{\partial}{\partial n'} \Phi_d(M', t) \right] dS_{M'}$$

where $\Omega(M)$ is the internal solid angle at point M and G holds for $G(M, M')$. In (21), Σ represents the instantaneous fluid domain boundary, including incident and diffracted components.

The global solution procedure of the initial boundary value problem for the diffracted potential and free surface elevation, Φ_d and η_d , is based on the consideration that free surface conditions (17) and (18) may be used to advance the solution in time from t to $t + dt$, once the boundary value problem has been solved at time t , by exploiting the integral representation (21). For this purpose, at a given time instant t , Φ_d on F and η_d (and thus Σ) are first evaluated from values at the previous time step through (17) and (18), while $\partial\Phi_d/\partial n$ on the body is explicitly given by (20). The integral representation (21) is thus recast into a Fredholm integral equation for $\partial\Phi_d/\partial n$ on the free surface F and Φ_d on Neumann boundaries. This integral equation is of the first kind for unknowns on the free surface (Dirichlet condition) and of the second kind for unknowns on Neumann boundaries. For example, when the control point M belongs to the free surface F , the integral equation writes:

$$\begin{aligned} & \int_F G(M, M') \frac{\partial \Phi_d(M', t)}{\partial n'} dS_{M'} \\ & - \int_{\Sigma-F} \Phi_d(M', t) \frac{\partial G(M, M')}{\partial n'} dS_{M'} \quad (23) \\ & = \int_F \Phi_d(M', t) \frac{\partial G(M, M')}{\partial n'} dS_{M'} \\ & - \int_{\Sigma-F} G(M, M') \frac{\partial \Phi_d(M', t)}{\partial n'} dS_{M'} - \frac{\Omega}{4\pi} \Phi_d(M, t) \end{aligned}$$

While for a control point on a material boundary supporting a Neumann condition, the last term

in the RHS of (22) would appear at the left-hand side. This solution procedure belongs to the family of mixed Euler-Lagrange methods and involves a combination of numerical schemes described in the following sections.

Calculation of wave loads

Time depending wave loads on material surfaces are evaluated by direct integration of the pressure over the body surface. In non-dimensional form, this writes:

$$p(M, t) = -\frac{\partial \Phi(M, t)}{\partial t} - \frac{1}{2} |\nabla \Phi|^2 - z \quad (24)$$

For practical calculations on time depending grids, the following expression is preferred, in which d/dt stands for the pseudo-material derivative following the motion of mesh nodes on the body surface and $\vec{V}(M)$ is the velocity of point M :

$$p(M, t) = -\frac{d\Phi(M, t)}{dt} + \vec{V}(M) \cdot \nabla \Phi - \frac{1}{2} |\nabla \Phi|^2 - z \quad (25)$$

The fluid force on the body is then given by:

$$\vec{F}(t) = \int_{S_b} p(M, t) \vec{n} dS \quad (26)$$

where the fluid pressure is integrated on each body panel as a linearly varying quantity, expressed from its values at panel vertices.

NUMERICAL TECHNIQUES

Boundary element method

A boundary element method is used for the solution of the boundary integral equation formulation of the problem. The method is based on iso-parametric triangular elements distributed over the different elementary surfaces composing Σ . A piecewise linear, continuous variation of the solution over each sub-boundary is assumed, and collocation points are placed at panel vertices. This level of discretisation is considered to be a good compromise between accuracy and versatility. The BEM solver has been devised with the view of preserving the possibility to solve a large variety of boundary value problems, including forced motions, diffraction, wave-current-body interaction problems, etc. Meshes are made of an assembly of different patches, with the assumption of continuous normal on each of them. On intersection lines between two patches, two collocation

points are considered for one single geometrical location, and the boundary conditions corresponding to the two elementary surfaces are both satisfied. This is particularly the case for points at the waterline of a surface-piercing body for which both the Neumann condition on the body surface *and* the free surface conditions are satisfied. Higher orders of multiplicity may also be accounted for, for instance at the intersection between a line of discontinuity of the normal vector on a material boundary, and the free surface (see figure 1)

This discretization scheme reduces the integral formulation to a linear algebraic system to be solved for the normal velocity on Dirichlet boundaries (free surface) and the potential on Neumann boundaries.

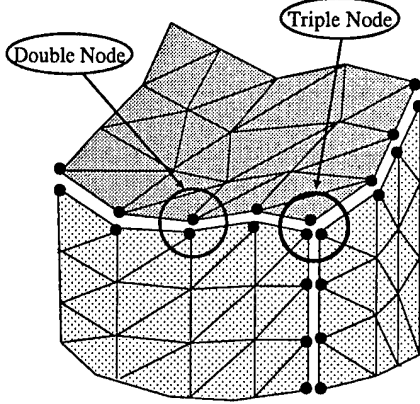


Figure 1: Multiple node arrangement at the intersection between elementary surfaces

This system is assembled from the influence coefficients of linearly varying distributions of sources and dipoles on boundary elements, and may be represented as follows, provided a proper renumbering scheme has been applied in order to place free surface nodes at the top of the global node vector:

$$\begin{bmatrix} S_{FF} & D_{BF} \\ S_{FB} & D_{BB} \end{bmatrix} \begin{bmatrix} \sigma_F \\ \mu_B \end{bmatrix} = \begin{bmatrix} D_{FF} & S_{BF} \\ D_{FB} & S_{BB} \end{bmatrix} \begin{bmatrix} \mu_F \\ \sigma_B \end{bmatrix} \quad (27)$$

In this full, non-symmetric, square system of linear algebraic equations, σ and μ represent respectively the source and normal dipole densities on Σ , and subscripts F and B refer to the free surface and body boundaries. Matrix elements in (27) are pointwise influence coefficients. If, for instance, we consider the potential induced at point M_i by a linear distribution of sources on the triangular panel P_j , we may write:

$$\Phi(i, j) = \sum_{iv=1}^3 \sigma(iv) s_{iv}(i, j) \quad (28)$$

Where $\sigma(iv)$ is the source density at vertex iv . Then the generic pointwise source influence coefficient in (27) is:

$$S_{ij} = \sum_{ip=1}^{npan(i)} s_{iv(i,ip)}[i, k(ip)] \quad (29)$$

Where $iv(i, ip)$ is the index of point i as a vertex of panel ip , $npan(i)$ is the number of panels having point i as a vertex, and k is the index of the considered panel in the global panel table. Identical equations apply for dipole influence coefficients. In (29), elementary coefficients $s_{iv(i,ip)}[i, k(ip)]$ are evaluated using analytical formulas for the near field, and different approximate formulas for the intermediate and far field.

Solution of linear systems of equations

In 3D non linear applications large systems of equations have to be solved at each time step, and any $O(N^3)$ solution algorithm is absolutely unsuitable. In the present formulation, the linear systems to be solved are full and non-symmetric. The now classical GMRES scheme of Saad & Schultz [24] is applied to the solution of these systems. The method is used with diagonal pre-conditioning, which reduces the necessary number of iterations by a factor close to 2, at no additional cost. Further reductions of the number of iterations may be obtained with more elaborate pre-conditioning techniques, but the cost of such pre-conditionings applied to full matrices is not negligible and may annihilate the advantage of the reduction of the number of iterations. Exploiting the monotonic convergence of residuals in the GMRES scheme, we also introduce a polynomial extrapolation of solution vectors at previous time steps as a first estimate of the new solution vector. This estimation slightly reduces the necessary number of iterations for a given convergence criterion, again at almost no cost.

Time marching scheme

After the solution of the boundary value problem and the computation of the fluid velocities and normal vector at the free surface, free surface conditions (17) and (18) considered as ODE for Φ and η are advanced in time. A fourth order Runge-Kutta scheme is used for that purpose, requiring four solutions of the boundary value problem per time step. In order

to reduce CPU times, results presented in this paper were obtained using the "frozen coefficient" approximation, in which influence coefficients are updated only once per time step, while four solutions of the boundary value problem are performed.

SCHEMES FOR THE FREE SURFACE

Standard procedure

Our fully nonlinear diffraction model, up to now, has been applied to a very simple free surface configuration, namely a circular annulus extending radially from the waterline of a circular cylinder. In this configuration, the mesh is structured in the azimuthal direction, that is nodes are distributed on circles surrounding the body, with a regular spacing on each circle. This situation allows us to apply a bi-cubic interpolation scheme for both the potential and the vertical co-ordinate at the free surface. These quantities are first interpolated at each radial station as functions of the azimuthal angle. Then interpolating splines are computed in the radial direction, at each free surface node. We are thus left with C_2 representations of Φ and η at the free surface, which allow accurate and straightforward evaluations of the velocity components and of the normal vector, by direct differentiation of the interpolating splines.

The structure of the free surface mesh is also exploited for the application of smoothing procedures at the free surface. This smoothing may become necessary for removing saw-tooth instabilities appearing during the simulation of strongly non-linear flows. In structured parts of the mesh we use five points formulas based on Chebyshev polynomials, applied sequentially in each parametric direction. The smoothing is applied typically every five time steps.

Extension to arbitrary geometries

The extension of our numerical model to more general geometries essentially requires the adaptation of three parts of the model, corresponding respectively to (i) grid generation, (ii) computation of tangential plane and fluid velocity at the free surface, and (iii) spatial filtering at the free surface. These three items are addressed in the following sections.

Grid generation

The choice of the grid generation method is in fact partly dictated by the interpolating and filtering procedure described in the following paragraphs.

Methods for triangulating arbitrary domains, such as Delaunay triangulation, or advancing front techniques are available, but do not always lead to regular meshes. They may become interesting for the automatic grid generation in very complicated configurations, when applied together with grid smoothing algorithms, and their inclusion in our model is left for future work.

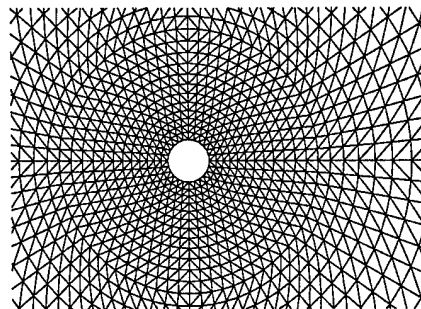


Figure 2: Free surface grid for a single vertical cylinder

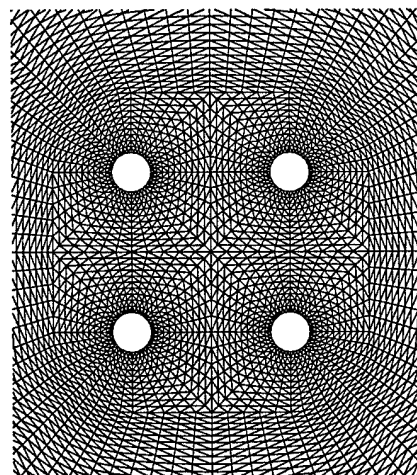


Figure 3: Free surface grid for a four-column structure

For the applications presented in this paper, we have devised a tailor-made procedure for triangulating the free surface in the vicinity of a four-column structure. Figures 2 and 3 give an idea of the grids used respectively in the standard case of a single vertical cylinder, and in the case of a four-column arrangement.

Tangential plane and fluid velocity

The problem here is to compute the fluid velocity and the components of a unique normal vector at the vertices of the free surface grid, which are chosen as control points in our formulation. This task essentially reduces to the problem of computing the derivatives of a function of horizontal coordinates (x, y) , with nodal values of the function on the free surface mesh as input data. The procedure already described and exploiting the polar topology of the free surface mesh around a single vertical cylinder is robust and accurate, but it cannot be directly applied on arbitrary geometries.

Different solutions may be considered for the extension to arbitrary free surface configurations.

polynomial is used as a local interpolant on a piecewise linear triangulation. Such a method has the advantage of a relatively straightforward application, without constraint on the mesh arrangement. A similar approach is used in [26] in the time domain simulation of the second order diffraction problem. However, in these approaches where the number of coefficients of the local interpolant is fixed, one is faced with the problem of selecting the set of neighboring points for which the local interpolant is fitted to nodal values, in order to obtain square systems of linear algebraic equations for the coefficients. This sometimes has to be done on a trial and error basis, for ill-conditioned systems are often encountered, depending on the local arrangement of the mesh. Another solution is to keep each first and possibly second level neighbor (see figure 4), and to solve the problem in a least-square sense. The scheme is then more robust, but also sensibly more computationally intensive.

In order to avoid such problems, we have been looking for a local interpolating method, with the constraints of good accuracy and adaptable number of coefficients, leading to square systems of equations for arbitrary number of nodes included in the neighborhood. Pseudo-polynomial splines and 'thin plate' splines described in [18] and [20] have been selected and tested.

Given P_o one node on a triangular grid, and $(P_i, i = 1, n)$ the selected (first or second level) set of neighbours of P_o , the pseudo-polynomial spline of order m interpolating the function of (x, y) to be differentiated is defined by:

$$\sigma_m(t) = \sum_{i=0}^n \alpha_i |t - t_i|^{2m-1} + P_{m-1}(t) \quad (30)$$

and the 'thin plate' spline by:

$$\sigma(t) = \sum_{i=0}^n \alpha_i |t - t_i|^2 \text{Log} |t - t_i| \quad (31)$$

$$+ \alpha_{n+1} + \alpha_{n+2}x + \alpha_{n+3}y$$

with:

$$t = (x, y) ; t_i = (x_i, y_i) \text{ nodes in the neighborhood}$$

$$|t - t_i| = [(x - x_i)^2 + (y - y_i)^2]^{1/2} \quad (32)$$

and

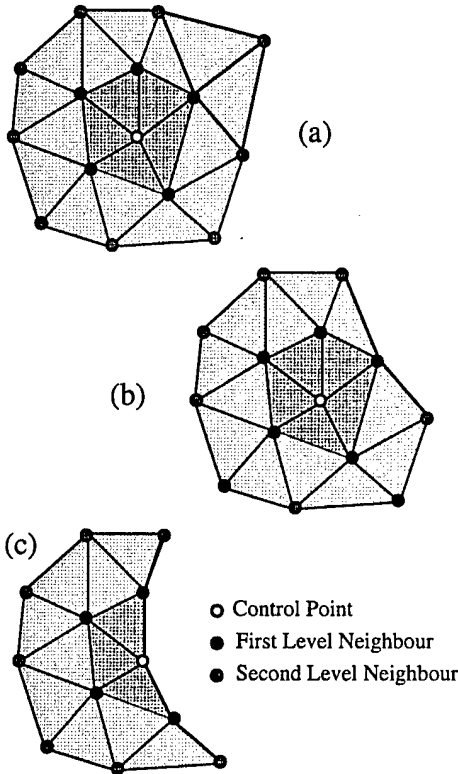


Figure 4: First and second level neighbourhood of a free surface node

a) standard case. b) control point close to a boundary. c) control point on a boundary

Most candidates belong to the wide family of local approximation methods, in which a locally defined analytical expression is first fitted to the field (potential or free surface elevation) in the vicinity of a given free surface node. Derivatives with respect to x and y are then obtained by differentiation of the local interpolant. In [3], for example, a quadratic

$$P_{m-1}(t) = \alpha_{n+1} + \alpha_{n+2}x + \alpha_{n+3}y + \dots \alpha_{n+m(n+1)/2}y^{m-1}$$

Conditions for interpolation at nodes ($P_i, i = 0, n$) and positivity of splines result in square systems of linear equations to be solved for the spline coefficients, see [18] or [20]. In the present study the 'thin plate' spline σ as well as the pseudo-polynomial splines σ_2 and σ_3 have been considered. σ and σ_2 have $n + 4$ coefficients, while $n + 7$ coefficients are needed for σ_3 (n is the number of considered neighbours of P_0). In terms of computing time, on the basis of a mean number of 6 neighbours, and solving the systems with a direct $O(n^3)$ method, this means that the computation of derivatives using splines σ_3 is about twice as long as with σ or σ_2 .

After solution, the derivatives at node P_0 (or in the vicinity of P_0) are obtained by direct differentiation of the local splines (30) or (31). After implementation, tests have been run by using the diffraction potential about a vertical cylinder bottom-mounted cylinder in regular waves (Mc Camy & Fuchs) as the function to be differentiated. For fixed discretizations of the free surface, σ and σ_2 gave similar levels of accuracy compared to the exact analytical derivatives, while a noticeable increase of accuracy was observed with σ_3 . On this simple geometry, the bi-cubic interpolation scheme referred to as 'standard procedure' gives an accuracy comparable to σ or σ_2 , and is overperformed by σ_3 .

The next step was to test the new schemes on the case of a multiple column structure, on a mesh similar the one depicted in figure 3, and by using the analytical spatial derivatives of the linearized diffraction potential given by Linton & Evans formulation [21] as a reference. It happened that the conditioning of systems for pseudo polynomial splines, estimated by a SVD solution procedure, became very high on this mesh. Computed values of the derivatives became completely meaningless in certain zones. On the contrary, conditioning was found to remain within reasonable bounds with the 'thin plate' spline σ , with an accuracy comparable with the one observed on the simplest free surface mesh.

On the basis of these observations, we selected the 'thin plate' σ as the local interpolating method for the computation of slopes and potential gradients at the free surface for simulation on arbitrary free surface grids. However, further investigations are planned on σ_3 , with the view of overcoming the bad conditioning, while retaining the better accuracy observed on the single cylinder test case.

Numerical filtering

Numerical filtering at the free surface is necessary in the presence of significant non-linearities. In the applications for multicolumn structures, we apply the filtering only in the close vicinity of the cylinders waterlines, where we keep a locally structured mesh. This has been found to be sufficient in moderately steep waves.

NUMERICAL RESULTS

Single Vertical Cylinder

Review of published results:

First results obtained with ANSWAVE on the diffraction of regular non linear waves about a vertical surface piercing cylinder were presented in 1995 [8], using a slightly different formulation in which the total flow was simulated, the separation between incident and diffracted components being exploited only in the damping zone, in order to ease the implementation of absorbing conditions. In 1996, the formulation with full separation of incident and diffracted components was implemented, and first results on higher order diffraction effects in long waves were obtained. Although not fully converged, these results presented in [9] allowed a first validation the third harmonic force components predicted by the third order frequency domain theory of Malenica & Molin [22]. The coupling with non linear vertical body motions was also incorporated in the model, see [9].

With the availability of faster computing resources, fully converged results for the higher harmonic components of the diffraction force in long waves were obtained, exhibiting both the convergence to higher order perturbation analysis in the low steepness regime, and the fully nonlinear influence of wave amplitude in more severe conditions. The detailed comparative study between fully non linear time domain diffraction theory and third order frequency domain theory is presented in [12], with also a comparison of nonlinear runup estimates with second order theory for a 'fat' vertical cylinder in the diffraction regime ($kh = 1.0$, $kR = 1.0$).

In the meanwhile, a comparison of higher harmonic diffraction forces in long waves with experimental results at small scale from the University of Oslo [13] had been undertaken, with strikingly good agreement both for the amplitudes and phases, up to the seventh harmonic, and for varying wave amplitudes [11].

Note that the model may also account for a current (or forward speed) superimposed to inci-

dent waves, allowing the study of non linear wave-current-body interactions. ANSWAVE has been used in this configuration, and results compared for cross-validation with a finite order time domain model, see [1]. Comparisons with experimental measurements from Ifremer on the runup about a vertical truncated cylinder in waves and current may also be found in [11].

Some examples:

Recovering results from higher order diffraction theory using a fully non linear model is a very demanding exercise. On one hand, the model has to be run in sufficiently low wave amplitude in order to remain within the domain of validity of Stokes expansion theory. On the other hand, asymptotically small components have to be extracted from the non linear time series for comparison with Stokes expansion force coefficients. An example of such a comparison is given by figures 5 to 8. For $kh = 8.0$ and $A/h = 0.0075$ (steepness $kA = 0.06$), with h the water depth, A the wave amplitude, simulations were run for a vertical bottom-mounted cylinder, with varying radius a , so that ka varies from 0.05 to 0.3. Time series of the inline diffraction force were submitted to a moving window Fourier analysis in order to obtain the harmonic components of the steady-state periodic wave load. Figures 5 to 8 give normalized force components, from the steady force to the third harmonic, compared to results of the frequency domain third order approach of Malenica & Molin [22]. Both sets of results appear to be very close, which indicates that Stokes expansion gives reliable estimates of the force components up to the third harmonic, for this low wave steepness.

One of the advantages of the present model, of course, is the possibility to investigate the influence of wave amplitude on the flow characteristics in a fully non linear manner. Especially, we are able to study the influence of the wave amplitude on harmonic force components, while Stokes expansion analysis gives constant normalized components asymptotically valid for vanishing wave steepness. An example of such an investigation is illustrated by figure 9, in which the variation of the normalized third harmonic inline force is given, for $ka = 0.2$, $kh = 0.8$, and for wave heights varying from $A/h = 0.005$ ($kA = 0.04$) to $A/h = 0.015$ ($kA = 0.12$). Components of the 3ω force obtained by fully non linear simulation are compared with third order values indicated by arrows. Non linear results are shown to converge pretty well towards third order Stokes expansion results when the amplitude is reduced. In larger amplitudes, an apprecia-

ble discrepancy is observed, with the onset of higher than third order effects. For example, for $kA = 0.12$, the 3ω force predicted by third order theory is 18% larger than the fully non linear result, with also a noticeable phase shift.

A the same trend is observed in figures 10 and 11 giving amplitude and phases of the third harmonic inline force on a vertical cylinder in regular waves, for $ka = 0.245$, and for varying amplitudes, compared with experimental values obtained by Huseby & Grue [13]. Despite oscillations of the experimental force module at lower amplitudes, probably due to the difficulty of extracting a very small part of the measured force time series, the agreement is very satisfying.

Runup profiles on a cylinder in regular waves have also been investigated. The runup at the waterline is a very sensible local quantity which is very demanding in terms of accuracy. Comparison of fully non linear runup profiles with first and second order estimations are given in figures 12 to 14. The body is a 'fat' cylinder, $a/h = 1.0$, and computations were run for regular waves of intermediate wave length, $kh = 1.0$. Runup profiles are given for $A/h = 0.005$, $A/h = 0.025$ and $A/h = 0.15$. For the smallest wave amplitude, figure 12, second order and fully non linear runup estimates are graphically identical, while a very small deviation from the first order solution is observed. For $A/h = 0.025$, figure 13, a small discrepancy between non linear and second order results appears at the rear part of the cylinder, while second order contribution is significant along the whole profile. For the largest wave amplitude, figure 14, there are considerable differences between fully non linear and second order runup profiles.

Figures 5 to 9 and 12 to 14 are reproduced from [12], while figures 10 and 11 come from [11]. More details on these validation studies, both with experimental and numerical data, may be found in these papers.

Four-column structure

As a first test, we have considered a square array of four bottom-mounted vertical cylinders, each of radius $r/h=0.1$, with a spacing $d/h=0.8$, where h is the water depth. The incident wave amplitude is 15% of the cylinders radius, $A/a = 0.15$, and the wavelength is $\lambda/h = 1.0$. This corresponds to a moderate steepness wave, $kA = 0.094$. The numerical scheme described in the preceding sections is applied with the local 'thin plate' spline interpolation method for the computation of derivatives

at the free surface. Each cylinder is meshed with 32 nodes on the waterline, and 7 stations in the vertical direction, with a local refinement at the waterline. The total number of panels is 7040, but the symmetry about the vertical plane xOz is accounted for to reduce the effective computational domain to 3520 triangular panels. 100 time steps per wave period are used in the simulation. the free surface mesh extends up to $R/\lambda=3.0$, and the outer part, from $R/\lambda=1.2$ to $R/\lambda=3.0$ is used as a damping zone for the absorption of the diffracted wave. In this simulation, smoothing has been applied only on the two first radial stations of the free surface mesh around each cylinder. The incident wave propagates in the positive x direction.

Figures 15 and 16 give the force on the two upwave and the two downwave cylinders, respectively. The simulation has been run over about 10 wave periods. A periodic steady state is obtained, and maintained until the end of the simulation, without apparent perturbation. One can notice that this steady state periodic force seems to be reached sooner on the downwave cylinder, while the amplitude of the force is sensibly lower.

A more thorough analysis results from the comparison of harmonic inline force components on front and aft columns.

Table 1 below gives for comparison normalized harmonic coefficients of the inline force F_x on the upwave and downwave cylinders.

$F_n/\rho g a^3 (A/a)^n$	F0	F1	F2	F3
Upwave cylinders	-0.03	14.7	1.2	5.4
Downwave cylinders	0.8	12.7	0.25	2.8

Table 1: harmonic inline force components on upwave and downwave cylinders.

$$a/h = 0.10; d/a = 8.; kh = .094; a/h = 0.015$$

A strong difference in the different components is observed. First, we observe that the major part of the drift force is concentrated on the downwave cylinder. On the contrary, higher harmonic forces are sensibly stronger on the upwave cylinder. The second harmonic is almost 5 times larger than on the downwave cylinders, while the ratio is close to 2 for the third harmonic.

These observations may be correlated with the analysis of the diffraction pattern around the structure. Figures 17 and 18 give maps of the maximum wave elevation observed in the steady state part of the simulation, after the initial transients. The elevation is normalized with the incident wave amplitude. Figure 17 corresponds to the non linear sim-

ulation described above, while Figure 18 has been obtained on the same mesh by running the model in the linear mode. Differences appear especially between the two upwave cylinders, where short resonant waves are highlighted by the non linear analysis. Strong higher harmonic forces observed on the upwave cylinders are probably connected with these short waves. At the moment, however, these observations are to be considered as qualitative, before confirmation by simulations on finer meshes.

Note also in figures 17 and 18 the attenuation of diffracted waves in the absorbing zone.

CONCLUSION

In this paper, we have extended our fully non-linear time domain diffraction model to arbitrary 3D geometries, essentially by implementing a new interpolation scheme for the computation of slopes and fluid velocities at free surface nodes.

The new capabilities of the model are illustrated by simulating the non linear diffraction of a regular wave about a four-column structure. Significant non linear phenomena, such as higher harmonic force components on different structure elements, and higher order free surface resonance between upwave columns of the structure are exhibited.

Future work include validation of computed higher harmonic force components with available experimental data or higher order Stokes expansion theory, with the objective of obtaining the same level of validation as on the single vertical cylinder.

The non linear description of resonant modes between offshore platforms columns, which may have major influence on deck clearance predictions, will be another interesting outcome of the model, with possible validation by comparison with existing second order or experimental results, see e.g. [25].

Acknowledgments: The author would like to thank Sirehna for the permission to use ANSWAVE as a basis for his research activities.

The fully non linear diffraction code ANSWAVE on which the present study is based has been developed during past years by the author while he was with Sirehna. The initial developments were funded by the Direction des Recherches, Etudes et Techniques (DRET), French Ministry of Defense. Further developments were funded by CEP&M through various Clarom projects.

Methods for the computation of non linear free surface flows about arbitrary 3D structures presented in this paper were developed in Division Hydrodynamique Navale, Laboratoire de Mécanique des Fluides, Ecole Centrale de Nantes.

Concerning validation studies in the single vertical cylinder case, many thanks to Bernard Molin and Sime Malenica for friendly and stimulating cooperation, and to John Grue for exchange of results.

References

- [1] Buchmann, Ferrant, P. and Skourup, J., 'Runup on a Body in Waves and Current. Fully Non-linear and Finite Order Calculations'. Proc. 13rd Workshop on Water Waves and Floating Bodies, Alphen aan den Rijn, The Netherlands, 1998.
- [2] Celebi, M.S., M.H. Kim, R.F. Beck, 'Fully Non-linear 3D Numerical Wave Tank Simulation', Journal of Ship Research, Vol.42(1), pp 33-45, 1998.
- [3] Chahine, G. L., 'Numerical Modelling of the Dynamic Behaviour of Bubbles in Non Uniform Flow Fields', Proc. Symposium on Numerical Methods in Multiphase Flows, Toronto, 1990.
- [4] Chen, X.B., B. Molin, F. Petitjean, 'Faster Evaluation of Resonant Exciting Loads on Tension Leg Platforms', in Offshore Engineering, Vol. 8, Pentech Press, 1992.
- [5] Di Mascio A., Landrini M., Lalli F., Bulgarelli U., '3D Non Linear Diffraction around a Fixed Structure', Proc. 20th ONR Symposium on Naval Hydrodynamics, Santa Barbara, 1994.
- [6] Eatock-Taylor, R. & F.P. Chau, 'Wave Diffraction-Some Development in Linear and Non Linear Theory', J. Offshore Mech. and Arctic Engg., 1993.
- [7] Ferrant, P., 'Radiation and Diffraction of Non Linear Waves in Three Dimensions', Proc. 7th Int. Conf. on the Behavior of Offshore Structures (BOSS'94), MIT, Boston, 1994.
- [8] Ferrant, P., 'Time Domain Computation of Non-linear Diffraction Loads upon Three Dimensional Floating Bodies', Proc. 5th International Offshore and Polar Engineering Conference (ISOPE'95), The Hague, 1995.
- [9] Ferrant, P., 'Simulation of Strongly Non Linear Wave Generation and Wave-Body Interactions using a 3D MEL Model', Proc. 21st ONR Symposium on Naval Hydrodynamics, Trondheim, 1996.
- [10] Ferrant, P., 'Runup on a Cylinder due to Waves and Current: Potential Flow Solution with Fully Non-Linear Boundary Conditions', Proc. 8th International Offshore and Polar Engineering Conference (ISOPE'98), Montreal, Canada, 1998.
- [11] Ferrant, P., 'Fully Nonlinear Interactions of Long-Crested Wave Packets with a Three-Dimensional Body', Proc. 22nd ONR Symposium on Naval Hydrodynamics, Washington, 1998.
- [12] Ferrant, P., Malenica, S., Molin, B., 'Nonlinear Wave Loads and Runup on a Vertical Cylinder', Chapter in: 'Nonlinear Water Wave Interaction', pp 101-136, Advances in Fluid Mechanics, Eds O. Mahrenholtz & M. Markiewicz, WIT Press, Computational Mechanics Publications, ISBN 1 85312 545 8, 1999.
- [13] Huseby, M. & J. Grue, 'An Experimental Investigation of Higher Harmonic Forces on a Vertical Cylinder in Long Waves', Proc. 13th Int. Workshop on Water Waves and Floating Bodies, Alphen an den Rijn, 1998.
- [14] Isaacson, M. & K.F. Cheung, 'Time Domain Second Order Wave Diffraction in Three Dimensions', J. Waterways, Port, Coastal & Ocean Engg., ASCE, Vol.118(5), pp 496-516., 1992.
- [15] Kim, M.H. & D.K.P. Yue, 'The Complete Second-Order Diffraction Solution for an Axisymmetric Body: Part 1: Monochromatic Incident Waves', J. Fluid Mech., Vol. 200, pp 235-264, 1989.
- [16] Kim, Y., D.C. Kring, P.D. Sclavounos, 'Linear and Nonlinear Interactions of Surface Waves with Bodies by a Three Dimensional Rankine Panel method', Applied Ocean Research, Vol. 19, pp 235-249, 1997.
- [17] Krokstad, J.R. & C.T. Stansberg, 'Ringling Load Models Verified against Experiments', Proc. OMAE Conference, 1995.
- [18] Lafranche, Y., 'Application de l'Interpolation Polynomiale au Dépouillement Graphique de Valeurs de R^3 ', Thesis, University of Rennes I, France, 1984. (in French).
- [19] Lee, C.H. & J.N. Newman, 'Second Order Wave Effects on Offshore Structures', Proceedings BOSS'94 Conference, Cambridge, MA, 1994.
- [20] Le Méhauté A., 'Interpolation et Approximation par des Fonctions Polynomiales par Morceaux dans R^n ', Sc.D. thesis, University of Rennes I, France, 1984. (in French).

- [21] Linton, C.M. & Evans, D.V., 'The Interaction of Waves with Arrays of Vertical Circular Cylinders', *Journal of Fluid Mech.*, vol. 215, 1990.
- [22] Malenica, S. & B. Molin, 'Third Harmonic Wave Diffraction by a Vertical Cylinder', *Journal Of Fluid Mechanics*, Vol.302 , pp 203-229, 1995
- [23] Rienacker, M.M. & Fenton, J.D., 'A Fourier Approximation Method for Steady Water Waves', *Journal of Fluid Mechanics*, Vol. 104, pp 119-137, 1981.
- [24] Saad, Y. & M.H. Schultz, 'A Generalized Minimal Residual Algorithm for Solving Non-Symmetric Linear Systems', *Research Report RR-254*, Yale University, 1983.
- [25] Scolan, Y.M., Malenica, S., 'Experimental and Numerical Second Order Diffracted Waves around an Array of 4 Cylinders'. *Proc. 13rd Workshop on Water Waves and Floating Bodies*, Alphen aan den Rijn, The Netherlands, 1998.
- [26] Skourup, J., B. Buchmann, H.B. Bingham, 'A Second Order 3D BEM for Wave-Structure Interaction', *Proc. 12th Workshop on Water Waves and Floating Bodies*, Carry-le-Rouet, France, 1997.

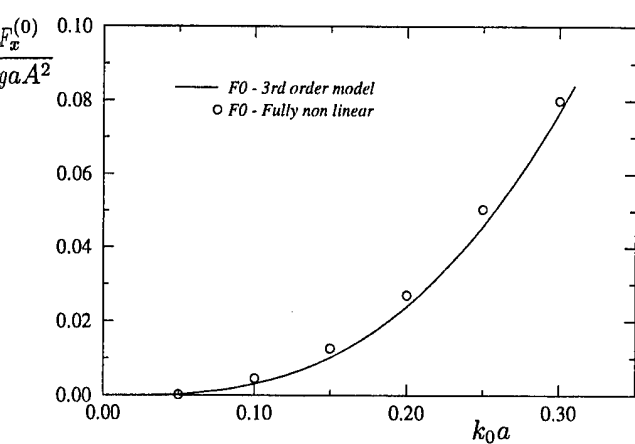


Figure 5: Normalized steady second order force versus wave number ka
Vertical cylinder, radius a ,
 $kh = 8.$, $A/h = 0.0075$

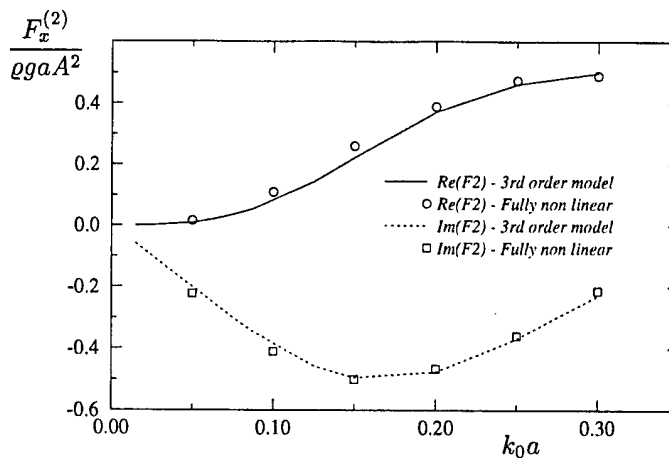


Figure 7: Normalized second harmonic force components
Vertical cylinder, radius a
 $kh = 8.$, $A/h = 0.0075$

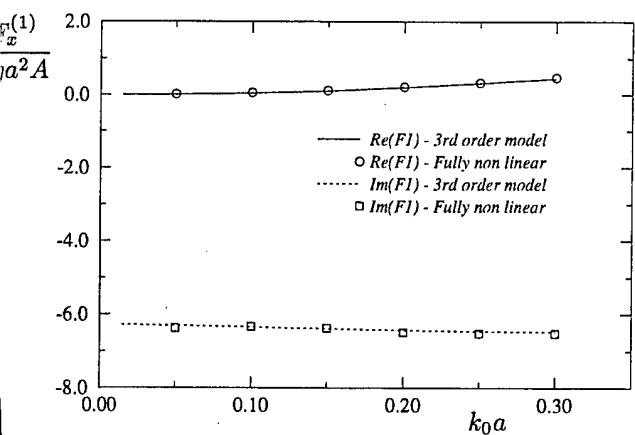


Figure 6: Normalized first harmonic force components
Vertical cylinder, radius a ,
 $kh = 8.$, $A/h = 0.0075$

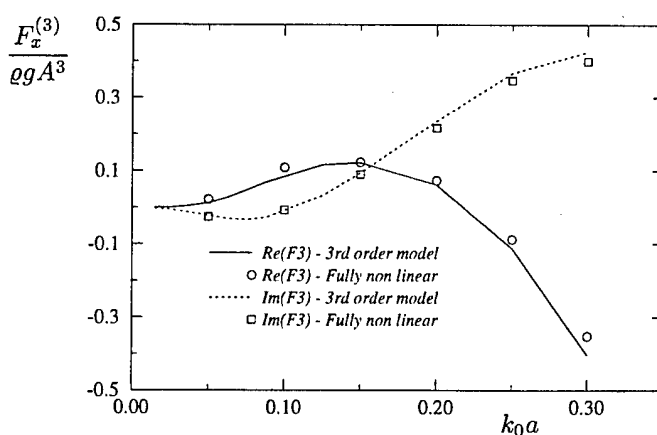


Figure 8: Normalized third harmonic force components
Vertical cylinder, radius a ,
 $kh = 8.$, $A/h = 0.0075$

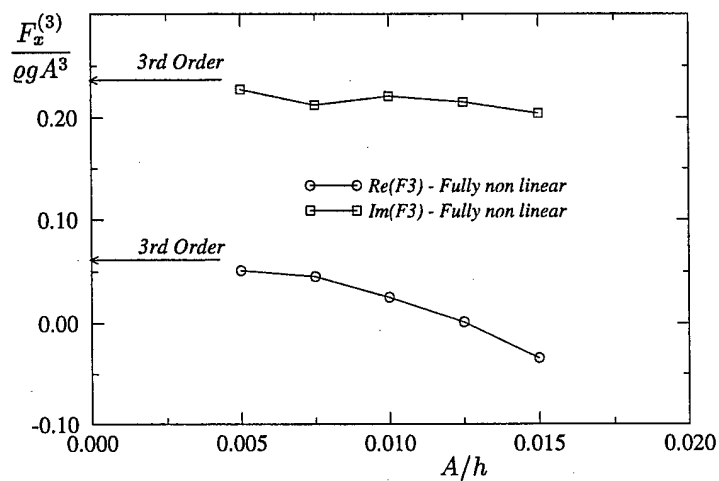


Figure 9: Influence of wave amplitude on third harmonic force components
Fully non linear simulations compared to 3rd order Stokes expansion results
 $kh = 8$, $ka = 0.2$

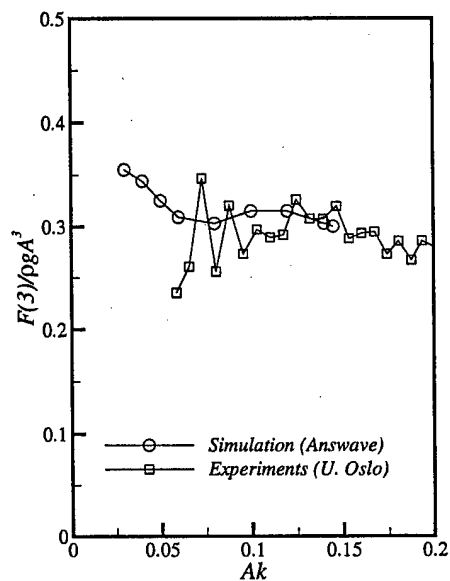


Figure 10: Influence of wave amplitude on third harmonic force coefficient; $ka = 0.245$
Fully non linear simulations compared to experiments from University of Oslo

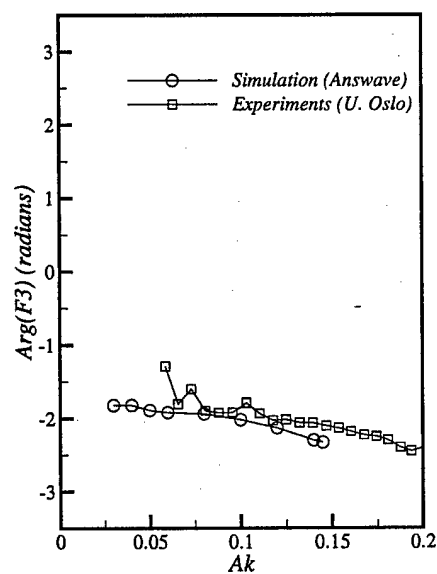


Figure 11: Influence of wave amplitude on third harmonic force phase; $ka = 0.245$

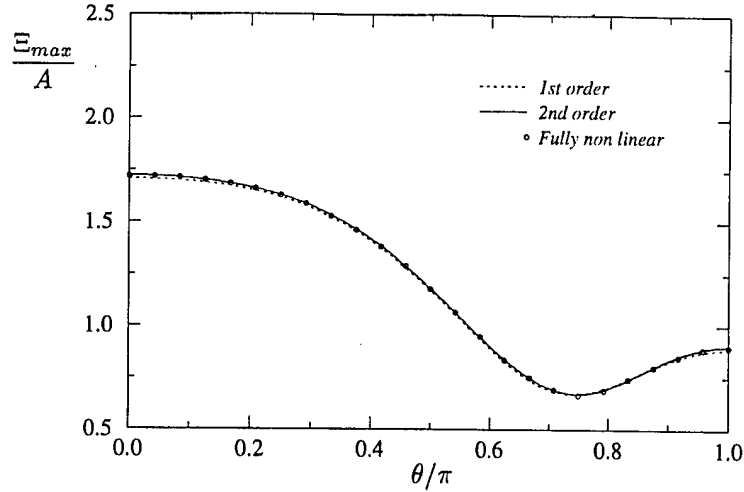


Figure 12: Runup profile on a large vertical cylinder in regular waves
Fully non linear model compared to first and second order theory; $a/h = 1.0$; $kh = 1.0$, $A/h = 0.005$

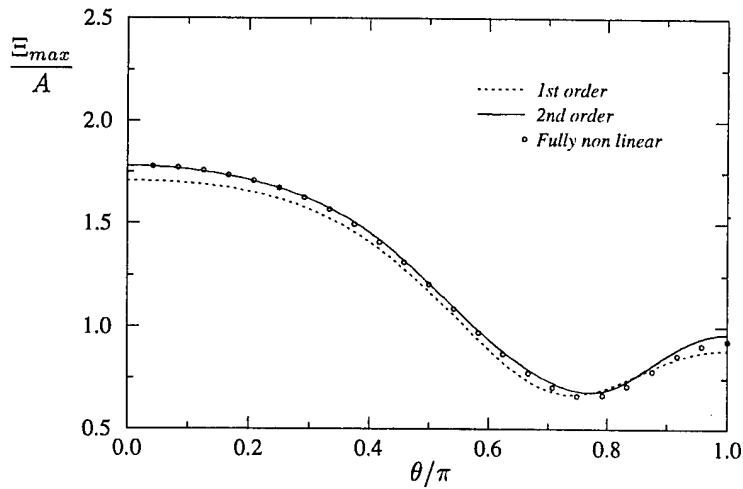


Figure 13: Runup profile on a large vertical cylinder in regular waves
Fully non linear model compared to first and second order theory; $a/h = 1.0$; $kh = 1.0$, $A/h = 0.025$

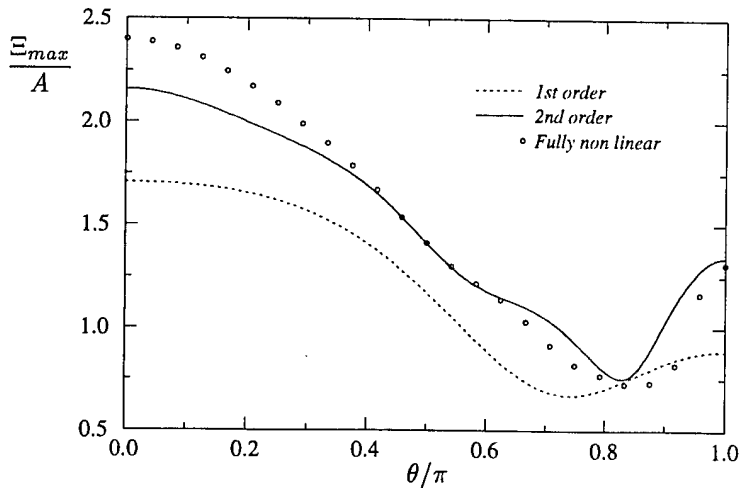


Figure 14: Runup profile on a large vertical cylinder in regular waves
Fully non linear model compared to first and second order theory; $a/h = 1.0$; $kh = 1.0$, $A/h = 0.15$

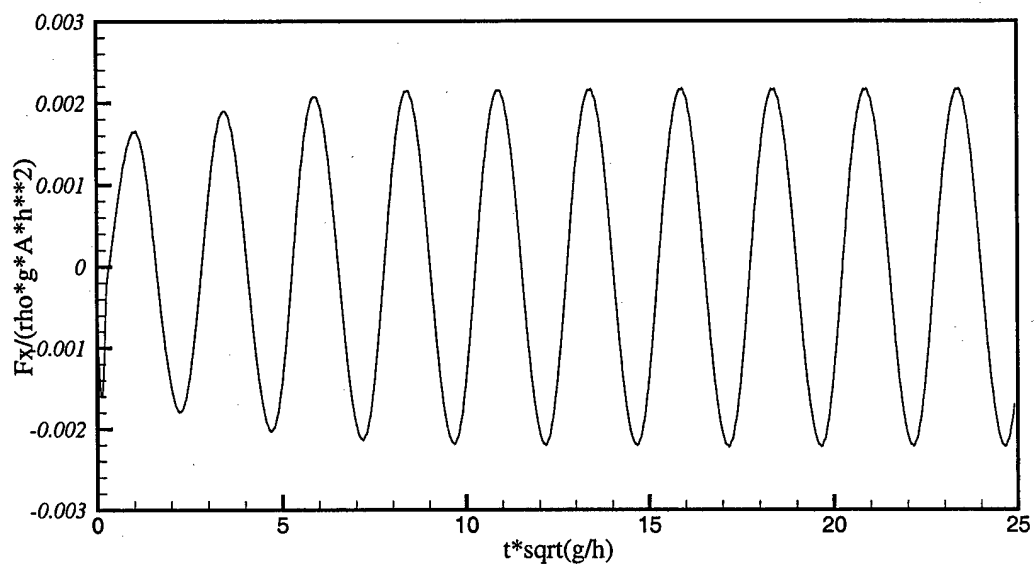


Figure 15: Four-column structure, Horizontal force on the upwave cylinders
 $a/h = 0.10$; $d/a = 8$; $kh = .094$; $a/h = 0.015$

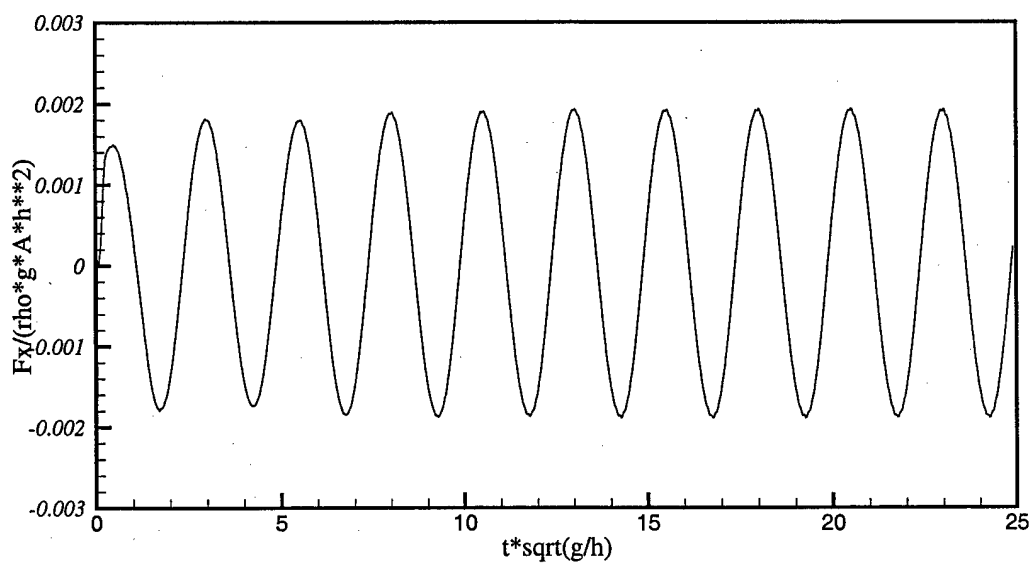


Figure 16: Four-column structure, Horizontal force on the downwave cylinders
 $a/h = 0.10$; $d/a = 8$; $kh = .094$; $a/h = 0.015$

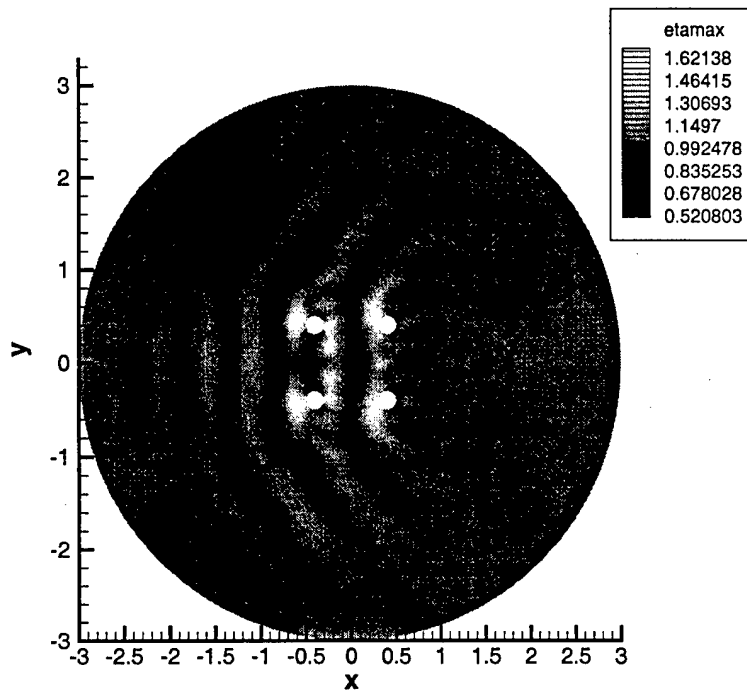


Figure 17: Contour map of the maximum wave elevation. Non linear simulation
 $a/h = 0.10$; $d/a = 8$; $kh = .094$; $a/h = 0.015$

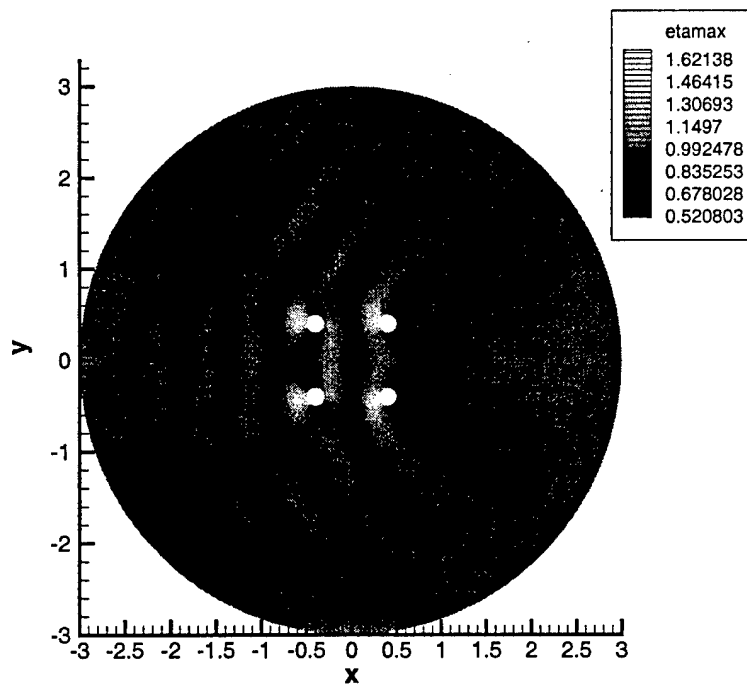


Figure 18: Contour map of the maximum wave elevation. Linear simulation
 $a/h = 0.10$; $d/a = 8$; $kh = .094$; $a/h = 0.015$

HYDROELASTIC ANALYSIS OF TWO DIMENSIONAL SLAMMING PHENOMENA

A. Iafrati¹, A. Carcaterra¹, E. Ciappi² and E.F. Campana¹

¹I.N.S.E.A.N., Istituto Nazionale per Studi ed Esperienze di Architettura Navale
Via di Vallerano 139, 00128-Roma, Italia

Fax: +39-06-5070619; E-Mail: a.iafrati@insean.it

² Dipartimento di Meccanica ed Aeronautica - Univ. "LA SAPIENZA"
Via Eudossiana 18, 00184-Roma, Italia

ABSTRACT

In this paper the hydroelastic interaction during the impact of a two mass oscillator over the water surface is analyzed. The system consists of a massive wedge, plunging the free surface, elastically connected to a carried mass. When the wedge impacts, the system is excited by the pulse hydrodynamic force and an oscillatory coupled motion takes place. The attention is focused on a parametric analysis of the maximum of both hydrodynamic and elastic forces originated by the collision. A simplified theoretical model is proposed starting from the slamming force estimated by similarity solutions of an impacting flat plate. This model is validated by comparisons with a numerical simulation of the fluid-structure interaction. The unsteady potential flow is computed through a boundary elements formulation and a fully non linear boundary condition is applied on the free surface. The hydrodynamic load is then used to force the dynamic system. A good agreement between numerical results and theoretical estimate has been found validating the simplified model.

NOMENCLATURE

x, y	Vector positions	ζ_1	Vertical position of the wedge
G	Two-dimensional Green's function	ζ_2	Vertical position of the suspended body
S	Boundary of the fluid domain	k	Elastic constant
ϕ	Velocity potential	F_h	Hydrodynamic force
ν	Inward unit normal vector	F_e	Elastic force
u	Fluid velocity	F^*	Maximum hydrodynamic force
S_B	Body contour	t^*	Time corresponding to F^*
S_F	Free surface	ζ^*	Depth corresponding to F^*
t	Time	β	Deadrise angle of the wedge
g	Acceleration of gravity	ρ	Water density
ζ	Vertical coordinate (positive downwards)	γ	Non dimensional added mass coefficient
$\dot{\zeta}$	Actual entry velocity	δ	Mass ratio m_2/m_1
v_0	Initial entry velocity	σ	Non dimensional elastic parameter
m_1	Mass of the impacting wedge	$S(f)$	Residual shock spectrum
m_2	Mass of the suspended body	$\mathcal{F}(f)$	Fourier spectrum of the shock signal
		f_{cr}	Critical natural frequency

INTRODUCTION

The problem of collision of an elastic structure over a fluid surface has a quite long tradition, starting from the pioneer studies of von Karman [1] during the thirties to investigate the seaplane floating landing. Although the curiosity for this subject never ceased to stimulate the scientific community, in this last decade a renewed interest has been brought by the design problem related to high speed vessels.

At the actual state of the art, though at least some basic phenomena seem to be quite well established for the rigid body entry, not a complete understanding of the complex mutual fluid-structure interaction is yet possible.

Under a general point of view, two distinct characteristic phases are recognized: the compressible and the incompressible one. In fact, although the water is commonly dealt with an incompressible assumption, in an early impact stage, especially for flat bottom geometry of the impacting body, water compressibility can claim its important role. Authoritative literature can be found [2] on this subject. In a second stage of the impact, the water density variation are negligible at all and a correct analysis can be carried on by using the more usual incompressible approach.

Rather simple but effective models to study the problem were introduced by von Karman [1] and Wagner [3] by assuming that the velocity field around the wetted part of the wedge can be approximated by that around an expanding flat plate. The von Karman model assumes a flat free surface while the Wagner approach accounts for a free surface deformation leading to a more reliable result.

More recently the water entry problem has been analyzed by a fully numerical approach by Zhao & Faltinsen [4]. Through a boundary element formulation, they simulated the flow about a wedge for different values of the deadrise angle. In view of the extension to three dimensional problems, the model has been successively applied to axisymmetric bodies [5].

In the previous mentioned works, as in the present analysis, several assumptions are made. These are related to particular phenomena as air cushion trapping, viscous and surface tension effects, that should be included in a complete analysis, but that strongly increase the complexity of the problem. Likely, some of them do not lead to dramatic changes in the evolution of the impact phenomenon. However, a particular mention deserves air trapping that, at least for very

flat bottom shapes in rough sea, certainly modifies the pressure load acting as a damper interposed between the water and the body. Neglecting the other effects, can be intended as a simplification of the problem but probably not as an oversimplified approach.

In this paper the behavior of a two degrees of freedom elastic oscillator hitting the fluid surface is investigated. In spite of the simplicity of the analyzed system, the investigation reveals to be significant under the theoretical point of view. In fact, some basic interaction phenomena related to the frequency spectrum of the hydrodynamic load as well to the natural frequency of the oscillator, disclose their mutual link in the response of the system.

Aim of the present paper is to investigate the water entry problem of a simple elastic system consisting of two masses, where the lower one is a rigid wedge directly impacting the water. The attention is focused on the incompressible stage and for this reason the deadrise angle is chosen large enough to avoid super-sonic edge conditions.

The flow about a wedge plunging the water surface is numerically studied by using a boundary elements formulation that solves the Laplace equation in terms of the velocity potential. A Neumann boundary condition is applied on the body contour, while the unsteady Bernoulli's equation is used on the free surface to update the velocity potential. Due to the velocity singularity at the edge, a thin jet layer occurs requiring a very fine mesh for an accurate description. For this reason, once a limit thickness is approached, the jet is cut off in a way similar to that proposed by Zhao & Faltinsen [4]. The hydrodynamic load acting on the wedge is used as a forcing term for the system dynamics that provides the elastic force and the actual drop velocity.

Along with a numerical investigation of the subject a theoretical model is developed based on a simplified representation of the hydrodynamic force in terms of the actual depth and drop velocity of the impacting body. The study of the impact of the single wedge provides an analytical solution of the problem that turns to be useful for the theoretical prediction of the occurrence of critical conditions in the case of impact of an elastic system.

The main aspects of the numerical approach will be described in the next section. Successively, the simplified theoretical model will be presented and comparisons between theoretical and numerical results will be discussed.

NUMERICAL SIMULATIONS

The flow about a wedge entering the free surface is numerically analyzed by assuming the flow to be ir-

rotational and the fluid inviscid. Moreover, the dead-rise angle of the impacting wedge is assumed to be large enough to avoid compressibility effects to be relevant. In this conditions the velocity field is expressed in terms of the velocity potential ϕ that satisfies the Laplace equation. This equation is solved by mean of a boundary elements formulation. By introducing the two dimensional free space Green's function of the Laplace operator G , at any point x inside the computational domain the velocity potential can be written as:

$$\phi(x) = \int_S \left[\frac{\partial \phi}{\partial \nu}(y) G(x-y) - \phi(y) \frac{\partial G}{\partial \nu}(x-y) \right] dS(y) \quad (1)$$

where S is the boundary of the fluid domain and ν is the unit vector normal to the boundary oriented inwards. Equation (1) completely describes the flow field $u = \nabla \phi$ once the velocity potential and its normal derivative are known throughout S .

The normal derivative of ϕ is assigned on the body contour S_B in order to satisfy the impermeability constraint, while, on the free surface S_F , the velocity potential is updated according to the unsteady Bernoulli's equation. Actually, the pressure on the free surface is assumed to be constant and, by using the kinematic condition, the Bernoulli's equation reads:

$$\frac{D\phi}{Dt} = g\zeta + \frac{|\nabla \phi|^2}{2} \quad (2)$$

where ζ is the vertical coordinate, positive downwards, with $\zeta = 0$ on the undisturbed water surface. In the initial phase of the impact the kinematic contribution to the right hand side of equation (2) is much stronger than the gravity term, hence the latter is usually neglected in using that equation.

This assumption makes simulations valid only in the short time analysis. However, it should be noted that the initial stage of the impact is the most important in terms of impact loads. Moreover, in performing long time simulations with such kind of approaches, suitable models should be employed in describing the flow separation [6]. Finally, difficulties may arise when the separated flow plunges onto the water surface and, to deal with this phase, other numerical techniques are needed [7].

On the free surface $\phi = 0$ is assumed as initial condition for equation (2). It should be remarked that this initial condition implies a zero tangential velocity all along the free surface and, as a consequence, the limit of the velocity field from the free surface toward the body violates the impermeability constraint at $t = 0$. This is due to the neglected surface tension effects that would avoid the discontinuity in the normal vector at the intersection between the free surface and the body.

The velocity potential on S_B and its normal derivative on S_F are determined by solving the integral equation obtained by applying equation (1) on the boundary of the fluid domain S . Once the velocity potential along the body surface is known, the dynamic pressure is computed by the unsteady Bernoulli's equation.

The problem stated above is numerically solved with a scheme similar to that employed by Zhao & Faltinsen [4] that is briefly described in the following. The boundary of the fluid domain is discretized with segments on which the velocity potential and its normal derivative are assumed to be constant and equal to the value they take at the centroid. The boundary integral equation is solved providing the velocity potential on the body contour and its normal derivative on the free surface. A second order Runge Kutta scheme is employed for the integration of the motion of mid-points on the free surface and of the velocity potential above it. A cubic spline is used to reconstruct the vertices distribution. For the sake of accuracy, at each time step, the panel distribution is refined in highly curved regions.

In the potential approximation the solution of the problem is highly challenging due to the velocity singularity occurring at the intersection between the free surface and the body contour [8]. This singularity leads to the formation of a water jet that needs a suitable procedure to be described numerically. A model, suggested by Zhao & Faltinsen [4], is employed here and some aspects of this procedure are given below.

In a first stage of the numerical simulation the free surface is assumed to intersect the body. Successively, a thin water jet develops, characterized by a strong velocity gradient normal to the body. An accurate description of the development of jet region would require a increasing number of elements with even smaller dimensions and, as a consequence, a dramatic reduction of the time step. For this reason when the distance between the midpoint of the first panel on the free surface and the body contour becomes smaller than a cut-off length, the first panel is replaced by a straight line panel \mathcal{P} normal to the body surface. In order to match both the body and the free surface boundary conditions a linear variation of the velocity potential is assumed along this panel. The tangential derivative is equal to the normal derivative assigned on the body contour while the velocity potential itself is assigned on the free surface side. During the time integration, whenever the first panel on the free surface beyond \mathcal{P} forms an angle with the body contour smaller than a limit value (usually 2°) it is excluded and the jet truncation is moved back. A sketch of the discretization employed close to the jet region

is shown in Fig. 1.

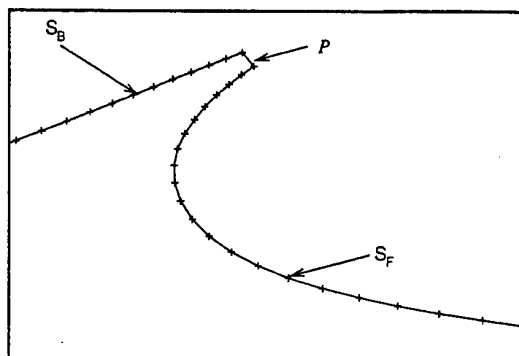


Fig. 1 Sketch of the panels distribution employed to avoid the jet description.

The flow about a wedge with a deadrise angle of 10° and a constant entry velocity $v_0 = 2\text{ms}^{-1}$ has been simulated. After a transient phase, in which the jet develops, the expected similarity solution [4] is achieved. In Fig. 2, free surface profiles obtained at several times are shown in a suitable non-dimensional form.

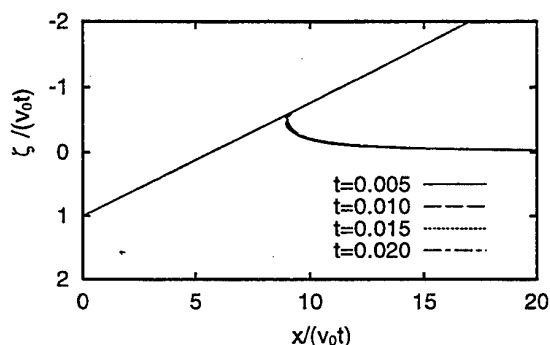


Fig. 2 Similarity solution for water entry at constant velocity of a wedge with deadrise angle 10° .

When analyzing the free fall impact of the elastic system (Fig. 7), the hydrodynamic load F_h is used as a forcing term of the dynamic equation

$$\begin{cases} m_1 \ddot{\zeta}_1 + k(\zeta_1 - \zeta_2) + F_h = 0 \\ m_2 \ddot{\zeta}_2 - k(\zeta_1 - \zeta_2) = 0 \end{cases}, \quad (3)$$

where m_1 and m_2 are the masses of the impacting wedge and of the suspended body, respectively, and k is the elastic constant of the spring.

In the solution of the dynamic equation of the elastic system an explicit numerical procedure is

used. More rigorously, the instantaneous hydrodynamic load should be computed in a coupled way with the wedge acceleration. However, due to the high refinement of the discretization, a very small time step is adopted and then the use of a more sophisticated implicit procedure, see for instance [9], is not really necessary.

Due to the treatment of the jet region, strong oscillations characterize the slamming load and a suitable filter has been applied to the numerical results.

SIMPLIFIED ANALYTICAL APPROACH

In this section, a simplified theoretical model for predicting the slamming force time history for a wedge plunging the water surface is proposed with applications to the rigid body case and to a simple elastic system. Following an approach developed in Carcaterra & Ciappi [10, 11], the method allows a simple analysis of the impact phenomenon leading to the analytical estimate of two basic quantities: the maximum slamming force F^* and the characteristic time delay t^* between the initial instant of the impact and the instant at which the force peak occurs. Both these parameters reveal their fundamental importance in the fluid-structure interaction. In fact, F^* affects directly the amplitude of the structure response while t^* controls the peak frequency of the hydrodynamic force spectrum. In particular, when a specified ratio between t^* and a natural period of oscillation of the system is approached, a critical situation is achieved, characterized by severe stress condition in the elastic system.

The hydrodynamic force acting on a massive wedge follows a characteristic evolution. On one hand the drop velocity decay causes a reduction in the slamming pressure while, at the same time, the wetted length is increasing. In the first stage of the impact the latter effect dominates over the former and an increasing trend of the force is observed. At t^* the two opposite phenomena find a balance and a characteristic maximum is reached. Successively, the velocity reduction prevails against the increase of the wetted length and the slamming force definitively decays.

In Carcaterra & Ciappi [10], on the basis of the acoustic approximation originally introduced by Skalak & Feit [12], this phenomenon is kept by a simple formulation and the hydrodynamic force is expressed only in terms of the body depth and velocity. In this way a solution of the body motion is provided in analytical form. Due to some hypotheses contained in the acoustic approximation, the analysis is only valid for a supersonic edge condition that implies a very small deadrise angle when analyzing a wedge entry.

This procedure has been generalized in Carcaterra & Ciappi [11] starting from the von Karman [1] approximation of the hydrodynamic force, valid for a constant drop velocity. Again, the force is suitably expressed only in terms of the body depth and velocity, and analytical results are determined.

Impact of the Rigid Body

Let us consider a two dimensional wedge of mass m per unit length, impacting on the water surface with an initial drop velocity v_0 . The equation of motion simply reads $m\ddot{\zeta} + F_h = 0$, where F_h and ζ are the hydrodynamic force (per unit length) and the depth, respectively.

By the potential theory, and by approximating the velocity field on the wetted length with the flow around a flat plate, the following expression for the hydrodynamic force is obtained: $F_h = \pi \rho \gamma v_0^3 t / \tan^2 \beta$, where β is the deadrise angle and γ , both in Wagner and von Karman approaches, is assumed to be a constant depending on the hypotheses made on the wetted length. More details about this coefficient are provided at the end of this section.

When a variable drop velocity is considered, a reasonable approximation for the hydrodynamic force can be used:

$$F_h = \pi \rho \gamma \dot{\zeta}^3 t / \tan^2 \beta \quad (4)$$

to obtain the equation of the body motion. However, in view of a closed form solution, the direct dependence of F_h on time can be eliminated by letting $t = \zeta / v_0$. In this case one obtains:

$$F_h(\zeta, \dot{\zeta}) = \frac{\pi \rho \gamma}{v_0 \tan^2 \beta} \dot{\zeta}^3 \zeta \quad (5)$$

and the equation of motion becomes:

$$\ddot{\zeta} + A \dot{\zeta}^3 \zeta = 0 \quad \text{where} \quad A = \frac{\pi \rho \gamma}{m v_0 \tan^2 \beta} \quad (6)$$

This nonlinear equation admits an analytical solution. By introducing the variable transformation:

$$\dot{\zeta} = \psi(\zeta) \Rightarrow \ddot{\zeta} = \frac{d\psi}{dt} = \frac{d\psi}{d\zeta} \frac{d\zeta}{dt} = \psi \frac{d\psi}{d\zeta} \quad ,$$

equation (6) takes the form:

$$\psi \frac{d\psi}{d\zeta} + A \psi^3 \zeta = 0 \quad (7)$$

whose solution is determined by separation of variables. In fact:

$$\frac{d\psi}{\psi^2} = -A \zeta d\zeta \Rightarrow \psi = \dot{\zeta} = \frac{2v_0}{2 + A v_0 \zeta^2} \quad (8)$$

where the integration constant is found by matching the initial condition $\dot{\zeta}(0) = v_0$.

The relationship between time and depth is found by integration of the previous equation, yielding:

$$t(\zeta) = \frac{\zeta}{v_0} + \frac{A \zeta^3}{6} \quad (9)$$

$$\zeta(t) = -6 \sqrt{\frac{2}{B(t)}} + \frac{1}{3 A v_0} \sqrt{\frac{B(t)}{2}}$$

where

$$B(t) = b_1 A^2 v_0^3 t + \sqrt{b_2 A^3 v_0^3 + b_3 A^4 v_0^6 t^2}$$

with $b_1 = 162$, $b_2 = 23328$ and $b_3 = 26244$. The new expression of $t(\zeta)$ can be considered as an higher order approximation with respect to $t = \zeta / v_0$, accounting for the velocity reduction.

By using equations (5) and (8), the hydrodynamic force versus the depth is:

$$F_h(\zeta) = m A \dot{\zeta}^3 \zeta = m A \left[\frac{2v_0}{2 + A v_0 \zeta^2} \right]^3 \zeta \quad (10)$$

that, through equation (9), provides $F_h(t)$. Starting from this equation, it is possible to obtain F^* and t^* . The former is the relative maximum of $F_h(\zeta)$ that follows from the solution of the algebraic equation:

$$\frac{dF_h}{d\zeta} = 0 \Rightarrow \zeta^* = \sqrt{\frac{2m \tan^2 \beta}{5\pi \rho \gamma}} \quad (11)$$

where ζ^* is the depth at which the maximum occurs. Hence, F^* is given by:

$$F^* = F_h(\zeta^*) = \left(\frac{5}{6}\right)^3 \sqrt{\frac{2\pi}{5} \rho \gamma m} \frac{v_0^2}{\tan \beta} \quad (12)$$

and t^* is found by using equation (9):

$$t^* = t(\zeta^*) = \frac{16}{15} \sqrt{\frac{2m}{5\pi \rho \gamma}} \frac{\tan \beta}{v_0} \quad (13)$$

It is interesting to notice that ζ^* is simply related to t^* . Actually, by combining equations (11) and (13), it follows that:

$$\zeta^* = \frac{15}{16} v_0 t^* \quad ,$$

indicating that, although responsible for the relative maximum of the slamming force, only a small reduction of the entry velocity occurs up to t^* .

A useful relationship between F^* and t^* can be also determined. In fact, simple mathematics leads to:

$$F^* t^* = \frac{20}{81} m v_0 \simeq 0.247 m v_0 \quad (14)$$

These results completely solve the problem related to the simple model represented by equation (6). Their use in predicting the response of the elastic system is discussed in the next section.

The choice of the γ coefficient deserves some further comments. The total force acting on a wedge falling with a constant velocity v_0 can be written as $F = d(\mu v_0)/dt$ where μ is the added mass coefficient. This coefficient can be expressed in terms of the product of γ and the added mass of a flat plate of width $2v_0 t / \tan \beta$, that is:

$$\mu = \gamma \rho \frac{\pi v_0^2 t^2}{2 \tan^2 \beta} \quad (15)$$

From the above considerations, the slamming force becomes:

$$F = \dot{\mu} v_0 = \gamma \pi \rho \frac{v_0^3 t}{\tan^2 \beta}, \quad (16)$$

and if $C_f = F/(\rho v_0^3 t)$ is the non dimensional force, it follows that:

$$\gamma = \frac{1}{\pi} C_f \tan^2 \beta. \quad (17)$$

This constant assumes the value $\gamma = 1$ in the theory suggested by von Karman while, due to the different assumption for the wetted length, it is $\gamma = \pi^2/4$ in the Wagner theory. It should be noticed that, although a dependence of γ on the deadrise angle is expected, both these theories predict γ to be constant. A brief review of works developed about this relationship is given by Vorus [13], while only few points are discussed below.

In Zhao & Faltinsen [4] the flow about a wedge plunging the water surface with a constant velocity is analyzed by using a numerical simulation and other two approaches: one based on the similarity solution originally formulated by Dobrovolskaya [14], and the other on a matched asymptotic expansion similar to that employed by Howinson *et al.* [15], which uses the Wagner [3] solution to describe the inner flow. Zhao & Faltinsen [4] compute the non dimensional force coefficient C_f at several deadrise angles by using the three different approaches and the corresponding values of γ obtained through equation (17) are depicted in Fig. 3. All curves exhibit a decay of γ for increasing values of the deadrise angle and, for $\beta \rightarrow 0$, tend to the value predicted by Wagner [3] in the small deadrise angle assumption. In the following the value of γ provided by the similarity approach will be used for the theoretical estimate.

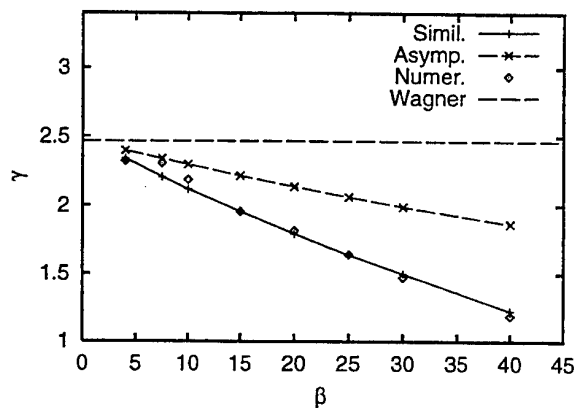


Fig. 3 Variation of the non dimensional added mass coefficient γ versus the deadrise angle.

To validate the theoretical formulation, a comparison with an experiment described in Kim *et al.* [16] is performed. The test case refers to a wedge with a deadrise angle of 23° , a mass per unit length of 398 kg and an initial drop velocity $v_0 = 6.9 \text{ m/s}$. The theoretical prediction of the vertical acceleration is in good agreement with experimental data (Fig. 4).

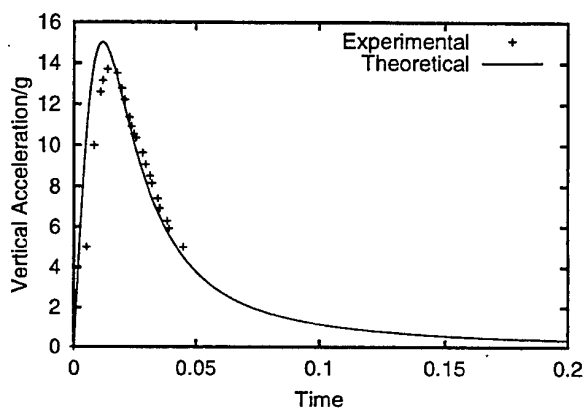


Fig. 4 Comparison between theoretical and experimental results for the impact at a constant entry velocity of a wedge with a deadrise angle of 23° .

The previous analysis can be considered acceptable only over a short time scale since buoyancy effects are not included in equation (6). In fact, they induce oscillations of the impacting wedge. However, the characteristic time scale T_{buoy} of the buoyancy phenomenon, trivially is:

$$T_{buoy} \approx \sqrt{\frac{m_1 \tan \beta}{4 \rho g^2}},$$

thus the ratio t^*/T_{buoy} can be easily obtained:

$$\frac{t^*}{T_{buoy}} \approx \sqrt[4]{\frac{\tan^3 \beta}{\gamma^2} \left(\frac{m_1 g^2}{\rho v_0^4} \right)}$$

Hence, the analysis is valid for

$$\frac{\tan^3 \beta}{\gamma^2} \left(\frac{m_1 g^2}{\rho v_0^4} \right) \ll 1,$$

i.e. when considering small deadrise angles and/or high impact velocities.

The same conclusion can be also drawn by directly considering the ratio between the buoy force corresponding to ζ^*

$$F_{buoy} = \rho g \zeta^{*2} / \tan \beta$$

and F^* . The wished ratio provides

$$\frac{F^*}{F_{buoy}} \approx \frac{\tan^2 \beta}{\gamma^{3/2}} \sqrt{\frac{m_1 g^2}{\rho v_0^4}}$$

By substituting the numerical values used for the previous application it follows

$$\frac{F^*}{F_{buoy}} \approx 95,$$

that allows to neglect at all any buoy effect.

Water entry of a Simple Elastic System

When the hydrodynamic force is modeled as shown in the previous section, equation (3) becomes:

$$\begin{cases} m_1 \ddot{\zeta}_1 + k(\zeta_1 - \zeta_2) + \frac{\pi \rho \gamma}{v_0 \tan^2 \beta} \dot{\zeta}_1^3 \zeta_1 = 0 \\ m_2 \ddot{\zeta}_2 - k(\zeta_1 - \zeta_2) = 0 \end{cases} \quad (18)$$

The numerical solution can be easily achieved and the comparison with results obtained by a numerical simulation is presented in the following section. However, some interesting conclusions about the maximum elastic force excited during the water impact can be determined in closed form.

Since in the previous section the evaluation of the hydrodynamic force was obtained, it is interesting to study under which conditions this force is almost independent of the elastic force, i.e. when the motion of m_1 is substantially independent of m_2 . In such a case the hydrodynamic force analysis developed is still considered valid.

Let us introduce, for the sake of simplicity, the non dimensional parameters $\sigma = \rho v_0^2 / k$ and $\delta = m_2 / m_1$. When the elastic force F_e satisfies the condition $F_e \ll F_h$, its effect on F_h is negligible. An estimate of the orders of magnitude of F_e and F_h is easily provided

by using results of the previous section. By wholly converting the initial kinetic energy of m_2 into elastic energy, corresponding to a sudden stop of m_1 , one has $F_e \propto \sqrt{k m_2} v_0$, while $F_h \propto v_0^2 \sqrt{\rho m_1} / \tan \beta$. Therefore:

$$\frac{F_h}{F_e} \propto \frac{\sqrt{\sigma}}{\sqrt{\delta} \tan \beta} \quad (19)$$

It can be concluded that when $\sqrt{\sigma / \delta} \gg \tan \beta$, F_h is weakly affected by F_e . Hence, the suspended mass behaves like a mass on a foundation that receives a known shock acceleration of the form $F_h(t) / m_1$, where $F_h(t)$ is given in 2.1.

In this case, the shock spectrum technique can be profitably used to predict the maximum response of the suspended mass as a function of the natural frequency $f = 1 / (2\pi) \sqrt{k / m_2}$ of the system itself. The residual shock spectrum $S(f)$ represents the maximum response of the system for $t > T$, where T is the time duration of the shock waveform. The absolute maximum is generally a good approximation of the overall maximum response [17, 18]. $S(f)$ is related to the Fourier transform \mathcal{F} of the shock signal by the following relationship:

$$S(f) = 2\pi f |\mathcal{F}(f)| \quad (20)$$

The concept of residual shock spectrum could not be introduced in a strict mathematical form for the slamming signal, since it vanishes only asymptotically and has not a finite time duration T . Nevertheless, the slamming force decays rapidly after the maximum and thus the use of the shock spectrum analysis does not reasonably introduce significant errors.

Even though equation (20) could be directly employed to provide the shock spectrum once the hydrodynamic force is known, a more general and even simpler result can be obtained by introducing a suitable non-dimensional form of the hydrodynamic load. If equations (9), (10) and the expression of $B(t)$ are rewritten in terms of the following non dimensional variables:

$$\bar{t} = \frac{t}{t^*}, \quad \bar{\zeta} = \frac{\zeta}{\zeta^*}, \quad \bar{F}_h = \frac{F_h}{F^*}, \quad (21)$$

they take the form below:

$$\begin{aligned} b(\bar{t}) &= \frac{b_1 \bar{t}}{\nu^2} + \sqrt{\frac{b_2}{\nu^3} + \frac{b_3 \bar{t}^2}{\nu^4}} \\ \bar{\zeta}(\bar{t}) &= -6 \sqrt[3]{\frac{2}{b(\bar{t})}} + \frac{1}{3} \sqrt[3]{\nu^3 \frac{b(\bar{t})}{2}} \\ \bar{F}(\bar{t}) &= \frac{81}{20\nu} \left[\frac{2}{2 + \bar{\zeta}^2 / \nu} \right]^3 \bar{\zeta}, \end{aligned} \quad (22)$$

where:

$$\nu = \frac{m}{\rho(v_0 t^*)^2} \frac{\tan^2(\beta)}{\pi \gamma(\beta)} = \frac{5}{2} \left(\frac{15}{16} \right)^2$$

Equation (22) is given once for any choice of the impact parameters. Only \tilde{F} and $\tilde{\zeta}$ are requested to be suitably scaled by using F^* and t^* .

In Fig. 5 the non dimensional force given by equation (22) is plotted versus the non dimensional time \tilde{t} . The shock spectrum of this signal:

$$\tilde{S}(\tilde{f}) = 2\pi \tilde{f} |\tilde{\mathcal{F}}(\tilde{f})|, \quad (23)$$

is represented in Fig. 6 versus the non dimensional frequency $\tilde{f} = ft^*$. The elastic force can be recovered by multiplying the residual shock spectrum by the maximum hydrodynamic force F^* and by the mass ratio δ .

By direct inspection of the shock spectrum curve it appears that the relative maximum occurs at $\tilde{f} \simeq 1/5$ and hence the critical frequency can be estimated as:

$$f_{cr} = \frac{1}{5t^*}. \quad (24)$$

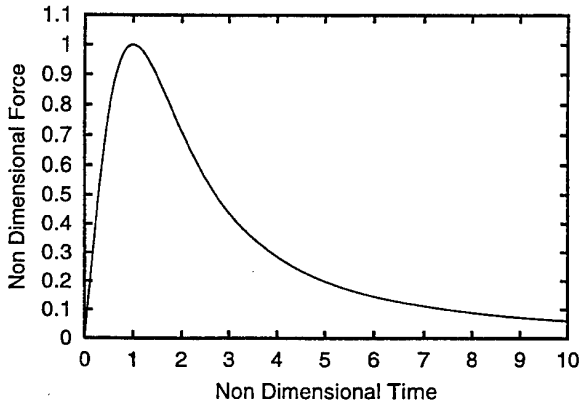


Fig. 5 Non dimensional slamming shock signal.

If one is interested to a critical value of the elastic constant k , it follows that $k_{cr} = m_2(2\pi f_{cr})^2$ and, in terms of the non dimensionless parameter σ , it becomes:

$$\sigma_{cr} = \frac{\rho v_0^2}{k_{cr}} = \frac{25}{4\pi^2} \frac{\rho v_0^2 t^{*2}}{m_2}. \quad (25)$$

By using the expression (13) for t^* , an equivalent expression for σ_{cr} is recovered:

$$\sigma_{cr} = \frac{25}{4\pi^3} \frac{1}{\delta \nu} \frac{\tan^2 \beta}{\gamma}. \quad (26)$$

On the basis of equation (24), besides k_{cr} , a complete set of critical values of the impact variables can be derived.

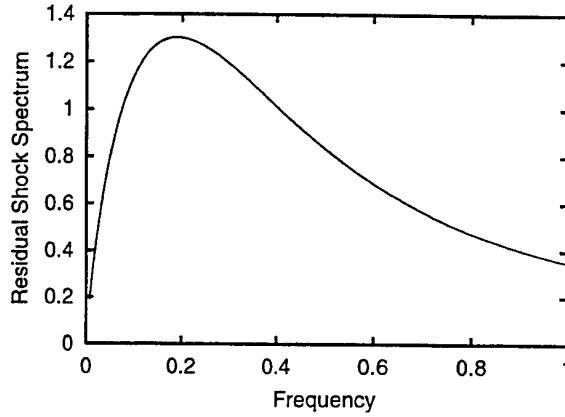


Fig. 6 Non dimensional residual shock spectrum of slamming signal.

It is apparent that, in correspondence of the critical condition, the maximum elastic force has the same order of magnitude of the hydrodynamic one being $\tilde{S}(\tilde{f}_{cr}) \simeq 1.3$ at least for a mass ratio $\delta = 1$. Therefore, in that case, it can be concluded that the initial assumption $F_e \ll F_h$ does not strictly hold. Nevertheless, this does not sensibly affect the estimate of the critical frequency. In fact, in the next section this severe case has been analyzed and the critical condition leading to the maximum elastic force agrees quite satisfactorily the corresponding numerical estimation. For smaller value of δ the condition $F_e \ll F_h$ holds and the estimated critical frequency should be definitively accepted.

DISCUSSION

In this section the water entry of the elastic system shown in Fig. 7 is analyzed by the numerical model and by the theoretical approach discussed in the last section.

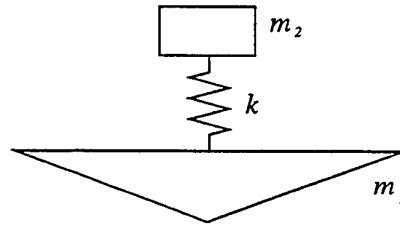


Fig. 7 Sketch of the elastic system.

The impacting wedge has a deadrise angle $\beta = 10^\circ$, an initial velocity $v_0 = 2 \text{ m s}^{-1}$, a mass $m_1 = 166.26 \text{ kg m}^{-1}$ and the mass ratio is $\delta = m_2/m_1 = 1$.

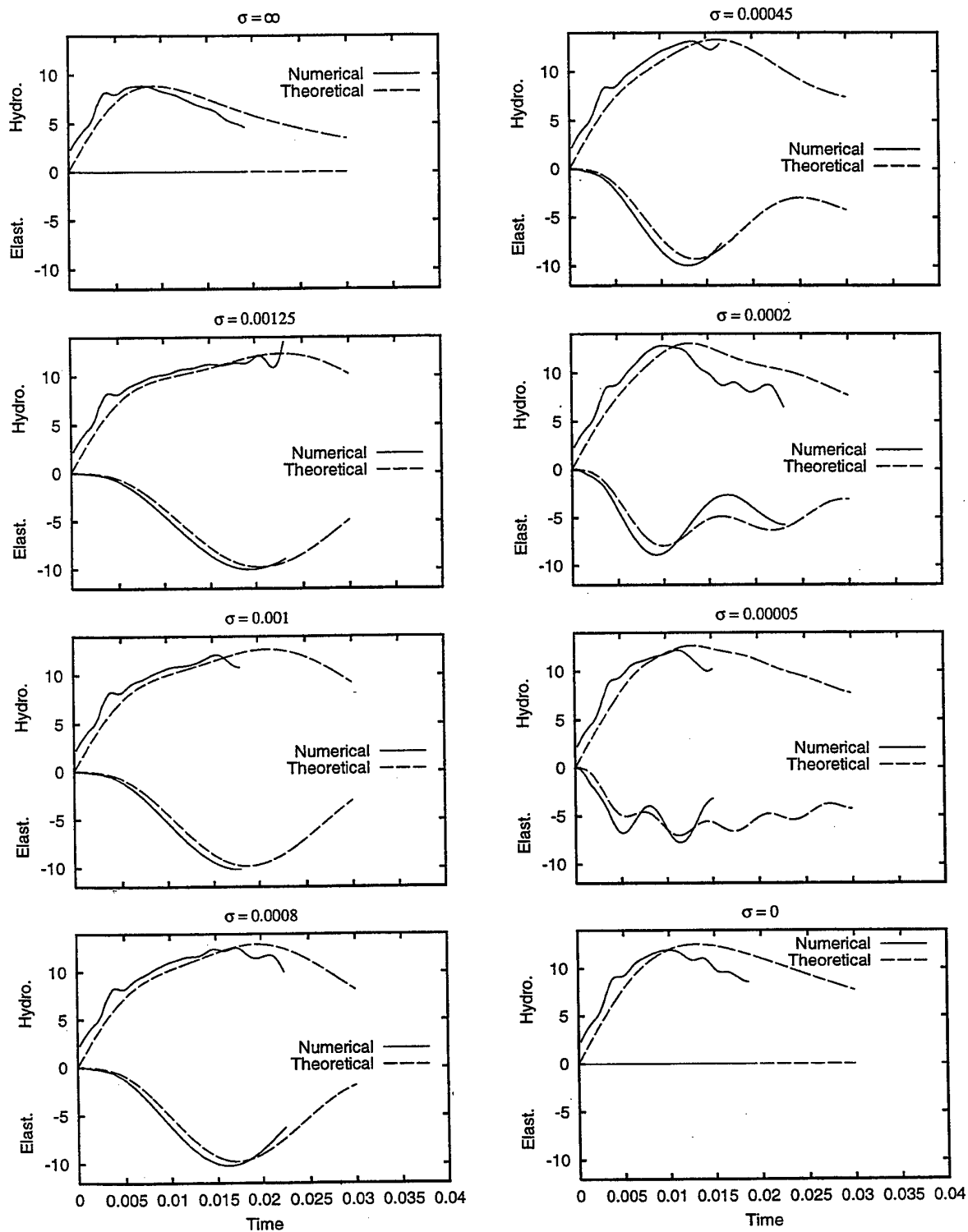


Fig. 8 Time histories of hydrodynamic and elastic forces for several stiffness parameters. ($\delta = 1$)

The value chosen for m_1 has been obtained by introducing a non dimensional mass parameter $m'_1 = m_1/(\rho L^2) = 1$, being L a reference length. For the semi-infinite wedge the reference length was assumed as $L = v_0^2/g$, that is the amplitude of the free oscillations of a buoy mass originally forced with a velocity v_0 .

The stiffness k of the elastic spring has been systematically varied from zero to infinity to study its effects on the elastic and hydrodynamic responses, that is, in terms of σ , from ∞ ($k = 0$) to 0 ($k \rightarrow \infty$). Since in both extreme cases the elastic force vanishes, they collapse into a rigid body impact with mass $m'_1 = 1$ and $m'_1 = 2$ for the former ($k = 0$) and the latter ($k \rightarrow \infty$) bound, respectively.

The time histories of the hydrodynamic and elastic forces, divided by the fluid density ρ , are shown for several values of the non-dimensional stiffness parameter in Figs. 8. For each case the hydrodynamic and the elastic (negative) forces are represented in the upper and lower side of the graph, respectively. The dashed curves represent the results obtained by solving the system (3) where the hydrodynamic force is modeled as in equation (5). On the other hand the solid lines refer to the solution of the same system (3) where the hydrodynamic load is determined from the numerical solution of the fluid dynamic problem.

A good agreement among the two approaches appears over the whole range of σ , although the slight differences in the hydrodynamic load of the two solutions deserves some remarks.

With respect to the theoretical prediction, numerical results seem to start from a non zero slamming force. Actually, in the initial development of the jet, the numerical hydrodynamic force grows rapidly from zero up to catch the slope predicted by the similarity solution.

Moreover, for all values of σ a marked peak occurs in the numerical results around $t = 0.004$, that is the time at which the jet is cut off for the first time. Hence this peak does not have a physical meaning but rather it is an effect related to the numerical algorithm. Nevertheless, after a few time steps, the effects of the jet cut off disappear and the curves catch again the previous trend.

Finally, after the maximum, the numerical hydrodynamic force decays faster than the theoretical one. However, the agreement of the latter with experimental data shown in Fig. 4 seems to validate its decay rate, thus differences should be due to an excessive damping in the numerical solution.

In Fig. 9 the maxima of the elastic force of each time history are plotted versus σ . Equations (25) and (26) provide for the stiffness parameter a critical value

at which the maximum elastic response occurs. In the present case it results $\sigma_{cr} \simeq 0.00135$ while the solution of the coupled system (18) gives $\sigma_{cr} \simeq 0.001$ and the numerical simulation provides $\sigma_{cr} \simeq 0.0008$. These differences mainly originate from the neglected interaction between the hydrodynamic and the elastic force in deriving equation (26). However, the comparison seems rather good especially considering the flat trends that characterizes the region of maxima.

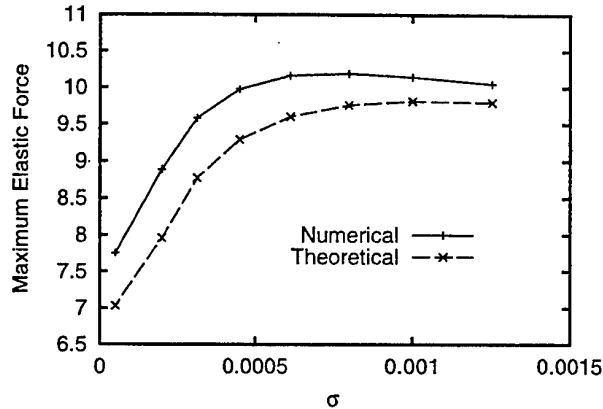


Fig. 9 Maximum elastic force versus σ .

In Fig. 10 the same comparison between theoretical and numerical predictions is performed in terms of hydrodynamic loads, and a good agreement is observed. It is interesting to remark that a value of the maximum hydrodynamic force larger than those predicted in both the extreme cases, $\sigma = 0$ and $\sigma \rightarrow \infty$, is found. Also a critical condition for the hydrodynamic force occurs, although it is not clear if and how it is related to σ_{cr} .

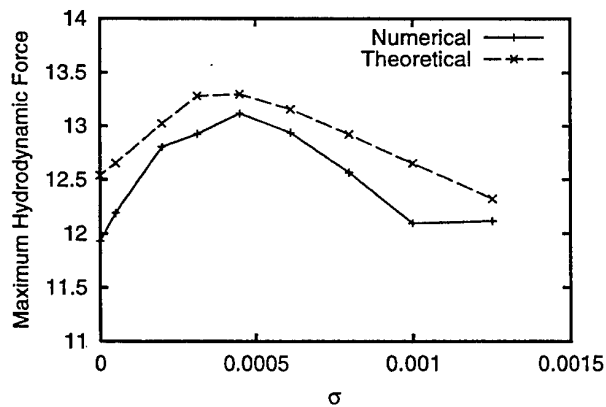


Fig. 10 Maximum hydrodynamic force versus σ .

CONCLUDING REMARKS

The effects of the impact of an elastic oscillator on the water surface have been analyzed. The hydrodynamic load acting on the impacting body is computed by a fully non linear boundary element technique. Since in this kind of problem the velocity reduction of the entering body plays a key role, the dynamic equations of the system are coupled with the hydrodynamic computed force. A critical condition in both elastic and hydrodynamic forces arises when varying the stiffness of the connecting spring, that shows an important hydroelastic coupling.

A theoretical approach to the problem is able to recover a closed form expression of the spring constant leading to a critical condition for the elastic force. The same model can be also directly used to predict the evolution in time of both hydrodynamic and elastic forces and a good agreement with the fully numerical simulation has been achieved.

ACKNOWLEDGMENTS

This work was supported by the *Ministero dei Trasporti e della Navigazione* in the frame of INSEAN research plan 1997-99.

REFERENCES

1. von Karman, T., "The impact of seaplane floats during landing," tn-321, 1929, NACA.
2. Korobkin, A., "Blunt-body impact on a compressible liquid surface," *J. Fluid Mech.*, Vol. 244, 1992, pp. 437-453.
3. Wagner, H., "über stoß- und gleitvorgänge an der oberfläche von flüssigkeiten," *Z. Angew. Math. Mech.*, Vol. 12, No. 4, 1932, pp. 192-215.
4. Zhao, R. and Faltinsen, O., "Water entry of two-dimensional bodies," *J. Fluid Mech.*, Vol. 246, 1993, pp. 593-612.
5. Zhao, R. and Faltinsen, O., "Water entry of axisymmetric bodies with and without flow separation," *Proceedings of the twenty-second Symposium on Naval Hydrodynamics*, Office of Naval Research, 1998.
6. R. Zhao, O. Faltinsen and Aarsnes, J., "Water entry of arbitrary two-dimensional sections with and without flow separation," *Proceedings of the twenty-first Symposium on Naval Hydrodynamics*, Office of Naval Research, 1996, pp. 408-423.
7. S. Muzaferija, M. Peric, P. Sames and Schellin, T., "A two-fluid navier-stokes solver to simulate water-entry," *Proceedings of the twenty-second Symposium on Naval Hydrodynamics*, Office of Naval Research, 1998.
8. Greenhow, M. and Lin, W.M., "Numerical simulation of nonlinear free surface flows generated by wedge entry and wavemaker motions," *Proceedings of the fourth International Conference on Numerical Ship Hydrodynamics*, Office of Naval Research, 1985, pp. 94-106.
9. Tanizawa, K., "A time domain simulation method for hydroelastic impact problem," *Proceedings of the second International Conference on Hydroelasticity in Marine Technology*, Kyushu University, 1998, pp. 119-127.
10. Carcaterra, A. and Ciappi, E., "Prediction of the compressible stage slamming force on rigid and elastic systems impacting on the water surface," *subm. to Non Linear Dynamics*, 1998.
11. Carcaterra, A. and Ciappi, E., "Impact of structures on the water surface: an upper bound analysis of the induced stress," *Proceedings of the twenty-third ISMA: International Conference on Noise and Vibration Engineering*, Vol. II, 1998, pp. 647-654.
12. Skalak, R. and Feit, D.A., "Impact on the surface of a compressible fluid," *Trans. ASME B: J. Engin. for Industry*, Vol. 88, No. b, 1966, pp. 325-331.
13. Vorus, W.S., "A flat cylinder theory for vessel impact and steady planning resistance," *J. of Ship Res.*, Vol. 40, No. 2, 1996, pp. 89-106.
14. Dobrovolskaya, Z.N., "On some problems of similarity flow of fluid with a free surface," *J. Fluid Mech.*, Vol. 36, 1969, pp. 805-829.
15. S.D. Howinson, J.R. Ockendon and Wilson, S.K., "Incompressible water-entry problems at small deadrise angles fluid with a free surface," *J. Fluid Mech.*, Vol. 222, 1991, pp. 215-230.
16. D.J. Kim, W. Vorus, A. Troesch and Gollwitzer, R., "Coupled hydrodynamic impact and elastic response angles fluid with a free surface," *Proceedings of the twenty-first Symposium on Naval Hydrodynamics*, Office of Naval Research, 1996, pp. 424-437.
17. Broch, J.T., *Mechanical Vibration and Shock Measurements*, Brüel & Kjær, 1980.
18. Meirovitch, L., *Elements of vibration analysis*, McGraw-Hill, 1986.

LIFTING SURFACES.

Chairman : L.Doctors

NUMERICAL INVESTIGATION ON SUBMERGED DOWNWARD LIFTING BODY AND ITS OPTIMIZATION WITH LOW WAVE RESISTANCE

Shigeki Nagaya¹, Kazu-hiro Mori², Yasuaki Doi²

¹Ship Performance Division, Ship Research Institute,

6-38-1, Shinkawa, Mitaka, Tokyo, 181-0004, JAPAN

Fax: +81-422-41-3053; E-Mail: nagaya@srinot.go.jp

²Faculty of Engineering, Hiroshima University

4-7-4, Kagamiyama, Higashi-Hiroshima, Hiroshima, 739-0046, JAPAN

Fax: +81-824-22-7194; E-Mail: kmori@ipc.hiroshima-u.ac.jp, doi@naoe.hiroshima-u.ac.jp

ABSTRACT

Wave making phenomenon of a submerged lifting body which generates downward lifting force is different from that of a conventional, upward lifting body. Theoretical analysis and experimental research suggest that wave making resistance of the submerged body with downward lifting force is less than that of a body without lifting force. Numerical investigations on the submerged lifting body are carried out to understand its characteristics.

For the numerical analysis, a direct boundary element method is introduced. To satisfy the Kutta condition at trailing edge, a wake sheet is placed behind the lifting body.

As the results of the computations, it is revealed that characteristics of the submerged downward lifting body is remarkably different from that of the upward one. An optimization method is applied to obtain a shape of lifting body with minimum drag.

NOMENCLATURES

x, y, z	: coordinate system	P_{TE+}, P_{TE-}	: pressure at TE^+, TE^-
U	: uniform incoming flow velocity	ΔP_{TE}	: $P_{TE+} - P_{TE-}$
g	: gravitational acceleration	$\Delta \phi_W$: potential jump on wake sheet
C	: chord length	H, G	: influence coefficient matrix
B	: span width	p, q	: nodal points
h	: submergence depth	T_p	: tent function around p
Λ	: aspect ratio, B / C	Ω_p	: region of all elements connect with p
ρ	: density of fluid	k_0	: wave number, g/U^2
α	: angle of attack	\mathbf{X}	: vector of unknown values
ϕ	: perturbation velocity potential	\mathbf{A}	: coefficients matrix of unknown values
∇^2	: Laplacian, $\partial^2/\partial x^2 + \partial^2/\partial y^2 + \partial^2/\partial z^2$	N	: total number of nodal points
\mathbf{n}	: normal direction of boundary, or time step it appears as superscripts	BS	: body surface
ϕ_n	: normal velocity, $\partial \phi / \partial n$	FS	: free surface
$\mathbf{n}_x, \mathbf{n}_z$: x, z component of normal vector	OB	: outer boundary
r	: distance between nodal points	W	: wake sheet
S	: boundary surface	\mathbf{B}	: coefficient matrix of wake contribution
t	: time	K	: number of vortex lines on wake sheet
ζ	: wave height	S_{PB}	: plane area of lifting body, $C \times B$
ζ_x, ζ_y	: derivatives of ζ with respect to x, y	C_P	: pressure coefficient
ϕ_x, ϕ_y, ϕ_z	: derivatives of ϕ with respect to x, y, z	C_D	: drag coefficient
P	: pressure	C_L	: lifting force coefficient
TE^+, TE^-	: trailing edge on upper and lower surfaces	C_B	: buoyancy force coefficient
		Fn	: Froude number, U / \sqrt{gC}

$z^+(x), z^-(x)$: offsets of upper and lower surface
$T(x)$: thickness function
$C(x)$: camber line function
X_T	: position of maximum thickness
T_m	: maximum thickness
α_{TE}	: angle at trailing edge
R	: curvature at leading edge
X_C	: position of maximum camber
C_m	: maximum camber
S_s	: sectional area of lifting body
LE, TE	: position of leading edge and trailing edge

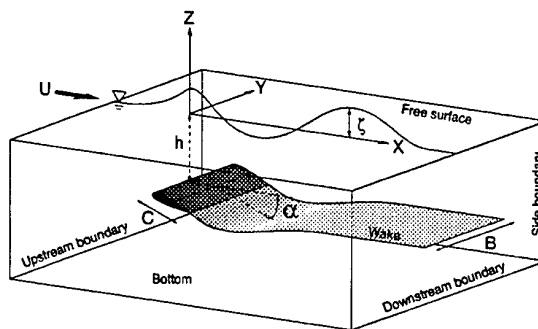


Figure 1: Coordinate system

INTRODUCTION

A submerged body which generates downward lifting force makes wave less than that which generates upward lifting force. Mori and et. al.[1] carried out an experimental research on a submerged ship which has foils generating downward lifting force to make the body submerged to reduce making waves. In the study, it is found that the total drag of the submerged body is less than that without wings; that is, the downward lifting force reduces the drag of the submerged body. And it is revealed that the reduction of the total drag comes from the component of wave making resistance. This phenomenon is very interesting from the view point of hydrodynamics, and it is useful also for the practical purpose.

On the other hand, theoretical investigations on the wave-less submerged body with downward force are done by Tulin and Tuck et. al. [2][3][4][5]. Their conclusion is that a singularity combination of a vertical dipole and anti-clockwise vortex can satisfies the free surface condition without free wave terms. It is suggested that, in 2-D case, the combined singularity with zero wave making resistance exists when it produces the downward force twice its buoyancy force.

As to the hydrofoils producing upward force, there are many researches in the past and their characteristics are well known as far as wave breaking does not takes place. However, wave making problem by a downward lifting body are not studied so far. Motivated by the above mentioned findings, in the present study, it is focused on the phenomenon found in [6][7]. The purpose is to reveal wave making resistance reduction by downward lifting force by numerical analysis. For the numerical method to solve free surface flow around a submerged lifting body, a boundary element method is used and jump of velocity poten-

tial on wake behind the lifting body is assumed to satisfy the Kutta condition.

As the results of computations, it is found that the wave patterns are much different from those of the body with upward lifting force and that a minimum drag is obtained when it generates downward force. Furthermore, an optimization method is applied to get shapes of the lifting body which has minimum drag. Through the optimization, the shape with low resistance is obtained which produces downward force.

COMPUTATIONAL METHOD

In the present paper, the viscosity and compressibility are neglected and an irrotational flow is assumed. Figure 1 shows a sketch of a submerged lifting body, computational domain and the coordinate system. The lifting body is fixed at the depth, h , and uniform incoming flow velocity U is assumed.

ϕ is the perturbation velocity potential around the submerged lifting body which satisfies the Laplace equation given by

$$\nabla^2 \phi = 0 \quad (1)$$

Applying the Green's theorem to the Laplace equation, following equation is obtained.

$$c\phi = \iint_S \frac{\partial \phi}{\partial n} \frac{1}{r} ds - \iint_S \phi \frac{\partial}{\partial n} \left(\frac{1}{r} \right) ds \quad (2)$$

where c is a solid angle of discretize panels.

Boundary conditions are given as follows,

· on body surface

$$\frac{\partial \phi}{\partial n} = -Un_x \quad (3)$$

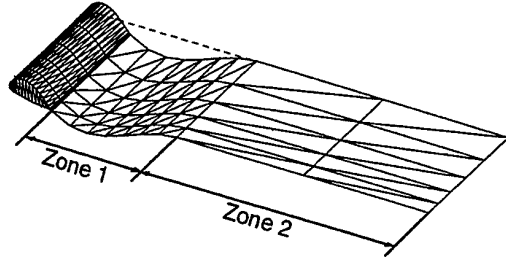


Figure 2: Wake sheet model

on free surface

$$\frac{\partial \zeta}{\partial t} = \phi_z - U\zeta_x - \phi_x\zeta_x - \phi_y\zeta_y \quad (4)$$

$$\frac{\partial \phi}{\partial t} = -g\zeta - U\phi_x - \frac{1}{2}(\phi_x^2 + \phi_y^2 + \phi_z^2) + \phi_z \frac{\partial \zeta}{\partial t} \quad (5)$$

The *Kutta* condition at the trailing edge of the lifting body is given by

$$\Delta P_{TE} = P_{TE^+} - P_{TE^-} = 0 \quad (6)$$

where TE^+, TE^- represent the nodal points on the upper and the lower trailing edges of the lifting body respectively. In order to satisfy the *Kutta* condition, a wake sheet is introduced. The wake sheet consists of a transitional zone (Zone 1) and a horizontal flat zone (Zone 2) as shown in Figure 2. The transitional zone starts from the trailing edge in the direction of the camber line of lifting body and extends to a certain location toward downstream. At the end of Zone 1, the wake sheet has a zero slope and the same height as that of the leading edge. Zone 2 extends far enough to the downstream. On the wake sheet, a velocity potential jump is assumed and its strength is iteratively determined so that the *Kutta* condition is satisfied. The strength is constant on each longitudinal line, but it varies in span direction.

Numerical Scheme

For the present computations, a direct boundary element method (BEM) is used [8]. Body surface, wake, free surface and outer boundary are divided into triangular elements, on which the values of functions are interpolated linearly. Equation (2) is discretized to the following system of linear equations

$$\sum_{q=1}^N H_{pq} \cdot \phi_q - \sum_{q=1}^N G_{pq} \frac{\partial \phi_q}{\partial n} = 0 \quad (7)$$

; $p = 1, 2, \dots, N$

H, G are influence coefficients as follows,

$$H_{pq} = \iint_{\Omega_q} T_q \frac{\partial}{\partial n} \frac{1}{4\pi r} d\Omega \quad (8)$$

$$G_{pq} = \iint_{\Omega_q} T_q \frac{1}{4\pi r} d\Omega \quad (9)$$

where T_q is the tent function around the node q .

Boundary conditions on the free surface Equations (4)(5) are discretized by following finite difference approximations.

$$\left(\frac{\partial f}{\partial x} \right)_{i,j} = \frac{2f_{i+1,j} + 3f_{i,j} - 6f_{i-1,j} + f_{i-2,j}}{6\Delta x} \quad (10)$$

$$\left(\frac{\partial f}{\partial x} \right)_{i,j} = \frac{f_{i,j+1} - f_{i,j-1}}{2\Delta y} \quad (11)$$

where f means ϕ and ζ and i, j is ordering number on free surface mesh in the direction of x, y respectively.

Upstream boundary conditions are given as follows.

$$\left(\frac{\partial \zeta}{\partial x} \right)_{i,j} \Big|_{i=1} = 0 \quad (12)$$

$$\left(\frac{\partial \phi}{\partial x} \right)_{i,j} \Big|_{i=1} = 0 \quad (13)$$

To make the numerical method computationally efficient, an implicit time-marching method is employed as follows,

$$\frac{\zeta_{i,j}^{n+1} - \zeta_{i,j}^n}{\Delta t} = \frac{\left(\frac{\partial \zeta}{\partial t} \right)_{i,j}^{n+1} + \left(\frac{\partial \zeta}{\partial t} \right)_{i,j}^n}{2} \quad (14)$$

$$\frac{\phi_{i,j}^{n+1} - \phi_{i,j}^n}{\Delta t} = \frac{\left(\frac{\partial \phi}{\partial t} \right)_{i,j}^{n+1} + \left(\frac{\partial \phi}{\partial t} \right)_{i,j}^n}{2} \quad (15)$$

where $\left(\frac{\partial \zeta}{\partial t} \right)_{i,j}^{n+1}$, $\left(\frac{\partial \zeta}{\partial t} \right)_{i,j}^n$ and $\left(\frac{\partial \phi}{\partial t} \right)_{i,j}^{n+1}$, $\left(\frac{\partial \phi}{\partial t} \right)_{i,j}^n$ are the finite difference forms of r.h.s.

of Equation (4) and (5) respectively. Because these two equations are both nonlinear and coupled with each other, they have to be solved by iterative procedure. The initial value for the iterative procedure is provided by the extrapolation of the solutions at two previous time steps.

For open boundary conditions, upstream boundary, side boundary, and bottom boundary, the *Neumann* condition is assumed.

$$\frac{\partial \phi}{\partial n} = 0 \quad (16)$$

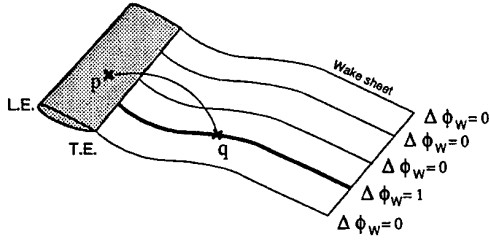


Figure 3: Sketch of unit $\Delta\phi_W$ contribution

On the downstream boundary, following condition is employed.

$$\frac{\partial\phi}{\partial n} = \frac{\partial\phi}{\partial n} \Big|_{z=0} \cdot e^{k_0 z} \quad (17)$$

where $\phi_n|_{z=0}$ is calculated by the differentiation of ϕ on the free-surface.

Depending on these boundary conditions, the known and the unknown variables of Equation (7) are separated into both sides as follows,

$$\begin{aligned} \sum_{q=1}^N A_{pq} \cdot X_q &= - \sum_q^{BS} G_{pq} \frac{\partial\phi_q}{\partial n} \\ &\quad - \sum_q^{FS} H_{pq} \cdot \phi_q - \sum_q^{OB} G_{pq} \frac{\partial\phi_q}{\partial n} \\ &\quad - \sum_q^W H_{pq} \cdot \Delta\phi_W \end{aligned} \quad (18)$$

; $p = 1, 2, \dots, N$

where X_q is a vector of the unknown values, A_{pq} coefficients matrix at node p against q .

$$X_q = \begin{Bmatrix} [\phi]_{BS} \\ [\phi_n]_{FS} \\ [\phi]_{OB} \end{Bmatrix} \quad (19)$$

$$A_{pq} = \left\{ \{H_{pq}\}_{q \in BS}, \{G_{pq}\}_{q \in FS}, \{H_{pq}\}_{q \in OB} \right\} \quad (20)$$

This system of linear equations is solved by iterative procedure.

In the present study, a wake sheet behind the lifting body is introduced and a jump of the velocity potential is assumed on the wake sheet in order to satisfy the *Kutta* condition. The strength of the jump is determined by solving following

system of equations.

$$\begin{aligned} \sum_{j=1}^K B_{ij}^{(l)} \cdot \left\{ \Delta\phi_{Wj}^{(l+1)} - \Delta\phi_{Wj}^{(l)} \right\} &= \\ \Delta P_{TEi}^{(l+1)} - \Delta P_{TEi}^{(l)} \end{aligned} \quad (21)$$

; $i = 1, 2, \dots, K$

where K shows the number of vortex lines on the wake sheet, i, j the ordering number of vortex line, l the number of iteration, and B the matrix of the coefficient given by,

$$B_{ij}^{(l)} = \frac{\partial(\Delta P_{TEi})}{\partial \Delta\phi_{Wj}} \approx \frac{\Delta P_{TEi}^{(l)} - \Delta P_{TEi}^{(l-1)}}{\Delta\phi_{Wj}^{(l)} - \Delta\phi_{Wj}^{(l-1)}} \quad (22)$$

; $i, j = 1, 2, \dots, K$

Equation (21) is solved iteratively so that $\Delta P_{TEi}^{(l+1)}$ becomes zero.

Equation (18) can be separated into the following two equations

$$\begin{aligned} \sum_{q=1}^N A_{pq} \cdot X_{0q} &= - \sum_q^{BS} G_{pq} \frac{\partial\phi_q}{\partial n} \\ &\quad - \sum_q^{FS} H_{pq} \cdot \phi_q - \sum_q^{OB} G_{pq} \frac{\partial\phi_q}{\partial n} \end{aligned} \quad (23)$$

$$\sum_{q=1}^N A_{pq} \cdot X_{Wq} = - \sum_q^W H_{pq} \cdot \Delta\phi_W \quad (24)$$

where X_0 is the solution without contribution of the wake and X_W represents its contribution.

The r.h.s. of Equation (24) can be written in the form of

$$\sum_q^W H_{pq} \cdot \Delta\phi_W = \sum_{j=1}^K \hat{H}_{pj} \cdot \Delta\phi_{Wj} \quad (25)$$

$$\hat{H}_{pj} = \sum_{q \in \text{line } j} H_{pq} \quad (26)$$

To avoid to solve Equation (24) at every time when $\Delta\phi_W$ is updated, the contribution of a unit strength distributed on each wake line is calculated in advance by solving the following equation

$$\sum_{q=1}^N A_{pq} \cdot \tilde{X}_{jq} = -\hat{H}_{pj} \quad (27)$$

where $\Delta\phi_{Wj} = 1$ on the line j and $\Delta\phi_W = 0$ on the other lines. The solution of Equation (24) can be obtained by taking a weighted summation of

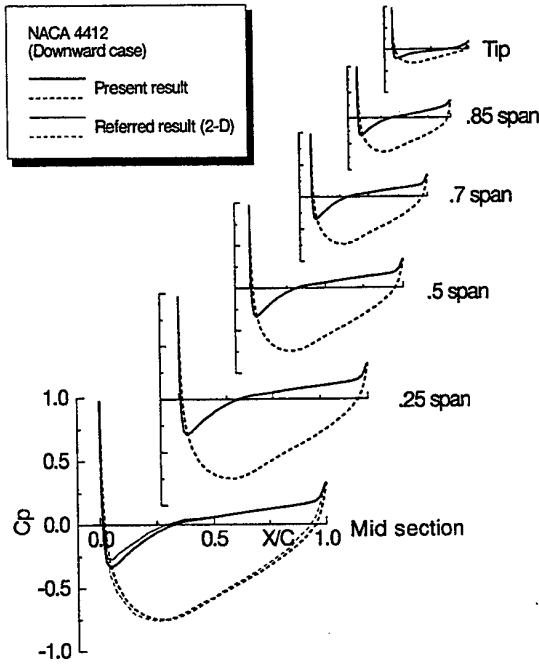


Figure 4: Comparison of pressure distributions on NACA4412

$\hat{\mathbf{X}}^{(k)}$ as follows,

$$\mathbf{X}_{Wq} = \sum_{j=1}^K \Delta\phi_{Wj} \cdot \tilde{\mathbf{X}}_{jq} \quad (28)$$

Finally, the solution of Equation (18) can be obtained by summing up \mathbf{X}_0 and \mathbf{X}_{Wq} .

$$\mathbf{X}_q = \mathbf{X}_{0q} + \mathbf{X}_{Wq} \quad (29)$$

The pressure acting on the body surface is determined by *Bernoulli's* equation.

$$\frac{\partial\phi}{\partial t} + \frac{P}{\rho} + \frac{(U + \phi_x)^2 + \phi_y^2 + \phi_z^2}{2} + g\zeta = \frac{U^2}{2} \quad (30)$$

The drag and the lift force coefficients, C_D and C_L , are calculated by the integration of the pressure on the body surface.

$$C_D = \frac{1}{S_{PB}} \int_{BS} C_P \cdot \mathbf{n}_x ds \quad (31)$$

$$C_L = \frac{1}{S_{PB}} \int_{BS} C_P \cdot \mathbf{n}_z ds \quad (32)$$

where C_P is the pressure coefficient normalized by $\frac{1}{2}\rho U^2$ and S_{PB} the plane area of the lifting body given by the product of the chord length and the span width.

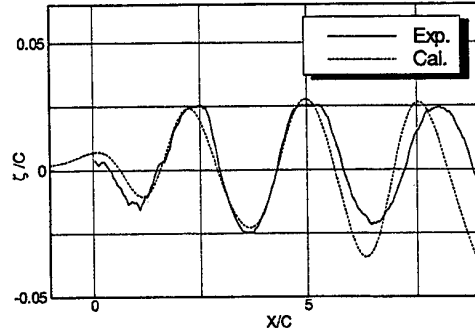


Figure 5: Comparison of wave profiles between the measured and the computed, along $Y = 2.48C$

COMPUTATIONAL RESULTS

The flow around a hydrofoil in a unbounded fluid domain is first computed in order to validate the numerical method for a lifting body. The body has NACA4412 sectional profile whose aspect ratio Λ is 14. The computation is carried out at zero attack angle. The pressure distribution on the foil is shown in Figure 4 together with a published 2-D result by Nakatake[9]. The computed pressure distribution in the mid-section agrees satisfactorily well with the published data.

Figure 7 shows a comparison of wave profiles by NACA4412 with negative camber whose aspect ratio Λ is 2, between the computed and the experimental results which are longitudinal cut data along $Y = 2.48C$ at $Fn = 0.7$ and the submergence depth is $h = 0.5C$. They agree well with each other. We can conclude that the present numerical scheme is well qualified for the numerical studies.

In the present paper, to simplify understanding the problem, a 3-dimensional rectangular hydrofoil which has a displacement volume and produces lifting force is studied as a lifting body.

First, to demonstrate the difference of wave making phenomenon between the submerged lifting bodies with upward and downward lifting force, flows around a lifting body with NACA0012 section are computed. The aspect ratio of the body Λ is 2 and it is fixed at the submergence depth of $0.5C$. The computations are carried out at the speed of $Fn = 0.9$.

Figure 6 shows the wave patterns for the cases where the angle of attack α is $+5^\circ$ and -5° . The cases of $\alpha = +5^\circ$ and $\alpha = -5^\circ$ correspond to the cases where the lifting force is upward and down-

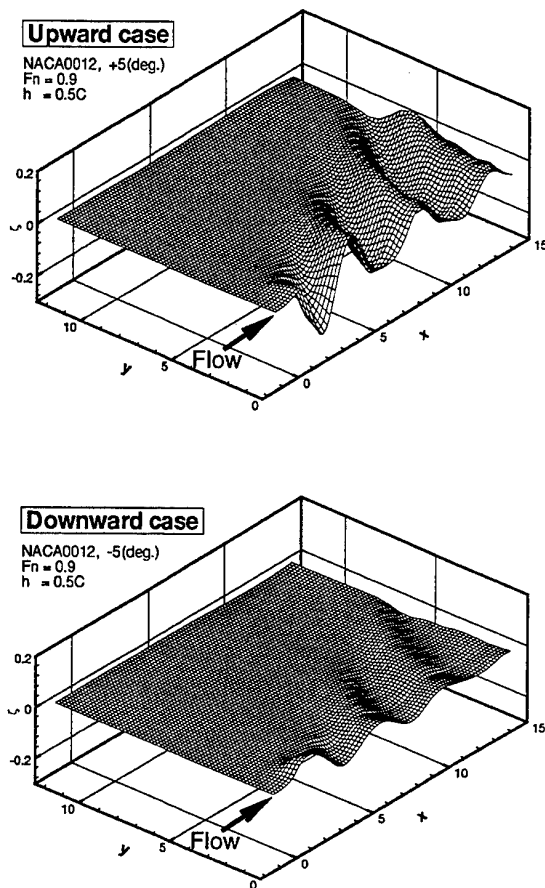


Figure 6: Comparison of wave patterns between the upward and the downward lifting forces

ward respectively. It is found that the two wave patterns are remarkably different each other. The maximum wave height of the downward case is almost half the upward case as shown in Figure 7.

The differences of the hydrodynamic force between them are shown in Table 1. Here the drag coefficient C_D represent the sum of the induced drag and the wave making resistance. C_L of the downward case is twice the upward case. However, C_D of the downward case is about 30% less than that of the upward case. It is confirmed that clear effects of the free surface interaction exist. The angle of attack of the lifting body changes the elevation of the free surface and it is expected that wave making resistance of the lifting body is reduced by the downward force.

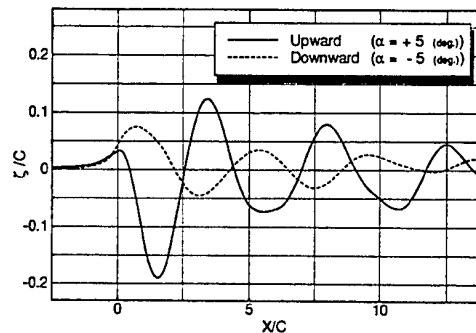


Figure 7: Comparison of wave profiles between the upward and the downward lifting forces

Table 1: Comparison C_D and C_L

	Upward (+5°)	Downward (-5°)
C_D	4.1×10^{-2}	2.8×10^{-1}
C_L	2.8×10^{-2}	-6.1×10^{-1}

Computations of the lifting body with various angle of attack are carried out to make clear the relation between the drag and the downward lifting force. The conditions of computations are the same as those mentioned above. Figure 8 shows the results of computation where the abscissa is C_L and the coordinate shows C_D where negative C_L means downward force and the positive upward. The angle of attack α is changed from -6° to $+6^\circ$ at every 2° . The C_D curve has a minimum value near $\alpha = 0^\circ$ where the lifting body produces downward force. In unbounded flow, drag of a symmetric lifting body becomes zero at zero angle of attack, because it does not produce lifting force. In free surface flow, however, minimum value of drag is obtained which produces downward lifting force. It seems the reason why the induced drag of a lifting body is increased with producing lifting force, but wave making resistance can be reduced by the downward lifting force, so balance of both component is important.

In Figure 8, the buoyancy force coefficient C_B of the lifting body is plotted, too. It is found that the downward lifting force of the lifting body is close to the buoyancy force of itself when the of it is minimum. The relation between downward force and buoyancy force of the lifting body in terms of the drag reduction will be studied in the future works.

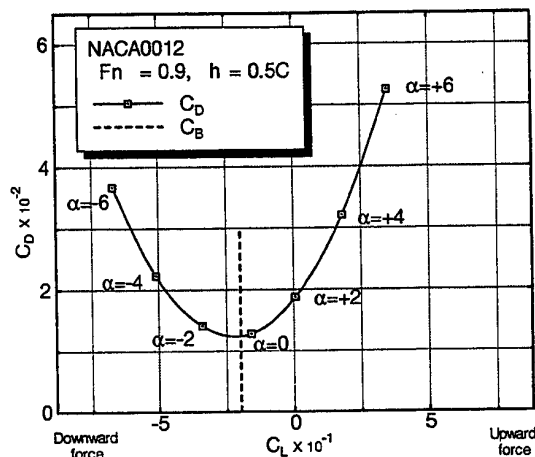


Figure 8: C_D vs C_L for angle of attack variation

OPTIMIZATION OF SUBMERGED LIFTING BODY WITH MINIMUM DRAG

Optimization method

In the present study, the optimization method is applied in order to obtain the sectional profile of lifting body whose drag is minimum. As the optimization method, the quasi-Newton method is used. This method is one of the local minimizing scheme without constraints.

In the optimization, the total drag of a submerged lifting body is estimated as the objective function, and the shape is expressed by functional form so that arbitrary shape of the lifting body can be formed. Here, the following parameters are fixed for the optimization.

- chord length
- span width
- angle of attack
- sectional area of the lifting body
- curvature at the leading edge

Definition of lifting body shape

The sectional profile of lifting body is defined by functional form. The sectional profile is expressed by the two functions which are similar to the definition of NACA four-digit series, thickness distribution $T(x)$, and camber line $C(x)$ respectively.

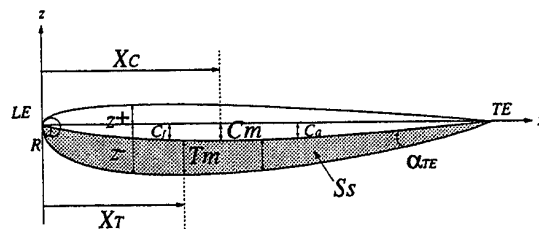


Figure 9: Definition of sectional profile

The offsets of the upper and the lower surfaces at the position x on the lifting body $z^+(x)$ and $z^-(x)$ are determined by sum of $T(x)$ and $C(x)$ as follows,

$$z^+(x) = C(x) + T(x) \quad (33)$$

$$z^-(x) = C(x) - T(x) \quad (34)$$

The thickness function $T(x)$ is formulated depending on the following conditions.

1. thickness is zero at the leading edge
2. gradient is infinite at the leading edge
3. curvature R is given at the leading edge
4. maximum thickness T_m is given at position X_T
5. gradient is zero at X_T
6. thickness is zero at the trailing edge
7. angle at the trailing edge α_{TE} is given by α_{TE}
8. sectional area is given by S_s
9. thickness is not zero except at the leading and trailing edges

Depending on these conditions, $T(x)$ is given by a following equation.

$$T(x) = \sqrt{x(TE-x)} \exp[t_0 + t_1x + t_2x^2 + t_3x^3 + t_4x^4] \quad (35)$$

$$(LE \leq x \leq TE)$$

where LE means the position of leading edge, and TE that of trailing edge. Condition 1, 2, 6 and 9 are included into the equation implicitly, and the

coefficients $t_0 \sim t_4$ can be obtained by solving following equations in terms of other conditions.

$$\begin{cases} T(X_T) = T_m \\ T'(X_T) = 0 \\ T'(TE) = -\tan(\alpha_{TE}) \end{cases} \quad (36)$$

$$R = \frac{(1 + T'(LE)^2)^{3/2}}{|T''(LE)|} \quad (37)$$

$$S_s = \int_{LE}^{TE} T(x) dx \quad (38)$$

Finally, $T(x)$ can be determined with the parameters X_T , T_m , α_{TE} , R and S_s .

$C(x)$ is separated into a forward part $C_f(x)$ and an after part $C_a(x)$ at X_C . Forward part of camber line $C_f(x)$ has following conditions.

- Camber is zero at the leading edge.
- Maximum camber C_m is given at position X_C .
- Gradient is zero at X_C .

and after part $C_a(x)$ has

- Maximum camber C_m is given at X_C .
- Gradient is zero at X_C .
- Camber is zero at the trailing edge

$$C_f(x) = c_1 + c_2 x^2 \quad (39)$$

$(LE \leq x \leq X_C)$

$$\begin{cases} C_f(X_C) = C_m \\ C'_f(X_C) = 0 \end{cases} \quad (40)$$

$$C_a(x) = c_3(x - TE) + c_4(x - TE)^2 \quad (41)$$

$(X_C \leq x \leq TE)$

$$\begin{cases} C_a(X_C) = C_m \\ C'_a(X_C) = 0 \end{cases} \quad (42)$$

The coefficients $c_1 \sim c_4$ are determined with X_C and C_m , and $C(x)$ is obtained.

The optimization computation can be carried out by tuning the coefficients sets of t_i and c_i for the drag to be minimum.

Computational results

In the optimization, the sectional area of the lifting body S_s and the curvature at the leading edge R are fixed to the initial values, and the other five parameters, X_T , T_m , α_{TE} , X_C , C_m , are optimized. Computations are carried out at $Fn = 0.9$

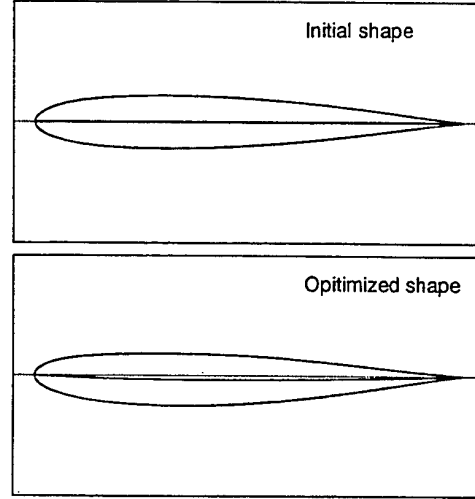


Figure 10: Comparison of profile, initial; NACA0012

Table 2: Comparison of coefficients, initial; NACA0012

	Initial	Optimized
C_D	1.3×10^{-2}	1.2×10^{-2}
C_L	-1.6×10^{-1}	-2.4×10^{-1}

and the submergence depth $h = 0.5C$. The angle of attack is 0° .

As the initial shapes for the optimization, two profiles are used; NACA0012 and NACA4412. NACA4412 has a negative camber and it produces much larger downward lifting force. The lifting force of NACA0012 is rather small and the drag of NACA4412 is also larger.

Figure 10 shows the sectional profile of initial body and that of optimized body. It is found that the camber line is slightly curved in negative direction but other parameters is not much changed. Hydrodynamic force is compared in Table 2. Minimized C_D is decreased to 90% of initial C_D . On the other hand, C_L of optimized body is increased by 50% from that of the initial one.

The optimized shape of NACA4412 is shown in Figure 11 together with its initial shape. C_D and C_L of optimized body from NACA4412 is shown in Table 3. In this case, minimized C_D is decreased to 55%, and C_L of optimized body is also decreased to half of initial value. It is interesting that the values of C_D and C_L of the two optimized shapes are the same although their op-

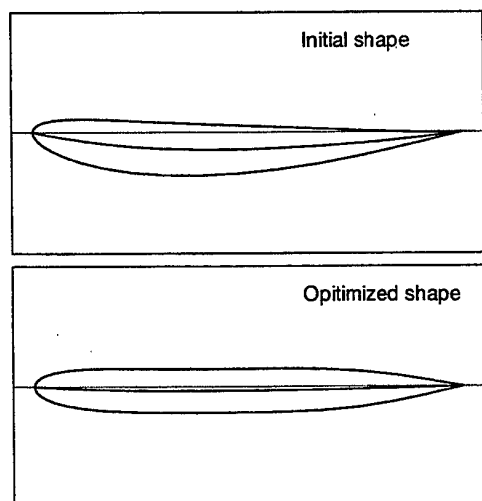


Figure 11: Comparison of profile, initial; NACA4412

Table 3: Comparison of coefficients, initial; NACA4412

	Initial	Optimized
C_D	2.2×10^{-2}	1.2×10^{-2}
C_L	-4.7×10^{-1}	-2.4×10^{-1}

timized shapes are different each other.

It is also interesting that the hydrodynamic forces of the two optimized bodies are the same although their initial lifting forces are much different each other.

Figure 12 shows the comparison of the pressure distributions on the optimized bodies between the two initial shapes of NACA0012 and NACA4412. Although C_D and C_L are the same, the pressure distributions are not always the same. Both C_D and C_L are the same as the minimum values of the C_D curve shown in Figure 8. It can be concluded that the lifting force is optimal for the body with a minimum drag of the lifting body under the given condition of Froude number, the submergence depth and the displacement volume.

CONCLUDING REMARKS

It is investigated by numerical computations that the downward lifting force reduces resistance of submerged body. The relation between the drag and the downward lifting force of a submerged lifting body is made clear. An optimization method is applied to minimize resistance of the

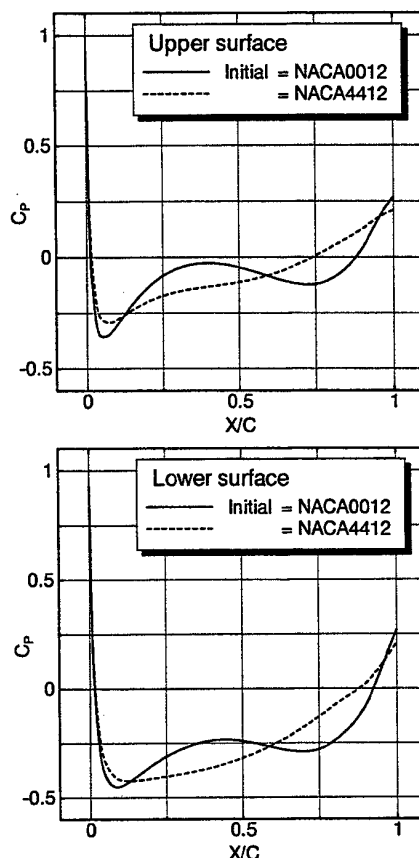


Figure 12: Comparison of pressure distribution on optimized body

lifting body by changing the shape. And a shape of the submerged lifting body is obtained whose resistance is less than the that of initial body.

By the present study, characteristics of a submerged downward lifting body are revealed. The study on the characteristic of the aspect ratio and an optimization of more practical 3-dimensional lifting body shapes are left for future works.

REFERENCES

1. Mori K., et.al., "A study on Semi-Submersible High Speed Ship with Wings," Jour. of Soc. of Naval Arch. of Japan, vol. 164, 1988.
2. Tulin, M. P., "Free Surface Flows without Waves," HYDRONAUSTICS, Incorporated Technical Report 8035-2, 1982.
3. Tuck, E. O., "A Submerged Body with Zero Wave Resistance," Journal of Ship Research, Vol. 33, No. 2, Jun. 1989, pp. 81-83.
4. Tuck, E. O., and Tulin, M. P., "Submerged

Bodied That Do Not Generate Waves," Proc. of 7th International Workshop on Water Waves and Floating Bodies, Val de Reuil, France, 1992,

5. Tulin, M. P., and Oshri, O., "Free Surface Flows without Waves," Proc. of 20th Symposium on Naval Hydrodynamics, Santa Barbara, USA, 1994,

6. Nagaya, S., Xu, Q., Mori, K. and Doi, Y., "Numerical Investigation on Low Wave Resistance Lifting Bodies," Proc. of the 2nd International Conference on Hydrodynamics, University of Hong Kong, 1996.

7. Nagaya, S., Xu, Q. and Mori, K., "On Resistance of a Submerged Lifting Body which Generates Downward Lifting Force," Jour. of Soc. of Naval Arch. of Japan, vol. 182, 1997.

8. Xu, Q. and Mori, K., "A Boundary Element Method for the Numerical Simulation of 3-D Nonlinear Water Waves Created by a Submerged Lifting Body," Jour. of Soc. of Naval Arch. of Japan, vol. 167, 1990.

9. Nakatake, K., et.al. "A Simple Calculation Method for Thick Wing," The West-Japan Society of Naval Architects, Vol.88, 1994.

NUMERICAL ANALYSIS OF VISCOUS FLOW PAST A ROUNDED LEADING EDGE OF A LIFTING FOIL WITH USE OF MATCHED ASYMPTOTICS

Kirill V. Rozhdestvensky, Wu-Chun-Kai
Department of Applied Mathematics and Mathematical Modeling
St. Petersburg State Marine Technical University
Lotsmanskaya St. 3, 190008 St. Petersburg, Russia
fax: (812)2197866, e-mail: xmas@infopro.spb.su

ABSTRACT

The authors consider a problem for a viscous flow near the leading edge of a thin lifting foil. In vicinity of a rounded leading edge of analytical foil the flow is reduced to that around an osculating parabola. Corresponding (inner) Navier-Stokes equations are rendered non-dimensional with use of radius of curvature of the edge and velocity of the local oncoming flow. Therewith, characteristic Reynolds number of the flow under consideration is two orders of magnitude smaller than based on the chord of the foil. Far from the parabolic edge the (outer) flow is considered inviscid and is constructed with use of a thin airfoil theory. The far-field condition to solve the (inner) Navier-Stokes equations is obtained through asymptotic matching and applied on the boundary of the inner domain. For the purpose of numerical computation of the Navier-Stokes equations the authors employ finite difference technique, implicit scheme of solution, the grid based on parabolic coordinates and appropriate turbulence model. To secure convergence of the solution for high magnitudes of local Reynolds number and provide more detailed viscous flow description in immediate proximity to solid boundary, use is made of a multi-block approach. Therewith, the flow data is iteratively transferred from one block to another, the computation being performed simultaneously within only one block. Results are presented on pressure and shear stress distribution along the contour of the parabola. It is shown that for certain degree of asymmetry of the flow, which can be translated into displacement of the stagnation point, there may occur separation of the flow from the contour of the parabola.

INTRODUCTION

Flows near leading edges are known to play significant role from viewpoint of efficiency of wings and propeller blades. These domains, albeit small in dimensions, are characterized by large surface curvature and contain regions of both stagnating and accelerating flow. The latter circumstance may cause occurrence of such phenomena as cavitation, separation, generation of noise and even ice accretion (in the case of airplane wings).

At the same time, both experimental and theoretical analysis of the flow in immediate vicinity of the leading edge is not easy because of required high resolution of corresponding numerical and measuring technique. (Note that for analytical foil sections, radius of curvature of the lead-

ing edge is proportional to the square of relative thickness of the foil).

An approach to analytical analysis of steady potential flow near leading edges of foils, supplementing (linear) thin airfoil theory, was advocated by Van-Dyke [1] and Lighthill [2] with use of singular perturbation technique, methods of matched asymptotic expansions (MAE) and strained coordinates. It was shown that for any analytical foil section, its geometry near rounded leading edge can be approximated by an osculating parabola. Resulting local flow solutions were shown to be of simple form and to contain two free parameters, defining position of stagnation point on the contour of the parabolic edge. The latter parameters were determined by means of asymptotic matching of the local flow description with the outer flow solution based on a thin air-

foil (linear) theory. In Darrozes [3], Rozhdestvensky [4], Rozhdestvensky & Mishkevich [5] and Rozhdestvensky, Mishkevich & Bubentsov [6] the approaches of [1] and [2] were extended to unsteady and three-dimensional case. In particular, in [5] it was demonstrated that for Strouhal numbers of the order of unity, the flow near the leading edge can be viewed as quasi-steady, and time derivative of the velocity potential in the Lagrange integral can be omitted with asymptotic error of $O(\delta^2)$, where δ is maximum relative thickness of the foil section. Also derived in [5] were simple closed expressions for the minimum of pressure on the parabola as well as for abscissas of stagnation point and that of minimum pressure. Several papers were dedicated to analysis of a viscous flow past a parabolic edge. Ermak [7] and Werle [8] performed calculations of a laminar boundary layer on a parabola. The outer potential solution, used in [7] as an input for boundary layer calculations was obtained by Lighthill method [2], and laminar boundary layer equations were expressed in terms of a stream function and new independent coordinates. Calculations of boundary layer (with and without suction) were conducted, starting from the stagnation point determined through local potential solution. Results were presented for a concrete case of an elliptic foil in terms of a shear stress function versus stretched arc coordinate S , measured from the vertex of the leading edge and related to its radius of curvature. Two relative foil thicknesses $\delta = 0.1$ and $\delta = 0.2$ and a range of angles of attack α were considered. It was found that for thin foils (independently of Reynolds number) the laminar boundary layer separated when the ratio α/δ reached values $0.6 - 0.7$ and at S close to $7 - 8$. Approximate study of laminar separation was carried out in [9], where integral relationship of momentum for an unsteady laminar boundary layer was integrated analytically with use of Kochin-Loitsyansky method and closed form solution for a potential flow past a parabola. For the case of elliptic foil this study predicted laminar flow separation at $\alpha/\delta \approx 0.65$ and stretched (related to the radius of curvature of the elading edge) abscissa $X \approx 5.8$. Later Tuck [10] proposed similar approach to find a simple criterium for prediction of laminar flow separation from the contour of osculating parabola.

An interesting asymptotic analysis of separation phenomena on the leading edge of a thin foil was conducted by Ruban [11] who used matched asymptotics and a concept of self-similar separation

to study conditions of appearance of a laminar separation bubble on the contour of the parabola. It should be noted that role of the bubble in the mechanism of leading edge separation was investigated by many researchers, see Tani [12]. According to existing experimental data, with growth of the incidence of the wing the flow pattern changes in the following way. For small angles of attack the flow in the vicinity of the leading edge is unseparated. Separation occurs when the angle of attack reaches a certain critical magnitude, depending on form of the foil and Reynolds number. Therewith, on the upper surface of the foil there is formed a closed stationary separation zone of small extent, which has practically no effect on the flow around the foil. Subsequent increase of the incidence results in a sudden destruction of that zone. As a result a new regime of flow is formed, characterized by a developed separation region, covering the whole upper side of the foil or, at least, its significant part. This process is accompanied by an abrupt change of characteristics of the foil toward diminution of lift and increment of drag. As indicated by Ruban, this phenomenon is of special interest from viewpoint of theoretical investigation. As a matter of fact, in normal conditions the Reynolds number based on leading edge radius, is still not large enough for turbulisation of the flow. Therefore, the flow around the leading edge of a thin foil (at least, in absence of separation) is described by stationary Navier-Stokes equations. At the same time, the Reynolds number is sufficiently large for application of asymptotic analysis. Interesting results, related to the problem of prediction of the leading edge separation and prediction of "burst" of laminar separation bubble, preceeding the global stall of the flow from the foil and subsequent drop of lift-to-drag ratio, are reported in [13]-[15].

FORMULATION AND SOLUTION OF THE PROBLEM

Description of the Farfield

The farfield solution makes use of analytical expressions for complex velocity potential $F(Z)$ for the flow past a parabola in inviscid flow. As per [1] and [4] this function can be shown to have the following form

$$F(Z) = U_1 F_s(Z) + U_2 F_c(Z), \quad (1)$$

where $Z = X + iY$ is a stretched complex coordinate with $X = (1 + x)/\rho_{le}$ and $Y = y/\rho_{le}$,

ρ_{le} represents radius of curvature of the leading edge (Note, that for analytical foil families with rounded leading edge the radius of curvature of the edge can be shown to be of the order of $O(\delta^2)$, where δ is maximum relative thickness of the foil). Complex functions $F_s(Z)$ and $F_c(Z)$ represent contributions to the complex velocity potential, associated correspondingly with symmetrical and circulatory flow past a parabolic nose, and are given by the following expressions

$$\begin{aligned} F_s(Z) &= Z - 1 - i\sqrt{2Z-1} \\ F_c(Z) &= \sqrt{Z-1/2}. \end{aligned} \quad (2)$$

Parameters U_1 and U_2 , depending on the geometry and kinematics of the foil, can be determined by means of asymptotic matching with a linear theory solution valid far from the edge, see [5]. Physically, these parameters can be viewed respectively as a local oncoming velocity in vicinity of the edge and velocity of the circulatory flow at the vertex of the parabola.

The complex conjugate velocity of the potential flow past a parabola can be found by way of differentiation of $F(Z)$ with respect to Z to give

$$\begin{aligned} \frac{dF}{dZ} &= V_x - iV_y = \\ &= U_1 \left(1 - \frac{i}{\sqrt{2Z-1}}\right) + U_2 \frac{1}{\sqrt{Z-1/2}}. \end{aligned} \quad (3)$$

The pressure coefficient at arbitrary point Z of the nearfield can be found as

$$\begin{aligned} p = 1 - V^2 &= 1 - V_x^2 - V_y^2 = 1 - \frac{dF}{dZ} \frac{d\bar{F}}{d\bar{Z}} \\ V &= \left| \frac{dF}{dZ} \right| \end{aligned} \quad (4)$$

It should be mentioned that for unsteady motions of the foil with Strouhal numbers of the order of unity the flowfield in the vicinity of the leading edge can be viewed as *quasi-steady* so that time derivative term in Lagrange integral can be omitted with the error of the order of $O(\delta^2)$, where δ is a maximum relative thickness of the foil. Using (3), it is easy to determine both velocity and pressure coefficient on the surface of the parabola, i.e. for $Z = X \pm i\sqrt{2X}$, through the following equations

$$V(X) = \sqrt{\frac{X}{X+1/2}} \left(U_1 \pm \frac{U_2}{\sqrt{X}} \right), \quad (5)$$

$$p(X) = 1 - \frac{X}{X+1/2} \left(U_1 \pm \frac{U_2}{\sqrt{X}} \right)^2. \quad (6)$$

Note, that \pm signs in equations (5) and (6) are associated respectively with the upper and lower sides of the parabola. Consideration of the expression (5) enables to find position of stagnation point within the potential flow formulation. Equating velocity on the surface of the parabola to zero, one finds

$$X_s = \frac{U_2^2}{U_1^2}. \quad (7)$$

One can also find position of the minimum of pressure (maximum suction) on the surface of the parabola by means of differentiating the equation (5) with respect to X and equating the result to zero. Denoting abscissa of the point of minimum pressure as X_m , one arrives at the following expression

$$X_m = \frac{U_1^2}{4U_2^2}. \quad (8)$$

It is interesting to see from the expressions (7) and (8) that within potential flow formulation the abscissas X_s and X_m are related to each other in the following way

$$X_s X_m = \frac{1}{4}. \quad (9)$$

The results expressed by the formulae (7), (8) and (9) were published in [5]. As follows from the previous analysis, all major quantities of the potential flow around a parabolic leading edge depend on two parameters, namely U_1 and U_2 . Some concrete expressions for U_1 and U_2 can be presented as examples with reference to [4] and [5]

- Elliptic foil

$$U_1 = 1 + \delta, \quad U_2 = \frac{\alpha}{\delta} \sqrt{2}. \quad (10)$$

- Symmetric foil NACA-66012, performing harmonic heave oscillations with the amplitude h_o

$$U_1 = 1 + 0.817\delta,$$

$$\begin{aligned} U_2(k, t) &= k \frac{h_o}{\delta} \sqrt{2} [G(k) \cos kt + \\ &\quad + F(k) \sin kt], \end{aligned} \quad (11)$$

where $k = \omega C_o / 2U_o$ is Strouhal number, $F(k)$ and $G(k)$ represent real and imaginary parts of Theodorsen function. Further on, analysis of the viscous flow past

a parabolic edge will be conducted versus parameter $a = U_2$ on an assumption that parameter U_1 is close to unity.

Near Field Description

In the near-field, i.e. close to the leading edge, description of the flow is based on Navier-Stokes equations, rendered nondimensional with use of the oncoming flow velocity and the radius ρ_{le} of the leading edge. Consequently, the Reynolds number of the flow is based on $\rho_{le} = O(\delta^2)$, i.e. *for a thin foil this number is two orders of magnitude less than that based on the chord of the foil*. The leading edge viscous flow equations are solved numerically in a local region on the outer boundary of which there are prescribed appropriate (far-field) potential flow quantities in accordance with relationships (3) and (4). Three optional numerical solution procedures are considered. The first option makes use of no mathematical model of turbulence. Therewith, if the local Reynolds number is not too large, and the cells of computational grid are not too small to allow direct numerical simulation (DNS), the resulting viscous flow can be viewed as *entirely laminar*. Associated computational scheme will be designated as *L-model*. This scheme enables to predict surface distributions of pressure, shear stress as well as conditions for which the laminar flow can separate from the leading edge. Another option makes use of Smagorinsky turbulence model which is known as the simplest way to conduct large eddy simulation (LES), [16]. Smagorinsky model is certain to reproduce turbulent flow conditions, whereas laminar and transitional regimes can be reproduced only with appropriate scaling (size) of the mesh. Third option of computation utilizes Smagorinsky turbulence model but on the basis of the first (*entirely laminar*) flow simulation, including laminar separation effects, if any.

Large-Eddy-Simulation (LES) with the Smagorinsky [16] constant coefficient subgrid-scale (CSGS) model, adopted to give a comparable turbulent solution, is designated as further on as a *T-model*. Whenever a criterion of inverse velocity gradient in normal direction at the first point downstream along the wall surface is viewed as a starting separation point, a transitional solution is introduced and defined as a laminar upstream and a turbulent downstream of that point. The corresponding computational scheme is designated as a *LT-model*.

In the computation the width of a box filter, Δ

, used in the expression of turbulent viscosity

$$\mu_t = C_s^2 \Delta^2 |\bar{S}_{ij}|,$$

as proposed by Smagorinsky [16], is related to the local grid size, h , say $\Delta_1 = h_1$ and $\Delta_2 = h_2$. The following definitions are also used for our two-dimensional problem: $\Delta = \sqrt{(3/2)(\Delta_1^2 + \Delta_2^2)}$, $|\bar{S}_{ij}| = \sqrt{\bar{S}_{ij}\bar{S}_{ij}}$. The stress tensor is defined as

$$S_{ij} = \frac{1}{2} \left(\frac{\partial u_i}{\partial x_j} + \frac{\partial u_j}{\partial x_i} \right), \quad i, j = 1, 2$$

as per Ferziger [17]. The Smagorinsky [16] constant, $C_s = 0.1$, is used in all of the computations.

Multi-block technique

Considered multi-block grid system comprises several blocks, which involve grids of drastically different scales, decreasing in direction of solid boundaries. The external block, surrounding and covering the internal one, is extended to farfield stream and is computed to give necessary outer boundary conditions for the internal one. The computation can then proceed within the internal block with the latest known outer boundary conditions, transferred from the previously calculated external block solution. If a satisfactory solution has not been reached, then the next internal block may be introduced, and the same procedure repeats. Note that different governing equations, different time steps and even turbulence models can be used in different blocks. The role of a block relative to other blocks is to supply updated boundary conditions for those other blocks through the process of iteration and interpolation. Hence, parallel-computing technique can be readily applied in this case.

A single block can be viewed as a particular case of the multiple block approach. In order to allow better, denser but less stretched (low slenderness ratio) grids to be used for numerical computation, it is needed to have some cut in the original outer block and to form a definite region where a new inner block is placed to help resolve the flow. Multi-block technique serves to considerably reduce the number of cells (hence the time of computation) in the computational grid by making them appropriately small only in the flow regions with large gradients. Note that for uniformly dense grids it becomes impossible to treat the whole flow field in a single block computation due to limited computer resources.

Numerical stability is very dependent on the flow gradients and on the employed cell sizes. The higher is the Reynolds number, the larger

will be the flow gradients near a wall surface, and still smaller grid size will be needed. Practically, to avoid divergence of computation, the time step should also be reduced. As a result one needs much more computer resources. Multi-block technique puts the cells of similar sizes into appropriate block.

In general, for a numerical scheme, discretization error decreases when one can utilize grids of more uniform sizes. Multi-block technique allows to use them in the internal blocks and hence can reduce the discretization error there. But because of the incompatibility of the grids at the interfaces of different blocks, flow patterns become discontinuous in the overlapping region. In these regions the flow information from finer grids can be lost when transferred to coarser grids, especially in the case of very unsteady flow patterns. It may cause concentration of numerical errors. So it is hard to say whether the multi-block technique removes or generates numerical errors. Nevertheless this technique gives us certain possibilities to redistribute numerical errors in the interface region between blocks by appropriate choice of position of the latter thus enabling better control of induced errors.

Construction of the Grid

There are two blocks, that is, an external and internal one, which constitute the multi-block grid system. The grid lines, orthogonal everywhere, are constitutive of the stream-function lines and the potential-function lines which can be found from the complex potential function $F_c(Z) = \sqrt{Z - 1/2}$.

The idea of using multi-block technology is to allocate most of the available computational resources to the inner (near wall) region. The density of the grid in the internal block is drastically refined not only due to decrease of its area but also because of increase of the used cell numbers.

The internal-block grids are established by making subdivisions upon the outer ones. For our cases, there are six subdivisions made along each direction. It means that there are $6 \cdot 6 = 36$ internal-block cells to compose an external-block cell.

NUMERICAL IMPLEMENTATION

In the work, the finite volume method is used to discretize the integral form of the conservative continuity and momentum equations. The quadratic upwind interpolation scheme with

third-order accuracy on a uniform mesh, proposed by Leonard [18], is used as a convection scheme for the momentum equations. Second order accuracy is maintained in time by using Crank-Nicolson implicit scheme and in space by using central differences.

All of the flow variables, velocities and pressure, are calculated in the control volume center and are arranged to be non-staggered. To avoid the checkerboard pressure oscillation, which is reported in a non-staggered grid, Rhie and Chow [19] proposed the pressure weighted interpolation method (PWIM), using the SIMPLE method as the framework of solution strategy. Their method can closely couple the pressure gradient with the interpolated control volume face velocity in one grid size and then can suppress the oscillation.

The purpose of pressure correction method is to introduce an inner iterative process. In each iterative loop the pressure correction term is found first and then the relative velocity correction can be determined to gradually approach the continuity equation. This iterative process also serves as a chance for the multi-block technique to transfer, release and update the latest boundary conditions for the neighboring blocks. Hence, the use of multi-block technique will not cause any additional computational cost.

To secure efficiency of the computation, one has to suitably choose the number of numerical sweeping (N_{swp}) in a whole block, the number of iterative loops (N_{itr}) for blocks and the overlapping region between blocks. In this work, $N_{swp} = 10$ and $N_{itr} = 20$ are chosen as a limit for solving of momentum transport equations and the pressure correction equation, respectively. Choose $N_{itr} = 4 - 8$, depending on the unsteadiness of flow patterns. Four strips of outer-block cells, overlapping a wide-range region in the subsequent internal block, serve as an effective overlapping interface region. The number of time steps is 5 for a particle of unit velocity to cover the distance equal to the nose radius, that is, 100 time steps (as a time period) are required for that particle to flow through the length of computational domain, $X=20$ for example. In general, 20 time periods are enough and executed in a computation.

Analytical potential solution is given as the initial condition and is kept as a farfield Dirichlet-type boundary condition for computation. The wall surface condition is non-slip. When considering the existing viscous boundary layer, Neumann-type boundary conditions are imposed

upon the near-wall part of the used external block, width of which is chosen the same as that of the internal block at the downstream location. They are a farfield condition for the velocity gradient and a specified pressure gradient, which is determined from the analytical potential solution.

Computations was carried out on an Intel Pentium II-450 personal computer under the Windows98 operating system. The installed memory size (RAM) was 128 Mbytes. Usually about 24 hours are required for a one-machine single-run case.

RESULTS AND DISCUSSION

Some results of the computation are presented in Figs 2-12. Figure 2 shows the effect of Reynolds number on distribution of the pressure coefficient along the upper and lower sides of the parabolic leading edge in the case of unseparated flow and within *L-model*. It shows clearly that as the Reynolds number increases the peak of suction on the upper side of the foil near the leading edge becomes more pronounced. At the same time the pressure distribution on the lower side is almost invariable within considered range of Reynolds numbers. Note, that the Reynolds number is based on the radius of the nose of the foil. Consequently, the Reynolds numbers based on the chord of the foil are two orders of magnitude larger.

Analysing distribution of friction coefficient for the same case (see Fig. 3), one can see that (outside of the region of the stagnation point) the shear stress does not become equal to zero, i.e. no separation occurs for $a = 0.9$. Naturally, the graph confirms that for lower Reynolds numbers the friction coefficient grows at a given station of X .

Figure 4 represents the influence of Reynolds number and asymmetry of the flow (magnitude of a) upon distribution of pressure coefficient within *L-model*. Prescribed magnitudes of $a = 0.9, 1.0$ correspond to unseparated and separated flow cases. Oscillatory character of the pressure distribution in the case of separated flow and Reynolds number of 10^4 reflects that fact that in this range the separation region splits in multiple vortical zones. Figures 5 and 6 shows friction coefficients, corresponding to the aforementioned case for more detailed variation of the asymmetry parameter a . It can be seen in particular from Fig. 5 that for $Re = 10^3$ laminar separation on the upper surface of the parabola occurs at $a \approx 0.98$ and

at stretched abscissa $X = X_{sep} \approx 9.2$. As follows from Fig. 6, the critical values of a for $Re = 10^4$ are somewhat smaller than for $Re = 10^3$. Besides, similarly to pressure graphs, the separation region for $Re = 10^4$ is subdivided into multiple albeit almost invisible vortical zones.

Velocity vector fields and streamlines of the leading edge flow (in *L-model* formulation) are presented in Figs 7 and 8 at $Re = 10^3$ for both unseparated and separated flow regimes. Velocity vector field for $a = 1.1$ reveal position and structure of laminar separation bubble. Similar data is presented in Fig. 9 within the *LT-model* (laminar+turbulent). Note, that for the case of separated flow both *L* and *LT-model* demonstrate unsteady flow pattern. Thus, the plots show instantaneous picture of the flow. For large $Re = 10^4$ the separation effects are not detectable from the observation of velocity vector field and streamline, calculated from *LT-model*. However, they can be observed in the Fig. 11, showing friction coefficient versus stretched abscissa X ($Re = 10^4$). Figure 11 also compares results for friction coefficient, obtained on the basis of *L*, *LT* and *T models* on the suction side for $a = 1.0$ and $a = 1.1$. Attention can be drawn in particular to the two curves predicted by means of *T-model*, showing transition of the flow from laminar to turbulent regime in downstream direction. Figure 12 displays dependence of pressure coefficient upon stretched abscissa X predicted by means of *L*, *LT* and *T models* for $Re = 10^3, 10^4$ and $a = 1.0, 1.1$.

In conclusion the authors would like to mention that the ideas of combining asymptotic and numerical methods have been known for years, see for example, Euvrard [20], but the computing power available today provides solid ground for their realization.

ACKNOWLEDGEMENT

The authors would like to thank Dr. Igor V. Tkachenko for the discussion of the work and some practical remarks.

REFERENCES

- [1] Van-Dyke, M.D. "Subsonic edges in thin wing and slender body theory", *National Advisory Committee for Aeronautics*, Ames Aeronautical Laboratory, Moffett Field, California, November 1954, 26 p.

- [2] Lighthill, M.J. "New approach to thin aerofoil theory", *Aeronaut. Quarterly*, vol. 3, part 3, November 1951, pp 193-210.
- [3] Darrozes, J.-S. "Behavior of a subsonic flow past a thin wing in the vicinity of a leading edge", *ONERA Note Techn.*, No. 16, 1976.
- [4] Rozhdestvensky, K.V. "Method of Matched Asymptotic Expansions in Hydrodynamics of a Wing", *Sudostroenie*, Leningrad, 1979, 208 p.
- [5] Rozhdestvensky, K.V. and Mishkevich, V.G. "Calculation of unsteady flow past a thin foil on the basis of the method of matched asymptotic expansions", *Voprosy Sudostroeniya, ser. Proektirovanie sudov*, vyp. 37, 1983, pp 60-73.
- [6] Mishkevich, V.G., Rozhdestvensky, K.V., Bubentsov, V.P. "Unsteady flows near leading edges of lifting surfaces: pressures, flow separation, cavities", *Proc. The 1993 ASME Winter Annual Meeting "Bubble Noise and Cavitation Erosion in Fluid Systems"*, New Orleans, Louisiana, November 28-December 3, 1993, pp 9-19.
- [7] Ermak, Yu.N. "Incompressible viscous flow past a rounded leading edge of a thin foil", *Trudy TSAGI imeni N.E. Zhukovskogo*, vyp. 1141, Moscow, 1969, pp 1-12.
- [8] Werle, M.J. and Davis, R.T. "Incompressible laminar boundary layers on a parabola at angle of attack: a study of the separation point", *J. Appl. Mech. Trans. ASME, Ser. E*, vol. 39, N 1, 1972.
- [9] Rozhdestvensky, K.V. and Mishkevich, V.G. "Equation of a parametric unseparated flow in CAD of lifting elements of ships", *Sb. NTO imeni akad. A.N. Krylova*, 1984, vyp. 8, pp 60-65.
- [10] Tuck, E.O. "A criterion for leading edge separation", *J. Fluid Mechanics*, vol. 222, 1991, 33-37.
- [11] Ruban, A.I. "Asymptotic theory of short separation zones on leading edges of a thin foil", *Mekhanika zhidkosti i gaza*, N 1, 1982, pp 42-51.
- [12] Tani, I. "Low-speed flows involving bubbles separations", *Progr. Aeronaut. Sci.*, vol. 5, Oxford, Pergamon Press, 1964.
- [13] Ely, W.L., Herring, R.N. "Laminar leading edge stall prediction for thin airfoils", *Proc. AIAA 11th Fluid and Plasma Dynamics Conference, AIAA Paper 78-1222*, Seattle, July 10-12, 1978, pp 1-12.
- [14] Tuncer, C., Khattab, A.A. and Schimke, S.M. "Separation and reattachment near the leading edge of a thin an oscillating airfoil", *J. Fluid Mechanics*, vol. 188, 1988, pp 253-274.
- [15] Ekaterinaris, J.A., Chandrasekhara, M.S. and Platzer, M.F. "Analysis of Low Reynolds Number Airfoil Flows", *Journal of Aircraft*, vol. 32, No. 3, May-June 1995, pp 625-630.
- [16] Smagorinsky, J., "General circulation experiments with the primitive equations, Part I: the basic experiment", *Monthly Weather Rev.*, 91, 1963, pp 99-164.
- [17] Ferziger, J.H. and Peric, M. "Computational methods for Fluid Dynamics", Springer, ISBN 3-540-59434-5, 2nd printing, 1997.
- [18] Leonard, B. P., "A stable and accurate convective modelling procedure based on quadratic upstream interpolation", *Comput. Methods Appl. Mech. Eng.*, 12, 1979, pp 59-98.
- [19] Rhie, C. M. and Chow, W. L., "Numerical study of the turbulent flow past an airfoil with trailing edge separation", *AIAA Journal*, vol.21, 1983, pp 1525-1532.
- [20] Euvrard, D. "A mutually profitable alliance: asymptotic expansions and numerical computations", *J. of Theoretical and Applied Mechanics*, 1986, pp 25-45.

2-block grid system

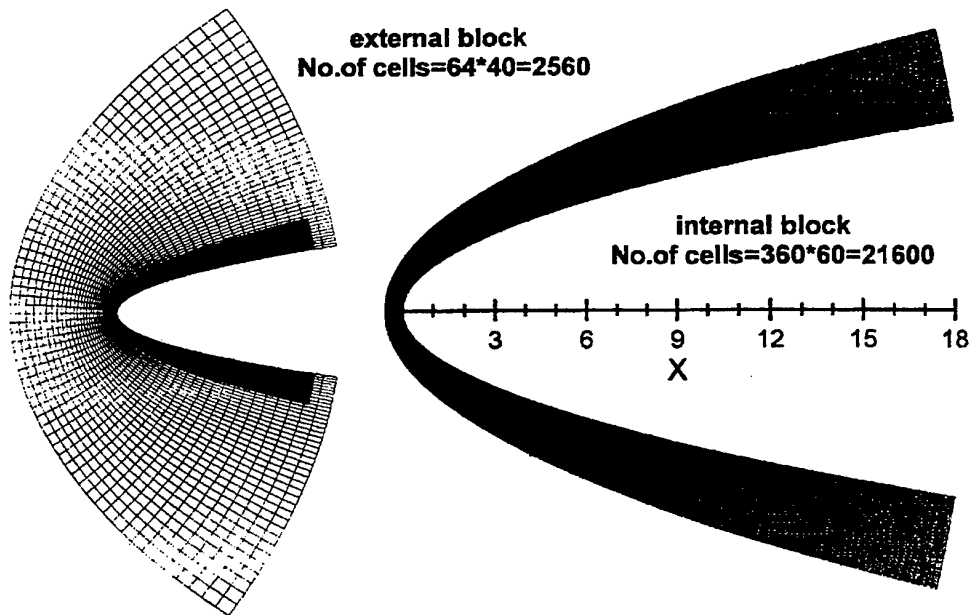


Figure 1: Two-block (parabolic) grid system employed for numerical calculation of Navier-Stokes equations in the vicinity of the leading edge: a. - the whole computational domain, containing two blocks; b. - the inner block

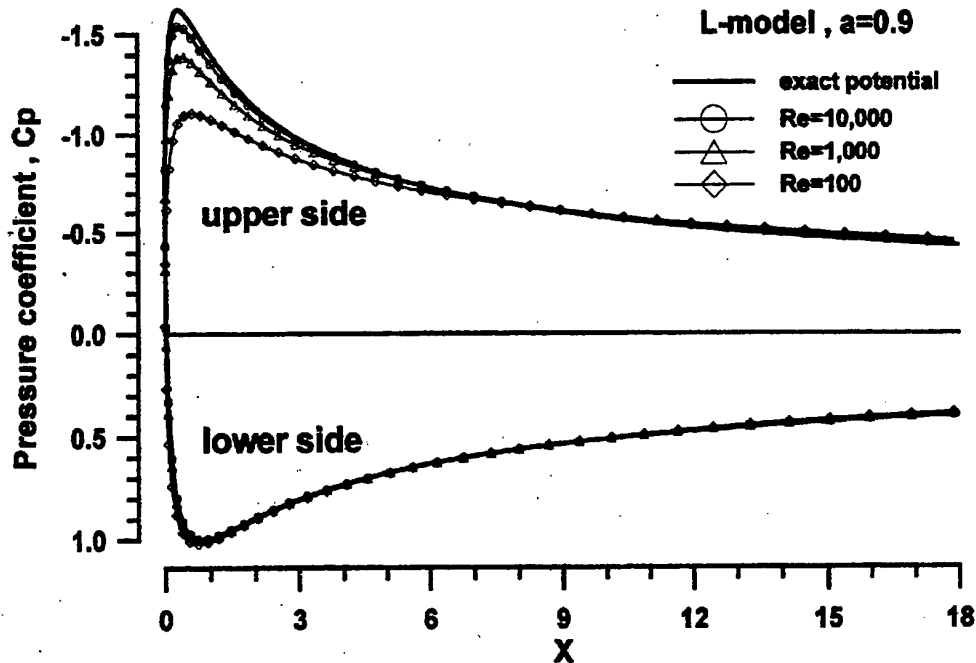


Figure 2: Viscous effect upon distribution of the pressure coefficient on the upper and lower side of the foil for different Reynolds numbers (*L-model*, no separation)

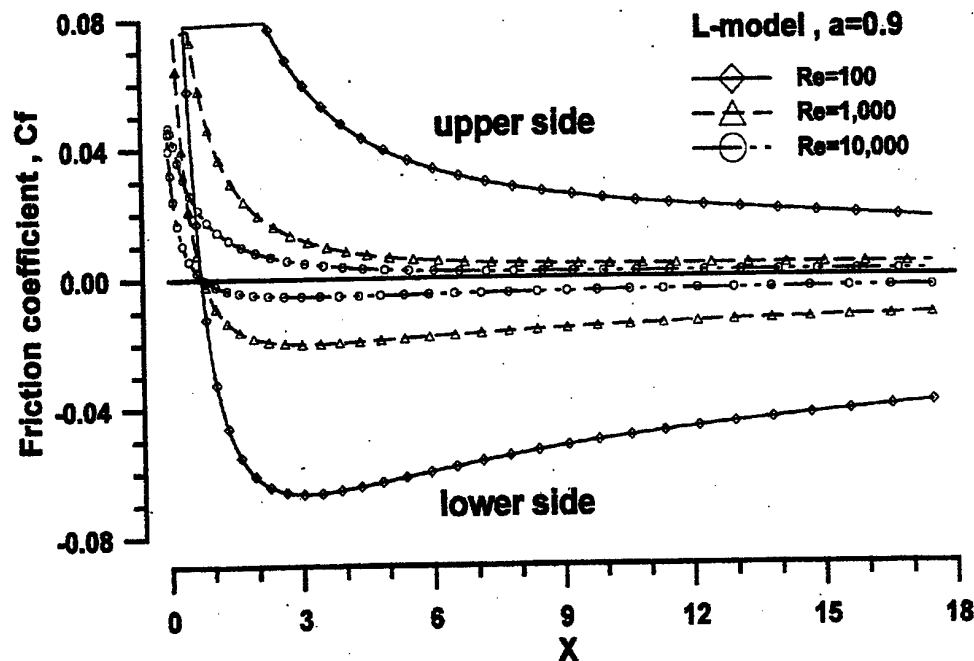


Figure 3: Distribution of local friction coefficient along the contour of parabolic leading edge for different Reynolds numbers (*L-model*, no separation). In definition of the friction coefficient clockwise direction of the arc coordinate is considered positive

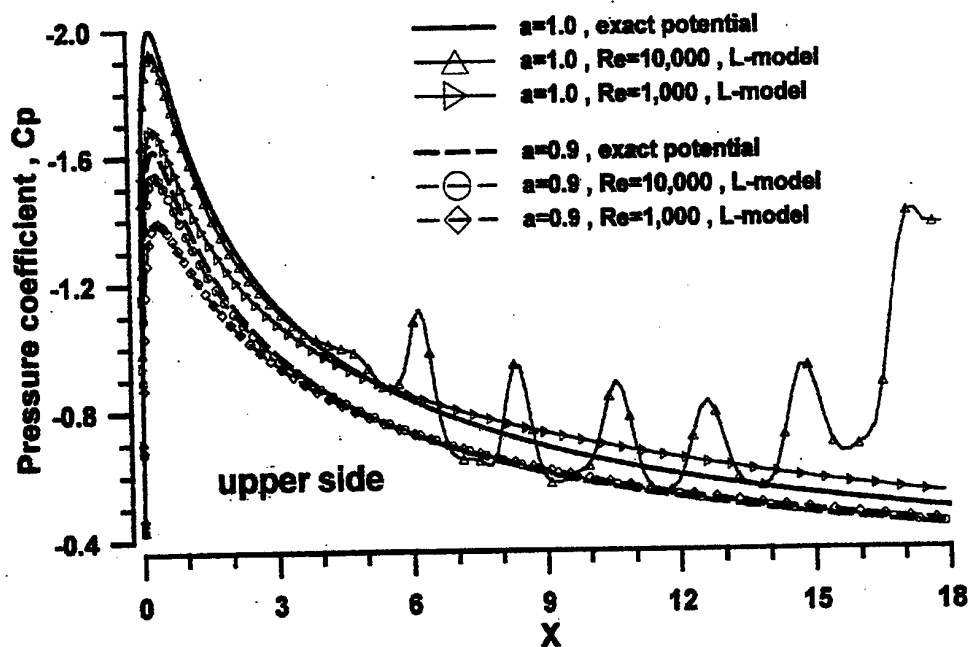


Figure 4: Viscous effect upon distribution of the pressure coefficient on the upper and lower side of the foil for different Reynolds numbers with and without separation (*L-model*)

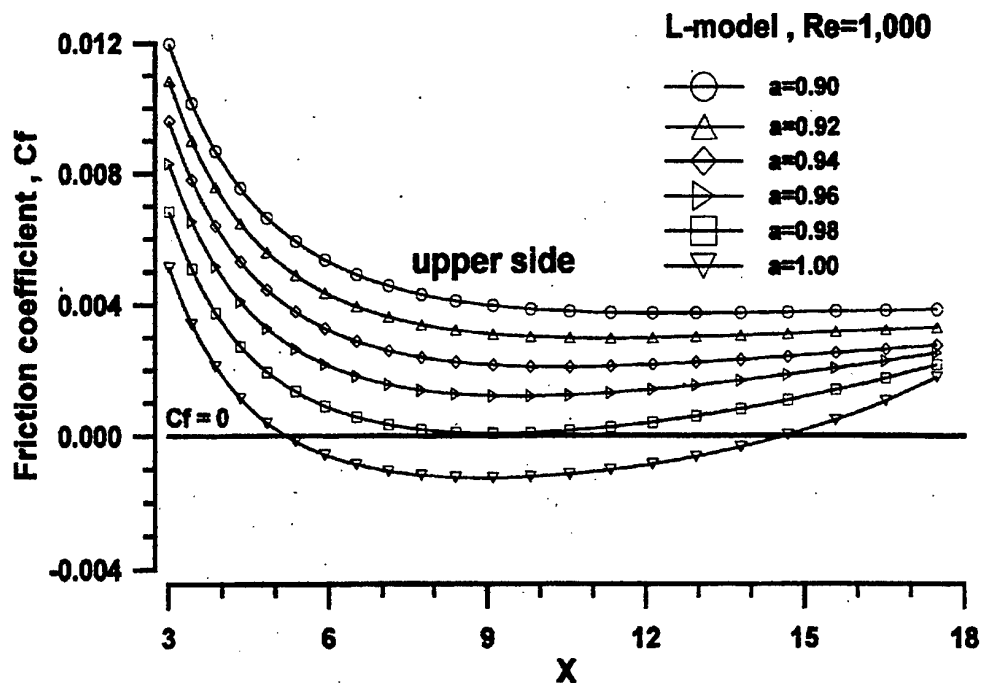


Figure 5: Distribution of friction coefficient along the suction side of the parabola for different magnitudes of parameter a and $Re = 10^3$ (L-model)

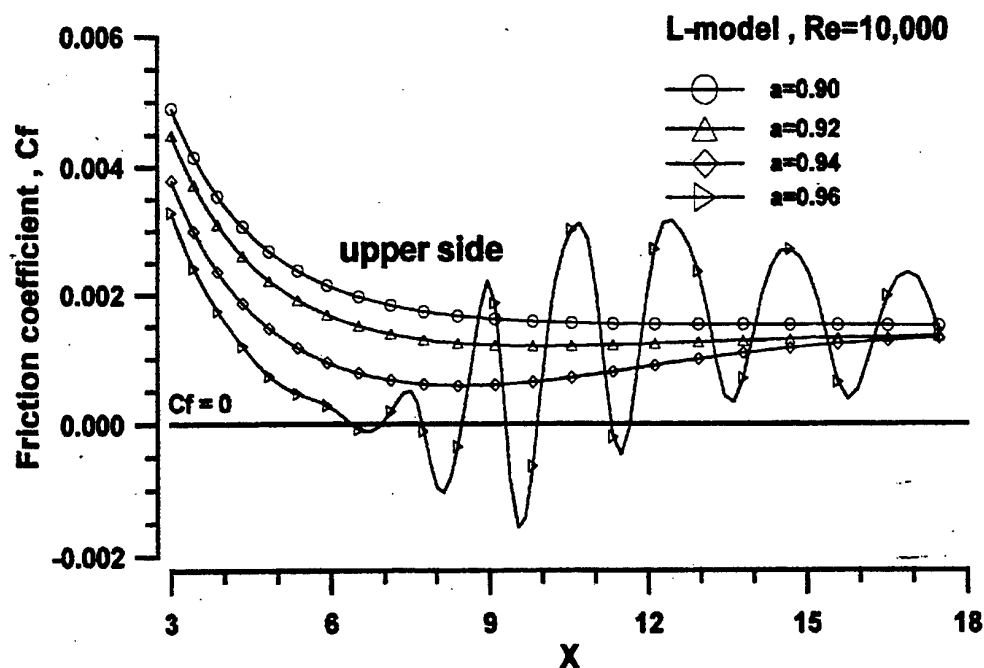


Figure 6: Distribution of friction coefficient along the suction side of the parabola for different magnitudes of parameter a and $Re = 10^4$ (L-model)

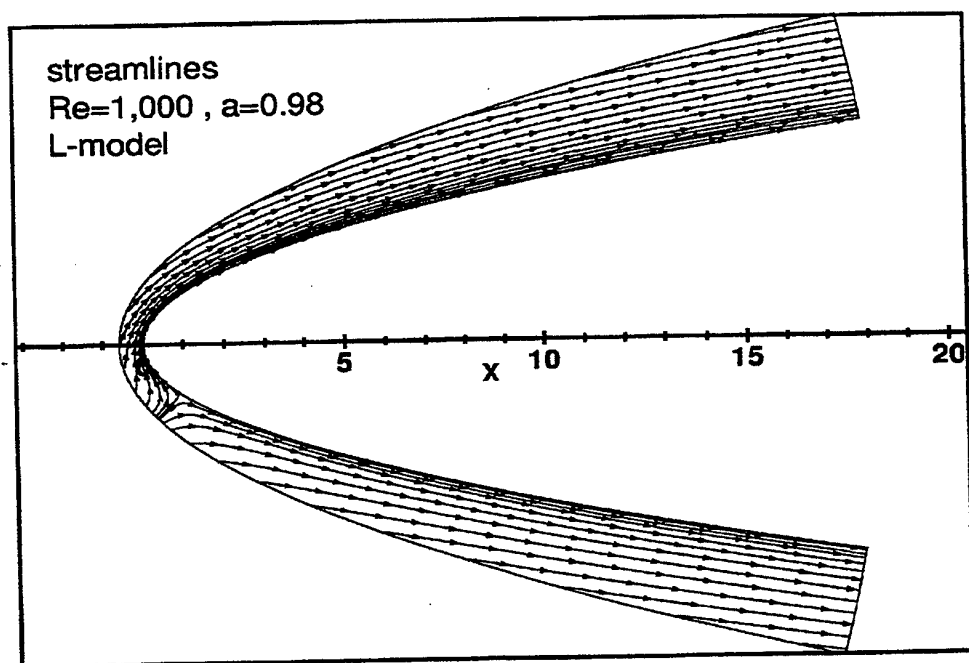
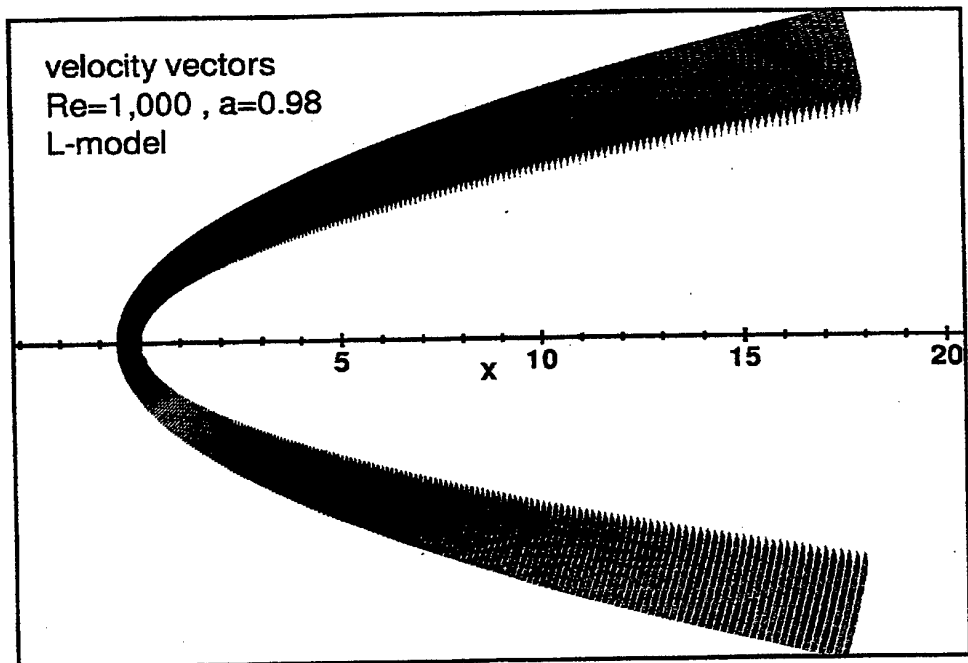


Figure 7: Velocity vector field and streamlines of the flow past a parabolic edge prior to separation
 (*L-model*)

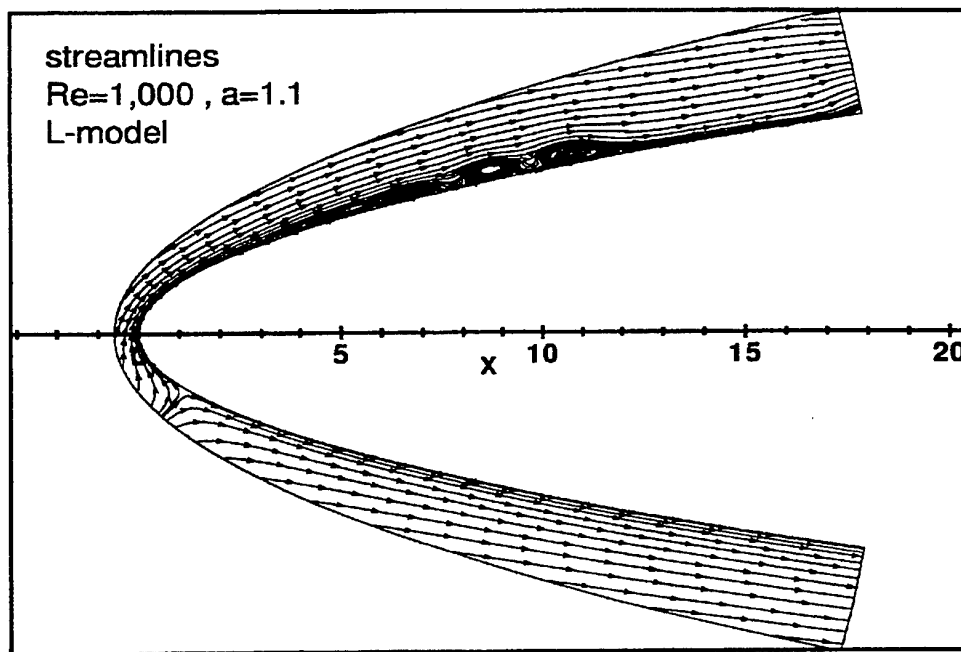
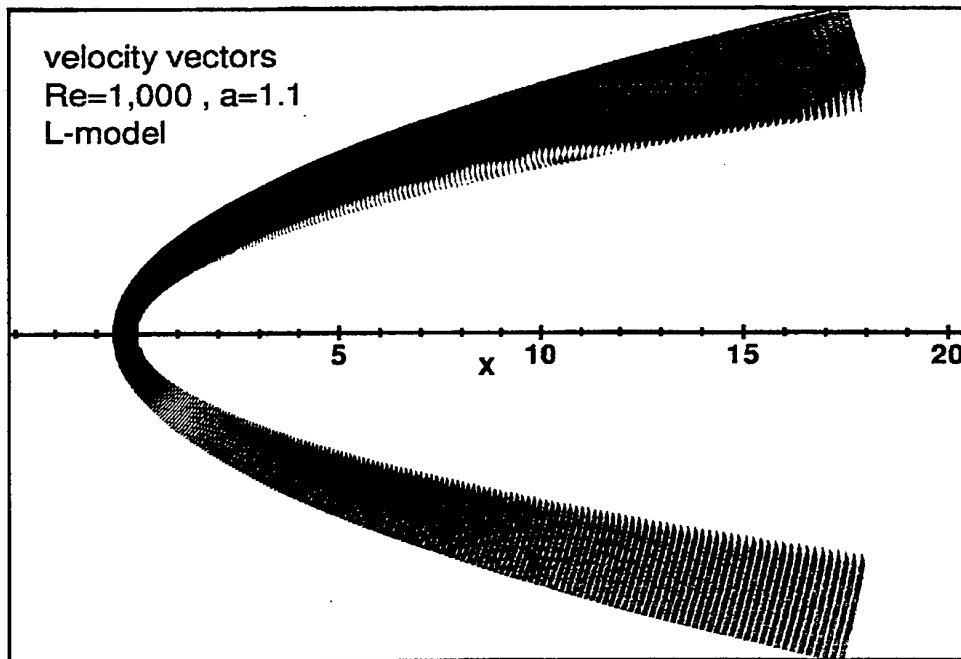


Figure 8: Velocity vector field and streamlines of the flow past a parabolic edge (*L-model*, laminar separation bubble)

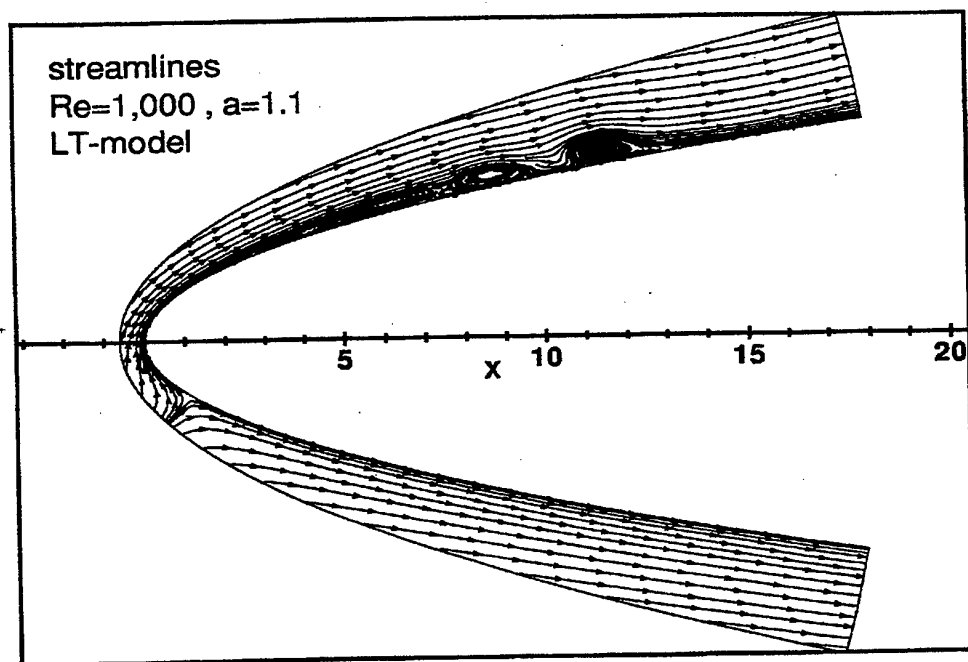
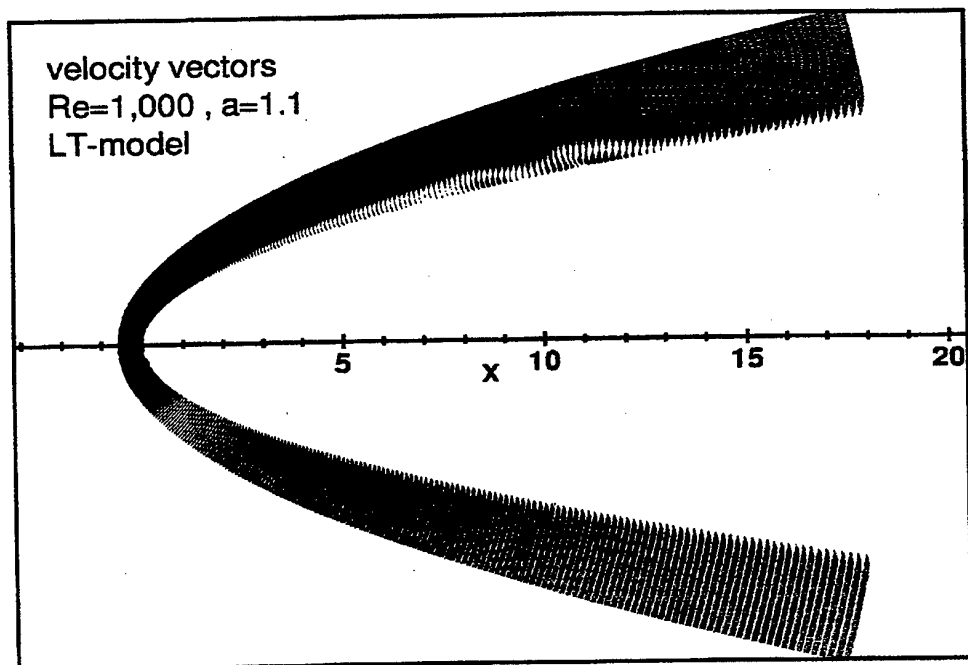


Figure 9: Velocity vector field and streamlines of the flow past a parabolic edge (*LT-model*, separation bubble, $Re = 10^3$)

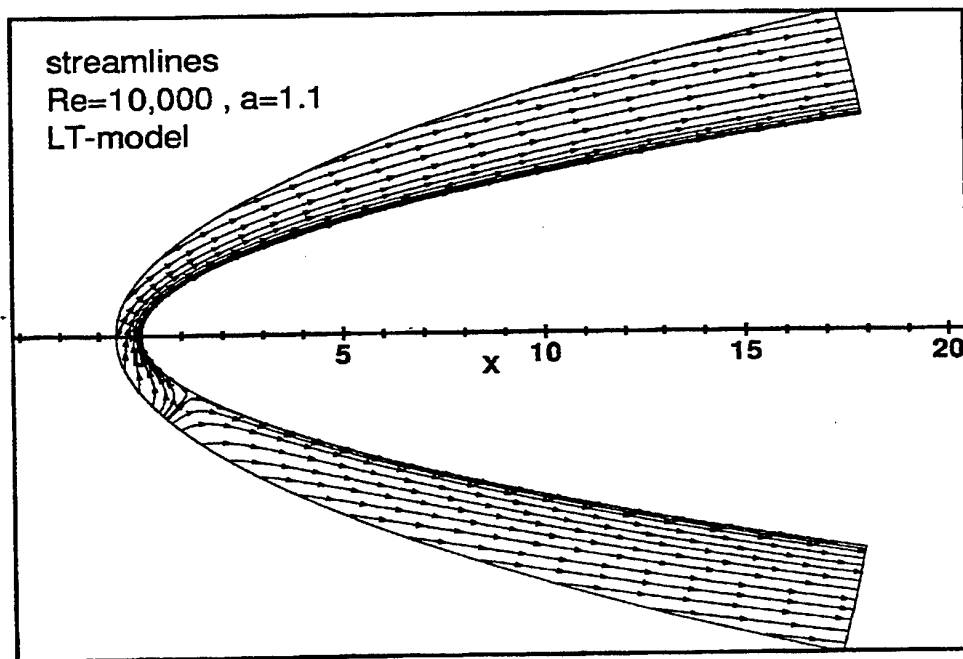
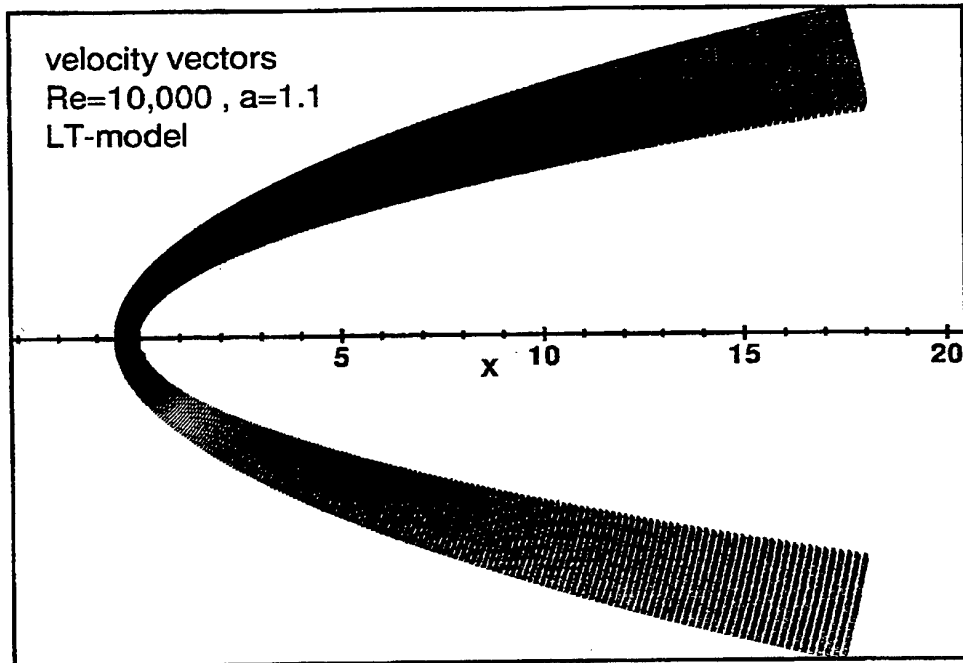


Figure 10: 10 Velocity vector field and streamlines of the flow past a parabolic edge (*LT-model*, very small separation bubble, $Re = 10^4$)

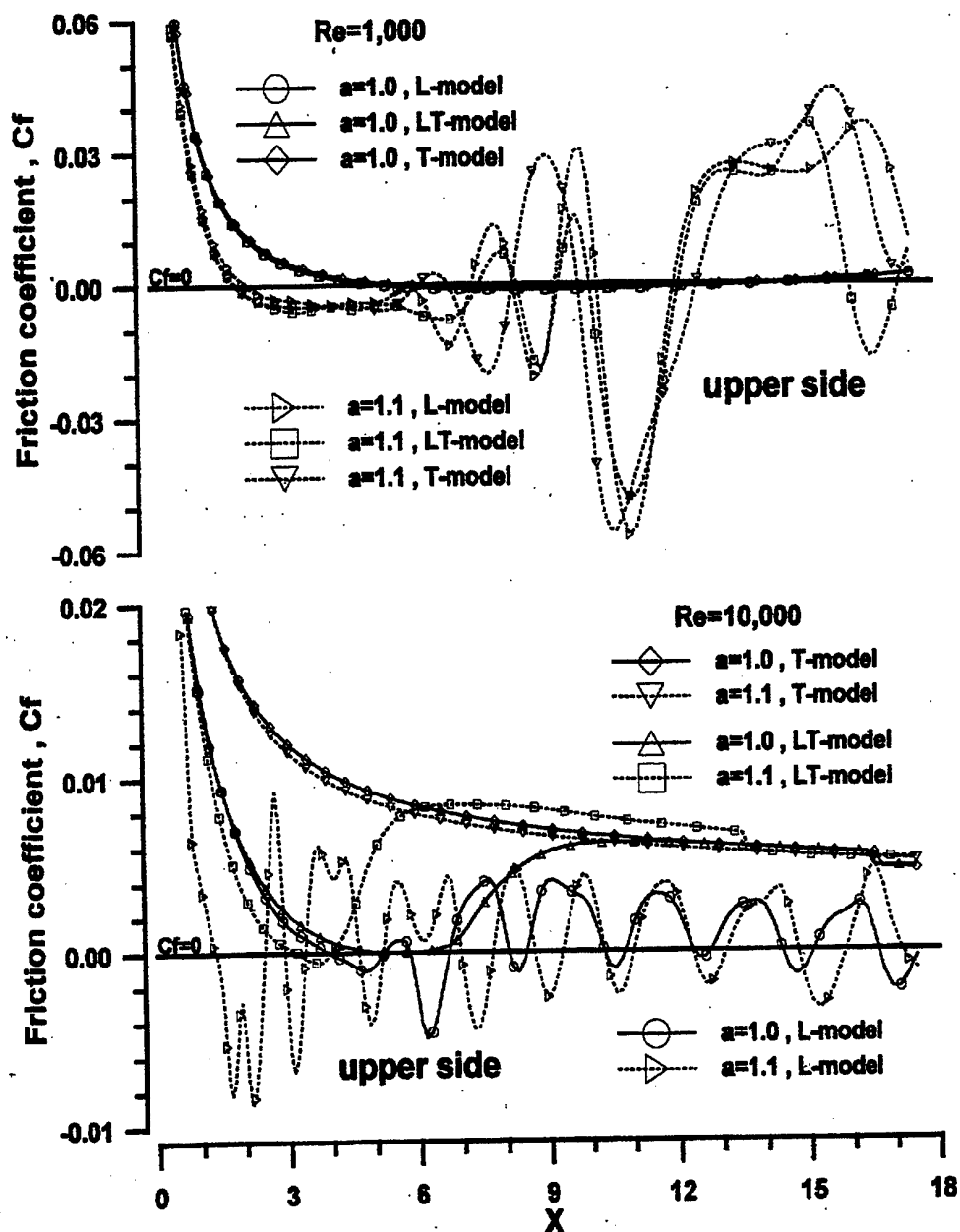


Figure 11: Distribution of friction coefficient along the upper side of the parabola calculated with help of different mathematical models of the flow (L , LT and T) for $Re = 10^3$ and $Re = 10^4$

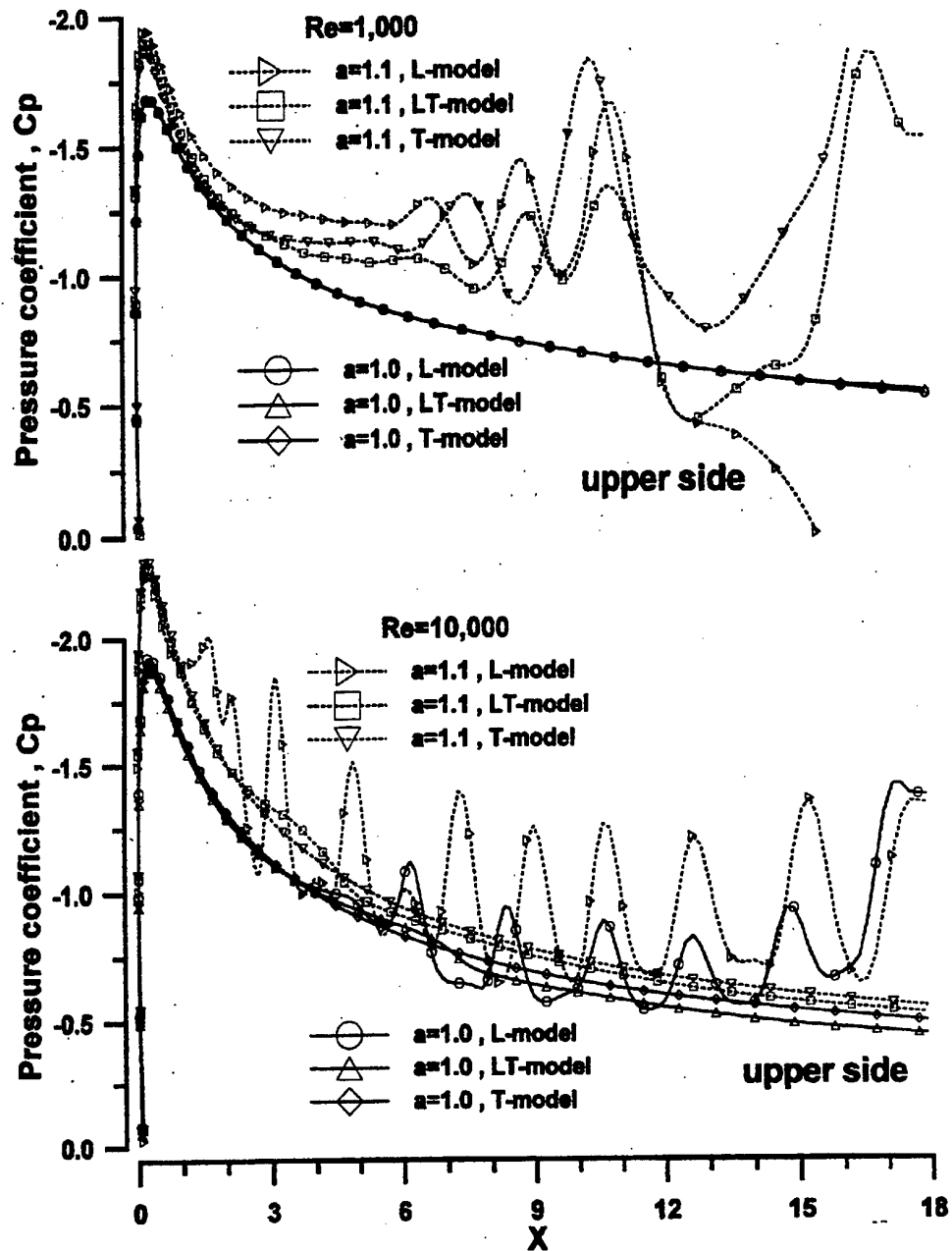


Figure 12: Distribution of pressure coefficient along the upper side of the parabola calculated with help of different mathematical models of the flow (L , LT and T) for $Re = 10^3$ and $Re = 10^4$

COMBINING NUMERICS AND ASYMPTOTICS TO ACCOUNT FOR THE INFLUENCE OF THE VORTEX ROLL-UP UPON HYDRODYNAMIC CHARACTERISTICS OF A WING

K.V. Rozhdestvensky, G.M. Fridman

Department of Applied Mathematics and Mathematical Modeling

St. Petersburg State Marine Technical University

Lotsmanskaya St. 3, 190008 St. Petersburg, Russia

fax: (812)2197866, e-mail: xmas@infopro.spb.su, grifri@brain.nw.ru

ABSTRACT

The paper is dedicated to theoretical investigation of the influence of the roll-up of the side edge vortex sheets upon hydrodynamic characteristics of a wing. It is demonstrated that for the wings of finite aspect ratio the size of the region of the roll-up in vicinity of the side edge is proportional to $\alpha^{2/3}$, where α is (small) angle of attack. Asymptotic analysis, conducted in the paper, shows that dynamic evolution of the side vortex sheets, occurring in the said neighbourhood of the wing tips, gives dominating nonlinear contribution to the dependence of the lift of the wing upon the angle of attack. The solution algorithm incorporates separate consideration of the flow in the regions close and far from the wing side tips with subsequent matching of corresponding asymptotic expansions of the solution. The outer field flow description contains both classical linear lifting surface term, satisfying the requirement of zero loading at the wing side tips, and a contribution revealing square root singularity of loading at the side tips. The strength of the tip singularities is shown to be proportional to the static moment of vorticity of the side edge rolled-up vortex sheet. Therewith the roll-up in the local region is carried out numerically. Some results are presented for the case of wings of small aspect ratio which are compared to the existing experimental data and semi-empirical formulae.

INTRODUCTION

One of the causes of nonlinearity of aerodynamic characteristics of wings of small and medium aspect ratio is due to the roll up of vortex sheets, emanating from side edges. Consequently, there appear changes in magnitudes of lift and drag forces, acting upon the wing. Both theory and experiments in this case show that the contribution of spiral discontinuities into aerodynamic characteristics of wings of small aspect ratio can attain 50%. In principle, the ideal fluid model admits flows past sharp corners of the body with generation of spiral surfaces of tangential discontinuity of the velocity field. Back in 1924 Prandtl expressed the opinion on practicality of investigation of "the second" possible form of the flow past sharp corners with birth and subsequent roll up of corresponding vortex sheets, [1]. Practically, analysis of both inception and evolution of a surface of tangential discontinuity can be reduced to consideration of dynamics of an equivalent sys-

tem of discrete vortices, [2]. Such an approach is not strictly justified and its success largely depends on skilfulness of the researcher, [3]. Typical instability of the process of modeling of dynamics of tangential discontinuities by means of discrete vortices is due to inherent instability of such surfaces. In the process of development of the aforementioned instability there play significant role numerical perturbations. The nature of the latter effect depends on both the method of rounding off numbers and on parameters of approximation of the surface of discontinuity by a discrete system, in particular upon the step of calculation. Another difficulty consists in the fact that during the evolution of the sheet there are formed near its edge the spirals with large number of turns. In the "tight" part of the spiral its approximation by a finite number of discrete vortices turns out to be impossible. Therefore, for its description with account of the "dense" core there is applied either asymptotics of the spiral near the

edge of vortex sheet or replacement of the "tight" part of the spiral by an equivalent single discrete vortex with a cut, connecting this vortex with finite part of spiral discontinuity, see for instance [4]. Kaden, [5] was the first to propose a similarity law (time)^{2/3} to describe roll up of a semi-infinite vortex sheet and derived an asymptotic form of the inner part of the spiral. Smith, [4] performed an investigation and calculation of parameters of self-similar solutions, corresponding to shedding of vortex sheet from leading edges of delta wing of small aspect ratio. Kaden's idea was further extended in research work of Moore [6] and Guiraud and Zetounian, [7] where correction was introduced towards ellipticity of preliminarily "circular" Kaden's spiral. In the work of Moore and Saffman [8] there was analysed the effect of viscosity upon diffusion of vorticity of the spiral with generation of vortical though inviscid outer part of the core and inner viscous part of the core. Nikolsky, [9,10,11] considered matters of dynamics of two-dimensional separated flows and deduced similarity laws for three-dimensional steady separated flows past bodies. Sudakov, [12] constructed an asymptotic solution of the problem for the flow past a small aspect ratio delta wing at small angles of attack. Seemingly, he was the first to have used the idea of matching of local descriptions of vortex sheet near the its edge with description of tangential discontinuity in the middle part of the wing. Molchanov [13] considered the approach based on singling out of the main nonlinear contribution to characteristics of a rectangular wing in a separated ideal fluid flow and showed how to construct the second approximation of the lifting surface theory with account of roll up of vortex sheets near side edges. In the present paper these ideas are illustrated on the basis of somewhat different approach utilizing in the second order outer approximation special solutions of the lifting surface theory with square root singularities of the loading at side edges, [14]. The essence of the approach consists in splitting of the flow field into zones with different characteristic scales of coordinates. In the vicinity of the edge there is singled out an "inner" zone, in which the roll up of vortex sheet is assumed to take place at small incidences. Asymptotic dimension of this zone is determined with help of the least degeneracy principle from equations of dynamics of the roll up of edge vortex sheet. It is shown that this dimension is of the order of $\alpha^{2/3}$, i.e. for small incidences α the roll up region is localized. The outer asymptotics of local solution shows

that the next term of the outer representation of circulation has the order $\alpha^{5/3}$ and should have a square root singularity at side edges. Corresponding outer solution was determined in form of a generalized Birnbaum-Prandtl series with square root singularities at side edges. Strength of these singularities was found by means of asymptotic matching of inner and outer solutions. It turned out that it can be interpreted as the moment of vorticity of rolled-up vortex sheets at corresponding lateral cross section $x = \text{constant}$.

OUTER ASYMPTOTIC EXPANSION FOR AERODYNAMIC LOADING

Consider an irrotational ideal fluid flow past an infinitely thin flat lifting surface of rectangular form and arbitrary aspect ratio λ with small angle of attack α . Assuming that lateral dimension of the roll up zone of the edge vortex sheet diminishes with decrease of incidence $\alpha \rightarrow 0$, seek the outer asymptotic expansion of loading in form combinations of acceptable solutions of a well known integral equation of linear lifting surface theory

$$\int_{-\lambda/2}^{\lambda/2} \int_{-1}^1 \frac{\gamma^0(\xi, \zeta)}{(z - \zeta)^2} \times \\ \times \left[1 + \frac{x - \xi}{\sqrt{(x - \xi)^2 + (z - \zeta)^2}} \right] d\xi d\zeta = -4\pi\alpha \quad (1)$$

namely

$$\gamma^0(x, z) = \delta_1(\alpha)\gamma_1^0(x, z) + \delta_2(\alpha)\gamma_2^0(x, z) + \dots \quad (2)$$

It follows from (2) that $\delta_1(\alpha) = \alpha$. Solution of the order α is standard and is sought in the class of function of loading γ_1^0 with behavior of the type $O(1/\sqrt{s})$ at the leading edge, and of the type $O(\sqrt{s})$ - at side edges and the trailing edge (where s is distance from corresponding edge). In angular variables $\cos \theta = -2z/\lambda$, $\cos \psi = -x$, $x \in [-1, 1]$, $z \in [-\lambda/2, \lambda/2]$ solution of the first order γ_1^0 and corresponding integral circulation Γ_1^0 have the form

$$\gamma_1^0(\psi, \theta) = \sum_{n=1}^{\infty} (a_{0n} \operatorname{ctg} \frac{\psi}{2} + \sum_{k=1}^{\infty} a_{kn} \sin k\psi) \sin n\theta, \\ \Gamma_1^0(\psi, \theta) = - \int_0^\psi \gamma_1^0(\psi, \theta) d\psi = \\ = -2 \sum_{n=1}^{\infty} \left[a_{0n} \ln \left| \cos \frac{\psi}{2} \right| + \sum_{k=1}^{\infty} a_{kn} \sin^2 \frac{k\psi}{2} \right] \sin n\theta,$$

where the coefficients a_{kn} are determined from the integral equation (1) by means of the collocation method. The inner asymptotics of the loading function γ_1^o and integral circulation Γ_1^o near side edges (for example, $z \rightarrow \lambda/2$, $\theta \rightarrow \pi$) can be found in the form

$$\gamma_1^o(\psi, \theta) = -\sqrt{2}\sqrt{1 - \frac{2z}{\lambda}} \times \sum_{n=1}^{\infty} (-1)^n n (a_{on} \operatorname{ctg} \frac{\psi}{2} + \sum_{k=1}^{\infty} a_{kn} \sin k\psi), \quad (3)$$

$$\Gamma_1^o(\psi, \theta) = 2a(x)\sqrt{1 - \frac{2z}{\lambda}} = 2\sqrt{2}\sqrt{1 - \frac{2z}{\lambda}} \times \sum_{n=1}^{\infty} (-1)^n n \left[a_{on} \ln |\cos \frac{\psi}{2}| + \sum_{k=1}^{\infty} a_{kn} \sin^2 \frac{k\psi}{2} \right] \quad (4)$$

LOCAL PROBLEM OF ROLL UP OF VORTEX SHEET NEAR SIDE EDGE

Introduce local coordinates in the plane perpendicular to the edge contour ($s = 2z/\lambda - 1$, y) and their complex combination $\chi = s + iy$. Write down complex potential F_1^o , corresponding to inner asymptotics of integral circulation of the first outer approximation $\Gamma_1^o = 2a(x)\sqrt{-s}$

$$F_1^o(\chi) = a(x)i\sqrt{\chi}, \quad \frac{dF_1^o}{d\chi} = \frac{a(x)i}{2\sqrt{\chi}}. \quad (5)$$

From physical viewpoint the local solution must "work" to extinguish infinite suction due to the flow around sharp side edge in the outer problem of the order $O(\alpha)$. This is realized at the account of shedding and subsequent evolution of vortex sheets.

Corresponding differential equation of evolution of vortex sheet from the leading edge in chordwise direction is

$$\frac{d\bar{\chi}}{dx} = \frac{dF^i}{d\chi}, \quad (6)$$

where "bar" designates complex conjugate. Simultaneously, it is necessary to impose the requirement of smooth detachment of vortex sheet from the side edge (analog of Kutta-Zhukovsky condition). The latter requirement can be formulated as

$$\operatorname{Im} \frac{dF^i}{d\chi} = 0, \quad \chi = 0. \quad (7)$$

Mapping the region of local flow (external with respect to a semi-infinite cut) upon an auxiliary

half plane $\operatorname{Im} \mu > 0$, $\mu = \mu_1 + i\mu_2$ by means of function $\mu = i\sqrt{\chi}$, one can re-write the evolution equations (6), (7) in the form

$$\frac{d\mu}{dx} = \frac{dF^i}{d\mu} \left(\frac{d\mu}{d\chi} \frac{d\mu}{d\chi} \right) = \frac{dF^i}{d\mu} \frac{1}{4|\mu|^2}, \quad (8)$$

$$\frac{dF^i}{d\mu} = 0 \quad \text{for} \quad \mu = 0.$$

Because the vortex system generated due to shedding and development of surfaces of tangential discontinuity "works" in a nonuniform potential flow with complex potential $F_1^i(\mu) = a(x)\mu$ and, in its turn, gives birth to induced complex potential

$$F_2^i(\mu) = \frac{1}{2\pi i} \int_L \gamma_v(l) \ln \frac{\mu - \mu(l)}{\mu - \bar{\mu}(l)} dl, \quad (9)$$

the evolution equations of vortex sheet (8) can be re-written

$$\frac{d\mu}{dx} = \frac{d}{d\mu} [\alpha a(x) + F_2^i] \frac{1}{4|\mu|^2}, \quad (10)$$

$$\alpha a(x) + \frac{dF_2^i}{d\mu} = 0, \quad \text{for} \quad \mu = 0.$$

Introducing stretched variables $\hat{\chi} = \chi/\sigma(\alpha)$, $\hat{\mu} = \mu/\sqrt{\sigma(\alpha)}$, $\hat{F}_2^i = F_2^i/\Delta_2(\alpha)$, perform scaling of the equation in the following fashion

$$\sqrt{\sigma(\alpha)} \frac{d\hat{\mu}}{d\hat{x}} = \left[\alpha a(x) + \frac{\Delta_2(\alpha)}{\sqrt{\sigma(\alpha)}} \frac{d\hat{F}_2^i}{d\hat{\mu}} \right] \frac{1}{4\sigma(\alpha)|\hat{\mu}|^2}. \quad (11)$$

wherefrom with account of the principle of the least degeneracy one can determine scale (stretching) functions for dependent and independent variables

$$\sigma(\alpha) = \alpha^{2/3}, \quad \Delta_2(\alpha) = \sqrt{\sigma(\alpha)}\alpha = \alpha^{4/3}. \quad (12)$$

Eventually, the evolution equations acquire the form

$$\frac{d\hat{\mu}}{d\hat{x}} = \left[a(x) + \frac{d\hat{F}_2^i}{d\hat{\mu}} \right] \frac{1}{4|\hat{\mu}|^2}, \quad (13)$$

$$a(x) + \frac{d\hat{F}_2^i}{d\hat{\mu}} = 0, \quad \text{for} \quad \hat{\mu} = 0.$$

Following Molchanov [13], one can write

$$\frac{d\hat{F}_2^i}{d\hat{\mu}} = \frac{1}{2\pi i} \int_L \hat{\gamma}_v(l) \left[\frac{1}{\hat{\mu} - \hat{\mu}(l)} - \frac{1}{\hat{\mu} - \bar{\hat{\mu}}(l)} \right] dl =$$

$$\frac{1}{2\pi i} \int_0^x \left[\frac{1}{\hat{\mu} - \hat{\mu}(\xi)} - \frac{1}{\hat{\mu} - \hat{\mu}(\xi)} \right] \frac{d\hat{\Gamma}}{d\xi} d\xi, \quad (14)$$

where ξ is abscissa of the point in which the vortex element under consideration has been shed from side edge of the wing, and $\hat{\Gamma}_v(\xi)$ represents a jump of the velocity potential at the moment of shedding of this vortex element

After the equation of evolution of vortex sheet has been solved the one term inner expansion of complex potential in the vicinity of side edge can be written in the following way

$$F^i(x, \mu) = \alpha^{4/3} a(x) \mu + \frac{\alpha^{4/3}}{2\pi i} \int_0^x \ln \left[\frac{\hat{\mu} - \hat{\mu}(\xi)}{\hat{\mu} - \hat{\mu}(\xi)} \right] \frac{d\Gamma_v(\xi)}{d\xi} d\xi. \quad (15)$$

Two term outer expansion of previous expression was found in the form

$$F^{io}(x, \mu) = \alpha a(x) \mu - \frac{\alpha^{5/3}}{\pi \mu} \int_0^x \mu_2(\xi) \frac{d\Gamma_v(\xi)}{d\xi} d\xi \quad (16)$$

On the surface of the wing $\mu = \pm\sqrt{-s}$, where "+" corresponds to the upper, and sign "-" to the lower surface of the wing. The outer asymptotics of integral circulation can be written as

$$\Gamma^{io} = 2\alpha a(x) \sqrt{-s} - \frac{2\alpha^{5/3}}{\pi \sqrt{-s}} \int_0^x \mu_2(\xi) \frac{d\Gamma_v(\xi)}{d\xi} d\xi, \quad (17)$$

wherefrom with account of the least degeneracy principle there can be determined gauge function and structure of the second term of the outer expansion of loading γ_2^o and integral circulation Γ_2^o .

$$\delta_2(\alpha) = \alpha^{5/3} \quad (18)$$

$$\gamma_2^i(\psi, \theta) = \sum_{n=0}^{\infty} \left[a_{on} \operatorname{ctg} \frac{\psi}{2} + \sum_{k=1}^{\infty} a_{kn} \sin k\psi \right] f_n(\theta); \quad (19)$$

$$\Gamma_2^o(\theta, \psi) = -2 \sum_{n=0}^{\infty} \left[a_{on} \ln \left| \cos \frac{\psi}{2} \right| + \sum_{k=1}^{\infty} a_{kn} \sin^2 \frac{k\psi}{2} \right] f_n(\theta), \quad (20)$$

where $f_0(\theta) = 1/\sin \theta$, $f_n(\theta) = \sin n\theta$ as $n \leq 1$.

Inner representation of (20) has the form

$$\Gamma_2^i(\theta, \psi) = -\sqrt{-\frac{2}{s}} \left[a_{on} \ln \left| \cos \frac{\psi}{2} \right| + \sum_{k=1}^{\infty} a_{kn} \sin^2 \frac{k\psi}{2} \right]. \quad (21)$$

Matching of outer and inner asymptotic expansions of circulation enables to establish the following correlation between the coefficients a_{kn}

$$a_{on} \ln \left| \cos \frac{\psi}{2} \right| + \sum_{k=1}^{\infty} a_{kn} \sin^2 \frac{k\psi}{2} = \frac{\sqrt{2}}{\pi} \int_0^\psi \mu_2(\psi_1) \frac{d\Gamma_v(\psi_1)}{d\psi_1} d\psi_1. \quad (22)$$

Condition (22) replaces in the outer flow region the standard requirement of zero loading at side edges of the wing in the case when account is taken of shedding and roll up of vortex sheets at side edges.

The structure of asymptotic expansion shows that the lift coefficient has the following asymptotic structure

$$C_y = C_1(\lambda) \alpha + C_2(\lambda) \alpha^{5/3} + \dots \quad (23)$$

As per the above algorithm the use of the method of matched asymptotic expansions in the problem of the flow past a wing with account of roll up of vortex sheets implies the following sequence of steps

- Within the linear lifting surface theory the first approximation is calculated with no account of vortex shedding from side edges.
- In vicinity of side edges and in variables stretched with gauge function $\alpha^{2/3}$ the equation of dynamics of the vortex sheet is solved accounting for information on behavior of integral circulation of the first order near side edge (4) and Kutta-Zhukovsky condition (7) of smooth detachment of vorticity.
- To the order of $O(\alpha^{5/3})$ there is solved homogeneous equation of the lifting surface in which a conventional condition of zero loading at side edge (22), containing the information on the rolled up vortex sheet.

The approach presented herein can also be applied in the case when the wing moves in proximity of a boundary. In this case the functions C_1 and C_2 , entering formula (23), will be dependent on type of the boundary, distance of the wing

form the boundary and, if the boundary is a free surface, upon the magnitude of Froude number.

CALCULATED RESULTS AND ANALYSIS

As per previous analysis, the first step of the calculation consists in performing the roll-up process in the local (physical) domain with dimensions of the order $O(\alpha^{2/3}\lambda^{2/3})$. Therewith, one employs an expression for the function $a(x)$, entering the equation of dynamic evolution of the side edge vortex sheet, on the basis of the theory of a slender wing. In the process of calculation of roll-up the corresponding integral contributions are approximated by appropriate system of discrete vortices, and the problem is reduced to numerical solution of associated algebraic equations. The computational procedure is known to be inherently unstable and requires application of special algorithms. In search of coherent structures an analysis has been performed of different methods of regularization. The most effective among the latter, as found out by the authors, is use of the concept of *finite thickness* of the shed vortical sheets. This approach to regularization is based on solution of a linear parabolic equation of dissipation of vortex cores. Another factor, affecting stability of computations was selection of initial position of discrete vortex closest to the tip of the side edge. In this connection, it has been concluded that this factor is strongly coupled with the time step of the numerical procedure of the roll-up. All calculation have been performed with use of the package *Mathematica 3.0* for Windows'95 operating system. Some representative results, obtained with use of the present asymptotic theory are given in Figs. 4-11. Figures 4-6 demonstrate evolution of the roll-up of the side edge vortex sheets for wings of small aspect ratio with different planforms. The resulting "curls" are plotted in stretched side edge domain. It should be noted that in most of the calculated examples the number of time (x -wise) steps varied from 80 to 100 which turned out to be more than sufficient for convergence of the roll-up procedure. It can be observed from comparative analysis of the Figures, associated with different planforms that the geometry of the wing has noticeable effect on the evolution of the vortex sheets.

As shown in the present theory the global characteristics of the wing are affected by static moment of vorticity of rolled-up sheets with respect to the side tip, accumulated at the trailing edge.

The resulting expression for the lift coefficient of a wing of small aspect ratio has been obtained in the form

$$C_L = \frac{\pi}{2}\alpha\lambda + 2\sqrt{2}M_{st}(\alpha\lambda)^{5/3}(n+1)^2, \quad (24)$$

where M_{st} represents static moment of vorticity of the rolled-up vortex sheet (with respect to the side tip) at the trailing edge, n is a parameter, governing the planform of the wing by means of the following span equation

$$l_o(x) = \frac{l}{2}x^n. \quad (25)$$

The following set of Figs. 7-10 illustrates behaviour of the lift coefficient of a slender wing with triangular planform versus angle of attack. For comparison on the same graphs are plotted some calculated results employing semi-empirical formulae as well as relevant experimental data. The aforementioned semi-empirical formulae have been borrowed from Rom [15], p. 171 and are listed below

- The relationship, proposed by Edwards [16]

$$C_L = \frac{\pi}{2}\alpha\lambda + \pi\alpha^{5/3}\lambda^{1/3}. \quad (26)$$

- The formula first developed by Lawrence and Flax [17] and later adopted by Küchemann [18]

$$C_L = \frac{\pi}{2}\alpha\lambda + 2\alpha^2 \quad (27)$$

- Empirical relationship, developed by Alexander [19] with use of measurements of Peckam [20], Kirby [21], Hummel and Srinivasan [22] and Barlett and Vidal [23]

$$C_L = 1.23\lambda^{0.77}\alpha + 1.59\lambda^{0.60}\alpha^{1.74} \quad (28)$$

- The equation, proposed by Poisson-Quinton and Erlich, reported to hold for $\lambda < 0.5$

$$C_L = 0.915 \frac{4.9}{4.9 + \lambda} \left(\frac{\pi}{2}\alpha\lambda + \pi\alpha^{5/3}\lambda^{1/3} \right). \quad (29)$$

REFERENCES

1. Prandtl L. Über die Entstehung von Wirbeln in der Idealen Flüssigkeit, *Vorträge aus Hydro- und Aerodynamik*, Berlin, 1924.
2. Belotserkovsky, S.M., Nisht, M.I. Separated and unseparated ideal fluid flow past thin wings, M., Nauka, 1978, 352 p.

3. Betyaev, S.K. Separated flows, AN SSSR, Sibirskoye otделение, Institut teoreticheskoi i prikladnoi mekhniki, *Preprint*, n.14-83, Novosibirsk, 1983, 29 c.
4. Smith J.H.B. Improved Calculations of Leading Edge Separation from Slender Delta Wings, *Proc. Roy. Soc.*, A306, 1968, pp. 67-90.
5. Kaden H. Aufwicklung einer unstabilen Unstetigkeitsfläche, *Ingenieur, Archiv*, 1931, Bd.2, Heft 2.
6. Moore D.W. A Numerical Study of the Roll-Up of a Finite Vortex Sheet, *J. Fluid Mechanics*, 1975, Vol. 63, pp. 225-235.
7. Guiraud J.P., Zetounian, R.Kh. A Double Scale Investigation of the Asymptotic Structure of Rolled-Up Vortex Sheets, *J. Fluid Mechanics*, 1977, Vol. 79, pp. 93-113.
8. Moore D.W., Saffman P.G. Axial Flow in Laminar Trailing Vortices, *Proc. Roy. Soc.*, 1973, A333, pp. 491-508.
9. Nikolsky, A.A. On "second" form of motion of ideal fluid near a body (investigation into separated vortex flows), *Dokladi AN SSSR*, 1957, Vol. 116, No. 2.
10. Nikolsky, A.A. Similarity laws for a three-dimensional steady separated fluid and gas flows past bodies, *Ucheniye Zapiski TSAGI*, Vol. 1, No. 1, 1970, pp. 1-7.
11. Nikolsky, A.A. Theoretical research in mechanics of fluids and gases, *Trudy TSAGI*, vyp. 2122, M., 1981, 285 p.
12. Sudakov, G.G. Calculation of separated flow past a thin delta wing of small aspect ratio, *Ucheniye Zapiski TSAGI*, Vol. 5, No. 2, 1974, pp. 10-18.
13. Molchanov, V.F. Method of separation of the principal part of nonlinear characteristics of a rectangular wing in ideal fluid flow, *Ucheniye Zapiski TSAGI*, 1980, Vol. XI, No. 1, pp. 12-17.
14. Rozhdestvensky, K.V. Derivation of the effect of vortex roll-up upon aerodynamic characteristics of a wing by the method of matched asymptotic expansions, *Proc. Second International Conference AiM'96 - Asymptotics in Mechanics*, St-Petersburg, October 13-16, 1996, pp. 215-222.
15. Rom, J. High Angle of Attack Aerodynamics: Subsonic, Transonic and Supersonic Flows, *Springer-Verlag*, 1993.
16. Edwards, R.H. Leading edge separation from delta wings, *J. Aeronaut. Sci.*, Vol. 21, No. 2, 1954, pp. 134-135.
17. Flax, A.H., Lawrence, H.R. The aerodynamics of low aspect ratio wings and wing-body combinations, *Third Anglo-American Aeronautical Conference*, 1951.
18. Küchemann, D. Aircraft shapes and their aerodynamics for flight at supersonic speeds, *Advances in Aeronautical Sciences*, Vol. 3, 1962, Pergamon Press.
19. Alexander, A.J. Correlation of total lift data for thin sharp-edged, low aspect ratio delta wings at low speeds, *The Aero. Journal, Royal Aeronautical Society*, 1971, pp. 569-570.
20. Peckham, D.H. Low speed wind tunnel tests on a series of uncambered slender pointed wings with sharp edges, *British ARC, R&M*, # 3186, 1961.
21. Kirby, D.A. An experimental investigation of the effect of planform shape on the subsonic longitudinal stability characteristics of slender wings, *British ARC, R&M*, # 3568, 1969.
22. Hummel, D., Srinivasan, P.S. Vortex breakdown effect on the low speed aerodynamic characteristics of slender delta wings in symmetrical flows, *Journal of the Royal Aeronautical Society*, Vol. 71, # 676, 1967, pp. 319-322.
23. Barlett, G.E., Vidal, R.J. Experimental investigation of influence of edge shape on the aerodynamic characteristics of low aspect ratio wings at low speeds, *Journal of the Aeronautical Sciences*, Vol. 22, #8, 1955, pp. 517-533.

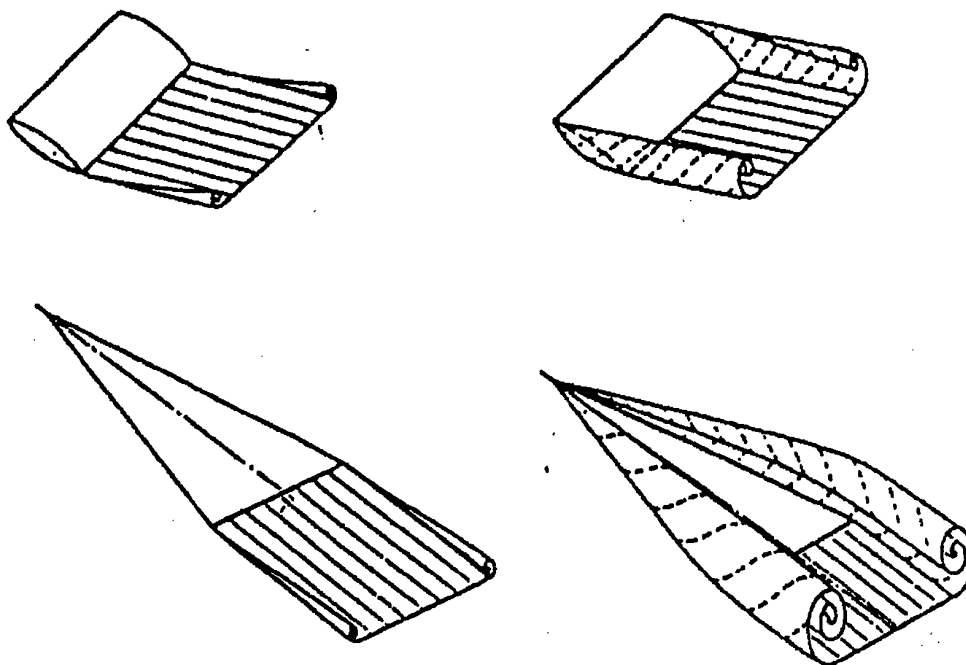


Figure 1: Trailing vortex sheet models in the linear and nonlinear lifting surface theories, from [15].

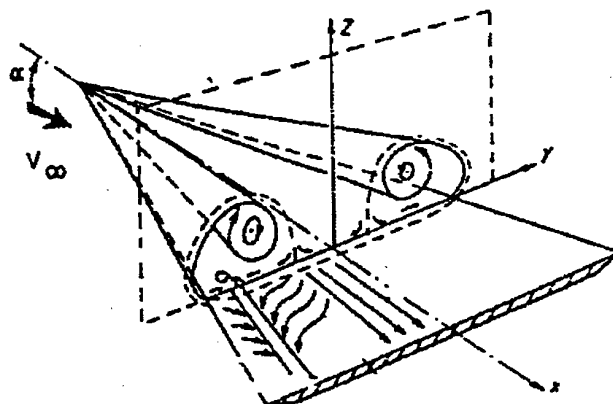


Figure 2: An example of the flow field around a delta wing featuring rolled-up vortex sheets.

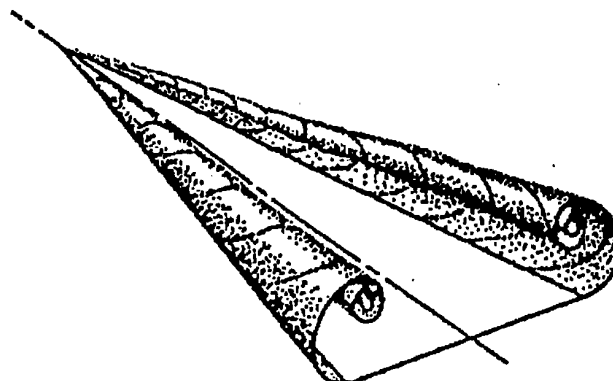


Figure 3: An example of a flow structure around a delta wing with a cross-section containing rolled-up vortex spirals.

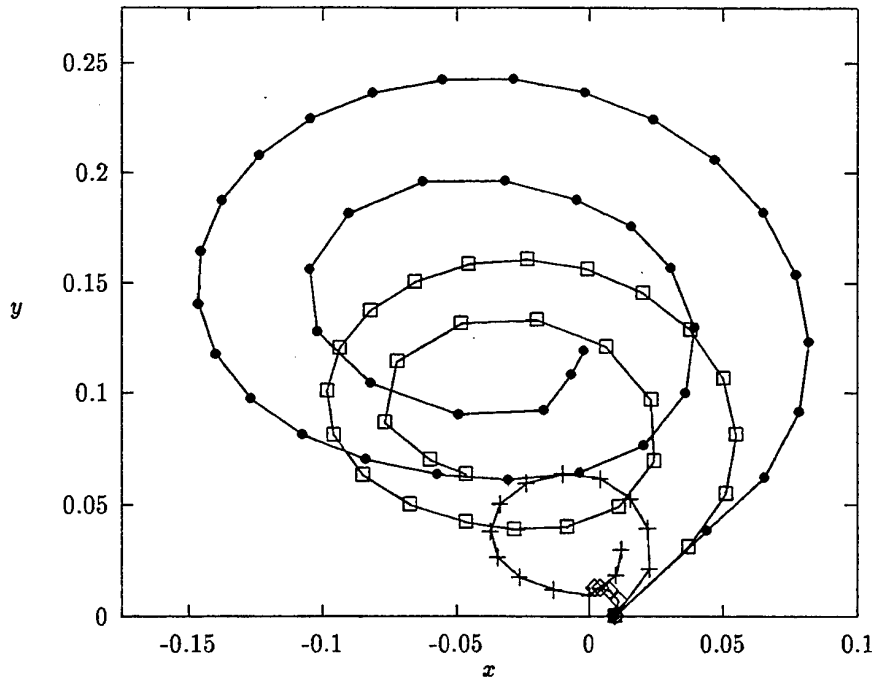


Figure 4: Chordwise roll up of the spiral vortex sheet over a slender delta wing.
 \diamond - 12.5% chord; $+$ - 37.5% chord; \square - 75% chord; \bullet - 100% chord.

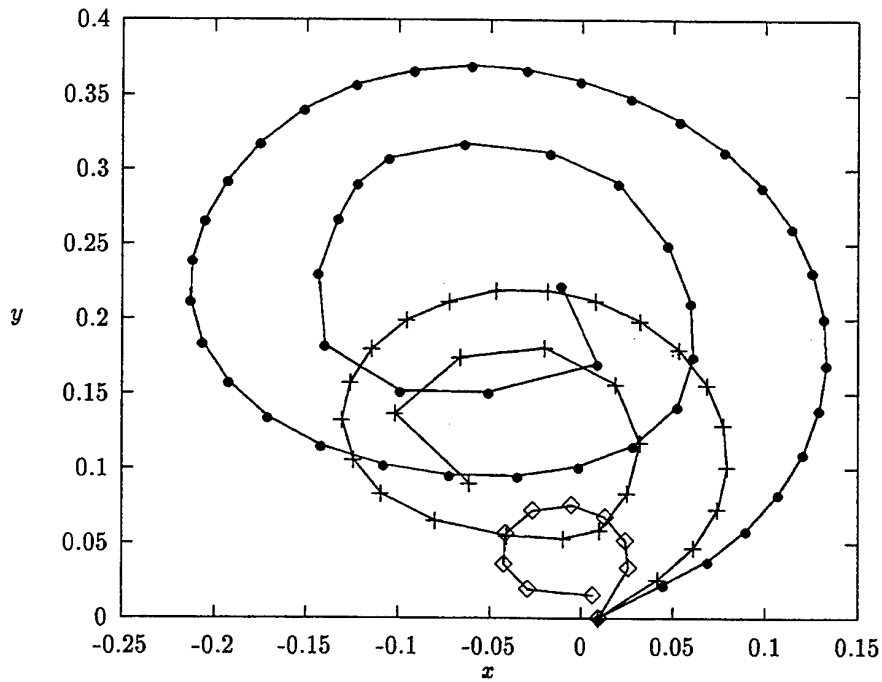


Figure 5: Chordwise evolution of vortex sheets for a slender wing of parabolic planform.
 \diamond - 20% chord; $+$ - 60% chord; \bullet - 100% chord.

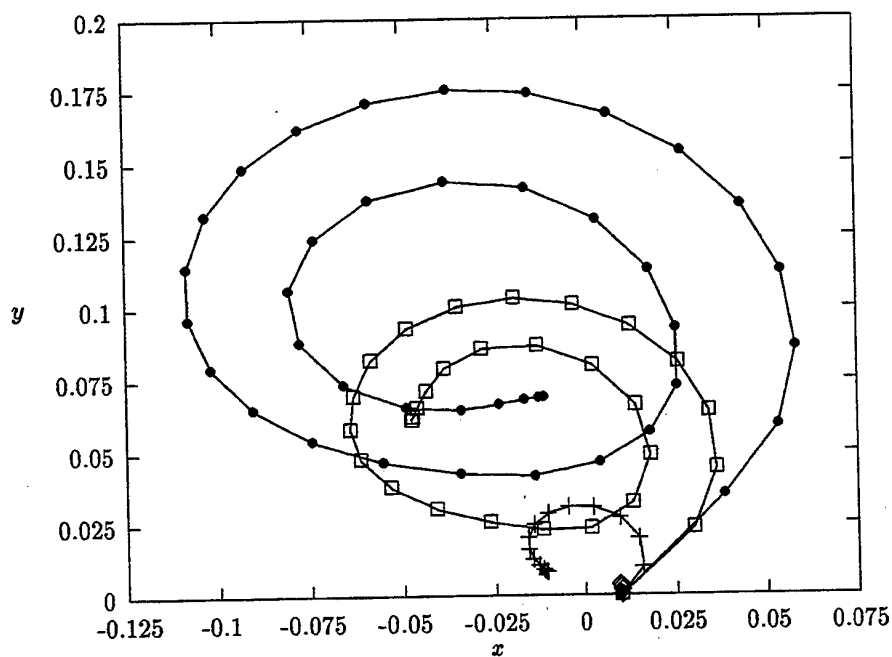


Figure 6: Chordwise evolution of vortex sheets for a slender wing of cusped planform.
 \diamond - 12.5% chord; $+$ - 37.5% chord; \square - 75% chord; \bullet - 100% chord.

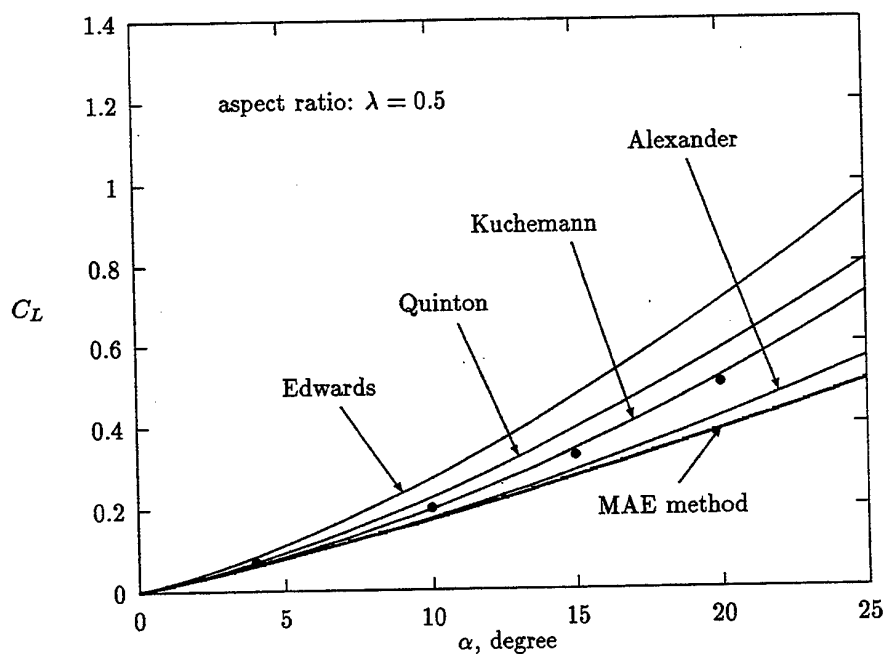


Figure 7: Comparison of the present (asymptotic) theory with semi-empirical formulae and experimental data for a slender wing of a triangular planform, $\lambda = 0.5$

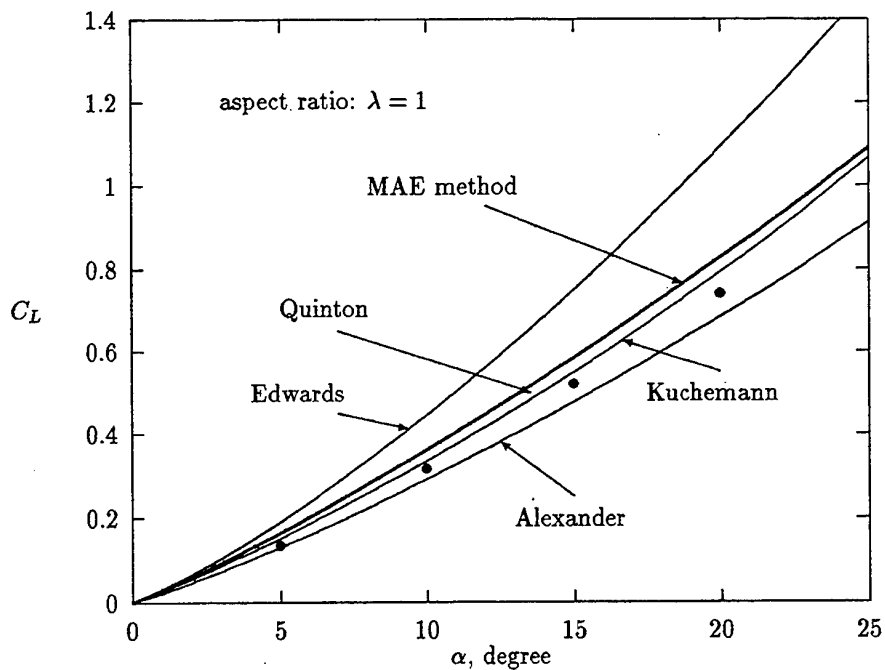


Figure 8: Comparison of the present (asymptotic) theory with semi-empirical formulae and experimental data for a slender wing of a triangular planform, $\lambda = 1.0$

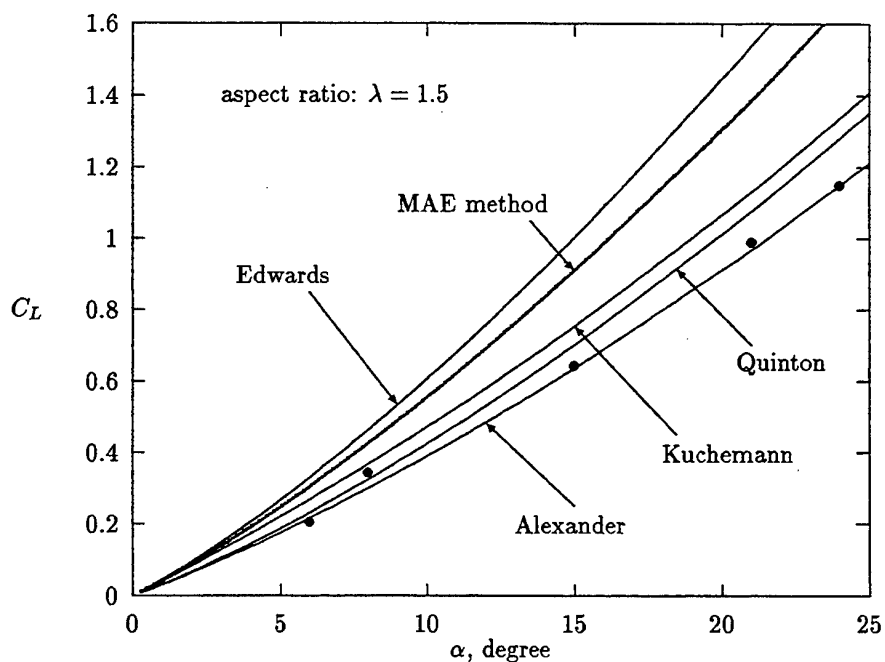


Figure 9: Comparison of the present (asymptotic) theory with semi-empirical formulae and experimental data for a slender wing of a triangular planform, $\lambda = 1.5$

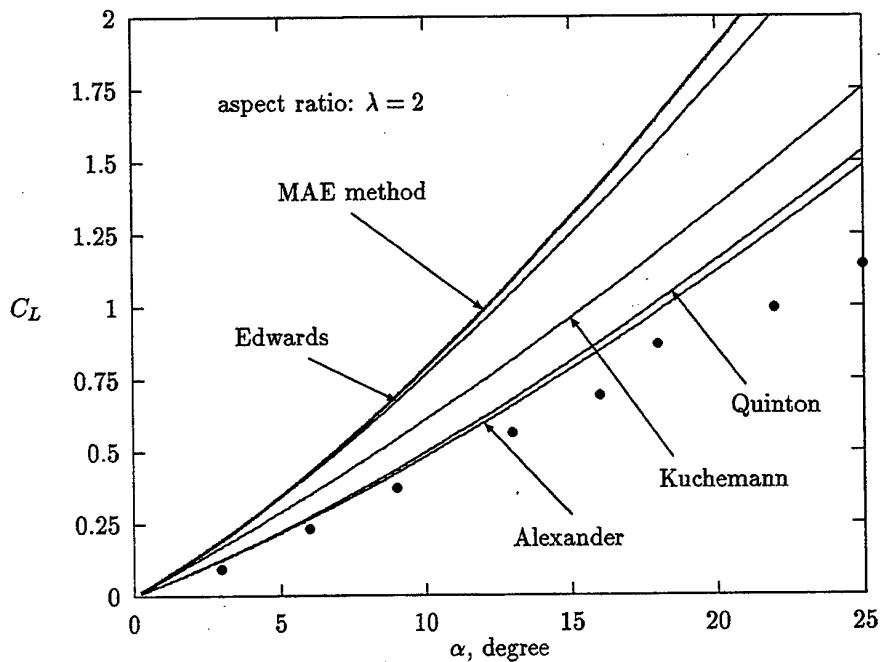


Figure 10: Comparison of the present (asymptotic) theory with semi-empirical formulae and experimental data for a slender wing of a triangular planform, $\lambda = 2.0$

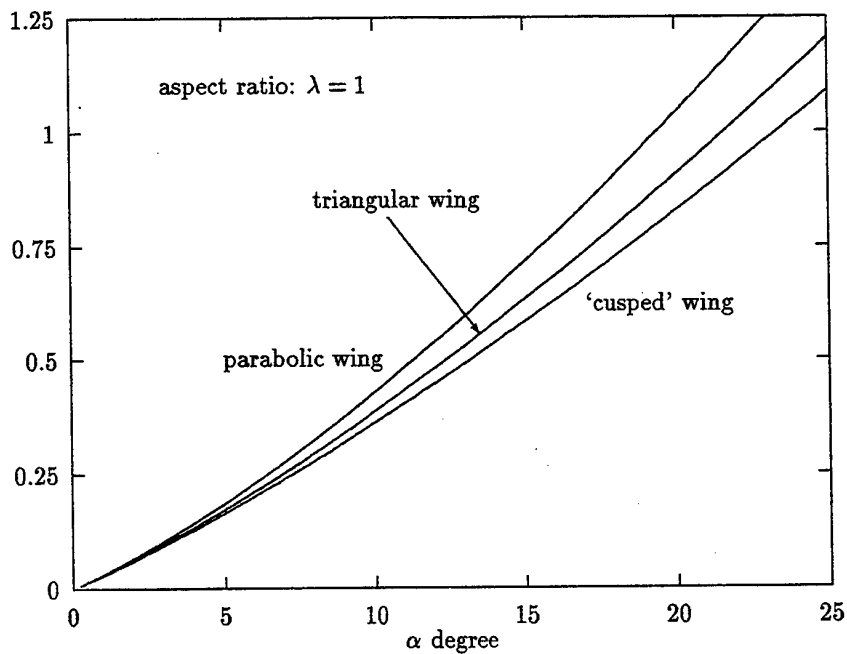


Figure 11: Lift coefficient of a slender wing versus parameter α for three representative planforms and $\lambda = 1$.

FREE-SURFACE VISCOUS FLOWS.

Chairman : C.H.Sung

THE NUMERICAL SIMULATION OF THE YAW FLOW OF A FREE SURFACE SHIP

A. Di Mascio¹ and E.F. Campana¹

¹I.N.S.E.A.N., Istituto Nazionale per Studi ed Esperienze di Architettura Navale
Via di Vallerano 139, 00128-Roma, Italia
Fax: +39-06-5070619; E-Mail: e.campana@insean.it

ABSTRACT

Numerical solution for the steady flow past a ship in straight course with a yaw angle have been obtained with a finite volume RANSE solver.

Two different turbulent models, namely the Baldwin - Lomax and the Spalart - Allmaras models, have been applied and the results have been validated against experimental measurements for boundary layer, wake and wave fields of a Series 60 hull in yaw motion.

Attention has been devoted to the verification of the numerical results, both for global quantities, for which monotonic convergence is obtained on the three finest grids, and for local variables.

Results obtained with the Baldwin-Lomax model agree well for global coefficients and wave profiles, but the contours of the axial velocity in some cross-planes reveal that most details of the measured data are not caught. Results for the axial velocity contours with the Spalart-Allmaras model are in better agreement with experimental data.

NOMENCLATURE

		ζ	Free surface elevation
		n_i	Normal unit vector
		t_i^t	Tangent unit vector
		D_{ijk}	Finite volume
		V_{ijk}	Volume of D_{ijk}
$x_i \quad i = 1, 2, 3$	Cartesian Coordinate		
x, y, z	Cartesian Coordinate		
t	Time		
$u_i \quad i = 1, 2, 3$	Velocity Components		
u, v, w	Velocity Components		
p	Pressure		
Re	Reynolds Number		
Fr	Froude Number		
Δt	Time Stepping		
ν_t	Eddy Viscosity		
k	Turbulent kinetic energy		
τ_{ij}	Stress Tensor		
δ_{ij}	Kronecker operator		
α	Yaw angle		

INTRODUCTION

The viscous, incompressible, free-surface flow past a hull advancing steadily with a yaw angle is relevant for the prediction of the hydrodynamic performances of a vessel in manoeuvring. As a matter of fact, these subject still heavily rely upon experimental data in manoeuvring tanks.

Alternatively, the motion of a vessel may be computed by coupling the rigid body dynamics with the solution of the flowfield about the hull. As well known, by means of the RANS (Reynolds-averaged Navier-Stokes) equations, the forces relevant to ship maneuverability are related to the vorticity generated and convected during the motion. From this point of view numerical solutions of the RANS equations for

this problem are also relevant in the development of simplified models. For instance, data about the location of separation lines and on the evolution of the wake can be used to calibrate and validate inviscid rotational models, which at present give satisfactory results only when the separation line is known [1]. The specification of these data requires a CFD solution unless the boundary layer separation is enforced at a sharp edge.

In these kind of problem the numerical simulation is difficult since the non-symmetric flow over the hull is fully three-dimensional and highly turbulent. Boundary layer separation and re-attachment often occurs, large wakes and complicated wave pattern are formed. Hence the analysis of the solution obtained by means of the commonly employed turbulent models is extremely interesting, as well as the use of models not applied before to ship hydrodynamics problems. Recently, a number of papers have been published on this subject, both with steady or unsteady numerical approach [2, 3, 4, 5]. Both algebraic and two-equations turbulence models have been used, namely the Cebeci-Smith, the Baldwin-Lomax and the $k - \omega$ model.

The new one-equation model by Spalart and Allmaras [6] is encountering an increasing popularity in the aeronautical community, whereas there is little experience on the use of this model in the naval hydrodynamic context. In this paper we have carried out a validation and verification test on the Spalart and Allmaras model by applying it to the simulation of the yaw flow past a Series 60 model. The results are compared with those obtained with the same flow solver with the Baldwin-Lomax model [7] and with the experimental data collected by Longo [8].

MATHEMATICAL AND NUMERICAL MODEL

The solution of the free-surface viscous steady flow past a ship hull can be obtained as the asymptotic solution of the unsteady pseudo-compressible Navier-Stokes equations, [9], which in non-dimensional form are:

$$\begin{aligned} \frac{\partial p}{\partial t} + \beta \frac{\partial u_i}{\partial x_i} &= 0; \quad i = 1, 2, 3 \\ \frac{\partial u_i}{\partial t} + \frac{\partial u_i u_j}{\partial x_j} + \frac{\partial p}{\partial x_i} - \frac{\partial \tau_{ij}}{\partial x_j} &= 0 \end{aligned} \quad (1)$$

where x_i is the i -th coordinate, u_i the i -th component of the velocity vector, $p = P + z/Fr^2$, P the pressure, Fr the Froude number, β the pseudo-compressibility factor, $\tau_{ij} = \mu_t \left(\frac{\partial u_i}{\partial x_j} + \frac{\partial u_j}{\partial x_i} \right)$

the stress tensor, $\nu_t = \frac{1}{Re} + \nu_{turb}$ the global kinematic viscosity, Re the Reynolds number and ν_{turb} the turbulent viscosity.

As to the boundaries, a no-slip condition $u_i = 0$ is enforced on the hull whereas the dynamic condition at the unknown free surface enforces continuity of normal and tangential stresses through the surface,

$$p + \tau_{ij} n_j n_i = \frac{\zeta}{Fr^2} \quad \tau_{ij} n_j t_i^l = 0 \quad (2)$$

air and surface tension effects have been neglected. In the above equations n_i is the normal unit vector, t_i^l ($l = 1, 2$) two unit tangent vectors, and $\zeta = \zeta(t, x, y)$ the surface elevation. The kinematic condition states that the free surface moves with the same velocity as the fluid particles

$$\frac{\partial \zeta}{\partial t} + u \frac{\partial \zeta}{\partial x} + v \frac{\partial \zeta}{\partial y} = w \quad (3)$$

The mathematical equations are approximated by a discrete finite volume model. The fluid domain D is divided into structured blocks, each with $N_i \cdot N_j \cdot N_k$ disjoint hexahedrons D_{ijk} . By integrating the equations on each volume, we get

$$\begin{aligned} \int_{V_{ijk}} \frac{\partial p}{\partial t} dV + \beta \sum_{s=1}^6 \int_{S_s} u_i n_i dS &= 0, \quad i = 1, 2, 3 \\ \int_{V_{ijk}} \frac{\partial u_i}{\partial t} dV + \sum_{s=1}^6 \int_{S_s} [u_i u_j n_j + p n_i - \tau_{ij} n_j] dS &= 0 \end{aligned} \quad (4)$$

S_s is the s -th face of the finite volume D_{ijk} with measure V_{ijk} . The viscous terms at the cell interfaces are computed by a finite volume approximation of the derivatives of the velocity vector. E.g., at the cell face $i + \frac{1}{2}, j, k$

$$\begin{aligned} \frac{\partial u_i}{\partial x_j} \Big|_{i+\frac{1}{2}, j, k} &= \frac{1}{V_{i+\frac{1}{2}, j, k}} \int_{V_{i+\frac{1}{2}, j, k}} \frac{\partial u_i}{\partial x_j} dV + O(\Delta^2) \\ &= \frac{1}{V_{i+\frac{1}{2}, j, k}} \int_{S_{i+\frac{1}{2}, j, k}} u_i n_j dS + O(\Delta^2) \end{aligned} \quad (5)$$

The integral is extended to the volume $V_{i+\frac{1}{2}, j, k}$ with boundary $\Sigma_{i+\frac{1}{2}, j, k}$ that includes the cell face $S_{i+\frac{1}{2}, j, k}$ and is overlapped to half the cell i, j, k and half the cell $i + 1, j, k$. The stress tensor at this cell interface is given by

$$\tau_{ij} \Big|_{i+\frac{1}{2}, j, k} = \nu_{i+\frac{1}{2}, j, k} \left(\frac{\partial u_j}{\partial x_i} + \frac{\partial u_i}{\partial x_j} \right) \Big|_{i+\frac{1}{2}, j, k} \quad (6)$$

Velocity and pressure at the interface, needed for the computation of the Eulerian fluxes, are evaluated by a second-order E.N.O.-type scheme [10]. These schemes, originally developed for compressible flows, were adapted to pseudo-compressible

flows in [11] The discrete equations to be solved can be rewritten in semi-discrete vector form as

$$\frac{\partial \mathbf{q}}{\partial t} \Big|_{i,j,k} + \frac{1}{V_{i,j,k}} \mathbf{L}_{i,j,k} = 0 \quad (7)$$

where \mathbf{L} represents the flux balance on the cell (i, j, k) . A Runge-Kutta type scheme updates the numerical solution from step n to step $n+1$. The general form of a N_p -stage explicit scheme is

$$\begin{cases} \mathbf{q}_{i,j,k}^0 = \mathbf{q}_{i,j,k}^n \\ \mathbf{q}_{i,j,k}^p = \alpha^p \mathbf{q}_{i,j,k}^0 + (1 - \alpha^p) \mathbf{q}_{i,j,k}^{p-1} - \gamma^p \frac{\Delta t_{i,j,k}}{V_{i,j,k}} \times \\ \quad \times \mathbf{L}_{i,j,k}(\mathbf{q}^{p-1}) \quad p = 1, \dots, N_p \\ \mathbf{q}_{i,j,k}^{n+1} = \mathbf{q}_{i,j,k}^{N_p} \end{cases} \quad (8)$$

where a local time step $\Delta t_{i,j,k}$ was chosen to improve the convergence rate. It can be seen that with a proper choice of N_p , α , and γ , most classical scheme can be recovered.

A multigrid scheme was used to enhance the convergence rate. A study of multigrid efficiency for ENO schemes can be found in [12].

Turbulence Models

In the simulations two different turbulent models have been employed: the Baldwin-Lomax algebraic turbulent model [13] and the Spalart-Allmaras one equation model [6]. Both these models are based on the eddy viscosity concept, i.e. on the assumption that the Reynolds stress tensor $(-\rho \overline{u'_i u'_j})$ is related to the mean strain rate through the eddy viscosity ν_T

$$-\overline{u'_i u'_j} = \nu_T \left(\frac{\partial \bar{u}_i}{\partial x_j} + \frac{\partial \bar{u}_j}{\partial x_i} \right) - \frac{2}{3} \delta_{ij} k \quad (9)$$

where k is the turbulent kinetic energy. For the sake of completeness, a brief description of the models is given in the following. For details, the reader is referred to [13] for a description of the Baldwin and Lomax model and to [6] for the Spalart and Allmaras model.

In what follows, it can be noted that the Spalart-Allmaras model is strictly "local", in the sense that the coefficients in the equations depends only on quantities that can be computed from the velocity field and its first order tensor in each point, and from the distance from the nearest wall. This property renders this

model very attractive when dealing with complex geometries and therefore with multiblock meshes or unstructured grids. On the contrary, the Baldwin-Lomax model requires the evaluation of the wall shear stress at the intersection of the "normal" to the wall; consequently, ambiguities often arises when simulating the flow past boundaries like, for instance, hull with appendages.

Baldwin-Lomax model

The Baldwin-Lomax model is an eddy viscosity zero-equation (algebraic) model, in which ν_T is given by

$$\nu_T = \begin{cases} \nu_T^i = \left[0.4d \left(1 - e^{-\frac{d u_\tau}{26\nu}} \right) \right]^2 \omega & d \leq d_c \\ \nu_T^o = 0.02688 F_{wake} F_{kleb}(d) & d \geq d_c \end{cases} \quad (10)$$

where d is the normal distance from the wall, d_c is the smallest value of d at which $\nu_T^i = \nu_T^o$, u_τ the friction velocity at the wall and ω the magnitude of the vorticity vector. Moreover, $F_{wake} = \min(d_M F_M, 0.25 d_M U_{dif}^2 / F_M)$, U_{dif} being the difference between the maximum and minimum of u in the profile at fixed x -station, d_M is the distance at which the function $F(d) = d\omega[1 - \exp(-\frac{d u_\tau}{26\nu})]$ attain its maximum value F_M . Finally, $F_{kleb}(d) = 1/[1 + 5.5(0.3d/d_M)^6]$ (Klebanoff intermittency factor).

Spalart-Allmaras model

In the Spalart and Allmaras model, the eddy viscosity ν_T is computed by means of an intermediate variable $\tilde{\nu}$

$$\nu_T = \tilde{\nu} f_{v1}(\chi), \quad \chi = \frac{\tilde{\nu}}{\nu}, \quad f_{v1}(\chi) = \frac{\chi^3}{\chi^3 + C_{v1}^3} \quad (11)$$

$\tilde{\nu}$ is computed from the solution of a partial differential equation

$$\begin{aligned} \frac{D\tilde{\nu}}{Dt} &= c_{b1} [1 - f_{t2}] \tilde{S} \tilde{\nu} \\ &- \left[c_{w1} f_w - \frac{c_{b1}}{k^2} f_{t2} \right] \left[\frac{\tilde{\nu}}{d} \right]^2 \\ &+ f_{t1} \Delta U \\ &+ \frac{1}{\sigma} [\nabla \cdot ((\nu + \tilde{\nu}) \nabla \tilde{\nu}) + c_{b2} (\nabla \tilde{\nu})^2], \end{aligned} \quad (12)$$

where $\tilde{S} = S + [\tilde{\nu}/(k^2 d^2)] f_{v2}$, S is the magnitude of the vorticity vector, d the distance from the wall, f_{t1} , f_{t2} , f_w , f_{v2} are functions that depends only on χ and the distance from the wall; finally, the c -s and k are constants. The first two terms in the right hand side represent production and destruction of $\tilde{\nu}$, respectively; the third one is the so-called "trip"

term, that allows to specify the laminar-turbulent transition point (in the results shown in the next section, this term was always turned off); the last part is a dissipation term, that contains also a non conservative portion $c_{b2}(\nabla \bar{v})^2$ which is responsible, together with the non-linear part of the diffusion term $\nabla \cdot (\bar{v} \nabla \bar{v})$, for the advection of a turbulent front into non-turbulent regions.

RESULTS

As a benchmark test for the comparison between the two turbulence models, the flow past a Series 60 hull with $C_b = 0.6$, moving in steady motion, was computed for yaw angles $\alpha = 0^\circ, 2.5^\circ, 5^\circ, 10^\circ$ at $Fr = 0.316$, $Re = 5.3 \cdot 10^6$. Detailed experimental data were collected by Longo *et al.* in [8] for the same configuration. In both the simulation and the experiments, 'port' is the pressure side, 'starboard' the suction side.

The two turbulence models have been tested by implementing the models on the same numerical code. Comparisons will be shown with both the models, although in the assessment of the characteristic of the numerical code only the Baldwin-Lomax model has been used.

As expected, the use of different turbulent models has no appreciable influence on the wave pattern and on the wave profile. Hence, comparison between the two turbulence models will be carried out by comparing the local velocity fields in some transversal sections of the fluid domain.

To assess the convergence and the order of accuracy of the developed numerical code, we decided to remove any possible source of uncertainty and fixed in the computations the hull position to the measured sinkage σ , trim τ , and heeling angle η . The fluid domain was divided into port and starboard blocks with O-O topology, each block with $96 \times 96 \times 64$ cells in stream-wise, normal, and girth-wise direction, respectively. Five coarser were generated by halving the number of cells in each direction in the previous finer grid. Although the coarsest grid is only $6 \times 6 \times 4$, and this mesh is too poor to get an accurate numerical solution, it is convenient to have such a coarse grid to speed up convergence with the full multigrid approach.

The different grid levels were used to get estimates of the grid convergence uncertainties for global quantities: C_t, C_s, C_m , following the suggestions by [14].

Fig. (1) shows the grid convergence index GCI:

$$GCI = \frac{F_x^{2h} - F_x^h}{F_x^h} \quad (13)$$

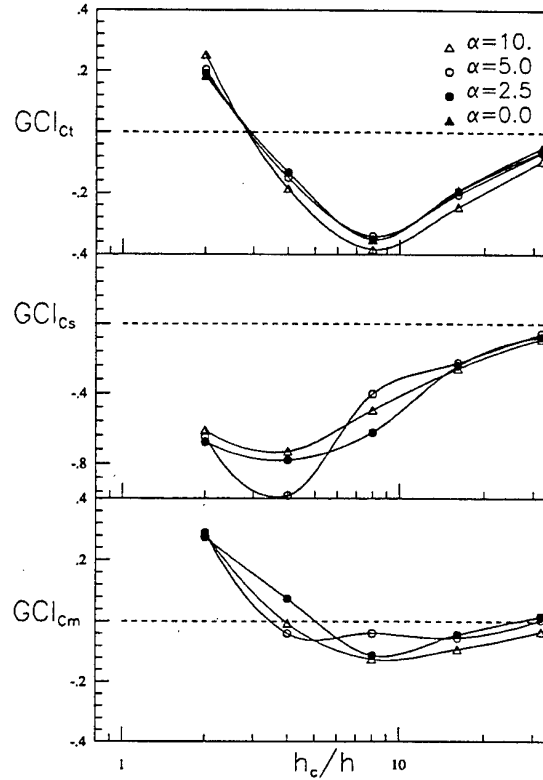


Figure 1: Grid Convergence Index for the hydrodynamic coefficients C_t, C_s, C_m for several yaw angles. $Fr = 0.316$, $Re = 5.3 \cdot 10^6$

and the computed values of hydrodynamic coefficients as a function of the grid refinement ratio h_c/h . h_c is the grid step in the coarsest grid. Monotonic convergence is obtained for the last three finer grids for all yaw angle. The GCI is not sufficient to assess grid convergence, because this analysis is meaningful only if the results are in the asymptotic range, i.e. when the leading order term in the truncation error dominates over the other terms, and therefore a asymptotic behavior can be extrapolated. An important indicator of the attained grid convergence is the apparent convergence order \tilde{N} , defined as

$$\tilde{N} = \frac{1}{\log 2} \log \left(\frac{f^{4h} - f^{2h}}{f^{2h} - f^h} \right) \quad (14)$$

Superscripts $h, 2h, 4h$ refer to three solutions computed on three different grid levels, obtained by doubling the grid size with respect to the previous coarser level. The computed values of \tilde{N} show that the asymptotic range was probably reached, at least for the force coefficients, since it is always close to the theoretical value 2, as shown in the following table

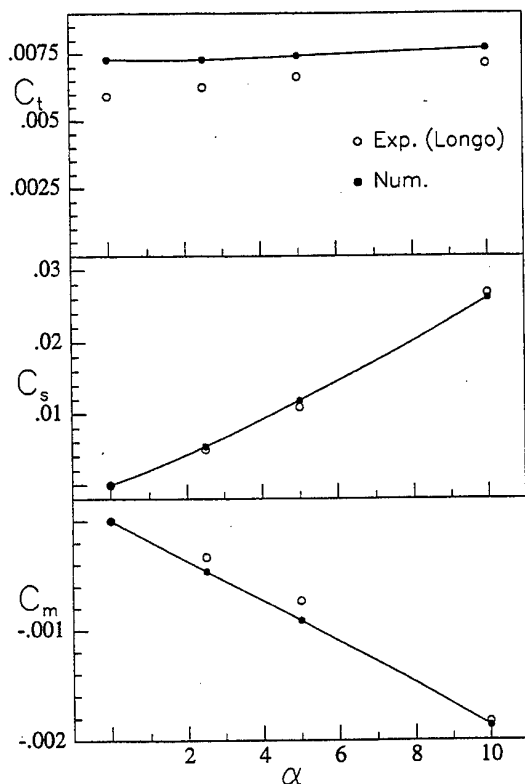


Figure 2: Hydrodynamic coefficients as a function of the yaw angle

for several yaw angle α .

α	0.0	2.5	5.0	10.0
\dot{N}_{C_t}	2.00	1.74	1.73	1.52
\dot{N}_{C_s}	—	1.75	2.05	1.67
\dot{N}_{C_m}	—	1.46	3.54	1.48

While the yaw moment and the side force coefficients show a significant increase with the yaw angle, the variation of the total resistance is less pronounced, fig. (2). The calculated coefficients agree well with experimental data for side forces and yaw moments, but the total resistance coefficient is over-predicted by up to 20%, especially for small yaw angles.

As an example, results obtained with both the turbulence models have been reported for the wave profiles along the hull. In the $\alpha = 5^\circ$ case the computed wave profiles on the finest grid level computed with the Baldwin-Lomax model are shown in figs (6), (7), while those obtained in the $\alpha = 10^\circ$ case with the Spalart-Allmaras model are shown in (4), (5). In both cases numerical results agree well with measured waves.

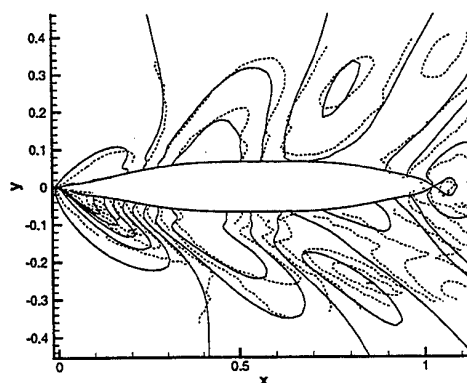


Figure 3: Numerical (solid) and experimental (dashed) wave pattern ($\alpha = 5^\circ$).

Fig. (3) compares computed and measured wave patterns for $\alpha = 5^\circ$. On the suction side (starboard), results agree well with troughs and crests in the correct positions. On the pressure side (port), measurements show a decreased diverging wave angle and shorter wave lengths. To maintain the same accuracy, more grid points would be needed in this region. However, for simplicity, we decided to use the same grid on both sides of the hull, allowing a less accurate resolution of the wave pattern in this region.

The comparison between the two turbulence models is carried out by comparing the local velocity fields in four transversal sections. The analysis has been focused on the starboard region, where viscous and wave effects are stronger.

In figs. (8), (9), (10), (11), the results obtained with the Baldwin-Lomax model have been compared with the experimental data, while in figs. (12), (13), (14), (15) results computed by using the Spalart-Allmaras model are shown. Contours of the axial velocity u are shown at $x = 0.2, 0.8, 0.9, 1.0$ for $Fr = 0.316$, $Re = 5.3 \cdot 10^6$, and $\alpha = 10^\circ$. We have chosen the ship length L_{pp} as reference length and a point on the waterplane at the bow as the origin of the x axis; then $x = 0.2$ is near the bow, $x = 1.0$ is the propeller plane.

With the Baldwin-Lomax model, although the global trends are predicted, the strong bilge vortex in the suction side in the numerical simulation is much weaker than in the experiment. The Reynolds stresses in the simulation seem to be too strong with respect to the actual situation, and therefore the shed vorticity too weak. This is illustrated in fig. (16), fig. (18), by comparing numerical and experimental streamlines for $x = 1.0$. In the experiments the vortex is approximately located

at $y = 0.02, z = -0.03$. The simulation predicts a less intense vortex, located at the same depth, but at $y = 0.01$. With the Spalart-Allmaras model, global trends are much better predicted. In all the computed transversal sections the agreement between numerical and experimental data is better than that obtained with the Baldwin-Lomax model. Furthermore, the strong bilge vortex in the suction side is much more like the one visualized in the experiment. This is illustrated in fig. (17), fig. (18), by comparing numerical and experimental streamlines for $x = 1.0$. The Spalart-Allmaras model predicts an intense vortex, located at a depth of $y = 0.015, z = -0.2$, close to the location of the measured vortex.

As a general comment, the departure of the numerical prediction obtained with the Baldwin-Lomax model from the experimental observation should be attributed to its simplified nature, which does not take into account any diffusion or convection effects of the turbulent viscosity. In fact, the Baldwin-Lomax model is purely algebraic, and therefore connected only to the local properties of the flow.

CONCLUSIONS

In the present study, numerical simulations have been carried out of the steady yaw flow past a ship with a RANS solver.

Two different turbulent models, namely the Baldwin-Lomax and the Spalart-Allmaras models, have been used and the results have been validated against experimental measurements for boundary layer, wake and wave fields of a Series 60 hull in yaw motion.

Numerical results compare favourably with experimental data with regards to the hydrodynamic coefficients and the wave profile. The main features of the flow phenomena are reproduced by the simulation and the behavior of the two turbulence models is pointed out in the analysis of the axial velocity contours and the transversal streamlines in the propeller region.

The Spalart-Allmaras turbulent model appears to be a promising trade-off between CPU cost and reliability of the results.

ACKNOWLEDGEMENTS

This work was supported by the Italian Ministry of Transportation in the frame of INSEAN research plan 1997-99.

REFERENCES

1. Landrini, M. and Campana, E.F., "Steady waves and forces about a yawing flat plate," J. Ship Res., Vol. 40, No. 3, 1996.
2. E.F. Campana, P.G. Esposito and Penna, R. "Numerical simulation of the drift motion of a ship," 20-th Sym. on Naval Hydro., Santa Barbara, California, USA, Vol. 1, 1994.
3. Alessandrini, B. and Delhommeau, G. "Viscous free surface flow past a ship in drift and in rotating motion," 22-th Sym. on Naval Hydro., Washington, D.C., USA, Vol. 1, 1998.
4. Cura Hochbaum, B. "Computation of the turbulent flow around a ship model in steady turn and in steady oblique motion," 22-th Sym. on Naval Hydro., Washington, D.C., USA, Vol. 1, 1998.
5. Y. Tahara, J. Longo, F. Stern and Himeno, Y. "Comparison of cfd and efd for the series 60 $c_b = 0.6$ in steady yaw motion," 22-th Sym. on Naval Hydro., Washington, D.C., USA, Vol. 1, 1998.
6. Spalart, P.R. and Almaras, S.R., "A one-equation turbulence model for aerodynamic flows," La Recherche-Aérospatiale, No. 1, 1994, pp. 5-21.
7. Di Mascio, A. and E.F. Campana, "Yaw flow simulation for the series 60," Ship Technology Research, to be published.
8. Longo, J.F., Effects of Yaw on model-scale Ship Flows, Iowa Institute Hydraulic Research, Iowa City, 1996.
9. Chorin, A.J., "On the convergence of discrete approximations to the navier-stokes equations," Math. Comput., No. 23, 1969, pp. 341-353.
10. A. Harten, B. Engquist, S. Osher and Chakravarthy, S.R., "Uniformly high order accurate essentially non-oscillatory schemes," J. Comp. Phys., Vol. 71, No. 231, 1987.
11. A. Di Mascio, R. Broglia and Favini, B. "Numerical simulation of free-surface viscous flow by eno-type schemes," 3-rd Int. Conf. on Hydro, Seoul (Korea), 1998.
12. B. Favini, R. Broglia and Di Mascio, A., "Multigrid acceleration of second order eno schemes from low subsonic to high supersonic flows," Int. J. Num. Meth. Fluids, No. 23, 1996.
13. Baldwin, B.S and Lomax, H., "Thin layer approximation and algebraic model for separated turbulent flows," AIAA Paper, Vol. 78, No. 257, 1978.
14. Coleman, W.H. and Stern, F., "Uncertainties and cfd code validation," J. Fluids Eng., Vol. 119, 1997, pp. 795-803.

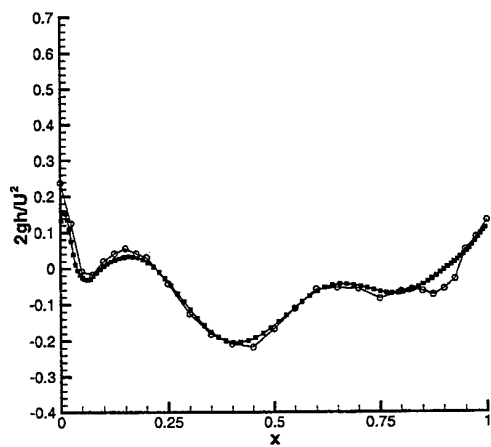


Figure 4: Numerical (●) and experimental (○) star-board wave profiles ($\alpha = 10^\circ$). Spalart and Allmaras model.

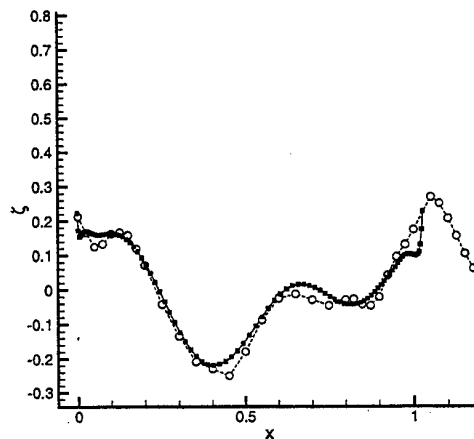


Figure 6: Numerical (●) and experimental (○) star-board wave profiles ($\alpha = 5^\circ$).

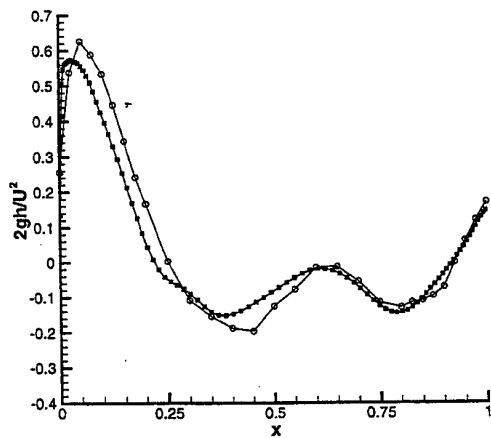


Figure 5: Numerical (●) and experimental (○) port wave profiles ($\alpha = 10^\circ$). Spalart and Allmaras model.

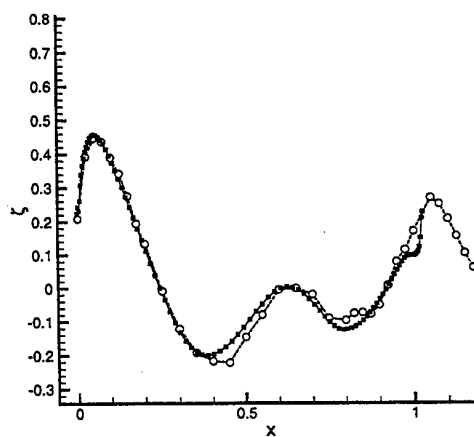


Figure 7: Numerical (●) and experimental (○) port wave profiles ($\alpha = 5^\circ$).

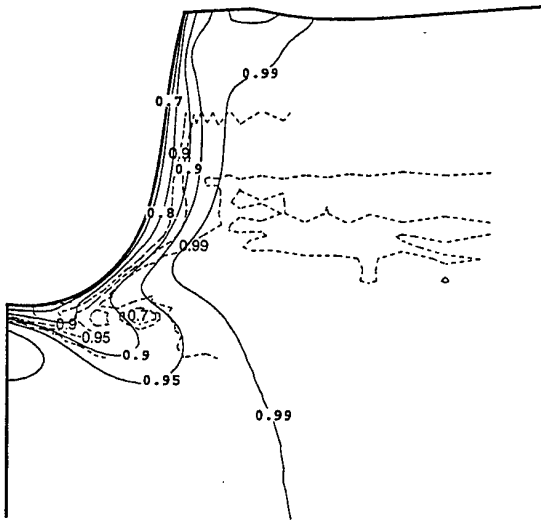


Figure 8: Numerical (Baldwin-Lomax, solid) and experimental (dashed) contours of the axial velocity u . Left $x = 0.2$, right $x = 0.8$. $Fr = 0.316$, $Re = 5.3 \cdot 10^6$, $\alpha = 10^\circ$

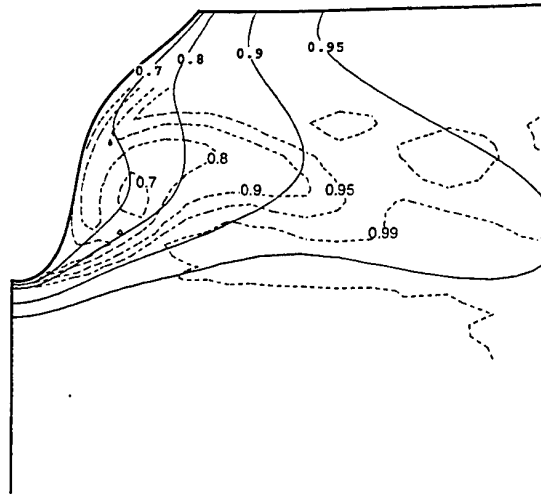


Figure 10: Numerical (Baldwin-Lomax, solid) and experimental (dashed) contours of the axial velocity u . Left $x = 0.9$, right $x = 0.9$. $Fr = 0.316$, $Re = 5.3 \cdot 10^6$, $\alpha = 10^\circ$

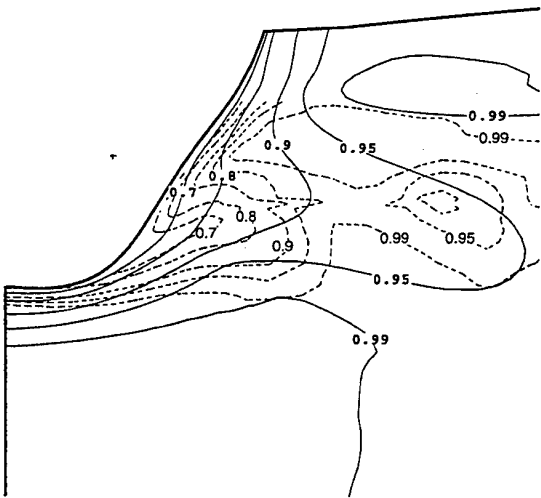


Figure 9: Numerical (Baldwin-Lomax, solid) and experimental (dashed) contours of the axial velocity u . Left $x = 0.8$, right $x = 0.8$. $Fr = 0.316$, $Re = 5.3 \cdot 10^6$, $\alpha = 10^\circ$

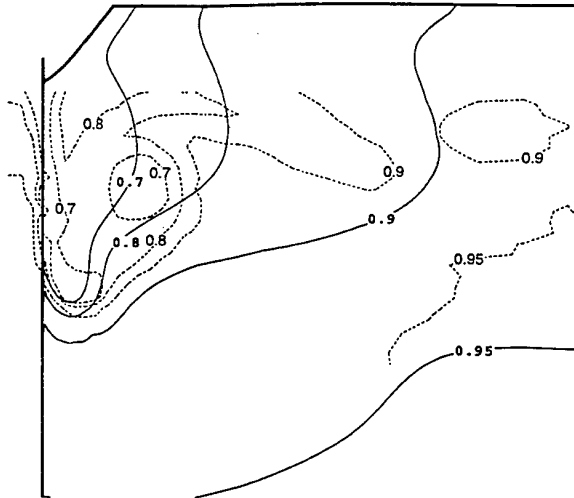


Figure 11: Numerical (Baldwin-Lomax, solid) and experimental (dashed) contours of the axial velocity u . Left $x = 1.0$, right $x = 1.0$. $Fr = 0.316$, $Re = 5.3 \cdot 10^6$, $\alpha = 10^\circ$

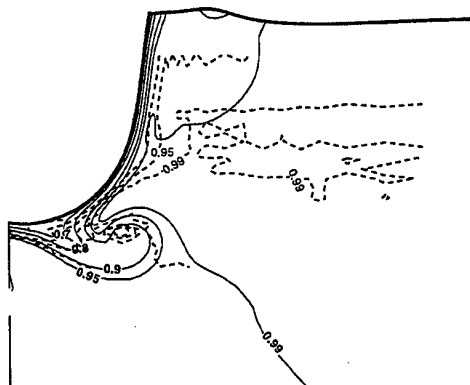


Figure 12: Numerical (Spalart-Allmaras, solid) and experimental (dashed) contours of the axial velocity u . Left $x = 0.2$, right $x = 0.8$. $Fr = 0.316$, $Re = 5.3 \cdot 10^6$, $\alpha = 10^\circ$

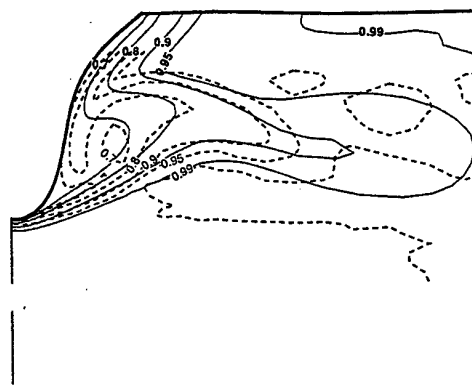


Figure 14: Numerical (Spalart-Allmaras, solid) and experimental (dashed) contours of the axial velocity u . Left $x = 0.9$, right $x = 0.9$. $Fr = 0.316$, $Re = 5.3 \cdot 10^6$, $\alpha = 10^\circ$

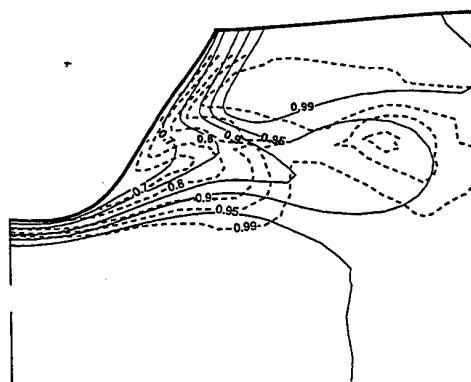


Figure 13: Numerical (Spalart-Allmaras, solid) and experimental (dashed) contours of the axial velocity u . Left $x = 0.8$, right $x = 0.8$. $Fr = 0.316$, $Re = 5.3 \cdot 10^6$, $\alpha = 10^\circ$

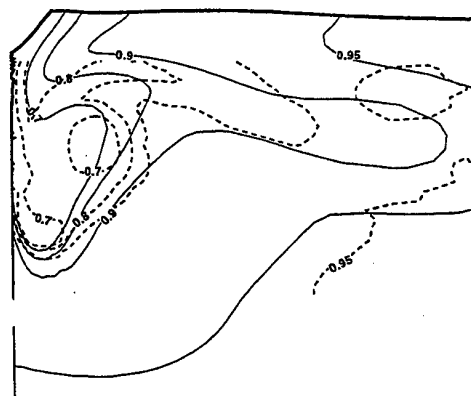


Figure 15: Numerical (Spalart-Allmaras, solid) and experimental (dashed) contours of the axial velocity u . Left $x = 1.0$, right $x = 1.0$. $Fr = 0.316$, $Re = 5.3 \cdot 10^6$, $\alpha = 10^\circ$

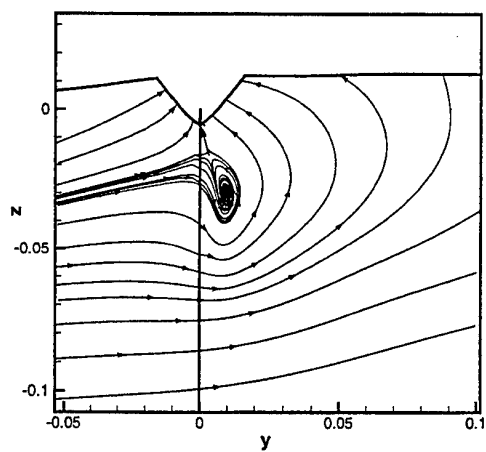


Figure 16: Cross-flow streamlines of the flow onto the (y, z) plane at $x = 1.0$. Numerical (Baldwin-Lomax) solution.

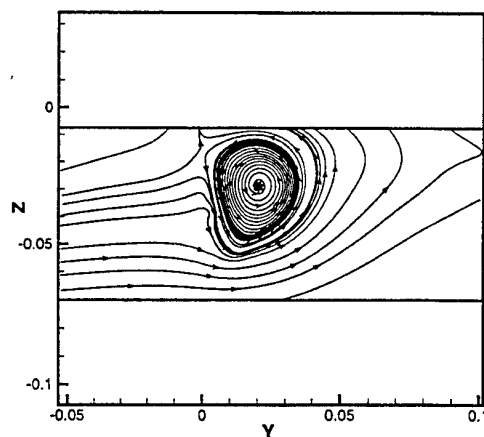


Figure 18: Cross-flow streamlines of the flow onto the (y, z) plane at $x = 1.0$. Experimental data.

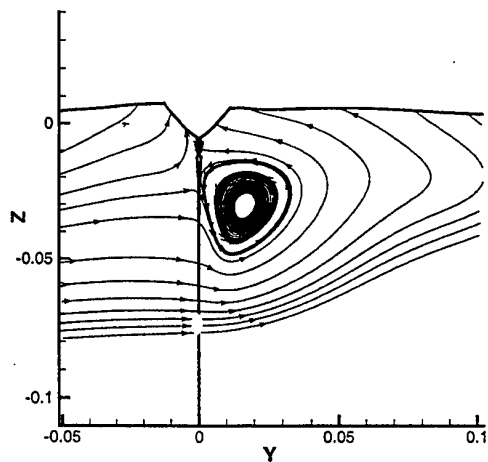


Figure 17: Cross-flow streamlines of the flow onto the (y, z) plane at $x = 1.0$. Numerical (Spalart-Allmaras) solution.

COMPUTATION OF BREAKING BOW WAVES FOR A VERY FULL HULL SHIP

R. AZCUETA¹, S. MUZAFERIJA², M. PERIĆ¹

¹Fluid Dynamics and Ship Theory Section, Technical University of Hamburg-Harburg
Lämmersiehl 90, D-22 305 Hamburg, Germany
Fax: +49 40 42832 3331; E-Mail: rodrigo@schiffbau.uni-hamburg.de

²ICCM Institute of Computational Continuum Mechanics GmbH,
Bramfelder Str. 164, D-22 305 Hamburg, Germany

ABSTRACT

Numerical simulations of the wave-breaking occurring at the bow of a very full hull ship model are presented. The computation is performed using a finite volume method with unstructured meshes and an interface-capturing scheme to determine the shape of the free surface. The wave-breaking occurs not only at the bow but also on the side of the hull, leading to nearly-periodic oscillations in drag. The hull is assumed to be fixed relative to the undisturbed water surface. Three grids with substantially different fineness in the free-surface region were used in order to assess the grid-dependence of the computed results. The comparison of flow features at the bow with experimental data provided by the Ship Research Institute, Tokyo, shows a reasonably good agreement.

INTRODUCTION

Bow-wave breaking is often observed, especially for a very full hull ships. Computational studies of this phenomenon are difficult and not very numerous; the authors are aware of only few such studies. Since the numerical uncertainties are relatively large, the need for experimental data to be used for validation purposes is obvious. At the Ship Research Institute (SRI) in Tokyo, measurements of wave flows in front of a blunt bow ship model are being conducted. The present study is an effort to numerically simulate the flow under the same conditions as in the experiments at SRI. At present, only a limited amount of experimental data is available for comparison purposes; future studies will be aimed at providing a more detailed validation of the computational model.

The results of computations presented here are meant to demonstrate the capabilities and limitations of an interface-capturing scheme [7] for a simulation of bow-breaking phenomena. In the following sections, the solution method will be described first, followed by the analysis of solutions obtained on three grids. Both the aspects of numerical accuracy and efficiency will be addressed. Finally, conclusions and directions for future research in this area will be summarized.

NUMERICAL METHOD

The interface-capturing method used in this study is described in detail in [7]; only a brief summary is presented here. Details about the underlying finite-volume method (FVM) can be found in [3].

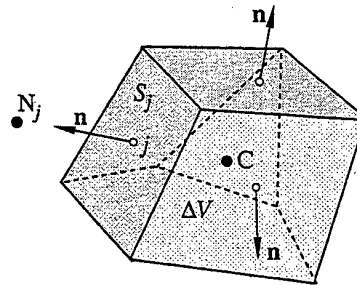


Fig. 1: A typical control volume and the notation used

The discretization method is of finite-volume type and uses control volumes (CVs) with an arbitrary number of faces, cf. Fig. 1. It also allows cell-wise local refinement of unstructured meshes, i.e. each CV can be subdivided in an arbitrary number of smaller volumes to locally increase the mesh resolution. Although the mesh refinement can in principle be automated (based on an error estimate, cf. [6]), in this study the refinement regions have been pre-selected

based on the expected variation of the position of free surface.

The mass and momentum conservation equations, which – complemented by the corresponding transport equations for the turbulent kinetic energy and its dissipation rate, which will not be given here – serve as the mathematical model of the flow, read in integral form:

$$\frac{d}{dt} \int_V \rho dV + \int_S \rho(\mathbf{v} - \mathbf{v}_b) \cdot \mathbf{n} dS = 0, \quad (1)$$

$$\begin{aligned} \frac{d}{dt} \int_V \rho u_i dV + \int_S \rho u_i \mathbf{v} \cdot \mathbf{n} dS = \\ \int_S (\tau_{ij} \mathbf{i}_j - p \mathbf{i}_i) \cdot \mathbf{n} dS + \int_V \rho b_i dV, \end{aligned} \quad (2)$$

where V is the CV-volume bounded by a closed surface S with a unit normal vector \mathbf{n} directed outwards, \mathbf{v} is the fluid velocity vector, ρ is fluid density, p is the pressure, b_i are the body forces per unit mass (here the gravity), and τ_{ij} are the effective stresses (the sum of viscous and Reynolds-stresses, the latter being modeled using the standard k - ϵ model based on the eddy-viscosity approach):

$$\tau_{ij} = \mu_{\text{eff}} \left(\frac{\partial u_i}{\partial x_j} + \frac{\partial u_j}{\partial x_i} \right) + \frac{2}{3} \delta_{ij} k, \quad (3)$$

with $\mu_{\text{eff}} = \mu + \mu_t$ being the effective dynamic viscosity of the fluid, δ_{ij} the Kronecker's delta and k the kinetic energy of turbulence.

The solution domain covers both water and air region around the hull; both fluids are considered as an effective fluid with variable properties, which are at any spatial location determined according to the volume fraction of one constituent fluid (e.g. water). The volume fraction c is obtained by solving the corresponding conservation equation, which reads:

$$\frac{d}{dt} \int_V c dV + \int_S c \mathbf{v} \cdot \mathbf{n} dS = 0. \quad (4)$$

In order to solve the conservation equations using FVM, they are applied to each CV and discretized in order to obtain one algebraic equation per CV; each such equation involves the unknown from the CV-center and from all neighbor CVs with which the current CV has common faces. Since the equations are non-linear, they have to be linearized in order to be solved by an iterative solution method. The equations are also coupled and are solved in a segregated manner, i.e. for each variable in turn, treating thereby other variables as known.

In the course of obtaining an algebraic equation for each CV, three levels of approximation are applied:

- The integrals over surface, volume, and time are evaluated using midpoint-rule approximations, which use the value of the integrand at the center of the integration domain.
- Since the variable values are calculated at CV centers only, values at cell-face centers required for the evaluation of integrals have to be obtained by interpolation; here, linear interpolation is used, except on very coarse grids, where linear interpolation is blended with an upwind-biased approximation.
- In order to evaluate stress terms (forces) at CV-faces, numerical differentiation is needed to compute derivatives of the Cartesian velocity components with respect to Cartesian coordinates. This is done using either Gauss method or polynomial fitting and central differences, cf. [7]. The time derivative at the current time level is computed by differentiating a parabola fit through values at the current and two previous time levels; the time integration interval is centered around the current time level (a fully implicit scheme).

All of the above approximations are nominally of second order. Deferred-correction approach is used to reduce the implicit part of the discretized equations to the nearest neighbors only; the difference between the simplified and full approximations is included at the right-hand side of the algebraic equations. This makes the matrix of the algebraic equation system smaller and allows the use of simpler iterative solvers; here, the conjugate-gradient type solvers are used (ICCG for symmetric and Bi-CGSTAB [8] for non-symmetric matrices).

The mass conservation equation is transformed into a pressure-correction equation following the well-known SIMPLE-algorithm for colocated arrangements of variables. The standard k - ϵ model with wall functions is used to compute the eddy viscosity μ_t .

The discretization of the volume-fraction equation requires special attention. Higher-order schemes violate the boundedness requirement, which requires that $0 \leq c \leq 1$; on the other hand, numerical diffusion of low-order schemes must be avoided in order to retain the interface between the two fluids as sharp as possible. Here, the high-resolution interface-capturing scheme (HRIC) is used, which computes the cell-face value of c as a blend of the upwind and downwind interpolation; see [7] for a detailed description. The choice of the blending factor depends on the local distribution of the volume fraction, relative position of the free surface to the cell face, and the local value of

the Courant number

$$Co = \frac{\mathbf{v} \cdot \mathbf{n} S_j \Delta t}{\Delta V_C}, \quad (5)$$

where S_j is the area of the CV-face j , ΔV_C is the volume of the cell centered around node C , and Δt is the time step. The Courant number indicates how much of one fluid is available in the donor cell and the scheme is tuned not to allow to drain more fluid out of one CV within one time step than was available in it. Another important factor is the orientation of the interface relative to the CV-face. The normal to the interface – which is assumed to lie where the volume fraction has the value $c = 0.5$ – is obtained by computing the gradient of c ; it is equal to zero everywhere except in the interface region.

Finally, the cell-face value of c is computed as:

$$c_j = \gamma c_C + (1 - \gamma) c_{N_j}, \quad (6)$$

where γ is a non-linear function of the profile of c , Courant number, and the orientation of the interface, and C and N_j denote the nodes on either side of the CV-face j ; more details are available in [7].

With this approach, the interface is usually smeared across two to three cells. The fluid properties are computed as:

$$\rho = \rho_1 c + \rho_2 (1 - c), \quad \mu = \mu_1 c + \mu_2 (1 - c), \quad (7)$$

where subscripts 1 and 2 denote the two fluids (e.g. liquid and gas). If one CV is partially filled with one and partially with the other fluid (i.e. $0 \leq c \leq 1$), it is assumed that both fluids have the same velocity and pressure.

The free surface does not represent a boundary and no boundary conditions need to be prescribed at it. If surface tension is significant at the free surface, this can also be taken into account by transforming the resulting surface-tension force into a body force [2].

Computation of three-dimensional flows with free surfaces – especially when they are unsteady, as is the case with breaking bow waves – requires a lot of both memory and computing time. It is therefore essential to be able to perform such simulations on parallel computers. The computer code used here is parallelized by domain decomposition in both space and time and can use either PVM or MPI message-passing libraries for communication between the processors. Both clusters of workstations and massively parallel computers can be used – as long as they support PVM or MPI standards. Details about parallelization of the present method can be found in [9] or [10].

DEFINITION OF THE TEST CASE

For the present study, the model of a very full hull towed at the Ship Research Institute in Tokyo was used. Figure 2 shows a sketch of this model. The waterplane shape is shown in the upper part of the figure (top view). The bow has the shape of a semi-circle with a radius of $R = 0.3$ m. It is followed by a parallel middle body 1 m long, and the stern 0.7 m long, prescribed as a spline. Thus, the total length of the model is 2.0 m and the beam is 0.6 m. The same shape of the waterplane extends 0.2 m above the load waterline up to the deck and 0.3 m beneath the load waterline. There, half a body of revolution, obtained by rotating the waterplane around its longitudinal axis, is attached to complete a total draft of 0.6 m. With the semi-circular bow, the hull can be seen as a blunt body.

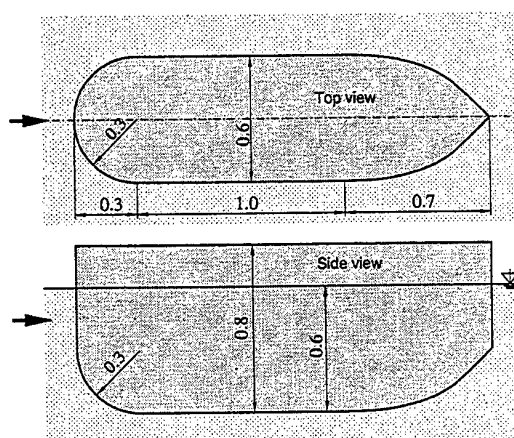


Fig. 2: Geometry of the hull model

As in the experiments, the model was held fixed in place, i.e. it was not allowed to sink and trim. The model speed was set at $v = 1.697$ m/s, which corresponds to a Froude number $Fr = 0.7$, based on the hull draft. The Reynolds number, based on the hull length and a water temperature of 19.2°C was around $3.4 \cdot 10^6$.

COMPUTATIONAL GRIDS

Computations were carried out on three numerical grids. The coarsest one had 103 950 CVs, the medium one had 411 180 CVs, and the finest one had 2 147 628 CVs. Figure 3 shows a perspective view of the coarsest grid. The inlet, outlet, lateral, and bottom boundaries are placed about 1.5 model lengths away from the model. Only one half of the model was considered, due to the symmetry of the flow. The grid

resolution is high at the model wall and in the proximity of the waterplane to capture the boundary layer and the free surface distortion better. It expands continuously in all directions away from the hull and the waterline. Due to the simple geometry of the model, the grids were easy to generate. The coarsest grid is a matching block-structured grid, with some cells being prisms. Above the deck, another block of 0.4 m height was added since, if the computational domain ended at the deck level, the air flow would accelerate appreciably between the bow wave and the upper boundary. The grid shows large variation in cell size due to the chosen grid generation strategy and the local grid refinement, but the numerical method can cope with this without noticeable problems.

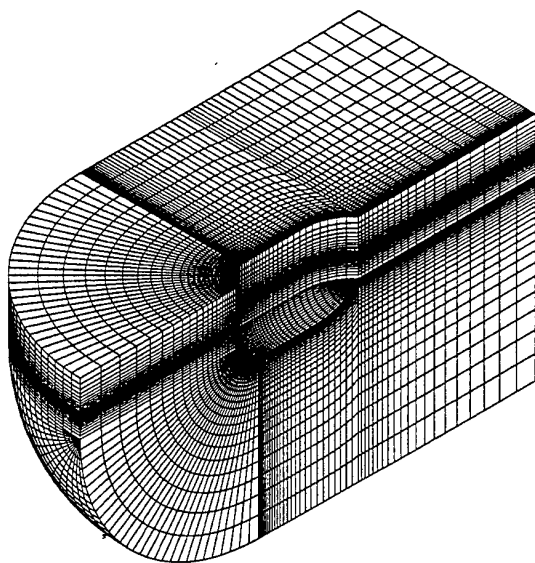


Fig. 3: Perspective view of the coarsest grid

The medium grid was obtained by refining the cells in all directions in a region extending horizontally over the whole computational domain and 0.16 m above and below the load waterline in the vertical direction. The size of this region was established using the free surface elevation previously obtained on the coarse grid as a reference. The finest grid was obtained by refining the medium grid but now in a region restricted horizontally to about half a model length around the model. Figure 4 shows the finest grid in the plan view and the cross-section. There, the extension of the local grid refinement can be seen.

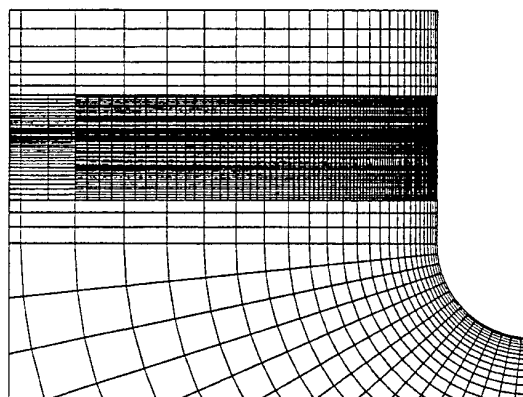
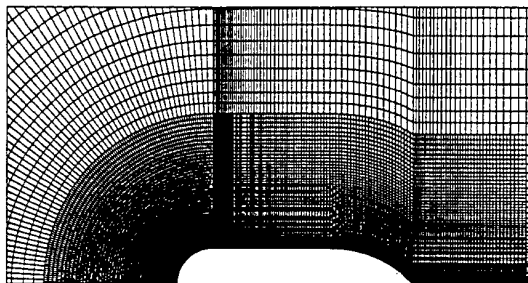


Fig. 4: Finest grid in the plan view (above) and the cross-section (below), showing the extent of the local grid refinement (only part of the solution domain is shown)

BOUNDARY CONDITIONS AND COMPUTATIONAL DETAILS

At the inlet, the velocity of both water and air was set equal to the hull velocity, and the turbulent parameters were derived from a turbulent intensity of 1 % and a turbulent viscosity in the same order of the molecular viscosity. Top, bottom and lateral boundaries were treated as slip walls. At the symmetry plane, the symmetry boundary condition was enforced. At the outlet, extrapolation in streamwise direction was used, and the hydrodynamic pressure was specified according to a prescribed water level.

As initial condition to start the simulation, the full model speed over the entire computational field was imposed without accelerating the flow from rest. The numerical method was shown to be robust enough to cope with this. No numerical damping of the radiating waves at the lateral boundary was applied because the waves dissipate sufficiently due to numerical diffusion in the larger outer cells.

The simulations on the coarse and medium grid were performed on a single-processor workstation,

while on the finest grid, eight processors on a parallel computer were used, see Table 1 for details on memory and CPU time requirement per time step. The simulations were carried out until a periodic oscillation of pressure drag was obtained over many periods. This was typically after about 4000, 6000 and 8000 time steps for the coarse, medium and fine grid respectively. This number of time steps corresponded to a simulation time of 40 seconds or the time taken for a particle of water to travel 20 model lengths. The time step Δt was chosen so that a Courant number of 1 was not exceeded.

Table 1. Some computational details for the simulations carried out on the three grids

	coarse	medium	fine
CVs	103 950	411 180	2 147 628
RAM	34 MB	133 MB	832 MB
CPU / Δt	9 s	54 s	54 s
Computer	DEC α	HP	8 \times HP
Model	500 MHz	PA-8200	PA-8200
Δt	0.02 s	0.01 s	0.005 s
No. of Δt	4 000	6 000	8 000

RESULTS AND DISCUSSION

The aim of performing the simulation on three grids was to assess the accuracy of the numerical solutions.

Grid-Dependence Analysis

Numerical solutions are always affected by three kinds of numerical errors:

- *Iteration errors*, which are due to stopping the iteration procedure at some stage. We control these errors by monitoring the norm of the residuals for all equations solved, after the matrix and right-hand side of equations are updated to account for non-linearity and inter-equation coupling. When the residual norm becomes three to four orders of magnitude smaller than an appropriate normalization quantity (usually the norm obtained by using zero-filled values of the variable in the interior of the solution domain), one can assume that the variable values will not further change on three to four most significant digits.
- *Discretization errors*, which are due to approximations introduced in the numerical integration, interpolation, and differentiation. These errors depend on the approximations used and on the fine-

ness of the grid; for a given discretization method, they depend only on the grid fineness and quality.

- *Modeling errors*, which are due to the fact that the equations solved are not exact (turbulence model, interface model etc.) and that both the geometry and the boundary conditions are also simplified to some extent. These errors can only be evaluated when the other two kinds of error are negligibly small and the exact solution is known within much smaller error bounds (e.g. from an accurate experiment or from a more accurate numerical study).

When the time step is small, as was the case in this study, the changes in solution from one time level to the next are also small; usually, only few outer iterations per time step are then needed. In the initial stage of the simulation one can actually use only one outer iteration per time step, without checking the convergence of outer iterations. Comparison of solutions obtained using just one outer iteration per time step and those obtained by satisfying the convergence criterion showed very small differences, indicating very low iteration errors. Especially when a steady solution is sought is it appropriate to use a fully-implicit method and one iteration per time step, since the temporal accuracy is not important.

The modeling errors can not be evaluated very accurately since the available information from an experiment is not detailed enough to allow a quantitative analysis of these errors. However, the aim of this study was not to determine friction resistance most accurately but primarily to analyze the bow-wave breaking, so the estimation of turbulence-modeling errors was not pursued further.

The ideal way of evaluating discretization errors is to systematically refine the grid, i.e. subdivision of each CV into eight smaller ones (for hexahedral CVs, as used in this study). However, this leads to an eightfold increase in the number of CVs from one grid to another, meaning that the third grid has 64 times as many CVs as the first one. There is not much incentive in using a first grid coarser than about 100 000 CV, as the discretization errors would be too large. Since our computing resources available for the present study did not allow the use of a grid with 6.4 million CVs, and since the errors are expected to be largest near the hull, we refined the grid only locally.

First, the integral quantities computed on the three grids are compared. In Table 2 the computed mean values of the pressure and viscous drag coefficients, defined as

$$C_p = \frac{R_p}{\frac{1}{2}\rho v^2 S}, \quad C_f = \frac{R_f}{\frac{1}{2}\rho v^2 S}, \quad (8)$$

are presented, where R_p and R_f denote the total pressure and viscous forces on the hull in x -direction (obtained by summing the forces computed for the individual boundary cell faces) and S is the wetted surface considering the distortion of the free surface.

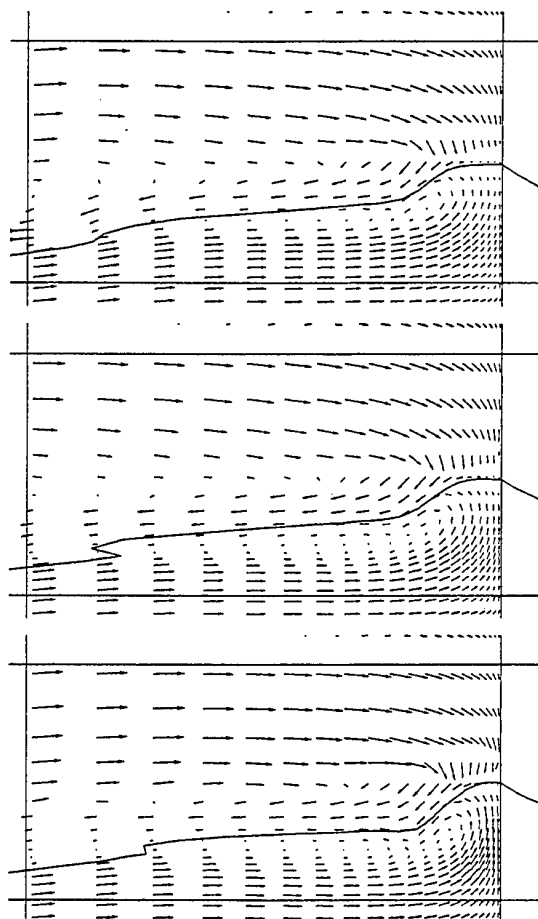


Fig. 5: Water level contour and velocity vectors in the symmetry plane ahead of the bow for three time instants within one oscillation period, as computed on the coarsest grid (the lower horizontal line denotes the undisturbed water surface, while the upper represents the height $z/R = 1.0$; the vertical line on the right-hand side denotes the bow, while that on the left-hand side represents the position $x/R = 2.0$ ahead of the bow)

Since the refinement is not strictly systematic (only part of the hull surface was refined), one can not apply Richardson extrapolation to estimate the discretization error, as suggested e.g. by Ferziger and Perić [4]. However, since the differences between the two finer grids are very small, and the differences between the finest and the coarsest grid are of the order of 6 %, one can assume that the solution on a still finer grid would not change the results by more than a few per

cent, regarding the drag coefficient.

Table 2. Computed pressure and viscous drag coefficients for the three grids

	coarse	medium	fine
C_p	$3.12 \cdot 10^{-2}$	$2.94 \cdot 10^{-2}$	$2.92 \cdot 10^{-2}$
C_f	$3.10 \cdot 10^{-3}$	$3.34 \cdot 10^{-3}$	$3.30 \cdot 10^{-3}$

While the friction drag remained nearly constant during the simulation, the pressure drag oscillated typically by about ± 5 % around the mean values shown in Table 2. The oscillation period for the pressure drag for all grids was about 2.5 seconds of simulation time, or the equivalent to the time taken for a particle of water to travel 2 model lengths. However, the period of the breaking bow-wave as could be observed in the animations of the computed flow was much smaller, about 0.6 seconds. This shows that the oscillations in C_p were more influenced by the much larger breaking wave at the side of the model.

Figure 5 shows the water level contour and the velocity vectors in the symmetry plane in front of the bow for three characteristic instants within one period, as computed on the coarsest grid. These figures show that both the level to which the water rises along the bow and the position of the breaking wave crest change in time.

Figure 6 shows isolines of water level ahead of the bow for three time instants within one oscillation period, as computed on the finest grid. They show that the water elevation changes within one oscillation period substantially in a large region around the hull. One of the figures shows an overturning bow wave, as the isolines cross each other. Similar patterns are also observed on the other grids.

Since the flow oscillates nearly periodically, the results were averaged over the last 10 seconds (about 16 periods of wave breaking) and the average field values obtained on the three grids are compared. This comparison is presented in Figs. 7 and 8. In Fig. 7 the velocity vectors are interpolated and presented on a uniform grid for easier comparison. The results show that the mean maximum water level at the bow is roughly the same on all three grids (about $z/R = 0.5$). However, with grid refinement the height of the breaking wave and its steepness increase substantially. Also, the range over which the breaking wave moves in time becomes narrower, as recognized from the velocity pattern in the air. On all grids the results agree qualitatively: water rises up along the bow, while air moves downwards towards the free surface.

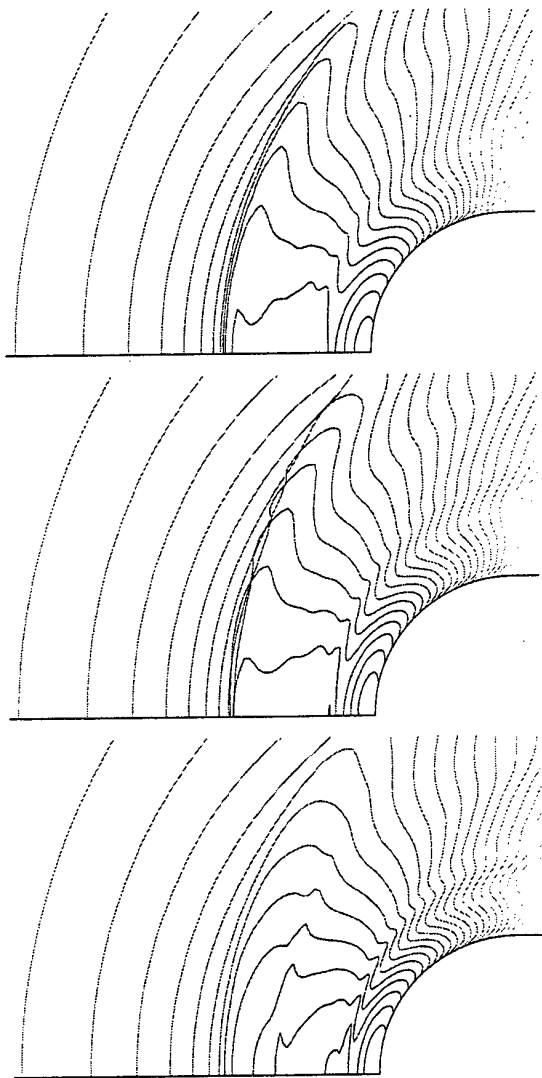


Fig. 6: Isolines of water level ahead of the bow for three time instants within one oscillation period, as computed on the finest grid, viewed vertically from above (interval between lines 0.01 m, the first line in front of the bow represents 0.14 m above load waterline)

Figure 8 shows average isolines of water level ahead of the bow, as computed on the three grids. These figures show that the mean pattern on the finest grid is substantially different from the instantaneous patterns showed in Fig. 6. One can also observe, that with grid refinement the breaking wave becomes sharper and somewhat closer to the bow and more extended to the side.

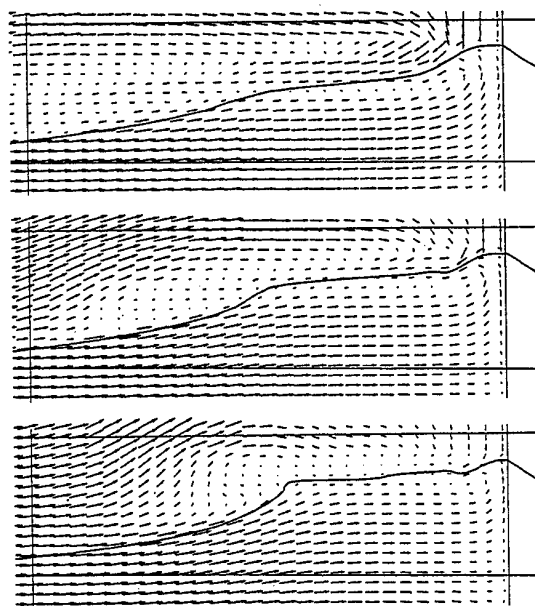


Fig. 7: Average water level contour and velocity vectors in the symmetry plane ahead of the bow for the three grids (coarse, medium, and fine, from top to bottom, respectively; the lower horizontal line denotes the undisturbed water surface, while the upper represents the height $z/R = 0.6$; the vertical line on the right-hand side denotes the bow, while that on the left-hand side represents the position $x/R = 2.0$ ahead of the bow)

Comparison with Experiment

Figure 9 is a photograph of the breaking wave ahead of the bow at some instant of time for the same Froude number as observed during the model experiments at the Ship Research Institute in Tokyo. In Fig. 10, an instant of the wave breaking as simulated on the finest grid is shown.

The photograph indicates that the free surface in the bow wave region is highly "turbulent" (i.e. non-smooth). The unsteadiness of the free surface on the small scale takes place at higher frequencies than those resolved in the unsteady RANS-simulation; the simulation takes into account only the low-frequency (nearly periodic) unsteadiness effects whose time scale is separated from the time scale of turbulence. Therefore, the simulation can not show such unsteadiness of the free surface as observed in the photograph – a large-eddy simulation (LES) would be required for that purpose.

The instantaneous shape of the bow wave taken from the simulation (Fig. 10) shows a nearly smooth free surface, except for the crest of the breaking wave about one bow radius ahead and another discontinu-

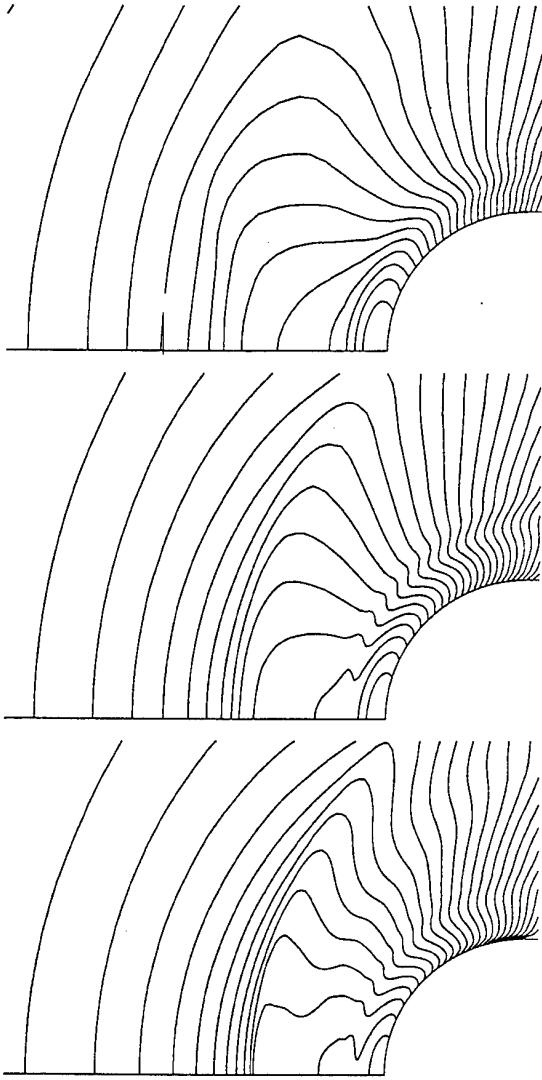


Fig. 8: Average isolines of water level ahead of the bow, as computed on the three grids, viewed vertically from above (from top to bottom: coarse, medium, and fine grid; interval between lines 0.01 m, the first line in front of the bow represents 0.14 m above load waterline)

ity closer to the bow where the upcoming flow along the bow overturns, cf. Figs. 5 and 7. This rol-over effect is also clearly seen in the photograph in Fig. 9. One could argue that a special “free-surface turbulence model” would be required to model the fine-scale disturbances of the free surface, which certainly dissipate the energy in the wave and affect both its spreading and dynamics. These effects are not taken into account in the simulation.

Figures 11 and 12 show a comparison of the time-averaged free-surface elevation in the bow-wave re-

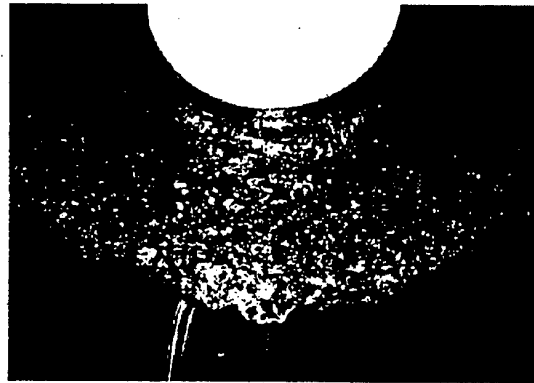


Fig. 9: Photograph of the instantaneous free surface ahead of the bow (courtesy of Ship Research Institute, Tokyo [5])

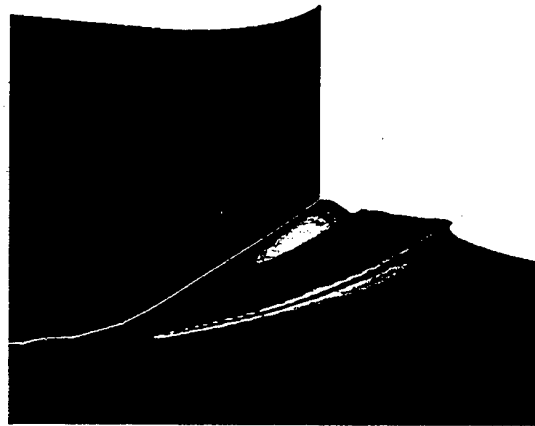


Fig. 10: Instantaneous shape of the free surface ahead of the bow, computed on the finest grid

gion computed on the medium and fine grid with experimental data from SRI. A very good agreement is observed between experiment and simulation on the medium grid, while the finest grid shows a shorter distance from the bow to the breaking wave crest. Similarly, the wave profile from experimental data shown in Fig. 13 is in closer agreement with the simulation result from the medium grid, cf. Fig. 7., than with that of the finest grid.

The reason for the fact that the finest-grid simulation does not agree with experimental data as well as the results from the medium grid can stem from three sources. One could be the above-mentioned fact that the small-scale free-surface disturbances introduce additional diffusion effects on the breaking wave which are not modeled in the simulation. Since it is obvious from Fig. 8 that the coarser grids show effects of numerical diffusion on the breaking wave, it may be that the amount of numerical diffusion on the medium grid is just of the right order to model the

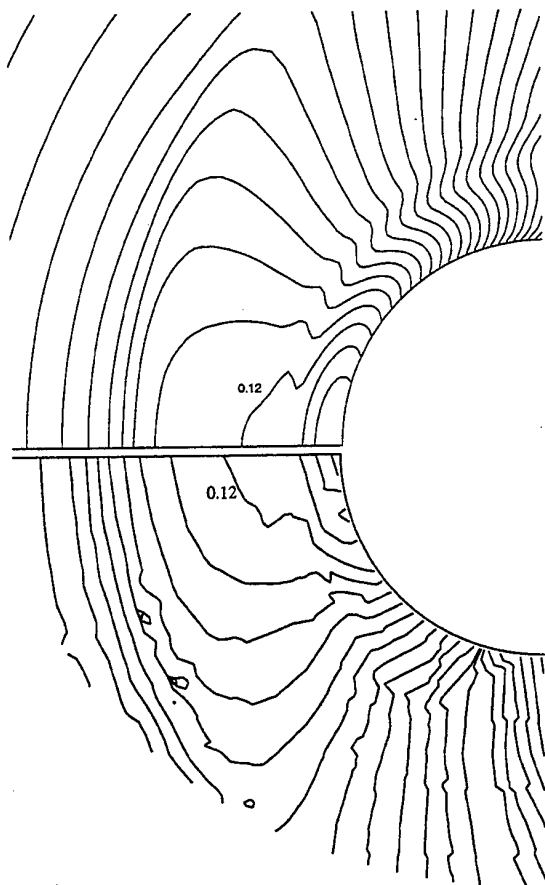


Fig. 11: Average free surface elevation ahead of the bow: measurement (below; courtesy of Ship Research Institute, Tokyo [5]) and calculation (top; medium grid). Interval between lines 0.01 m

above effects. With a finer grid but without resolving the small-scale turbulent fluctuations of the free surface, the wave becomes too sharp and hence also shorter.

Another explanation could be the air-entrainment in the breaking wave and the more complex two-phase flow than modeled in the simulation. The third possible reason for disagreement could be the measurement uncertainty. Future studies of the bow-wave breaking phenomena will be devoted to clarifying these issues.

Discussion of Flow Features

Figure 14 shows the instantaneous pressure distribution on the hull surface, computed on the finest grid. Dashed lines show the region in which the grid was refined, cf. Fig. 4.

The maximum pressure at the bow corresponds to the stagnation pressure. The minimum values result in

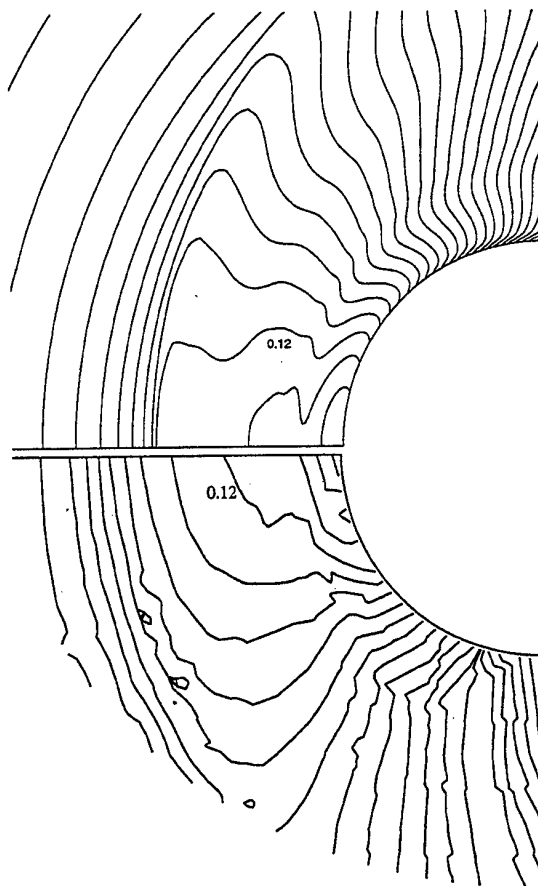


Fig. 12: Average free surface elevation ahead of the bow: measurement (below; courtesy of Ship Research Institute, Tokyo [5]) and calculation (top; finest grid)

the area of transition from curved to straight wall in the main flow direction, and at the bottom of the side wave, about one model width behind the bow. The under-pressure is here of the same order as the stagnation pressure (pressure coefficient equal -1). The pressure distribution on the hull did not change much with grid refinement – the pressure contours look very much the same.

In Fig. 15 the computed instantaneous distribution of the shear stress along the hull surface in the bow region (medium grid) is shown. The shear stress in the air is obviously negligible compared to that over wetted surface, which is indicated by the free-surface contour (the undisturbed waterline is also shown for reference). The maximum shear stress occurs in the region of downward flow near the lowest water level.

Finally, Fig. 16 shows the instantaneous free-surface shape around the whole model. It shows that the water level drops very low (over 200 mm below undisturbed waterline) shortly behind the bow, then

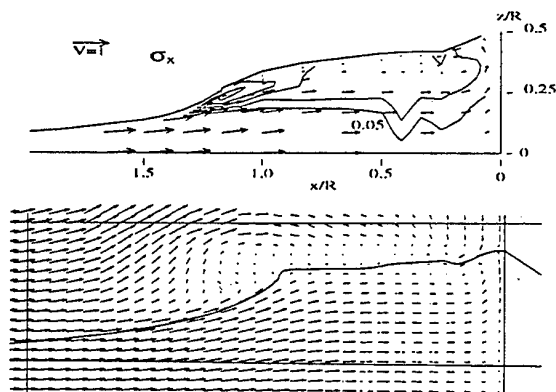


Fig. 13: Average wave profile and velocity vectors measured in the symmetry plane ahead of the bow (above) and the simulation data obtained on the finest grid (below); experimental data also shows standard deviation of the streamwise velocity component (measurement data courtesy of Ship Research Institute, Tokyo [5])

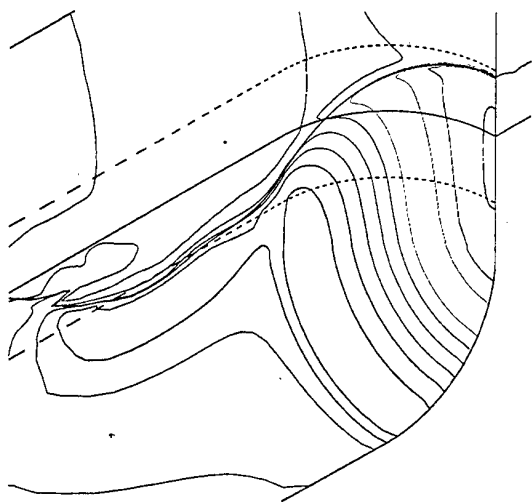


Fig. 14: Computed instantaneous pressure distribution along the hull surface in the bow region (finest grid; dashed lines show the region which was refined compared to the medium grid)

rises again to another breaking wave, followed by one more trough shortly before the model end. This figure shows that the wave breaking is more severe at the side and aft waves than at the bow wave. An animation of the computed free-surface deformation as a function of time shows that the side wave moves both vertically and longitudinally. At present no experimental data for this region is available to judge the accuracy of the simulation; from the changes observed in the course of grid refinement, one can conclude that

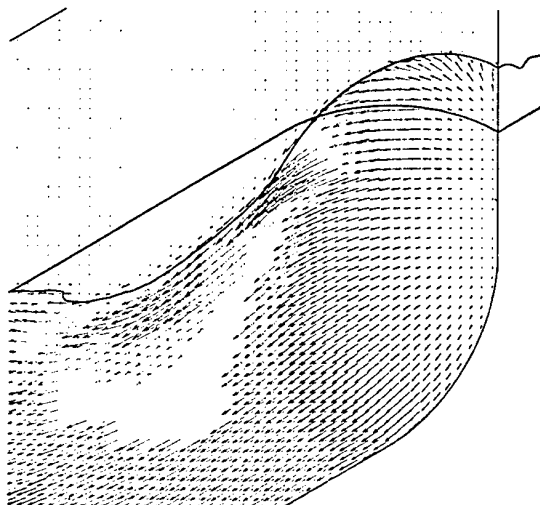


Fig. 15: Computed instantaneous distribution of the shear stress along the hull surface in the bow region (medium grid)



Fig. 16: Computed instantaneous free surface elevation around the hull

the typical structure of the free surface shown in Fig. 16 is qualitatively identifiable on all grids.

CONCLUSIONS

The results of the computations presented above lead to the conclusion that the interface-capturing method used in this study is suitable for the analysis of breaking-wave phenomena around ship hulls or other surface-piercing or submerged bodies. The time-averaged features of the breaking bow wave are qualitatively – and to some extent also quantitatively – in good agreement with experimental observations conducted at the Ship Research Institute in Tokyo. Further studies will be devoted to a more detailed comparison of simulation results and experimental data in order to be able to estimate the modeling errors and possibly improve the modeling of turbulence effects on the free surface.

ACKNOWLEDGMENTS

The authors are indebted to Dr. Munehiko Hinatsu and his colleagues at the Ship Research Institute in Tokyo for initiating this study and for providing their experimental data for comparison with present simulations. The computations and the visualization of the results were performed using the *Continuum mechanics engineering tool (Comet)* of ICCM GmbH, Hamburg.

REFERENCES

1. Azcueta, A., Muzaferija, S., Perić, M., "Computation of water and air flow around ships", Proc. EUROMECH 374 Symposium *Recent Computational Developments in Steady and Unsteady Naval Hydrodynamics*, pp. 185–195, April 27–29, 1998, Poitiers, France.
2. Brackbill, J.U., Kothe, D.B., and Zemaach, C., "A continuum method for modeling surface tension", *J. Comput. Physics*, Vol. 100, pp. 335–354 (1992).
3. Demirdžić, I. and Muzaferija, S., "Numerical method for coupled fluid flow, heat transfer and stress analysis using unstructured moving meshes with cells of arbitrary topology", *Comput. Methods Appl. Mech. Engrg.*, Vol. 125, pp. 235–255 (1995).
4. Ferziger, J.H., and Perić, M., *Computational Methods for Fluid Dynamics*, 2nd ed., Chap. 11, Springer, Berlin, 1999.
5. Hinatsu, M., Takeshi, H., and Kawashima, H., "Measurement of Wave-Breaking Flows Occurring in front of a Blunt Bow ship" Abstract Note of 64th General meeting of SRI, (in Japanese), (1994).
6. Muzaferija, S. and Gosman, D., "Finite-volume CFD procedure and adaptive error control strategy for Grids of arbitrary topology", *J. Comput. Phys.*, Vol. 138, pp. 766–787 (1997).
7. Muzaferija, S. and Perić, M., "Computation of free surface flows using interface-tracking and interface-capturing methods", Chap. 3 in O. Mahrenholtz and M. Markiewicz (eds.), *Nonlinear Water Wave Interaction*, Computational Mechanics Publications, Southampton, 1998.
8. Van den Vorst, H.A., "BI-CGSTAB: a fast and smoothly converging variant of BI-CG for the solution of non-symmetric linear systems", *SIAM J. Sci. Stat. Comput.*, Vol. 13, pp. 631–644 (1992).
9. Schreck, E. and Perić, M., "Computation of fluid flow with a parallel multigrid solver", *Int. J. Numer. Methods in Fluids*, Vol. 16, pp. 303–327 (1993).
10. Seidl, V., Muzaferija, S., and Perić, M., "Parallel DNS with local grid refinement", *Appl. Scientific Research*, Vol. 59, pp. 379–394 (1998).

SIMULATION OF GREEN WATER LOADING USING THE NAVIER-STOKES EQUATIONS

G. Fekken¹, A.E.P. Veldman¹
B. Buchner²

¹University of Groningen, Department of Mathematics,
P.O. Box 800, 9700 AV Groningen, The Netherlands
E-Mail: G.Fekken@math.rug.nl

²Maritime Research Institute Netherlands (MARIN)
P.O. Box 28, 6700 AA Wageningen, The Netherlands
E-mail: B.Buchner@marin.nl

ABSTRACT

Simulating viscous flows with a free surface causes special difficulties, since its position will change continuously. Therefore, besides solving the Navier-Stokes equations, the position of the free surface must be determined every time step. In the present method, the Navier-Stokes equations are solved on a three-dimensional Cartesian grid. A Volume-of-Fluid function is used for the position of the fluid. Since the method is able to handle arbitrary forms of the geometry, many types of industrial flow problems can be simulated. In this paper the problem of green water loading on the foredeck of a ship is discussed and a comparison is made with experimental results. Waterheights, pressures and water contours are produced and compared with model tests. Also forces on different structures placed on the deck are compared and analyzed.

INTRODUCTION

When a ship at sea is sailing or moving in the waves, it may get water on the foredeck. This water, which flows on the deck in high waves when the relative wave motion around the bow is exceeding the deck level, is called *green water*. As a result of this green water loading, damage to superstructures on the deck is still a common occurrence. The Maritime Research Institute Netherlands (MARIN) has done extensive model test research to this phenomenon during the last few years [1], [2]. In the paper a simulation method will be described with which this phenomenon can be investigated numerically.

The simulation of green water flow on the foredeck of a ship is a complex problem, since the water will behave wildly when it flows on the deck, causing effects like air bubble entrapment. The tests also show complex high velocity flow patterns on the deck. Besides the model test research MARIN has done, it also investigated the non linear relative wave motions around the bow with a boundary integral method, modeling the flow with a potential function [3]. However, fluid flow is best described by the complete Navier-Stokes equations. In 1995, at the University of Groningen (RuG), the development of a computer program called ComFlo has been started which can solve fluid flow with free surfaces in 3D-complex

geometries. Here the Navier-Stokes equations are solved on a Cartesian grid. No motion of the geometry has been implemented yet, so this will cause some differences between the tests and the simulation. The inflow conditions at the boundaries of the domain will be determined by the data of the model tests instead of simulating an incoming wave.

MATHEMATICAL MODEL

The motion of water, and in general the motion of a viscous, incompressible fluid can be described by the incompressible Navier-Stokes equations, consisting of conservation of mass and conservation of momentum:

$$\nabla \cdot \mathbf{u} = 0 \quad (1)$$

$$\frac{\partial \mathbf{u}}{\partial t} + (\mathbf{u} \cdot \nabla) \mathbf{u} = -\frac{\nabla p}{\rho} + \nu \Delta \mathbf{u} + \mathbf{F} \quad (2)$$

where $\mathbf{u} = (u, v, w)$ is the velocity, ρ is the density, p is the pressure, ∇ is the gradient operator, $\nabla \cdot$ is the divergence operator, and Δ is the Laplace operator. Further ν is the kinematic viscosity and $\mathbf{F} = (F_x, F_y, F_z)$ is an external body force, e.g. gravity.

Further, boundary conditions are required for the solid boundary, the free surface and eventually in- and outflow boundaries. At the solid boundary a no-slip condition is used: $\mathbf{u} = 0$.

Free-slip walls are also possible, resulting in the conditions $u_n = 0$ and $\tau = 0$. Here $u_n = \mathbf{u} \cdot \mathbf{n}$ is the component of the velocity perpendicular to the wall, $\tau = \frac{\partial u_t}{\partial n}$ is the tangential stress, where u_t is the velocity component in the tangential direction.

At the free surface the boundary conditions consist of two components:

$$-p + 2\mu \frac{\partial u_n}{\partial n} = -p_0 + 2\gamma H \quad (3)$$

$$\mu \left(\frac{\partial u_n}{\partial t} + \frac{\partial u_t}{\partial n} \right) = 0 \quad (4)$$

where μ is the dynamic viscosity, p_0 is the atmospheric pressure, γ is the surface tension and $2H$ is the total curvature of the surface. These boundary conditions describe the continuity of normal and tangential stresses at the free-surface. Further, for the free surface displacement an equation is required: Suppose the position of the free surface is described by $s(x, t) = 0$, then the movement of the free surface becomes

$$\frac{Ds}{Dt} = \frac{\partial s}{\partial t} + \mathbf{u} \cdot \nabla s = 0. \quad (5)$$

At inflow boundaries the velocity \mathbf{u} is prescribed, and at outflow boundaries the homogeneous Neumann condition $\frac{\partial \mathbf{u}}{\partial n}$ is used. This is better than prescribing the normal component of the velocity, since then a boundary layer could easily be created. Further, at outflow boundaries the pressure p is set equal to the atmospheric value p_0 .

NUMERICAL MODEL

In this section the mathematical model will be discretized to obtain a numerical model.

Description of geometry and free surface

First a Cartesian grid is laid over the three dimensional domain. The discretization is done on a totally staggered grid, which means that the pressure will be set in the cell centers and the velocity components in the middle of the cell faces between two cells (figure 1). Like all figures of the discretization of geometries in this paper, this is a 2-dimensional example. Extension to 3D is straightforward.

Since complex geometries are used, the grid cells will run through the boundaries in several ways. This is also the case for the free surface, with an extra complexity since the free surface is time-dependent. Also the main reasons why Cartesian grids are used, can be inferred from this. In the first place each cell has the same orientation which is an advantage with respect

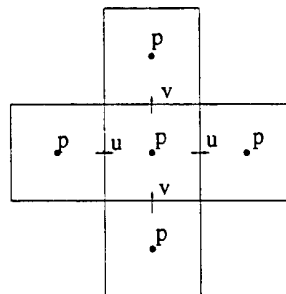


Figure 1: Location of the pressure and velocity components

to the transportation of the free surface. In the second place when the geometries become more complex, the creation of boundary-fitted grids will become very complex and time consuming. A disadvantage of the Cartesian approach is the discretization of the boundary conditions, since in general the grid will not be fitted in the boundary. Now the method which takes care of the complex shape of the geometry and the free surface is discussed.

Apertures

An indicator function is used in the form of so-called *apertures*, which are divided into two classes:

1. volume apertures

In every cell, the geometry aperture F_b defines the fraction of the cell where fluid is able to flow. The (time-dependent) fluid aperture F_s defines the fraction of the cell which is occupied by fluid. Of course $0 \leq F_s \leq F_b \leq 1$.

2. edge apertures

The edge apertures A_x, A_y, A_z define the fraction of a cell surface which is contained in the flow domain, so A_x indicates the fraction of the cell surface through which fluid is able to flow in x -direction, A_y in y -direction and A_z in z -direction.

Figure 2 shows a 2-dimensional example of a grid cell using apertures. Here $F_b = F_b \setminus F_s + F_s = 0.8$.

Labels

After calculating the apertures, every cell will be given a *cell label*, to make distinction between the boundary, the fluid and the air, and because the pressure is treated differently near the wall and near the free surface. Since the free surface is time-dependent, two classes of labeling are introduced,:

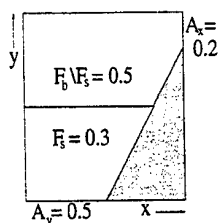


Figure 2: Example of a grid cell with geometry and fluid apertures

1. geometry cell labels

This labeling class is time-independent, consisting of three different labels:

- **F**-cells: All cells with $F_b \geq \frac{1}{2}$
- **B**-cells: All cells adjacent to an **F**-cell
- **X**-cells: All remaining cells

2. free-surface cell labels

Free-surface labels are time-dependent and they are a subdivision of the **F**-cells:

- **E**-cells: All cells with $F_s = 0$
- **S**-cells: All cells adjacent to an **E**-cell
- **F**-cells: All remaining **F**-cells

Figure 3 shows an example of this labeling.

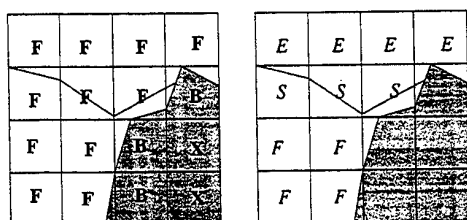


Figure 3: Example of geometry cell labeling (left) and free-surface cell labeling (right)

For the treatment of the velocity, the velocities between cells have to be labeled, too. So we introduce *velocity labels*, which, like the cell labels, have to be subdivided in a time-dependent and a time-independent class:

1. geometry velocity labels

These (time-independent) labels are a combination of the labels of the geometry where the velocities lie in between. Five combinations are possible: **FF**, **FB**, **BB**, **BX** and **XX**.

2. free-surface velocity labels

These labels are time-dependent and they are a combination of the labels of the free surface. The following combinations are possible: **FF**, **FS**, **SS**, **SE**, **EE**, **FB**, **SB** and **EB**.

Further, there is one more class of labeling, namely inflow and outflow labels, resp. **I**- and **O**-cells. They are just a specific subset of the **B**-cells.

Discretization of the Navier-Stokes equations

When all cells and velocities are labeled, the Navier-Stokes equations can be discretized in time and in space. First the Navier-Stokes equations are written more simplified as:

$$\nabla \cdot \mathbf{u} = 0 \quad (6)$$

$$\frac{\partial \mathbf{u}}{\partial t} + \nabla p = \mathbf{R} \quad (7)$$

Here $\frac{\partial}{\partial t}$ is replaced by p (p is normalized to 1) and $\mathbf{R} = \nu \Delta \mathbf{u} - (\mathbf{u} \cdot \nabla) \mathbf{u} + \mathbf{F}$, containing all convective, diffusive and body forces.

Discretization in time

The explicit first order Forward Euler method is used:

$$\nabla \cdot \mathbf{u}^{n+1} = 0 \quad (8)$$

$$\frac{\mathbf{u}^{n+1} - \mathbf{u}^n}{\delta t} + \nabla p^{n+1} = \mathbf{R}^n \quad (9)$$

Here $n+1$ and n denote the new and old time level respectively, and δt is the time step. Equation (8) and the pressure in (9) are treated on the new time level, to make sure the new \mathbf{u} is divergence free.

Discretization in space

The spatial discretization can be explained using the scheme in figure 4.

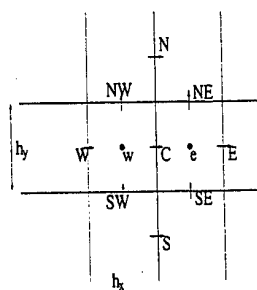


Figure 4: Discretization scheme

Equation (8) is applied in the centers of the cells and a central discretization is used. In the cell with center w the discretized equation becomes:

$$\frac{u_C^{n+1} - u_W^{n+1}}{h_x} + \frac{v_{NW}^{n+1} - v_{SW}^{n+1}}{h_y} = 0 \quad (10)$$

The momentum equation (9) is applied in the centers of the cell faces, for instance the discretization in point C becomes:

$$\frac{u_C^{n+1} - u_C^n}{\delta t} + \frac{p_e^{n+1} - p_w^{n+1}}{h_x} = R_C^n. \quad (11)$$

The diffusive terms in R_C^n are discretized centrally, and for the convective terms upwind or central discretization is possible. For wildly moving fluids mostly an upwind discretization is used, since central discretization may cause stability problems (see [4] section 2.4).

Discretization near the free surface

Near the free surface besides F -cells, S -cells and E -cells appear. In E -cells the pressure is set to the atmospheric value p_0 . In S -cells the pressure is determined by linear interpolation between the pressure in F -cells and the free surface. The pressure p_F in F -cells is obtained from the pressure Poisson equation which is handled in the next section. The pressure at the free surface p_f is obtained from equation (3), where the term $2\mu \frac{\partial u_n}{\partial n}$ is neglected because μ is small in relation to the other terms. So $p_f = p_0 - 2\gamma H$. The pressure p_S now becomes

$$p_S = \eta p_f + (1 - \eta) p_F. \quad (12)$$

Here $\eta = \frac{h}{d}$ (figure 5).

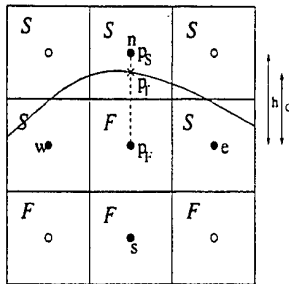


Figure 5: Pressure interpolation in S -cells

For the velocities in equation (4) there are a number of possibilities. The velocities FF , FS and SS are obtained solving the momentum equations. But when

discretizing derivatives SE - and EE - velocities are needed. SE -velocities are computed by demanding mass conservation in the corresponding S -cell. This velocity can then be computed from the five other (not unknown) velocities appearing in the equation for mass conservation. However, it is possible that two or more of these velocities are SE , in which case other decisions have to be made, e.g. setting derivatives like $\frac{\partial u}{\partial x}$ to zero. EE -velocities not surrounded by at least one SS -velocity are set to zero. Other EE -velocities are computed using the discrete simplified version of 3, existing of equations like

$$\frac{\partial u}{\partial z} + \frac{\partial w}{\partial x} = 0 \quad (13)$$

The determination of these velocities is more extensively treated in [5].

In- and outflow discretization

In- and outflow cells are a specific subset of the B -cells.

- Inflow
The velocity between an I -cell and an F -cell gets a prescribed value and is labeled as FI .
- Outflow
In an O -cell two velocities have to be labeled: FO and OX . The FO -velocity is computed from the momentum equations and then the OX -velocity is set equal to the FO -velocity, to satisfy the condition $\frac{\partial u}{\partial n} = 0$.

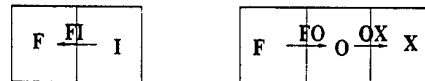


Figure 6: In- and outflow cells

The pressure Poisson equation

The pressure p^{n+1} in (9) has to be determined in such a way that equation (8) holds. This can be attained by substituting (9) into (8), resulting in the following equation:

$$\Delta p^{n+1} = \nabla \cdot \left(\frac{\mathbf{u}^n}{\delta t} + \mathbf{R}^n \right) \quad (14)$$

This equation is known as the Poisson equation for the pressure. No boundary conditions for the pressure are available for this equation, since they only involve the velocity \mathbf{u} . Therefore we first discretize equations 8 and 9, and then substitute the boundary conditions

for u , and after that we substitute these discretized equations to create the discretized Poisson equation. It will follow that no more boundary conditions for the pressure are required now (see [4] section 4.4).

After discretization it follows that the discrete analogon for the Laplace operator (Δ) consists of a central coefficient C_p and six coefficients C_n, C_s, C_w, C_e, C_u and C_d , related to the six neighbouring cells. When we denote the right hand side of (14) by f_p , the Poisson equation can be written as:

$$C_p p_p + C_n p_n + C_s p_s + C_e p_e + C_w p_w + C_u p_u + C_d p_d = f_p \quad (15)$$

The Poisson equation is solved by SOR-iteration (Successive Over Relaxation), which has some advantages:

- simple implementation, immediately using every new value.
- easy vectorization and parallelization, using a Red-Black ordering of the cells.
- rapid convergence, using an automatically adjusted relaxation parameter ω [6].

When the SOR-iteration has finished the pressure in every cell is known at the new time step, and the new velocities can now be computed.

Free surface displacement

When the velocities at the new time step are known, the free surface can be displaced. The sequence of actions that have to be done to achieve this are:

1. *compute fluxes between cells*
The fluxes between cells are computed by velocity times the area of the cell, taking into account the edge apertures.
2. *compute new fluid apertures F_s*
Using the fluxes between the cells, the new F_s can be computed.
3. *adjust free-surface labeling*
When the new fluid apertures are known the free-surface labeling can be adjusted.

This algorithm is called the Donor-Acceptor algorithm, which means that fluid is transported from a donor cell to an acceptor cell. A few things have to be taken into account: A donor cell cannot lose more fluid than it contains and an acceptor cell cannot receive more fluid than the amount of flow space that is available in the cell. Further, in S -cells the fluid has to stay coherent, which is accomplished by making use of a local height function (see [7]).

The CFL-number

One can imagine that when the fluid is moving very wildly, the time step has to be smaller than when the fluid is moving very calm. It would be useful to adjust the time step to these changes, to achieve an improvement in the computation time. Therefore the Courant-Friedrichs-Levy number (CFL-number) is introduced:

$$CFL = \frac{|u|\delta t}{h_x} + \frac{|v|\delta t}{h_y} + \frac{|w|\delta t}{h_z} \quad (16)$$

Here h_x, h_y and h_z denote the distances between the cell centers in x -, y - and z -direction. The condition to keep the computation stable, which can be proved by Fourier analysis (see [4]), turns out to be $CFL \leq 1$. This means that the fluid is transported over no more than one cell in one time step, which corresponds with our intuitive approach of stability. In ComFlo the maximum of the CFL-number over all cells is determined, and with respect to this number the time step is adjusted: The time step is immediately halved when the CFL-number becomes larger than a certain constant $C_1 < 1$, and the time step is doubled when the CFL-number is smaller than another constant C_2 which is small enough to be sure the time step can be doubled; typically $C_1 = 0.5$ and $C_2 = 0.1$.

RESULTS

Now the results of the green water simulations, computed by ComFlo will be presented and compared with experimental results. First the initial conditions used in the simulation will be explained. Then the results of the simulation of green water loading, consisting of water heights on the deck, the pressure at one place on the deck and contours of the waterfront will be discussed. Finally, the results of pressures and forces on different structures placed on the deck will be compared with experiments and analyzed. A detailed description of the physical behaviour of green water can be found in [1], [2].

Initial conditions

It will be clear that the simulation of a moving bow in large waves is a complex problem. Since the first goal was to investigate the possibilities to predict the behaviour of the green water on the deck using a numerical simulation program, simpler boundary conditions have been used for a first start.

Examining the situation of green water flow on the deck, a good resemblance for this appeared to be the theoretical dambreak problem (see [1]): A wall of water is placed around the bow and at time zero the water starts to flow onto the deck. Therefore this

dambreak problem was used as an initial condition for the green water problem on the deck. To compare the results of simulations and model tests carried out by MARIN [1], the precise configuration of the dambreak problem had to be adjusted to the data of the tests. This means that this configuration had to be tuned, to create more or less the same results with respect to the contour plots of the progressing water-front on the deck and heights at different positions at the deck. In the future the model will be extended with realistic deck(ship) motions and realistic inflow.

One of the model tests was chosen to be approximated, namely the regular wave test with a bow flare angle of 30 degrees, wave amplitude of 8.65 m and wavelength/shiplength = $\frac{\lambda}{l} = 0.75$. The width of the deck was 47 m and it was approximated by a parabola as shown in figure 7. More details on the tests can be found in [1].

A reasonable approximation for the test mentioned before, seemed to be the dambreak problem with a vertical wall of water of 13 m height at the most forward point of the bow, linearly decreasing to 5 m below the deck level 25 m behind this point (see figure 8). In the simulation no bowflare is used. The total flow domain was a box with dimensions $-40m \leq x \leq 15m$, $-30m \leq y \leq 30m$, $-6m \leq z \leq 20m$ where $z = 0$ corresponds with the deck level and $y = 0$ is the symmetry axis. A free-slip boundary condition is used at the sides $y = -30m$ and $y = 30m$. Further, to prevent an upward movement of the water at these sides of the domain, an outflow boundary condition is used from $-40m$ to $-12m$ (figure 7). Also an outflow boundary condition is used at the aft wall of the fluid domain where the flow is not interesting. At all other walls of the flow domain no-slip boundary conditions were used.

Green water simulation

The simulation used a uniform grid of $66 \times 72 \times 32$ cells in the x -, y - and z -direction respectively. The computation time was about 4 hours for a duration of 10 seconds full scale on a workstation with a specfp95 of 16.3 and 140 Linpack Mflops. At 30 m from the ships fore perpendicular (fpp) in the middle of the deck a flat vertical structure was placed with a height of 20 m and a width of 15 m. The load on this structure was used as a reference for the load on the other structures. First the heights of the water were measured at three different points at the axis of the deck: at $x = 0$, $x = -10$ and $x = -20$. Further the pressure at the deck was determined at the position $x = -12.5$ (see figure 9).

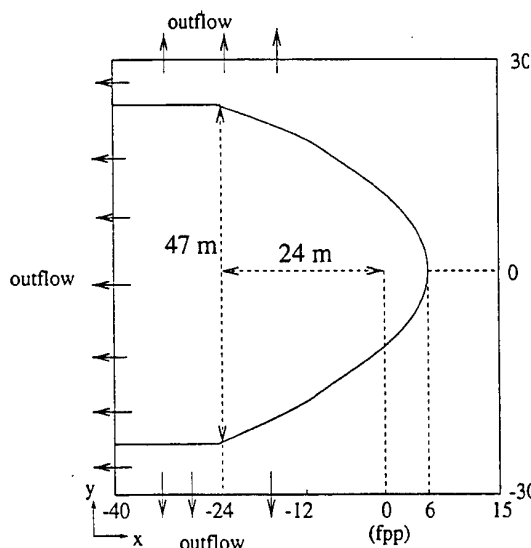


Figure 7: Initial situation in xy -plane

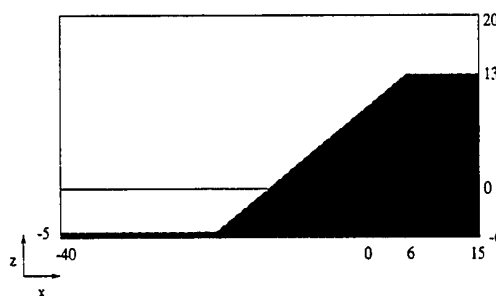


Figure 8: Initial situation in xz -plane

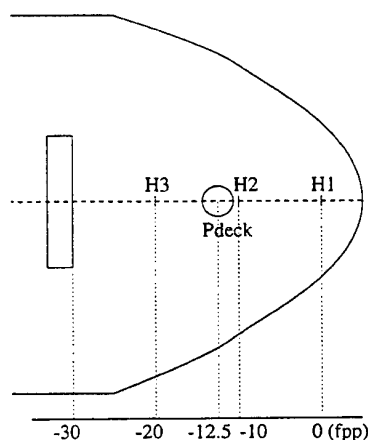


Figure 9: Measure positions for height and pressure

The following results are found for the water heights H1 to H3 on the deck:

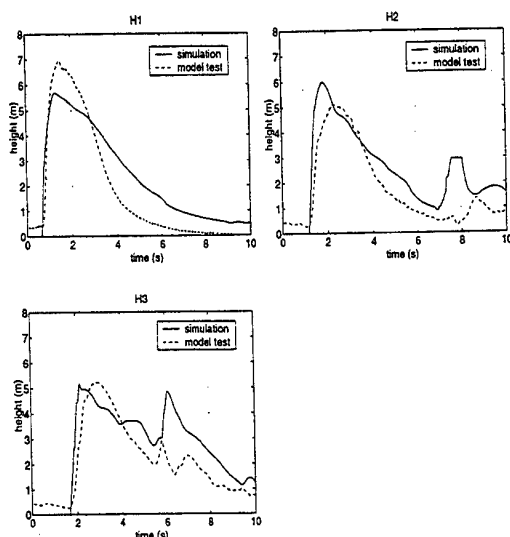


Figure 10: Results for the heights on the deck

Comparing these results, the resemblance between the model test and the simulation is clear. At H1, H2 and H3 the water rises very quickly and after reaching the maximum height it is slowly going down to a more or less zero value. At H3 a second peak is observed, due to the reflection of the water that was built up in front of the structure. This behaviour is also recognized in the simulation (see snapshot in figure 13 on the next page). A few variations are found in the maximum heights, but the behaviour of the water is quite the same.

To compare both situations also in the transverse direction of the deck, the water contours of the waterfront were plotted in figure 11 (model test) and figure 12 (simulation). The time between the contours is 0.31 seconds.

Having a look at Figures 11 and 12, it is obvious that a high velocity water 'tongue' arises in the middle of the deck both in the simulation and the experiment. However, some differences are observed between the test and the simulation. The waterfront in the simulation seems to be a bit sharper, due to a very shallow part of the front which has no big influence, so this difference looks bigger than it really is. It should also be noted that the contours from the model test are based on visual observation. The contourlines at the sides of the bow are somewhat different too. In the simulation the water almost immediately flows onto the deck around the full bow,

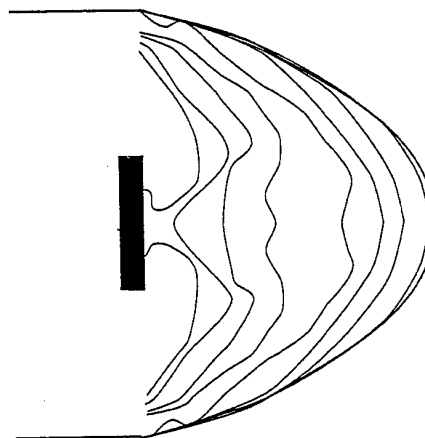


Figure 11: Contours of waterfront (model test), time step 0.31 s

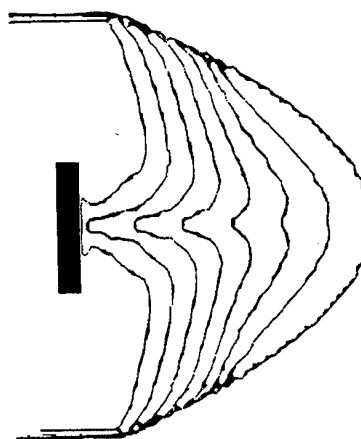


Figure 12: Contours of waterfront (simulation), time step 0.31 s

but in the test, likely because of the bowflare that pushes the water away from the bow, the water flows more gradually onto the deck around the bow. Also the vertical and angular motion of the deck can play a role here.

However, the global behaviour is similar, and the heights of the water are comparable, so a further investigation in the behaviour of the green water should be possible with this simulation.

The appearance of the high-velocity water 'tongue' is very well visible in a movie of this simulation, which is shown below, created by the visualization system AVS. Also the impact on the structure and the returning of the water which causes the second

maximum in the heights and pressure are clearly visible.

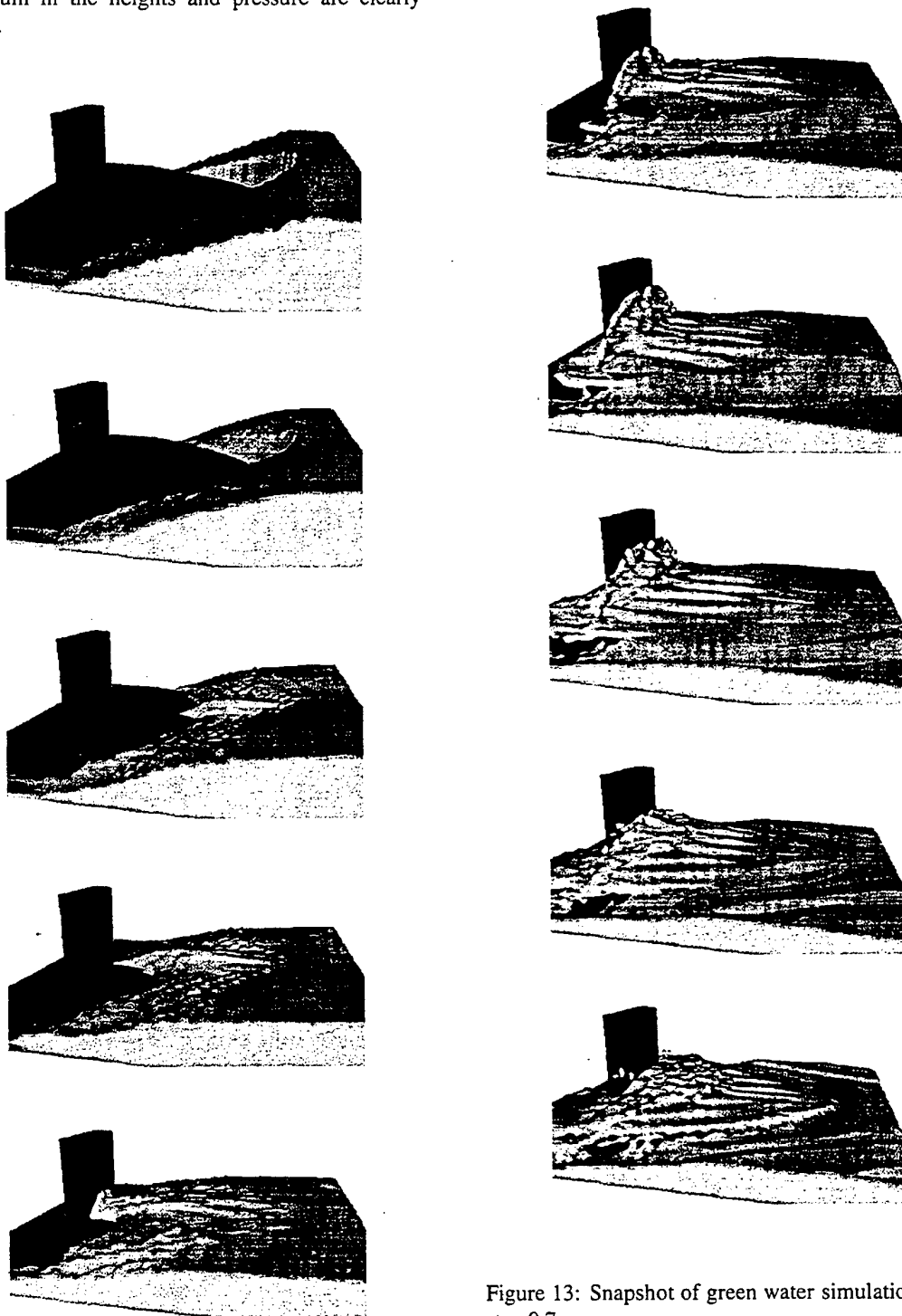


Figure 13: Snapshot of green water simulation, time step 0.7 s

The photos on the next page give an impression of the model test and how the water behaves on the deck in comparison with the simulation. Also the high velocity water 'tongue' is again clearly visible.

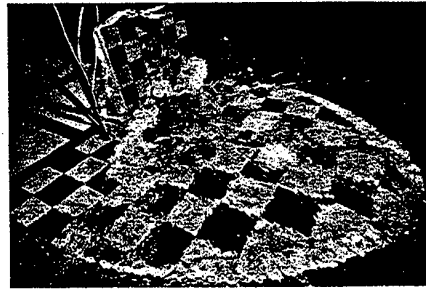
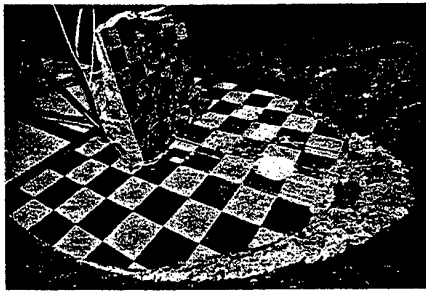
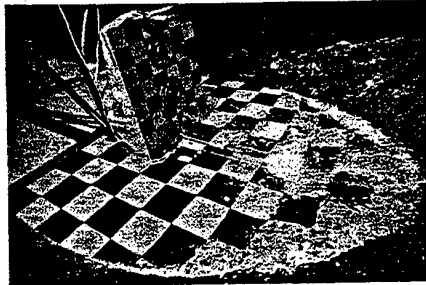


Figure 14: Photos of a model test, time step 0.31 s



Now a comparison between the model test and the simulation is made for the pressure at the deck (figure 15).

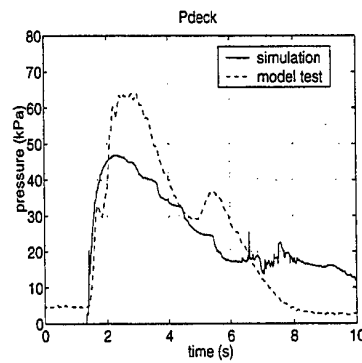
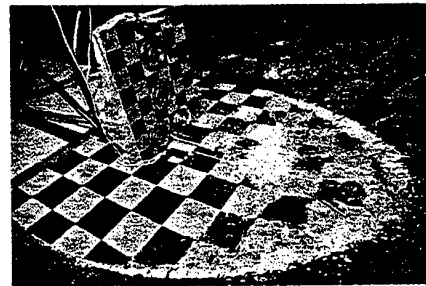
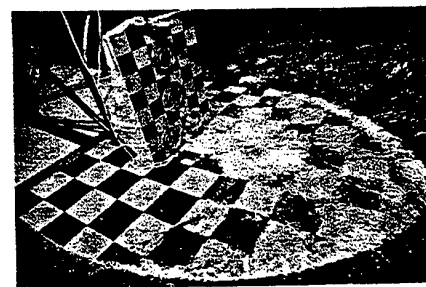
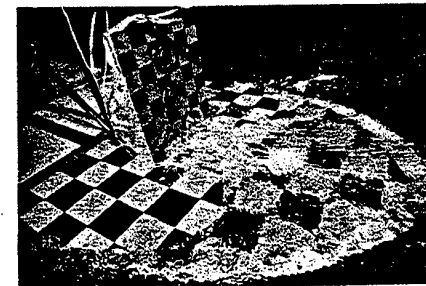


Figure 15: Pressures for simulation and experiment



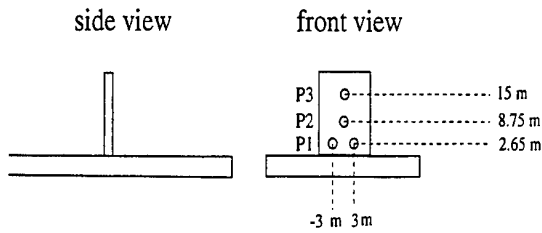
Like the heights, the pressure increases very fast and then, after the maximum pressure is reached, slowly decreases. Since the vertical velocity and acceleration of the deck is not simulated, the pressure for the simulation only exists of a hydrostatic component : $p = \rho gh$. This is the reason why the pressures in the tests are higher than in the simulation. A complete expression for the pressure on the deck, including the effects of the vertical velocity and acceleration can be found in [1]. This pressure will be found when the vertical motion of the deck is included in the method.



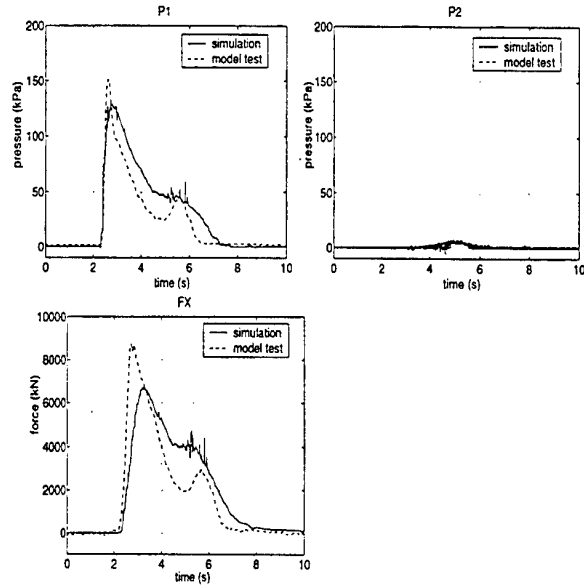
Pressures and forces on different structures

To determine the effect of different structural shapes on green water loading, MARIN has carried out some model tests with a number of different structures placed on the deck. The following structures were used in the tests (positions are with respect to deck level and the ships centerline):

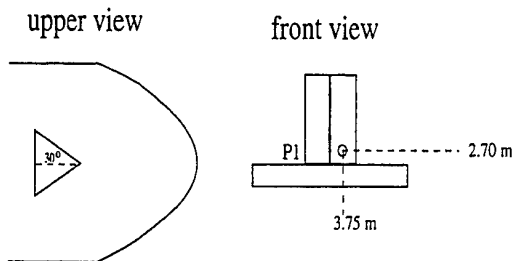
Structure 1: Squared structure



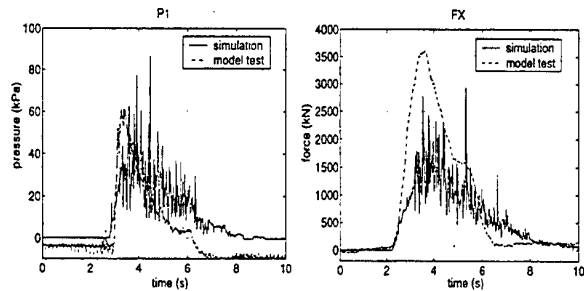
Structure 1 (squared)



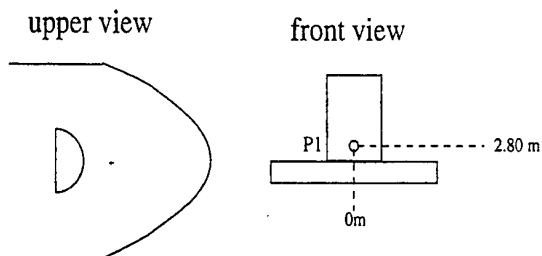
Structure 2: Triangular 30 degrees



Structure 2 (triangular 30 degrees)



Structure 3: Cylindrical front



Structure 3 (cylindrical front)

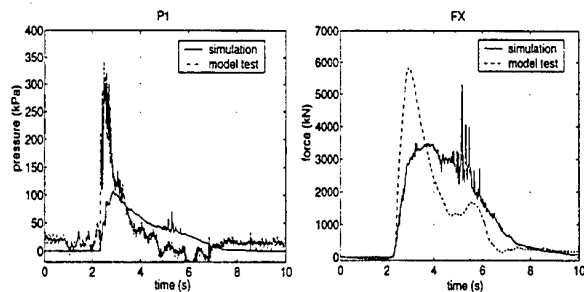


Figure 16: Different structures used in the tests

All structures are placed with their front at 30 m from the fore perpendicular, their height is 20 m and their width is 15 m. Pressures are measured at the pressure panel positions which are drawn in the figures (front view), the area of the circular pressure panels (2.7 m diameter) is 5.7255 m^2 . Further, the total force in x -direction F_x is measured on every structure.

Below a comparison is made between the pressures and total loads on the different structures.

Figure 17: Comparison of measured and calculated pressures and total loads on the different structures

Recapitulating the results of the different structures, it can be concluded that the global behaviour of the water is similar as in the tests, but also that there are differences in the absolute load values. It should be noted that impact phenomena are sensitive to small

changes. In the model tests for instance a significant variation of impact loads was found even in regular waves, as can be seen in figure 18.

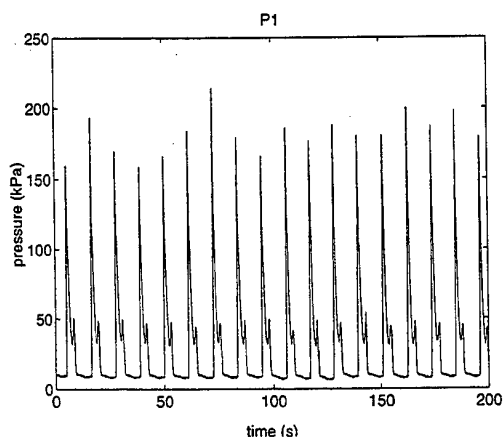


Figure 18: Sensitivity of the pressure in experiments

Looking at structure 1, at P1, the global shape of the pressure graphs correspond to each other, but in the maximum values of the pressure some differences occur. For P1, the maximum value in the simulation is 132 kPa, and for the tests, the mean value of the maxima, corresponding with a mean maximum height H_3 of 4.93 m, is 167 kPa with a standard deviation of 13.1 kPa. The standard deviation is $\sigma = \sqrt{\frac{1}{N} \sum_{i=1}^N (p_i - \bar{p})^2}$, where N is the total number of measured maxima in the test and \bar{p} is the mean value of the maxima. A difference of about 25 % in the maximum pressure is observed, but also the differences in the heights are about 25 %. At P2 almost nothing is observed in both simulation and test. P3 is left out in the figure, since the pressure was equal to the atmospheric value in both situations. A reason for the differences in the pressure may be the fact that the pressure in the simulation is determined in the cell centra and not exactly at the structure. Extrapolation of the pressure would be useful here, but since the solution near the structure is not very smooth, this is left out. It is also possible that the impact velocity is a bit different there, which may cause the difference in the pressure, since a small difference in the velocity means a squared difference in the pressure.

Looking at the total force in x -direction, the shape of the force graphs look similar, although the maximum force differs about 20-30 %.

To get an impression of the pressure distribution at the structure, in figure 19 the pressure distribution

at the structure is plotted at times 2.5, 3, 3.5 and 4 seconds (the force peak is observed between 3 and 3.5 seconds). In figure 20 this pressure distribution is plotted as function of the height above deck for the situation at the centerline of the structure.

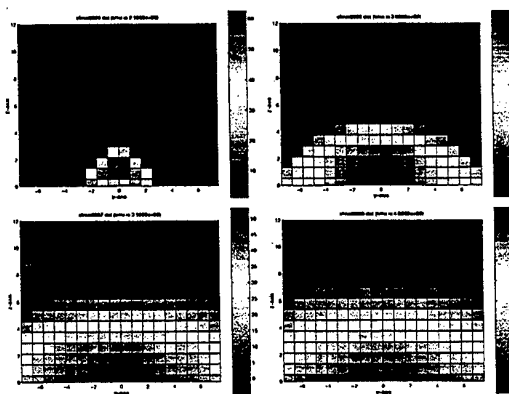


Figure 19: Pressure profile at structure at different moments in time

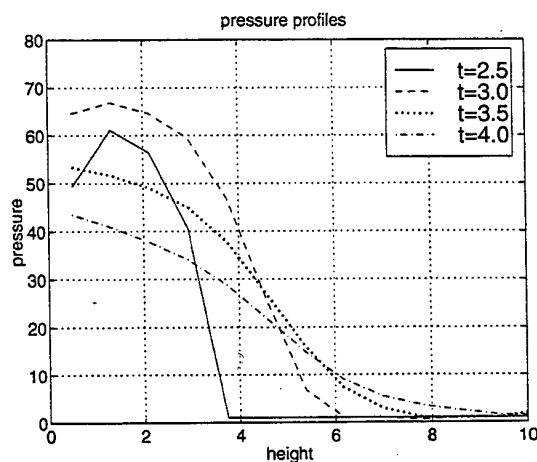


Figure 20: Pressure versus height at the centerline of the squared structure at different time steps

From this figure it becomes clear that initially the pressure is limited to the lower part of the structure (similar to the incoming waterheight). The pressure is high due to the fact that the momentum in the fluid is destroyed by the structure. In a later stage the pressure reaches also the higher positions at the structure, but the pressure is lower and only a result of the quasi-static water pressure due to the water in front of the structure.

For structures 2 and 3 the behaviour of the simulated pressure turned out to be very oscillatory, especially for the triangular structure. It is likely that these numerically observed pressure spikes should be attributed to numerical noise. However, to find out the nature of this noise, further investigation is required and compressible air flow has to be included in the model, see [8]. Also significant differences are visible in the level of the pressures, and the force turned out to be lower than the tests in structure 2 and 3. Some reasons for this may be:

- The initial conditions of the real situation, with the movement of the ship and the water inflow, differ from the simulation.
- No pressure is defined in B-cells, which can cause some problems when using smooth geometries for the structures. In this case, for the computation of the force the pressure is taken from an F-cell close to this B-cell. This approach can cause a smaller force than desired on structures 2 and 3, since the pressure will increase when moving towards the structure. In the case of structure 1 this problem does not occur (see figure 21).

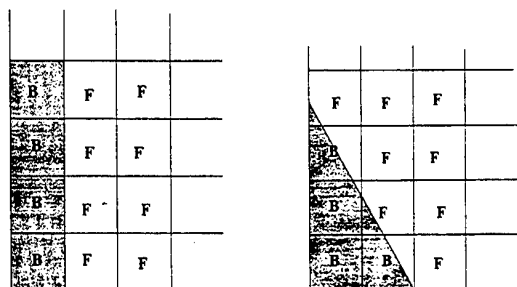


Figure 21: F-cells and B-cells near different structures

- The coarseness of the grid. One cell is about 1 x 1 x 1 meter, so for a pressure panel with a diameter of 2.7 meters, only two or three grid cells are contained in it.

These aspects are the subject of investigations at the moment.

CONCLUSIONS

In this research project the feasibility of numerically simulating green water loading by means of a Navier-Stokes model has been investigated. It was found that

the global physical behaviour of the water on the deck is described quite well by the simulation. The high water 'tongue', as observed in the tests, is also visible in the simulation. Although differences appear between the tests and the simulations, the computed forces and pressures at the structures and at the deck are similar. The differences can partially be explained by numerical noise, on which some improvements will be made in the treatment of the B-cells in the future, and partially by physical differences. Referring to the purpose of this project, it can be concluded that further development of the simulation of green water is worth working on. Some aspects that will be investigated in the future are:

- Motion of the ship: A ship at sea is not fixed in space, but is moving in vertical and horizontal direction, this means that the geometry will be changing continuously.
- Creation of a wave field around the ship and realistic inflow (taking into account the effect of the bowflare). This will make the situation significantly more realistic.

References

1. Buchner, B., On the Impact of Green Water Loading on Ship and Offshore Unit Design, PRADS '95, September 1995. Seoul.
2. Buchner, B., A New Method for the Prediction of Non-Linear Relative Wave Motions, OMAE98, June 1998. Lisbon.
3. Buchner, B. and Cozijn, J. L., An investigation into the numerical simulation of green water, MARIN, February 1997.
4. Veldman, A. E. P., Numerieke Stromingsleer, March 1994. Lecture Notes.
5. Gerrits, J., "Three-dimensional liquid sloshing in complex geometries," Master's thesis, RUG, August 1996.
6. Botta, E. F. F. and Ellenbroek, M. H. M., "A modified sor method for the poisson equation in unsteady free-surface flow calculations," J. Comp. Phys. 60, 1985, pp. 119-134.
7. Loots, E., "Free surface flow in 3d complex geometries using enhanced boundary treatment," Master's thesis, RUG, June 1998.
8. Sabeur, Z. E., Cohen, J. E., Stephens, J. R. and Veldman, A. E. P., Investigation on Free Surface Flow Oscillatory Impact Pressures with the Volume of Fluid Method, In K.W. Morton and M.J. Baines, editors, Numerical Methods for Fluid Dynamics, volume VI. Oxford Science Publications, pp. 493-498.

FLOATING BODIES, WAVE LOADS & SEAKEEPING.

Chairman : G.Delhommeau.

LINEAR DRIFT-FORCE CALCULATIONS INCLUDING ALL FORWARD-SPEED EFFECTS

T.H.J. Bunnik and A.J. Hermans¹

¹Department of Applied Mathematics, Delft University of Technology
Mekelweg 4, 2628CD Delft, The Netherlands
Fax: 31 15 278 7209; E-Mail: bunnik@twi.tudelft.nl

ABSTRACT

When a sailing ship encounters waves, a time-varying force is experienced that can have a non-zero mean value, and which, therefore, increases the resistance of the ship. In oblique waves, also a lateral force exists that causes the ship to drift away from its mean position. These additional forces are called drift forces, and they become more important when the speed of the ship is increased.

To predict these forces, we use a mathematical model that splits the wave pattern into a steady wave and an unsteady wave. The steady wave is approximated by the non-linear wave pattern and calculated by the program RAPID [1]. The calculation of the unsteady wave is based on a linearization about this steady wave and is performed in the time domain. To test this model, we compare the resulting drift forces on, and the ship motions of an LNG carrier with model-test measurements from the MARIN.

NOMENCLATURE

B	: breadth	[m]	$\tilde{\alpha}$: total displacement	[m]
D	: draught	[m]	β	: phase difference	[-]
\vec{F}	: force	[N]	γ	: phase difference	[-]
Fn	: Froude number	[-]	ϵ	: small parameter	[-]
G	: Green's function	[m ⁻¹]	ζ	: wave height	[m]
H	: mean wetted hull surface	[m ²]	θ	: angle of incidence	[-]
L	: ship length	[m]	ρ	: density	[kg m ⁻³]
M	: mass matrix	[kg]	σ	: source strength	[ms ⁻¹]
\vec{M}	: moment	[Nm]	ϕ	: time-dependent potential	[m ² s ⁻¹]
Q	: free-surface function	[-]	ω	: frequency of encounter	[s ⁻¹]
T	: transfer term	[m s ⁻³]	ω_0	: earth-fixed frequency	[s ⁻¹]
U	: forward speed	[m s ⁻¹]	Δz	: vertical distance	[m]
\vec{X}	: translational motion	[m]	Δ	: mean submerged volume of the ship	[m ³]
g	: gravitational constant	[m s ⁻²]			
h	: fluid depth	[m]			
k	: wave number	[m ⁻¹]			
k_{xx}	: transverse gyradius	[m]			
k_{yy}	: longitudinal gyradius	[m]			
\vec{n}	: normal vector	[-]			
p_s	: steady pressure	[kg m ⁻¹ s ⁻²]			
t	: time	[s]			
\vec{x}	: coordinates	[m]			
(x, y, z)	: coordinates	[m]			
Φ	: total potential	[m ² s ⁻¹]			
Φ_s	: stationary potential	[m ² s ⁻¹]			
$\vec{\Omega}$: rotational motion	[-]			

INTRODUCTION

A ship sailing at sea experiences time-varying forces due to current and waves. These forces may have a positive average value and add to the wave resistance that the ship experiences in calm water. This results in a decrease in speed, or causes the ship to drift away from its mean position if oblique waves are involved. For this reason, it is important to have an accurate prediction of these additional forces, known as drift forces, at a wide range of incoming-wave frequencies and incoming-wave angles. The influence of the forward speed, and of the ship's motions, on these drift forces is very important, so accurate predictions of

the steady flow around the ship, and of its motions are necessary.

A mathematical model is therefore introduced that meets these demands. This model is based on an accurate prediction of the steady flow, which enables us to simulate the behaviour of the ship at moderate and high speeds also. This prediction is calculated by RAPID, a method that has been developed at the MARIN, that takes into account the steady trim and sinkage of the ship, and the non-linear wave pattern.

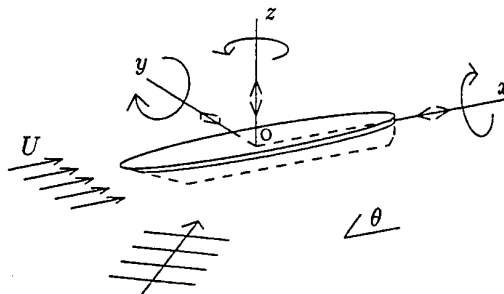
Numerical techniques are used to approximate the solution of this model in the time domain with a computer simulation. To test the validity of the model, the results of the simulation for an LNG carrier are compared with model tests performed in a towing tank at the MARIN. We compare the motions and added resistance at several cruising speeds, several incoming-wave angles and a wide range of incoming-wave lengths. A similar method has been developed by Bertram in the frequency domain, and applied to tee Series 60 [2].

MATHEMATICAL MODEL

There are a number of ways to model the water flow around a ship. Some of these are very complex, and it must therefore be considered whether these formulations are really necessary to capture the most important physics. The most exact description of the flow of water is given by the Navier-Stokes equations, which take into account the water's viscosity. Viscosity in ship hydrodynamics can be important in turbulent areas like, for example, near a rudder, propulsor or a sharp edge of the hull, but none of these are considered here. Near the hull, a small boundary layer exists in which viscous effects dominate, but this layer does not really affect the large-scale interactions of ocean waves and ship motions. The effect of viscosity is therefore neglected and potential theory is used to describe the flow of water. This means a velocity potential Φ is introduced, which gradient is the fluid velocity, and that satisfies the equation of Laplace

$$\Delta\Phi = 0$$

inside the fluid domain. In this fluid domain, a symmetrical ship sails at a constant speed U in incoming waves that make an angle θ with the forward direction of the ship. Figure 3 shows this configuration, where the coordinate system is attached to the ship. In this coordinate system, it is like the ship has no forward speed, and like there is a stream with velocity U . The ship is free to rotate around or translate along any of its axes. This sketched situation is non-linear due to the presence of a moving free surface and a moving surface-piercing ship. The non-linear condition



on the free surface states that the pressure must equal atmospheric pressure, and that a fluid particle cannot leave the free surface. On the moving hull of the ship, the normal velocity should equal the normal velocity of the water. It is very hard and time consuming to solve the Laplace equation combined with these conditions, especially when the ship has forward speed, which forces us to linearize these equations. This can be done if the time-dependent behaviour of the flow is small in some sense. We therefore have to assume that the amplitudes of the unsteady waves and the ship motion are small. If we do that, the velocity potential can be perturbed according to

$$\Phi = \Phi_s + \epsilon\phi^{(1)}(\vec{x}, t) + \epsilon^2\phi^{(2)}(\vec{x}, t) + \dots \quad (1)$$

where ϵ is a small parameter. Φ_s is the solution of the steady flow, that satisfies the non-linear steady free-surface condition and a zero-flux condition on the hull. This base flow is assumed to be known, and an approximation of this flow can very efficiently be calculated by RAPID.

The perturbation of the potential automatically results in a perturbation for the wave elevation ζ

$$\zeta = \zeta_s + \epsilon\zeta^{(1)} + \epsilon^2\zeta^{(2)} + \dots$$

It can easily be shown that the zeroth and first-order contributions satisfy

$$\begin{aligned} \zeta_s &= -\frac{1}{2g} \left(\vec{\nabla}\Phi_s \cdot \vec{\nabla}\Phi_s - U^2 \right) \quad \text{on } z = \zeta_s \\ \zeta^{(1)} &= -\frac{1}{gQ} \left(\frac{\partial\phi^{(1)}}{\partial t} + \vec{\nabla}\Phi_s \cdot \vec{\nabla}\phi^{(1)} \right) \quad \text{on } z = \zeta_s \end{aligned}$$

where

$$Q = 1 + \frac{1}{2g} \frac{\partial}{\partial z} \left(\vec{\nabla}\Phi_s \cdot \vec{\nabla}\Phi_s \right) \quad \text{on } z = \zeta_s$$

We see that the total wave elevation is the sum of the steady wave elevation, which can be seen when

the ship sails at constant speed in calm water, and small, time-dependent perturbations of this steady wave, consisting of incoming, diffracted and radiated waves. If the perturbation series (1) is substituted in the non-linear unsteady free-surface condition and we make use of the fact that the steady potential Φ_s satisfies the non-linear steady free-surface condition, the following linear condition is obtained for the first-order potential

$$\frac{\partial^2 \phi^{(1)}}{\partial t^2} + 2\vec{\nabla}\Phi_s \cdot \vec{\nabla} \frac{\partial \phi^{(1)}}{\partial t} + \vec{\nabla}\Phi_s \cdot \vec{\nabla} (\vec{\nabla}\Phi_s \cdot \vec{\nabla}\phi^{(1)}) + \frac{1}{2}\vec{\nabla}\phi^{(1)} \cdot \vec{\nabla} (\vec{\nabla}\Phi_s \cdot \vec{\nabla}\Phi_s) + g \frac{\partial \phi^{(1)}}{\partial z} + T\zeta^{(1)} = 0 \quad \text{on } z = \zeta_s \quad (2)$$

T is a transfer term that is included because the condition must be transferred from the actual, unknown, free surface $z = \zeta$ to the known surface $z = \zeta_s$ with a Taylor expansion. The transfer term is given by

$$T = \frac{\partial}{\partial z} \left(\frac{1}{2} \vec{\nabla}\Phi_s \cdot \vec{\nabla} (\vec{\nabla}\Phi_s \cdot \vec{\nabla}\Phi_s) + g \frac{\partial \Phi_s}{\partial z} \right) \quad (3)$$

To linearize the boundary condition on the hull of the ship, a Taylor expansion is made around the mean position of the ship. This boundary condition then becomes

$$\frac{\partial \vec{\alpha}^{(1)}}{\partial n} = \left(\frac{\partial \vec{\alpha}}{\partial t} + (\vec{\nabla}\Phi_s \cdot \vec{\nabla}) \vec{\alpha} - (\vec{\alpha} \cdot \vec{\nabla}) \vec{\nabla}\Phi_s \right) \cdot \vec{n} \quad (4)$$

where $\vec{\alpha}$ is the displacement of the ship as obtained from the equation of motion. It consists of a translational motion \vec{X} , and a rotational motion $\vec{\Omega}$ around the centre of gravity of the ship. This condition was, amongst others, derived by Timman and Newman [3]. Both conditions contain derivatives of steady velocities. These steady velocities are calculated by RAPID with an accuracy of the order of the grid size, because RAPID uses a first-order panel method. These inaccuracies might enlarge when the velocities are differentiated with a difference scheme, so some investigation has to be carried out to check if these derivatives are grid independent i.e. if they converge when the grid size is decreased.

Forces and Moments

In a non-viscous flow, forces and moments can be obtained by means of a pressure integration over the wetted part of the hull. Because the wetted part of the hull is not known, and because all fluid quantities are known on the average position of the hull instead of

the actual position, a perturbation series for the forces and moments has to be derived similar to (1), that only involves fluid quantities on the mean position of the hull. This means we write for the forces and moments

$$\vec{F} = \vec{F}^{(0)} + \epsilon \vec{F}^{(1)} + \epsilon^2 \vec{F}^{(2)} + \dots$$

$$\vec{M} = \vec{M}^{(0)} + \epsilon \vec{M}^{(1)} + \epsilon^2 \vec{M}^{(2)} + \dots$$

The zeroth-order force is the steady force, which contribution in x -direction equals the wave resistance, and which contribution in z -direction equals the weight of the ship. The zeroth-order moments are all zero because the ship is in equilibrium as far as buoyancy is concerned. The first-order forces and moments cause the first-order motions of the ship and have a mean value which is zero. The second-order forces and moments are the drift contributions, and they can have a mean value which is non-zero because they contain products of first-order quantities. After some extensive calculations, very long formulas can be derived for the second-order forces and moments. It turns out that the most important contributions in the drift force are

$$I : \frac{1}{2} \int_{wl} \frac{\partial p_s}{\partial z} (\zeta^{(1)} - \alpha_3)^2 \vec{n} dl \quad (5)$$

$$II : -\frac{1}{2} \rho \iint_H \vec{\nabla}\phi^{(1)} \cdot \vec{\nabla}\phi^{(1)} \vec{n} dS \quad (6)$$

$$III : -\rho \iint_H \vec{\alpha} \cdot \vec{\nabla} \left(\frac{\partial \phi^{(1)}}{\partial t} + \vec{\nabla}\Phi_s \cdot \vec{\nabla}\phi^{(1)} \right) \vec{n} dS \quad (7)$$

$$IV : \vec{\Omega} \times \left(M \frac{\partial^2 \vec{X}}{\partial t^2} \right) \quad (8)$$

The first contribution is a line integral of the relative wave height over the steady water line of the ship. It is therefore important to have an accurate prediction of both the motions and the wave elevation at the water line of the ship. The second contribution is an integral of unsteady velocities over the mean wetted surface of the ship. These velocities can be obtained directly from the source strengths. The third contribution is an integral of the derivative of the first-order pressure, in the direction of the motion, over the mean wetted surface. Because the pressure contains unsteady velocities, difference schemes on the hull are used to determine this derivative. The fourth contribution is the outer product of the rotational motion and all first-order forces.

The mean value of the first element of this force is the added resistance and causes a decrease in speed.

The mean value of the second element is a lateral force and will cause the ship to drift away from its mean position. The third element is a vertical force that will alter the sinkage of the ship. For the drift moments similar formulas can be derived. Because all forces that we want to evaluate only contain first-order quantities, only the first-order potential has to be solved, which from now on we will refer to as ϕ .

NUMERICAL MODEL

In general, no analytical solution to the presented mathematical model exists, so we have to construct a numerical approximation which limit must equal the exact solution if grid sizes approach zero.

The first thing to do is to reduce the area on which we calculate this approximation, to a finite one. This gives problems at the edges of the created computational domain, because waves that reach that edge may reflect instead of propagate further like they should. This problem can be solved by adding some numerical damping to the free-surface condition near the edges where waves may show up. This makes sure that the amplitude of these waves will decrease to almost zero when the edge is reached.

To solve the Laplace equation, we use a boundary-integral method. On the boundaries of the fluid domain a source distribution is placed which makes sure the velocity potential satisfies the Laplace equation. By making use of mirror sources, the no-flux condition on the bottom of the water is satisfied. The source strength is still an unknown function, which is discretized by assuming that it is piecewise constant on the boundary. This means that we have to divide the steady free surface and the hull in a number, say N , of small panels, resulting in the following expression for the velocity potential

$$\phi(\vec{x}) = \sum_{j=1}^N \sigma_j \iint_{\partial\Omega_j} G(\vec{x}, \vec{\xi}) dS_{\xi} \quad ; \quad G = \frac{-1}{4\pi r}$$

where $\partial\Omega_j$ is one of the panels. The advantage of this formulation is that the fluid velocities on the hull, required to calculate the pressure, can accurately be determined from the source strengths once they are known. The unknown, finite set of source strengths is found by substituting this expression into the two boundary conditions and by applying these conditions in the centre of the panels.

The boundary condition on the hull (4) is easy to apply. The condition on the free surface (2) is more difficult to apply, because it contains time and space derivatives of the potential. The time derivatives are discretized by using second-order difference schemes

with a uniform time step, that relate the derivatives to values of the potential at the current and previous time levels. This means that at each time level the potential has to be recalculated from the potential at previous time levels. The result is a time-domain method, which takes more computational time than a frequency-domain method, but which has the advantage that the time dependence does not have to be harmonic. In a time-domain simulation, care must be taken with the description of the spatial derivatives, because the stability of the time stepping strongly depends on it. It turns out that for moderate or higher speeds of the ship, upwind difference schemes have to be used for the tangential derivatives in (2) to guarantee stability. The more accurate central difference schemes can only safely be used in case of low speeds and large grid sizes, as shown by Bunnik and Hermans [4].

The first-order wave elevation consists of three parts; a radiated wave, an incoming wave and a diffracted wave. Radiated waves are waves that occur because the ship performs small rotations and translations. The resulting forces and the motions can be related to each other by calculating frequency-dependent added mass and damping coefficients. When this relation is known, the behavior of the ship in incoming waves can be simulated. For the incoming-wave potential we use

$$\phi_{inc} = \frac{g\zeta_a}{\omega_0} \cos(\omega t - kx \cos \theta - ky \sin \theta) f(z)$$

where

$$f(z) = \frac{\cosh(k(z+h))}{\cosh(kh)}$$

This potential satisfies the Kelvin condition on the calm-water plane and the zero-flux condition on the bottom, $z = -h$. This means that near the ship, this wave does not satisfy the free-surface condition. This gives no problems because this is corrected in the diffracted wave. To calculate the drift forces we need three separate simulations. First, the added mass and damping are determined. Second, the diffracted wave is determined and the first-order forces and moments on the ship in waves. From these forces the equation of motion is solved and a simulation is run to calculate the total wave pattern. When all the first-order quantities are known, the drift forces can finally be calculated. To save memory and time, the symmetrical and asymmetrical parts of the wave pattern are calculated separately on the starboard side of the ship only.

LNG CARRIER

Natural gas is a bulky form of energy and must be concentrated before it can be transported economically. Over the years, for obvious economic reasons, the use of natural gas increased most rapidly in zones close to production sites, such as the United States, Russia and Western Europe. This explains why, even today, only 19% of world gas production is exported. Most exports are transported by pipeline, but gas can also be liquefied and shipped by sea in special carriers. Today, liquefied natural gas (LNG) accounts for 26% of all gas exports, and the stage is set for a strong and continuing increase in gas use and international gas trade.

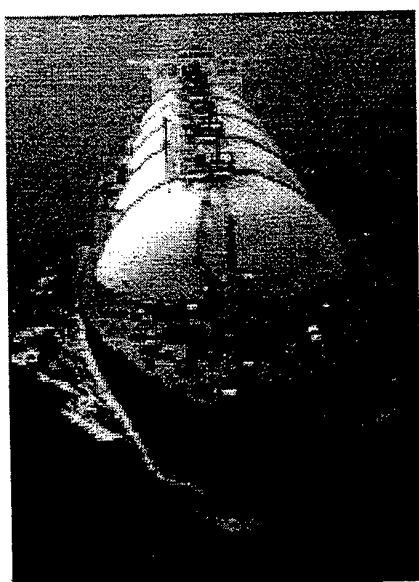


Figure 1: LNG carrier sailing at sea.

Table 1: Main particulars of the LNG carrier.

Denomination	Symbol	Unit	Value
Length	L	m	273.0
Breadth	B	m	42.0
Draught	D	m	11.5
Displacement	Δ	m^3	98740.0
Longitudinal c.o.g. from aft perpendicular	\overline{AG}	m	138.7
C.o.g. above base	\overline{KG}	m	13.7
Longitudinal gyradius	k_{yy}	% L	24.0
Transverse gyradius	k_{xx}	% B	35.0

We applied our model to such a Liquefied Natural Gas carrier sailing at its maximum speed and slightly

below that, corresponding to moderate Froude numbers of 0.2 and 0.17, in water with a depth $h = 175m$. The particulars of this tanker are listed in table 1, where c.o.g. is used to abbreviate 'center of gravity'. At these Froude numbers, it is expected that the influence of the steady wave profile on the unsteady waves is too large to allow the use of simple approximations, like uniform flow or double-body flow. Our method, that incorporates the fully non-linear steady characteristics of the ship, must therefore be applied to obtain correct results.

Steady velocities, derivatives and their convergence

The first step is to calculate the non-linear steady free surface, the fluid velocities on that surface, and the fluid velocities on the hull of the carrier. Only the steady solution at Froude number 0.2 will be discussed here.

To calculate the steady flow, a panel distribution of the carrier is required. We used a panel distribution that had 2380 panels, and which is shown in figure 2. In the calculations only the starboard side of the ship is used, because use is made of the symmetry of the wave pattern. The steady wave and the steady

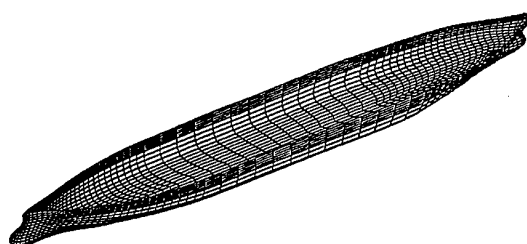


Figure 2: Panel distribution on LNG carrier.

velocities were calculated twice; First on a grid that had 60 panels per steady wave length ($2\pi Fn^2$), and then on a grid that had 120 panels per steady wave length. This made it possible to check the convergence of the steady wave, and the velocity derivatives that are required in the free-surface condition (2). Because RAPID only calculates velocities, these derivatives have to be obtained with difference schemes. Likely, the transfer term (3) will give most problems, because it is a second derivative of the velocity field. The other derivatives are all first derivatives, and less problems are expected with them.

The non-linear wave elevation was calculated on an area stretching from $x = -1.3L$ to $x = 1.7L$, and from $y = 0$ to $y = 0.6L$, with panels arranged

in strips that approximately follow the steady streamlines, making numerical differentiation easier.

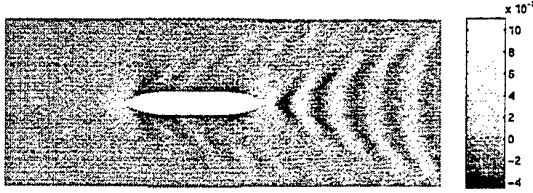


Figure 3: Top view of the steady wave pattern, $Fn=0.2$.

Figure 4 shows the wave pattern on the strip of collocation points that lies closest to the ship. First 60, and then 120 panels per wave length were used. The bow and stern waves can be seen, which have an amplitude of about one half times the Froude number squared. Almost no differences can be seen between the prediction that uses 60, and the prediction that uses 120 panels per wave length, so we may conclude that the wave pattern converges extremely well.

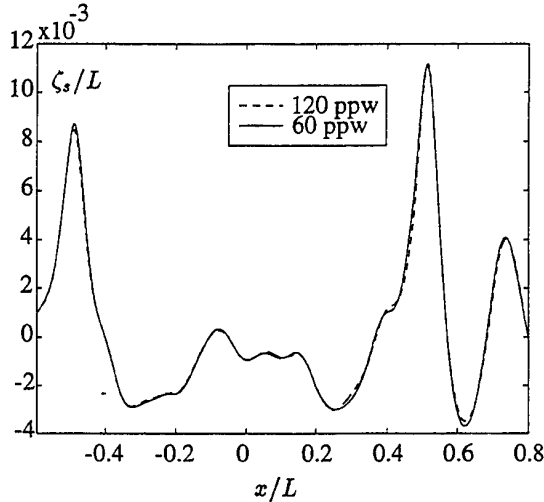


Figure 4: Steady wave elevation for 60 and 120 panels per wave length, on the free-surface strip closest to the ship.

Figure 5 shows the longitudinal tangential derivative of $\vec{\nabla}\Phi_s \cdot \vec{\nabla}\Phi_s$ on the free-surface strip closest to the ship. Hardly any differences can be seen due to the fact that only a part of this derivative must be obtained with a difference scheme, when use is made of the free-surface condition

$$\frac{1}{2} \vec{\nabla}\Phi_s \cdot \vec{\nabla} (\vec{\nabla}\Phi_s \cdot \vec{\nabla}\Phi_s) + g \frac{\partial \Phi_s}{\partial z} = 0 \quad \text{on } z = \zeta_s$$

It relates the change of the squared velocity in the direction of the velocity to the vertical velocity. Be-

cause the main component of the velocity is mostly in longitudinal direction, this equation only has to be adjusted slightly to obtain the derivative shown in figure 5.

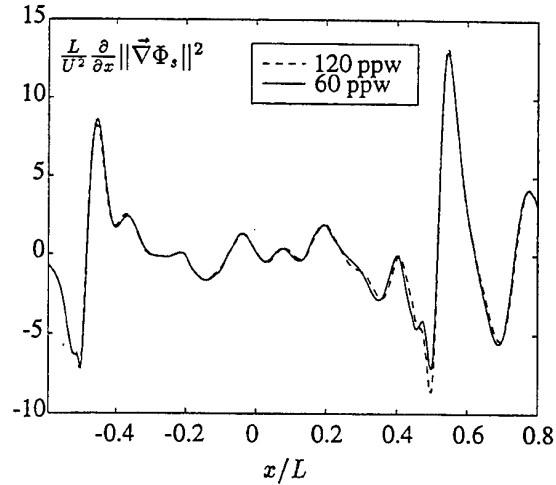


Figure 5: Tangential derivative in x -direction of the squared velocity for 60 and 120 panels per wave length, on the free-surface strip closest to the ship.

The transfer term (3) will likely give more problems, because an additional vertical derivative has to be calculated. To determine this vertical derivative, the velocities are not only calculated on the free surface, but also on two parallel planes at distances Δz and $2\Delta z$ below the free surface. This only requires the determination of some extra influence coefficients, and costs not much extra work. The vertical derivative is then obtained with a three point, second-order difference scheme. The distance between the planes must be such, that $k\Delta z \ll 1$, where $k = \frac{g}{U^2}$ is the steady wave number. Because at the bow and the stern, the velocity gradients are largest due to the presence of stagnation points, most problems are expected in these areas. Figure 6 shows the transfer term near the bow. As can be seen, large differences occur at some points, and a filtering technique must be used to obtain reasonably correct results.

Figure 7 shows the transfer term in the midship region, between bow and stern. Near bow and stern differences can be seen, but further away from them, these disappear and the transfer term converges very well. At larger lateral distances from the ship no large differences were found anymore, but these results are not shown here. Therefore, we may conclude that, apart from bow and stern, the transfer term converges on the entire free surface, making its use in the unsteady free-surface condition possible.

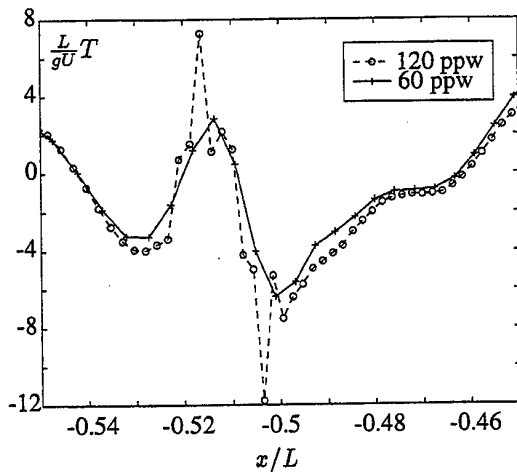


Figure 6: Transfer term on the free-surface strip closest to the ship and near the bow for 60 and 120 panels per wave length, $\Delta z = 0.00102L$.

Motions

The convergence of the steady velocities and derivatives enables us to apply the unsteady free-surface condition (2), so we can start with the calculation of the time-dependent flow. First, we will determine the motions of the ship.

To determine the motion of the ship, all quantities in the equation of motion have to be known, such as added mass and damping, restoring force coefficients, and mass and moments of inertia. The restoring force coefficients are estimated from the forces and moments on the ship, when it is moved from its mean position. For the mass and moments of inertia of the ship, empirical values are used, part of which are listed in table 1. To obtain the added mass and damping coefficients, 6 simulations have to be run in which the ship is given one of the 6 possible motions, while no incoming waves are considered. By relating the resulting hydrodynamic forces to the motions, the appropriate values of added mass and damping can be found.

The motion of the ship can be found by calculating the diffracted and incoming waves. After calculating the corresponding first-order forces and moments, the equation of motion can be solved, which results for the translational motions in

$$X_i = |X_i| \sin(\omega t - kx_g \cos \theta + \beta_i) \quad i = 1, 2, 3$$

and for the rotational moments in

$$\Omega_i = |\Omega_i| \sin(\omega t - kx_g \cos \theta + \gamma_i) \quad i = 1, 2, 3$$

The phases β and γ are the phase differences between

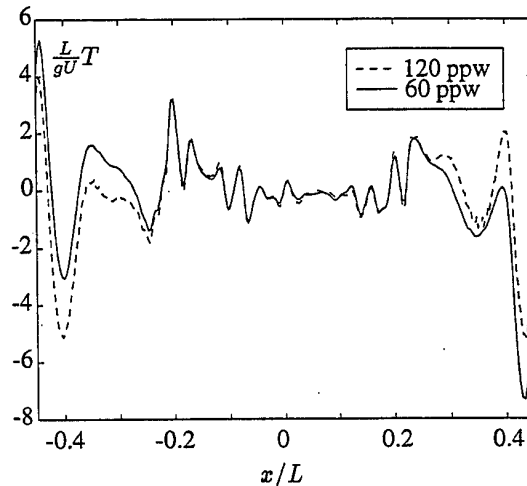


Figure 7: Transfer term on the free-surface strip closest to the ship between bow and stern for 60 and 120 panels per wave length, $\Delta z = 0.00102L$.

the incoming-wave elevation at the centre of gravity, x_g , and the motion.

We calculated the motions in head waves and bow-quartering waves, at Froude numbers 0.17 and 0.2. The wave length ranged from $\lambda = 0.37L$ to $\lambda = 1.4L$. At each Froude number, all calculations were done on the same grid, stretching from $x = -L$ to $x = L$ and from $y = 0$ to $y = 0.9L$, divided in 24 strips of 95 panels. The same grid had to be used because the calculation of the influence coefficients takes a lot of time, so a re-gridding at each wave length was too costly. This may give problems for very long waves, because they are truncated at a relative small distance from the ship. Very short waves may be represented inaccurately because too little panels per wave length are used. The area between $y = 0.5L$ and $y = 0.9L$ was used to damp waves by adding artificial damping to the free-surface condition. No damping zone in front of, or behind the ship was required, because only downstream waves are considered in this particular case.

Figure 8 shows the amplitude and phase differences of the three symmetrical motions (surge, heave and pitch), at Froude numbers 0.17 and 0.2, in head waves and bow-quartering waves. There is a very good agreement between our calculations and the measurements of the amplitudes, especially for short waves. The surge amplitude shows some differences for long waves, and the pitch amplitude for long bow-quartering waves. To predict surge and pitch motion, an accurate prediction of the steady-velocity derivatives (m-terms) on bow and stern is required. For this ship that is very difficult because of the presence of

stagnation points, and the consequent large velocity derivatives. Another factor that may cause the differences between measurements and calculations is the fact that the waves are quite long compared to the size of the grid. Because the distance from the stern to the downstream edge of the computational free surface is only half a ship length, long waves may easily be represented inaccurately. One must bear in mind that the diffracted bow-quartering waves have an even larger wave length, because the encounter frequency is lower than the encounter frequency of head waves with the same length. The encounter frequency of a bow quartering wave at $Fn=0.2$ with length $\lambda = 1.4L$, for example, is the same as the encounter frequency of a head wave with length $\lambda = 1.61L$. This explains why more differences can be seen in long bow-quartering waves than in long head waves. A solution might be to enlarge the size of the computational free surface. To represent the steady wave and the derivatives of the steady velocities accurately, however, a minimum number of panels per steady wave length ($2\pi Fn^2$) is required. One look at the transfer term (figure 7), for example, shows that a lot of points are required to represent it. A large grid with a small grid size leads to a large number of panels. On the workstation that we used in our calculations, the number of panels was restricted to 3500, a number which is reached quite fast, also because an accurate description of the hull requires 1000 to 1500 panels. Therefore, to represent large waves accurately, a more powerful computer is required.

The phase difference in surge is very hard to predict, especially the 90 degrees phase shift that occurs at the point where the amplitude takes on its minimum. The main reason, again, is an incorrect prediction of the steady-velocity derivatives. Note that the phase difference in heave is zero in long waves, which means that the motion tends to follow the waves. In pitch, there is a 90 degree phase difference, so the motion is in phase with the wave slope.

Figure 9 shows the asymmetrical motions (sway, roll and yaw), at Froude numbers 0.17 and 0.2, in bow-quartering waves (there are no asymmetrical motions in head waves because of the symmetry of the ship). It is impossible to predict roll motion correctly with our model, because of the absence of viscosity. A correct prediction may be obtained with an empirical correction of the damping (viscous roll damping), but that has not been done here. In short waves, the agreement for the other two motions is again remarkable. In long waves, however, differences in amplitude can be seen again. This may be caused by two facts. First, the waves may be too long to fit on the grid. Second, incorrect

restoring-force and moment coefficients may have been used, which are especially important at low frequent motions. To determine the restoring-force coefficients, the gradient of the steady pressure has to be calculated, which is very difficult at the bow and the stern. Empirical values are, unfortunately, not available. Because the prediction of the asymmetrical motions is incorrect in long waves, the predicted added resistance will probably also differ from the measurements.

Added resistance

The most important contributions to the added resistance were discussed before, and summarized in (5), (6), (7) and (8). Our calculations show, that the most important contribution is the waterline integral, which means an accurate prediction of the wave elevation at the waterline, and the vertical motion (determined by heave, roll and pitch) is required. The other motions however, also influence the wave elevation, so in fact all motions should be predicted accurately. The previous section showed the difficulties in predicting the roll motion and the other motions in long waves, so differences are likely to be found between the calculated and the measured added resistance.

Figure 10 shows the added resistance at $Fn=0.17$ and 0.2 in head waves and bow-quartering waves. The results in head waves are in good agreement with the measurements, showing only small differences. In bow-quartering waves larger differences can be seen, especially in long waves. The reasons for this has already been mentioned; an inaccurate prediction of roll and an inaccurate prediction of the other motions in long waves.

SUMMARY

To predict the motions and the added resistance of a ship sailing in waves, a mathematical model was formulated that incorporates an accurate description of the steady flow. This makes it possible to use the model for ships sailing at moderate and high speeds. With numerical techniques, the model has been translated in a computer program, and then applied to a Liquid Natural Gas carrier sailing at Froude numbers 0.17 and 0.2. The motions and the resistance in head and bow-quartering waves were compared with measurements done at the MARIN. In head waves, a very good agreement was found between our predictions and the measurements, especially for waves with short to medium wave length. In bow-quartering waves, the sway, roll and yaw motion become important. It was found that it is impossible to predict the roll motion accurately in the absence of viscous

damping. Empirical formulas for the roll damping exist which can be implemented in the future. In long waves, sway and yaw also differed from the measurements, probably because the dimensions of the grid were too small, and because it is not possible to calculate the derivatives of the steady flow on the bow and stern accurately. The first problem can only be solved if a computer is used with more memory and a faster processor. The second problem can be solved by using a higher-order panel method to calculate the nonlinear steady flow. Because the added resistance depends directly on the motion, differences were found between calculations and measurements in long, bow-quartering waves. If the motion is predicted correctly, these differences will not occur.

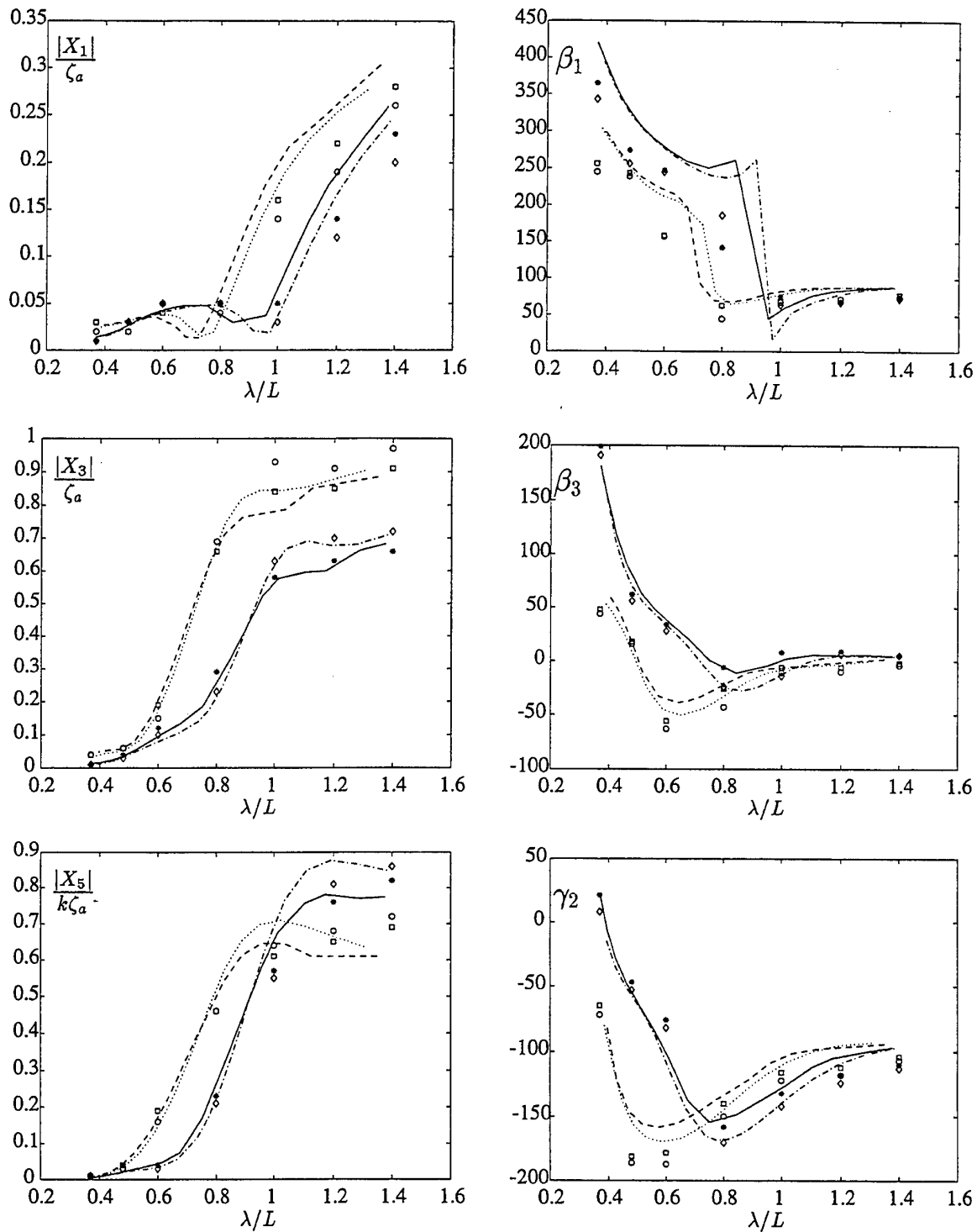


Figure 8: Amplitude and phase difference (in degrees) of surge, heave and pitch motion, at $F_n=0.17$ in head waves (— calculated, * measured) and bow-quartering waves (- - calculated, \square measured), and at $F_n=0.2$ in head waves (-·-·- calculated, \diamond measured) and bow-quartering waves (··· calculated, \circ measured).

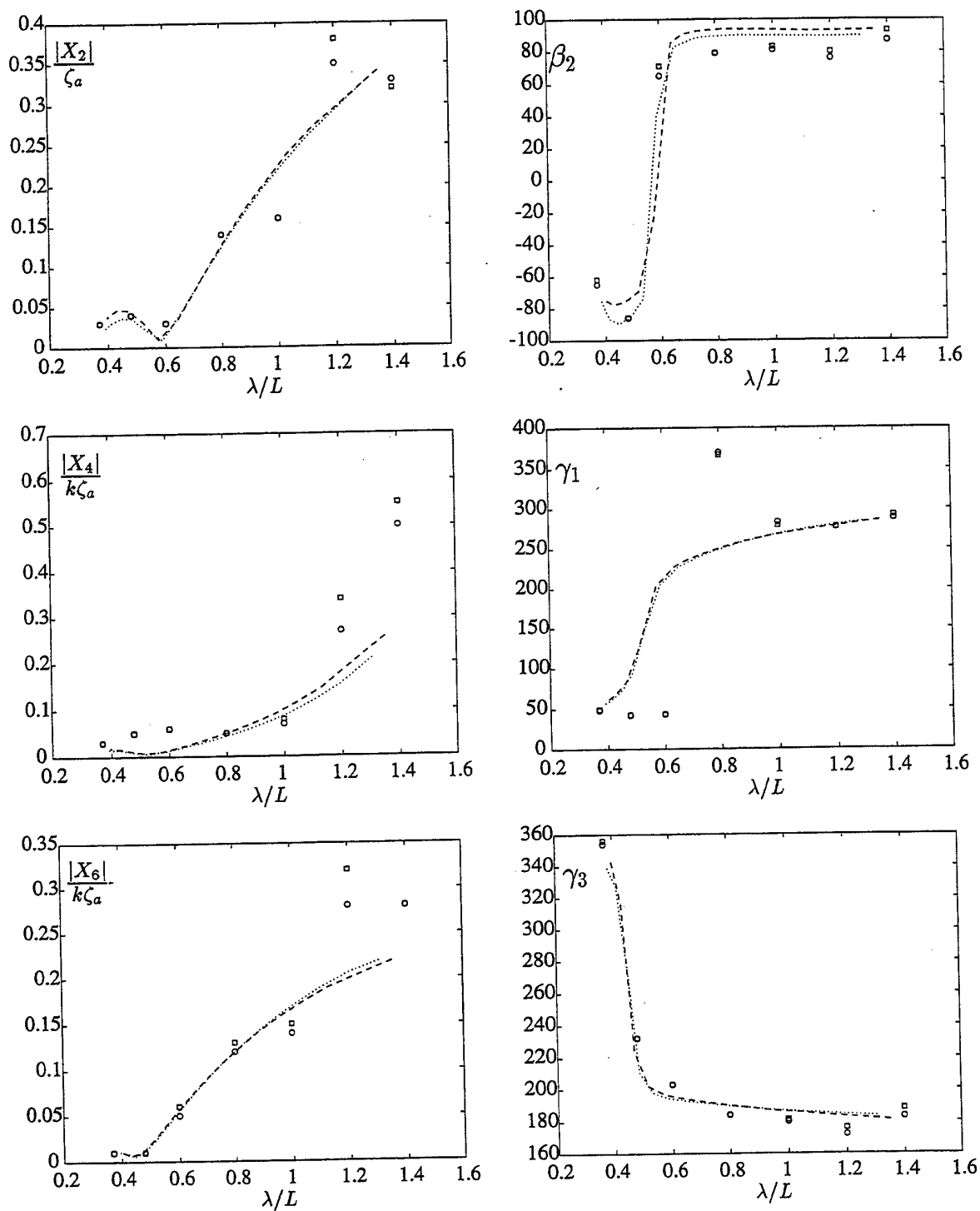


Figure 9: Amplitude and phase difference (in degrees) of sway, roll and yaw motion, at $F_n=0.17$ in bow-quartering waves (- - calculated, \square measured), and at $F_n=0.2$ in bow-quartering waves (\cdots calculated, \circ measured).

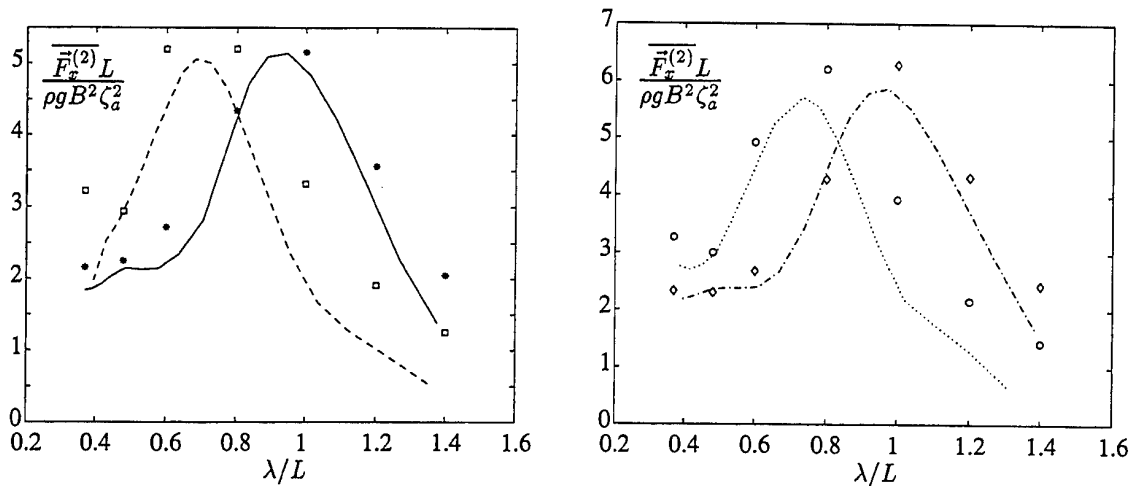


Figure 10: Added resistance at $F_n=0.17$ in head waves (— calculated, * measured) and bow-quartering waves (- - calculated, \square measured), and at $F_n=0.2$ in head waves (---- calculated, \diamond measured) and bow-quartering waves (\cdots calculated, \circ measured).

REFERENCES

1. Raven, H.C., "A Solution Method for the Nonlinear Ship Wave Resistance Problem," PhD Thesis, Delft University of Technology, The Netherlands, 1996.
2. Bertram, V., "A 3-D Rankine Panel Method to Compute Added Resistance of Ships," Technical Report 566, 1996, Technical University of Hamburg, Germany.
3. Timman, R. and Newman, J.N., "The coupled damping coefficients of a symmetric ship," Journal of ship research 5, 1962, pp. 1-7.
4. Bunnik, T.H.J. and Hermans, A.J., "Stability analysis for the 3D unsteady free-surface condition with raised panels." Proceedings of the 13th International Workshop on Water Waves and Floating Bodies, 1998.

USING DIFFERENTIAL PROPERTIES OF THE GREEN FUNCTION IN SEAKEEPING COMPUTATIONAL CODES

A.H Clément

¹Laboratoire de Mécanique des Fluides, Ecole Centrale de Nantes
1 Rue de la Noë, B.P. 92101, 44321 Nantes Cedex 3, France
Fax: 332 40 37 25 23; E-Mail: Alain.Clement@ec-nantes.fr

ABSTRACT

The Green function of linear time-domain hydrodynamics has been recently proven to satisfy a simple fourth order ordinary differential equation (ODE) [5]. As a first application of this remarkable property, the present paper shows how it can be used to evaluate the kernel of the convolution integrals in the BEM solution of seakeeping problems, in the linear time-domain approach. The Green function is obtained by integrating these ODE from one time-step to another instead of being computed by the usual methods. Several Runge-Kutta algorithms were tested and compared; it is shown how an optimal time step can be derived from a stability analysis. The *cpu*-time savings brought by this new method are then evaluated. Numerical results are given for three test cases: the heaving hemisphere, a standard series-60 ship hull, and a TLP offshore platform. Impulse response functions are calculated and Fourier transformed to recover the classical frequency domain hydrodynamic coefficients as a check for validity and accuracy.

INTRODUCTION

The solution of time-domain seakeeping problems in the framework of linear potential flow theory generally requires to resolve a boundary integral problem involving convolution integrals. These integrals may be regarded as the memory of the free-surface fluid; their kernel features the time-domain Green-function of linear free-surface hydrodynamics, and its spatial gradient. The numerical evaluation of this function, analytically defined as an integral over an unbounded domain, is quite time consuming by itself. Furthermore, since the convolution integrals extend from the initial state of rest up to the current time t , the mass storage and *cpu* time required for their computation grow roughly quadratically with time. Since 1995 [3], we are developing a "system" approach to the problem, which is aimed at speeding up these calculations and at reducing the storage demand. It is based on a major result stating that the time-domain Green-function of linearized free-surface hydrodynamics satisfies an exact fourth order ordinary differential equation [4, 5]. If the coefficients of this ODE were constant with respect to the time variable, the convolution integrals could be completely suppressed

and replaced by a simple filtering numerical process. Unfortunately, the ODE coefficients being polynomial with respect to the time variable, such a simplification does not occur. Nevertheless, this differential property provides us with an alternative method for the on-line computation of the Green function during the calculation of the convolution integrals. In this paper, we present an application of this approach to the computation of the free-surface flow resulting from an impulsive motion of a floating body around its equilibrium position; the practical output of such computations being the matrix of impulse response functions (IRFs) of the body. The aim of this very first application of our ODEs was primarily to establish the feasibility of the method, and to estimate the savings it could bring in terms of computation time. The problem is posed in the linear potential theory, and solved by a direct, zeroth order, BEM method. The Green functions in the kernel of the convolution integrals are computed by either the classical series expansion, a tabulation procedure, or integrating the new ordinary differential equation. The computational aspects of these three methods are presented and compared.

MATHEMATICAL FORMULATION

Let us make the usual assumptions of linearized potential flow theory. We shall denote by $\Phi(x, y, z; t)$ the velocity potential which depends on the nondimensional space variables (x, y, z) and the time variable t . The fluid velocity at a field point $M(x, y, z); z \leq 0$ is then given by $\mathbf{V} = \nabla\Phi$. All space variables will be reduced by a typical length h , and the time variables by $\sqrt{h/g}$, g being the gravity acceleration.

We shall focus here on the impulsive wave radiation problem which may be formulated as: given a floating body at rest in its equilibrium position \mathcal{C} , it is impulsively set into motion, at $t = 0$, in one of its six degrees of freedom. The resulting velocity potential associated with the waves radiated from the body will be the unknowns of the problem. Let us denote by \mathbf{V}_i the velocity vector for a motion on the i th mode.

The velocity potential is sought as the solution, in the fluid domain \mathcal{D} , of the following initial boundary value problem (IBVP).

Laplace's equation

$$\Delta\Phi(x, y, z; t) = 0 \quad ; M \in \mathcal{D}, t \geq 0 \quad (1)$$

Free-Surface condition:

$$\frac{\partial^2 \Phi(x, y, 0; t)}{\partial t^2} + \frac{\partial \Phi(x, y, 0; t)}{\partial z} = 0 \quad ; t \geq 0 \quad (2)$$

No-Flux body boundary condition:

$$\frac{\partial \Phi(x, y, z; t)}{\partial n} = \mathbf{V}_i \cdot \mathbf{n} \quad ; M \in \mathcal{C} \quad (3)$$

Initial conditions:

$$\Phi(x, y, z; t) = \frac{\partial \Phi(x, y, z; t)}{\partial t} = 0 \quad ; M \in \mathcal{D}, t \leq 0 \quad (4)$$

Let us now introduce the Green function of the impulsive source problem which satisfies intrinsically Laplace's equation (1), the linearized free surface condition (2) and the initial conditions (4). It may be written as the sum of an impulsive part and a memory part, like :

$$G(M, t, M', t') = -\frac{1}{4\pi} [\delta(t - t') G_0(M, M')] - \frac{1}{4\pi} [H(t - t') \mathcal{F}(M, t, M', t')] \quad (5)$$

where δ and H refer respectively to the Dirac and to the Heaviside distributions. Full expressions of this function, together with some interesting

differential properties, will be given in the next section. Applying the Green's formula to the unknown potential Φ and to this function yields the following Fredholm-Volterra integral equation :

$$\begin{aligned} \frac{\Phi(M, t)}{2} - \iint_{\mathcal{C}} \Phi(M', t) \frac{\partial}{\partial n'} G_0(M, M') d\mathcal{C} = \\ - \iint_{\mathcal{C}} G_0(M, M') \mathbf{V}_i \cdot \mathbf{n}(M', t) d\mathcal{C} \\ + \int_0^t dt' \iint_{\mathcal{C}} \left[\Phi(M', t') \frac{\partial}{\partial n'} \mathcal{F}(M, t, M', t') \right. \\ \left. - \mathcal{F}(M, t, M', t') \mathbf{V}_i \cdot \mathbf{n}(M', t') \right] d\mathcal{C} \quad (6) \end{aligned}$$

A direct Boundary Element Method may then be derived from this integral equation by discretizing the body surface into plane panels, and representing the unknown functions over each panel by a suitable functional approximation. The details of the numerical solution of (6) will be presented in a later section.

The j^{th} component of the transient hydrodynamic forces consecutive to the i^{th} impulsive motion can be computed afterwards by integrating the potential over the body surface, namely :

$$M_{ij}(t) = \iint_{\mathcal{C}} \Phi_i(M', t) n_j(M') d\mathcal{C} \quad (7)$$

and differentiating with respect to the time variable to return to the pressure on the body surface :

$$L_{ij}(t) = \iint_{\mathcal{C}} \frac{\partial \Phi_i(M', t)}{\partial t} n_j(M') d\mathcal{C} = \frac{\partial M_{ij}(t)}{\partial t} \quad (8)$$

This *impulse response function* (IRF) is homogeneous to a force and will be given, in the following sections, as a coefficient defined by : $CL_{ij} = L_{ij}/\rho gh^3$.

Before examining the numerical method for the solution of the boundary integral equation (6), let us first recall some important results about the impulsive time-domain Green function and its differential properties.

THE TIME-DOMAIN GREEN FUNCTION

The function (5) which satisfies (1), (2) and (4) is the basic element of the so-called Kelvin BEM methods. Its impulsive part G_0 is nothing but the

free space Green-function associated with its anti-mirror image about the linearized free-surface, namely :

$$G_0(M, M') = \frac{1}{R} - \frac{1}{R_1} \quad (9)$$

where : $r = \sqrt{(x-x')^2 + (y-y')^2}$, $R = \sqrt{r^2 + (z-z')^2}$, $R_1 = \sqrt{r^2 + (z+z')^2}$ while the memory part is given by :

$$F(M, t, M', t') = F(r, \zeta, t) = R_1^{-\frac{3}{2}} \tilde{F}(\mu, \tau) \quad (10)$$

with $\tilde{F}(\mu, \tau) =$:

$$2 \int_0^\infty J_0(\lambda \sqrt{1-\mu^2}) e^{-\lambda \mu} \sqrt{\lambda} \sin(\sqrt{\lambda} \tau) d\lambda \quad (11)$$

The set of variable $(r, \zeta = z+z', t)$ will be referred to as the *initial variables*, while (μ, τ) , defined as :

$$\mu = -\frac{z+z'}{R_1} \quad \text{and} \quad \tau = t/\sqrt{R_1} \quad (12)$$

will be named the *natural variables* of the function. One may notice that the geometric parameter μ lies in the bounded range $[0, 1]$. Approaching this limit, the function is more and more oscillating but remains convergent at infinity, as illustrated by fig.1. In the limit $\mu = 0$, where both source and field points belong to the free-surface $z = 0$, and only in this case, it is divergent, linearly in t .

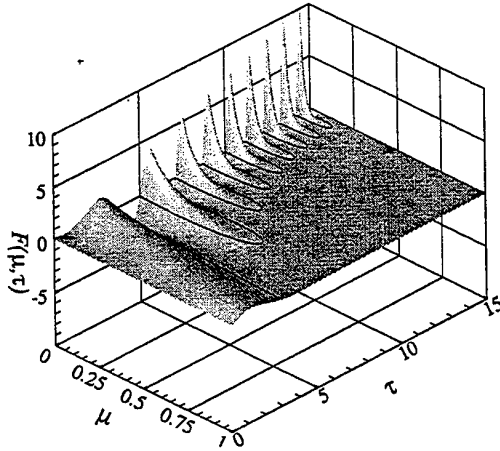


Figure 1: The Green function (eq.11) in natural variables (μ, τ)

In a recent paper [5], we derived a general lemma stating that the family of functions $A_{\nu,l}(\mu, \tau)$ of

the form:

$$A_{\nu,l}(\mu, \tau) = \int_0^\infty \lambda^l e^{-\lambda \mu} J_\nu(\lambda \sqrt{1-\mu^2} \sin(\sqrt{\lambda} \tau)) d\lambda$$

satisfy a fourth order differential equation with polynomial coefficients of second degree with respect to the time variable. The time-domain Green function and its space derivatives belonging to the family, they are shown to satisfy the following ODEs:

$$(r^2 + \zeta^2) \frac{\partial^4 F}{\partial t^4} - \zeta t \frac{\partial^3 F}{\partial t^3} + \left(\frac{t^2}{4} - 4\zeta \right) \frac{\partial^2 F}{\partial t^2} + \frac{7t}{4} \frac{\partial F}{\partial t} + \frac{9}{4} F = 0 \quad (13)$$

$$(r^2 + \zeta^2) \frac{\partial^4 F_r}{\partial t^4} - \zeta t \frac{\partial^3 F_r}{\partial t^3} + \left(\frac{t^2}{4} - 6\zeta \right) \frac{\partial^2 F_r}{\partial t^2} + \frac{11t}{4} \frac{\partial F_r}{\partial t} + \frac{21}{4} F_r = 0 \quad (14)$$

$$(r^2 + \zeta^2) \frac{\partial^4 F_\zeta}{\partial t^4} - \zeta t \frac{\partial^3 F_\zeta}{\partial t^3} + \left(\frac{t^2}{4} - 6\zeta \right) \frac{\partial^2 F_\zeta}{\partial t^2} + \frac{11t}{4} \frac{\partial F_\zeta}{\partial t} + \frac{25}{4} F_\zeta = 0 \quad (15)$$

where F_r (resp. F_ζ) denotes the horizontal (resp. vertical) gradient of $F(r, \zeta, t)$. The initial conditions, also derived in their general form in [5], become in this case:

$$\begin{cases} F(r, \zeta, 0) = 0 \\ \frac{\partial F}{\partial t}(r, \zeta, 0) = -2 \frac{\zeta}{(r^2 + \zeta^2)^{\frac{3}{2}}} \\ \frac{\partial^2 F}{\partial t^2}(r, \zeta, 0) = 0 \\ \frac{\partial^3 F}{\partial t^3}(r, \zeta, 0) = 2 \frac{r^2 - 2\zeta^2}{(r^2 + \zeta^2)^{\frac{5}{2}}} \end{cases} \quad (16)$$

$$\begin{cases} F_r(r, \zeta, 0) = 0 \\ \frac{\partial F_r}{\partial t}(r, \zeta, 0) = 6 \frac{r\zeta}{(r^2 + \zeta^2)^{\frac{3}{2}}} \\ \frac{\partial^2 F_r}{\partial t^2}(r, \zeta, 0) = 0 \\ \frac{\partial^3 F_r}{\partial t^3}(r, \zeta, 0) = 6 \frac{r(4\zeta^2 - r^2)}{(r^2 + \zeta^2)^{\frac{5}{2}}} \end{cases}$$

$$\begin{cases} F_\zeta(r, \zeta, 0) = 0 \\ \frac{\partial F_\zeta}{\partial t}(r, \zeta, 0) = \frac{4\zeta^2 - 2r^2}{(r^2 + \zeta^2)^{\frac{3}{2}}} \\ \frac{\partial^2 F_\zeta}{\partial t^2}(r, \zeta, 0) = 0 \\ \frac{\partial^3 F_\zeta}{\partial t^3}(r, \zeta, 0) = -6 \frac{\zeta(3r^2 - 2\zeta^2)}{(r^2 + \zeta^2)^{\frac{5}{2}}} \end{cases}$$

We shall see in a later section that the major part of the computation time required to solve the

integro-differential integral equation (6) is spent in evaluating this function (and its gradient) a huge number of time ($\sim O(10^8)$). Then, the choice of the method for the calculation of F , F_r and F_C requires a particular attention if one wants to keep the global *cpu*-time within reasonable limits. Two families of methods were available up to now. The new method proposed here constitutes a third alternative.

• *series expansions method*. Obviously, the original expression (11) is not well suited for direct numerical evaluation; then, from the early eighties, several authors [12, 15, 13, 20, 19] have developed numerical procedures to compute the Green function in its natural variables. The best choice among all the available methods is local in both space and time; it depends on the values of μ and τ . Asymptotic expansions are used in the large time range, series expansions for moderate μ and τ , Filon quadrature for moderate τ and larger μ , and finally recursive Bessel relations in the vicinity of $\mu = 1$ (see [13] for details). Following B.W. King (1987), a set of subroutines devoted to this task has been developed in our laboratory, and will be used in the sequel as the first alternative for the numerical solution of (6).

• *tabulation method*. A second numerical method for the evaluation of (11) is based on a bi-linear interpolation in a pre-computed table [9, 16]. This is made possible by the fact, first pointed out by Jami (1981), that the Green function is a function of only two natural variables (μ, τ), the first one varying in a bounded domain. Because the maximum of the τ variable reached during a given computation is not known a priori, the table must be quite large in that direction, and the preceeding (series expansion) method must be also available in case of the function should be evaluated beyond the table boundary τ_{max} . Nevertheless, we shall see later that this method yet allows considerable saving in *cpu*-time compared to the first one.

• *ODE-integration method*. Because eq. (6) is to be solved sequentially in a time marching procedure from given initial conditions, the above set of ODEs may be used to update the right hand side from a time step to the next one rather than evaluating the Green function by one of the two above mentioned methods as usual. Runge-Kutta ODE integration algorithms are used for this purpose in the present study. Details about the stability of this new method will be given in a forthcoming section.

SOLUTIONS TO THE BOUNDARY INTEGRAL PROBLEM

Since the early eighties, several authors have proposed numerical algorithms to solve the above boundary integral equation, or some variants [15, 13, 14, 9, 17, 2, 1]. From (6), one may consider the potential in the fluid domain as generated by a distribution of both sources and doublets with density distributions : $\sigma = \frac{\partial \Phi}{\partial n}$, resp $\nu = -\Phi$, on the body surface C . Discretizing this surface into simple sub-elements and approximating the unknown functions on each one by some low-order functional, the continuous integral equation (6) is transformed into a discrete set of linear algebraic equations which can be solved numerically afterwards. Various order of approximations for both the type of geometric sub-element and the functional representation of the solutions may be found in the related literature.

The present implementation of the method follows a previous work done by Ferrant (1988b), who used a zeroth order direct BEM method with constant singularity distributions (σ, ν) over quadrilateral and/or triangular plane panels. Because his code has served as a starting basis in the present study, this constant distribution option was kept. Furthermore, a step velocity excitation of the body hull, $\mathbf{V}_i = \mathbf{n}_i H(t)$, is considered here for numerical convenience; the hydrodynamic responses for an actually impulsive velocity input then follow straightforwardly by simple differentiation. Due to the constant density distribution over the panels, the discretized integral equation (6) is written at the centroid of each panel, leading to the discrete set of linear algebraic equations :

$$[D_{ij}][\nu_j(t)] = -H(t)[S_{ij}][\sigma_j(0)] - \int_0^t [s_{ij}(t')][\sigma_j(0)] dt' + \int_0^t [d_{ij}(t-t')][\nu_j(t')] dt' \quad (17)$$

where :

$$\begin{aligned} D_{ij} &= \iint_{C_j} \frac{\partial}{\partial n_j} G_0(M_i, M_j) dC_j \\ S_{ij} &= \iint_{C_j} G_0(M_i, M_j) dC_j \\ d_{ij}(t) &= \iint_{C_j} \frac{\partial}{\partial n_j} \mathcal{F}(M_i, t, M_j, 0) dC_j \end{aligned} \quad (18)$$

$$s_{ij}(t) = \iint_{C_j} \mathcal{F}(M_i, t, M_j, 0) dC_j \quad (19)$$

The constant coefficient matrices $[D_{ij}]$ and $[S_{ij}]$ are computed by the classical Hess & Smith formula. Being time independent, they can be evaluated once for all at the onset. Furthermore, $[D_{ij}]$ is inverted once for all by a Gaussian procedure, and stored.

The time variable is also discretized into equal time-steps. The solution of (17) at each time step is then obtained by a simple matrix product after updating the RHS. This later task requires the computation of convolution products of the past solution on the body with the Green function and its gradient. The convolution integrals are computed by a simple trapezoidal rule, and, in this very first application of the method, the surface integrals in (19) are computed by means of single point Gauss quadrature. Despite of these low order algorithms, these computations remain the most time consuming part of the overall numerical process due to the complexity of the Green function [14, 17]. All the memory coefficients (19) from the first to the current time step are theoretically needed to perform the time integration in (17). The best choice is therefore to keep all these coefficient matrices in RAM memory during the execution, as long as the computer memory size permits doing so; when it does not, which essentially occur when running the *tabulation* method on a small computer, we are constrained to store them on disk, resulting in slowing down the program by multiplying disk input/output (I/O) (see fig.9left).

In the present study, the three above mentioned computational methods were implemented. In the *series expansion* approach, several methods are used to compute the Green function in its natural variables, depending on the values of μ and τ . These methods do not share the same performances in terms of *cpu*-time, and during the same time step, the choice of an algorithm may be different from one couple of points to an other due to the dependency of the time variable $\tau = t/\sqrt{R_1}$ upon the relative position of field point and source point. The local *cpu* time thus depends on time and meshing, making the global *cpu* time quite unpredictable.

In the *tabulation* method, the Green function $\tilde{F}(\mu, \tau)$ is precomputed on a grid of the (μ, τ) plane and stored in a permanent file. In the present study, a (1000, 24000) grid was used with

$\delta\mu = 0.001$ and $\delta\tau = 0.005$, resulting in a 96Mbyte file in single precision, in order to cover the whole time-range in the simulations. This long time range tabulation avoids the algorithm to switch to asymptotic expansion method in long time simulations, and permits a better comparison with the ODE-integration method afterwards. The table has to be implemented in RAM memory during execution to avoid too much disk access; then, depending upon the total memory available to him, the user may be obliged to store the memory coefficient matrices (19) on disk files as mentioned above. We happened to be in that case in the computations reported herein, as we shall see later.

STABILITY AND CONVERGENCE

ODE integration scheme

The new method proposed above for the on-line evaluation of the Green function is based on the numerical integration of ordinary differential equations featuring time-varying polynomial coefficients. In the wide choice of numerical schemes available to perform this task, we paid a special attention to the class of Runge-Kutta algorithms which has the advantages of being sufficiently robust and which does not require the knowledge of previous values to advance in time as it is the case with predictor-corrector method. Furthermore, the evaluation stage of the ODEs right hand side, in the present case, is so unexpensive (in term of *cpu* time indeed) that economizing the number of evaluations is not a key point as it may be in other circumstances. (see matrix eq.20).

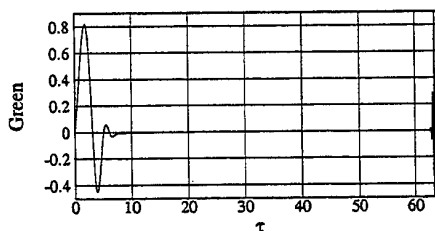


Figure 2: Typical instabilities in the determination of the Green function by ODE integration ($\mu = 0.5$, $d\tau = 0.1$), method=RK4

The most important point to be investigated carefully here is the stability of the integration scheme which must be ensured whatever the kind of body being tested and the level of mesh re-

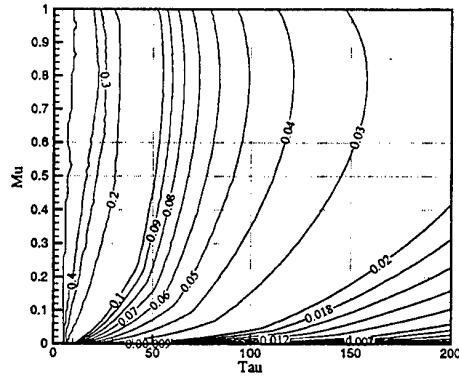


Figure 3: stability limits RK2 method

finement. The figure (2) shows a typical instability occurring at $\tau \approx 62$ when computing $\tilde{F}(0.5, \tau)$ by a standard fourth order Runge-Kutta method. Such an instability will occur systematically at some (large) value of the time variable τ for a given value of the geometrical parameter μ . Then, before using this method to compute the whole set of s_{ij} and d_{ij} influence coefficients, one must address the problem of finding the optimum time step to avoid such a phenomenon in a given computation range $0 \leq t \leq t_{max}$, for a given meshing of the floating body.

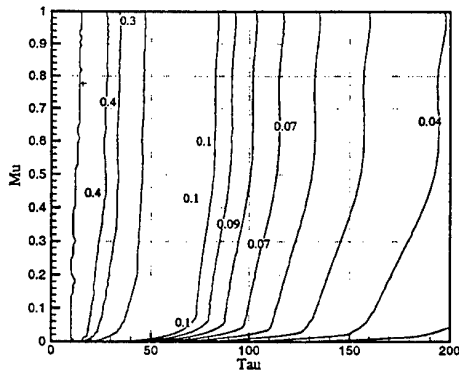


Figure 4: stability limits RK5 method

First of all, one must remember that the Green function is a function of two variables in the system of natural variables (μ, τ) defined by (12), and of three variables (r, ζ, t) when we considered the function in its initial set of variables. The computation of the convolution integral in (17)

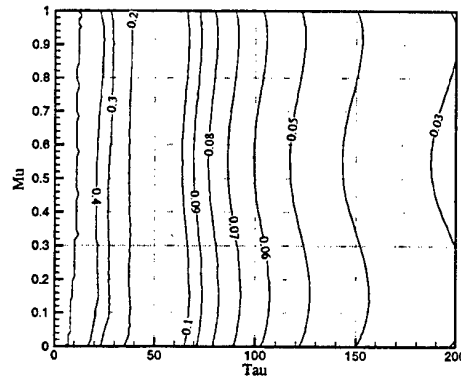


Figure 5: stability limits RK4 method

must be performed in the later one while the stability can be investigated in the former one. The natural variable τ depends on the time variable t through the relation $\tau = t(\tau^2 + \zeta^2)^{-\frac{1}{2}}$; therefore, it is scaled by the space variables depending on the couple of source and field points being considered. It means that the maximum (natural) time step $\Delta\tau_{max}$ determined by the stability analysis has to be converted into a maximum (system) time step Δt_{max} by considering the minimum value of the distance R_1 among all the couples of points defined by the hull panelization.

Usually, the stability analysis of differential equations starts from examining some basic features of the matrix $[A]$ defined by expressing the high order differential equation as a system of first order ODE, namely:

$$\dot{\mathbf{F}} = [A] \mathbf{F}$$

For the Green function ODE (13) under consideration, the so-called companion matrix $[A]$ would read:

$$[A] = \begin{bmatrix} 0 & 1 & 0 & 0 \\ 0 & 0 & 1 & 0 \\ 0 & 0 & 0 & 1 \\ -\frac{9}{4} & -\frac{7\tau}{4} & \left(4\mu - \frac{\tau^2}{4}\right) & -\mu \end{bmatrix} \quad (20)$$

The most common stability criterion requires all the eigenvalues of $[A]$ to have a negative real part. But this theorem holds only for constant coefficients matrix systems, and not for varying matrices as in the present case (see [18] p113). This prevents us from proceeding to the standard analysis straightforwardly.

Nevertheless, this point is not crucial because the Green function, which is the solution we are

concerned with, is known to be stable everywhere except at $\mu = 0$. Furthermore, this parameter μ belongs to the bounded range $[0, 1]$.

The stability of the various Runge-Kutta integration algorithms was therefore investigated from this argument, by numerical experiments in the (μ, τ) plane. Three schemes were tested: a second order (RK2) a fourth order (RK4) and a fifth order (RK5). The first and the second one are the classical algorithms which can be found in the literature. According to Press et al. [21] we chose the set of Cash-Karp parameters for the fifth order scheme. This permits a precise time step optimization by using an embedded fourth order formula and the Fehlberg method. The coefficients for this fifth order scheme are given in Appendix. With each method, the parameter range $0 < \mu < 1$ was thoroughly swept, and the time step leading to the stability limit was determined numerically for each couple (μ, τ_{max}) by detecting instabilities like in fig.2. The corresponding results are plotted in figures 3, 5 and 4 for RK2, RK4 and RK5 methods respectively. In these plots, the labels on the curves indicates the time step. As it can be observed, we recover the expected behaviour : the smaller the time step, the later the divergence for a given RK scheme, and also : the higher the scheme order, the later the divergence for a given time step. Considering now the behaviour in the vicinity of the axis $\mu = 0$, the fourth order scheme appears to be far more robust than the two others. This point is important and it must be kept in mind when one designs the time-step maximization algorithm, as we did in the following manner. As a starting point, the mesh and the maximum simulation time are given by the user. From the former, one may derive the minimum value of R_1 , and then, from both of them, a map of all the points in the

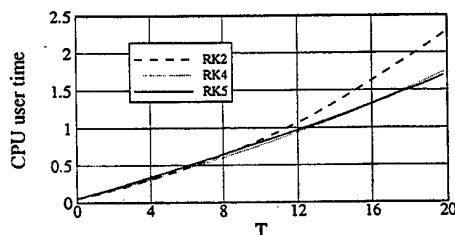


Figure 6: Heaving hemisphere. comparison of overall cpu time using various RK schemes to integrate the Green function ODEs.

scheme	maximum time-step	local error
RK2	.083	$O(7.10^{-3})$
RK4	.11	$O(1.5 \cdot 10^{-4})$
RK5	.15	$O(7.6 \cdot 10^{-5})$

Table 1: stability limit time-steps and error magnitude for the three considered Runge-Kutta methods. 4*25 panels, floating hemisphere.

(τ_{max}, μ) plane may be established. Now, for a given RK scheme, a $(d\tau, \mu)$ map may be drawn with the help of the corresponding figure 3, 5 or 4 depending on the algorithm being considered; returning, at last, to the (dt, μ) map, the smaller value of dt ensuring the stability over the whole mesh can be determined easily.

A preprocessor of our time-domain code ACHIL3D was built on this model. When applied to the heaving hemisphere test problem discretized into 4*25 panels, it gave the stability limit time-steps shown in table 1. Nevertheless, the final choice of a method cannot be based on these items only. The natural advantage of RK5 should be moderated by the fact that this scheme needs six evaluations of the RHS of the ODE while it is four with RK4 and only two with RK2. Therefore, the comparisons must be done on the overall computation time to obtain a more objective ranking. Figure 6 finally shows that RK4 and RK5 are practically equivalent in terms of *cpu* time when each method is run at its stability limit time-step (minus epsilon of course!). The choice left to the user is therefore based on other arguments like time-integration accuracy, which gives the leadership to RK5, or robustness of the time-step maximization which rather favours RK4 (compare fig.5 and 4). Furthermore, the accuracy argument in favour of the fifth order scheme, should be moderated by consistency consideration, if we remember that we have chosen a zeroth order BEM with one Gauss point by panel for this first implementation of our ODE method. The two RK algorithms were finally implemented in our code in such a way that the user may easily switch from one to the other; the fourth order algorithm is the most commonly used.

Convergence with mesh refinement

Being a well documented test case, the floating hemisphere was chosen as the first model body for the convergence tests. The two geometric symmetries of this simple hull were naturally taken into

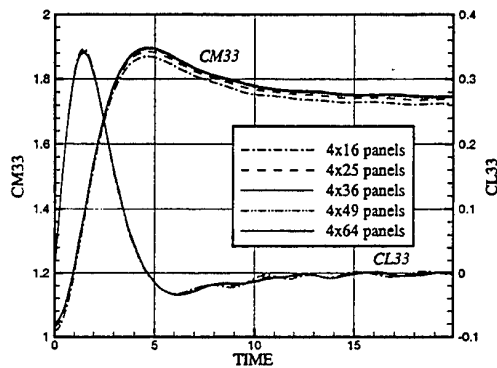


Figure 7: Floating hemisphere : impulse response function / mesh refinement

account and only a quarter-body was meshed. The impulse response function for an impulsive heave motion CL_{33} was selected as the output for checking the overall accuracy. Several different meshing were used with 16, 25, 36, 49 and 64 panels on a quarter-body, and the convergence with regard to the mesh size (characterized by the average panel area) was investigated. The curves of $CL_{33}(t)$ (eq.8) and $CM_{33}(t)$ (eq.7) are plotted in figure 7. The accuracy was checked by comparing with the same result obtained with 144 panels by Korsmeyer (1988) [14]. An excellent agreement was observed. Zooming around the first peak at $CL_{33}(1.475)$ (see fig.7) revealed that a 1% local relative error was achieved with 100 panels (4x25) on the hemisphere. The oscillations observed in the tail of the response for $t \geq 6$ are the time-domain counterpart of the well known "irregular frequencies", and arise from the same origin. Since we were mainly interested here in *cpu* time statistics, we did not tried to suppress this phenomenon by the help of the usual dedicated methods. This is left as a further development of the code. A linear convergence rate was observed when plotting the error on the impulse response function CL as a function of the typical average area of the panels (at the peak value where a maximum discrepancy is expected). The same convergence tests were also achieved on the ISSC TLP and the results are plotted in figure 8 which illustrates this linear behaviour perfectly well.

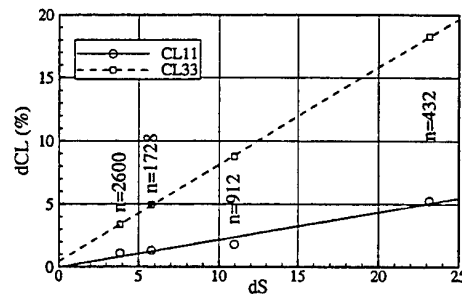


Figure 8: ISSC TLP impulse response function in heave and sway. Global convergence with respect to typical panel size (n the total number of panels)

CPU-TIME SAVING WITH ODE METHOD

The first goal of this study was to assess the feasibility of the ODE-integration method. The results presented in the previous section show that it has been reached. The second one was to give a first estimate of the savings it can bring in terms of computing time. The three methods were then implemented in three parallel "brother" codes differing only by this point, and tested intensively varying the mesh, the time-step, the Runge-Kutta method order, ... Impulse response functions were computed not only for the floating hemisphere, but also on the ISSC TLP platform (fig.12) and a standard Series60-06 ship hull (fig.14).

To sets of curves are plotted in Fig:9. On the left side, the total *cpu*-time including the system part is shown, whereas the user part only is plotted in the right figure. The difference between these two measures is spent mainly in I/O operations to and from the disk storage. As pointed earlier, we were obliged to write the coefficient matrices (19) on disk files when using the *tabulation* method, whereas they stayed in memory in the two other approaches. This explains the differences between the dashed lines in the left and in the right frames of figure 9. For the two other methods, the time spent in I/O is negligible and the curves are quite the same in both sides. In other words, one may assume that the right view of figure 9 can always be obtained provided one run a computer with a sufficient amount of memory. Let us thus focus on this view as a basis for comparisons.

The structure of the convolution process sug-

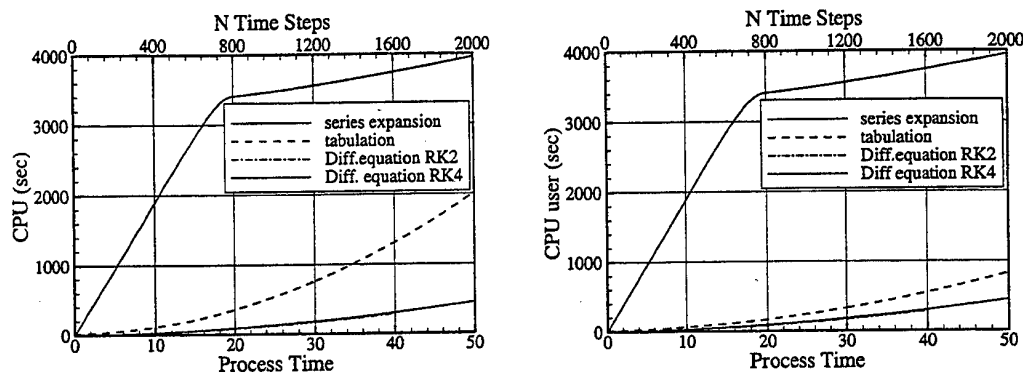


Figure 9: Floating Hemisphere (4x49 panels; $\delta t=0.025$) ; left : total *cpu*-time (user+I/O) ; right : user *cpu*-time only.

gests a quadratic growth of the computing time. Such a behaviour can be observed with both the *tabulation* and the ODE-integration methods, whereas the series expansion method presents two different regimes. For $t < 18$, we observe a quasi-linear growth of the *cpu*-time. In that range, the Green function is evaluated by different algorithms, according to the relative position of source and field points as explained before. These methods are far more time consuming than the asymptotic expansion which is used later, when $\tau \geq 14$. So, once all the couples of points satisfy this condition, the program speeds up and a quadratic behaviour is recovered. The benefit of using the two other methods is clearly illustrated by Fig:9. Between them, the advantage goes to the ODE-integration method ; the *cpu*-time ratio with the *tabulation* method lies in the range [2,4], depending on whether or not you can keep all the arrays in RAM during the program execution.

In the present comparison all the methods were run using the same constant time-step $\delta t = 0.025$. We limit ourselves to RK2 and RK4 methods; RK5 was disregarded. The fourth-order, four steps Runge-Kutta method requires twice as many floating operations as the second order two steps method. Nevertheless, the tiny difference between the RK4 and RK2 curves in Fig:9 proves that, with the ODE-integration method, the time spent in Green function evaluations has become marginal compared with the time for the overall process. On the contrary, it means that, by selecting RK5 algorithm, we could increase the precision of the ODE integration at practically no extra *cpu* cost.

One should notice that these curves correspond to quite long simulations. In the present case of

a heaving hemisphere, a simulation up to $t = 20$ should be sufficient from a practical point of view (see Fig:7). It would result in computing times shown in the table below, when running a DEC Alpha 500 workstation, at 330MHz.

Method	user+I/O	user (sec)
Series	3408	3405
Tabulation	356	164
ODE-RK4	88	87
ODE-RK2	82	82

Table 2. *cpu*-time requirements (sec), floating hemisphere (4x49 panels), $t=20$.

The ISSC Tension Leg Platform

The computer code was used afterwards to compute the IRFs of a more realistic body. Results for the ISSC platform in heave and surge motions were presented by Ferrant (1988)[9]. We therefore selected it as a test geometry for our code **ACHIL3D**. Several meshes were generated using the mesh generator **MACAO**. All the results reported here were obtained with a 912 panels mesh illustrated by Fig:12. The fourth-order Runge-Kutta integrator was used with a fixed time step $\delta t = 0.02$.

As a check for the computer code, our surge/surge impulse response function CL_{11} (fig.10a) was compared with the results obtained by Ferrant using a 1200 panels mesh; the agreement was found excellent.

In figures 10b and 11, the diagonal IRF for heave, roll and yaw motions are presented together with their Fourier transform which are nothing but the classical *added mass* and *damping* coefficients of the frequency domain approach to

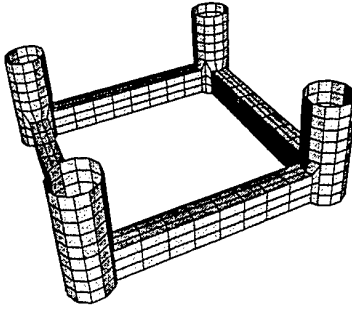


Figure 12: Meshing of the ISSC TPL. (912 panels)

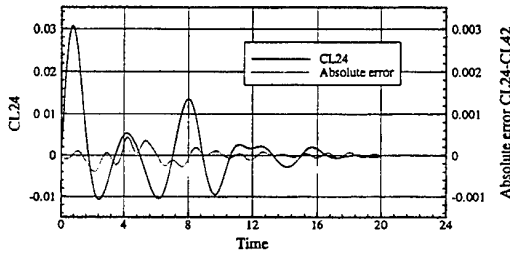


Figure 13: ISSC Tension Leg Platform - 912 panels Sway/Roll IRF CL24 ; symmetry (absolute) error

the seakeeping problem, the correspondence being given by :

$$A_{ij}(\omega) = M_{ij}(0) + \int_0^\infty L_{ij}(t) \cos(\omega t) dt$$

$$\frac{B_{ij}(\omega)}{\omega} = \int_0^\infty L_{ij}(t) \sin(\omega t) dt \quad (21)$$

These frequency domain coefficients CA_{ij} CB_{ij} , deduced from the present time-domain approach by Fourier transformation have been compared to those obtained directly by running frequency domain panel codes like **AQUADYN** (ECN) and **WAMIT** (MIT) (data in [10]). The agreement is again excellent, within a few percent. In figure 13, the off-diagonal IRF coefficients CL_{24} and CL_{42} and the difference between them (ten times magnified) are presented. These coefficients should theoretically be equal; the gap between is therefore a good measure of the overall accuracy of the computation method. In the present case, the maximum difference is approximately one percent of the maximum of the CL_{24}/CL_{42} curve.

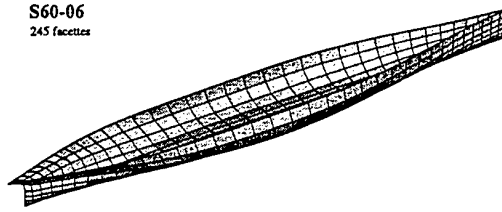


Figure 14: S60-06 meshing; 2x245 panels

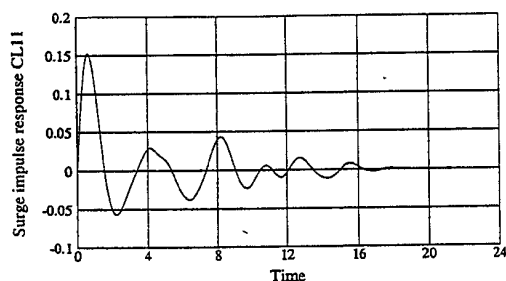
SERIES60-06 SHIP HULL

The bodies used in the previous section have two symmetry plane. This property was naturally exploited to reduce the number of unknowns, hence the system matrix size. The computer code was afterwards extended to bodies with a single symmetry plane. The standard Series 60-06 ship (fig.14) hull was then used as a test case for this further release. The hull was panelized with 2x245 plane quadrilateral panels.

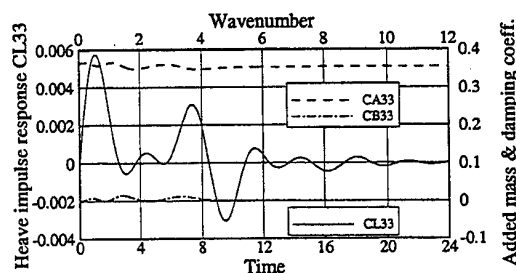
The optimal time step determined by the pre-processor as explained previously was found to be $\delta t = 0.00484$ when the ship length is taken as the reference length. A RK5 scheme was used in the reported computations. The impulse response functions were computed up to $T = 10$ which was found sufficient to reach a quasi-null response state as shown in fig.15 to 20. These time-domain results were then Fourier transformed by (21) in order to be compared to those obtained directly in the frequency domain by the diffraction-radiation code **AQUADYN** [7, 8] developed at LMF laboratory in the eighties. In terms of order of approximation, this code is equivalent to **ACHIL3D** but in the frequency domain. It solves the linearized (to the first order) seakeeping problem by a zeroth-order BEM featuring a mixed sources-dipoles distribution of Kelvin type Green function on the discretized hull.

Time-domain and frequency domain results are plotted in figures 15 to 20 hereafter. We give only diagonal coefficients here, to save space, but the whole set of non-zero responses has, of course, been computed.

The fit between the frequency domain and the time-domain approaches is generally excellent ($O(10^{-2})$), except near the "irregular" frequencies already mentioned in this paper. This phenomenon is particularly sensitive on the frequency-domain results for heave and pitch motions, in figures 17 and 19. These results con-

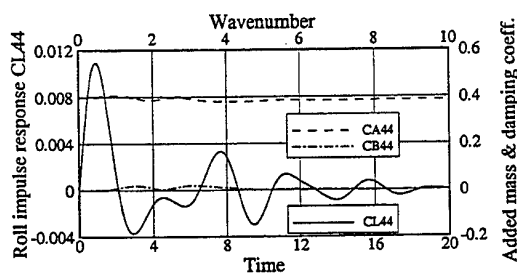


(a) CL11. Surge/Surge IRF

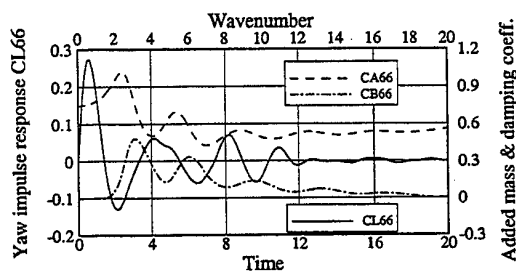


(b) CL33, CA33 and CB33 Heave/Heave coefficients

Figure 10: ISSC Tension Leg Platform - 912 panels



(a) CL44, CA44 and CB44 Roll/Roll coefficients



(b) CL66, Yaw/Yaw coefficient

Figure 11: ISSC Tension Leg Platform - 912 panels

firm that the present time-domain approach can be used as a robust alternative method to obtain the usual frequency domain hydrodynamic coefficients. The opposite is not true due to the slow asymptotic decrease of these coefficients as the wavenumber tends to infinity (see fig.15 to 20). The inverse Fourier transform which has to be performed numerically from these data imposes a truncation at very high frequencies where the convergence of the frequency domain solution would surely be problematic.

CONCLUSION

A new method for the calculation of the Green function during the computation of convolution integrals occurring in time-domain seakeeping simulations has been proposed. It is based on differential properties of the time-domain Green function which are used to speed up this numerical process. The performance, in terms of *cpu* time requirements, of the new alternative method

was compared with the two usual approaches to the problem, based either on series expansions or tabulation of the Green function. The proposed ODE-integration method runs faster than the tabulation method, in a ratio between two and four, depending on the memory capacity of the computer. The stability analysis of the Green function ODE provides a mean to optimize the choice of the time step depending on the RK algorithm finally selected. The accuracy of the code has been checked by tests on well documented bodies as the hemisphere, the ISSC TLP platform and a serie60-06; the frequency domain coefficients of these bodies were recovered by Fourier transform with an excellent accuracy.

This work was financially supported by the *Direction des Recherches, Etudes et Techniques* of the French Ministry of Defence (DGA).

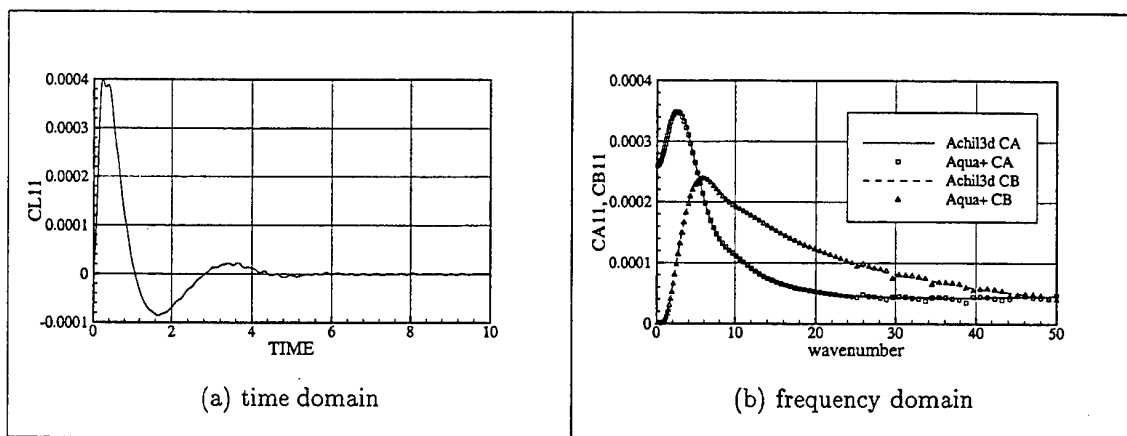


Figure 15: Series 60-06 (2x245 panels). Surge/Surge hydrodynamic coefficients

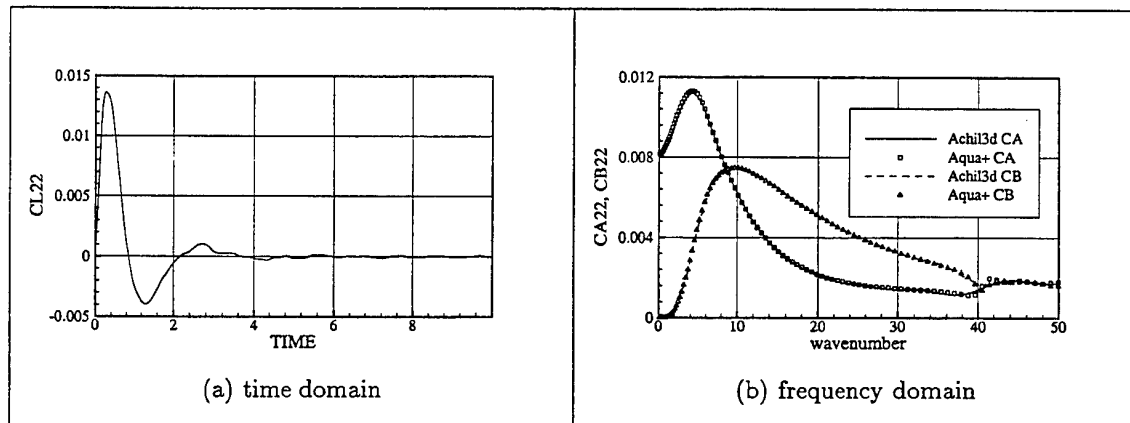


Figure 16: Series 60-06 (2x245 panels). Sway/Sway hydrodynamic coefficients

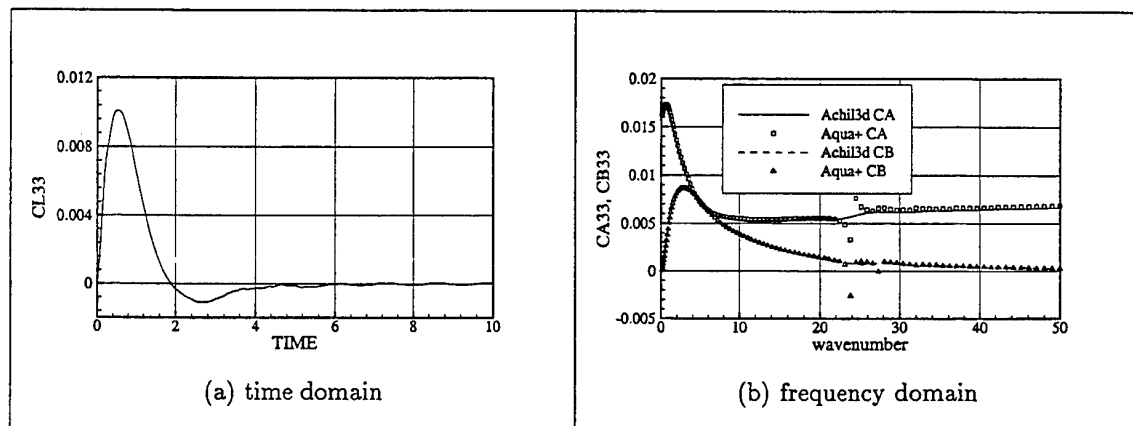


Figure 17: Series 60-06 (2x245 panels). Heave/Heave hydrodynamic coefficients

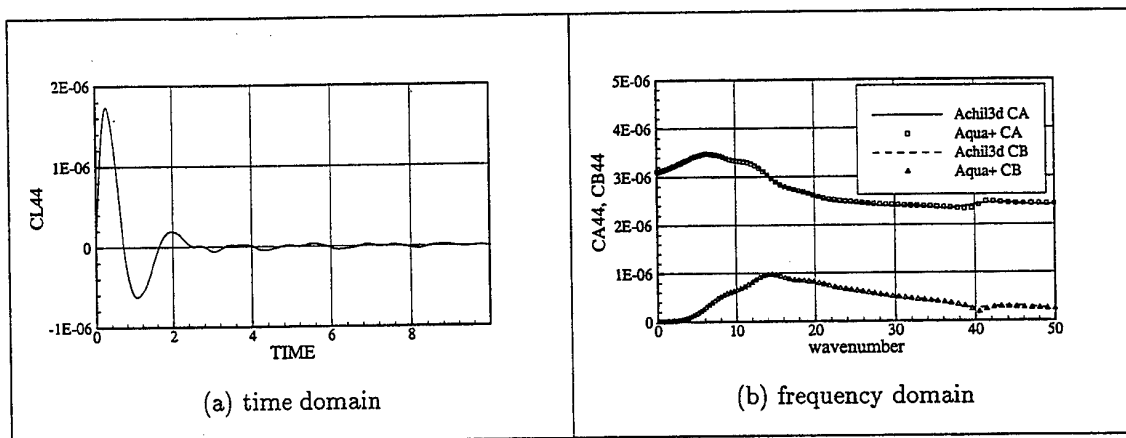


Figure 18: Series 60-06 (2x245 panels). Roll/Roll hydrodynamic coefficients

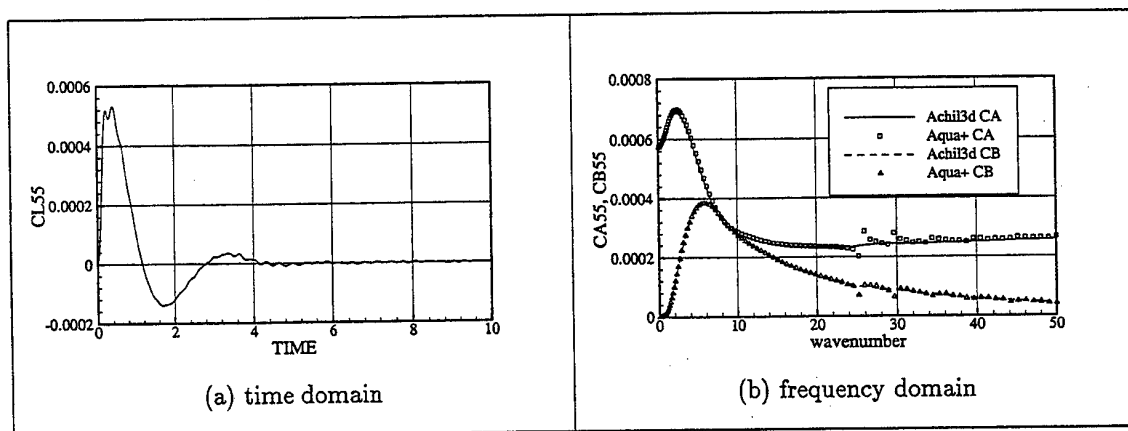


Figure 19: Series 60-06 (2x245 panels). Pitch/Pitch hydrodynamic coefficients

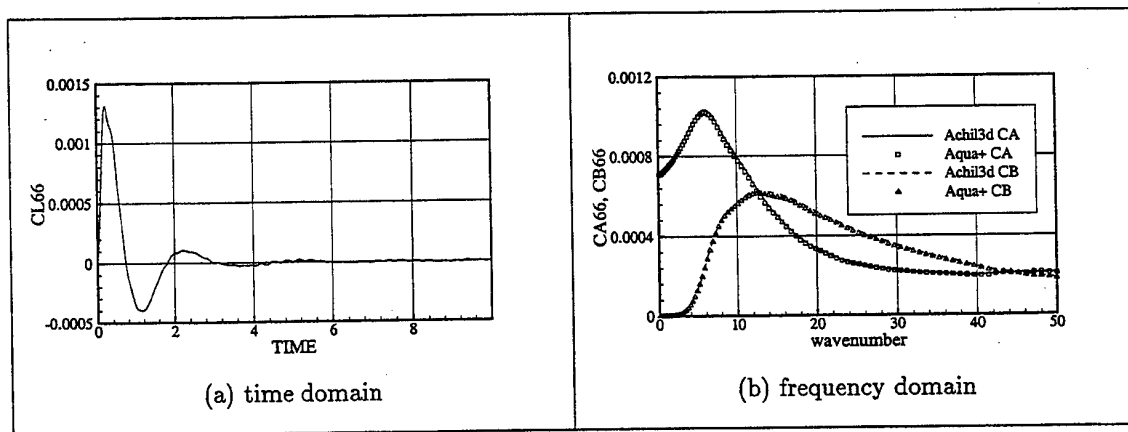


Figure 20: Series 60-06 (2x245 panels). Yaw/Yaw hydrodynamic coefficients

REFERENCES

1. H.B. Bingham (1994), Simulating ship motions in the time domain. PhD . M.I.T.
2. H.B. Bingham, F.T. Korsmeyer, J.N. Newman and G.E. Osborne (1993), The simulation of ship motions. In : Proc. 6th Intl Conf. Num. Ship Hydrod., Iowa City.
3. A.H. Clément (1995): Identification de la fonction de Green de l'hydrodynamique transitoire par des modèles continus . Proc. 5èmes Journées de l'Hydrodynamique, Rouen, pp.319/332.
4. A.H. Clément (1997) : A shortcut for computing time-domain free-surface potentials avoiding Green function evaluations. - Proc. 12th Int. Workshop on Water Waves and Floating Bodies, Marseille, pp.37-43.
5. A.H. Clément (1998a) : An ordinary differential equation for the Green function of time-domain free-surface hydrodynamics. Journal of Engineering Mathematics. 33 (2), pp201-217.
6. A.H. Clément (1998b) : Computation of impulse response functions using differential properties of the time-domain Green function. - Proc. 13th Int. Workshop on Water Waves and Floating Bodies, Alphen aan den Rijn, pp.21-24.
7. G. Delhommeau (1989), Amélioration des performances des codes de calcul de diffraction radiation au premier ordre. in Proc. 2èmes Journées de l'Hydrodynamique, Nantes, pp.69-88.
8. G. Delhommeau, P. Ferrant and M. Ferrant (1992), Calculation and measurements of forces on a high speed vehicle in forced pitch and heave. Applied Ocean Research, 14-2, pp.119-126.
9. P. Ferrant (1988a), A fast computational method for transient 3D wave-body interaction. Proc. Int. Conf. Comp. Model. Ocean Engng. Venice.
10. P. Ferrant (1988b), Radiation d'ondes de gravité par les déplacements de grande amplitude d'un corps immergé: comparaison des approches fréquentielles et instantanées. Thèse de Doctorat de l'Université de Nantes.
11. A. Hulme (1982), The wave forces acting on a floating hemisphere undergoing forced periodic oscillations. J. Fluid Mech., 121, pp. 443-463
12. A. Jami (1981), Etude théorique et numérique de phénomènes transitoires en hydrodynamique navale. Thèse de Doctorat ès Sciences. ENSTA, Paris.
13. B.W. King (1987) Time-domain analysis of wave exciting forces on ships and bodies. PhD Univ. Michigan.
14. F.T. Korsmeyer (1988), The first- and second order transient free surface wave radiation problem. PhD Diss. M.I.T.
15. S.J. Liapis (1986), Time-domain analysis of ship motions. PhD Diss. Univ. Michigan.
16. A.R. Magee and R.F. Beck (1989). Vectorized Computation of the Time-Domain Green Function. Proc. 4th Workshop Water Waves & Floating Bodies. Oystese.
17. A.R. Magee (1991). Large amplitude ship motions in the time domain. PhD Thesis. Univ. Michigan.
18. R.M.M. Mattheij and J. Molenaar (1996), Ordinary Differential Equations in Theory and Practise. John Wiley & Sons Eds.
19. J.N. Newman (1992). The approximation of free-surface Green functions. in: Wave Asymptotics. P.A. Martin & G.R. Wickham ed, pp. 107-135. Cambridge University Press.
20. J.N. Newman (1985). The evaluation of free-surface Green functions. Proc. 4th Intl Conf. Numer. Ship Hydrod. Washington.
21. W.H. Press, S.A. Teukolsky, W.T. Vetterling and B.P. Flannery (1992), Numerical Recipes. Cambridge University Press Eds.

APPENDIX. COEFFICIENTS OF THE 5TH ORDER RUNGE-KUTTA SCHEME

The differential equation being symbolically written as

$$\dot{y}(t) = f(t, y)$$

and the time step being denoted by h . Let us define the i^{th} stage of the method by:

$$k_i = hf \left(t_n + a_i h, y_n + \sum_{j=1}^{i-1} b_{ij} k_j \right)$$

and the final estimate as

$$y_{n+1} = y_n + \sum_i^I c_i k_i$$

The Cash-Karp coefficient set of the fifth order Runge-Kutta scheme we have selected is given in

the tables below [21]. Applying the stored coefficients c_i^* provides the embedded fourth-order estimation necessary to optimize the time-step by the Fehlberg method.

i	a_i	b_{ij}				
1						
2	$\frac{1}{5}$	$\frac{1}{5}$				
3	$\frac{3}{10}$	$\frac{3}{40}$	$\frac{9}{40}$			
4	$\frac{3}{5}$	$\frac{3}{10}$	$-\frac{9}{10}$	$\frac{6}{5}$		
5	1	$-\frac{11}{54}$	$\frac{5}{2}$	$-\frac{70}{27}$	$\frac{35}{27}$	
6	$\frac{7}{8}$	$\frac{1631}{55296}$	$\frac{175}{512}$	$\frac{575}{13824}$	$\frac{44275}{110592}$	$\frac{253}{4096}$
$j =$		1	2	3	4	5

i	c_i	c_i^*
1	$\frac{37}{378}$	$\frac{2825}{27648}$
2	0	0
3	$\frac{250}{621}$	$\frac{18575}{48384}$
4	$\frac{125}{594}$	$\frac{13525}{55296}$
5	0	$\frac{277}{14336}$
6	$\frac{512}{1771}$	$\frac{1}{4}$

SHIP DESIGN.

Chairman : H.Raven

SHAPE OPTIMIZATION OF PRACTICAL SHIP HULL FORMS USING NAVIER-STOKES ANALYSIS

Takanori Hino (+)

(+) Ship Research Institute

6-38-1, Shinkawa, Mitaka, Tokyo 181-0004, Japan.

Fax: +81-422-41-3053; E-Mail: hino@srinot.go.jp.

ABSTRACT

As a practical design tool using a CFD (Computational Fluid Dynamics) technique, a hydrodynamic shape optimization system for ship hull forms has been developed. A nonlinear programming method, SQP (Sequential Quadratic Programming) is used as an optimizer which automatically determines the values of design variables in such a way that an objective function is minimized with subject to the design constraint. In the present system, an objective function is obtained from a flow field computed by a Navier-Stokes solver. Design variables are chosen to efficiently manipulate ship hull shapes during an optimization process. The gradients of the objective function with respect to design variables (sensitivity coefficients) required in the SQP procedure are computed by the adjoint variables method which solves the linear equation system derived from the Navier-Stokes equations. Finally, an optimization of an aft body of a practical tanker hull for the minimum viscous resistance is carried out to demonstrate the applicability of the present method. Also a trial computation is made for the minimization of total resistance including wave-making resistance of the Series 60 ($C_B = 0.6$) hull using a Navier-Stokes solver for free surface flows.

NOMENCLATURE

$B_i(x)$	basis function in x direction for shape modification
C_i	constraint for optimization
C_f	frictional resistance coefficient
C_p	pressure resistance coefficient
C_t	total resistance coefficient
C_v	viscous resistance coefficient
D	design variables for optimization
d	search direction of optimization procedure
E, F, G	inviscid flux in (x, y, z) direction
E^v, F^v, G^v	viscous flux in (x, y, z) direction
F	objective function of optimization
Fn	Froude number
H	transformed inviscid flux
H^v	transformed viscous flux
h	wave height

p	pressure
$p(z), p_0(z)$	modified and original bow profiles
Q	flow variables
R	residual of NS equations
R^*	1st order upwind approximation of R
Rn	Reynolds number
S_x, S_y, S_z	area vectors of cell interfaces
t	time or step size in optimization
u	Lagrange multiplier of optimization procedure
u, v, w	(x, y, z) component of velocity
V	cell volume
$w(x, z)$	weight function for hull shape modification
$w_p(z)$	weight function for bow profile modification
β	artificial compressibility parameter
λ	adjoint variables
ν_t	turbulent eddy viscosity

INTRODUCTION

CFD (Computational Fluid Dynamics) techniques have expanded their field of applications in past decades. In ship hydrodynamics, Navier-Stokes solvers are now being used as a practical tool for ship hull design. In most cases CFD is used to obtain a flow field around a ship hull of a given shape. In other words, a CFD analysis is used as a replacement of tank testing. This 'numerical tank' approach has advantages over the real tank testing in terms of cost reduction and quantities of flow field informations when appropriate numerical schemes and carefully examined grids are used.

Recently, efficient CFD algorithms and advanced computer hardware enable more extensive use of CFD for a ship hull design. That is a shape optimization using CFD in which an optimal body shape with the lowest resistance or other fluid dynamic extremities is automatically searched using a numerical optimization method.

In ship hydrodynamics, shape optimization problems have a long history. Linear wave-making theories using velocity potential can be easily combined to linear optimization methods such as a variational method and a number of wave-making minimization theories have been proposed. Later, these approaches are extended to numerical procedures using panel methods. Boundary layer theories are also applied to shape optimization with respect to viscous flow properties. More recently, the shape optimization methods using CFD techniques are applied to ship design problems[1, 2, 3, 4].

These shape optimization methods based on CFD are expected to be a powerful design tool, because CFD methods can simulate turbulent flows around a ship hull reasonably well. On the other hand, these optimization problems are highly nonlinear and the large amount of CPU time is required to solve them, because a usual CFD analysis which is already time-consuming should be repeated many times during an optimization procedure. Therefore, efficient algorithms which reduce the CPU time requirement must be developed for practical applications of the methods.

In this paper, a hydrodynamic shape optimization system for practical ship hull forms is presented. The system is composed of a nonlinear optimizer, a Navier-Stokes solver and a sensitivity analysis tool together with a shape modification method and a grid generator. The system was first developed for a two-dimensional body[5] and then extended to cope with a simple three-dimensional shape[4]. The effect of shape modification methods was also investigated for a two-dimensional body[6].

The features enhanced here are the extension of the Navier-Stokes solver to include a free surface effect and the development of a shape modification method suitable to practical ship hull forms. In the sections below, numerical algorithms are described followed by the presentation of the results of applications to shape optimization of a practical tanker hull and the Series 60 ($C_B = 0.6$) hull.

OPTIMIZATION METHOD

Optimization Procedure

A fluid dynamic shape optimization problem can be described in a mathematical form as follows:

$$\begin{aligned} &\text{Minimize} && F[D, Q(D)] \\ &\text{Subject to} && C_i[D, Q(D)] = 0, \quad i = 1, M_E \\ & && C_i[D, Q(D)] \geq 0, \quad i = M_E + 1, M \end{aligned}$$

F is an objective function to be minimized and it is dependent on D and Q where D is the vector of design variables which determines a hull shape and Q is the vector of flow variables. The flow field Q is obviously the function of a shape and therefore expressed as $Q(D)$. $C_i = 0$ and $C_i \geq 0$ are equality and inequality constraint, respectively. Note that C_i is either the function of D only (geometric constraint) or the function of D and Q (fluid dynamic constraint). Here, a relation between a shape D and a flow field Q is given by a Navier-Stokes analysis, which means that the objective function F is a nonlinear function of the design variables. Therefore, a nonlinear programming procedure should be used as an optimizer. The SQP (Sequential Quadratic Programming) method adopted here is one of such methods which can solve general nonlinear optimization problems with constraint. The SQP method requires the gradients of the objective function and the constraint with respect to the design variables which are called sensitivity coefficients.

The nonlinear optimization procedure can be described as follows:

1. Set the initial values of design variables D which correspond to the initial body shape.
2. Define a body shape geometrically from the numerical design variables. A shape modification tool is required for this purpose.
3. Generate a computational grid around a given body or modify an existing grid conforming a deformed body shape. This is an essential preprocess for a CFD analysis.
4. A Navier-Stokes solver is used to compute a flow field Q using a grid obtained in 3.

5. An objective function F and constraint are computed using the flow field Q and the geometry D .
6. Sensitivity analysis is carried out to obtain gradients of an objective function and constraint for the current design.
7. The SQP procedure is used to search the new values of design variables D which decrease the objective function F from the current value. This is done by setting the search direction followed by the line search along that direction. Several CFD computations together with grid modifications are required in this search process.
8. If the current design satisfies certain criteria, then the process terminates and the current design is considered to be an optimal body shape. Otherwise return to 2.

The optimization procedure shown above consists of several elements. These are a shape modification, a grid generation, a Navier-Stokes solver, a sensitivity analysis and a nonlinear optimizer. The brief description for each element is given below.

Shape Modification and Grid Generation

The role of a shape modification is to provide a link between design variables and a body shape which should be defined geometrically. In an optimization system, design variables and a shape modification method should be selected with a compromise between flexibility and simplicity. Since an optimization procedure searches an optimal solution in the space defined by the design variables, the final shape is optimal among the shapes which can be defined by the combination of design variable values. Thus design variables and a shape modification method should be flexible enough to cover a wide variety of body shapes. On the other hand, the number of design variables should be as small as possible and a shape modification should be as simple as possible from the efficiency point of view.

A shape modification method used here is based on a weight function. First, the initial ship hull form is assumed to be

$$y = f_0(x, z) \quad (1)$$

In case of practical ship hull forms, f_0 does not necessarily take an explicit functional form. Instead, it is given numerically as the coordinates of a body surface grid.

A modified shape is then defined as

$$y = f_0(x, z)w(x, z) \quad (2)$$

where $w(x, z)$ is a weight function and the design variables are the parameters defining $w(x, z)$.

Thus a grid point on an original body surface whose locations is given by (x_o, y_o, z_o) moves to $(x_o, w(x_o, z_o)y_o, z_o)$ on a modified body. A new surface grid is obtained with the re-distribution of grid points along the grid lines in the girth direction.

When a bow profile is to be modified, before applying the above procedure, the new profile $x = p(z)$ is defined as

$$p(z) = x_{\text{mid}} + w_p(z)(p_0(z) - x_{\text{mid}}) \quad (3)$$

where $x = p_0(z)$ is the original profile and $w_p(z)$ is a weight function for a profile modification. Also x_{mid} is the x coordinate at midship. Using the new profile the grid points on the original hull are re-distributed along the longitudinal grid lines. The definition of weight functions are case-dependent and will be given in the following section.

It is important that the system has a capability to generate or modify a computational grid automatically when a body shape is re-defined during an optimization process. In the present system, an initial grid around an initial body shape is generated a priori and given to the system as a part of the initial conditions. In the optimization process, whenever the design variable values change, the body surface grid corresponding to the modified body shape is generated as described above.

The volume grid covering a computational domain is generated based on the flexible grid method[7] with slight modification. In the original method, the grid point coordinates along the grid line in the direction from the body surface to the outer boundary are modified as follows:

$$X_k^{\text{new}} = X_k^{\text{old}} + w_k(X_1^{\text{new}} - X_1^{\text{old}}) \quad (4)$$

where the subscript k is the grid indices and X_1 is a grid point on a body surface. w_k is the weight whose values are 1 on the body surface and 0 on the outer boundary and linearly distributed in-between using the arc length of the grid line. This method is modified as follows to enhance robustness. X_1 above is replaced by X_2 which is a grid point next to a body. X_2^{new} is determined using the given grid distance and the outward normal vectors of the new body surface defined by X_1^{new} . At the same time, the definition of w_k is modified in such a way that $w_k = 1$ at $k = 2$ and $w_k = 0$ on the outer boundary.

Navier-Stokes Solver

Efficiency of an optimization procedure is strongly dependent of the speed of a flow solver, since

the Navier-Stokes analysis is most time-consuming among the elements of an optimization system. Furthermore, the Navier-Stokes computations are carried out several times in each design cycle for a line search process and nonlinear optimization requires tens of design cycles. Thus the number of flow analysis as a whole becomes quite large.

In the present study, a newly developed Navier-Stokes solver[8] is used. This is a finite-volume method for simulating incompressible turbulent flows with or without a free surface. Due to the implicit time integration with the Newton relaxation scheme and the convergence acceleration by a multigrid method and local time stepping, the solver is highly efficient in obtaining steady state solutions.

The governing equations are the 3-D incompressible Navier-Stokes equations. With the introduction of artificial compressibility, they can be written in the non-dimensional form as

$$\frac{\partial Q}{\partial t} + \frac{\partial(E - E^v)}{\partial x} + \frac{\partial(F - F^v)}{\partial y} + \frac{\partial(G - G^v)}{\partial z} = 0 \quad (5)$$

where $Q = (p, u, v, w)^T$ and

$$(E, F, G) = \begin{bmatrix} \beta u & \beta v & \beta w \\ u^2 + p & uv & uw \\ uv & v^2 + p & vw \\ uw & vw & w^2 + p \end{bmatrix}$$

$$(E^v, F^v, G^v) = \begin{bmatrix} 0 & 0 & 0 \\ \tau_{xx} & \tau_{xy} & \tau_{xz} \\ \tau_{xy} & \tau_{yy} & \tau_{yz} \\ \tau_{xz} & \tau_{yz} & \tau_{zz} \end{bmatrix}$$

with

$$\tau_{ij} = \left(\frac{1}{Rn} + \nu_t \right) \left(\frac{\partial u_i}{\partial x_j} + \frac{\partial u_j}{\partial x_i} \right)$$

In the above, (x, y, z) or (x_1, x_2, x_3) are the Cartesian coordinates and (u, v, w) or (u_1, u_2, u_3) are the velocity components in (x, y, z) directions. In case of free surface flow computations, pressure p is modified from the original pressure p^* as

$$p = p^* + z/Fn^2$$

where Fn is the Froude number. This modification removes the hydrostatic component from the original pressure and eliminates the gravitational acceleration term from the z -momentum equation. Rn is the Reynolds number and ν_t is non-dimensional kinematic eddy viscosity determined from a turbulence model. β is the parameter of artificial compressibility. Turbulence models implemented are the algebraic model by Baldwin and Lomax[9] and its variant[10].

A finite-volume method is adopted for spatial discretization. First, a computational domain is divided into hexahedral cells. Flow variables (pressure, velocity and eddy viscosity) are stored in the center of each cell. Integration of the governing equation (5) over a cell yields

$$\int_V \frac{\partial Q}{\partial t} dV + \oint_{\partial V} ((E - E^v) dS_x + (F - F^v) dS_y + (G - G^v) dS_z) = 0 \quad (6)$$

where the divergence theorem is applied to the momentum and the mass flux integration. V is the volume of a cell and ∂V is its boundary. (S_x, S_y, S_z) are the area vector components of cell boundaries.

Control volumes should be time dependent when a grid is fitted to the moving free surface boundary. However, since the present computations require only a steady state solution, all terms associated with cell volume change and grid movement velocity are neglected, although the flow solver has capability to cope with moving control volumes.

In the discretized form, Eq.(6) is written as

$$\frac{\partial Q_{ijk}}{\partial t} + R(Q) = 0 \quad (7)$$

where

$$R(Q) = \frac{1}{V_{ijk}} \sum_{\text{Faces}} (H - H^v) = 0 \quad (8)$$

ijk is the cell numbering and H and H^v are the inviscid and the viscous fluxes on cell interfaces. The sum is taken for six interfaces of a cell.

The inviscid flux H is expressed as

$$H \equiv S_x E + S_y F + S_z G = \begin{bmatrix} \beta U \\ uU + pS_x \\ vU + pS_y \\ wU + pS_z \end{bmatrix} \quad (9)$$

where

$$U = S_x u + S_y v + S_z w \quad (10)$$

is an unscaled contravariant velocity. The flux H is numerically evaluated by the third-order upwind scheme based on the flux difference splitting.

The viscous flux H^v can be written similarly as

$$H^v \equiv S_x E^v + S_y F^v + S_z G^v \quad (11)$$

Application of the divergence theorem to a control volume surrounding a cell interface gives velocity

gradients at a cell interface which are required in the evaluation of H^v .

The backward Euler scheme is used for the time integration[8] in which Eq.(7) is written as

$$\frac{Q_{ijk}^{(n+1)} - Q_{ijk}^{(n)}}{\Delta t} + R^{(n+1)} = 0 \quad (12)$$

where the superscripts denote the time step. Δt is the time increment which can be either globally constant or determined cell by cell with the local CFL condition (local time stepping).

The approximated Newton relaxation scheme is applied to Eq.(12) to get $Q^{(n+1)}$. This yields

$$\left(\frac{I}{\Delta t} + \left\{ \frac{\partial R^*}{\partial Q} \right\}^{(n+1),m} \right) \Delta Q_{ijk}^{(n+1),m} = - \left(\frac{Q_{ijk}^{(n+1),m} - Q_{ijk}^{(n)}}{\Delta t} I_a + R^{(n+1),m} \right) \quad (13)$$

where

$$\Delta Q^{(n+1),m} = Q^{(n+1),m+1} - Q^{(n+1),m}$$

R^* is an approximation to R where the inviscid flux is evaluated using the first-order upwind scheme and I_a is a 4×4 identity matrix whose first diagonal element is set zero in order to satisfy the continuity condition at each time step. The superscript m denotes the iteration count and $Q^{(n+1),1} = Q^{(n)}$. The equation above is a linear equation for ΔQ and it is solved by the Symmetric Gauss-Seidel (SGS) iteration together with a multigrid method.

A multigrid method is known as the extremely efficient way to obtain fast convergence. The concept of the multigrid time stepping is to compute corrections to the solution on a fine grid by the time-stepping on a coarser grid. The successively coarser grids can be generated by deleting the alternate points along grid lines of the finer grids.

When a free surface flow is computed, free surface boundary conditions should be imposed. The free surface conditions consist of dynamic and kinematic conditions. By neglecting surface tension and tangential stress of air, the dynamic condition is simplified as follows. From the condition of zero tangential stress, the viscous flux H^v on a free surface vanishes and the velocity boundary condition on a free surface is given as the zero gradient extrapolation. The condition for normal stress can be given as the Dirichlet condition for pressure on a free surface:

$$p = p_{air} + h/Fn^2 \quad (14)$$

where $p_{air}(=0)$ is the atmospheric pressure and h is a wave height.

The kinematic condition is used to update a free surface configuration. This is formulated based on the mass conservation consideration[11] as follows:

$$\frac{\Delta \zeta}{\Delta t} = \frac{S^{FS} \cdot u^{FS}}{S^{FS} \cdot r} \quad (15)$$

where S^{FS} is an area vector of a cell interface on a free surface and u^{FS} is a velocity vector on a free surface. $\Delta \zeta$ is a displacement of a free surface along a grid line whose direction is given by a unit vector r .

In order to avoid reflection of free surface waves in the outer boundaries of a computational domain, the wave damping method is applied to the free surface kinematic condition[11]. Also, to avoid singular behavior at the contact line between a free surface and a solid body, the wave height in the region close to a body is extrapolated from the outside.

The control volume for Eq.(15) is constructed around a grid point on a free surface. Spatial discretization is based on a finite-volume method with a third-order upwind manner. Time integration of Eq.(15) is carried out in the similar way as the flow equations and also the same multigrid strategy is used for the convergence acceleration.

Since the free surface fitted grid is used, the grid should be re-generated after the free surface shape is updated at each time step. This is done by using a reference grid. A reference grid covers the domain below and above the still water level. When free surface locations are obtained as a part of solution, the computational grid at the next time step is generated by the cubic spline interpolation in the girth direction along each grid line of a reference grid.

Sensitivity Analysis

Sensitivity analysis provides the gradients of an objective function and constraint with respect to the design variables. The gradients, ∇F and ∇C_i , are called sensitivity coefficients.

The simplest way to compute the sensitivity coefficients is to use the finite-difference of solutions with the slight perturbation of design variables. In this case, a grid generation and a flow computation should be repeated as many times as the number of design variables. This procedure is not efficient, because CFD analysis is most time-consuming. The more sophisticated methods such as the implicit gradient method or the adjoint variable method [12, 13] offer better efficiency than the finite-difference method. The adjoint variable method described below is adopted in the present study.

The sensitivity coefficients can be analytically expressed as follows (though only an objective function F is used in the following discussion, the fluid dynamic constraint can be treated similarly):

$$\nabla F \equiv \frac{\partial F(\mathbf{D}, \mathbf{Q})}{\partial \mathbf{D}} = \left(\frac{\partial F}{\partial \mathbf{D}} \right)_Q + \left(\frac{\partial F}{\partial \mathbf{Q}} \right)_D^T \left\{ \frac{\partial \mathbf{Q}}{\partial \mathbf{D}} \right\} \quad (16)$$

where the subscripts means that the corresponding variables are kept fixed in the partial differencing process. $(\partial F / \partial \mathbf{D})_Q$ and $(\partial F / \partial \mathbf{Q})_D$ can be computed easily by a finite-difference method. On the other hand, $\{\partial \mathbf{Q} / \partial \mathbf{D}\}$, the change of flow field due to the change of a body shape, is determined implicitly by the Navier-Stokes equations and is difficult to evaluate. In that sense, the Navier-Stokes equations can be viewed as the additional implicit constraint of the optimization, because at every design stage the flow field around the current body shape should be the solution of the Navier-Stokes equations.

The discrete steady state Navier-Stokes equations can be written as

$$\mathbf{R}(\mathbf{Q}, \mathbf{D}) = 0 \quad (17)$$

where \mathbf{R} is the function of \mathbf{D} since \mathbf{D} determines a body shape and hence a computational grid.

The fact that the Navier-Stokes equations should be satisfied at every design stage yields that the partial differencing of Eq.(17) with respect to \mathbf{D} is always zero, i.e.:

$$\left\{ \frac{\partial \mathbf{R}}{\partial \mathbf{D}} \right\} = \left\{ \frac{\partial \mathbf{R}}{\partial \mathbf{Q}} \right\}_D \left\{ \frac{\partial \mathbf{Q}}{\partial \mathbf{D}} \right\} + \left\{ \frac{\partial \mathbf{R}}{\partial \mathbf{D}} \right\}_Q = 0 \quad (18)$$

that is,

$$\left\{ \frac{\partial \mathbf{Q}}{\partial \mathbf{D}} \right\} = - \left\{ \frac{\partial \mathbf{R}}{\partial \mathbf{Q}} \right\}_D^{-1} \left\{ \frac{\partial \mathbf{R}}{\partial \mathbf{D}} \right\}_Q \quad (19)$$

The following equation is obtained by substituting Eq.(19) into (16),

$$\nabla F = \left(\frac{\partial F}{\partial \mathbf{D}} \right)_Q - \left(\frac{\partial F}{\partial \mathbf{Q}} \right)_D^T \left\{ \frac{\partial \mathbf{R}}{\partial \mathbf{Q}} \right\}_D^{-1} \left\{ \frac{\partial \mathbf{R}}{\partial \mathbf{D}} \right\}_Q \quad (20)$$

Let the adjoint variable λ satisfy the following relation

$$\lambda^T = \left(\frac{\partial F}{\partial \mathbf{Q}} \right)_D^T \left\{ \frac{\partial \mathbf{R}}{\partial \mathbf{Q}} \right\}_D^{-1} \quad (21)$$

then the sensitivity coefficients are evaluated as

$$\nabla F = \left(\frac{\partial F}{\partial \mathbf{D}} \right)_Q - \lambda^T \left\{ \frac{\partial \mathbf{R}}{\partial \mathbf{D}} \right\}_Q \quad (22)$$

To obtain λ the following equation should be solved:

$$\left\{ \frac{\partial \mathbf{R}}{\partial \mathbf{Q}} \right\}_D^T \lambda = \left(\frac{\partial F}{\partial \mathbf{Q}} \right)_D \quad (23)$$

where $\{\partial \mathbf{R} / \partial \mathbf{Q}\}_D^T$ and $(\partial F / \partial \mathbf{Q})_D$ are evaluated using a finite-difference method. The advantage of the adjoint variable method is that Eq.(23) is independent of the design variables \mathbf{D} . Thus Eq.(23) must be solved only once, regardless of the number of the design variables. The gradient for all the design variables can be computed from Eq.(22).

The number of unknowns λ is identical to that of the flow field \mathbf{Q} and the $\{\partial \mathbf{R} / \partial \mathbf{Q}\}_D^T$ is the transpose of the Jacobian matrix appears in the implicit solution method for the Navier-Stokes equations (see Eq.(13)). Thus the size of adjoint equation system is the same as the Navier-Stokes equation system except that the adjoint equation is a linear equation system. Since the direct inversion of Eq.(23) is too expensive for both the storage size and the CPU time requirement, an iterative method described below is used.

First, Eq.(23) is written in incremental form as

$$\begin{aligned} \left\{ \frac{\partial \mathbf{R}}{\partial \mathbf{Q}} \right\}_D^T \Delta \lambda^{(m)} &= - \left\{ \frac{\partial \mathbf{R}}{\partial \mathbf{Q}} \right\}_D^T \lambda^{(m)} + \left(\frac{\partial F}{\partial \mathbf{Q}} \right)_D \\ \lambda^{(m+1)} &= \lambda^{(m)} + \Delta \lambda^{(m)} \end{aligned} \quad (24) \quad (25)$$

where the superscript m denotes the iteration count. To enhance diagonal dominance of the left-hand-side, the Jacobian $\{\partial \mathbf{R} / \partial \mathbf{Q}\}$ is evaluated using the first order upwind scheme for the inviscid terms (expressed as $\{\partial \mathbf{R}^* / \partial \mathbf{Q}\}$) and the pseudo-time derivative is added:

$$\begin{aligned} \left(\frac{\mathbf{I}}{\Delta t} + \left\{ \frac{\partial \mathbf{R}^*}{\partial \mathbf{Q}} \right\}_D^T \right) \Delta \lambda^{(m)} &= \\ - \left\{ \frac{\partial \mathbf{R}}{\partial \mathbf{Q}} \right\}_D^T \lambda^{(m)} + \left(\frac{\partial F}{\partial \mathbf{Q}} \right)_D \end{aligned} \quad (26)$$

Eq.(26) is solved by the Symmetric Gauss-Seidel method together with a multigrid acceleration.

Note that when a free surface effect is taken into account, an objective function is dependent on a wave height in addition to \mathbf{Q} and \mathbf{D} . Since a wave height is a part of flow variables and at the same time is a part of a grid, this dependence makes the adjoint variable formulation above more complicated. However, this effect is not included in the present implementation.

Nonlinear Optimizer

The SQP (Sequential Quadratic Programming) method is a general method for solving nonlinear optimization problems with constraint. Suppose that an optimization problem is written as

$$\begin{aligned} &\text{Minimize} && F[D] \\ &\text{Subject to} && C_i[D] = 0, \quad i = 1, M_E \\ & && C_i[D] \geq 0, \quad i = M_E + 1, M \end{aligned}$$

where F is an objective function and $C_i = 0$ and $C_i \geq 0$ are constraint. When the current design point $D^{(k)}$ is given, the next design point $D^{(k+1)}$ is determined as follows. First, the following quadratic programming problem is solved to obtain the modification d :

$$\begin{aligned} &\text{Minimize} && \nabla F[D^{(k)}]^T d + \frac{1}{2} d^T B^{(k)} d \\ &\text{Subject to} && C_i[D^{(k)}] + \nabla C_i[D^{(k)}]^T d = 0, \\ & && \quad i = 1, M_E \\ & && C_i[D^{(k)}] + \nabla C_i[D^{(k)}]^T d \geq 0, \\ & && \quad i = M_E + 1, M \end{aligned}$$

In the above, an objective function F is approximated as the quadratic function of $D^{(k)}$ and the constraint are approximated as the linear functions of $D^{(k)}$. B is approximation to the Hessian matrix of the Lagrangian function $L[D, u]$:

$$B \approx \nabla^2 L[D, u] = \nabla^2 \left(F[D] - \sum_{i=1}^M u_i C_i[D] \right)$$

where $u = (u_1, u_2, \dots)^T$ are the Lagrange multipliers.

The next design point $D^{(k+1)}$ is obtained by the line search along the vector d . Step size t is determined in such a way that the penalty function with r being a penalty parameter

$$F[D] + r \left(\sum_{i=1}^{M_E} |C_i[D]| + \sum_{i=M_E+1}^M |\min(0, C_i[D])| \right)$$

becomes smaller than a certain value. Finally, the next design point is computed by

$$D^{(k+1)} = D^{(k)} + t^{(k)} d^{(k)}$$

and the iteration continues until the convergence criteria are satisfied.

APPLICATIONS

Optimization of a Tanker Hull

The first application is for optimization of a tanker hull form with respect to the minimum viscous resistance. A free surface effect is neglected in this case and a water plane is treated as a symmetric plane.

Table 1: Principal particulars.

Length between perpendiculars	320m
Breadth	58m
Draft	19.3m
C_B	0.802

The initial ship hull is a practical VLCC with bow and stern bulbs. The principal particulars of a ship is shown in Table 1.

Shape modification methods

Only the aft part of a hull is optimized and the fore part is kept fixed. Two kinds of weight functions are used for a shape modification. First one (denoted as CASE-A hereafter) is expressed as follows.

Four basis functions in x -direction B_i ($i = 1, 4$) are defined as

$$B_i(x) = \begin{cases} 1 & \text{if } x < a_i \\ 1 + c_i \sin\left(\frac{\pi}{2}\xi\right) & \text{if } x \geq a_i \end{cases} \quad (27)$$

where a_i is the location at which modification starts. ξ is defined as

$$\xi = \min \left(\left(\frac{\tilde{x}}{b_i} \right)^3, \left(\frac{1 - \tilde{x}}{1 - b_i} \right)^3 \right)$$

and \tilde{x} is a normalized distance defined as

$$\tilde{x} = \frac{x - a_i}{x_{\text{MAX}} - a_i}$$

x_{MAX} is the x coordinate of the aft-end of a hull. c_i is a weighting factor corresponding to a peak value and b_i is a parameter to specify a location of a peak. $B_i(x)$ is designed in such a way that

$$B_i(a_i) = 1, \quad \frac{\partial B_i(a_i)}{\partial x} = \frac{\partial^2 B_i(a_i)}{\partial x^2} = 0$$

and this guarantees the smooth transition from the unmodified zone. Three parameters a_i, b_i, c_i are used for each function $B_i(x)$ as shown in Fig.1.

For a given x , the four values, $B_1(x)$ through $B_4(x)$, are computed. To obtain the weight function $w(x, z)$ the cubic spline interpolation in z -direction is used (see Fig.2). Assume that $S(\tilde{z})$ is the spline function where \tilde{z} is a normalized z coordinate and $\tilde{z} = 0$ corresponds to a bottom and $\tilde{z} = 1$ to a water plane. The four control points are set as

$$S(\tilde{z}_i) = B_i(x), \quad \tilde{z} + \frac{i-1}{3}, \quad i = 1, 4$$

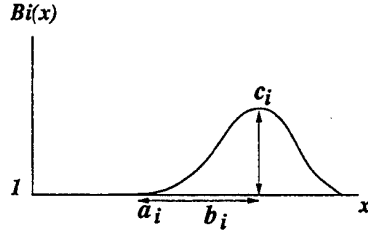


Figure 1: Parameters for basis function in x direction (CASE-A).

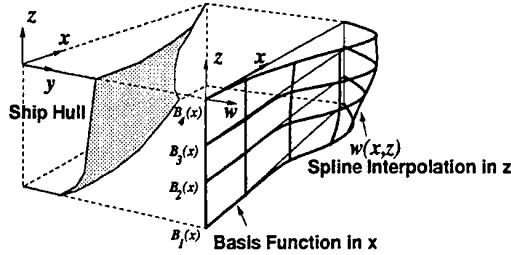


Figure 2: Weight function for hull form modification.

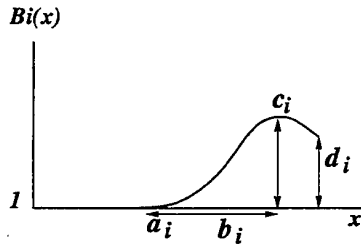


Figure 3: Parameters for basis function in x direction (CASE-B).

and the boundary conditions are

$$\frac{\partial^2 S(0)}{\partial \bar{z}^2} = \frac{\partial^2 S(1)}{\partial \bar{z}^2} = 0$$

From these, the cubic spline function can be determined. Total number of design variables in this case is 12 ($a_i, b_i, c_i, d_i, i = 1, 4$).

The other shape modification (CASE-B) also uses four basis function in x -direction defines as

$$B_i(x) = \begin{cases} 1 & \text{if } x < a_i \\ 1 + c_i \sin\left(\frac{\pi}{2} \left(\frac{\bar{x}}{b_i}\right)^3\right) & \text{if } x \geq a_i \text{ and } \bar{x} < b_i \\ 1 + \frac{d_i - c_i}{(1 - b_i)^2} (\bar{x} - b_i)^2 + c_i & \text{if } x \geq a_i \text{ and } \bar{x} \geq b_i \end{cases} \quad (28)$$

where \bar{x} is the same as before

$$\bar{x} = \frac{x - a_i}{x_{\text{MAX}} - a_i}$$

and this function also guaranteed the smooth transition from the unmodified zone as well as CASE-A. As shown in Fig.3, this basis function can have the non-zero value d_i at the aft-end, i.e., $x = x_{\text{MAX}}$. The cubic spline interpolation in z direction is also used. Again, $S(\bar{z})$ is assumed to be the spline function. The control points are

$$S(\bar{z}_i) = B_i(x), \bar{z} + \frac{i-1}{3}, \quad i = 1, 4$$

and one more point as below is added:

$$S(0.9) = B_4(x)$$

The boundary conditions are

$$\frac{\partial^2 S(0)}{\partial \bar{z}^2} = \frac{\partial^2 S(1)}{\partial \bar{z}^2} = 0$$

By this definition of the spline function, frame lines of a modified hull are enforced to be parallel to the original frame lines in the region close to a water plane. The number of design variables increases to 16 ($a_i, b_i, c_i, d_i, i = 1, 4$).

Constraint

An optimization problem is formulated to minimize the viscous resistance of a ship under the constraint below.

1. The displacement does not decrease from the initial value.
2. Minimum width is given for certain locations in the Square Station 7/8. This constraint comes from a practical requirement for the engine arrangement.
3. Appropriate limits are imposed for each design variable.

Computational conditions

The computational grid consists of $45 \times 25 \times 23$ points in longitudinal, girth and outward directions, respectively. This is the minimum sized grid for computing viscous resistance. Reynolds number is set to 1.9×10^6 which corresponds to a model scale. Flow is assumed to be turbulent and modified Baldwin-Lomax turbulence model[10] is used.

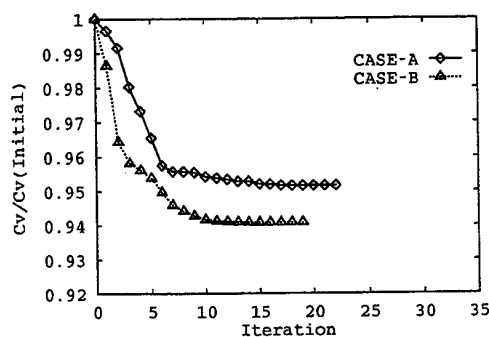


Figure 4: Optimization history.

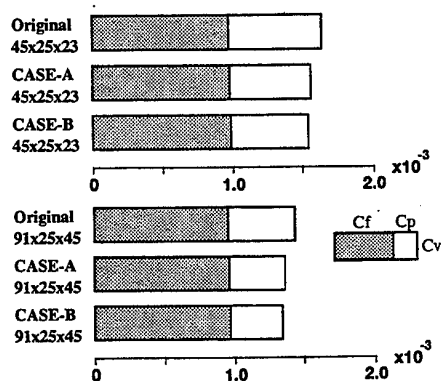
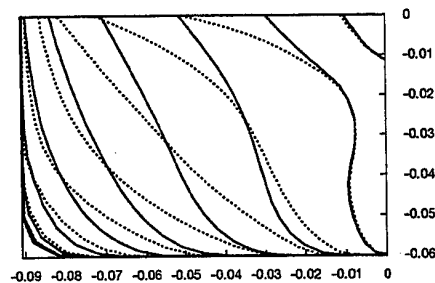


Figure 5: Resistance components.

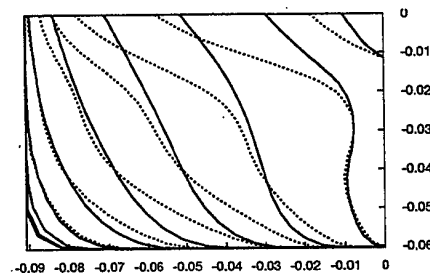
Results

History of the objective function value (viscous resistance) in the optimization process is shown in Fig.4. In CASE-A, the viscous resistance decreases about 5% of the original value with 22 iterations, whereas in CASE-B about 6% reduction is achieved with 19 iterations. Fig.5 shows the computed resistance coefficients nondimensionalized with $0.5\rho U^2 L^2$ where ρ is a density of water and U and L are speed and a length of a ship. Also shown are the results computed with the fine grids of $91 \times 25 \times 45$ after the optimal shape is obtained. In both CASES-A and B, the frictional resistance increases slightly (as much as 1% of the original frictional resistance), while pressure components decrease significantly and achieve the total resistance reduction. The results with the fine grids show the same tendency as those with the coarse grids.

Fig.6 shows the comparison of the aft part of body plans. In CASE-A, the frame lines of the modified hull (dotted lines) become V-shaped while the original hull (solid lines) has the U-shaped frame



Original (solid lines) and CASE-A (dotted lines)



Original (solid lines) and CASE-B (dotted lines)

Figure 6: Comparison of body plans (Top: Original (solid lines) and CASE-A (dotted lines), Bottom: Original (solid lines) and CASE-B (dotted lines)).

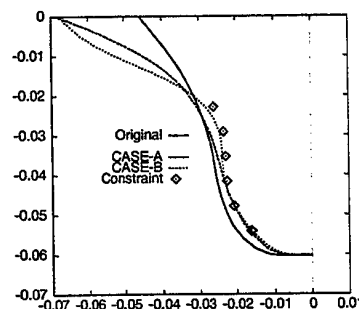


Figure 7: Framelines and constraint at S.S.7/8.

lines. The CASE-B has the same tendency but the deformation is larger than the CASE-A. Further differences of modification can be seen in the inclination of the frame lines at a water plane. The frame lines of CASE-B have tendency to go into a water plane parallel to the original frame lines. Also, the hull modification near the aft-end is very small in CASE-A, because a weight function $w(x, z)$ tends to be zero at the aft-end. It is seen that shape modification methods affects the final hull form and hence the amount of resistance reduction.

In Fig.7 the frame lines at the Square Station

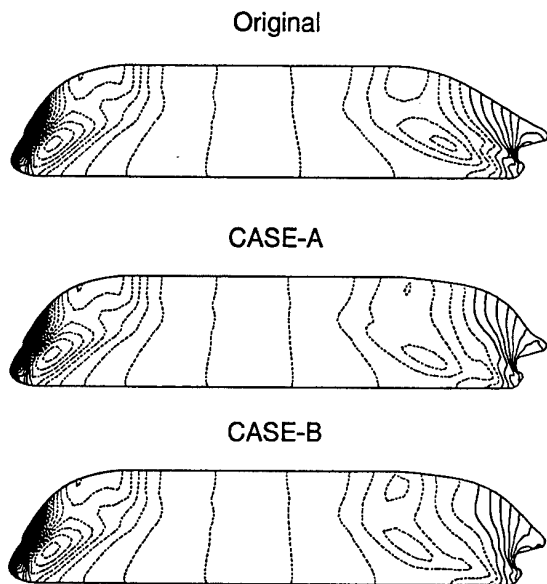


Figure 8: Hull surface pressure distributions. Contour interval: $\Delta C_p = 0.04$ (Top:Original, Middle:CASE-A, Bottom:CASE-B).

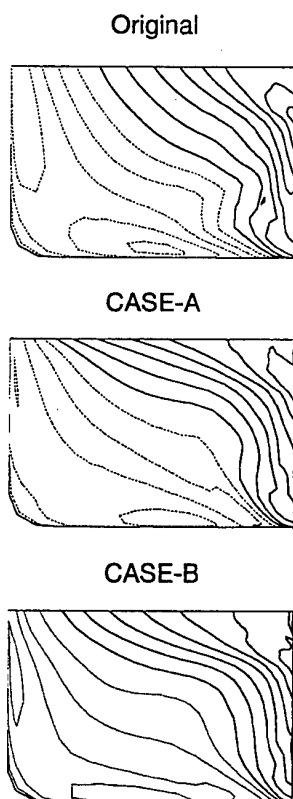


Figure 9: Surface pressure distributions of aft part. Contour interval : $\Delta C_p = 0.04$ (Top:Original, Middle:CASE-A, Bottom:CASE-B).

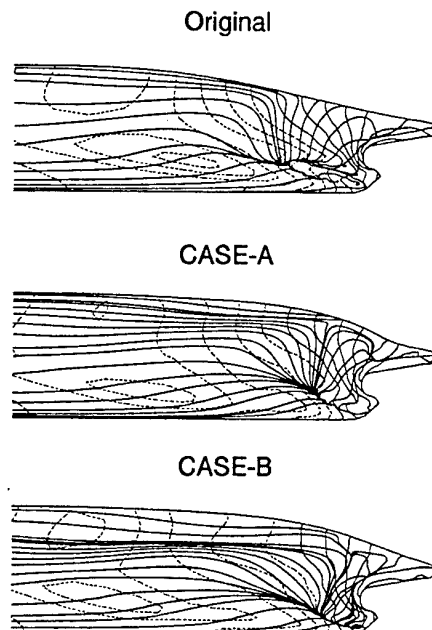


Figure 10: Limiting streamlines and surface pressure contours (Top:Original, Middle:CASE-A, Bottom:CASE-B).

7/8 are plotted together with the minimum width given as constraint. The frame lines of the modified hulls again change their shape from U-type to V-type. The constraint effectively limits the decrease of width in the lower region.

Hereafter the flow data computed with the fine grids ($91 \times 25 \times 45$) are examined. Hull surface pressure distributions are compared in Fig.8. Views from behind the ship are also shown in Fig.9. The fore part of each hull are identical and therefore the pressure patterns does not show any differences. The pressure patterns differ most significantly at the low pressure zone at the bilge of the stern region. In both CASES-A and B, the lowest pressure points move forward and the amplitude of pressure peaks becomes small compared with the original hull.

The limiting streamlines of the three hulls are compared in Fig.10. The separation areas of modified hulls slightly decrease from that of the original hull which is consistent with the fact that the frictional resistance of the modified hulls increases about 1% from the original hull.

The longitudinal distributions of frictional and pressure components of resistance are shown in Fig.11. Difference of frictional resistance cannot be seen in these plots. The pressure resistance components of modified hulls decrease around $x = 0.3$

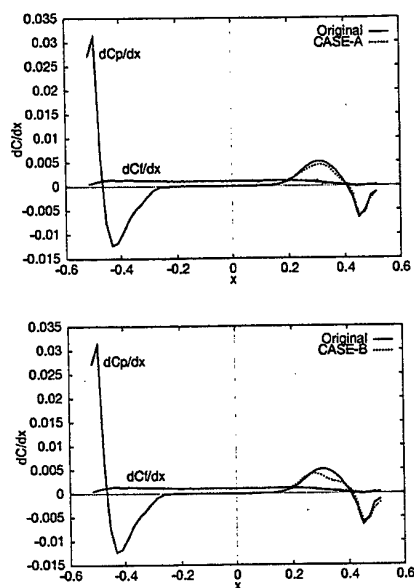


Figure 11: Longitudinal distributions of frictional and pressure resistance components. Top:(Original(solid lines) and CASE-A (dotted lines), Bottom:(Original(solid lines) and CASE-B (dotted lines).

which corresponds to the location of the low pressure peak in the stern bilge. The amount of decrease is larger in CASE-B than in CASE-A.

Velocity distributions at the AP ($x = 0.5$) plane are shown in Fig.12. The longitudinal vortex and the 'hook' shape of the original hull can be observed since the turbulence model used[10] is tuned up for the use with this kind of ships. The longitudinal vortices of modified hulls are weaker than those of the original hull due to the fact that the frame lines are modified from U-shaped to V-shaped. In the present optimization, wake pattern associated with propulsive efficiency is not taken into account as constraint. From the practical point of view, optimization of propulsive performance is more interesting. The Navier-Stokes analysis with propeller effects should be linked to an optimization system for this purpose.

Optimization of Series 60 ($C_B = 0.6$) Hull

For the second example, a well known hull shape, Series 60 ($C_B = 0.6$) is selected as an initial body shape. The objective function in this case is total resistance including both wave-making resistance and viscous resistance. Therefore, a free surface effect is taken into account in the Navier-Stokes analysis.

Shape modification method

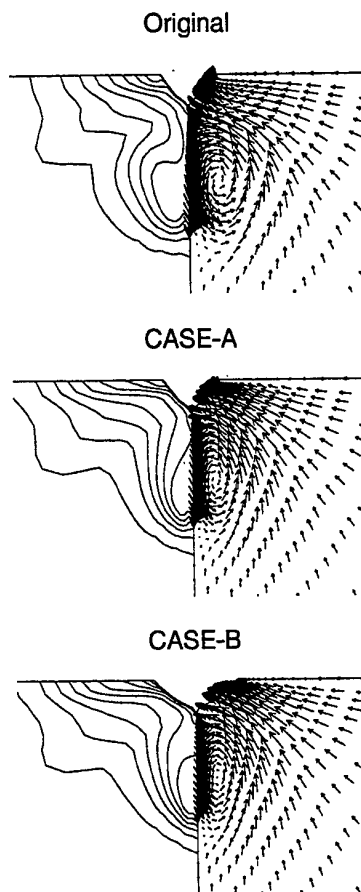


Figure 12: Wake contours and cross flow vectors at AP plane (Top:Original, Middle:CASE-A, Bottom:CASE-B).

Since wave-making resistance is taken into account and the original Series 60 hull does not have a bow bulb, it is desirable that a bow profile can be modified in an optimization process in addition to frame lines.

The weight function for a bow profile modification $w_p(z)$ in Eq.(3) is defined in a similar way as a basis function for CASE-B above:

$$w_p(z) = \begin{cases} 1 & \text{if } z > a_p \\ 1 + c_p \sin\left(\frac{\pi}{2} \left(\frac{\bar{z}}{b_p}\right)^3\right) & \text{if } z \leq a_p \text{ and } \bar{z} < b_p \\ 1 + \frac{d_p - c_p}{(1 - b_p)^2} (\bar{z} - b_p)^2 + c_p & \text{if } z \leq a_p \text{ and } \bar{z} \geq b_p \end{cases} \quad (29)$$

where \tilde{z} is the normalized z coordinate

$$\tilde{z} = \frac{z}{z_{\text{BOTTOM}}}$$

z_{BOTTOM} is the z coordinate at the bottom. $\tilde{z} = 0$ at the still water plane and 1 at the ship bottom.

For the modification of frame lines, the basis function in x direction is extended to handle shape modification both in fore and aft bodies. The new basis function is written as

$$B_i(x) = \begin{cases} 1 + \frac{h_i - g_i}{(1 - f_i)^2} (\tilde{x}_1 - f_i)^2 + c_i & \text{if } x \leq e_i \\ & \text{and } \tilde{x}_1 \geq f_i \\ 1 + g_i \sin\left(\frac{\pi}{2} \left(\frac{\tilde{x}_1}{f_i}\right)^3\right) & \text{if } x \leq e_i \\ & \text{and } \tilde{x}_1 < f_i \\ 1 & \text{if } e_i < x < a_i \\ 1 + c_i \sin\left(\frac{\pi}{2} \left(\frac{\tilde{x}_2}{b_i}\right)^3\right) & \text{if } x \geq a_i \\ & \text{and } \tilde{x}_2 < b_i \\ 1 + \frac{d_i - c_i}{(1 - b_i)^2} (\tilde{x}_2 - b_i)^2 + c_i & \text{if } x \geq a_i \\ & \text{and } \tilde{x}_2 \geq b_i \end{cases} \quad (30)$$

where the parameters from a_i to d_i are for the modification of the aft part and they are the same as the CASE-B above. The parameters from e_i to h_i are used for the modification of the fore part in the same way as the aft part. e_i is the location where the fore modification starts and f_i is the peak location. g_i and h_i are the peak value and the value at the fore-end, respectively. The normalized distances \tilde{x}_1 and \tilde{x}_2 are defined as

$$\tilde{x}_1 = \frac{x - e_i}{x_{\text{MIN}} - e_i}$$

$$\tilde{x}_2 = \frac{x - a_i}{x_{\text{MAX}} - a_i}$$

x_{MIN} and x_{MAX} are the x coordinates of the fore-end and the aft-end of a hull. The parameters of the basis function are shown in Fig.13.

Interpolation in z -direction is similar to the CASE-B in the previous optimization. In case of free surface flows, a hull modification has to be extended to the region above the still water plane. This is accomplished by assuming that the weight function above the still water plane has the same value as that at the still water plane.

The total number of design variables are 36 (a_p, b_p, c_p, d_p and $a_i, b_i, c_i, d_i, e_i, f_i, g_i, h_i, i = 1, 4$).

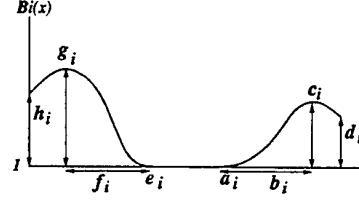


Figure 13: Parameters for basis function in x direction.

Constraint

Constraint considered in this case is as follows:

1. The displacement does not decrease from the initial value.
2. The maximum width does not exceed the initial value.
3. The length of bow bulb is less than 5% of L_{pp} .
4. Appropriate limits are imposed for each design variables.

Computational conditions

The grid used for optimization procedure is $53 \times 25 \times 29$. Froude and Reynolds numbers are 0.316 and 4×10^6 . The original Baldwin-Lomax turbulence model is used.

Results

The optimization procedure stopped after two iterations and the objective function, total resistance, reduced about 3.5%. It appeared that the optimizer could not find the proper search direction at the second iteration. One possible reason for this is that the sensitivity coefficients of an objective function may not be computed appropriately because, as stated earlier, in the adjoint equation formulation for free surface flows, the dependence of an objective function on wave height is ignored. Further investigation is required to estimate the effect of this simplification.

Despite of convergence problem, the final hull is still improved from the original hull with respect to total resistance and it is worthwhile to examine the result. The computations with the finer grid of $105 \times 25 \times 57$ were also carried out for both the original and modified hulls after the optimization run. The resistance components nondimensionalized by $0.5\rho U^2 L^2$ are compared in Fig.14. In the coarse grid case, the frictional resistance of a modified hull increases about 1 % of the original total resistance but the pressure resistance reduces about 4.5 % and hence

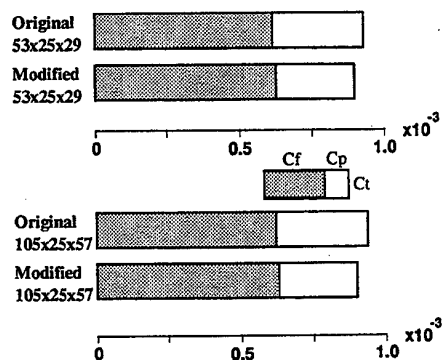


Figure 14: Resistance components.

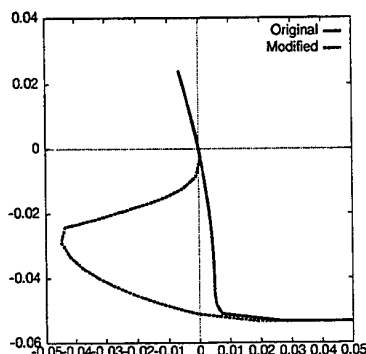


Figure 15: Bow profiles: Series 60 (solid lines) and a modified hull(dotted lines).

total resistance decreases about 3.5%. The fine grid case shows the same tendency and the reduction of total resistance is about 4%.

The bow profiles are shown in Fig.15. A bow bulb is generated for a modified hull and its length is limited by constraint. It is expected that a more practical bulb profile can be obtained if the profile modification function $w_p(z)$ is carefully designed.

The body plans of original and modified hulls are shown in Fig.16. The frame lines of the fore part become U-shaped for the modified hull, this effectively makes a water plane narrower and moves the volume of upper region to lower region. The frame lines of the aft part shows that the modified hull becomes wider than the original hull to compensate a displacement loss at the bow.

Hereafter the results computed using the fine grids ($105 \times 25 \times 57$) are shown. The hull surface pressure distributions are compared in Fig.17. The steep pressure gradient at bow of the original hull becomes mild due to a bow bulb of the modified hull and the low pressure zone near the midship increases for the modified hull. On the other hand, the pressure

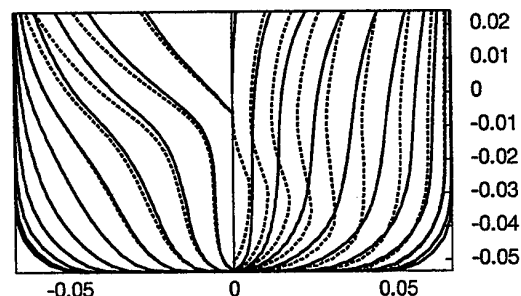


Figure 16: Body plans: Series 60 (solid lines) and a modified hull(dotted lines).

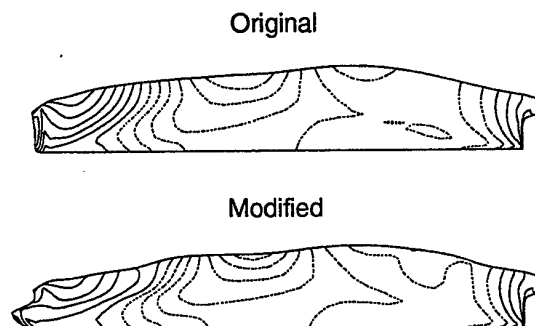


Figure 17: Hull surface pressure distributions. Contour interval: $\Delta C_p = 0.04$ (Top:Original (Series 60), Bottom:Modified).

distributions near the aft-end do not show significant difference.

The wave profiles along the ship hull are compared in Fig.18. Also plotted is the measured data for the Series 60 hull[14]. The computed profile of the original hull is in good agreement with the measured one. The modified hull generates a smaller bow wave and a slightly larger fore shoulder wave beginning at $x = 0.2$. The amplitude of stern waves is almost the same for both hulls. These wave-making properties are consistent with the surface pressure distributions in Fig.17

The wave contours are shown in Fig.19. The difference of wave fields generated by both hulls are clearly observed. The modified hull generates waves of lower amplitude.

CONCLUSIONS

A hydrodynamic shape optimization system has been developed. The system is based on the nonlinear optimizer, SQP (Sequential Quadratic Programming), the Navier-Stokes solver, and the adjoint variable method for sensitivity analysis. Shape modi-

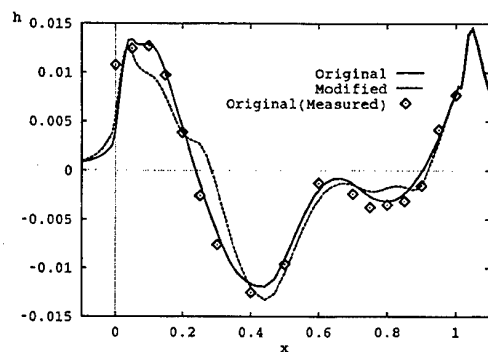


Figure 18: Wave profiles along the ship hull.

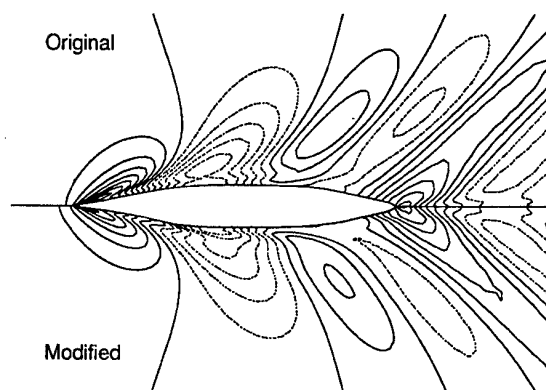


Figure 19: Wave contours. Contour interval: $\Delta h = 0.002$ (Top: Original (Series 60), Bottom: Modified).

modification is carried out using the weight function multiplied to the breadth or the bow profile coordinates of an original hull.

The system is applied to two optimization problems. The first one is for a tanker hull with the minimum viscous resistance. A free surface effect is not taken into account in this case. Two types of weight functions are used for a shape modification of an aft body. The results show both methods can reduce the viscous resistance about 5 to 6 % by deforming the frame lines from U-shaped to V-shaped.

The second problem is the minimization of total resistance including wave-making resistance. The Series 60 ($C_B = 0.6$) hull is selected as an initial shape. Design variables are set to enable modification of both a bow profile and frame lines. Although there seems to be a problem of convergence, total resistance can be reduced about 3.5% in two iterations. The modified hull is equipped with a bow bulb which is missing in the original hull and this contributes the reduction of pressure resistance by suppressing bow

waves.

CPU time used for the execution of CASE-B of the tanker hull optimization is about 51 hours using a single processor of DEC Alpha (500MHz). This run consists of 140 Navier-Stokes computations and 39 sensitivity analyses.

Further investigations on shape modification methods and the combination with more complicated flow models such as self-propulsion or seakeeping analyses will enable the system to be applicable to practical ship hull designs.

ACKNOWLEDGMENT

This research was partly carried out as the collaborative research project between Ship Research Institute and the Shipbuilding Research Association of Japan. The author is grateful to the SR229 committee for providing the initial ship hull form and the constraint for a tanker hull optimization. The author also gratefully acknowledges the suggestions and discussions from Dr. Y. Kodama and Dr. N. Hirata, Ship Research Institute.

REFERENCES

1. Janson, C. and Larsson, L., "A Method for the Optimization of Ship Hulls from a Resistance Point of View", *Proc. of 21st Symposium on Naval Hydrodynamics*, 1996, pp.680-693.
2. Hamasaki, J., Himeno, Y. and Tahara, Y., "Application of Computational Fluid Dynamics to Ship Hull Optimization Problem", *Proc. the Second International Conference on Hydrodynamics*, Vol.1, 1996, pp.23-28.
3. Tahara, Y. and Himeno, Y., "An Application of Computational Fluid Dynamics to Tanker Hull Form Optimization Problem", *Proc. the Third Osaka Colloquium on Advanced CFD Applications to Ship Flow and Hull Form Design*, 1998, pp.515-531.
4. Hino, T., Kodama, Y. and Hirata, N., "Hydrodynamic Shape Optimization of Ship Hull Forms Using CFD", *Proc. the Third Osaka Colloquium on Advanced CFD Applications to Ship Flow and Hull Form Design*, 1998, pp.533-541.
5. Hino, T., "Fluid-dynamic Shape Optimization using Sensitivity Analysis of Navier-Stokes Solutions", *Journal of the Kansai Society of Naval Architects, Japan*, No.226, 1996, pp.49-54.
6. Kodama, Y. and Hino, T., "Effect of Body Geometry Expression and Grid Resolution on the Optimization of a Two-Dimensional Symmetric Wing", *Proc. ASME/JSME Joint Fluids Engineering Conference*, 1999 (to appear).

7. Burgreen, G.W. and Baysal, O., "Three-Dimensional Aerodynamic Shape Optimization of Wings Using Sensitivity Analysis", AIAA Paper 94-0094, 1994.

8. Hirata, N. and Hino, T., "An Efficient Algorithm for Simulating Free-Surface Turbulent Flows around an Advancing Ship", Journal of the Society of Naval Architects of Japan, Vol.185, 1999, pp.1-8, (to appear).

9. Baldwin, B.S. and Lomax, H., "Thin Layer Approximation and Algebraic Model for Separated Turbulent Flows", AIAA Paper 78-257, 1978.

10. Kodama, Y., "Scope of CFD for Computing Ship Flows", Proc. the Third Osaka Colloquium on Advanced CFD Applications to Ship Flow and Hull Form Design, 1998, pp.395-405.

11. Hino, T., "A Study of Grid Dependence in Navier-Stokes Solutions for Free Surface Flows around a Ship Hull", Journal of the Society of Naval Architects of Japan, Vol.176, 1994, pp.11-18.

12. Frank, P.D. and Shubin, G.R., "A Comparison of Optimization - Based Approaches for a Model Computational Aerodynamic Design Problem", Journal of Computational Physics, Vol.98, pp.74-89, 1992.

13. Jameson, A., "Optimum Aerodynamic Design Using CFD and Control Theory", AIAA Paper 95-1729-CP, 1995.

14. Toda, Y., Stern, F. and Longo, J., "Mean-Flow Measurements in the Boundary Layer and Wake and Wave Field of a Series 60 $C_B = 0.6$ Ship Model — Part 1: Froude Numbers 0.16 and 0.316.", Journal of Ship Research, Vol.36, No. 4, 1992, pp.360-377.

FRONTIER PROBLEMS IN HYDRODYNAMICS.

Chairman : K.Rozhdestvenski

UNSTEADY FLOW CALCULATIONS PAST VENTILATED HYDROFOILS

V. N. Semenenko

National Academy of Sciences – Institute of Hydromechanics

8/4 Zhelyabov str., Kyiv, 252057, Ukraine.

Fax: 38 044 446 42 29; E-Mail: vns@vnsh.pp.kiev.ua.

ABSTRACT

Two numerical-analytic methods for calculation of low-disturbed flow around two-dimensional supercavitating and ventilated hydrofoil at harmonic time dependence are considered. An approximate approach to calculation of time dependence of a cavity length is described. An effect of the variable cavity length on unsteady hydrodynamic characteristics of hydrofoil is analyzed. The influence of free surfaces on stability of two-dimensional ventilated cavity is investigated.

NOMENCLATURE

b	Chord length	(m)
c_m, c_y	Moment and lift coefficients	(-)
Eu	Euler number	(-)
g	Gravity acceleration	(m/s ²)
h	Mean immersion depth	(-)
i, j	Imaginary units	(-)
k	Reduced frequency	(-)
l	Cavity length	(-)
p'	Local disturbed pressure	(Pa)
p_c	Cavity pressure	(Pa)
p_∞	Pressure at infinity	(Pa)
q	Source intensity	(-)
Q	Cavity volume	(-)
t	Time	(-)
v_y	Disturbed velocity	(-)
V_∞	Free-stream velocity	(m/s)
z	Complex coordinate	(-)
α	Angle of attack	(-)
β	Similarity parameter	(-)
γ	Vortex intensity	(-)
ε	Small parameter	(-)
θ	Acceleration potential	(-)
κ	Oscillation amplitude	(-)
λ	Real part of μ	(-)
λ_w	Wave length	(m)
μ	Exponential power	(-)
ρ	Liquid density	(kg/m ³)
σ	Cavitation number	(-)
Φ	Complex acceleration potential	(-)
ω	Circular frequency	(1/s)

INTRODUCTION

Hydrofoils of high-speed ships usually are slender and low-curved. The linear theory is successfully applied to calculate them. The cavitation arises on the hydrofoils at high speed of motion. While the velocity increases the following cavitation types sequentially are replaced: bubble, sheet, partial and super-cavitation.

Now an attention of investigators is concentrated mainly on study of initial stages of cavitation which are accompanied with noise and erosion. Sheet and partial cavitation on hydrofoils and propeller blades are also of great interest (see Proceedings of Third International Symposium on Cavitation, Grenoble, France, April 1998). Such flows may be named "naturally" unsteady ones. For numerical modeling of such flows mainly direct methods are used.

Supercavitation flow around the hydrofoils is developed at the very high velocity of motion. It is usually close to the stationary regime. Foundations of the linear theory of the supercavitating hydrofoils have been developed in the classical work [1]. A lot of partial results and practical calculations have been obtained on its basis in 70s (e.g. see monographs [2-6]).

The ventilated cavities past the hydrofoil may be formed both in natural way – by suction of atmospheric air and artificially – by blowing air into the cavity.

At stationary flow a shape and dimensions of nat-

ural (vapor) and ventilated cavities are practically identical providing that cavitation number

$$\sigma = \frac{2(p_\infty - p_c)}{\rho V_\infty^2} \quad (1)$$

is the same and buoyancy force is neglected. In this case the cavitation number σ is a key similarity parameter of the flow.

Besides σ the second similarity parameter takes an important role at unsteady flow

$$\beta = \frac{Eu}{\sigma}, \quad (2)$$

where $Eu = 2p_\infty / \rho V_\infty^2$ is the Euler number. It is obvious that always $\beta \geq 1$, value $\beta = 1$ corresponds to the natural supercavitation. Influence of gas elasticity in the cavity increases when the parameter β grows. Similarity parameter β is a key parameter at investigation of instability and dynamical behavior of gas-filled cavities [7-10]. In this paper forced non-stationarity of the supercavitating flow around the hydrofoil is considered. It may be caused by the several causes:

- hydroelastic instability and the hydrofoil flutter [11], vehicle oscillations at sea-way;
- nonhomogeneity of mainstream at the hydrofoil motion under the wave surface [2, 12];
- instability and self-induced oscillations of a ventilated cavity itself [7-10].

Two calculation methods of the low-disturbed unsteady flow past two-dimensional supercavitating hydrofoils in the case of harmonic time dependence are considered. A key point of our approach is that the cavity pressure p_c is considered dependent of time. Such a dependence of pressure on time is natural for unsteady ventilated (gas-filled) cavities.

The variable cavity length $l(t)$ is determined in sequential moments by numerical solving the equation of balance of gas mass in the cavity (in the case of natural supercavities – by condition of the cavity pressure to be constant). For each iteration, the unsteady part of solution is calculated at $l = const$.

1. FORMULATION OF PROBLEM

We consider a supercavitating and ventilated two-dimensional hydrofoil with chord b moving horizontally with velocity V_∞ at distance h from the middle level of the free water surface (Fig. 1). Liquid is considered to be ideal, incompressible and weightless.

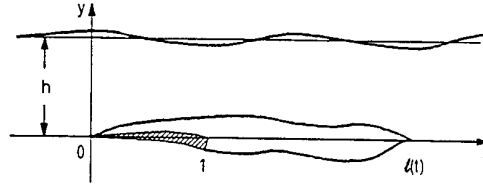


Fig. 1. Supercavitating hydrofoil under a waved surface

The two-dimensional hydrofoil $y = f(x, t)$ is considered to be slender and low-curved (a plate), the cavitation number is small:

$$\|f(x, t)\| \sim O(\varepsilon), \quad \sigma(t) \sim O(\varepsilon).$$

Hence, the problem may be linearized.

Let the sea-way influence develops nonhomogeneity in the mainstream stipulated by orbital motion of liquid particles in a wave. As follows from the linear theory of surface waves, in this case the following distribution of the vertical velocity is induced on the two-dimensional hydrofoil:

$$v_y(x, t) = -a \sqrt{\frac{2\pi g}{\lambda_w}} e^{-\frac{2\pi h}{\lambda_w}} \cos\left(\nu_w t - \frac{2\pi}{\lambda_w} x\right), \quad (3)$$

where λ_w is the wave length; a is the wave half-height ($a \ll \lambda_w$); $c = \sqrt{g\lambda_w}/2\pi$ is the wave velocity; $\nu_w = 2\pi(V_\infty \pm c)/\lambda_w$ is the seeming frequency of the hydrofoil meeting with the wave. For high-speed ships with hydrofoils usually $b < \lambda_w$ and $V_\infty \gg c$, hence the reduced frequency of the hydrofoil meeting a wave is equal

$$k = \frac{\nu_w b}{V_\infty} \approx 2\pi \frac{b}{\lambda_w}. \quad (4)$$

Then formula (3) for dimensionless variables gets the form

$$v_y(x, t) = -\kappa(k) \cos k(t - x), \quad (5)$$

$$\kappa(k) = \frac{a}{V_\infty} \sqrt{\frac{gk}{b}} e^{-\frac{k\lambda}{b}}.$$

Thus, the problem of motion of the hydrofoil under conditions of regular sea-way at $V_\infty \gg c$ is deduced to the problem on uniform flow having a harmonic burst of the vertical velocity around the two-dimensional hydrofoil.

Measurements [2] show that at motion in wave flow the pressure in the artificial cavity is pulsing with dimensionless frequency k and changing

synchro along the cavity length. Hence, the cavitation number may be written in the form of a sum of the mean and disturbed components

$$\sigma(t) = \sigma_m + \operatorname{Re}\{\sigma^* e^{jkt}\}, \quad \sigma_m \neq 0. \quad (6)$$

We introduce a harmonic function – the potential of disturbed accelerations:

$$\theta = -\frac{p'(x, y, t)}{\rho V_\infty^2} = \operatorname{Re}\{\theta^*(x, y) e^{jkt}\}, \quad (7)$$

$$\Delta\theta(x, y, t) = 0,$$

where p' is unsteady perturbation of the pressure. Below all the values marked by sign "*" are considered to be complex with respect to j (complex amplitudes):

$$\theta^* = \theta_1 + j\theta_2, \quad \sigma^* = \sigma_1 + j\sigma_2 \quad \text{etc.}$$

The real parts of results have meaning.

On the flow boundaries the following conditions for the complex amplitude must be fulfilled:

$$\theta_y^* = \left(jk + \frac{d}{dx}\right) v_y^*(x) \quad \text{on the foil}, \quad (8)$$

$$\theta^* = \sigma^*/2 \quad \text{on the cavity}, \quad (9)$$

$$\theta^* = 0 \quad \text{on the free surface}. \quad (10)$$

Here, $v_y(x, t) = -\alpha + \operatorname{Re}\{v_y^*(x) \exp(jkt)\}$ is the given normal velocity on the two-dimensional hydrofoil; $\alpha \sim O(\varepsilon)$ is angle of attack.

In addition, the kinematic condition for disturbed velocity must be fulfilled on the two-dimensional hydrofoil:

$$\int_{-\infty}^x \theta_y^*(s) e^{jk(s-x)} ds = v_y^*(x). \quad (11)$$

To solve the boundary value problem (8)–(10) it is possible to apply two different numerical-analytical methods:

- 1) method of integral equations (IE method, named also as method of singularities) [3, 13];
- 2) method of boundary value problem for analytic function (BVP method) [5, 12].

In each case, the most suitable scheme of cavitation flow around the hydrofoil is chosen.

2. METHOD OF INTEGRAL EQUATIONS

Boundary conditions (8)–(10) show that the acceleration potential experiences a discontinuity

at passage through the two-dimensional hydrofoil projection onto axis Ox , and its normal derivative experiences a discontinuity at passage through the cavity projection onto the same axis. It is known [14] that simple or double layers distributed along intervals of axis Ox would have these properties, i.e. layers formed by vortices and sources provided that their intensities are equal respectively

$$\begin{aligned} \gamma^*(x) &= \theta^*(x, +0) - \theta^*(x, -0), \\ \left(jk + \frac{d}{dx}\right) q^*(x) &= \theta_y^*(x, +0) - \theta_y^*(x, -0). \end{aligned}$$

Using the method of mapping of singularities relative to the free boundary, we write a solution of the problem in the form of a sum of the potentials of simple and double layers

$$\begin{aligned} \theta^*(x, y) &= \frac{1}{2\pi} \int_0^1 \gamma^*(s) \left[\frac{y}{(x-s)^2 + y^2} + \right. \\ &\quad \left. + \frac{y-2h}{(x-s)^2 + (y-2h)^2} \right] ds + \int_0^l q^*(s) \times \\ &\quad \left[\frac{x-s}{(x-s)^2 + y^2} - \frac{x-s}{(x-s)^2 + (y-2h)^2} + \right. \\ &\quad \left. + jk \ln \sqrt{\frac{(x-s)^2 + y^2}{(x-s)^2 + (y-2h)^2}} \right] ds. \end{aligned} \quad (12)$$

Computing values $\theta^*(x, y)$ and $\theta_y^*(x, y)$ at $y \rightarrow \pm 0$ [15] and substituting in the boundary conditions (8), (9), we obtain a system of two singular integral equations relatively intensities of the distributed vortices $\gamma^*(x)$ and sources $q^*(x)$:

$$\begin{aligned} q^*(x) + \frac{1}{\pi} \int_0^l q^*(s) L_1(x-s) ds + \frac{1}{\pi} \int_0^1 \gamma^*(s) \times \\ \left[L_2(x-s) - jke^{-jkx} \int_{-\infty}^x e^{jk\lambda} L_2(\lambda-s) d\lambda \right] ds = \\ = -2v^*(x), \\ H(1-x) \left[\gamma^*(x) - \frac{1}{\pi} \int_0^1 \gamma^*(s) L_1(x-s) ds \right] + \\ + \frac{1}{\pi} \int_0^l q^*(s) [L_3(x-s) + jkL_4(x-s)] ds = \sigma^*. \end{aligned} \quad (13)$$

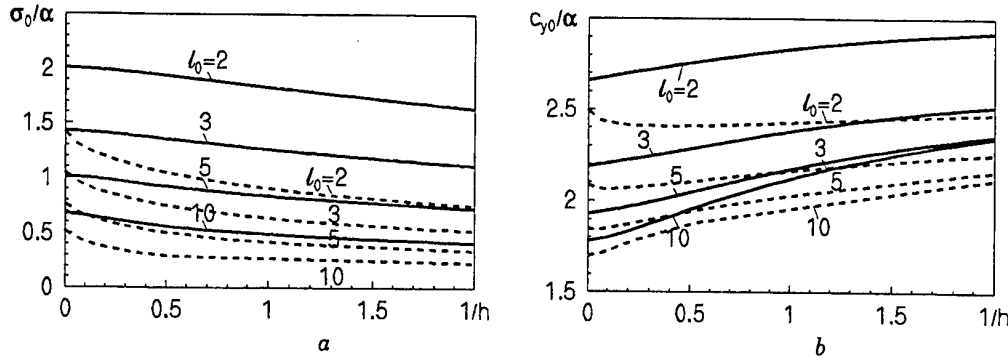


Fig. 2. Stationary solutions: — IE method, --- BVP method

where is designated

$$\begin{aligned} L_1(x-s) &= \frac{2h}{(x-s)^2 + 4h^2}, \\ L_2(x-s) &= \frac{1}{x-s} + \frac{x-s}{(x-s)^2 + 4h^2}, \\ L_3(x-s) &= \frac{1}{x-s} - \frac{x-s}{(x-s)^2 + 4h^2}, \\ L_4(x-s) &= \ln \frac{|x-s|}{\sqrt{(x-s)^2 + 4h^2}}, \end{aligned}$$

$H(x) = 0$ at $x < 0$, $H(x) = 1$ at $x \geq 0$. The internal integral in (13) may be expressed by the integral exponential function.

Since the cavitation number σ^* disturbance and cavity length l are also unknown and act as dependent parameters, two relations have to be added to the equations (13), (14) to get a complete system.

At $\beta > 1$ and assuming the process is isothermal it yields, to take into account dynamic properties of ventilated cavities an equation of balance of gas mass in the cavity is to be attracted:

$$\frac{d}{dt} [(\beta - \bar{\sigma}(t)) Q(t)] = \beta [\dot{Q}_{in} - \dot{Q}_{out}(t)], \quad (15)$$

where $\bar{\sigma} = \sigma(t)/\sigma_m$; $Q(t)$ is the cavity volume; \dot{Q}_{in} , $\dot{Q}_{out}(t)$ are the volumetric rates of gas blowing in the cavity and leakage from the cavity. It is assumed that pressure $p_c(t)$ changes synchro along the cavity length. In the case of natural supercavitation ($\beta = 1$), equation (15) transforms into a condition of the cavity pressure to be constant $\bar{\sigma}(t) = 1$.

There is not a single option to choose the second relation that would make the system complete. It might be either a condition of the cavity to

be close or condition of the boundary problem solvability. Here we use the Neyman condition of solvability of the external boundary value problem for the velocity potential [14]:

$$\int_0^l [\varphi_y](s, t) ds = \int_0^l q(s, t) ds = 0. \quad (16)$$

Here, $[\varphi_y](x, t)$ is a jump of the vertical velocity at passage through the axis $0x$. Condition (16) ensures the solution (12) to be finite in the case of the unbounded flow $h \rightarrow \infty$. In the case of steady flow the equation (16) is a condition of the cavity to be closed [3]. In the case of unsteady flow the cavity is unclosed.

After determination of intensities γ^* , q^* it is possible to calculate the unsteady cavity thickness

$$\delta(x, t) = \alpha \int_0^x q_m(s) ds + \quad (17)$$

$$+ \kappa \operatorname{Re} \left\{ e^{jk(t-x)} \int_0^x q^*(s) e^{jks} ds \right\}$$

and perturbations of the unsteady hydrodynamic forces acting on the hydrofoil

$$\begin{aligned} c_y^* &= 2\kappa \int_0^1 \gamma^*(s) ds, \\ c_m^* &= 2\kappa \int_0^1 \gamma^*(s) s ds. \end{aligned} \quad (18)$$

The system of equations (13)–(16) is nonlinear as a whole. Specifically, non-harmonicity of the

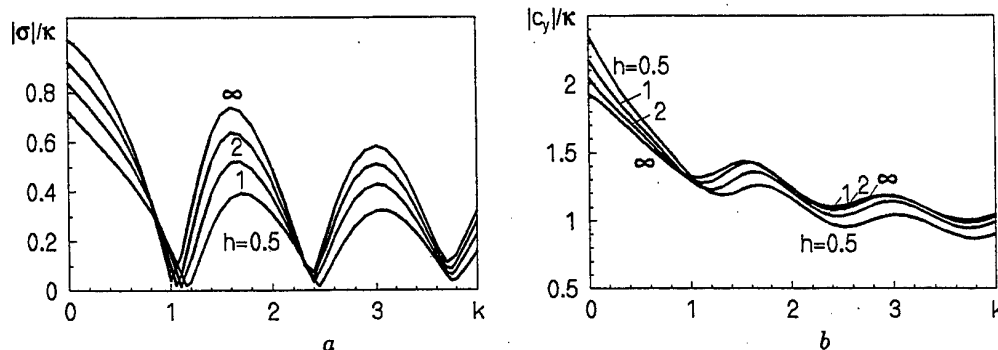


Fig. 3. Influence of the immersion depth h on frequency responses of σ and c_y , IE method, $l_m = 5.0$

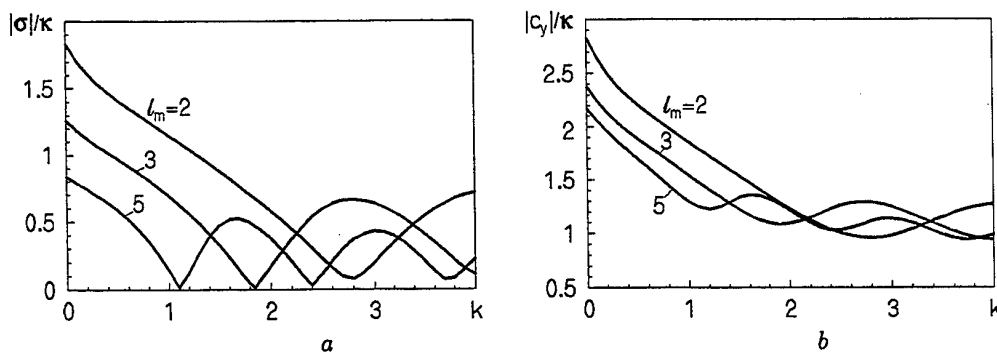


Fig. 4. Influence of the mean cavity length l_m on frequency responses of σ and c_y , IE method, $h = 1.0$

unknown function $l(t)$ to be found makes the system difficult to solve. Its variation is of order of unit while $v_y(x, t) \sim O(\varepsilon)$ and $\sigma(t) \sim O(\varepsilon)$.

It is known from experiments that the processes at the tail cavity part weakly influence on the hydrodynamic characteristics of the supercavitating hydrofoils at small σ . In our works [12, 13], the cavity length is considered to be known, constant and equal to its value l_m at $\kappa = 0$. In this case the system of equations (13), (14), (16) becomes linear and may be effectively solved numerically by method of discrete singularities. This method is described for cavitation problems in [3].

In this work, a real dependence $l(t)$ is calculated in sequential moments $t^{(m)} = t^{(m-1)} + \Delta t$ by numerical solving the equation (15). In this case the complete problem solution is used in the form of sum of the quasistationary and unsteady dis-

turbed components:

$$\begin{aligned}\gamma(x, t^{(m)}) &= \alpha \gamma_m(x) + \kappa \operatorname{Re}\{\gamma^*(x) e^{jkt^{(m)}}\}, \\ q(x, t^{(m)}) &= \alpha q_m(x) + \kappa \operatorname{Re}\{q^*(x) e^{jkt^{(m)}}\}.\end{aligned}$$

The unsteady cavity volume $Q(t^{(m)})$ is calculated by numerical integrating the expression (17). For each iteration, the unsteady part of solution is calculated at $l = \text{const}$ by using the linear system of equations (13), (14), (16).

A result of application of this algorithm to calculate of natural supercavity is given below. In this case equation (15) is substituted by the condition of cavitation number to be constant.

The numerical method of discrete singularities is a method of approximation of integral equations derived from continuous distribution of vortices and sources with a system of linear algebraic

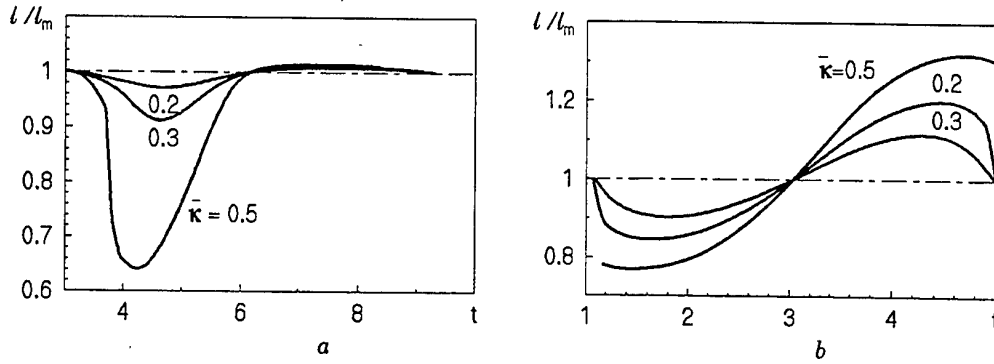


Fig. 5. Cavity length history,
 $h = \infty$, $l_m = 5.0$, $a - k = 1.0$, $b - k = 1.6$

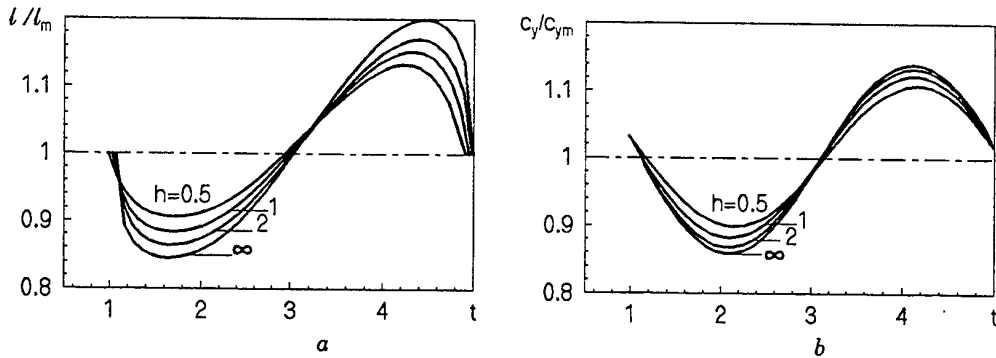


Рис. 6. Influence of the immersion depth h on $l(t)$ and $c_y(t)$,
 $l_m = 5.0$, $k = 1.6$, $\bar{\kappa} = 0.2$

equations that correspond to discrete distribution of singularities of the same type.

Preliminarily, change of variables $x \rightarrow x^2$, $s \rightarrow s^2$ is done in all the integrals [3]. Projections of the hydrofoil and cavity are divided on $M\sqrt{l_m}$ equal intervals. A position order of the discrete singularities and points, where the boundary conditions are satisfied, is determined by function classes, in which a solution is found, and also the best convergence requirement of this method [3]. As a result, we obtain a system of $4M + 2M(\sqrt{l_m} - 1) + 2$ linear algebraic equations after decoupling the real and imaginary parts.

We note that another variant of the singularity method is applied to calculate the flow around the oscillating supercavitating two-dimensional hydrofoils in [16, 17]. An advantage of the method of integral equations is that it is easy

distributed for the case of systems of hydrofoils and wings of finite span. So the stationary supercavity shape in span past the rectilinear hydrofoil has been succeed to determine in the work [18].

Mathematical background of the numerical method of discrete vortices is given in [19]. An analysis of accuracy of the solution obtained shows that an error monotonically increases with growth of reduced frequency k (as an exponential function of k) provided a total number of singularities on the hydrofoil M is fixed. For practically important values of the reduced frequency $k < 2$ and $M \geq 20$ the method error does not exceed 2%.

The influence of cavity length l_0 and immersion depth h on σ_0/α and c_{y0}/α for the steady flow case $k = 0$ is shown by solid lines in Fig. 2.

The frequency responses

$$|\sigma|(k) = \sqrt{\sigma_1^2 + \sigma_2^2}, \quad |c_y|(k) = \sqrt{c_{y1}^2 + c_{y2}^2}$$

at fixed value $l_m = 5.0$ and various values of the depth h are shown in Fig. 3. It is seen that the dependencies $|\sigma|(k)$ and $|c_y|(k)$ have brightly expressed resonance behavior. The position of minimums and maximums practically does not depend on h .

The influence of value of l_m on frequency response for constant value of $h = 1.0$ is shown in Fig. 4.

3. OSCILLATION OF HYDROFOIL WITH VAPOUR SUPERCAVITY

A resonance behavior of dependencies $|\sigma|(k)$ and $|c_y|(k)$ obtained in calculations at $l = \text{const}$ is internal property of equations (13), (14). Taking account of equation (15) does not result in qualitative change of resonance behavior. It just increases the phase lags

$$\arg(\sigma) = \arctan \frac{\sigma_2}{\sigma_1}, \quad \arg(c_y) = \arctan \frac{c_{y2}}{c_{y1}}$$

In the case of natural supercavitation ($\beta = 1$) the pressure in the cavity must remain constant and equal to its mean value, and the cavity length l must change in time. To determine it we propose the following approach.

We consider the cavity length $l(t)$ as a free time parameter and determine it from the condition that the cavitation number is equal to its mean value $\sigma_m(l_m)$ in each moment. As a result, we get the equation

$$\sigma_m(l) + \bar{\kappa} [\sigma_1(l) \cos kt - \sigma_2(l) \sin kt] = \sigma_m(l_m), \quad (19)$$

where $\bar{\kappa} = \kappa/\alpha$, which is solved numerically for sequential moments $t^{(m)} = t^{(m-1)} + \Delta t$.

The time dependences of the cavity length and lift coefficient at various values of the oscillation amplitude $\bar{\kappa}$ and two values of the reduced frequency is shown in Fig. 5. Value $k = 1.0$ corresponds to the first minimum of function $|\sigma|(k)$ (see Fig. 3, a), value $k = 1.6$ corresponds to its first maximum. As is visible at increase of κ the cavity length oscillations are the more different from harmonic ones and become separate at exceeding some limiting value of κ . The calculated form of the cavity length oscillations qualitatively corresponds to the experimental data [17].

On the contrary, oscillations of the lift coefficient c_y remains sinucoidal at any values of κ . In this

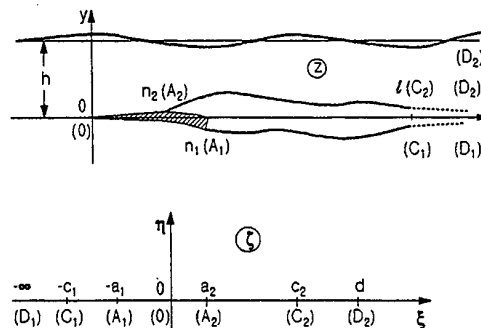


Fig. 7. Boundary value problem by 2nd M.Tulin scheme

case their amplitude is not practically changed comparing to the calculation at $l = \text{const}$. Hence, the important conclusion follows that the resonance nature of dependence $|c_y|(k)$ has a physical sense and it is possible to talk that the supercavities of finite length have fundamental frequencies developing at forced oscillations.

A comparison with results of the theory of two-dimensional gas-filled cavities [9, 10] shows that obtained resonance frequencies are close to the fundamental cavity frequencies. In this case the minimal cavity length for oscillation period l_{min} should be used:

$$kl_{min} \approx 2\pi n, \quad n = 1, 2, 3, \dots \quad (20)$$

Influence of the immersion depth h on $l(t)$ and $c_y(t)$ is shown in Fig. 6. As we can see, the oscillation amplitudes of both $l(t)$ and $c_y(t)$ increase when h increases.

4. METHOD OF BOUNDARY VALUE PROBLEM FOR ANALYTIC FUNCTION

The used above cavitation scheme is equivalent to the one known as the first M.Tulin scheme [1]. In the case of steady flow it is a kinematically closed cavity scheme.

Now, we consider the same problem using the second M.Tulin scheme with infinite wake past a cavity [1] (Fig. 7, a). Let $n_1 = 1$, n_2 are x-coordinates of the streamline separation points on the hydrofoil; l is x-coordinate of points separating the cavity boundaries and the wake boundaries. The cavity pressure is equal $p_c(t)$, the wake pressure is equal p_∞ .

We can manage the streamline separation in the arbitrary point $0 \leq n_2 \leq 1$ of upper hydrofoil surface by air supply or using the cavitating spoiler. In this case the condition on the wake boundaries is added to the boundary conditions (8)-(11)

$$\theta^* = 0, \quad l < x < \infty, \quad y = \pm 0. \quad (21)$$

The obtained problem is deduced to the mixed boundary value problem for analytic function $\Phi^*(z) = \theta^*(x, y) + i\xi^*(x, y)$ in parametrical half-plane $\text{Im } \zeta > 0$ conformally mapping onto the flow zone by formula

$$z = -2d \left[\zeta + d \ln \left(1 - \frac{\zeta}{d} \right) \right], \quad d = \sqrt{\frac{h}{2\pi}}.$$

Correspondence of points at conformal mapping is shown in Fig. 7, b. The boundary condition for χ^* is easily obtained with the help of Cauchy-Riman condition from (8):

$$\chi^*(x) = \chi^*(0) - \int_0^x \left(jk + \frac{d}{ds} \right) v_y^*(s) ds. \quad (22)$$

In the considered case of the harmonic gust $v_y^*(x) = -\kappa \exp(-jkx)$, and the second term in the formula (22) is equal to zero. A solution of the obtained mixed boundary value problem in the respective class of functions is given by Keldysh-Sedov formula [15]

$$\Phi^*(\zeta) = \frac{\sqrt{(a_1 + \zeta)(a_2 - \zeta)}}{\pi i \zeta} \times \quad (23)$$

$$\times A \int_{-c_1}^{c_2} \frac{s}{\sqrt{(a_1 + s)(a_2 - s)}} \frac{ds}{s - \zeta},$$

where $A = i\chi^*(0)$ at $-a_1 < \xi < a_2$, $A = \sigma^*/2$ at $-c_1 < \xi < -a_1$, $a_2 < \xi < c_2$.

To determine the two complex constants $\chi^*(0)$, σ^* it is necessary to have two additional conditions. One of them is easy to obtain from (11):

$$-\chi^*(0) + jk \int_{-\infty}^0 \chi^*(s) e^{jks} ds = v_y^*(0). \quad (24)$$

The condition of the wake thickness to be finite at $x \rightarrow \infty$ is used as the second closing condition. It is equivalent to requirement of equality to zero of the total intensity of sources-sinks modeling the unsteady cavity and wake perturbations

$$[\chi^*](0) + \int_0^\infty [\chi_s^*](s) e^{jks} ds = 0. \quad (25)$$

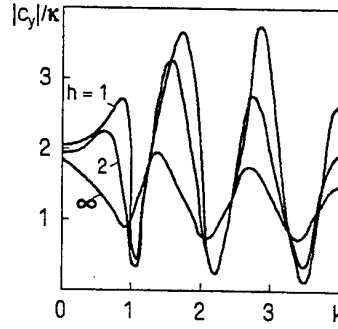


Рис. 8. Frequency response of c_y , BVP method, $n_2 = 0$, $l_m = 5.0$

Here, the quadratic brackets designate a jump of corresponding value at passage through axis $0x$ in the physical plane.

Thus, the problem solution is represented by means of quadratures that have to be calculated numerically. This method is formally applicable at arbitrary frequency values k . Restrictions come from the problem linearization conditions only.

The coefficients of unsteady components of the lift acting on the two-dimensional hydrofoil and also moment about the frontal edge are calculated by formulae

$$c_y^* = (n_1 - n_2) \sigma^* + 2 \int_{-a_1}^{a_2} \theta^*(\xi) \frac{dx}{d\xi} d\xi, \quad (26)$$

$$c_m^* = \frac{n_1^2 - n_2^2}{2} \sigma^* + 2 \int_{-a_1}^{a_2} \theta^*(\xi) x(\xi) \frac{dx}{d\xi} d\xi.$$

The influence of cavity length l_0 and immersion depth h on σ_0/α and c_{y0}/α in the steady flow case is shown in Fig. 2 by dashed line. A comparison with calculation by the method of integral equations (solid lines) and experimental data [4, 6] shows that the BVP method gives underestimated values of both σ_0 and c_{y0} . It is explained by using the cavitating scheme with the wake. This scheme gives the smaller cavity length l_0 than the kinematically closed cavity at the same value of σ_0 [1].

The frequency responses of the cavitation number and unsteady lift coefficient are given in Fig. 8 at $l = 5.0$, $n_2 = 0$ for various values of h . The calculated results show that resonance frequency values are low-changed with decreasing the immersion depth. At the same time the free

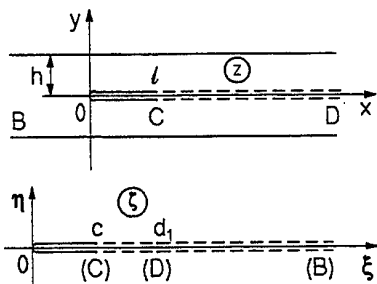


Fig. 9. Scheme of "pure" supercavity in free jet

surface closeness results in considerable growth of amplitude of the force pulsation on the two-dimensional hydrofoil.

When the separation point n_2 displaces to the tail hydrofoil edge, the resonance phenomena becomes weakly, also influence of the separation point position decreases at decreasing h . The case, when $n_2 = n_1$ corresponds to the unseparated flow around an oscillating plate.

A comparison with Fig. 3 shows that both the calculation methods result in close values of the resonance frequencies. The different form of the frequency responses $|\sigma|(k)$ and $|c_y|(k)$ is explained by use of the different cavitation schemes.

5. INSTABILITY OF VENTILATED CAVITY IN A FREE JET

We investigated stability of the plane gas-filled cavity in unbounded stream basing on the 1st and 2nd M.Tulin linearized schemes [9, 10]. In the first case (closed cavity scheme) a logarithmic singularity of the pressure at infinity $p_\infty(t)$ is assumed. It is caused by variability of the unsteady cavity volume. In the second case (infinite wake scheme) the pressure at infinity is finite in any moment. A good agreement of the solution and experimental data [7] was achieved.

To estimate the influence of the free surface on the cavity stability we consider the two-dimensional problem on unsteady cavity in free jet. For simplicity, the flow is considered symmetric about axis Ox , and a cavitator is small in comparison with a cavity (known as "pure" cavity). The linearized flow zone representing a band having the slit along the positive axis Ox is shown in Fig. 9, a. We conformally map it onto

a plane with a slit by function

$$z = -d_1 \ln \left(1 - \frac{\zeta}{d_1} \right),$$

where $d_1 = h/\pi$, h is the jet half-width. A correspondence of the flow stream points and parametric plane ones is shown in Fig. 9, b. The tail point of the cavity $x = l(t)$ is mapped to the point c :

$$c = d_1 \left(1 - e^{-\frac{l}{d_1}} \right). \quad (27)$$

The dynamic condition $p = p_\infty$ must be fulfilled on both the jet and the wake boundaries. Hence, we have the mixed boundary value problem in the upper parametric half-plane $\text{Im } \zeta > 0$:

$$\begin{aligned} \chi &= 0, & -\infty < x < 0, \\ \theta &= \frac{\sigma(t)}{2}, & 0 < x < c(t), \\ \theta &= 0, & c(t) < x < \infty. \end{aligned} \quad (28)$$

The first of boundary conditions (28) follows from the symmetry of flow. A solution of the mixed boundary value problem in the upper half-plane $\text{Im } z > 0$ has the form:

$$\Phi(\zeta, t)/\sigma_0 = -\frac{i}{\pi\sqrt{\zeta}} + \frac{\bar{\sigma}(t)\sqrt{\zeta}}{2\pi i} \int_0^{c(t)} \frac{ds}{\sqrt{s(s-\zeta)}}. \quad (29)$$

where $\bar{\sigma} = \sigma(t)/\sigma_0$. Here and below all the values are related to the cavity length l_∞ when $h \rightarrow \infty$. To determine two time functions $\bar{\sigma}(t)$, $l(t)$ it is necessary to have two additional equations. The equation (15) is the first of them. In the work [9], we used approximation of the experimental data [7] to compute rates of gas supply and leakage:

$$\dot{Q}_{in} = \gamma_0 b_0 V_\infty \left(1 - \frac{\sigma_0}{Eu} \right), \quad (30)$$

where γ_0 is an empirical coefficient. The value $\gamma_0 \approx 2.5 \cdot 10^{-4}$ follows from [7] for stationary cavities. A detailed analysis of influence of the parameter γ_0 on the supercavity stability [9] has shown that it is negligible at such values of γ_0 . Here, we assume that $\gamma_0 = 0$. In this case the equation (15) becomes a condition of the mass of gas in the cavity to be constant.

As the second "closing" equation we use condition of the wake width at infinity to be finite

$$\lim_{x \rightarrow \infty} \int_0^x \chi_t(s, t-x+s) ds = 0, \quad (31)$$

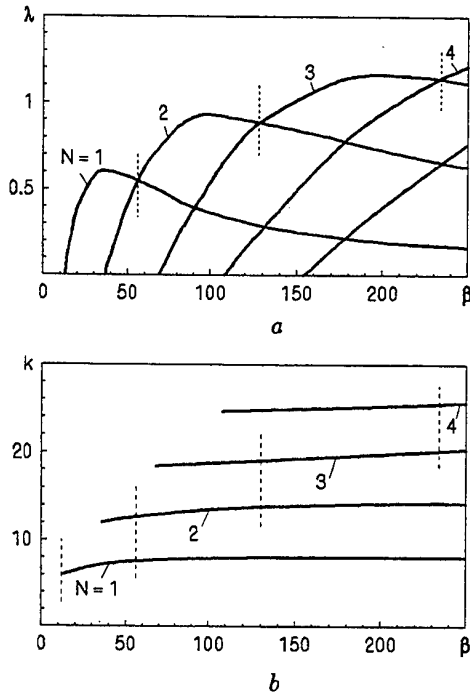


Fig. 10. Complex roots of characteristic equation, $h = \infty$

which is also a condition of the total cavity and wake volume time variation to be finite. To investigate the steady ventilated cavity stability with respect to small oscillations we represent the unknown time functions in the form

$$\bar{\sigma}(t) = 1 + \varepsilon a e^{\mu t}, \quad l(t) = l_0 + \varepsilon b e^{\mu t},$$

where $\mu = \lambda + jk$; $k = \omega l_0 / V_\infty$ is the reduced frequency; ω is the circular frequency; a, b are constants. We linearize the equations (15), (31) in neighborhood of the steady solution $\bar{\sigma} = 1$, $l = 1$ and obtain a system of two linear uniform equations for coefficients a, b .

Equating the system determinant to zero, we obtain a characteristic equation to research the complex roots $\mu = \lambda + jk$ in dependence on two parameters h, β . When $\lambda < 0$, the cavity is asymptotically stable. When $\lambda > 0$, the cavity is unstable. Accepting $\lambda = 0$ and dividing the real and imaginary parts, we obtain a system of two equations to determine the parameters of fundamental cavity oscillation β_n, k_n .

A numerical analysis of the complex roots of the characteristic equation has shown that loss of the ventilated cavity stability happens identically by

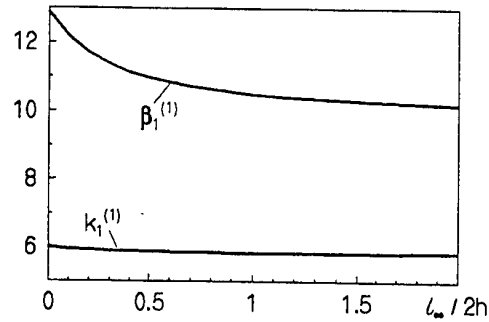


Fig. 11. Influence of the jet width on cavity fundamental frequency

the 1st and 2nd M.Tulin schemes [9]. In the case of $\lambda = 0$ the characteristic equation has two series alternating pure imaginary roots i. e. fundamental oscillation frequencies $k_n^{(1)}, k_n^{(2)}, n = 1, 2, \dots$. We have $\lambda < 0$ at $k < k_1^{(1)}$ and $\lambda > 0$ at $k_n^{(1)} < k < k_n^{(2)}, n = 1, 2, \dots$. In the second case, the cavity is unstable related to oscillations having frequencies $k > k_1^{(1)}$.

Graphs of the real and imaginary parts μ versus β are given in Fig. 10, a, b. We can see that the cavity is asymptotic stable when $1 \leq \beta < \beta_1^{(1)}$ and unstable when $\beta > \beta_1^{(1)}$. Oscillations with reduced frequency $k_n^{(1)}$ are excited when the parameter β passes through the value $\beta_n^{(1)}$.

It is natural to suppose that the frequency k is realized having the highest value of the increment power λ . This assumption permits to evaluate the limits of cavity self-induced oscillation modes $\beta_N^{min}, \beta_N^{max}, N = 1, 2, 3, \dots$. They are shown by vertical dashed lines in Fig. 10, a, b.

Kinematic waves extending with the velocity V_∞ arise due to the pressure pulsation on the unstable cavity. Approximately N waves are packed along the cavity length at the N th oscillation mode.

Graphs of the first reduced fundamental frequency of cavity $k_1 = \omega l_0 / V_\infty$ and corresponding value of the parameter β_1 versus the jet half-width h are shown in Fig. 11. It is seen that variation of the jet width influences very weakly on the reduced frequency k_1 . A influence of the jet width on the parameter β_1 becomes weak when $h < l_\infty / 2$, and this effect decreases when the number n increases.

CONCLUSION

Two numerical-analytical methods for calculation of the flow past the supercavitating and ventilated two-dimensional hydrofoils at harmonic time dependence are compared. Both the methods give resonance frequency responses of the cavity pressure oscillation and the hydrodynamic force oscillation.

The method to calculate the variable length of the unsteady supercavity $l(t)$ is proposed. It is shown that taking account of the cavity length variability does not essentially influence on frequency response of the hydrodynamic forces. Thus, the simple numerical algorithm with the constant cavity length may be used to calculate the unsteady forces.

A stability of the ventilated cavity in a free jet is investigated. It is shown that the decrease of the free jet half-width h weakly influences on the cavity fundamental reduced frequencies k_n which are undimensioned with respect to the undisturbed cavity length in jet $l_0(h)$. Also corresponding values of the parameter β_n decrease when h decreases. However, this influence is weak. These conclusions are valid for evaluation of limits of the cavity pulsation modes β_N , k_N as well. The obtained results are in good agreement with experimental data on pulsation of two-dimensional ventilated cavities [7, 8].

The developed calculation methods are of use practically. Having data about the fundamental cavity frequencies and the sea-way parameters, we can avoid undesirable resonance modes by changing the air supply rate into the cavity, i.e. the cavity length in formula (20).

REFERENCES

1. Tulin, M.P., "Supercavitating Flows — Small Perturbation Theory", *Journal of Ship Research*, Vol.7, No.3, 1964, pp.16–37.
2. Yegorov, I.T., ed., Sadovnicov, Yu.M., Isaev, I.I., Basin, M.A., *Artificial Cavitation*, Sudostroenie, Leningrad, 1971, 283 p. (in Russian).
3. Yefremov, I.I., *Linearized Theory of Cavitating Flow*, Naukova dumka, Kyiv, 1974, 156 p. (in Ukrainian).
4. Rozhdestvensky, V.V., *Cavitation*, Sudostroenie, Leningrad, 1971, 248 p. (in Russian).
5. Gurevich, M.I., *Theory of Ideal Liquid Jets*, 2nd ed., Nauka, Moscow, 1979, 536 p. (in Russian).
6. Basin, M.A., Shadrin, V.P., *Hydrofoil Hydrodynamics near Boundary of Medium Division*, Sudostroenie, Leningrad, 1980, 304 p. (in Russian).
7. Silberman, E., Song, C.S., "Instability of Ventilated Cavities", *Journal of Ship Research*, Vol.5, No.1., 1961, pp.13–33.
8. Michel, J.-M., "Ventilated Cavities. A Contribution to the Study of Pulsation Mechanism", *Non-Steady Flow of Water at High Speeds. Proceedings of the IUTAM Symposium held in Leningrad*, Nauka, Moscow, 1973, pp.343–360.
9. Semenenko, V.N., "Instability of a Plane Ventilated Supercavity in an Infinite Stream", *International Journal of Fluid Mechanics Research*, Vol.23, Nos.1 & 2., 1996, pp.134–143.
10. Semenenko, V.N., "Instability and Oscillation of Gas-Filled Supercavities", *Proceeding of Third International Symposium on Cavitation*, Vol.2., Grenoble, France, 1998, pp.25–30.
11. Brennen, C., Oey, K.T., Babcock, C.D., "Leading-Edge Flutter of Supercavitating Hydrofoils", *Journal of Ship Research*, Vol.24, No.3, 1980, pp.135–146.
12. Semenenko, V.N., "Calculation of Unsteady Hydrodynamic Characteristics of Ventilated Two-Dimensional Hydrofoil near Waved Water Surface", *Journal of Hydromechanics*, No.48, 1983, pp.6–10 (in Russian).
13. Yefremov, I.I., Semenenko, V.N., "Cavitating Flow around Oscillating Two-Dimensional Hydrofoil", *Izvestiya AN SSSR. MZhG*, No.1, 1975, pp. 163–166 (in Russian).
14. Vladimirov, V.S., *Equations of Mathematical Physics*, 2nd. ed., Nauka, Moscow, 1971, 512 p. (in Russian).
15. Gahov, F.D., *Boundary Value Problems*, 2nd ed., Fizmatgiz, Moscow, 1963, 640 p. (in Russian).
16. Nishiyama, T., "Unsteady Supercavitating Hydrofoil Theory at Non-Zero Cavitation Number", *Technology Reports, Tohoku Univ.*, Vol.37, No.2, 1972, pp.259–282.
17. Nishiyama, T., "Unsteady Cavity Flow Model for Two-Dimensional Super-Cavitating Hydrofoils in Oscillation", *Technology Reports, Tohoku Univ.*, Vol.46, No.2, 1982, pp.199–216.
18. Makaseev, M.V., "On Bounded Flow around a Supercavitating Hydrofoil of Finite Span", *Izvestiya AN SSSR, MZhG*, No.4, 1985, pp.64–68 (in Russian).
19. Belotserkovsky, S.M., Lifanov, I.K., *Numerical Methods in Singular Integral Equations*, Nauka, Moscow, 1985, 256 p. (in Russian).

SHIP WAVE MAKING OVER A NATURAL TOPOGRAPHY

Xue-Nong Chen

VBD-European Development Centre for Inland and Coastal Navigation,

Klößnerstr. 77, D-47057 Duisburg, Germany.

Tel: +49 203 993 69-0; Fax: +49 203 36 1373

ABSTRACT

The problem of ship wave making and propagation in shallow water over a varying topography is studied. A shallow water model, namely a varying-coefficient Kadomtsev-Petviashvili type equation, and the improved slender body theory are developed and used for such problem. The computer code SHALLOWTANK, which dealt previously only with ship motion on a constant-depth shallow water, is further extended for the transversally varying depth. A typical case, a container ship in a natural waterway for which the hydraulic model experiments were carried out at the Coastal Division, Federal Waterways Engineering and Research Institute, Hamburg, is numerically simulated. It shows that the effects of topography on generation and propagation of ship waves are significant. The phenomenon of ship wave shoaling is clearly observed in the numerical result. The calculated free surface elevations at five points are compared to the measurements. Satisfied agreements are achieved.

INTRODUCTION

This paper concerns the problem of ship wave-making in shallow water over a varying topography. Ship waves will become serious, if the ship speed and size are increased and the topography of a waterway is not homogeneous. The large ship size makes coastal and inland waterways relatively shallow. A ship at a high speed in shallow water generates huge waves. The inhomogeneous bottom topography of a natural waterway may cause the ship waves even more complicated and more harmful to the river-bed and banks. These actually pose a new task for computational shallow-water ship hydrodynamics in conjunction with hydraulic engineering.

Traditionally, the ship wave-making problem is investigated in numerical calculation, or even in towing tank experiment, for the idealised case of uniform water depth and, usually without taking explicit account of wave-bank interaction, e.g. to see Graff *et al.* (1964), Bertram (1997) and Uliczka & Bertram (1997). This paper is an attempt to overcome these limitations. Direct numerical simulation including the effect of un-

even topography and the interaction with banks is intended. A shallow water model is proposed for such problem. By reasonable assumptions, a Kadomtsev-Petviashvili (KP) type equation with varying coefficients due to the topography is derived. The computer code SHALLOWTANK, which dealt previously with ship motion in a channel with vertical sidewalls of uniform depth (Chen & Sharma 1994, 1995), is further extended for the transversally varying depth.

A typical example of a large container ship in a section of the river Elbe is calculated. The effect of the topography on ship motion and wave-making is shown. The calculated results of wave profiles are compared with measurements that were carried out at the Coastal Division, Federal Waterways Engineering and Research Institute (BAW-AK), Hamburg, Germany. The agreement is satisfied. It is also seen that the ship wave shoaling takes place, i.e. ship waves propagate onto and back from river shallow banks. The study of this phenomenon is of importance from a hydraulic engineering point of view, namely, in river bank protection.

MATHEMATIC MODEL

It is considered that a slender ship of length l^* , free to heave and pitch, moves at a constant speed U^* in a natural inland waterway of a typical depth h_0^* . Because of both asymmetric ship motion and the bottom topography, the flow is generally asymmetric about the straight line, along which the ship moves. A typical situation is shown in Figure 2, which was investigated experimentally at the BAW-AK and is simulated numerically tentatively in this paper. The flow is assumed to be incompressible and irrotational. The water is assumed to be relatively shallow with respect to ship length. For the bottom topography it will be provided that the bottom varies slowly in the transverse direction and even more slowly in the longitudinal direction.

For the conventional problem of ship moving in a constant-depth shallow water, Chen & Sharma (1994, 1995) developed a nonlinear theory. Based on matched asymptotic expansions the whole flow field is divided into near and far-fields. In the near-field the slender body theory is improved by considering higher-order effects, while in the far-field a modified KP equation is used. The matching condition provides a boundary condition in the position of the ship for the mKP equation. The treatment of near-field and the matching condition is same as in previous papers, but the far-field equation must be changed, since the effect of inhomogeneous bottom must be taken into consideration. In the following we give briefly a derivation of the far-field equation and list the matching condition as much as necessary.

Due to uneven bottom two Cartesian coordinate systems must be used. A coordinate system $Oxyz$, namely, moving reference frame, moving at the same speed as the ship is set with origin O located in the midship section, Ox along the direction of motion, plane Oxy on the quiet free surface, and z positive upward. The other $Ox'y'z'$, namely, quiet reference frame, is fixed at the earth.

In the regime of Boussinesq theory there are two small parameters defined by

$$\varepsilon = \alpha^*/h_0^*, \quad \mu = h_0^*/L^*,$$

where α^* and L^* are typical wave amplitude and length. Without loss of generality, for ship wave-making problem, we set $\mu = \sqrt{\varepsilon}$. The starting point of the formulation of the far-field is a

concise form of Boussinesq equations derived by Chen (1989), in terms of quiet coordinates,

$$\zeta_{t'} + \nabla' \cdot [(h + \varepsilon\zeta)\nabla'\Phi_0] = \frac{\mu^2}{6} \nabla'^2 [\nabla' \cdot (h^3 \nabla'\Phi_0)] + O(\mu^4, \varepsilon\mu^2), \quad (1)$$

$$\left[1 - \frac{\mu^2}{2} \nabla' \cdot (h^2 \nabla')\right] \Phi_{0t'} + \zeta + \frac{\varepsilon}{2} \nabla'\Phi_0 \cdot \nabla'\Phi_0 = O(\mu^4, \varepsilon\mu^2). \quad (2)$$

where

$$\begin{aligned} \frac{\zeta^*}{\varepsilon h_0^*} &\rightarrow \zeta, \quad \frac{\Phi^*}{\sqrt{\varepsilon h_0^*} \sqrt{g^* h_0^*}} \rightarrow \Phi, \quad \frac{h^*}{h_0^*} \rightarrow h, \\ \frac{p^*}{\rho^* g^* h_0^*} &\rightarrow p, \quad \frac{\mu t^* \sqrt{g^* h_0^*}}{h_0^*} \rightarrow t, \\ \frac{\mu}{h_0^*} (x^*, y^*) &\rightarrow (x, y), \quad \frac{z^*}{h_0^*} \rightarrow z, \end{aligned} \quad (3)$$

where all variables carrying asterisk $*$ are dimensional.

What follows is to derive a Kadomtsev-Petviashvili type equation that is much easier to solve numerically than Boussinesq equations. Further assumptions should be proposed: (i) the water depth varies slowly in the transversal direction and even more slowly in the longitudinal direction; (ii) the time-varying is even slower than permitted in Boussinesq equations. It may be more convenient to employ the depth-averaged potential that is defined as

$$\varphi = \frac{1}{h + \varepsilon\zeta} \int_{-h}^{\varepsilon\zeta} \Phi dz. \quad (4)$$

By shallow water expansions, we have

$$\varphi = \Phi_0 - \frac{\mu^2}{6} h^2 \nabla^2 \Phi_0 + O(\mu^4, \varepsilon\mu^2),$$

or inversely

$$\Phi_0 = \varphi + \frac{\mu^2}{6} h^2 \nabla^2 \varphi + O(\mu^4, \varepsilon\mu^2).$$

Transforming equations (1), (2) in moving coordinates, i.e. $\partial/\partial t' \rightarrow \partial/\partial t - U\partial/\partial x$, where $U = U^*/\sqrt{g^* h_0^*}$ is the depth Froude number, and substituting ζ in (1) into (2), we obtain an extended KP equation,

$$\begin{aligned} 2\varepsilon U \varphi_{x\tau} + (h - U^2) \varphi_{xx} + h \varphi_{yy} + h_y \varphi_y \\ + \frac{\mu^2}{3} h^2 U^2 \nabla^2 \varphi_{xx} + \frac{3\varepsilon U}{2} (\varphi_x^2)_x \end{aligned}$$

$$+2\epsilon U \varphi_{xy} \varphi_y + \epsilon U \varphi_x \varphi_{yy} = 0 \quad (5)$$

In fact, the above equation is precise to same order as Boussinesq equations (1) and (2). Discussion on stationary dispersion relation of its linearised form given by Chen & Sharma (1996) shows that the term φ_{xyy} will make the dispersion relation differ more from the exact one of linear finite depth theory than without it in the subcritical and transcritical speed ranges. Hence, it is believed heuristically that the equation without φ_{xyy} will produce better results than that with it. So we choose the following equation as the governing equation in the far-field,

$$\begin{aligned} 2\epsilon U \varphi_{x\tau} + (h - U^2) \varphi_{xx} + (h + \epsilon U \varphi_x) \varphi_{yy} \\ + h_y \varphi_y + \frac{\mu^2}{3} h^2 U^2 \varphi_{xxx} \\ + \frac{3\epsilon U}{2} (\varphi_x^2)_x + 2\epsilon U \varphi_{xy} \varphi_y = 0, \end{aligned} \quad (6)$$

which is still of KP-type.

The boundary condition at the ship location is derived by the matching asymptotics and the improved slender body theory, see Chen & Sharma (1994) for details. Here we only list the necessary results. The boundary condition at the ship location reads

$$\begin{aligned} \frac{\partial \varphi}{\partial y} \Big|_{y=\pm 0} = \mp \frac{\sqrt{\epsilon}}{2} \frac{1}{1 + \epsilon \zeta_0} \frac{d}{d\hat{x}} \left[\hat{S}(\hat{x}, \tau) (U - \epsilon u_0) \right] \\ + \frac{\sqrt{S_0^*}}{l^*} \frac{\varphi|_{y \rightarrow +0} - \varphi|_{y \rightarrow -0}}{2\epsilon^2 C(\hat{x}, \tau)}, \end{aligned} \quad (7)$$

where $\hat{x} = x^*/l^*$, $C = C^*/\sqrt{S_0^*}$ is the blockage coefficient and \hat{S} is the dynamic instantaneous cross-sectional area, that can be expressed approximately as

$$\begin{aligned} \hat{S}(\hat{x}, \tau) = \frac{S^*(\hat{x})}{S_0^*} + \frac{h_0^*}{S_0^*} b^*(\hat{x}) \times \\ \left[\frac{l^*}{h_0^*} (s(\tau) - \hat{x} \theta(\tau)) + \epsilon \zeta_0 \right] \end{aligned}$$

The small parameter ϵ is determined by the normalisation of the boundary condition as

$$\epsilon^{3/2} = \frac{S_0^*}{l^* h_0^*}.$$

Since the problem is almost locally symmetric about the longitudinal ship hull axis, i.e. $\varphi|_{y \rightarrow +0} - \varphi|_{y \rightarrow -0}$ is almost zero, the blockage coefficient has a very small effect. Therefore it can be evaluated by any reasonable estimation. Here it is evaluated by the formula for the rectangular cross section with small under-keel clearance given by Taylor (1973).

EXPERIMENTS

The measurements were carried out by the BAW-AK in the range of the project "Adapting the Lower and Outer Elbe Fairway to Container Shipping - Ship Induced Loading" in order of the Federal Waterway and Shipping Administration of Germany (Uliczka 1998). The hydraulic model (scale 1:40) covered a section of the Elbe estuary of about 1.8 km² (river-km 644.6 to river-km 645.2; bearing from 1992), where the Wedel Wadden area was reproduced up to Höhenkoten at mean sea level. The modelled topography consisted of steep southern banks (Lühe) and mild slopes in the northern part (Wedel). The test basin including acceleration and stopping zones had dimensions of about 100 m × 35 m × 0.6 m. The ship model that has the same scale as the hydraulic model is made for a PANMAX-Containership of length $l^* = 280$ m, beam $b_0^* = 32.2$ m, draft $d^* = 13.8$ m and block coefficient $C_B = 0.695$.

In the cross section of the river, probes registered at 21 points the water level and at 11 locations the 2D-current. 3D-current was measured 2 m above the bottom in the line of the incoming ship track and pressure at bottom was taken near the 3D-current meter. The ship speed and the squat were measured by a laser beam and rectangular and triangular sheets using the method published by Eryuzlu *et al.* (1994). The accuracy of the measurements were carried out with a standard deviation of $\sigma < 0.05$ m and $\sigma < 0.05$ m/s, the ship speed was measured with $\sigma < 0.1$ knots in field scale.

The incoming and outgoing container vessels sailed with a bank clearance of about one ship width, so that the navigation axis was situated parallel to the fairway boundary for a stretch of 60 m. The passing distance for an incoming ship was about 220 m to the Lühe landing-pier and for an outgoing ships about 410 m to the Wedel groyne head. The model ship was wireless-controlled and driven by a propeller with fixed number of revolutions. The model was directed by a guide cable and was trimmed "highly stable" in order to minimise any random outer influences on the ships' movement and thus on the loading induced by the ships. The influence of navigating the bend on the local wave picture and the

current conditions was determined by measurements taken during test runs with a steersman in the model ship and by drift angle runs compared to cable runs. The differences in the ship induced loading in the measurement cross-section were negligible.

The ship-length relevant Froude numbers $F_{nl} = U^*/\sqrt{l^*g^*}$ were between $0.08 < F_{nl} < 0.22$. The depth-Froude numbers $F_{nh} = U^*/\sqrt{h_0^*g^*}$ were between $0.25 < F_{nh} < 0.63$. The Reynolds numbers $R_n = U^*l^*/\nu^*$ for the model experiments were $3 \times 10^6 < R_n < 8 \times 10^6$. The prediction capability of the model was thus guaranteed.

The large values of the drawdown and the current near the steep bank showed the effect of the asymmetric cross section for incoming ships and the ship speed. At ship speeds of more than 12 knots the hydraulic loads on the river bed, due to the container ship, increase greatly and the risk of demolition of banks and revetments increases, too.

NUMERICAL RESULTS

The previous computer code SHALLOWTANK (Chen & Sharma 1994, 1995) is now equipped by an uneven bottom, so that one can use it to solve the problem of ships over an uneven topography. The topography used in the following example is simplified to be varying only in the transversal direction, i.e. $h = h(y)$.

We numerically simulate the container ship of IV. Generation PANMAX in the section of the river Elbe, which is almost in the same situation as in the experiment as described in the last section. The principal dimensions are listed: ship length $l^* = 280$ m; beam $b_0^* = 32.2$ m; draft $d^* = 13.8$ m; volume displacement $V = 87,200$ m³; wetted surface area $S_w = 13,500$ m². The cross-sectional area and the beam curve at the waterline are shown in Figure 3. The ship speed in full scale is $U^* = 15.4$ knots, corresponding depth Froude number $U = 0.586$ with respect to the local water depth $h_0^* = 18.65$ m at the ship track.

The profile of a cross section of the river Elbe is shown in Figure 2. Five measure points are selected. The calculated wave pattern is shown by a 3-D plot in Figure 4 and a contour plot in Figure 5. A detailed 3-D plot is shown in Figure 6. Since the simulation is on a large scale, it is quite time-consuming. The present grid size $\Delta x^* \times \Delta y^* = 7 \times 10$ m² does not seem to be enough fine, see Figure 6. Calculations on finer

grids will be tried.

The calculated wave elevations are transformed to be processes of time at the five earth fixed points, at which the measurements are available. The comparison is shown in Figure 7. The calculated results agree satisfactorily with those of the experiment, especially at Points P1 and P2, which are nearest points to the river bank and the ship, respectively. The maximum of the calculated wave elevation at P1 is almost same as the measured value, which can supply a norm for the hydraulic engineering. Figure 8 shows a temporal series of the ship waves at a river cross-section. As the ship is going through this section, the generated waves propagate onto river banks and then are reflected by river banks. Note that the river bank is not a vertical wall, but a slowly varying bottom topography. This phenomenon is called ship wave shoaling, which is of importance in hydraulic engineering, saying more precisely, in river bank protection. The present computation shows the prognosis capability, however, the computer program will be further verified by the detailed measurements.

CONCLUSION

A mathematic model is developed for the problem of ships in shallow natural waterways and the corresponding computer program is made for the case of the transversally varying topography. A typical example of a container ship in a natural waterway is numerically simulated, for which the measurements were carried out at the BAW-AK. The tentative numerical results agree satisfactorily with measurements.

ACKNOWLEDGEMENT

The authors is supported by a research project (03-KI7ST1-4) sponsored by the German Federal Ministry of Education, Science, Research and Technology (BMBF) and thanks Dr.-Ing. K. Uliczka at the BAW-AK, Hamburg, for his helpful cooperation and, especially, for providing the experiment data.

References

- [1] Graff, W, Kracht, A. & Weinblum, G. 1964 Some extension of D: W. Taylor's standard series. *Trans. Soc. Nav. Arch. Mar. Engrs.* 72, pp. 374-401.

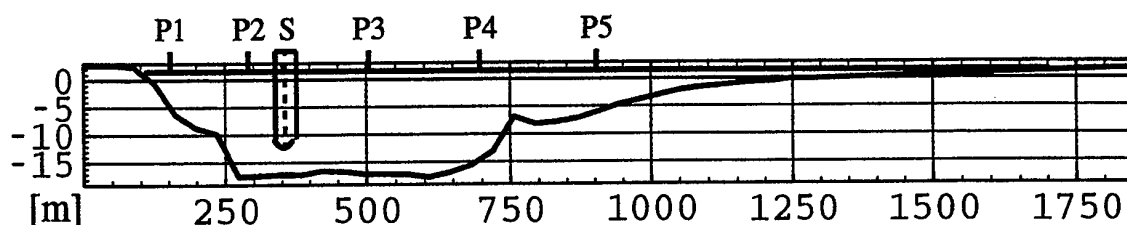


Figure 2: The profile of a cross section of the river Elbe with the ship position S (353 m) and five measure points: P1 (149 m), P2 (288 m), P3 (499 m), P4 (688 m), P5 (895 m). The water depth at the ship track $h_0^* = 18.65$ m.

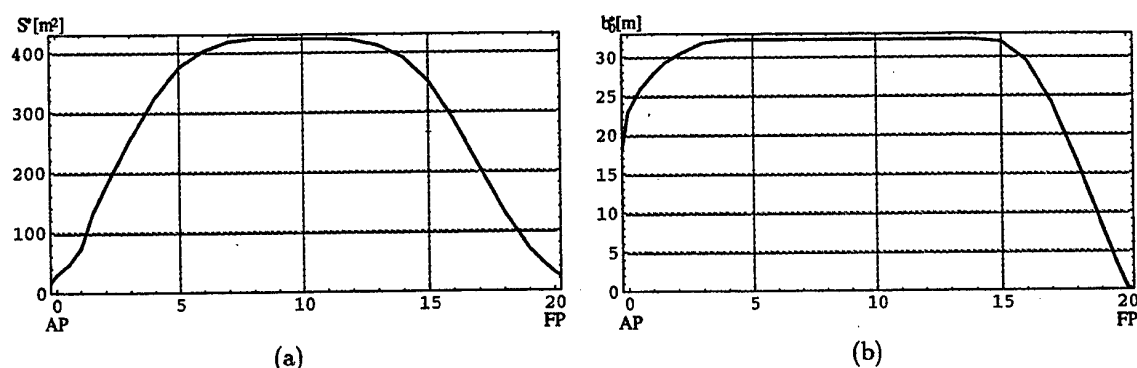


Figure 3: (a) The cross-sectional area S^* in square meter vs stations; (b) the beam b^* at the water-line in meter vs stations.

- [2] Bertram, V. 1997 Schwellprognose per Computer für ein SES. *Binnenschiffahrt* 52. Jahrgang Nr. 11, Juni-Ausgabe, pp.32-33.
- [3] Uliczka, K. & Bertram, V. 1997 Stellungnahme zum Artikel von Dr.-Ing. V. Bertram und Stellungnahme des Verfassers. *Binnenschiffahrt* 52. Jahrgang Nr. 13, Juli-Ausgabe, pp.34-35.
- [4] Chen, X.-N. & Sharma, S. D. 1994 Nonlinear theory of asymmetric motion of a slender ship in a shallow channel. *20th Symposium on Naval Hydrodynamics*, Santa Barbara, California, (ed. E. P. Rood), pp.386-407. US Office of Naval Research.
- [5] Chen, X.-N. & Sharma, S. D. 1995 A slender ship moving at a near-critical speed in a shallow channel. *J. Fluid Mech.* 291, 263-285.
- [6] Chen, X.-N. 1989 Unified Kadomtsev-Petviashvili equation. *Phys. Fluids A* 1, 2058-60.
- [7] Chen, X.-N. & Sharma, S. D. 1996 On ships at supercritical speeds. *21st Symposium on Naval Hydrodynamics*, Trondheim, Norway, (ed. E. P. Rood), pp.147-158. US Office of Naval Research.
- [8] Taylor, P. J. 1973 The blockage coefficient for flow about an arbitrary body immersed in a channel. *J. Ship Res.* 17, 97-105.
- [9] Uliczka, K. 1998 Interaction between sea-going ship and estuary fairway. *29th PIANC International Navigation Congress*, Hague, Netherlands, Section II, Subject 1, pp. 27-30.
- [10] Eryuzlu, P., Cao, Y.L. & D'agnolo, F. 1994 Underkeel requirements for large vessels in shallow waterways. *28th Int. Navigation Congress of PIANC*, Section II-2, Seville, Canada.

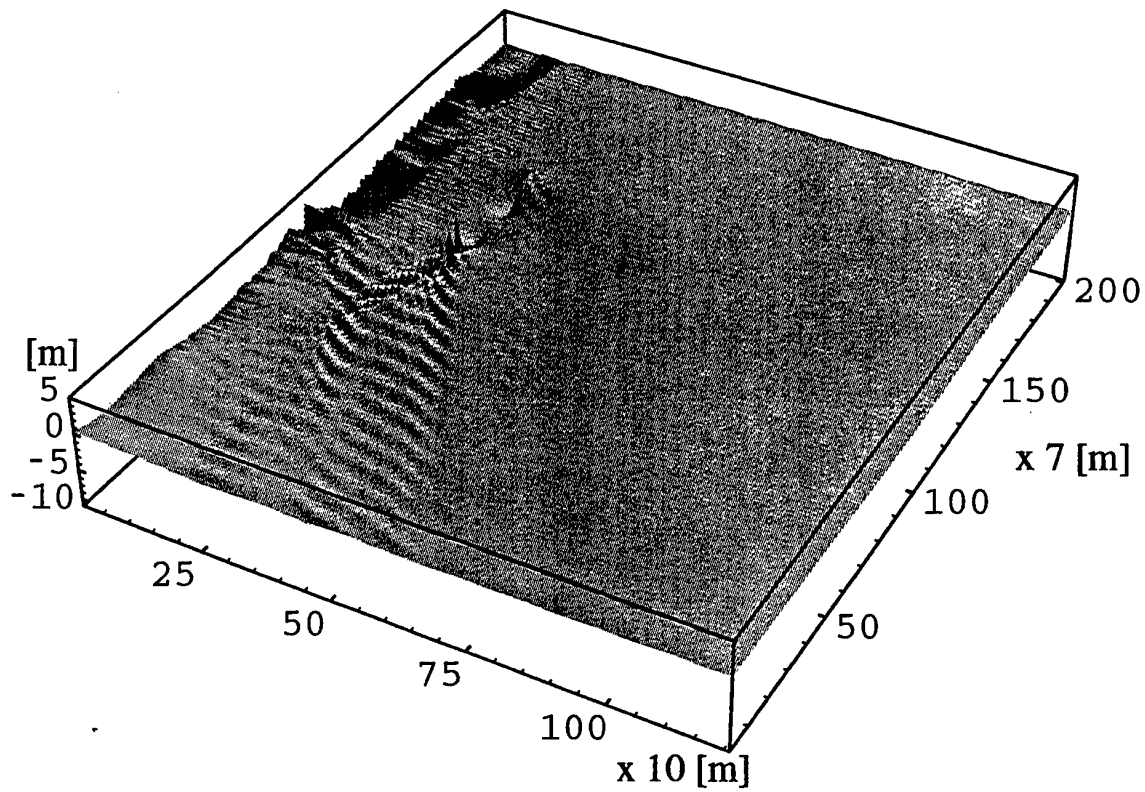


Figure 4: 3-D plot of the calculated ship wave pattern over the varying topography, where the vertical scale is exaggerated 15 times for the sake of clarity.

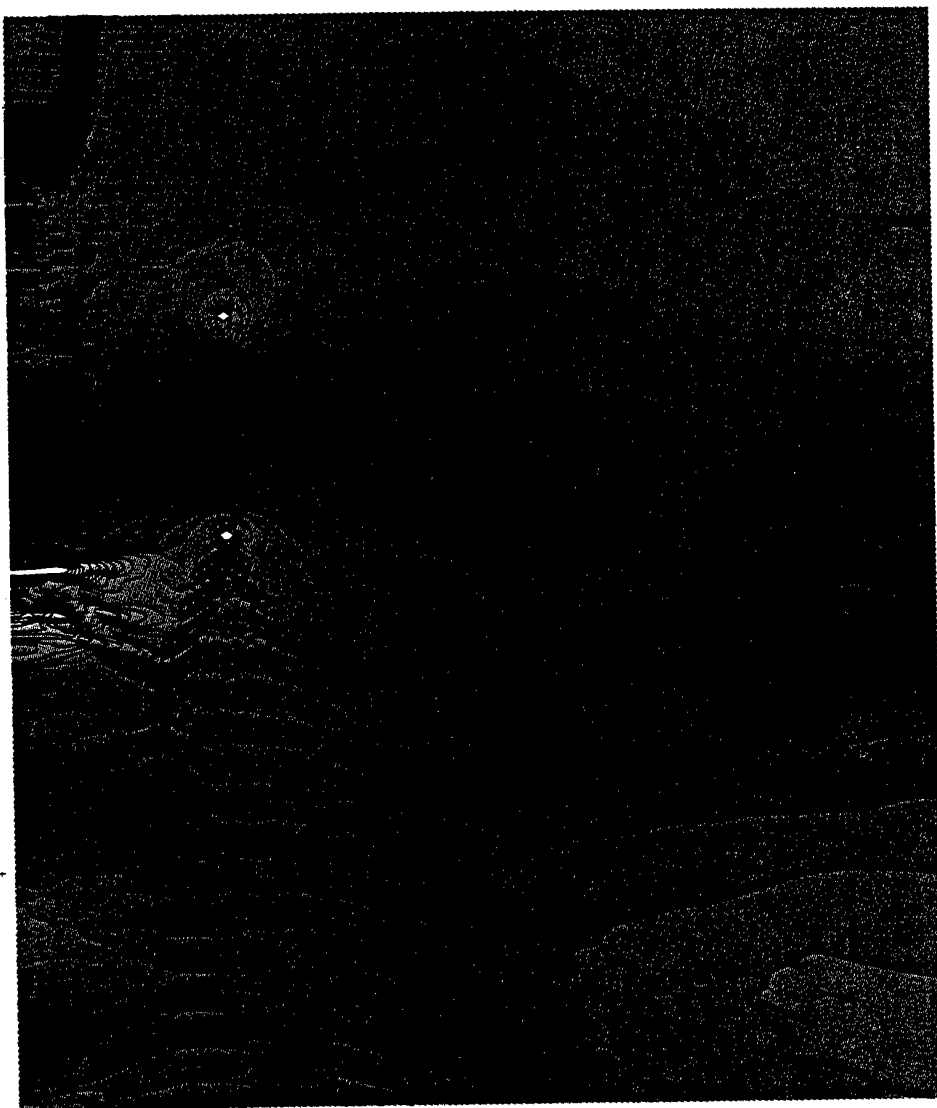


Figure 5: Contour plot of the same calculated ship wave pattern.

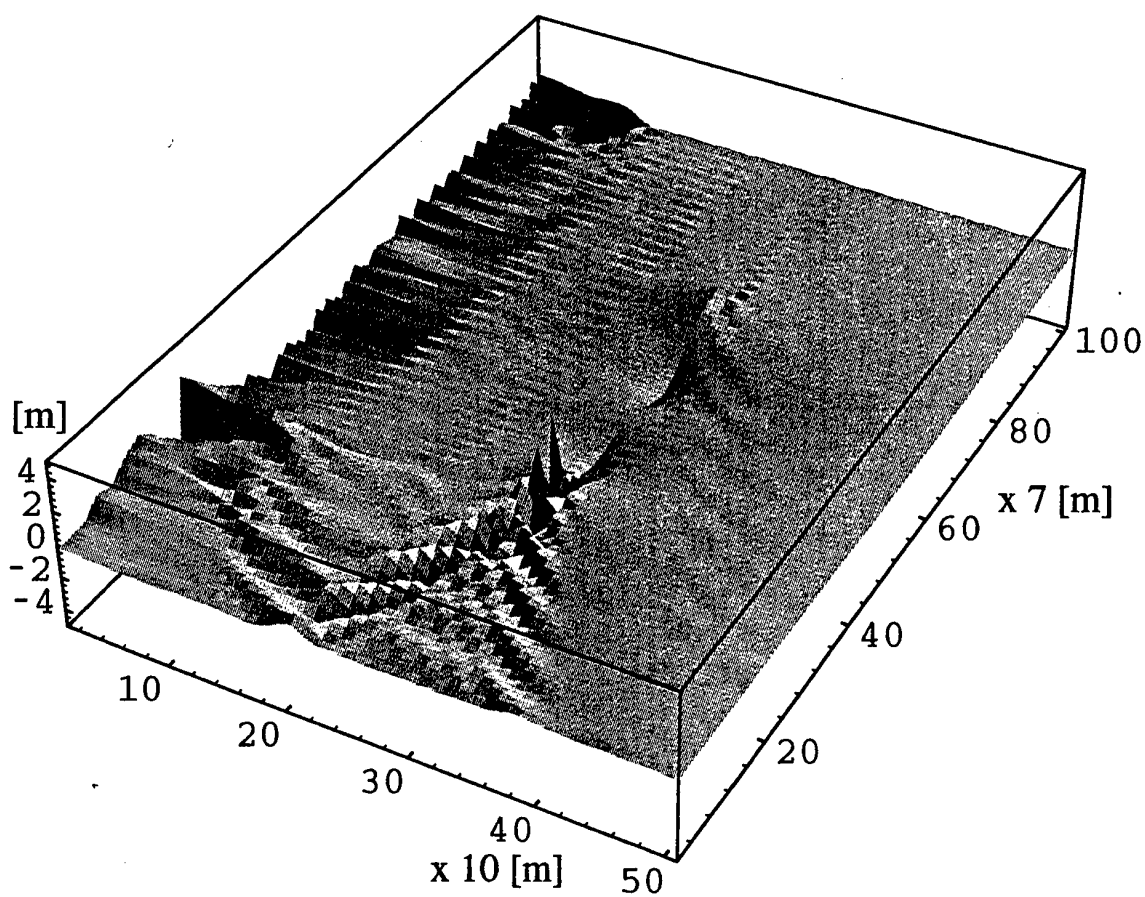


Figure 6: 3-D graph of the same wave pattern around the ship in detail ($500 \times 700 \text{ m}^2$), where the vertical scale is exaggerated 15 times.

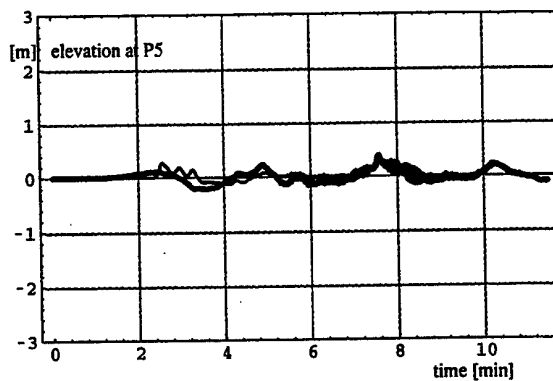
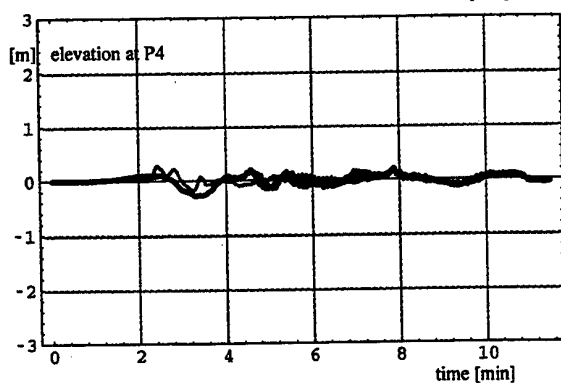
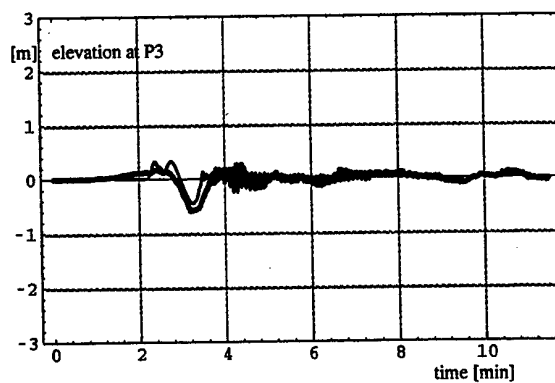
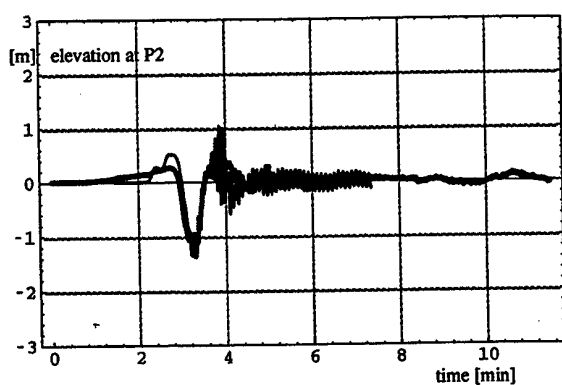
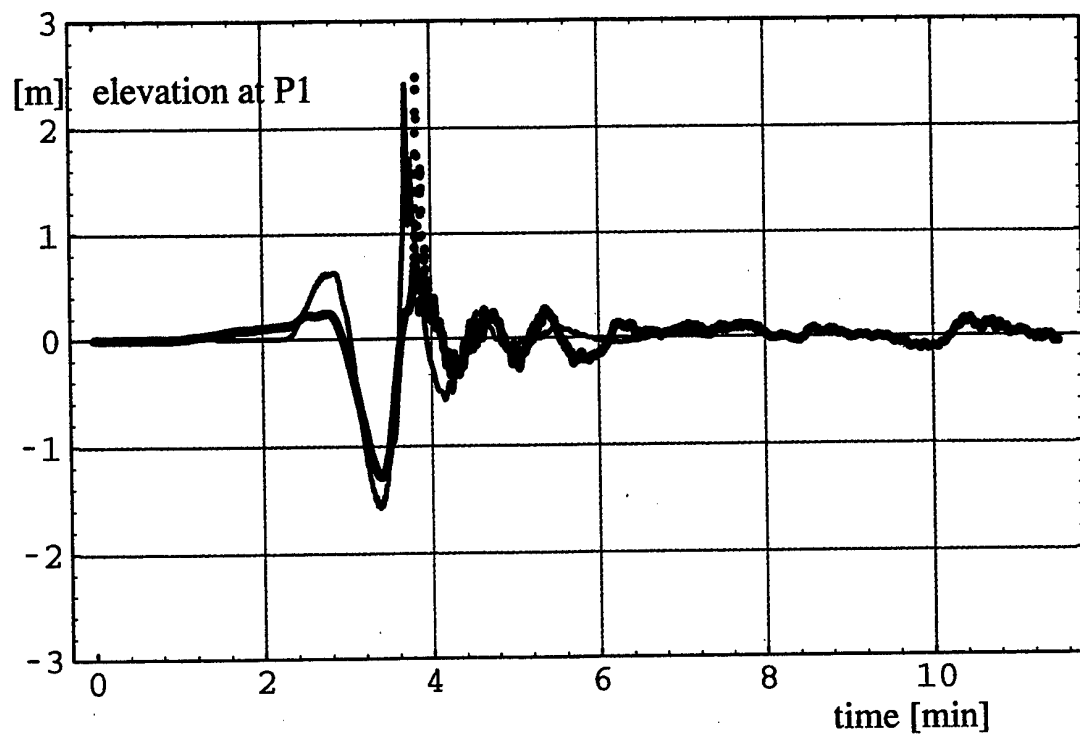


Figure 7: The calculated wave elevations at the five points as processes of time are compared to measurements, thin and thick lines stand for calculated and measured results, respectively.

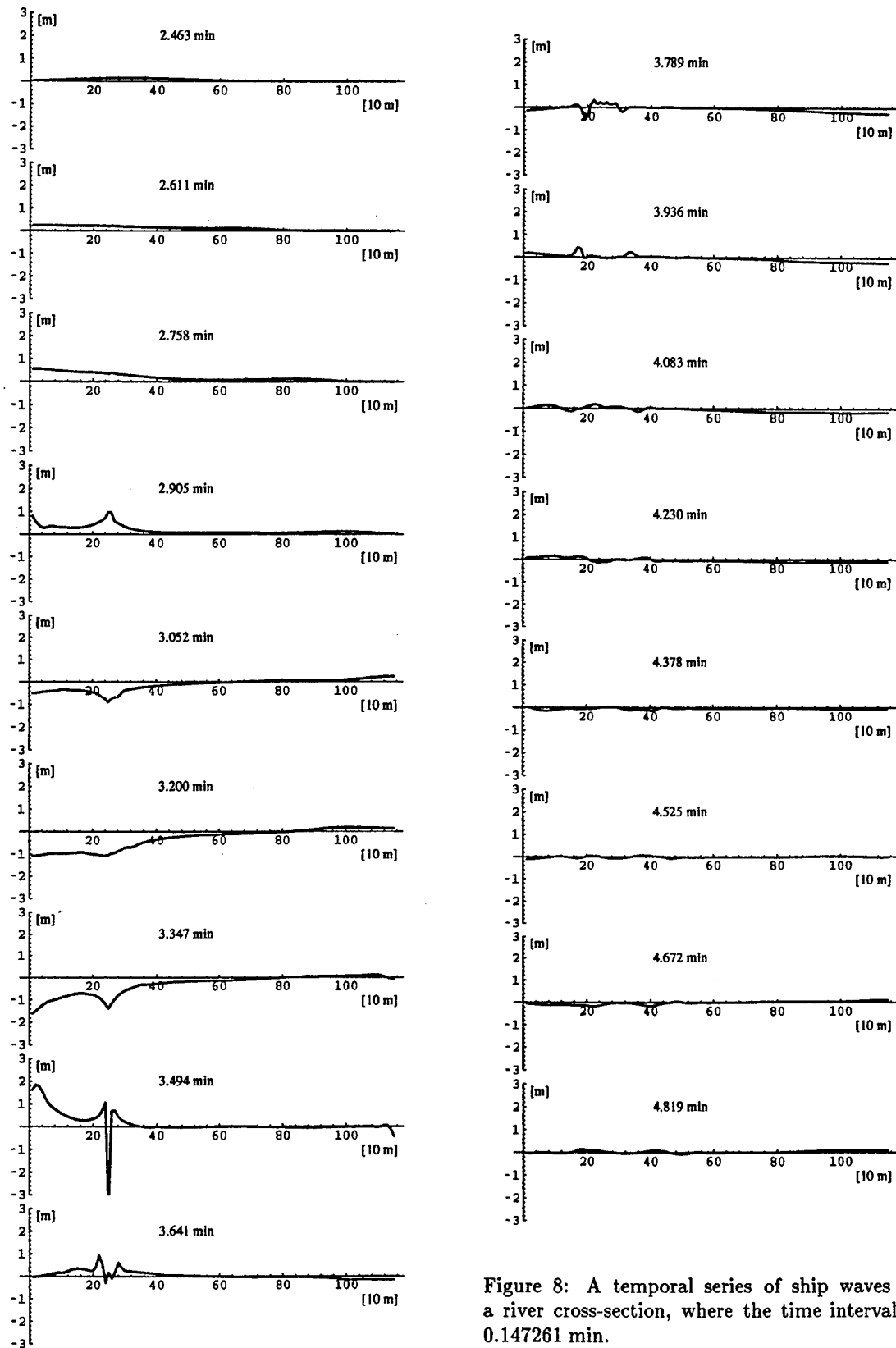


Figure 8: A temporal series of ship waves at a river cross-section, where the time interval is 0.147261 min.

PERIODIC WAVE IMPACT ONTO AN ELASTIC PLATE

A. A. Korobkin and T. I. Khabakhpasheva

Laboratory of Hydroelasticity, Lavrentyev Institute of Hydrodynamics,
15 pr. ac. Lavrentyeva, Novosibirsk 630090, Russia.
Fax: 3832 33 16 12; E-Mail: KAA@hydro.nsc.ru, TANA@hydro.nsc.ru

ABSTRACT

A computational analysis is presented for the impact of an elastic plate dropped against regular long waves. The problem is considered within the linear potential flow theory. The liquid flow is two-dimensional and the plate is modelled by an Euler beam. The analysis is based on the normal mode method with hydroelastic behaviour of the plate being of main interest. Different impact conditions are considered, to study the dependence of the total energy of the plate-liquid system on impact geometry and plate properties. The contributions of kinetic and potential energies to the total energy are analysed. It is shown that the kinetic part of the system energy is small at the instant of time when bending stresses in the beam approach their maximum values. Estimations of both the total energy and the maximum of bending stresses are presented. Main part of calculations are performed for the conditions of experiments carried out in MARINTEK. A range of the problem parameters is considered also, to reveal peculiarities of the unsteady interaction between falling elastic plate and surface waves.

1 Introduction

The plane unsteady problem of an elastic plate falling down onto liquid free surface covered with regular long waves is considered. Initially ($t' = 0$) the plate touches the wave profile and starts to move down thereafter with a constant velocity V . The position of the left edge of the plate at the initial moment is taken as the origin of the Cartesian coordinate system $x'Oy'$ (dimensional variables are denoted by a prime). The wave is assumed linear and its shape before the impact given by the equation

$$y' = a[\cos(\nu[x' - x'_1] - \omega t') - 1], \quad (1)$$

where a is the wave amplitude, ω is the wave frequency, ν is the wavenumber, $\omega^2 = g\nu$ for a deep water, x'_1 is the distance of the impact point from the left edge of the plate (see Figure 1), g is the gravity acceleration, and $T_W = 2\pi/\omega$ is the wave period. The wave is assumed long, $a\nu \ll 1$. The

plate length $2L$ and the wave length $\lambda = 2\pi/\nu$ are of the same order, hence we have also $a/L \ll 1$. The impact velocity is assumed to be much less than the sound velocity in the resting liquid c_0 . Initially the plate is horizontal and undeformed. It corresponds to the interval $y' = 0, 0 < x' < 2L$. The shape of the plate is changed owing to its in-

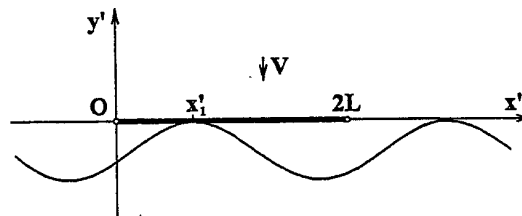


Figure 1: Elastic plate and the free surface at the impact moment.

teraction with the liquid. The plate is dry at the initial moment, $t' = 0$, and only partially wetted

at the first stage of the process, which is referred to as the impact stage. During the second stage (penetration stage) the plate is totally wetted and continues to interact with the liquid. The presence of the contact points between the free surface and the elastic plate during the impact stage is the main feature of the problem. The positions of these points are unknown in advance and must be determined together with the liquid flow and the plate deflections. We shall successively determine the plate deflection and bending stresses in the plate, estimate the maximum stresses and analyse their dependence on impact conditions, initial shape of the liquid free surface and properties of the plate.

The analysis is based on the following assumptions: (1) the liquid is ideal and incompressible; (2) the liquid flow is two-dimensional and potential; (3) the plate deflection is governed by the Euler beam equation; (4) the beam edges are simply supported; (5) influence of the air as well as both external mass forces and surface tension are negligibly small; (6) the wave length is comparable to the beam length; (7) the wave amplitude is much smaller than the beam length; (8) duration of the impact stage T_i is much smaller than the greatest period of free vibrations of the plate in the liquid T_w and much greater than the time scale L/c_0 of the acoustic effects; (9) the elastic plate is the bottom of a rigid structure which penetrates the liquid with a constant velocity V ; (10) during the impact stage the contact points move monotonically with time; (11) the ratio VT_w/L is much less than unity.

Motivations for the present research come from ship hydrodynamics, where wave impact onto the wetdeck of a catamaran can be very severe and may lead to local damage of the wetdeck. This problem was intensively studied during the last seven years experimentally [1], [2], numerically [2]–[6] and theoretically [2], [7]. The study carried out by Norwegian researchers is based on the experiments by Aarsners [1] exclusively. Attempts to generalize the derived predictions to other experiments (see, for example, [8], [9]) were not done (see [2]). It should be noted that other experiments did not receive so intensive theoretical analysis as Norwegian ones. Preliminary theoretical analysis of the experiments by Zhu & Faulkner [9] was given by Korobkin [10] with account for three-dimensional effects. The present study is based on the Norwegian experiments also. In addition to the theoretical analysis already carried out by Faltinsen and his group:

- 1) Modified method of normal modes is used. After modifications (a) calculations of the hydrodynamic loads are not required; (b) matrix of hydrodynamics coefficients is evaluated analytically; (c) positions of the contact points are governed by ordinary differential equations, which are incorporated into the system for the principal coordinates of the normal modes; (d) there are no obstacles to start numerical simulations from the initial moment, at which the size of the wetted area is zero; (e) there is no need to introduce the acoustic stage to describe formation of the contact region from a single point;
- 2) The study is focused on global characteristics of the interaction, which make it possible to explain energy redistribution during the impact and to estimate maximum stress amplitude;
- 3) A range of the problem parameters is considered to reveal peculiarities of the interaction. This may be helpful to design future experiments on elastic plate impact.

It is worth noting that assumptions (8) and (11) provide some limitations. The greatest period of free vibrations of the plate placed in unbounded liquid, T_w , is of the order $O([\rho L^5/EJ]^{1/2})$, where ρ is the liquid density, E is the elasticity modulus, J is the inertia momentum of the beam cross-section, $J = h^3/12$ for a beam of constant thickness h [2]. For a plate of length $2L$ comparable to the wavelength λ the duration of the impact stage T_i is of the order $O(a/V)$. In order to consider also the case of very long regular waves with $2L \ll \lambda$, radius of the curvature at the wave crest R is introduced, where $R = (av^2)^{-1}$. The wave profile can be approximated by the parabolic contour $y' = -(x' - x_1')^2/(2R)$ close to the impact point. Neglecting both the free surface deformation and the plate deflection during the impact stage, we can estimate the order of the impact stage duration as $L^2/(RV)$. This quantity is of the same order as a/V , where $L/\lambda = O(1)$, and of higher order, where $L/\lambda \ll 1$. Assumption (8) provides inequalities

$$\frac{L}{c_0} \ll \frac{L^2}{RV} \ll \sqrt{\frac{\rho L^5}{EJ}},$$

which lead to the following limitations for the impact velocity

$$[EJ/\rho L]^{1/2} \ll VR \ll c_0 L. \quad (2)$$

Experiments [5] were performed under the following conditions: $L = 0.25$ m, $E = 21 \cdot 10^{10}$ N/m², $\rho = 10^3$ kg/m³, $h = 0.008$ m, $c_0 = 1500$ m/s.

We obtain $(EJ/\rho L)^{1/2} \approx 6 \text{ m}^2/\text{s}$ and $c_0 L \approx 375 \text{ m}^2/\text{s}$. If the product VR approaches the lower bound in (2), the quantities T_i and T_W are comparable to each other. If the product approaches the upper bound, $c_0 L$, acoustic effects must be taken into account during the impact stage [11]. Assumption (8) is essential for theoretical analysis because it makes possible to separate the impact stage, during which large impact forces occur, and the penetration stage, at which the bending stresses approach their maximum values, and also to disregard the acoustic stage of the impact [2].

Assumption (11) gives $V \ll 24 \text{ m/s}$. This inequality guarantees that the bending stresses take their maximum values sufficiently before the penetration depth of the plate becomes comparable to the length scale L of the problem. Assumptions (7) and (11) indicate that, as a first approximation, we can put the boundary conditions on the line $y' = 0$ and to linearize them and the equations of motion. The ratio L/R , which is small, can be taken as the parameter of linearization.

At the leading order the liquid flow before the impact can be neglected compared to the flow caused by the impact for $t'/T_W = O(1)$ if and only if $\nu L^5 \ll EJ/\rho g$, which gives $L/\lambda \ll 32$ for the experiment conditions. We obtain $T_W \approx 0.01 \text{ s}$, which is much smaller than the period 0.7 - 5.0s of regular waves used in the experiments [2]. Therefore within the experiment conditions, wave motion can be neglected and the liquid can be considered as being at rest at the impact instant with its free surface described by equation (1), where $t' = 0$.

It should be noted that even after all possible simplifications the problem is coupled (hydrodynamic loads are dependent on the beam deflection and vice versa) and nonlinear at the impact stage (dimension of the contact region is unknown in advance and has to be determined together with the liquid flow and the beam deflection). At the penetration stage the problem is linear and its solution can be readily found if the beam deflection and velocities of beam elements are given at the beginning of this stage. Those values are determined by the nonlinear solution of the problem at the impact stage.

Both the impact stage and the penetration stage of the plate-liquid interaction are analysed in the three main cases: (i) central impact (Figure 3); (ii) edge impact (Figure 4); (iii) impact with a cavity formation (Figure 8), with the help of the normal mode method [3]. After the modi-

fications [12] this method leads to infinite system of ordinary differential equations with respect to principal coordinates of the beam deflection and dimensions of the contact region. Computer programs developed for the three cases distinguished are combined to describe the plate impact under arbitrary conditions.

Numerical simulations are performed to determine details of the interaction during both the impact and penetration stages, the kinetic energy of the plate, its potential energy and the kinetic energy of the liquid flow. It was found that in spite of the short duration of the impact stage, the peculiarities of the initial shape of the free surface and the impact conditions are of great importance, the hydrodynamic loads are very high and are dependent on the velocity of the contact region expansion [13]. In the case of the edge impact it was revealed that within the framework of incompressible liquid model the velocity of the contact region expansion and, therefore, the hydrodynamic loads on the beam can be beyond all bounds owing to flexibility of the beam only. This phenomenon is of geometrical nature and occurs when the angle between the beam and the liquid free surface close to the periphery of the contact region tends to zero. In naval hydrodynamics this phenomenon is known as the bow flare slamming. In the case of the impact with a cavity formation the loads are unbounded for any parameters of the beam and waves. This is due to the observation that the angle is very small at the moment of the cavity collapse. In this case the contact region consists of two parts which are separated with a cavity. The presence of air in the cavity is not taken into account.

The mathematical formulation of the problem and general description of the present approach are given in Section 2. Modifications of the normal mode method are presented in Section 3 for the simplest case of central impact ($x'_1 = L$). The method is applied to the problem of edge impact ($x'_1 = 0$), which is a part of the original problem, in Section 4. Peculiarities of the impact stage are discussed and comparisons are presented for the beam behaviours at the end of the impact stage for both the central impact and the edge impact. Elastic plate impact with a cavity formation is analysed in Section 5. Vibration of the plate during the penetration stage is studied in Section 6 with the focus on comparison between the theoretical predictions and the experimental results. One of the features of the theoretical prediction for maximum bending stress evolution is overes-

timination of high mode contributions. Generation of high-frequency components of the bending stresses is investigated in Section 7. Global characteristics of the impact and their evolution in time are studied in Section 8. Energy conservation law and the results of numerical simulations of the impact are used in Section 9 to derive estimations of maximum bending stress amplitude. Main findings of the present study are formulated in Conclusion.

2 Formulation of the problem

The plane problem of the impact of an elastic beam onto the slightly curved free surface of an ideal incompressible liquid is considered in non-dimensional variables. The scales of the independent variables are chosen the same as in the rigid-body impact problem. They are: L is the length scale, $L^2/(RV)$ is the time scale, V is the velocity scale, $\rho V^2 R/L$ is the pressure scale, where ρ is the liquid density, Eh/R is the bending stress scale. In numerical analysis we use the scales, which characterize the impact stage. Generally speaking, we need to introduce another scales [2] to describe the process during the penetration stage. In particular, it is reasonable to take T_W as the time scale of the penetration stage and the product VT_W as the displacement scale. However, the description of the penetration stage is much simpler than that of the impact stage. That is why we do not expect any difficulties with its numerical study even if the choice of scales for the penetration stage is not optimal. More details about the orders of unknown quantities during the penetration stage can be found in [2] and [14].

Within the framework of the linearized impact theory, which is referred to as the Wagner theory [15], the flow domain coincides with the half-plane $y < 0$. The liquid flow is governed by the Laplace equation for the velocity potential $\varphi(x, y, t)$, and the plate deformation by the Euler beam equation for the deflection $w(x, t)$. The conditions on the liquid boundary are linearized and put on the line $y = 0$. The part of the boundary $x \in D(t)$, $y = 0$ corresponds to the contact region of the elastic beam with the liquid, and the part $x \notin D(t)$, $y = 0$ corresponds to the free surface where the pressure is zero at all times. The last statement follows from assumptions (5) and (10). Despite the fact that both the equations of motion and the boundary conditions are linearized, the problem remains nonlinear as the contact region $D(t)$ is

unknown in advance. The coupled problem has the form

$$\alpha \frac{\partial^2 w}{\partial t^2} + \beta \frac{\partial^4 w}{\partial x^4} = p(x, 0, t) \quad (0 < x < 2, t > 0), \quad (3)$$

$$w = w_{xx} = 0 \quad (x = 0, x = 2, t \geq 0), \quad (4)$$

$$w = w_t = 0 \quad (0 < x < 2, t = 0), \quad (5)$$

$$p = -\varphi_t \quad (y \leq 0), \quad (6)$$

$$\varphi_{xx} + \varphi_{yy} = 0 \quad (y < 0), \quad (7)$$

$$\varphi = 0 \quad (y = 0, x \notin D), \quad (8)$$

$$\varphi_y = -1 + w_t(x, t) \quad (y = 0, x \in D), \quad (9)$$

$$\varphi \rightarrow 0 \quad (x^2 + y^2 \rightarrow \infty). \quad (10)$$

Here $p(x, y, t)$ is the hydrodynamic pressure, $D \subset [0, 2]$, $\alpha = M_B/(\rho L)$, $\beta = EJ/(\rho L R^2 V^2)$, M_B is the beam mass per unit length. The bending stress distribution on the upper side of the beam $\sigma(x, t)$ is given in the dimensionless variables as $\sigma(x, t) = w_{xx}(x, t)/2$. In the non-dimensional variables the shape of the plate with respect to the initial position of the liquid free surface is described by the equation $y = (L/R)y_b(x, t)$,

$$y_b(x, t) = \frac{1 - \cos[\eta(x - x_1)]}{\eta^2} - t + w(x, t), \quad (11)$$

where $\eta = 2\pi(L/\lambda)$ and L/R is the parameter of linearization. In particular, for very long waves, $\eta \rightarrow 0$, and $|x - x_1| = O(1)$ equation (11) leads to the parabolic approximation of the wave profile

$$y_b(x, t) \approx \frac{1}{2}x^2 - t + w(x, t),$$

which was used by Korobkin [13] and Khabakhpasheva & Korobkin [16].

Initially ($t = 0$) the beam touches the liquid free surface at a single point x_1 , where $0 \leq x_1 \leq 1$ (Figure 2). Central impact corresponds to $x_1 = 1$, and edge impact to $x_1 = 0$. In general case ($0 < x_1 < 1$) the dimension of the contact region, which appears at the impact moment, is described by two functions $c_1(t)$ and $c_2(t)$, where $dc_1/dt < 0$ and $dc_2/dt > 0$ according to assumption (10) and $c_1(0) = c_2(0) = x_1$. At the first phase, $0 < t < t_1$, of the impact stage we obtain $D(t) = \{x \mid c_1(t) < x < c_2(t)\}$, where $c_1(t_1) = 0$. During the second phase, $t_1 < t < t_2$, the dimension of the contact region is described by the function $c_2(t)$ only, we have $D(t) = \{x \mid 0 < x < c_2(t)\}$. It should be noted that both deformations of the liquid free surface and the beam deflection are not shown in Figure 2 for simplicity. Wetted parts of the plate

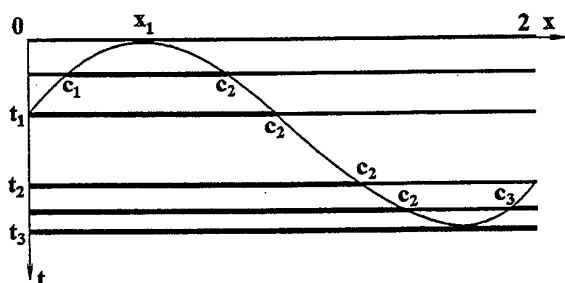


Figure 2: Three phases of the impact stage.

are shown with thick lines and the dry parts with thin lines.

It is possible that the right edge of the beam touches the disturbed liquid free surface well before the plate is totally wetted. If so, a cavity is formed close to this edge. The cavity collapses thereafter providing there is no air entrapped. Two reasons may be responsible for this scenario. They are: (1) special shape of the initial free surface (see Figure 8); (2) elastic deflection of the beam (blockage phenomenon). In any case, the second part of the contact region may appear, dimension of which is described by the function $c_3(t)$ (Figure 2). In this case $D(t) = \{x \mid 0 < x < c_2(t), c_3(t) < x < 2\}$. This phase of the impact stage, $t_2 < t < t_3$, is referred to as the third phase. This phase is over at the instant t_3 , when the cavity collapses, $c_2(t_3) = c_3(t_3)$.

The penetration stage starts at $t = t_3$. During this stage the problem is linear but coupled. It should be noted that for given impact conditions some phases may be absent. For example, in the central impact problem studied in Section 3 there is only the first phase with $c_1(t) = 2 - c_2(t)$.

The initial conditions for the first phase are given by (5) and for both the following phases and for the penetration stage it is required that the beam deflection $w(x, t)$ and its first derivative in time $w_t(x, t)$ change continuously at $t = t_j$, $j = 1, 2, 3$,

$$w(x, t_j + 0) = w(x, t_j - 0),$$

$$w_t(x, t_j + 0) = w_t(x, t_j - 0). \quad (12)$$

The formulation of the problem will be completed if the equations for the functions $c_1(t)$, $c_2(t)$ and $c_3(t)$ are obtained. Those equations follow from the condition that displacements of the liquid particles are finite at the contact point: $x = c_1(t)$ and $x = c_2(t)$ for $0 < t < t_1$, at $x = c_2(t)$ for $t_1 < t < t_2$, and at $x = c_2(t)$ and

$x = c_3(t)$ for $t_2 < t < t_3$. The equations are derived for each phase separately. They are equivalent to the well-known Wagner conditions [13]. Wagner conditions in their traditional forms lead to system of singular, non-linear integral equations [2], which are not easy to solve numerically even for undeformable bodies. This is why modified Wagner conditions are used here [13]. Modified Wagner conditions are transformed to non-linear ordinary differential equations, which are incorporated into the system for principal coordinates of the beam deflection.

3 Central impact

The problem, where initially the wave crest touches the plate centre, is the simplest one. In this case it is convenient to take the middle point of the plate as the origin of the Cartesian coordinate system xOy (in this section only). Initial shape of the free surface is symmetrical with respect to the Oy axis, which indicates that the flow is symmetrical with respect to the new coordinate system also (Figure 3). The central impact problem has the same features as the problem for the first phase of the impact stage but is more suitable to demonstrate main peculiarities of both the method of analysis and the numerical algorithm.

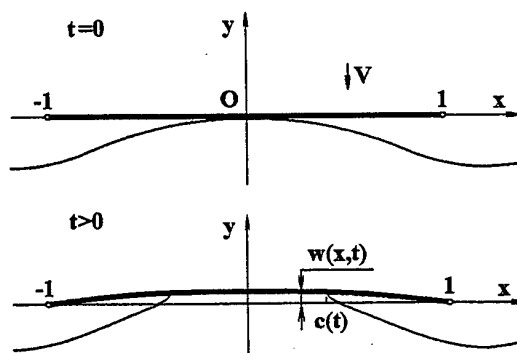


Figure 3: Central impact.

The contact region dimension is described by a function $c(t)$, where the interval $y = 0, -c(t) < x < c(t)$ corresponds to the wetted part of the plate. Equation (11) is replaced in the new coordinate system by

$$y_b(x, t) = \eta^{-2}(1 - \cos(\eta x)) - t + w(x, t), \quad (13)$$

where $w(-x, t) = w(x, t)$. In symmetrical case

the Wagner condition leads to the equation [13]

$$\int_0^{\pi/2} y_b[c(t) \sin \theta, t] d\theta = 0. \quad (14)$$

Substitution of (13) into (14) gives

$$t = \frac{1 - J_0(\eta c)}{\eta^2} + \frac{2}{\pi} \int_0^{\pi/2} w[c \sin \theta, t] d\theta. \quad (15)$$

It is convenient to introduce new unknown function $d(x, t) = \alpha w_t(x, t) + \varphi(x, 0, t)$, $-1 < x < 1$, which makes it possible to rewrite the beam equation (3) with account for (6) in the form

$$d_t + \beta w_{xxxx} = 0, \quad (16)$$

$$\alpha w_t + \varphi(x, 0, t) = d(x, t). \quad (17)$$

The boundary-value problem (16), (17), (4), (5), (7)-(10), (15) is solved with the help of normal mode method. This method leads to infinite system of ordinary differential equations with respect to principal coordinates of the beam deflection $w(x, t)$, $-1 < x < 1$. Within the framework of the normal mode method the beam deflection $w(x, t)$ and the function $d(x, t)$ are sought in the forms

$$w(x, t) = \sum_{n=1}^{\infty} a_n(t) \psi_n(x), \quad (18)$$

$$d(x, t) = \beta \sum_{n=1}^{\infty} \lambda_n^4 d_n(t) \psi_n(x). \quad (19)$$

Here $\psi_n(x)$ are the non-trivial solutions of the homogeneous boundary-value problem

$$\frac{d^4 \psi_n}{dx^4} = \lambda_n^4 \psi_n \quad (-1 < x < 1), \quad (20)$$

$$\psi_n = \frac{d^2 \psi_n}{dx^2} = 0 \quad (x = \pm 1),$$

and λ_n are the corresponding eigenvalues. Moreover, the eigenfunctions $\psi_n(x)$ satisfy the orthogonality condition

$$\int_{-1}^1 \psi_n(x) \psi_m(x) dx = \delta_{nm}, \quad (21)$$

where $\delta_{nm} = 0$ for $n \neq m$ and $\delta_{nn} = 1$. In the case of simply supported beam and central impact the eigenfunctions $\psi_n(x)$ are given as ($n \geq 1$)

$$\psi_n(x) = \cos(\lambda_n x), \quad \lambda_n = \pi(n - 1/2). \quad (22)$$

It is convenient to take the principal coordinates $a_n(t)$ of the beam deflection as the new unknown functions and to express the other quantities with their help.

On the interval of the liquid boundary, $y = 0$, $-1 < x < 1$, which contains the contact region, $-c(t) < x < c(t)$, $c(t) \leq 1$, the velocity potential can be presented as

$$\varphi(x, 0, t) = \sum_{n=1}^{\infty} b_n(t) \psi_n(x), \quad (23)$$

$$b_n(t) = \int_{-c(t)}^{c(t)} \varphi(x, 0, t) \psi_n(x) dx.$$

This follows from equations (17)-(19) and (8). In order to find the dependencies of the coefficients $b_m(t)$ on the principal coordinates $a_n(t)$, where $m, n \geq 1$, we must consider the hydrodynamic part (7)-(10) of the original problem. We introduce the harmonic in the lower half-plane functions $\varphi_n(x, y, c)$, which satisfy equations

$$\frac{\partial^2 \varphi_n}{\partial x^2} + \frac{\partial^2 \varphi_n}{\partial y^2} = 0 \quad (y < 0),$$

$$\varphi_n = 0 \quad (y = 0, |x| > c(t)),$$

$$\frac{\partial \varphi_n}{\partial y} = \psi_n(x) \quad (y = 0, |x| < c(t)),$$

$$\varphi_n \rightarrow 0 \quad (x^2 + y^2 \rightarrow \infty).$$

Here $n = 0, 1, 2, \dots$ and $\psi_0(x) \equiv 1$. We obtain

$$\varphi(x, 0, t) = -\sqrt{c^2 - x^2} + \sum_{n=1}^{\infty} \dot{a}_n(t) \varphi_n(x, 0, c),$$

$$b_m(t) = -f_m(c) + \sum_{n=1}^{\infty} \dot{a}_n(t) S_{nm}(c), \quad (24)$$

$$f_m(c) = \int_{-c}^c \sqrt{c^2 - x^2} \psi_m(x) dx,$$

$$S_{nm}(c) = \int_{-c}^c \varphi_n(x, 0, c) \psi_m(x) dx,$$

where dot stands for the derivatives in time. Green's second identity gives that the matrix S with the elements $S_{nm}(c)$, where $m, n = 1, 2, \dots$, is symmetrical. Taking (22) into account, we find

$$f_m(c) = \pi c^2 J_1(\lambda_m c) / (\lambda_m c),$$

$$S_{nm}(c) = \frac{\pi c}{\lambda_n^2 - \lambda_m^2} [\lambda_n J_0(\lambda_m c) J_1(\lambda_n c) - \lambda_m J_0(\lambda_n c) J_1(\lambda_m c)] \quad (n \neq m),$$

$$S_{nn}(c) = \frac{\pi}{2} c^2 [J_0^2(\lambda_n c) + J_1^2(\lambda_n c)],$$

where $J_0(z)$ and $J_1(z)$ are the zero- and first-order Bessel functions.

Substituting (18), (19), (23) and (24) into (16), (17) and taking into account the orthogonality condition (21), we arrive to the infinite system of ordinary differential equations with respect to the principal coordinates

$$\frac{d\vec{a}}{dt} = (\alpha I + S)^{-1}(\beta D\vec{d} + \vec{f}), \quad (25)$$

$$\frac{d\vec{d}}{dt} = -\vec{a}. \quad (26)$$

Here $\vec{a} = (a_1, a_2, a_3, \dots)^T$, $\vec{d} = (d_1, d_2, d_3, \dots)^T$, $\vec{f} = (f_1(c), f_2(c), f_3(c), \dots)^T$, I is the unit matrix and D is the diagonal matrix, $D = \text{diag}\{\lambda_1^4, \lambda_2^4, \lambda_3^4, \dots\}$. The right-hand side of system (25) and (26) depends on \vec{a} , \vec{d} and c but not on the time t , which is why it is convenient to take the quantity c as a new independent variable ($0 \leq c \leq 1$) instead of time t . Time t is the function of c now, $t = t(c)$. This substitution is justified under the condition $dc/dt > 0$, which follows from assumption (10). Differential equation for the unknown function $t(c)$ can be obtained from equation (15) after its differentiation with respect to c :

$$\frac{dt}{dc} = Q(c, \vec{a}, \vec{d}), \quad (27)$$

$$Q(c, \vec{a}, \vec{d}) = \frac{\eta^{-1} J_1(\eta c) + (2/\pi)(\vec{a}, \vec{\Gamma}_c(c))}{1 - (2/\pi)(\vec{a}, \vec{\Gamma}(c))},$$

$$\Gamma_n(c) = \int_0^{\pi/2} \psi_n(c \sin \theta) d\theta, \quad \vec{\Gamma}_c(c) = d\vec{\Gamma}/dc.$$

For simply-supported beam, we obtain $\Gamma_n(c) = (\pi/2)J_0(\lambda_n c)$ and $(\Gamma_c)_n = -(\pi\lambda_n/2)J_1(\lambda_n c)$.

Multiplying equations of system (25), (26) by dt/dc and taking (27) into account, we find

$$\frac{d\vec{a}}{dc} = \vec{F}(c, \vec{d}) Q(c, \vec{a}, \vec{F}(c, \vec{d})), \quad (28)$$

$$\frac{d\vec{d}}{dc} = -\vec{a} Q(c, \vec{a}, \vec{F}(c, \vec{d})),$$

where $\vec{F}(c, \vec{d}) = (\alpha I + S(c))^{-1}(\beta D\vec{d} + \vec{f}(c))$ and $\vec{a} = \vec{F}(c, \vec{d})$. The initial conditions for system (27), (28) are

$$\vec{a} = 0, \quad \vec{d} = 0, \quad t = 0 \quad (c = 0). \quad (29)$$

The system (27), (28) is suitable for numerical evaluation. Indeed, for small times we have $c(t) = O(t^{1/2})$, $w(x, t) = O(t^{3/2})$, $w_t = O(t^{1/2})$, $w_{tt} = O(t^{-1/2})$, and therefore, one cannot start numerical calculations for system (25), (26) with

homogeneous initial conditions. Kvålsvold & Faltinsen [3] described the difficulties with initial conditions for system of differential equations with respect to principal coordinates $a_n(t)$ and their derivatives $\dot{a}_n(t)$, where the time t is taken as the independent variable. On the other hand, $t = O(c^2)$, $w = O(c^3)$, $w_t = O(c)$, $w_{tt} = O(c^{-1})$ as $c \rightarrow 0$, and there are no problems with initial conditions for system (27)-(28).

Details of numerical analysis of the initial-value problem (27)-(29) are given by Korobkin [12]. Estimation of the optimal step Δc and its dependence on the number of modes taken into accounts are discussed.

In order to explain the present approach and outline its main features compared to standard approaches to numerical analysis of water impact, we consider a simple initial-value problem

$$v_{tt} + v = t^{-1/2} \quad (t > 0), \quad v(0) = v_t(0) = 0. \quad (30)$$

This equation is similar to the beam equation (3). It is worth noting that $p(0, 0, t) = O(t^{-1/2})$ as $t \rightarrow 0$ [17]. Standard approach is based on the decomposition of (30) as

$$v_t = u(t), \quad u_t = -v + t^{-1/2},$$

$$v(0) = 0, \quad u(0) = 0.$$

The right-hand side of the ordinary differential system is singular as $t \rightarrow 0$ (compare with system (25)). This is the main difficulty to start numerical procedure. There are three possible ways to overcome this difficulty: (1) to resolve the singularity of the forced term, $t^{-1/2}$, from physical point of view [6]; (2) to obtain asymptotics of the solution as $t \rightarrow 0$ and to start numerical simulation from that approximate solution at $t = t_\epsilon$, where $0 < t_\epsilon \ll 1$ [18]; (3) to use another decomposition (see below).

Equation (30) can be rewritten in the form

$$(v_t - 2t^{1/2})'_t + v = 0,$$

which leads to another way of the problem decomposition

$$v_t = a(t) + 2t^{1/2} \quad a_t = -v, \quad v(0) = a(0) = 0 \quad (31)$$

the present approach is based on (the function $a(t)$ is equivalent to the function $d(x, t)$ introduced in (16), (17)). The initial problem (31) is already suitable for numerical analysis. However, higher derivatives of the solution are singular at $t = 0$, which can lead to loss of accuracy for small t . This is a reason to introduce new independent

variable $\tau = t^{1/2}$, with the help of which problem (31) can be rewritten as

$$v_\tau = 2\tau a(t) + 4\tau^2, \quad a_\tau = -2\tau v(\tau), \quad (32)$$

$$v(0) = a(0) = 0.$$

This change of the independent variable is equivalent to the replacement of time t for c in system (28). The right-hand side of system (32) is analytic with respect to the independent variable τ and the unknown functions $v(\tau)$ and $a(\tau)$. This implies that the solution is the analytical function of τ also and it can be readily computed.

4 Edge impact

It was shown by Kvålsvold & Faltinsen [4] that wave impact on the bow part of the wetdeck of a catamaran is possible and that this phenomenon needs particular attention. In Section 2 it was also pointed out that the edge impact problem corresponds to the second phase of an elastic plate impact and its solution has to be incorporated into the computer code to treat the impact under arbitrary conditions. Theoretical analysis of the edge impact problem was given by Korobkin [19] within one-mode approximation and by Korobkin & Khabakhpasheva [20] using the normal mode method.

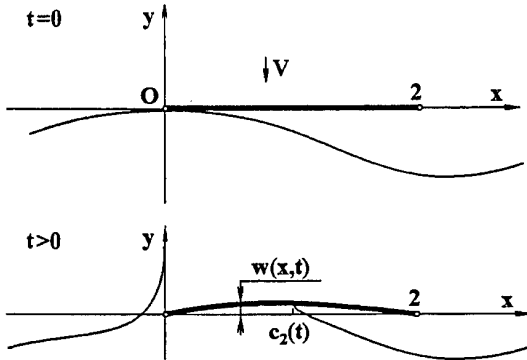


Figure 4: Edge impact.

In the case of edge impact (Figure 4) the liquid flow and the plate deflection are governed by the boundary-value problem (3)–(10), where $D = \{x \mid 0 < x < c_2(t)\}$ and $x_1 = 0$ in (11). The modified Wagner condition (14) has to be changed into (see [19])

$$\int_0^{\pi/2} \sin^2 \theta y_b[c_2(t) \sin^2 \theta, t] d\theta = 0, \quad (33)$$

which with account for (11) provides

$$t = \frac{1 - g(\eta c_2)}{\eta^2} + \frac{4}{\pi} \int_0^{\pi/2} \sin^2 \theta w[c_2 \sin^2 \theta, t] d\theta,$$

where

$$g(z) = \int_0^1 \frac{\sqrt{\sigma} \cos(z\sigma)}{\sqrt{1-\sigma}} d\sigma.$$

We use the same decomposition of the beam equation as in Section 3 and seek the plate deflection $w(x, t)$ and the function $d(x, t)$ in forms (18) and (19), where now $\psi_n(x) = \sin(\lambda_n x)$, $\lambda_n = \pi n/2$, $n = 1, 2, \dots$ and $0 < x < 2$. Representations of the velocity potential (23), (24) have to be replaced by (see [20])

$$\varphi(x, 0, t) = \sum_{n=1}^{\infty} b_n(t) \psi_n(x) \quad (0 < x < 2),$$

$$b_m(t) = -f_m(c_2) + \sum_{n=1}^{\infty} \dot{a}_n(t) S_{nm}(c_2),$$

$$f_m(c_2) = \frac{\pi c_2 \sin(\lambda_m c_2/2)}{2\lambda_m} v_m \quad (34)$$

$$S_{nm}(c_2) = \frac{c_2}{2\pi\lambda_m} \left[\cos \frac{\lambda_m c_2}{2} \cos \frac{\lambda_n c_2}{2} S_{nm}^{(1)}(c_2) - \sin \frac{\lambda_m c_2}{2} \sin \frac{\lambda_n c_2}{2} S_{nm}^{(2)}(c_2) \right],$$

$$S_{nm}^{(1)} = \frac{\pi^2 \lambda_m}{(\lambda_n^2 - \lambda_m^2)} [\lambda_m u_m v_n - \lambda_n u_n v_m],$$

$$S_{nm}^{(2)} = \frac{\pi^2 \lambda_m}{(\lambda_n^2 - \lambda_m^2)} [\lambda_m v_m u_n - \lambda_n v_n u_m],$$

$$S_{nn}^{(1)} = -\pi^2 u_n v_n - S_{nn}^{(2)},$$

$$S_{nn}^{(2)} = -\frac{\pi^2 \lambda_n c_2}{4} [u_n^2 + v_n^2],$$

$$u_m = J_0\left(\frac{\lambda_m c_2}{2}\right), v_m = J_1\left(\frac{\lambda_m c_2}{2}\right).$$

By taking (33) and (34) into account, we arrive to systems (25)–(26) and (27)–(28), where the function $Q(c_2, \vec{a}, \vec{a})$ is obtained by differentiation of (33) with respect to c_2 .

The initial-value problem (27)–(29) in the case of the edge impact, where the elements of the system are given by (34), is solved numerically by the Runge-Kutta method. The approach used is valid only in the case where the velocity of the contact region expansion dc_2/dt is positive and finite. If the velocity vanishes and becomes negative, the liquid particles from the contact region escape onto the liquid free surface, and a vortex layer,

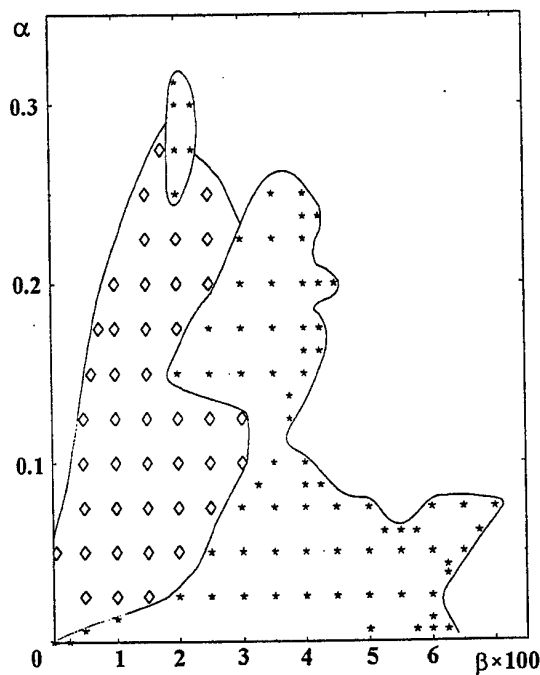


Figure 5: Plane of parameters α, β . The regions, where $dc_2/dt < 0$ (\diamond), and where dc_2/dt is unbounded (\star), are distinguished. The Wagner approach is valid outside these two regions only.

which is ignored in the present model, is formed. If the velocity grows and becomes comparable to the sound velocity in the liquid, acoustic effects must be taken into account. Therefore, in general, the plane of parameter (α, β) is divided into three parts (Figure 5): (1) dc_2/dt becomes negative with time; (2) dc_2/dt is unbounded; (3) dc_2/dt is positive and finite during the impact stage. It is seen that the Wagner approach is valid for beams of high rigidity. It is well-known that the total hydrodynamic force grows beyond all bounds as $dc_2/dt \rightarrow +\infty$. This phenomenon is referred to as blockage. In this case the rate of the added-mass increase is very high, which is due to the elastic deflection of the beam mainly. This result is of practical importance because it indicates that flexibility of impacting surfaces may lead to hydrodynamic loads, which are greater than those for equivalent rigid surfaces.

Analysis of the blockage phenomenon shows that the liquid flow may be more complicated than this is predicted by the Wagner theory. Namely, the right edge of the plate enters the liquid before the velocity of the contact point becomes very high (Figure 6). The distance between the right edge of the beam and the disturbed

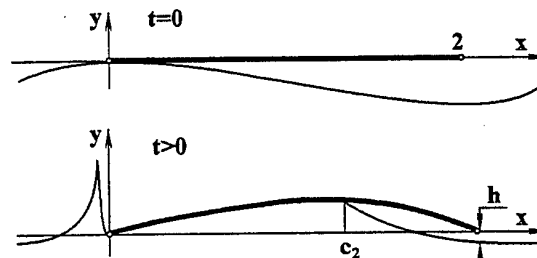


Figure 6: Blockage phenomenon.

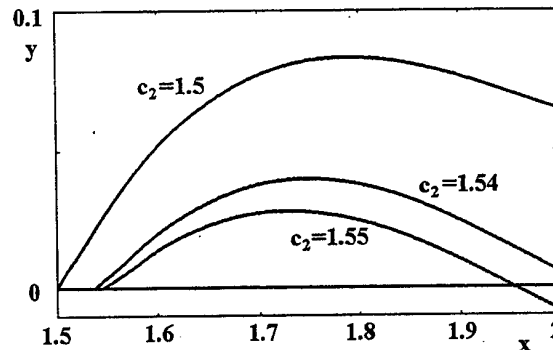


Figure 7: Distance between the elastic plate and the disturbed liquid free surface at different time instants ($c_2 < x < 2$).

free surface is shown in Figure 7 for $\alpha = 0.157$, $\beta = 0.0294$ as function of the contact region dimension c_2 . If the blockage phenomenon has been detected in numerical calculations, the cavity formation near the right edge of the beam is expected. The presence of the air in the cavity may essentially change the process of the plate-liquid interaction. This problem is not considered here. The blockage was not observed in central impact case, which means that the impact conditions are responsible for this phenomenon.

Comparison between edge impact (curves 2) and central impact (curves 1) is presented in Figure 8. Distributions of the beam deflection, velocity of the beam elements and the bending stresses along the beam are shown at the end of the impact stage. The impact conditions in both cases are identical, except the impact point. Curves 1 are symmetrical with respect to the beam centre, $x = 1$. Calculations were performed for $\alpha = 0.314$ and $\beta = 0.311$, which corresponds to the impact of elastic plate onto wave crest with the radius of curvature $R = 10$ m. The plate of length 1 m and thickness 2 cm is made of mild steel and hits the waves at velocity 3m/s. In dimensional variables, the duration of the impact stage

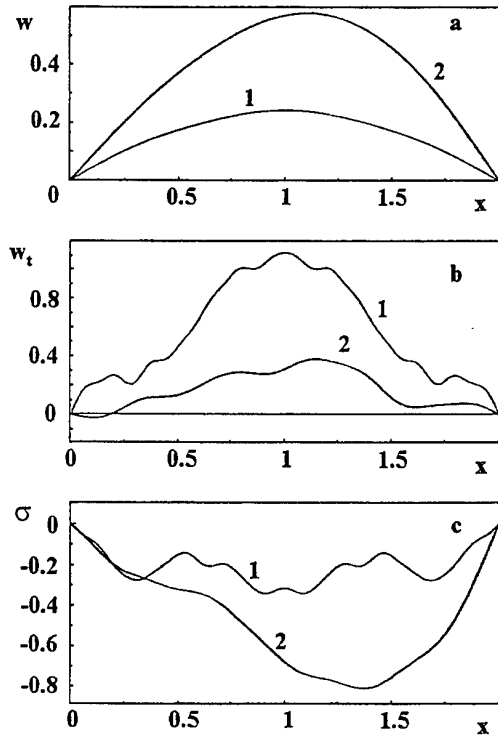


Figure 8: Distributions of the beam deflection (a), beam velocity (b), and the bending stresses (c) along the beam at the end of the impact stage for central impact (curves 1) and edge impact (curves 2).

is 0.36 for the central impact and 1.537 for the edge impact. It is seen that the increase of the impact stage duration leads to more than double increase of the deflection amplitude, significant decrease in the kinetic energy of the beam and increase in the potential energy of the deformed beam. Figure 8 demonstrates that the position of the impact point has a strong effect on the beam behaviour at the end of the impact stage, with other conditions being equal.

5 Impact with attached cavity

The interaction between an elastic plate and the liquid during the third phase of the impact stage, $t_2 < t < t_3$, is governed by the boundary-value problem (3)–(10), where $D = \{x \mid 0 < x < c_2(t), c_3(t) < x < 2\}$ (Figure 9). The initial conditions are given by (12) at $t = t_2$. The presence of air in the cavity, $y = 0$, $c_2(t) < x < c_3(t)$, is neglected. We consider only the case, where $dc_2/dt > 0$ and $dc_3/dt < 0$. Formulae (16)–(21)

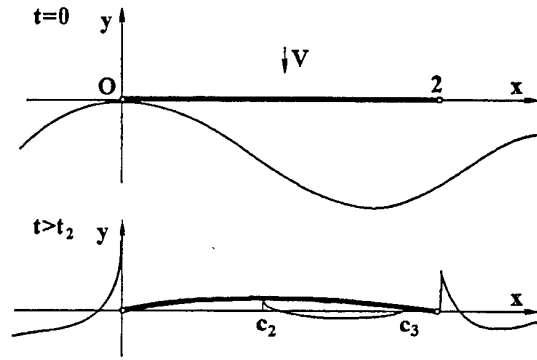


Figure 9: Impact with attached cavity.

are still valid and the eigenfunctions $\psi_n(x)$ are the same as in the edge impact problem (see Section 4).

In order to derive equations for functions $c_2(t)$, $c_3(t)$, we consider the vertical displacement of the liquid free surface [21]

$$Y(x, 0, t) = \frac{1}{\pi W(x)} \left(\int_0^{c_2} \frac{y_b(\tau, t) W(\tau)}{\tau - x} d\tau - \int_{c_3}^2 \frac{y_b(\tau, t) W(\tau)}{\tau - x} d\tau + F(t) \right), \quad (35)$$

where $x \notin D(t)$. The characteristic function $W(x)$ of the contact region is given as

$$W(x) = \sqrt{x(x - c_2)(c_3 - x)(2 - x)},$$

and $F(t)$ is an arbitrary function of time. The vertical displacement $Y(x, 0, t)$ is bounded at the contact points $x = c_2$ and $x = c_3$ if and only if

$$\begin{aligned} & \int_0^{c_2} y_b(\tau, t) \sqrt{\frac{\tau(2 - \tau)}{(c_2 - \tau)(c_3 - \tau)}} d\tau - \\ & - \int_{c_3}^2 y_b(\tau, t) \sqrt{\frac{\tau(2 - \tau)}{(\tau - c_2)(\tau - c_3)}} d\tau = 0, \\ & \int_0^{c_2} y_b(\tau, t) \sqrt{\frac{\tau(2 - \tau)(c_3 - \tau)}{c_2 - \tau}} d\tau + \\ & + \int_{c_3}^2 y_b(\tau, t) \sqrt{\frac{\tau(2 - \tau)(\tau - c_3)}{\tau - c_2}} d\tau = F(t). \end{aligned}$$

Differentiation of these equations with respect to time leads to the following system for the derivatives \dot{c}_2 and \dot{c}_3 (dot stands for the time derivative)

$$a_{11}\dot{c}_2 + a_{12}\dot{c}_3 = b_1, \quad (36)$$

$$a_{21}\dot{c}_2 + a_{22}\dot{c}_3 = b_2 + \dot{F}(t),$$

initial conditions for which are

$$c_2(t_2) = c_2(t_2 - 0), \quad c_3(t_2) = 2. \quad (37)$$

Here a_{11} , a_{12} , a_{21} , a_{22} , b_1 and b_2 are given functions of c_2 , c_3 and t . The vertical velocity of the liquid free surface is given by

$$\varphi_y(x, 0, t) = \frac{1}{\pi W(x)} \left(\int_0^{c_2} \frac{\varphi_y(\tau, t) W(\tau)}{\tau - x} d\tau - \int_{c_3}^2 \frac{\varphi_y(\tau, t) W(\tau)}{\tau - x} d\tau + C(t) \right), \quad (38)$$

where $x \notin D(t)$ and $\varphi_y(\tau, 0, t) = -1 + w_t(\tau, t)$. Far from the contact region, $x \rightarrow +\infty$, $y = 0$, equations (35) and (38) provide

$$Y(x, 0, t) \sim \frac{F(t)}{\pi x^4}, \quad \varphi_y(x, 0, t) \sim \frac{C(t)}{\pi x^4},$$

which with account for the equality $Y_t = \varphi_y$ yield the equation

$$\frac{dF}{dt} = C(t). \quad (39)$$

The function $C(t)$ is determined from the condition $\varphi(c_3, 0, t) = 0$, which is used in the following form

$$\int_{c_3}^2 \varphi_x(x, 0, t) dx = 0, \quad (40)$$

where

$$\frac{\partial \varphi}{\partial x}(x, 0, t) = -\frac{1}{\pi W(x)} \left(\int_0^{c_2} \frac{W(\tau) \varphi_y(\tau, 0, t)}{\tau - x} d\tau - V.p. \int_{c_3}^2 \frac{W(\tau) \varphi_y(\tau, 0, t)}{\tau - x} d\tau + C(t) \right) \quad (c_3 < x < 2).$$

Integrals in equations (36) and (40) are transformed into forms, which are suitable for their numerical evaluation by the Simpson rule.

Principal coordinates $a_n(t)$ are governed by the system of ordinary differential equations (25)-(26), (36) and (39), where now ($n \geq 1$)

$$f_m = S_{0m}(c_2, c_3), \quad \psi_0(x) = 1, \quad \psi_n(x) = \sin \lambda_n x,$$

$$S_{nm}(c_2, c_3) = \frac{1}{\lambda_m} \left(\int_0^{c_2} \cos(\lambda_m x) \frac{\partial \varphi_n}{\partial x} dx + \int_{c_3}^2 \cos(\lambda_m x) \frac{\partial \varphi_n}{\partial x} dx \right), \quad (41)$$

and

$$\frac{\partial \varphi_n}{\partial x} = \frac{1}{\pi W(x)} \left(V.p. \int_0^{c_2} \frac{W(\tau) \psi_n(\tau)}{\tau - x} d\tau - \int_{c_3}^2 \frac{W(\tau) \psi_n(\tau)}{\tau - x} d\tau + C_n \right) \quad (0 < x < c_2),$$

$$\frac{\partial \varphi_n}{\partial x}(x, 0, t) = -\frac{1}{\pi W(x)} \left(\int_0^{c_2} \frac{W(\tau) \psi_n(\tau)}{\tau - x} d\tau - V.p. \int_{c_3}^2 \frac{W(\tau) \psi_n(\tau)}{\tau - x} d\tau + C_n \right) \quad (c_3 < x < 2),$$

the constants C_n are determined by condition (40). Integrals in (41) are evaluated numerically by the Simpson rule.

Numerical calculations were performed with 5 and 10 elastic modes for two cases. In the first case the wave profile was approximated by parabolic contour ($\eta \rightarrow 0$), and in the second case - was given by equation (1). It was revealed that even in the first case the air can be trapped close to the right edge of the impacting plate ($\alpha = 0.157$ and $\beta = 0.03$). After the cavity has been formed, the contact points are accelerated. The cavity is very thin and exists for a short period only. The hydrodynamic pressures during the cavity collapse are very high but they are of short duration. In fact, second hydrodynamic impact onto the plate occurs with loads being much higher than at the beginning of the plate-liquid interaction. It should be noted that the deflections change just a little during the third phase and the main effect of the high pressures is on the bending stresses, which grow significantly.

It was obtained that the value t_2 , which has to be determined together with the liquid flow and the beam deflection, must be evaluated very precisely to make the numerical scheme stable. It was proved that system (36) provides $(dc_3/dt)(t_2) = 0$. This equality is used to start simulation of the interaction during the third phase.

In the second series of calculations the initial shape of the liquid free surface is given by (11) in non-dimensional variables with $\eta = 3\pi/4$, which implies that the wave length is $4/3$ of the total plate length, and $\alpha = 0.248$, $\beta = 0.0573$, which corresponds to the experiment conditions (see Faltinsen et al 1997). The experiment conditions are the steel plate of thickness 8mm and the length 0.5m falls down from the height 1m against regular waves with the radius of curvature at the wave crest equal to 10m. Cavity during the impact stage is formed due to geometry of the initial shape of the liquid surface. The cavity size and the duration of the third stage are much greater than in the first case. The trajectories of the contact points are shown in Figure 10. Bending stresses and deflections change during the third phase smoothly.

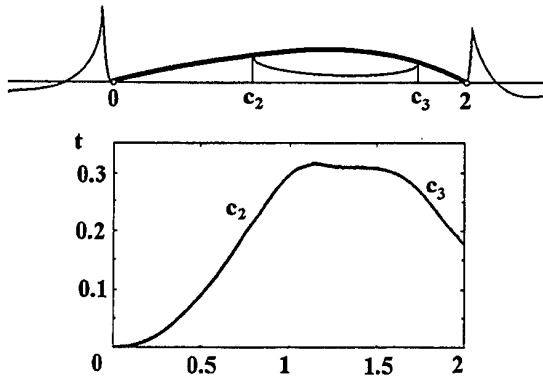


Figure 10: Trajectories of the contact points.

6 Penetration stage

During the penetration stage the beam is totally wetted but continues to interact with liquid. The process is described by the boundary value problem (3)–(10), where $D = (0, 2)$ and the initial conditions (5) have to be changed for

$$w(x, t_3) = w(x, t_3 - 0), \quad w_t(x, t_3) = w_t(x, t_3 - 0), \quad (42)$$

where $w(x, t_3 - 0)$ and $w_t(x, t_3 - 0)$ are the beam deflection and the beam velocity, respectively, at the end of the impact stage. This problem is equivalent to that of a floating elastic plate, which starts to enter the liquid at $t = t_3$ with a constant velocity and both the initial deflection of the plate and the initial velocity of its elements being prescribed. Theoretical analysis of this stage was given by Faltinsen [7], see also [14]. In the last paper the problem is formulated with respect to the hydrodynamic pressure $p(x, y, t)$ and the beam deflection $w(x, t)$. The scales of time and those of the unknown functions are chosen in accordance with recommendations by Faltinsen [7]. The beam deflection is sought with the help of eigenfunctions of spectral problem for a floating elastic plate. The orthogonality conditions (21) is not valid for this spectral problem. The eigenfunctions and the corresponding eigenvalues are dependent on the parameter α but not on β . Calculations were performed for $\alpha = 0.252$ and spring conditions at the beam edges [2]

$$\frac{\partial^2 w}{\partial x^2} \pm k \frac{\partial w}{\partial x} = 0, \quad (43)$$

where plus is for $x = 2$ and minus for $x = 0$, k is the nondimensional rigidity of the spring. It was taken $k = 2.85$ in calculations. Details of the

analysis of "wet" modes and formulae for the elements of the matrix of hydrodynamic coefficients S_{nm} (see (25)) can be found in [14]. It was obtained that the first "dry" and "wet" modes are practically identical, difference between the second modes is less than 8%, the third – 7% and that of the fourth modes – 6%. Therefore, it is reasonable to use "dry" modes, shapes of which are given analytically, to describe the beam deflection during the penetration stage.

It should be noted that numerical analysis of the plate-liquid interaction during the penetration stage does not require a special treatment of the original boundary-value problem and can be performed with the help of the numerical scheme described in Section 4 for the edge impact case. We need only to omit equation (33) because $c_2 \equiv 2$ during this stage and to replace c_2 in (34) by 2. Both the matrix S and the vector \vec{f} do not depend on time now and system (25), (26) can be readily integrated numerically. Within the experiment

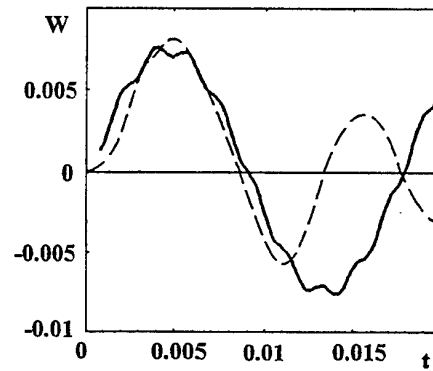


Figure 11: Deflection at the beam centre. *Solid line*, calculations; *broken line*, experiments.

conditions ($\alpha = 0.2512$, $\beta = 0.0551$, $k = 2.85$) the calculations were performed with 15 dry modes for problem (3), (6)–(10), (42) and (43) in the case of central impact. Comparison between experimental and numerical results are shown in Figure 11 for the plate deflection and in Figure 12 for the amplitude of bending stresses at the beam centre point, $x = 1$. Predicted deflection at the plate midpoint corresponds to the measured deflection at this point (see also the comparison in [2]). Predicted stresses clearly overestimate contributions of higher modes, which are depressed in experimental data. Similar overestimation can be found in theoretical results by Faltinsen et al [2], which were obtained for the same model we use in this paper but with simplified initial con-

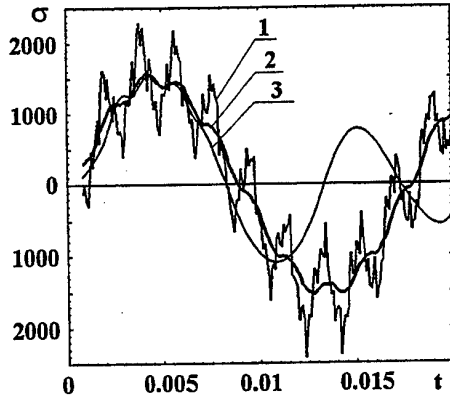


Figure 12: The strains (in μs) at the beam centre as a function of the time (in seconds) during the penetration stage. Direct computations (curve 1), average stresses (curve 2), experiments (curve 3).

ditions

$$w(x, t_3) = 0, \quad w_t(x, t_3) = 1.$$

Explanation of the higher mode generation is given in Section 7. However, there is a simple possible explanation based on parameters of the stress gauges used in experiments. Resonance frequency of the stress gauges is not reported in [2], that is why, to estimate this frequency, data reported in [22] were used. In this paper hydroelastic behaviour of circular elastic cylinder was studied with the help of the stress gauges, resonance frequency of which is 5kHz. If we assume the resonance frequency of stress gauges in the Norwegian experiments being 3kHz, we may average the numerical results over the time interval $2.25 \cdot 10^{-3}s$. Averaged numerical curve fits the experimental one fairly good (see Figure 12).

7 Generation of higher modes

There are several reasons for higher modes to be generated during the impact stage. Those are: (1) initially very high hydrodynamic pressures are localized close to the impact point; (2) pressure distribution along the wetted part of the plate is highly non-uniform and is unbounded at the moving contact points; (3) the area, along which the hydrodynamic loads act, grows with time. Calculations were performed to demonstrate that the third reason, which is the main feature of

the impact stage, is responsible for generation of higher modes.

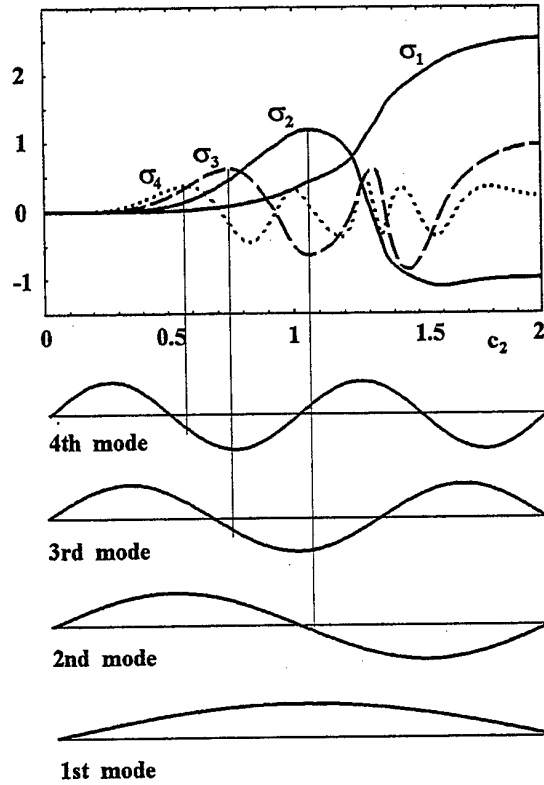


Figure 13: Contributions of normal modes to the bending stresses.

We consider the edge impact problem ($\alpha = 0.247$, $\beta = 0.05733$, $\eta = \pi/6$) for simply supported beam. The nondimensional stress amplitude is given by

$$\sigma(x, t) = \sum_{n=1}^{\infty} \sigma_n(t) \psi_n(x),$$

where $\psi_n(x) = \sin(\lambda_n x)$, $\lambda_n = \pi n/2$, $\sigma_n(t) = -a_n(t) \lambda_n^2/2$ and $a_n(t)$ are the principal coordinates of the beam deflection. Functions σ_n , $n = 1, 2, 3, 4$, as functions of the dimension of the contact region c_2 , $0 < c_2 < 2$, are shown in Figure 13 together with the shapes of corresponding modes. It is seen that $\sigma_1(c_2)$ is the monotonical function, and $\sigma_2(c_2)$ peaks at the instant, where the contact point passes the node of the second mode. Correspondingly, the amplitude of the third mode contribution to the bending stresses, $\sigma_3(c_2)$, peaks at the instant, when the contact point passes the first node of the third mode, and so on. After their first peaks the functions $\sigma_n(c_2)$ do not grow

essentially. The magnitudes of the peaks decrease monotonically as the number n increases. We may conclude that the highest modes are generated just after the impact instant and are influenced by fine details of the flow at the very beginning of the impact, but their amplitudes are rather small. The modes with moderate numbers are generated much later, and their amplitudes are influenced by the velocity of the contact region expansion. The first mode does not reach its maximum at the impact stage. This preliminary analysis makes it possible to think that correct description of high mode contributions to the bending stresses is connected neither with fine details of the very initial stage of the impact, when the speed of the contact point is very high and acoustic effects have to be taken into account, nor with fine details of the pressure distribution close to the contact points, where non-linear effects are of importance, but with the effect of moving load.

We may assume that the amplitudes of higher modes decay during the penetration stage due to the sound radiation. Indeed, the period of the second "dry" mode for the plate used in the experiments but simply supported, is 0.00125s, the scale of acoustic effects is of the order 0.0003s (the initial length of the beam, 0.5m, divided by the sound velocity, 1500m/s), and the bending stresses reach their maximum values at 0.005s approximately. Taking into account that the acoustic radiation of energy is more intensive for high frequencies than for lower ones, we may conclude that acoustic effects may be responsible for depressing the higher modes sufficiently before the stresses reach their maximum.

8 Global characteristics of the impact stage

Previous sections of this paper show that the interaction between an elastic plate and the liquid can be very complicated during the impact stage. On the other hand, in order to evaluate the maximum amplitude of the bending stresses in the plate within the Wagner's theory, we need to determine the plate deflection and its velocity at the end of the impact stage only. This means that we need to obtain the initial conditions to start numerical calculations for the penetration stage, during which the bending stresses approach their maximum values. According to the algorithm described in Section 3-5 several possibilities of the process development have to be considered, which

are essentially dependent on the initial shape of the liquid free surface. However, both the position of the free surface at the impact instant and this instant itself are not usually well defined in practice. This means that we may hope only to obtain estimations of the bending stress maximum, which is of the main practical interest, for a certain range of impact conditions but not the stress values. If so, we shall study quantities, which are weakly dependent on the impact conditions, and use them to estimate maximum bending stresses. Experimental analysis of the dependency of the maximum stresses on impact conditions (place of the impact, radius of the curvature at the wave crest) was given by Faltinsen et al [2]. But the maximum of bending stresses is a local characteristic, that is why in theory it is not easy to estimate this quantity directly. We use another approach based on estimations of global characteristics (kinetic energy of the liquid flow, kinetic energy of the beam deflection and potential energy of the deformed plate), which are much easier to obtain. It is shown in this section that the global characteristics are strongly depend on the impact conditions (it is clearly seen from Figure 8) but the total energy of the plate-liquid system is highly conservative and is mainly dependent on the impact velocity and the plate parameters. In order to determine the global characteristics under consideration, we use the energy conservation law for non-linear liquid flow and linear elasticity of the beam. This point is very important because the correct result can not be derived within the linear theory of liquid flow, which is used for numerical simulations of the impact. The reason is that the energy conservation law has to include the kinetic energy of spray jets, which is of the same order of magnitude as the kinetic energy of the main flow [23], but the spray jets are neglected within the Wagner approach used in this paper.

The kinetic energy of the non-linear liquid flow

$$T_L'(t') = \frac{1}{2}\rho \iint_{\Omega(t')} (\nabla' \varphi')^2 dx' dy', \quad (44)$$

where ρ is the liquid density, $\Omega(t')$ is the flow region and $\varphi'(x', y', t')$ is the velocity potential of the non-linear flow. $T_L'(t')$ is equal to the external work done to generate the flow

$$T_L'(t') = - \int_0^{t'} \left(\int_{D(\tau')} p' \frac{\partial \varphi'}{\partial y'} \right) d\tau', \quad (45)$$

which follows from the energy conservation law for the liquid motion. Here $D(\tau')$ is the contact region between the entering elastic plate and the liquid at the instant τ' (prime stands for dimensional variables). It should be noted that the change of the plate shape owing to its flexibility is not taken into account in equation (45). This approximation comes from the assumption that the amplitude of elastic plate deflections is small compared to both the plate length and the dimension of the contact region and gives negligibly small contribution to the liquid flow. The interaction between the liquid and the entering elastic plate is mainly due to decrease of the impact velocity

$$\frac{\partial \varphi'}{\partial y'} = -V + \frac{\partial w'}{\partial t'}(x', t') \quad (46)$$

but not due to variation of the plate shape.

Multiplying the beam equation (3) rewritten in dimensional variables by $\partial w'/\partial t'$ and integrating the result along the plate and in time with account for the edge conditions (4), we obtain

$$T'_B(t') + P'_B(t') = \int_0^{t'} \left(\int_{D(\tau')} p' \frac{\partial w'}{\partial t'} dx' \right) d\tau', \quad (47)$$

where $T'_B(t')$ is the beam kinetic energy,

$$T'_B(t') = \frac{1}{2} M_B \int_0^{2L} \left(\frac{\partial w'}{\partial t'} \right)^2 (x', t') dx', \quad (48)$$

and $P'_B(t')$ is the potential energy of the deformed plate,

$$P'_B(t') = \frac{1}{2} E J \int_0^{2L} \left(\frac{\partial^2 w'}{\partial x'^2} \right)^2 (x', t') dx'. \quad (49)$$

The left-hand side of the energy conservation law for the elastic plate (47) will be more complicated for beam equations different from the Euler one and other edge conditions.

Combining equations (45) and (47) and taking (46) into account, we find

$$T'_B(t') + P'_B(t') + T'_L(t') = V \int_0^{t'} F'(\tau') d\tau',$$

where $F'(t')$ is the total hydrodynamic force on the plate, and in the dimensionless variables

$$T_B(t) + P_B(t) + T_L(t) = 2 \int_0^t F(\tau) d\tau \quad (50)$$

with the quantities $\frac{1}{2}\rho V^2 L^2$ and $\rho V^2 R$ being the energy scale and the force scale, respectively.

The kinetic energy of the liquid flow can be approximately decomposed as $T_L = T_{LM} + T_{jet}$, where $T_{LM}(t)$ is the energy of the main flow and $T_{jet}(t)$ is the kinetic energy of the spray jets. The energy $T_{LM}(t)$ can be determined within the Wagner theory with $\Omega(t)$ being approximated by the lower half-plane $y \leq 0$. The velocity potential $\varphi(x, y, t)$ is decomposed as

$$\varphi(x, y, t) = \varphi_R(x, y, t) + \varphi_E(x, y, t),$$

where $\varphi_R(x, y, t)$ satisfies equations (7)–(10) with $w \equiv 0$ and $\varphi_E(x, y, t)$ satisfies the same equation with condition (9) being changed for $\partial \varphi_E / \partial y = w_t(x, t)$. The potential $\varphi_R(x, y, t)$ can be referred to as the velocity potential of the flow caused by rigid motion of the plate and $\varphi_E(x, y, t)$ as the velocity potential of the flow generated by the plate elastic deflection. It should be noted that both potentials depend on the geometry of real contact region $D(t)$. We find

$$T_{LM}(t) \approx \iint_{y < 0} (\nabla \varphi)^2 dx dy = \int_{D(t)} \varphi_R \frac{\partial \varphi_R}{\partial y} dx + 2 \int_{D(t)} \varphi_E \frac{\partial \varphi_R}{\partial y} dx + \int_{D(t)} \varphi_E \frac{\partial \varphi_E}{\partial y} dx. \quad (51)$$

On the other hand,

$$2 \int_0^t F(\tau) d\tau = 2 \int_0^t \int_0^2 (-\varphi_t(x, 0, \tau)) d\tau dx = -2 \int_0^2 \varphi_R(x, 0, t) dx - 2 \int_0^2 \varphi_E(x, 0, t) dx. \quad (52)$$

Substitution of (51) and (52) into (50) and account for the equalities $(\partial \varphi_R / \partial y)(x, 0, t) = -1$, where $x \in D(t)$, and $\varphi_R(x, 0, t) = \varphi_E(x, 0, t) = 0$, where $x \notin D(t)$, yield

$$T_B(t) + P_B(t) + T_{LE}(t) \approx T_{LR}(t) - T_{jet}(t). \quad (53)$$

Here

$$T_{LE}(t) = \int_{D(t)} \varphi_E \frac{\partial \varphi_E}{\partial y} dx, \\ T_{LR}(t) = \int_{D(t)} \varphi_R \frac{\partial \varphi_R}{\partial y} dx.$$

The kinetic energy of the spray jets $T_{jet}(t)$ grows with time during the impact stage and is constant at the penetration stage because the jets separate the main flow region at $t = t_3$ and are independently moving thereafter. The total energy of the jets at the penetration stage, $T_{jet}(t_3)$, is denoted

by T_{jet}^* . The kinetic energy $T_{LR}(t)$ grows during the impact stage also, is equal to $\pi/2$ at the end of the impact stage and keeps constant thereafter.

It is worth noting that for an equivalent rigid plate the left-hand side in (53) is zero and we obtain the well-known result $T_{LR}(t) \approx T_{jet}(t)$, which implies that the kinetic energy of spray jets is equal to the kinetic energy of the main flow at every instant of time [23].

The sum on the left-hand side of equation (53) is referred to as the total elastic energy of the plate-liquid system and is denoted by $U(t)$. It is clear that

$$U(t) \approx \frac{\pi}{2} - T_{jet}^*$$

during the penetration stage, $t > t_3$. We denote $U(t_3)$ by U_* , for which

$$U_* \leq \pi/2. \quad (54)$$

Dependency of U_* on impact conditions was studied numerically for $\eta = 3\pi/4$ and the steel plate used in the Norwegian experiments. It was revealed that U_* weakly depends on the impact location, $U_* \approx 1.27$ for $0 \leq x_1 \leq 1$, which is less than $\pi/2$, and on the initial geometry of the liquid free surface: $1.21 < U_* < 1.28$ for $7.5m < R < 75m$. This means that the total elastic energy U_* is dependent mainly on impact velocity and the plate flexibility and weakly on the initial shape of the liquid free surface. Inequality (54) can be improved with account for the energy of spray jets. This problem is not considered here.

9 Estimation of maximum bending stresses

In order to illustrate how to estimate the maximum amplitude of the bending stresses in the plate, the central impact case is considered. The corresponding analysis for the edge impact is described in [24].

The parts $T_B(t)$, $P_B(t)$ and $T_{LE}(t)$ of the total elastic energy U_* during the penetration stage are depicted in Figure 14 as functions of time t . It is seen that the main contribution to the total energy U_* at the beginning of the penetration stage comes from the kinetic energy of the liquid flow T_{LE} and there is a time instant t_m , when the total energy is concentrated in the potential energy of the deformed plate

$$P_B(t_m) \approx U_*. \quad (55)$$

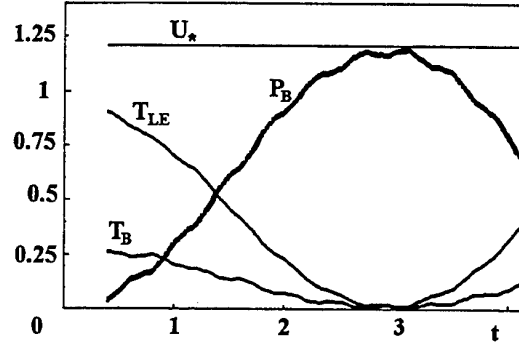


Figure 14: Components of the 'elastic' energy U_* as functions of time during the penetration stage.

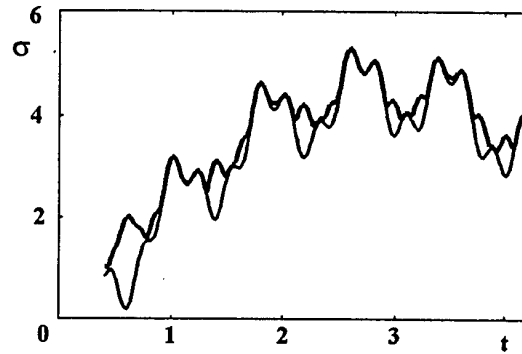


Figure 15: Non-dimensional stresses in the plate during the penetration stage: *thick line* is for maximum stresses, *thin line* is for the bending stress at the plate centre.

The maximum stress in the plate (thick line) and the stress at the plate midpoint (thin line) are shown in Figure 15. We may conclude that the stresses at the plate centre can be used to approximate the absolute maximum value of bending stresses. It is important to notice that the bending stresses approach their maximum value at $t \approx t_m$ approximately.

Within the normal mode approach the potential energy $P_B(t)$, $t > t_3$, is the sum of each mode contributions. Relative contributions of modal potential energies are depicted in Figure 16, where $P_1(t)$ is the potential energy of the first dry mode

$$P_1(t) = \beta \lambda_1^4 a_1^2(t) \quad (56)$$

and

$$\tilde{P}(t) = \beta \sum_{n=2}^{10} \lambda_n^4 a_n^2(t)$$

is the contribution to the total potential energy of the modes from second to tenth. It is seen that the first mode gives the main contribution to the

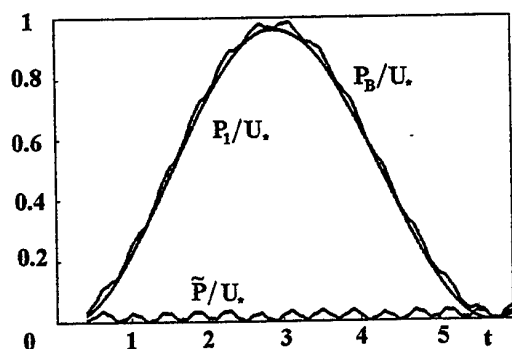


Figure 16: Relative contributions to the 'elastic' energy U_* of the total potential energy, P_B/U_* ; the potential energy due to the first mode, P_1/U_* ; the potential energy due to the modes from second to tenth, \tilde{P}/U_* .

potential energy of the deformed plate. Therefore, we obtain from (55) and (56) that

$$a_1^2(t_m) \approx \frac{U_*}{\beta \lambda_1^4}, \quad (57)$$

where $U_* < \pi/2$.

Within the one-mode approximation, which is used here to describe the hydroelastic behaviour of the plate during the penetration stage, system (25)–(26) gives

$$(\alpha + S_{11})\ddot{a}_1 + \beta \lambda_1^4 a_1 = 0 \quad (t > t_3), \quad (58)$$

where $\lambda_1 = \pi/2$, $S_{11} = (\pi/2)[J_0^2(\pi/2) + J_1^2(\pi/2)]$, and the term f_1 in (25) is zero after the plate is totally wetted. The general solution of equation (58) has the form

$$a_1(t) = C_1 \sin(\omega t + \delta), \quad (59)$$

where $\omega = \lambda_1^2 \sqrt{\beta/(\alpha + S_{11})}$, and C_1 and δ have to be determined from initial conditions. We suppose that the one-mode approximation correctly describes the evolution of the beam potential energy with time. Equations (57) and (58) yield

$$C_1 = \sqrt{U_*/\beta \lambda_1^2}, \quad t_m = (\pi/2 - \delta)/\omega. \quad (60)$$

The quantity δ can be found by matching either potential or kinetic energy at the beginning of the penetration stage. For example, if $P(t_3)$ is specified, we obtain the following equation

$$\beta \lambda_1^4 C_1^2 \sin^2 \delta = P(t_3). \quad (61)$$

Dimensional bending stresses are given as

$$\sigma'(x', t') = -(E z_a / R) w_{xx}(Lx, (L^2 / RV)t), \quad (62)$$

where z_a is the distance from the neutral axis in the beam cross-sectional area to the point where the stress is evaluated [2]. For a beam of constant thickness h , we have $z_a = h/2$. Within the one-mode approximation the absolute maximum of the bending stresses σ'_{max} and the time t'_m can be found using (60)–(62) as

$$\begin{aligned} \sigma'_{max} &\approx \sqrt{U_*} V z_a \sqrt{\frac{\rho L E}{J}}, \\ t'_m &\approx \frac{2L^2}{\pi} \left(1 - \frac{2\delta}{\pi}\right) \sqrt{\frac{M_B + S_{11} \rho L}{EJ}}, \\ \delta &= \arcsin \sqrt{P(t_3)/U_*}. \end{aligned} \quad (63)$$

In the experiment conditions for the steel plate, formulae (63) provide $\sigma'_{max} \approx 1867 \mu s$ and $t'_m \approx 0.0075 s$ with $\delta = 0$, which reasonably correspond to the measured values $\sigma'_{max} = 1600 \mu s$ and $t'_m = 0.005 s$. It should be noted that the connection between the elastic plate and the structure was more complicated in the experiment than in the simplified theoretical analysis here. By taking into account more realistic edge conditions, we may hope to reduce the differences between the estimated and the measured values.

The non-dimensional 'elastic' energy U_* in (63) has to be evaluated from the numerical solution of the original problem at the impact stage with all peculiarities of this stage taken into account. This fact reduces the practical importance of the approximate formula (63) for the value σ'_{max} . On the other hand, we can use inequality (54) to estimate the stresses. The corresponding bound is depicted in Figure 17 by the broken line.

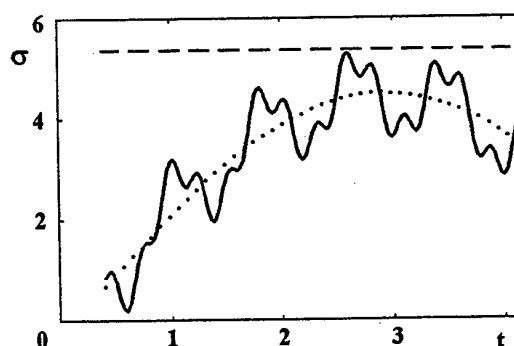


Figure 17: Non-dimensional stresses in the plate during the penetration stage: solid line is for bending stresses at the centre, broken line is the theoretical estimation of the bending stresses, dotted line is for bending stresses given by one-mode approximation.

Let us denote the total length of the beam by L_B , then (54) and (63) lead to

$$\frac{|\sigma_{max}|}{\left(\frac{z_a}{L_B}\right) V} \sqrt{\frac{J}{\rho E L_B^3}} \leq \sqrt{\frac{\pi}{4}},$$

where $\sqrt{\pi/4} \approx 0.88$. Experimental results for the same ratio and different impact velocities, plates and impact conditions [2] provide the corresponding upper bound as 0.7. The obtained theoretical estimation overpredicts the experimental estimation but is simple and can be recommended for structural analysis of plates subject to wave impact loads.

10 Conclusion

It is demonstrated in the present paper that the normal mode method is a powerful tool to treat the unsteady problem of elastic plate impact onto the liquid free surface, which is slightly curved. The method was modified to avoid calculations of hydrodynamic loads. The study is focused on deflections of the plate and distribution of bending stresses. The original problem is reduced to the system of ordinary differential equations for the principal coordinates of normal modes. Positions of the contact points are governed by nonlinear differential equations, which are incorporated into the system for the principal coordinates. It is important to notice that numerical solution can be started from the initial instant of time, when the dimension of the plate wetted area is zero. The numerical algorithm allows PC computations, is not time-consuming and makes it possible to investigate details of the plate-liquid interaction.

Impact stage, during which the plate is wetted only partially, is divided into three phases. Peculiarities of the interaction are investigated for each phase. Impact conditions, for which the Wagner's theory can be used, are distinguished. The phenomenon of the load increase due to plate flexibility was revealed (blockage phenomenon). It is shown that a cavity attached to the plate may be formed just before the hydrodynamic loads become unbounded. Impact of an elastic plate with attached cavity is analysed.

Maximum bending stresses are obtained numerically and compared with the measured data. Calculated stresses overestimate the contributions of higher modes. Explanations of the higher mode generation is given. Higher modes are generated during the impact stage and are due to the effect of wetted area expansion.

It is shown that the components of the energy of the plate-liquid system are strongly dependent on the impact conditions but the total energy not. The greater kinetic energy of the spray jets, the smaller potential energy of the deformed plate. The obtained estimate of the potential energy leads to the estimate of the absolute maximum of the bending stresses, which reasonably corresponds to the experimental results. The obtained theoretical estimation can be used in structural analysis of plates subject to wave impacts.

This work was supported by the Russian Foundation for Fundamental Research (projects N96-15-96882, N97-01-00897 and N96-01-01767).

References

1. Aarsnes, J. V., "An experimental investigation of the effect of structural elasticity on slamming loads and structural response," Technical Report, MARINTEK A/S, 1994.
2. Faltinsen, O.M., Kvålsvold, J. and Aarsnes, J. V., "Wave impact on a horizontal elastic plate," J. Marine Science and Technology, Vol.2, No.2, 1997, pp.87-100.
3. Kvålsvold, J. and Faltinsen, O., "Hydroelastic modelling of slamming against the wetdeck of a catamaran," Proc. Second Int. Conf. Fast Sea Transportation, FAST'93, Japan, 1993, pp.681-697.
4. Kvålsvold, J. and Faltinsen, O., "Slamming loads on wetdeck of multihull vessels," Proc. Int. Conf. Hydroelasticity in Marine Technology, Trondheim, Norway, 1994, pp.205-220.
5. Kvålsvold, J. and Faltinsen, O., "Hydroelastic modelling of wetdeck slamming on multihull vessels," J. Ship Res. Vol.39, 1995, pp.225-239.
6. Kvålsvold, J., "Hydroelastic modelling of wetdeck slamming on multihull vessels," Dr.Ing. Thesis, Department of Marine Hydrodynamics, Norwegian Institute of Technology, MTA-rapport 100, 1994.
7. Faltinsen, O.M., "The effect of hydroelasticity on ship slamming," Phil.Trans.R. Soc.Lond., Vol.A355, 1997, pp. 575-593.
8. Chuang, S.L., "Experimental Investigation of Dynamic Interaction Between Rectangular Elastic Plate and Fluid during Flat-Bottom Slamming," Report 2411, Naval Ship Research and Development Center, 1967.
9. Zhu, L. and Faulkner, D., "Slamming

Drop Tests for Small Scale SWATH Characteristic Model," NAOE-94-34, Department of NAOE, University of Glasgow, 1994, 63pp.

10. Korobkin, A.A., "Elastic Effects on Slamming," NAOE-96-39, Department of NAOE, University of Glasgow, 1996, 134pp.

11. Korobkin, A.A., "Acoustic approximation in the slamming problem," J.Fluid Mech., Vol.318, 1996, pp. 165-188.

12. Korobkin, A.A., "Wave impact on the center of an Euler beam," Zh.Prikl.Mekh.Tekh.Fiz., Vol.39, No.5, 1998, pp.134-147 (in Russian).

13. Korobkin, A.A., "Water impact problems in ship hydrodynamics," Advances in Marine Hydrodynamics, ed. M. Ohkusu, Southampton, Computational Mech. Publ., 1996, pp.323-371.

14. Korobkin, A.A. and Khabakhpasheva, T.I., "Plane linear problem on penetration of an elastic plate into ideal and incompressible liquid," Zh.Prikl.Mekh.Tekh.Fiz., 1999 (in press).

15. Wagner, H., "Über Stoss- und Gleitvorgänge an der Oberfläche von Flüssigkeiten," Z. Angew. Math. Mech., Vol.12, H.4, 1932, S.193-235.

16. Khabakhpasheva, T.I. and Korobkin, A.A., "Wave impact on elastic plates," Proc. 12th Intern. Workshop on Water Waves and Floating Bodies, Carry-le-Rouet, France, 1997, pp.135-138.

17. Korobkin, A.A. and Pukhnachov, V.V., "Initial stage of water impact," Ann. Rev. Fluid Mech., Vol.20, 1988, pp.159-185.

18. Korobkin, A.A., "Initial asymptotics in the problem of blunt body entrance into liquid," Ph.D.thesis, Lavrentyev Institute of Hydrodynamics, 1985.

19. Korobkin, A.A., "Wave Impact on the Bow End of a Catamaran Wet Deck," Journal of Ship Research, Vol.39, No.4, Dec. 1995, pp.321-327.

20. Korobkin, A.A. and Khabakhpasheva, T.I., "Plane problem on asymmetrical wave impact on an elastic plate," Zh.Prikl.Mekh.Tekh.Fiz., Vol.39, No.5, 1998, pp.148-158.

21. Khabakhpasheva, T.I. and Korobkin, A.A., "One-side inequalities in the problem of the wave impact," Proc. 13th Intern. Workshop on Water Waves and Floating Bodies, Alphen aan den Rijn, Netherlands, 1998, pp.67-70.

22. Shibue, I., Ito, A. and Nakayama, E., "Structural response analysis of cylinders under water impact," Hydroelasticity in Marine Technology, Rotterdam, Balkema, 1994, pp.221-228.

23. Korobkin, A.A., "Blunt-body penetration

into a slightly compressible liquid," 20th Symposium on Naval Hydrodynamics, University of California, Santa Barbara, California, 1994.

24. Khabakhpasheva, T.I. and Korobkin, A.A., "Energy conservation law in the problem of elastic plate impact onto liquid free surface," Proc. 14th Intern. Workshop on Water Waves and Floating Bodies, Michigan, 1999.